GEOTECHNICAL AND GEOPHYSICAL SITE CHARACTERISATION 5

ISC'5

Barry M. Lehane,
Hugo E. Acosta-Martínez &
Richard Kelly
Editors

VOLUME 2

Proceedings of the

5TH INTERNATIONAL CONFERENCE ON GEOTECHNICAL AND GEOPHYSICAL SITE CHARACTERISATION

IN PURSUIT OF BEST PRACTICE

ISC'5, Gold Coast, Queensland, Australia, September 5–9, 2016

SIMSG ISSMGE

AUSTRALIAN GEOMECHANICS SOCIETY

PROCEEDINGS OF THE FIFTH INTERNATIONAL CONFERENCE ON GEOTECHNICAL AND GEOPHYSICAL SITE CHARACTERISATION (ISSMGE TC-102 – ISC'5), GOLD COAST, QUEENSLAND, AUSTRALIA, 5-9 SEPTEMBER 2016

Geotechnical and Geophysical Site Characterisation 5

Editors
Barry M. Lehane
School of Civil, Environmental & Mining Engineering, The University of Western Australia, Australia

Hugo E. Acosta-Martínez
AECOM, Perth, Australia

Richard Kelly
SMEC and The University of Newcastle, New South Wales, Australia

VOLUME 2

AUSTRALIAN GEOMECHANICS SOCIETY

Published by: Australian Geomechanics Society
PO Box 955, St Ives, NSW 2075, Australia
e-mail: secretary@australiangeomechanics.org
www.australiangeomechanics.org

For Volume 1, ISBN 978-0-9946261-1-0
For Volume 2, ISBN 978-0-9946261-2-7

Geotechnical and Geophysical Site Characterisation 5 – Lehane, Acosta-Martínez & Kelly (Eds)
© 2016 Australian Geomechanics Society, Sydney, Australia, ISBN 978-0-9946261-2-7

Table of contents

Theme 1. Developments in Technology & Standards

Theme 2. Penetration Testing

Theme 3. Interpretation of In-Situ Testing

Theme 4. Laboratory Testing and Sampling

Theme 5. Liquefaction Assessments

Theme 6. Pavements and Fills

Theme 7. Pressuremeter and Dilatometer

VOLUME 2

Theme 8. Geophysics

Theme 9. General Site Characterisation

Theme 10. Characterisation in Rock and Residual Soil

Theme 11. Characterisation of Non-standard soils

Theme 12. Design Using In-situ tests

Theme 13. Case Histories

Theme 14. Application of Statistical Techniques

Theme 15. Environmental Testing

Theme 8. Geophysics

Geotechnical and Geophysical Site Characterisation 5 – Lehane, Acosta-Martínez & Kelly (Eds)

Multi-dimensional Electrical Resistivity Tomography (ERT) for the mapping of the zones with (or without) cavities in Hofuf KSA

S.N. Abduljauwad
Civil and Environmental Engineering Department, King Fahd University of Petroleum and Minerals (KFUPM) Dhahran, Saudi Arabia.

H.R. Ahmed, M.A. Shafiq & M. Abdul-Waheed
Department of Geophysical & Geotechnical, Riyadh Geotechnique & Foundations Co. Eastern Province, Al Khobar, Saudi Arabia.

ABSTRACT: The Hofuf area in Eastern Saudi Arabia is featured by subsurface sinkholes, solution cavities, voids, karst and caves. These features have resulted in hazards to the human safety and stability of the structures founded in them. The development of the area involved the construction of flyover bridges in Hofuf city. For these structures, several investigations were attempted including conventional geotechnical investigations using boreholes and cavity probing, however, these did not provide necessary information to visualize the subsurface zones with cavities. Finally, Electrical Resistivity Tomography (ERT) survey was selected to map the shallow subsurface strata at proposed construction sites with the aims to detect and map the subsurface cavities. ABEM Lund Imaging System consisting of Terrameter with Automatic Electrode Selector was used to acquire apparent resistivity data during the survey. Cables with 2m to 5m electrode spacing take-outs were used with a total of 84 to 400m surface spreads using Wenner-Schlumberger configuration. Windows based software; RES2DINV and RES3DINV developed by Geotomo Software were used for the inverse modeling of the acquired apparent resistivity data resulting in 2-D and 3-D absolute / true resistivity models of the subsurface conditions. The results revealed several anomalous locations which were subsequently verified by drilling boreholes. This study resulted in most feasible recommendations for the design and construction of safe and economical foundation systems for the proposed structures.

1 INTRODUCTION

Hofuf area of the Eastern Province of Saudi Arabia is part of the Shedgum Plateau positioned at the eastern edge of the greater As Summan Plateau (Hussain et. al., 2006). Hydrogeologic processes during the Miocene age of Hofuf formation and Quaternary period has resulted in the formation of large and continuous zones having cavities in the shallow subsurface strata of the Hofuf area. The Shedgum Plateau, including the Hofuf area, is marked with numerous karstic features including sinkholes, solution cavities and caves (Pint, 2000, 2003). Edgell (1990a, 1990b) reported over 58 caves in an area of 500 km^2 in the As Sulb area of the Summan Plateau. Vicinity map of Hofuf is shown in Figure 1 while typical surface karstic features of the area are highlighted in Figure 2.

The karstic zones in Al Hofuf area have always been a hazard to the stability of the structures founded in such type of strata. Recent development projects taken up by Al-Hassa Municipality include the construction of fly-over bridges at most of the heavily trafficked intersections in the Hofuf city. Several efforts including geotechnical investigations using boreholes have yielded imprecise information that could not be successively used for the safe design and construction of the structures in the area. This entails the requirement of a precise 2-D and 3-D mapping and delineation of the zones with cavities using geophysical technique(s). Several geophysical techniques including Electrical Resistivity Tomography (ERT), Seismic refraction / crosshole, Ground Penetrating Radar (GPR) and Gravity were considered to be used for the project. Owing to the limited applicability of the other techniques to the specific site and subsurface conditions, ERT was selected as most feasible among its counterparts. This paper explains the details of geophysical exploration of two proposed flyover sites using Electrical Resistivity Tomography (ERT). Based on the results of the exploration, most feasible and safe foundation

system(s) have also been suggested for the proposed structures.

Figure 1. Vicinity Map of Hofuf City

Figure 2. Typical Karstic Features of the Area

2 STUDY AREA

The study area is situated in Hofuf City, Al Hassa District Eastern Province Saudi Arabia. Two proposed fly-over locations at Mobarraz interchange and Al-Hassa three level interchange were selected for the cavities exploration.

The project site is covered with sand and underlain by flat lying sedimentary rocks of continental origin, known collectively as the Hofuf formation. The Hofuf formation in general, consists of red to reddish brown, gray to rarely off-white conglomerate, sandstone, sandy limestone, sandy marl, and sandy shale.

The surface rock of the area is highly weathered, at places, transformed to the residual soil. Underlying the weathered rock surface, fresh-water hard sandy LIMESTONE / LIMESTONE layers exist. Typical of Hofuf formation, a calcareous duricrust caps the surface rock of the rest of the area and provides resistance to weathering of the underlying rock. The depressions in the area are filled with eolian dune sand and fine gravel-sized weathered rock particles.

Another notable feature of the area, in general, is the innumerable dry valleys or wadis that traverse the rocky strata. The steep slopes of wadis are covered with dune sand. The wadis were cut by ancient streams flowing during the humid climates.

3 RESEARCH METHODOLOGY

3.1 Electrical Resistivity Tomography

Electrical Resistivity Tomography (ERT) was proposed to be carried out along the proposed pile foundation grid at the abutment and pier foundation locations. This paper presents details of ERT investigations and provides the assessment and 2D-3D mapping of the subsurface cavities at all the proposed structure locations.

The measurement protocol used for the data acquisition was a combination of Wenner-Schlumberger configuration ensuring both vertical and horizontal precision. Using the designed electrode spacing of 2.0 to 5.0m and a spread of 160 to 400m, maximum depth of investigations achieved was about 12 to 70m below the ground surface. Based on the designed configuration, a total of 68 and 80 tests were conducted at Mobarraz and Al-Hassa three level interchange locations respectively.

3.1.1 Investigation design & data acquisition

ABEM Lund Imaging System consisting of Terrameter SAS 4000 and Automatic Electrode Selector ES10-64C was utilized for the acquisition of apparent resistivity data during the survey. Cables with 2.0 to 5.0m electrode take-outs spacing was used with a total of 160 to 400m spread layout in both the directions.

Data acquisition process initiates with the plugging of a total of 81 electrodes into the ground at the selected spacing and connected to the multi-core cables using the jumper cables. The multi-core cables were in turn connected to the auto electrode selector which is directly operated by the Terrameter SAS4000. Terrameter generates current and records the corresponding voltage across any set of electrodes selected automatically via the electrode selector. The data acquisition process was completely controlled by the software that verifies the connectivity and grounding of all the 81 electrodes before actual acquisition of the data was started. As surface strata of the terrain exhibited extremely dry conditions, proper grounding of the electrodes was ensured using the saline water at the contact points where needed. During the execution of the designed protocol, data was being automatically stored in the Terrameter.

3.1.2 Data Processing and Analysis

RES2DINV and RES3DINV software developed by GEOTOMO were used for the processing and inverse modelling of the acquired apparent resistivity data. True resistivity models were interpreted by using 2.5D smoothness constrained inversion, employing a quasi-Newton technique with precision of the models was established through a maximum RMS error of 5%. A typical processed 2-D resistivity cross-section is shown in Figure-3.

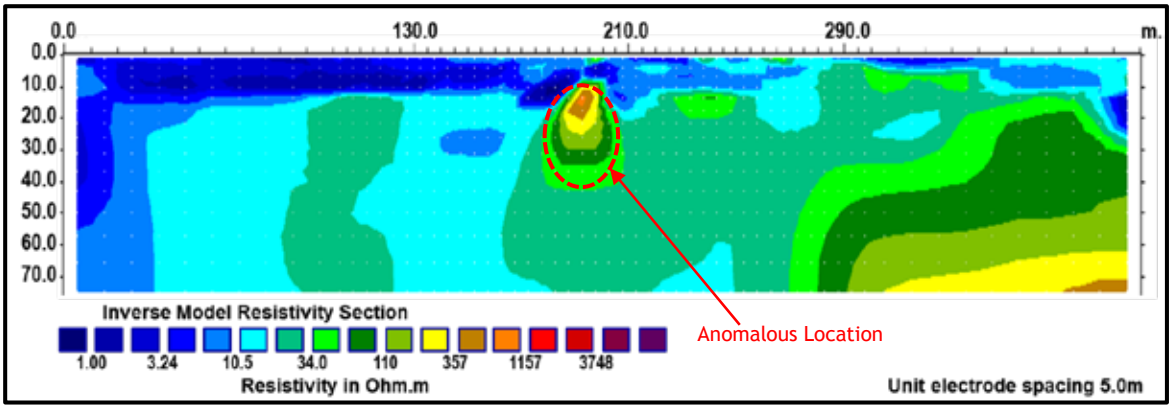

Figure-3. A typical 2-D Processed ERT Data

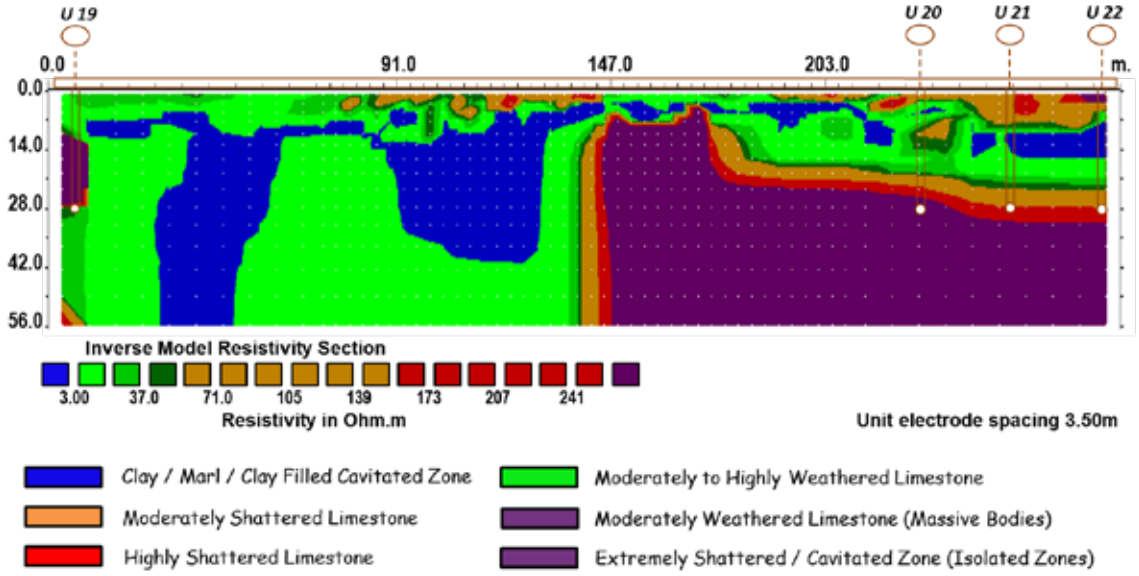

Figure 4. A typical 2-D sampling

The processed ERT sections were then analysed for the identification of various subsurface features and anomalies. Background resistivity of the subsurface strata encountered at site was assessed and used to demarcate the anomalies at various horizons. An anomaly in ERT testing campaign was assessed by several indicators. These indicators were determined for each specific site using the geologic knowledge and subsurface strata information acquired through the borehole drilling. Upon identification of such anomalies, physical confirmation of these locations was carried out as a next phase of the exploration process. Processed and analysed 2-D ERT cross-sections were drawn in the RES2DINV editor.

3.2 Data verification & calibration

Calibration of ERT data for these sites have been carried out using the subsurface strata information acquired generally through the geologic knowledge / setting of the area and specifically through the borehole drilling and sampling at the known anomalous locations. This is accomplished through the performance of probe / boreholes and the strata at the identified locations.

By associating the entire spectrum of the resistivity from the ERT sections and the physical data acquired from the boreholes and the knowledge of the geology, electrical resistivity cross-sections were transformed into interpreted subsurface strata cross-sections. After assigning the specific resistivity ranges, the interpreted sections consisted of the details of the depth, lateral extent and nature of each type of stratum and the associated engineering characteristics. A typical interpreted ERT cross-section is shown in Figure 4.

For the creation of 3-D modelling from this ERT data, an algorithm was used to perform a unified processing of the parallel 2-D lines data at a particular location. 3-D sections were digitized in RockWorks software by RockWare. The 3-D ERT model is presented in Figure-5.

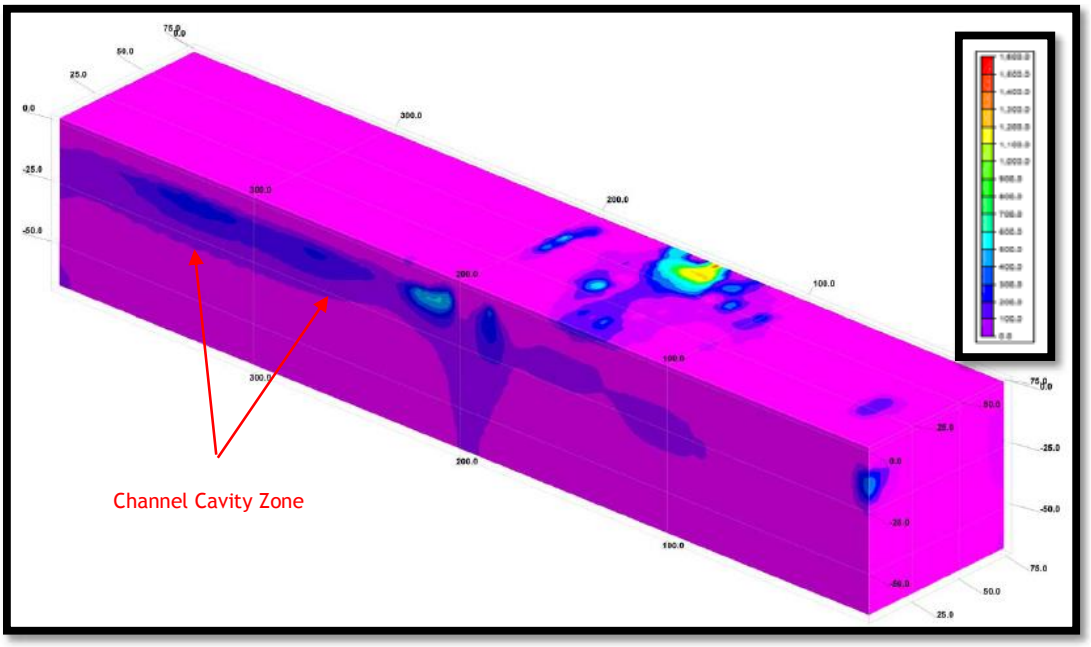

Interpreted ERT Cross-section
Figure 5. 3D ERT Model

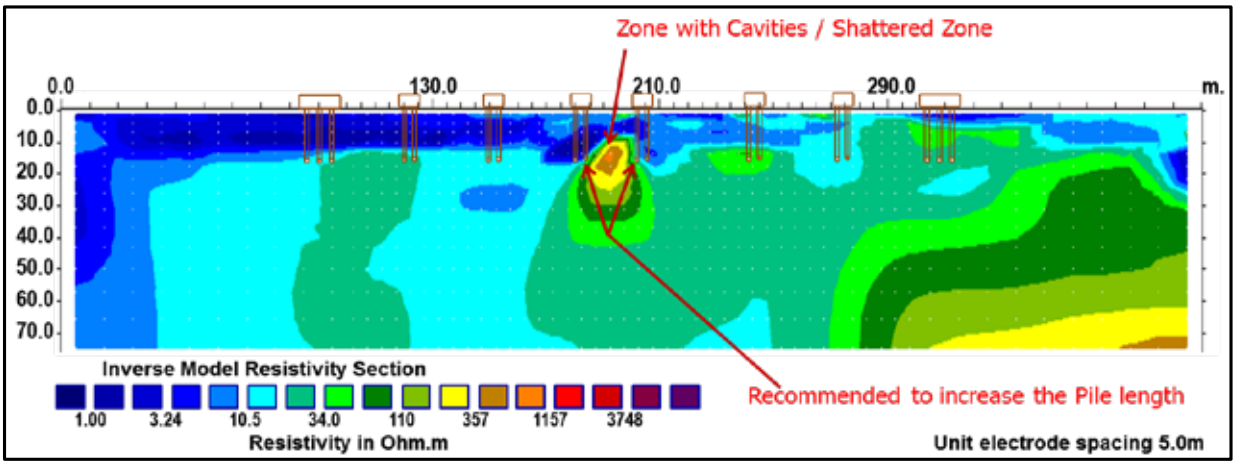

Figure 6. Design of pile foundations

4 CONCLUSIONS

Electrical Resistivity Tomography and borehole drilling revealed that two distinct types of strata exist in the subsurface i.e. Sandy / Silty / Clayey Soil deposits overlying rocky strata as MARL / Marly LIMESTONE / LIMESTONE with varying degree of weathering. Generally, the site could be divided into two different zones, namely "Zones with cavities" and "Zones without cavities".

These zones with (or without) cavities could be further divided into different sub-zones, as described below:

- Clay / Marl
- Clay Filled Zones with Cavities (Isolated Zones)
- Moderately to Highly Weathered Limestone
- Moderately to Highly Shattered Limestone
- Extremely Shattered Limestone (Isolated Zones)

The subsurface strata contain seams of clay material, intercalated / filled in the cracks present in Limestone rock. Based on the final conclusive results, loose filled cavities / extremely shattered zones have been encountered in a depth range of 18 to 25m, therefore it was suggested to design the pile lengths to ensure proper pile tip socketing in the strong bearing stratum to a minimum of 28m depth as shown in Figure 6.

5 ACKNOWLEDGEMENTS

The authors highly acknowledge patronage and support of King Fahd University of Petroleum & Minerals (KFUPM) and the Mayor of Al Hassa Municipality, Adil Al-Mulhim in the execution of the projects.

6 REFERENCES

Edgell, H. S. 1990a. Geological Framework of Saudi Arabian Groundwater Resources, *Journal of King Abdulaziz University, Jeddah, Earth Sciences*, 3 (special issue): 267–286.

Edgell, H.S. 1990b. Karst in northeastern Saudi Arabia, *Journal of King Abdulaziz University, Jeddah, Earth Sciences*, 3 (special issue): 1st Saudi Symp. on Earth Sci., Jeddah, 1989, 81–94.

GEOTOMO Software

Hussain, M., Al-Khalifah, F. and Khandaker, N. 2006. The Jabal Al Qarah Caves of the Hofuf Area, Northeastern Saudi Arabia: A geological investigation, *Journal of Cave and Karst Studies*, 68(1): 12–21.

Pint, J. 2003. The Desert Caves of Saudi Arabia: Stacey International, London, 120.

Pint, J. 2000. The Desert Cave Journal 1998–2000: *NSS News* 58 (10): 276–281.

Geotechnical and Geophysical Site Characterisation 5 – Lehane, Acosta-Martínez & Kelly (Eds)

Preliminary results of P-wave and S-wave measurements by seismic dilatometer test (SPDMT) in Mirandola (Italy)

S. Amoroso
Istituto Nazionale di Geofisica e Vulcanologia, L'Aquila, Italy

C. Comina
University of Turin, Department of Earth Sciences, Torino, Italy

S. Foti
Politecnico di Torino, Department of Structural, Geotechnical and Building Engineering, Torino, Italy

D. Marchetti
Studio Prof. Marchetti Srl, Rome, Italy

ABSTRACT: A trial seismic dilatometer-V_P (SPDMT) has been recently developed to measure the compressional wave velocity V_P, in addition to the shear wave velocity V_S and to the DMT geotechnical parameters. The new SPDMT is the combination of the traditional mechanical flat dilatometer (DMT) with an appropriate seismic module placed above the DMT blade. The SPDMT module consist in a probe outfitted with two receivers for measuring the P-wave velocity, along with two receivers for measuring the S-wave velocity. The paper describes the SPDMT equipment, the test procedure and the interpretation of V_P and V_S measurements, together with some considerations on the potential geotechnical applications which can benefit from the contemporary measurement of the two propagation velocities. Finally, the paper illustrates preliminary results of P-wave and S-wave measurements by SPDMT compared to several cross-hole, down-hole and suspension logging data at the Mirandola test site (Italy), a soft alluvial site which was investigated within the InterPACIFIC (Intercomparison of methods for site parameter and velocity profile characterization) project.

1 INTRODUCTION

During the last decades, there has been a considerable shift from laboratory testing to in situ testing at a point that, today, in situ testing often represents the major part of a geotechnical investigation. Therefore the incoming need of acquiring multiple parameters of the soil stratigraphy with the use of the same investigation tool. In this respect the addition of one or more seismic receivers (geophones or accelerometers) to traditional CPT cone or DMT blade has become a standard practice. These new testing procedures are addressed as the seismic cone penetrometer test (SCPT - Robertson et al. 1986) or the seismic dilatometer test (SDMT - Marchetti et al. 2008), respectively. These tests provide the measurement of the shear wave velocity V_S, in addition to the usual CPT or DMT parameters, extending the scope of site characterization. Recommendations given in recent State-of-the-Art papers (e.g. Mayne et al. 2009) indicate that direct-push in situ tests, such as SCPT and SDMT, are, at intermediate investigation depths, fast and very convenient tests for routine site investigations if compared to other invasive seismic tests.

This paper introduces a trial seismic dilatometer-V_P (SPDMT), recently developed to measure also the compressional wave velocity V_P, together with the common DMT geotechnical parameters and shear wave velocity V_S. The new equipment is the combination of the traditional mechanical flat dilatometer (DMT) with a seismic module placed above the DMT blade. Accurate in situ P-wave and S-wave velocity profiles can give a significant support to the geotechnical characterization in both static and dynamic analyses where the small strain elastic parameters are input variables into the models (Finn 1984). Moreover, porosity evaluation and liquefaction assessment can be performed based on these data.

The InterPACIFIC (Intercomparison of methods for site parameter and velocity profile characterization) project provided a valuable case study to compare SPDMT results to independent cross-hole (CH), down-hole (DH) and suspension logging data at the Mirandola test site (Italy) and to verify the reliability of the new tool particularly concerning the P-wave velocity measurement.

2 THE SEISMIC DILATOMETER WITH COMPRESSION WAVE MEASUREMENTS (SPDMT)

The trial seismic dilatometer-V_P (SPDMT) is the combination of the traditional mechanical flat dilatometer (DMT) with a SPDMT seismic module placed above the DMT blade (Figures 1a, 1b). The new system has been recently developed in Italy and it is an upgrade of the seismic dilatometer (SDMT) introduced by Marchetti et al. (2008). The SPDMT module is a probe outfitted with two uniaxial (vertical) geophones, spaced 0.604 m, for measuring the P-wave velocity V_P, along with two uniaxial (horizontal) geophones, spaced 0.500 m, for measuring the S-wave velocity V_S. Geophones have appropriate frequency and sensitivity characteristics to determine the seismic wave train arrival according to ASTM D7400-14 (2014). Two different seismic sources are adopted: an impulsive source, such as a 8 kg-hammer, hits vertically a steel squared base to produce identifiable compressional waves; a pendulum hammer (≈ 10 kg) hits horizontally a steel rectangular base pressed vertically against the soil (by the weight of the truck) and oriented with its long axis parallel to the axis of the receivers, in order to offer the highest sensitivity to the generated shear wave.

The P-wave and the S-wave seismic sources are connected to two different external triggers to record respectively the response of the P-wave geophones and of the S-wave geophones. The signal is amplified and digitized at depth. The recording system consists of different channels, one for each geophone, having identical phase characteristics and adjustable gain control.

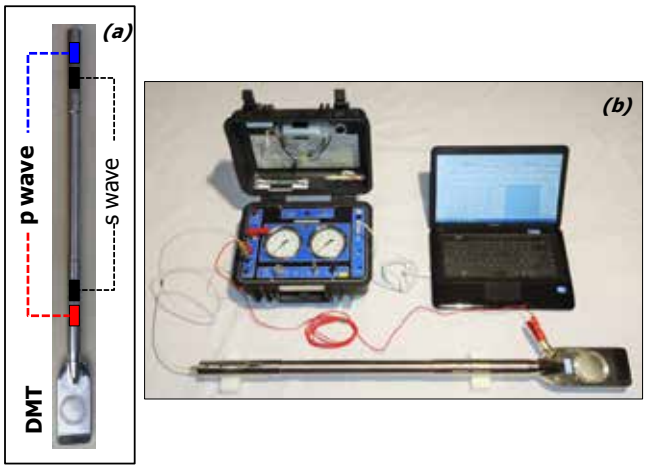

Figure 1. Trial seismic dilatometer-VP (SPDMT): (a) DMT blade and SPDMT module; (b) SPDMT equipment.

The interpretation of the seismic waves arrival times can rely both on the *direct method*, considering the whole set of travel-times at different depths or on the *true-interval* considering for each realization of the test the time delay between two receivers. In the first case the arrival time at each receiver position during penetration is determined by first break picking (Tp). Then all the arrival times are corrected to account for the ray-path inclination:

$$Tc = \left(\frac{SD}{d}\right) \cdot Tp \qquad (1)$$

where SD is the source distance and d is the depth for each receiver position. All the corrected arrival times Tc are then plotted as a function of depth and homogeneous velocity intervals are searched with interpolation of linear branches of the travel time curve. This first interpretation approach is commonly used in the analysis of down-hole data (Auld 1977). This method is convenient when subsoil layering has to be determined. The interpretation reduces inaccuracy in the travel time determinations by mediating among several arrival times over homogeneous velocity layers. In the second case, seismic velocity is obtained as the ratio between the difference in distance between the source and the two receivers (SD_2-SD_1) and the delay of the arrival of the impulse from the first to the second receiver (Δt). The *true-interval* test configuration with two receivers avoids possible inaccuracy in the determination of the "zero time" at the hammer impact, sometimes observed in the *direct method* one-receiver configuration. Moreover, the couple of seismograms recorded by the two receivers at a given test depth corresponds to the same hammer blow and not to different blows in sequence, which are not necessarily identical. Hence the repeatability of velocity measurements is considerably improved. The determination of the delay in the seismograms can be based both on the direct picking of the first arrival times in the recorded traces or on the cross-correlation algorithm. This second approach is generally better conditioned being based on a wide portion of the two seismograms – in particular the initial waves – rather than on the first break or specific marker points in the seismogram.

2.1 *Potential geotechnical applications*

The use of the SPDMT dilatometer allows the measurement of the compressional wave velocity V_P, in addition to the shear wave velocity V_S and to the DMT geotechnical parameters obtained using current DMT correlations (Marchetti 1980, Marchetti et al. 2001), by means of the material index I_D (soil type), the constrained modulus M, the undrained shear strength c_u

and the horizontal stress index K_D (related to the over-consolidation ratio). Beyond the usual geotechnical applications provided by the seismic dilatometer (SDMT), the seismic dilatometer-V_P (SPDMT) can the potentially support site scale porosity evaluation and the liquefaction assessment using V_P and V_S measurements, commonly obtained from in situ geophysical surveys, such as cross hole (CH) and down-hole (DH) tests.

According to Foti et al. (2002) and Foti & Lancellotta (2004) the theory of linear poroelasto-dynamics in the low-frequency limit, developed by Biot (1956a, 1956b), can profitably be used for determining the porosity n in fluid-saturated porous media from measured P-wave and S-wave velocities. The determination of the porosity from CH, DH or SPDMT tests has particular relevance in coarse materials, which are difficult to sample. However this procedure gives a simple but effective way to estimate the porosity in situ in fine and coarse soils.

Moreover in situ P-wave and S-wave velocities have the potential to identify the degree of saturation of soils, in terms of saturation ratio S_r and pore pressure coefficient B, and hence the liquefaction resistance of a partially saturated sand. According to Tsukamoto et al. (2002) V_P tends to increase from about 500 m/s to about 1800 m/s when the B-value increases from 0.00 to 0.95 corresponding, respectively, to the saturation ratio S_r of about 90 % and 100 %. Results of cyclic loading tests on partially saturated sands indicated the cyclic resistance ratio CRR tends to increase significantly with a decrease in V_P, particularly when P-wave velocity become less than 500 m/s and where the B-value drops to less than 0.1 with a saturation ratio S_r of 90 %. Alternatively CRR begins to increase sharply when the ratio V_P/V_S drops to a value of about 3. Conventional liquefiability assessment, carried out according to the "simplified procedure" by Seed & Idriss (1971), is modified introducing a partial saturation factor PSF inferred from compression wave velocity V_P or the ratio V_P/V_S, to correct the cyclic resistance ratio CRR derived from SPDMT or other in situ geotechnical or geophysical investigations. Examples can be found in EQC (2013) and Amoroso et al. (2015).

3 MIRANDOLA TEST SITE (ITALY)

3.1 Interpacific project

The InterPACIFIC project (Garofalo et al. 2016) was aimed at assessing the reliability, resolution, and variability of geophysical methods (invasive borehole methods and non-invasive surface wave methods) in estimating the shear wave velocity profile for seismic ground response analyses. A series of blind tests has been organized in which several participants performed both invasive and non-invasive techniques at each site without any *a priori* information about the site. Three different subsoil conditions were selected as test sites. The present study is focused on invasive tests performed at the Mirandola test site by means of DH, CH and suspension logging methods and is aimed at comparing the results of SPDMT data within the comparable depths.

Mirandola is located in the Po river plain. The Secchia river, a stream of the Po river, flows north-south on the west side of the test site. The area was affected by a couple of strong earthquakes in May 2012 (Anzidei et al. 2012). The station of the Italian Accelerometric Network placed in Mirandola provided strong-motion records in the vicinity of the epicenter for both shocks. For this reason, Emilia Romagna Region planned a specific site investigation. In particular two boreholes placed at 6.8 m from each other were drilled to a depth of 125 m to reach the geological and seismic bedrock, and DH and CH tests were performed by different teams. A SPDMT sounding was also carried out up to roughly 20 m depth in the nearby area. The site is characterized mainly by alluvial deposits with an alternating sequence of silty-clayey layers of alluvial plain and sandy horizons. V_S and V_P estimations are generally in good agreement over the entire investigation depth. The geological substratum consists of marine and transitional deposits of lower-middle Pleistocene age. It was found at a depth of 118 m in the borehole and it was consistently identified by seismic borehole methods. The boreholes detected the water table at a depth of approximately 4 m below the ground surface as suggested also by P-wave velocity values.

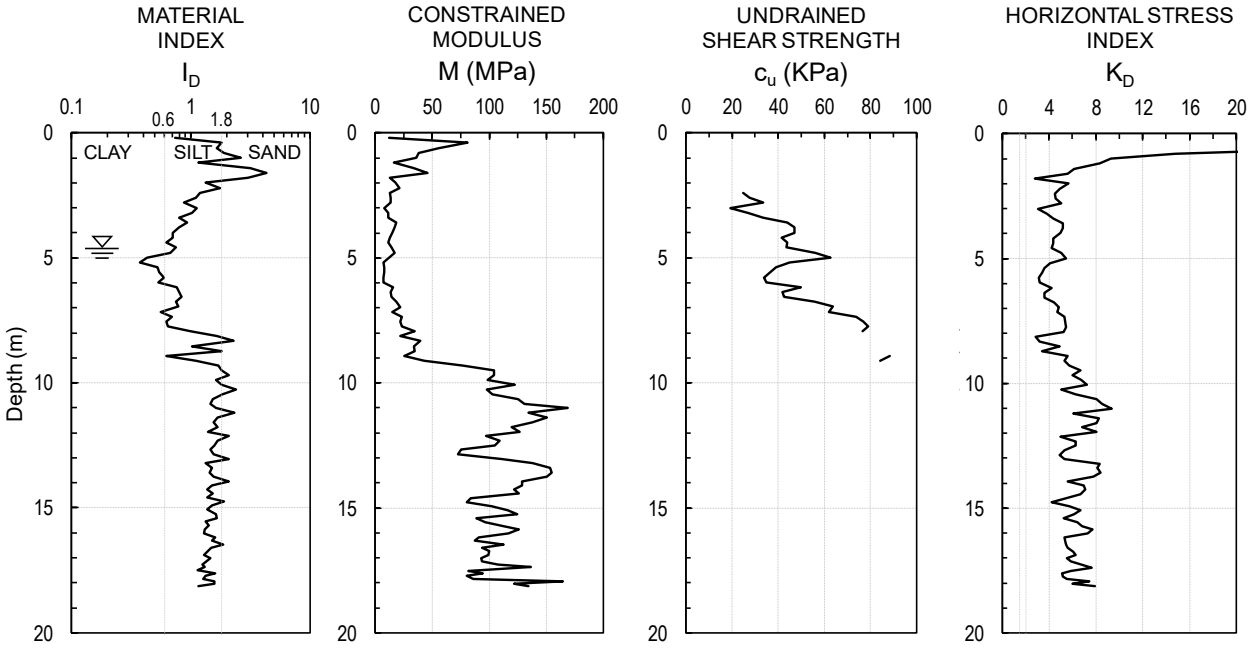

Figure 2. Geotechnical parameters from SPDMT profiles at Mirandola test site.

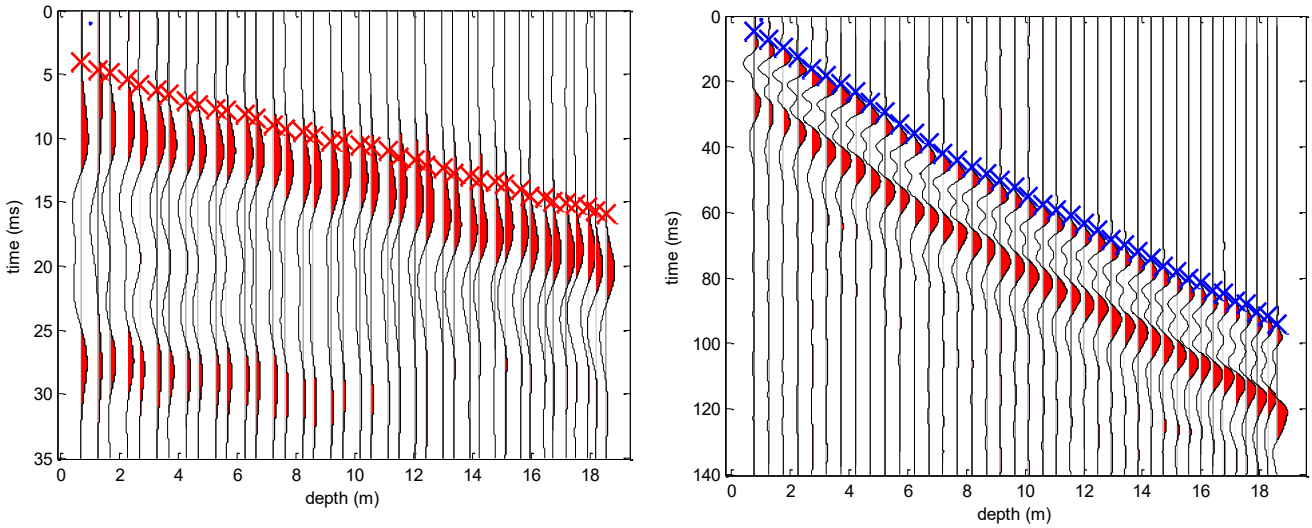

Figure 3. SPDMT recorded seismic traces at Mirandola test site for P-waves (left) and S-waves (rigth).

3.2 SPDMT survey

The profiles with depth of the DMT parameters at Mirandola test site are reported in Figure 2, in terms of material index I_D (indicating soil type), constrained modulus M, undrained shear strength c_u, and horizontal stress index K_D (related to stress history/OCR), obtained using common DMT interpretation formulae (Marchetti 1980, Marchetti et al. 2001). The ground water level was detected at 4.6 m depth by means of the C-readings (see Marchetti et al. 2001). According to the lithological classification based on I_D, the Mirandola test site is characterized by silty sand and sandy silt (i.e. $I_D > 1.2$) in the upper 3.6 m depth, and then a silty clayey and clayey silty layer with low stiffness and strength parameters is encountered up to 7.7 m depth. A lens of silt and sandy silt is found between 7.7 m and 9.1 m depth before entering in a succession of silty sand and sandy silt characterized by high geotechnical properties. These lithologies partially correspond to the geological borehole log, considering that I_D is not a grain size distribution index but it infers the mechanical soil behaviour.

For seismic wave velocity determination the S-wave pendulum hammer was 0.8 m far from the rods,

while the P-wave impulsive source was located at 1.5 m from SDMT axis. The data recording equipment was able to record 700 samples at a sampling time of 50 μs and 200 μs respectively for P-wave and S-wave, using two different external triggers. Recorded seismic traces for all the sensors and for both methods are reported in Figure 3 together with the first break picking used in the determination of velocities. For both seismic waves, a high quality of the traces has been obtained after appropriate filtering of the raw data. Nevertheless travel time determination for P-waves resulted difficult due to the time resolution required for a correct determination and due to the oscillating nature of the arrival times in some portion of the stratigraphy (particularly for the first 5 m from the ground surface).

3.1 Comparisons of the results

At Mirandola test site V_S and V_P values from SPDMT are compared to the DH, CH and suspension logging profiles provided by the InterPACIFIC teams as shown in Figure 4. Shear wave velocity data estimated from the trial SPDMT are in very good agreement with the other invasive results with all the interpretation methods considered. The *true-interval* velocity analysis by means of the cross-correlation of seismic traces provided more stable results with respect to the first break picking. Instead, compression wave values from SPDMT are only in broad accordance with the InterPACIFIC interpretations. An higher variability in the *true-interval* velocity can be observed in the data reflecting the lower resolution in time delay determination due to the higher velocity of P-waves. Particularly in the first 5 m investigation depth cross-correlation of seismic traces provided very coarse result not reported in the figure. Conversely the *direct method* interpretation, mediating the inaccuracies over wide intervals is able to provide a reference profile which is more in agreement with other available data. Results can be therefore considered acceptable considering also the seasonal fluctuations of the ground water table that can create some variability in the partial/full saturation of the upper portion of the soil deposit (5.0-7.5m).

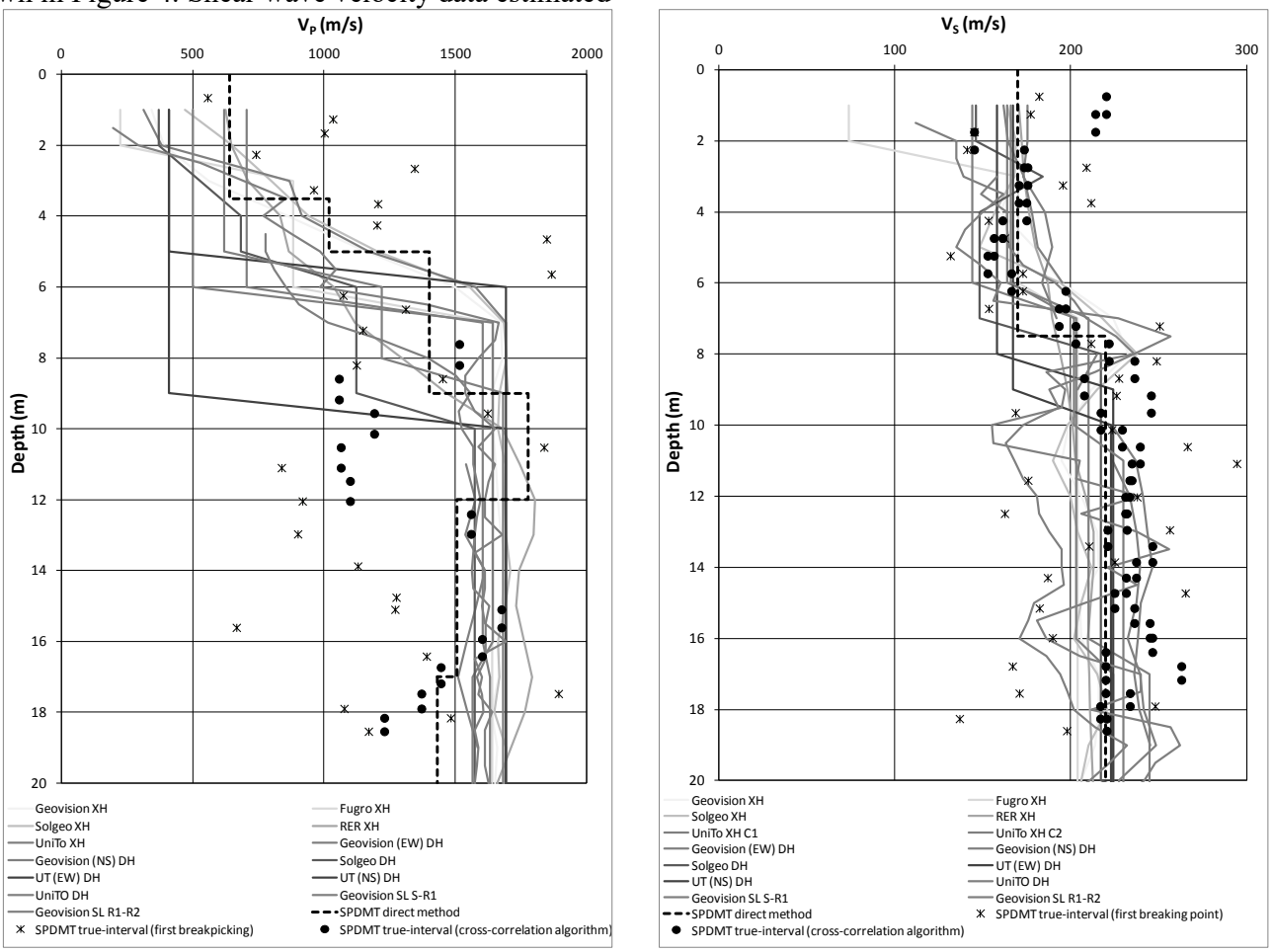

Figure 4. Comparisons between CH, DH suspension logging results of the InterPACIFIC project (grey lines, Garofalo et al. 2016) and SPDMT results (black line and symbols) in terms of V_S and V_P values at Mirandola test site.

4 CONCLUSIONS

This article reports on the first application a trial seismic dilatometer-V_P (SPDMT) recently developed to measure the compressional wave velocity V_P, in addition to the shear wave velocity V_S and to the DMT geotechnical parameters. Results have confirmed the high reliability of V_S determination from the SDMT test and an acceptable agreement in terms of V_P.

Further tests are required to improve the quality of acquired P-wave traces by improving the sensors response in order to increase reliability also of true interval determinations. Trials are ongoing to reduce eventual presence of tube waves by mechanically disconnecting the SPDMT seismic module from the rods.

5 ACKNOWLEDGEMENTS

The InterPACIFIC data were collected for a research project financed by the Research & Development Program SIGMA funded by EdF, Areva, CEA and ENEL and by CASHIMA project, funded by CEA, ILL and ITER. Regione Emilia Romagna made available borehole data and additional geophysical surveys at Mirandola test site. SPDMT test was funded by FIRB-Abruzzo project (http://progettoabruzzo.rm.ingv.it/it) and Studio Prof. Marchetti (Italy).

6 REFERENCES

Amoroso, S., Monaco, P., Rollins, K.M., Holtrigter & M., Thorp A. 2015. Liquefaction assessment by seismic dilatometer test (SDMT) after 2010-2011 Canterbury earthquakes (New Zealand).*6th International Conference on Earthquake Geotechnical Engineering - 6ICEGE, 1-4 November 2015, Christchurch, New Zealand*.

Anzidei, M., Maramai, A. & Montone, P. 2012. The Emilia (northern Italy) seismic sequence of May-June, 2012: preliminary data and results. *Annals of Geophysics, special issue*, 55 (4).

Auld, B. 1977.Cross-Hole and Down-Hole VS by Mechanical Impulse.*J. Geotech. Engrg. Div., ASCE*, 103(GT12), 1381-1398.

ASTM D7400-14 2014.Standard Test Methods for Downhole Seismic Testing.*ASTM International*.

Biot, M. A. 1956a.Theory of propagation of elastic waves in a fluid-saturated porous solid.I Lower frequency range.*J. Acoust. Soc. Am.*, 28, 168-178.

Biot, M. A. 1956b.Theory of propagation of elastic waves in a fluid-saturated porous solid. II Higher frequency range. *J. Acoust. Soc. Am.*, 28, 179-191.

EQC 2013. Ground Improvement Trials Project.*Draft Project Resources 2013* (under preparation).

Finn, W.D.L. 1984. Dynamic response analysis of soils in engineering practice.In *Mechanics of engineering materials. John Wiley & Sons Ltd*., New York. Chapter 13.

Foti S. & Lancellotta R. 2004. Soil porosity from measured seismic velocities.*Géotecnique, Tech. Note*, 54, 8, 551-554.

Foti S., Lai C.G. & Lancellotta R. 2002. Porosity of fluid-saturated porous media from measured seismic wave velocities., *Géotecnique*, 5, 359-373.

Garofalo, F., Foti, S., Hollender, F., Bard, P.Y., Cornou, C., Cox, B.R., Dechamp, A., Ohrnberger, M., Perron, V., Sicilia, D., Teague, D. & Vergniault, C. 2016.InterPACIFIC project: comparison of invasive and non-invasive methods for seismic site characterization. Part II: Intra-comparison of surface wave methods. *Soil Dynamics and Earthquake Engineering,* 82, 241-254.

Marchetti, S. 1980. In Situ Tests by Flat Dilatometer. J. *Geotech. Engrg. Div., ASCE*, 106(GT3), 299-321.

Marchetti, S., Monaco, P., Totani, G. & Marchetti, D. 2008. In situ tests by seismic dilatometer (SDMT). *Proc. From Research to Practice in Geotechnical Engineering*, ASCE Geotech. Spec. Publ. No. 180 (honoring J.H. Schmertmann): 292-311.

Marchetti, S., Monaco, P., Totani, G., & Calabrese, M. 2001. The flat dilatometer test (DMT) in soil investigations—A report by the ISSMGE Committee TC16. *Proc., 2nd Int. Conf. on the Flat Dilatometer, R. A. Failmezger and J. B. Anderson, eds., In-Situ Soil Testing, Lancaster, VA*, 7–48.

Mayne, P.W., Coop, M.R., Springmanm, S.M., Huang, A. & Zornberg, J.G. 2009. Geomaterial behavior and testing, *Proc. 17th ICSMGE Alexandria, Egypt*, Eds Hamza et al., 4, 2777-2872.

Robertson, P.K., Campanella, R.G., Gillespie, D. & Rice, A. 1986. Seismic CPT to measure in-situ shear wave velocity.*ASCE, Journal of Geotechnical Engineering*, Vol. 112, No. 8, August 1986, 791-804.

Seed, H.B. &Idriss, I.M. 1971. Simplified procedure for evaluating soil liquefaction potential. J. *Geotech. Engrg. Div., ASCE*, 97(9), 1249–1273.

Tsukamoto, Y., Ishihara, K., Nakazawa, H., Kamada, K. & Huang, Y. 2002. Resistance of partly saturated sand to liquefaction with reference to longitudinal and shear wave velocities. *Soils and foundations*, 6(2), 93-104.

Geotechnical and Geophysical Site Characterisation 5 – Lehane, Acosta-Martínez & Kelly (Eds)

Geophysical characterisation of marine and quick clay sites: field and laboratory tests

S. Bazin, H. Anschütz, G. Sauvin
Norwegian Geotechnical Institute, Oslo, Norway

T. E. Helle
NTNU, Trondheim, Norway

S. Gribben, S. Donohue
Queen's University, Belfast, UK

M. Long
University College Dublin, Ireland

ABSTRACT: Quick clay is a highly sensitive, post-glacial marine clay characterized by a remolded shear strength of less than 0.5 kPa. Such deposits pose a serious geohazard in Scandinavia and North America and need to be delineated in detail. Therefore, there has recently been a considerable amount of work published on the use of geophysical methods for their mapping. Two of them, especially electrical resistivity but also seismic measurements are tested for their consistency. In situ and laboratory measurements of resistivity and shear wave velocity (V_s) were acquired to characterise two clay sites in Norway. At the first site, resistivity changes are monitored while salt is artificially diffused in a quick clay deposit. Three successive ERT (electrical resistivity tomography) surveys and R-CPTu (resistivity CPTu) were acquired around the diffusion wells to monitor the salt plume over time as resistivity is closely related to pore water chemistry. At the second site, an ERT and seismic survey were carried out to characterise a non-sensitive clay deposit. In addition, resistivity and V_s were measured on high quality block samples. These laboratory data combined with the field data enable a study of how resistivity and V_s correlate to salt content in clay. The primary aim is to better employ geophysical methods for quick clay site characterisation.

1 INTRODUCTION

The Scandinavian post-glacial marine clays are deposited in marine environment during and after the last ice age, entrapping pore water of high salt content (~30-35 g/l) in the voids. Leaching of the pore water by meteoric groundwater flow has diluted the pore water salinity in some clays to less than 5 g/l. At low salt content the repulsive forces between the clay particles increase, and the structure easily collapses and the clay minerals float in their own pore water. The salt content in quick clays is often less than 2 g/l (Torrance 1979). The most reliable method to confirm quick clay is sampling and index testing in the laboratory to measure the remolded shear strength and sensitivity. However these tests are costly for systematic quick clay hazard zonation. As resistivity is closely correlated to the pore water salinity in clays, and quick clay is indicated by higher resistivity than low-sensitive clay, ERT is a suitable approach. Indeed, its use for quick clay mapping has increased during the last decade, also thanks to recent advances in the data acquisition (protocols and instruments) and processing tools.
Based on 2D ERT models Solberg et al. (2012) proposed the following ranges of resistivity for Norwegian clays:

- unleached marine clay: 1-10 Ωm
- leached, possibly quick clay: 10-80/100 Ωm
- dry crust clay, slide deposits, coarser material like sand and gravel and bedrock: >100 Ωm

However, increasing numbers of case studies reveal that this resistivity range is often influenced by local conditions. ERT is however considered as a useful mapping tool for landslide risk assessment at comparably lower costs than extensive drilling (e.g. Pfaffhuber et al. 2013, Bazin et al. 2014). Here, the limitations of the technique is considered by comparing resistivity values obtained with ERT, borehole logging and laboratory measurements. Furthermore, MASW (multichannel analysis of seismic waves) has also been used successfully to characterise Norwegian clays (e.g. Long & Donohue 2010). Since the V_s is directly connected to the small-strain shear stiffness G_{max} ($G_{max}=\rho V_s^2$, where ρ is the density in kg/m^3), it seems reasonable to investigate the effect of quick clay on V_s. The velocity change due to the removal of the salt content is expected to be weak and possibly within the measurement error (Donohue et al. 2012, Sauvin et al. 2014). Here, the measurement accuracy is considered by comparing V_s measurements obtained with MASW, borehole logging and laboratory tests.

The two marine clays included in this paper were deposited after the last glaciation about 10.000 years ago, and they are in the Trondheim (Dragvoll site) and

Oslo (Onsøy site) areas. These two sites have been investigated in connection with research projects and are well characterized. However the three types of measurements (ground-based geophysics, borehole logging, and laboratory) do not all exist for the two sites. Dragvoll clay is low saline, with a remolded shear strength of less than 0.1 kPa, while Onsøy clay has a high salt content and a remolded shear strength from 2 to 6 kPa.

2 QUICK CLAY SITE: DRAGVOLL, NORWAY

2.1 *Research site*

The NTNU research site at Dragvoll is located 156 m above current sea level and the clay deposit is up to 40 m thick (Fig. 1 upper). To investigate the effect of potassium chloride (KCl) on geotechnical properties, six salt wells filled with KCl were installed in January 2013 (Helle et al. 2015). Vertical 63 mm diameter pipes allow the salt to diffuse into the quick clay layer from 4 to 8 m depth. They are regularly refilled with granular KCl to maintain a high concentration (~4 mol/kgw). R-CPTu around one of the salt wells and ERT surveys were carried out to inspect the migration of the salt plume.

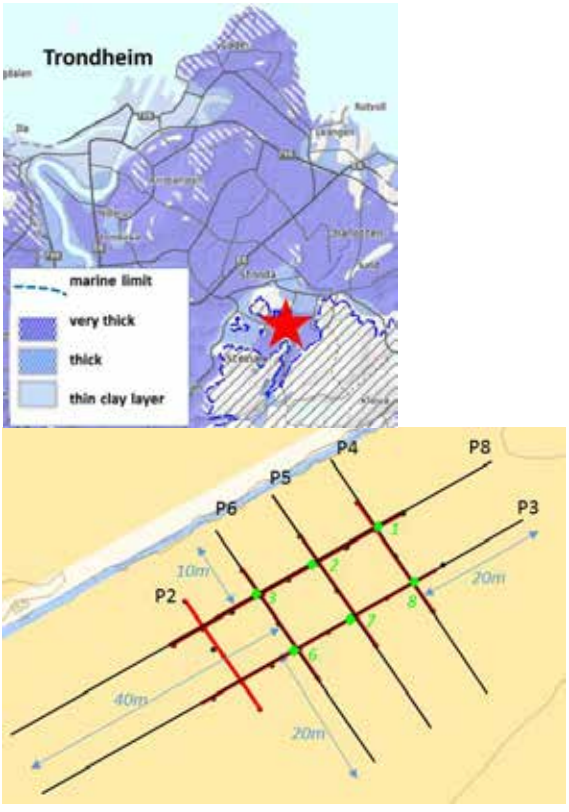

Figure 1. Upper: Dragvoll site. Lower: The ERT survey before salt-well installation is illustrated in thick red lines while the two later surveys are in thin black lines. The salt wells are numbered in green (1, 2, 3, 6, 7, and 8).

2.2 *ERT surveys*

2.2.1 Monitoring surveys

Six ERT profiles with varying electrode spacings (0.25, 0.5 or 1 m spacing) and varying lengths (20, 40 or 80 m long) were acquired once before installing the salt wells, and twice after (Fig. 1 lower) to monitor resistivity changes over time (time-lapse). The surveys were performed with a 12-channel Terrameter LS recording unit (ABEM 2010). The multiple gradient array was chosen for the acquisition protocol, it has been designed for use in multichannel systems (Dahlin & Zhou 2006) and is optimal for this instrument. The penetration depth was 3.8, 7.2 and 15.6 m depending on the electrode spacing. Datasets acquired with different electrode spacings but along the same line were concatenated to improve the model resolution. The raw data were inverted with software RES2DINV (Loke 2016) to obtain the model resistivity distribution. The following options were chosen for the inversion: half unit cell spacing, manual removal of noisy data points, smooth inversion with reduced side-block effects, and time-lapse resistivity inversion between consecutive surveys.

One selected resistivity profile is presented in Figure 2. The data fit is very good (RMS = 0.96% at iteration 4). The top is marked by a ~1 m thick dry crust layer. The clay is very homogeneous and typical of leached clay (ρ ~ 50 Ωm). The clay thickness is greater than the penetration depth (15 m). One selected time-lapse resistivity change, almost 3 years after salt-well installation, is presented in Figure 3. The ERT monitoring is not able to detect any conductive anomalies near the salt wells. Only a strong elongated anomaly is observed in the first 1.5 m, due to the seasonal water table fluctuations (Fig. 3 inset).

2.2.2 Resolution tests

To illustrate the resolution of the ERT survey, a synthetic test was carried out. The synthetic model is displayed in Figure 4 and contains several geological units with three different resistivities: a 1 m thick resistive dry crust (ρ = 150 Ωm), a background typical of leached clay (ρ = 50 Ωm), three conductive salt wells between 4 to 8 m depth (ρ = 0.3 Ωm). A synthetic data set is obtained by perturbing the theoretical solution of the forward problem with 5 % Gaussian noise using RES2DMOD package (Loke 2002). It is computed assuming a multiple gradient array with 81 electrodes at 1 m spacing, which is the geometry of a real survey.

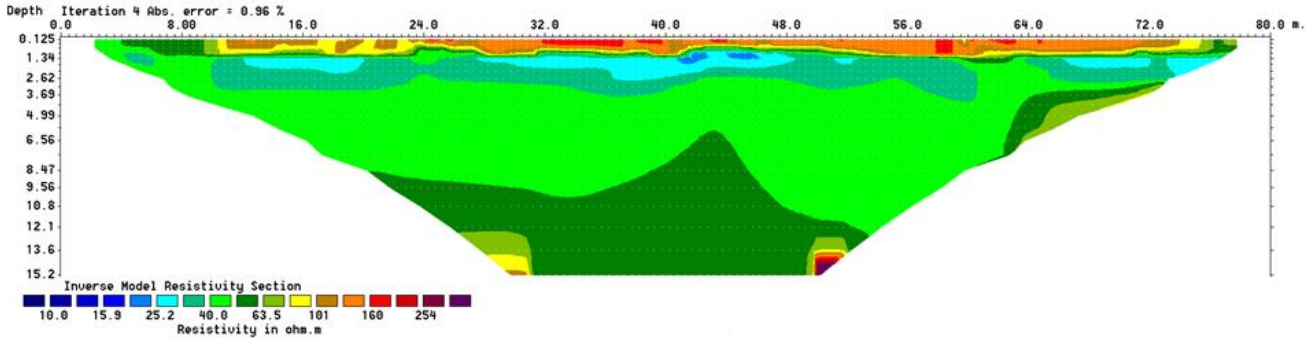

Figure 2. Representative ERT depth section (profile P3).

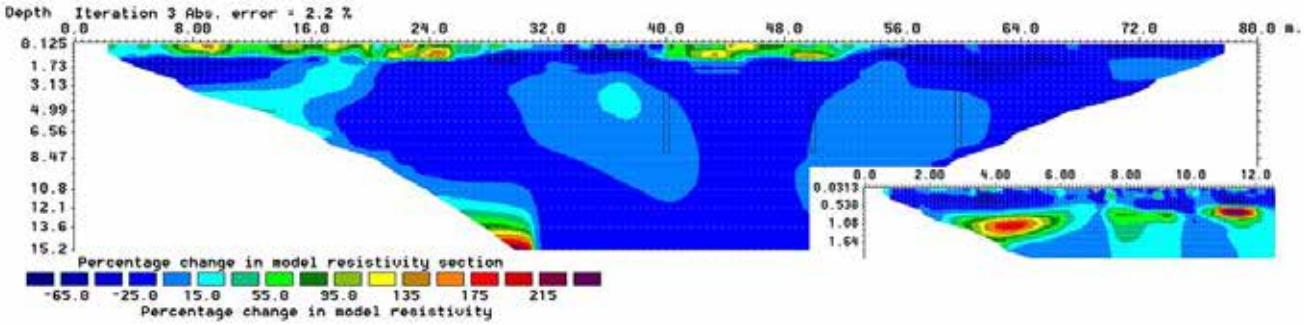

Figure 3. Time-lapse resistivity changes along P3. The inset shows a shallow profile illustrating seasonal variations.

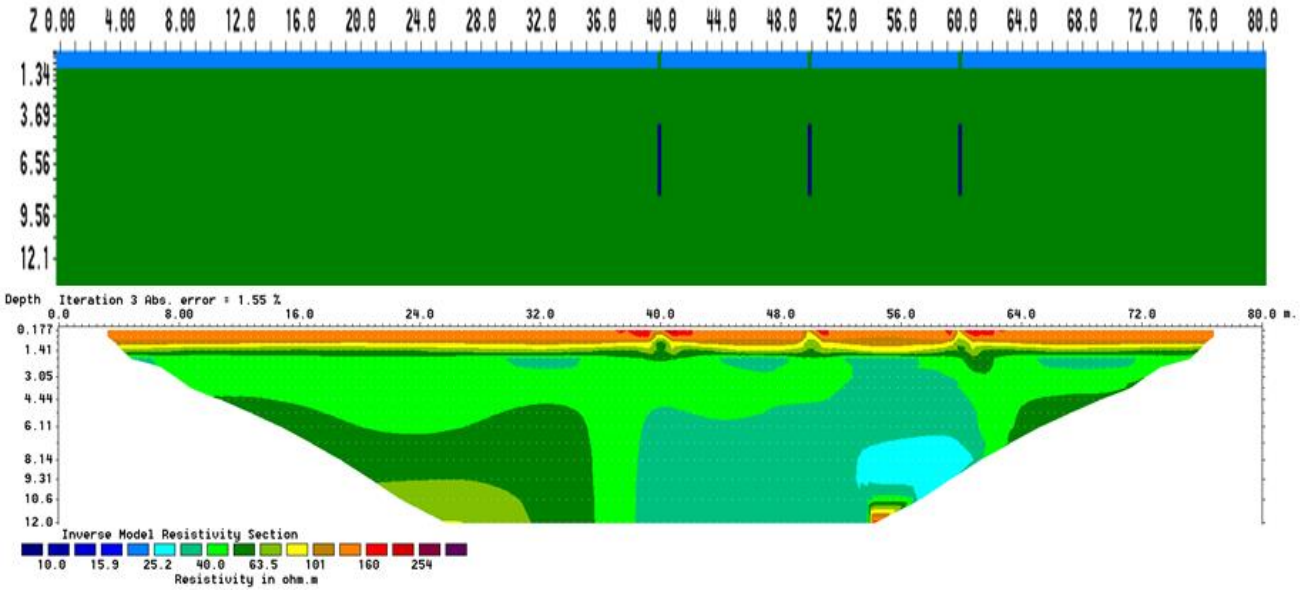

Figure 1. Resolution test: the synthetic model is shown at the top while the recovered resistivity model is shown at the bottom.

This synthetic data set is then inverted with RES2DINV using similar parameters as for the real datasets. The data fit is already good (RMS = 1.5 %) after 3 iterations. The synthetic response shows that dry crust layer and the average resistivity are well retrieved. However the narrow salt wells are not detected and instead the inverted model images a 20 m wide conductive anomaly. This illustrates the low resolution at depth of the surface-based ERT method and its inadequacy to detect slim salt plumes below 4 m depth. Cross boreholes surveys would be recommended for such a target.

2.3 *R-CPTu survey*

A resistivity module is attached to a conventional CPTu: the probe is 80 cm long with 4.4 cm diameter and holds four ring electrodes. Two outer rings, 20 cm

apart, inject a current while two inner rings measure the voltage (Fig. 5 right). R-CPTu readings are therefore small-scale compared to ground-based geophysics. Several R-CPTu logs acquired in October 2015 (2 years and 9 months after wells installation) around one of the salt wells (from 50 cm to 1.5 m away) clearly illustrate how far and in which direction the salt plume has migrated (Fig. 5 left). The maximum resistivity reduction due to the increased salt content goes from 50 to 8 Ωm. Further analysis of the R-CPTu profiles are presented in Helle et al. (2016). The resistivity depth profiles extracted from the two perpendicular ERT profiles (P3 and P4) are also shown for comparison. They are in very good agreement with the resistivity values obtained with the R-CPTu. However, they fail to detect the resistivity reduction near the salt well, as already noticed in Figure 3.

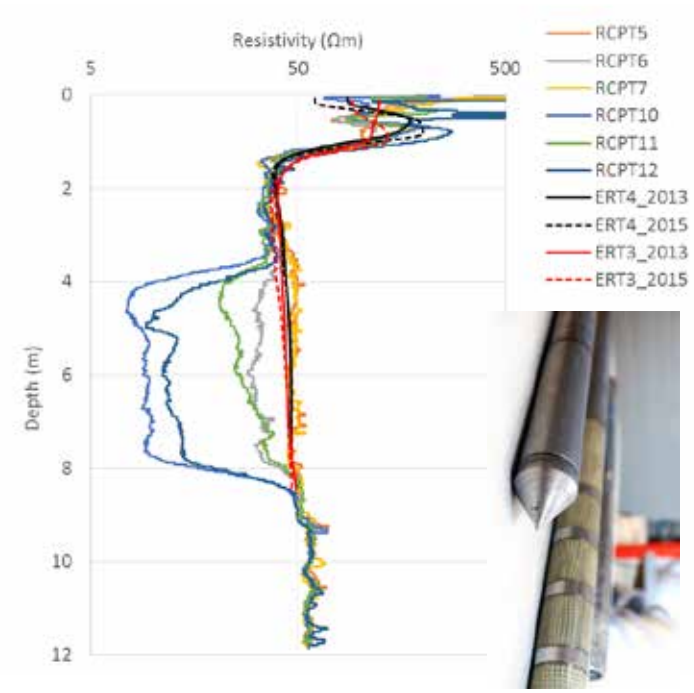

Figure 2. Left: R-CPTu and ERT depth profiles around well 8 during the salt diffusion test in Dragvoll. Right: R-CPTu tool.

3 LOW-SENSITIVE CLAY SITE: ONSØY, NORWAY

3.1 *Research site*

Onsøy is located within the marine clay deposits in SE Norway close to the town of Fredrikstad (Fig. 6). The area is near present sea level. NGI has been using this site for research testing for several decades because of the high thickness (up to 44 m) of the clay deposit and its highly uniform nature.

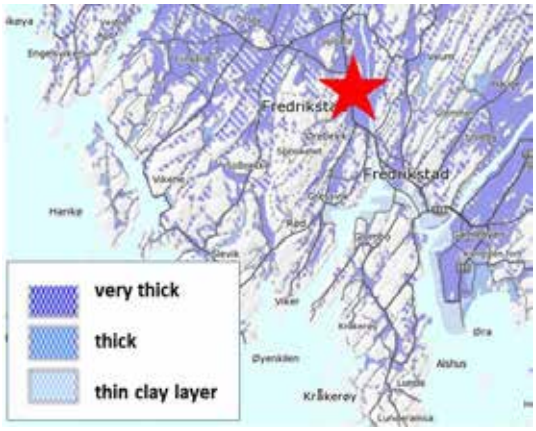

Figure 6. Onsøy site, Norway.

3.2 *Seismic survey*

Six MASW profiles were carried out in 2005 using a RAS-24 seismograph and Seistronix software. A sledgehammer was used as a source and 4.5 and 10 Hz vertical geophones were planted every 1 or 2 m. Data processing was performed by selecting dispersion curves from a phase velocity-frequency spectra, generated using a wavefield transformation method (Park et al. 1999). V_s models were inverted with the software Surfseis using the least squares approach of Xia et al. (2003). In addition, three V_s borehole logs were acquired in 1984 using the Univ. of British Columbia S-CPTu (Eidsmoen et al. 1985, Lunne et al. 2003) and in 2004 by the Univ. of Massachusetts (Landon 2007). The V_s depth profiles are depicted in Figure 7.

3.3 *ERT survey*

A 80 m ERT profile with 1 m electrode spacing was acquired in 2016. The profile was positioned as close as possible to where the block samples were collected for direct comparison with laboratory data. The survey was performed with the same instrument and same data processing work flow as in Dragvoll. The resistivity profile is presented in Figure 8. The data fit is very good for (RMS = 2.5 % at iteration 4). The top is marked by a ~1 m thick dry crust layer. The clay appears very homogeneous and extremely conductive (ρ ~ 1Ωm). The clay thickness (44 m) is much greater than the penetration depth (15 m).

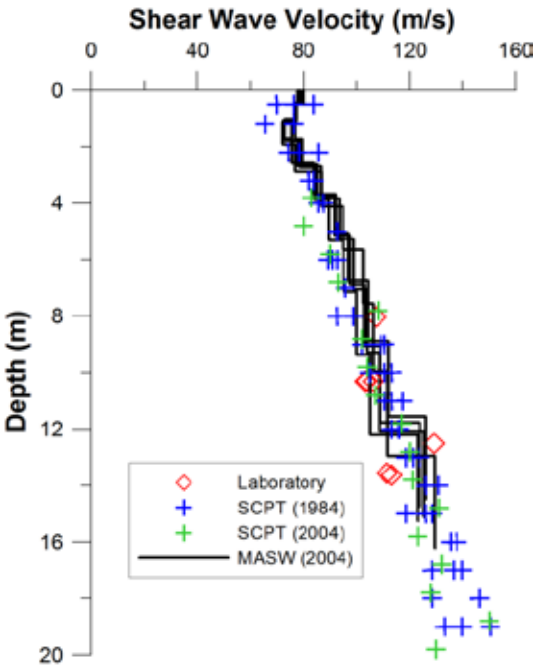

Figure 7. V_s depth profiles in Onsøy.

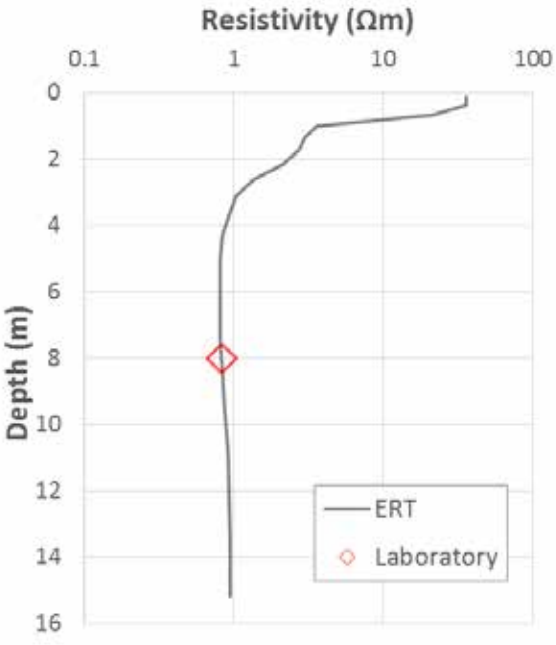

Figure 9. Resistivity depth profile in Onsøy.

3.4 *Laboratory tests*

A major difficulty in soil geotechnics is to retrieve undisturbed samples that maintain the clay structure. NGI has been using a specially designed block sampler from the Univ. of Sherbrooke Québec (Lefebvre & Poulin 1979) since 1982. Tests on block samples show that they are of high quality (Karlsrud & Martinez 2013). Specimens from Onsøy block samples, with a diameter equal to 71 mm and height ~70 mm, were mounted into specially modified triaxial cell, then incrementally and anisotropically consolidated to their in-situ stress. Three resistivity and seven V_s measurements were acquired longitudinally. Laboratory data points are compared with the V_s and the resistivity depth profiles in Figure 7 and in Figure 9. The agreement with ground-based geophysics is very good, probably thanks to the homogeneity and isotropy of the clay layer.

4 CONCLUSIONS

As all geophysical techniques, ERT depth sections suffer from some methodical limitations. The weakness illustrated at Dragvoll is the lack of resolution at depth. Nonetheless, the comparison between ERT, R-CPTu and laboratory data confirms the good agreement between 2D profile, borehole and sample resistivity data. Hence, the ERT method is satisfactory in accuracy (property to measure the right resistivity). It is however weak in resolution (property to detect small-scale anomalies) at depth and synthetic modeling is for that reason advisable to design an effective survey geometry.

MASW models suffer from similar weaknesses. Nonetheless, the comparison between MASW, S-CPTu and laboratory data confirms also a good

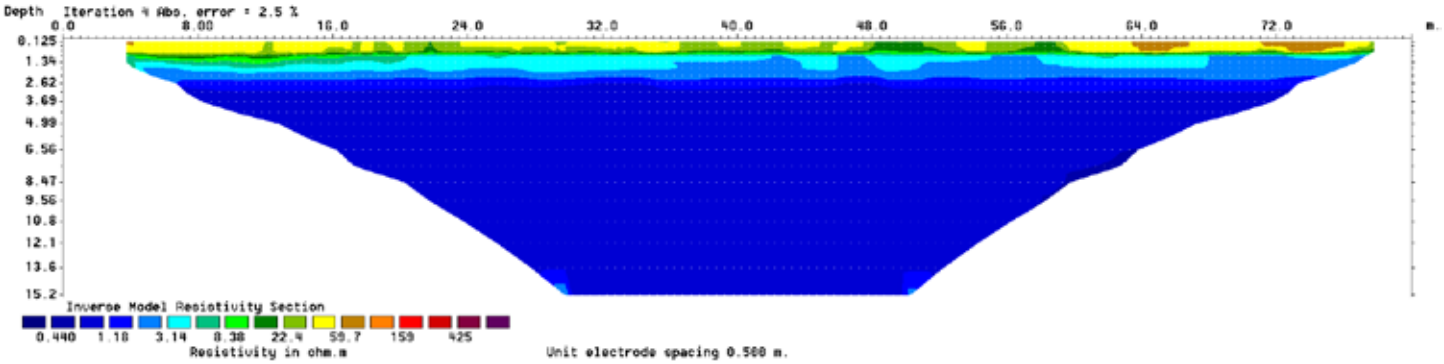

Figure 8. ERT depth section in Onsøy.

agreement between seismic profiling, borehole and laboratory bender element measurements. Hence the V_s method is also satisfactory in accuracy (property to measure the right velocity) thanks to the clay homogeneity and isotropy. Further work is however necessary in order to quantify the velocity change due to leaching for quick clay applications (Gribben et al. 2016).

5 ACKNOWLEDGEMENTS

Funding was provided by the Research Council of Norway through NGI research programs, the Norwegian Public Roads Administration, the Norwegian research program "Naturfare - infrastruktur, flom og skred (NIFS)" and NGI Schmertmann Research Laboratory.

6 REFERENCES

ABEM 2010. Terrameter LS Instruction Manual. <http://abem.se>, p63.

Bazin, S. & Pfaffhuber, A.A. 2013. Mapping of quick clay by electrical resistivity tomography under structural constraint. *J. Appl. Geophys*. (98): 280–287.

Dahlin, T. & Zhou, B. 2006. Gradient array measurements for multi-channel 2D resistivity imaging. *Near Surface Geophysics* (4): 113-123.

Donohue, S., Long, M., O'Connor, P., Helle, T.E., Pfaffhuber, A.A., & Rømoen, M. 2012. Multi-method geophysical mapping of quick clay. *Near Surface Geophysics* (10): 207- 219.

Eidsmoen, T. Gillespie, J., Lunne, T. & Campanella, R.G. 1985. Tests with the UBC seismic cone at three Norwegian sites. *NGI report* No. 59040-1, 30/11/85, Oslo.

Gribben, S., Bazin, S., L'Heureux, J.-S., Sivakumar, V., & Donohue, S. 2016. Geophysical methods for assessing the geotechnical properties of sensitive clays. *GeoVancouver conference*.

Helle, T.E., Bryntesen, R. N., Amundsen, H., Emdal, A., & Norda, S. 2015. Laboratory setup to evaluate the improvement of geotechnical properties from potassium chloride saturation of a quick clay from Dragvoll, Norway. *GeoQuebec conference*.

Helle, T.E., Aagaard, P., Emdal, A., & Nordal, S. 2016. Monitoring the plume of potassium chloride from wells used as ground improvement in highly sensitive clay. *5th International Conference on Geotechnical and Geophysical Site Characterization* (ISC'5), Gold Coast, Australia.

Karlsrud, K., & Hernandez-Martinez, F.G. 2013. Strength and deformation properties of Norwegian clays from laboratory tests on high-quality block samples. *Can. Geotech. J.* (50): 1273-1293.

Landon, M.M. 2007. Development of a non-destructive sample quality assessment method for soft clays. *Ph.D. Dissertation*, University of Massachusetts Amherst, Amherst, MA.

Lefebvre, G. & Poulin, C. 1979. A new method of sampling in sensitive clay. *Can. Geotech. J*. (16): 226-233.

Loke, M.H. 2002. RES2DMOD version 3.01.80. Rapid 2D resistivity forward modeling using the finite-difference and finite element methods. Instruction Manual. Geotomo Software, <http://www.geotomosoft.com>

Loke, M.H. 2016. RES2DINV version 6.1. Geoelectrical Imaging 2D and 3D. Instruction Manual. Geotomo Software, <http://www.geotomosoft.com>

Long, M. & Donohue, S., Characterisation of Norwegian marine clays with combined shear wave velocity and CPTU data. *Canadian Geotechnical Journal* (47): 709-718.

Lunne, T., Long, M., & Forsberg, C.F. 2003. Characterisation and engineering properties of Onsøy clay. *Proceedings International Workshop on Characterisation and Engineering Properties of Natural Soils.* NUS Singapore (1): 395-428.

Park, C.B., Miller, R.D., & Xia, J. 1999. Multichannel analysis of surface waves. *Geophysics* (64): 800-808.

Pfaffhuber, A.A., Bazin, S., & Helle, T.E. 2014. An integrated approach to quick-clay mapping based on resistivity measurements and geotechnical investigations. Landslides in sensitive clays. *Advances in Natural and Technological Hazards Research* (36): 193-204.

Sauvin, G., Lecomte, I., Bazin, S., Hansen, L., Vanneste, M., & L'Heureux 2014. On the integrated use of geophysics for quick-clay mapping:The Hvittingfoss case study, Norway. *J. Appl. Geophys*. (106): 1-13.

Solberg, I.L., Hansen, L., Rønning, J.S., Haugen, E., Dalsegg, E., & Tønnesen, J.F. 2012. Combined geophysical and geotechnical approach to ground investigations and hazard zonation of a quick clay area, Mid Norway. *Bull. of Eng. Geology and the Environment* (71): 119-133.

Torrance, J.K., 1979. Post-depositional changes in the pore water chemistry of the sensitive marine clays of the Ottawa area, eastern Canada. *Engineering Geology (*114): 135-147.

Xia, J., Miller, R.D., Park, C.B. & Tian, G. 2003. Inversion of high frequency surface waves with fundamental and higher modes. *J. Appl. Geophys.* (52): 45–57.

Geotechnical and Geophysical Site Characterisation 5 – Lehane, Acosta-Martínez & Kelly (Eds)

Near-surface geophysical scanning for exemplar landslide projects in Poland

Z. Bednarczyk
Poltegor-Institute Institute of Opencast Mining, Wroclaw, Poland

ABSTRACT: The paper present usage of shallow geophysics in landslide investigations. The GPR method carefully scaled by others geotechnical engineering tests were useful for recognition of landslides and its internal structure to the depths from few to even 18 m. Totally over 27 km of scanning was performed on 24 landslides. The investigations were conducted for protection of public roads and infrastructure. The depth of scanning was depended on types of equipment used and local soil conditions. The best scanning results were obtained with 100 MHz antennas. Caution was paid to proper calibration of GPR results because in this method detected stratification is interpretation result. Therefore the GPR was carefully calibrated by the boreholes. In the paper conclusion from usage of this method is presented. Near-surface geophysical scanning was very effective, low cost and fast method of investigations. However, due to same limitations, caution should be paid in geotechnical interpretation of the results, its careful calibration by monitoring measurements.

1 INTRODUCTION

Landslides became a serious problem in southern Poland. Its density is there the highest in the country. According to the newest data of Polish Geological Survey (PGI), 60 000 of landslides were registered in Polish Carpathians (Chowaniec et al. 2015). High economic losses, damaged roads together with different types of infrastructure and private buildings are reported in Poland every year. In May-June 2010 after the flood its costs reached 2.9 bln EUR. (Chowaniec et al. 2015). Author of the paper had opportunity to perform same of these landslide investigations and counteraction projects for public roads and local authorities. These works financed by Polish State budget and loan from the European Investment Bank were conducted in years 2006-2015. The main objective of the research was to define possibilities and methods of landslide remediation. Landslides built from soil-rock type flysch deposits, were difficult for in-situ and laboratory tests. Complex and effective techniques of investigations were required. Some types of in-situ tests proper for soils were not always useful. The site investigations required core impregnated boreholes. These were very important but time consuming, costly not always answering all the geotechnical questions. The near-surface geophysical and geotechnical methods delivered valuable data for slope stability analysis. The Ground Penetration Radar scanning were found to be a one of very useful methods in conjunction with other in-situ and laboratory geotechnical tests. It was very effective, low cost and fast method of investigations. However, it had also same limitations connected with forest areas, powers supply lines and specific soil conditions. Caution was paid in geotechnical interpretation of the GPR results, its careful calibration by boreholes and in-situ monitoring.

2 LANDSLIDE CHARACTERIZATION

Investigated 24 landslides were localized in three regions located in Beskid Niski Mts. (No 1-20), Beskid Sredni Mts. (No 21-23) and Carpathian Foreland (No 24). Exemplar landslides are presented on the map (Fig. 1). List of investigated landslides and its parameters are presented in Table 1.

Figure 1. Investigated landslide localization

Table 1. Landslide parameters and GPR scanning length

Location	Inclin.	Volume	Depth	Type	GPR length
No	deg	mln m^3	m	*	m
1-6. Szymbark	6-18	2.2	1.3-15	R	2170
7-8. Szymbark	6-12	0.5	6-13	R	940
9-11. Bystra	6-9	2.5	2.7-5	R	2240
12-14. Bystra	9-12	1.3	2.5-9	R	2400
15. Szalowa	6-12	10.8	9-16	R	990
16. Sekowa	6-12	0.4	2.7-5.1	R	1257
17. Wapienne	6-9	1.9	2.5-9	R	6155
18. Strzeszyn	9-16	0.3	1.4-10	R	460
19. Sitnica	6-9	0.1	1.2-5	R	360
20-21.Tarnawa	6-12	0.9	10-15	N 2006/R	2795
22. Sitarzowka	6-19	1.6	10-12	N 2010	3520
23. Zarebki	8-10	1.8	2-13	R	1845
24. Strachocina	5-18	0.6	10-12	R	2130

* R – reactivated N-new formed.

Investigated landslides occurred at specific mountain locations under certain morphology and geotechnical engineering conditions. Its volume varied from 0.1-2.2 mln m^3. Mass movements were localized on mountain slopes dip from 5° to 19°. Landslide depths varied 1.0 m to 16 m. The most active zones were usually situated at landslide tongues. Colluviums were built from shale's and sandstones. Flysch layers involved in slides represent Neogene marine clastic sedimentation folded during Alpine Orogenesis. Intensive erosion in river valleys and high groundwater level, during the Holocene era, characterized by thick weathering zones activated huge numbers of landslides (Raczkowski 2002). Deposits were built from many thin layers of flysch type marine sandstones and claystones. Colluviums represented soil-rock type of landslides (Cruden 1996). Saturated claystones in colluviums had mechanical parameters as a weak cohesive soils. Sandstones interlayer's allowed water infiltration. Failure occurred as a combination of different mechanism and was depend on hydrology, geology and topography factors. Low friction angle, cohesion high moisture and variation of pore pressure values often influencing the slope stability (Rybar at al. 2002). On slopes built of clayey deposits failure developed over periods of months as a creep process. Clayey soils with very low geotechnical parameters were often interbeded by medium stiff to stiff rocks such as claystones or sandstones with different degree of digenesis. The groundwater levels were 0.5-1.5 m bellow the natural terrain level. Groundwater regime conditions had a dominant influence on landslide activation. Intensive rainfalls together with floods, erosion in river valleys, snow melting and pore pressure fluctuations inside soil layers were enhancing the sliding activity (Bednarczyk 2004-2015). The previous studies (Starkel 2011) shows that the activity of the landslides were increasing after long-term precipitations in 20-40 days, which exceeds the sum of monthly rainfalls of 400-550 mm. Especially, if the rain in a few days exceed 250 mm. Three of investigated landslides No 20, 22, 23 were new formed others twenty one landslides were reactivated in wet periods many times.

3 GEOPHYSICAL SCANNING PRINCIPLES

Landslide slopes internal stratification and colluvium depths were detected using 2D GPR RAMAC scanning. It allowed more accurate measurements of changes of colluviums and bedrock layers dielectric properties between the boreholes. The GPR scanning is based on the Electromagnetic Reflection Theory (EMR). In this method pulses of ultra high electromagnetic frequency waves were transmitted down from transmitter (T) into the landslide body through antennas (Burton 2009). Part of the GPR waves were reflected from flysch sediments layers boundaries, while the rest of the waves passed through to the next layers or contacts between landslide colluviums and bedrock layers. Reflected signals returned and were received by the digital control unit – receiver (R) which registered the reflections against two-way travel time in nanoseconds and then amplified the signals. The data control unit allowed generation of radar energy coordinates together with displaying and recording the time of received reflections returns. The speed of the electromagnetic energy travelling trough the colluviums and bedrock layers was directly related to its dielectric properties. The lower the dielectric, the faster waves travel. More precisely, data logger registered returned reflections of the radar waves. The depths of GPR survey with100 MHz antennas were as deep as 10-18 meters depending on the local conditions. Scanning usually had not very high resolutions at depths below 15 m but allowed general landslide depth and internal structure recognition. Lower frequency 100 MHz unshielded antennas allowing relatively deeper penetration were chosen for the scanning of 23 landslides (Fig. 2).

Figure 2. GPR, 100 MHz unshielded antennas, landslide No 21

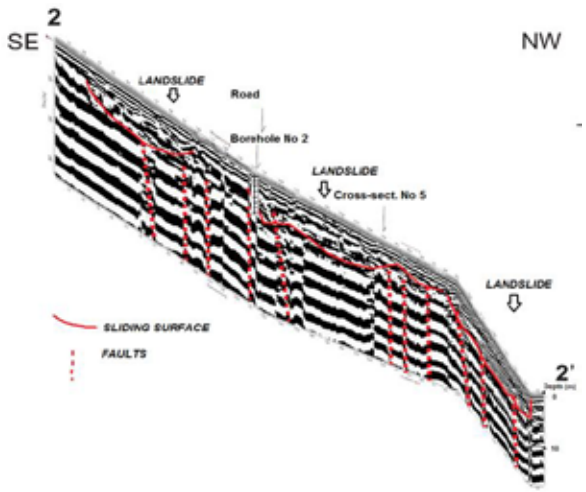

Figure 3. GPR longitudinal scanning profile, landslide No 23

Figure 4. GPR scanning close to the borehole, landslide No 23

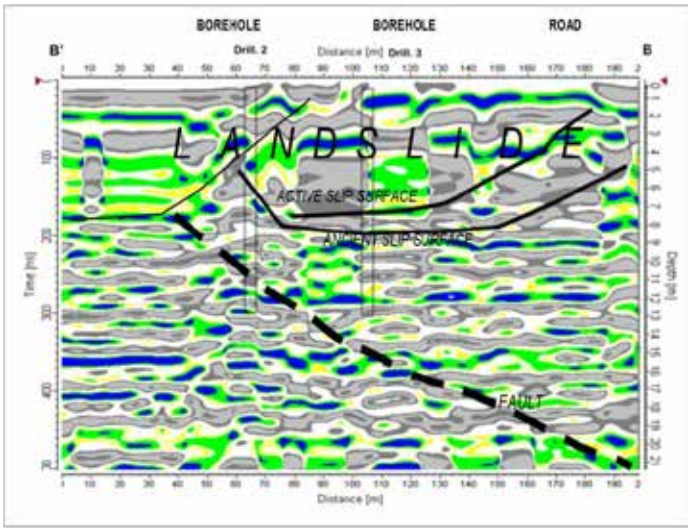

Figure 5. GPR longitudinal scan. profile I-I', landslide No 16

On one landslide No 23, 100 MHz shielded antennas were used (Figs. 3 & 4). For shallow parts of the landslides 3-5 m depth, better resolution had 250 MHz antennas. The post-processing and interpretation Ground Vision software was used for data interpretation. The output signal voltage peaks were plotted on the profile as different colour bands by the digital control unit (Fig 5).

The calibration of the depth scale was calculated after boreholes data: thickness of colluviums and type of bedrock below. It was necessary to include in the interpretation software dielectric parameters for different types of soils and rocks. For colluviums, built from clayey wet deposits, the attenuation (dBm^{-1}) as 6, relative permittivity range as 30 and relative permeability 30. For dry claystones, the attenuation (dBm^{-1}) as 10, relative permittivity range as 9 and relative permeability 9. For fine sandstone, the attenuation (dBm^{-1}) as 10, relative permittivity range as 5 and relative permeability 10 (see: Daniels 2004, Bednarczyk, Szynkiewicz 2008). The GPR raw data was processed in program. On scanning results interpreted colluviums depth, faults and folds were indicated. As a result of scanning, two dimensional images of the landslide colluviums, calibrated by boreholes were indicated on the cross-sections. Obtained results were corrected for slope morphology. On the cross-sections geographical directions, control points, boreholes, faults, colluviums depths were marked. The georadar cross-sections showed that colluviums had approximate depths of 1-15 m. The GPR profiling was essential for construction of geotechnical cross-sections. It allowed recognition of landslide colluviums and inclinations of layer and faults. For example, on landslide No 16, under the public road, the colluviums were recognized to depths of 2.8-4.5 m (Figs. 5-6). The total length of GPR profiles was over 27,2 km on 24 landslides. It varied from 360 m on landslide No 19 to 6150 m on landslide No 17 depending on the mass movements size and slope accessibility. Interpreted by GPR method and boreholes sandy and clayey layers was helpful in identification of water infiltration prone zones.

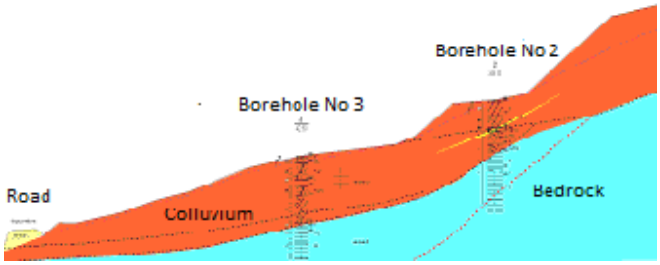

Figure 6. Geotechnical cross-section I-I', landslide No 16

4 CORRELATION WITH OTHER METHODS

4.1 *Calibration by core boreholes*

In GPR method the interpreted layers depths are affected by included in the software rocks and soils dielectric input parameters. Therefore the detailed pro-

files of new drilled boreholes were used for GPR surveys calibration and scaling. The oldest GPR profiles didn't included morphology.

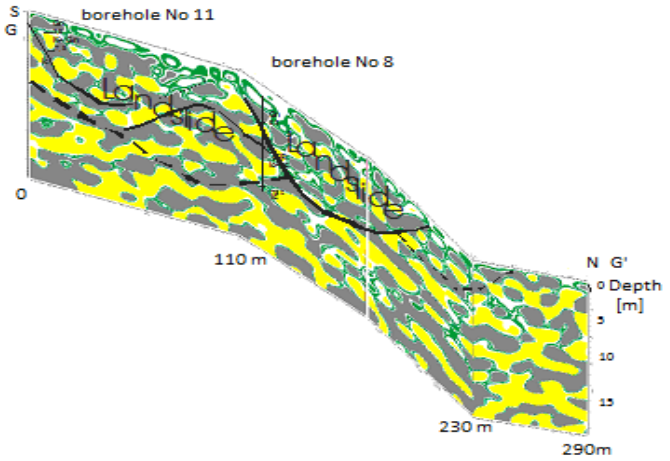

Figure 7. GPR longitudinal scanning profile, landslide No 18

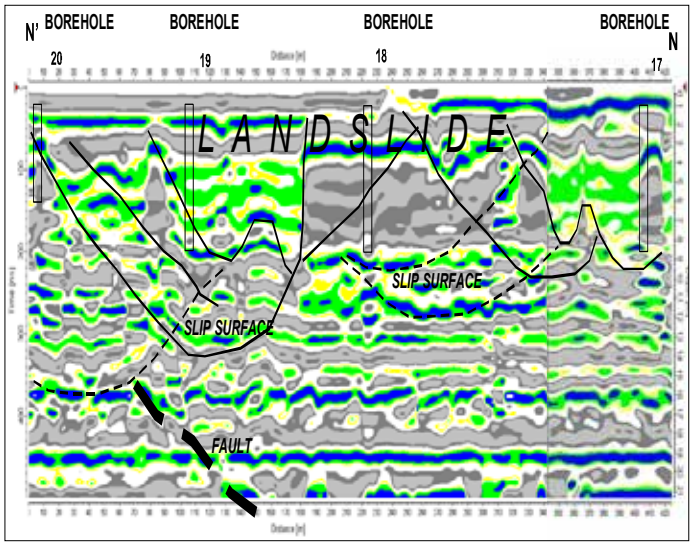

Figure 8. GPR transverse scanning profile, landslide No 15

More recent scanning profiles were corrected for slopes morphology (Fig. 7). In same cases faults inside the deeper parts of flysch sediments were detected (Fig. 8). The GPR method helped in identification of slope internal stratification in areas where no any other geological data were available. In many cases it was also valuable for initial identification of slip surfaces depths. In the most cases on the scanning results colluviums were characterized by "mixed" not regular areas. These interpretation were compared with detailed geotechnical description of core from the boreholes. In same cases it was possible to recognize slip surfaces in the core. However, in same cases it required complex comparison of different geological data including reference monitoring results. In order to facilitate the interpretation the GPR surveys were located between the previously drilled boreholes located 50-200 m one from the other. The obtained data were used for construction of geotechnical cross-sections. The georadar scanning interpretation was always based on few longitudinal and transverse cross-sections. On every landslide, depending on its size 6-10 longitudinal and transverse GPR survey were performed. To eliminate the fault scanning results in same cases the same scanning works were conducted twice, for example in W-E and E-W directions. The locations of the profiles in the field and on the map were compared to normalize scanning profiles to the real distances in areas of variable morphology. The longitudinal scanning were performed with slope inclination. These profiles were conducted from area above the main landslide scarp downhill. The crossing of longitudinal and transverse scans were indicated at the field and measured by GPS.

4.2 *Calibration by monitoring and in-situ tests*

The GPR surveys were also compared with the different types of in-situ measurements and tests. Inclinometer and piezometer monitoring was performed at 30 monitoring locations. The measurements started depending on the location 2006-2008 and are conducted till now (Fig.9).

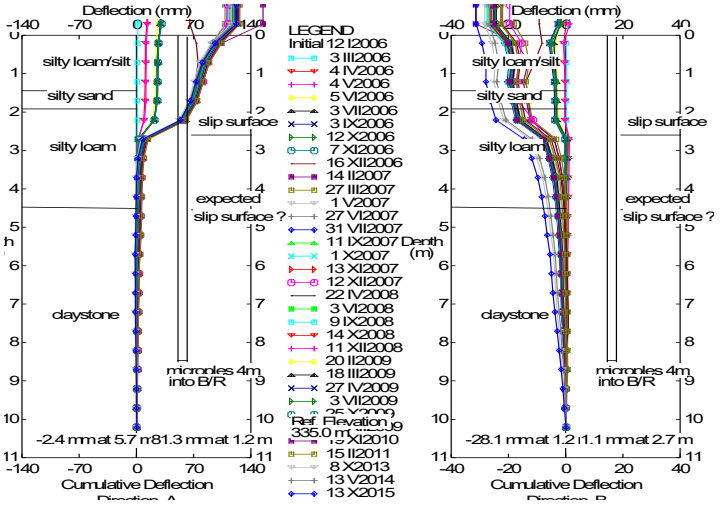

Figure 9. Inclinometer measurements, landslide No 16

The changes in ground profile were measured every 0.5 m by inserting an inclinometer probe into vertical ABS inclinometer tube and recording how far out of vertical the probe was at various depths within the tube (Dunnicliff 1993). It allowed detection of sliding surfaces depths and ground movement size with accuracy of 0.05 mm. Together with pneumatic and automatic VW pore pressure and groundwater level depths monitoring it delivered detailed data for comparison

with GPR scanning results. The GPR survey on landslide No 16 detected that the main active slip surface under the public road was at depth of 2.4 m while another at the depth of 4.7 m below the natural terrain level (Fig. 9). Inclinometer measurements detected that second deeper surface was not active. The GPR results together with monitoring measurements were included in slope stability analysis for this landslide. It allowed to lower up to 30% the costs of remediation works using more effective design of micropiles lengths. At landslide No 17 (Fig. 8) the slip surfaces were detected at different depths of 2 m and between 7.2-9.0 m bellow the natural terrain level. The results of drillings and GPR profiling on this landslide indicated that few slip surfaces had complicated shapes. The monitoring measurements and slope stability analysis detected that remediation of this landslide will be not possible due to economical reasons. Exemplar instrumentation on landslide No 1-6 is presented on figure 10. Monitoring measurements on these landslides reported slip surface at the depth initially detected by GPR. The pore pressure values of 14-98 kPa were reported at the sliding surface. The values of pore pressures rose over 90 kPa after high precipitation in July 2008, May-June 2010 and May 2013. The groundwater level was usually very shallow and varied mainly between 0.8-1.5 m below the natural terrain level. The ground movements occurred at the different depths and they varied in magnitudes due to the flysch lithology nature. In same colluviums built of clayey soils in-situ vane tests were performed in boreholes every 1 m depth. For example on landslide No 20 the values of shear strength in vane tests reported in stiff clays of 0.67 MPa was decreasing to 0.037 MPa at the slip surface depth.

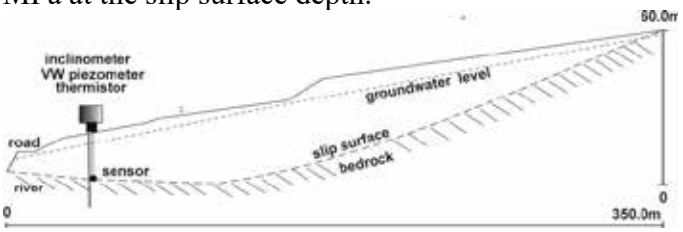

Figure 10. Localization of monitoring landslide No 6

4.3 *Correlation with the laboratory results*

The recognition of geotechnical engineering conditions by laboratory tests allowed better identification of landslide zones. Geotechnical laboratory tests included index tests (grain size, moisture content, liquid and plastic limits, unit weight, and soil particles unit weight), direct shear tests and incrementally loaded (IL) odometer tests. Flysch soils used for these tests represented silty loams, silty clays to claystones (rock). Soils inside the sliding surface usually had very high moisture content 20-36%, liquidity index up to 0.5, cohesion from 6.5 kPa, angle of shearing resistance 9-11 degree. Very high values of soil moisture and plasticity index up to 50% were usually recognized at the sliding surface depths. Soils were characterized also by high 2-10% content of organic (bituminous) material. Results of oedometer consolidation tests detected high compressibility of clayey soils at the slip surface. Index laboratory tests results indicated that on landslide No 1-6 sliding surface depth of 10.5 m detected by monitoring measurements and GPR was in quite good relation with the highest values of moisture content and plasticity index of 15-40% (Fig. 11). At landslide No 16 similar conclusions for two slip surfaces at 2.8 m and 4.5 m depth were obtained (Fig. 12).

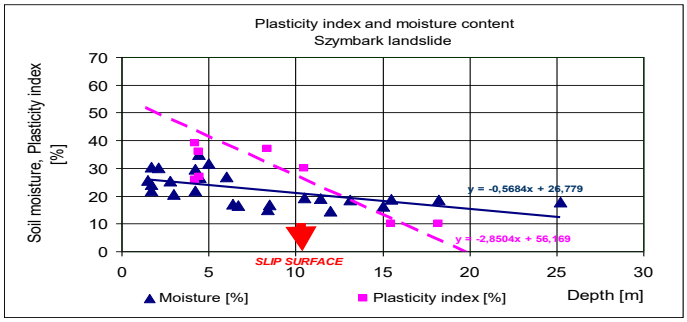

Figure 11. Plasticity index and moisture, landslide No 1-6

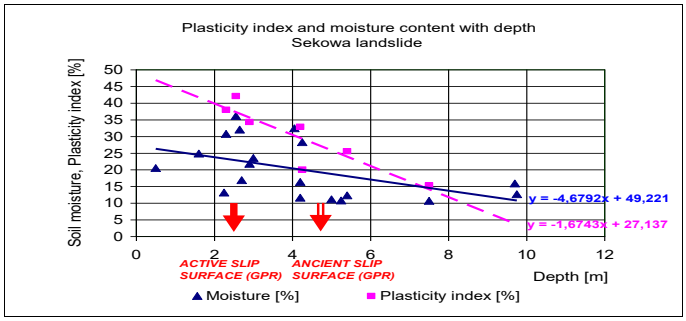

Figure 12. Plasticity index and moisture, landslide No 16.

4.4 *Implementation of GPR results in slope stability analysis and remediation works*

The GPR scanning results were the basis for construction of landslide geotechnical engineering cross-sections. Together with monitoring and laboratory results it delivered valuable data for slope stability LEM and FEM analysis. For example on landslide No 16, values of relative factor of safety F_s, calculated by Bishop LEM method, were slightly above Fs=1.13 before stabilization and 1.58 after it. Using FEM methods and linear elastic model it was predicted that expected displacements of 120 mm and could be dangerous for the public road. Proposed counteraction

method was checked by LEM method, included 60 piles length of 11 m, gabions retaining walls on 300 micropiles foundation length of 6 m, culvert and surface draining system length of 300 m. These works safeguarded the public road. This was confirmed by the monitoring measurements conducted up to 9 years after remediation (Fig. 9). After the remediation displacements were reduced to +/-5 mm. The pore pressure value of 45 kPa before remediation was lowered to 30 kPa after it. Groundwater level depths were also lowered from 1.3-1.8 m to 2-2.2 m.

5 CONCLUSIONS

The Ground Penetration Radar method carefully calibrated by boreholes and others methods was quick and inexpensive way of landslide investigations. Together with other geotechnical engineering methods it made possible recognition of mass movement's areas. It allowed delivery of detailed site investigation reports to the depth of 5-18 m. One of the main advantages of GPR was its efficiency. It allows recognition of geological stratification and tectonic structures. The results indicated that GPR scanning with proper correlation by other geotechnical engineering methods could help in recognition of internal landslide geology and was used for slope stability calculations. Interpretation and calibration of GPR results is very important. In same specific soil conditions and due to others external factors this method could not deliver high quality data. At any new landslide site it is important to know what natural undisturbed slope geological stratification looks like. Therefore scanning should be performed also in the nearest to the landslide border areas. Then it is easier to identify colluviums layers which are not ordinary for natural slope stratification and often characterized by "mixed" structures. The most crucial practice is careful interpretation and calibration by other methods including core drillings to gaining experience in each investigated landslide area. Landslide monitoring helped in precise mass movement's prediction for civil engineering landslide remediation projects. One of the main advantages of the GPR method was its ability of data collection. On some landslides over 2 km of GPR scanning was performed in one day time. Limitations were connected mainly with the penetration depth and resolution, which depended on the ground conditions. On some landslides due to the electric power supply lines or in the forest areas some difficulties were also observed. The obtained results indicated that with proper interpretation and correlation by other methods GPR could detect colluviums and bedrock depth. This method also allows recognizing many internal geological structures together with faults and folds. Calibrated by core drillings, inclinometer measurements, pore pressure monitoring and laboratory tests the GPR method allowed indication of failure zones between the boreholes and was used for slope stability calculations for landslide stabilization projects. However, not every research method is suitable for every landslide type. Caution should be paid in type of the equipment and the antennas used for the scanning, correct interpretation of the GPR results. Very important is careful calibration of GPR results by the boreholes and in-situ monitoring results.

6. REFERENCES

Bednarczyk, Z. 2015 Landslide surveys for road remediation projects in Polish Carpathians, Geotechnical Engin. for Infrastructure and Development, ICE Edinburgh UK: 1707-1711.

Bednarczyk, Z, Szynkiewicz A. 2014, Applied Engineering Geology Methods for Exemplar Infrastructure Projects in Malopolskie and Podkarpackie Provinces Engineering Geology for Society and Territory – Volume 6 Springer.: 203-210

Bednarczyk Z. Szynkiewicz A., 2009. Ground Penetrating Radar GPR Scanning In Geological And Geotechnical Recognition Of Mountain Site For Polish Oil & Gas Company", 22 SAGEEP Symp. Fort Worth, Texas USA EEGS,731-738

Bednarczyk Z. 2008. Landslide geotechnical monitoring network for mitigation measures in chosen locations inside the SOPO Landslide Counteraction Framework Project Carpathian Mountains, Poland. The First World Landslide Forum, Tokyo ICL, UN, Kyoto University, pp. 41-45.

Bednarczyk, Z. 2004. Landslide investigations by static sounding with pore pressure measurements CPTU, GPR and other chosen methods PGI Spec. Pap. 15: 19-29.

Burton C., 2009 The art and Science of GPR, Short Course, SAGEEP Symposium, Forth Worth USA: 1:51

Chowaniec, Wojcik, Mrozek, Raczkowski et al. 2015 Osuwiska w województwie malopolskim. Praca Zbiorowa. Panstwowy Instytut Geologiczny. Wyd. Compas, Krakow:1-33

Cruden, D.M., D.J. Varnes D.J. 1996. Landslides Types and Processes, in: A.K. Turner, R.L. Schuster, Landslides - Investigation and Mitigation, Washington D.C., National Academy Press, Tran. Res. Board Spec Report 247, 36-75.

Daniels D.J. 2004 Ground-penetrating radar – 2nd ed. IEE Radar, sonar, navigation & avionics series 15: 726. The Institution of Electrical Engineers, London, MPG Books

Dunnicliff, J. 1993. Geotechnical Instrumentation for Monitoring Field Perform. J. Wiley & Sons .

Raczkowski W., Mrozek T. 2002. Activating of landsliding in the Polish Flysch Carpathians by the end of 20th century. Studia Geom.. Carpathos-Balcanica 36,: 91 – 111.

Rybar, J., Stemberk, Wagner, P 2002. (Eds): Landslides - Proceedings of the First European Conference on Landslides, Prague, Czech Republic 1:219.

Starkel L. 2011 Temporal and spat. complexity of extreme rainfalls. Landform Analysis. Vol. 15

Geotechnical and Geophysical Site Characterisation 5 – Lehane, Acosta-Martínez & Kelly (Eds)

Imagery of nonlinear soil behaviour using in-situ and laboratory tests

K. Çami & J. Garcia
Geoslab, France

L.-F. Bonilla-Hidalgo & J.-L. Tacita
University Paris-Est / IFSTTAR, The French institute of science and technology for transport, development and networks, France

S. Perlo
CEREMA, Center for studies and expertise on risks, environment, mobility, and urban and country planning, Paris, France

ABSTRACT: Soil is known to behave nonlinearly when large strains are attained. The aim of the present paper is to establish a 2D strain-dependent imagery of the nonlinear soil behaviour of a foundation site located in the Paris suburban area. The experimental program includes in situ measurements such as surface wave methods and pressuremeter tests. The laboratory experiments include resonant column tests to characterize the shear modulus degradation up to moderate soil strains, cyclic triaxial tests and standard triaxial tests to obtain the material strength at failure. All laboratory tests are conducted on specimens from the on-site soil samples. Finally, a 2D shear modulus reduction model is constructed combining all these tests.

1 INTRODUCTION

Geoengineering design and analysis require to represent in a realistic way the mechanical behaviour of soils. In ordinary practice, this is mainly achieved based on classical laboratory tests, such as triaxial tests, or in situ tests, such as pressuremeter tests (widely used in the French practice) or SPT. Although these tests do provide useful information on soil behaviour and most rupture mechanisms, they do not allow fully characterizing the soil behaviour from very small to very large deformations. One of the most important geoengineering properties is the stiffness of the material. Soil stiffness is known to decay as deformation increases (Kramer 1996). As it is known, the shape of the modulus reduction curve (Fig. 1) depends on several factors such as mean effective confining pressure, soil plasticity, void ratio, overconsolidation ratio, and number of loading cycles. Mean effective confining pressure and soil plasticity play the most important role.

A site in the east of Paris, France has been selected for carrying out an experimental program designed to obtain shear modulus reduction curves from various types of tests and for increasing strain level. The experimental program includes in-situ and laboratory tests. More specifically, surface wave methods (MASW) have been used, standard and cyclic pressuremeter tests, resonant column tests, as well as cyclic triaxial and monotonic triaxial tests have been performed.

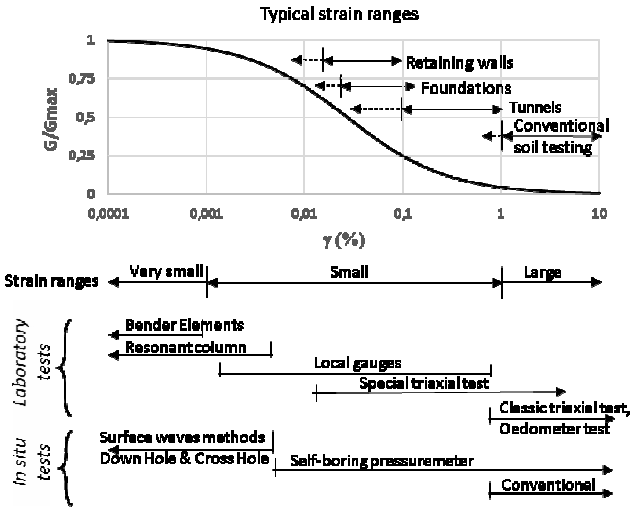

Figure 1. Schematic variation in shear modulus with different shear levels for different geoengineering applications, in-situ tests and laboratory tests (modified after Atkinson & Sallfors 1991, Mair 1993).

2 EXPERIMENTAL PROGRAM

2.1 *Materials*

The site chosen for running the experimental program is characterized by silty soils in the first 3 meters from the surface. Beneath this level, clay and sand was found together with some calcareous blocs.

The soils were sampled on-site by rotary core tube sampling in order not to cause soil disturbance and to get intact material for laboratory experiments. Sample quality assessment using volumetric strain was found to be fair to good (after Andersen & Kolstad, 1979). Soil identification and classification tests such as particle size distribution, Atterberg limits, water content and soil mass density were carried out.

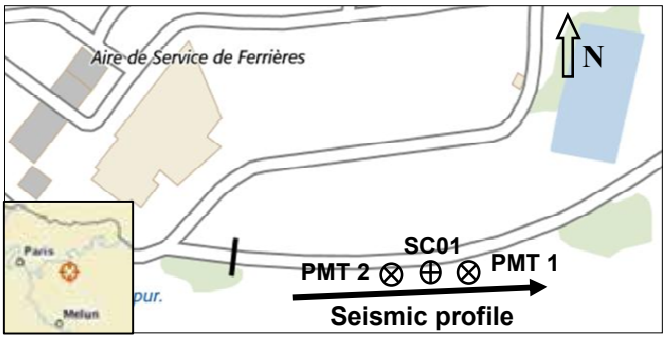

Figure 2. Site location (Geoportail/IGN) and in situ measurements emplacement).

The core SC01 (Fig. 2) revealed a 3-m deep layer of silty soil with an Ip = 19 %, followed by 2 m of calcareous clay with an Ip = 40 %. Then, sand (Ip = 7%) constitutes the rest of the 10-m soil column sampled on site. Two calcareous blocs were found at a depth of 9.30 m and 9.80 m in the soil column. Their size was respectively 0.25 m and 0.17 m. Standard pressuremeter test (PMT 1) and cyclic pressuremeter test (PMT 2) were run at both sides of SC01, at a distance of 5 m.

2.2 *Testing procedures*

To fully characterize the shear modulus reduction curve for the soil, an experimental program was established. The program includes in situ and laboratory tests with on-site soil samples.

2.2.1 *Surface wave methods*

Surface waves methods have gained in popularity for being less expensive and non-intrusive methods for characterizing soils and providing useful information on stiffness profile.

Multichannel analysis of surface waves (Park et al. 1999) was realized on site to define the 1D and 2D shear wave velocities profiles of the site. Knowledge of Vs allows defining in situ low strain shear modulus, G_{max}, with the relationship:

$$G_{max} = \rho V_S^2 \quad (1)$$

where ρ = soil density [kg.m-3]; and V_S = shear wave velocity [m.s-1].

For this experiment, 24 geophones of a frequency of 4.5 Hz were placed in a line on the ground with a distance of 2 m from one to another. The line was moved by steps of 4 m to cover a 80-m long linear profile. A manual penetrometer mass was used as a hitting mass causing the required shock to start signal acquisition.

To obtain the shear wave velocity profile, the data recorded on site were treated by SeisImager and Geopsy. The shear velocity profiles obtained by both computer programs have been compared. SeismImager performs a basic inversion, mainly based on depth and layer thickness, using the least squares method. Geopsy needs prior information to be implemented and uses another method of inversion known as the neighbourhood algorithm. For this study, only the shear velocity profiles obtained with SeisImager were taken into account because the use of Geopsy led to slightly higher Vs values.

2.2.2 *Resonant column tests (RC)*

Resonant column tests were performed to determine the shear modulus from very small strains (~10^{-4}%) (G_{max}) up to shear strains of 10^{-2}%.
Resonant column tests were performed following the standard procedure ASTM D 4015–92 on clayey and sandy material using undisturbed solid cylindrical specimens (D = 50 mm and H = 100 mm). The specimens went through saturation (Skempton's coefficient checked) and consolidation phase before taking undrained tests on them. The shear modulus is calculated from:

$$G = \rho(2\pi L)^2 (f_T / F_T)^2 \quad (2)$$

where L = specimen length [m], f_T = system resonant frequency for torsional motion [s-1], and F_T = dimensionless frequency factor.

2.2.3 *Cyclic triaxial tests (CT)*

The cyclic triaxial tests were run on solid cylindrical undisturbed specimen (D = 50 mm and H = 100 mm) following the standard procedure ASTM D 3999–91. All specimens went through saturation (Skempton's coefficient checked) and consolidation phase before undrained cyclic loading. The single specimen went through staged loading, which means application of progressively increasing levels of load. Each stage consists of 40 loading cycles with the first half cycle loaded in compression. The loading frequency chosen for all the tests was 0.75 Hz. The presented results concern only the modulus determined from the tenth cycle of loading. As stipulated in the standard procedure, the Young's modulus, E, is derived (3) from the test and a shear modulus can then be deduced (4).

$$E = \frac{L_{DA}}{S_{DA}} \times \frac{L_S}{A_S} \quad (3)$$

$$G = \frac{E}{2(1+v)} \quad (4)$$

where L_{DA} = double amplitude load [kN]; S_{DA} = double amplitude deformation [mm]; L_S = height of the specimen after consolidation [mm]; A_S = area of the specimen after consolidation [mm-2]; and v = Poisson's ratio, which for the undrained condition is assumed to be equal to 0.5.

2.2.4 *Monotonic triaxial tests (MT)*

To obtain the reference shear strain, which is a key quantity to derive shear modulus reduction curve, monotonic undrained triaxial tests were realized. Undisturbed solid cylindrical specimens have been used according to French standards NF P 94-070 and NF P 94-074. These tests allowed determining cohesion (c') and internal friction angle (ϕ') for soils. The shear modulus can be obtained by the equation (4) and shear strain, γ, can be calculated from the following equation:

$$\gamma = (1 + v)\varepsilon \quad (5)$$

where ε = axial strain.

2.2.5 *Pressuremeter test and cyclic pressuremeter test (PMT and PMTr)*

The pressuremeter test was developed in France and can be credited to Louis Ménard.

The pressuremeter is a cylindrical device that uses a flexible membrane to apply a uniform pressure to the walls of a borehole. Deformation of the soil can be measured by the volume of the fluid injected into the flexible membrane. After correcting the measured pressures and volume changes, a pressure-volume curve can be obtained and used to compute the stress-strain soil behaviour. Then, useful soil parameters can be obtained, such as: pressuremeter modulus E_M, soil limit pressure p_L and the creep pressure p_F.

To align this test with the logic of shear modulus reduction curve, some precision needs to be added. In fact the theory of the cylindrical cavity expansion relies on Lamé's (1852) equation:

$$\frac{\Delta R}{R} = \frac{1}{2G}\Delta p \quad (6)$$

where G = the shear modulus; R = the radius of borehole; and ΔR = the radius increase as a function of the increase of the pressure Δp on the borehole's wall.

Ménard modified this relation by introducing the Poisson's coefficient (v) conventionally taken to be equal to 0.33. He obtained from it the pressuremeter modulus E_M also called the Ménard's modulus. Since the fifties, the pressuremeter test hasn't stop developing to become nowadays the most used in-situ test in the French geotechnical practice.

Pressuremeter tests were executed following the French standards NF P 94 110-1 and XP P 94 110-2. For the experience realized for this case study, a 44-mm probe was inserted in a slotted tube with a diameter of 56 mm and a test was performed every meter to a depth of 9m. The loading program was realized using an automated pressure-volume controller. As cited above, cyclic pressuremeter tests were realized on site. The probe was inflated to a pressure close to the creep pressure and then deflated to a pressure close to the contact pressure and inflated again to end as an increasing pressure program. This is realized to observe a loop on the pressure-volume diagram, which makes it possible to deduce a reload modulus G_R.

3 RESULTS

The results of all laboratory tests and pressuremeter tests are plotted together in the following charts. All laboratory tests were conducted under the same mean effective confining pressure (that is 60 kPa for silty and clayey specimens and 100 kPa for sandy specimens). To represent shear modulus reduction curve of soils on site, a modified hyperbolic model was fitted to the data. The chosen hyperbolic model reads:

$$\frac{G}{G_{max}} = \frac{1}{1+a\left(\frac{\gamma}{\gamma_r}\right)^b} \quad (7)$$

where a and b = material constants; γ= shear strain; γ_r = reference shear strain calculated as τ_{max}/G_{max}; and τ_{max} = shear stress at failure.

τ_{max} was determined based on shear strength envelopes derived from the consolidated undrained monotonic triaxial tests by using the Mohr-Coulomb failure criterion, as reported by Benz (2007).

As often reported in the literature (Tatsuoka et al. 1995, Pitilakis & Anastasidis 1998, Stokoe & Santamarina 2000) $G_{max}^{in-situ}$ is known to be larger than G_{max}^{lab}. This fact was also verified in this study because it is known that disturbance due to soil sampling and specimen preparation in laboratory causes reduction of low strain shear modulus (Ishihara 1996, Benz 2007). For this purpose Tatsuoka's (1995) normalization was accepted to provide more reasonable results (Pitilakis & Anastasiadis 1998).

Nevertheless, the low strain modulus obtained from shear wave velocity values seemed to be very large (sometimes 4 to 5 times the laboratory low strain modulus) considering the soils encountered on site and the small depth investigated. The use of this

modulus could lead to rapid decrease of the normalized shear modulus, which can be true for low plasticity soils, but it is not always the case in this study. For the reasons cited above, the relation provided by Jamiolkowski et al. (1995) leads to a much more realistic approach for the low strain shear modulus.

$$G_{max}^{in-situ} = \frac{600 \cdot \sigma'^{0.5}_m p_a^{0.5}}{e^{1.3}} \quad (8)$$

where σ'_m = mean effective confining pressure, p_a = reference pressure (equal to 100 kPa), and e = void ratio.

Maximum shear modulus obtained by resonant column tests, G_{max}^{lab}, were chosen to be raised to the $G_{max}^{in-situ}$ values, because of the fact that these types of tests do provide the lowest strains generated in laboratory in our experimental program. Thus the ratio in equation (9) was raised at this value.

$$G(\gamma) = \frac{G(\gamma)^{lab}}{G_{max}^{lab}} G_{max}^{in-situ} \quad (9)$$

The results of all tests were normalized by the $G_{max}^{in-situ}$ values for the three types of soils. Here below are presented the normalized shear modulus reduction curves for clay and sand.

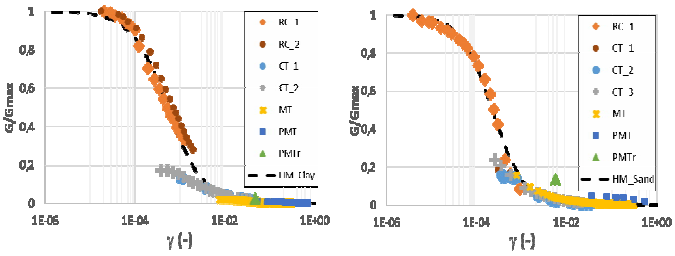

Figure 3. Normalized modulus reduction curve for clayey soil (left) and sandy soil (right)

The normalized modulus reduction curves for the 3 types of soils encountered on site helped developing a strain dependent imagery of the in situ shear modulus. As an example, Figure 4 presents the shear modulus imagery for $\gamma = 10^{-1}$%. This was realized using a basic nodal model based on low strain shear modulus, soil ruptures characteristics, soil density and mean effective confining pressure.

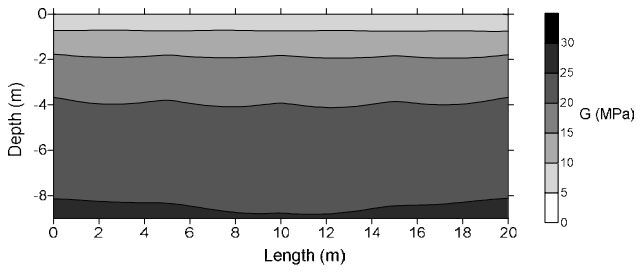

Figure 4. Shear strain-dependent imagery of shear modulus

4 CONCLUSION

An experimental program was applied to a site near Paris in order to fully characterize the modulus reduction curve of soils encountered on site. The program includes in-situ tests such as surface wave methods and pressuremeter tests and laboratory tests such as resonant column tests, cyclic triaxial and monotonic triaxial tests. These tests helped determining the normalized shear modulus reduction curves for the on-site soils. The presented curves do exceed the threshold shear strain of 1% often reported in the literature linked to soil dynamics, in this way we do have modulus values beyond this limit. The strain dependent imagery of the site has been presented.

The in-situ shear modulus obtained by using shear waves velocity values is large. At the moment, we are not capable of establishing how much the presence of calcareous blocs on site does influence the shear velocity profile because we do not know the on-site distribution of these blocs and their dimensions.

5 REFERENCES

Andersen, A. & Kolstad, P. 1979. The NGI 54 mm sampler for undisturbed sampling of clays and representatives sampling of coarser materials. *Proceedings of International Symposium of Soil Sampling,* Singapore, pp. 13-21.

ASTM D3999-91. 2003. Standard Test Methods for the Determination of the Modulus and Damping Properties of Soils Using Cyclic Triaxial Apparatus. *Annual Book of ASTM Standards, ASTM International*, *West Conshohocken, PA*.

ASTM D4015-92. 2000. Standard Test Methods for Modulus and Damping of Soils by Resonant-Column Method. *Annual Book of ASTM Standards. ASTM International*, *West Conshohocken, PA*.

Atkinson, J. H. & Sallfors G. 1991. Experimental determination of soil properties. *In Proc. 10th ECSMFE*, 3, p. 915-956.

Benz, T. 2007. Small-strain stiffness of soils and its numerical consequences. *Ph.d. thesis*, Universität Stuttgart.

Darendeli, M. 2001.Development of a new family of normalized modulus reduction and material damping curves. *PhD thesis*. University of Texas.

El Mohtar, C. S., Drnevich, V. P., Santagata, M. & Bobet, A. 2013. Combined resonant column and cyclic triaxial tests for measuring undrained shear modulus reduction of sand with plastic fines. *Geotechnical Testing Journal*, Vol. 36, No. 4, pp. 1–9.

Geopsy 2005. Sesame European Project, www.geopsy.org.

Ishihara, K. 1996. *Soil behaviour in earthquake geotechnics, chapter 7. Strain dependency of modulus and damping*, pages 127–151. Clarendon Press, Oxford University Press, Oxford, UK.

Jamiolkowski, M., Lo Presti, D.C.F., & Pallara, O. 1995. Role of in-situ testing in geotechnical earthquake engineering.

3rd International Conference on Recent Advances in Geotechnical Earthquake Engineering and Soil Dynamic, State of Art 7, Vol. 3, pp. 1523-1546.

Kramer, S. 1996. *Geotechnical earthquake engineering*. Prentice-Hall, New Jersey, United States of America, 1st edition.

Lamé, G. 1852. *Leçons sur la théorie mathématique de l'élasticité des corps solides*. Bachelier, Paris.

Mair, R.J. 1993. Unwin memorial lecture 1992. Developments in geotechnical engineering research: application to tunnels and deep excavation. *Proceedings of the ICE —Civil Engineering* 97 (1), 27–41.

NF P 94-070. 1994. Essais à l'appareil triaxial de révolution, Généralités – Définitions.

NF P 94-074. 1994. Essais à l'appareil triaxial de révolution, Appareillage – Préparation des éprouvettes – Essai (UU) non consolidé non drainé – Essai (CU+u) consolidé non drainé avec mesure de pression interstitielle – Essai (CD) consolidé drainé.

NF P 94-110-1 .2000. Essai pressiométrique Menard, Partie 1 : Essai sans cycle.

Park, C.B., Miller, R.D. & Xia, J. 1999. Multichannel analysis of surface waves. *Geophysics*, Vol. 64, NO. 3, p. 800–808.

Pitilakis, K. & Anastasiadis, A. 1998. Soil and site characterization for seismic response analysis. In ECEE, editor, *XI European Conference on Earthquake Engineering*, Paris, France. Invited Lecture.

SeisImager/2D/SW. 2009. Geometrics, Inc.

Stokoe, K. H. & Santamarina, J.C. 2000. Seismic-wave-based testing in geotechnical engineering. *GeoEng 2000: An International Conference on Geotechnical and Geological Engineering*, volume 1, pages 1490-1536, Melbourne, Australia. Technomic Publishing Company.

Tatsuoka, F., Lo Presti, D., & Kohata, Y. 1995. Deformation characteristics of soils and soft rocks under monotonic and cyclic loads and their relationships. In Prakash, editor, *Third Int. Conf. on Recent Advances in Geotechnical Earthquake Engineering and Soil Dynamics*, volume 2, pages 851–879, St Luois, MO, USA.

XP P 94-110-2. 1999. Essai pressiométrique Menard, Partie 2 : Essai avec cycle.

Geotechnical and Geophysical Site Characterisation 5 – Lehane, Acosta-Martínez & Kelly (Eds)

An Investigation into the Effects of Material Properties on Shear Wave Velocity in Rocks/Soils

N. Campbell
Jacobs, Brisbane, Australia

C. Fenton
University of Canterbury, Christchurch, New Zealand

S. Tallett-Williams
Imperial College London, London, United Kingdom

ABSTRACT: The shear wave velocity (V_s) in the near surface geology has many uses in seismic design including site classification, ground motion prediction equations and evaluation of liquefaction resistance. V_s also allows assessment of rippability, small strain stiffness and verification of soil improvement work. As part of a broader study into site classification for hazard assessment in the United Kingdom, a database of V_s results from around the world was compiled to investigate the effect of different material parameters on V_s. Through statistical analysis, the effect of origin, fracture spacing and weathering state was explored for rock materials tested in both the laboratory and field. The database of soil results was examined to assess the effects of depositional environment. From the dataset analysed, weathering class has the greatest effect; there is a 52% decrease in V_s for rock as the weathering increases from slightly to moderately weathered. The effect of the depositional environment of soils shows that diverse transportation and deposition processes (wind, water, gravity, glacial or in situ) result in different levels of variability in V_s records. This is related to the degree of grading.

1 INTRODUCTION

The shear wave velocity (V_s) of geological materials has become an important input for earthquake seismic design, where it is primarily used to categorise seismic site conditions. Borcherdt *et al.* (1991) showed a correlation between the average shear wave velocity in the top 30m (V_s30) and the amplification of ground motion. This led to the development of site classification schemes based on V_s measurements used worldwide. As part of a project aiming to improve site classification for hazard assessment in low seismicity countries, the effects of geological history on V_s for differing rock types was investigated. This involved:

a) Compilation of a database of V_s values obtained from studies globally, to understand the controlling factors for V_s in different geological units

b) Investigation of the relationships among depositional environment, geological age and other factors with V_s.

2 DATABASE

In order to investigate the influence of various physical properties on V_s, a statistically significant quantity of data was required to be sourced and analysed. Results from site investigations that included both V_s data directly from in situ testing and the corresponding invasive, geological information were obtained from multiple sources and national databases (Table 1). Correlations with standard penetration test (SPT) results were not considered.

These results were then rationalised to account for differences in local/national terminology and classification standards. This was required to ensure consistency between the results. Where this could not be performed (i.e., the reference standard was unavailable), the data was analysed separately, so as not to mix potentially incompatible V_s data.

Each record collected for the database contains a V_s measurement with corresponding depth and a borehole log, providing details of the subsurface materials, ideally including; the material name, USCS classification, structure (bonding, cementation, laminations, stratification), origin (e.g., alluvial, residual, colluvium, aeolian) and geological age. For rock tests, the degree of weathering and fracture spacing was also recorded.

Table 1. Sources of V_s data

Source	Method	No. of sites	No. of records
United Kingdom (Campbell, 2014)	SCPT	60	258
	Crosshole	27	543
	Downhole	14	109
	CSW	1	4
	Refraction	36	72
	PS Logger	7	229
San Francisco Bay (Gibbs *et al.*, 1975, 1977)	Downhole	58	127
LA County and Oxnard-Ventura (Gibbs *et al.*, 1980) (Fumal *et al.*, 1981, 1982b, 1984)	Downhole	84	203
Central California (Fumal *et al.*, 1982a)	Downhole	10	32
Loma Prieta, California (Gibbs *et al.*, 1992, 1993, 1994a)	Downhole	26	172
Turkey (Middle East Technical University, 2014)	MASW	136	1129
Canada (Natural Resources Canada, 2013a, 2013b)	Downhole	20	60
	SCPT	1	4
	Piezoelectric transducer	-	2882
Washington (Cakir & Walsh, 2010, 2011, 2012)	MASW and MAM	67	249
Taiwan (National Centre for Research on Earthquake Engineering & Central Weather Bureau, 2012)	PS Logger	25	306
Bucharest, Romania (Bala *et al.*, 2006, 2007, 2009)	Downhole	21	110
Laboratory database of silicate rocks (Birch, 1960)	Piezoelectric transducer	-	64
TOTAL		593	6553

3 ANALYSIS

The influences of a number of material parameters on V_s values were examined. These included rock type, discontinuity spacing and weathering for rocks and depositional environment for soils. The results are presented as a box and whisker plot, showing the lower quartile, median and upper quartile (box) within the minimum and maximum values (whisker). The average value is also plotted.

3.1 *Origin (rock)*

The database of laboratory tests on rock samples (n=2946) was examined with respect to their identified origin as sedimentary, metamorphic or igneous. The general trend observed was that sedimentary rocks have the lowest V_s, whilst metamorphic rocks have the highest V_s (Figure 1).

The database of in situ V_s results contains 1096 tests in rock, all of which can be primarily classified as sedimentary, metamorphic or igneous. The quality of the rocks varies according to the weathering and fracture spacing which will be addressed in subsequent sections. However initially, the effect of rock origin was investigated (Figure 1).

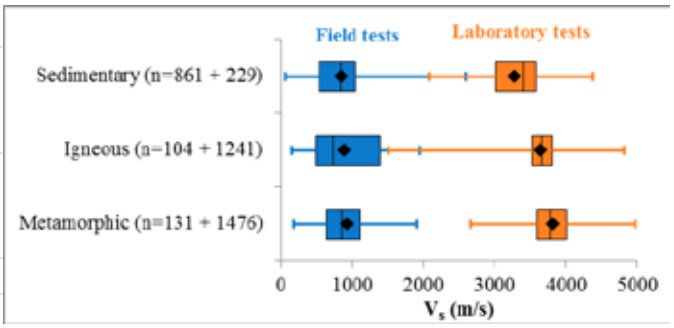

Figure 1. Comparison between field and laboratory V_s results categorized by rock type

The laboratory tests on intact, fresh samples result in higher V_s values compared to tests in the field, with the mean value being 3.8 times higher in sedimentary rock to 4.1 in metamorphic rock. The order of slowest to fastest mean velocity (sedimentary, igneous then metamorphic) is apparent in both data sets, but the magnitude of the increase is larger for the laboratory results.

The reason for discrepancies between the field and laboratory tests is expected to be due to a combination of factors such as accuracy of the test methods, accuracy of material classification (logging), scale effects, boundary conditions, weathering state, confining stress, fracture spacing and anisotropy. Several of these factors will be explored in subsequent sections:

3.2 *Fracture Spacing*

The majority of V_s records which included companion fracture spacing descriptors came from two sources; the Turkish national database and USGS reports (Table 1). The qualitative terms for fracture spacing used in the Turkish logs could not be directly compared with the quantitative categories used in the USGS database, therefore these datasets have been analysed independently, with the Turkish results presented in this paper.

A preliminary analysis of the Turkish data (Figure 2) indicate a possible decrease in V_s as the degree of fracturing increased (i.e., fracture spacing decrease). However two of the six categories do not conform to this trend, namely 'moderately to slightly jointed' (n=3) and 'crushed to highly jointed' (n=5) materials. This may be due to the fact that these two categories contain the lowest number of records of the six defined fracturing classes. Furthermore, four of the five results in the 'crushed to highly jointed' category are identified as Paleozoic aged sandstone, which would be expected to have likely undergone metamorphism and could potentially be a quartzite of much higher strength and therefore velocity than materials typical of sandstone. The effect of geological age was also investigated and it was found that in general, older materials have higher shear wave velocities (N.B., the majority of data in the conforming categories are Cenozoic or Mesozoic in age).

Figure 2. V_s results according to fracture classification [Turkish Data (Middles East Technical University, 2014)]. The linear trend between V_s and fracture density is shown by the dashed line.

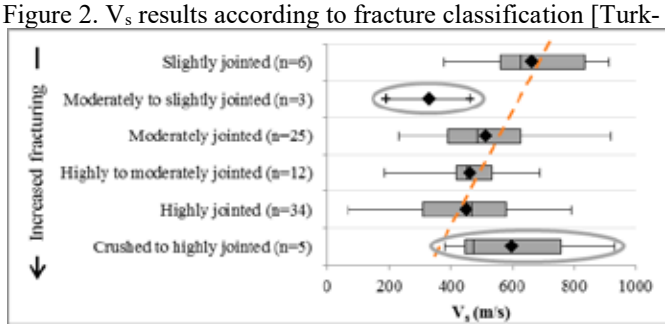

3.3 *Weathering*

Within the compiled database 461 V_s measurements are accompanied by a description of the weathering state of rock materials. The highest V_s values, on average, are observed in fresh rock, continually decreasing to the slowest V_s in completely weathered material (Figure 3).

There is a notable change at the moderately to slightly weathered gradational boundary. Less weathered rocks resulted in an average value of approximately 1050m/s whereas the more weathered material was approximately 500m/s (a 52% decrease). The boundary between slightly and moderately weathered, marks the state of weathering where mineral grain decomposition begins, producing some 'soil like' material. Overall, soils have a lower velocity than rock, so the decrease observed at this grade is expected.

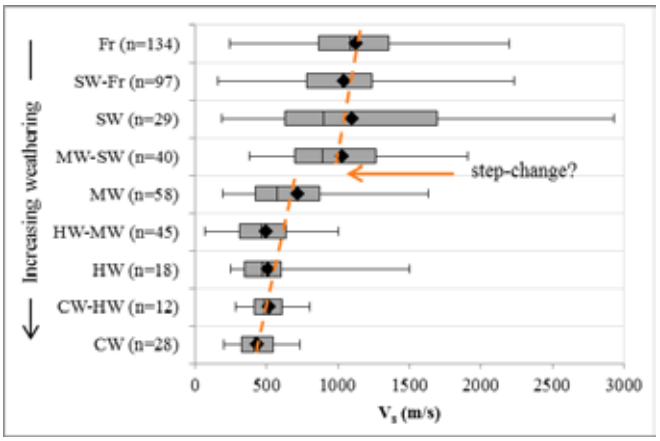

Figure 3. V_s results grouped by weathering category. Dashed line indicates a linear trend between weathering and V_s, with a step-change at the slightly to moderately weathered boundary.

3.4 *Depositional Environment / Origin*

Of the 2471 V_s records for soil, 1954 (79%) contained information relating to the material origin or depositional environment. Although numerous descriptions of origin were provided on the logs and in original reports, these were reviewed and simplified in order that they could be grouped into seven categories (Figure 4).

Residual soils (i.e., weathered in situ from parent rock) show high variability of V_s results with a coefficient of variation (CoV) of 60%. This has been attributed to the dataset covering a range of material types (clay, silty clay, gravelly sand, gravelly clay, etc) and the records also span a number of geological eras (Paleozoic, Mesozoic and Cenozoic).

The least variable data is the aeolian material, having an interquartile range of V_s = 202 - 325m/s and CoV = 33%. This dataset has been compiled from observations made across numerous sites in three countries (Turkey, USA and Romania, Table 1), yet the results remain relatively consistent across all locations. The transportation process (wind) results in selective material sorting, predominantly silt, therefore aeolian data is likely to be the most uniform material in terms of grain size.

Visual inspection of the resultant plot (Figure 4) indicates that all the depositional environments essentially present a similar total range of results (i.e., minimum ~ 100m/s to maximum ~ 1050m/s). The estuarine, alluvial and aeolian environments display similar average V_s values (category 1, V_s = 280m/s), with a second grouping identified for the colluvial, glacial and residual environments (category 2, V_s = 450m/s). The average Category 1 value is 38% less than the Category 2 results.

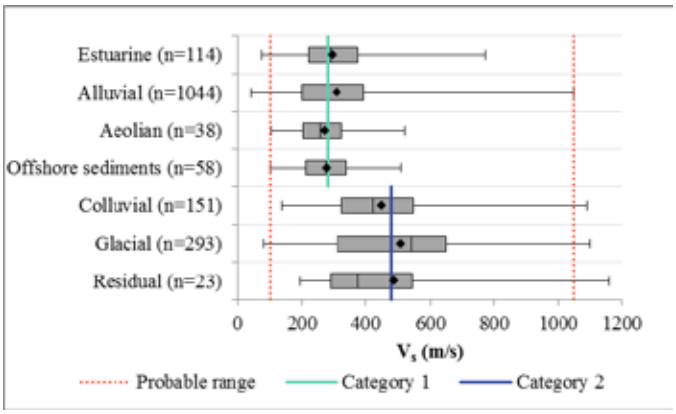

Figure 4. V_S results for soils according to depositional environment

Considering the nature of each of the environment categories, the colluvial, glacial and residual materials (category 2) are most likely to be predominantly well graded as the materials are not sorted during the transportation process. The opposite was expected for the estuarine, alluvial, aeolian and offshore environments, whereby the transportation process (water or wind) would lead to selective transportation and thus sorting of the materials. Wind or water transport would likely result in a comparatively uniform grain size at any particular location. This is in agreement with the observations of Wills *et al.* (2000), who reported that dune sands, basin, lake and beach, deposits have a distinctive (inferred to suggest uniform) grain size distribution, and this material parameter would lead to less variation in V_s values when compared to most bedrock units.

4 CONCLUSION

A global database containing 6531 individual measurements was compiled to examine the influence of various geological characteristics on V_s. This involved the sourcing and assessment of 594 ground investigation site records from 11 different sources. These data allowed statistical analyses of the effects of various parameters on V_s values. Weathering class has the greatest effect; with a 52% decrease in V_s as the weathering increases from slightly to moderately weathered. The effect of the depositional environment of soils shows that diverse transportation and deposition result in different levels of variability in V_s record, related to the degree of grading

5 ACKNOWLEDGMENTS

The authors would like to thank the UK industry partners for providing many sources of data. International data were obtained, with thanks, from Dr Andrei Bala of the National Institute of Earth Physics, Romania, Mr Rudolfo Puglia of the Intituto Nazionale di Geofisica e Vulcanologia, Italy, Mr Hung-Hao Hsieh of the National Center for Research on Earthquake Engineering, Taiwan, Mr Warner Miles of the Geological Survey of Canada and Dr Oz Yilmaz for information on the Turkish database. Without their contributions, the research database would not have been nearly as diverse.

6 REFERENCES

Bala, A., Balan, S. F., Ritter, J. R. R., Dannich, D., Huber, G. & Rohn, J. (2007) Seismic site effects based on in situ borehole measurements in Bucharest, Romania. International Symposium on Strong Vrancea Earthquakes and Risk Mitigation. 4-6 October 2007, Bucharest, Romania.

Bala, A., Grecu, B., Ciugudean, V. & Raileanu, V. (2009) Dynamic properties of the Quaternary sedimentary rocks and their influence on seismic site effects. Case study in Bucharest City, Romania. Soil Dynamics and Earthquake Engineering. 29 (1), 144-154.

Bala, A., Raileanu, V., Zihan, I., Ciugudean, V. & Grecu, B. (2006) Physical and dynamic properties of the shallow sedimentary rocks in the Bucharest metropolitan area. Romanian Reports in Physics. 58 (2), 221-250.

Birch, F. (1960) The velocity of compressional waves in rocks to 10 kilobars, part 1. Journal of Geophysical Research. 65 (4), 1083-1102.

Borcherdt, R. D., Wentworth, C. M., Janssen, A., Fumal, T. & Gibbs, J. (1991) Methodology for predictive GIS mapping of special study zones for strong ground shaking in the San Francisco Bay region, California. 4th International Conference on Seismic Zonation. 26-29 August, California. pp.545-552.

Cakir, R. & Walsh, T. J. (2010) Shallow seismic site characterisations of near-surface geology at 20 strong-motion stations in Washington State. Washington Department of Natural Resources. Report number: G09AP00021.

Cakir, R. & Walsh, T. J. (2011) Shallow seismic site characterisations at 23 strong-motion stations in and near Washington State. Washington Department of Natural Resources. Report number: G10AP00027.

Cakir, R. & Walsh, T. J. (2012) Shallow seismic site characterisations at 25 ANSS/PNSN stations and compilation of site-specific data for the entire strong-motion network in Washington and Oregon. Washington Department of Natural Resources. Report number: G11AP20045.

Campbell. (2014) An investigation into the effects of material properties on shear wave velocity in rocks and soils (Unpublished master's dissertation). Imperial College London, United Kingdom.

Fumal, T. E., Gibbs, J. F. & Roth, E. F. (1981) In situ measurements of seismic velocity at 19 locations in the Los Angeles, California region. California, USGS. Report number: 81-339.

Fumal, T. E., Gibbs, J. F. & Roth, E. F. (1982a) In situ measurements of seismic velocity at 10 strong motion accelerograph station in Central California. California, USGS. Report number: 82-407.

Fumal, T. E., Gibbs, J. F. & Roth, E. F. (1982b) In situ measurements of seismic velocity at 22 locations in the Los Angeles, California Region. California, USGS. Report number: 82-833.

Fumal, T. E., Gibbs, J. F. & Roth, E. F. (1984) In situ measurements of seismic velocity at 16 locations in the Los Angeles, California region. California, USGS. Report number: 84-681.
Gibbs, J. F., Fumal, T. E., Boore, D. M. & Joyner, W. B. (1992) Seismic velocities and geologic logs from borehole measurements at seven strong-motion stations that recorded the Loma Prieta earthquake. California, U.S. Geological Survey. Report number: 92-287.
Gibbs, J. F., Fumal, T. E. & Borcherdt, R. D. (1975) In situ measurements of seismic velocities at twelve locations in the San Francisco Bay region. California, U.S. Geological Survey. Report number: 75-564.
Gibbs, J. F., Fumal, T. E., Borcherdt, R. D. & Roth, E. F. (1977) In situ measurements of seismic velocities in the San Francisco Bay region: Part III. California, U.S. Geological Survey. Report number: 77-850.
Gibbs, J. F., Fumal, T. E. & Powers, T. J. (1993) Seismic velocities and geologic logs from borehole measurements at eight strong-motion stations that recorded the 1989 Loma Prieta, California, earthquake. California, U.S. Geological Survey. Report number: 93-376.
Gibbs, J. F., Fumal, T. E. & Powers, T. J. (1994a) Seismic velocities and geologic logs from borehole measurements at seven strong-motion stations that recorded the 1989 Loma Prieta, California, earthquake. California, U.S. Geological Survey. Report number: 94-222.
Gibbs, J. F., Fumal, T. E. & Roth, E. F. (1980) In situ measurements of seismic velocity at 27 locations in the Los Angeles, California region. California, USGS. Report number: 80-378.
Middle East Technical University - Earthquake Engineering Research Centre. (2014) Strong ground motion database of Turkiye. [Online] Available from: http://kyhdata.deprem.gov.tr/2K/kyhdata_v4.php [Accessed 17 June 2014].
National Centre for Research on Earthquake Engineering & Central Weather Bureau. (2012) Engineering geological database for TSMIP [Online] Available from: http://egdt.ncree.org.tw/news_eng.htm [Accessed 25 June 2014].
Natural Resources Canada. (2013a) Borehole Geophysical Logs in Surficial Sediments of Canada. [Online] Available from: http://geogratis.gc.ca/api/en/nrcan-rncan/ess-sst/-/%28urn:iso:series%29borehole-geophysical-logs-in-surficial-sediments-of-canada [Accessed 30 June 2014].
Natural Resources Canada. (2013b) Earth Sciences Sector (Aeromagnetic, Gravity or Radioactivity data). [Online] Available from: http://gdr.agg.nrcan.gc.ca/gdrdap/dap/index-eng.php?productid=1576 [Accessed 3 July 2014].
Wills, C.J., Petersen, M., Bryant, W., Reichle, M., Saucedo, G., Tan, S., Taylor, G. & Treiman, J. (2000) A site-conditions map for California based on geology and shear-wave velocity. Bulletin of the Seismological Society of America. 90 (6B), S187-S208.

Geotechnical and Geophysical Site Characterisation 5 – Lehane, Acosta-Martínez & Kelly (Eds)

Integrated use of terrestrial laser scanning and thermal imagery for characterization of hydrothermally altered granites

J.S. Coggan, D.M. Pascoe, & M.L.Eyre
University of Exeter, Cornwall, UK

J.H.Howe
IMERYS Minerals Ltd, Cornwall UK

ABSTRACT: The assessment of material properties is a fundamental component of geotechnical characterization of slopes in hydrothermally altered granite, as potential slope failure mechanisms are controlled by kaolinization intensity, discontinuity characteristics (such as orientation, persistence and spacing) and the detrimental effects of groundwater. In order to assess the potential advantages of remote mapping technologies for improved spatial cover both laser scanning and photogrammetry have been evaluated within the china clay operations for use in rock mass characterization. The results presented also focus on application of the remotely captured data for use in design of china clay slopes in southwest England. A key benefit of the detailed geo-referenced point cloud data is the ability to measure and evaluate discontinuity characteristics such as orientation, spacing, persistence and volumetric data which are key factors that dictate the size of any potential failure. In addition to capturing rock mass characteristics, accurate slope geometries and digital terrain models can be derived for more effective slope management. Through use of photo-overlays and coloured point cloud data captured from use of terrestrial laser scanning, based on red green blue (RGB) values, it was also possible to evaluate discontinuity type, such as tourmaline veins within the point cloud. Integration of laser scanning derived data with overlays from infra red and thermal images was also performed to assist identification of alteration zones within a slope. The results highlight the benefits of using remote mapping technologies for rock mass characterization and acquisition of spatial data for planning purposes.

1 INTRODUCTION

1.1 *Geological Setting*

Kaolinized china clay areas of the granite batholith can be found in Cornwall, including the centrally positioned deposits in St Austell. The long history of china clay extraction, since deposits were first discovered by William Cookworthy in 1746, has left a legacy of historical pit faces which were designed prior to the Quarry Regulations (Health and Safety Executive, 2013).

This paper discusses the combination of 3-D laser scanning and thermal infrared imaging which was used to map historic bench faces in the china clay pits to provide input parameters for rock mass characterisation to allow slope stability analyses to be carried out.

1.2 *Kaolinization of Granite*

Kaolin (china clay) is produced by the alteration of granite, through the interaction of hydrothermal fluids and groundwater with feldspar causing hydrothermal decomposition to form kaolinite (Wilson, 2006).

Lower temperature (<100ºC) high salinity hydrothermal fluids also played a major role in the kaolinization process (Psyrillos *et al*., 1998; Manning *et al*., 1996) also indicated that meteoric water was also involved. It is also considered that both hydrothermal and low-temperature weathering processes were contributing factors (Bristow and Exley, 1994). The grading system for the china clay deposits in Cornwall used by Imerys is shown in Table 1.

In lower grades of kaolinized granite, in particular Grades II and III, slope failures are most likely to be kinematically controlled by discontinuities within the rock mass, causing wedge, toppling and plane failure along with general rockfall from the bench crests. Rock fall due to unfavourably aligned joint surfaces in a higher bench may affect development at lower levels towards the toe of the slope. Rock-trap design to overcome this safety risk is of great importance.

In more highly kaolinized granite (Grades IV and V), rotational failures through the body of the rock are more likely and require continuum modelling of

slope stability, although relict discontinuities can still have an effect. Thus the degree of kaolinization highly influences the design of pit slopes, with overall slope angles in highly kaolinized zones being as low as 25 degrees.

Table 1. China clay grading (altered from Stead et al. 2000)

Grade	Description	Characteristics	Geological hammer blows (break)	Unconfined Compressive Strength (UCS) values based on Schmidt hammer rebound value
I	Fresh rock	No visible alteration	Multiple	n/a
II	Slightly altered	Slight discolouration and weakening	More than one	>45 MPa
III	Moderately altered	Considerable weakening, penetrative discolouration	Single	25-45 MPa
IV	Highly altered	Large pieces broken by hand	n/a	0-25 MPa
V	Completely altered	Considerably weakened, original texture preserved, slakes readily in water	Geological pick penetrates	50-250 kPa
VI	Residual soil	Soil mixture with no rock	n/a	<50 kPa

In less kaolinized zones, individual benches can be near vertical as demonstrated in Figure 1, where the slope of this historic bench face is approximately 26 m high at an inclination of 80+/-5 degrees with significant rock traps constructed to manage risk. Also shown in the photograph is the presence of several narrow highly kaolinized zones within this mostly poorly kaolinized bench face which have been oriented using remote methods, as described in this paper.

Figure 1. Photograph of a section of historical bench face (striking N-S) with several sub-vertical kaolinized zones, found within poorly kaolinized rock. Discontinuities sets of high angle joints striking sub parallel to the face subject to possible toppling failure.

2 STRUCTURAL ORIENTATIONS

Tectonic, lithostatic and thermal stresses and pore pressures set up strain in rock leading to the formation of discontinuities. Stead *et al.*, (2000) reported that the kaolinization in the St. Austell granite is structurally controlled and generally occurs in association with greisen, tourmaline and quartz veining. The kaolinized zones are often orientated parallel to NW-SE and ENE-WSW striking structures due to the in-situ stresses at the time of formation. NNW-SSE trending wrench faults known as cross courses also occur throughout the Cornubian orefield. Some of the outcropping kaolinized zones are up to several hundreds of metres across and tend to be funnel-shaped or trough-like in cross section, narrowing downwards with stems more than 300m below surface. An understanding of these structural controls on discontinuities and alteration grade, can be gained using remote sensing methods required to enable safe slope design.

2.1 *Remote Sensing*

The excavated slopes investigated within the china clay area, exhibit various levels of stability, making direct access to the faces unattainable. This inaccessibility necessitates the use of remote sensing, preferably using a combination of methods: 3-D laser scanning and thermal infrared imaging as described in this paper.

2.2 *3-D Laser Scanning*

Terrestrial LiDAR scanners are based on electromagnetic distance measurement. Using the known constant speed of light, the range to the target can be calculated. In addition, angular measurement is also obtained electronically. Multiple scans from different locations along the slope face minimized the blinding effect (occlusion) of a single line of sight (Sturzenegger and Stead, 2009). The individual scans were joined together in Cyclone software to produce the combined image in Figure 2 (consisting of 20 million points). The point cloud was split vertically into five sections to speed the processing in Split-FX software (Split-FX, 2013) which was used to analyse the three dimensional point cloud data.

The laser scan in Figure 2 shows the coloured point cloud based on the RGB (red, green, blue) values. This technique has the potential for a further degree of identification of discontinuity type – vein, joint, fault etc. For instance, the tourmalinized joints can be picked out by their dark grey/black colouration.

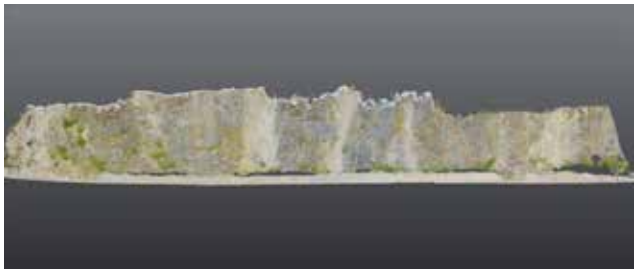

Figure 2. Coloured point cloud of an historic excavated face in a china clay pit

2.3 *Analysis of point clouds using Split FX software*

Point cloud data was imported into Split-FX software, to enable the orientation of discontinuities to be identified. Zones where no patches could be fitted

corresponded mostly with highly altered zones where the joints have been obscured by the process of kaolinization. Where discontinuities were striking almost perpendicular to the bench face it was not always possible to fit patches to the surface of the discontinuity and 'traces' were fitted, enabling orientation of these joints to be determined as demonstrated in Figure 3.

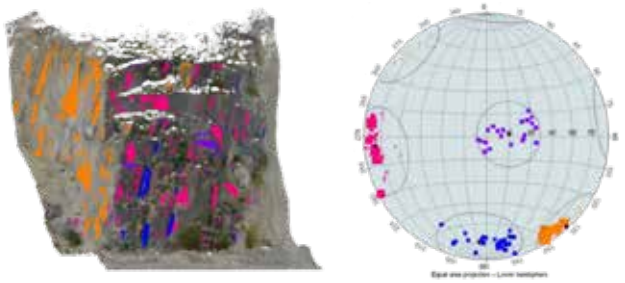

(a) (b)

Figure 3. a) 3-D laser scan of section of pit benches indicating patches (angular) and traces (ovoid) added b) Stereoplot of section of NE face pit bench indicating poles of patches (angular) and traces (ovoid) with each joint set colour-coded.

Orientation data for each of the major sets identified in each of the four sections of the slope are shown in Table 2.

Table 2. Orientation data for major joint sets in 5 sections of the bench.

Set number	Dip	Dip Direction	Fisher K
1	81	082	134.5
2	86	310	154.9
3	77	348	147.8
4	18	251	47.9

The major planes plot indicates the average pole for each set identified from cluster data and these results are given in Table 3. Contouring is enabled in Dips using the "floating cone" method in which pole counting is done on the 3-D sphere. Fisher's constant (K), which gives some measure of the degree of clustering in a given set.

Dominant joint set 1 is preferentially sampled as it strikes almost parallel to the bench face, dipping into the slope face at 81 degrees towards 082°. Set 4 is nearly horizontal and has the lowest k value.

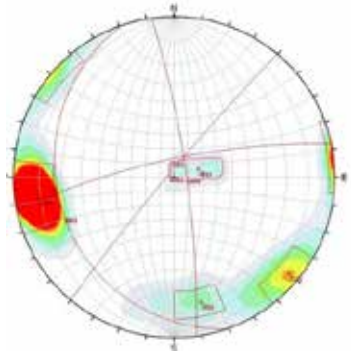

Figure 4. Contoured lower hemisphere equal angle stereographic projection of discontinuities in combined sections 1- 5.

Table 3. Mean poles of major joint sets and Fisher constants in east face of Melbur Pit

Section	Set 1 (pink) Orientation (Dip/Dip Dir.)	Set 2 (orange) Orientation (Dip/Dip Dir.)	Set 3 (blue) Orientation (Dip/Dip Dir.)	Set 4 (purple) Orientation (Dip/Dip Dir.)
1	82/076	88/298	79/007	05/257
2	77/083	78/304	74/355	14/270
3	77/082	87/317	75/004	15/264
4	85/078	84/316	70/355	21/267
5	74/073	84/294	79/344	14/241

It is also possible to determine estimates of the true spacing and persistence of discontinuities using Split-FX, achieved by measuring the perpendicular distance between fitted traces and patches. The probability density distributions of both total discontinuity lengths and spacings are shown in Figure 5. Individual joint set spacings from sections 2, 3 and 4 are presented in Table 4.

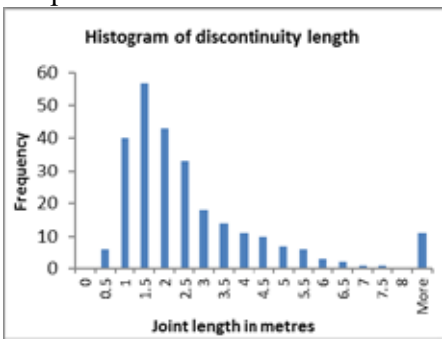

Figure 5. Histogram of discontinuity length.

Table 4. Mean poles of major joint sets and Fisher constants in east face of Melbur Pit

Set 1 (pink)				
	Spacing			
Section	Mean	Maximum	Minimum	Standard deviation
1	0.7	2.37	0.15	0.54
2	0.47	1.06	0.11	0.29
3	0.64	1.54	0.24	0.4
4	0.5	1.27	0.07	0.3
Set 2 (orange)				
	Spacing			
Section	Mean	Maximum	Minimum	Standard deviation
1	0.91	1.8	0.22	0.47
2	1.31	2.21	0.59	0.53
3	1.12	3.92	0.12	1.1
4	1.07	2.06	0.23	0.57
Set 3 (blue)				
	Spacing			
Section	Mean	Maximum	Minimum	Standard deviation
1	1.24	2.47	0.46	0.63
2	1.13	2.25	0.44	0.53
3	2.41	5.8	0.26	1.41
4	0.94	1.67	0.34	0.44
Set 4 (purple)				
	Spacing			
Section	Mean	Maximum	Minimum	Standard deviation
1	0.84	1.73	0.23	0.39
2	0.68	1.25	0.25	0.33
3	1.67	3.99	0.21	1.25
4	1.69	3.09	0.79	0.62

Measurements of true persistence were exported directly from Split-FX, shown in Table 5. It can be seen, traces in section 2 appear to be approximately twice as long as in the other sections. Upon reviewing the point clouds data there are two very long individual traces of 20.8 and 24.41m listed which skew the data.

Table 5. True trace lengths exported from sections of NE face of Melbur Pit.

Section	Mean true lengths	Standard deviation
1	1.83	1.33
2	4.02	4.6
3	2.27	2.01
4	2.50	1.86
5	2.47	2.49

2.4 *Kinematic Analysis*

Based on the data described above, the preliminary kinematic analysis which quantifies the likelihood of plane, wedge and toppling failures was carried out for the east face of the pit and the results are shown in Figure 6 (a)-(d) where the pink shaded areas identify the critical sets or intersections of joint sets for each failure mode.

Kinematically, the opportunities for both direct/oblique and flexural toppling failures are predominant with planar and wedge failure being much less significant. Input data included a slope dip of 70, dip direction of slope of 270° and angle of internal friction of 30°. As seen in Figure 6(a), plane failure analysis indicated that of the 796 discontinuities created by fitting patches and traces to the point cloud, only 15 (1.9%) were deemed critical. Figure 6(b) shows there is a low possibility of wedge failure with an estimated 4.3% of joint intersections being classified as critical due to them daylighting in the slope and the chosen friction angle of 30° exceeded. For direct toppling, including oblique toppling to occur, high angle joints dipping into the slope face are required plus an intersection with another high angle joint set, to form the vertical slabs. Of a possible total of 316,180 intersections 5.2% were critical. For oblique toppling however, 47% of the intersections were critical. As demonstrated in Figure 6(d), Set 1 is the most critical joint set for flexural toppling and this mode of failure is deemed to be of most importance in slope stability in this bench area. Pre-split blasting to re-profile parts of this slope is described in Keverne *et. al.,* 2015.

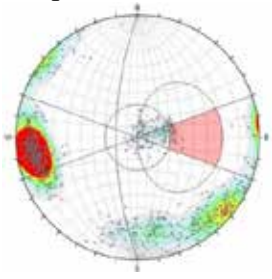

6 (a) Planar failure

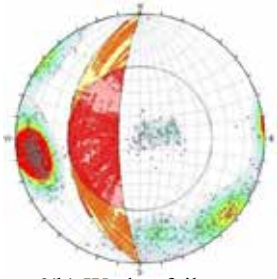

6(b) Wedge failure

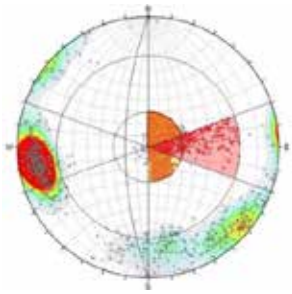

6(c) Direct toppling

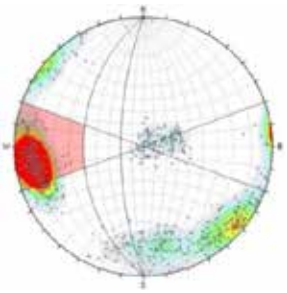

6 (d) Flexural toppling

	Critical	Total	%
Direct toppling (intersection)	16451	316180	5.2
Oblique toppling (intersection)	148110	316180	46.8
Base plane (all)	96	796	12.1
Base plane (set 4)	57	63	90.5

	Critical	Total	%
Flexural toppling (All)	327	796	41.1
Flexural toppling (Set 1)	296	304	97.4

Figure 6. Kinematic analysis of East face of Melbur Pit.

3 THERMAL INFRARED IMAGING

Objects at a temperature of less than 500 °C emit thermal radiation in the infrared spectrum. Thermography is a Non-Destructive Testing (NDT) technique in which temperature changes on the surface of rock exposures can be used to assess underlying conditions and interior discontinuities in some cases. Radiometric images or thermograms can be generated by a thermal imager in the infrared (IR) band, roughly 9,000–14,000 nanometers. When rock is loaded, the thermal infrared radiation of the rock surface changes.

3.1 *Previous work linking TIR studies with geomechanics*

McHugh and Girard (2002) investigated thermal imaging to distinguish geomechanical structure in mining environments. They considered that the differential cooling as a result of water saturation levels and flows in wall rocks have the potential to map geologic faults, contacts, and altered zones. Temperatures are greater in high-stress areas than low-stress areas and according to Liu et al, 2011 tension fractures appear as temperature-decrease anomalies. They determined that a thermal imager could detect a loose rock block in a mine tunnel. The same authors presented the results of infrared imaging of a slope in an opencast mine. Two lower temperature areas correlated with a compressive zone and a fault separated by a higher temperature zone between them. Although this may seem counter-intuitive, they postulated that fractured rock in the two areas contained more water so the temperature in the fault and the compressive zone are lower.

The infrared thermograms obtained by Martino and Mazzanti (2013) identified positive and negative anomalies in the temperature variations which corresponded to joint sets and discontinuities within the face of the slope. Thermal imaging was used in slope stability analysis and the implications of ground water in the slope face were assessed by Zwissler (2013). Due to the instability of the cliffs, no invasive soil sampling or testing was performed on the cliffs, however thermal imagery was used in the assessment of ground water. The FLIR thermal IR imaging indicated a band of lower temperature with respect to the temperature of the surrounding soil, which was associated with moisture (Zwissler (2013)).

3.2 *TIR imaging within china clay pits*

The aim was to investigate the changes in temperature in a bench section of a china clay pit. Data was collected and images taken during June and July 2014. The thermographic images were created using a FLIR ThermaCAM$_{TM}$ B2. 3-D laser scans obtained from the same location were merged with both infrared and digital photographic images using Cyclone 9 software and Photoshop. To correct the target pit face temperature, the IR camera software required inputs for the emissivity of the object, atmospheric attenuation and temperature, and temperature of the ambient surroundings. The emissivity value was standardised at 0.82 for the granite as the surface was rough and weathered (Danov *et al*., 2007). Batch photographs were taken from the same location which allowed for an overlay/blending of the images afterwards. At each site the IR camera settings were altered with an approximate atmospheric temperature. The majority of the images were standardised within a temperature range of 8–19˚C based on measured temperatures of the ambient surroundings. Another method of calibration involves measuring the temperature of several points on the scanned object using a thermocouple. However, in remote monitoring situations this is not possible.

The IR camera was manually adjusted to focus on the required slope. The temperature range was also altered on site to provide a clearer representation of the slope; however, this was problematic later on in the process when collating the images due to the influence of the sun.

3D analysis of thermographs was also achieved by overlaying the thermal images onto point clouds of the same bench face position.

3.3 *Example results*

Figure 7 shows firstly, an example of overlapping the rectangular thermal images onto a digital photograph and secondly draping the thermal images onto a 3-D point cloud. The blue areas indicate colder zones which are postulated to be structures which, at some stage of their genesis, have been subject to alteration by fluids penetrating along lower stress discontinuities in the rock. These may still be conduits for groundwater flow. The advantage of draping thermal images over the point cloud is that the orientation of specific discontinuities can then be determined in Split FX. Several features of interest are noted on the images in Figure 8, numbered 1, 2 and 3.

1. A sub-horizontal discontinuity coloured blue in the infrared image, suggesting that moisture also infiltrated horizontally at this point.

2. Intersection of two discontinuities is clearly visible in an area devoid of shadow.

3. Major sub-vertical discontinuities striking perpendicular to the face are indicated by dark blue features in the infrared images. These correspond to Set 2 (blue) shown in Figure 3. From the mean pole of this set indicated in the major plane plot in Figure 6 and data in Table 3 the mean pole of this set is orientated at 77°/348°.

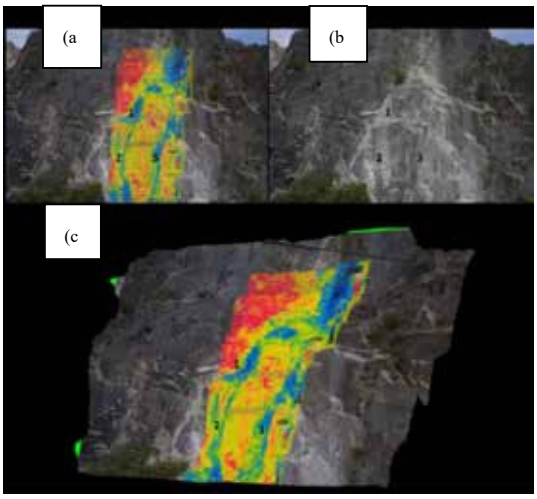

Figure 7. (a) 2D thermal overlay on RAW format digital image. (b) Digital RAW format photograph. (c) 3-D manipulation of thermal image draped over the point cloud. The numbering on the images represents key areas of interest explained in the text above.

Figure 7 also demonstrates that surfaces of discontinuities that have been subject to alteration have a different thermal response to unaltered rock faces. The highly kaolinized zone to the left hand side of the thermograms in Figure 8(a), indicated by numbers 2 and 4, is characterized by dark blue coloured thermographic imaging indicating the lowest temperatures equating to approximately 8°C. The orientation of this particular highly kaolinized discontinuity surface corresponds to Set 4 (orange) in Figure 3. In Table 2 the mean orientation of this major joint set in this section of the bench is seen to be 86°/310°.

Figure 8. (a) Thermal images draped over point cloud of same position depicted in figures 6 and 10 (b) Raw format digital image of same exposure aids identification of specific features.

4 CONCLUSIONS

This preliminary study of combined remote methods produced promising results. The results of 3-D laser scanning provided input data for kinematic slope stability analysis. In more conventional scan-line mapping of a single section carried out by geotechnical personnel, a bias occurs in the mapped discontinuity orientation data depending on the orientation of the scanline, hence it is recommended that three orthogonal scans be carried out. The effect of scanline direction with respect to particular discontinuity orientations is different for 3-D laser scanning but a bias still occurs. In order to obtain a more representative sample of joint at least two orthogonal faces were scanned in each pit and this will be explored in a further paper. In addition, for each exposure, scans were obtained from several different orientations to reduce occlusion.

For this research patches and traces were fitted individually in Split-FX rather than automatically. Images obtained from Terrestrial Infrared (TIR) imaging, combined with 3-D laser scans were used to identify particular joint orientations associated with alteration/fluid flow. Ideally future work should be undertaken using a 3-D laser scanner which incorporates a thermal camera which would avoid any errors in fitting the digital and laser images together. Zones where no patches could be fitted to the point cloud in Split-FX corresponded mostly with the wider kaolinized zones where the joints have been obliterated by the process of kaolinization. Using infrared thermal imaging the kaolinized zones in the slope were not only identifiable due to the low temperature profiles but the more precise positions of altered zones were identifiable within areas covered with superficial coating of washed out clay. The clear depiction of vegetation in thermograms is an issue however in that underlying discontinuities are obscured meaning that only clean faces can be fully analysed using thermography.

Kinematic analyses can be carried out using actual slope angles and directions in critical zones rather than representative values. Orientation of kaolinized zones can be determined using the combined thermal IR (TIR) images draped onto the 3-D laser scans. This research has demonstrated the potential use of combined remote methods for slope characterization, understanding of groundwater flow and mineralogical recognition.

5 ACKNOWLEDGEMENTS

Application of remote technology for data capture leading to improved rock mass characterization is part of research within the STOICISM project. The STOICISM research project has been supported by the European Commission under the 7th Framework Programme through the grant number 310645.

6 REFERENCES

Bristow and Exley, 1994. Historical and geological aspects of china clay industry of southwest England. Transactions of the Royal Geological Society of Cornwall, 21 (1994): 247–314.

Cyclone 9 software. 2014. *http://www.leica-geosystems.com/en/hds-software-leica-cyclone_6515.htm*

Danov, M., Petkov, D., Tsanev, V. 2007. 'Investigation of thermal infrared emissivity spectra of mineral and rock samples'. New developments and challenges in remote sensing. http://www.gbv.de/dms/tib-ub-hannover/531900762.pdf

Dips 6, Rocscience. 2006. Structural data processing software, Toronto. *http://www.rocscience.com/products/1/Dips*

FLIR Quick report software. *http://www.flir.co.uk/instruments/display/?id=60093*

Health and Saftety Executive. 2013. Health and safety at quarries. The Quarries Regulations 1999. Approved Code of Practice ISBN: 9780717663354

Keverne, B., Howe, J., Pascoe, D., Eyre, M., Coggan, J. 2015. 'Remediation of a hazardous legacy slope face using pre-split blasting' Eurock 2015. In preparation

Liu, S., Xu, Z., Wu, L., Ma, B., Liu, X. 2011. 'Infrared Imaging Detection of hidden dangers in mining engineering'. Progress in Electromagnetics research symposium proceedings.

Manning, D.A.C., Hill, P.I. & Howe, J.H. 1996. 'Primary lithological variation in the kaolinized St Austell Granite, Cornwall, England'. *J. of the Geological Society*, London, 153: 827-838.

Martino, S., Mazzanti, P. 2013 .Integrating geomechanical surveys and remote sensing for sea cliff slope stability analysis: the Mt. Pucci case study (Italy). Natural hazards and earth system sciences. 14: 831-848.

McHugh, E.L., Girard, J.M. 2002. Evaluating techniques for monitoring rock falls and slope stability.

Psyrillos, A. Manning, D.A.C. & Burley, S.D. 1998. 'Geochemical constraints on kaolinization in the St Austell granite, Cornwall, England. *Journal of the Geological Society*. 155: 829-840

Split-FX 64. Split Engineering. 2013. Version 2.1.0 *http://www.spliteng.com/products/split-fx-software/*

Stead D, Coggan JS, Howe JH. 2000. Engineering geology and hazard assessment of excavated china clay slopes, Geoscience in South West England, 10, PT 1 2000 (10): 72-76.

Sturzenegger, M. and Stead D. 2009. 'Close-range terrestrial digital photogrammetry and terrestrial laser scanning for discontinuity characterization on rock cuts'. *Engineering Geology*, Volume 106, Issues 3–4, 12 June 2009: 163-182

Zwissler, B.E. 2013. 'A study of the thermal impacts of freeze-thaw on cliff recession at the Calvert Cliffs in Calvert County, Maryland'. Michigan Technological University.

Geotechnical and Geophysical Site Characterisation 5 – Lehane, Acosta-Martínez & Kelly (Eds)

Soil discrimination using an electrical logging method

M. Fujii & K. Watanabe
Tokai University, Hiratsuka,Kanagawa, Japan

T. Fukaya & K. Takechi
Japan Home Shield Corporation,sumida,Tokyo, Japan

ABSTRACT: The Swedish Weight Sounding (SWS) test is widely used as a research method to evaluate the bearing capacity of residential sites. However, a disadvantage of the SWS test is its inability to determine soil. We believe it is possible to perform soil determination, (sandy soil or cohesive soil) evaluations using electrical resistivity data obtained from SWS test holes. We found that the electrical logging method of attaching electrodes to the SWS test hole is effective. The evaluation of the fine fraction content of soil is possible to obtain using electrical resistivity data from laboratory tests. This data can then be used to complete estimation equations. In this study, field experiments at ten sites were performed to determine the accuracy of the soil estimation equation of the SWS laboratory tests.

1 INTRODUCTION

More than 25,000 houses were affected by liquefaction caused by the Tohoku-Pacific Ocean Earthquake, which occurred on March 11, 2011(Wakamatsu 2012 and Yasuda 2012). As a result, countermeasures against liquefaction and methods to evaluate liquefaction for detached houses have been recognized as important challenges, and the need for remedial construction methods for liquefied ground is increasingly gaining public attention (Kim and Fujii 2013). A notable issue under these circumstances is the use of a ground survey method that allows precise determination of liquefaction in residential grounds (Shinagawa and Fujii 2015).

As an existing survey method to assess residential grounds, the Swedish Weight Sounding (SWS) test is being widely used as a method that is generally simpler, more economical, and quicker than the Standard penetration test (SPT). This method has a history of about 60 years since it was introduced into Japan from Sweden in 1954, and has become a popular method to survey residential grounds in the building industry (Fujii et al. 2002 and AIJ 2008). The SWS test has been established as a standard method to survey residential grounds. On the other hand, a disadvantage of SWS test is inability to determine the nature of the soil and the groundwater level. The determination of the soil type is based on the experience of the operator. Information obtained from the results of the SWS test is insufficient to evaluate the residential ground (Fujii et al. 1996).

If it were possible to incorporate a determination of the soil type by electrical resistivity using SWS test hoes, a lot of information will be gained. An electrical logging method using electrodes in the SWS test hole would be ideal. The purpose of this study is intended to clearly determine the classification of soil by an electrical logging method using a SWS test hole.

2 PHOTOGRAPHS AND FIGURES

The typical ground survey method used in Japan is the Standard Penetration Test (SPT). However, SPT has some problems with its size and cost in the narrow residential sites common in Japan. So, SPT is rarely carried out on the site. The most popular survey method in residential sites is the Swedish Weight Sounding (SWS) test. The SWS test is a very simple and easily obtains information about the strength of the soil. On the other hand, information on the particle size of a soil is obtained by the electrical resistivity method. Therefore, combining the results obtained from SWS test and electrical resistivity is effectively producing the same information as that obtained from the SPT.

We have previously conducted laboratory tests of the relationship between the electrical resistivity and the fine content and we have found that there is a relationship like equation (1) between them (YuanHao and Fujii 2014). Equation (1) was demonstrated to be applicable to clay (YuanHao et al. 2015). However, it has not yet been performed for ground with sandy soil.

$$A = 9.81RW^{-1.24} \cdot Fo1.41^{(9.81Rw^{-1.24})^{0.03}} \quad (1)$$

A: Fine fraction content (%)
Rw: Resistivity of pore water(Ω・m)
Fo : Rw/Ro
Ro : Resistivity of soil (Ω・m)

3 OUTLINE OF EXPERIMENT

3.1 *Kinds of tests and location*

Three types of tests were performed in this study: the SPT, SWS test and electrical resistivity. The tests were conducted at 10 sites, with three test results being compared at each site. The SPT and the SWS tests were conducted at a distance of up to 3 m. The electrical resistivity was performed using the SWS test hole. Measurement of the electrical resistivity was conducted in a state where the SWS test hole was filled with ground water.

3.2 *Measuring equipment*

The equipment used for measuring the electrical resistivity of soil is an automatic SWS testing device shown in Figure 1. The in–situ measurement electrode is attached to the screw point as shown in Figure 2. The electrical resistivity was measured for each depth at 25 cm intervals. The measurement circuit for the electrical resistivity is shown in Figure 3

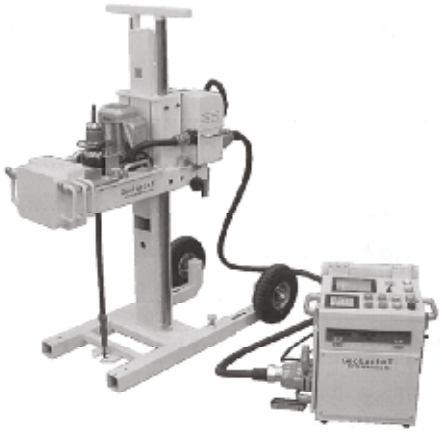

Figure 1. Automatic SWS testing device

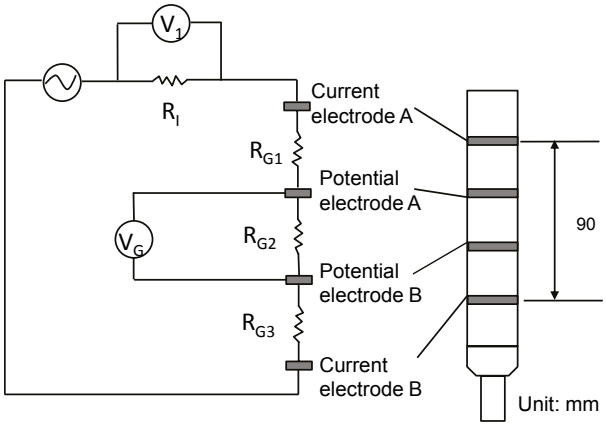

Figure 3.Measurement circuit of the electrical resistivity

and its specifications in Table 1. The rotary connector shown in Figure 4 was used to prevent twisting the electrode conductors as the screw turned. Transmission of the detection signal between the turning side (rod side) and the fixed side (cable side) is carried out by this connector. By this mechanism, the electrical resistivity is measured with the cable in a fixed position with respect to the turning of the rod. The electrode which is used to measure the electrical resistivity of the ground water in the laboratory is part of the commercially available portable conductivity meter shown in Figure 5. The dimension are shown in Figure 6 and its specifications in Table 2. Ground water was drawn up using the vessel shown in Figure 7 which was inserted in the SWS test hole. When ground water floods from the tip of the vessel, a ball moves to the top. The ball falls by its own weight with time and close the opening of the tip of the vessel

3.3 *Experimental method*

The method of measuring electrical resistivity is shown in Figure 8. In this case, the electrode may be in contact to the remolded soil with water. Since the electrical resistivity is measured in the water present in the SWS test, the application range of this method is limited to ground water. An actual measurement situation is shown in Figure 9.

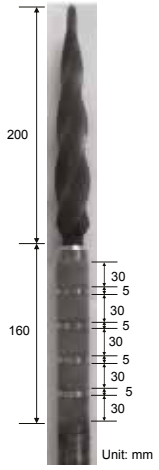

Figure 2. Electrode for in-situ measurement

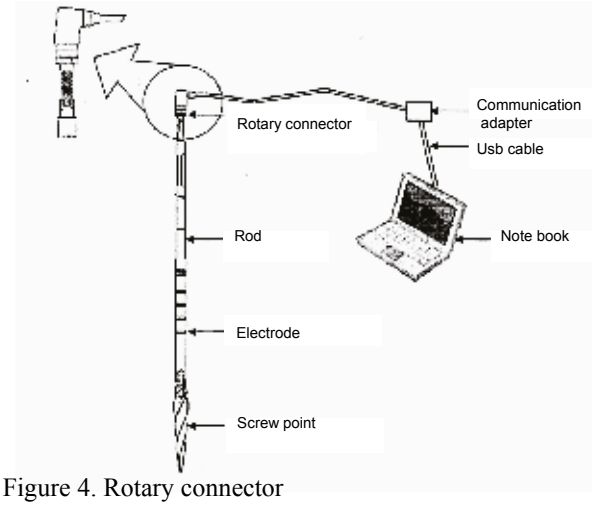

Figure 4. Rotary connector

Figure 5.Portable conductivity meter

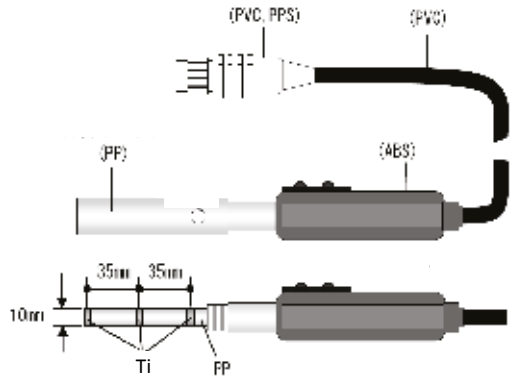

Figure 6. Portable electric conductivity meter

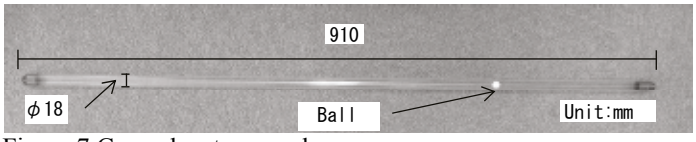

Figure 7.Ground water sampler

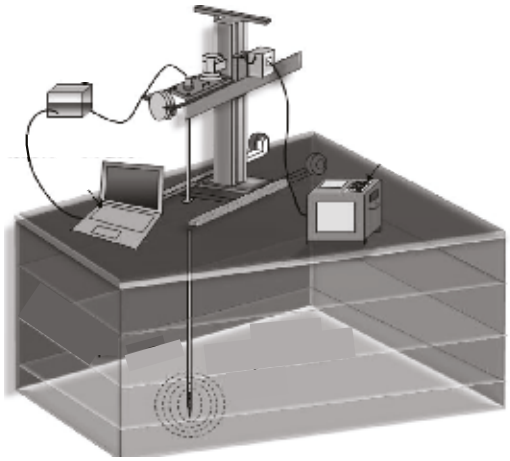

Figure 8. Measuring method

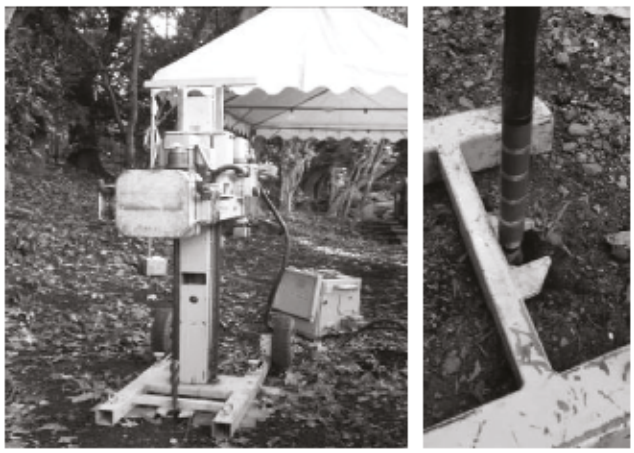

Figure 9. Measurement situation

Table 1. Specifications of electrode for in-situ measurement

Measurement range switching	0.1mA - 20mA
Electrical resistivity measurement range	0.5Ω・m – 20KΩ・m
Power-supply	DC100V
Temperature range	0℃ - 50℃
Humidity range	<80RH%

Table 2. Specifications of Portable conductivity meter

Model number	CT-27112B
Electrical resistivity measurement range	0.5Ω・m - 20KΩ・m
Temperature range	0℃ - 80℃
Humidity range	<95RH%

4 OUTLINE OF EXPERIMENT

4.1 *Test results*

Figure 10~19 show the experimental results from the SPT, SWS and electrical resistivity measurements. From Figures 10 to 19, we can discover the boundaries between layers based on the change in the electrical resistivity. If the electrical resistivity is more than 60Ωm, the soil is judged to be mostly sandy soil. If the electrical resistivity is less than 30Ωm it is judged to be mostly cohesive soil. Fig.20 shows the maximum value and minimum value of the resistivity at each site. Discrimination of sandy soil or cohesive soil is possible on the based on Fig.20.

4.2 *Discussion of the use of equation (1) for the fine fraction content*

When the electrical resistivity of soil and pore water is known, it is possible to estimate the fine fraction content of the soil from equation (1). Therefore, we examined the applicability of equation (1) at these sites. Figure 20 shows a comparison of the fine fraction content obtained by calculation using equation (1) and the measured grain size analysis from 10 sites. From Figure 21, we can see that both sets of values correspond very well with each other. Thus discrimination of sandy soil or cohesive soil from Figure 21 is possible.

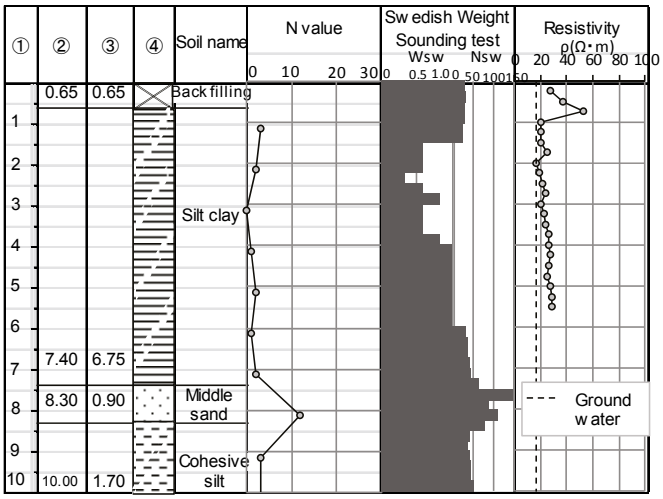

*①Level(m) ②Depth(m) ③Thickness(m) ④Symbol

Figure 10.Test results in Kawashima

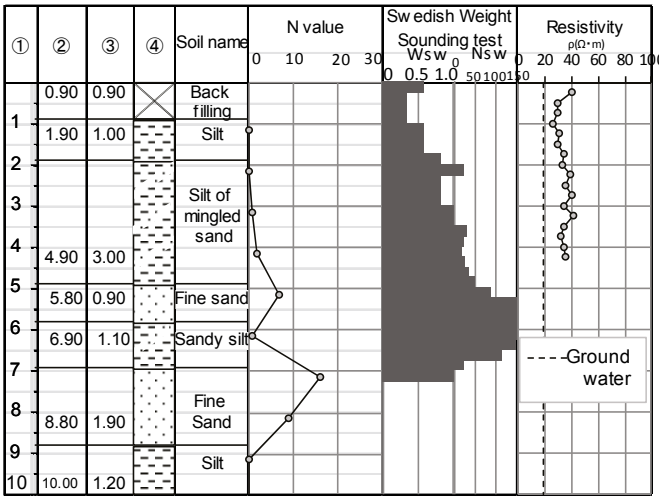

*①Level(m) ②Depth(m) ③Thickness(m) ④Symbol

Figure 11.Test results in Yanaka

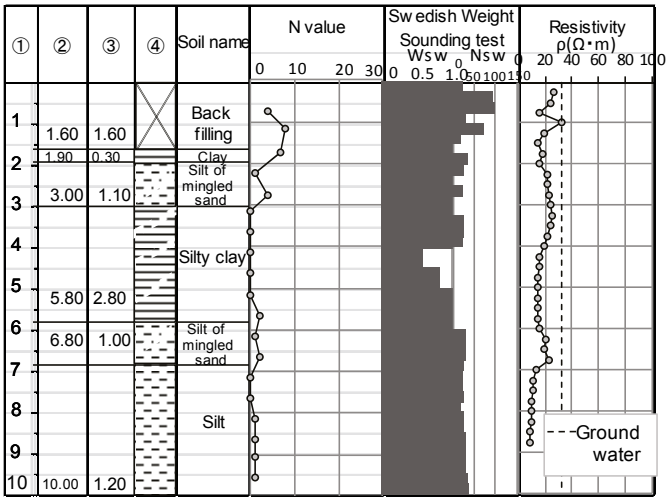

*①Level(m) ②Depth(m) ③Thickness(m) ④Symbol

Figure 12.Test results in Masudo

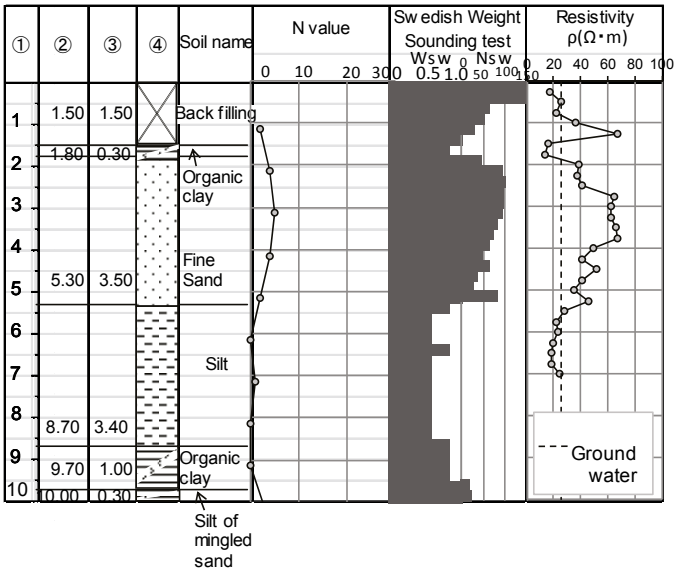

*①Level(m) ②Depth(m) ③Thickness(m) ④Symbol

Figure 13.Test results in Kikuma(1)

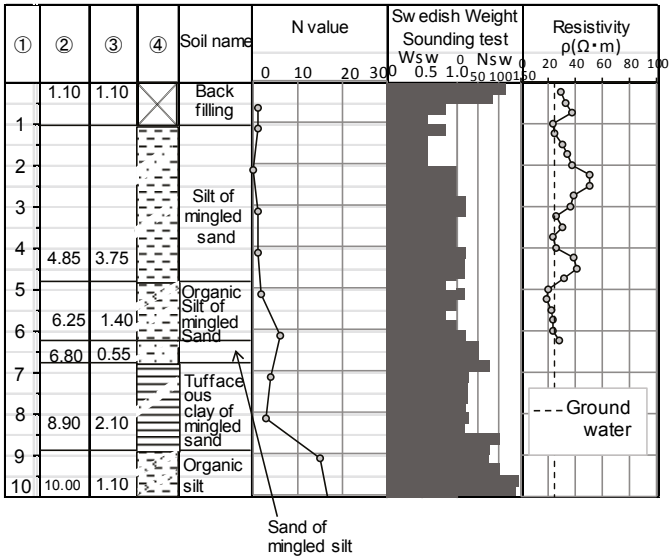

*①Level(m) ②Depth(m) ③Thickness(m) ④Symbol

Figure 14.Test results in Kitaterao

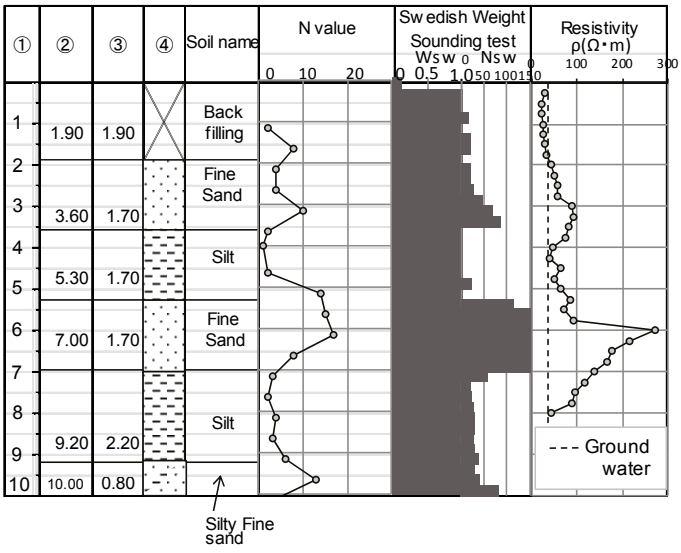

*①Level(m) ②Depth(m) ③Thickness(m) ④Symbol

Figure 15.Test results in Ajika-cho

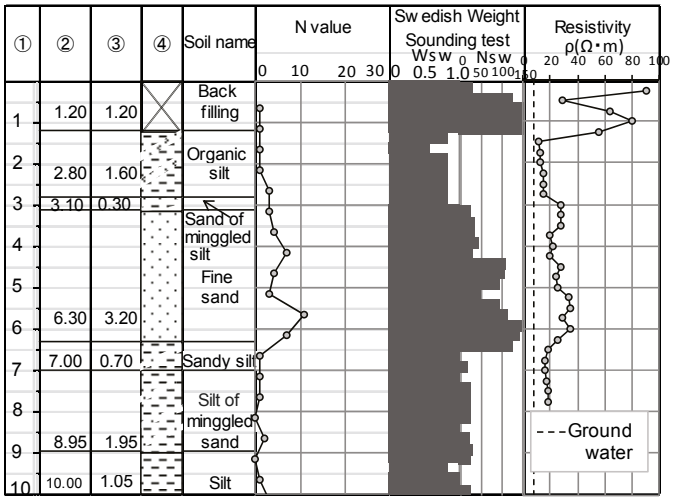

*①Level(m) ②Depth(m) ③Thickness(m) ④Symbol

Figure 16.Test results in Kikuma(2)

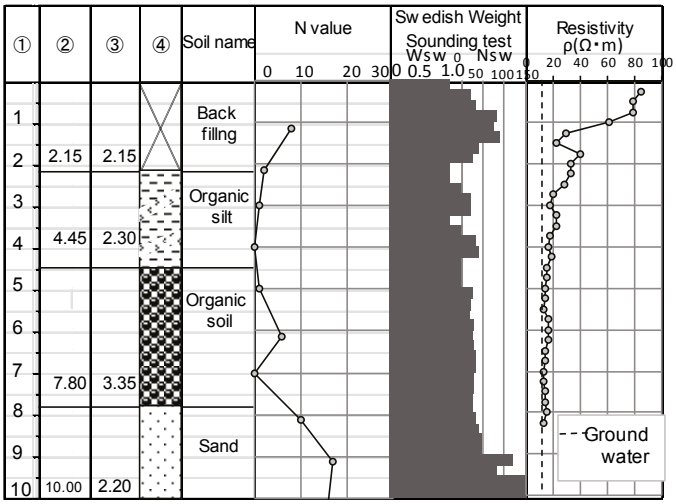

*①Level(m) ②Depth(m) ③Thickness(m) ④Symbol

Figure 17.Test results in Okusa-cho

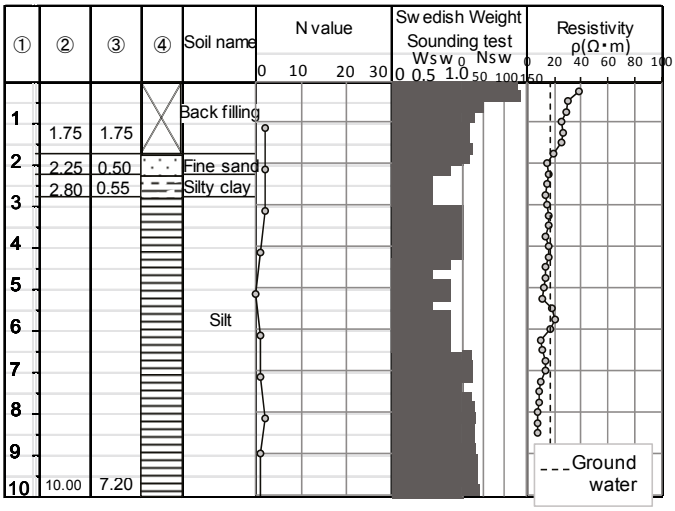

*①Level(m) ②Depth(m) ③Thickness(m) ④Symbol

Figure 18.Test results in Shinmeikan

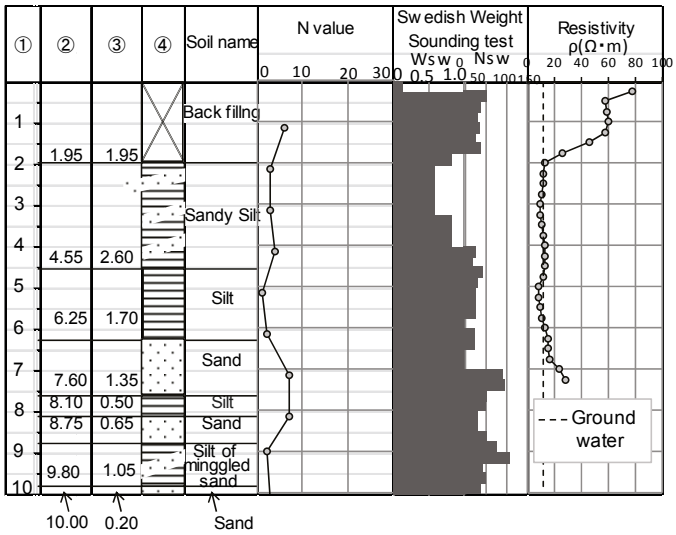

*①Level(m) ②Depth(m) ③Thickness(m) ④Symbol

Figure 19.Test results in Matsushima

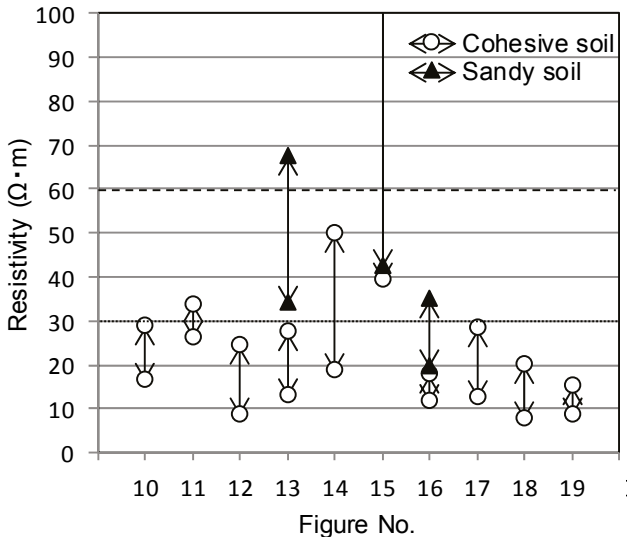

Figure 20. Maximum resistivity and minimum resistivity at each site

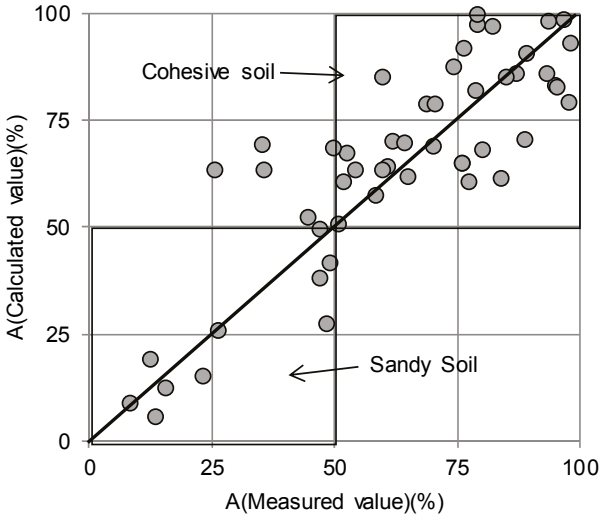

Figure 21. Comparison of the measured and calculated values of fine fraction content(A)

5 CONCLUSIONS

By combining SWS with electrical resistivity measurement we obtained the following conclusions.

- The soil is judged to be mostly sandy soil if the electrical resistivity of the soil is more than 60 Ωm.
- The soil is judged to be mostly cohesive soil if the electrical resistivity of the soil shows less than 30 Ωm.
- It is possible to distinguish the borders of the layers by comparing the results of the electrical resistivity.
- Equation (1) is very useful to evaluate the fine fraction content. Thus it is possible to determine the soil discrimination, (sandy soil or cohesive soil).

From the above-mentioned conclusions, we can say that the combination of the SWS test and the electrical resistivity results can produced the same information as the ground features obtained from the SPT.

6 ACKNOWLEDGEMENTS

This study was conducted with the cooperation of the Japan electrical resistivity association. We wish to sincerely thank the members concerned.

REFERENCES

Wakamtsu, K. 2012. Geomorphological and geotechnical conditions of liquefied sites in Tohoku region during the 2011 East Japan Earthquake, *Proceeding of the 47th japan National Conference on JSSMFE*: 1506-1507.

Yasuda, S. 2012. Analysis about effects that sphere of surface ground improvement give settlement of houses, *Proceeding of the 47th japan National Conference on JSSMFE*: 809-810.

Fujii, M. & Shinagawa, K. 2013. A survey on damage of small building due to liquefaction by the pacific coast of Tohoku Earthquake, *18th Southeast Asian Geotechnical Conference*: 1003-1009.

Kim, C. & Fujii, M. 2013. Study on measuring the groundwater level and soil classification for detached houses, *AIJ Journal Technol*., Vol.19, No.41: 89-94.

Shinagawa, K. & Fujii, M. 2015. Investigation based on consciousness of residents of detached houses in a liquefaction area and study of differential settlement caused by liquefaction in the Tohoku Earthquake, *Japanese Geotechnical Journal*, Vol.10, No.2: 285-293.

AIJ.2008. *Recommendations for designing of small buildings foundations*, Tokyo: Maruzen Publishing

Fujii, M., Tamura, M. & Ijuin, H. 2002. The evaluation method and issue of Swedish Weight Sounding test performed in the site of small buildings, *Journal Structure Construction Engineering*, AIJ, No. 557: 121-128.

Fujii, M., Futaki, M., Ijuin, H., Kazama, S., Tamura, M. & Abe, A. 1996. Relation between Nsw of Swedish Weight Sounding and N-value of Standard Penetration Test, *AIJ Journal Technol*., No.3: 64-68.

YuanHao, G. & Fujii, M. 2014. Estimation of fine fraction content in soil by electrical resistivity, *Proceedings of the Twenty-fourth International Ocean and Polar Engineering Conference*: 723-730.

YuanHao, G., Fujii, M., Mochida, Y., Takechi, K. & Adachi, Y. 2015. Evaluation of the fine fraction content using electrical logging method, *AIJ Journal Technol.*, Vol.21, No.48: 557-562.

Geotechnical and Geophysical Site Characterisation 5 – Lehane, Acosta-Martínez & Kelly (Eds)

Inversion of effective phase velocity seismic surface wave data by partial least squares regression

G. Heymann, D.N. Wilke & S. Kok
University of Pretoria, Pretoria, South Africa

ABSTRACT: Inversion of seismic surface wave data is an important stage in the process to obtain the profile of shear and compression wave velocities of a ground profile. Basic inversion techniques often assume that Rayleigh waves are propagated by the fundamental mode. For normally dispersive ground profiles this may be a reasonable assumption, but for inversely dispersive profiles or profiles, with high velocity contrasts, higher modes will also contribute strongly at high frequencies of excitation. Most inversion strategies for such profiles require that the phase velocity be propagated at one dominant mode at any given frequency of interest with a clear discontinuity when the phase velocity moves from one mode to the next. In practice this may sometimes be achieved by employing a large number of geophones, but for complex profiles the number of geophones needed may be impractical. For such profiles, using the number of geophones typical for surface wave testing, the effective phase velocity will be measured where mode superposition occurs with a gradual transition from one mode to the next. Inversion of such data is not possible with conventional techniques, as each mode can not be identified separately and requires the effective phase velocity dispersion data to be inverted directly. This paper proposes a partial least square regression strategy for the inversion of effective phase velocity dispersion data.

1 INTRODUCTION

Seismic surface wave testing has become popular for geotechnical site characterization (eg. Foti et al. 2015, Stokoe et al. 2004). These tests are relatively fast to perform, cost effective and non-invasive. Numerous active surface wave tests have been developed where an active seismic source is used such as a vibrator, sledge hammer or explosive source. Active tests include CSW - continuous surface wave test (e.g. Matthews et al. 1996), SASW - spectral analysis of surface waves (e.g. Stokoe et al. 1994) and MASW - multichannel analysis of surface waves (e.g. Park et al. 1999). In addition a number of passive surface wave techniques have been developed which uses background vibration as seismic source. Passive tests typically target low frequencies and therefore allow characterisation of deep layers and are often used to complement active surface wave tests. Passive tests include SPAC - spatial autocorrelation (Aki 1957) which uses regularly shaped geophone arrays such as L-shaped, T-shaped, circular or triangular and ReMi - Refraction Microtremors (Louie 2001) which uses linear geophone arrays.

The dispersion data lies central to surface wave testing, and it is measured experimentally. Inversion of the dispersion data is required to construct a profile of seismic wave velocity with depth. Most analytical techniques used for inversion of dispersion data assume that the energy is propagated by discrete modes, be it the fundamental mode only, or the fundamental mode together with other discrete higher modes. This is only true for very long geophone arrays placed sufficiently far from the seismic source. For typical active surface wave testing this is often not the case and mode superposition occurs in which case the effective phase velocity is measured. The continuous surface wave test has the advantages of using a vibrator (Heymann 2013), which allows good quality control in the field and a short geophone array. Foti et al. 2015 noted that with a short geophone array there is less risk of insufficient signal to noise ratio, high frequency attenuation and spatial aliasing as well as lateral variations of the soil properties. However when using a short geophone array it is likely that the effective phase velocity will be measured and not discrete modes as often assumed by inversion algorithms. Robust techniques for inversion of effective phase velocity are therefore required.

It is well known that surface wave inversion is ill-posed. Various least squares inversion strategies have been proposed and additional information can

be incorporated to alleviate the ill-posed nature of the problem (Rix 2005). Least squares strategies require the minimisation of the least squares error in experimental and modelled response, by changing the soil profile characteristics. Alternatively, the maximum deviation from the reference response can be minimised using a minimum-maximum formulation.

In this study an alternative approach is consider to characterise soil profiles by directly mapping the effective phase velocity to the soil properties. A map is first constructed by conducting a number of independent analyses to compute the effective phase velocity for randomly chosen soil profiles. These runs are then used to correlate information between the effective phase velocity and soil characteristics to obtain a lower dimensional description of the simulated data. Linear regression is applied to the lower dimensional description of the effective phase velocity to the lower dimensional description of the soil characteristics. Once the direct mapping has been done, the inversion of experimental field data is much faster than conventional inversion techniques.

There are practical benefits for fast direct inverse approaches, as opposed to the conventional minimisation approach as statistical quantification of the ill-posed nature of the problem is computationally efficient. This may be used to create technology that allows the sufficiency of the experimental measurements to be statistically evaluated in real-time in the field.

In this study we conduct a simulated experiment to quantify the accuracy, robustness and degree of ill-posedness of the problem as well as the suitability of a partial least squares regression strategy.

2 FORMULATION OF THE PROBLEM

Typical geotechnical experiments measure seismic surface wave phase velocity at specific frequencies. A soil characterisation inverse analysis aims to identify the soil layer characteristics that match a model dispersion curve to the experimentally measured data. The construction of the dispersion curve requires the phase velocity - frequency relationship of every mode, which requires the roots of the secular function to be computed at every experimentally measured frequency.

The dispersion curve is numerically computed by finding the roots of the secular function to give the dispersion modes. The dispersion curve is then computed as the combined participation of the various modes (Rix 2005). To compute the modes, an analysis tool `mat_disperse`, was used to compute the roots of the secular Rayleigh function. The secular Rayleigh function S for waves, requires the computation of roots for a specific wave number k and frequency f.

The secular function S has the following form:

$$S(k,f) = \frac{\det(E(k,f))}{g(k,f)} \tag{1}$$

where E is a 2 by 2 matrix and g is a scalar function. The secular function is a complex function that takes real inputs. The complex modulus can be computed by computing the magnitude of the complex function, often referred to as the absolute value of a complex number. A *Matlab* or *Octave* implementation of the secular function is freely available (Rix 2005), and defined in the user defined function `secular.m`. However, computing the roots may prove challenging especially for inversely dispersive profiles (Wilke et al. 2014). We opted to compute the dispersion modes using Dinver (Wathelet et al. 2004) and `mat_disperse` to compute the effective phase velocity.

A virtual experiment was conducted in which a target soil profile was chosen and the reference soil profile computed using the *Matlab* analysis tool `mat_disperse`. As the root finding can be challenging and often fails to find all the modes or complete modes, an *a priori* analyses was conducted to give N observations. These observations were used to construct radial basis interpolation fields.

A soil profile typically has four independent unknowns namely the shear wave velocity (V_s), compression wave velocity (V_p), density (ρ) and thickness (t). In the virtual experiment it was assumed that each layer only has two unknowns; shear wave velocity, and thickness. The density was assumed to be known and the Poisson's ratio, which relates compression wave velocity to shear wave velocity, was also assumed to be known. The aim of the virtual experiment was to estimate the shear wave velocity profile for three soil layers from the effective phase velocity dispersion curve.

2.1 *Partial least squares regression*

Before the partial least squares regression can be constructed it is necessary to first use known soil characteristics and obtain the effective Rayleigh phase velocities. `Dinver` (Wathelet et al. 2004) was used to calculate the first seven discrete modes and `mat_disperse` to compute the effective phase velocity. The shear wave velocities were taken to range between 200 m/s and 600 m/s and the soil layer thicknesses for the upper two layers were chosen to range between 1 m and 20 m with the third layer infinitely thick. A Latin Hypercube was constructed for 1000 soil profiles $\mathbf{Y}$. These profiles were then analysed in parallel as they are completely independent, to obtain the effective phase velocity $\mathbf{X}$. `Dinver` was only able to successfully compute the dispersion modes for 556 of the 1000 profiles.

The partial least squares regression is constructed as follows:

1. Both **X** and **Y** are normalised as z-scores i.e. the data sets have zero mean and is divided by their standard deviation.

2. The user chooses the number of latent variables (modes) M.

3. Set $\mathbf{X_1} = \mathbf{X}$ and $\mathbf{Y_1} = \mathbf{Y}$.

4. Solve the optimisation problem in which the covariance is maximized as follows:

$$\max_{w_i} cov(\mathbf{X}_1\mathbf{w}_1, \mathbf{Y}_1), \text{ subject to } \mathbf{w}_1^{\mathrm{T}}\mathbf{w}_1 = 1 \qquad (2)$$

5. Compute $\mathbf{X}_2 = \mathbf{X}_1 - \mathbf{t}_1\mathbf{p}_1^{\mathrm{T}}$

$$\min_p \left\| \mathbf{X}_1 - \mathbf{t}_1\mathbf{p}^{\mathrm{T}} \right\|^2, \text{ with } \mathbf{t}_1 = \frac{\mathbf{X}_1\mathbf{w}_1}{\left\| \mathbf{X}_1\mathbf{w}_1 \right\|} \qquad (3)$$

6. Compute $\mathbf{Y}_2 = \mathbf{Y}_1 - \mathbf{t}_1\mathbf{c}_1^{\mathrm{T}}$

$$\min_c \left\| \mathbf{Y}_1 - \mathbf{t}_1\mathbf{c}^{\mathrm{T}} \right\|^2, \qquad (4)$$

7. Repeat steps 4 - 6 using $\mathbf{X}_k$ and $\mathbf{Y}_k$ for k = 2, 3,..M

8. Construct **T** that consists of $\mathbf{t}_k$, **W** that consists of $\mathbf{w}_k$, **P** that consists of $\mathbf{p}_k$ and **C** that consists of $\mathbf{c}_k$.

9. For linear regression $\mathbf{x}\beta$, the regression coefficients $\beta = \mathbf{W}(\mathbf{T}^{\mathrm{T}}\mathbf{X}\mathbf{W})^{-1}\mathbf{T}^{\mathrm{T}}\mathbf{y}$.

The procedure outlined above is packaged in *Matlab* under the function `plsregress`. This allows for the efficient and convenient construction of inverse maps.

The only unknown parameter is the number of components to use in the partial least squares regression.

Computing the mean difference between the desired profile and the simulated profiles ranks the data points. We used responses that had the lowest difference. The number of points depends on the number of components and we used 4 times the number of components as the number of points used in the partial least squares regression. The reason is that partial least squares regression is a linear map and therefore not very flexible and by focussing the data around the solution a more accurate specialised map is obtained as opposed to an inaccurate generic map.

3 NUMERICAL EXPERIMENT

The soil profile investigated in the numerical experiment is shown in Table 1, with the Rayleigh modes and effective phase velocity depicted in Figure 1. `Dinver` was used to compute the fundamental modes and `mat_disperse` is used to compute the effective phase velocity.

Table 1. Initial profile parameters.

Thickness m	Vs m/s	Vp m/s	Density kg/m^3
5	350	600	1800
10	400	700	1800
∞	450	800	1800

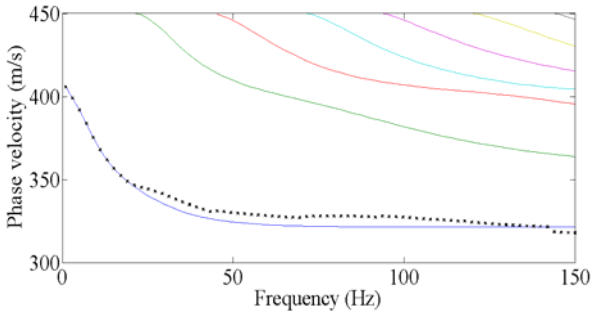

Figure 1. Rayleigh modes and effective phase velocity for the soil profile.

The sampled frequencies were 1; 3; 5; 7; 9; 12; 15; 18; 22; 26; 30; 34; 38; 42; 46; 50; 55; 60; 65; 70; 80; 90; 100; 125; 150 Hz. A short geophone array of five geophones with spacing 0.75m, typical of continuous surface wave (CSW) testing, were used with the geophones located at 1.5; 2.25; 3; 3.75 and 4.5 metres from the source to compute the effective phase velocity.

1000 independent simulations were conducted using Latin Hypercube sampling assuming the shear wave velocity to range between 200 m/s and 600 m/s and the soil layer thicknesses between 1 m and 20 m. `Dinver` was able to solve only 556 of the profiles. Figure 2 shows every tenth response as well as the effective phase velocity we aim to recover as a solid line. In addition Figure 3 depicts the variation of each variable as a box and whisker plot, with a range of one standard deviation and mean of 0.5 together with the solution we aim to recover.

Three simulated experiments were conducted:

1. Recover only shear wave velocity, given the rest of the profile.
2. Recover only thickness, given the rest of the profile.
3. Recover both shear wave velocity and thickness.

The aim of experiment 1 was to recover the shear wave velocity for each layer. Poisson's ratio is assumed to be known to compute the compression wave velocity. The layer thickness as well as the density (1800kg/m^3) was assumed to be known.

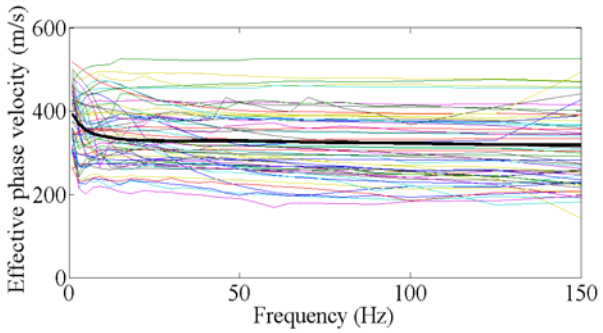

Figure 2. Response samples generated.

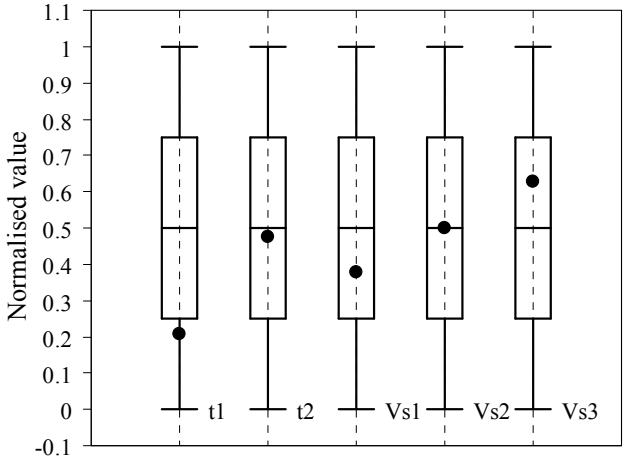

Figure 3. Variation of each variable for the generated samples.

Table 2 shows the shear wave velocity recovered from experiment 1 and Figure 4 shows the effective phase velocities for using 1 to 5 components in the partial least squares regression.

Table 2. Recovered shear wave velocity.

Components	Vs 1 m/s	Vs 2 m/s	Vs∞ m/s
1	348.27	416.82	443.48
2	348.04	403.70	446.88
3	348.50	404.21	451.10
4	349.17	403.21	451.51
5	348.79	403.86	449.82
Solution	350	400	450

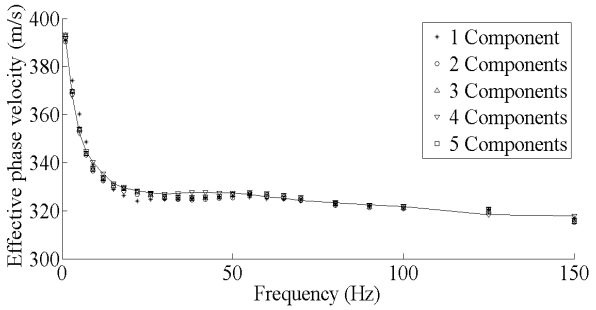

Figure 4. Response from the estimated shear wave velocities.

For experiment 2 all the soil parameters were assumed to be known except the thickness of layer 1 and layer 2. Table 3 shows the thickness recovered and Figure 5 shows the effective phase velocities.

Table 3. Recovered thickness.

Components	Thickness 1 m	Thickness 2 m
1	4.81	9.97
2	4.84	9.92
3	4.83	10.69
4	4.83	10.93
5	4.86	11.10
Solution	5	10

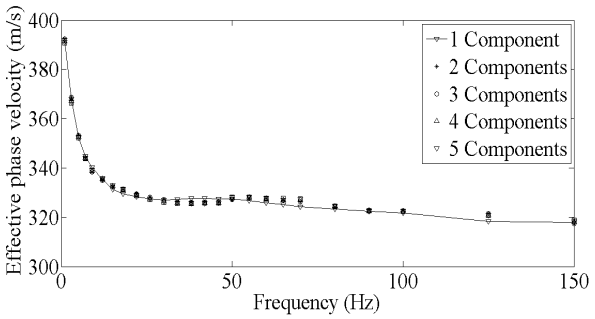

Figure 5. Response from the estimated layer thicknesses.

The aim with virtual experiment 3 was to recover the layer thickness for the top two layers and the shear wave velocity for all three layers. Poisson's ratio was assumed to be known to compute the compression wave velocity and the density was assumed to be known and taken as 1800kg/m^3. Table 4 shows the recovered layer thicknesses and shear wave velocities and Figure 6 show the effective phase velocities using 1 to 5 components in the partial least squares regression

Table 4. Recovered shear wave velocity and thickness.

Comp	Vs 1 m/s	Vs 2 m/s	Vs∞ m/s	Thick 1 m	Thick 2 m
1	350.95	401.62	441.08	5.31	15.92
2	347.32	389.45	443.60	5.71	10.66
3	345.48	414.92	446.53	7.40	11.15
4	344.19	439.04	413.33	4.96	8.04
5	351.74	445.72	430.57	7.36	13.80
Solution	350	400	450	5	10

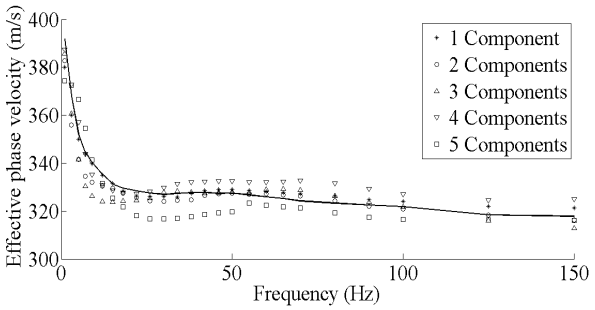

Figure 6. Response from the estimated shear wave velocities and layer thicknesses.

4 DISCUSSION

The main advantage to use the direct mapping inverse approach is the time required for the inversion analysis. Once the map has been constructed, the inversion analysis to find the ground profile which best fits the measured dispersion data, takes about 17 micro seconds using a 2.4 GHz Intel Core i5 processor. Using a conventional inversion analysis approach typically takes a few minutes using the same processor. Such fast inversion analysis may allow technology to be developed which allow inversion to be conducted in the field.

Table 5 shows the results for experiment 1 which attempted to recover the shear wave velocities for the three layer model. The shear wave velocities recovered by the inversion analysis were within approximately 1% of the true value for all layers if more than two components are used for the least squares regression. Figure 4 show that the calculated effective phase velocities closely matched the true effective phase velocity of the ground profile.

Table 5. Error in recovered shear wave velocity.

Components	Vs 1 %	Vs 2 %	Vs∞ %
1	-0.49	4.21	-1.45
2	-0.56	0.93	-0.69
3	-0.43	1.05	0.25
4	-0.24	0.80	0.34
5	-0.34	0.97	-0.04

The error of the recovered layer thicknesses for virtual experiment 2 are shown in Table 6. The layer thickness recovered by the least squares regression for layer 1 was within 4% of the true layer thickness, but for layer 2 it was 11%. This appears to suggest that the accuracy with which layer thickness can be determined is less than the accuracy with which shear wave velocity can be determined. In addition the accuracy appears to be better for shallow layers. No advantage is evident for increasing the number of components of the least squares regression.

Table 6. Error in recovered layer thickness.

Components	Thickness 1 %	Thickness 2 %
1	-3.66	-0.28
2	-3.12	-0.73
3	-3.33	6.97
4	-3.25	9.30
5	-2.65	11.03

Table 7 shows the error when attempting to simultaneously recover both shear wave velocity and layer thickness. It may be observed that the accuracy is worse in both cases compared with attempting to recover only shear wave velocity or layer thickness. The accuracy with which the shear wave velocity was recovered was 11% as opposed to 1% when the layer thicknesses were known. The accuracy with which the layer thicknesses were recovery reduced to approximately 60% compared with 11% when the shear wave velocities were known. Again, no advantage is evident for increasing the number of components of the least squares regression.

Figure 6 shows the effective phase velocities when both the layer thickness and wave velocity is recovered. It indicates that the scatter of the calculated wave velocities are significantly more than when either the layer thickness is known (Figure 4), or shear wave velocity is know (Figure 5).

Table 7. Error in recovered shear wave velocity and thickness.

Comp	Vs 1 %	Vs 2 %	Vs∞ %	Thick 1 %	Thick 2 %
1	0.27	0.41	-1.98	6.27	59.21
2	-0.76	-2.64	-1.42	14.25	6.65
3	-1.29	3.73	-0.77	48.10	11.56
4	-1.66	9.76	-8.15	-0.67	-19.51
5	0.50	11.43	-4.32	47.26	38.09

5 CONCLUSIONS

A number of conclusions may be drawn from the inversion of effective phase velocity seismic surface wave data by partial least squares regression. The technique applies a direct mapping inverse approach and once the map has been constructed the inversion analysis to find the ground profile which best fits measured dispersion data is significantly faster than conventional inversion techniques.

The results suggest that if *a priori* information is available regarding the thickness of the soil layers for a given profile, the shear wave velocity of the layers may be computed with a high degree of accuracy. However, simultaneous inversion of both layer thickness and shear wave velocity reduces the computational accuracy.

The efficiency with which the inverse analysis can be computed using the direct inverse map, will allow the variation of the recovered ground profile parameters to be quantified statistically.

REFERENCES

Aki, K. (1957). Space and time spectra of stationary stochastic waves, with special reference to microtremors, Tokyo University, Bulletin of the Earthquake Research Institute, Vol. 25, pp.415-457.

Foti, S., Lai C. G., Rix G. J. and Strobbia, C. (2015). Surface Wave Methods for Near-Surface Site Characterization. CRC Press, Boca Raton, pp. 467.

Heymann, G (2013). Vibratory sources for continuous surface wave testing. Geotechnical and Geophysical Site Characterization (ISC'4), Coutinho & Mayne (eds). Taylor and Francis Group, London, pp.1381-1386.

Louie, J.L., 2001, Faster, Better: Shear-wave velocity to 100 meters depth from refraction microtremor arrays, Bulletin of the Seismological Society of America, Vol. 91, 347-364.
Matthews, M.C., Hope, V.S. and Clayton, C.R.I. (1996). The use of surface waves in the determination of ground stiffness profiles. Proceedings of the Institution of Civil Engineers: Geotechnical Engineering, Vol.119, pp.84-95.
Park, C. B., Miller, R. D., and Xia, J. (1999). Multichannel analysis of surface waves: Geophysics, v. 64, p.800-808.
Rix, G. (2005). Surface Waves in Geomechanics: Direct and Inverse Modelling for Soils and Rocks. Chapter: Near-Surface Site Characterization Using Surface Waves, Volume 481. CISM International Centre for Mechanical Sciences.
Stokoe, K.H., Joh, S. and Woods, R. D. (2004). Some contributions of in situ geophysical measurements to solving geotechnical engineering problems. Proceedings ISC-2 on Geotechnical and Geophysical Site Characterization. Viana da Fonseca & Mayne (eds.), Millpress, Rotterdam, pp.97-132.
Stokoe, K.H., Wright, S.G., Bay, J.A. and Roesset, J.M. (1994). Characterization of geotechnical sites by SASW method. Geophysical Characterization of Sites (ISSMFE Technical Committee no. 10) by R.D. Woods, Oxford and IBH Publications, pp. 15-25.
Wathelet M., Jongmans D. and Ohrnberger M. (2004). Surface-wave inversion using a direct search algorithm and its application to ambient vibration measurements. Near Surface Geophysics, pp. 211-221.
Wilke, D.N., Kok, S. and Heymann, G. (2014). Comparison of two inverse strategies to characterize soil profiles, Proceedings of the 4th International Conference on Engineering Optimization (EngOpt2014), pp. 1005-1010, Lisbon, Portugal, 8-11 September, 2014. ISBN: 978-1-138- 02725-1.

Geotechnical and Geophysical Site Characterisation 5 – Lehane, Acosta-Martínez & Kelly (Eds)

Use of GPR on two sites with voids to enable safer work and targeted probing

C.G.C. Hughes & K.J. Read
Opus International Consultants Ltd, Auckland Office, New Zealand.

M. Watson
ScanTec Ltd, Whangarei Office, New Zealand.

ABSTRACT: In this paper we describe two case studies where a combination of geophysics and 'conventional' geotechnical techniques was used to characterise the sites for risk associated with voids in near surface soils that could potentially collapse. One is a former mine site where collapse of mineshaft back fill has occurred. Before intrusive investigations were carried out desk studies highlighted the possibility of other shafts on the site and voids below demolition rubble. In order to assess the potential risk from these an initial Ground Pene-trating Radar (GPR) survey was carried out and possible voids identified. This enabled targeted ground inves-tigation and safe siting of plant and workers. The second case is an electricity substation where 'tomos', (shal-low and potentially large voids created by piping erosion in pumice rich sands) were suspected. To improve the likelihood of striking a tomo in a borehole, reduce the risk of provoking an unexpected collapse and of striking buried services, a GPR survey was first carried out. In both cases further intrusive investigation is necessary to locate voids but this has potential for collapse, threatening the health and safety of site users and those carrying out investigation(s). By firstly characterising these sites through desk studies and GPR, we could carry out fu-ture works more safely and optimise our intrusive investigation.

1 INTRODUCTION

Investigations to determine the size and location of underground voids present a number of health and safety and remediation challenges for engineering consultants. The characterisation of sites with the potential risk of void collapse needs to be properly managed in order to maintain the health and safety of both the site users and those carrying out the ground investigations.

The purpose of this paper is to discuss two sites where the potential for void collapse was identified early in the preliminary geotechnical appraisals of these projects. These sites were then investigated using GPR, to characterise them ahead of conventional intrusive investigative works. This approach assisted us in optimising the scope and location of the intrusive investigations as well as assisting with our health and safety planning.

2 CASE STUDY 1: MINE SHAFT SITE - THAMES

2.1 *Background and site inspection*

Case study 1 is a site in an urban area of Thames, North Island, New Zealand (Fig. 1) where a mine shaft has been exposed. The shaft cover collapsed sometime in 2014, causing the shaft to become exposed at ground level. In order to protect the public in the immediate and short term the site was cordoned off using safety fencing to prohibit site access.

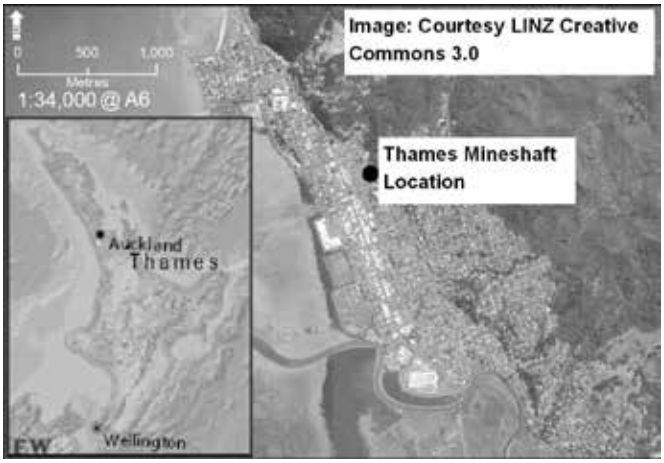

Figure 1. Site location, Bella Street, Thames

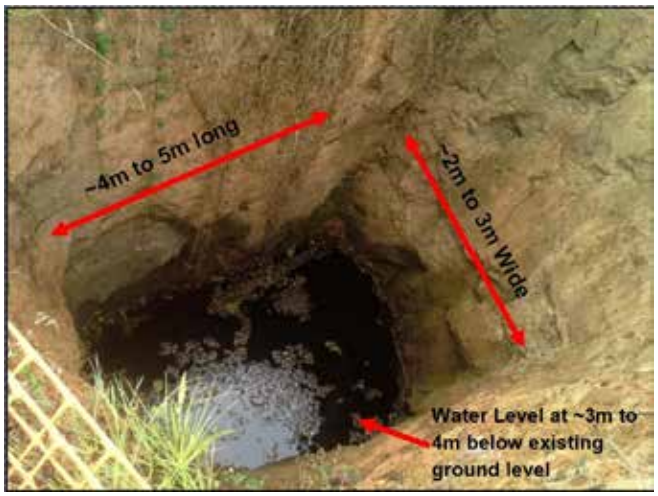

Figure 2. Photograph of mine shaft

At the time of inspection the exposed unlined shaft was approximately 4m to 5m long, 2m to 3m wide and broadly rectangular in shape (Fig. 2). There was a tension crack close to one edge of the shaft and groundwater was present in the shaft at approximately 3m to 4m depth below existing ground level (m begl). There were two smaller (approx. 1.5m to 2m diameter) circular depressions located to the south of the shaft. The ground surface to north of the large shaft was hummocky and appeared to have been disturbed.

Following the inspection, we then scoped and carried out a desk study, followed by a GPR survey of the site in order to help characterise the site and to confirm if the circular depressions and hummocky ground on site might reflect possible voids.

2.2 *Desk Study*

From review of the published geological information for the site (Edbrooke, 2001 and Fraser, 1910) the site was indicated to be underlain by igneous rock comprising andesite and dacite intrusives, lava flows, volcaniclastites and volcanic epiclastites, with extensive hydrothermal alteration. The mine shaft on site was identified by the geological information as the 'Bird in Hand Shaft Site' (Fig. 3 and 4). The cross section clearly labels the 'Bird In Hand N^{o} 2 Shaft'.

The shaft was completed in 1874, to about 70m depth, and work in the mine is thought to have ceased in 1914, and a cap placed over the shaft at that time (Barker, 2014). A house was constructed on site sometime post-mining and prior to 1916. That house is thought to have burned down in the mid 1980's, with demolition occurring in 1987.

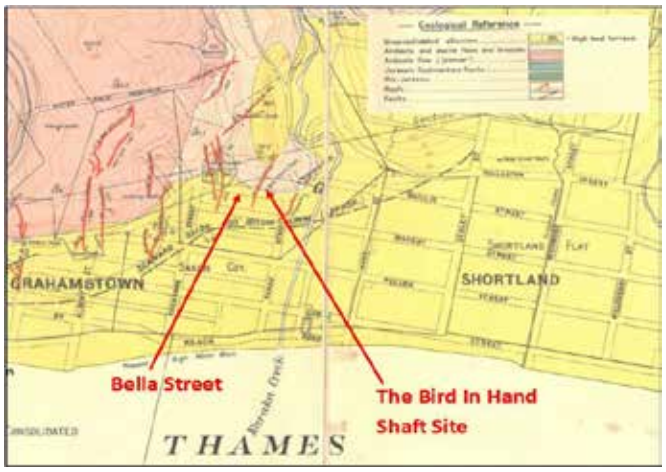

Figure 3. Geological map information extract (C Fraser 2010)

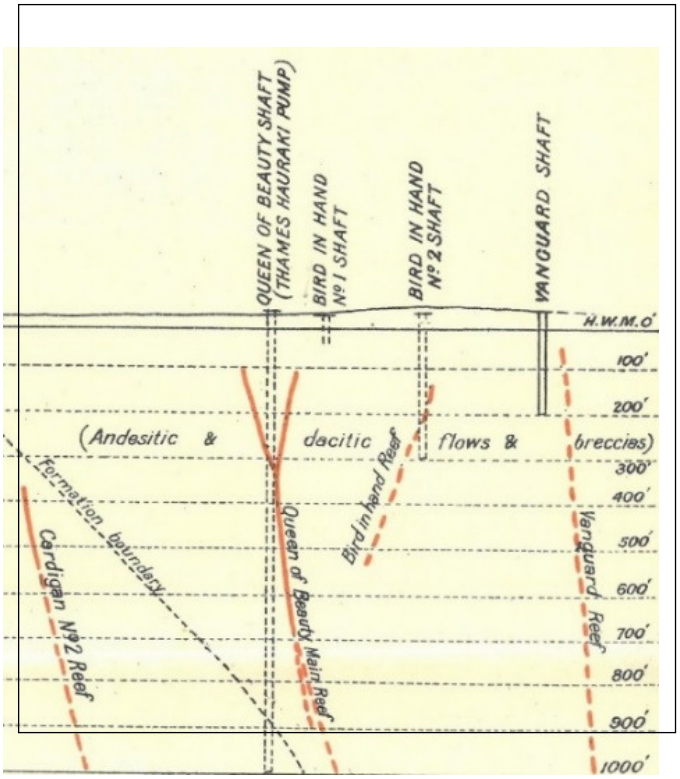

Figure 4. Geological information extract, cross section (C Fraser 2010)

2.3 *Ground Penetrating Radar Survey*

After the Desk Study, GPR was carried out at the site. Health and safety measures included a requirement for all staff working on site to be appropriately tethered.

The GPR survey identified diffraction anomalies at five locations on the site which may be cavities. The locations of these (labelled A to E) are shown on Figure 5. Locations B to E are previously unidentified potential hazards.

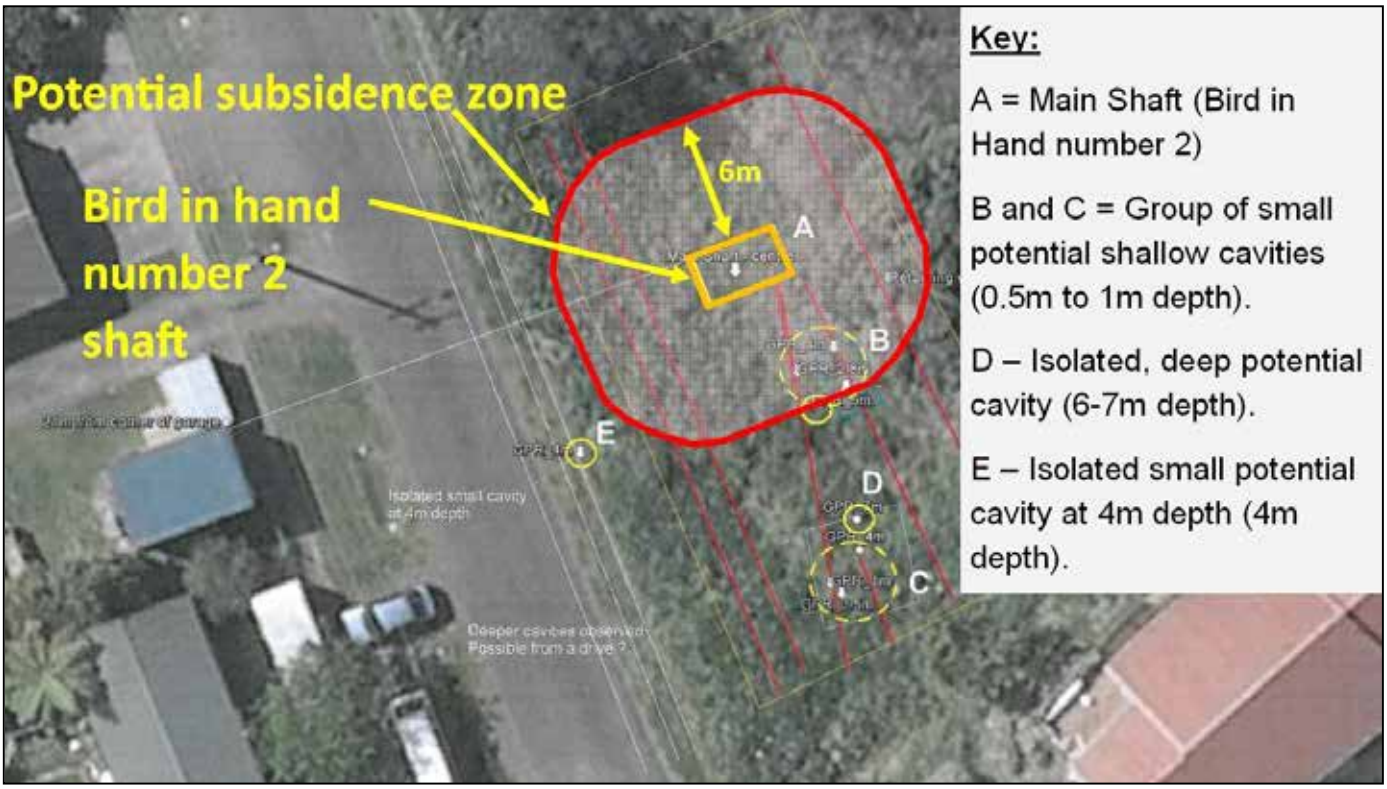

Figure 5. GPR results and anomalies A to E (Image from Scantech report – source Google Earth)

There was signal character, attenuation and linear reflections in the GPR data at about 4m depth (Fig. 6).

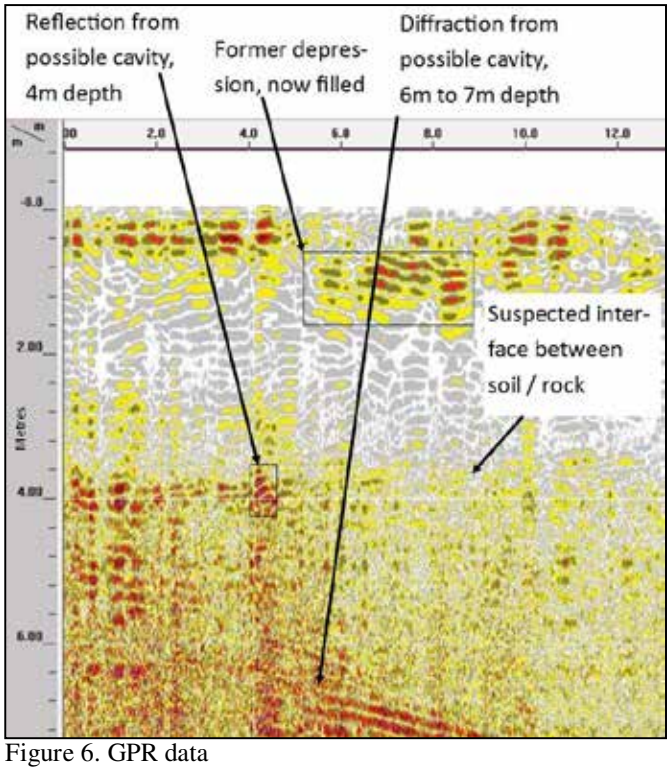

Figure 6. GPR data

We suspect that this may be the interface between soil / rock layers but it may also be the groundwater level. Equally this interface may be that between disturbed ground/fill and weathered andesite, or the interface between weathered and less weathered andesite. From our inspection of the shaft sides we could not determine which was the case

With respect to the anomalies B to E, there may be a number of possible causes for these, including:

1 **Mining related features** – localised contrast between rock/mining waste/fill/soils, buried equipment in the fill around the main shaft, unrecorded air/exploratory drive shafts, mining subsidence or partial collapse of mining related voids.

2 **Ancillary surface features** - Unrecorded structures around the mine shaft relating to the former mining activities, such as huts / sheds, railway sidings. Foundations to the former residential dwelling and associated underground services. Possible water well for the residential property.

Some gravitational survey was also performed at this site. The gravitational survey indicated a local-ised disturbance in the gravitational field in the vicini-ty of the 'Bird in Hand N^{o} 2 Shaft', but did not indi-cate the presence of cavities in the anomalies B to E.

This would / may suggest that GPR is a more effective method of identifying cavities than gravita-tional survey in these type of ground conditions.

2.4 *Health and safety / investigation scoping*

Following the methodology set out in the CIRIA guidance (Healey et al. 2002) and in the absence of site specific data we estimated the extent of the potential subsidence zone that could form from collapse of the 'Bird In Hand N^{o} 2 Shaft'. The calculated horizontal distance from the edge of the shaft to the edge of a potential crater was approximately 6m (Fig. 5). There is also a risk of shaft side collapse within the rock portion which we suspect may be from below 4m depth. However, on balance, and bearing in mind the shaft appears to be backfilled to approximately 8m begl we consider collapse of the rock portion to be lower risk compared to collapse within the upper more weathered soil part.

The GPR survey assisted us greatly in scoping out a phased intrusive investigation of locations we may not otherwise have considered high risk and for setting out the requirements for health and safety. The scope of the next phase includes:

1 Test pits using a long reach mechanical excavator to investigate the anomalies B to E. The pits will be progressed after carefully inspecting and removing the topsoil and upper 0.5m to 1m of soils across each of the zones with the excavator positioned a safe distance outside of the anomalies.
2 If no obvious features are found we will reduce the excavator bucket size to approximately 600mm and excavate a conventional test pit as deep as safely possible (~4m) in order to investigate the deeper soil zones.
3 All staff will be harnessed and tethered to a fixed point.
4 A protocol in the health and safety plan will be used to guide staff on the actions to be taken in the unlikely event that a void collapse occurs and is required to be made safe.

3 CASE STUDY 2: ELECTRICITY SUBSTATION SITE – EDGECUMBE, BAY OF PLENTY

3.1 *Background*

Case study 2 is an electricity substation site located in Edgecumbe, North Island, New Zealand (Fig. 7).

Opus were engaged by the client to carry out a site inspection and provide recommendations to investigate holes (tomos) that had appeared within the substation grounds.

The site is located on a low lying flood plain approximately 80m east of the Rangitaiki River.

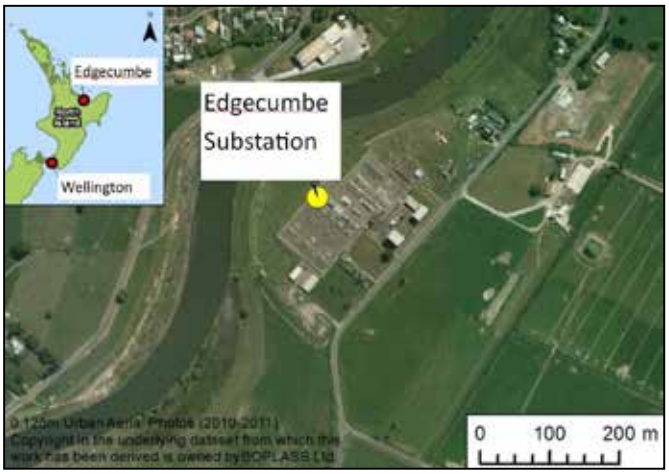

Figure 7. Site location

3.2 *Initial site walkover / on site testing*

A site walkover and-on site testing comprising two hand augers and Scala tests was carried out. The aim of the walkover and initial testing was to assess the immediate risk to the substation components.

Figure 8. Tomo 2

We noted two key areas where tomos had formed on site and where surface expression of voids was evident. The first area (Tomo 1) was a broadly circular hole in the gravel surface roughly 0.7m diameter and 0.3m deep. The ground around the hole appeared to be within a slight depression of approximately 2.5m diameter. There was silt build up around the location of the tomo that was thought at the time of the visit to be indicative of surface water ponding around this area. The second area referenced Tomo 2 (Fig. 8) was roughly oval in shape and 0.9m long by 0.5m wide. The void extended laterally (below ground level) by up to approximately 1.5m. There were similar tomos located around supply poles within the open grass land west of the substation.

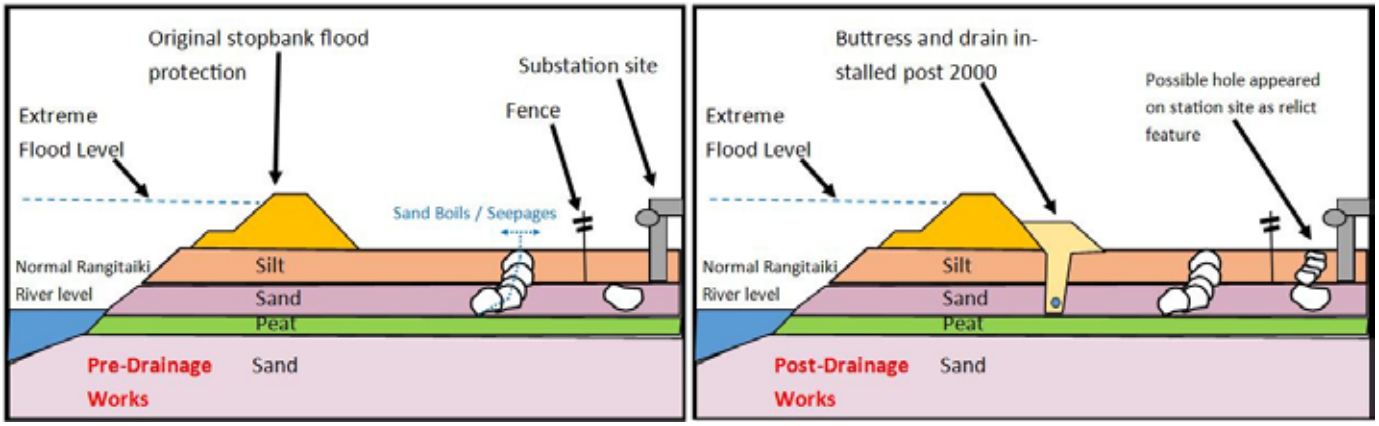

Figure 9. Site characterisation and concept ground model for tomo formation

From our discussions with the substation staff we determined that Tomo 1 appeared around March 2013, whilst Tomo 2 appeared around June/July 2013.

Gravel is present from ground level to between 0.25m and 0.35m across the substation site. Loose grey brown fine to medium sand / soft sandy silt was identified in the area of the tomos to a depth of around 2.5m. The sands are rich in pumice, easily erodible and prone to piping. The sand / silt soils are underlain by a peaty (20% to 50% organics) dark brown soft silt to a depth of between 2.70m and 3.1m depth below ground level.

The peat component of the soil is amorphous to fibrous. Below the peat is a medium dense light brown medium to coarse pumiceous sand. The auger holes all refused within this material.

3.3 *Desk study and concept ground model*

From our review of the published geological map (Leonard et al. 2010), the site was indicated to be underlain by recent swamp deposits comprising dark brown to black peat, organic rich muds, silt and sand. The Edgecumbe Fault is located approximately 14km to the east of the site.

The site lies on a flood plain next to the Rangitaiki River. The river is constrained by stop bank flood protection bunds and there is a history during flood events of piping erosion through the pumice sands causing flooding, sand boils and tomo formation on the downstream sides of the bunds. In 2000 substantial improvement works comprising toe bunds and drainage measures were constructed adjacent to the banks to protect the surrounding land (Fig. 9).

The desk study found historical evidence of tomos occurring outside the sub-station site during pre-2000 flood events but there was no correlation between the tomos observed on site and any recent flood events.

3.4 *GPR survey*

A GPR survey was carried out to assess the possible presence of further sub-surface voids (tomos) on the site. Carrying out a GPR survey in the substation environment was challenging; however despite interference patterns from the substation metal structures and electromagnetic noise fields a number of possible features were identified from the GPR data. These included earthing cables, underground services, layering in sediments, paleo-channels, possible rock blocks and possible cavities.

No significant large cavities (of size greater than 2m) were interpreted from the GPR data. However, a number of features or anomalies (Fig. 10) that could comprise voids or other features such as boulders or paleo-channels were identified. Paleo-channels are old river or tributary channels that have since been buried or in-filled by sediment from the natural meandering of the river.

The GPR survey also identified a lot of small features that have the characteristics of cavities but could also be natural features within the sediment. Many of these features were indicated to be present within the upper 1m to 2m and be of possibly 200mm to 300mm in size.

The GPR aided development of a more complex ground model for the site including buried ‘natural’ channels and possible flow paths in service trenches both of which may promote rapid and/or concentrated groundwater flows leading to piping of the pumice sands and tomo formation.

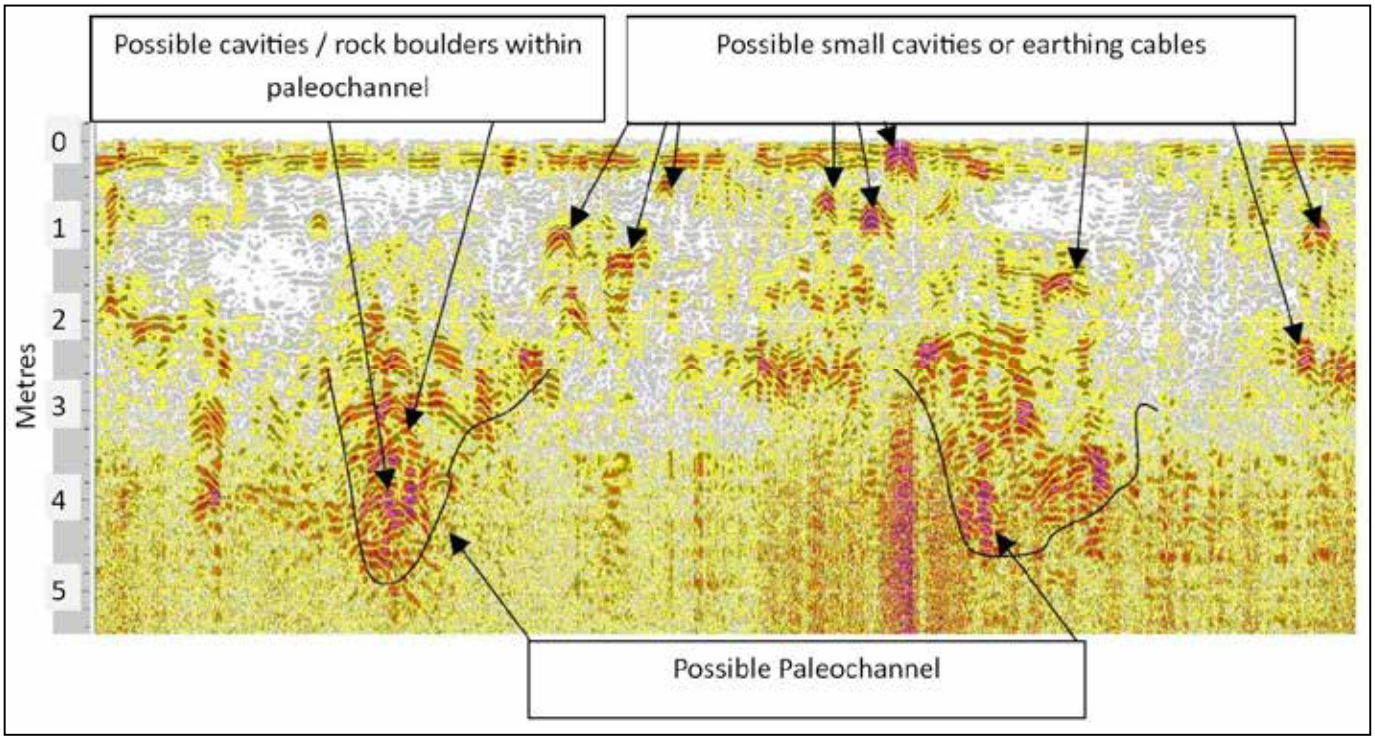

Figure 10. GPR Data and further site characterisation

4 CONCLUSIONS

At the time of preparing this paper further intrusive works for both the case studies discussed had not yet been carried out.

However, the walkover/desk studies in conjunction with the GPR surveys have allowed us to scope and optimise the positions of the proposed intrusive works to improve the likelihood of striking voids at these sensitive sites and aided development of appropriate ground models. This approach also allowed us to mitigate health and safety risks at these sites for both the site users and those carrying out intrusive investigations.

5 ACKNOWLEDGEMENTS

The authors would like to acknowledge the clients Colliers International Ltd, Land Information New Zealand (LINZ) for the mineshaft site and our client for the substation site for their permission to discuss these two case studies.

6 REFERENCES

Edbrooke, S.W. 2001. Geology of the Auckland Area, 1:250,000 scale Map 3, Institute of Geological & Nuclear Sciences.

Fraser, C. (1910) The Geology of the Thames Subdivision, Hauraki, Auckland. New Zealand Geological Survey, Department of Mines.

Barker, T. 2014. Archaeological Assessment of Effects: 204 Bella Street, Thames, Former Bird in Hand No.2 Shaft Site. Heritage NZ, Pouhere Taonga.

Healey P.R., Head, J.M. 1984. Construction over abandoned mine workings'. CIRIA Special Publication 32, PSA Civil Engineering Technical Guide 34.

Leonard, G.S. Begg, J.G. and Wilson, C.J.N. 2010. Geology of the Rotorua Area'. 1:250,000 Geological Map sheet 5, Rotorua. GNS Science.

Geotechnical and Geophysical Site Characterisation 5 – Lehane, Acosta-Martínez & Kelly (Eds)

Assessment of underground karst caves using geophysical tests: A case study for Lajamgir dam site, Iran

F. Jafarzadeh
Civil Engineering Department, Sharif University of Technology, Tehran, Iran

M.M. Shahrabi, M. Banikheir & N. Eskandari
Abgeer Consulting Engineers, Tehran, Iran

A.A. Garakani & H. F. Jahromi
Civil Engineering Department, Sharif University of Technology, Tehran, Iran

ABSTRACT: Karst features have caused serious problems in many engineering projects because of their permeability and high leakage potential; a clear example is Lar Dam, 84 km northeast of Tehran in which normal water level has never been reached since the filling of its reservoir in 1980. Sometimes conventional methods of studying karst features (e.g., borings and sampling) fail to precisely reveal their underground structure and this may result in inaccurate design, extensive leakage and creation of sinkholes. In the present paper, an under-study dam site in Lajamgir, Zanjan province, northern Iran is investigated. Ground observations indicated the possibility of presence of Karst caves while borings showed no such feature. Detailed studies by means of geoelectrical (Electrical Resistivity Tomography, ERT) and geo-radar (Ground Penetrating Radar, GPR) tests demonstrated what was claimed by site observations and proved that a simple group of geophysical tests can effectively help reveal the general condition of underground karst caves which can be followed by a set of dense borings to assess the details.

1 INTRODUCTION

Karst features are mainly formed in limestone and other dissolvable lithological units and they cover approximately 33% of the earth's surface (Milanovic, 1981). Surface karst features are distinguished through geomorphologic maps, whereas, underground features are extended from the uppermost layers of the ground surface to great depths and are not easily discoverable. Thickness of the underground features varies normally from a few decimeters to tens of meters (Klimchouk, 1996). Leakage is one of the main problems associated with cavities and gaps formed in karstic zones. Recurring drainage in the foundation of dams result in their malfunction as water storage structures, therefore, a thorough survey is needed in the primary phase investigations of any dam to avoid such problems.

Geophysical techniques have proven to be very useful to engineers and geologists in order to identify anomalies related to underground cavities and gaps and have developed recently. Among the most favored geophysical tests used for this purpose, one can name electrical resistivity tomography (ERT) or geoelectrical imaging and an electromagnetic survey referred to as GPR (Ground Penetrating Radar) or geo-radar test. In ERT method, electrical current is applied into the soil by means of two electrodes. The electrical potential generated in another pair of electrodes is measured and the electrical resistivity (or its inverse electrical conductivity) of the subsoil is obtained. The electrical resistivity of the geomaterials can give a reasonable insight into their mechanical properties and is used to recognize different rock and soil formations, including the presence of caves and discontinuities. Various types of arrays are introduced for the purpose of geoelectrical testing including Wenner, Schlumberger, and dipole–dipole (Zhou et al, 2002).

GPR has also been widely applied to locate karst features (Robert and de Bosset, 1994; Grandjean and Gourry, 1996; Freeland et al, 1998; Doolittle and Collins, 1998; Cunningham, 2004; Kofman et al, 2006). It takes advantage of electromagnetic pulses that are produced by an antenna and received by another one which detects the changes in the dielectric permittivity of the subsoil. The method typically involves a systematic moving of both the generating and the receiving antenna in parallel lines in a way to entirely cover the surveying area. In the present paper, both ERT and GPR tests have used to detect the underground karst features at Lajamgir Dam site in Zanjan Province in northern part of Iran. Results obtained by both methods are presented followed by a discussion on the effectiveness and accuracy of geophysical tests as non-invasive investigations for detection of underground karst caves.

2 GEOLOGICAL SETTINGS

Lajamgir Dam is an under-study embankment dam located about 60 km west of the City of Zanjan in the Zanjan Province of Iran. The dam is planned to be constructed on the Lajamgir River, one of the main tributaries of Ghezel-Ozan River in a drainage basin with very high flooding potential. The study area is located in the Western Alborz-Azarbaijan structural zone with outcrops of sedimentary sequences from Oligo-Miocene to Miocene. The most important lithological units in the dam site include (old to new): (1) lower marl unit, (2) lower marly limestone unit, (3) middle marl unit, (4) upper limestone unit, (5) upper marl unit, (6) gypsiferous marl unit, (7) quaternary alluvial deposits. The upper limestone unit is underlain by a marl unit, has a thickness of 30-40 meters and is outcropped at the dam axis (Figure 1). As shown in Figure 1, this unit contains several dissolved karst caves and has a great potential for leakage. As a consequence, several geoelectrical and georadar tests were planned to be conducted on the axis of dam, on the river stream route and on the abutments of the dam. Figure 2 demonstrates the geological section of the dam foundation based on previous geotechnical investigations. It is clearly shown that sequences of limestone and marly limestone exists under the axis of the dam, proving the necessity of further underground investigations to locate any cavities and gaps and consider required measures to prevent leakage from the foundation and abutments.

3 FIELD INVESTIGATIONS

A total of 23 georadar arrays and 9 geoelectrical arrays (1 Schlumberger and 8 dipole-dipole) were designed on the axis of dam, on the river stream route and on the abutments of the dam as depicted in Figure 3.These investigations were concentrated mainly in locations where the possibility of the presence of underground karst features was the most. In order to improve the effectiveness and efficiency of the georadar method, multiple arrays were planned and performed in which the distance between the emitter and the receiver is varied.

In the dam site under study, the Schlumberger array for geoelectrical testing was feasible only on the river bed (array No. 10). A total number of 12 vertical sockets were placed at every 25 meters, perpendicular to the dam axis. The achieved processed section is shown in Figure 4(a). Anomalies which may be attributed to the dissolving karst caves are shown in circles. However, for a more accurate assessment, these anomalies should be compared to those achieved by georadar tests. The sections obtained by dipole-dipole arrays were also processed and two sections are shown as examples in figures 4(b) and 4(c). Lithological units, fractures and anomalies (marked with circles) can be seen through these sections.

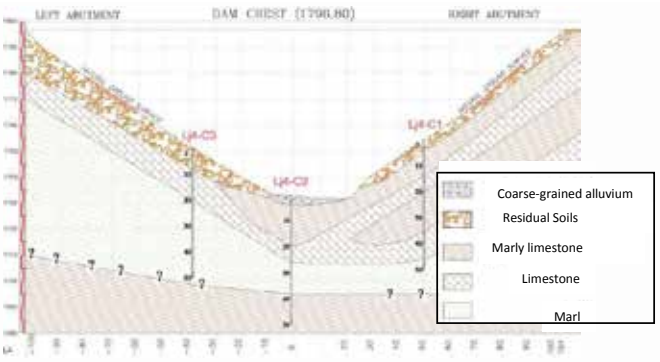

Figure 2. Geological section of the dam foundation under the axis

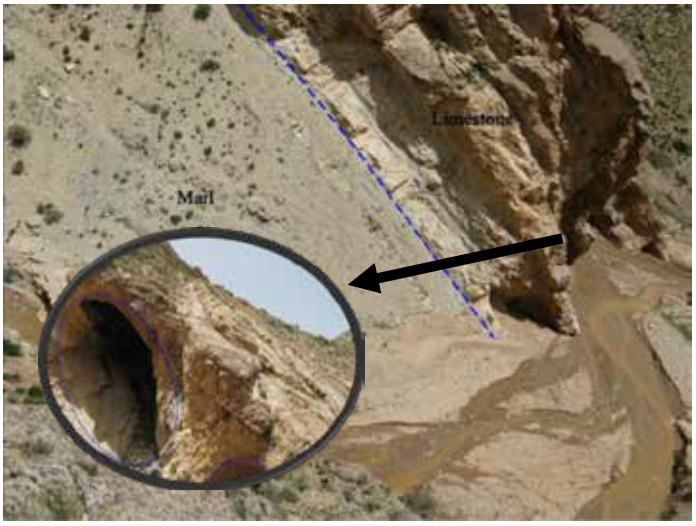

Figure 1. Limestone outcropping on the axis of Lajamgir Dam (large dissolved karst caves)

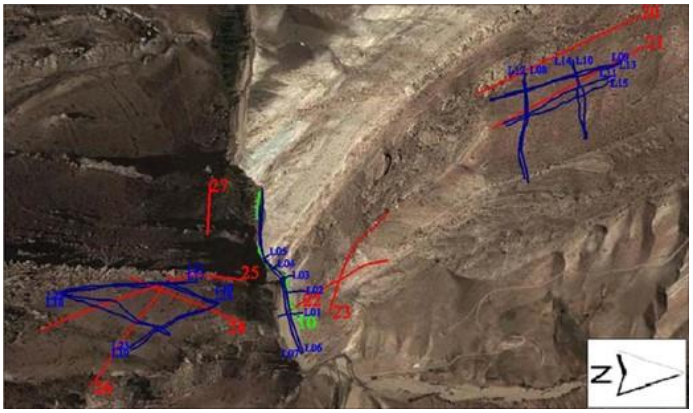

Figure 3. Location of geophysical arrays at the dam site, georadar arrays (L01-L23), geoelectrical arrays, dipole-dipole (1-9) and Schlumberger (10).

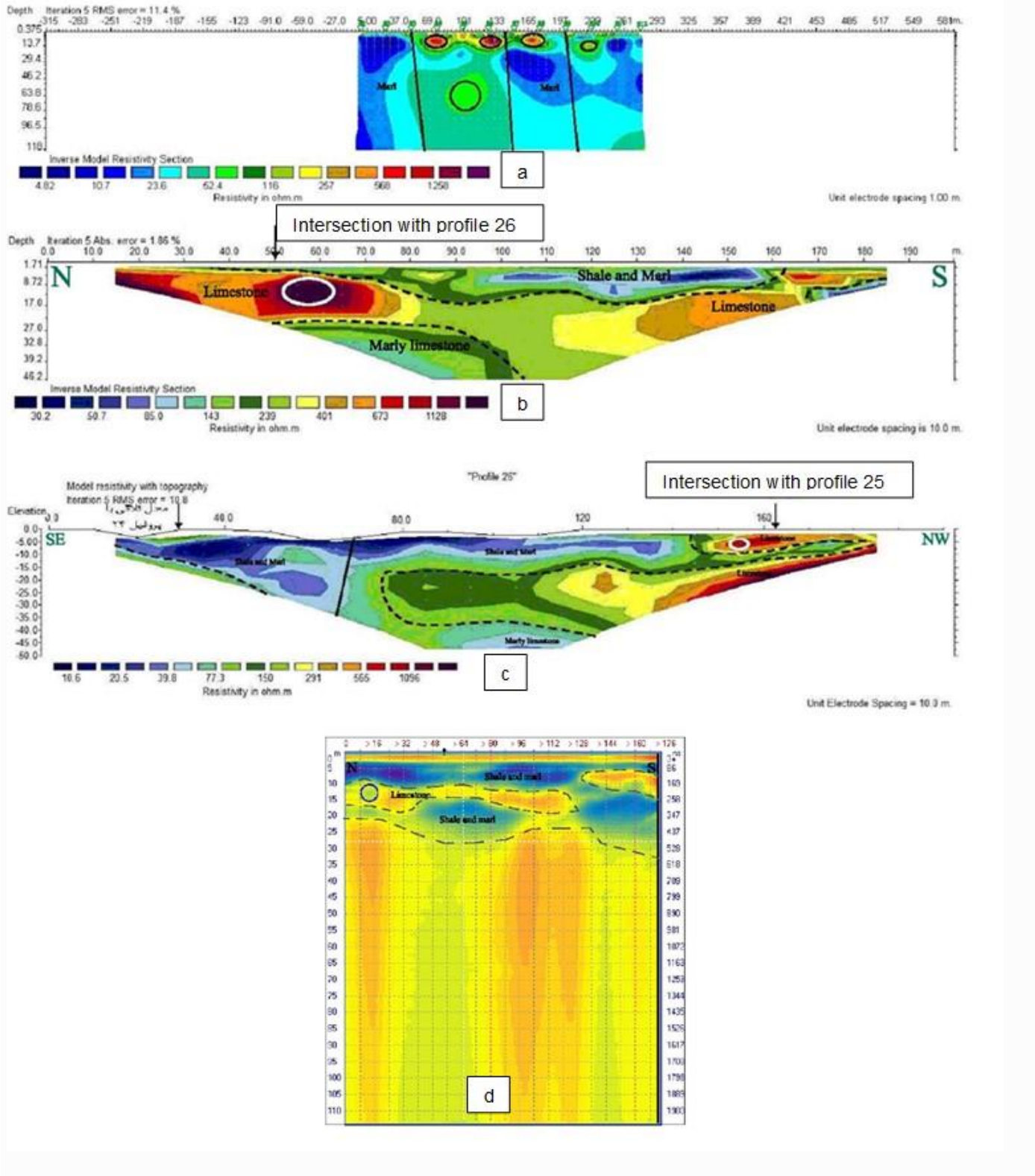

Figure 4. Typical results obtained by geoelectrical tests and Georadar tests; (a) Schlumberger array No.10, (b) dipole-dipole array No.25, (c) dipole-dipole array No.26, (d) georadar array No.L17.

Figure 5. Location of geophysical arrays at the dam site and the observed anomalies (shown in circles)

By comparing figures 4(b) and 4(c), it is observed that at the intersection of arrays No.25 and 26, an anomaly exists showing a very small electrical resistivity that can be ascribed to a karst cave.

For georadar testing, 27 arrays were designed on the river bedding, right and left abutments. Typical result obtained from the array No. L17 is shown id Figure 4(d). The section clearly defines different lithological units and the observed anomalies (marked with circles). As mentioned before, not all the anomalies detected through georadar tests are caused by karst features. Therefore, a detailed comparison should be made between the results obtained by geoelectrical and georadar tests to better prove the presence of any karst cave in the dam site.

All of the surveys demonstrated that at Lajamgir Dam site, anomalies are limited to depths of less than 20 meters. The results obtained by both geoelectrical and georadar tests prove that although anomalies are spread at the river bedding, left and right abutments (shown by circles in Figure 5), most of them are concentrated at shallow depths smaller than 5 meters under the river bedding. In general, it was observed that both methods provide valuable information on the present underground anomalies especially at shallow depths (<40 m), however, the results of geoelectrical tests are more reasonable in terms of accurate interpretation. Therefore, it is suggested that geoelectrical tests may be used solely for determination of underground karst features at dam sites and that georadar tests should be followed by a set of geotechnical borings to achieve a complete perception of underground lithological formations.

4 CONCLUSIONS

Lajamgir Dam site is located near the City of Zanjan in the Zanjan Province of Iran on the Lajamgir River, a tributary of Ghezel-Ozan River. The presence of limestone in the river bedding and the resulting leakage potential is an important issue about the Lajamgir Dam site studied in this paper. Two mostly used geophysical tests (geoelectrical and georadar) were performed to assess the underground lithological units and obtain information on karst features. In total, 23 georadar and 9 geoelectrical (1 Schlumberger and 8 dipole-dipole) tests were designed and performed on the axis of dam, on the river stream route and on the abutments of the dam. Surveys showed that most anomalies are shallow and mainly concentrated under the river bedding below the axis of the dam. Both georadar and geoelectrical approaches were proved to give reasonable information on presence of anomalies at small depths (<40 m). Nevertheless, it was observed that georadar tests were less accurate than geoelectrical tests and they need to be followed by a set of geotechnical surveys (boreholes) to better evaluate the presence of underground karst caves.

5 REFERENCES

Zhou, W., Beck, B.F. & Adams, A.L. 2002. Effective electrode array in mapping karst hazards in electrical resistivity tomography. *Environmental Geology* 42: 922-992.

Robert, A. & de Bosset, C. 1994. Application du géoradar à la localisation de cavités, de nids de gravier et de zones karstiques. *Journal of Applied Geophysics* 31 (1–4): 197–204.

Grandjean, G. & Gourry, J.C. 1996. GPR data processing for 3D fracture mapping in a marble quarry (Thassos, Greece). *Journal of Applied Geophysics* 36 (1): 19–30.

Freeland, R.S., Yoder, R.E. & Ammons, J. T. 1998. Mapping shallow underground features that influence site-specific agricultural production. *Journal of Applied Geophysics* 40(1–3): 19–27.

Doolittle, J.A. & Collins, M. E. 1998. A comparison of EM induction and GPR methods in areas of karst. *Geoderma* 85(1): 83–102.

Kofman, L., Ronen, A. & Frydman, S. 2006. Detection of model voids by identifying reverberation phenomena in GPR records. *Journal of Applied Geophysics* 59(4): 284–299.

Cunningham, K. J. 2004. Application of ground-penetrating radar, digital optical borehole images, and cores for characterization of porosity hydraulic conductivity and paleokarst in the Biscayne aquifer, southeastern Florida, USA. *Journal of Applied Geophysics* 55(1–2): 61–76.

Milanovic, P.T. 1981. *Karst Hydrogeology*. Water Resources Publications, Colorado, U.S., 434pp.

Klimchouk, A. 1996. Hydrogeology of gypsum formations. Gypsum karst of the world. *International Journal of Speleology* 25: 83-89.

Geotechnical and Geophysical Site Characterisation 5 – Lehane, Acosta-Martínez & Kelly (Eds)

A comparison of in-situ and laboratory resistivity measurements in soft clay

R. Kelly
SMEC, Brisbane, Queensland, Australia
J.A. Pineda & L. Suwal
ARC Centre of Excellence for Geotechnical Science & Engineering, University of Newcastle, Australia

ABSTRACT: In-situ resistivity data obtained using a hydrostatic profile tool are compared with resistivity measurements obtained from soil and water samples in the laboratory. Resistivity was then compared with porosity measurements to demonstrate that Archie's law can be used in natural soft clay deposits. Archie's law is then used to convert *in-situ* bulk conductivity measurements made with a hydrostatic profile tool to po-rosity. Porosities estimated using the hydrostatic profile tool were found to be similar to the measured porosi-ties.

1 INTRODUCTION

That a relationship between void ratio (or porosity) and electrical conductivity of pore fluid and bulk soils exists is well known (e.g Archie, 1942; Mitchell, 1993; Grellier et al, 2007; Kim et al, 2011). Mitchell (1993) classifies these relationships into nonconductive particle models and conductive particle models. Nonconductive models include Archie's Law, capillary models and cluster models. Conductive particle models include the Waxman and Smits two parallel resistor model and three element network models. While the models have varying levels of complexity, Archie's law is often used due to its simplicity and efficacy, mainly in granular soils (e.g. Atkins and Smith, 1961; Jackson et al, 1978; Campanella and Weemees, 1990; Salem and Chilingarian, 1999).

Archie's law relates the conductivity of the pore fluid (σ_w) to the bulk soil conductivity (σ_T) and the porosity (n) in the form:

$$F = \frac{\sigma_W}{\sigma_T} = an^{-m} \quad (1)$$

where a and m are empirical constants, commonly related to tortuosity and cementation, respectively. In Equation 1, F is known as the formation factor.

The hydrostatic profile tool (HPT Geoprobe™) is an in-situ penetration test that measures resistivity of the bulk soil. The HPT is 44.5mm in diameter and is equipped with a 4 pin electrical conductivity array located on the shaft of the tool behind the probe tip. It can be used to estimate the porosity of the soil if the constants in Equation 1 can be obtained along with the conductivity of the pore fluid. Pineda *et al* (2016) have measured bulk and pore fluid electrical conductivities as well as the porosity of soils at Australia's National Soft Soil Field Testing Facility in Ballina, northern NSW. In situ resistivity measurements have been carried out using the HPT probe. In situ and laboratory measurements are combined in this paper to assess the potential of the HPT to estimate porosity of Ballina clay.

2 LABORATORY AND FIELD TEST DATA

Soil samples were obtained using an hydraulic fixed-piston Osterberg sampler (89 mm in external diameter) from borehole Inclo 2 (see Figure 1) drilled up to 13 m depth using a mounted rig. In the laboratory, bulk electrical conductivity (σ_T) was measured by inserting an electrical conductivity probe into the soil mass. This soil was then compressed, under very slow strain-controlled mode, to squeeze out 15 cm^3 of pore fluid required to measure the pore fluid electrical conductivity (σ_w). Four measurements per tube were obtained by using the soil from top and bottom ends.

In the field, test HPT8 was performed approximately 100m north-west from borehole Inclo2 (see Figure 1), was pushed into the ground at 20mm/s using a conventional cone penetration rig and conductivity was recorded with depth.

The soil stratigraphy is shown in Figure 2(a) superimposed on cone penetrometer CPT8 which was performed next to HPT8. The stratigraphy comprised an upper clayey silty sand upper crust approximately 1.5m thick underlain by estuarine clay to approximately 11m depth which is in turn underlain

by a clean sand layer. The groundwater table lay at about 0.5m below ground surface at the time of sampling. The mineralogical composition of the estuarine deposits varies along the profile. In order of importance, the specimens are composed of amorphous minerals, kaolinite, illite, quartz, interstratified illite/smectite, plagioclase, pyrite, K-feldspar, mica and calcite.

Bulk and fluid electrical conductivities measured in the laboratory and in the field are presented in Figure 2(b). Bulk electrical conductivity measurements vary with depth from 4 mS/cm to 15 mS/cm. The reduction in bulk conductivity at about 11.1m depth confirms the change in soil composition. Bulk electrical conductivities measured in the laboratory are similar to those measured in the field. Differences between the two data sets might be due to spatial variation of soils or to subtleties of the different measurement techniques. Values of pore fluid electrical conductivity are larger than bulk conductivity. Pore fluid electrical conductivity varied from 7 mS/cm to 36 mS/cm (average below 5 m). Lower values measured at shallow depths may be due to dilution by fresh water from the ground surface.

Laboratory bulk and pore fluid electrical conductivity measurements have been combined here to estimate the variation of the Formation Factor in Ballina clay. The variation of the Formation Factor with depth is shown in Figure 3. Values of soil porosity estimated from laboratory test samples using mass and volume measurements as well as density of solid particles are also included in Figure 3. The Formation Factor shows an average value around 3 for the soft clay and increases up to 6.5 in the sandy layer encountered below 11 m depth. Porosity ranges from 0.5 at shallow depths to 0.75 which is the average value for the soft clay.

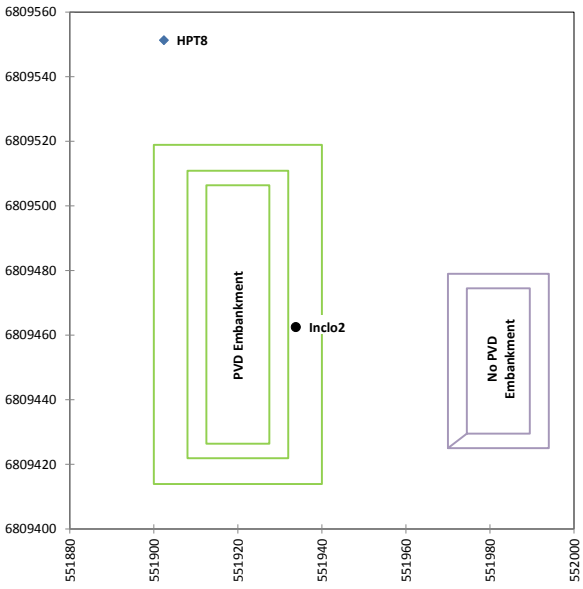

Figure 1. Site Plan: vertical axis Northings, horizontal axis Eastings

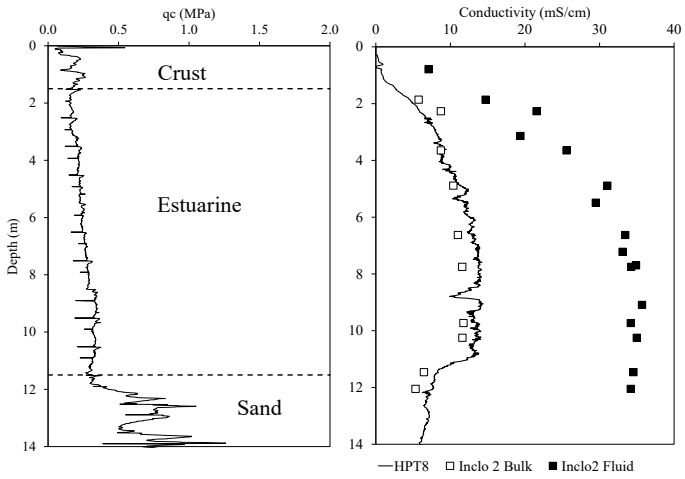

Figure 2.(a) CPTu results (b) bulk and fluid conductivities

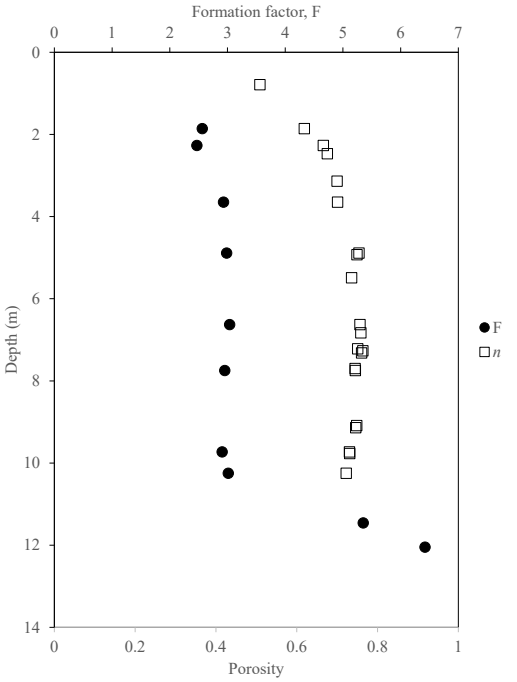

Figure 3. Formation Factor and Porosity

3 CALIBRATION OF ARCHIE'S LAW

Archie's Law can be re-written by taking logarithms of Equation 1, which is presented in Equation 2.

$$\log \sigma_T = m \log n + \log \sigma_w - \log a \qquad (2)$$

The logarithm of bulk electrical conductivity is compared with the logarithm of porosity, for data pairs taken from all samples in Figure 4. The slope of the line shows that the constant m is equal to 3.19. The intercept value of 1.46 is equal to the logarithm of the average of the pore fluid electrical conductivity measurements which implies that the constant a equals 1.0.

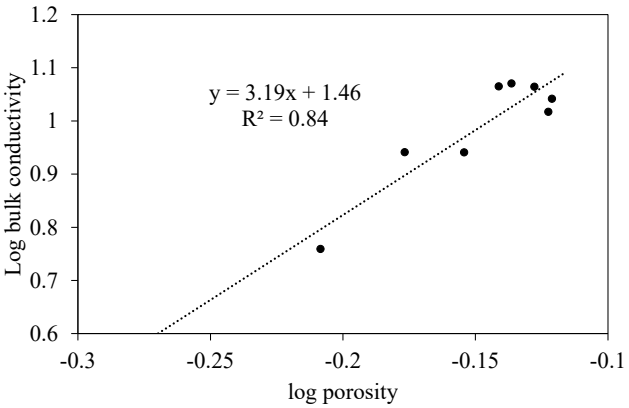

Figure 4. Calibration of Archie's law

The data set has been subdivided in Figure 5 to represent the different soil strata indicated previously in Figure 2(a). Here, the constant *a* is assumed to equal 1 and the fluid conductivity is assumed to equal the bulk conductivity when the logarithm of the porosity is zero (i.e., porosity = 1; implying no solids). Linear trend lines have been fitted through data sets representing 1.86m depth, 2.3m to 4.9m depth and greater than 5m depth. It can be seen that the slopes of the trend lines (constant *m*) vary with logarithm of the fluid conductivity. Average pore fluid electrical conductivity for the three data sets shown in Figure 5 are plotted against *m* values in Figure 6. An exponential fit to the data results in Equation 3.

$$m = 1.19e^{0.033\sigma_w} \quad (3)$$

It can be noted that *m* reduces with the pore fluid electrical conductivity and the soil composition. For σ_w=0, *m* is equal to 1.19 which is similar to the values reported in the literature for sandy materials (e.g., Jackson et al, 1978; Campanella and Weemees, 1990; Salem and Chilingarian, 1999)

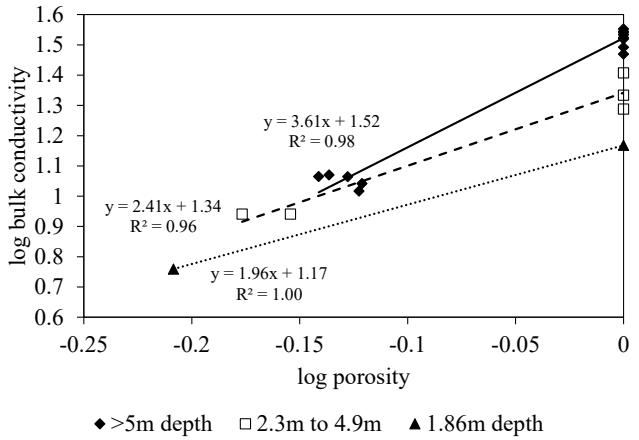

Figure 5. Calibration by soil layer

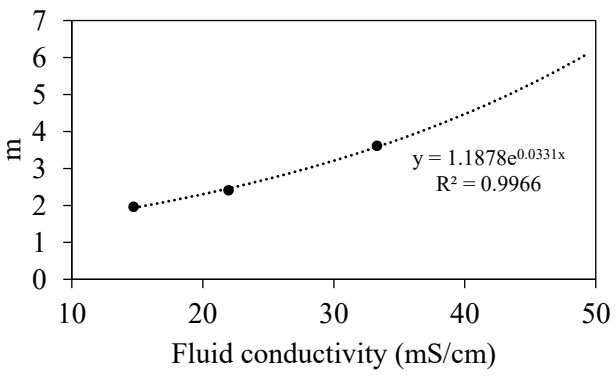

Figure 6. Relationship between σ_w and *m*

The data presented in Figures 4 and 5 have been used to correlate bulk conductivities measured by the HPT to porosity. The correlations are shown in Figure 7. The parameters adopted for the 'average' and 'by layer' series are presented in Table 1.

Table 1 Parameters used to fit HPT data

Parameter	*Average*	*By layer*
A	1.0	1.0, 1.0, 1.0
M	3.19	1.96, 2.41, 3.61
σ_w (mS/cm)	34.4	14.8, 21.9 33.1

The 'average' series fits the measured porosities reasonably well below about 5m depth and to a first approximation between 2m and 5m depth. The 'by layer' series improves the correlation between 3m and 5m depth but fits the data less well between 8m and 11m depth. There 'by layer' approach does not provide enough improvement in the correlation between the HPT measured bulk conductivity and porosity to warrant the additional effort required to define the parameters for Ballina clay.

Use of Archie's law to interpret HPT data in practice requires knowledge of the *a* and *m* constants along with the pore fluid electrical conductivity. While *a* can be assumed equal to 1.0, constant *m* and the pore fluid electrical conductivity will not be known in general. However, the observations that the Formation Factor for Ballina clay is about 3 and *m* is related to fluid conductivity through Equation 3 can be used to as a first approximation in Ballina clay. Using this approach, porosities have been estimated from HPT data. The results are shown in Figure 7 where data inferred from the average parameter set and the parameter set with F=3 are similar. Therefore, it is possible to assume a value (or values) for the Formation Factor without any prior knowledge, calculate the corresponding *m* value through Equation 3 and obtain a reasonable estimate for porosity.

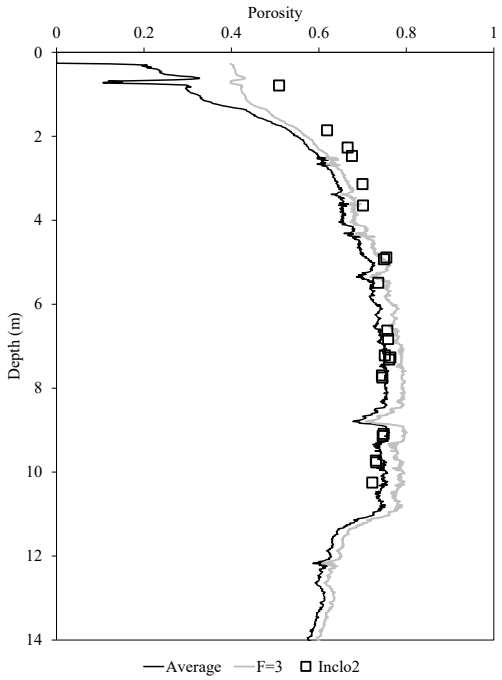

Figure 7. HPT and laboratory porosity with Depth

4 CONCLUSIONS

Laboratory measurements of bulk soil conductivity, fluid conductivity and porosity have been found to be related in accordance with Archie's law. Archie's law is a non-conductive particle model and the highly conductive saline pore fluid may dominate the bulk conductivity such that the contribution of the surface conductance of the clay particles is small (Mitchell, 1992). Values of a=1 and m=3.2 for Ballina clay are consistent with literature reported by Kim *et al* (2011), albeit with m=3.2 lying slightly above the upper end of the range of reported values.

Porosities interpreted from HPT data using Archie's law has been shown to represent measured values reasonably well to a first approximation.

Archie's law can be used with HPT data in practice by assuming a=1.0, assuming the Formation Factor, F=3 and adopting Equation 3 for Ballina clay.

Further work is required to assess whether Equation 3 can be used with other clays and to assess whether in-situ resistivity measurements can be used to estimate values of soil parameters depending on porosity, such as permeability.

5 ACKNOWLEDGEMENTS

The authors wish to acknowledge the support of the Australian Research Council Centre of Excellence for Geotechnical Science and Engineering and its industry partners Advanced Geomechanics (now Fugro), Coffey and Douglas Partners.

6 REFERENCES

Archie, G. E. _1942_. "The electrical resistance log as an aid in determining some reservoir characteristics." Trans. Am. Inst. Min., Metall. Pet. Eng., 146, 54–62

Atkins ER Jr and Smith GH (1961) The significance of particle shape in formation factor-porosity relationships, *J Pet. Technol.* 13(3), 285-291

Campanella RG and Weemees I (1990) Development and use of an electrical resistivity cone for groundwater contamination studies, *Can Geotech J*, 27, 557-567

Campanya J, Jones AG, Vozar, J, Rath, V, Blake, S, Delhaye, R and Farrell, T (2015) Porosity and Permeability Contraints from Electrical Resistivity Models: Examples using Magnetotelluric *Data, Proc World Geothermal Congress*, Melbourne, Autralia, 1-8

Grellier S, Reddy KR, Gangathulasi, J, Adib, R and Peters CC (2007) Correlation between Electrical Resistivity and Moisture Content of Municipal Solid Waste in Bioreactor Landfill, GSP No 163, ASCE, 1-14

Jackson PD, Taylor-Smith D and Stanford PN (1978) Resistivity-porosity-shape relationships for marine sands, *Geophysics*, 43(6), 1250-1268

Kim JH, Yoon H-K and Lee, J-S (2011) Void Ratio Estimation of Soft Soils using Electrical Resistivity Cone Probe, *J Geot and Geoenv Engineering*, ASCE, 86-93

Mitchell JK (1993) Fundamentals of Soil Behaviour, Second Edition, Wiley.

Pineda J.A., Suwal L.P., Kelly R.B., Bates L. & Sloan S. (2016) Characterization of the Ballina clay. Geotechnique (in print), doi: 10.1680/jgeot.15.P.181.

Salem HS and Chilingarian GV (1999) The cementation factor of Archie's equation for shaley sandstone reservoirs, J. Pet. Sci. Eng., 23, 83-93

Geotechnical and Geophysical Site Characterisation 5 – Lehane, Acosta-Martínez & Kelly (Eds)

Geophysical Characterisation for Dredging of the Marine Industry Park, Darwin

J. Lean
Douglas Partners Pty Ltd, New South Wales, Australia

S. Williams
GBG Australia Pty Ltd, New South Wales, Australia

ABSTRACT: The Marine Industry Park is a major state development requiring significant dredging of sediments, soils and meta-sediments including quartzite's. To characterise the subsurface for dredgeability assessment, a marine geophysical investigation was carried out by Douglas Partners and GBG Australia in 2015, comprising multi-beam bathymetry, side scan sonar, magnetics, seismic reflection and seismic refraction, with geotechnical control from vibro-coring and onshore drilling. High resolution bathymetry allowed calculation of total dredge volumes and added morphological detail to sonar and vibro-core data, for characterisation of seabed materials ranging from silty clays to mobile sand bodies to lateritic gravels (dominating the magnetic response) and for mapping of dredging hazards including wrecks. Seismic reflection record character allowed the extent of the sand bodies to be inferred and allowed mapping of an inferred buried laterite or residual soil horizon. A deeper reflector, mapped throughout the area, was interpreted as the bedrock surface, indicating significant volumes of bedrock within the proposed dredge volume. To characterise both the sub-seabed and sub-bedrock materials in terms of dredgeability, extensive seismic refraction profiling was carried out for construction of a "full volume" tomographic inversion velocity model, sliced vertically and horizontally for velocity contouring. The distribution of high velocities, reaching over 3000 m/sec within the proposed dredge volume, provided a clear indication of anticipated zones of hard dredging and provided parameters for assessment of the impacts of dredging and blasting.

1 INTRODUCTION

The Land Development Corporation of the Northern Territory commissioned a combined geotechnical and geophysical site characterisation of the proposed site for a Marine Industrial Park (MIP) lying between the current East Arm port facility and Hudson's Creek to the East of Darwin City. The proposed MIP development will focus on marine related industries to service the offshore energy industry in the Timor and Arafura Seas.

The investigation work was undertaken by a combined team from Douglas Partners, GBG Australia and Astute Surveying and comprised multiple marine geophysical techniques backed up by limited marine vibro-coring along with onshore cone penetration tests, test pits and boreholes.

The over-water investigations were required as part of the overall preliminary geotechnical investigations for feasibility and design purposes for the proposed dredging of access channels, turning bays and the wharf facilities. Figure 1 shows site location and extents.

The marine geophysical program was planned and undertaken in line with the scope specified by the client's engineering consultant. This entailed collection of the following quantities of data:

- Multi –beam bathymetry - 183 line kilometres
- Side Scan Sonar – 147 line kilometres
- Horizontal marine magnetic Gradiometer – 191 line kilometres
- Seismic Reflection profiling - 111 line kilometres
- Continuous Marine Seismic Refraction – 136 line kilometres

At the time of confirming the program, the spacing requirement of 25m in both directions for marine seismic refraction had been considered potentially excessive. However, as shown in this paper, on completion of the processing and in the reporting stage this quantity of information proved invaluable in characterizing the bedrock for dredging purposes.

Figure 1: outline of full investigation site and local features.

2 OVERVIEW OF GEOLOGY

Rock outcrops are present over parts of the site, particularly in areas of high terrain and in some of the intertidal zone. The outcrops typically comprise meta-siltstone of the Burrell Creek Formation (BCF), with minor meta-sandstone and quartz sandstone or quartzite. The intertidal zone is generally dominated by thin tidal mud with laterite gravels and outcropping meta-siltstone. The proposed dredge channel is in an area where frequent large tidal movements occur, and this was expected to limit depositional sediments to coarser materials such as sand gravel. The dredge channel also passes by Catalina Island and a small shoal exposed at low tides and shown on existing navigation charts. Both of these areas are considered likely to comprise bedrock belonging to the BCF that has remained after erosion of the surrounding weaker rocks. The BCF typically strikes in a near north-south direction, and steeply dips to the east or west, so the near vertical bedding planes of strong bedrock observed on Catalina Island are expected to continue to the north and south, through the proposed dredge channels and berthing pockets

3 FIELD WORK

Offshore geophysical field work comprised:

- Multi-beam bathymetric mapping was undertaken by an Australian Hydrographic Society Certified Practitioner (AHSCP), Level 1 (Hydrography), for the full extent of the Common Access Channel, Approach Channel and proposed near shore dredging areas east and west of the northern end of the Approach Channel. The multi-beam survey extended over the full width of all required investigation areas plus an extra 100 m outside of proposed dredge zones;
- Side scan sonar mapping to provide a full seabed image of the proposed dredge areas and extended area outline above;
- Horizontal magnetic gradiometer profiling to assess the proposed dredge and extended areas for possible Unexploded Ordnance (UXO) and other significant debris;
- Marine seismic reflection (boomer) profiling to interpret the sub bottom sediments and the interface with the bedrock;
- Continuous marine seismic refraction profiling using a 24 channel, 2m separation hydrophone array and 20 cubic inch airgun source to enable an assessment of the consistencies and strengths of the materials to be dredged

During the collection of the bathymetric and seismic reflection data, onboard evaluation of the data suggested that the ground conditions between the southern end of the proposed north – south approach and the existing Inpex channel turning basin (a distance of approximately 140m) might comprise sands and gravels rather than rock, thus suggesting easier than expected dredging conditions. After consulting with the client about the possibilities of extending into the Inpex channel, the bathymetric, seismic reflection and refraction were extended through this section, thus providing a potential alternative channel option. Figure 2 presents bathymetry and raw (boomer) reflection data from this extended section.

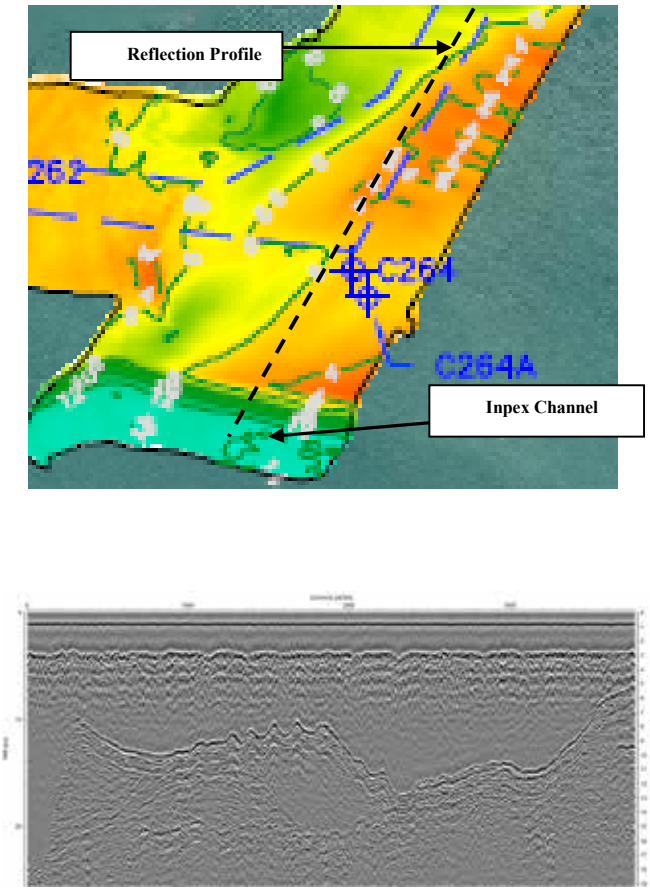

Figure 2: Bathymetry Boomer profile over sand bar into Inpex

Data collection for the majority of the survey was undertaken from a 6.5m aluminum vessel. However, due to the extent of the seismic refraction survey, a larger local 12m commercial vessel was chartered to enable the use of a compressor to supply the air gun source and enough deck space to load the marine streamer and ancillary equipment. The full survey was completed in 5 weeks on site.

4 DATA HANDLING AND REPORTING

The survey produced large volumes of digital data which were initially processed on site each day to minimize the office time and to provide Quality control. The bathymetry and Sonar data were processed and reported using Hypack 2015 (Hypack) and Sonarwiz v5.8(Chesapeake Software), the magnetic data was processed using Magmapper 2000 (Geometrics freeware) and Surfer v13 (Golden Software). The seismic reflection processing and reporting was undertaken using Reflex v 7.5 (Sandmeier) and the initial processing of the refraction data (first arrival picking) was undertaken with Rayfract v3.3 (Intelligent resources) prior to transfer to Tomoplus (Geotomo) to create the 3d velocity models.

The output from all these software programs was imported into CivilCAD and ACAD 2015 for provision to the client. This allowed provision of sections, images and depth-slice plan views at RL values set by the client, in line with the proposed dredging program. This ability allowed a much more accurate assessment of dredging extents and volumes for the site for a staged construction approach.

4.1 Results

The bathymetric survey mapped the seafloor in 0.5m gridded bins providing high resolution imaging of the seabed with contouring at 1m intervals. The bathymetry showed variation in seabed topography between 6m above LAT (Lowest Astronomical Tide) to 20m below LAT over the site. Consequently, a considerable amount of the site will require dredging to meet the design declared depth of 6.2m below LAT.

The sonar was utilized to locate sea bed obstructions and classify seabed type. A number of wrecked boats were observed in the Mangrove areas to the north of the site and variation between exposed rock, fine mud and sand were observed. However, one of the most important images was that of a wrecked Catalina Flying boat sunk during the war and listed as a heritage site. The approximate position was already known. However, multibeam bathymetry and sonar confirmed its exact position and condition, noting that it is in the middle of the proposed approach channel. Figure 3 (over the page) clearly outlines the body of the plane and the separate wing section.

The magnetic response data identified an abundance of targets at the northern end of the survey site, in the mangroves, and in the channel areas. However, research of WW2 archives suggested that there would be little likelihood of UXO in this area as it was well away from the main bombing runs on Darwin.

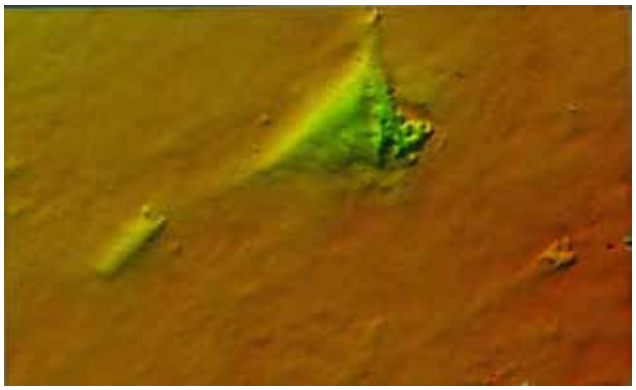

Figure 3: Catalina Flying boat wreck in sonar and backscatter Multi-beam record. Main body and wing section

Seismic reflection profiles, calibrated against vibro-core data, were used to interpret the bedrock elevation and to help in classifying the marine sediments. The X,Y & Z coordinates for the interpreted bedrock surface were used to create 3D models and plan view depth slices at proposed dredging stages to enable extent and volume modeling of

sediment and rock materials. For quality control, selected velocity profiles, produced using the 3D Geotomo software, were compared with corresponding seismic refraction profiles.

The seismic refraction data were collected with high density to create detailed velocity models for the subsurface materials. This was considered extremely important at this site because of the steep dip of the meta-sediments and varied mixture of hard and soft layers. Previous experience of dredging these materials in Darwin indicated that strengths based on limited geotechnical investigations had proved inadequate for the design of dredging and rock-removal works. The process used to assess the dredgeabilty of the MIP is discussed in detail below.

5 SEISMIC REFRACTION PROFILING, TOMOGRAPHIC MODELING AND DEPTH SLICING

An extraordinarily dense (25 m x 25 m) seismic refraction grid was specified for this project, leading to almost 140 line-km of continuous underway profiling. A computer-controlled shot interval of 10 m created a daunting dataset of almost 14,000 shot records saved to a Geode seismograph, however the benefits of such a dense grid became apparent during processing.

The ability to characterize the proposed dredge volume over the full design area, at all design depths, was achieved by creating velocity models from an initial dataset comprising: shot and receiver positions; seabed depths; and picked first break arrival times, for each shot. The dataset for selected lines was used as input to GeoTomo's, TomoPlus software for inversion to initial, coarse, 2D velocity-depth models for these lines, followed by comparison of velocities on intersecting and neighboring lines and calculation of velocity anisotropy parameters for use as subsequent model constraints. As expected in an area of vertically foliated bedrock, velocities measured along strike were seen to exceed those measured across strike, by approximately 10%. In order to produce a model which accommodated both along-strike and across-strike data, an anisotropy parameter was used to weight the velocities determined in the vicinity of intersections, biased towards the higher values for a conservative outcome in terms of dredge ability. The dataset was then expanded to include more lines and was re-gridded with a finer cell size for further inversion, when convergence was achieved.

Contoured 2D vertical velocity-depth sections (e.g. Figure 4), were first extracted from the model along selected alignments, for correlation with the interpreted bedrock surface from seismic reflection profiling and with graphic vibro-core and onshore borehole logs. These sections indicated relatively low velocity (1600 – 1900 m/s) material draped over zones of higher velocity material comprising sub-vertical velocity blocks. This pattern appeared consistent with the expected geology of the area, comprising layers of clay, silt and sand overlying meta-sediments with near-vertical foliations, containing quartz sandstone interbeds, frequent quartz veins and minor quartz pebble conglomerate.

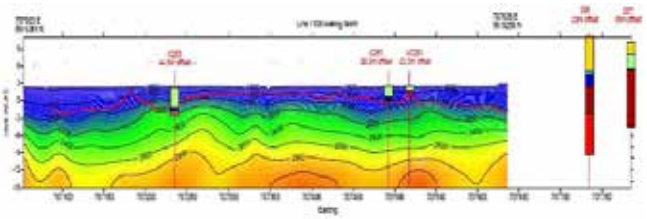

Figure 4: Interpreted refraction section with velocity contours, bedrock reflection and core logs

Next, a "full volume" or 4-dimensional (X,Y,Z,Velocity) model was produced by a similar recursive inversion process, leading to velocity values in each cell of a 3D grid covering the entire investigation area, to depths exceeding the proposed ultimate dredge depth. Finally, depth slicing was carried out by extracting all (X,Y,Velocity) data at selected depths throughout the area and contouring the velocities, to produce a "stack" of maps to demonstrate the areal and vertical distribution of velocities for dredgeability assessments. Figure 5 presents the interpreted velocity distribution at a depth of 6 m below Chart Datum, with velocities of over 3000 m/sec at the upper end of the contour-spectrum (highlighted within the red rectangle). The *"Transparent zones" within the channels, presented on Figure 5, are where the seabed depth exceeds the slice depth.*

Site characterization for dredging purposes is heavily dependent on the distribution of velocities. To present the 3D distribution of velocities considered significant to the feasibility and means of dredging, in a practical way rather than a 3D "fly through" visualization, three slices in the velocity "stack" (0 m, 3 m and 6 m below chart datum) were re-classified to show areas exceeding 2300 ms^{-1} and were overlain in plan view – an example, indicating a near-shore portion is presented in Figure 6. The velocity value of 2300 ms^{-1} was based on correlations made by others in an adjacent area of East Arm, between mapped velocities and reported dredging difficulties ("shudder" and "ladder bounce"), although considered below that indicative of the need for rock blasting. Figure 6 indicates that the area of which *velocities exceed 2300 m^{-1} (expected difficult dredging expands rapidly with depth*

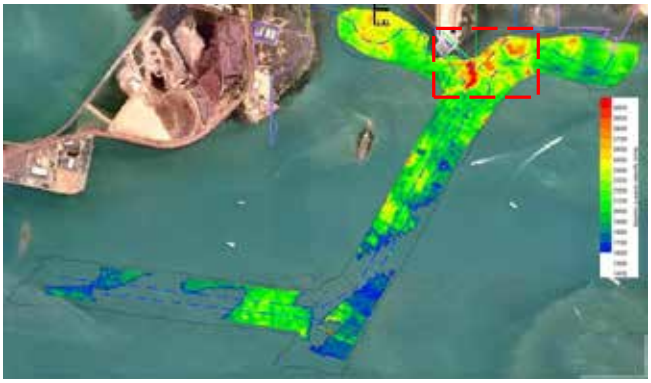

Figure 5: Velocity model sliced at a depth of 6 m below LAT.

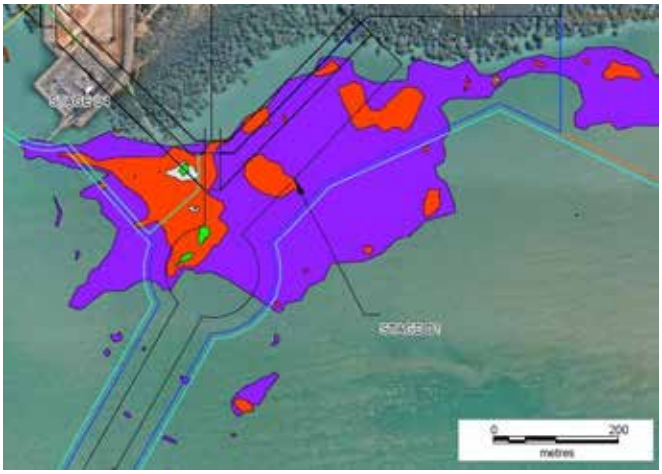

Figure 6: Velocity model slices from 0 m, 3 m and 6 m below LAT

6 SITE CHARACTERISATION SUMMARY

The Marine Industry Park geophysical investigation enabled site characterisation firstly by direct, high resolution bathymetric mapping to provide basic data for dredge design and calculation of dredge volumes.

Characterisation was extended by interpretive methods based on side scan sonar mapping and seismic reflection profiling, controlled by comparisons with elevations interpreted from vibro-core logs and onshore borehole logs. Seabed and sub-seabed materials were inferred to comprise: sandy, silty marine clays near shore; and clayey marine sands, mobile ripple-marked clayey, silty marine sands and areas of laterite or residual soil and sub-cropping meta-sedimentary bedrock in the offshore channels. Some distributed lateritic gravel was inferred within the shallow sediments, mapped from the magnetic gradient response.

Intensive processing and computer modeling of seismic refraction data enabled sub-seabed velocity mapping over the investigation area, presented in velocity-depth sections and contoured velocities on horizontal depth slices. Velocities alone enable a qualitative assessment of dredgeability by highlighting areas of higher velocities, associated with harder dredging. To further characterise the site with respect to dredgeability, reference was made to: published empirical relationships between velocities, material types and geotechnical properties (Ohkubo and Teresaki 1977; Hawkins and Whiteley (undated)); locally reported correlations (confidential company reports); and to geotechnical properties from onshore boreholes drilled in conjunction with this investigation. By these means, the following inferences were made:

- Marine sediments with velocities as low as 1600 m/sec increasing towards 1900 m/sec;
- Laterite and residual soil with velocities up to 1900 m/sec;
- Extremely weathered or fractured BCF, increasing in strength as velocities increase from 1900m/sec towards 3400m/sec
- High strength BCF, with velocities measured as high as 3400 m/sec.

Adoption of the nominal lower velocity limit (2500 m/sec) above, for rock requiring blasting, enabled locations and depths to be extracted from the velocity model for use by the client's blasting consultant in progressing the project towards environmental impact assessments.

7 CONCLUSIONS

Geophysical investigation can provide valuable data towards characterization of a site proposed for dredging, independently of other data in the first instance but with much greater effect when interpretation is controlled by targeted geological and geotechnical data. At this site, a suite of geophysical methods, including multi-beam echo-sounder, side-scan sonar, magnetic survey, seismic reflection and seismic refraction, were used.

The extraordinarily dense grid of seismic refraction profiles specified for the investigation enabled an extremely detailed 4D velocity model to be developed for the site. This enabled enhanced interpretations of the surface and sub-surface ground conditions for dredging assessments

The identification of an additional potential channel alignment confirms that experience-based, in-field assessment of site conditions and collaborative relationships between consultant and client can lead to valuable outcomes.

8 ACKNOWLEDGEMENTS

The authors are grateful for the collaborative nature of the working arrangement between Douglas Partners, GBG Australia and the Land Development Corporation and for the Corporation's permission to publish this paper.

Geotechnical and Geophysical Site Characterisation 5 – Lehane, Acosta-Martínez & Kelly (Eds)

Generalization and Standardization of Multi-station Surface Wave Method for Site Investigation

C.P. Lin & C.H. Lin
National Chiao Tung University, Hsinchu, Taiwan

ABSTRACT: The application of surface wave method for site investigation becomes more and more popular in practical uses due to its non-intrusive tests and convenient operations. However, various methods have been developed with different approaches in the field testing and dispersion analysis, with the SASW and MASW methods being the two major groups. The data reduction method for dispersion relation in a surface wave testing is conventionally associated with certain method of data acquisition. In this paper, it is pointed out that, while the channel number of a seismograph may restrict the field testing procedure, it does not necessarily prescribe the method of dispersion analysis. Limited to the two channel data, conventional dispersion analysis of SASW suffers from possible phase un-wrapping errors, inefficient data filtering and synthesis, and inability to distinguish multiple modes. The MASW method is generalized to accommodate SASW data. Numerical simulations were performed to demonstrate its feasibility and advantages for analyzing SASW data. The MASW method is further examined to show tradeoffs involved in the testing configuration when spatial resolution, effect of lateral heterogeneity, spectral resolution, investigation depth, and near and far field effects are considered. Some efforts are made in this paper to resolve the dilemma and put forth a more definitive guideline for MASW testing and analysis.

1 INTRODUCTION

Field testing methods conventionally used in geotechnical site investigations are mainly penetration methods (e.g. standard penetration test, SPT, cone penetration test, CPT, and dilatometer test, DMT). Those methods are primarily large-strain methods that provide better prediction for ground strength than ground stiffness. Shear wave velocity (Vs) from seismic tests, on the other hand, measures small-strain modulus. Soils exhibit nonlinear variation in shear modulus with shearing strain (G –log γ curve) and in shear stress with shearing strain (τ –γ curve). However, in addition to dynamic response, the importance of small-strain modulus from Vs measurement on static deformation analysis has also been pointed out, especially for analyses of settlement and soil structure interaction (see, for example, Shibuya et al. 1994; Jardine et al. 1998; Jamiolkowski et al. 2001; Di Benedetto, et al. 2003). Furthermore, Stokoe et al. (2004) showed that Vs measurement in the field is a critical component in evaluating sample disturbance and in predicting nonlinear G – log γ and τ – γ curves.

The main advantage of surface wave method for Vs measurements is essentially related to its non-destructive and non-invasive nature that allows the characterization of hard-to-sample soils without the need for boreholes that makes the subsurface seismic methods (such as down-hole and cross-hole methods) expensive and time consuming. Surface wave testing is not affected by sample disturbance or insertion effects and is capable of sampling a representative volume of the ground even in difficult materials such as fractured rock or gravelly deposit. The method has been successively applied to various problems, such as profiling sub-ground stiffness (Foti 2003), delineating potential liquefaction area (Lin et al. 2004), evaluating thickness and condition of pavement (Ryden et al. 2004), evaluating efficiency of soil improvement (Lin et al. 2012), and characterizing waste disposal site (Haegeman and Van Impe 1999).

Three steps are involved in a surface wave test: (1) field testing for recording surface waves, (2) determination of the experimental dispersion curve from the field data, and (3) inversion of shear wave velocity profile from the experimental dispersion curve. The data reduction method for dispersion relation in a surface wave testing is conventionally associated with a certain method of data acquisition. At present, the two-station spectral analysis of surface wave and multi-station analysis of surface wave are the most popular methods used worldwide. The

two-station SASW method is based on the phase difference between two receivers as a function of frequency (Nazarian and Stokoe 1984), while Multi-station MASW method are based on the relation between phase angles and source-to-receiver offset (Lin and Chang 2004), or 2D wavefield transformation of surface wave (see, for example, McMechan and Yedlin 1981; Gabriels et al. 1987; Park et al. 1998; Xia et al. 2007). It can be confusing to geotechnical engineers as to their differences and which method performs better.

This study attempted to clarify their differences and suggest preference. It is pointed out that, while the channel number of a seismograph may restrict the field testing procedure, it does not necessarily prescribe the method of dispersion analysis. Limited to the two channel data, conventional dispersion analysis of SASW suffers from possible phase unwrapping errors, inefficient data filtering and synthesis, and inability to distinguish multiple modes. The MASW method is generalized to accommodate SASW data. Numerical simulations were performed to demonstrate its feasibility and advantages for analyzing SASW data. The MASW method is further examined to show tradeoffs involved in the testing configuration when spatial resolution, effect of lateral heterogeneity, spectral resolution, investigation depth, and near and far field effects are considered. Some efforts are made in this paper to resolve the dilemma and put forth a more definitive guideline for MASW testing and analysis.

2 GENERALIZATION OF DISPERSION ANALYSIS

In a conventional two-station SASW test, the two recording stations are in line with the source and typically have the same spacing as the near offset (distance between the source and nearest receiver). By Fourier transform, the phase shift between the two signals can be determined for each frequency. The phase velocity $v_a(f)$, or more precisely the apparent phase velocity since the wave may propagate in more than one mode, can then be calculated as

$$v_a(f) = \frac{2\pi f}{\frac{\Delta\phi(f)}{\Delta x}} \tag{1}$$

where f is the frequency in Hz, Δx is the receiver spacing, and $\Delta\phi$ is the phase shift between the two receivers after unwrapping. To overcome the near field and far field effects, the tests are typically repeated with various receiver spacings, each of which analyzed for its associated appropriate frequency range. The testing sequence can be arranged in so-called common source array or common midpoint array.

The introduction of SASW method using only two-channel recording greatly contributed to the wide-spread use of surface wave testing in geotechnical engineering in its time. However, both its strength and weakness are related to the minimum number of stations used for phase velocity determination. Using only a pair of receivers, different modes of propagation cannot be differentiated, and the data reduction for correcting possible unwrapping errors is tedious. As multi-channel recording system became readily available, methods based on multi-station receivers sprouted. Multi-station methods sample the wavefield at multiple locations. The sampling periods in the time and space domain are Δt and Δx; and the numbers of samples in the time and space domain are M and N, respectively. The analysis of the multi-station signals may begin with Fourier transform as

$$U(f, x_n) = \sum_{m=0}^{M-1} u(t_m, x_n) \exp\left(-j2\pi f t_m\right) \tag{2}$$

where u is the ground motion (typically velocity) recorded by the receivers with space interval Δx and time interval Δt, U is the DFT of u, $j = \sqrt{-1}$, $t_m = m\Delta t$, and $x_n = n\Delta x$. The subscripts n and m in Eq. (2) are integer indices to represent respectively discrete points in the space and time domain. The most straight-forward algorithm of dispersion algorithm is the 2-D Fourier transform, which is often referred to as the *f-k* transform (Gabriels et al. 1987). For each frequency component of interest in Eq. (2), the wavefield U is a harmonic function of space. By taking another Fourier transform with respect to the space (i.e. spectral analysis in the space domain),

$$Y(f, k) = \sum_{n=0}^{N-1} U(f, x_n) \exp\left(-j2\pi k x_n\right) \tag{3}$$

where 2-D spectrum $Y(f, k)$ represents the wavefield in the frequency-wavenumber domain, the wavenumbers (spatial frequency, inverse of wavelength) of propagating modes for each frequency can be identified at amplitude peaks of the spectrum $Y(k)$. The phase velocity is then determined by the definition $v=2\pi f/k$. Alternatively, the *f-v* spectrum can be derived from Eq. (3) by simply changing the variable $k = 2\pi f/v$ as

$$\hat{Y}(f, v) = \sum_{n=0}^{N-1} U(f, x_n) \exp\left(-j\frac{2\pi f}{v} x_n\right) \tag{4}$$

where 2-D spectrum $\hat{Y}(f, v)$ represents the wavefield in the frequency-velocity domain, which will be used throughout this paper. The peaks of the amplitude of the frequency-velocity domain spectrum constitute the experimental dispersion curve. Spectra in other domains can be derived from (3) by simply changing the variable $k=2\pi fp$ for the frequency–slowness domain and $k= 2\pi/\lambda$ for the frequency–

wavelength domain. Other 2-D transform algorithms are also available, such as, *p-f* transform (McMechan and Yedlin 1981), the phase shift (Park et al. 1998), and the frequency decomposition and slant stacking (Xia et al. 2007). But they are essentially or physically equivalent to Eq. (3) and Eq. (4).

The dispersion analysis in a surface wave testing is conventionally associated with a certain method of data acquisition, for example, the phase angle analysis in the two-station SASW method and the 2-D multi-station wavefield transformation in the MASW method. While the channel number of a seismograph may restrict the field testing procedure, it does not necessarily prescribe the method of dispersion analysis. In fact, the 2-D wavefield transformation can be extended to accommodate the two-station SASW data. Two-D wavefield transformation formulated in the form of Eq. (3) or Eq. (4) can be used to process each pair of SASW data. To demonstrate this approach, numerical simulations were performed using two distinct earth models. One is a normal profile with a dominant fundamental mode and the other is a reversal profile with multiple dominant modes. The parameters of the earth models used are listed in Table 1. Both SASW and MASW testing are numerically simulated. The common-midpoint receiver spacings for the SASW testing include 2 m, 4 m, 8 m, 16 m, 32 m, and 64 m. The receiver spacing for the ordinary MASW testing is 2 m. Synthetic waveforms for the surface wave testing were simulated by the modal summation method programmed by Herrmann and Ammon (2002).

The results of 2-station MASW analysis for the normal case is shown in Fig. 1. The spectral resolution of the dispersion image increase with increasing receiver spacing. However, as receiver spacing gets longer, aliasing patterns are observed. Fortunately, the dispersion curve typically has a shape different and can be differentiated from the aliasings. Dispersion curve can be picked starting from the shortest receiver spacing at high frequencies.

Table 1. Parameters of earth models used in numerical simulations.

Model	Layer	V_s(m/s)	V_p(m/s)	Layer Thickness(m)	Density(g/cm³)
1	1	300	600	10	1.8
	2	400	800	∞	1.8
2	1	300	600	4	1.8
	2	250	500	8	1.8
	3	400	800	∞	1.8

Figure 2 shows the picked dispersion curve, in which the usual filtering criterion ($\lambda/3$ < geophone spacing < 2λ) was applied to mitigate effects of near field and far field. The dispersion curve obtained from 2-station wavefield transformation is basically identical to that from the conventional SASW analysis using Eq. (1). However, the wavefield transformation avoids the ticklish and error-prone phase-unwrapping procedure. It is also more tolerant to measurement errors (e.g. noises and waveform clipping) than the two-station phase analysis using Eq. (1). Similar results are obtained for the case of reversal profile with multiple dominant modes, as shown in Fig. 3 and 4.

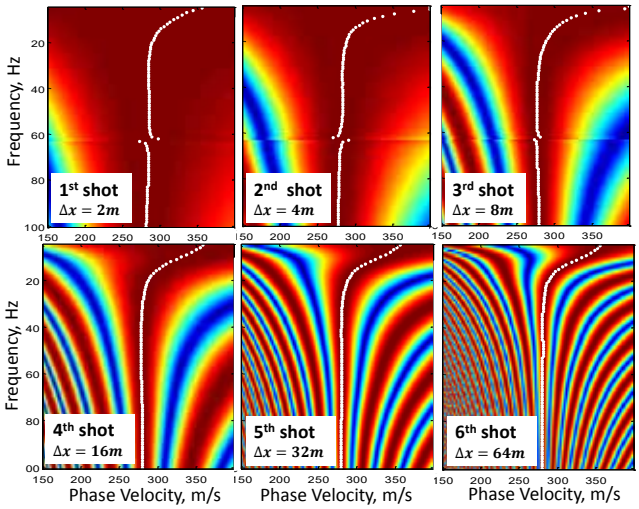

Figure 1. Results of 2-station wavefield transformation on each pair of SASW data for Model 1.

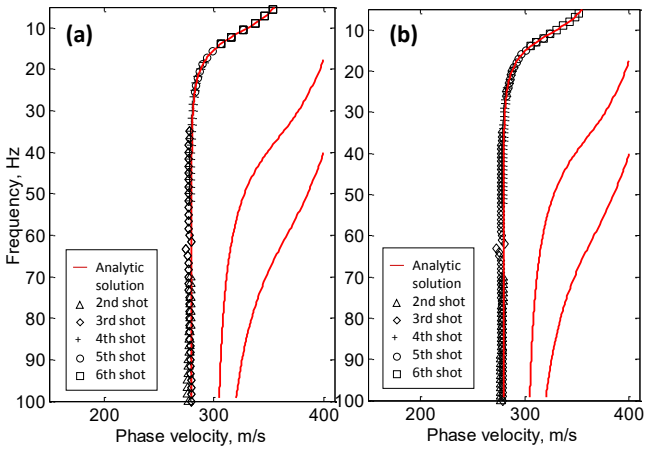

Figure 2. The dispersion curve obtained by (a) SASW method and (b) 2-station wavefield transformation for Model 1.

Limited to the two-station data and aliasing, the wavefield transformation is not able to separate different dominate modes. Instead of analyzing each pair of 2-station data, all SASW data can be combined by the source-to-receiver distance gather. Each pair of signals from different shots in a SASW testing is identified by the source-to-receiver distance. The SASW data is then rearranged in ascending order of source-to-receiver distance. Between two adjacent shots, signals having the same source-to-receiver distance can be simply stacked and averaged. The combined multi-offset data is a spatially non-uniform sampling of the wavefield. Equation (3) and (4) stem from of discrete-space Fourier trans-

form. But taking the form, they can be relaxed to accommodate data in that x_n is non-uniformly spaced.

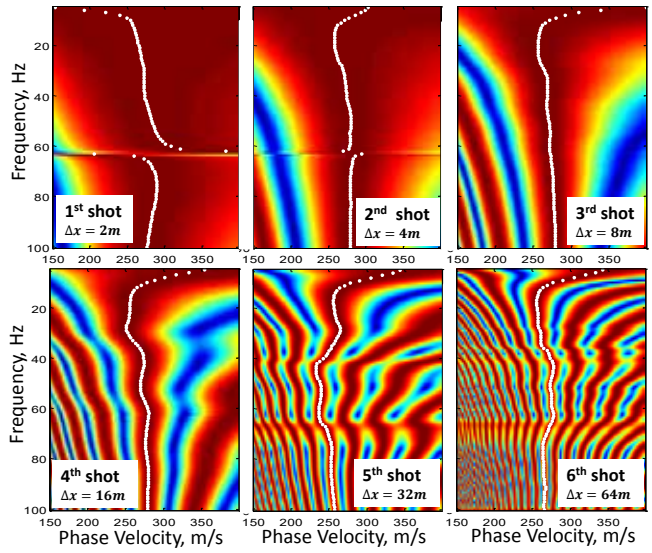

Figure 1. Results of 2-station wavefield transformation on each pair of SASW data for Model 2.

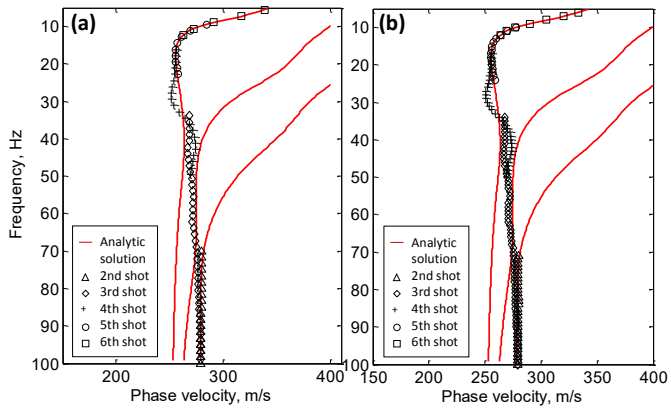

Figure 2. The dispersion curve obtained by (a) SASW method and (b) 2-station wavefield transformation for Model 2.

The result of non-uniform MASW analysis using SASW data for the normal case is shown in Fig. 5(a). For comparison, the dispersion analysis using uniformly spaced MASW data of the same offset range is shown in Fig. 5(b). The non-uniform wavefield transformation from the SASW testing shows some aliasing patterns in the 2-D spectrum due to sparse sampling in the space domain. Yet the correct dispersion curve can be clearly distinguished from the aliasing pattern in the *f-v* domain. The results for the case of reversal profile are shown in Fig. 6. Although there are some aliasing effects due to non-uniform spatial sampling, particularly in the left part of the spectral image (Fig. 6a), dominated modes can still be recognized successfully. On the contrary, the apparent experimental dispersion curves extracted from the conventional SASW analysis (Fig. 4) gradually sway from one mode to another. It is difficult to tell whether higher modes dominate at certain frequency range. The SASW method samples phase angles at only two locations, and yields location-dependent apparent velocities from the linearized slope of the phase angle versus distance. This inconsistency in the experimental dispersion data between difference receiver spacings (locations) is often misinterpreted as a result of laterally variable profile. The MASW method, on the other hand, provides visualization of dispersion relation through 2-D wavefield transformation, which yields consistent experimental dispersion curve and allows identification or separation of multiple modes.

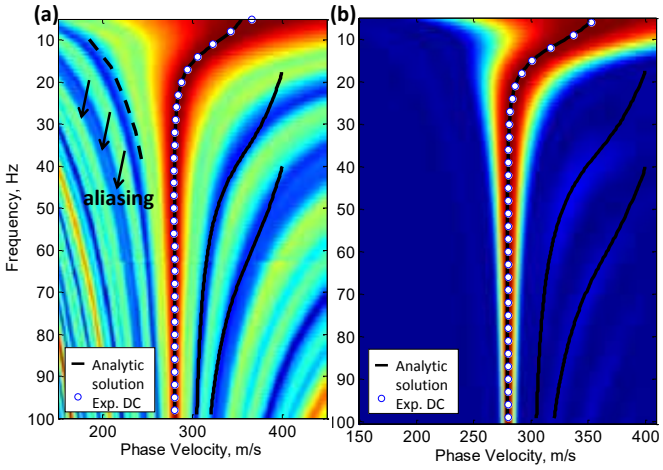

Figure 5. (a) Non-uniform MASW analysis using 6-shot SASW data vs. (b) Uniform MASW analysis using equally-spaced multi-station data of the same offset range for Model 1.

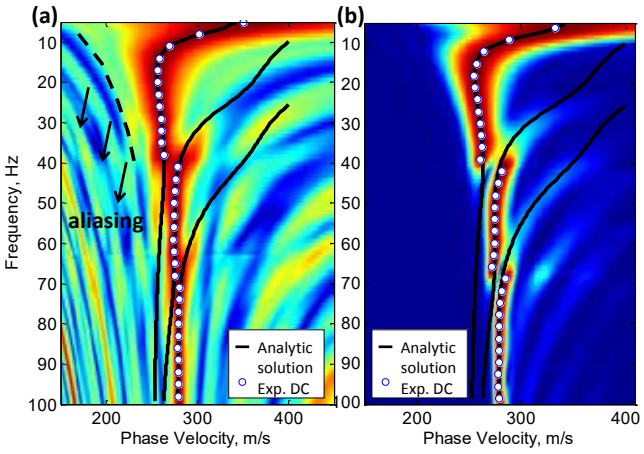

Figure 6. (a) Non-uniform MASW analysis using 6-shot SASW data vs. (b) Uniform MASW analysis using equally-spaced multi-station data of the same offset range for Model 2.

3 DILEMMAS IN FIELD TEST CONFIGURATION

The 2-D wavefield transformation can be generalized to accommodate SASW data. It has been demonstrated that the multi-station wavefield transformation is superior in dispersion analysis. It avoids unwrapping of phase angles, a major source of human error in conventional SASW analysis, enable

identification and separation of multiple modes, and provides visual appraisal of complicated dispersion phenomenon. With modern seismograph, the multi-station data is normally collected by a number of receivers with constant receiver spacing. In a MASW survey, three spatial parameters need to be decided, including near offset (x_0), receiver spacing (Δx), and receiver spread length ($L=N\Delta x$). To avoid spectral aliasing in the space domain, receiver spacing should be sufficiently short. This will limit the spread length with finite channels of the seismograph. On the other hand, spread length should be as long as possible to have good depth coverage and identify different dominant modes. However, too long of a receiver spread is more susceptible to lateral variation and has poor lateral resolution. As to the near offset, short x_0 is desired to avoid far field effect while long x_0 is preferred to avoid near offset. These tradeoffs in selecting proper x_0, Δx, and L make the field testing ambiguous and subjective.

4 STANDARDIZED MASW SURVEY

Tradeoffs are involved when selecting the testing configuration. To resolve the aforementioned dilemmas, a multi-shot common receiver configuration survey is proposed as a standard approach to acquire multi-station data for 2-D wavefield transformation. The multi-shot common receiver configuration is illustrated in Fig. 7, in which the geophone spread is fixed and data of different source-to-receiver distance are collected by gradually increasing the near offset in multiples of receiver spacing. More equally-spaced data can be recorded by these walk-away shots, which allows assembling MASW-imitating data by the source-to-receiver distance gather. The offset range is initially from x_0 to (x_0+L) when using the conventional multi-station configuration. After K consecutive walk-away shots, all collected field data can be synthesized into one seismic record according to the source-to-receiver offset. The synthesized seismogram has an extended offset range from x_0 to (x_0+KL).

The receiver spacing Δx ideally is set to be half of the minimum depth of exploration. This can be relaxed since the aliasing can often be differentiated from the surface wave dispersion. The nearest offset x_0 is about the same distance as the minimum depth of exploration. The receiver spread L is set to be in the target range of interest. The number of walk-away shots times the spread length L should be greater than if not doubled the desired depth of exploration. This way, requirements of the lateral resolution and depth of investigation can be meet simultaneously. Even with a small number of receiving channels, the receiver interval can be kept small enough without sacrificing the total offset range. The near field and far field effects can also be mitigated since it establishes an expansive offset range in the same spatial range by synthesizing seismic records with different nearest source-to-receiver offsets.

The dispersion analysis of the SASW test can be replaced by the wavefield transformation technique. However, there is a nice feature about the SASW field testing. The near offset is proportional to the receiver spacing and different types of source are often adopted from small hammer in short spacing to large weight drop in long spacing, while single shot is normally used to conveniently collect the MASW data. The useful frequency range of dispersion curve is affected not only by receiver spread length, but also by the type of source. For example, when a large hammer is used, it is difficult to obtain high frequency component regardless of how small the offset is. Likewise, when a small hammer is used to generate high-frequency component, it is difficult to obtain low frequency component regardless of how long the receiver spread is. Using the multi-shot common receiver MASW survey, different types of sources can be used for different walk-away shots. As a general rule of thumb, handheld hammer, sledge hammer, and large weight drop can be used for short, intermediate, and long near offset, respectively. To maximize the bandwidth of dispersion curve, multiple sources can be used for each walk-away shot. For each frequency component, the optimal combination of source and offset can be selected to mitigate the near and far field effects as well as maximize the obtainable bandwidth for the dispersion curve.

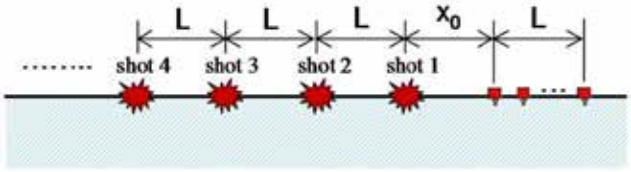

Figure 7. The multi-shot common receiver configuration.

A field example was conducted to demonstrate the advantages of the multi-shot common receiver survey. The test was carried out on a grass field in the campus of National Chiao Tung University, Taiwan. An area about 50 m long was to be tested with a desired investigation depth up to 30 m using a 24-channel seismograph. The receiver spread consisted of 24 geophones with 2 m spacing used. A small handheld hammer and large 12-lb sledge hammer were used as the sources at near offset 4 m and 27 m, respectively. The results of dispersion analysis using each single shot and the multi-shot source-to-receiver distance gather are shown in Fig. 8. The small handheld hammer at short near offset yielded good high frequency components from 30 Hz to 120 Hz, while the big sledge hammer at long near offset produced low frequency energy from 15 Hz to 55 Hz. The bandwidth of experimental dispersion curve is rather limited by either case. A higher

resolution dispersion image and larger bandwidth of experimental dispersion curve were obtained by multi-shot source-to-receiver distance gather, as shown in Fig. 8c. The improvement from the multi-shot common receiver configuration is quite pronounced.

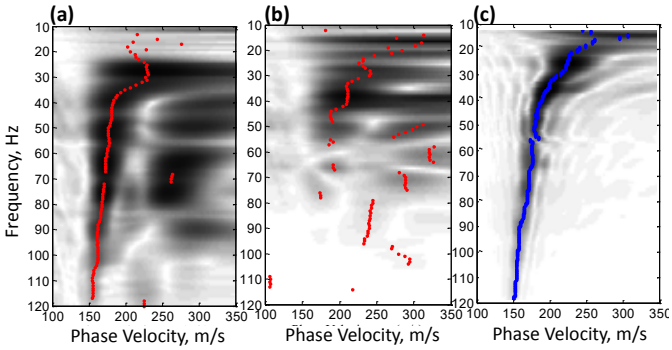

Figure 8. The dispersion analysis for (a) single shot at x_0 = 4m with a small handheld hammer, (b) single shot at x_0 = 27m with a small handheld hammer, and (c) two shots combined by source-to-receiver distance gather.

5 CONCLUSIONS

The data reduction method for dispersion relation in a surface wave testing is conventionally associated with certain method of data acquisition. Typical examples are phase angle analysis in the two-station SASW method and 2-D multi-station wavefield transformation of surface wave in the MASW method. Limited to the two channel data, conventional SASW dispersion analysis suffers from possible phase un-wrapping errors, inefficient data filtering and synthesis, and inability to distinguish multiple modes. The MASW method is generalized to accommodate SASW data. Numerical simulations were performed to demonstrate its feasibility and advantages for analyzing SASW data. It avoids unwrapping of phase angles, a major source of human error in conventional SASW analysis, enable identification and separation of multiple modes, and provides visual appraisal of complicated dispersion phenomenon.

Tradeoffs are involved in the MASW testing configuration when spatial resolution, effect of lateral heterogeneity, spectral resolution, investigation depth, and near and far field effects are considered. To resolve the dilemmas in the field configuration, a multi-shot common receiver configuration survey is proposed to acquire multi-station wavefield for 2-D wavefield transformation analysis. A field example demonstrated that this new approach provides a more definitive guideline for MASW testing and maximize the obtainable bandwidth for the dispersion curve.

6 REFERENCES

Shibuya, S., Mitachi, T., and Miura, S. (Eds.) 1994. Symposium on Pre-Failure Deformation Characteristics of Geomaterials, Two Volumes, Sapporo, Japan.

Jardine, R.J., Davies, M.C.R., Hight, D.W., Smith, A.K.C., and Stallebrass, S.E. (Eds.). 1998. "Pre-Failure Deformation Behavior of Geomaterials.'', Thomas Telford Publishing, London, 417 p.

Jamiolkowski, M., Lancellotta, R., and Lo Presti, D. (Eds.). 2001. "Pre-Failure Deformation Characteristics of Geomaterials.'', A.A. Balkema Publishers, Tokyo , 1 and 2.

Di Benedetto, H., Doanh, T., Geoffroy, H., and Sauzeat, C. (Eds.) 2003. "Deformation Characteristics of Geomaterials.'', A.A. Balkema Publishers, Tokyo, 1425 p

Stokoe II KH, John SH, Woods RD. 2004. "Some contributions of in situ geophysical measurements to solving geotechnical engineering problems.'' Proceedings of 2nd International Conference on Site Characterization, Porto, Portugal, 1, 97-132.

Foti, S. 2003. "Small-strain stiffness and damping ratio of Pisa clay from surface wave tests." Geotechnique , 53, 455-461.

Lin C-P, Chang C-C, Chang T-S. 2004. "The use of MASW method in the assessment of soil liquefaction potential.'' Soil Dynamics and Earthquake Engineering, 24, 689-698.

Ryden N, Park CB, Ulriksen P, Miller RD. 2004. ''Multimodal approach to seismic pavement testing.'' Journal of Geotechnical and Geo-environmental Engineering, 130, 636-645.

Lin, C.-P., Lin, C.-H., Dai, Y.-Z, and Chien, C.-J. 2012. "Assessment of Ground Improvement with Improved Columns by Surface Wave Testing," Grouting and Deep Mixing 2012, Geotechnical Special Publication, No. 228, pp. 483-492.

Haegeman W, Van Impe WF. 1999. "Characterization of disposal Sites from surface wave measurements.'' Journal of Environmental and Engineering Geophysics, 4, 27-33.

Nazarian S., and Stokoe K.H., II. 1984. "Nondestructive testing of pavements using surface waves." Transportation Research Record, 993, 67-79.

Lin C-P. and Chang. T-S. 2004. "Multi-station analysis of surface wave dispersion" Soil dynamics and earthquake engineering, 24, 877-886.

McMechan GA, Yedlin MJ. 1981. "Analysis of dispersive waves by wave-field transformation.'' Geophysics, 46, 869-874.

Gabriels, P., Snieder, R., and Nolet, G. 1987. "In situ measurements of shear-wave velocity in sediments with higher mode Rayleigh waves." Geophys. Prospect., 35, 187-196.

Park CB, Miller RD, Xia J. 1998. "Imaging dispersion curves of surface waves on multi-channel record.'' 68th Annual International Meeting, Society of Exploration Geophysicists, Expanded Abstracts, 1377-1380.

Xia, J., Xu, Y., and Miller, R.D. 2007. "Generating image of dispersive energy by frequency decomposition and slant stacking'' Pure and Applied Geophysics, 164, 941-956.

Herrmann, R. B., and Ammon, C. J. 2002. "Computer Programs in Seismology version 3.20.'', St. Louis University, Missouri.

Geotechnical and Geophysical Site Characterisation 5 – Lehane, Acosta-Martínez & Kelly (Eds)

Characterisation of Small Strain Rock Modulus from Ultrasonic Pulse Velocity Testing

B. Look
Foundation Specialists Pty Ltd, Brisbane, Queensland, Australia

S. Schneider & C. Gallage
Queensland University of Technology, Brisbane, Queensland

ABSTRACT: Small strain rock shear modulus is increasingly being used in routine design by applying a reduction factor applicable to foundations under normal serviceability conditions. While, the velocity measurement provides a reliable means of determining the small strain modulus, this represents only an upper bound, and an appropriate modulus degradation factor is required. A database of various rock types in South East Queensland, tested with the intact rock modulus derived from both a non - destructive pulse velocity and traditional UCS testing to failure are compared. Ultrasonic pulse velocity (UPV) testing was used to establish if this would be a reliable test method on Brisbane rock cores and provided the modulus at low strain. The UCS – modulus ratios at low strain levels and at failure are also compared. The results suggest that a strong relationship exists between the pulse velocity and mechanical properties of rock in the Brisbane.

1 INTRODUCTION

The International Society for Rock Mechanics and the American Society for Testing and Materials have standardized the procedure for measuring uniaxial compressive rock strength (UCS) and Young's modulus (E), but this method is time-consuming and expensive (Bakar, 2007). The UCS is often derived using the point load index (PLI) test, but rock specific correlations need to be established for soft rocks. For example, Look and Griffiths (2001) found the UCS/PLI ratio of 11 for soft rocks (R^2 = 0.4) in Brisbane, whereas a ratio of 23 is the most common ratio quoted in the international literature. A UCS to Young's modulus conversion factor in the range of 200 to 500 (Deere & Miller, 1966) is typically applied to approximate the Young's modulus from UCS.

The UCS and E of rocks can also be estimated by non-destructive methods, such as ultrasonic pulse velocity (UPV) testing (Hudson & Harrison, 2007).

The Pundit (Portable Ultrasonic Non-destructive Digital Indicating Tester) is relatively new to the Queensland industry. This equipment measures the velocity, which can then be converted to a modulus value. The objective was to first independently assess its reliability (with the default correlations), and then to establish correlations between the PUNDIT measured velocities and other laboratory-tested properties of Brisbane rock cores. This would add credence as an acceptable measuring device.

2 ULTRASONIC PULSE VELOCITY TESTING

Non-destructive testing such as ultrasonic pulse velocity testing can be used for rock characterization. The modulus is directly related to the pulse velocity (Equations 1 - 3) of the rock (Yasar & Erdogan, 2004), who found strong correlations ($R^2 \geq 0.8$) for carbonate rocks. A.S. 1170.4 (2007) uses shear wave velocity (V_s) directly for rock definitions with the lowest rock classification of V_s = 300m/s and a UCS > 0.8 MPa. Strong rocks would have an average shear velocity of 1500 m/s.

Proceq produces a portable UPV testing instrument for the non-destructive testing of the material properties of metal, concrete, rock, paper and composites. The "Pundit PL-200" provides a wide range of measurements, including UCS and E (Proceq, 2014). The uniaxial compressive strength is estimated by a pre-determined correlation between measured velocity and known UCS values. However, this "universal" correlation needed to be validated for Brisbane rocks.

The shear modulus obtained from the Pundit is an idealized value and is referred to as G_{max} or G_0, i.e. the modulus under very small strain (Schneider, Hoyos, Mayne, Macari, & Rix, 1999). In practice, as the strain increases the shear modulus will decrease, as shown in Figure 1. The secant modulus may be 20% to 40% of G_{max} for a practical range of factor of safety (Poulos, 2015).

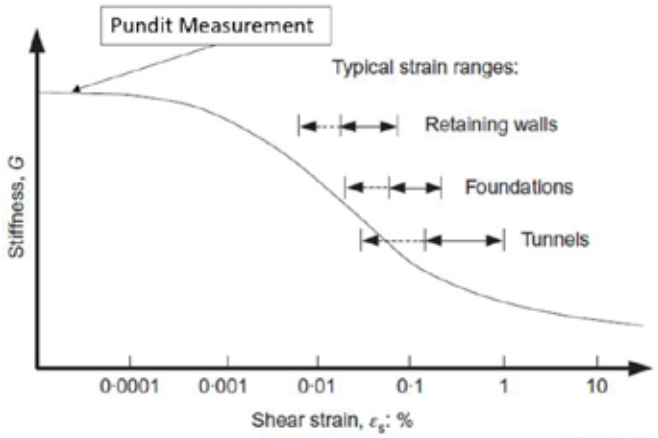

Figure 1. Stiffness variation and strain ranges (Clayton, 2011).

The Young's modulus (E) is also proportional to velocity using P-wave (compression) and S-wave (shear) measurements. By measuring P-wave transmission time and S-wave transmission time, the P-wave modulus (M) and the shear modulus (G_{max}) can be determined.

$$M = \rho V_p^2 \quad \text{and} \quad G_{max} = \rho V_s^2 \qquad (1)$$

Where: ρ = density of the material
V_p = pulse velocity of P waves
V_s = pulse velocity of S waves

Poisson's ratio (ν) can then be determined by:

$$\nu = (M - 2G) / (2M - 2G)$$
$$\nu = (V_p^2 - 2V_s^2) / [2(V_p^2 - V_s^2)] \qquad (2)$$

The small-strain Young's modulus can then be calculated using:

$$E_0 = 2G (1 + \nu) \qquad (3)$$

3 METHODOLOGY

The rock cores were of different rock types, varying degrees of weathering and were from projects (past and present) around Brisbane, Queensland, Australia. The rock types included Brisbane Tuff, Phyllite, Argillite, Spillite, Coal, Greywacke and Sandstone. The degree of weathering ranged from distinctly weathered (DW) to fresh rock (Fr). A total of 149 samples were tested. The measured pulse velocities were correlated against the UCS and E values. In addition, the measured E-modulus values were compared to the E-modulus obtained from the stress-strain curve in the laboratory testing results.

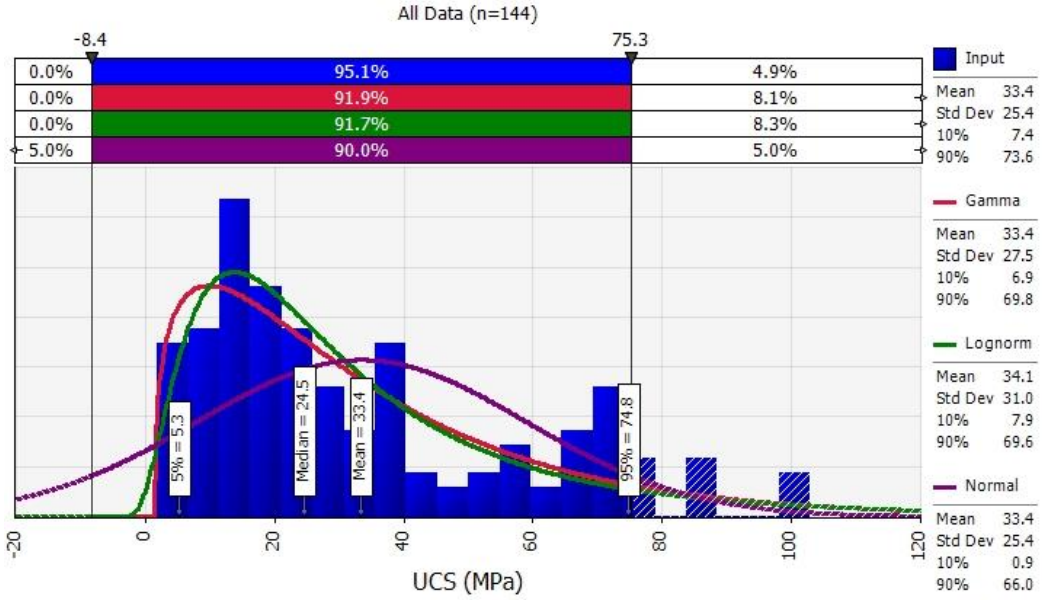

Figure 2. Probability Distribution for UCS (All Data).

Goodness of fit tests were used to determine best fit Probability Distribution Functions (PDF) and regression analysis (trend analysis) was used to determine correlations between the data obtained. The data was analyzed as a whole data set, as well as broken down into smaller data sets to analyze effects of rock type, weathering, specimen length and RQD on the correlation results (Schneider, 2015).

Various test lengths were also compared. Test lengths of 200 – 250 mm had a UCS – Velocity (V_p) relationship with $R^2 = 0.8$ as compared to shorter lengths with $R^2 = 0.4$. This is opposite of what was expected based on ASTM (2008). The data below does not differentiate lengths as test were carried out on available or standard sample sizes.

4 TEST RESULTS AND DISCUSSION

4.1 *Probability Distribution of UCS and Modulus*

Figure 2 shows the probability distributions for all data. Using all the data (*n*=144), the best fit distribution is the Gamma PDF. The coefficient of variation (CV) is 82% with a mean of 33.4 MPa.

Table 1. Summary of UCS (MPa) Fit Comparisons

Rock Type	No. of Samples	Best Fit Distribution	Mean	Standard Deviation	Percentile		Coefficient of Variation (CV, %)
					10th	90th	
All Data	144	Gamma	33.4	27.5	6.9	69.8	82
Argillite	53	Gamma	34.1	26.5	7.6	69.3	78
Brisbane Tuff	34	Weibull	30.5	16.9	13.4	53.4	55
Sandstone	26	Laplace	17.4	11.4	4.4	30.4	66
Spillite	18	Laplace	73.6	35	33.8	113.4	48

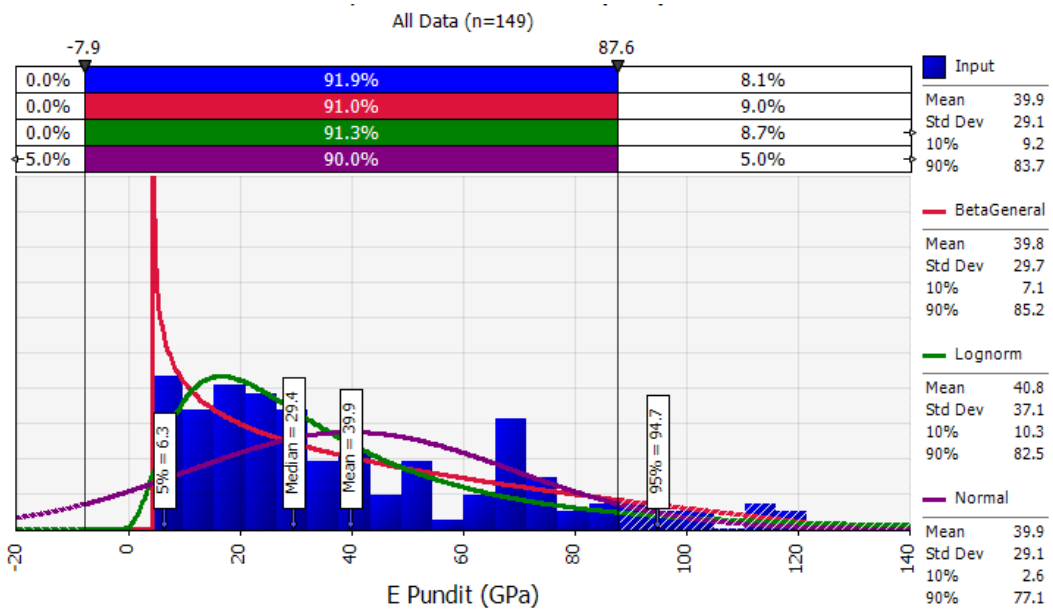

Figure 3. Probability Distribution of All E – Pundit data.

Table 2. Summary of E_o (GPa) Pundit Fit Comparisons

Rock Type	No. of Samples	Best Fit Distribution	Mean	Standard Deviation	Percentile		Coefficient of Variation (CV, %)
					10th	90th	
All Data	149	BetaGeneral	39.8	29.7	7.1	85.2	75
Argillite	55	Triangular	46.7	24.6	17.2	83.3	53
Brisbane Tuff	34	Logistic	23.3	8.7	12.8	33.8	37
Sandstone	27	BetGeneral	24.8	17.2	5.9	50.2	69
Spillite	18	Laplace	90.8	24.3	63.2	118.4	27

The normal distribution if applied would have a 5 percentile value of −8.4 MPa which shows the error in assuming a normal distribution. The lognormal, while not best ranked, closely follows the best fit distribution and would not produce the errors of the normal distribution (Look 2015). The results of the UCS fit comparisons are summarized in Table 1.

The data for E_0 obtained from the Pundit was analyzed in a similar fashion (Figure 3). The CV for all combined data is 75% with a mean of 39.8 GPa. The normal distribution, if applied, would have a 5 percentile value of −7.9 GPa. This negative value again shows the error in assuming a normal distribution. The results of the E Pundit fit comparisons are summarized in Table 2. Overall, less variation is obtained for the modulus as compared with the UCS.

A higher ratio applied to the low strength rocks, while a lower ratio applied to the high strength rocks, excluding Sandstone. The sandstone and Tuff have a relatively minor change in E_0/UCS ratios, while the argillite and Spillite have a very high ratio difference between low to high strength rocks.

Tables 1 and 2 show that lumping all data together results in a large spread of results with a CV of 82% and 75% for the UCS and modulus respectively. When that data is analyzed for Spillite only, the spread of results reduces to as low as 48% and 27% for the UCS and E, respectively.

The results from the UCS/ E Pundit PDF analysis from Tables 1 and 2 were then combined to calculate E_0/UCS ratios for rock type and overall PDF (Figures 4 and 5, respectively).

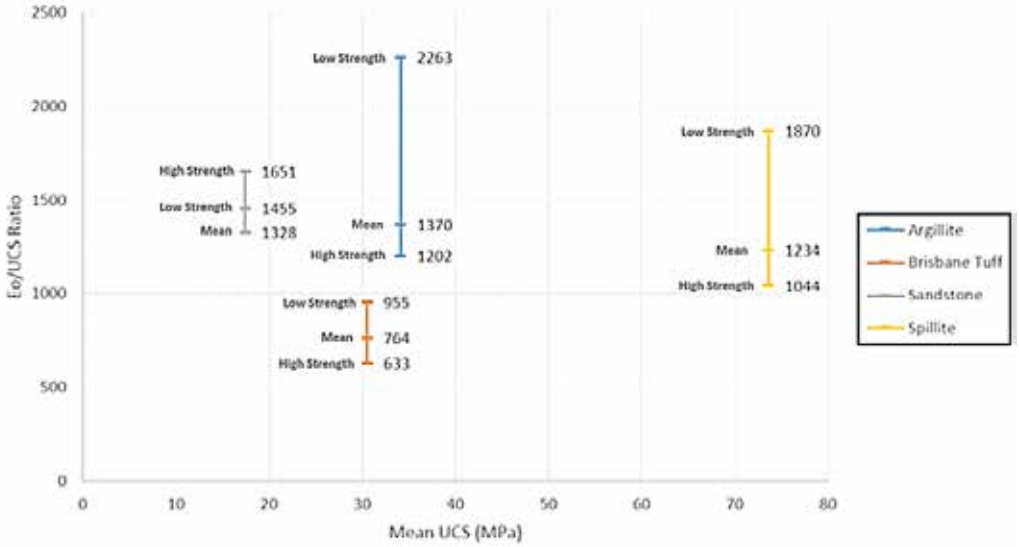

Figure 4. E_0/UCS Ratio for Rock Types.

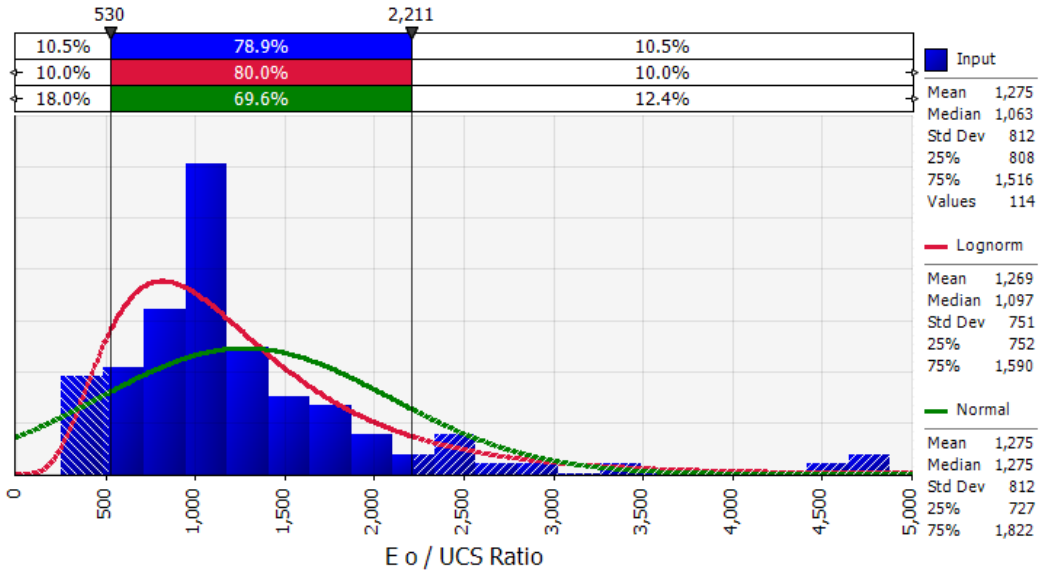

Figure 5. PDF of E_0/UCS Ratio for combined data.

The Poisson's ratio obtained through the velocity testing was also analyzed for each rock type. Using all the data (n=149) the best fit distribution is the normal. The CV is 23% with a mean of 0.22 for rocks in the Brisbane region.

4.2 *Primary Velocity versus Young's Modulus Correlation*

The primary velocity, measured by the Pundit, was correlated with the Young's Modulus (both secant and tangent), obtained through laboratory testing (Figure 6). The secant Modulus is measured at 0% to 50% of maximum UCS while the tangent Modulus is at 50% of UCS. There is an excellent exponential relationship (R^2 =0.9) between primary velocity and Young's modulus, using all data.

4.3 *Young's Modulus (Pundit) versus Young's Modulus (Lab Tested)*

The Young's modulus obtained with the Pundit is a low (0%) strain (E_0 value), whereas the laboratory tested Young's modulus (E_{Lab}) is at a measured strain relative to ultimate failure. Therefore, E_0 was correlated with E_{Lab}, (Figure 7) to determine the appropriate reduction for this strain difference (Figure 1).

Table 4 outlines the reduction factor required to convert E_0 to E_{Lab} for different modulus values and the typical rock associated weathering. Higher strength rocks requires less of a reduction factor, whereas lower strengths rocks require a greater reduction is required.

There was little difference between the secant and tangent modulus.

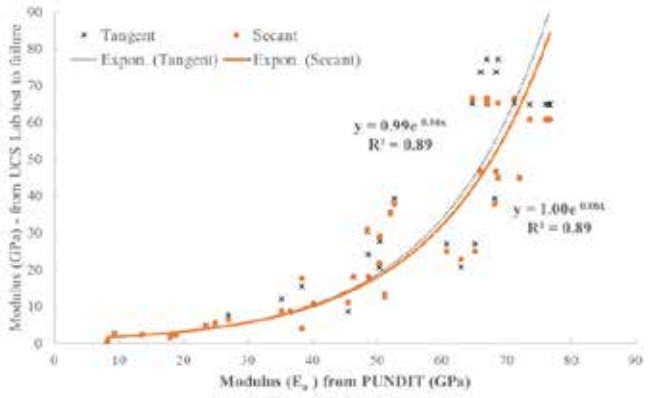

Figure 6. Lab Modulus from UCS testing vs Primary Velocity.

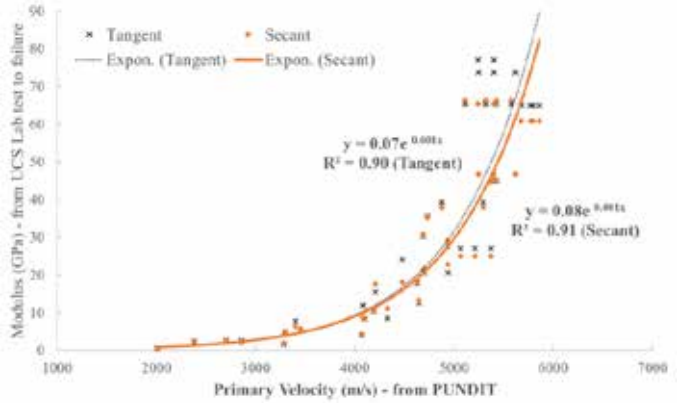

Figure 7. Lab Modulus from UCS testing vs Modulus (Pundit).

Table 3. E_{Lab} / E_0 Ratio

E_0 Pundit (GPa)	Typical Weathering	E_{Lab} (GPa)	E_{Lab} / E_0
20	DW	3.2	0.2
30	DW - SW	5.8	
40	SW	10.3	0.3
50	SW - Fr	19	0.4
60	Fr	33	0.6
70	Fr	60	0.9

Figure 8 shows the $E_{Lab\ Failure}$ / $UCS_{Lab\ Failure}$ of 800 (median) to 900 (mean) for all data, are significantly higher for this data set, compared to the typically reported values of 200 to 500. The Lognormal PDF is used in the evaluation.

An alternative approach with reduction factor applied to E_0 (Figures 4 and 5) shows this E/ UCS ratio typically varies from 750 to 1,600 for individual data (Table 4) but varies between rock types.

Table 4. Modulus / Strength Ratio

Rock Type		Strength	E_0/UCS	E_{Lab}/E_0	E_{Lab}/UCS
Sedimentary	Sandstone	Low (15 MPa)	1400	0.16	~ 220
	Argillite	Typical (35 MPa)	1300	0.3	~ 400
	Spillite	High (70MPa)	1200	0.9	~ 1,000
Igneous	Brisbane Tuff	Low	900	0.2	~ 180
		Typical (35 MPa)	900		~ 150
		High	750		~ 110

5 CONCLUSIONS

The results show the PUNDIT is a reliable tool for measuring rock core properties. Figure 9 compares the traditional strength modulus conversion method versus the UPV method which measures Modulus directly. The latter seems to be more reliable approach to obtain the rock properties with less uncertainty for obtaining UCS and the Modulus. However this is offset by introducing a strain reduction factor. The UCS ~ E_0 /1200 but this varied with rock, type, strength and weathering. Understanding this requires more research.

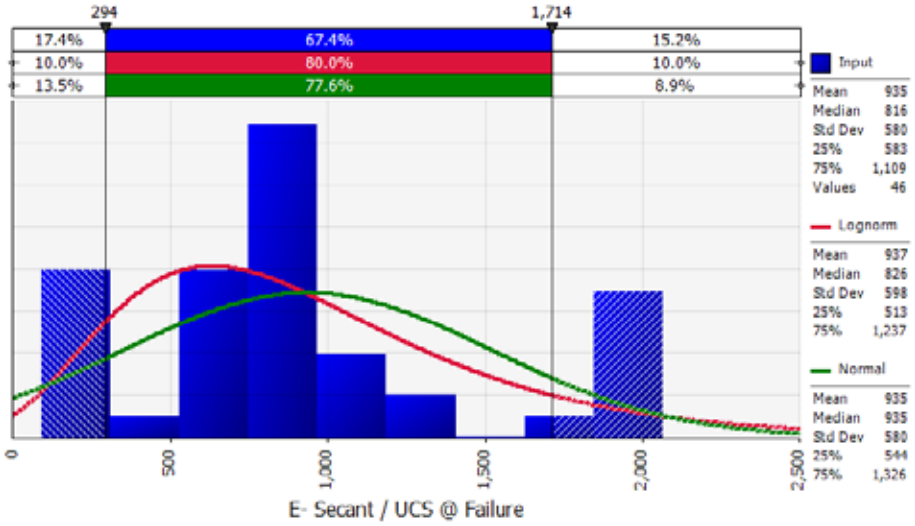

Figure 8. PDF for E (Secant) vs UCS at failure

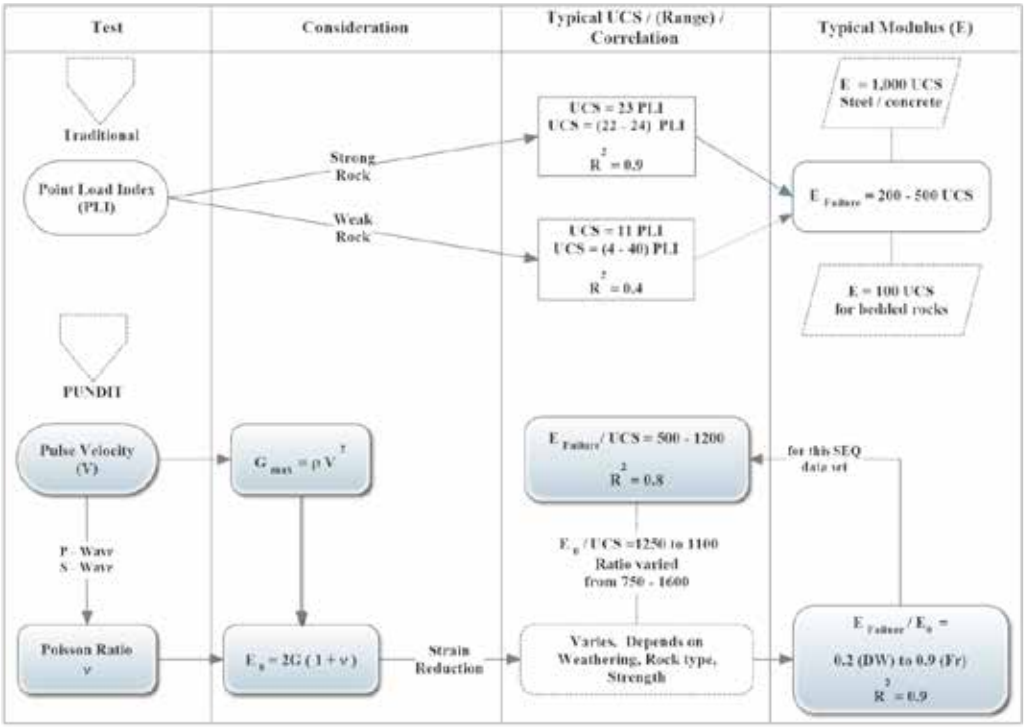

Figure 6. Traditional Method vs UPS method to indirectly determine UCS and modulus.

The E_{Lab}-V_p correlation relationship was less affected by rock type, specimen length, weathering or RQD, whereas the UCS-V_p relationship was heavily influenced by these parameters.

On a cost basis, this UPV approach would be comparable with using the PLI with its correlations for obtaining UCS or Modulus values.

6 ACKNOWLEDGEMENTS

The authors would like to thank Brisbane City Council for granting access to the rock cores, background information and assistance in particular Gary Bruyeres, Heidi Mahler and the laboratory team.

7 REFERENCES

American Society for Testing and Materials. 2008. *Laboratory Determination of Pulse Velocities and Ultrasonic Elastic Constants of Rock.* ASTM D2685.

Australian Standards. 2007. *A.S. 1170.4 – Structural Design Actions - Part 4: Earthquake Actions in Australia*.

Bakar, M. A. 2007. Correlation between Uniaxial Compressive Strength and Point Load Index for Salt-Range Rocks. *Pak J. Engg. & Appl. Sci*. Vol. 1 July 2007, pp. 1-8.

Clayton, C. 2011. Stiffness at small strain: research and practice. *Geotechnique*, pp. 5-37.

Deere D.U. & Miler R.P. 1966. *Engineering clasification and index properties of intact rock*. Report AFWL-TR-65-116. Air Force Weapon Laboratory, New Mexico.

Hudson, J. & Harrison, J. 2007. *Engineering Rock Mechanics - An Introduction to the Principles*. Elsevier.

Look, B. G. & Griffiths, S.G. 2001. An Engineering Assessment of the Strength and Deformation Properties of Brisbane Rocks, *Australian Geomechanics Journal*, Vol 36, No. 3, pp. 17 – 30.

Look, B. (2015). Appropriate distribution functions in determining characteristic values, *12th Australia New Zealand Conference in Geomechanics*, Wellington, New Zealand, P014

Poulos, H. 2015. Design Challenges for Tall Building Foundations. *International Conference on Geotechnical Engineering* (pp. 1-14). Colombo: ICGE.

Proceq. 2014. *Pundit PL-200 Operating Instructions*, available from: http://www.proceq.com/fileadmin/documents/proceq/products/Concrete/PL-200/English/Pundit_PL-200_Operating_Instructions_English_low.pdf

Schneider, J., Hoyos, L., Mayne, P., Macari, E. & Rix, G. 1999. Field and Laboratory Meaurements of Dynamic Shear Modulus of Piedmont Residual Soils. *Behavioural Characteristics of Residual Soils*, pp. 12-25.

Schneider S. 2015. *An investigation into Brisbane rock core properties using ultasonic pulse velocity measurements*, Queensland University of Tecnhology Report

Vallejo, L., & Ferrer, M. 2011. *Geological Engineering*. London: CRC Press.

Yasar, E. & Erdogan, Y. 2004. Correlating sound velocity with the density, compressive strength and Young's modulus of carbonate rocks. *International Journal of Rock Mechanics and Mining Sciences*, pp. 871-875.

Geotechnical and Geophysical Site Characterisation 5 – Lehane, Acosta-Martínez & Kelly (Eds)

Use of Geophysical Logs to Map Aquifers Electrofacies

R. Macari & A. S. P. Peixoto
UNESP – Univ Estadual Paulista, Dept. Civil and Environmental Engineering, Bauru, Brazil

G. G. Nery
Hydrolog Serviços de Perfilagens Ltda., Bauru, Brazil

ABSTRACT: Map of geophysical parameters in different depth and their corresponding geological interpretations are analyzed based on an automatic geostatistical method to aquifers electrofacies identification using geophysical well logging curves of electrical resistivity, gamma ray and sonic transit time. The methodology for the spatial analysis of the variability of petrophysical characteristics considering their borehole geophysical responses, useful in oil industry, is extended here in water research. For that, they were used 65 geophysical logs scattered throughout the metropolitan region of São Paulo (Brazil) carried on between 1997 and 2012. In addition, the combined use of these three parameters has led to a better understanding of the subsurface rocks in the complex stratigraphy of Paleogene São Paulo Basin, Brazil, in order to future projects of planning groundwater wells.

1 INTRODUCTION

The city of São Paulo is fully urbanized and so it has no exposed geological outcrops making it difficult to study the subsoil. Thus, the use of existing data on artesian wells can help studies for urban planning, building construction and underground water extraction. That city is one of the largest urban centers of the Planet and it suffered an unprecedented water crisis in recent years leading to the necessity of choosing cost-effectively solutions.

The use of geophysical logs in groundwater wells is a commonplace and often essential to improve the water flow. In fact, after the construction of the well, the test results are stored. However, a better destination for them would be the use to plot 2D / 3D map information in order to help the geological knowledge of the exploited areas.

It is presented methodology using well logging data and ordinary softwares in order to better plan the construction of artesian wells leading to increase the flow of the artesian wells. The aquifers electrofacies were identified based on geophysical well logging curves of electrical resistivity, gamma ray and transit time of 65 well logs performed between the years of 1997 and 2012.

Also this work aims a better understanding of the subsurface layers in the basin of São Paulo, quite complicated stratigraphy, helping in better visualization and project planning of wells for groundwater extraction in the state capital.

2 METHODOLOGY

2.1 *Theoretical concepts*

According to Kearney et al (2013), the gamma rays are pure electromagnetic radiation released from excited nucleus during disintegrations and can be obtained by scintillation sensors. The gamma ray profile is one of the best indicators of lithological sedimentary rocks. The most important hydrogeological application of the technique is the identification and quantification of clay intervals choice of appropriate intervals for the placement of filters in groundwater wells. The American Petroleum Institute (API) normalized the gamma ray measurement as API unit.

A gamma ray shale index, I_{GR}, for a given layer is defined by Equation 1:

$$I_{GR} = \frac{(GR - GR_{cl})}{(GR_{sh} - GR_{cl})} \quad (1)$$

where GR = log response in the zone of interest, API units; GR_{cl} = log response in clean beds, API units; and GR_{sh} = log response in shale beds, API units

The induction logging provides the resistivity measurements in two ways: induction (DIR) and short normal (SN).

The DIR is obtained as follows: the surrounding rock is energized by an electromagnetic field of approximately 20 kHz, which generates currents by

electromagnetic induction. The secondary electromagnetic field created is recorded in a receiver that allows a direct estimate of the apparent resistivity with the unit in ohm-m.

The test use four coils, two transmission and two reception. The induced electromagnetic field flows in circular paths around the borehole. Such an arrangement provides a depth of penetration of about twice the transmitter-receiver separation.

The short normal, SN, is obtained as follows: a constant current is sent between a transmitter electrode, A, and the receiver electrode, B. It creates current lines crossing a certain amount of mud and rock. The tool reads the potential difference between the measuring electrodes M and N.

The borehole compensated sonic (BCS) also known as the continuous velocity or acoustic log, determines the seismic velocities of the formations traversed. The sonde normally contains two receivers about 0.30m apart and an acoustic source some 0.9–1.5m from the nearest receiver, Kearney et al (2013). These waves propagate in 3D shape inside the well and the formation. They are captured by an receiver located at a fixed distance from the transmitter. These receptors basically read the time between emission and arrival of the ultrasonic wave (transit time, DT) in μs/ft, as standardized by the API (e.g. 3.28 x 10^{-6} s/m).

2.2 *Study area*

The study area is located in the São Paulo Basin, Paleogene Age (Figure 1). The most wells are located between the Tietê River and the Pinheiros River, (Figure 2).

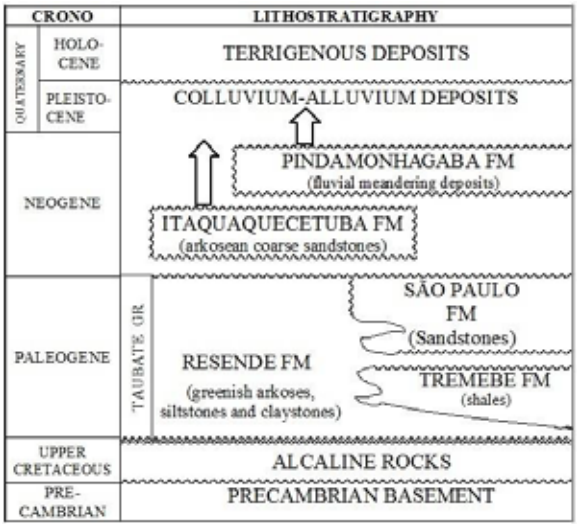

Figure 1. Stratigraphic Column São Paulo Basin. Modified of Riccomini et al (1989).

The typical log example of Figure 3 shows the high variability of the geology in the area with successive high-low values of transit time, resistivity and gamma anomalies peaks, as result of clay and sandy lenses. Below 110 meters there is altered basement igneous rock, visible by the low values of transit time, e.g. lower than 70 μsc/ft (2.3 x 10^{-4} s/m).

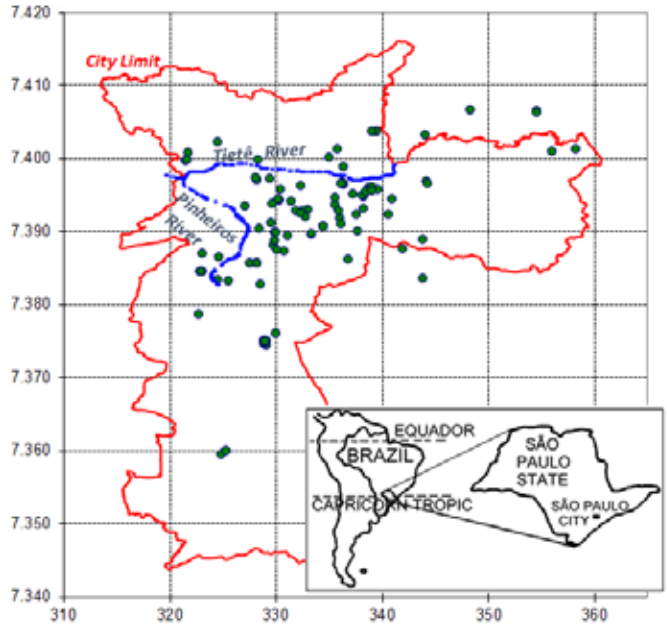

Figure 2. Location Map of São Paulo Wells Drilled

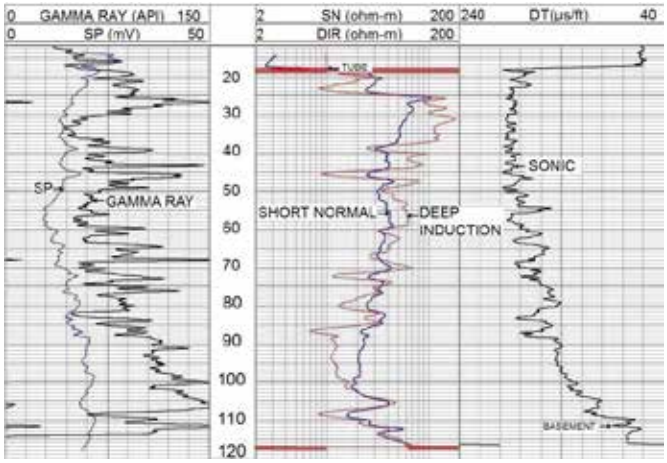

Figure 3. Typical Log in the São Paulo Basin.

The dashed line in Figure 4 shows the top of the crystalline rocks, since most of the logged well was drilled through the sedimentary layer. According to Takira (1991), the maximum continuous thickness of sediments in the is 250 meters in that place, but Figure 4 shows at most 185 meters of sediment.

The recent origin of the basin with discontinuous, unconsolidated and lenticular layers became quite complex geology and the establishment of a correlation between the logs a difficult task.

2.1 *Database*

The files of all 65 logs have been converted from the acquisition format (db) to Las text format (LAS - Log Ascii Standard) compatible with commercial

spreadsheet software. An example of spreadsheet used is detailed in Table 1.

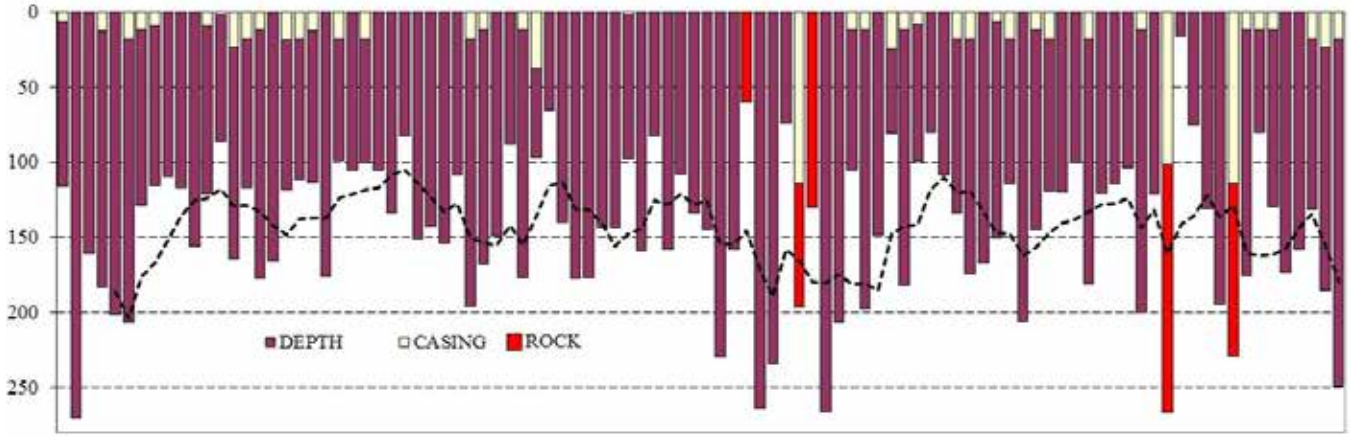

Figure 4. Depths (m) of the 65 wells used.

Table 1. Spreadsheet used in database

WELL nr	LOGS	DEPTH (m)	UTME	UTMN
Number given to logging.	IEL and GR (All Wells); DT	Depth reached.	UTM coordinates	

DIR (xm)	GR (xm)	DT (xm)	DIR (n)... GR (n) etc.
Resistivity value at the depth of "x" meter (ohm-m)	Value of Gamma Ray at the depth of "x" meter (GAPI).	Value of the Sonic Transit Time at the depth of "x" meter (μs/ft).	And so on according to the same scheme.

Induction logging and gamma ray datas were avaliable in all analysed wells but not all had sonic logging. In this way, the type of tool was considered in the analyzes. The wells were identified by number well (nr), the reached depth and UTM coordinate. It was done a separeted collumn for each meter depth of the values of induction resistivity, gamma ray and sonic.

The deep resistivity values of induction (DIR) above 200 ohm-m were set as 200ohm.m for interpolation the purposes, since resistivity changes above that value has little geological significance. The maps has been limited up to coordinate UTM 400,000 although some outliers wells located above this coordinate has been used for sake of interpolations.

3 MAPS

Maps of resistivity values, DIR (ohm-m), gamma rays, GR (GAPI) and transit time, DT (μs/ft) were done at each 10 meter depth from the top of layers. Neighboring wells correlation scale ranges were chosen in accordance to authors experience in the field, as seen in Table 2.

The Figures 5 show an example of 50m depth results from Krigging interpolation method according to Sturaro & Landim (1997) for the three curves resistivity values (DIR), gamma rays (GR) and transit time (DT).

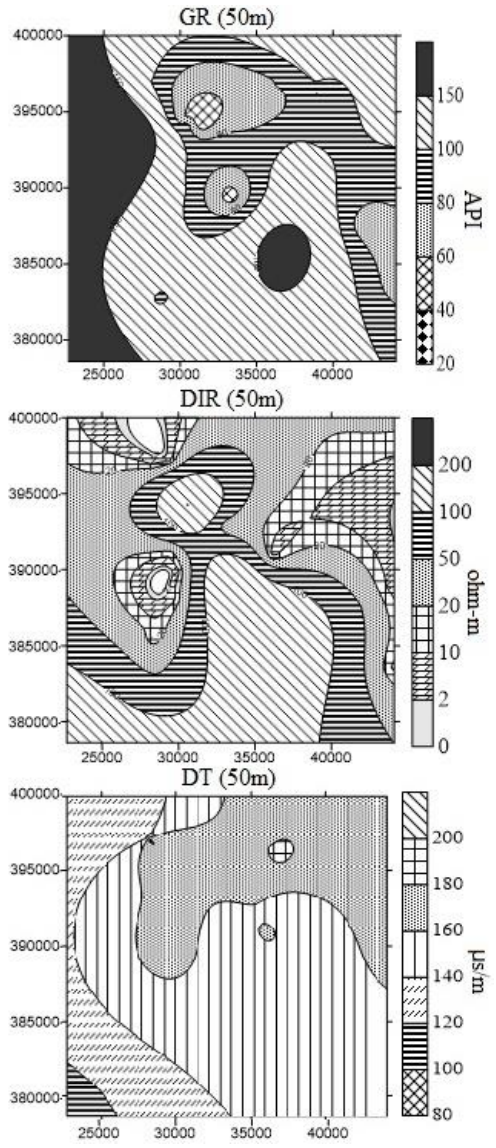

Figure 5. Example of Electrofacial Maps at 50 meters depth.

Table 2. Correlation between Gamma Ray, Transit Time and Deep Resistivity, range and lithology.

GAMMA RAY - GR		SONIC TRANSIT TIME - DT	
GAPI	INTERPRETED LITHOLOGY	μs/ft	INTERPRETED LITHOLOGY
40 - 60	Clean Sand	60 - 80	Well consolidated rock or sediment
60 - 80	Clay Sand	80 - 100	Consolidated sandstone or weathered rock
80- 100	Very Clayey Sand / Shale	100 - 120	Unconsolidated sandstone and clay
100-150	Shale/Clay/ Arkosic Sandstone	120 - 140	Low consolidated sediment
> 150	Arkosic Sandstone	140 - 160	Very low consolidated sediment
INDUCTION DEEP RESISTIVITY - DIR			
Ohm-m	INTERPRETED LITHOLOGY	Ohm-m	INTERPRETED LITHOLOGY
0 - 2	Clay/Shale	50 - 100	Water Sandstone
2 - 10	Sandy Clay	100 - 200	Water Sandstone or weathered rock
10 - 20	Sandstone clay		
20 - 50	Sandstone	> 200	Basement Rock or dry sandstone

4 ANALYSIS OF RESULTS

Clays, silts and fine clayey arkosic sands, with occurrences of coarse sand and fine gravel, compose the lithology of sedimentary basin of São Paulo. These sediments are textural and mineralogical immature. The coarser fractions are mainly in the central part of the basin.
Considering the probe samples and taking into account the low level of total salts in water, it was carried out the following analysis for each map.

4.1 *Gamma Ray*

The Figure 6 shows the gamma ray values maps. The higher GAPI values observed at all depths demonstrate the predominance of immature sediments. Arkosic sandstones are explained by the high gamma values due to ^{40}K (radiative) of potassium feldspar. It is almost difficult to correlate the presence of sand based only in low GAPI. There is a sand trend to north of studied area and possibly a sandy body delimited to 40 meters in the northern portion center. This layer has a clayey intercalation after 80 meters depth. It turns to be sandy at 90 meters depth, almost disappearing at 100 meters depth.

4.2 *Deep Induction*

The analyses of the induction curves show higher values (100-200 ohm-m) in the SW portion of the map, Figure 7, due to the presence of the crystalline basement in place. In this way, DIR is the profile that best characterizes the area because it is not be influenced by the lack of maturity of the sediments.

The lower resistivity values (2-50 ohm-m), between 50 and 70 meters lead to a possibly existence of clay material. At 80 meters there is high resistivity layer (possibly a sandy layer) that does not have continuity at greater depths. The portion of NW has consistently low values indicating more clay material for all depths. The SE portion shows intermediate values interlayered with sandy layers in sandy clay.

In addition, the alternating layers with high resistivity (sandy layers) in the central part of maps can be noted in Figure 7. Noteworthy is a high resistivity layer, with low gamma ray and high transit time up to 60 meters. There is a sandy layer with a good log correlation. Bellow 70 meters, the increase of gamma values increase with decrease of resistivity.

4.3 *Borehole Compensated Sonic (BCS)*

In the depth up to 30m, the high transit time values indicate low textural maturity and high porosity, map DT 20 of Figure 8. The reduction of the transit time values in the SW direction (below 100 μs/ft) suggests a change in to the crystalline basement, map DT100 of Figure 8.

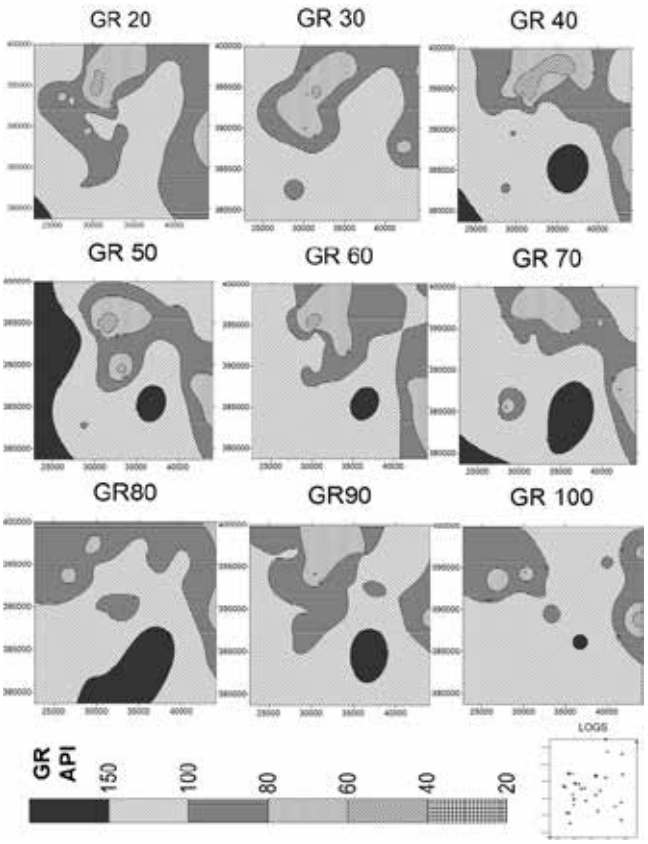

Figure 06. Gamma Ray (GAPI) Electrofacial Composite Maps at each 10 meters depth.

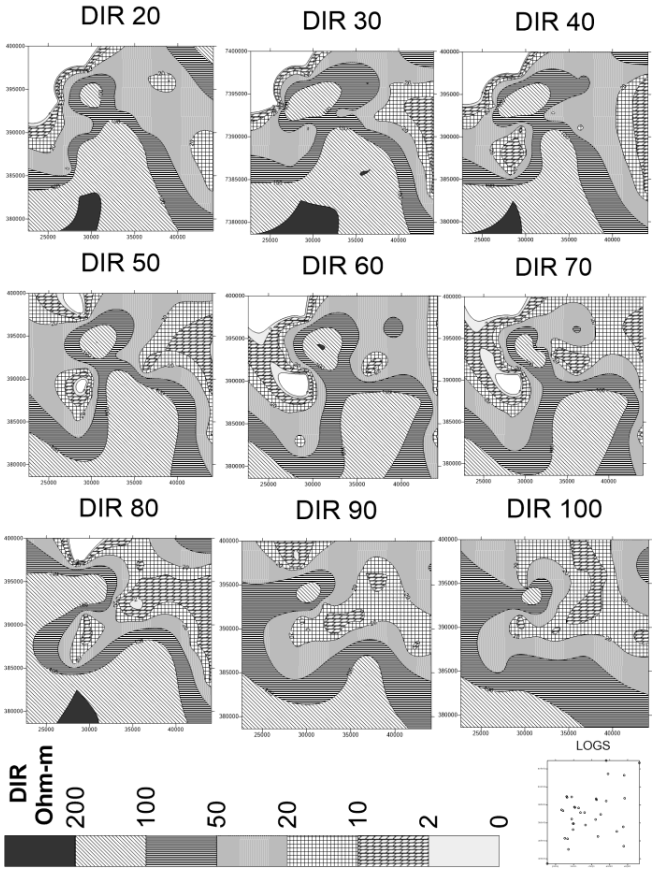

Figure 07 - Transit Time (μs/ft) Electrofacial Composite Maps at each 10 meters depth.

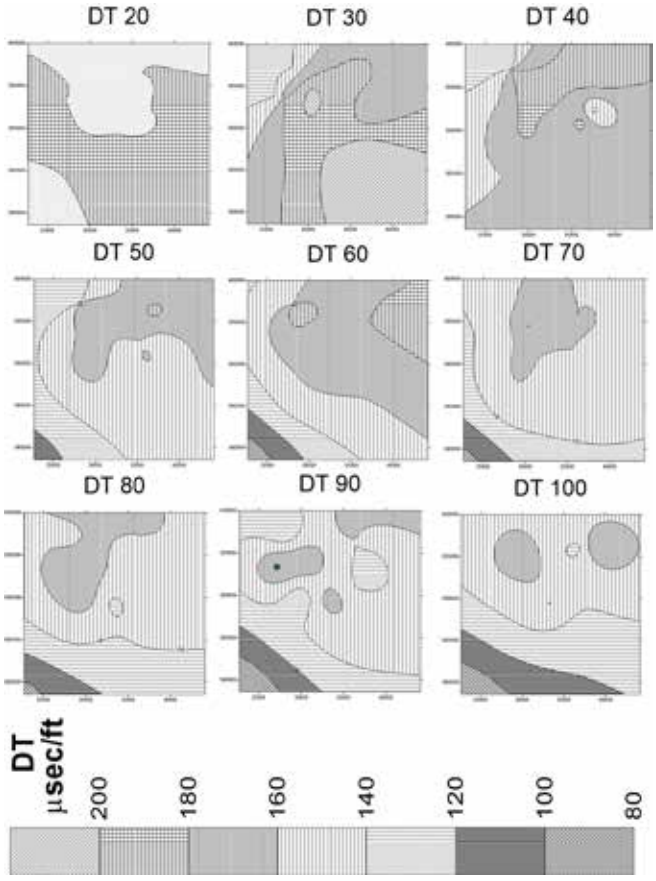

Figure 08 –Deep Induction (ohm.m) Electrofacial Composite Maps at each 10 meters depth.

4.4 *Stratigraphic Section*

The analysis of the curves DIR and GR led to the interpretation of existence of four layers (A, B, C and D) that were identified by results of the log correlation (Figures 9 and 10) with well-defined resistivity characteristics. The upper layer above the layer defined as a layer A represents the changed portion.

The major operational difficulties for the method are: sometimes different lithofacies have similar values in the same type of well log; in the same lithofacies values of a given logs can vary depending on variables such as thickness, pit geometry, texture, etc. Therefore, lithofacies recognition becomes more effective when it employs statistical techniques to allow simultaneous analysis of several logs.

4.4.1 *Layer A*

The layer A has a maximum thickness of 15m and has characteristic resistivity peak. Moreover, the lithology is composed of immature sandstone, with low gamma ray values, with occasional spikes due to the presence of potassium feldspar (arkosic sandstone). This layer when below the water level is a good groundwater catchment.

4.4.2 *Layer B*

The Layer B is the thickest one (40 to 70 meters) and it is composed by shale and clay sediments. Thus, it is no good for groundwater catchment.

4.4.3 *Layer C*

The Layer C is sandier than the layer A and consequently is more favorable to water potential. Its thickness is about 20 meters. In addition, when C is above the crystalline basement, it further increases its water storage.

4.4.4 *Layer D*

The Layer D represents the transition between sediments and crystalline rocks.

5 CONCLUSIONS

The authors do not intend to show a detailed faciological mapping methodology, but rather way to assess the feasibility of the procedures. The major difficult found in São Paulo area was the complexity stratigraphy of the recent sediments in the area. It will be more easy to work in geologically simpler areas, especially where occur mature sandstones without feldspar minerals and also in areas with consolidated materials in a more uniform stratigraphic column.

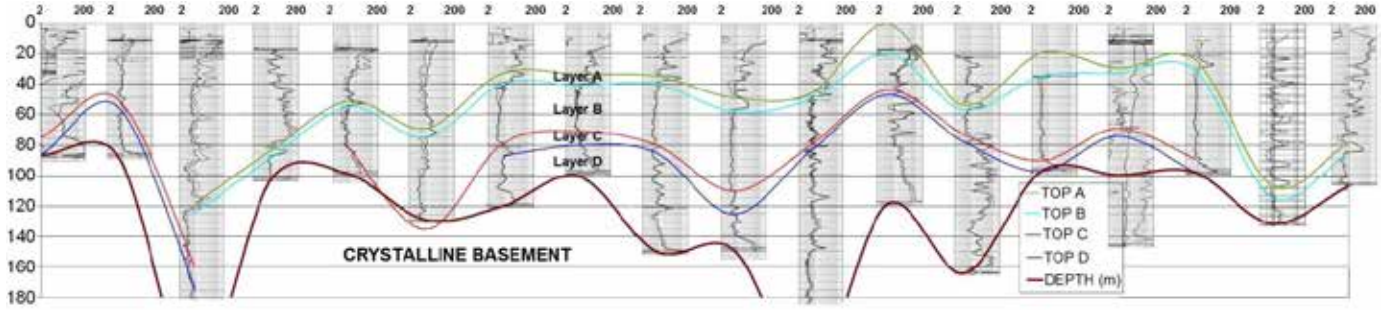

Figure 9. Electrofacies Section NS of study area.

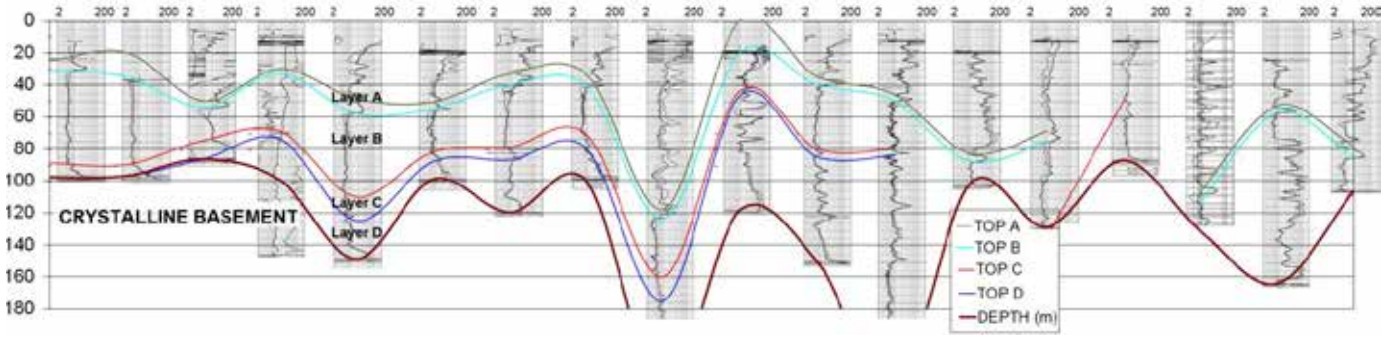

Figure 10. Electrofacies Section EW of study area.

It was possible a better correlation in the business centre area of the map, because of a higher density of logged water wells**.** Although the results showed this methodology can also be applied in areas with comples gelology, they provide a sufficient number of wells to desired detail (design of wells and stratigraphic evaluation).

It can also be interesting to use the same specific software for mining purpose in the data processing to minimize interpolation problems.

6 ACKNOWLEDMENTS

The authors would like to thank the company HYDROLOG Serviços de Perfilagens Ltd for well logs data.

The second author also would like to thank the grants 16/06214-0 and 07/06085-7, São Paulo Research Foundation (FAPESP).

7 REFERENCES

Kearey, P.; Brooks, M. & Hill, I. 2013. An Introduction to Geophysical Exploration. 3rd ed. Oxford: Blackwell Science.

Riccomini, C.; Peloggia, A ; Saloni, J ; Kohnke, M &; Figueira, R. 1989. Neotectonic activity in the Serra do Mar rift system (southeastern Brazil). Journal of South American Earth Sciences JCR, England, v. 2, p. 191-197.

Sturaro, J R; Landim, P. M. B. 1997. Indicator Kriging For Gis'S Maps Integration. Proc. Third Annual Conference of the International Association for Mathematical Geology. Barcelona. Spain International Center for Numerical Methods in Engineering (CIMNE) v. 02, p. 699-704.

Takira, H. 1991. Aplicação dos métodos quantitativos espaciais a dados geológicos da Bacia de São Paulo. M.Sc. Dissertation. Instituto de Geociências da Universidade de São Paulo, São Paulo, 109pp.

Geotechnical and Geophysical Site Characterisation 5 – Lehane, Acosta-Martínez & Kelly (Eds)

Multichannel Analysis of Surface Waves (MASW) for Offshore Geotechnical Investigations

T. McGrath & M. Long
University College Dublin, Dublin, Ireland

P. O'Connor & A. Trafford
Apex Geoservices, Gorey, Wexford, Ireland

D. Ward
In Situ Site Investigation, Battle, East Sussex, United Kingdom

ABSTRACT: The multichannel analysis of surface waves (MASW) technique is widely used in onshore geotechnical investigations. It provides shear wave velocity (V_s) from which G_{max} can be obtained for input into foundation design. The objective of this research project was to develop the MASW technique for offshore use and to compare the results against those obtained from direct investigations. This will allow its application with some confidence to geotechnical investigations for offshore platforms, pipelines and other offshore hydrocarbon infrastructure. The technique is performed offshore in a similar manner to a traditional land based seismic acquisition. In this paper the acquisition and processing used is described in detail and the results for work carried out at a site in Dublin Bay are presented. The V_s values and geotechnical parameters obtained indirectly from the MASW technique are then compared to those obtained directly by seismic cone testing (SCPTU), showing good agreement between all three methods of investigation.

1 INTRODUCTION

Multichannel analysis of surface waves (MASW) is a non-invasive technique which allows estimation of seismic shear wave velocity (V_s). This is a key parameter for the evaluation of the small strain shear modulus (G_{max}) of a soil, which is used for a range of geotechnical design applications. As the name suggests, the strains involved are considered small, of 10^{-3}% or less. G_{max} is calculated using the density (ρ) and V_s with the formula:

$$G_{max} = \rho . V_s^2 \qquad (1)$$

where G_{max} is in Pa, ρ in kg/m^3, and V_s in m/s.

There are several techniques commonly used to measure V_s in both the field and laboratory. However a number of these techniques are difficult to implement in marine environments. These difficulties include logistical issues regarding working in marine environments, adverse weather conditions, and the problems associated with obtaining high quality samples for laboratory testing. MASW is a geophysical technique which can be used to overcome many of these issues. It has been used for onshore applications for a number of years, and is considered a cheap and reliable method for determining V_s (and hence G_{max}).

This paper will present the results of an MASW survey carried out of the east coast of Dublin, Ireland, comparing the measurements of V_s of both onshore and underwater MASW (or UMASW) in the intertidal zone, along with seismic cone testing (SCPTU) on this site.

2 THEORECTICAL BACKGROUND

Surface waves are seismic waves that travel along a boundary between two media, which can be of gas, liquid or solid state. If the interface is between gas and solid the surface wave is of Rayleigh type, which is the wave under consideration when performing MASW on land. However when moving offshore the interface is between water and an elastic solid (soil), which means the surface wave is no longer of Rayleigh type, but is now a Scholte wave or Stoneley-Scholte wave. Scholte waves have a similar particle motion and dispersive nature to that of Rayleigh waves, but they propagate at 88% to 99% of the Rayleigh wave velocity, depending on the thickness of the water layer (Grant & West 1965).

In general there are three parts to the MASW method: generating and recording the propagation of the surface waves; processing to construct the dispersion curve; and back calculation of the V_s profile from the calculated dispersion curve.

To generate the surface waves for MASW an impulsive source (sledgehammer or weight drop), vibrator, or a passive source (earthquake shaking or road traffic) can be used. The chosen source inputs

energy into the subsurface, two thirds of which is converted into surface wave energy, whether Rayleigh or Scholte type (Richart et al, 1970). These waves propagate at different velocities through strata with different properties, including but not limited to soil type, and stiffness.

Since there is significant layering in the subsurface the depth of penetration is dependent on the frequency (or wavelength) content produced by the source. Higher frequencies (i.e. short wavelengths) will be influenced by the more shallow material. Lower frequencies (i.e. long wavelengths) reflect the properties of deeper materials (Mouton & Robert, 2014). To optimise the depth of penetration the field set up can be altered by changing the source or interval distance between receivers.

After the data has been recorded in the field it is used to generate a dispersion curve which plots phase velocity versus frequency. As an initial estimate, the depth of penetration, z, can be interpreted as a fraction of the wavelength, λ.

$$z = (\lambda/n) \qquad (2)$$

where n is a constant, usually chosen as either 2 or 3 based on the preference of the interpreter (Donohue et al, 2004).

When processing the dispersion curve the MASW method generally uses only the fundamental mode for the inversion analysis. However higher modes can be incorporated into the inversion process, when necessary, particularly when dealing with complex stiffness profiles. Once the desired modes have been measured the inversion procedure can be implemented to produce a shear wave velocity versus depth profile, having converted from shear wave phase velocity (V_R).

The MASW technique has been performed successfully on land in various places including Ireland (Donohue et al, 2004) and Norway (Long & Donohue, 2010), proving it to be a trustworthy geophysical investigation method.

3 SITE

The site involved in this study is located on Bull Island off the east coast of Dublin, Ireland, as shown in Figure 1. Bull Island is a wedge shaped narrow portion of land orientated southwest-northwest, approximately 5 km in length, while the width ranges from 1 km to 200 m at opposite ends. It was formed towards the end of the 19th century after the construction of the North Bull Wall causing the deposition in a north easterly direction. The primary area of interest is a section of beach on the southeast side of the island approximately 1 km from the southwest end of the island.

This site is generally well characterized by a number of agencies, including boreholes at the St. Anne's golf club and in Dublin Harbour. The sediments in the sub-surface are made up of alluvial

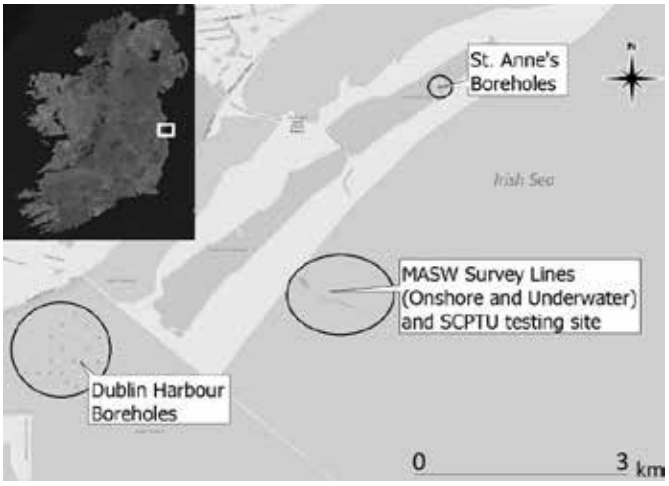

Figure 1. Map of the site on Bull Island, Ireland

clays, gravels, sands and marine deposits (Gibson et al, 2012). The upper stratum ranges in thickness from 3 m to 9.5 m, and consists of sand. A stratum of stiff boulder clays lies beneath this, with an approximate thickness of 3 m. The corresponding bulk density values of these are 1.8 Mg/m^3 and 1.9 Mg/m^3 respectively. There is also a stratum of glacial and glaciofluvial deposits that lies just above the bedrock, which was derived from the limestone bedrock (O'Meara, 2012) at the end of the last ice age some 10,000-20,000 years B.P.

The bedrock underlying the site and most of Dublin is "Calp" Limestone, deposited in a shallow sea environment during the Lower Carboniferous period. Marchant & Sevastopulo (1980) describe it as an argillaceous limestone interbedded with calcareous shales or mudstones. The bedrock at this location is at a depth of between 10 m and 13 m.

4 DATA ACQUISITION METHODS

4.1 *Onshore MASW*

The onshore portion of the survey was carried out in one day in good weather conditions. Four separate MASW survey lines were performed as part of the onshore tests. The MASW lines were all perpendicular to the shoreline, collinear with one another, and located at 12 m intervals. The field set up for each of these lines included: 24 receivers (4.5 Hz geophones) with 3 m spacing between consecutive receivers; a 5 kg sledgehammer and steel plate were used to produce the impulse to generate the surface waves located 9 m from the north western end of the spread; and a seismic recorder for collection of the data.

All data from the onshore MASW survey were processed using the program SurfSeis 4.0, to plot the

dispersion curve and perform the inversion procedure. The inversion procedure used by this program is a least squares approach (Xia et al, 1999). It is an iterative method that requires an initial earth model, including the S-wave velocity, P-wave velocity, density and thickness of each layer. This model can be specified by the user, if correlating with other pre-existing data sources, or the program can create a model, as was the case for the tests on Bull Island. Once the model has been specified a synthetic dispersion curve is then generated. Since the dominant influence on a dispersion curve in a high frequency range (>5 Hz) are the S-wave velocities, they are updated after each iteration, until the synthetic curve closely matches the field curve, and thus a shear wave velocity-depth profile is produced.

4.2 *Underwater MASW*

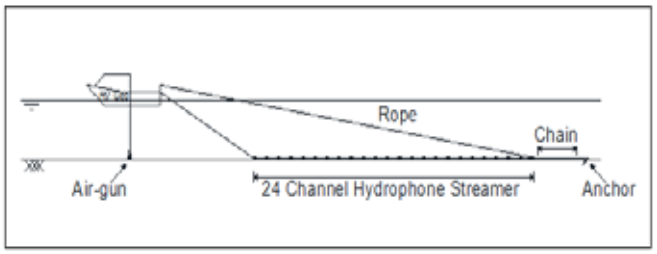

Figure 2. Underwater MASW set up

The offshore survey was completed over two days in fair weather conditions. The field work had to be repeated on the second day as the presence of electrical noise, due to a lack of an earth, negatively affected the dispersion curve plots from the first day. Five separate MASW survey lines were performed in a similar location to the onshore MASW survey lines, to test the repeatability and maximise the confidence in the results. The MASW lines were parallel with the onshore MASW lines and were located at intervals between 10 m and 15 m moving out from the shore. These spreads included 24 receivers, however low frequency hydrophones are used in place of geophones, as the former can be as effective if laid on or near the sea bottom (Park et al 2000). The spacing between receivers was 3.125 m as this was the standard spacing of the streamer as supplied, but also matches well with the onshore MASW spacing. When laying this on the sea floor the hydrophone streamer was tensioned by hand, whilst a rope, chain, and anchor were used to take strain off the streamer and prevent damage, while holding the vessel in place. The full field set up is depicted in Figure 2.

With a water column of up to 3 m now above the soil a seismic source, capable of imparting more energy into the subsurface than a sledgehammer and steel plate to generate surface waves, was required. Thus a 12 cu.in air gun was chosen as the impulsive source. This source was located approximately 9 m collinear from the end of the streamer.

All other equipment was kept on board the deck of the research vessel including a seismic recorder and gun trigger. All communications from deck to underwater equipment and vice versa were relayed through an umbilical, to ensure coordinated energy input and data recording.

The data was later processed using the SurfSeis 4.0 program once more, to maintain consistency. It should be noted that SurfSeis is designed to perform inversions on Rayleigh waves. However there is negligible degrading of the confidence level waves in the inversion process if treating Scholte waves as Rayleigh waves (Park et al, 2000).

4.3 *SCPTU*

Figure 3. Performing SCPTU test on Bull Island

The seismic cone testing was carried out in one day at low tide in good weather conditions. A probe containing two geophones as the receivers, was pushed into the earth using a hydraulic ram. A sledgehammer hitting a steel plate horizontally, fitted with 45 degree grooves for improved beam to soil contact, acted as the seismic source and was offset 0.5 m from the penetration hole. The first metre of soil was not tested, and three readings were taken every 0.5 m thereafter, to ensure better consistency and accuracy. A total of four locations along the lines of the UMASW and onshore MASW spreads, perpendicular to the line of the shore were performed. The final depths of penetration ranged between 6.5 m and 9.0 m before refusal.

5 RESULTS

Figure 4 shows a direct comparison between the onshore method of MASW, using a sledgehammer and steel plate, and the underwater MASW method, using an air gun. The images depict the data recorded (shot signals) on site, and the dispersion curves produced by SurfSeis during processing.

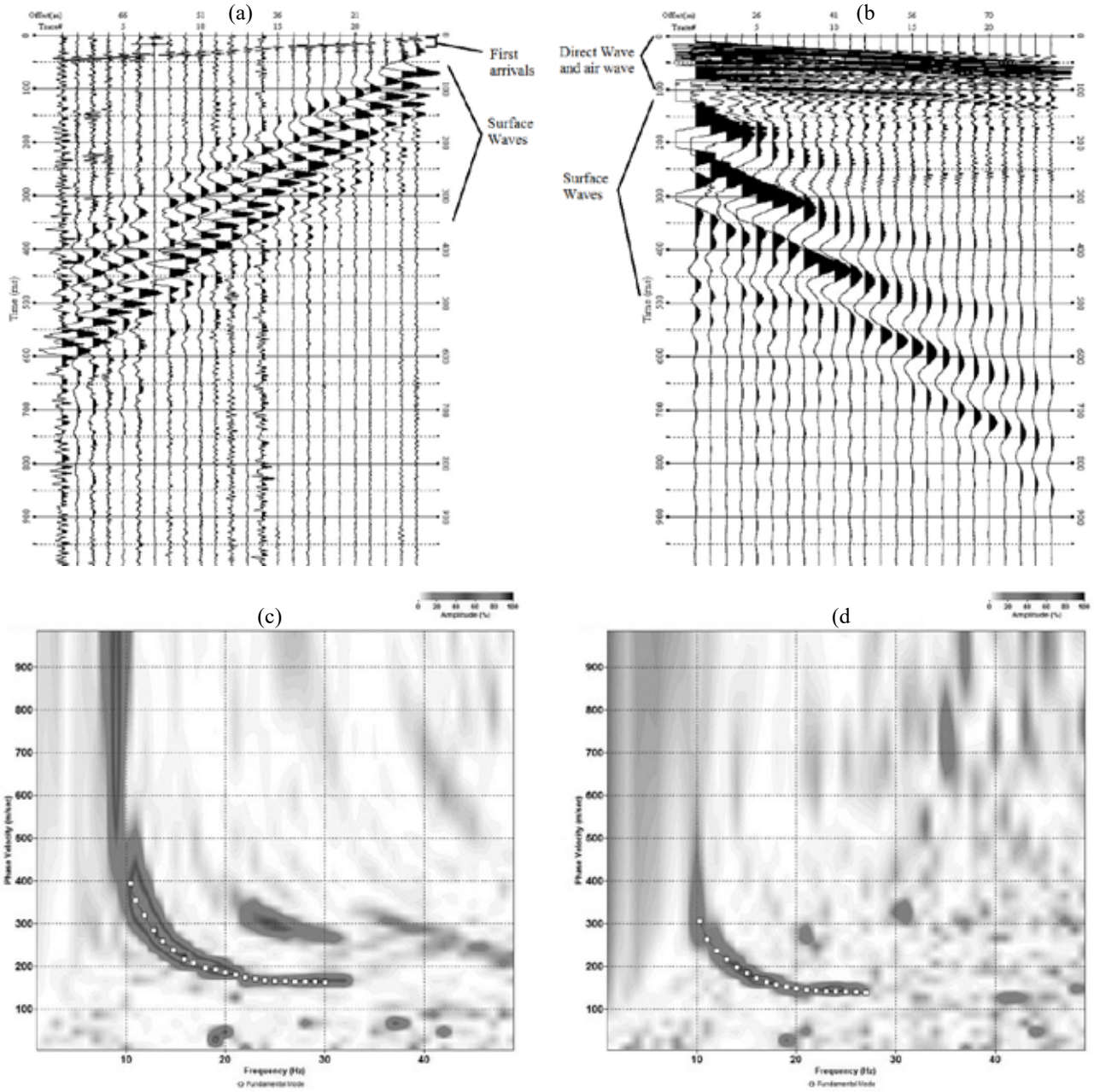

Figure 4. MASW shot signals by (a) 4.5Hz Geophones on land at 3 m spacing and (b) Hydrophones in shallow water at 3.125 m spacing, and dispersion curves from these (c) and (d) respectively

Focusing on the shot signals 4(a) and 4(b), there are noticeable differences. In the onshore method the first arrivals, usually used for P-Wave analysis, are clearly evident in the first 50 ms of the recording. In the UMASW recording there is a lot more activity occurring in this time period. The first arrivals are masked by the air waves generated by the load blast, while some of this data could be related to the water in the soil, since it is fully saturated, as these waves arrive at the approximate P-wave velocity of water (1480 m/s). It should be noted that while these waves are present they do not affect the picking of a fundamental mode dispersion curve as these waves typically travel much faster than the surface waves as seen above. Examination of the body waves shows good correlation between the two methods. However there appears to be a loss of some of the frequency content in the UMASW as the visible wavelengths appear longer than those in the onshore recording.

Moving to the dispersion curves 4(c) and 4(d), the assumption of a loss of frequency content is confirmed. In the onshore MASW recordings the highest frequency picked was between 30 Hz and 33 Hz, while the highest frequency with UMASW was 27 Hz. While this change is relatively small, it reduces confidence in the results of the shallowest strata.

There is also some change in the lower frequency range, although this is less likely due to the different testing environments, but more a result of equipment limitations, including the capability of the sources to produce lower frequencies, and the sensitivity of the

receivers (4.5 Hz geophones and approximately 10 Hz hydrophones).

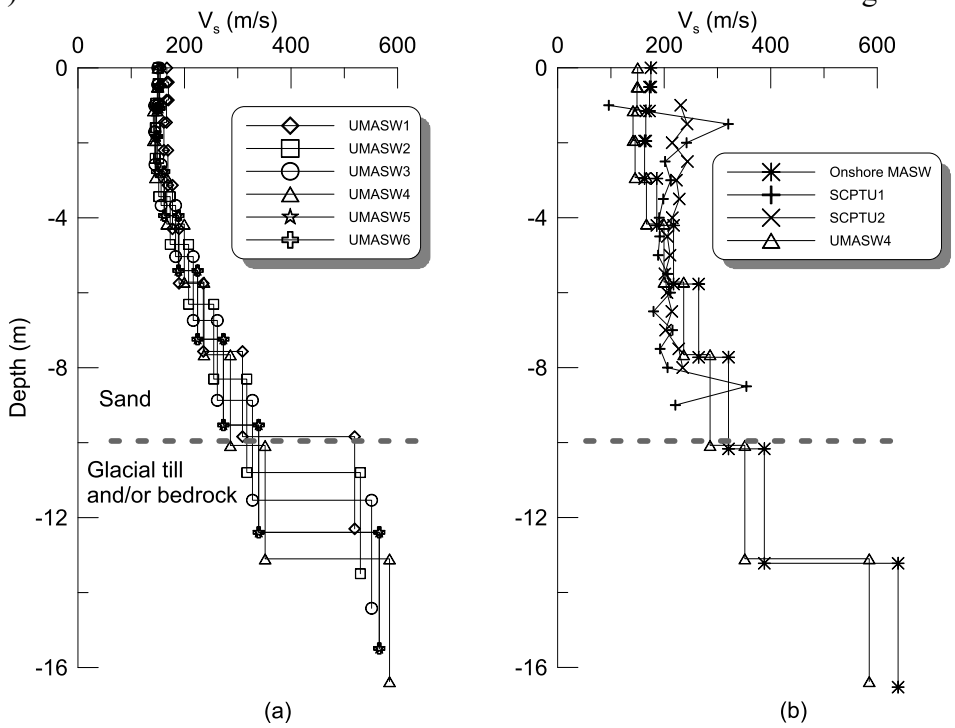

Figure 5. (a) UMASW profiles and (b) comparison of V_s from UMASW, onshore MASW and SCPTU)

Figure 5a is a plot of six separate underwater MASW shots taken using the same spread. All of the profiles are consistent with one another, showing good repeatability of the technique. The most obvious separation of the profiles occurs when defining the depth of the last layer, i.e. to half space.

Each profile estimates it to be at a different depth. This is due in part to the pick of the fundamental mode dispersion curve before the final inversion process, particularly in the lower frequencies where interpretation can become more difficult.

Equation (2) can be used to gauge the approximate depth of this layer, using the point picked with the lowest frequency. The pick of each curve is also dependent on the interpretation and experience of the individual processing the data.

Results of SCPTU testing are shown on Figure 6. The plot shows corrected cone resistance (q_t), sleeve friction (f_s), friction ratio (R_f) and pore pressure (u_2) versus depth. These data suggest a sand layer is present to the depth of the test.

The sand appears to reduce in density and perhaps become more silty with depth.

The comparison of the underwater MASW technique with the other site investigation methods is illustrated in Figure 5b. For clarity only one UMASW, one onshore MASW and two SCPTU results have been plotted. In general the UMASW an MASW data are very similar, The UMASW Vs values are typically 15% less than those from MASW. This is consistent with the theory suggesting that Scholte waves propagate at a slower

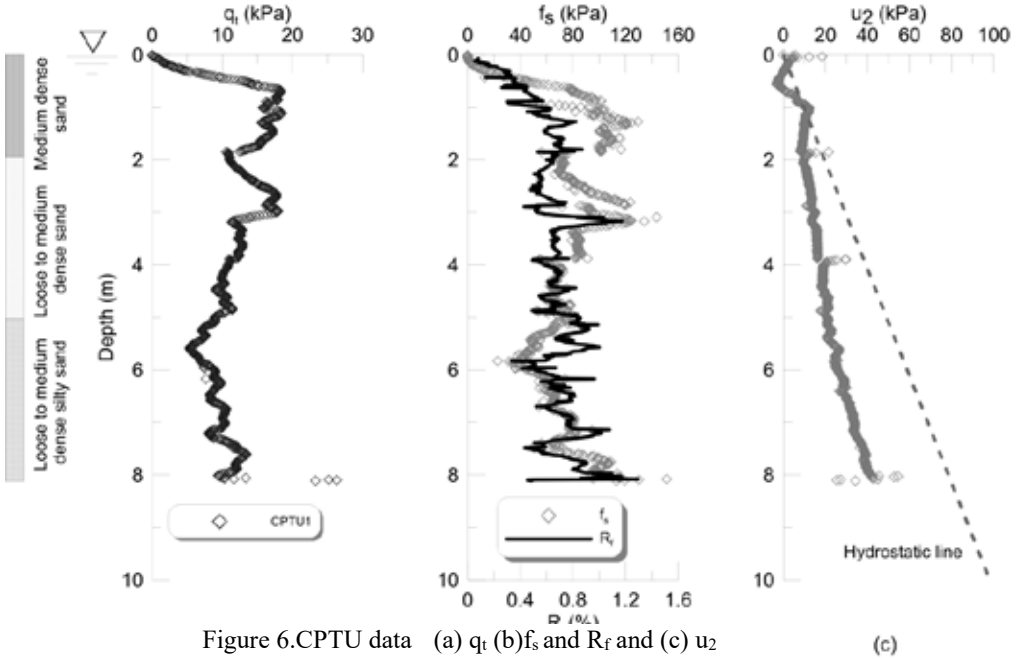

Figure 6.CPTU data (a) q_t (b)f_s and R_f and (c) u_2

velocity than Rayleigh waves. The SCPTU correlates well with the other two data sets up to its penetration depth of 9 m. At this depth the tests had to be terminated as the cone could not penetrate the stiffer lower strata, which may also have been the result of cobbles and boulders present within them. Just prior to termination the SCPTU method registered an increase in shear wave velocity, indicating the beginning of a stiffer layer which correlates with the UMASW and MASW results.

The SCPTU also recorded a high V_s value in a layer less than 2 m from the surface, which neither of the MASW methods determined. This layer is likely to be real as there was significant resistance to penetration when performing the CPTU tests. Returning to Equation (2) focusing on the highest frequency picked on the fundamental mode dispersion curve, and using the more conservative approach of selecting n = 2, it was determined that the frequency content relating to the top 2.5 m of the MASW profiles lies outside the range picked, thus a lowered confidence in the final output of this upper stratum. Despite this anomaly the UMASW results are considered to be satisfactory for site investigation in shallow water depths.

6 CONCLUSIONS

This paper presents the shear wave velocity profiles measured in the intertidal zone on Bull Island, Dublin, Ireland, with the aim of assessing the repeatability, accuracy, and reliability of the underwater MASW (UMASW) technique. Measurements were taken using three different methods: UMASW, standard onshore MASW and seismic cone testing (SCPTU).

The results of the tests indicate that hydrophones at the bottom of a water column can produce surface wave data of similar quality to that produced by geophones on land. The agreement between numerous shots taken at a similar location indicate good repeatability of the UMASW. The two MASW techniques managed to penetrate to the expected stiff soil depth of 13m, while the seismic cone testing penetration depth was limited to 9 m by the stiffer soils in the lower strata. All results from the different techniques are consistent with one another and are in line with the site stratigraphy.

The underwater tests outlined in this paper were performed in water depths up to a maximum of 3 m. Tests using the same equipment have since been completed in depths of up to 25 m. Good quality data is produced in these depths, similar to the shallow work, with good frequency ranges present in the dispersion curves.

7 ACKNOWLEDGEMENTS

The authors wish to thank the National Parks & Wildlife Service & the Geological Survey of Ireland. This project is funded by the Irish Shelf Petroleum Studies Group (ISPSG) of the Irish Petroleum Infrastructure Programme (www.pip.ie). The ISPSG comprises: Atlantic Petroleum (Ireland) Ltd, Cairn Energy Plc, Chrysaor E&P Ireland Ltd, Chevron North Sea Limited, ENI Ireland BV, Europa Oil & Gas (Holdings) plc, ExxonMobil E&P Ireland (Offshore) Ltd., Kosmos Energy LLC, Maersk Oil North Sea UK Ltd, Petroleum Affairs Division of the Department of Communications, Energy and Natural Resources, Providence Resources plc, Repsol Exploración SA, San Leon Energy Plc, Serica Energy Plc, Shell E&P Ireland Ltd, Sosina Exploration Ltd, Statoil (UK) Ltd, Tullow Oil Plc and Woodside Energy (Ireland) Pty Ltd.

8 REFERENCES

Donohue, S., Long, M., O'Connor, P., Gavin, K. 2004. Use of multichannel analysis of surface waves in determining G_{max} for soft clay. *Proceedings 2nd. Int. Conf on Geotechnical Site Characterisation, ISC.* 2: 459-466.

Gibson, P.J., Caloca Casado, S., Jiminez-Martin D. 2012. Integrated Coastal Mapping of Dublin Bay Geomorphology based on geophysical data, satellite inferred bathymetry and 3D integration with INFOMAR datasets. *INFOMAR Report: INF-11-07-GIB*.

Grant, F.S., West, G.F. 1965. Interpretation theory in applied geophysics. *McGraw-Hill Book Company,* New York.

Long, M., Donohue, S. 2010. Characterization of Norwegian marine clays with combined shear wave velocity and piezo-cone cone penetration test (CPTU) data. *Canadian Geotechnical Journal*, *47*(7): 709-718.

Marchant, M.R., Sevastopulo, G.D. 1980. The Calp of the Dublin District. *Journal of Earth Sciences*, 3(2):195-203.

Mouton, E., Robert, D. 2014. Combination of Seismic Refraction and Marine Surface Wave to Characterize Near Surface Marine Sediments. *Proceedings of the 1st Applied Shallow Marine Geophysics Conference,* Athens.

O'Meara, D. 2012. Investigating the Geotechnical Properties of the Geological Units Underlying Dublin Bay. *M.Sc. Thesis*, Queens University Belfast.

Park, C.B., Miller, R.D., Xia, J., Ivanov, J., Hunter, J.A., Good, R.L., Burns, R.A. 2000. Multichannel analysis of underwater surface waves near Vancouver, Canada, *SEG Tech. Program Expanded Extracts 2000:* pp.1303-1306.

Park, C.B., Miller, R.D., Xia, J. 1999. Multichannel analysis of surface waves. *Geophysics*, Vol. 64(3): pp.800-808.

Richart, F.E., Woods, R.D., Hall, J.R. 1970. *Vibration of Soils and Foundations,* Prentice-Hall.

Stokoe, K.H., Wright, S.G., Bay, J.A., Roesset, J.M. 1994. Characterization of geotechnical sites by SASW method. *Geophysical characterization of sites*, Woods, R.D. (ed.), Oxford Publishers.

Xia, J., Miller, R.D., Park, C.B. 1999. Estimation of near-surface shear-wave velocity by inversion of Rayleigh waves. *Geophysics*, Vol. 64(3):.691-700.

Geotechnical and Geophysical Site Characterisation 5 – Lehane, Acosta-Martínez & Kelly (Eds)

In-situ detection of sensitive clays from a geophysical perspective

A. A. Pfaffhuber, S. Bazin, K. Kåsin, H. Anschütz
Norwegian Geotechnical Institute, Oslo, Norway

R. Sandven, A. Montafia, A. S. Gylland
Multiconsult, Trondheim, Norway

M. Long
The University College of Dublin, Ireland

ABSTRACT: Sensitive and quick clays are typically found in Norway, Sweden and Canada and are characterised by a remoulded undrained shear strength which is considerably lower than the intact undisturbed shear strength. In geotechnical engineering the presence of sensitive clays poses a major challenge. The landslides at Rissa in 1978, and more recently at the Skjeggestad bridge in Norway, are devastating reminders of the potential threats related to such soils. For the geotechnical engineer in a construction project it is hence important to 1) determine if there is sensitive clay present and 2) determine the extent of the deposit. This is currently done based on interpretations of soundings and to some extent geophysical methods. However, for verification of quick clay, sampling and laboratory testing must be performed. A set of updated and new guidelines for classification of sensitive clays from in-situ measurements were recently compiled. The aim was to provide the geotechnical engineer with a practical classification tool where all available information is utilized and combined efficiently. An extensive database of Norwegian test sites formed the basis for the work. Here, we focus on the geophysical tools that are suggested in these guidelines: cone penetration test with resistivity measurements (R-CPTu), electrical resistivity tomography (ERT) and airborne electromagnetics (AEM). The results show that the above mentioned site investigation methods hold information that complement each other to form a solid basis for detecting the location of sensitive clays. In turn this opens for more efficient site investigations where all available data is interpreted in a systematic manner leading to more reliable mapping of sensitive clay deposits.

1 INTRODUCTION

The Scandinavian post-glacial marine clays were deposited in a marine environment during and after the last ice age some 10 000 years ago, entrapping pore water of high salt con-tent in the voids. Leaching of the pore water by meteoric groundwater flow has diluted the pore water salinity in some clays. Without its salt, the clay structure can easily collapse and the clay becomes quick. A quick clay is a clay which in the remoulded state has a shear strength c_r less than 0,5 kPa. The most reliable method to confirm quick clay is sampling and index testing in the laboratory to measure the remoulded shear strength and sensitivity. However these tests are costly for systematic quick clay hazard zonation.

The electric resistivity (the ability to conduct electrical current) of soils and rocks is generally a function of porosity, the ion content of the pore water, salinity, clay content and presence of charged minerals such as graphite and some sulphides. For clays in general and for leached clays in particular, it is mainly the salt content that influences the resistivity of the clay (Montafia 2013), at least for salt contents down to about 1 g/l. The resistivity is normally higher in leached clay than in the intact marine clays. By measuring the soil resistivity, one may hence be able to deduce the potentially leached zones according to the classification by Solberg et al. (2012) for Norwegian clays:

- Unleached marine clay: 1-10 Ωm
- Leached, possibly quick clay: 10-80/100 Ωm
- Dry crust clay, slide deposits, coarser material like sand and gravel and bedrock: >100 Ωm

However, increasing numbers of case studies reveal that these resistivity ranges are often influenced by local conditions (Rømoen et al. 2010, Long et al. 2012).

2 METHODS

As resistivity is closely correlated to the pore water salinity in clays, and quick clay is indicated by higher resistivity than low-sensitive clay, measuring it in-situ appears as a suitable approach (Pfaffhuber et al. 2014, NIFS 2015). Measuring electrical resistivity in the field can be done downhole (R-CPTu), from the terrain surface (ERT) or from the air (AEM). The different geometries imply different advantages and limitations.

2.1 *Resistivity - CPTu*

The sounding equipment used for R-CPTu consists of an ordinary CPTu probe and a resistivity module mounted behind the probe (Fig. 1). To enable direct measurements of the resistivity, the electrodes need to be in contact with the soil volume where the measurements shall take place. The module is powered by batteries, and it can read, store and transmit measured data acoustically through the rods or via an electric cable to a receiver on the surface. The measured data can also be stored on a digital memory-card mounted in the probe. Scandinavian manufacturers of R-CPTu equipment have chosen to equip their resistivity probes with four ring-electrodes. The two outer electrodes transmit electric current into the soil, whereas the two inner electrodes measures the difference in potential. The distance between the electrodes defines the configuration. The resistivity depth profile is only limited by the maximum borehole penetration depth (on the order of 50 - 70 meters). In the Nordic countries, R-CPTU is mainly used for detection of leached clays, whereas in the rest of the world the method is used for tracing of contaminants in the ground.

Figure 1: RCPT-u probe (Geotech).

2.2 *Electrical resistivity tomography*

ERT is a geophysical method that uses DC current for measurement of the resistivity distribution in the ground. The current is applied on the soil volume by using short steel electrodes installed at the terrain surface, penetrating 10-20 cm into the ground (Fig. 2). By measuring the differences in electric potential, a measure of the soil resistance is obtained for all electrode locations. The measuring profiles are organized in one or more straight lines. Present day equipment can measure potentials on several parallel channels, and the total time of measurements in a profile takes approximately one hour. By processing the data and running an inversion algorithm, a 2D or 3D resistivity (ρ) model of the ground is obtained. A general estimate of the investigation depth is a reach of about 10-20 % of the profile length, depending on the resistivity distribution in the soil.

By integration of the resistivity model with data from borings and the geological knowledge of the area, the resistivity can be interpreted in terms of a geological ground model. This principle rests on the assumption that the resistivity mainly is determined by sediment or rock type. Its use for quick clay mapping has increased during the last decade, thanks to recent advances in the data acquisition (protocols and instruments) and processing tools.

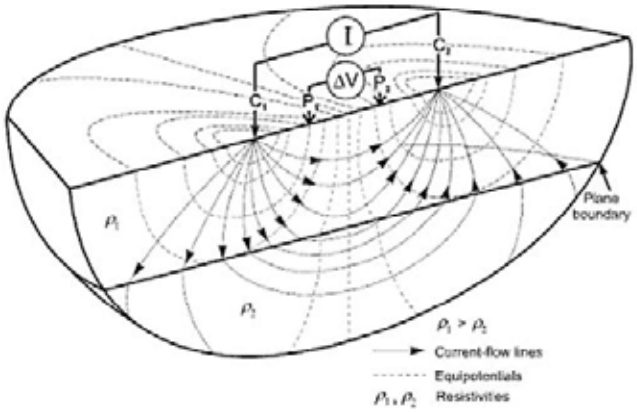

Figure 2: Principal sketch of ERT measurements. Electric current is send through the soil by 2 electrodes (C), while the power is measured on several locations (two in the illustration, P) (Knödel et al 2007).

2.3 *Airborne electromagnetics*

AEM measurements are used to map the electrical resistivity of the ground in a larger area. The method is traditionally used in the mining industry for tracing minerals in the ground, but modern airborne systems may have sufficient resolution to allow use in hydrological and geotechnical applications. Different AEM systems are available, some adapted to the need of large penetration depths for mineral tracing, others for more shallow applications in hydrogeology and geotechnics. All systems have in common that a magnetic field generated by the antenna induces current in the ground, which distributes downward and outwards. The rate of change in the electromagnetic field these currents produce, is recorded by a secondary coil. By inversion of the measured data points, the resistivity distribution in the ground can be modelled (Fig. 3). Interpretation of AEM resistivity data with regard to sediment properties has so far been done manually and is an advanced task

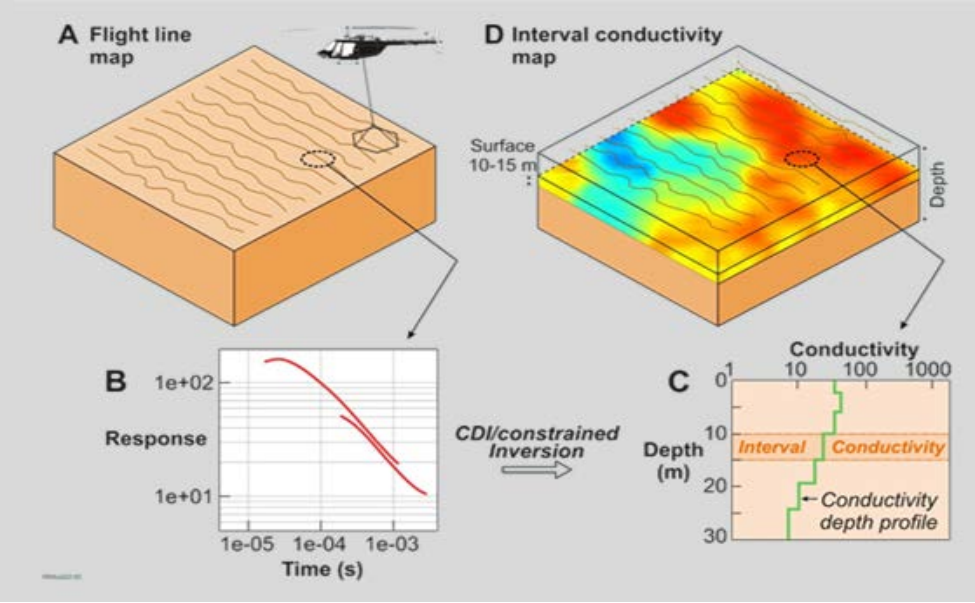

Figure 3: Principal sketch of AEM: The measurements are collected along flylines and are inverted to a resistivity model (Source: crcleme.org.au).

that requires both geophysical and geotechnical knowledge and skills.

The possible investigation depth may vary from 50 m to about 500 m, depending on the geology and type of soil in the area, the AEM system and the influence of noise from surrounding infrastructure.

3 DATA RESOLUTION

3.1 *R-CPTu resolution*

The distance between the electrode rings is in the order of 20 cm, R-CPTu readings are therefore small-scale compared to ground-based or airborne geophysics. No inversion is required during the data acquisition and therefore the measurement resolution is constant throughout the whole borehole. The module needs to be regularly calibrated in brine solutions of salt and water to ensure correct readings. In addition, a depth correction needs to be applied to the measurements, which is not always automatically done by the manufacturer software.

3.2 *ERT resolution*

The resolution obtained depends on the electrode spacing. Near the surface, the resolution in depth and along the profile is about half the electrode spacing, but becomes poorer with depth due to the increase in the influenced soil volume. Good planning of the measuring profile and synthetic modelling are hence important, but one usually has to compromise between investigation depth and resolution in the measurements. It is however possible to measure a number of adjacent profiles with several different electrode spacing to obtain a combination of high resolution and sufficient penetration depth. High resolution is particularly important if the aim is to separate the small differences in resistivity between salt and leached clay.

ERT results are computed by inverse modelling of the measured data. Usually resistivity is gradually in- or decreased laterally and in depth until the model fits the data, leading to a smooth resistivity model. This means that the transition from marine clay with low resistivity to rock with very high resistivity may be misleading, particularly if the thickness of the clay layer is limited. The resistivity of the clay will then appear higher than the real value, which can cause misleading interpretation of the clay (see examples in sections 4.1 and 4.2).

There exists no unique resistivity model for an ERT measurements, and use of different calculation models can illustrate the uncertainty (Bazin et al. 2015).

3.3 *AEM resolution*

The vertical resolution may be as good as 3-6 m close to the surface, but it gradually gets poorer with depth. The lateral resolution is determined by the size of the soil volume where current is induced. A typical estimate is that > 90 % of the signal from the ground origins from a perimeter about 3-4 times the flying height of the antenna. This means that one measurement defines a half-sphere with about 100 - 150 meter diameter. The resolution is also influenced by the processing method. Experience shows that structures falling steeper than 30° will not be correctly depicted, but will appear with a gentler slope compared to the true conditions.

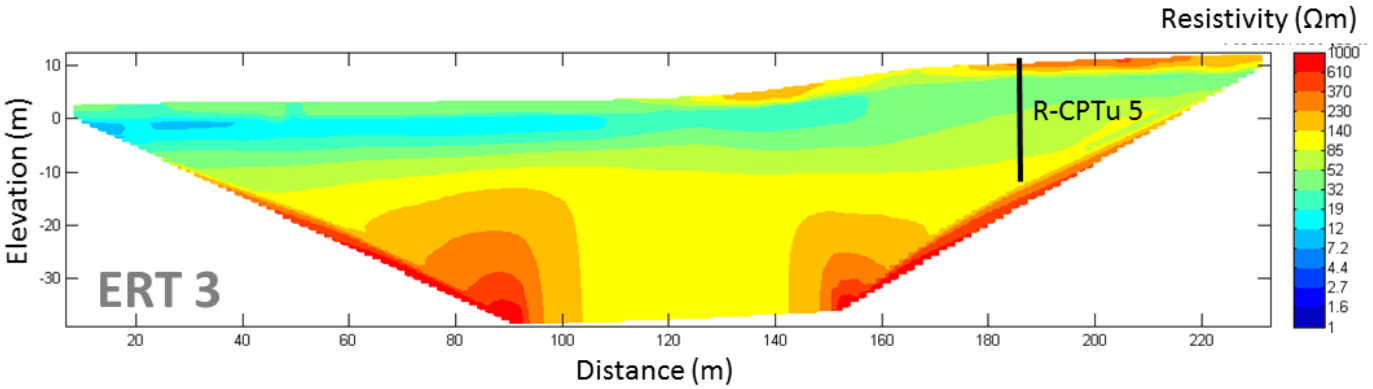

Figure 4: A representative ERT profile in Verdal. The resistivities at x < 160m (ρ < 20 Ωm) indicate intact marine clay while the resistivities at x > 160m (ρ > 20 Ωm) indicate leached clay.

High-resolution AEM has since 2013 been used in several large-scale road or railroad projects in Norway to obtain bedrock depth information, but the sediment characteristics requires even higher resolution.

4 DATA CORRELATION FROM CM- TO M-SCALE

The new guidelines for quick clay investigation are based on an extensive database of Norwegian test sites. Here, some representative examples are selected to illustrate the agreement between the three mentioned resistivity measuring methods.

When comparing resistivity measurements, it is important to be aware that these are influenced by a soil volume involving some centimetres to some tens of centimetres for R-CPTu, some meters to tens of meters for ERT and finally some tens of meter to some hundreds of meters for AEM.

4.1 *RCPT-u versus ERT*

A small scale ERT survey was acquired in 2015 in Verdal, 70 km NE of Trondheim, for a quick clay hazard investigation (NGI, 2015). The survey covered two sides of a major railway line, which therefore need to be studied with care. Five ERT profiles from 140 m to 400 m length were acquired, with 2, 3 or 5 m electrode spacing. In addition,, six CPTus were carried out, three with a resistivity module (R-CPTu 1, 3, and 5). A representative ERT profile is shown in Figure 4. The top is marked by a 1-2 m thick dry crust layer (ρ > 100 Ωm). The clay appears more leached (ρ > 20 Ωm) on one side of the profile than on the other side (ρ < 20 Ωm). Indeed, laboratory tests on clay collected in the boring marked in Fig. 4, indicate quick clay at 7 and 10 m depth. The transition to the resistive bedrock is smoothened out by the inversion process. A 3D overview of the survey is depicted in Fig. 5. The R-CPTu are presented with the ERT measurements for comparison (Fig. 6).

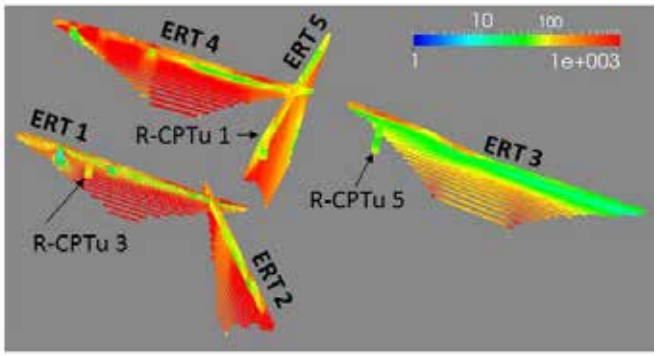

Figure 5: 3D view of the five ERT profiles and relative positions of the three R-CPTu loggings.

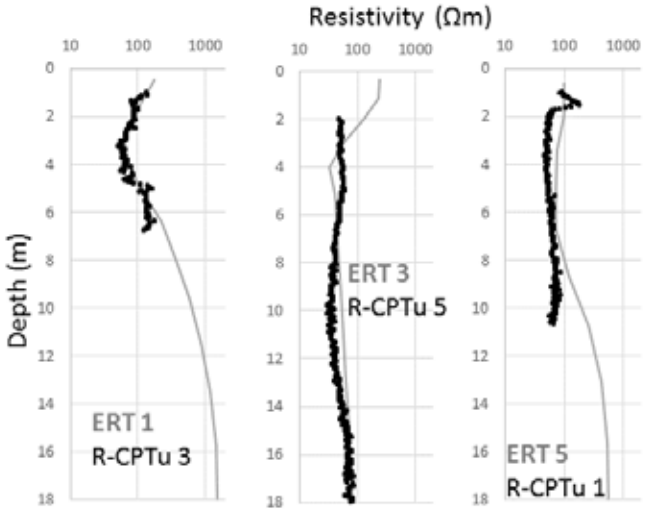

Figure 6: Resistivity measurements with R-CPTu (black) compared to ERT (grey) for three locations in Verdal. For thin sediments, (ERT 1 and ERT 5) the ERT-measurements are influenced by high resistivity bedrock.

The values measured by R-CPTu agree well with those obtained by ERT, whereas ERT-measurements below 6 m in this case, are influenced by the resistive bedrock. Except from these conceptual limitations, experience shows that the measurements agree well where the soil conditions are favourable.

4.2 *ERT versus AEM*

A SkyTEM 302 AEM survey was flown in 2013 in Norway to complete a new major highway between eastern Norway and Sweden (Anschütz et al., in prep.). The survey covers a planned road with known deposits of quick clay. In order to obtain more information in the near surface, a 600 m long ERT profile was acquired in 2014 along one AEM flight line in a known quick clay zone, near Vorma 50 km NE of Oslo. ERT and AEM data were processed and inverted using similar constraints with the Aarhus Workbench software.

Figure 6 demonstrates that ERT and AEM models agree very well. The AEM model (Fig. 6 upper) displays internal structures in the clay layer. The unconstrained ERT model (Fig. 6 middle) illustrates that the transition from conductive clay to resistive rock is smoothed out by the inversion process. Furthermore, the constrained ERT model (Fig. 6 lower) using the bedrock depth from the boreholes, obviously depicts a clear interface, but it is also possible to retrieve pockets of intact marine clay ($\rho < 10$ Ωm) at depth. Those are identified by boring (marked as blue in the boreholes).

This example demonstrates that AEM in principle can be used to distinguish marine, unleached clay from leached and potentially quick clay, provided the sediment layer is thick enough. Vertical variations in the resistivity distribution appear to be overestimated in the AEM method compared to the ERT method (Figure 7), a result/bias of the inversion algorithm used.

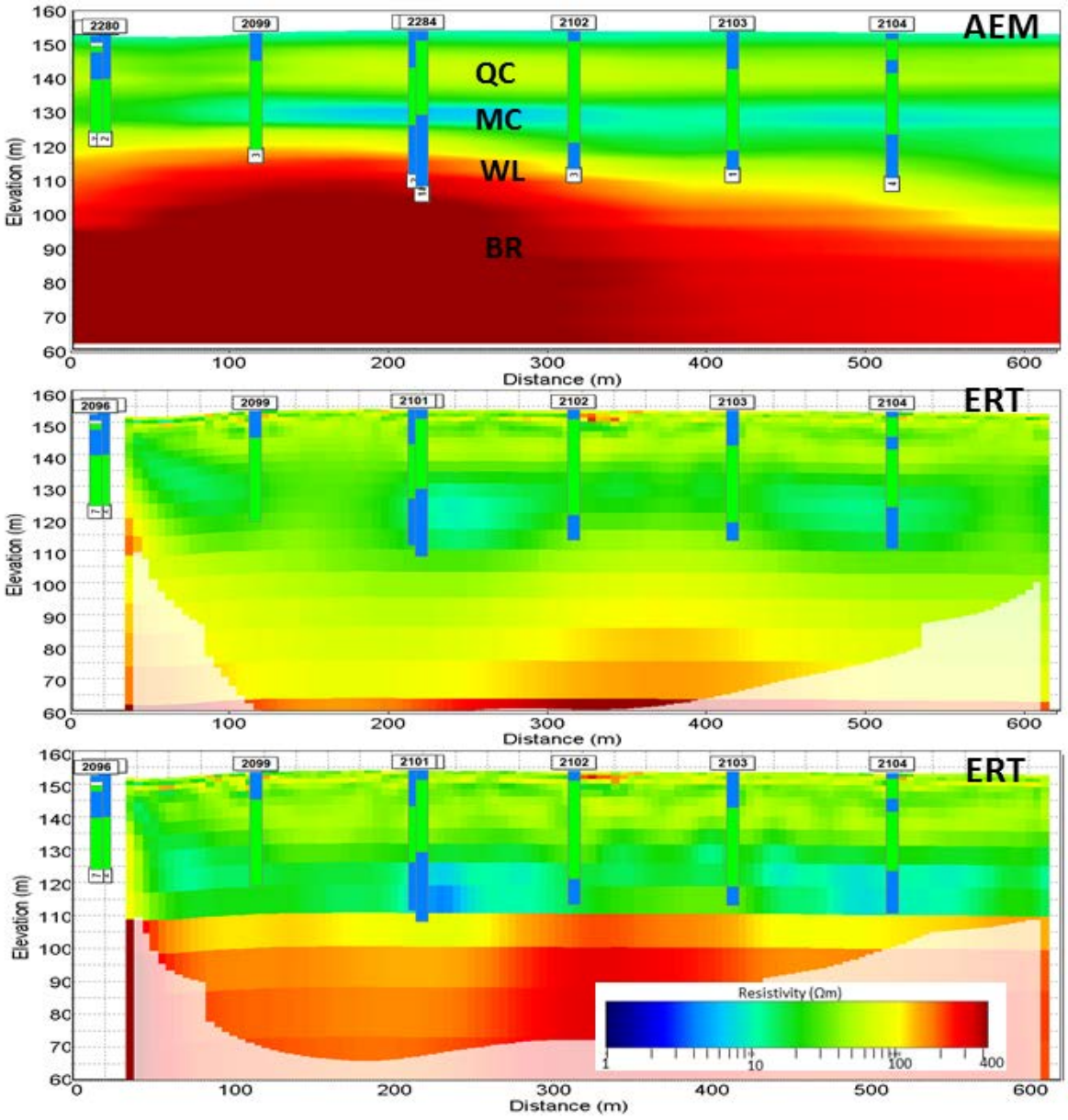

Figure 6: AEM model (upper), ERT model unconstrained (middle), and ERT model constrained (lower) by bedrock depth from boreholes. The letters in the top panel mark the four main layers: possible quick clay (QC), marine clay (MC), weathered layer (WL), and bedrock (BR). Quick clay identified with borings is marked in green. Figure from Anschütz et al., in prep.

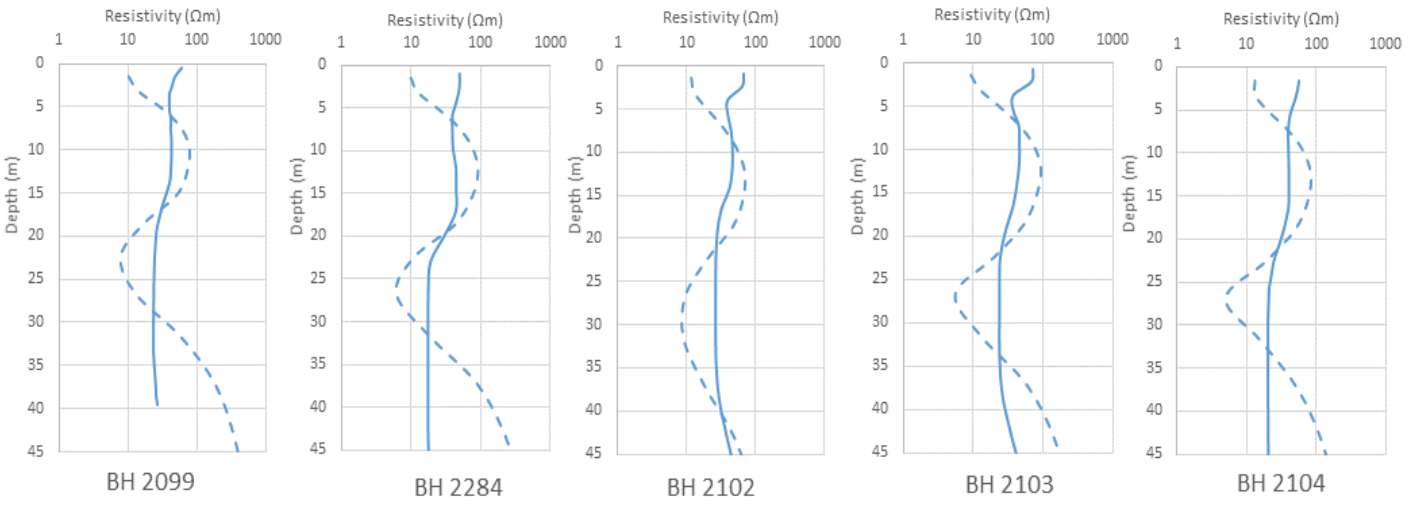

Figure 7: Vertical resistivity distribution from AEM (dash line) and ERT (solid line) at the boreholes positions shown in Figure 6. Figure from Anschütz et al., in prep.

5 CONCLUSIONS

Resistivity is directly related to salt content and therefore connected to sensitivity, and can indicate the spatial extent of leached clay. Although the three resistivity methods sample soil volume with different order of magnitude (centimetres, meters, to tens of meters) they hold information that agree and complement each other.

As AEM allows for a large coverage within a short time period and at reasonable costs, compared to borehole data and even to ERT surveys, regional information should be acquired in the initial phase of the mapping project. Indeed, the likelihood of sensitive clays can be used as a cost-saving tool for placing of further geotechnical investigations and ERT profiles. The proposed workflow in medium to large scale projects is thus AEM – ERT – soundings – sampling.

Proximity to bedrock or other resistive layers can bias the ERT and AEM soundings. Multimethod investigations can mitigate this uncertainty by complementing the resistivity information (e.g. Sauvin et al. 2014) or by constraining the resistivity inversion (e.g. Bazin et al. 2013).

ACKNOWLEDGEMENTS

The "Naturfare - infrastruktur, flom og skred (NIFS)" project is a joint venture between the Norwegian Water Resources and Energy Directorate (Norges Vassdrags- og Energidirektorat NVE), The Norwegian Railroad Administration (Jernbaneverket NNRA) and the Norwegian Public Roads Administration (Statens vegvesen NPRA). Funding was provided by NIFS, the Norwegian Geotechnical Society (NGF) and by the Research Council of Norway through NGI research programs.

REFERENCES

Anschütz, H., Bazin, S., Kåsin, K., Pfaffhuber, A.A. & Smaavik, T.F. submitted. Airborne sensitive clay mapping - stretching the limits of AEM resolution and accuracy, submitted to *Near Surface Geophysics*.

Bazin, S. & Pfaffhuber, A.A. 2013. Mapping of quick clay by electrical resistivity tomography under structural constraint. *J. Appl. Geophys*. (98): 280–287.

Knödel, K., Lange, G. & Voigt, H.-J. 2007. Environmental geology, *Handbook of field methods and case studies*, Eds. Springer, ISBN 978-3-540-74669-0, Berlin, Tyskland.

Long, M., Donohue, S., L'Heureux, J.S., Solberg, I.-L., Rønning, J.S., Limacher, R., O'Connor, P., Sauvin, G., Rømoen, M. & Lecomte, I. 2012. Relationship between electrical resistivity and basic geotechnical parameters for marine clays. *Can. Geotech. J.,* DOI 10.1139/T2012-080

Montafia, A. 2013. Influence of physical properties of marine clays on electric resistivity and basic geotechnical parameters. *Master thesis*, Department of Civil and Transport Engineering, NTNU, Trondheim.

NGI 2015. Detaljkartlegging Stjørdal-Steinkjer. Datarapport – grunnundersøkelser. *NGI report* 20150042-02-R, pp106.

NIFS 2015. Detection of brittle materials. Summary report with recommendations. Final report. *NIFS Report no. 126/2015* , pp150. (www.naturfare.no)

Pfaffhuber, A.A., Bazin, S., & Helle, T.E. 2014. An integrated approach to quick-clay mapping based on resistivity measurements and geotechnical investigations. Landslides in sensitive clays. *Advances in Natural and Technological Hazards Research* (36): 193-204.

Rømoen, M., Pfaffhuber, A. A., Karlsrud, K. and Helle, T. E. 2010. Resistivity of marine sediments retrieved from R-CPTU soundings: A Norwegian case study. In Proceedings of CPT'10, pp. 9-11.

Sauvin, G., Lecomte, I., Bazin, S., Hansen, L., Vanneste, M., & L'Heureux 2014. On the integrated use of geophysics for quick-clay mapping:The Hvittingfoss case study, Norway. *J. Appl. Geophys*. (106): 1-13.

Solberg, I.L., Hansen, L., Rønning, J.S., Haugen, E., Dalsegg, E., & Tønnesen, J.F. 2012. Combined geophysical and geotechnical approach to ground investigations and hazard zonation of a quick clay area, Mid Norway. *Bull. of Eng. Geology and the Environment* (71): 119-133.

Geotechnical and Geophysical Site Characterisation 5 – Lehane, Acosta-Martínez & Kelly (Eds)

Regional geotechnical railway corridor mapping using airborne electromagnetics

A. A Pfaffhuber, H. Anschütz, T. Ørbech, S. Bazin, A. O. K. Lysdahl, M. Vöge, G. Sauvin, I.-K. Waarum, H. C. Smebye, K. Kåsin & G. Grøneng
NGI, Oslo, Norway

A.-L. Berggren
Norwegian National Rail Administration, Oslo, Norway

J. B. Pedersen & N. Foged
Aarhus University, Department of Geoscience, Aarhus, Denmark

ABSTRACT: The Norwegian National Rail Administration (Jernbaneverket) is planning 230 km of railway construction and upgrades adapting for high speed trains to reduce commuting times to and from Norway's capital Oslo. Parts of the project are in areas with little or no prior geotechnical knowledge. To enable an efficient and economic ground investigation program, we conducted a high-resolution airborne electromagnetic mapping (AEM) campaign covering 600 km2 in summer 2015. The investigation area includes various types of geotechnical and geological challenges and the AEM data contribute to the detailed railway alignment design. Primary delivery is depth to bedrock varying from tens of meters glaciomarine clay to few meters moraine or coarse-grained sediments. Detailed analysis of the final AEM resistivity models leads to quick clay appraisal, alum shale detection and indications for major bedrock weakness zones. A tight integration of accurate geophysical models and sparse geotechnical data is a key element in this project.

1 INTRODUCTION

After decades with minor investments, linear infrastructure development has recently become a significant factor for the Norwegian geotechnical industry. Tens to hundreds of km with upgraded and new roads and railroads are currently being planned, designed and constructed. The typically demanding topography and geology requires extensive pre-investigations, which so far were carried out from the ground.

High-resolution time-domain AEM has been used previously in Norway for bedrock mapping with great success for both road and railway design projects. Christensen et al. (2015) present a geotechnical case study using AEM to assess bedrock depth for a planned highway section northeast of Oslo. It has been shown that in favorable cases AEM may even distinguish saline, marine clay from leached and potentially sensitive clay (Anschütz et al. 2016a). These results and experiences provided the basis for the large-scale survey discussed here:

A high resolution airborne electromagnetic (AEM) survey was carried out during 6 weeks in summer 2015, covering about 600 km2 extending over 9 separate geotechnical project areas. The AEM data were used to create a geomodel for the detailed railway alignment and design: the primary purpose was to obtain information of depth to bedrock in areas with little or no prior geotechnical knowledge. Bedrock topography is indeed the main target for geotechnical surveys in terms of stability and mass balance as well as for tunnel planning in terms of bedrock topography at portals and expected rock cover along the tunnel.

To illustrate the various aspects of the project we show three data examples that demonstrate the deliveries in terms of (a) bedrock topography in general in an area with good to moderate contrast, (b) indications for leached marine clay (quick clay) in a small area that is known to contain quick clay units and finally (c) a tunnel example where the data show lacking rock cover and a thrust zone crossing the tunnel alignment.

2 METHOD

The survey was flown with a SkyTEM304 system (Sørensen and Auken, 2004) with one turn in the low moment and a peak moment of 3000 Am^2 and four turns in the high moment with a peak moment of 150 000 Am^2. The resulting time gates range from < 10 μs to 2 ms. This bandwidth provides an excellent trade-off between high near surface depth resolution and moderate penetration depth. Nominal line spacing was 100 m throughout the entire area of investigation. Around 6000 line-km of AEM data were acquired within six weeks. Processing and inversion was done with the Aarhus Workbench spatially constrained inversion (SCI, Viezzoli et al. 2008) with moderately loose vertical and horizontal constraints

and automatic starting models to account for the heterogeneous geology ranging from outcropping resistive bedrock to tens of meters with conductive, marine clay. Bedrock topography interpretation involved a combination of resistivity thresholds, vertical resistivity gradient, manual picking and sparse geotechnical boreholes (Anschütz et al. 2016b).

3 GEOLOGICAL BACKGROUND

The demanding topography and geology in Norway requires costly and long lasting pre-investigation phases for major geotechnical projects. The extent and thickness of marine clay and other glacial sediments as well as the occurrence of toxic black shale or bedrock weakness zones are factors that determine feasibility and construction costs and are all suitable targets for an AEM survey. Figure 1 gives typical examples of encountered quaternary sediments. Bedrock mostly comprises medium to highly metamorphic sedimentary and igneous rocks with a high abundance of gneiss, schist and phyllite. With the exception of highly conductive cambro-silurian black shales found around Oslo, the bedrock is highly resistive and makes a suitable AEM contrast to the conductive sediments. Tracking bedrock topography from AEM is feasible for large parts of the investigated lowlands. A minor part of the more than 6.000 km AEM data acquired in 2015 was not transferable to a bedrock model due to lacking resistivity contrast between bedrock and electrically resistive moraines or shallow surface weathering. In the highlands, above the marine limit and thus free of conductive marine sediments, bedrock topography tracking is limited to wetlands (bogs) that pose a good enough resistivity contrast for AEM.

4 RESULTS

The main task is to convert the 3D AEM resistivity models into bedrock topography. We have previously computed detailed bedrock models based on spatial correlation of the AEM data combined with sparse boreholes (Christensen et. al. 2015). For most of the data discussed here, we combine automatic and manual interpretation (Anschütz et. al. 2016b) largely based on the resistivity models and geological maps validated by boreholes at only a few locations (Figure 2).

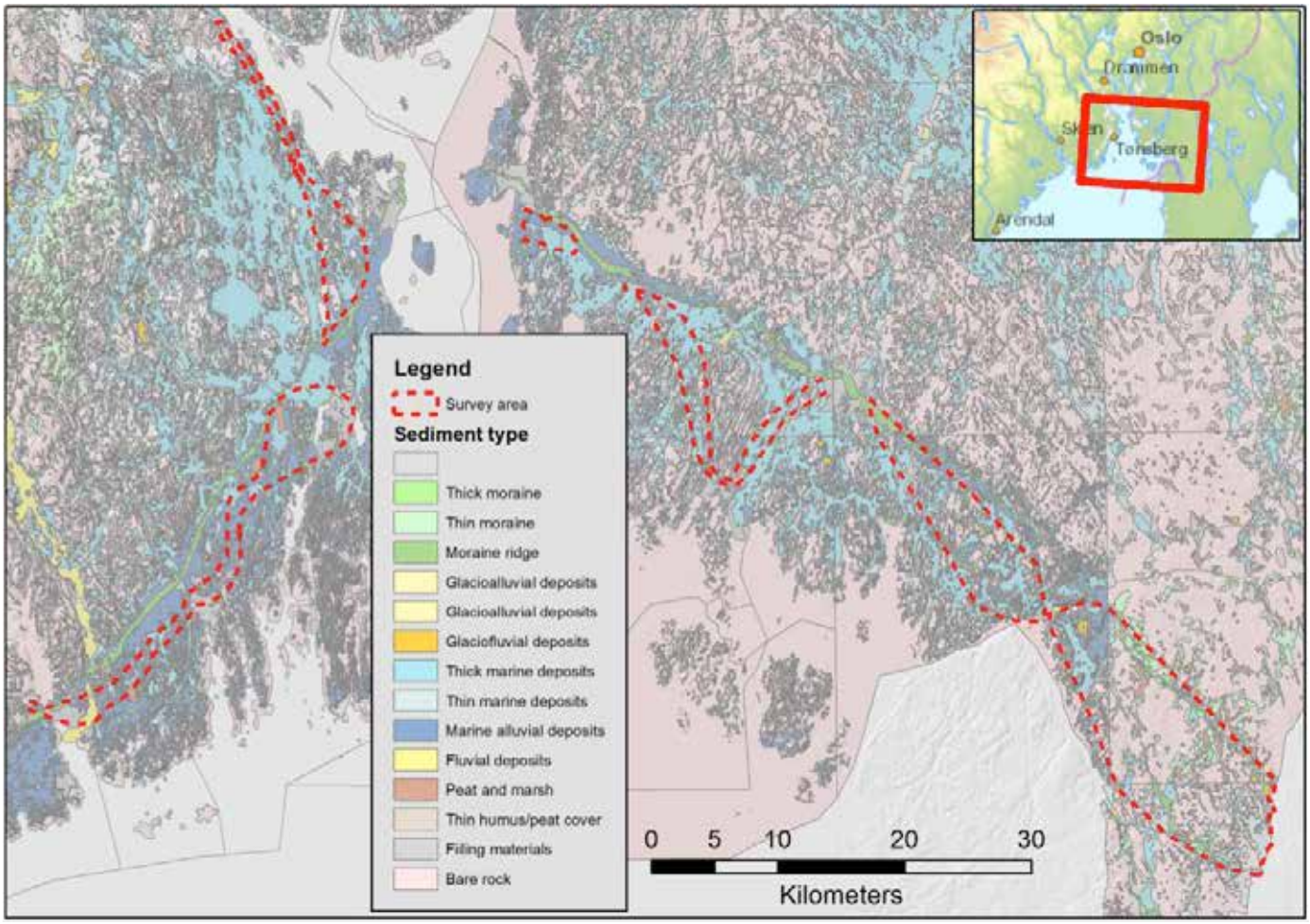

Figure 1. Quaternary geological map of the southern survey area covering five of the nine project areas. Approximate survey extent drawn for illustration, a grid of flight lines with 100 m spacing covers close to 600 km2 in total.

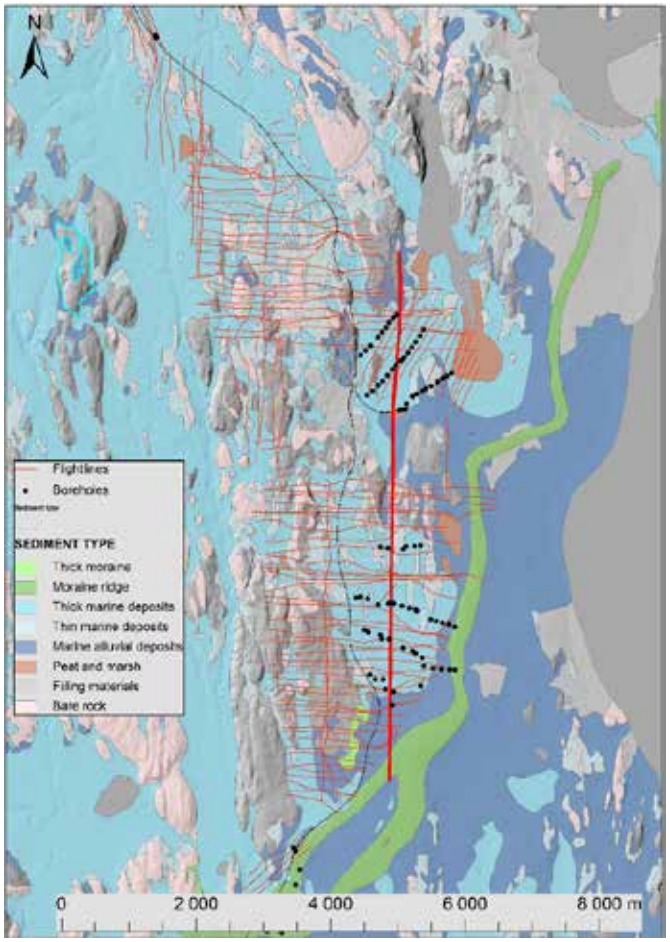

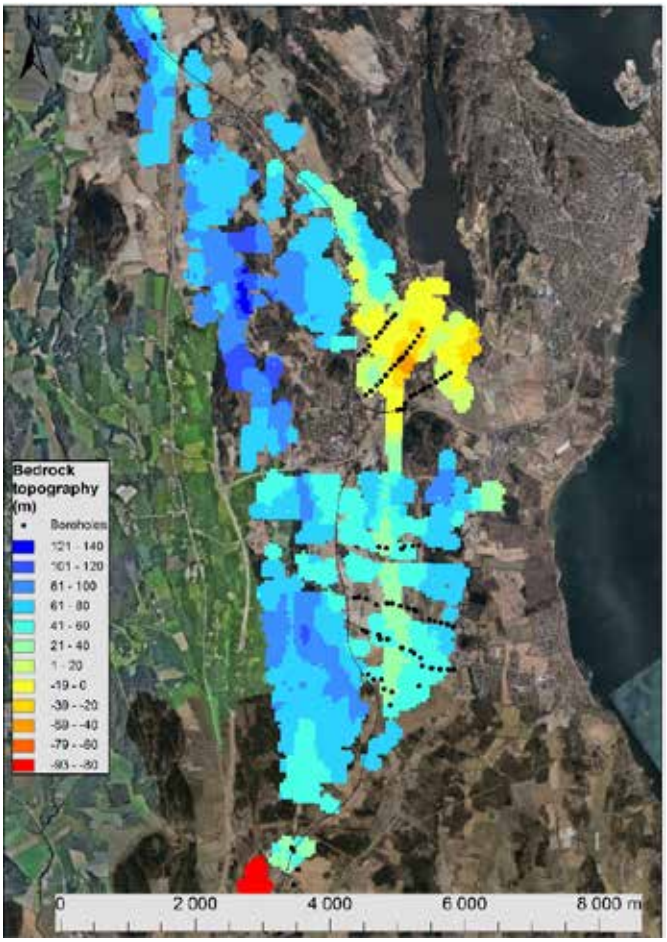

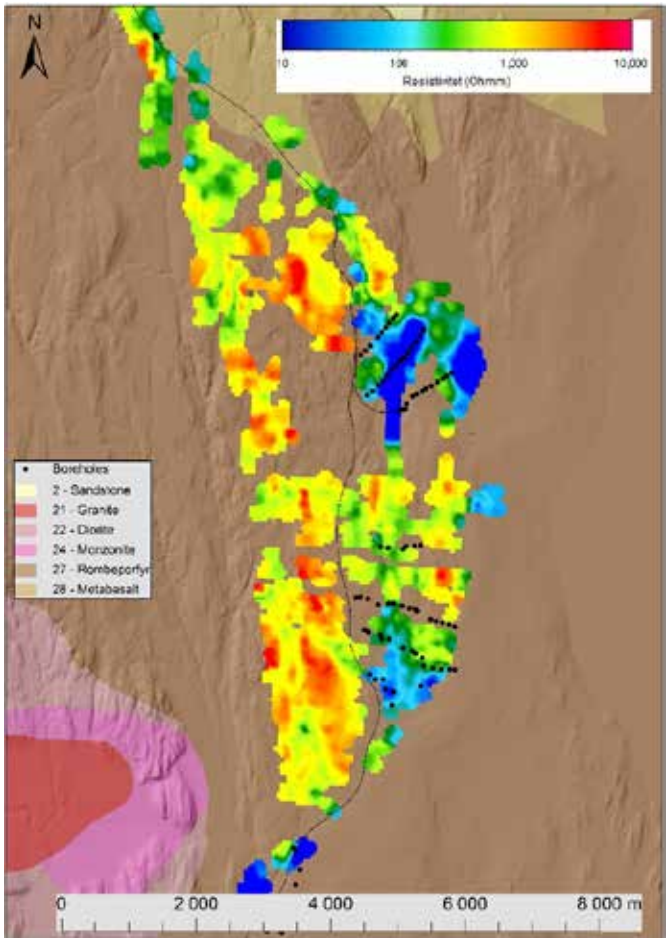

Figure 2a: Left: Quaternary geology map along with flight lines (red) and existing railway (thin black). Bottom: Bedrock types and resistivity depth slice with average resistivity from 15 to 30 m below ground with geological map outlining various volcanic units over shaded DEM. Right: Bedrock topography model derived from AEM data over an aerial image

To quantify uncertainty we pick a maximum and minimum bedrock elevation, subjectively chosen based on resistivity contrast, depth, distance to boreholes, consistency with a priori data, etc. Sediment thickness varied from meters to tens of meters and the bandwidth and signal to noise ration of the AEM data was sufficient to resolve sediment depths within the geotechnical relevant range. In some cases, we were able to interpret bedrock beneath up to 100 m of marine clay with resistivity lower than 10 Ωm, albeit with a higher uncertainty.

Further to bedrock delineation, characterizing the sediment type is of additional value. Norway is prone to so-called quick clay, highly sensitive formerly marine clay that liquefies at failure and poses a serious geohazard. Electrical resistivity is a valuable factor when it comes to distinguishing unleached (stable) and leached (sensitive) clay (Rømoen et al. 2010). The resistivity contrasts are subtle and consequently only accurate and high resolution resistivity models can provide the desired information.

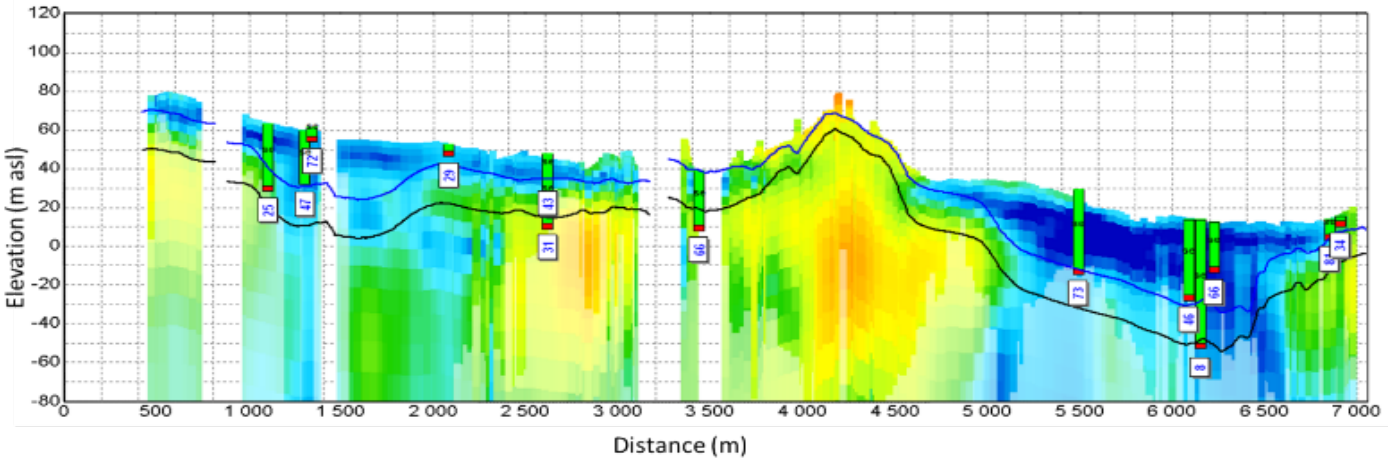

Figure 2b: Resistivity model (same resistivity colour scale as on map) from S-N along one of the very few profiles with boreholes close to the AEM data (thick red line in left map). Off-line distance of boreholes denoted in meters below the bars, the bars extend until assumed bedrock. The blue and black lines illustrate the lowest and highest assumed bedrock.

Previous field trials (Anschütz et. al. 2016a) have shown that this criteri-on is met for our data and we thus use the acquired resistivity models as indications of clay salinity and consequently probability for quick clay, provided the sediment layer is thick enough. The profile in Figure 3 clearly shows a valley filled with some tens of meters marine clay with some tens of Ωm resistivity, typical for leached marine clay. Geotechnical drillings confirmed the assumption and found sensitive quick clay. We are currently extending our interpretation to quick clay probability maps, based on a spatial search for sediments with resistivity typical for quick clay.

The results discussed so far focus on geotechnical issues such as depth to bedrock and sediment properties (indications for leached clay). For near surface AEM systems the depth of investigations typically extends to some hundred meters depending on the geology. We utilize this deeper part of the data in areas that will be crossed with tunnels. Geophysical targets are major weakness zones and/or existence of black shale due to their impact on tunnel

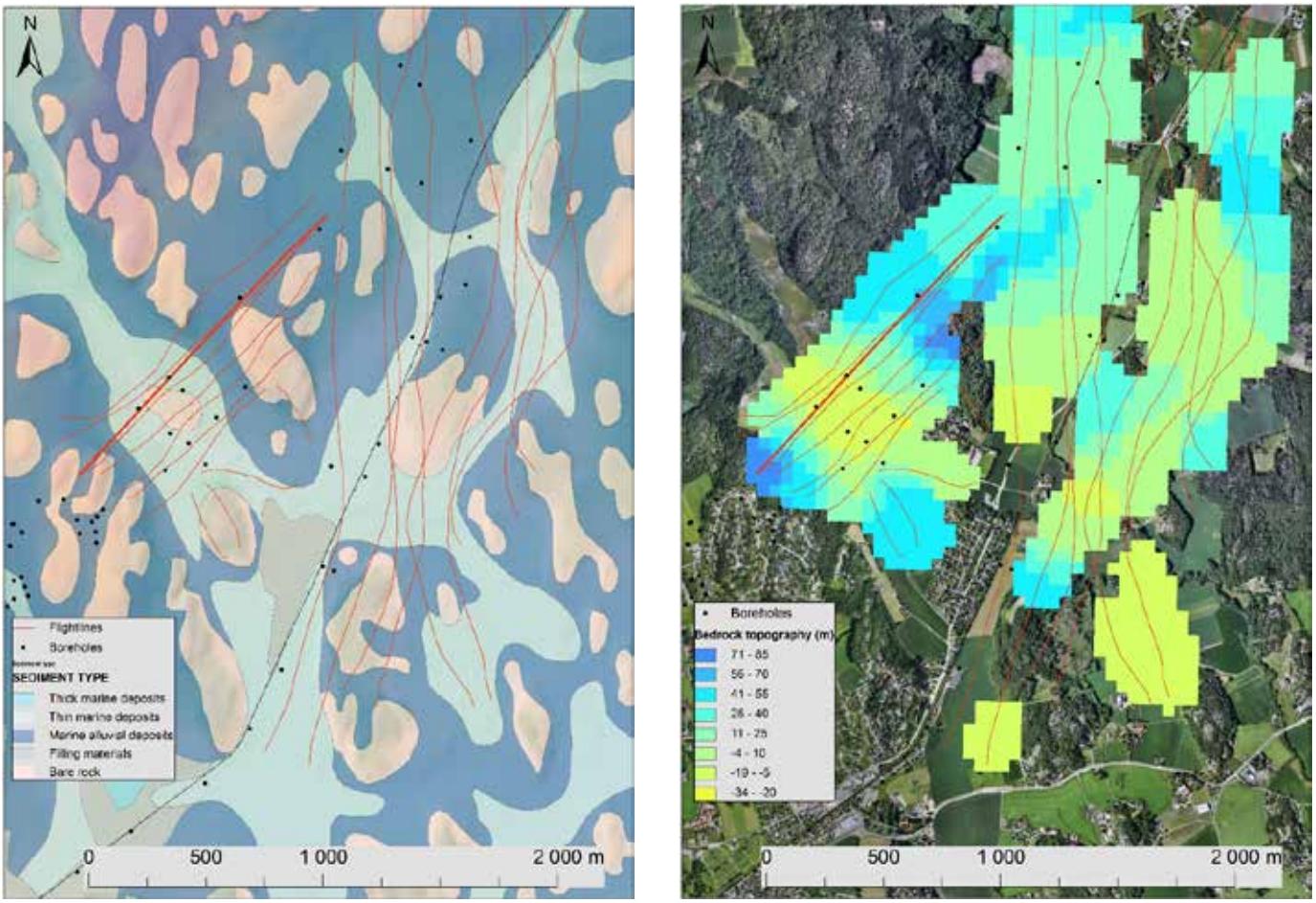

Figure 3a: Left: Quaternary geology map along with flight lines (red) and existing railway (black). Right: Bedrock topography model derived from AEM data over an aerial image.

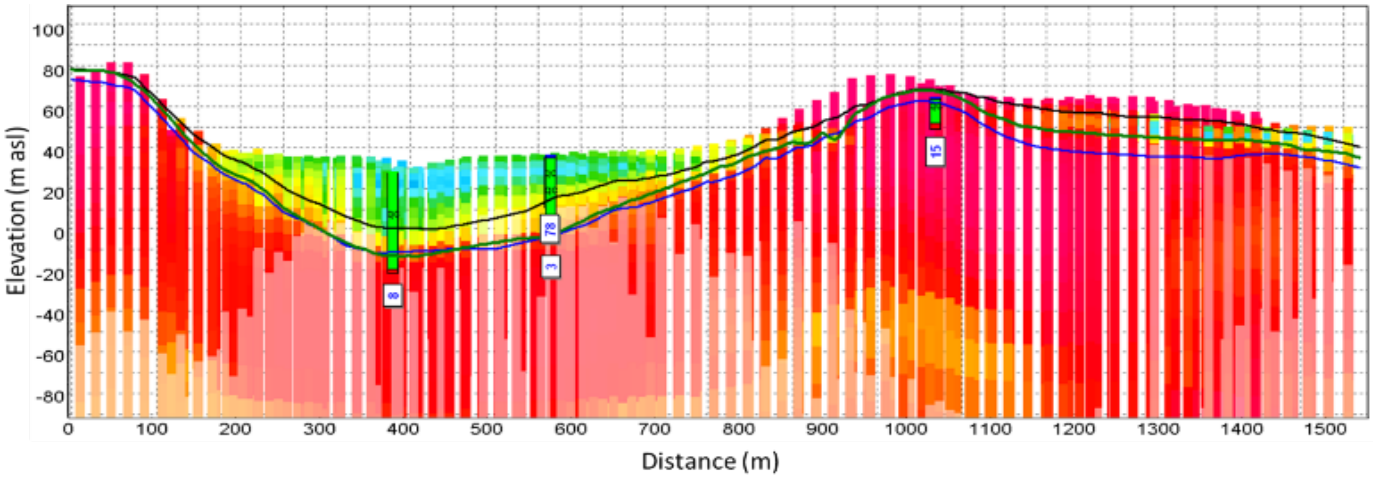

Figure 3b: Resistivity model (same resistivity colour scale as on map) from SW-NE along the profile drawn on the left map. The green line shows an adjusted bedrock model, based on the boreholes. The resistivity models result from a constrained inversion based on the green bedrock interface. Note the subtle variation in clay resistivity from below to above 10 Ωm indicating leached marine clay and thus a chance for sensitive quick clay.

construction costs. In areas prone to the occurrence of uranium rich black shales the models outline highly con-ductive structures (resistivity around and below 1 Ωm) that can consequently be avoided if possible (not shown). The final data example (Figure 4) shows a potential tunnel alignment that was finally considered as not feasible due to lack of rock cover in the western part. The model also shows a strong electrical conductor crossing the alignment, a thrust zone where phyllite has been reworked to clay. It is worth mentioning that this zone most probably isn't as thick as it appears in the resistivity section due to decreasing resolution with depth; The zone may rather be meters, than tens of meters thick. Note that not all areas with low near surface resistivity are due to sedimentary cover. In the eastern part of the survey, low resistivity indicates outcropping thrust zones rather than marine sediments.

The high efficiency, beneficial economics, survey robustness and data accuracy of modern AEM makes it a strong candidate for early phase investigations both in terms of geotechnical design (e.g. bedrock topography and stability) and engineering geology (e.g. major weakness zones). Based on our experience, the AEM vertical resistivity resolution is very close to ground measurements (ERT) with the exception of the very first meters.

Processing, inversion and interpretation is the crucial element of AEM investigations as for any other geophysical data. Without a geophysical contrast, no parameter such as bedrock topography can be derived though (resistive cover over resistive bedrock). A remaining challenge is to quantify depth uncertainty: transferring data standard deviation and inversion sensitivity to a bedrock model uncertainty in meters is neither state of practice nor firmly established in academia.

5 CONCLUSIONS

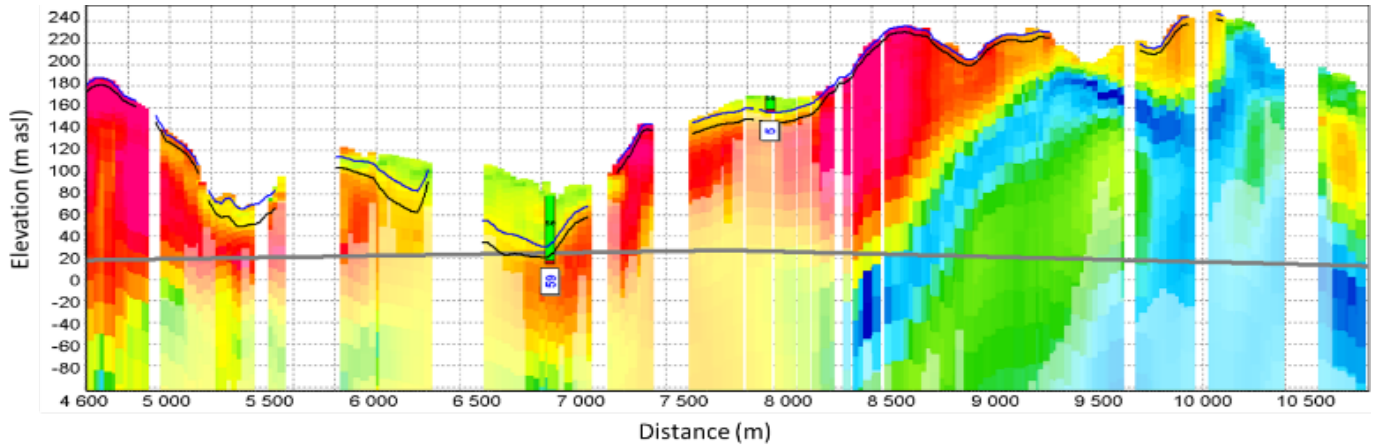

Figure 4a: Resistivity model (same resistivity color scale as on map) from SW-NE along the profile drawn on the map. The grey line sketches a potential tunnel alignment that would encounter a lack of rock cover at profile coordinate 6 500 – 7 000 m and crosses a low resistivity zone at 8 500 m as well as further east.

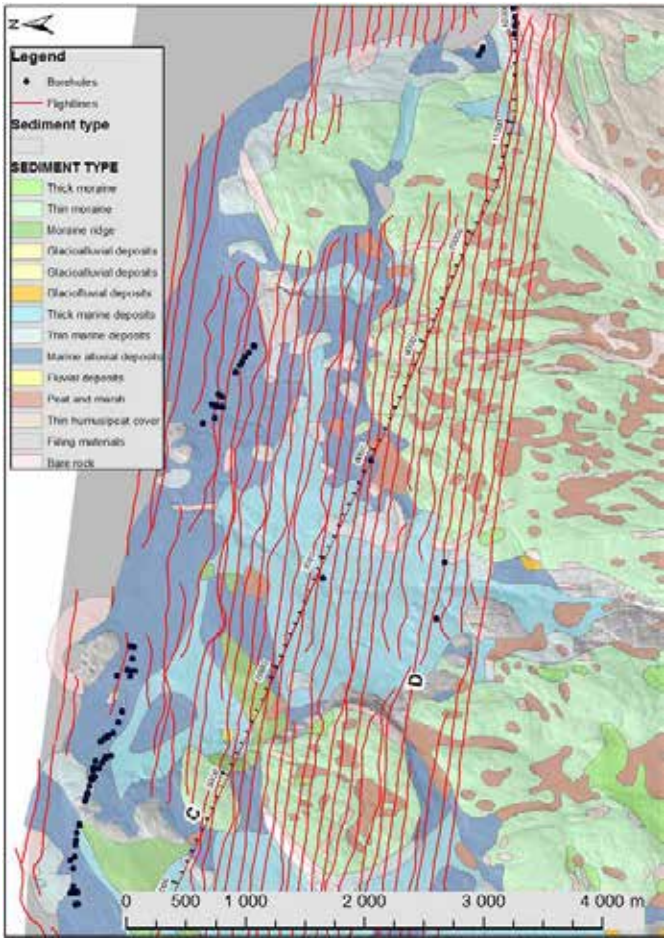

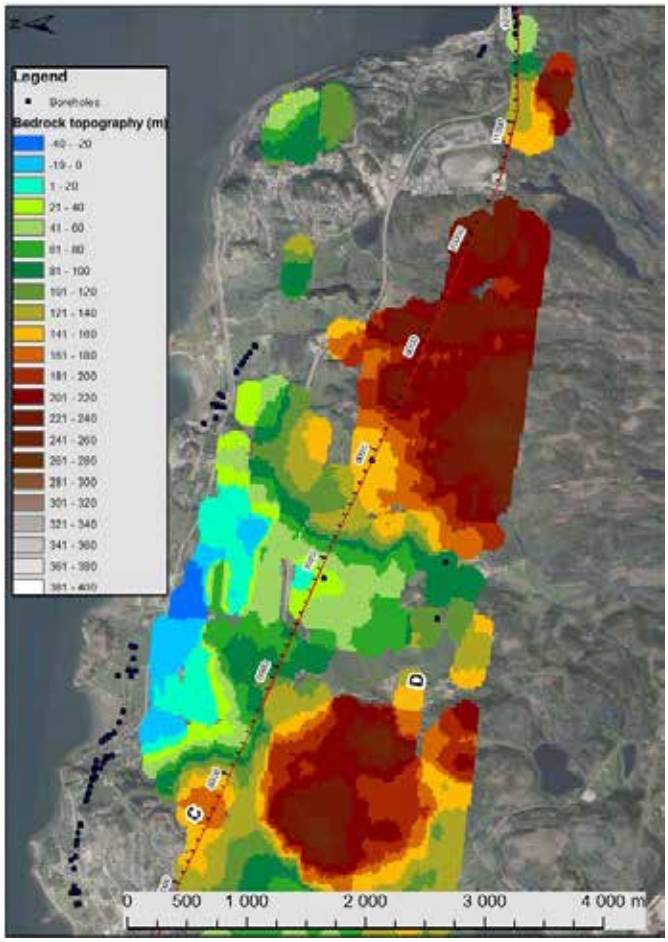

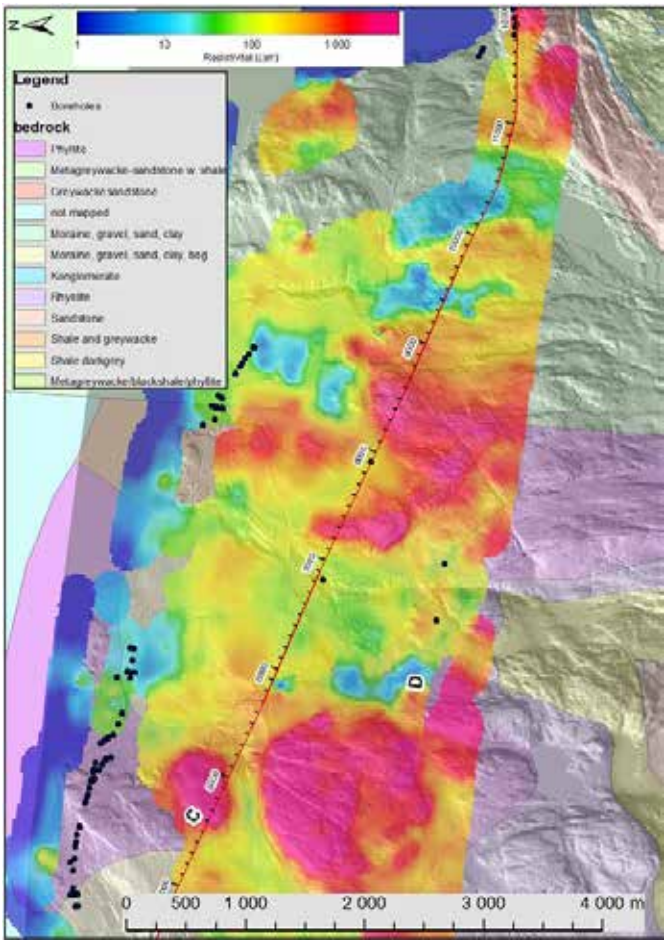

Figure 4b: Survey maps as in Figure 2 with one exception: Resistivity depth slice from 10 to 20 m below ground.

6 ACKNOWLEDGMENTS

The Norwegian National Rail Administration, the owner of all shown results, gave permission to publish these data,

7 REFERENCES

Anschütz, H., Bazin, S., Kåsin, K., Pfaffhuber, A. A. & Smaavik, T. F. 2016a. Airborne sensitive clay mapping - stretching the limits of AEM resolution and accuracy. *Near Surface Geophysics*, submitted.

Anschütz, H., Vöge, M., Bazin, S., Sauvin, G., Lysdahl, A. O., Pfaffhuber, A. A. & Berggren, A. L. 2016b. From manual to automatic AEM bedrock mapping. Journal of Environmental and Engineering Geophysics, submitted.

Christensen, C. W., Pfaffhuber, A. A., Anschütz, H. & Smaavik, T. F. 2015. Combining airborne electromagnetic and geotechnical data for automated depth to bedrock tracking. *Journal of Applied Geophysics* 119 179-191, doi:10.1016/j.jappgeo.2015.05.008.

Rømoen, M., Pfaffhuber, A. A., Karlsrud, K. & Helle, T. E. 2010. Resistivity on marine sediments retrieved from RCP-TU-soundings: a Norwegian case study. *International symposium on cone penetration testing, 2, CPT'10, Huntington Beach, CA.* Proceedings 2, 289-296

Viezzoli, A., Christiansen, A. V Auken, E. & Sørensen, K. 2008. Quasi-3D – modeling of airborne TEM data by Spatially Constrained Inversion. *Geophysics* 73 F105-F113.

Geotechnical and Geophysical Site Characterisation 5 – Lehane, Acosta-Martínez & Kelly (Eds)

Fractures location on karstified limestone surfaces by Electrical Resistivity Tomography Characterization

Porres-Benito, J.A., Ibanez, S.J., Ortiz-Palacio, S., López-Ausín, V.
INGITER S.L.-University of Burgos, Burgos, Spain

ABSTRACT: The location of main surface fault zones, identified by means of the geophysical technique is nowadays being resolved successfully. The aim of this research is to develop a suitable methodology for the interpretation of Electrical Resistivity Tomography (ERT) 2D images, specifically applied to the preliminary detection of surface faults and structural characterization of active and non-active fault on limestone sites. This work compiles tests and research performed on well-known objectives and analyses the effects of the main factors that condition resistivity images, in order to help in the resistivity profile interpretation. In relation to the study, we highlight the good correlation between the laboratory test and the field works.

1 INTRODUCTION

There has been a significant increase in Geoelectrical prospecting applied in geophysical investigation to hydrological studies, mining and geotechnical research (Dahlin 2001; Griffiths and Barker 1993; Daily and Ramirez 2000, Maillol et al. 1999), as well as in environmental studies and archaeology (Griffiths and Barker 1994; Piro et al. 2000 and 2001; Chambers et al, 2002; Astin et al. 2007; Drahor et al. 2008; Cardarelli and Di Filippo 2009; Papadopoulos et al. 2006 and 2010; Tsokas et al. 2009), proving its utility as non-destructive technique for subsurface exploration. The application of Electrical Resistivity Tomography (ERT) for imaging of discontinuities and lithological contacts is well documented (Beresnev et al. 2002).

At the same time, other studies have contributed successfully in faults location (Giano et al. 2000; Storz et al. 2000; Demanet et al. 2001; Caputo et al. 2007; Rizzo et al., 2004; Fazzito et al. 2009; Terrizzano et al., 2012).

Electrical Resistivity Tomography (ERT) constitutes an important advance in the geoelectric methods because it solves automatically the data acquisition, instead the manual change of electrodes characteristic of the classic geoelectrical methods. In this way, ERT facilitates the management and fast processing of a large number of data, constituting a useful non-destructive method to detect subsurface structures.

Electrical tomography is a geoelectrical surveying method that analyzes subsoil materials according to their electrical impedance, which, in other words, allows them to be differentiated according to their resistivity (Aracil et al., 2002 and 2003; Zhou 2000). Factors that condition the presence of a greater or lesser concentration of ions depend on the nature and composition of the rocks, and their texture that may be more or less altered, or compact, or porous, in relation to their fluid content and their nature. Fault movements develop a high secondary porosity, why the water content is increased and a drop in resistivity values occurs.

Greater mobility of these ions has as a consequence, greater conductivity, or conversely less resistivity, which is the parameter used in electrical resistivity tomography (Orellana, E. 1982).

The resistivity or conductivity of the water, as the greater the conductivity of the water, the lower the resistivity of the rock formation in which it is found (Sumanovac and Weisser 2001).

According to Equation (1), Heiland's amplified equation (Heiland 1946), the resistivity in the rock will depend fundamentally on four factors:

$$[\rho] = [F/v][\rho w][1/Fs] \qquad (1)$$

Where [ρ] is the resistivity of the rock, [F] is the formation factor, [v] is the porosity factor, [ρw] is the resistivity of the water contained in the rock or soil, and [Fs] is the saturation factor.

The porosity factor is defined as the proportion in volume of cavities in the rock. It takes values between 0.08-0.15 for sand, sandstone, porous limestone and compact clays. This definition of [v] coincides with that of porosity [n], for which reason

reference will henceforth be made to [n]. The formation factor depends on the form and distribution of the pores. The rocks that are most affected by factor [F] are sandstones, quartzites, limestones and shales. The data for this study were collected by measuring 2D Dipole-Dipole and Wenner-Schlumberger profiles, carried out with a SYSCAL R1+ Switch 72 geo-resistivitimeter, made by Iris Instruments Company. The apparent resistivity values from field measurement are processed by means of the RES2DINV software (Loke 1999)

The results of this type of geophysical surveying are the electrical tomography profiles (Figure 1) that are simply vertical sections of the ground that are colour coded with the different resistivity measurements. The colour coding is shown in a legend at the bottom of each profile.

Consequently, once the geo-electrical prospecting research using ERT is underway different resistivity values will be determined and attributed to materials that will permit identification of lithological units of differing natures, lithologies with different textures or degrees of deterioration, structural (fractures) and geomorphologic aspects (caves and infills), etc.

The data acquisition requires the positioning of an array of, each separated at a particular distance according to the required degree of resolution (Porres 2003). Each one of these resistivity data measure, is attributed to a particular geometric point in the subsurface. The electrical images are, in fact, cross-sections of land that reflect the distribution of resistivity values at different depths corresponding to the different layers of investigation (Loke 1996-2011).

The investigation depth, therefore, will depend on the spacing between electrodes and the selected layout may easily run deeper than 100m in depth, even though shallower test boreholes into the subsurface have the definite advantages of greater resolution, as there is generally less separation between electrodes. As a rule, the resolution of the investigation decreases logarithmically in relation to the depth (Dahlin and Loke 1998).

2 LABORATORY TESTS: ELECTRICAL RESPONSE OF KNOWN MODELS

In order to meet the electrical response of different geological conditions, laboratory tests were carried out on small-scale models. Figure 1 shows the data acquisition process for an air-filled big hole in a layer of sand, trying to simulate a geology similar to a limestone place, showing an air-filled karst cavity as well as a large area fractured unfilled in a full scale test.

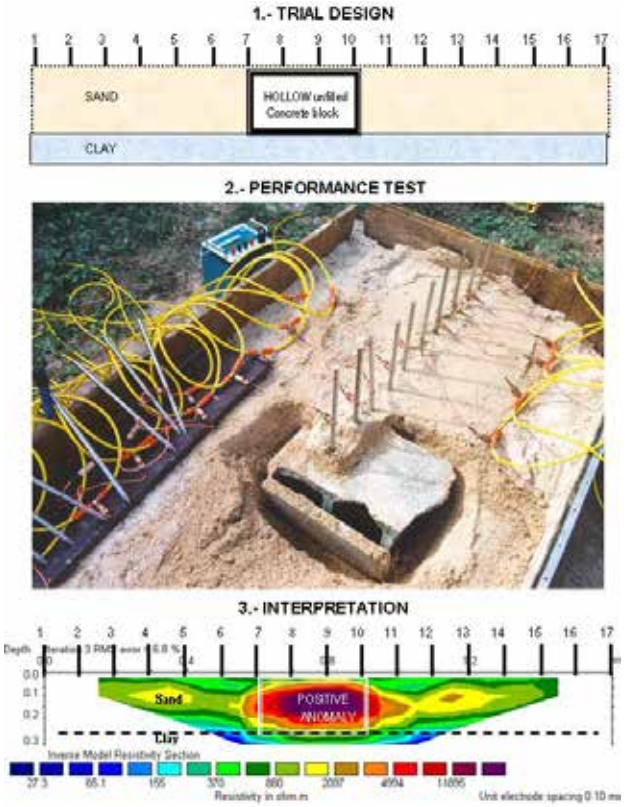

Figure 1. Electrical Resistivity Tomography laboratory test, and its corresponding 2D profile image interpretation. (Porres, J.A., 2003).

Multitude of test were conducted on a small scale, observing the influence of 5 variables in the 2D images obtained: 1- Electrode array (Schlumberger-Wenner and Dipole-Dipole), 2- Separation distance between electrodes, 3- Depth of investigation, 4- Size and shape of the discontinuities investigated, 5- Kind of filling inside the faults.

The results showed the best choice of electrode array to locate vertical fractures and high-angle faults is Dipole-Dipole array, consistent with most other works (Loke, 1996-2011; Fleta et al., 2000; Caputo et al., 2007; Rizzo et al., 2004). However, the Schlumberger-Wenner array allows higher investigation depth, and often gets good resolution images

3 FIELD WORK: LOCATION OF DISCONTINUITIES AND FAULTS ON LIMESTONE SURFACES

Electrical Resistivity Tomography profiles were taken to identify the characteristics of the subsoil, with the specific objective of identifying fractures or faults affecting the limestone massif in different places of Burgos, Spain. The geomorphology of karst in this bedrock, is clearly related with the tectonic structure (Zhou, W. et al., 2000).

The application of appropriate geophysical surveying methods to each objective provides knowledge of the subsoil materials and their layout

to a greater or lesser degree of precision. Concretely, this geophysical survey method well used will allow the materials at different depths to be studied at different degrees of resolution (Martínez-Pagán et al. 2005).

The field work sections were carried out with the resistivity device SYSCAL R1 PLUS Switch72, and were processed using the software RES2DINV ver.3.42 (Locke 1999). In every section, we applied Schlumberger-Wenner and Dipole-Dipole electrode arrays. Most of the profiles present similar results using the Dipole-Dipole and Schlumberger-Wenner arrays, although in a few profiles they differ substantially, especially in those where the prospection depth is increased. In these cases, the Dipole-Dipole array showed the highest root-mean-squared errors. Also the Schlumberger-Wenner profiles provide more realistic images according to the endokarstic and geological structures observed in the "Cueva Peluda" control profile (Figure 2), what initially seems contradictory with the laboratory previous test.

In addition, the sections were drawn without vertical exaggeration, in order to facilitate georeferencing and projection of the karstic passage topography. The topography of the geophysical sections was elaborated from topographic surveys.

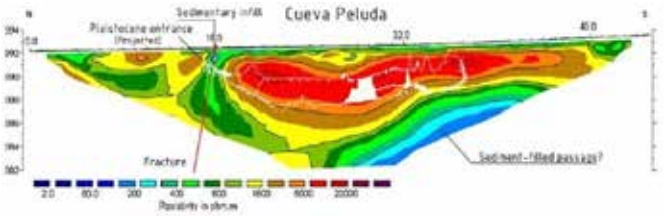

Figure 2. ERT profile recorded over "Cueva Peluda" karstic passage in Atapuerca, Spain. The whiteline shows the internal wall of the cave (Ortega, A.I. et al 2010).

The Pleistocene paleoanthropological sites of Atapuerca (Burgos, Spain), was one of the places studied on this work. The geophysical interpretation of these sections was supported by archaeological and geological field observations, 1:50.000 and 1:10.000 geological and geomorphological surface maps (Pineda, 1997; Benito, A. 2004; Benito-Calvo, A. 2008), and using the geomorphology of the known endokarst system, elaborated by detailed surveying (Ortega, 2009).

Section represented on Figure 2 was carried out along the well-known shallow main passage of the Peluda Cave and was used as a first control for the resistivity response of the fractures, cavities, sediments and limestone materials. In this section, the Dipole-Dipole and Schlumberger-Wenner arrays show similar results. Figure 2 presents a closed structure denoted by the highest resistivity values (> 1500 ohm.m, corresponding to the empty cavity of Cueva Peluda, barely a few meters (1-2 m) under the current floor. This structure is surrounded by rock, Upper Cretaceous carbonates, defined by a wide range of resistivities (> 400 ohm.m), according to its fracturation degree, local facies and stratification. In the profile, a third zone with the lowest resistivity values (< 400 ohm.m) can be distinguished. The latter correspond to non-consolidated and higher porosity material, which correspond to a sediment-filled old entrance and passage, such as was observed in several sections carried out in the site.

A similar place is the Roman City called "Colonia Clunia Sulpicia" also located in Burgos, Spain. The geology of Clunia and surrounding areas is limestone outcrops that crown the upper Miocene tertiary series. This Micritic limestone is sometimes brecciated, whose thickness ranges from 5 to 15 meters. Under the limestone in the series is a section of marls inter-bedded with lenticular sand bodies that gradually give way to carbonate crusts where Miocene limestone occur as described above. In this sense, it seems that the Roman city is located in a very favorable place for the development of karst aquifers on carbonate formations.

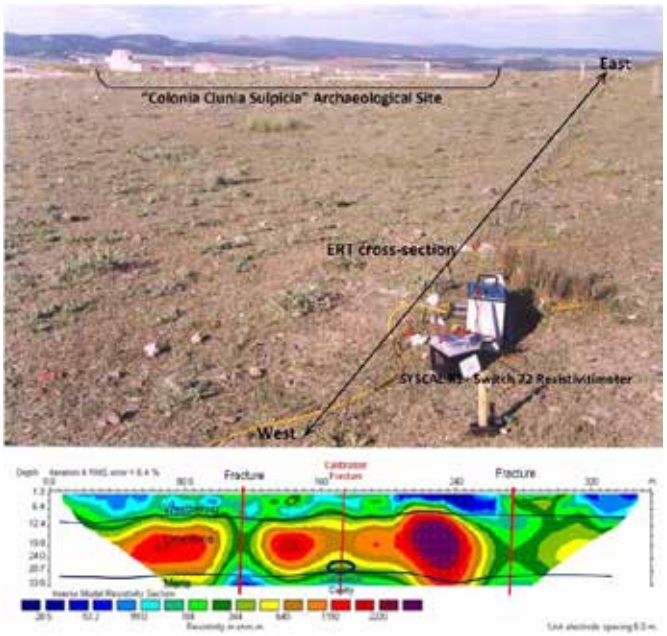

Figure 3. ERT profile recorded over a karstic passage in "Colonia Clunia Sulpicia" archaeological site, Spain. The central line shows a calibration fracture and cavity which shape and depth was well known, and the two other red lines are negative anomalies who shows Fractures or Faults. (Porres 2003).

The morphology and layout of the cavities must have been highly conditioned by the presence of fractures which would have logically been the conduits through which the water passed, which caused the formation of these caves. An effort has been made to analyze these fractures using the same type of geophysical surveying but with the profiles located on the external surface of the limestone massif. These profiles, taken with different equipment to reach greater depths, identified certain anomalies which, on account of their morphology and their resistivity values, must be fractures in which the circu-

lation of water and the deposits of clays would give them their characteristically low resistivity values in this type of geophysical profile (Negative anomaly at figure 3).

The calibration of Profile showed in Figure 3 was possible because we know the existence of a cave and fracture under the ERT profile. The dimensions of the calibration cavity is 10 m wide and 3 m high, and is located at a depth of 25 m, following the structural discontinuities of the limestone, where the weathering is easier. The profile has 5 m as electrode spacing, so it shows 355 m lengh and 33,8 m depth. There are two clear low resistivity anomalies (<350ohm.m) in figure 3, that seems clear fracture evidence, since the normal resistivity values in the limestone itself is located, which could be around 650 ohm.m.

4 CONCLUSIONS

Electrical tomographic images show low resistivity values associated with fractures in limestone rocks, as well as significant resistivity contrast across faults in the subsurface. It has been shown an experience which permitted, through the interpretation of electrical resistivity profiles, the characterization of the geometry of fault zones, detecting the depth, size, shape and filler of surface fractures, specifically applied to karstified limestone bedrock.

To image the geometry of fault planes and tectonic structures, is essential to select the most suitable electrical arrangement and configuration, that must be used on each case to locate faults and tectonic structures. Electrical Resistivity Tomography (ERT) has been a useful non-destructive geophysical method for imaging the subsurface structures of the Sierra de Atapuerca and Clunia sites, as well as its endokarst system. The use of detailed geomorphological and geological maps of the tectonic system and the surface landscape was essential to reduce the uncertainty of the geophysical interpretation. High resolution ERT prospecting made it possible to detect and analyze structures related to the site formation and distribution, such us bedrock morphologies, fractures continuity, cavities geometries and thickness of sedimentary infills.

Deeper prospecting, related to longer length and lower resolution sections, was suitable to analyze deeper geological structures which controlled the development of the tectonic structure.

5 ACKNOWLEDGEMENTS

The writers would like to express their gratitude to A.I. Ortega, A. Benito-Calvo and A. Pérez-González, Research National Centre of Human Evolution (CENIEH) & Atapuerca Research Team.

6 REFERENCES

Aracil, E.; Maruri, U.; Porres, J.A.; Espinosa, A.B., 2002. La tomografía eléctrica: una herramienta al servicio de la obra pública. Rock Máquina, 76 (30-34).

Aracil, E.; Maruri, U.; Vallés, J.; Martínez Pagán, P.; Porres, J.A., 2003. Evaluación de problemas medioambientales mediante tomografía eléctrica. Ingeopress, 122 (34-39).

Astin, T., Eckardt, H. and Hay, S., 2007. Resistivity Imaging Survey of the Roman Barrows at Bartlow, Cambridgeshire, UK. Archeological Prospection 14: 24-37.

Benito, A., 2004. Análisis geomorfológico y reconstrucción de paleopaisajes neógenos y cuaternarios en la Sierra de Atapuerca y el valle medio del río Arlanzón. PhD Tesis, Universidad Complutense, Madrid, Spain, 381 pp, ISBN 84-669-2585-6.

Benito-Calvo, A., Pérez-González, A. and Parés, J. P., 2008. Quantitative reconstruction of late Cenozoic land-scapes: a case study in the Sierra de Atapuerca (Burgos, Spain). Earth Surface Processes and Landforms 33: 196-208.

Beresnev, I. A.; Hruby, C. and Davis, C., 2002. Exploration Geophysics. Journal of Applied Geophysics 49: 245-254.

Caputo, R., Salviulo, L., Piscitelli, S., Loperte, A., 2007. Late Quaternary activity along the Scorciabuoi fault (southern Italy) as inferred from electrical resistivity tomographies. Annals of Geophysics 50 (2), 213e223.

Cardarelli, E. and Di Filippo, G., 2009. Integrated geo-physical methods for the characterisation of an archaeological site (Massenzio Basilica – Roman forum, Rome, Italy). Journal of Applied Geophysics 68: 508-521.

Chambers, J. E., Ogilvy, R. D., Kuras, O., Cripps, J.C. and Meldrum, P. L., 2002. 3D electrical imaging of know targets a controlled environmental test site. Environmental Geology 41: 690-704.

Dahlin, T., 2001. The development of DC resistivity imaging techniques. Computer and Geosciences 27: 1019-1029.

Dahlin, T., Loke, M.H., 1998. Resolution of 2D Wenner resistivity imaging as assessed by numerical modelling. Journal of Applied Geophysics, 38. pp. 249

Daily, W. and Ramirez, A. L., 2000. Electrical imaging of engineered hydraulic barriers. Geophysics 65: 83-94.

Demanet, D., Pirard, E., Renardy, F., Jongmans, D., 2001. Application and processing of geophysical images for mapping faults. Computers and Geosciencies 27, 1031e1037.

Drahor, M. G., Berge, M. A., Kurtulmus, T. Ö., Hartmann, M. and Speidel, M. A., 2008. Magnetic and Electrical Resistivity Tomography Investigations in a Roman Legionary Camp Site (Legio IV Scythica) in Zeugma, Southeastern Anatolia, Turkey. Archaeological Prospection 15: 159-186.

Fazzito, S.Y., Rapalini, A.E., Cortés, J.M., Terrizzano, C.M., 2009. Characterization of Quaternary faults by electric resistivity tomography in the Andean Precordillera of western Argentina. Journal of South American Earth Sciences 28, 217-228.

Fleta, J., Santanach, P., Martinez, P., Goula, X., Grellet, B., Masana, E., 2000. Geologic, geomorphologic and geophysic approaches for the paleoseismological analysis of the Amer fault (NE Spain). In: Workshop Proceedings of HAN2000: Evaluation of the Potential for Large Earthquakes in Regions of Present Day Low Seismic Activity in Europe, Han-sur-Lesse, Belgium, pp. 63-66.

Giano, S.I., Lapenna, V., Piscitelli, S., Schiattarella, M., 2000. Electrical imaging and self-potential surveys to study the geological setting of the Quaternary slope deposits in the Agri High Valley (southern Italy). Annali di Geofisica 43 (2), 409e419.

Griffiths D.H.; Barker R.D., 1993. Two-dimensional resistivity imaging and modelling in areas of complex geology. Journal of Applied Geophysics, 29,211-226.

Griffiths, D.H. and Barker, R.D., 1994. Electrical Imaging in Archaeology. Journal of Archaeological Science 21:153-158.

Heiland, C.A., 1946. Geophysical Exploration. Prentice Hall Inc New York 634.

Loke, M. H., 1999. RES2DINV ver. 3.42, Geoelectrical Imaging 2D & 3D, User Manual.

Loke, M.H., 1996-2011. Tutorial: 2-D and 3-D Electrical Imaging Surveys. Geotomo Software.

Maillol, J. M., Seguin, M.-K., Gupta, O. P., Akhauri, H. M., and Sen, N. (1999). Electrical resistivity tomography survey for delineating uncharted mine galleries in West Bengal, India. Geophys Prospect 47: 103-116.

Martínez Pagán, P.; Aracil, E.; Maruri, U.; Faz, Á., 2005. Tomografía eléctrica 2D/3D sobre depósitos de estériles mineros. Ingeopress, 138 (34-36).

Orellana, E. 1982. Prospección Geoeléctrica en Corriente Continua. 2ª ed. Madrid. Paraninfo Vol.1.

Ortega, A. I. (2009). Evolución geomorfológica del Karst de la Sierra de Atapuerca (Burgos) y su relación con los yacimientos pleistocenos que contiene. Unpublished PhD Thesis, Universidad de Burgos, Burgos, Spain, 624 pp.

Ortega, A.I., Benito-Calvo, A., Porres, J., Pérez-González and Martin-Merino, M.A., 2010. Applying Electrical Resistivity Tomography to the Identification of Endokarstic Geometries in the Pleistocene Sites of the Sierra de Atapuerca (Burgos,Spain). Archaeological Prospection, Published online in Wiley Online Library (wileyonlinelibrary.com) DOI: 10.1002/arp.

Papadopoulos, N. G., Tsourlos, P., Tsokas, G. N. and Sarris, A., 2006. Two-dimensional and three-dimensional Electrical Imaging in Archaeological Site Investigation. Archaeological Prospection 13: 163-181.

Papadopoulos, N. G., Yi, M.-J., Kim, J.-H., Tsourlos, P. and Tsokas, G. N., 2010. Geophysical investigation of tumuli by means of surface 3D Electrical Resistivity Tomography. Journal of Applied Geophysics 70: 192-205.

Pineda, A., 1997. Mapa Geológico de España escala 1:50.000, 2ª Serie (MAGNA). Hoja de Burgos, 200 (19-10). IGME, Madrid, 93 pp.

Piro, S., Mauriello, P. and Cammarano, F., 2000. Quantitative Integration of Geophysical Methods for Archaeological Prospection. Archaeological Prospection 7: 203-213.

Piro, S., Tsourlos, P. and Tsokas, G. N., 2001. Cavity detection employing advanced geophysical techniques: a case study. European Journal of Environmental and Engineering Geophysics 6: 3-31.

Porres, J.A., 2003. Caracterización de cavidades en el subsuelo mediante la interpretación de perfiles de Tomografía Eléctrica: Aplicación al yacimiento arqueológico de Clunia. Phd. Thesis, University of Burgos, Spain. ISBN 978-84-96394-55-1.

Rizzo, E., Colella, A., Lapenna, V., Piscitelli, S., 2004. High-resolution images of the fault-controlled High Agri Valley basin (southern Italy) with deep and shallow electrical resistivity tomographies. Physics and Chemistry of the Earth 29, 321e327.

Terrizzano, C.M., Fazzito, S.Y., Cortés, J.M., Rapalini, A.E., 2012. Electrical resistivity tomography applied to the study of neotectonic structures, northwestern Precordillera Sur, Central Andes of Argentina. Journal of South American Earth Sciences 34, 47e60.

Tsokas, G. N., Tsourlos, P. I., Stampolidis, A., Katsonopoulou, D. and Soter, S. (2009): Tracing a Major Roman Road in the Area of Ancient Helike by Resistivity Tomography. Archaeological Prospection 16: 251-266.

Storz, H., Storz, W., Jacobs, F., 2000. Electrical resistivity tomography to investigate geological structures of the earth's upper crust. Geophysical Prospecting 48, 455e471.

Sumanovac, F.; Weisser, M. 2001. Evaluation of resistivity and seismic methods for hydrogeological mapping in karst terrains. Journal of Applied Geophysics, 47. 13-28

Zhou, W.; Beck, B.F.; Stephenson, J.B., 2000. Reliability of dipole-dipole electrical resistivity tomography for defining depth to bedrock in covered karst terranes. Environmental Geology, 39 (7), 760-766.

Geotechnical and Geophysical Site Characterisation 5 – Lehane, Acosta-Martínez & Kelly (Eds)

Site characterization of seismic stations based on downhole tests to 30 m depth in South Korea

C.G. Sun
Earthquake Research Center, Korea Institute of Geoscience and Mineral Resources, Daejeon, Korea

J.M. Jeong & K.S. Kim
Heesong Geoetek Co., Ltd., Gyeonggi-do, Korea

I.S. Jang
Underwater Construction Robotics R&D Center, Korea Institute of Ocean Science and Technology, Gyeonggi-do, Korea

ABSTRACT: Earthquake ground motions inducing catastrophic losses are strongly influenced by the local site characteristics. To observe the ground motions during an earthquake, seismic monitoring stations have been installed at a number of locations, not only in strong seismicity regions but also in moderate seismicity regions, including the Korean Peninsula, where most sites have shallow bedrock depths of less than 30 m. As part of the evaluation of seismic responses of regional seismic stations, this study carried out a series of site investigations involving borehole drilling and downhole seismic tests at 53 stations in South Korea. The site conditions at the seismic stations were categorized using several earthquake engineering parameters, which can be determined using the shear wave velocity (V_S) profile to 30 m depth or to bedrock depth. Most of the stations in Korea were site class C based on the mean V_S to 30 m depth for earthquake-resistant design, rather than site class B indicating rock condition. In terms of engineering parameters and their correlations, the site characteristics of the seismic stations in Korea were compared with those in other strong seismicity regions. The regional comparisons showed that the Korean seismic stations have region-specific geotechnical characteristics differing from those of regions with strong seismicity.

1 INTRODUCTION

The Korean Peninsula is a region of the Eurasian plate with moderate seismicity (Sun et al. 2005). Since seismic monitoring began in the late 1970s and early 1980s, few earthquake motion data recorded in Korea have shown substantial magnitudes or intensities. Therefore, the reference earthquake ground motion is determined from seismic hazard maps based on historical earthquake records. To obtain earthquake hazard data for the Korean Peninsula, additional seismic monitoring stations have been installed and there are now more than 100 stations in South Korea. Most stations are operated by the Korea Meteorological Administration (KMA) and Korea Institute of Geoscience and Mineral Resources (KIGAM) and their data are shared in real-time.

This paper examined the site characterization of the seismic response by performing in situ geotechnical dynamic investigations composed of borehole drillings and downhole seismic tests at 53 seismic monitoring stations in South Korea. Besides the borehole drilling or invasive methods, the characterization of seismic stations has been carried out using nondestructive methods, such as surface wave techniques and microtremor survey. Particularly, the microtremor observation is usually adopted to H/V (horizontal to vertical) spectral ratio indicating fundamental frequency (or site period) at a site, and for the seismic monitoring station, the H/V ratio would be determined using earthquake records or continuous noises (Nakamura 2008). In this study, the direct seismic method in a borehole was however applied not only for site characterizing but also for obtaining shear wave velocity (V_S) profile to be utilized in site-specific seismic response analyses.

The downhole seismic tests measured the V_S profiles of the near-surface materials at each seismic station. As a representative in situ dynamic property, the V_S profile has a profound influence on the characteristics of earthquake ground motion, which may be recorded at a seismic station. Moreover, site conditions such as bedrock depth (H) and soil stiffness associated with V_S affect the amplification of ground motions, because the earthquake motions of bedrock can be drastically modified in frequency and amplitude during propagation of the seismic waves through the soil column over the bedrock. Based on the in situ investigation results, region-specific site conditions, related to the seismic site effects and resulting in the amplification of earthquake ground motions, were assessed in terms of several geotechnical earthquake engineering parameters at 53 seismic monitoring stations in Korea.

2 SITE INVESTIGATIONS AT SEISMIC MONITORING STATIONS IN KOREA

The Korean Peninsula, located at the eastern margin of the Eurasian continent, is an ancient landform in geomorphological formed by continual erosion. This erosion is especially prominent in inland areas of Korea, which are mainly covered by plains, hills, and small mountains (Fig. 1). The peninsula is covered by various geological strata formed from the Precambrian to the Cenozoic Era. The southern part of the peninsula is composed of crustal blocks of Archean to middle Proterozoic high-grade gneisses and schists (Sun 2015). The surface soils over the bedrock in the region were generally formed by fluvial actions or weathering processes and are alluvial and weathered residual soils.

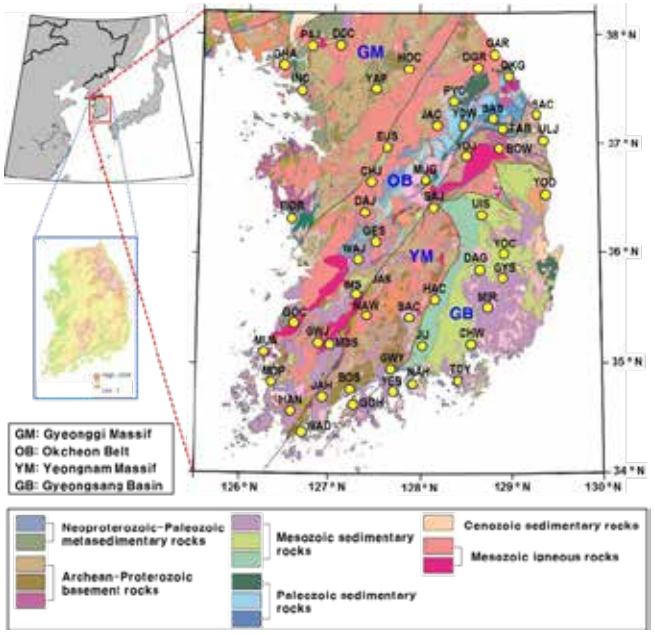

Figure 1. Geographic locations of the seismic stations subject to in situ investigations with a base map of the geological setting of South Korea.

Intensive site investigations involving borehole drilling and downhole seismic tests were conducted to obtain V_S profiles, with the goal of understanding the geological conditions at 53 seismic monitoring station sites in South Korea (Fig. 1). The boreholes were drilled to at least 30 m depth at the sites with bedrock shallower than 30 m, and to bedrock at the sites with bedrock deeper than 30 m. The depth of 30 m from the ground surface is used to compute the mean V_S to a depth of 30 m (V_{S30}), as a criterion for site classification of earthquake-resistant designs (Dobry et al. 2000). After borehole drilling at a site, a downhole seismic test inside the PVC-encased borehole was conducted to obtain seismic wave signals, including the shear wave, according to increasing depth, as depicted in Figure 2. V_{S30} is calculated from the time taken by a shear wave to travel from a depth of 30 m to the ground surface. For a profile consisting of n soil or rock layers, V_{S30} can be calculated as

$$V_{S30} = 30 / \sum_{i=1}^{n} \frac{d_i}{V_{Si}} \quad (1)$$

where d_i and V_{Si} are the thickness and V_S of each soil or rock layer to a depth of 30 m (30 m = Σd_i), respectively.

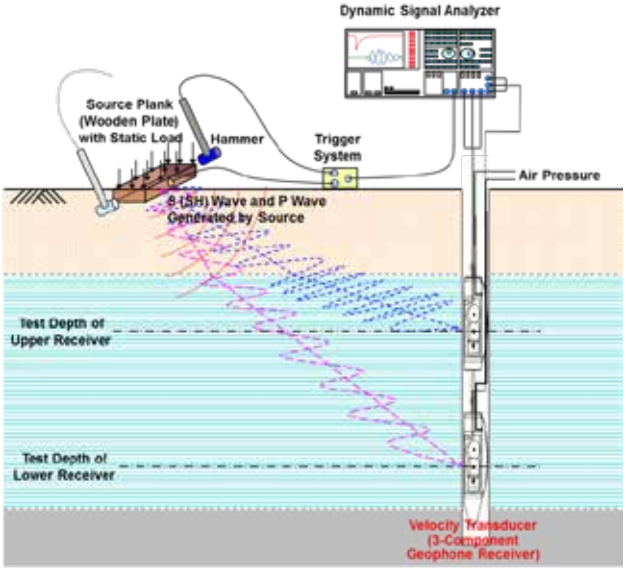

Figure 2. Schematic diagram of an in situ downhole seismic test in a borehole.

The two methods used most commonly for determining the ground motion are site classification based on V_{S30} and site-specific seismic response analysis using the V_S profile of soil strata and the unique V_S of infinite-assumed bedrock. Recently several researchers (Rodriguez-Marek et al. 2001; Sun 2010) have proposed another method of site classification that uses the site period (T_G) determined by equation (2). The site period is based on the thickness of the soil layers overlying the bedrock at each site and their V_S values:

$$T_G = 4 \sum_{i=1}^{n} \frac{D_i}{V_{Si}} \quad (2)$$

where D_i and V_{Si} are the thickness ($H = \sum D_i$) and V_S, respectively, of the ith layer above bedrock.

Table 1 lists the site characteristics at the seismic stations assessed using boring investigations and downhole tests. Lee et al. (2012) suggested using the mean V_S of the soil layers above bedrock ($V_{S,soil}$) in Table 1 as a parameter to classify site conditions including the depth to bedrock (H). $V_{S,soil}$ can be calculated from equation (3). More than half of the station sites in this study fall within site class C based on V_{S30}, because the sites are located in the inland region. Of the 53 station sites, 11, 32, and 10 sites were site classes B, C and D, respectively.

$$V_{S,soil} = \sum_{i=1}^{n} D_i \Big/ \sum_{i=1}^{n} \frac{D_i}{V_{Si}} \quad (3)$$

Table 1. Site parameters derived from in situ investigations at 53 seismic stations in South Korea.

Site name	H (m)	V_{S30} (m/s)	$V_{S,soil}$ (m/s)	T_G (s)	Site class*
PAJ	13.5	784	533	0.1050	B
WAJ	6.0	749	301	0.0797	C
MDS	4.0	852	384	0.0416	B
DGR	3.2	607	268	0.0448	C
TAB	2.0	611	339	0.0236	C
MUG	0.8	1122	507	0.0079	B
GYS	2.5	925	282	0.0426	B
MIR	13.0	533	378	0.1377	C
CHW	1.5	901	259	0.0309	B
TOY	10.0	560	300	0.1334	C
HOC	14.2	452	292	0.1916	C
GAR	15.2	302	188	0.3196	D
OKG	7.0	679	309	0.0905	C
SAC	7.5	433	199	0.1608	C
SAB	3.0	686	283	0.0425	C
PYC	12.5	435	270	0.1929	C
JAC	28.8	384	378	0.3067	C
EUS	5.0	812	259	0.0772	B
DAJ	16.0	473	343	0.1866	C
CHJ	36.0	291	308	0.4677	D
BOR	27.5	286	272	0.4121	D
IMS	16.7	513	367	0.1853	C
NAW	24.2	471	424	0.2262	C
JAS	34.0	387	412	0.3299	C
GWY	11.5	397	288	0.1667	C
YES	19.5	323	246	0.3255	D
BOS	30.0	212	212	0.5670	D
JAH	34.7	309	328	0.4273	D
WAD	5.5	865	312	0.0768	B
HAN	36.1	273	301	0.4783	D
MOP	6.6	488	239	0.1170	C
MUA	17.5	434	331	0.2177	C
GOC	12.0	433	248	0.1936	C
GWJ	20.5	380	305	0.2750	C
GHA	33.0	331	339	0.3889	D
GOH	5.6	746	390	0.0615	C
GES	30.0	305	305	0.3932	D
HAC	30.0	279	279	0.4295	D
NAH	20.0	414	281	0.2993	C
DDC	10.5	804	543	0.0811	B
SAC	13.3	437	270	0.1923	C
INC	9.0	511	336	0.1071	C
JIJ	0.7	765	313	0.0128	B
YOW	4.5	599	247	0.0808	C
DAG	2.0	708	217	0.0369	C
BOW	7.0	631	307	0.0912	C
SAJ	25.5	469	441	0.2361	C
YOD	0.5	787	486	0.0082	B
YOJ	27.0	442	419	0.2575	C
YOC	3.5	775	342	0.0468	B
ULJ	30.5	523	526	0.2358	C
UIS	5.7	534	289	0.0831	C
YAP	29.0	624	1133	0.1024	C

* Sites are categorized based on the site classification system with the criterion of V_{S30} adopted in current codes such as NEHRP and IBC.

3 STATISTICAL DISTRIBUTION OF SITE PARAMETERS IN KOREA

The depth to bedrock at each seismic monitoring station site was examined based on borehole drilling and the V_S profile was determined by performing a downhole test. To analyze the continuous V_S profile according to depth at a site, the discrete data per meter of depth were stored in a spread sheet. Figure 3 shows the V_S profiles for the 53 station sites in South Korea, together with the average V_S profile to 30 m depth and two V_S profiles reflecting the standard deviation (SD). As expected, the profiles show that V_S increases with depth.

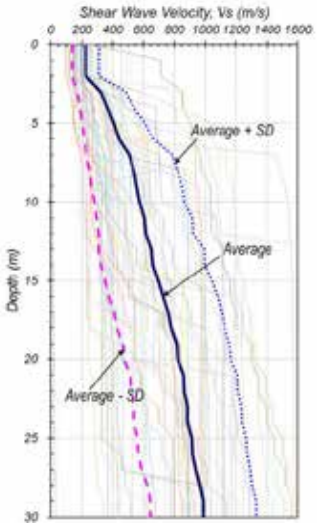

Figure 3. Average V_S profile to 30 m depth based on the V_S profiles at the sites in South Korea.

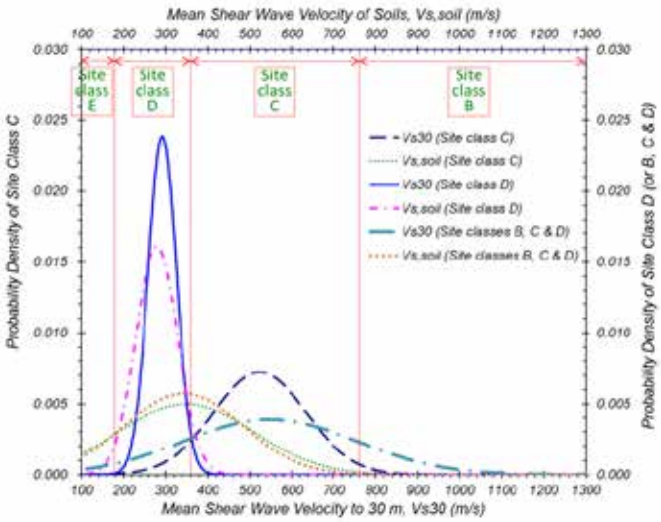

Figure 4. Probability distributions of V_{S30} and $V_{S,soil}$ for seismic station sites in South Korea.

To estimate the distributions of both V_{S30} and $V_{S,soil}$ for site classification, the probabilistic distributions of parameters, V_{S30} and $V_{S,soil}$, were examined for 53 seismic station sites in South Korea, as illustrated in Figure 4. The parameters were assumed to have Gaussian distributions. The V_{S30} and $V_{S,soil}$

for three site classes (B, C and D) have similar distribution ranges to those of site class C, because the seismic stations predominantly fall into site class C ($360 < V_{S30} \leq 760$). The mean values of V_{S30} and $V_{S,soil}$ were roughly 550 m/s and 340 m/s, respectively. However, the $V_{S,soil}$ values for site classes B, C and D are very close to 360 m/s, which is the boundary value between site classes C and D.

In addition, the site period (T_G) was examined based on the probabilistic distributions (Fig. 5). For the T_G of site classes B, C, and D, the distribution has a mean of about 1.8 s, which is similar to that of site class C, rather than site class D. Based on both V_{S30} and T_G for seismic stations in South Korea, the correlation presented in Figure 6 was calculated and compared with a correlation based on the data for historical earthquake hazard sites in Korea suggested by Sun (2010). The decay in the correlation in the present study is greater than that of the correlation calculated by Sun (2010) because the soils of the seismic station sites are stiffer than those of the historical earthquake hazard sites.

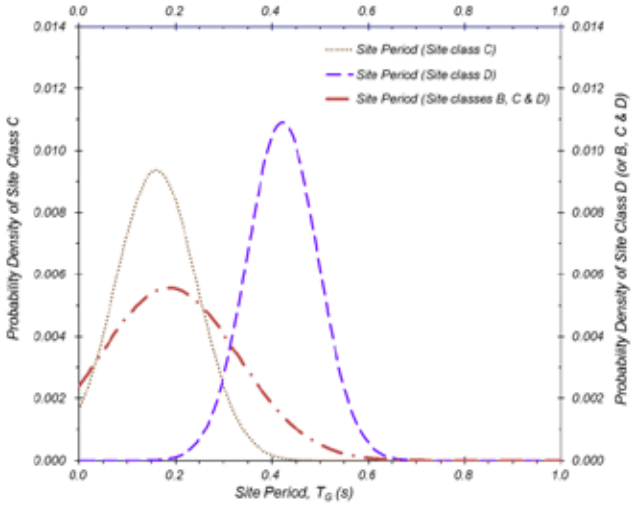

Figure 5. Probability distribution of T_G for seismic stations in South Korea.

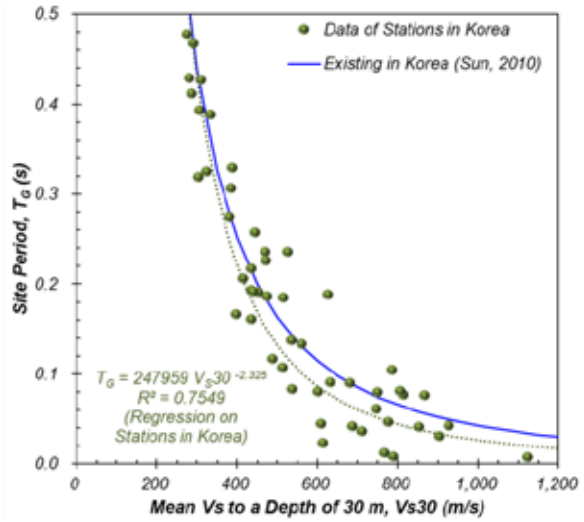

Figure 6 Comparison of the correlations between T_G and V_{S30} in Korea.

4 COMPARISONS OF SITE PARAMETERS BETWEEN KOREA AND OTHER REGIONS

The geotechnical characteristics influencing on the seismic site response differ by region. We evaluated three other V_S profiles and borehole datasets for seismic monitoring stations in strong seismicity regions: western US (WUS), Japan, and Turkey. These were compared with the site response parameters. Figure 7 shows the V_S profiles at sites in WUS, Japan, and Turkey, and their average profiles and SD. The profile data for these three areas were compiled from database websites for the Resolution of Site Response Issue from the Northridge Earthquake (ROSRINE) project (Bardet et al. 1998), the Kiban Kyoshin network (KiK-net) (NIED 2015), and the Strong Ground Motion Database of Turkey (AFAD 2015), respectively.

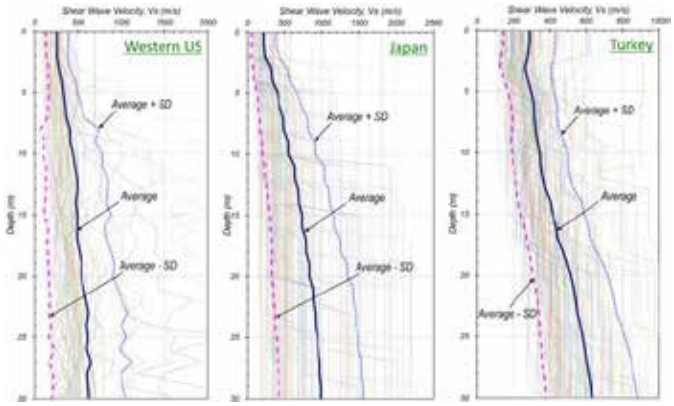

Figure 7. Average V_S profile to 30 m depth based on V_S profiles at sites in strong seismicity regions.

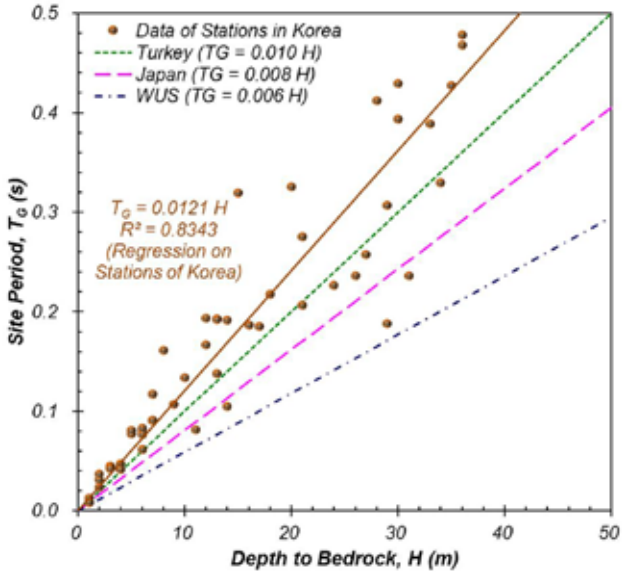

Figure 8. Comparison of the correlations between T_G and H for seismic stations in Korea and strong seismicity regions.

Regional differences in site conditions can be identified by comparing the probability distributions of the site response parameters and their correlations. We investigated the correlations between T_G

and H in Korea and other regions of strong seismicity (western US, Japan, and Turkey), as presented in Figure 8. The slope of the regression reflects the stiffness of the soils above bedrock, and decreases for softer soils. Examining the slopes of the regressions shows that the soil layers at the seismic stations in Korea are stiffer than those in the other three strong seismicity regions.

Of the various site parameters, the probabilistic distributions of T_G for site classes C and D in Korea were compared with those in the other three regions, as shown in Figures 9 and 10, respectively. For Korea, T_G is generally smaller than for strong seismicity regions, regardless of site class, owing to the shallow bedrock in Korea. For Japan and western US, T_G is distributed across a wide range compared with T_G for Korea and Turkey. These differences in geotechnical site conditions, such as the soil stiffness and the depth to bedrock, between the strong seismicity regions and Korea would result in different site responses at the seismic monitoring stations.

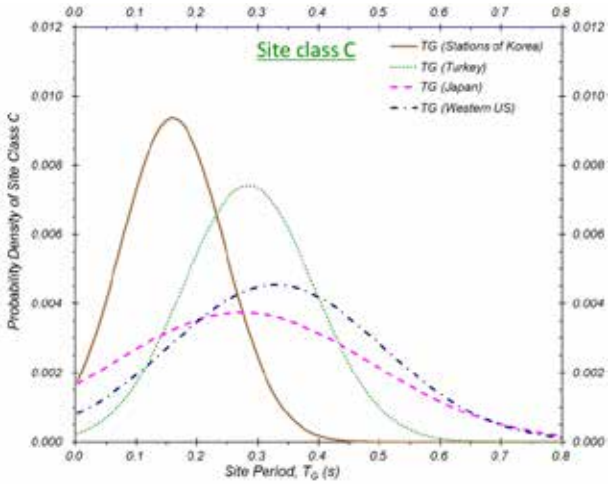

Figure 9. Comparisons of the probability distributions of T_G for seismic stations of site class C in Korea and strong seismicity regions.

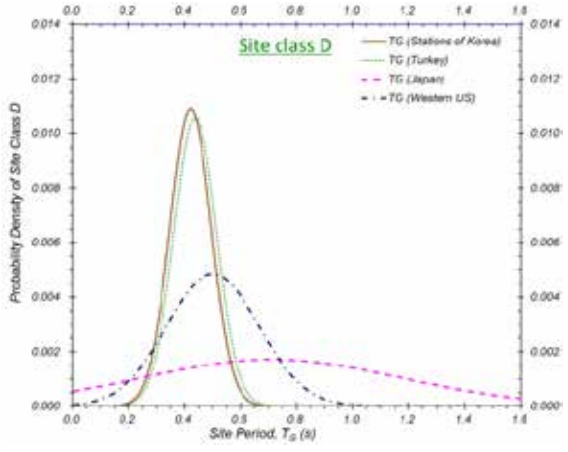

Figure 10. Comparisons of the probability distributions of T_G for seismic stations of site class D in Korea and strong seismicity regions.

5 CONCLUSIONS

Site characterization was performed at 53 seismic monitoring stations in Korea using in situ investigations up to at least 30 m depth and including downhole seismic tests. Most of the stations were categorized into site class C according to V_{S30}. The average values of the site parameters at the stations in Korea were 550 m/s for V_{S30}, 340 m/s for $V_{S,soil}$, and 0.18 s for T_G. Comparing the site conditions at seismic stations in Korea with other strong seismicity regions, the depth to bedrock in Korea is shallower, and the soils are stiffer, comparing to those in western US, Japan and Turkey.

6 ACKNOWLEDGEMENTS

This study was supported by the Basic Research Project of the Korea Institute of Geoscience and Mineral Resources (KIGAM).

7 REFERENCES

AFAD. 2015. Strong ground motion database of Turkey. http://kyhdata.deprem.gov.tr/2K/kyhdata_v4.php, Accessed 19 January 2015.

Bardet, J.P., Nielsen, E. & Villacorta, R. 1998. ROSRINE data dissemination. http://geoinfo.usc.edu/rosrine, Accessed 12 June 2015.

Dobry, R., Borcherdt, R.D., Crouse, C.B., Idriss, I.M., Joyner, W.B., Martin, G.R., Power, M.S., Rinne, E.E. & Seed, R.B. 2000. New site coefficients and site classification system used in recent building seismic code provisions. *Earthquake Spectra* 16(1): 41-67.

Lee, S.H., Sun, C.G., Yoon, J.K. & Kim, D.S. 2012. Development and verification of a new site classification system and site coefficients for regions of shallow bedrock in Korea. *Journal of Earthquake Engineering* 16(6): 795-819.

Nakamura, Y. 2008. On the H/V spectrum. *Proc. 14th World Conference on Earthquake Engineering*, Beijing, China, Paper ID: 07-0033.

NIED. 2015. Site list of soil condition data: KiK-net. http://www.kyoshin.bosai.go.jp/kyoshin/db, Accessed 16 February 2015.

Rodriguez-Marek, A., Bray, J.D. & Abrahamson, N.A. 2001. An empirical geotechnical seismic site response procedure. *Earthquake Spectra* 17(1): 65-87.

Sun, C.G. 2010. Suggestion of additional criteria for site categorization in Korea by quantifying regional specific characteristics on seismic response. *Jigu-Mulli-Mulli-Tamsa* 13(3): 203-218 (in Korean).

Sun, C.G. 2015. Determination of mean shear wave velocity to 30 m depth for site classification using shallow depth shear wave velocity profile in Korea. *Soil Dynamics and Earthquake Engineering* 73: 17-28.

Sun, C.G., Kim, D.S. & Chung, C.K. 2005. Geologic site conditions and site coefficients for estimating earthquake ground motions in the inland areas of Korea. *Engineering Geology* 81(4): 446-469.

Geotechnical and Geophysical Site Characterisation 5 – Lehane, Acosta-Martínez & Kelly (Eds)

Design and application of a low-cost, 3D printed crosshole seismic system- Preliminary assessment

M.B. Sylvain, M.A. Pando, M.J. Whelan & V.O. Ogunro
UNC Charlotte, NC, USA

Y. Park
EPIC Engineer, UNC Charlotte, NC, USA

ABSTRACT: This paper presents the design and construction of an inexpensive crosshole testing (CHT) system constructed for shear wave velocity (V_s) determination. The paper also presents a validation carried out at the geotechnical test pit at the University of North Carolina at Charlotte (UNCC). The test pit is backfilled with a compacted silty, clayey sand (SC-SM) underlain by dense in-situ soil. Details are provided concerning the design of the crosshole system and the validation of the CHT V_s data which is based on a comparison with V_s measurements from two separate conventional methods.

1 INTRODUCTION

Crosshole testing (CHT) is a geophysical test that involves direct measurements of shear wave velocity (V_s) at depths of interest. The test provides an efficient means of evaluating in-situ geotechnical conditions such as layering, and engineering properties of a soil profile in-situ (Ballard et al. 1983, Campanella 1994). This paper presents details of the design and construction of a low-cost, in-house developed CHT system. The transmitter and receiver housing system used for the CHT was economically fabricated through the use of 3D printing. In addition to the sensor housing, the paper describes the sensors used in the system for generating and receiving the shear waves. This CHT system developed in-house is validated by comparing V_s measurements at a geotechnical test pit with V_s measurements using MASW and seismic CPTu soundings. This cost effective CHT system was found to provide reliable V_s measurements which can be especially useful for projects which have limited budgets.

2 DESCRIPTION OF CROSSHOLE SYSTEM

The major components of the low-cost CHT system are shown in Figure 1.

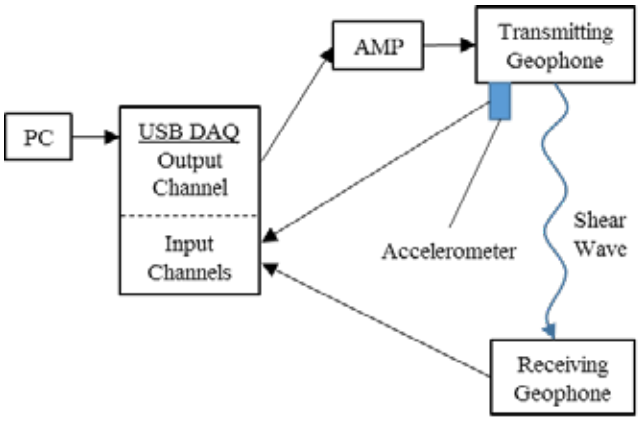

Figure 1. Main components of CHT system.

The CHT system included a microprocessor computer running the test software, a data acquisition system (DAQ) to send and receive analog signals from the sensors, a power amplifier to drive sufficient current through the transmitting geophone, and the transmitting and receiving geophones. The system involved placing low-cost R.T. Clark 10 Hz vertical and horizontal geophones (less than US$25 per geophone). The geophone specifications included a natural frequency of 10 Hz, a coil resistance of 395 Ohms, and a moving mass of 11 g. The CHT transmitter and receiver used plastic sensor casings that were designed and 3D printed in-house at a minimum cost. The CHT transmitter contained a vertically oriented geophone and the CHT receiver contained one vertical and two horizontal geophones. The design of

the plastic housing is shown in Figure 2. The plastic housing for each sensor type was secured against the PVC pipes using pneumatic actuators that were placed in the geophones and were used to extend and retract a 3D printed foot that was used to provide clamping pressure. These actuators were connected to a source of pressurized air. The pressurized foot shown in Figure 2 was effectively used to lock the sensors in place against the wall of the PVC pipe at the target depth.

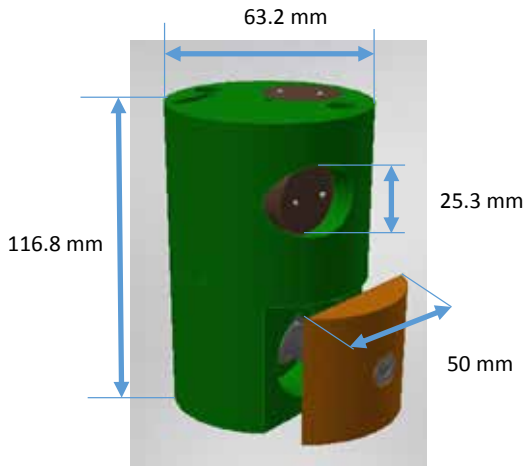

Figure 2. Drawing of 3D printed sensor casing.

The transmitter sensor used the vertical geophone as a source of excitation. An impulsive seismic source was generated by driving the coil of the transmitting geophone with a pulse wave output from a digital output of the DAQ that was passed through a Bruel & Kjaer Type 2706 power amplifier. The power amplifier increased the current of the signal which was then sent to the vertical geophone encased in the transmitting sensor casing. The current applied to the coiled wire within the geophone excited the magnetic internal moving mass, and in turn the movement of the moving mass generated the seismic source wave upon striking the geophone casing. The generated shear wave is a horizontally propagating shear wave with particle motion in the vertical direction. An accelerometer, Model 353B31 manufactured by PCB Piezotronics, was attached to the transmitting geophone to help determine the timing of the generated source wave. The time of transmission of the shear wave is given by the peak velocity derived from the accelerometer data. The analog signals from the three sensors in the receiving geophone as well as the accelerometer on the transmitting geophone were sampled by a 16-bit analog-to-digital converter in a National Instruments USB-6341 at a sampling rate of 100,000 Hz. Figure 3 presents a schematic demonstrating the signal transmission used to generate the plane shear wave. Photos of the CHT test setup are shown in Figure 4.

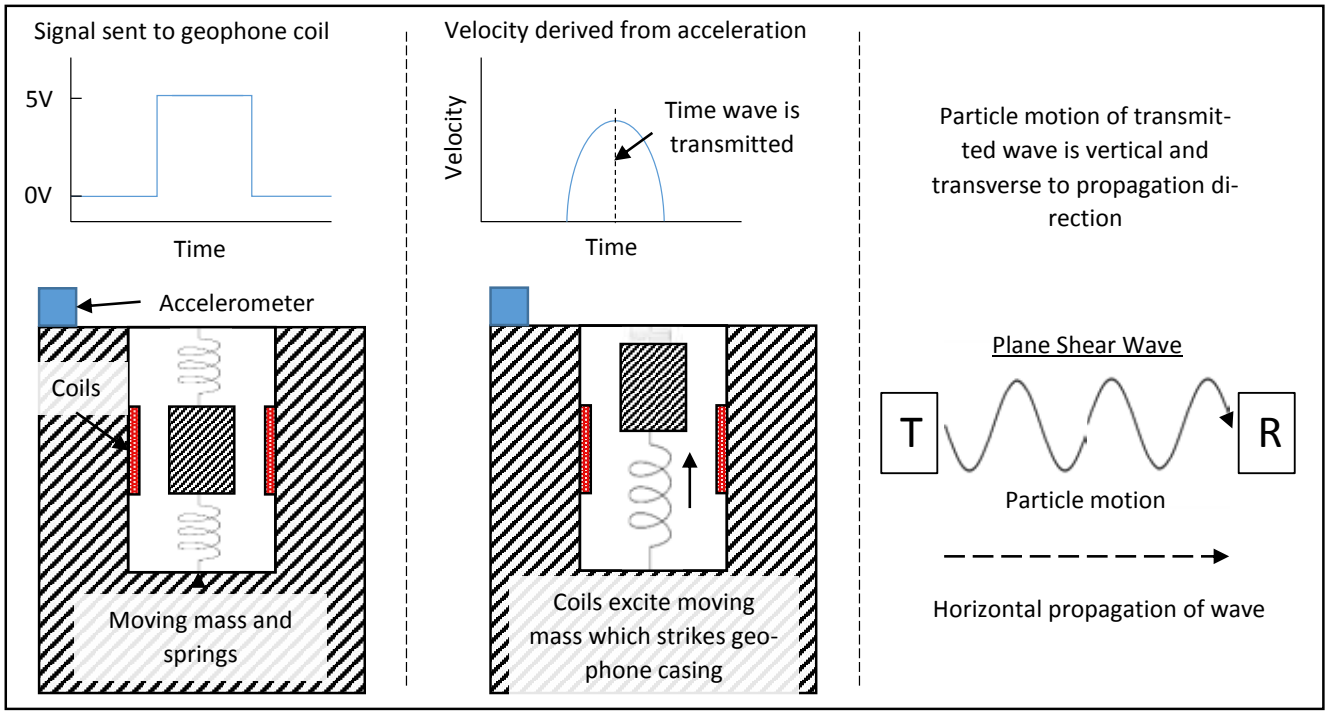

Figure 3. Schematic of generation of shear wave and transmission time.

a.) Test pit and PVC pipes. b.) Sensor housing. c.) Test setup.

Figure 4. Photos of CHT system.

The CHT test results presented in this paper were carried out in general accordance with the methodology proposed by the ASTM Standard D4428 (ASTM 2014). The arrival times were chosen in the time domain based on visual inspection of the seismic measurements versus time (Hoar & Stokoe II 1978; ASTM 2014). A set of representative images of the recorded data, after processing, are presented in Figure 5. In this figure the transmitted wave was recorded by the accelerometer in the transmitting sensor. The second wave shown was recorded by the receiving geophone and the black 'X' represents the selected arrival time for this wave. The final selection of the peak was made after considering different peaks representing arrival of the S wave. Different peaks were considered in order to obtain consistent results with measurements made above and below a given depth. The next section presents details of the validation carried out at the geotechnical test pit at UNC Charlotte.

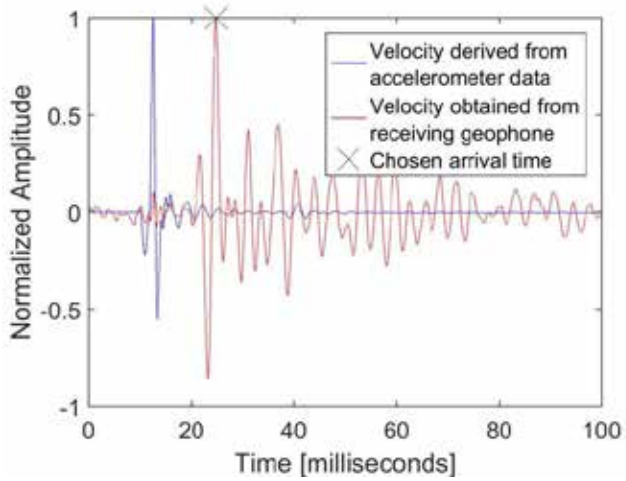

Figure 5. Example of transmitted and received signals and preliminary selection of arrival time.

3 VALIDATION OF CROSSHOLE SYSTEM

3.1 *Geotechnical testing of test pit*

The crosshole system described in the previous section was validated at the geotechnical test pit at UNC Charlotte. The geotechnical test pit has a 3.66 m × 3.66 m square footprint formed by concrete walls. The pit is approximately 3.05 m deep and its base is open to in-situ soil which consists of a very dense, residual, gravelly sand. The residual soil at the base of the pit was dry and had a total unit weight of about 21 kN/m^3. A photo of the UNCC geotechnical test pit is shown in Figure 6. Figure 6(a) shows the pit empty prior to backfilling and Figure 6(b) shows the pit completely backfilled. Prior to fill placement, two rows of PVC pipe were placed vertically inside the pit along the north and south edges of the pit. A total of ten, 3.05 m long sections of PVC pipe were placed in two rows approximately 0.61 m away from the north and south edges of the pit. These PVC casings were later used for crosshole testing. The PVC pipes had an inside diameter of approximately 7.62 cm and were held vertically in place with wooden frames. Verticality of the pipes was carefully checked during the backfilling process.

a.) Empty test pit with PVC casings.

b.) Backfilled test pit showing top of PVC casings.

Figure 6. Geotechnical test pit at UNC Charlotte.

For this study, the test pit was backfilled with a silty, clayey sand soil with a unified soil classification ranging from SC to SC-SM. The main index properties and the results of Standard Proctor compaction tests are presented in Table 1. The backfill was placed in lifts with a thickness of approximately 10 cm when in a loose state. Compaction was achieved through the use of a vibratory plate compactor, model MVC-88VGH by Multiquip, as well as with large hand tamping plates that were used for compacting soil in areas of the pit difficult to compact with the plate compactor. The vibratory plate compactor was able to apply a centrifugal force of 1,564.9 kg and could apply 5,800 vibrations per minute. Soil was compacted to achieve a minimum target relative compaction of 90% with respect to the Standard Proctor dry unit weight (γ_{dry}= 18.66 to 18.86 kN/m^3) as defined in ASTM D698 (ASTM 2012).

During compaction the backfill water content was kept at ±2% of the Standard Proctor optimum water content (w_{opt} = 12.2 to 12.3%). The level of compaction achieved and water content were assessed using the nuclear density, drive cylinder, and sand cone test methods. In general this testing revealed that the target compaction was achieved for the majority of depths tested.

Table 1. Index properties and compaction test results for backfill soil.

USCS Classification		SC to SC-SM
C_u		103.2 to 118.1
D_{50} (mm)		0.17 to 0.42
G_s		2.68 to 2.72
Standard Proctor	$(\gamma_{dry})_{max}$	18.66-18.86 kN/m^3
	w_{opt}	12.2-12.3%

Note: Ranges provided based on multiple tests

3.2 *Geotechnical testing of test pit*

Several conventional geotechnical tests were performed on the compacted backfill material. These tests included standard penetration tests (SPT), seismic cone penetration tests (SCPTu), and flat dilatometer tests (DMT), as well as several tests carried out to control the placement moisture and dry unit weight of the compacted fill material. The location of the geotechnical tests are summarized in Figure 7.

A summary of the main results of the geotechnical tests is presented in Figure 8. As shown in Figure 8, results of SPT testing indicated an average corrected SPT blow count, $(N_1)_{60}$, of 12 blows per 0.3 m. At depths where the test encountered the in-situ residual soil at the bottom of the pit, blow counts were in excess of 50 blows per 0.3 m. The results of SCPTu testing indicated average cone tip and sleeve resistance values of 4.1 MPa and 0.038 MPa, respectively. Results of density testing indicate the compacted backfill has an average dry unit weight of approximately 17 kN/m^3, which corresponds to an average relative compaction of 90 to 91% with respect to the Standard Proctor maximum dry unit weight presented in Table 1. The DMT, I_D indices values obtained are also shown in Figure 8. The I_D values indicate a soil that can be classified as silt ($0.6<I_D<1.8$) and sand ($1.8< I_D<(10)$) (Marchetti 1980).

Figure 7. Layout of geotechnical tests.

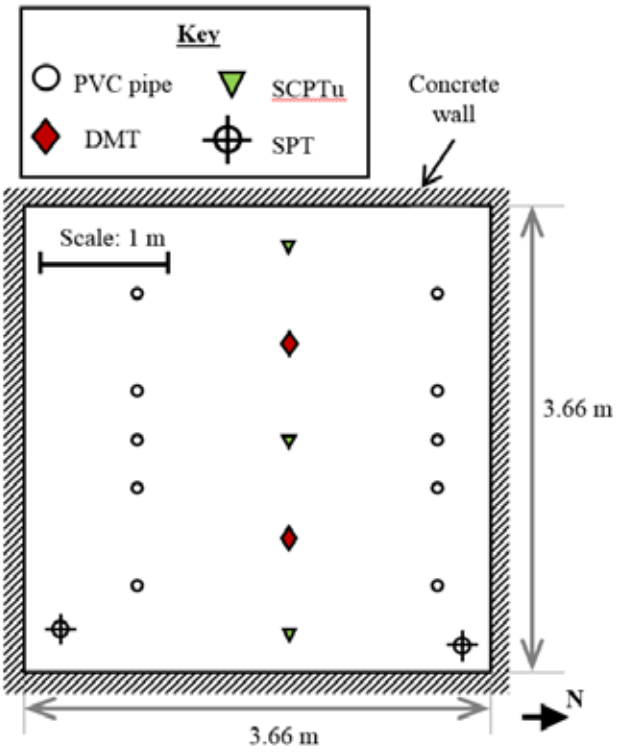

3.3 *Comparison of CHT with other geophysical tests*

To validate the CHT system, the V_s measurements obtained with this system were compared with results obtained from two other geophysical tests performed at the geotechnical test pit. The two other geophysical tests were the Multichannel Analysis of Surface Waves (MASW) and downhole tests carried out as part of the Seismic CPTu soundings. The MASW methodology is described by Park et al. (1999) and Lee et al. (2002). The MASW test results were obtained from three different geophone arrays oriented in the N-S direction as well as in a diagonal direction.

The CHT tests used direct paths in the N-S direction using different pairs of PVC casings. A summary of the CHT results for a single path is presented in Figure 9. In this figure, the chosen arrival times for the shear waves are marked with black 'X's.

The location of the seismic CPTu soundings were shown in Figure 7. For these tests, the shear wave excitation was generating by striking a steel beam at the ground surface of the pit located at a horizontal distance of approximately 1 meter from the CPT sounding.

A comparison of the shear wave velocity values measured using the in-house, cost effective CHT system with the values obtained from the MASW and seismic CPTu soundings is presented in Figure 10. The figure presents results from the three different methods considered with data obtained from the center path in the test pit. The CHT Vs values compare reasonably well with the values obtained from the MASW and SCPTu tests. Measurements taken from the CHT were on average higher than values measured using MASW. This is in part because the MASW values represent average values based on an inversion process of a soil model volume centered along the different sensor arrays. The comparison with the SCPTu based values is reasonably close but again represents a different path (downhole versus the horizontal path used for the CHT).

Overall the values are considered to compare reasonably well and thus the developed CHT system was considered adequate for V_s measurements for geotechnical applications, such as the one used in the validation. However, the adequacy of the pulse, in terms of energy and frequency, may need to be evaluated and modified for different soil conditions and for increased path lengths.

4 ACKNOWELDGEMENTS

The authors wish to thank the assistance and support received from S&ME for the geotechnical and geophysical testing. Additionally, the support by Dr. C. Park in the processing of the MASW data is greatly appreciated.

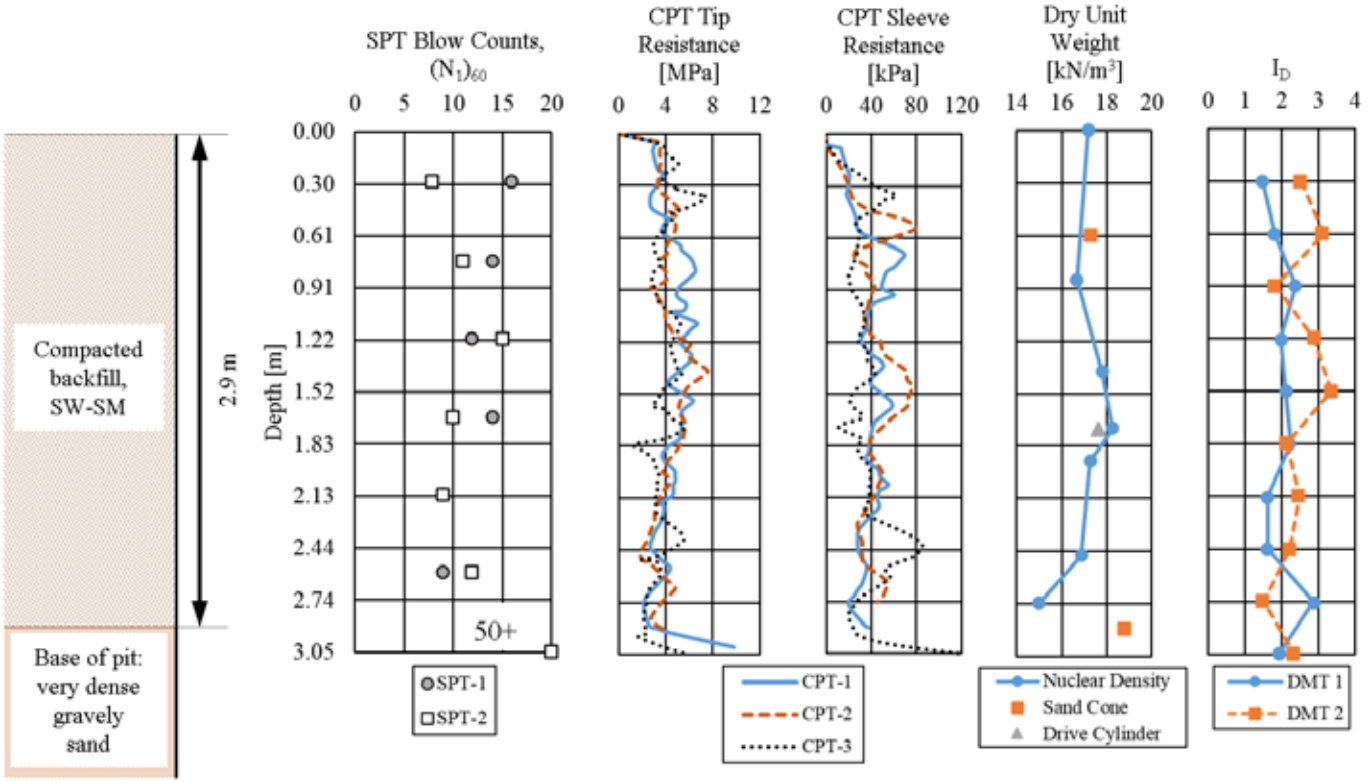

Figure 8. Stratigraphy of geotechnical test pit and summary of geotechnical test results.

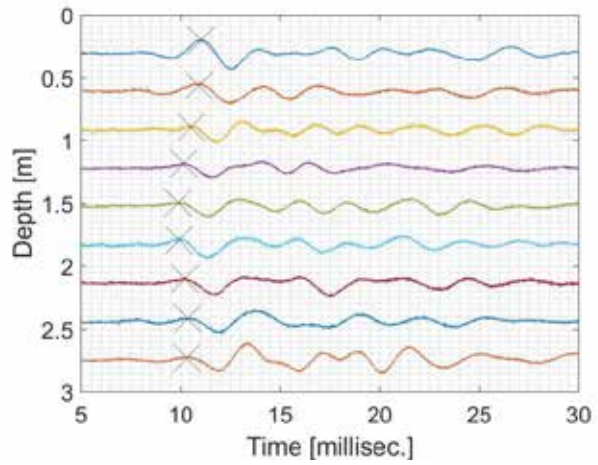

Figure 9. Waterfall plot of typical crosshole data obtained with depth.

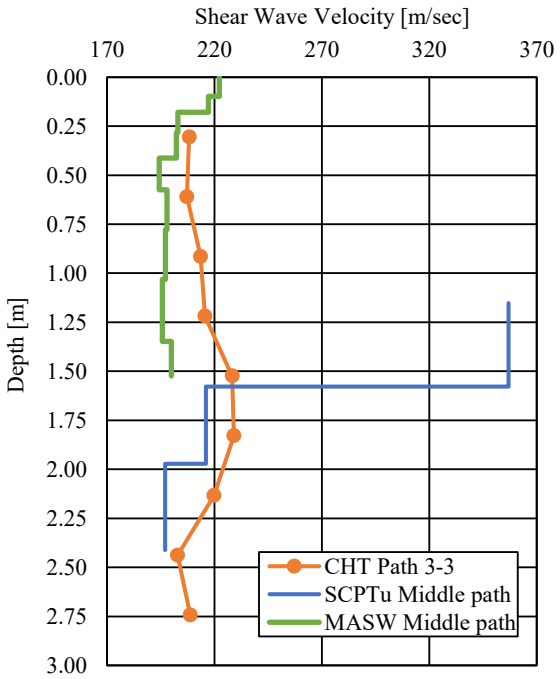

Figure 10. Comparison of the CHT shear wave velocities with values obtained from MASW and SCPTu tests

5 REFERENCES

ASTM. 2011. D5777 Standard guide for using the seismic refraction method for subsurface investigation. American Society for Testing and Materials, West Conshohocken, PA: 14 pp.

ASTM. 2011. D1586 Standard test method for standard penetration test (SPT) and split-barrel sampling of soils. American Society for Testing and Materials, West Conshohocken, PA: 9 pp.

ASTM. 2012. D5778 Standard test method for electronic friction cone and piezocone penetration testing of soils. American Society for Testing and Materials, West Conshohocken, PA: 20 pp.

ASTM. 2012. D698 Standard test methods for laboratory compaction characteristic of soil using standard effort (12400 ft-lbf/ft^3 (600 kN-m/m^3)). American Society for Testing and Materials, West Conshohocken, PA: 13 pp.

ASTM. 2014. D4428 Standard test methods for crosshole seismic testing. American Society for Testing and Materials, West Conshohocken, PA: 7 pp.

ASTM. 2014. D7400 Standard test methods for downhole seismic testing. American Society for Testing and Materials, West Conshohocken, PA: 10 pp.

ASTM. 2015. D6635 Standard test methods for performing the flat plate dilatometer. American Society for Testing and Materials, West Conshohocken, PA: 16 pp.

Ballard, R. F., Stokoe, K. H., II, & McLemore, R. 1983. Proposed standard test methods for cross-hole seismic testing. *Geotechnical Testing Journal, GTJODJ* 6(4): 210-219.

Butler, D. K., & Curro, J. R. 1978. Crosshole seismic testing—Procedures and pitfalls. *48th Annual International SEG Meeting,* San Francisco, CA: 23-29.

Campanella, R.. 1994. Field measurements for dynamic geotechnical testing: an overview of capabilities and needs. *ASTM STP 1213*: 21 pp.

Hall, L., & Bodare, A. 2000. Analyses of the cross-hole method for determining shear wave velocities and damping ratios. *Soil Dynamics and Earthquake Engineering* 20(1-4): 167-175.

Hoar, R. J., & Stokoe, K. H., II. 1978. Generation and measurement of shear waves *in situ*. *Dynamic Geotechnical Testing, ASTM STP 654*, American Society for Testing and Materials: 3-29.

Lee, W. H. K., Kanamori, H., Jennings, P. C., and Kisslinger, C. 2002. *International Handbook of Earthquake and Engineering Seismology*. San Diego: Academic Press.

Park, C. B., Miller, R. D., & Xia, J. 1999. Multichannel analysis of surface waves. *Geophysics*. 64(3): 800-808.

Marchetti, S. 1980. In situ tests by flat dilatometer. *ASCE Jnl GED* 106(GT3): 299-321.

Wong, J., & Stewart, R. R. 2006. Development of a vibratory source for shallow reverse VSP applications. *CREWES Research Report* 18: 12 pp.

Geotechnical and Geophysical Site Characterisation 5 – Lehane, Acosta-Martínez & Kelly (Eds)
© 2016 Australian Geomechanics Society, Sydney, Australia, ISBN 978-0-9946261-2-7

S-wave borehole tomography for geotechnical site characterization

J.K. von Ketelhodt & T. Fechner
Geotomographie GmbH, Neuwied, Germany

M.P.E. de Kleine
Deltares, Delft, The Netherlands

ABSTRACT: High-resolution tomographic investigations between boreholes are routinely applied for the exploration of development sites considered for larger building projects, such as power stations, dams and high-rise buildings. Currently, almost exclusively P-wave tomography is employed to predict the spatial continuity of lithological structures. However, the P-wave is highly influenced by the ground water table and its application for deriving geotechnical parameters is limited. Up to now, little effort has been made to develop equipment enabling an efficient acquisition of S-wave tomographic data. In this paper we present results of a newly developed S-wave tomography system, which has been tested at sites in the Netherlands. A horizontally polarizing borehole S-wave source was used with a multi station, three axial geophone array to receive the signals. P-wave tomography was also acquired along with the S-wave tomography. Results show a significantly higher velocity contrast for the S-wave tomograms (factor 3) compared to the P-wave tomograms (factor 1.5). Thus, the soils S-wave velocity structure is imaged in much more detail compared to the structure resolved with the P-wave. Furthermore, the S-wave tomogram covers both the saturated and unsaturated soil, with the water table not influencing the S-wave. The results obtained during the experiments show the potential of routinely carrying out S-wave tomography in addition to P-wave tomography.

1 INTRODUCTION

The shear modulus G is an important elastic soil parameter for foundation and construction design because it influences the force transfer between the structures and the soil. Depth dependent shear modulus profiles are needed as input to geotechnical numerical models. However, the shear modulus is strain dependent and in principle the dependency between the shear modulus and the shear strain needs to be described for a wide range of shear strains. This relationship is shown in Figure 1.

Among these is the maximum shear modulus G_0 at small shear strains, which is used as a starting value for numerical models. This maximum shear modulus G_0 can be calculated from geophysical tests that employ shear waves, since

$$G_0 = \rho V_s^2 \quad (1)$$

with the density ρ and the shear wave velocity v_s.

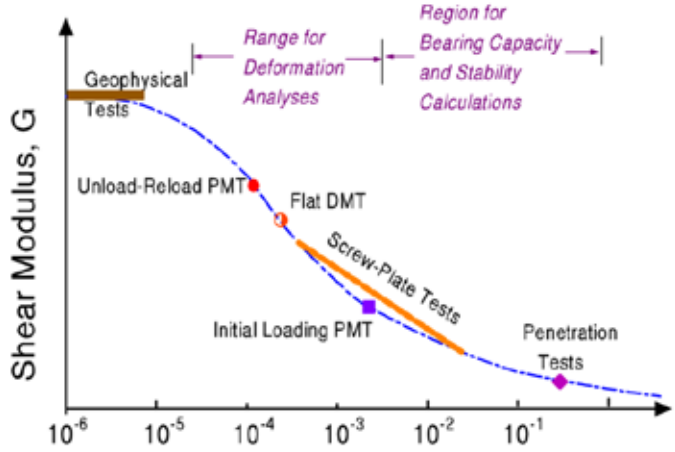

Figure 1. The shear modulus G as a function of the shear strain, from Mayne (2001)

Surface and borehole methods such as downhole and cross-hole testing are able to provide average S-wave velocity values. Among these methods cross-hole testing provides the most accurate and reliable values. However, the S-wave velocity is given as a function of depth only. The derived S-wave velocities are averaged values, since the two assumptions are made that the ray paths between the source and receiver are straight and that the material is laterally homogeneous.

Since the cross-hole testing method is applied between boreholes at small distances of 3 – 5 m, it is not meant to resolve structures between the boreholes. Consequently, the development of cross-hole S-wave tomography is required.

Up to now, only little effort has been made to develop equipment enabling the competitive acquisition of S-wave cross-hole tomographic data. Possible reasons for this could be the availability of reliable borehole S-wave sources as well as borehole receivers with multiple seismic channels. Furthermore, the S-wave data acquisition is more time consuming compared to standard P-wave tomography and the subsequent processing of S-wave data requires more sophisticated and skilled personnel.

2 DATA ACQUISITION

2.1 *Instrumentation*

To acquire S-wave tomographic data efficiently, an S-wave generating source and a tri-axial receiver string is needed. Conventionally borehole geophones are used for downhole and crosshole testing. These borehole geophones usually consist of three orthogonal receivers. However, to acquire S-wave tomographic data efficiently, more than one tri-axial receiver is desirable. Thus, a multi-station receiver system was developed (MBAS). A total of 10 stations can be connected, with each station consisting of a digital tri-axial geophone and the coupling to the borehole wall is achieved by two pneumatic cylinders per station. It is important to know the orientation of the stations for later data processing. Therefore, the stations are connected by a rotationally stiff hose, which enables the alignment of all stations from surface.

A horizontally polarizing S-wave source was used for the field testing. The source is powered by a high voltage generator from surface, with the energy releasing through a number of electromagnetic coils in the source. Subsequently, the source produces an impact to the side of the borehole wall, thereby generating both compressional and horizontally polarized shear waves. Due to this mechanism, the source can be used both in dry and water filled boreholes, with the signal being highly repeatable which allows vertical stacking of the data. Clamping is achieved by a pneumatic packer and the orientation is controlled from surface.

2.2 *Field acquisition*

The receiver string and the source are lowered into two boreholes which are between 3 and 25 m apart. The receiver string is aligned, that one of the two horizontal receivers in each station is facing the source borehole and the other is aligned perpendicular to the source borehole. The SH-source shoots twice per depth in 90° and 270° angles to the receiver borehole. This enables the overlaying of two opposing shooting directions at the processing stage, which results in an easier identification of the first arriving S-wave that is often obscured by the P-wave train.

3 PROCESSING SEQUENCE

3.1 *Re-sorting the data*

Data processing follows several steps in order to accurately determine the travel times for the seismic waves and to convert these into a tomographic image. The first step in the data processing is to resort the data into the respective X, Y and Z components. Experience has shown that more channels in a spread produces better and more consistent picking results. The number of channels are limited when using the MBAS system. A maximum of 10 stations can be connected, which results in a maximum of 30 channels, of which 10 horizontal channels are usually used for traveltime picking. However, the number of shots usually exceeds 10, since shooting starts below, and ends above the receiver spread. Thus, resorting the data from shot gathers to receiver gathers increases the, now artificial, spread length and increases the consistency of the traveltime picks.

3.2 *Picking traveltimes*

Traveltimes are determined manually by overlaying shots with two different strike directions. Subsequently, all the picked traveltimes are analyzed for their consistency, by ordering them by receiver and source positions. Oftentimes, the picking process follows a number of iterations which improves the underlying traveltime data for the following tomogram calculation.

3.3 *Tomogram calculation*

A SIRT algorithm is used to invert the traveltimes and to produce a shear wave velocity tomogram. Thereby, the residual of the observed and calculated seismic travel times is minimized by a correction of the seismic slowness, i.e. the reciprocal of the seismic velocity in each cell. The calculation is carried out along a 3D grid, with ray bending and the borehole deviation being incorporated in the calculation, Jackson & Tweeton (1996).

4 TEST SITE IN THE NETHERLANDS

4.1 *Test configuration*

A field test was carried out at a site in the Netherlands, close to the German border. Three boreholes were available in an L-shaped arrangement, with each borehole about 30 m deep. The geology at the test site is mainly composed of unconsolidated sediments, i.e. sands, gravel and clay. Both a P-wave tomography and an S-wave tomography survey were carried out with source and receiver intervals of 1 m. A hydrophone string was used to receive P-wave signals and the MBAS was used to receive S-waves.

Due to good transmission properties of the soil, it was decided to use the same source for both the P- and S-wave tomographic measurements. Therefore, the SH-wave source was used for both P- and S-wave measurements. The seismic strike direction was aligned towards the receiver borehole in order to generate P-waves with the highest amplitude. To generate S-waves, the seismic strike direction was aligned perpendicular to the receiver borehole. To acquire the opposite strike direction the source was

rotated by 180°. For each shot direction a separate seismic record was acquired and stored. An example of the collected data is shown in Figure 2.

4.2 *Tomography results*

Seismic traveltimes were picked for P-wave and S-waves. In total about 1800 traveltimes were determined for the P-wave and about 950 travel times for S-wave tomogram. The resulting tomograms are shown in Figure 3 and Figure 4.

4.3 *Calculation of elastic parameters*

Having determined both the P-wave and S-wave tomograms now enables the calculation of elastic soil parameters in 2D, such as the shear modulus G, Young's modulus E, the bulk modulus K and Poisson's ratio.

4.4 *Discussion*

Both P-wave and S-waves have on average a wavelength of about 1 m, indicating that the structural resolution is similar. However, the results show a significantly higher velocity contrast for the S-wave tomograms (factor 3) compared to the P-wave tomograms (factor 1.5). Thus, the soils S-wave velocity structure is imaged in much more detail compared to the structure resolved with the P-wave. Furthermore, the S-wave tomogram covers both the saturated and unsaturated soil, with the water table not influencing the S-wave.

The tomograms also show that the compressional wave velocity and shear wave velocity may not necessarily show the same structures. For example, the P-wave tomogram shows a low velocity zone of only about 1200 m/s in a depth of 6 to 8 m, even though the soil is saturated almost to surface. This low velocity zone is clearly missing in the S-wave tomogram. This may indicate that a high concentration of organic material in this zone decays, thereby producing gases which lower the P-wave velocity substantially, even at low concentrations, Murphy (1982).

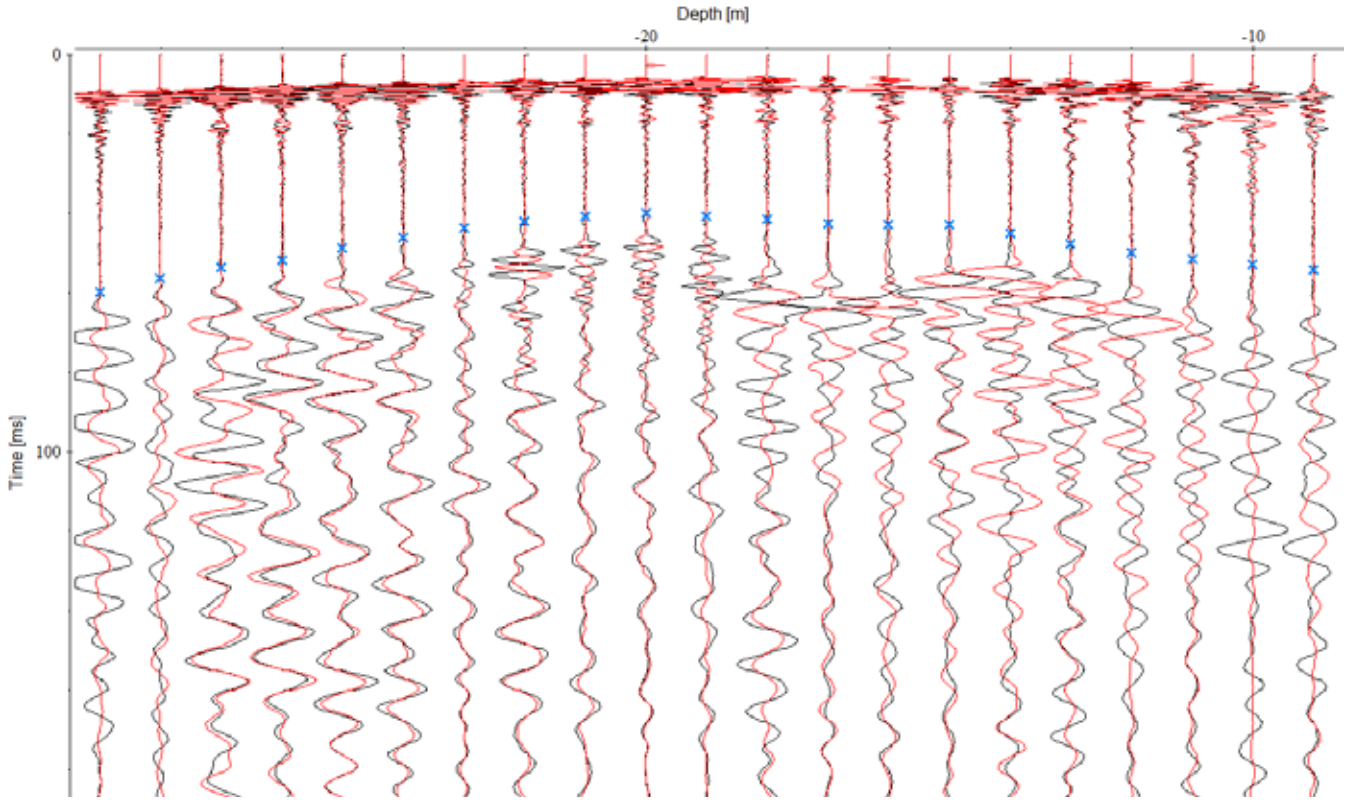

Figure 2. Raw data example from a test site in the Netherlands. The traces are re-sorted and show the horizontal channels of two opposing strike directions. The picked S-wave traveltimes are indicated by the blue crosses.

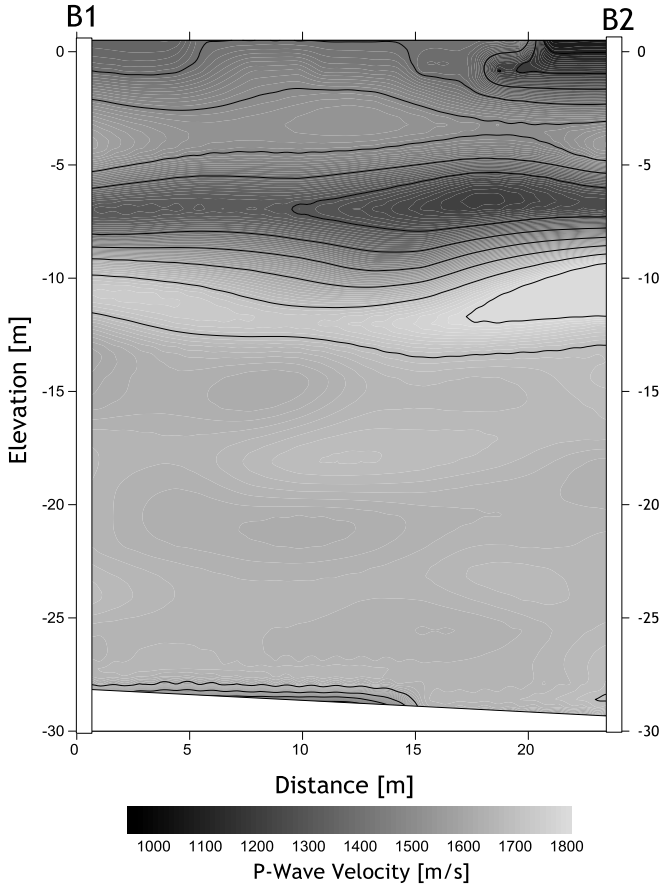

Figure 4. P-wave tomogram from a test site in the Netherlands.

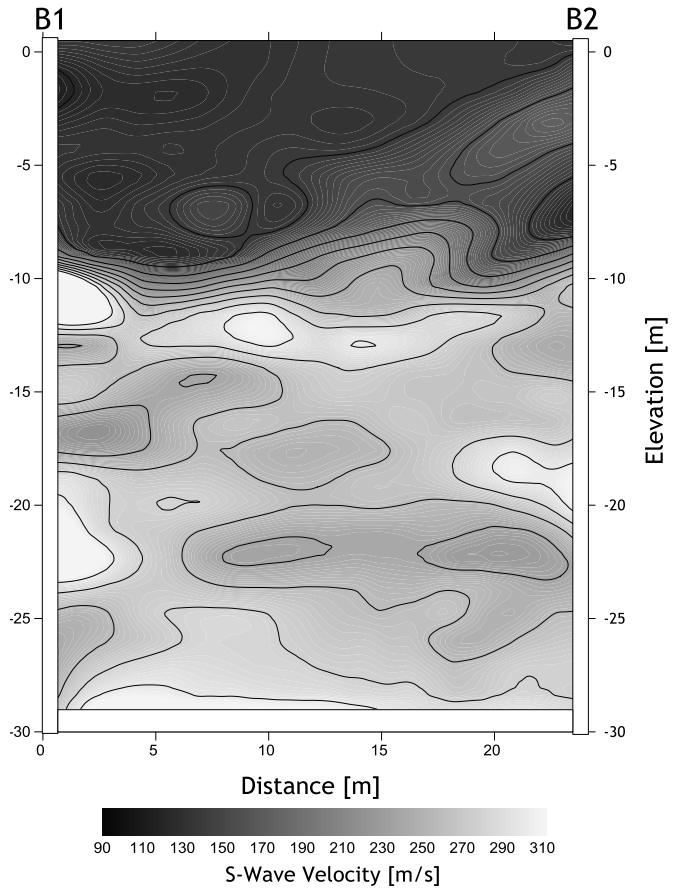

Figure 3. S-wave tomogram from a test site in the Netherlands.

5 CONCLUSION

The results obtained during the experiments show the potential of routinely carrying out S-wave tomography in addition to P-wave tomography. Different lithological structures are detectable and the resolution is generally higher for S-wave tomography due to a higher relative dynamic range compared to P-wave surveys. Carrying out both tomography surveys enables the calculation of several elastic parameters in high resolution and in 2D, among them the shear modulus.

6 REFERENCES

Jackson, M.J. & Tweeton, D.R. 1996. 3DTOM: Three-dimensional geophysical tomography. US Department of the Interior, Bureau of Mines.

Mayne, P.W. 2001. Stress-strain-strength-flow parameters from enhanced in-situ tests. Proceedings, International Conference on In-Situ Measurement of Soil Properties & Case Histories. Bali, Indonesia. May 21-24, 2001. pp. 27-48.

Murphy, W.F. 1982. Effects of partial water saturation on attenuation in Massilon sandstone and Vycor porous glass. The Journal of the Acoustical Society of America. Vol. 71. No. 6. pp. 1458-1467.

Geotechnical and Geophysical Site Characterisation 5 – Lehane, Acosta-Martínez & Kelly (Eds)

Analysis of Active MASW Test Data for a Convergent Shear Wave Velocity Profile

S. S. Kashyap, A.M. Krishna & A. Dey
Indian Institute of Technology Guwahati, India.

ABSTRACT: Shear wave velocity is a direct indicator of stiffness of an isotropic medium which is frequently used to represent the subsurface stratification. Non-invasive seismic survey like Multichannel Analysis of Sur-face Waves (MASW), in both active and passive forms, is widely used in professional practice due to its rapid implementation. Various stages in analysis viz. preprocessing (muting, filtering, etc.), obtaining dispersion curve and inversion govern the accuracy and reliability of final shear wave velocity profile. This paper high-lights the effects of several factors involved in each stage of analysis. Active MASW tests were conducted at a test site with a particular test configuration and the recorded data were analyzed using SurfSeis. The conver-gence study for contributory factors at every stage is carried out for the reliable results. The efficacy of the in-version procedure is highlighted without any a-priori information on the site subsurface stratigraphy.

1 INTRODUCTION

The application of geophysical methods for geotechnical purposes has been appreciated from a few decades. The seismic survey methods which use seismic or elastic waves viz. P-waves, S-waves, Rayleigh waves etc. has their trademark in this area due to its rapid implementation and low cost methodologies. Seismic methods utilize the elastic properties of the medium such as Lame's parameters, shear modulus and elastic modulus to define the wave propagation in the medium. The behavior of waves is delineated to trace back the mechanical properties of the medium. Multichannel Analysis of Surface Waves (MASW) is one of the trending non-invasive seismic method which use the dispersive characteristics of the surface waves with a multi receiver approach for the stratification of, mostly, the assumed vertically heterogeneous subsurface conditions. Active and passive MASW are different forms which are classified based on the source considered for the generation of surface waves (Park *et al.* 1999). MASW was developed over other former surface wave methods of similar approach. They are steady state vibration method (Jones 1955) and spectral analysis of surface waves (Heisey *et al.* 1982). Any application of surface wave methods, including MASW, typically consists of three stages. They are data acquisition, dispersion analysis and inversion. Each stage is dependent on the previous. Data acquisition is related to the acquiring of the response of the subsurface particles due to the energy transmitted. A linear array of 12 or more receivers convert the particle vibration into electric voltage at respective locations. Typically, equipment required for active MASW testing include a sledge hammer as source of energy, geophones as receivers and data acquisition system to qualify and store the acquired data. It is a basic assumption that the subsurface is transversely homogeneous. As wave propagates a lag is expected from one receiver to the next. Dispersion is a property of surface waves that is defined as the dependence of phase velocity on the frequency. In the other words, wave of a particular frequency originating from the source point will traverse certain depth and passes through certain number of layers. The propagation velocity of that particular frequency of wave is decided by the mechanical properties of the layers it traversed through. In this manner, different frequencies are expected to have different phase velocities owing to the fact that they travel through different number of layers. This variation of phase velocity with frequency is called as dispersion (Park *et al.* 1998). Due to reasons such as stiffness reversals and lateral heterogeneities, a wave of a particular frequency may be observed to possess more than one phase velocity. This possession describes the phenomenon of multimodal dispersion (Xia et al 2000). In dispersion imaging scheme, the normalized amplitude is imaged on a 2D plane of phase velocity and frequency. Theoretical dispersion curve obtained from any of the methods available (Ke *et al.* 2011) is optimized towards experimental dispersion curve such that RMS error is minimum. This theoretical

dispersion curve is optimized towards the experimental dispersion curve by updating the model properties such that the RMS error will be minimal, which is achieved through sequential and iterative model parameter updating scheme. The model which lead to the optimized theoretical dispersion curve is decided to be the final model which will be further used to obtain the subsurface stratigraphy profile

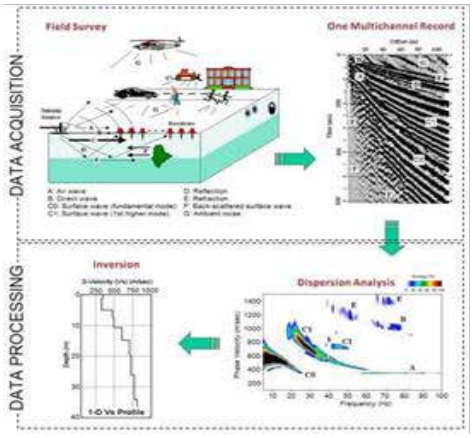

Figure 1. Overall procedure of MASW survey

There are many software available for data analysis i.e. dispersion analysis and inversion. SurfSeis, EasyMASW and Geopsy are the most prominent software available. The present study is based on active MASW tests carried out at Indian Institute of Technology Guwahati, India. The aim of this article is to highlight few of the most important parameters that govern each and every step of the testing and analysis. In the present study, SurfSeis is considered for the analysis. This is a commercially available software developed by Kansas Geological Society. This software is equipped to analyze both 1-D and 2-D data. In the present study, SurfSeis v3.45 is used for the analysis. From the literature and also the software tool methodology, it can be understood that many governing parameters are available. An attempt to decide the parameter or methodology to be considered during testing and analysis such that the solution converges is dealt and reported in this article. Commencing from the time sampling parameters in the field testing to the modeling parameters in inversion, crucial steps had been discussed elaborately. Few of the parameters that are exclusively available during analysis with SurfSeis viz. depth conversion ratio are also discussed. Most of the flaws that are more prone to happen involuntarily especially with SurfSeis are discussed.

2 DATA ACQUISITION DETAILS

2.1 *Site Details*

The study site is located at Indian Institute of Technology Guwahati, India. The site is used as cricket field. The latitude and longitude of the test site are 26.190494^0 and 91.696658^0 respectively. Next to the site, a lake is observed and so the ground water table is expected to be very near to the surface. Available bore logs at the site showed that the water table is at 1.5 to 2m from the ground surface. Other information available regarding the site is that the subsurface mostly contained silty clay and clays.

Figure 2. Satellite image of testing site location

2.2 *Testing Details*

Active MASW testing was conducted at the site specified above. A 10 kg sledge hammer with a steel base plate is used as source of energy. 4.5Hz geophones are used as receivers and a 24 bit data acquisition system is used for acquiring data. Figure 3 shows the linear array of geophones used for testing. Time sampling details of the testing include sampling frequencies of varied range are used for the convergence analysis. 500 Hz, 3750 Hz and 7500 Hz data is extracted at 5120 number of samples. Park *et al.* (2001, 2002) and Zhang *et al.* (2004) are few of the informative documents available for deciding the optimum field parameters. However such optimum parameters are observed to be site dependent. A receiver spacing of 2m was adopted with 24 number of receivers which makes as spread length of 46m. Foti el al. (2015) reported that the availability of a powerful preprocessing tool can sufficiently allow for a nominal near offset distance which efficiently overcomes the possibility of losing surface wave data with extremely larger near offset distances. Hence in the present study, a distance of 4m was used.

Figure 3. Linear array of geophones

2.3 *Time Sampling Parameters*

Time sampling parameters include number of data points to be recorded and sampling frequency. The ratio of number of samples to sampling frequency determines the recording time. The recording time needed depends on the site characteristics. Stiffer stratum lets the wave propagate faster than loose stratum, and hence requires lesser time of acquisition. The effect of the said time sampling parameters can be clearly observed from the amplitude spectra and phase spectra of the data. For 5120 number of samples, the effects of three different sampling frequencies (500 Hz, 3750 Hz and 7500 Hz) are shown in Figure 4 and 5. It can be observed that the total frequency content ranges from 5 Hz to 180 Hz though the effective range may be substantially smaller than this. Within this range the variability generated for the 500 Hz condition is far different from the other two scenarios. This spectrum is found to be very unclear and noisy unlike the other two cases. Similar behavior can be observed in the normalized phase spectrum as well. In comparison to the 500 Hz case, the 7500 and 3750 Hz cases have a nearly linear phase without much distortion. Based on these observations, 7500 Hz sampling frequency was selected for further study. It was observed that the effect of number of samples is negligible on both the phase and amplitude spectra of the data. This is evident from the spectrum of the 7500 Hz sampled data with different samples (5120, 10240 and 20480). All the three conditions are compared and are shown in Figure 6 and 7. In the absence of any substantial variation, in order to maintain the recording to be minimum of 600ms, 5120 number of samples is considered for the testing, choice of which lead to an actual recording time of 683ms.

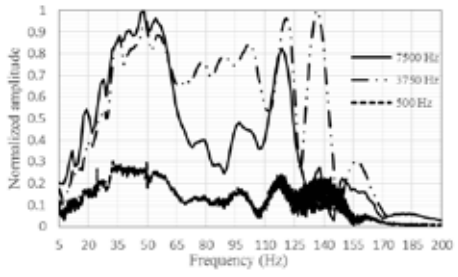

Figure 4. Normalized amplitude spectrum (different sampling frequency)

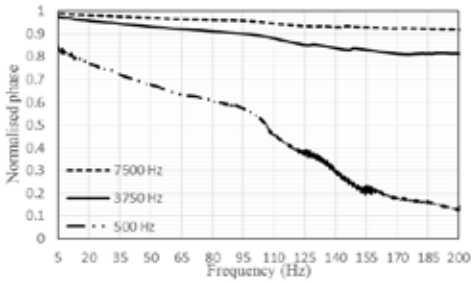

Figure 5. Normalized phase spectrum (different sampling frequency)

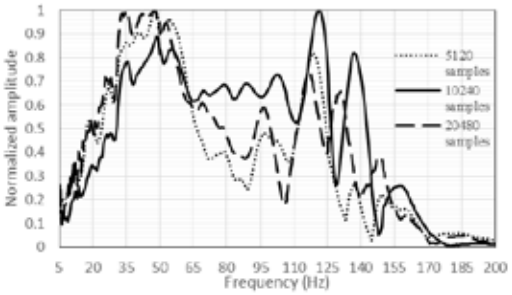

Figure 6. Normalized amplitude spectrum (different samples)

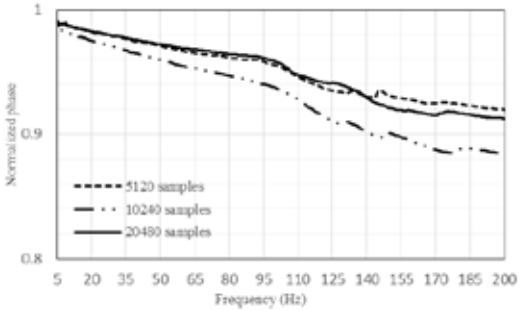

Figure 7. Normalized phase spectrum (different samples)

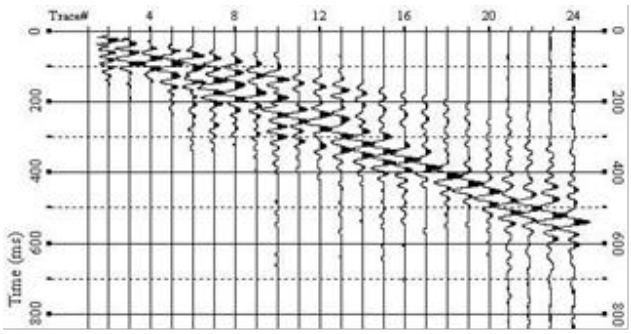

Figure 8. Raw wave field

3 DATA ANALYSIS AND DISCUSSIONS

3.1 *Preprocessing – Muting and Filtering*

Before the development of dispersion image, the raw wave field as in Figure 8 has to be groomed to create a dispersion image of high resolution. This renders the task of extraction of dispersion image (i.e. selection of high amplitude points) more subtle. Muting is one of the preprocessing task which is aimed at muting down the body wave intrusions and other low amplitude noises in the wave field. Muting is performed by selecting a slope on the wave field, above and below of which the events will be muted for top and bottom muting, respectively. In case of higher modes in the wave field, muting has to be carefully done. Filtering is another preprocessing task that is most common in any signal processing applications. The raw wave field is expected to contain both coherent and incoherent noise intruded into the wave field. This can be observed from the irregularities in amplitude and phase spectrum. Filtering reduces the

noise in the signal i.e. increases signal to noise ratio. In SurfSeis, four kinds of filtering are possible viz. low cut, high cut, band stop and band pass. Filtering is done based on the response of the amplitude spectrum to the applied filter. Figure 4 shows that the amplitude spectra for all the cases seem to possess effective content in 5 Hz to 90 Hz. Hence a band pass filter should be perfect for the case. After top and bottom muting and applying a band pass filter of 5-30-60-90 Hz specifications, the wave field appears to be as shown in Figure 9. The effect of preprocessing on the dispersion image can be checked and if any changes are required, the preprocessing can be manipulated at any time.

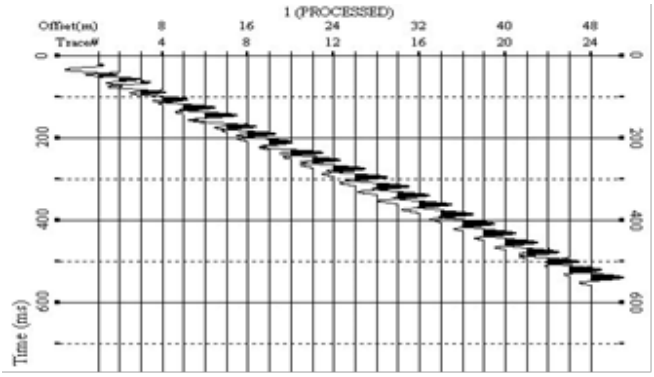

Figure 9. Wave field after preprocessing

3.2 *Dispersion Curve Extraction*

Dispersion image is a three dimensional variation of frequency and phase velocity with summed amplitudes over all the offsets. Generally the amplitudes are normalized and a contour of energy on the frequency-phase velocity plane is considered to be dispersion image. The points of maximum amplitude are selected and inversion is carried out. There are few precautions that are needed to be taken care while extracting the data points. Based on the spread length and the receiver spacing, the respective maximum and minimum wavelengths to be considered for inversion analysis are decided. For the present study the maximum waveleng th of 46 m and minimum wavelength of 2 m. The values are expected to be within this range but not out of the bounds. The data points for inversion are to be selected with in this range for reliable and practically possible results. Within the desired wavelength range peak amplitude points are selected for inversion. Two cases are presented here for understanding the criticality in proper selection of data points. A regular and smooth curve is extracted in one case (Case -1) and an irregular curve is extracted in another case (Case – 2). All the further analyses are carried out for both these cases. The typical dispersion curves and data points selected on them are shown in Figures 10 and 11 respectively. In both the cases the maximum and minimum wave lengths are 38.94m and 5.35m, respectively.

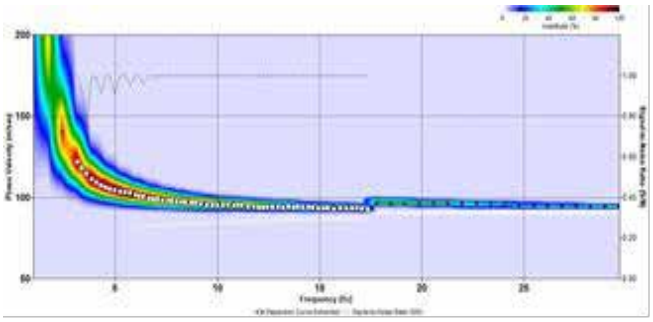

Figure 10. Dispersion curve extraction - smooth trend (Case-1)

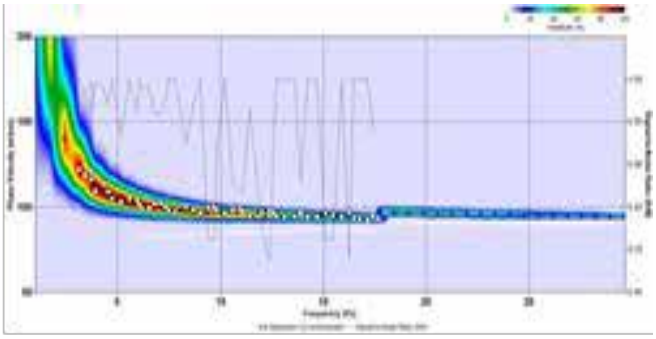

Figure 11. Dispersion curve extraction – irregular trend (Case-2)

3.3 *Inversion Process*

Depth conversion ratio (in percentage) determines the ratio between the wavelength and its corresponding depth of analysis. A 100% DCR indicates that the depth of half-space is equal to maximum wavelength available. A 0% DCR indicates automatic selection of modeling as per Park *et al.* (1999). Hence the variation of final shear wave velocity profiles with different DCR values are compared. All the analyses are carried out with a default 10 layer model in SurfSeis. The RMS errors with respect to phase velocity for each variation in DCR is plotted. Figure 12a and 12b show S-wave velocity variation with depth for different DCR values for case-1 and case-2 dispersion curves, respectively. DCR values from 100% to 60%, which includes practically possible and useful range of depth of analysis are adopted for analysis. In case-1, it can be observed from the figure that all the cases converge up to a depth of around 23m and then variability is seen. But in case-2 the depth decreased to around 12m and even up to 12m, the convergence is not as uniform as seen in case-1. At no depth, the observed variation is more than 10m/s. Owing to Figure 12a, based on the requirement of depth of analysis, any DCR value could be used subject to the condition that the maximum and minimum wavelengths of data points are in comparison with the field configuration adopted. DCR values which represent lesser depths i.e. less than 50% show unacceptable results. This is shown with respect to the RMS error associated as in Figure

13. The figure depicts that for a given change in the initial model (represented in terms of the DCR value), lesser change in the final model is expected which is possible with proper selection of data points and proper choice of DCR values corresponding to the wavelengths available in the data points for inversion.

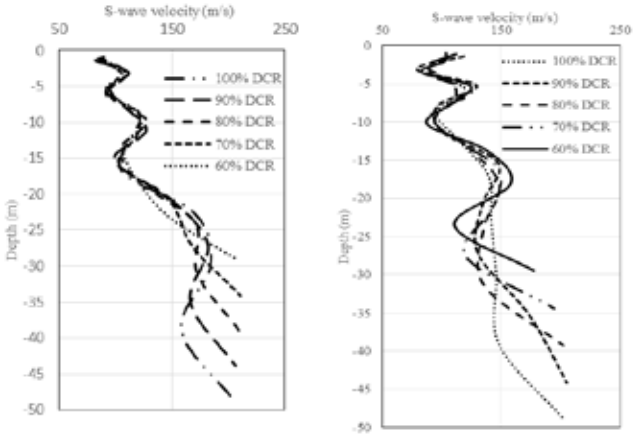

(a) (b)

Figure 12. S-wave velocity variation with depth for different DCR (a) Case-1 (b) Case-2

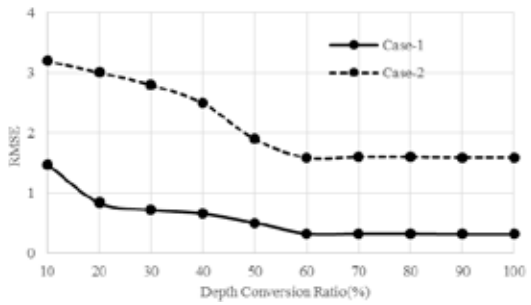

Figure 13. RMSE variation with DCR

In SurfSeis, layer modeling is discontinuous i.e. properties are considered to be constant in each layer of certain thickness. Hence the given depth of half-space will be divided into required number of layers. For the present study, a range from 2 to 20 number of layers are considered in the model for inversion (Maximum and minimum available with SurfSeis). For all the layer conditions 60% DCR is used. From Figure 14, after certain number of layers, there is not much change in the RMSE values and similar was the case with shear wave velocity profiles. Few of the instances are shown in Figure 15a and 15b.

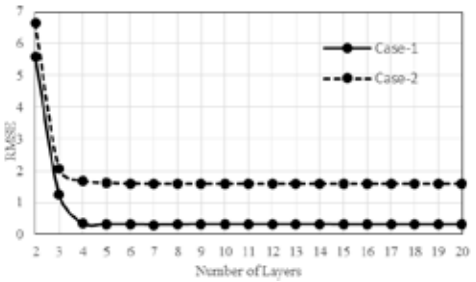

Figure 14. RMSE variation with number of layers

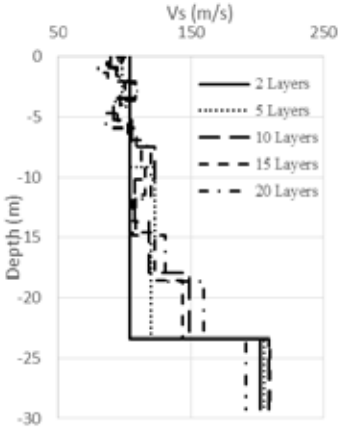

(a)

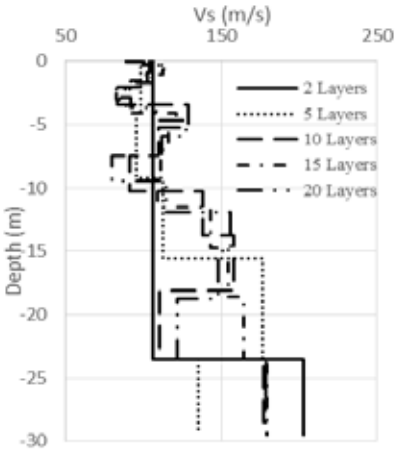

(b)

Figure 15. S-wave velocity variation with depth for different number of layers (a) Case-1 (b) Case-2

When the number of layers are more, there are exists more number of variables and corresponding matrix elements to represent the system accurately. Hence higher number of layers are to be considered for the model though it takes a little more time but acceptable. As expected from the observations in previous section, case-2 has more observed variation than case-1 due to the irregularity in the data points.

Initial models in SurfSeis are generated based on Park *et al.* (1999) as mentioned in manual. Selection of equal thickness model is possible in SurfSeis. The selected depth of half-space will be equally divided into the selected number of layers. For this study, a 60% DCR that corresponds to half-space depth of

around 23m and 15 layers are considered. Both variable and equal thickness models are compared as shown in Figure 16 for both case-1 and case-2. It can be observed from Figure 16a that there is not much difference with either of the model. This is due to the proper dispersion curve extraction. Thickness hence has not much influence on the inversion process if and only if the dispersion curve trend is smoother.

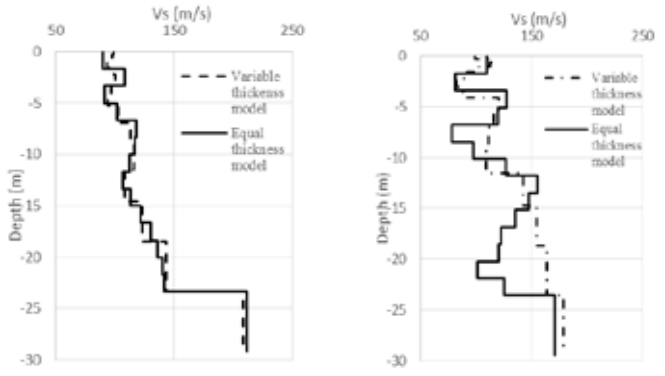

(a) (b)

Figure 16. S-wave velocity variation with depth for different thickness models (a) Case-1 (b) Case-2

4 CONCLUSIONS

An attempt was made to understand the influence of various parameters at different stages of MASW testing and analysis with the leverage of one of the robust and sophisticated tool SurfSeis. It was observed that at any number of samples, higher sampling frequencies provided appealing results. However this can further be understood on continuing the analysis up to dispersion image development. During preprocessing, top and bottom muting and then bandpass filtering was observed to be more useful. During the extraction of data points from the dispersion image, selecting the peaks with a regular and smooth trend is very much necessary. The users had to consider the field configuration adopted while selecting the maximum and minimum wavelength points for inversion. If the data points are in the practical limits, any DCR value would give a reliable result and it is up to the user to adopt a particular DCR value. Zero DCR would not always provide accurate results and so required DCR value is to be adopted. Number of layers adopted in the discontinuous model also govern the robustness and uniqueness of the final profile. Greater the number of layers, greater the number of unknowns and equations to solve and so greater will be the convergence. A variable thickness and an equal thickness models are compared at 60% DCR and 15 number of layers. They are almost matching with each other in case of a regular trend, ascertaining that thickness is not an important parameter for inversion. It can be discerned that selection of data points is one of the most critical steps in analysis. A perfectly extracted dispersion curve with regular and smooth trend within the correct wavelength limits would provide a convergent and robust final shear wave velocity profile.

5 REFERENCES

Foti, S., Lai, C.G., Rix, G.J., Strobbia, C. 2015. *Surface Wave Methods for Near-Surface Site Characterization*. Boca Raton: CRC Press.

Heisey, J.S., Stokoe II, K.H., and Meyer, A.H. 1982. *Moduli of pavement systems from Spectral Analysis of Surface Waves.* Transportation Research Record (852): 22-31.

Jones, R. 1955. *A Vibration Method for Measuring the Thickness of Concrete Slab In-Situ.* Magazine of Concrete Research (7): 97-102.

Ke, G., Dong. H., Kristensen, A., and Thompson, M. 2011. *Modified Thomson–Haskell Matrix Methods for Surface-Wave Dispersion-Curve Calculation and Their Accelerated Root-Searching Schemes.* Bulletin of the Seismological Society of America. 110(4):1692-1703.

Park, C.B., Miller, R.D., and Xia, J. 1998. *Imaging dispersion curves of surface waves on multi-channel record.* 68th Annual International Meeting of Society of Exploration Geophysics. Expanded Abstracts:1377-1380.

Park, C.B., Miller, R.D., and Xia, J., 1999. *Multichannel analysis of surface waves.* Geophysics:64(3):800-808.

Park, C.B., Miller, R.D., and Xia, J. 2001. *Offset and resolution of dispersion curve in multichannel analysis of surface waves (MASW).* Proceedings of the SAGEEP. Denver.

Park, C.B., Miller, D.M., and Miura, H. 2002. *Optimum field parameters of an MASW survey*. Proceedings of the 6th SEG-J International Symposium. Tokyo:22–23.

Park, C.B., R.D. Miller, J. Xia, and J. Ivanov. 2007. *Multichannel Analysis of Surface Waves (MASW) - Active and Passive Methods.* The Leading Edge. January.

Xia, J., Miller, R.D., and Park, C.B. 1999. *Estimation of near-surface shear-wave velocity by inversion of Rayleigh waves.* Geophysics. 64(3):691-700.

Zhang, S.X., Chan, L.S., and Xia, J. 2004. *The Selection of Field Acquisition Parameters for Dispersion Images from Multichannel Surface Wave Data.* Pure Application Geophysics (161):185-201.

Geotechnical and Geophysical Site Characterisation 5 – Lehane, Acosta-Martínez & Kelly (Eds)

Development of an unmanned aircraft mounted software defined ground penetrating radar

J. F. Fitter, A. B. McCallum & J. X. Leon
University of the Sunshine Coast, Sippy Downs, Australia

ABSTRACT*:* UAV technology is rapidly developing and increased payloads are available from more affordable platforms. Similarly, the development of Software Defined Radio (SDR) technology provides opportunities for configuration of lightweight and low-cost ground-penetrating radar (GPR) systems. (McCallum and Fairweather, 2013) briefly discussed the potential for UAV-mounted GPR systems for remote area glaciology. This discussion paper builds upon that work and examines the contemporary viability of UAV-mounted SDR GPR systems for site investigation of remote area or inaccessible geo-materials.

1 INTRODUCTION

1.1 *Background*

The use of unmanned aircraft ('drones') for commercial and scientific purposes has increased significantly in recent years, due largely to improvements in motion sensors, power systems, and digital processing capacity. Small drones configured as multicopters are of particular interest for geophysical survey in hazardous locations. They are portable, easily deployed, simple to operate, extremely stable, and due to their low cost, expendable. However, drones have numerous operational and performance limitations that need to be managed if they are to be used successfully for survey tasks.

Motion and position sensors used in small drones are prone to high levels of noise and drift, power systems generally allow only missions of short duration with very limited payload capacity, and power systems are often severely affected by environmental conditions, such as temperature extremes. Wind and turbulence influence small drones more than larger aircraft adding further constraints to any planned mission profile.

Despite these limitations small drones are extremely agile and can operate in environments hazardous to humans, close to obstacles, under conditions of poor visibility, and with low mission overhead. Being low capital cost items, they can be considered expendable and can therefore be operated with lower safety margins than larger, more costly drones or manned aircraft. In summary, the small drone is capable of performing some tasks that would be impossible, impractical, unsafe, or uneconomic to perform utilizing a larger drone or manned aircraft.

This research focuses on exploiting the operational and logistical advantages of using small drones to conduct geophysical surveys over hazardous terrain. We also examine the impact on these tasks of the operational and technical limitations of small drones.

1.2 *Drone Specification*

The desired specifications for drones under consideration are as follows:

- Small, portable, and able to be handled by a single person.
- Total weight below the industry accepted limit for manual handling of 14kg.
- Easily deployed with low maintenance requirements.
- Easily transportable by air or land vehicle.
- Medium payload capability of approximately 5kg.
- Mission endurance capability of over 1 hour.
- Exceptionally stable to optimise sensor performance.
- Able to operate in harsh or cold environments.
- Low operator skills required.

1.3 *GPR Specification*

The desired specification of the GPR for the study is as follows:

- Compact and lightweight.
- Power consumption below 20W.
- Total payload cost under $5K.
- Resolution (1m resolution at 10m depth is the initial desired goal).
- Local data storage of over 1TB.
- Rapidly re-configurable.
- Precise positioning and tracking even in the absence of visible GPS satellites.

– Telemetry for essential flight/sensor data.

1.4 *Software Defined Radio*

"Software Defined Radio" (SDR) describes a radio system in which many of the signal processing components, traditionally implemented in hardware, are instead implemented in software using either general purpose embedded processors or application specific digital signal processors.

Direct digital sampling and reconstruction of the radio frequency signal would define the ideal SDR, however, technology limitations presently preclude the realization of this technique. Modern SDRs utilize existing hardware methods such as oscillators, mixers, and filters to facilitate the conversion of the RF signal to and from an intermediate frequency, or baseband. Digital techniques implemented in software and utilizing high speed wideband analog to digital and digital to analog converters perform the processing of the baseband signal.

SDRs typically available for non-military research purposes fall into the category of *"scientific and amateur use"*. These radios utilize a direct conversion receiver based on a quadrature sampling detector and quadrature sampling exciter, high performance wide dynamic range analog to digital converters and high speed digital signal processors, often aided by non-clocked processors such as programmable gate arrays. Advantages of using SDR for this research include:

– Wide bandwidth available on the newest generation of SDRs.
– Effective use of software-defined antennas is possible through the tight integration of the radio management software and the antenna definition.
– Control of transmitted power and bandwidth utilization.
– Flexible modulation schemes and baseband processing.
– Ability to perform adaptive signal generation and processing.

(Ralston and Hargrave, 2012) explored the practicality of SDR technology to implement GPR and the challenges of ensuring sufficient bandwidth, timing accuracy, and power budget. They conclude that GPR development has a rich future as hardware becomes more available, lower cost, and higher performance. In the four years since they published, much of this has come to fruition, and practical, high performance GPR with useful penetration and imaging performance is now possible (circa 2016).

Early work on the practical realization of GPR with SDR include (Patton, 2007) whose successful construction of a GPR based on an Ettus Research USRP1 with RFX2400 daughterboard and Gnu Radio open source software highlighted the performance limitations of this hardware with respect to instantaneous bandwidth and RX/TX isolation. Subsequent works using more recent hardware have addressed these limitations. In particular (Salvador et al., 2013) realized a high performance GPR using an Ettus Research USRP N210 and National Instruments LabView software capable of generating signal bandwidths to 10MHz over a carrier frequency range of 400MHz through to 4GHz. A recently introduced product, the Ettus Research USRP B200Mini extends this performance significantly while reducing the size of the hardware to credit card size and the power consumption to levels that can be accommodated by a small drone.

While NI LabView is an excellent tool for SDR laboratory development, GNU Radio offers lower overhead and the ability to run under Linux enabling the use of a wide selection of very small, low power, high performance single board computers, ideal for integration into a small drone.

1.5 *Envisaged Method*

Sources of measurement error will be examined with reference to how these errors are generated and propagated by the control hardware and motion dynamics of a small drone. How these errors could be mitigated through innovative engineering and software design will also be investigated. Simulations will be performed at a task level for both the GPR task and the flight dynamics and positioning of the drone, for the purpose of establishing baseline performance capability prior to field testing. Analysis of the simulation results will be used to design optimised sensors and antennas, specify GPR operating parameters, and determine desired specifications for the flight dynamics and positioning capability of the drone. A drone will be configured to these specifications and field tests performed to validate the theoretical concepts.

A structured, parameterized method will be developed to enable a small drone to be configured to match a specific sensor based survey task and mission profile. This method will initially be developed for the use of GPR only. However, the extension of the method to other sensors is discussed, and will likely form the basis of future research.

2 METHODOLOGY

2.1 *Introduction*

For the purpose of this research a GPR was configured using an Ettus Research USRP B200Mini and GNU Radio, an open-source software development toolkit that provides signal processing blocks to implement software defined radios. The software was supported on an Odroid single board computer running the Linux operating system. For the initial basic research the GPR was configured to transmit broadband Ricker pulses using a simple dipole antenna.

Before GPR trials were commenced the characteristics of an optimum multicopter drone sensor platform were examined. These include:

- Endurance modelling.
- Stability.
- Positioning and geo-referencing.
- A review of electric power systems.

2.2 *Endurance modelling*

For research and data acquisition purposes, the most common figure of merit is the maximum mission endurance with some pre-defined payload. There is little benefit in fitting a drone with a sophisticated and capable sensor if the drone itself is not capable of achieving a mission profile that will yield useful quantities of scientific data. Many factors contribute to this capability; however endurance is a key factor and a high priority for research.

Conceptually it would appear that increasing the endurance of the multicopter would merely require increasing the capacity of the battery, however this does not necessarily work. A larger battery weighs more and needs larger motors to lift it, and the larger propellers necessitate a larger airframe, which must also be more rigid to manage the additional power from the larger motors. The increased power drain from the larger motors negates the expected increase in endurance.

There is a limit to the endurance potential of a conventional multicopter, and attempts to increase endurance beyond that limit result in rapid weight increases and endurance decreases. In order to assess the endurance limit quantitatively, a theoretical model of a multicopter was developed and the results of the model analysed for various values of motor specific power, motor constant, and battery specific energy.

Studies of drone endurance have been conducted, notably (Gatti et al., 2015) and (Abdilla et al., 2015). In (Gatti et al., 2015) an endurance expression is derived as a function of known airframe parameters and derived figures of merit for various components. Battery capacity is estimated using Peukert's equation, and although it is questionable whether this is the best option for LiPo batteries (Doerffel and Sharkh, 2006), it nevertheless makes little difference to the results. In (Abdilla et al., 2015) the propellers are modelled using momentum theory in addition to including a large number of known parameters specific to particular drones.

In both of these studies, endurance was estimated based on specific and well defined design parameters. Analysis conducted in this research project estimates the endurance of a drone of unknown design with very few provided design parameters. The analytical procedure itself designs the optimum drone based on a few provided parameters, and therefore the question being answered is not "what is the endurance of this (defined) drone?", rather it is "what kind of drone has this (defined) endurance?". It is therefore unsurprising that the results of the modelling will yield greater endurance for a specified weight drone than that predicted in the aforementioned studies which are based on experimental results using real drones. The real drones are not necessarily optimised designs whereas the modelling presented here derives an optimum design. Nevertheless, the shapes of the Endurance vs Weight curves are similar in all of the studies.

Figure 1 is an example output from the modelling, in this case for 100KV motors, showing an Endurance vs Weight relationship typical of that found by other researchers.

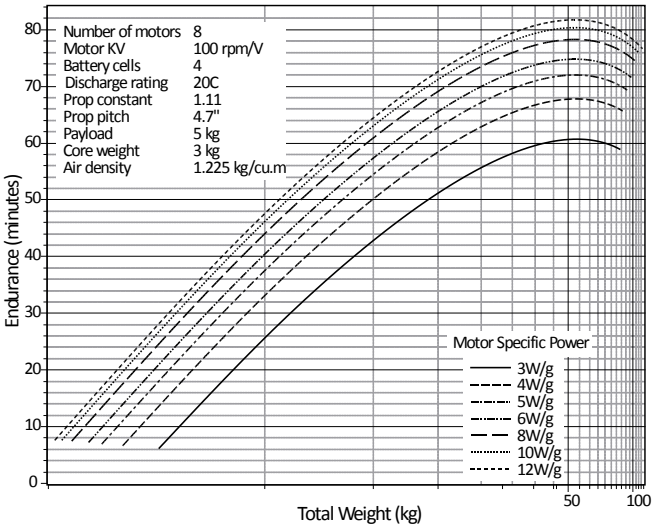

Figure 1 Endurance vs Total Weight for 100KV motors of various specific powers.

A conventional *"rule of thumb"* for multicopter design is that the maximum battery weight should not exceed the bare airframe weight. This is clearly demonstrated in the results of the modelling, Figure 2, and is similar to the experimental results of (Gatti et al., 2015) obtained using small commercially available quadrotor drones.

3 STABILITY

When discussing the mounting of a sensor on a drone it is necessary to consider the influence of the drone motion dynamics on the performance of the sensor and as a source of sensor error. The control and stability of a drone is based on inputs from motion and position transducers. In the case of small drones, these transducers are generally low cost consumer grade components and are rarely designed for avionics applications, instead being mainly targeted to mobile phone, automotive, and computer pointing device applications. These transducers are prone to rapid drift and high levels of noise

Transducer errors will add to the inherent errors of the sensor, therefore it is important to understand the nature and magnitude of these errors in order to either

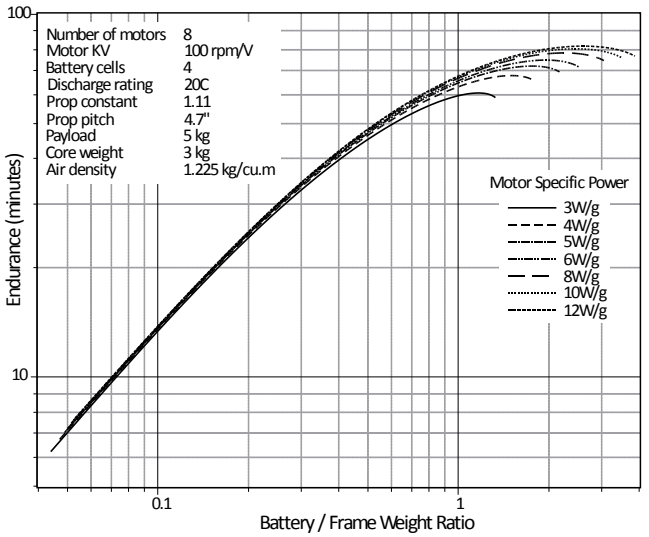

Figure 2 Endurance vs Battery/Frame Weight Ratio for 100KV motors and various specific powers.

correct the sensor data, to make an informed selection of suitable sensors that may not need correction at all, or to incorporate sensor mounting arrangements that limit the propagation of these errors, including the option to mount the sensor on an independently driven motion platform, or gimbal.

An additional design consideration in the case of a gimbal mounted sensor is that powerful gimbal motors and a high moment of inertia sensor can adversely affect the stability of the drone.

Studies into the influence of drone stability are currently ongoing with no publishable results yet available.

3.1 *Positioning and Geo-referencing*

Key to any survey task intended to gather scientific data is the ability to precisely define the location of the sensor in the world coordinate frame. In the modern environment this can be accomplished by the use of the global positioning system (GPS). Recent advances in receiver and antenna design in addition to the use of multiple receivers and differential techniques has yielded positional accuracies in the centimetre scale.

For surveys in locations where GPS cannot be used or is inaccurate such as in polar regions, other positioning methods must be investigated. The placement of markers and VSLAM navigation techniques offer potential worthy of further investigation.

3.2 *A review of electric power systems*

Small portable drones are generally powered by 3-phase brushless DC motors and this research will focus on such drones. These motors have very high power to weight ratios, are reliable and robust, require very little maintenance, and operate without the residue and exhaust associated with internal combustion motors. The limitation of electric motors is the need to carry a source of electrical energy, either stored energy in the form of a battery, or an energy generator such as a chemical fuel cell.

Modelling of maximum achievable endurance against energy source specific energy indicates, as would be expected, a linear relationship, as shown in Figure 3

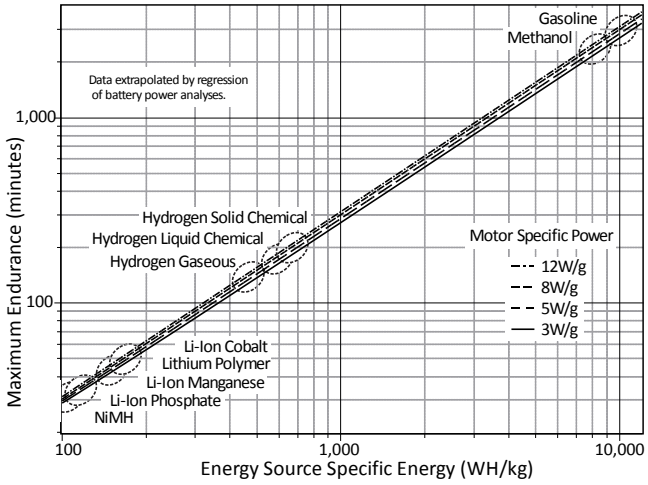

Figure 3 Endurance of Multicopter for various Energy sources.

It should be noted that the battery specific energies used in modern small multicopters are in the region of 150 to 200WH/kg. Gasoline has a specific energy of 12,000WH/kg and the specific energy of Ethanol is 8,000WH/kg. Assuming a mechanical efficiency of around 40% for internal combustion engines, the effective specific energies are 4,00WH/kg and 3,200WH/kg respectively. Both of these fuels are used frequently in drones powered by piston engines, especially helicopters and fixed wing drones. Piston engines are almost never used in multicopters due to the mechanical complexity of the drive train and complex vibration issues consequently resulting in high cost and low mechanical reliability.

Since the region from 150 to 200WH/kg represents over 30 years of incremental technological development, it would seem logical to search for alternative energy sources for short term solutions to the limited endurance of multicopters.

A promising alternative is the polymer electrolyte membrane hydrogen fuel cell (PEM HFC) stack. Presently available commercial lightweight systems offer specific energies of 400WH/kg and newer systems under development are offering in excess of 700WH/kg.

3.2.1 *Lithium Ion Polymer pouch cells*

The Lithium Ion Polymer pouch cell is a conventional LiIon chemistry cell, often with the addition of an electrolyte plasticiser, encased in a flexible polymer pouch.

Released onto the general market circa 1995 and colloquially referred to as LiPo cells, their extremely

high energy density foresaw a revolution in electric power for drones and other small unmanned aircraft.

The pouch cell offers a simple, flexible and lightweight solution to battery design, but with certain caveats. LiPo cells are sensitive to high humidity and temperature extremes above 60C and below -5C, all of which can shorten service life considerably. Charging below 5C or above 40C is dangerous, as is overcharging. Misuse can result in internal changes that may lead to explosion and fire, even after the use of the cell has ceased.

It is for these reasons that carriage of LiPo cells on commercial transport is severely restricted, which is a problem for a scientific research apparatus designed to be taken to remote locations anywhere on the earth.

3.2.2 *Lithium Ion cylindrical cells*

Li-Ion cylindrical cells, in particular the 18650 size, have been the subject of much research in recent years due to their increasing use in power tools, automotive vehicles, and domestic solar energy storage systems. Their advantage over Li-Ion pouch cells is higher specific energy, more robust construction, greater safety, and the ease of multi-cell assembly. Because the cell is contained within a rigid cylindrical metal enclosure the normal expansion resulting from gas liberation at high states-of-charge experienced by lithium cells does not cause operational problems.

Presently available commercial cells have specific energy ratings from 180 to 220WH/kg.

Because multicopters have high average current demands the major obstacle to the use of cylindrical Li-Ion cells is their high internal resistance relative to LiPo pouch cells, however with ongoing development the difference is decreasing and Li-Ion cylindrical cells are becoming a viable energy source for multicopters

3.2.3 *PEM Hydrogen Fuel Cell stack*

Recent advances in light weight hydrogen fuel cell technology have made practical the application of these power sources to unmanned aircraft (HES, 2016). Currently available systems fall into three categories:

- Gaseous hydrogen. These systems feature the lowest operating cost and are the best solution for large drones, in particular aeroplanes, however they are bulky and require a large aircraft to house them. Specific energy is around 450Wh/kg
- Liquid chemical fuel. These systems are generally lighter than the gaseous fuel systems and the fuel is easier to handle, however a reactor is needed to convert the fuel to pure hydrogen. Specific energy is 450Wh/kg but there is a progressive reduction in fuel weight throughout the flight enabling an overall specific energy up to 650Wh/kg. Fuel weight is approximately 1kWh/kg.
- Solid chemical fuel. No reactor is needed and the cartridges operate without a catalyst and without releasing any waste by-product. These systems are capable of achieving specific energies in excess of 700Wh/kg

Currently available HFC systems suitable for unmanned aircraft, though capable of great endurance, have limited on-demand current source capability. A 2kg fuel cell stack is able to deliver a maximum continuous current of 40A, which is acceptable for appropriately designed aeroplanes but inadequate for multicopters, which typically have very high continuous current demands.

A significant advantage that HFCs have over LiPo batteries is that they can operate efficiently at temperatures below those at which LiPo batteries are impractical. HFCs can be "winterized" to operate down to -5C, but more importantly their performance is predictable at these low temperatures, unlike LiPo performance.

Despite the limitations of HFCs for use on multicopters, the potential exists for endurance increases of a factor of two or more over existing lithium batteries, and this is therefore considered a fruitful area of research.

4 EXPECTED OUTCOMES

A key objective of this research is build a multicopter sensor platform fitted with a SDR GPR, flight control and power management systems, and scientific data management facilities. This multicopter will be the basis for further development of the SDR, the antenna, and associated data processing tasks.

4.1 *Costs*

Basic research is not expensive. Commercial quality multicopters generally cost less than AUD10K (circa 2016) and SDRs are under AUD5K. Lightweight, high performance embedded processors are available for less than AUD1K, such as the Odroid XU4 and the UDOO x86, either of which is capable of running the SDR in addition to processing the data from it and handling telemetry tasks. All software tools are available through the *"Open source"* community which offers quality tools and an open, cooperative development environment.

4.2 *BOM*

- 1.5M CFRP Octacopter airframe with 8 BLDC motors, speed controllers, and CFRP propellers (SteadiDrone).
- Flight control system with 32bit high speed embedded controller and high reliability RTOS (PixHawk)
- 2.4GHz radio control system for manual control (Multiplex Profi 5000).
- BLDC motor driven gimbal (generic).

- Ground control station consisting of a laptop computer and telemetry receiver/transmitter.
- SDR development hardware (Ettus Research USRP B200Mini and various test antennae).
- General purpose embedded computer (UDOO x86 with 2.6GHz dual core Intel processor).
- 5.2GHz HDMI video transmitter and receiver for cable free development (Nyrius Aries Pro).

5 CONCLUSION

The viability of using small electrically powered drones for scientific and geophysical survey tasks is dependent on two factors. The first is the ability of the drone to perform the mission to a standard required by the sensor systems in use. This implies sufficient flight endurance, stability, and positioning precision to enable the acquisition of quality data. The second is the availability of lightweight, low power sensor systems that can deliver survey data to a defined level of quality.

Multicopters, power systems, and the sensors required to meet these specifications are in early stages of development and there is yet considerable research to be done before small multicopters will be able to conduct practical scientific surveys.

6 REFERENCES

Abdilla, A., Richards, A. & Burrow, S. Power and Endurance Modelling of Battery-Powered Rotorcraft. *2015 IEEE/RSJ International Conference on Intelligent Robots and Systems (IROS), 2015 2015* Hamburg, Germany.

Doerffel, D. & Sharkh, S. A. 2006. A critical review of using the Peukert equation for determining the remaining capacity of lead-acid and lithium-ion batteries. *Journal of Power Sources,* 155**,** 395-400.

Gatti, M., Giulietti, F. & Turci, M. 2015. Maximum endurance for battery-powered rotary-wing aircraft. *Aerospace Science and Technology,* 45**,** 174-179.

HES. 2016. *HES Energy Systems Pty. Ltd.* [Online]. http://www.hes.sg/#!in-the-air/c15wk.

McCallum, A. B. & Fairweather, H. 2013. UAV-mounted GPR for remote area radioglaciology.

Patton, L. K. 2007. *A GNU radio based software-defined radar.* MSc (Engineering), Wright State University.

Ralston, J. & Hargrave, C. Software defined radar: An open source platform for prototype GPR development. *14th International Conference on Ground Penetrating Radar (GPR), 2012* Shanghai, China. 172-177.

Salvador, M. J., Jimenez, V., Lopez, R. G. & Von Borries, R. Platform for research and education on ground penetrating radar. *Proceedings of SPIE - The International Society for Optical Engineering 2013.*

Geotechnical and Geophysical Site Characterisation 5 – Lehane, Acosta-Martínez & Kelly (Eds)

Simplified seismic soil classification: the velocity-frequency-impedance (VfZ) matrix

S. Castellaro
Dep. Physics and Astronomy, University of Bologna, Italy

ABSTRACT: Site effect assessment studies aim at predicting the effect of seismic shaking on structures by modeling the subsoil as an oscillator coupled to another oscillator representing the construction. The resulting amplification functions and response spectra depend on so many strong assumptions and parameters that, in the standard engineering practice, simplified seismic classifications appear preferable to complex modeling procedures which can only offer an illusory better accuracy. Since stratigraphic seismic amplification is not related to the absolute rigidity of subsoil but to impedance contrasts, the standard simplified approaches based on the 'average' rigidity of subsoil in the first few meters (e.g. Vs30) can hardly be effective. Here it is proposed a simplified soil classification approach that takes into account the basic Physics of seismic amplification and its parameters, i.e. the average shear wave velocity of the cover layer, the resonance frequency and the impedance contrast between the cover and the bedrock, which we summarize as VfZ. A possible classification approach is illustrated through a set of examples.

1 INTRODUCTION

The assessment of seismic site effects at the scale of urban planning (shake maps, seismic microzonation) or at the scale of the single construction (building codes) requires the knowledge of the mechanical properties of subsoil down to the bedrock and of the 'characteristic' bedrock motion expected at the site. As output, it normally provides the SH-wave bedrock-to-surface amplification function - that is the ratio between the Fourier spectra of the accelerogram on the surface and on the bedrock - and the response spectrum - that is the expected maximum acceleration/velocity/displacement on a single degree of freedom oscillator of a specified damping and eigen-period, which mimics the behavior of a building. The first function mostly depends on the subsoil properties, while the latter is dependent on the input ground motion.
Determining the input needed for this kind of analysis requires the measurement of a large number of parameters (P and S-wave velocity profile down to the bedrock, density profile, depth of the water table, shear modulus dependence with strain, etc.) and the analysis itself is based on several assumptions, such as the existence of a characteristic earthquake and the dominance of vertically propagating SH-waves, which are in many cases contrary to available evidence.
As a consequence, taking into account all uncertainties associated to the inputs, reveals the huge uncertainty associated to the output of the current numerical modelling procedures.
The need for quick simplified alternatives to seismic soil response assessment for the standard daily practice appears scientifically justified. Despite a number of approaches presented in the literature, at present, the best known simplified procedure is based on Vs30, that is the shear-wave velocity of a homogeneous layer equivalent to the first 30 m depth, which is used as a proxy to the SH amplification factor, i.e. the maximum of the amplification function (Borcherdt, 1994). This approach, which was developed on a purely empirical basis, has been shown to suffer from statistical (Castellaro *et al*., 2008) and physical problems (Lee and Trifunac, 2010).
In this paper we try to cast the basis for an alternative simplified approach by first assessing what are the minimum physical parameters necessary to quantify seismic stratigraphic amplification. Then we show that the same effort currently used to measure Vs30 can produce subsoil classifications based on more physically meaningful parameters.

2 WHAT CONTROLS STRATIGRAPHIC SEISMIC AMPLIFICATION?

Seismic amplification has several causes (Anderson, 2007), the most important of which is stratigraphic amplification. This is due to the existence of impedance contrasts ($Z = \rho V$, density x seismic wave velocity) in the subsoil (Aki e Richards, 1980), which rule seismic wave reflection and transmission at the interfaces, determining wave interference and 'guided wave' effects.

At a specified frequency, amplification would theoretically be given by the ratio between the seismic impedance at the source depth Z_0 and the impedance averaged over the quarter-wavelength depth $\langle Z_i \rangle$ (Joyner *et al*., 1981; Day, 1986). It is therefore clear that it is not the *absolute* Vs value that controls seismic amplification but the size of the impedance contrast.

3 THE VFZ APPROACH

In order to characterize how seismic amplification is related to impedance contrasts, we study the 1D equivalent linear response of 600 subsoil models characterized by different levels of impedance contrasts (cover layer vs. bedrock) at different depths and different absolute stiffness.

In the modeling we used the same shear modulus and damping vs. strain curves. The specific choice of these curves clearly affects the fundamental mode amplitude and the amplitude decay of higher modes of the amplification function but the absolute values are not of primary interest in a methodological paper like the present one.

To avoid the incongruence of using whole accelerograms to model input motion, and in order to minimize the number of variables, the input motion function (the earthquake) is kept as simple as possible assuming it as a Ricker wavelet with frequency of 1 Hz and 0.5 Hz. This represents the onset of the SH-wave of intermediate-small and intermediate-large earthquakes, respectively. PGA_0 is set equal to 0.35 g. The 1D equivalent-linear site response simulations for the 585 models is run by using the computer code for equivalent linear earthquake site response analysis of layered soils by Bardet *et al.* (2000).

Let us now plot only the maximum amplification for each tested Vs of the cover layer as a function of its frequency of occurrence, which depends on the bedrock depth and we obtain the plots shown in Fig. 1. Each line in these plots connects the points characterized by the same impedance contrast between the cover layer and the bedrock. These are slices of a 4D function of the type: $Fa = f(\langle Vs \rangle, f_0, Z)$.

This function, only graphically defined, allows to get a quick estimate of the maximum SH-wave amplification factor Fa from the average <Vs> of the cover layer, its resonance frequency f_0 and the impedance contrast Z between the cover layer and the bedock.

<Vs>, f_0 e Z (or VfZ) constitute the minimal physical basis for a simplified classification of the stratigraphic site amplification potential.

It is to be noted that the absolute values of Fa depend on many other variables not explicitly considered in the modeling. Fig. 1 is therefore to be read only in relative sense (high or low amplification).

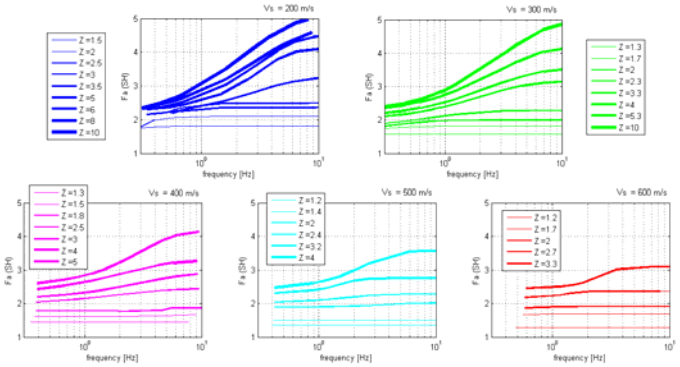

Figure. 1. Amplification factors for the SH wave expected at the resonance frequency as a function of Vs of the cover layer and of the impedance contrasts Z (for simplicity, Z is the simply the ratio between the Vs of two layers, being density the same for all layers). The input motion used for the calculation is a Ricker wavelet with 1 s period. The Fa values must be interpreted only as relative (not in absolute sense) because they depend on many other variables and assumptions.

4 VFZ VS VS30

It is not our intention to set boundaries between new seismic site classes. However, let us discuss what would potentially be the benefits of a subsoil classification based on <Vs>, f_0 e Z rather than on Vs30.

VfZ

We group our 585 soil modes in terms of the expected amplification at low (< 1 Hz) or high frequency (≥ 1 Hz) and in terms of low (< 1.5), intermediate (1.5-2) and high (> 2) amplification. We name these classes C1, C2, … C6 as shown in Fig. 2. The effects of the proposed classification (Fig.2 on the response spectra for an input ground motion Ricker wavelet with frequency 1 Hz are given in Fig. 3. We find that the maximum acceleration in the response spectrum is expected on soils with Fa ≥ 2 and f_0 ≥ 1 Hz, which is intuitive. The minimum acceleration is expected on soils with Fa < 1.5 and f_0 < 1 Hz.

For the 0.5 Hz input motion, the maximum acceleration is expected on soil classes with Fa ≥ 2 and f_0 < 1 Hz, which is again intuitive. The minimum ac-

celeration is expected on soils with Fa < 1.5 and $f_0 \geq$ 1 Hz.

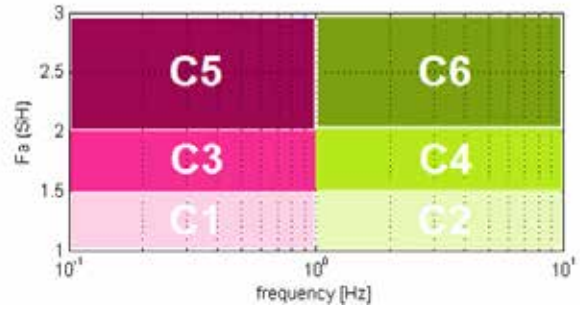

Figure. 2. Example of seismic site classes defined on the basis of the expected amplification frequency (odd classes: $f_0 < 1$ Hz; even classes: $f_0 \geq$ 1Hz) and value (Fa).

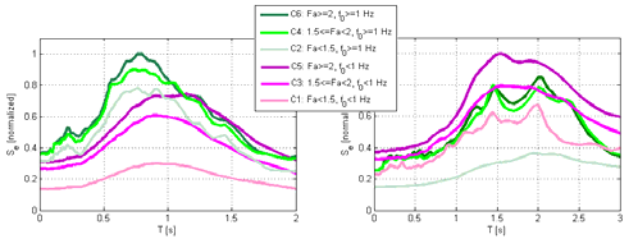

Figure. 3. Average response spectra for C1-C6 site classes for *(left)* input ground motion which is a Ricker wavelet with 1 Hz frequency and *(right)* input ground motion which is a Ricker wavelet with 0.5 Hz frequency.

Vs30

The VfZ matrix and the related subsoil classes (Fig. 2) are conceived to distinguish amplification factors and frequencies and, as it has just been shown, this implies a 'predictive power' on the response spectra, as a function of the earthquake magnitude.

Approaches based on Vs30 do not have the same capability because they do not explicitly take into account the main reason for stratigraphic amplification, that is the existence of an impedance contrast. As a further verification, we group the amplification maxima (and related frequencies) of the 585 models as a function of their Vs30 soil class as defined by the Italian Building Code (NTC, 2008). Note that the Vs30 soil classes are very similar worldwide, what changes is mostly the class-labeling (A, B, C…).

Results are illustrated in Fig. 4 and show that Vs30 cannot effectively discriminate neither different soil amplifications, nor different frequencies of amplification. Subsoils classified as B, C and D give completely overlapped amplification levels and frequencies of amplification. Class B and Class E results are largely overlapped, too. Additionally, soils classified as B or C can result in any size of amplification at any frequency of engineering interest. Since the bedrock-to-surface amplification function is little sensitive to the specific ground motion input, this result does not change with the specific input.

Class A, representing subsoils with maximum 5 m cover overlying a stiff bedrock (Vs_0 > 800 m/s), obviously leads to amplification at high frequency only. However, it is still largely overlapped to soils E and B.

We now analyze the average response spectra derived from our models grouped in their Vs30 site class. Differently from the bedrock-to-surface amplification functions, response spectra are strongly sensitive to the specific input ground motion used. In Fig. 5A we show the results when the input motion is the 1 Hz Ricker wavelet. We see that at short periods the highest accelerations are expected for buildings on soil classes C and E while at long periods there is no significant difference between the classes. When the input motion is a Ricker wavelet with a lower frequency (e.g. 0.5 Hz in Fig. 5B), the pattern changes at long periods, where the D and C class (those having the bedrock at higher depths) show the maximum response spectra. The frequency band of the maxima shifts from shorter to longer periods, consistently with the input motion dominant period.

The low class D normalized acceleration values at short periods might appear unexpected while they are not since D classes are associated, according to our models, to very deep bedrocks, therefore damping plays a major role at short periods and is responsible for low acceleration values.

The simplified numerical-modeling approach suggests that the Vs30 parameter is not an ideal site response proxy even when response spectra are considered, because the latter are very sensitive to the specific frequency content of the input motion compared to the subsoil eigen-frequency, information which is not included in the Vs30 parameter.

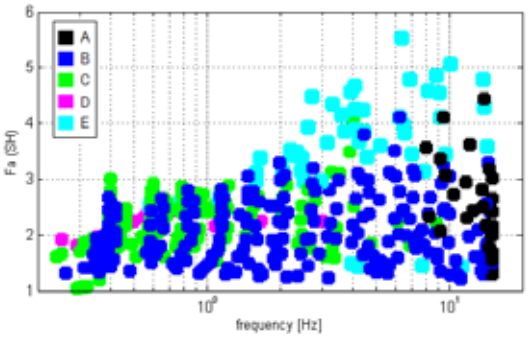

Figure. 4. SH wave amplification factors expected at the resonance frequency for the 585 subsoil models, grouped according to their Vs30 site class. The complete overlap of class B, C, D and, in large part, E, can be observed.

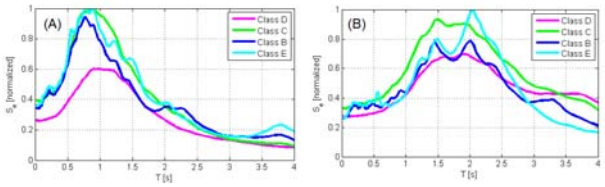

Figure. 5. Average response spectra for the Vs30 site classes. A) input ground motion is a Ricker wavelet with 1 Hz frequency, B) input ground motion is a Ricker wavelet with 0.5 Hz frequency.

In summary, a simplified subsoil classification has to rely on the minimum physical information needed to predict stratigraphic amplification, that is on <Vs>, f_0, Z or similar combinations. Note that Vs30 classes, are not unambiguously related neither to Fa, nor to f_0.

Since the final goal of site effect assessment studies is to predict the behavior of an oscillator (the structure) founded on another oscillator (the subsoil) and since such behaviors are both a function of frequency, shifting the reasoning from a depth-dependent approach (Vs30) to a frequency dependent approach (f_0), appears very natural.

5 DISCUSSION AND CONCLUSIONS

Since the final goal of site effect assessment studies is to predict the behavior of an oscillator (the structure) coupled to another oscillator (the subsoil), it is convenient to shift the reasoning from a depth-dependent approach (Vs30) to a frequency dependent approach (f_0).

By observing that the main cause for stratigraphic seismic amplification is the existence of impedance contrasts in the subsoil, we propose a simplified seismic site classification scheme based on three parameters: <Vs>, f_0 and Z (in short, VfZ), that is the average velocity of the cover layer, the resonance frequency of the subsoil and the impedance contrast between the cover and the bedrock or pseudo-bedrock.

The 1D numerical analysis of seismic response of several subsoils (all characterized by increasing Vs with depth) allows to generate a 4D function relating the amplification factor expected for the SH-wave, Fa, to (<Vs>, f_0, Z).

VfZ constitutes the minimum physical basis for a first-order approximation of stratigraphic amplification and can be measured with the same instrumental effort required to measure Vs30. Among the several techniques available, the joint fit of surface-wave based multichannel techniques and H/V or – under favourable circumstances – the H/V alone accompanied by an adequate knowledge of the site stratigraphy appear to offer the best cost effective performance. In particular, the H/V provides a sufficiently reliable estimate of f_0 while the joint fit of dispersion curves and H/V provide an adequate estimate of <Vs> down to f_0. Z can be inferred from the H/V peak amplitude or from the Vs profile.

A common objection to the proposed method is that, once the VfZ parameters are known for a site, one could – with a modest additional effort – perform a complete 1D numerical modeling rather than applying the simplified procedure.

Actually, the application of numerical models require the study of seismic response with several (3 to 9, depending on the specific regulation) different inputs (earthquakes), in order to provide an average value and its uncertainty (which is often ignored because not requested by law) and also requires the user to operate several other input choices (water table position, shear modulus and damping curves as a function of strain rate for all layers, position of the source, choice of the characteristic earthquake, etc.). All this makes the 1D numerical procedure more cumbersome and give results with often just an illusory accuracy, as discussed in the introduction. The use of full accelerograms in 1D numerical models conceived to model vertically incident SH waves is not fully justified and is the reason why we have based our models on simple Ricker wavelets.

The VfZ matrix could also help in the interpretation of the H/V curves. In fact, it allows a rough estimate of the expected SH-wave amplitude from the H/V peak amplitude and allows to understand the amplification potential of the observed peaks.

It is important to emphasize that the Fa values provided by the VfZ matrix (and in general by any simplified procedure) should only be interpreted as relative values (low or high amplification) because they depend on a very large number of other parameters and assumptions not explicitly taken into account in the models.

6 REFERENCES

Aki K. and Richards P.G., 2002. *Quantitative Seismology*, University Science Books, 700 p.

Anderson J.G., 2007. Physical Processes that control strong ground motion in *Treatise on Geophysics*, *Earthquake Seismology*, G. Schubert ed., Elsevier, Amsterdam.

Bardet J.P., Ichii K, Lin H., 2000. *Equivalent-linear Earthquake site Response Analyses Layered Soil*, comp. program.

Borcherdt, R.D., 1994. Estimates of site-dependent response spectra for design (methodology and justification), *Earthquake Spectra*, 10, 617–653.

Castellaro S., Mulargia F., Rossi P.M., 2008. VS30: Proxy for seismic amplification?, *Seismol. Res. Lett.*, 79, 540-543.

Day M.S., 1996. RMS response of a one-dimensional half-space to SH, *Bull. Seism. Soc. Am.*, 86, 363-370.

Joyner W.B., Warrick R.E. and Fumal T.E. (1981). The effect of Quaternary alluvium on strong ground motion in the Coyote Lake, California, earthquake, 1979, *Bull. Seism. Soc. Am.*, 71, 1333-1349.

Lee W., Trifunac M.D., 2010. Should average shear-wave velocity in the top 30 m of soil be used to describe seismic amplification? *Soil Dynamics and Earthquake Engineering*, 30, 1250-1258.

Geotechnical and Geophysical Site Characterisation 5 – Lehane, Acosta-Martínez & Kelly (Eds)

The complementarity of H/V and dispersion curves

S. Castellaro
Dep. Physics and Astronomy, University of Bologna, Italy

ABSTRACT: In the geotechnical and seismic practice, S-wave velocity profiles are frequently derived from the inversion of dispersion curves of surface waves and single-station passive H/V curves, mostly using a blind joint fit of the two. Here we emphasize the benefits of carrying out H/V reconnaissance surveys *prior* to any array acquisition and data analysis. The premise is that H/V data manifest diagnostic characteristics indicative of key features of the subsurface structure, e.g., the presence of lateral heterogeneities, large impedance contrasts at shallow depths and velocity reversals. Equipped with such a prior knowledge, practitioners could make better-informed decisions about array acquisition geometries, source/surface wave types and inversion strategies, which are strongly conditioned from the subsurface structure. In the end, we present the key points into a best-practice workflow for combining H/V techniques and dispersion curve analyses.

1 INTRODUCTION

The analysis of surface and interface waves is widely used for the geotechnical and seismic characterization of shallow soils. Through the analysis of the dispersion properties of Rayleigh, Love, Scholte or Stonely waves, it is possible to retrieve V_S (shear wave velocity) profiles. This can be done by using waves generated from active sources as in SASW (Nazarian and Stokoe, 1984), MASW (McMechan and Yedlin, 1981; Park et al., 1999), MUSIC (Schmidt, 1986), MOPA (Strobbia and Foti, 2006), and similar geotechnical approaches (Mulargia et al., 2015) or waves from passive ambient noise, as in the 2D arrays of SPAC (Aki, 1957) and ESAC (Ohori, 2002) or in the 1D of ReMi^{TM} (Louie, 2001) and SSASP (Mulargia and Castellaro, 2013). Apart from the variety of names, these techniques, which differ mostly for details of processing and acquisition, share essentially the same concepts, advantages and weaknesses (see Foti et al., 2014 for a review), which often make the interpretation of the dispersion curves difficult.

Surface wave propagation in layered media is a multimodal phenomenon. Higher modes often dominate the scene, resulting in so-called 'effective' or 'apparent' dispersion curves (Tokimatsu et al., 1992). The first problem is that these vary with the specific source used, which never has an ideal white spectrum, and this makes the interpretation difficult. This occurs particularly, but not only, in presence of velocity inversions and in presence of strong impedance contrasts at shallow depths (Tokimatsu et al., 1992; Gukunski and Woods, 1992). The second problem of these methods is the usually limited penetration depth, particularly in presence of stiff layers at shallow depth and particularly when high-frequency sources (sledgehammer, seismic gun) are used to excite the soil. The third problem is that the inversion of any dispersion curve holds only for 1D plane-parallel stratigraphy, which is not known in advance.

In order to by-pass some of these limitations, surface wave techniques have sometimes been used together with traditional P (or S) wave refraction seismic prospections, which share the same acquisition set up (Foti et al., 2003). However, also the refraction method suffers from several limitations, such as a poor penetration depth compared to surface waves, the incapacity to detect velocity inversions and the fact that under the water table the P wave arrivals do not allow to detect layers with P-wave velocity lower than the P wave velocity in water (~ 1500 m/s).

The H/V method, proposed by Nogoshi and Igarashi in 1970, promoted by Nakamura in 1989 and 'standardized' in 2004 within the SESAME (2004) project, is at present the most common technique to experimentally assess the subsoil amplification frequencies. In recent years the joint fit of H/V and dispersion curves was proposed (Parolai et al., 2005; Picozzi et al., 2005; Castellaro and Mulargia, 2010; 2014; Roser and Gosar, 2010; Zor et al., 2010; Foti

et al., 2011) and V_S profiles capable to match both the experimental H/V and dispersion curves are commonly considered better constrained than models based on the match of the curve from a single technique. However, this joint fit is usually a blind operation.

The microtremor H/V curves are diagnostic of other key features of the subsurface structure. First, they indicate, through the peak amplitudes, whether stiff layers are present and, through the peak frequencies, their relative depth (this clearly needs an assumption on V_S, as discussed in Castellaro and Mulargia, 2008). Second, their variation in space usually reflects lateral heterogeneities in the subsoil. Third, they can show velocity reversals (Castellaro and Mulargia, 2009). Such a prior knowledge could help practitioners in making better-informed decisions about array acquisition geometries, source/surface wave types and inversion strategies, which are strongly conditioned from the subsurface structure. Through a set of theoretical considerations and practical examples, we illustrate the complementarity of the H/V and the surface-wave array methods, aiming at a less 'blind' joint fit of the two curves. In the end, we present the key points into a best-practice workflow for combining H/V techniques and dispersion curve analyses.

2 BASIC PRINCIPLES

2.1 *H/V*

The microtremor spectra recorded at a site largely vary, particularly above 2 Hz, as a function of anthropic activity, being usually larger at daytime compared to nighttime. Gutenberg (1931; 1947; 1958) observed that the microtremor spectra largely vary also below 2 Hz, as a function of the weather (barometric pressure) at the recording site. Specifically, spectra under foul weather are higher in amplitude than under good weather conditions. However, it has been shown that the division of the horizontal (H) by the vertical (V) components has an effective normalization power (Nogoshi and Igarashi, 1970; Nakamura, 1989): it clears the source and enhances the path (i.e. the subsoil) response, so that and the H/V ratio remains essentially unchanged with time.

The European SESAME project (2004) and following literature (Lachet and Bard, 1994; Lermo and Chavez-Garcia, 1994; Fäh et al., 2001; Malischewsky & Scherbaum 2004; Haghshenas et al., 2008; Malischewsky et al., 2008) agree on the fact that the frequency of the H/V peak is a good proxy to the SH-resonance frequency f_0, which depends both on the V_S value and on the thickness H of the resonating layer. In a single-layer above bedrock resonator:

$$f_0 = \frac{V_S}{4H} n, \qquad n = 1, 3, 5 \ldots$$

where n is the mode number. Bonnefoy-Claudet et al. (2008) showed that this holds both if microtremors are composed mostly of body and/or surface waves.

Understanding the composition of microtremor is important, particularly to model the H/V curves in terms of V_S profiles. Over the years, different authors have attempted to explain the H/V phenomenology in terms of SH waves (Nakamura, 1989; Herak, 2008), of Rayleigh waves (Lermo and Chavez-Garcia, 1994; Fäh et al., 2001; Malischewsky and Scherbaum, 2004; Arai and Tokimatsu, 2004; Tuan et al., 2010) and by adding the effects of Love waves (Bonnefoy-Claudet et al., 2008; Van del Baan, 2009). Recent studies somehow consider the role of all waves, the so called total field (Lunedei and Albarello, 2010; Sanchez Sesma et al., 2011). It was found that results differ not only as a function of the waves considered, but also as a function of the temporal and spatial distribution of the sources and their strength. The inversion of the H/V curve requires not only the knowledge of the specific sources acting at the site but also several other soil parameters (Poisson's ratio, damping of each layer, 2D effects, etc.) often not easy to determine. This makes the H/V inversion an intrinsically imprecise process, but imprecise does not mean useless or not important.

The maximum amplitude of motion in an oscillating system occurs at the system resonance frequency: this implies that a local maximum is expected in the horizontal spectra of microtremor at the SH-wave resonance frequency f_0. Love waves are expected to show up with the same spectral feature. Rayleigh waves show up, instead, with a trough in the vertical spectral component at the resonance frequency f_0 and a peak at $\sim 2f_0$, as numerically derived in Fäh et al. (2001) and Tuan et al. (2010). In other words this means that Rayleigh waves have an almost pure horizontal component at f_0 and a dominant vertical component at $2f_0$. This results in H/V curves showing a maximum at f_0 and descending to H/V $\leq$ 1 at $\sim 2f_0$. Sometimes this pattern can be masked by the presence of other H/V peaks close to $\sim 2f_0$.

The observation of the single microtremor spectral components at a number of sites show that the contribution of the different wave types varies from site to site, but the Rayleigh wave signature (local minimum of the vertical spectral component) is always present, because surface waves attenuate less than body waves with distance from the source and because they have less stringent existence conditions compared to Love waves. This ubiquitous feature is what allows to distinguish H/V peaks of stratigraph-

ic origin from H/V peaks of anthropic origin, which is an essential task prior to any interpretation.

2.2 *Dispersion curves*

Surface waves of different wavelengths explore the soil at different depths and travel with the specific velocity that characterizes the soil at the different depths. Short wavelengths normally propagate slower (due to the low velocity of the shallow layers) while long wavelengths propagate faster. This property, called dispersion, is only proper of surface waves, such as Rayleigh and Love waves in layered media.

The techniques to retrieve dispersion curves from active or passive sources at 2 or more receivers undergo a variety of names and acronyms depending on sometime minor details regarding the geometry of the receivers, the type of source, etc. Here we just mention, among the active methods: SASW, Spectral Analysis of Surface Waves (Heisey et al., 1982; Nazarian et al., 1984); MASW, Multichannel Analysis of Surface Waves (Park et al., 1999) and, among the passive methods: SPAC, Spatial AutoCorrelation (Aki, 1957); ESAC, Extended Spatial Autocorrelation (Ohori, 2002); ReMi^{TM}, Refraction Microtemor^{TM} (Louie, 2001); SSAP, Statistical Self-Alignment Property (Mulargia and Castellaro, 2013). The basis of all these techniques is the slant-stack (or the correlation) of the signal recorded from different receivers, which allows to determine the velocity of propagation of waves of different frequencies travelling between them. None of these techniques outperforms the others, however, when using linear arrays with passive sources, assessing the real rather than an apparent velocity may in some cases be problematic (Strobbia and Cassiani, 2011; Mulargia and Castellaro, 2013; Strobbia et al., 2015).

From the seismic signal recorded at different positions (a minimum of two) over time, basically slant-stack and FFT procedures produce the so-called phase/group velocity spectra, which indicate the most probable velocity of the surveyed surface waves at each frequency. From this, a forward or inverse modeling procedure makes it possible to reconstruct a V_S model for the surveyed soil. V_S is linked to the Rayleigh and Love wave velocity (normally 10-15% larger) through the Poisson's ratio, as from the elastic theory of waves.

Surface waves have many modes of propagation, this implies that in the velocity spectra several relative maxima are possible at the same frequency value. In the case of an ideal impulsive source (i.e. with a white spectrum), ideal receiver geometry (i.e. equally well tuned on all frequencies, which is not possible in pratice), and ideal soil (e.g., isotropic, laterally homogeneous, with velocity gradually increasing with depth), the fundamental mode must be dominant in terms of energy, but in the real cases, as it will be discussed later, this does not always occur.

Selecting the dispersion curve of the fundamental mode or correctly sorting the higher modes implies a degree of subjectivity and is not an easy task (Gucunski and Woods, 1992; Tokimatsu et al., 1992; Cercato, 2009, 2011). When this is done by extracting only the maximum slant-stack value for each frequency, information is lost.

It is an experimental evidence (supported from theoretical facts) that active approaches, which rely on mid-to-high frequency artificial sources, usually provide better results in the high frequency range, that is, shallow depth. Passive approaches, relying on ambient noise, which is ubiquitous and spans a wider frequency interval, have the theoretical potential to perform better in the mid-to-low frequency range, which is pertinent to mid-to-large depths.

3 DISCUSSION AND CONCLUSIONS

Surface wave dispersion curves are, at present, among the most widely adopted geophysical non-invasive techniques in the geotechnical and seismic practice. Acquiring surface waves is a simple task, but the interpretation of their dispersion curves poses a number of challenges at different levels, that were reviewed in this paper. Here we propose to use the H/V curves as a complementary method in order to solve some ambiguities characteristic of the multi-channel surface wave methods, such as:

1D vs 2D STARTIGRAPHIES: The 1D plane-parallel soil condition is an essential assumption in the dispersion curve inversion/modeling. Verifying it by comparing the dispersion curves acquired from segments within the array or by moving the source at the two array ends is not reliable. Other causes such as scatterers external to the array line and differences in the source energy can produce the same effect. Taking a few H/V recordings along the array line helps in assessing the plane-parallel nature of the subsoil. H/V curves differing considerably along the array line indicate a 2D subsoil and also indicate where the array can be placed/cut to keep the 2D effect to the minimum. The joint fit of dispersion curves and H/V also allows to produce seismic stratigraphic sections. Acquiring H/V curves takes less time than acquiring an array, due to the different set-up times. When the survey is done for geotechnical interest, which is normally limited to the upper 10-20 m, the H/V acquisitions can be very short (even less than 5 min) since the frequencies of interest are normally above 3-5 Hz.

PENETRATION DEPTH: The H/V curve can predict the depth of penetration of standard arrays. Sites characterized by mid-to-high resonance frequencies stand for strong impedance contrasts at shallow depth and usually poor array penetration. Sites char-

acterized by flattish H/V curves stand for slowly increasing V_S with depth and usually higher array penetrations. The combined use of H/V also allows to extend the V_S profiles to larger depths and to identify the seismic bedrock, which is of paramount importance in many types of studies, even when the array penetration depth is severely limited by other shallower impedance contrasts.

VELOCITY INVERSION: The sensitivity of dispersion curves to velocity inversions and their interpretation pose a number of problems since the apparent dispersion curve can often both be interpreted as a real velocity inversion or as a mode jumping/mode superposition in a normally dispersive profile. The H/V curve in presence of velocity inversions has, on the opposite, a rather clear pattern (H/V < 1 for a wide frequency interval, particularly at the high frequencies-shallow depths of geotechnical interest), thus being of great help in reducing some ambiguities of interpretation of the dispersion curves.

CHOICE OF LOVE OR RAYLEIGH WAVES: Love wave-based arrays are highly inefficient in all the cases characterized by velocity inversions (included those induced by stiff artificial layers, pavements, asphalt etc.). When Vs decreases with depth, Love waves become leaky and harder to be observed since their dispersion equation has no real roots. Additionally, they hardly provide information to large depths, particularly when shallow stiff layers confine them waves in the soft layer, which will on the opposite be well characterized. An H/V survey conducted prior to the deployment of a surface wave array can identify both cases (velocity inversions and strong reflectors at shallow depth), thus addressing towards the use of Rayleigh or Love waves. A flat H/V curve suggests the absence of strong reflectors, which is an ideal condition for a good performance of Rayleigh wave on soft soils (e.g. deep sedimentary basins) or will be associated to poor dispersion curves on stiff (poorly dispersive) media, like rock. The dispersion of Love waves in both these cases is less efficient than Rayleigh waves.

MODE JUMPING: Numerical analyses have shown that mode jumping/superposition is expected particularly in presence of velocity inversions and shallow stiff reflectors. In the latter case, dispersion curves obtained from conventional sources reach only shallow depths and the apparent dispersion curve interpretation is not straightforward and strongly dependent on the array geometry.

Again, these two cases are indicated by 1) a persistent H/V < 1; 2) a high frequency peak in the H/V curve. The H/V curve can therefore be used not only to predict the effects on the dispersion curve (mode jumping) but also to guide the array geometry.

Both the multichannel and single station methods clearly have – when used alone - more limitations in comparison with their use in combination. However, we caution against the blind use of inversion algorithms, included the joint H/V-array inversion algorithms. In order to benefit from the combined use of the two techniques, the interpretation requires an active intervention of the user, who has to constrain the automatic inversion algorithms within well defined resolution/depth/velocity patterns limits, as the joint observation of the two techniques suggests. A summary of the proposed actions to take on the field and in the office is given in a flow chart (Fig. 1).

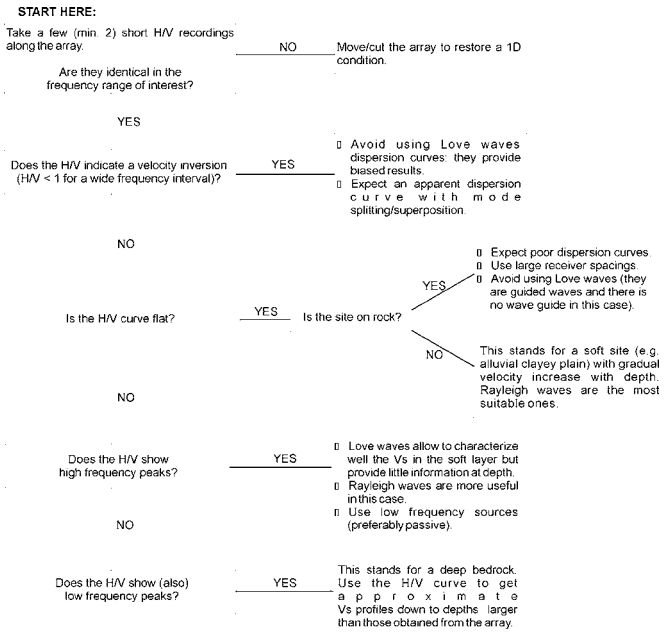

Figure 1. Summary of the proposed actions to take on the field when using surface wave methods.

4 REFERENCS

Aki K., 1957. Space and time spectra of stationary stochastic waves, with special reference to microtremors, *Bull. Earthq. Res. Inst.*, 35, 415–457.

Arai H., Tokimatsu K., 2004. S-wave velocity profiling by joint inversion of microtremor dispersion curve and horizontal-to-vertical (H/V) spectrum, *Bull. Seism. Soc. Am.*, 95, 1766-1778.

Bonnefoy-Claudet S., Köhler A., Cornou C., Wathelet M., Bard P.Y., 2008. Effects of Love Waves on Microtremor H/V Ratio, *Bull. Seism. Soc. Am.*, 98, 288-300.

Castellaro S., Mulargia F., 2009. The effect of velocity inversions on H/V, *Pure Appl. Geophys.*, 166, 567–592.

Castellaro and Mulargia, 2010. How Far from a Building Does the Ground-Motion Free-Field Start? The Cases of Three Famous Towers and a Modern Building, *Bull. Seism. Soc. Am.*, 100, 2080-2094.

Castellaro S., Mulargia F., 2014. Simplified seismic soil classification: the VfZ matrix, *Bull. Earthq. Eng.*, 12, 735–754.

Castellaro S., Panzeri R., Mesiti F., Bertello L., 2015. A geophysical approach to liquefaction, *Soil Dyn. Earthq. Eng.*, 77, 35-46.

Cercato M., 2009. Addressing non-uniqueness in linearized multichannel surface wave inversion, Geophysical Prospecting, 57, 1365-2478.

Cercato M., 2011. Global surface wave inversion with model constraints, Geophysical Prospecting, 59, 210-226.

Fäh D., Kind F., Giardini D., 2001. A theoretical investigation of average H/V ratios, *Geophys. J. Int.*, 145, 535–549.

Foti S., Lai C.G., Rix G.J., Strobbia C., 2014. *Surface wave methods for near-surface site characterization*, CRC Press, New York, 467 pp.

Foti S., Sambuelli L., Socco L. V., Strobbia C., 2003. Experiments of joint acquisition of seismic refraction and surface wave data, *Near Surface Geophys.*, 1, 119-129.

Foti S., Parolai S., Bergamo P., Di Giulio G., Maraschini, Milana G., Picozzi M., Puglia R., 2011. Surface wave surveys for seismic site characterization of accelerometric stations in ITACA, *Bull. Earthq. Eng.*, 9, 1797-1820.

Gukunski N., Woods R.D., 1992. Numerical simulation of the SASW test, *Soil Dyn. Earthq. Eng.*, 11, 213-227.

Gutenberg B., 1931. Microseisms in North America, *Bull. Seism. Soc. Am.*, 21, 1- 24.

Gutenberg B., 1947. Microseisms and weather forecasting, *Meteor.*, 4, 21–28.

Gutenberg B., 1958. Two types of microseisms, *J. Geophys. Res.*, 63, 595–597.

Haghshenas E., Bard P.Y., Theodulilis N., 2008. Empirical evaluation of microtremor H/V spectral ratio, *Bull. Earthq. Eng.,* 6, 75–108.

Herak M., 2008. ModelHVSR – a Matlab tool to model horizontal-to-vertical spectral ratio of ambient noise. *Comput. Geosci.*, 34, 1514–1526.

Heisey J.S., Stokoe K.H., Meyer A.H., 1982. Moduli of pavement systems from spectral analysis of surface waves, *Transport Res. Rec.*, 852, 22-31.

Hudson J.A., 1980. *The excitation and propagation of elastic waves*, Cambridge University Press, Cambridge.

Ibs-von Seht M., Wohlenberg J., 1999. Microtremor Measurements Used to Map Thickness of Soft Sediments, *Bull. Seism. Soc. Am.*, 89, 250-259.

Jones R.B., 1958. In situ measurement of the dynamic properties of soil by vibration methods, *Geotechnique*, 8, 1-21.

Jones R.B., 1962ì. Surface wave technique for measuring the elastic properties and thickness of roads: theoretical development, *British Journal of Applied Physics*, 13, 21-29.

Lachet C., Bard P.-Y., 1994. Numerical and Theoretical Investigations on the possibilities and limitations of Nakamura's technique, *J. Phys. Earth*, 42, 377–397.

Lermo, J., Chavez-Garcia F.J., 1994. Are microtremors useful in site response evaluation?, *Bull. Seismol. Soc. Am.*, 84, 1350–1364.

Louie J., 2001, Faster, better: Shear-wave velocity to 100 meters depth from refraction microtremor arrays: *Bull. Seism. Soc. Am.*, 91, 347–364.

Lunedei E., Albarello D., 2010. Theoretical HVSR curves from full wavefield modelling of ambient vibrations in a weakly dissipative layered Earth, *Geophys. J. Int.*, 181, 1093-1108.

Malischewsky P.G., Scherbaum F., 2004. Love's formula and H/V-ratio (ellipticity) of Rayleigh waves, *Wave Motion*, 40, 57–67.

Malischewsky P.G, Scherbaum F., Lomnitz C., Tran Thanh T., Wuttke F., Shamir G., 2008. The domain of existence of prograde Rayleigh-wave particle motion for simple models, *Wave Motion,* 45, 556–564.

McMechan G.A., Yedlin M.J., 1981. Analysis of dispersive waves by wave field transformation, *Geophys.*, 46, 869-874.

Miller R.D., Pullan S.E., Waldner J.S., Haeni F.P., 1986. Field comparison of shallow seismic sources, *Geophys.*, 51, 2067-2092.

Mulargia F., Castellaro S., 2008. Experimental Uncertainty on the Vs(z) Profile and Seismic Soil Classification, *Seism. Res. Lett.*, 80, 985-988.

Mulargia F., Castellaro S., 2013. A seismic passive imaging step beyond SPAC and ReMi^{TM}, *Geophys.*, 78, KS63-KS72.

Mulargia F., Castellaro S., Vinco G., 2015. Measuring shear wave velocity, Vs, of a hidden layer: An application to soil improvement under roads, *Can Geotech. J.*, 52, 721-731.

Nakamura Y., 1989. A method for dynamic characteristics estimates of subsurface using microtremor on the round surface, *QR of RTRI*, 30, 25-33.

Nazarian S., Stokoe K.H., 1984. In situ shear wave velocities from spectral analysis of surface waves. In: 8th Conference on Earthquake Engineering, San Francisco, CA, July 21-28, 31-38.

Nogoshi M., Igarashi T., 1970. On the propagation characteristics of microtremors, *J. Seism. Soc. Japan*, 23, 264-280.

Ohori M., Nobata A., Wakamatsu K., 2002. A comparison of ESAC and FK methods of estimating phase velocity using arbitrarily shaped microtremor arrays, *Bull. Seism. Soc. Am.*, 92, 2323–2332.

Park C.B., Miller R.D., Xia J., 1999. Multichannel analysis of surface waves, *Geophys.*, 64, 800–808.

Parolai S., Picozzi M., Richwalski S.M., Milkereit C., 2005. Joint inversion of phase velocity dispersion and H/V ratio curves from seismic noise recordings using a genetic algorithm, considering higher modes, *Geophys. Res. Lett.*, 32, L01303.

Picozzi M., Parolai S., Richwalski S.M., 2005. Joint inversion of H/V ratios and dispersion curves from seismic noise: Estimating the S-wave velocity of bedrock, *Geophys. Res. Lett.*, 32, L11308.

Sanchez Sesma F.J., Rodriguez M., Iturraran-Viveros U., Luzon F., Campillo M., Margerin L., Garcia-Jerez A., Suarez M., Santoyo M.A., Rodriguez-Castellanos A., Geophys. J. Int., 186, 221-225.

Schmidt R.O., 1986. Multiple emitter location and signal parameter estimation, IEEE Trans. Antenn. Propag., 34, 276-280.

SESAME Project, 2004. Guidelines for the implementation of the H/V spectral ratio technique on ambient vibrations: Measurements, processing and interpretation, SESAME European Research Project WP12, deliverable no. D23.12, http://sesame-fp5.obs.ujf-grenoble.fr/Papers/HV_User_Guidelines.pdf (last accessed 11 May 2012).

Socco L.V. and Strobbia C., 2004. Surface-wave method for near surface characterization: A tutorial, *Near Surface Geophysics*, 2, 165–185.

Strobbia C. and Cassiani G., 2011. Refraction microtremors: Data analysis and diagnostics of key hypotheses, *Geophys*., 76, MA11–MA20.

Strobbia C. and Foti S., 2006. Multi-offset phase analysis of surface wave data (MOPA), *J. App. Geophys.*, 59, 300-313.

Strobbia C., Boaga J., Cassiani G., 2015. Double-array refraction microtremors, *J. Appl. Geophys.*, 121, 31-41.

Roser J., Gosar A., 2010. Determination of Vs30 for seismic ground classification in the Ljubljana area, Slovenia, *Acta Geotecnica Slovenica*, 1, 61-76.

Tokimatsu K., Tamura S., Kojima H., 1992. Effects of multiple modes on Rayleigh wave dispersion characteristics, *J. Geotech. Eng*., 118, 1529-1543.

Tuan T., Scherbaum F., Malischewsky P.G., 2010. On the relationship of peaks and troughs of the ellipticity (H/V) of Rayleigh waves and the transmission response of single

layer over half-space models, *Geophys. J. Int.*, 184, 893-800.

Van der Baan M., 2009. The origin of SH-wave resonance frequencies in sedimentary layers, Geophys. J. Int., 178, 1587-1596.

Zor E., Özalaybey S., Karaaslan A., Tapırdamaz M.C., Özalaybey S.C., Tarancıoğlu A., Erkan B., 2010. Shear wave velocity structure of the İzmit Bay area (Turkey) estimated from active–passive array surface wave and single-station microtremor methods, *Geophys. J. Int.*, 182, 1603-1618.

Theme 9. General Site Characterisation

Geotechnical and Geophysical Site Characterisation 5 – Lehane, Acosta-Martínez & Kelly (Eds)

Characterisation of Halden silt

Ø. Blaker, R. Carroll, J.-S. L'Heureux
Norwegian Geotechnical Institute, Oslo & Trondheim, Norway

M. Klug
Geological Survey of Norway, Trondheim, Norway

ABSTRACT: NGI recently established a research site on a natural silt deposit to accommodate some of the challenges related to intermediate soils. This study briefly summarises the geological history and the preliminary geotechnical characteristics of the Halden silt deposit. The stratigraphy at the site consists of four main units. Two structureless silt units sit between a 4.5 m thick layer of sand and a 6 m thick deposit of clay. Soil behaviour type charts classify the silt deposit as transitional soils/silts to low I_r clays. Classification tests indicate that these soils are low plasticity silts with very similar mineralogical content. The results presented will form a useful reference to engineers working on similar intermediate soils worldwide.

1 INTRODUCTION

Intermediate silty soils are still considered challenging materials in geotechnical engineering, and limited information in on the engineering properties and how these relate to the geological background is available. This is primarily due to uncertainty in material behaviour, difficulties associated with sampling undisturbed material and the interpretation of *in situ* and laboratory test data. There is a need to provide guidance to practicing geotechnical engineers regarding characterization of silty material. To this aim, the Norwegian Geotechnical Institute (NGI) recently established a research site on a natural silt deposit.

The Halden Research Site is located in southeastern Norway, approximately 120 km south of Oslo (Fig. 1). Here the marine silt deposit is up to 10 m thick and uniform in nature. Over the last two years a series of geophysical, geological and geotechnical investigations have been carried out in the field and in the laboratory to characterize the natural silt deposit. This information will provide a basis for understanding the main factors controlling the engineering properties.

The purpose of this study is to present preliminary results summarizing the geological history and the geotechnical characteristics of the silt deposit at the Halden Research Site. The results presented will form a useful reference to engineers working on similar intermediate soils worldwide. Due to restrictions on the length of this study, we focus on the most significant properties.

2 GEOLOGICAL SETTING

The Halden Research Site is a recreational park area surrounded by hills, minor ravines and landslide scars. The site elevation is about 29 m above sea level and it slopes gently to the SW/W. Deposits at the site consists of marine and fjord marine sediments that emerged from the sea following a fall in relative sea level in the Oslofjord region during the last c. 11 000 years. During the post-glacial period, the depositional environment mainly led to hemipelagic deposition in a fjord marine environment. Due to the steady isostatic uplift in the Holocene and the fact that the sediments deposited continuously during a single period of submergence (Kenney, 1964), the soils in the study area are expected to be essentially normally consolidated except for some surface weathering, desiccation or in the vicinity of slide scars.

3 FIELD AND LABORATORY METHODS

3.1 *Field tests*

Several investigation methods are combined to provide information on the natural silt deposit and facilitate the understanding of the geotechnical behaviour and its link to the geological history. At present, geotechnical site investigation methods include Electrical Resistivity Tomography (ERT), several Total Pressure Soundings (TPS), Cone Penetration Tests with pore pressure measurements (CPTU), Seismic

Figure 1. Location of Halden Research Site.

Cone Penetration Testing (SCPT), Resistivity Cone Penetration Testing (RCPT), dissipation tests (Paniagua et al. 2016) and soil sampling. The latter was performed using two different Geonor thin walled stationary piston samplers; the K-100 54 mm composite sampler with zero inside clearance ratio (ICR) and a 10° cutting edge and the K-200 sampler modified to 72 mm inside diameter, ICR = 0 and a 5° cutting edge.

3.2 *Laboratory tests*

The samples were sent to the NGI and Geological Survey of Norway (NGU) laboratories in Oslo and Trondheim, respectively, for soil identification, classification, and assessment of index properties and advanced testing. Laboratory tests include; (i) Grain size distribution analyses by wet sieving (NSF, 1990), falling drop method (Moum, 1965) and hydrometer method (BSI, 1990); (ii) water content and Atterberg limits; (iii) unit weight of solid particles; (iv) mineralogical analyses using X-ray diffraction (XRD) and Scanning Electron Microscopy (SEM); (v) CAUC triaxial tests and (vi) constant rate of strain oedometer tests (CRS); (vii) geological and sedimentological analysis of the sediment using X-ray imaging and Multi-Sensor Core Logging techniques (magnetic susceptibility and gamma density) on 54 mm whole core samples. Whole core Gamma density (i.e. wet bulk density) and magnetic susceptibility (MS) were measured using the GEOTEK Standard Multi-Sensor Core Logger (MSCL-S) at 0.5 cm resolution with 5 s exposure/measurement time, see Figure 2. Total carbon (TC) and total organic carbon (TOC) measurements were performed on 7 samples.

4 SOIL CHARACTERISATION

4.1 *Stratigraphy*

The stratigraphy at the site is divided into four main units based on laboratory and *in situ* testing results, see Figure 2. It consist of c. 4.5 m of silty sand (Unit I) above c. 11 m of silt (Units IIA, IIB and III) and the final clay unit (Unit IV). Groundwater level was measured from an *in situ* stand pipe to be 2.5 m below ground level.

X-ray analyses show that both the Units II and III are structureless to mottled. Bioturbation has likely destroyed most of the primary sedimentary features. Such structureless sediments are common in fjord-marine environments subjected to hemipelagic sedimentation and seafloor biological activity (Hansen et al. 2010). In contrast, the Unit IV shows some weak laminations and the occasional presence of drop stones (sand/gravel particles) interpreted as ice rafted debris (IRD).

4.2 *Water content and Atterberg limits*

Natural water content (w) in Unit II generally falls between 28% and 31%. In Unit III the water content decreases with depth from about 27% at 12 m depth to about 21% at 15 m with an average value of 24%. The liquid limit (w_L) in Unit II varies between 31% and 37%, while in Unit III w_L is about 28%. Plastic limit (w_p) values are between 22% and 25% in the upper 11 m while below w_p = 20% - 22%. This gives plasticity indices (I_p) between 8% - 13% for Unit II. The average I_p is 10 % between 4.5 m and 10.5 m. The plasticity data for Units I and IIa fall on and below the A-line while Unit IIb and III data points are on and above the A-line, respectively (see Fig. 3). The average I_p of Unit I and III (12 – 13 m depth) is 7.5% and 8%, respectively. Based on the data in Figure 3 the Unified Soil Classification System (USCS) classifies the soils as silty clay with sand to lean clay with sand.

4.3 *Total unit weight and magnetic susceptibility*

The total unit weight (γ_t), both estimated from whole core gamma density measurements and that based on water content, are presented in Figure 2. Total unit weight in Unit II generally falls between 18.9 kN/m^3 and 19.2 kN/m^3. In Unit III the total unit weight increase with depth from about 19.5 kN/m^3 at 12 m to about 20.5 kN/m^3 at 15 m, with an average value of 19.9 kN/m^3.

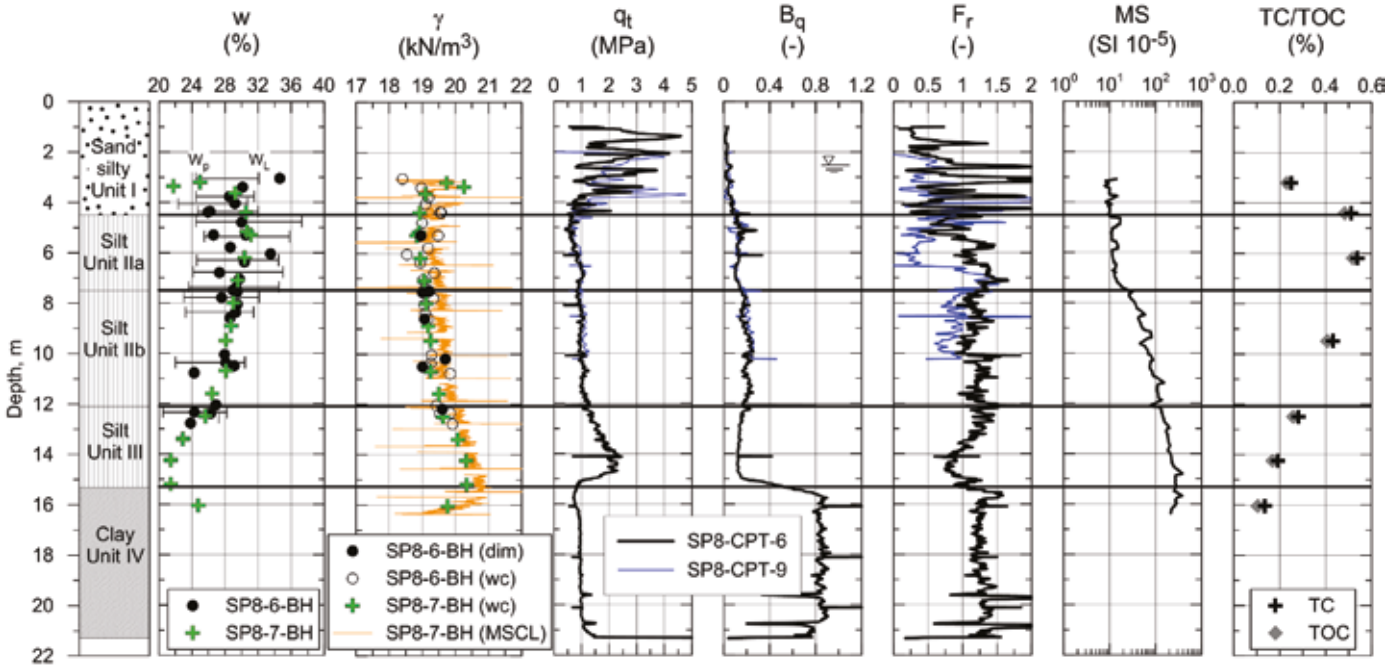

Figure 2. Basic parameters for Halden Research Site, corrected cone resistance, qt, normalised pore pressure, Bq, normalised friction, Fr, versus depth from CPTU, magnetic susceptibility from MSCL, and TC/TOC. Whole core Gamma density (i.e. wet bulk density) is shown in yellow on the total unit weight log.

Results from MSCL-S show an increase in wet bulk density (or total unit weight) in Unit II. The trend is similar to that obtained from laboratory results based on direct measurements and from water content. However, the wet bulk density values from the MSCL-S are slightly higher than those from direct measurement or values based on water content analysis (Fig. 2). This may be due to whole core measurements where wet bulk density measurements integrate the entire sample thickness. The MS results show constant values in the first c. 2 m of Unit II and thereafter a linear increase with depth until culminating at the upper boundary of Unit IV.

4.4 *Grain size distribution*

Figure 4 presents typical grain size distributions for the silt in Units II and III. All results are from the falling drop method (Moum, 1963). However, there is a trend of lower clay content based on the hydrometer method and the clay content determined by this method varies between 4% and 8% in Units II and III.

4.5 *Carbon content and mineralogy*

In Unit II the average Total Carbon (TC) was measured to 0.486% with a range from 0.432% - 0.539%. In Unit III the average TC is 0.238%, ranging from 0.193% - 0.282%. Meanwhile the Total Organic Carbon (TOC) in Unit II average is 0.464% while the average is lower in Unit III at a value of 0.215%.

Table 1 presents the result of XRD analyses performed on soil from Unit II and III. They reveal very similar mineralogical content for the silt Units II and III. Both units contain similar amounts of quartz, plagioclase, mica (muscovite and possibly illite), chlorite and amphibole. A Scanning Electron Microscope (SEM) image of a specimen from 6.4 m depth is presented in Figure 5.

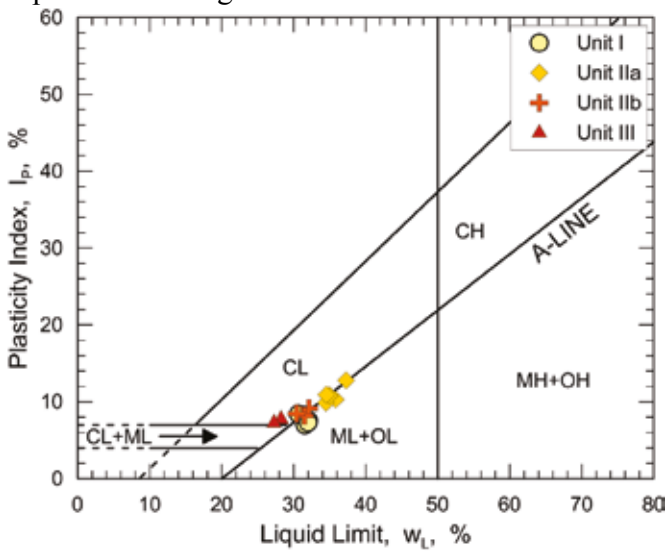

Figure 3. Plasticity chart, Unit I to III.

Table 1. Results from XRD analyses on silt Units IIa and IIb.

Depth (Unit)	Q*	K-F*	P*	M/I*	C*	A*	P*
m	%	%	%	%	%	%	%
6.2 (Unit IIa)	41	12	30	8	3	6	trace
9.5 (Unit IIb)	40	13	29	8	4	6	trace
13.4 (Unit III)	44	12	30	7	2	5	trace

* Q – Quartz, K-F – Potassium Feldspar, P – Plagioclase, M/I – Muscovite/Illite, A – Amphibole, P – Pyrite

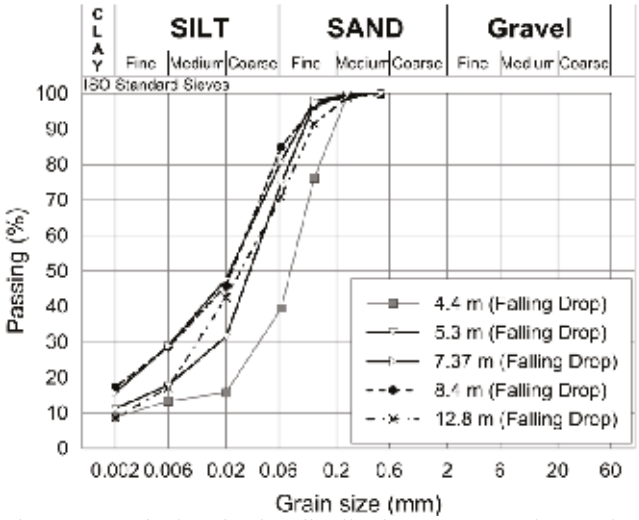

Figure 4. Typical grain size distribution curves, Unit II and III.

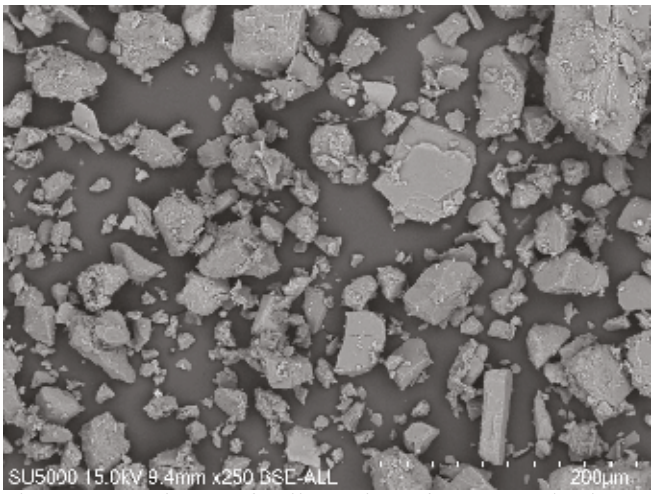

Figure 5. SEM image of a silt specimen from 6.4 m depth.

5 CONE PENETRATION TESTING

5.1 *Corrected cone resistance and pore pressure*

The corrected cone resistance (q_t) from CPTU tests, SP8-CPT-6 and SP8-CPT-9, are presented in Figure 2. The higher cone resistance in Unit I compared to the other units reflects the silty sand extending to about 4.5 m depth. Unit II has a uniform cone resistance throughout with q_t in the order of 1.0 MPa. In Unit III q_t increases from 1 MPa to 2.0 MPa between 12 m to 14.5 m before reducing to 1.0 MPa in the clay Unit IV. Pore pressure, u_2, is not presented but increases steadily with depth to approximately 380 kPa at 14 m depth. There is a clear change in rate of increase in u_2 from 15 m to 17 m which coincides with the upper boundary of Unit IV. Below 17 m u_2 increases steadily with depth.

5.2 *Soil behaviour type and soil classification charts*

Figure 6 presents the traditional SBT chart from Robertson (1990) combined with the more recent classification chart from Schneider et al. (2008). This system is based on Q_t and B_q and using Schneider et al. (2008) lines. Depth bias is known to occur when using soil classification charts if q_{net} and Δu_2 are not normalised, especially for sites with changes in OCR with depth. In this case only normalised charts are used for analysis. Unit I is classed as transitional. Unit IIa and IIb are classified as Transitional soil changing to Silts and low I_r (rigidity index) clays with depth. Unit III falls on the border between Transitional soils and Silts and low I_r clays before the deeper Clay Unit IV is identified. The Robertson (1990) classification chart, see Figure 6, indicates that Unit I is a Silt mixture with some transition into Sand mixture and Sands. Using this chart, Unit IIa, IIb and III are all Clays (clay to silty clay) with some transition into the Silt mixtures. Unit IV also a Clay (clay to silty clay) plots on the far right of the figure.

The Schneider et al. (2008) classification chart in Figure 7 presents a slightly different classification for the soil units as Units IIa and IIb both fall in Silts and low I_r clays classification and do not cross into the Transitional soils area. The classification for Unit III is Silts and low I_r clays before the deeper Clays / Sensitive Clays. Overall this Q_t-$\Delta u_2/\sigma_{v0}$' chart from Schneider et al. (2008) shows a clear classification of Silts and low I_r clays. It is also notable that Unit IIa and IIb are grouped separately within this classification. Unit I is a distinctively different material and clearly falls in the transitional soils classification in contrast to Unit II.

6 ENGINEERING PROPERTIES

Two CAUC tests were performed on 72 mm specimens from Units IIa and IIb, from 5.3 m and 8.6 m depth, respectively. Both specimens were consolidated to a best estimate vertical effective stress σ_{v0}' using K_0 of 0.5. The change in $\Delta e/e_o$ during sample consolidation was less than 0.02 for both specimens. Sample quality is therefore qualified as very good to excellent for and OCR of 1 - 2 according to Lunne et al. (1997). However it is noted that this criteria was developed for marine clays and might not be applicable to intermediate soils. The normalised shear stress with strain behaviour showed a steady increase in shear stress for both samples. At 10% axial strain the samples had normalised shear stress in the region of τ_f/σ_{v0}'. = 0.7 - 0.9. The normalised pore pressure reached a peak in the region of $\Delta u/\sigma_{v0}$' = 0.14 before 1% strain and the test specimens dilated strongly. The stress paths showed a clear 'S' shaped response before dilation. The samples had clay contents of 11% and 17% determined by the falling drop method. The silt content was approximately 65% and I_p was less than 10% for both samples. At peak pore pressure the normalised shear stress is in the range of 0.4 - 0.45. The measured response from

the tube samples is thought to be representative of good quality silt samples considering the corresponding index data.

7 DISCUSSION

Initially the silt deposit at the Halden Resesarch Site showed to be very homogenous. No layering was observed and the sediment proved to be structureless even with X-ray imaging. However, combining the data obtained from *in situ* testing, classification testing and the Multi Sensor Core Logger one can observe two distinct silt units. Units II and III differ slightly in terms of water content, total unit weight and magnetic susceptibility. This correlates also with an increase in corrected cone penetration resistance from 12 m. Reasons for this gradual change are not fully understood, but one possibility is that such subtle changes are linked to variation in organic matter as observed in both units. This interpretation is corroborated by other studies of geotechnical properties of marine sediments which showed to be altered to varying degrees by subtle changes in organic content (e.g. Keller 1982, Booth & Dahl 1986). Organic matter absorbs water and causes clay-sized particles to aggregate forming an open fabric. This causes an increase in water content and plasticity, and a decrease in the total unit weight. Since the mineralogical contents of both Units II and III are almost identical, the changes in magnetic susceptibility and gamma density obtained from MSCL-S could be linked to the observed patterns of organic matter and water contents (c.f. St-Onge et al. 2007).

The variations between the different SBT charts highlight the importance of cross checking CPTU interpretation of soil classification or behaviour type with index data. Falling drop grain size data for Unit IIa and IIb show average clay content of 13.4% and Unit III lower at 9% clay content. There is evidence that clay contents may be lower based on hydrometer results. For example, in Units IIa and IIb the clay content is in the range of 7.8% and 3% to 7% in Unit III. Clay contents at the lower bounds are questionable as Atterberg limits were measured on the material in Unit III. The plasticity index data for Unit IIa and IIb agrees well with the clustered results in the soil classification charts as Unit IIa is just on and below the A-line and has a higher I_p while Unit IIb plots on the A-line and has a lower I_p. Unit I, a transitional soil plots just below the A-line and has a low I_p which agrees well with the classification charts for both Robertson (1990) and Schneider et al. (2008). The soil classification based on CPTU results in Units IIa and IIb plot in a similar region of the Q-B_q chart (Schneider et al. 2008) as CPTU data from a silt site, Halsen, in Northern Norway tested by Sandven (2003).

A very limited program of advanced tests are carried out on the Halden silt. However, the normalised shear stress τ_f'/σ_{v0}' interpreted at peak pore pressure in the CAUC tests are in the range of 0.4 to 0.45. This is slightly below the ratios presented by Brandon et al. (2006) for Yazoo and LMVD silt, but within the range reported by Long (2007) for the estuarine Sligo silt.

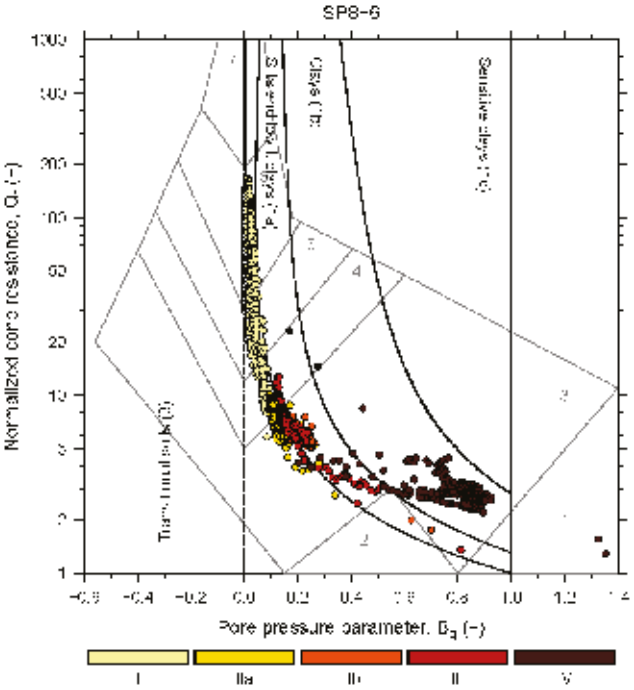

Figure 6. Robertson (1990) soil behaviour type chart for SP8-CPT-6.

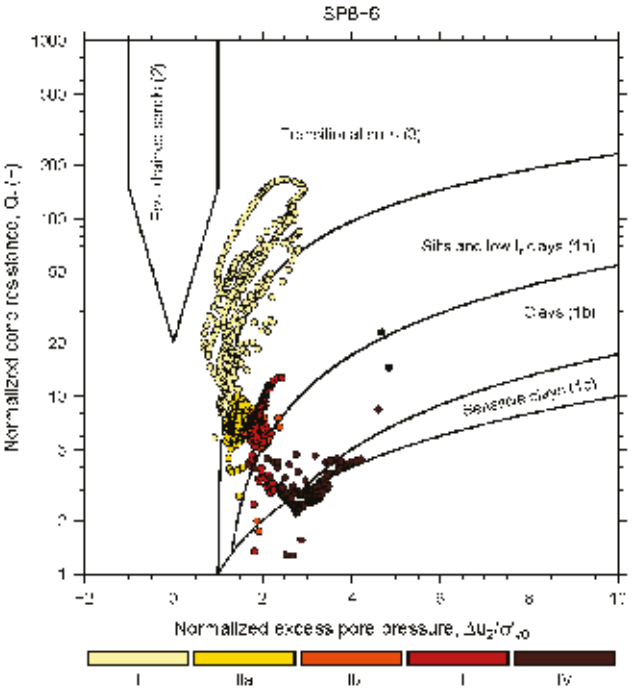

Figure 7. Schneider et al. (2008) soil behaviour type chart for SP8-CPT-6.

8 CONCLUSIONS

This study has detailed some characteristics and engineering properties of the Halden silt, a 11 m thick deposit of fjord marine silt in south-eastern Norway. NGI recently established a research site on this deposit to accommodate some of the challenges related to intermediate soils. A variety of *in situ* and laboratory tests have been performed to investigate its properties. Some preliminary conclusions are:

(i) The silt is considered normally consolidated and is of low plasticity, with a clay content between 8% – 18%.

(ii) Similar mineralogical content of the silt layers, Units II and III, is found. The soil consists mainly of quartz, K-feldspar and plagioclase, with 7% - 8% muscovite/illite.

(iii) Corrected cone resistance from CPTU in Unit II and III shows a 1 MPa to 2 MPa response, while pore pressures are positive and steadily increasing with depth down to the clay layer.

(iv) Patterns of water content, unit weight, magnetic susceptibility and cone penetration resistance could be attributed to subtle changes in organic content. Reasons for these gradual change are not fully understood and will need further studies.

(iv) Various SBT charts classify the soils as transitional soils or silts to low I_r clays. The Schneider et al. (2008) Q_t-$\Delta u_2/\sigma_{v0}$' chart shows a clear classification of Unit II-IV as Silts and low I_r clays, and separates Unit IIa and IIb from each other.

(v) The variation between the different SBT charts highlights the importance of cross checking CPTU interpretation of soil classification or behaviour type with laboratory index data.

(vi) CAUC tests on 72 mm silt specimens from Unit II indicate a normalised shear stress at failure the region of $\tau_f'/\sigma_{v0}' = 0.4 - 0.9$, depending on the failure criteria selected.

The results contribute to the developing global knowledge of properties and behaviour characteristics of intermediate soils. Further studies are planned at this site to better understand factors controlling the mechanical response of intermediate soils.

9 ACKNOWLEDGEMENT

This work is funded by the Norwegian Research Council (NRC) through the strategic research project SP8 – GEODIP at NGI. The contributions from other colleagues at NGI and Geological Survey of Norway are also highly appreciated.

REFERENCES

Booth, JS, and Dahl A.G. 1986. A note on the relationships between organic matter and some geotechnical properties of a marine sediment. *Marine Geotechnology* 6(3): 281–297.

Brandon, T. L., Rose, A. T. & Duncan, M. J. 2006. Drained and undrained strength interpretation for low-plasticity silts. *Journal of Geotechnical and Geoenvironmental Engineering* 132(2): 250-257.

BSI (1990). British Standard methods of test for soils for civil engineering purposes: Part 2 Classification tests. *BS1377,* British Standards Institution, London.

Keller, G. H. 1982. Organic matter and the geotechnical properties of submarine sediments. *Geo-Marine Letters* 2(3): 191–198.

Kenney, T.C. 1964. Sea-level movements and the geological histories of the post-glacial marine soils at Boston, Nicolet, Ottawa and Oslo. *Géotechnique* 14(3): 203–230.

Long, M. 2007. Engineering characterization of estuarine silts. *Quarterly Journal of Engineering Geology and Hydrogeology* 40(2): 147-161.

Lunne, T., Berre, T. and Strandvik, S. 1997. Sample disturbance in soft low plastic Norwegian clay. M. Almeida (Ed.), *Recent Developments in Soil and Pavement Mechanics*, Balkema, Rotterdam, pp. 81–102.

NSF 1990. Geotechnical testing. Laboratory methods. Grainsize analysis of soil samples. *NS 8005:1990*. NSF, Oslo.

Moum, J. 1965. Falling drop used for grain-size analysis of fine grained materials. *Sedimentology* 5(4): 343–347.

Paniagua-López, P., Carroll, R., Blaker, Ø., L'Heureux, J.-S., Nordal, S. 2016. Monotonic and dilatory excess pore water dissipations in silt following CPTU at variable penetration rate, Int. conf. on Geotech. and Geophys. Site Char., Gold Coast, Australia, 5-9. September, 2016.

Robertson, P. K. 1990. Soil classification using the cone penetration test. *Canadian Geotechnical Journal* 27(1): 151–158.

Sandven, R. 2003. Geotechnical properties of a natural silt deposit obtained from field and laboratory tests. In Tan, T.S., Phoon, K.K., Hight, D.W. & Leroueil, S. (ed.) *Characterization and engineering properties of natural soils; Proc. Int. Workshop*, NUS Singapore, 2-4 December, 2002, Balkema, Rotterdam, 2, 1121-1148.

Schneider, J. A., Randolph, M. F., Mayne, P. W. & Ramsey, N. R. 2008. Analysis of factors influencing soil classification using normalized piezocone tip resistance and pore pressure parameters. *Journal of Geotechnical and Geoenvironmental Engineering* 134(11): 1569–1586.

St-Onge G., Mulder T., Francus P., & Long B. 2007. Chapter Two; Continuous Physical Properties of Cored Marine Sediments. *Developments in Marine Geology*, Elsevier: 63–98.

Sørensen, R. (1979). Late Weichselian deglaciation in the Oslo fjord area, South Norway. *Boreas* 8: 241–246.

Geotechnical and Geophysical Site Characterisation 5 – Lehane, Acosta-Martínez & Kelly (Eds)

In situ behavior of clay soils over different drought-rewetting conditions

A. Denis, R. Fabre & J.F. Lataste
University of Bordeaux, Talence, France.

ABSTRACT: An experimental site was established to enable the continuous full-scale monitoring of the mechanical, geophysical and moisture behavior of the Brach clay geological formation at this site. We present the results of this in situ monitoring of the behavior of the clay soil over six consecutive years using various instruments (borehole extensometers, hygrometers, and a meteorological station). Displacement measurements (shrinkage and swelling) recorded at the experimental site were then related to soil moisture and temperature variations, which were in turn related to climatic variations observed at the site. By determining the cumulated soil hydrical condition over time, we showed a correlation between this parameter and the periods of shrinkage-swelling. The cumulated hydrical condition, as defined in this study, is a good indicator of the behaviour of soil under shrinkage and swelling.

1 INTRODUCTION

Mineralogical composition, suction, and microstructure are predisposing factors in shrinkage-swelling phenomenon in clay soils (Lin & Cerato, 2014, Burton et al., 2014). Associated with strong climatic variations and, in particular, with a succession of periods of intense drought, clayey soils cause many incidents of damage to private houses and buildings with shallow foundations (Jahangir et al., 2013). Many soil classifications in relation to water sensitivity and swelling and shrinkage potential (Holtz & Gibbs, 1956; Seed et al., 1962; etc.) have been built from laboratory-based studies on the behavior of clay soils. However, few studies have examined the behavior of clay soils in situ (Li & Zhang, 2011) and very few analyses have been conducted on shrinkage-swelling in situ in comparison to laboratory studies (Puppala et al., 2012).

The aim of this article is to present and analyze the results of an in situ monitoring study of the shrinkage-swelling of a clay soil in relation to variations in soil moisture and soil-temperature due to climatic conditions to better understand the shrinkage and swelling of clay soils under natural conditions. We concentrated this study on a particular part of a district near to Bordeaux (France) where many cases of damage to individual houses have occurred. All these cases are associated with the presence of clay soils and followed several exceptional drought periods. Due to a lack of information regarding the sensitivity of the geological formation responsible for the damage (the Brach formation – Upper Pleistocene) to shrinkage-swelling, a prior geological and geotechnical study of the damage-prone area was undertaken using laboratory measurements (measurements of the index of plasticity and methylene blue value, odometer tests, and other measurements). Then, an experimental site was established to enable the continuous full-scale monitoring of the mechanical, geophysical and water content behavior of the Brach clay geological formation at this site.

We present the results of the in situ monitoring of the behavior of the clay soil over six consecutive years using various instruments (borehole extensometers, hygrometers, and a meteorological station). Displacement measurements (shrinkage and swelling) recorded at the experimental site were then related to soil moisture and temperature variations, which were in turn related to climatic variations observed at the site. We discuss the influence of soil moisture on vertical soil movements observed in situ and introduce an indicator of the intensity of the shrinkage-swelling of a clayey soil; the cumulative hydrical condition.

2 MATERIAL AND METHOD

2.1 *Site location and lithological investigation*

The experimental site is situated approximately 2 km to the south-east of the district subject to damage in the geological formation of Brach clays. This district is located on the boundary between two geolog-

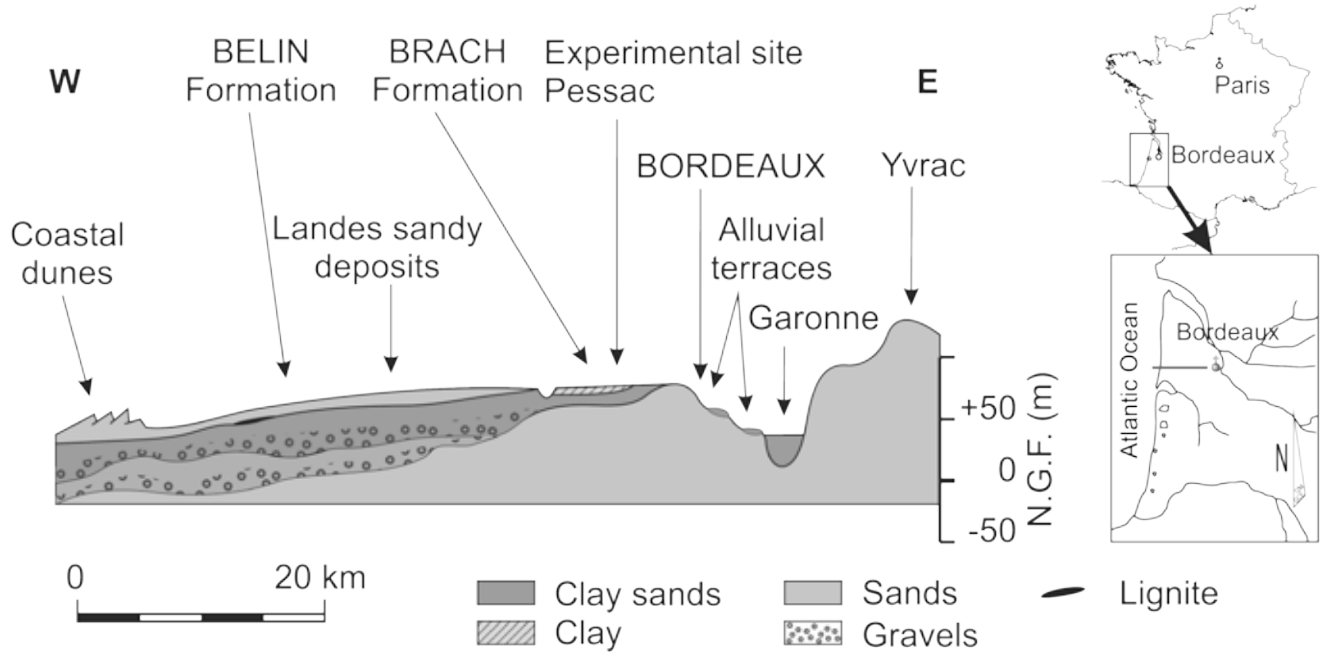

Figure 1. Geological section from the Atlantic Ocean to Bordeaux (Dubreuil and al., 1995)

ical areas: to the East lie the Quaternary alluvial terraces of the Garonne, and to the West lie the Pleistocene deltaic deposits of the Landes (the Brach and Belin formations), Figure 1. The Brach formation consists essentially of gray-blue to gray-black clay soils with traces of ochre-colored oxidization (Dubreuil and al., 1995).

The experimental site of Pessac consists of three distinct zones, which have been delimited by many geotechnical investigations. We describe only the section where instrumentation and sensors used were installed. This zone shows after 80 cm of sand a grayish clayey facies with ochre flecks (named A/BOG facies) to a depth of at least 10 m with more or fewer sandy lenses in the first few meters.

Analyses of the mineralogical composition of the Brach formation clay facies show that it is principally represented by the facies A/BOG, which consists essentially of kaolinite between [60 - 88%], and illite (muscovite) [9 - 20%] with very few smectites [2 - 10%]. The geotechnical characteristics of the clay facies measured in the laboratory exhibit also considerable variability (Fernandez and al 2015). The various clay facies encountered exhibited a wide variation in clay particle (< 2 μm) content, ranging from 10 to 83%. This demonstrates the textural heterogeneity of the facies. The laboratory results are not compared with the in situ results in this article (Andrieux et al., 2011).

2.2 *Instrumentation used at the experimental site*

We provide some details of instruments that were used at the experimental site; these instruments measure vertical movement (extensometer), soil moisture variations (hygrometer), temperature and precipitation (meteorological station), as well as variations in the resistivity (geophysical device) of the Brach formation soil (Chrétien and al, 2014).

The experimental site includes a continuous measurement station, which was used during 2008-2015. This station includes/enables the following instruments/methods:

1) Two systems of borehole extensometers, one manual WR-Flex – Telemac type (range 50 mm; accuracy +- 0.003 mm; precision 0.01 mm) and two automated devices, one of which was of the GKSE 12 – Glötz type (range 50 mm; accuracy +- 0.003 mm; precision 0.001 mm). The automated extensometers included potentiometric sensors placed at various depths (0.5, 1, 2, and 3 m) relative to fixed anchor points situated at depths of between 10 and 15 m. These devices enabled the measurement of ground vertical movements.

2) Three procedures for soil moisture measurement permitting soil moisture profiles to be established to a depth of 3 m by measuring the dielectric constant of the soil, which can be linked to the water content (volume/volume) using:

- the TDR (Time Domain Reflectrometry with tube access probe) method, which allows measurement of the dielectric constant of the soil. One measurement was made each 10 cm along a 3 m-deep bore using a tube probe. A manual measurement was made each two or four weeks.
- the FDR (Frequency Domain Reflectometry) method, which uses Thetaprobe probes placed at 0.5, 1, 2 and 3 m in depth (measurements were recorded automatically each three hours).
- the FD (Frequency Domain) method, which uses capacitive probes placed at 0.5, 1, 2 and 3 m (measurements were recorded automatically each hour).

Subsequently, we will present only the results of soil moisture profiles established using the TDR tube probe. This device provides information about the drying trend along a regular profile. The other types of sensors were installed at fixed depths and provide only a temporal record of water content with abrupt hydric variations that are not always physically explicable (possibly due to an electrical problem).

3) A series of soil thermometers placed at 0.5, 1.0, 2.0, 3.0 and 5.0 m in depth. Automatic measurements were recorded each hour from 2008 to 2010.

4) A meteorological station for recording air temperature, raw rainfall, atmospheric pressure, wind speed and air humidity.

3 RESULTS

3.1 *Experimental site climate*

The meteorological station at the experimental site enabled us to record the in situ micro-climate from 2008 and to compare this climate to that during the years of exceptional drought. Table 1 shows the gross precipitation recorded from 2008 to 2015, as well as 2003 and 2005, which were years of exceptional drought (cumulative precipitation of 734.8 mm and 595.8 mm, respectively). In both 2003 and 2005, many houses exhibited significant damage due to soil movement. The normal annual rainfall in the district is about 1000 mm.

Two other years of drought were experienced in 2011 and 2015 (annual rainfall, 687.6 mm and 605 mm respectively). The year 2011 was thus one of exceptional drought and was comparable to the reference years of 2003 and 2005 in terms of annual rainfall. In each year of drought, low raw rainfall was observed during spring.

The minimum and maximum average air temperatures during spring and autumn in 2011 and 2015 were 3 to 5°C greater than those observed during 2009 and 2010. The temperature during the spring of 2011 was equivalent to those during spring in 2003 and 2005. Autumn 2011 was warmer than the autumns of 2003 and 2005. The warmest springs were those of 2003 and 2005, and the minimum average temperatures during these years were 2 to 3 °C greater than those observed during the other years. The maximum average annual temperature for 2011 was greater than 19°C and approached that recorded during 2003 (19.5°C). The maximum average annual temperature for 2015 was greater than 2003 with 19.7°C.

Thus, compared to 2003 and 2005, 2011 and 2015 were years of exceptional drought in terms of temperature and precipitation, resulting, for 2011, in many cases of damage to private houses. For 2015, cases of damage are not yet listed and may be due to a cumulative precipitation of 243.5 mm only for January 2016.

Table 1. Seasonal and annual raw rainfall data for 2003 and 2005, and from 2008 to 2015.

	Raw rainfall (mm)				
Year	Winter	Spring	Summer	Autumn	Annual
2003	212.4	102.6	158.6	270.8	744.4
2005	109.4	130.4	108.2	241.2	589.2
2008	92.8	324.8	171.4	286.2	875.2
2009	221.8	262	129.2	354.5	967.4
2010	226.8	197.8	57.2	398.4	880.2
2011	144.4	74.4	188.8	280	687.6
2012	105.6	318.6	68.9	358.5	851.6
2013	283.9	348.2	136	278.2	1046.3
2014	466.4	210.9	188	216.5	1081.8
2015	219.6	119.4	154.4	111.6	605

3.2 *Soil moisture variations of the clayey subsoil in an annual cycle*

From our experiences during the last six years, the most convincing results used to determine the variations in water content as a function of depth and time were those obtained using the "TDR" method with tube access probe. Three hydric profiles, measured at intervals of 0.1 m down to a depth of approximately 3.0 m, were monitored at the experimental site on a monthly basis. Volumetric water content was calculated based on electrical permittivity, which was measured using a probe that produces a magnetic field in the ground. The probe that was used to measure water content was calibrated in the laboratory using a test sample. Because of the surface effect and the presence of humus-bearing soils, the measurements recorded in the top 0.5 m were of lesser quality than deeper measurements.

Figure 2 shows one of the soil moisture profiles for 2009, 2010, 2011 and 2015 including, for each graph, two extreme profiles: wet (reached in January during 2009 and 2011 and in February during 2010 and 2015) and dry (reached in October during 2009 and 2010 and in November during 2011and 2015). During wet periods, the lowest water contents in the soil were observed in 2015 where a-water content between 30 and 32% was measured at a depth greater than 1 m. In contrast the wet periods of 2009 and 2010 exhibited volumetric water content between 40 and 44 %. January 2011, was also a wet period with a low water content between 32 and 40 %.

The water content observed, during dry periods, was very similar for the four years between 1 and 1.75 m. However, the dry period of 2015 showed a lower water content than the other three years at depth greater than 1.75 m (about 22 %).

Without considering the surface measurements (in the topsoil), we observed that the greatest variations between wet and dry periods in the water content of clayey soils (approximately 19 to 24%) oc-

curred approximately at a depth of 1.50 m, and variations of only 16 to 20% occurred at 1.00 m (Fig. 2). One explanation of this phenomenon is dehydration/hydration; the circulation of water is affected by sandy drains, which are present at levels that vary according to depth. The difference in water content between wet and dry periods at 1.75 m and deeper was in the range of 6 to 12%.

3.3 . *In-situ shrinkage-swelling in six drought-rewetting cycles*

Extensometers at the experimental site enabled the continuous monitoring of movements of the clayey soil at various depths. We present here the results of measured displacement (ΔH) at depths of between 1.0 and 10.0 m obtained using the Telemac manual extensometer.

These movement records cover the periods from March 2008 to January 2016; thus, the records cover seven summers (from 2009 to 2015). Despite this, we found that the soil displacement was distributed between depths of 1 and 10 m.

Approximately 50% of the displacement occurred at depths between 1 and 3 m (Fig. 3), and the remaining displacement occurred at depths between 3 and 10 m depth. Therefore, the water content variations that were observed at depths of up to 3 m affected the displacement of this 2-m-thick layer. The layer deeper than 3 m also experienced significant displacement; thus, some water loss also occurred in the top part of this clay soil layer.

Each year is marked by a period of compaction and a period of swelling of the clayey soil. Between September 2008 and November 2015, seven phases of shrinkage and six phases of swelling were observed. Shrinkage accrued over the first three years, and swelling phases were insufficient to compensate for this shrinkage. The shrinkage that occurred in 2012 and 2013 were not so important; thus, the swelling of the clayey soil increased during these two cycles.

The periods of swelling starting between 2009 and 2011 were of short duration, from 161 to 190 days each years. The swelling phases starting in 2008 and 2012 were longer: 232 and 278 days. However, the duration does not affect the magnitude of the swelling. Indeed, the swelling values were between 1.80 mm (2008-2009) and 1.20 mm (2011-2012). The first rains in October or November initiated the swelling. The clayey soil was displaced rapidly; the soil reached 50 to 80% (depending on the rain intensity and duration) of its total swelling in approximately 60 days. Thereafter, the soil exhibited a more or less marked stabilization period, depending on the year, and the trend of the swelling depended on rainfall.

The shrinkage phases began at different periods. In 2010 and 2011, the shrinkage period began in April; these two years correspond to years with a raw rainfall in spring of less than 200 mm (Table 1). For 2009, 2012 and 2013, the raw rainfall in spring was between 262.0 and 348.2 mm, and the shrinkage periods began between mid-May and June. When shrinkage periods begin early, they are of longer duration. The period was longer than 187 days in 2010 and 2011, and lasted for 134 days in 2009 and 2012. The shrinkage period was of shorter duration in 2013 (96 days) and began at the end of June. The value of shrinkage seems to be related to the duration of the shrinkage period except for 2011 where sensors were in anomaly between September 2011 and December 2011. Indeed, greater shrinkage values were observed in 2009, 2010 and 2015 (about 2 mm). For the shorter period (2013), the shrinkage value was least (0.5mm). The shrinkage values in 2012 and 2014 were about 1 mm. The maximum displacement for the soil was about 5 mm.

Note that these results were also observed from the Glötz extensometer but with a stronger intensity

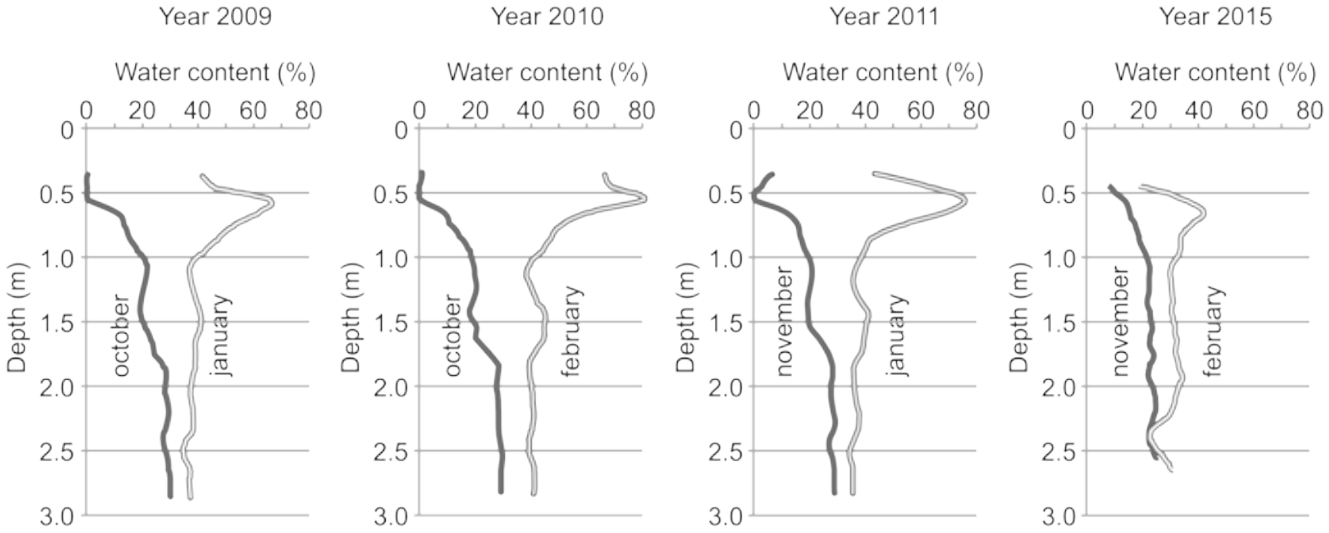

Figure 2. Maximal and minimal soil moisture profiles for 2009, 2010, 2011 and 2015.

for the shrinkage (about 4 mm).

4 THE HYDRICAL CONDITION OF THE SOIL

Our study linked many parameters to soil displacement during shrinkage and swelling. Here we use a new parameter to characterize the state of soil moisture, which characterized the studied site for a defined period. Let us first define the hydrical condition (HC) of the soil because this will enable us to determine the periods of hydration by effective rain (ER) and the periods of dry soil. This parameter is calculated based on raw rainfall (RR) and evapotranspiration. We distinguish two types of evapotranspiration: potential evapotranspiration (PET, the evaporative capacity of the atmosphere on a soil with a plant cover and having available water) and real evapotranspiration (RET, corresponding to the loss of water from a soil when water becomes scarce, considering the useful reserves in the soil). Effective rain (water that penetrates deeply into the soil), when the soil is hydrated, is defined as raw precipitation (RR) minus real evapotranspiration (RET). RET is very difficult to access, and we admit the hypothesis that RET corresponds to PET for a low plant cover that is supplied with water.

The hydrical condition is then defined by the following relationship:

$$HC(t) = RR(t)-PET(t) \quad (1)$$

with RR(t) : raw rainfall per day, PET(t) : potential evapotranspiration per day and t the time (one day).

From (Eq.1) three cases are possible:

1) HC(t) < 0 → one day water loss (soil drying)
2) HC(t) > 0 → one day water gain (soil hydration)
3) HC(t) = 0 no modification in drying or hydration

The hydrical condition gives the state (loss of water or gain of water) of the soil moisture for one day.

For a long period, one month, a season or one or more years we defined the cumulated Hydric Condition for a period T as follows:

$$HCc(T) = \sum_{t0}^{t} HC(t) \quad (2)$$

Where t0 is the initial time, t a date in day and T the interval in day (T = t – t0).

From Eq.2, we obtain a value for a given interval T (one month or one or more years). When HCc(T) is positive for a given interval T, the soil gains water while if HCc(T) is negative the soil loss water.

We can also define the cumulative Hydrical Condition over the time t as follows:

$$HCc(t) = \sum_{t0}^{t} HC(t) \quad (3)$$

In this last case, a positive slope of the curve of the cumulated Hydrical Condition represents a gain of water, while a negative slope represents a water loss (soil drying).

Raw rainfall (RR) and Potential evapotranspiration (PET) data were supplied, respectively, by the meteorological station of the experimental site and

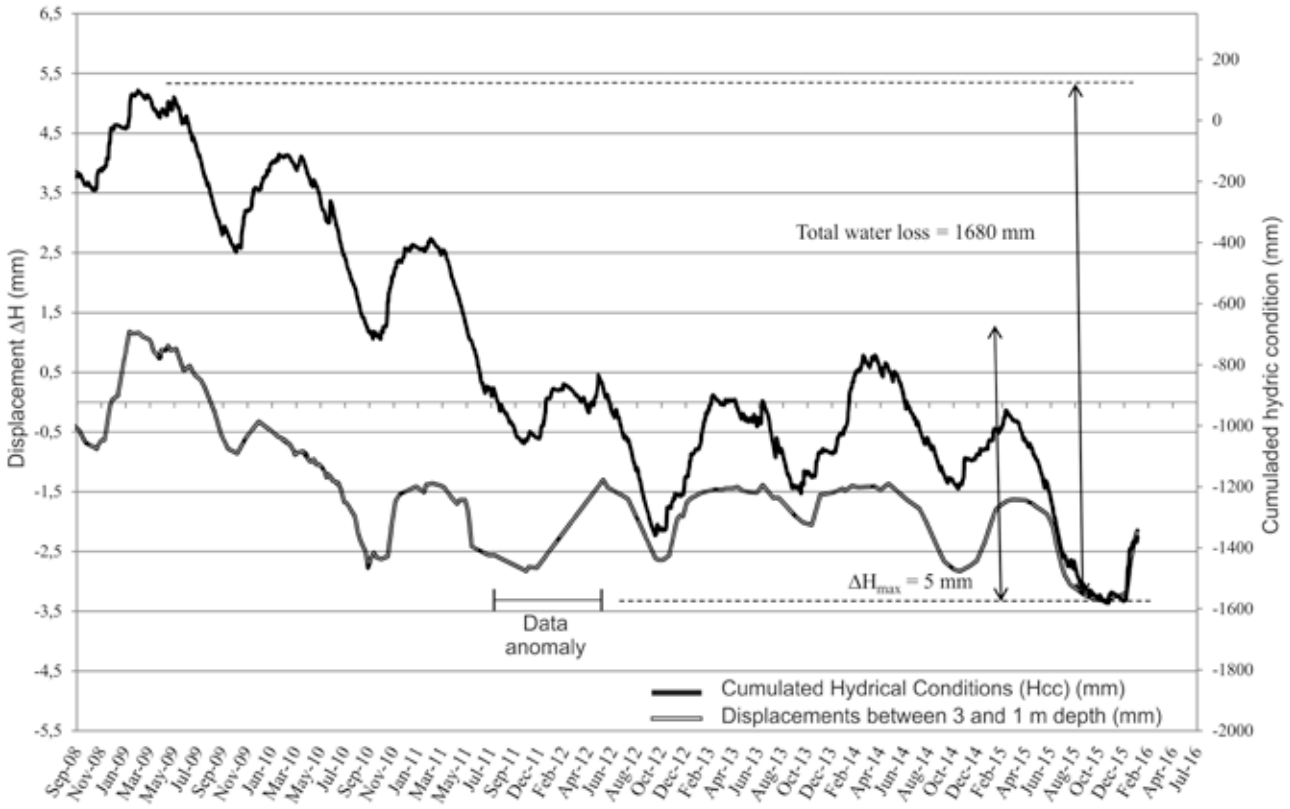

Figure 3. Displacement at depths of between 1 and 3 and the cumulated hydrical condition

by the meteorological station of Merignac (approximately 5 km from the experimental site.

The cumulated hydrical condition function (equation 3) is presented in Figure 3, with t in days and t0 is 19/03/2008. Three different parts can be discerned. In the first one the cumulated hydrical condition decreases from April 2009 to October 2012, showing that evaportranspiration is greater than raw rainfall. The second part of the time series shows a stabilization of the values of HCc(t) from October 2012 to April 2015, raw rainfall and evapotranspiration are equilibrated. The last part from April 2015 to December 2015 shows again a negative slope of the HCc(t) curve.

In details and for each years, the HCc(t) curve shows a positive slope from October to March and a negative slope to April to October. It is interesting to see that a negative slope fits with shrinkage period and a positive slope with swelling period. The zero-lag correlation between the two variables (HCc and ΔH) gives a correlation coefficient of 0.84. Note that a cross correlation does not give greater value at other lags.

The results obtained through in situ monitoring show that a cumulative shrinkage over several years with non-negligible soils movements can occur. This settlement of the soil can cause damage to light individual constructions without wall-ties or steel reinforcement and with shallow foundations constructed on this type of clay soil (Denis et al. 2011). Damage observed in the district near the site in 2011-2012, is largely due to the cumulative shrinkage of clay soils rather than to their swelling and fully explain by the deficit in soil water content (general negative trend of the HCc(t) curve) from 2008 to 2012.

5 CONCLUSION

In situ monitoring of the behavior of a clayey soil using various sensors and over six consecutive years was used to analyze the shrinkage-swelling movements. As expected, the variations in temperature and volumetric water content at a depth of 3 m are significant. The total displacement is about 5 mm (6.5 mm from another extensometer). However, displacements deeper than 3 m are also important, particularly for the top of the layer between 3 and 10 m depth. The cumulated hydrical condition as indicator of the intensity of the shrinkage-swelling of a clayey soil appears reliable, at least for this experimental site but should be confirmed in other contexts.

6 REFERENCES

Andrieux, C, Chrétien, M, Denis A, Fabre, R. & Lataste, JF. 2011. Shrinkage and swelling of clay soil. Comparison between laboratory and in–situ measurements. *European J. of Environ. and Civ. Eng.* 15, 819-838.

Burton, J.G., Sheng, D. & Airey, D. 2014. Experimental study on volumetric behaviour of Maryland clay and the role of degree of saturation. *Can. Geot. J.* 51, 1449-1455.

Chrétien, M., Lataste, J.F., Denis, A. & Fabre R. 2014. Electrical resistivity tomography to understand clay behavior during seasonal water content variations. *Eng. Geol.* 169, 112-123.

Denis, A., Elachachi, S.M., Niandou, H. 2011. Effects of longitudinal variability of soil on a continuous spread footing. *Eng. Geol.*, 122, 179-190.

Dubreuilh, J.P. & Capdeville, J.P. & Farjanel, G. & Karnay, G. & Platel, J.P. & Simon-Coinçon, R., 1995. Dynamique d'un comblement continental néogène et quaternaire: l'exemple du bassin d'Aquitaine, *Géologie de la France n°4,* pp. 3-26.

Fernandez, M., Denis, A., Fabre, R. & Lataste, J.F. 2015. In situ study of the shrinkage-swelling of a clay soil over several cycles of drought-rewetting. *Eng. Geol.* 192, 63-75.

Holtz, W.G. & Gibbs, H.B., 1956. Engineering properties of expansive clays. *ASCE*, vol. 121, pp.641-677.

Jahangir, E., Deck, O., & Masrouri, F., 2013. An analytical model of soil-structure interaction with swelling soils during droughts. *Comp. Geotch.* 54, 16-32.

Li, J.H. & Zhang, L.M. 2011. Study of desiccation crack initiation and development at ground surface. *Eng. Geol.* 123, 347-358.

Lin, B. & Cerato, A.B. 2014. Applications of SEM and ESEM in microstructural investigation of shale-weathered expansive soils along swelling-shrinkage sycles. *Eng. Geol.* 177, 66-74.

Puppala, A.J., Manosuthkij, T., Nazarian, S., Hoyos, L.R. & Chittoori, B. 2012. In situ matric suction and moisture content measurements in expansive clay during seasonal fluctuations. *Geotech. Test. J.* 35 (1), 74-82.

Seed, H.B., Woodward, R.J. & Lundgren, R. 1962. Prediction of swelling potential for compacted clays. *J.Soil Mech. and Found. Eng. Div. ASCE*. 88, 107-131.

Geotechnical and Geophysical Site Characterisation 5 – Lehane, Acosta-Martínez & Kelly (Eds)

Geotechnical site investigations for dredging works - Port of Townsville

M. Jaditager & N. Sivakugan
College of Science, Technology and Engineering, James Cook University, Townsville, QLD, Australia

ABSTRACT: In order to accommodate larger vessels with greater draughts, the Port of Townsville has conducted a major capital dredging campaign in 1993 to deepen its access channels and inner harbour from -10.7 m to -12.0 m Lowest Astronomical Tide . To determine the subsurface conditions of the dredging project site, the port has conducted offshore geotechnical site investigations. The factual information obtained on soil stratigraphy, classifications, and geotechnical properties has guided dredgeability assessment, cost estimates and dredging operations planning. Subsequent to provisions of guidance to design and tendering stages, the geotechnical site information reduced dredging project risk levels and contributed to a successful project execution without major delays or cost overruns for unforeseen ground conditions. This paper describes the geotechnical site characterisation for dredging works that were undertaken by the Port of Townsville, emphasising on site geological setting, scope of the investigations, field works, laboratory testing, and the obtained results.

1 INSTRUCTIONS

The Port of Townsville contributes to the North Queensland regional economy by servicing various industries including agriculture, mining, defense, retail and general cargo (Port of Townsville 2012). As with all marine ports, to improve navigational safety of vessels and to cater for larger ships with deeper draughts, the Port of Townsville has conducted a capital dredging campaign in 1993 to deepen its access channels and inner harbor from -10.7 m to -12 m Lowest Astronomical Tide (LAT). Dredging is generally characterised as a highly professional, capital intensive and risky industry, where, variations in soil and rock characteristics contribute the greatest cost uncertainty (Kinlan 2014). Thus, successful design, tendering and execution of a capital dredging project require adequate knowledge of dredging site subsurface conditions, beside bathymetric and environmental parameters in which dredging vessels will be operating (PIANC 2000).

In-situ soil geotechnical parameters that are essential for dredging works are those which assist in determining the optimal type of dredging plant to be used and help in identifying options for transporting, unloading, and using/ disposing of dredged material (PIANC 2014). To determine stratification, physical and mechanical properties of material to be dredged, the Port of Townsville in collaboration with its geotechnical consultants has carried out offshore geotechnical site investigations.

Figure 1 . The Port of Townsville Location

2 SCOPE OF SITE GEOTECHNICAL INVESTIGATIOS

The main objectives of the geotechnical site investigations for dredging projects are to obtain the most complete and accurate estimates of the subsurface profile and dredgeability properties of soil material to be dredged (Spigolon 1995). These objectives can be achieved by evaluating volume and distribution of material to be dredged, soil physical and mechanical characteristics that derive dredgeability, and dredged material suitability for land reclamation (ISSMGE 2005). For the Port of Townsville's clayey and cohesive silt soil profile, index properties, strength,

carbonate content, and particle shape dictate the dredgeability of the seabed material and its suitability as structural fill material (Table 1). To satisfy the necessary dredging site geotechnical requirements of identification of the successive layers below seabed, determination of in-situ soil geotechnical properties and sampling for laboratory testing, the port has undertaken the following field and laboratory testing works:

- Drilling of 49 bores,
- Six vibrocoring of near surface,
- Collection of soil samples,
- In-situ testing -Standard Penetration Test ,and
- Laboratory testing for soil: index, strength, carbonates content, particle shape, settling rate, consolidation and compressibility properties.

Table 1. Soil parameters relevant to dredging processes

Soil parameter	Application to dredging process
In-situ density	Excavation, production, slope stability and dredged material reuse
PSD*	Excavation and dredged material reuse
Shear strength	Excavation, production, transportation and slope stability.
Carbonate content	Excavation, production, transportation and dredged material reuse
Particle shape	Excavation, transportation, unloading and dredged material reuse

* Particle Size Distribution.

2 SITE GEOTECHNICAL SETTINGS

The geology of Townsville region comprises Quaternary aged alluvium and colluvium sediments underlain by Late-Palaeozoic age granite (Queensland department of mines 1986). The Townsville geological map indicates that the terrain to the south of the Port of Townsville is of Quaternary age estuarine deposits of mud, clay, silt and sand, then Permian age granite at depth of 20 to 23 m LAT (Figure 2). The near surface lithology of the Port of Townsville encompasses Holocene sediments more than 12,000 years old, including recent silt, mud and sand described as coastal tidal flats, mangrove flats and supratidal saltpans (Golder Associates 2008).

Figure 2. Townsville geological map (QLD department of mine 1986).

3 FIELD WORKS

The geotechnical site investigations of bore holes drilling, vibrocore sampling, in-situ and laboratory testing of the Port of Townsville access channels and inner harbour deepening were undertaken during 1992. The boring, standard penetration test (SPT) and vibrocoring works were performed from a cantilevered timber deck platform that mounted on the rear of a 25 m long X 10 m wide barge vessel (Douglas Partners 1992).The vessel was held on test positions by four anchors and associated air winches; satellite navigation system was used to establish bores and vibrocores locations. The boreholes were drilled at 250 to 300 m spacing (Figure 3) using a drill rig that deploys a floating head system. The boreholes were extended to depths range from 0.9 m to 8.95 m using rotary drilling with water or mud flush techniques through 100 mm diameter top casting. SPT or undisturbed tube samples of 50 mm and 70 mm diameter of strata were taken at 1 m depth intervals. The vibrocoring was conducted using a 3 m long X 65 mm diameter sample tube, the sample tube was driven into the seabed by mean of a high frequency air operated vibrator attached to the tube top. On completion of the tube driving, negative pressure was applied to the top of the tube to facilitate withdraw. The vibrocoring discontinued upon nominal refusal at depths of 0.45 m to 1 m below seabed level.

Figure 3. Inner harbor bore holes plan (Douglas Partner 1992)

4 LABORATORY TESTING

The laboratory tests on disturbed and undisturbed samples collected from a site are integral part of a site investigation exercise (Sivakugan & Das 2010). As complementary component to the geotechnical site investigations for dredging works, laboratory testing were conducted to assist in evaluating the likely engineering properties of the Port of Townsville's in-situ soils . Representative soil samples recovered from the bores were taken to a National Association of Testing Authorities (NATA) accredited laboratories for testing. The selected soil samples were laboratory tested for: index, shear strength, carbonates content, particle shape, settling rate, consolidation and compressibility properties.

The plasticity of the material to be dredged was evaluated by conducting thirty nine Atterberg limits and thirty six linear shrinkage tests, beside forty three natural moisture content tests. For particle size distribution, forty four wet sieving analyses and nineteen sedimentation (hydrometer) tests were performed to appreciate sand, silt and clay fractions of the soil. Undrained shear strength parameters of cohesion (c_u) and friction angle ($Ø_u$) were examined by testing seventeen undisturbed samples in quick, untdrained, unconsolidated Triaxial compression test. Bulk density of these seventeen undisturbed soil samples was also investigated.

Six soil samples with known dry weight were tested for carbonate content by treating the samples with dilute (10% weight for weight) hydrochloric acid until visible chemical reactions are complete. The loss in weight that results from the chemical reactions represents carbonate content of each soil sample. The particle shape of sand fractions from the particle size distribution tests were inspected under a hand magnifying glass to observe the particle angularity. Four samples of dredged mud slurry for material collected from four different bores were poured into graduated cylindrical tubes; changes in water turbidity and solid accumulation at the tubes bases versus elapsed time were recorded to study sedimentation of these mud samples. Sedimentation and consolidation behavior of dredged mud samples that taken from the port's inner harbour and access channels were simulated in laboratory. One dimensional consolidation (oedometer) tests on reconstituted dredged mud samples were performed to estimate the anticipated consolidation duration and settlement amount.

5 GEOTECHNICAL SITE INVESTIGATION RESULTS

5.1 *Field investigation results*

The bores and vibrocores encountered variable conditions over the Port's access channel and inner harbour dredging project site (Table 2 & 3). The dominant subsurface condition was broadly found to be a thin veneer of soft grey clay at 0.1 m to 0.5 m , overlaying dense to very dense clayey sand and sand inter-bedded with stiff to hard sandy and silty clays.

Table 2. The port's inner harbor subsurface stratigraphy

Depth	Strata description
Seabed level to 0.5 m	Very soft, grey clay
0.5 m to 3.5	Clayey sand and sand generally in dense condition.
3.5 m to 6.7 m	Stiff to very stiff sandy clays and silty clays, becoming hard with depth, some zones of dense to very dense clayey sand & sand up to 1 m thick are inter-bedded with clays.

Table 3. The port's access channel subsurface stratigraphy

Chainage (km)	Depth (m)	Strata description
1 - 1.7	0.4-1.3	Soft clayey silt
1 – 1.7	1- 3.05	Dense clayey sand & sand
1.7 – 3.5	0.2- 0.7	Soft clay silt
1.7 – 3.5	0.8 -3.0	Stiff to very stiff sandy clays & silty clays
3.5 -5	0.1-0.5	Soft clayey silt
3.5 - 5	0.6-5.0	Dense sand & clayey Sand
5.0- 6.1	0.2 -0.4	Soft clayey silt
9.5 -13.7	0.1- 2.8	Loose clayey sand & clayey silt

5.2 *Laboratory testing results*

The plasticity test results showed that the Port of Townsville's cohesive soil strata is generally of medium and high plasticity, while the non-cohesive clayey sand is of low to medium plasticity. The strength properties of un-drained cohesion (c_u) and the un-drained angle of internal friction ($Ø_u$) are presented on (Table 4). The coefficient of vertical consolidation (C_v) of the soft clayey dredged material was estimated to be in order of 4 m² / year and reclaim land total settlement of 400 mm to 480 mm is expected for 6 m high fill material on natural firm clay at 50 kPa loading condition.

Table 4. The Port's access channel soil strength properties

Bore (#)	Depth (m)	Soil description	Strength c_u (kPa)	Strength $Ø_u$ (°)
1-3	0 -1.3	Soft clayey silt	-	-
4 - 8	0.2 -3.	Clays	32 -102	2 - 3
9 -11	0.1 - 5	Clayey sand	-	-
12 -15	0 - 0.2	Clay silt	48 - 79	11
12 - 15	0.3 - 3	Clayey sand	37	19
16 - 27	0 - 4.5	Clayey sand	87- 89	3-14
28 - 36	0 - 4.0	Clayey sand	50 - 64	2-19

6 GEOTECHNICAL DATA INTERPRETATION

The Port of Townsville interpretation of geotechnical site investigation data indicated that the subsurface condition of the dredging project site comprise soft/loose Holocene alluvium overlying generally hard/dense older alluvium, overlying granitic weathered rock. Bore logs data were integrated into the Port of Townsville's historical bore logs register; dredging site longitudinal profile and material hardness contour (Figure 4) were established. The dredging contractor made their own interpretation of the factual geotechnical data, subsequently, has elected a

cutter suction dredge plant as the optimal vessel for the port's inner harbour dredging and trailer suction hopper dredge for the access channel dredging.

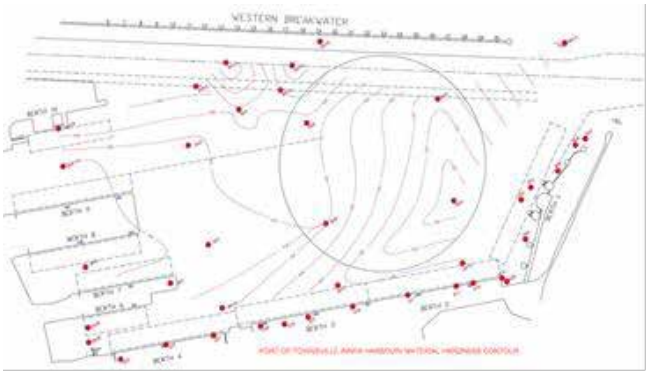

Figure 4. Inner harbor material hardness contour

7 CONCLUSIONS

The site geotechnical investigation results provided knowledge of the volume, distribution, classification and physical characteristics of material to be dredged has enabled the following practical applications:

- Determination of optimal dredge plant and dredging methods,
- Derivation of dredging production rates, project cost estimate , and dredging project risk levels assessment,
- Reduced the dredging project geotechnical risk levels and subsequently contributed to overall success of the dredging campaign.
- Slope stability analysis, dredged material suitability as structural fill assessment, estimation of reclaimed land consolidation duration, expected settlement amount and reclaimed land ground improvement alternatives.
- Comparison of actual dredging production rates with estimates and the actual dredged material properties with the site investigation findings to appreciate adequacy and comprehensiveness of the geotechnical site investigations plan.

8 REFERENCES

Douglas Partners Pty Ltd. 1992. Factual report on geotechnical investigations for access channel and inner harbor dredging. The Townsville Port Authority.

Golder Associates Pty Ltd. 2008. Report on offshore geotechnical investigations. The Port of Townsville.

International society for soil mechanics and geotechnical engineering (ISSMGE). 2005. Geotechnical and geophysical investigations for offshore and nearshore developments.

Kinlan, D. 2014. Adverse physical conditions and the experienced contractor. Delft Academic Press Leeghwaterstraat42, 2628 CA Delft, the Netherlands.

Permanent international association of navigation congresses (PIANC). 2014. Classification of soils and rocks for the maritime dredging processes. Report no. 144, PIANC general secretariat, B3B-1000 Brussels, Belgium.

Permanent international association of navigation congresses (PIANC). 2000. Site investigation requirements for dredging works. Supplement to bulletin no. 103, PIANC general secretariat, B 3B-1000 Brussels, Belgium.

The Port of Townsville. 2012. Navigation safety channel widening annual report. Port of Townsville Engineering Library.

Queensland Department of Mines. 1986. Geological Survey of Queensland- Townsville 1:100,000 Geological Series Sheet" Brisbane.

Sivakugan, N. and Das, B. 2010. Geotechnical engineering A practical problem solving approach. J Ross Publishing, Inc., Fort Lauderdale, FL, USA.

Spigolon, S.J. 1993. Geotechnical factors in the dredgeability of sediments. Department of civil and environmental engi--neering, Tulane University, New Orleans, Louisiana 70118, USA.

Geotechnical and Geophysical Site Characterisation 5 – Lehane, Acosta-Martínez & Kelly (Eds)

Using Multi-Channel Analysis of Surface Waves and Cone Penetrometer Tests to delineate an in-filled palaeochannel during routine investigations – A Christchurch Earthquake Case Study

R. Kamuhangire & T. Plunket
Aurecon, Christchurch, New Zealand

C. Rüegg
Southern Geophysical Ltd, Christchurch, New Zealand

ABSTRACT: The major events of the Canterbury Earthquake Sequence (CES) caused significant land and building damage in Christchurch between September 2010 and December 2011. The extensive damage necessitated detailed ground investigations and liquefaction hazard assessments to inform repair and rebuild options. Relying solely on intrusive testing to provide sufficient information for ground characterisation, risk assessments and design is often costly, particularly for large sites, and can be limited by site access. Combining traditional intrusive methods with non-intrusive geophysical investigations has proven to be an economical and time-saving approach and can aid in delineating abrupt changes in ground stratigraphy.
This paper presents a case study site where a combination of Multi-channel Analysis of Surface Waves (MASW) profiles and Cone Penetrometer Tests (CPTs) were used to outline the extents of an in-filled palaeochannel. The contrasting land and building damage at the site is described, together with the importance of a detailed desktop study. The MASW and CPT results are correlated with observations of damage, and the effectiveness of combining the two investigation techniques is highlighted.

1 BACKGROUND

The four major earthquakes and aftershocks of the Canterbury Earthquake Sequence (CES) between 4th September 2011 and 23rd December 2011 caused significant land and building damage. This has led to an estimated rebuild industry of NZ$40 billion (Potter et al 2015). There were around 15,000 residential houses and properties with severe damage from liquefaction and lateral-spreading related phenomena (Kaiser et al 2012).

The late Quaternary (Holocene-age) near surface geology of the Christchurch area is made up of coastal and marine deposits (Christchurch Formation) and fluvial deposits (Springston Formation) (Brown et al 1995). The variability in depositional environments since the last glaciations has led to significant lateral and vertical variability in the near surface, including numerous buried palaeochannels. The loose, water saturated, and uniformly graded sand and silt units within the Christchurch and Springston Formations are susceptible to liquefaction (e.g. Brown et al 1995). Differential behavior of the near surface soils caused extensive damage during the CES (Kaiser et al 2011).

Significant effort during the rebuild has therefore been put into ensuring that adequate geotechnical investigations are undertaken to quantify liquefaction potential and to support the design of resilient foundations and ground remediation strategies. Relying solely on intrusive investigations, in particular boreholes and cone penetrometer tests (CPTs), can be costly and sometimes logistically difficult in developed residential areas with limited access. An appropriate combination of intrusive testing and non-intrusive geophysical methods can often provide cost effective and detailed ground characterisation in areas with variable ground stratigraphy and difficult access.

Geophysics has been used to support intrusive investigations at a large number of complex sites in Christchurch. This paper describes one case study that highlights many of the advantages associated with this approach. The study site had considerable variability in ground conditions and there was significant but 'localised' land and building damage. A combination of geophysical methods and CPTs were used to delineate the structure of an in-filled palaeochannel crossing the site, to evaluate site ground conditions, to explain the observed land and building damage, and to inform development options. The investigation provided a more cost effective and timely ground investigation compared to alternative traditional intrusive investigations.

2 THE SITE AND NATURE OF DAMAGE

The site is located at Cresselly Place, St Martins Christchurch, within a 'point bar' of the Heathcote River (see Figs 1 & 2 below).

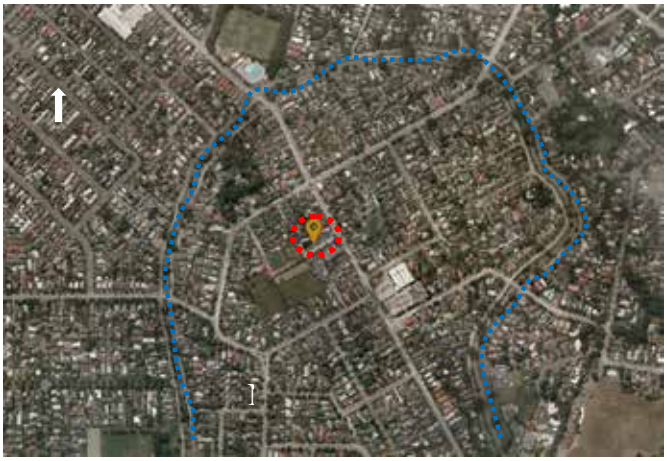

Figure 1 – Site location and relation to Heathcote River (blue dashed line). Image background from LINZ Crown Copyright Reserved.

Figure 2 – Site detail (note building locations). Image background from LINZ Crown Copyright Reserved.

The site experienced land damage in the form of ground settlement and ground cracks which were recorded by the Earthquake Commission (EQC, a Crown Entity) and its partners (CGD, 2016). A desktop review highlighted a global settlement pattern indicating a potential in-filled channel crossing the site, based on LiDAR data from the Canterbury Geotechnical Database (CGD) (Figs 3 & 4).

Building D, which appeared to straddle the edge of the channel, showed significant hogging (Fig 5). Building C sagged towards the middle, which correlates with its location near the centre of the in-filled channel. There was also up to 40 mm lateral stretch across Building D foundations and veneer around the inferred channel boundaries. Damage observed around other buildings also supported the hypothesis of the in-filled channel shown on Figure 4.

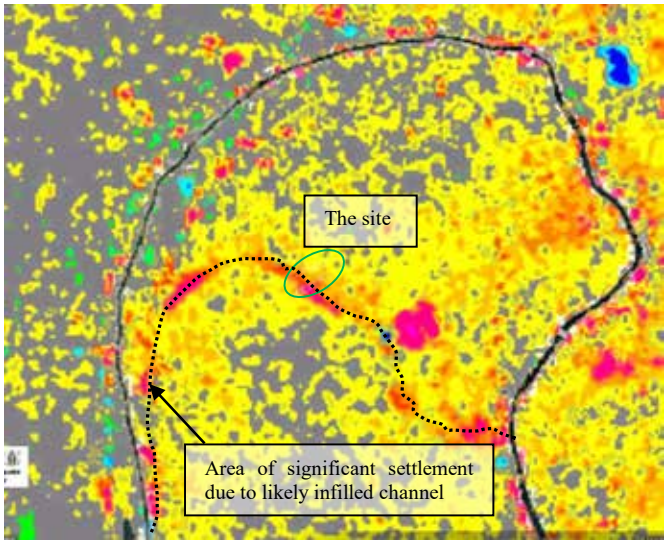

Figure 3 – LiDAR vertical movement (no tectonic component) from CES events between 4th September 2010 and 23rd December 2011. Sourced from CGD (2016).

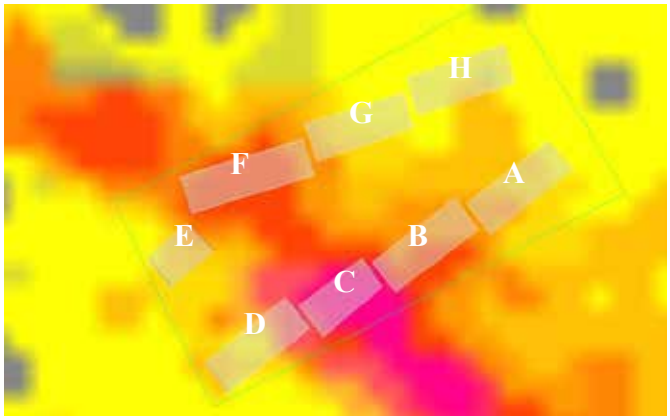

Figure 4 – LiDAR Vertical Movement from CES (site detail with building locations).

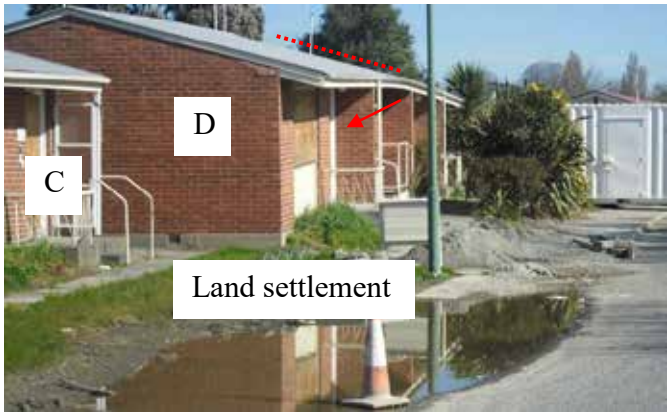

Figure 5 – Building D differential settlement (view roof line). Building 'broken' around dotted line.

3 SITE INVESTIGATION METHODS

3.1 *Desktop review and site walkover*

Prior to proposing geotechnical and geophysical investigations, a desktop review and site walkover was undertaken. The review indicated that damage at the site was likely related to changes in ground stratigraphy from a historical channel. The in-filled channel hypothesis contrasted earlier investigations, which proposed lateral spreading as the cause of land and building damage. It is noted that Cresselly Place is at least 300m from the nearest bank of the Heathcote River and previous studies probably did not have the benefit of reviewing the CGD global settlement data, which shows ground settlement occurred along a lineament, interpreted here to be a palaeochannel feature.

3.2 *Site Investigations*

A combination of eight CPTs and four MASW survey lines were undertaken in 2013 to delineate the extents of the in-filled channel and soil stratigraphy across the site. The investigation locations are shown on Figure 6, and include an additional seismic CPT and machine drilled borehole undertaken by others in 2015 (CGD, 2016).

Figure 6 – Extent of investigations undertaken.

A staged approach was adopted with MASW soundings completed first and used to plan the distribution of the CPT positions.

3.3 *MASW*

MASW is a geophysical technique that uses the dispersive nature of surface waves to model the shear-wave velocity (Vs) versus depth of the subsurface (Park et al 1999). The propagation velocity model of the recorded surface waves is inverted to find the Vs velocity model that best fits the observed propagation velocity pattern (Park et al 1999).

MASW shot records were collected at 5m spacing along the survey lines using a 24 channel towed seismic array with 1m geophone spacing and a source offset of 10m. The field records were processed using the Kansas Geological Survey software package SurfSeis4©. The velocity data was interpolated into two dimensional Vs profiles for the MASW lines.

The orientation of the MASW survey lines (Fig 6) was planned to optimise coverage across the site and to identify any abrupt changes in Vs.

3.4 *Cone Penetration Tests (CPTs)*

Eight CPTs were undertaken with positions based on results from geophysical testing and site access constraints along the northern and southern site boundaries. The CPTs targeted the middle and edges of the inferred channel, as well as ground outside the channel. The CPTs were conducted to 18m depth, near the top of the Riccarton Gravels Formation, which underlies the Springston Formation. The CPTs were not extended into the Riccarton gravels to minimise potential issues with artesian flow.

3.5 *Liquefaction Assessment*

A liquefaction hazard assessment was undertaken based on Idriss and Boulanger (2008), and Zhang et al (2002). The aim of the assessment was to identify the soil layers that could have liquefied during the major earthquakes of the CES and the likely magnitude of settlement. For this paper, back-analysis of the 22 February 2011 Mw6.2 earthquake has been re-run based on Boulanger and Idriss (2014) to highlight contrasting liquefaction potential at either ends of the inferred channel.

4 RESULTS

4.1 *CPT Results*

A summary of the CPTs is presented on Figures 7 and 8 indicating normalized cone penetration resistance (Qt) and Soil Behavior Type Index (Ic) with depth. The results indicate the following:

- The logs of CPT1 and CPT2, at the eastern end of the site with less observed settlement, show dense sands and gravelly sands from 3m to 4m depth extending to at least 10m depth. This relatively thick dense layer is generally absent in all other CPTs at shallow depth.
- The logs of CPT4 and CPT6 located in the ‘middle’ of the inferred channel, show soils with relatively low Qt cone resistance to minimum 14m depth. Organic layers are also interpreted between 11m and 13m depth in CPT6.
- Other CPTs show varying ground conditions, with the medium dense to dense layer only encountered in thin layers and generally not as strong as in CPT1 and CPT2.

Based on the CPT results, it can be inferred that CPT1 and CPT2 are outside the infilled channel, CPT4 and CPT6 are in the channel, and the rest are probably in transition zones. The CPT results therefore support the hypothesis that there is a historical channel and the nature of land and building damage is directly related to variability in ground conditions.

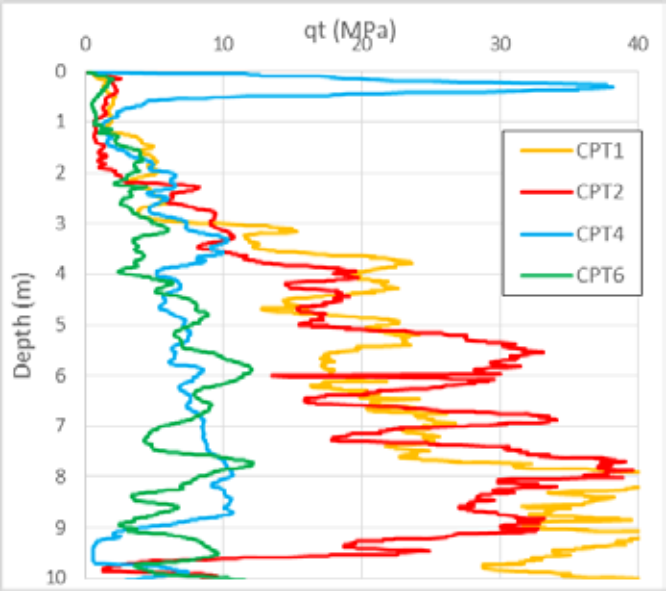

Figure 7 – Normalised cone resistance Vs depth (upper 10m profile and only CPTs 1, 2, 4, 6 shown for clarity).

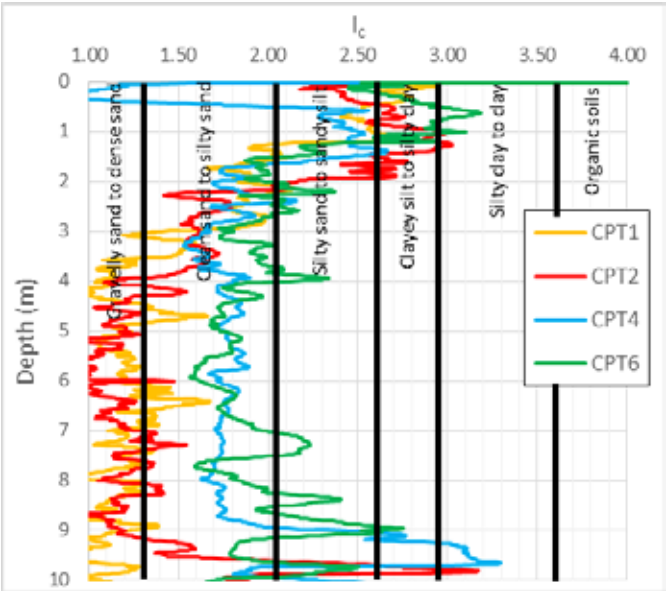

Figure 8 – Soil Behaviour Type Index (Ic) Vs depth (upper 10m profile and only CPTs 1, 2, 4, 6 shown for clarity).

4.2 *Liquefaction Assessment Results*

The liquefaction assessment results for CPTs 1, 2, 4, and 6 are presented in Figures 9 and 10 for the upper 10m profile. The results show the following:

- CPTs 1 and 2, at the eastern end of the site with less settlement, show no liquefiable layer below 3m depth to at least 10m. The assessed liquefaction settlement is generally less than 50mm.
- CPTs 4 and 6, located in the middle of the inferred channel, have potentially liquefiable layers from below the groundwater table to at least 10m depth. The assessed liquefaction induced settlement is generally more than 150mm.

The results of the liquefaction assessment were consistent with site observations. Areas where more liquefaction induced settlement was observed were assessed to have thicker calculated liquefaction layers and larger magnitudes of calculated free field settlement. The liquefaction assessment also supports the hypothesis of a historical channel and that the nature of observed damage is directly related to variability in ground conditions.

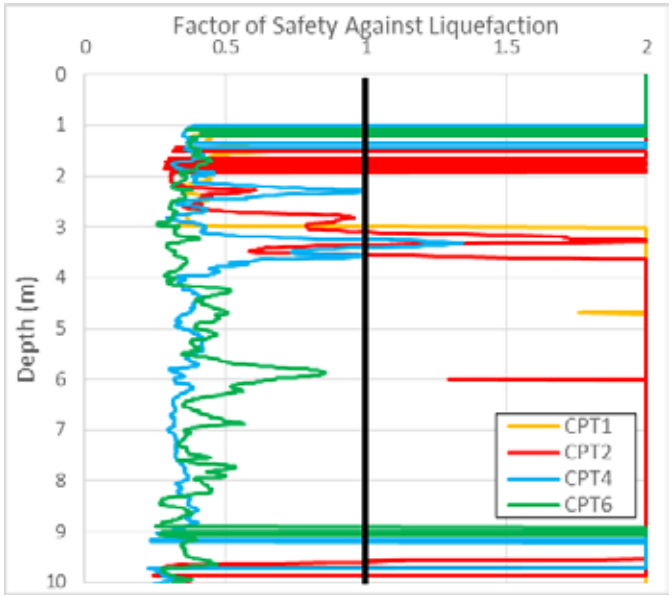

Figure 9 – Factor of Safety Against Liquefaction Vs depth (upper 10m profile and only CPTs 1, 2, 4, 6 shown for clarity).

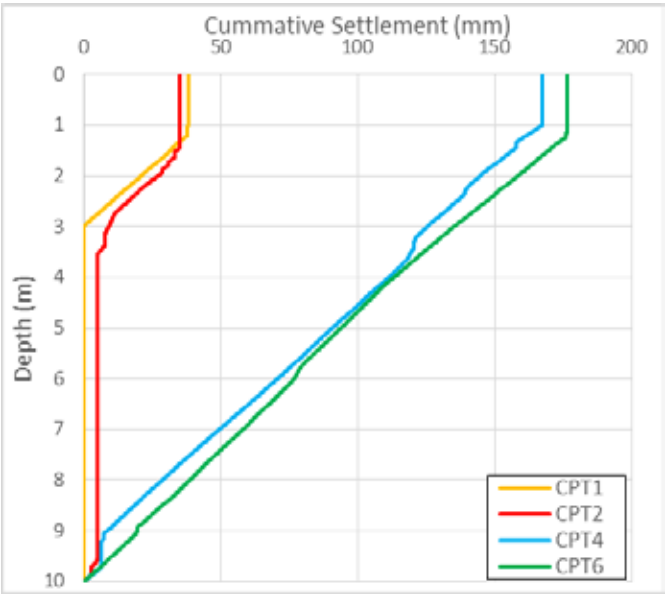

Figure 10 – Liquefaction Induced Reconsolidation Settlement Vs depth (upper 10m profile and only CPTs 1, 2, 4, 6 shown for clarity).

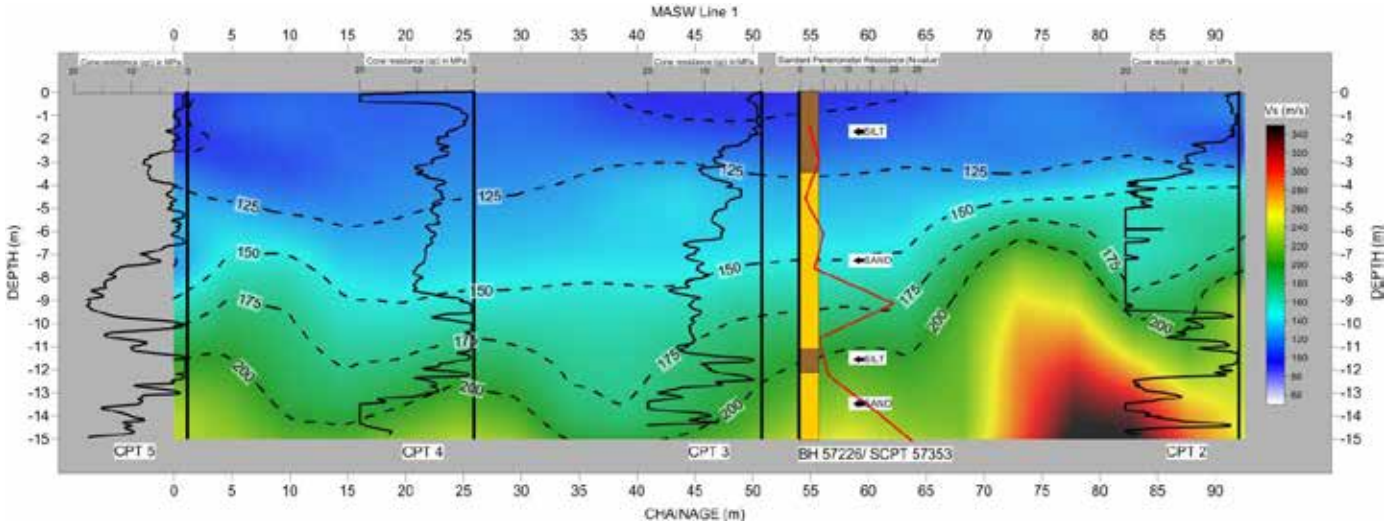

Figure 11 – MASW Line 1 plot superimposed with results of intrusive investigations.

4.3 *MASW*

The MASW results show low V_s (<100 m/s to 175 m/s) material in the upper 4m on the eastern end of the site thickening to over 10m depth near the centre of the site and then thinning towards the western end.

MASW Line 1 represents a typical west to east MASW profile across the site (Fig 11). Figure 11 includes CPTs 2, 3, 4, 5 and BH_57226 superimposed onto the plot for comparison purposes. The plots show good correlations between inferred strata based on MASW shear wave velocities and that from CPT tip resistance and borehole SPT tests. It can be inferred, based on the results, that the base of the paleochannel is coincident with shear wave velocities in the range of 170m/s to 180m/s.

It is worth noting that the MASW plot does not clearly show the weaker layers beneath stronger layers, such as in CPT5 below 11m depth (see Fig 11). While this is not critical for this study, care should be taken when interpreting MASW plots with V_s inversions. In such cases, it is recommended to review the raw shear wave velocity data and inversion modeling parameters if relying on the strength of specific layers for engineering purposes.

4.4 *Implication of results and observed damage*

A comparison between MASW and CPT profiles, borehole records, and the nature of observed damage shows the following:

- The MASW plots generally correlate well with CPT profiles and show the depth to the dense sandy layer. This is interpreted to be the base of a historical infilled palaeochannel.
- The nature of observed land damage is directly related to variability in ground stratigraphy. More settlement was recorded towards the western end of the site in locations similar to those identified on CPT and MASW plots with less dense sands and silts.
- Building damage can be explained based on building locations in the inferred channel profile. Building D straddled the low V_s part of the channel profile and transition zones while Building C was in the middle where larger magnitudes of settlement could be expected based on ground stratigraphy.
- Ground cracks recorded at the site appear to coincide with areas of sudden changes in ground stratigraphy based on MASW plots.

A combination of MASW and CPTs can therefore be effectively used to delineate sudden changes in ground stratigraphy and inform likely future land and building damage in liquefaction prone areas.

5 CONCLUSIONS

This case study at Cresselly Place highlights the potential for MASW to identify in-filled channels and abrupt changes in ground stratigraphy, which can have a significant influence on future land and building damage particularly in liquefaction prone areas.

At Cresselly Place, it was demonstrated that MASW findings correlated with CPTs, boreholes, and observed damage. MASW, with the ability to collect more data points at relatively low cost, can therefore be used in forensic and routine site investigations to produce 2D profiles between intrusive investigation points.

At Cresselly Place, it was possible to complete MASW lines in some areas where even small CPT rigs could not access. The versatility of the system has been successfully adopted for numerous site investigations in Christchurch.

Finally, the desktop review found critical information on the site, the advantage of which when planning site investigations cannot be overstated. At Cresselly Place, without the benefit of global vertical

settlement data, CPTs supplemented with one or two boreholes could have been considered appropriate for the redevelopment. However, CPTs and boreholes on their own could not have provided a complete explanation for the differing ground conditions, and may have led to conservative rebuild and remediation strategies based on unknown risks.

6 RECOMMENDATIONS

The following should be noted when utilising MASW (and any other non-intrusive investigation technique) for ground characterisations in the course of a geotechnical investigation:

- MASW investigations should be combined with intrusive investigations such as CPTs or boreholes, to allow for physical sampling and geological correlation of V_s variations.
- A staged approach should be adopted where practicable, to allow preliminary findings from MASW to be used to inform targeted and more expensive intrusive investigations.
- MASW may not be appropriate for some subsurface conditions, and may be limited in its ability to model high jumps in V_s (i.e. soil to bedrock), V_s inversions (i.e. gravels to marine silts), and sharp vertical changes in V_s (i.e. steeply dipping channel edges or fault planes). Engineers should consult with a qualified geophysicist to identify limitations specific to a site, and alternative solutions.

7 ACKOWLEDGEMENTS

The authors wish to thank Christchurch City Council, particularly Lee Sampson, for the opportunity to be involved in their rebuild portfolio, their support during the investigations, and for giving us the permission to share details about Cresselly Place. The authors also wish to thank their respective employers, Aurecon and Southern Geophysical Ltd, for the time and support during the project work and preparation of this paper.

8 REFERENCES

Canterbury Geotechnical Database (CGD), 2015. Retrieved March 2016 from https://canterburygeotechnicaldatabase.projectorbit.com/

Boulanger, R. W. and Idriss, I. M., 2014. *CPT and SPT based liquefaction triggering procedures*. *Report No. UCD/CGM-14/01*. Center for Geotechnical Modelling, Department of Civil and Environmental Engineering, University of California, Davis, California.

Brown, L.J., Beetham, R.D., Paterson, B.R., and Weeber, J.H. 1995 Geology of Christchurch, New Zealand. *Environmental and Engineering Geoscience*. I:4: 427-488.

Kaiser, A., Holden, C., Beaven, J., Beetham, D., Benites, R., Celentano, A., Collet, D., Cousins, J., Cubrinovski, M., Dellow, G., Denys, P., Fielding, E., Fry, B., Gerstenberger, M., Langridge, R., Massey, C., Motagh, M., Pondard, N., McVerry, G., Ristau, J., Stirling, M., Thomas, J., Uma, S.R., and Zhao, J., 2012. The M_w 6.2 Christchurch Earthquake of February 2011: preliminary report. *New Zealand Journal of Geology and Geophysics*. 55:1: 67-90.

Park, C.B., Miller, R.D., Xia, J. 1999. Multichannel analysis of surface waves. *Geophysics*. 64:3: 800-808.

Potter, S.H., Becker, J.S., Johnston, D.M., Rossiter, K.P. 2015. An overview of the impacts of the 2010-2011 Canterbury earthquakes. *International Journal of Disaster Risk Reduction* 14 (2015): 6-14.

Zhang, G., Robertson, P.K., Brachman, R.W.I. 2002. Estimating liquefaction-induced ground settlements from CPT for level ground. NRC Research Press J:19: 1168-1180

Geotechnical and Geophysical Site Characterisation 5 – Lehane, Acosta-Martínez & Kelly (Eds)

CPTU crossing existing boreholes in the soil

K. Kåsin
Norwegian Geotechnical Institute, Oslo, Norway

ABSTRACT: One of the most difficult deviations to explain, has been an unexpected drop in measured values inside a homogenous clay layer. Using the correlations from Karlsrud et al (2005), the interpreted CPTU sounding show a drop in undrained strength far below a normally consolidated soil at some sites. The paper shows that the drop in cone resistance and interpreted shear strength is due to disturbance and remoulding of the clay caused by previous investigations at the same location, as it is common practise to at least perform either a Norwegian total sounding or a rotary pressure sounding at a location where a CPT is performed. Using the inclination of the probe registered during the CPTU soundings, and the thickness of the disturbed and remoulded layer in the profile, the horizontal extent of the disturbed zone around the previous sounding is estimated to be around 60 cm in diameter, or around 8 - 12 times the diameter of the drill bit that is 57 mm in diameter.

1 INTRODUCTION

During the last 15 years the use of CPTU has developed into becoming one of the most widely used ground investigation methods in Norway. CPTU is used to classify soil type behaviour and to provide interpretation basis for a range of strength and deformation parameters for the soil in geotechnical calculations. As the use of CPTU has spread, NGI have collected a number of CPTU soundings where the results deviate from what is expected. The results presented in this paper come from an internal research project at NGI, and are presented in Kåsin (2011), which looked into several different types of anomalies in CPTu soundings.

2 SIMULTANEOUSLY LOW TIP RESISTANCE, SIDE FRICTION, AND PORE PRESSURE

One of the deviations that has been most difficult to explain is an unexpected drop in the tip resistance, q_c, side friction, f_s, and pore pressure, u_2, within what appears to be a homogenous clay layer. Such a drop in the measured data from each of these sensors would normally indicate that there is a weaker layer at this interval. If the data from these CPTU are interpreted according to Karlsrud et al (2005), as is common practise at NGI, the clay in these layers appears to be far below the strength of a normally consolidated clay. However, to have a weaker layer of clay, with a strength that appears to be far below the strength of a normally consolidated clay is unrealistic, especially when other data like geological history or data from investigations nearby are taken into account. The anomaly can not be reproduced by performing a new CPT at the same location.

Figure 1 shows a typical example of this type of anomaly, with both a total sounding, and the CPT with the anomaly present in the depth interval between ca. 9.7 m and ca. 12.7 m. The total sounding does not show any indication that the clay is weaker in the same layer. The total sounding and CPT were performed in central parts of Oslo, just east of Gamlebyen gravlund, at a borehole location 411. The tests were performed by Rambøll in 2009 with a Geotech CPTu type Nova. Figure 2 shows the same CPTu sounding where the undrained shear strength is interpreted using the correlations presented in Karlsrud (2005). Between 9.7 m and 12.7 m the strength of the soil is below the trend at the site, and between 10.5 m and 12.4 m the interpreted strength is below 0.3 x P_0', that can be used as an estimate of the shear strength for a normally consolidated clay in the area. Both the total sounding and the CPT indicate homogeneous, sensitive clay, with an interpreted over-consolidations ratio, OCR, between OCR=3 just below the dry crust at 5 m, and reducing with depth down to around OCR=1.8 at 20 m. The anomaly can be seen between 10 m and 12.9 m where the measured values in both the tip resistance, qc, side friction, fs, and the excess pore pressure, u2, are lower than the rest of the profile.

3 POSSIBLE EXPLANATIONS FOR THE LOWER MEASUREMENTS

Several different explanations for the anomaly have been suggested:

1. Sensor malfunction in the CPTU probe.
2. CPTu test executed erroneously, leading to lower or wrong values.

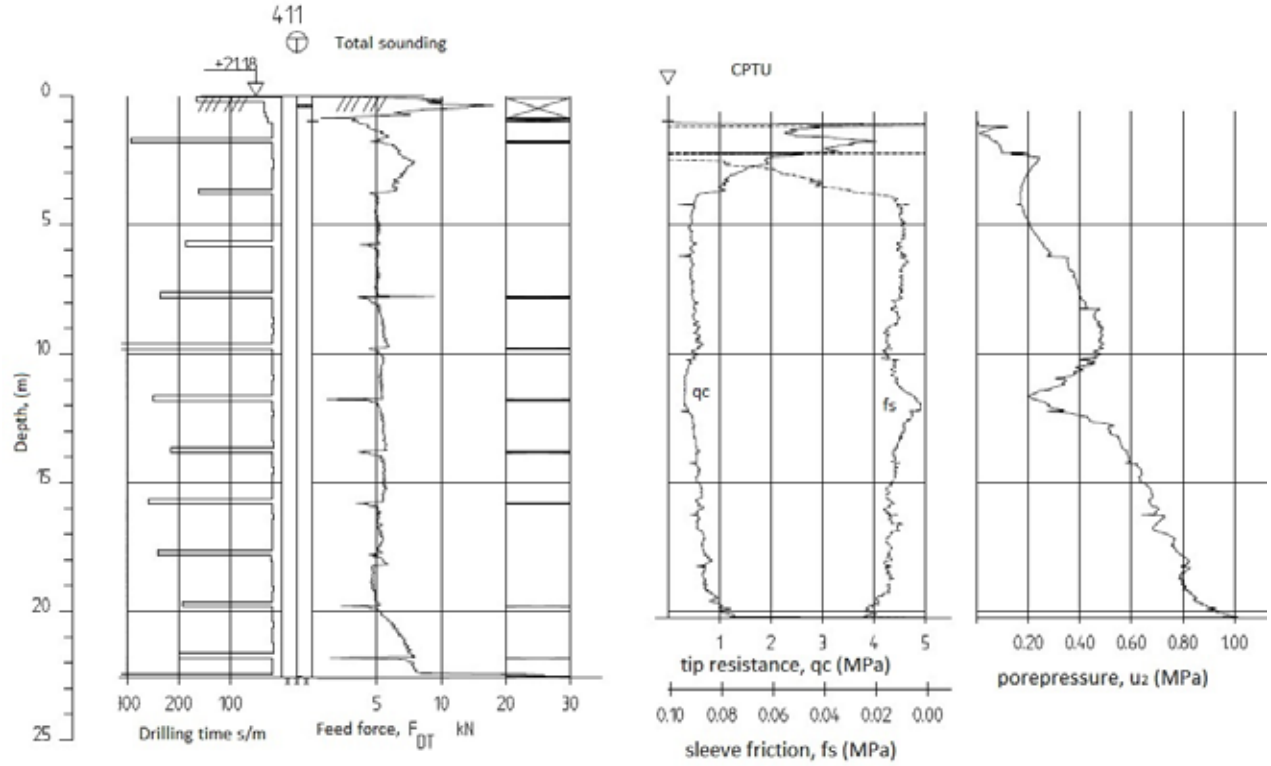

Figure 1: Plot of total sounding and CPT sounding in borehole 411, Oslo

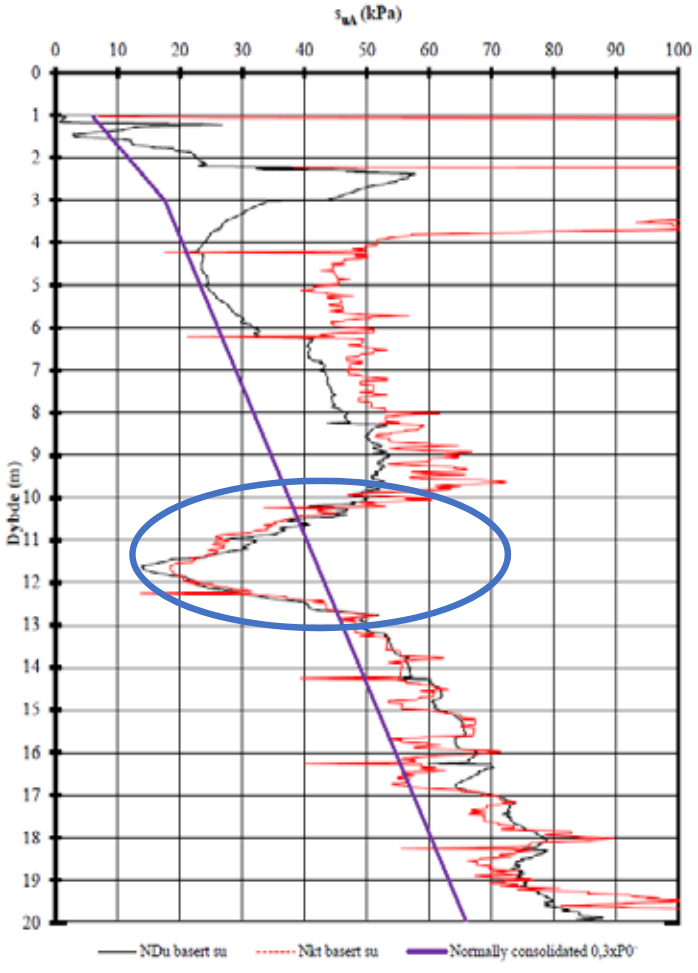

Figure 2. Interpreted shear strength

3. The strength of the clay layer is lower in just this interval – some kind of under-consolidated clay.
4. The strength is lower in the interval because of a shear band in the ground, reducing the strength of the soil.
5. The strength is lower in the interval because the CPTU passes through a previously drilled hole in the ground at an angle

Explanations 1 and 2 are often the "go to explanation" when geotechnical engineers receive data that does not conform to what is expected from the field, especially when the phenomenon cannot be replicated with another test at the same site, or if only one of several tests in the same deposit show an anomaly.

As this type of anomaly has been present in data collected from several locations with different types of clay, and from several renowned Norwegian geotechnical companies, and from both common CPT equipment manufacturers, it seems like it is not a problem with neither the personnel nor the equipment. Through the raw data files from the soundings, there are no indications that there is anything erroneous with the execution of the works in the field or with the sensors on the probe. To add to this it is in the authors opinion unlikely that a type of random error in the CPTUs sensors presents itself across several different probes of different makes, or

that several drilling crews are performing the CPTu test wrongly in some way in just one interval.

Explanations 3 and 4 are also unlikely, as the anomaly normally is not reproducible if the CPTu test is redone at the same location. If the soil at the location actually has a lower shear strength, either because of a shear band or because of some other phenomenon, one should expect to be able to detect this if the CPT tests are redone.

4 CROSSING OF PREVIOUS BOREHOLES

It is in this authors opinion that the most likely cause of these anomalies is that the CPT probe crosses through the disturbed and possibly remoulded zone around a previously drilled borehole or sounding.

This is supported by the fact that in Norway, it is common practise to perform either a total sounding or a rotary pressure sound at any given borehole location, before a CPTu is performed. The purpose of these soundings would be to collect data that CPT does not provide (eg. depth to bedrock, mapping of sensitive layers), and to map layers of elements in the ground that can damage the CPT-probe itself.

After performing the total sounding, the drill rig is moved 1 – 2 m, and the CPT-sounding is executed. The Norwegian practice follows Norges Geotekniske Forening melding 5 (2010), which specifies that a CPT has to be performed either 2 m or minimally 20 times the diameter, from a previous borehole to avoid performing the CPT in soil affected by the previous investigation. For the total sounding and rotary pressure soundings, these diameters are 57 mm and 56-51 mm, respectively. This corresponds to 1.14 m to 1.02 m if the latter requirement is to be used.

It is also common practice to predrill through hard layers of top soil or dry crust, as these hard layers are often dilatant, and can suck out the saturation fluid in the pore pressure sensor and can damage the probe. This practice of predrilling, often means that even in the start of the sounding, the CPT can be somewhat out of verticality, as the rods often will be unsupported horizontally within the predrilled hole at the start of the sounding. Any small rock or pebble at the bottom of the borehole will then push the CPT sideways, because of the long unsupported drill string in the hole.

As shown in Figure 3, which shows the horizontal deviation vs the true depth for CPT 411, the horizontal deviation of the CPT can be significant, and certainly more than the 1 – 2 m that is common practice to move the drill rig in between different tests at the same location. The horizontal and vertical deviations in each depth increment is calculated using the following equations:

$$\Delta h = \sin(\alpha), \Delta v = \cos(\alpha)$$

where α is the measured inclination angle in each increment in degrees. These incremental values can then be used to see how far the CPT has travelled horizontally during the penetration.

Going back to the sounding at location 411CPT and applying this, one can see that at 9.7 m depth, where the start of the layer with apparently lower shear strength, the CPT has moved a horizontal distance of 0.85 m, at 12.7 m the distance is 1.45 m, and at 20 m the horizontal distance travelled is over 3 m. The CPT travels around 60 cm horizontally within the 3 m thickness of the layer with lower shear strength, indicating that the width of a disturbed zone that is at least this wide.

Looking back to Figure 2, the interpreted shear strength is falling between 9.7 m and 11.6 m where the interpreted strength is at the lowest. From 11.6 m the strength increases strongly with depth to 12.7 m. This points to the CPT seeking the path of least resistance as it is passing through the less disturbed soil furthest away from the previous sounding, and then passing through or close to the center of the borehole at 11.6 m. From the center of the previous borehole the probe goes through less and less disturbed soil until it reaches undisturbed soil at around 12.7 m. This fits well with an assumption that the disturbance or remoulding effect of the previously drilled sounding is greatest near the center of the drilled, and reducing with distance from the center.

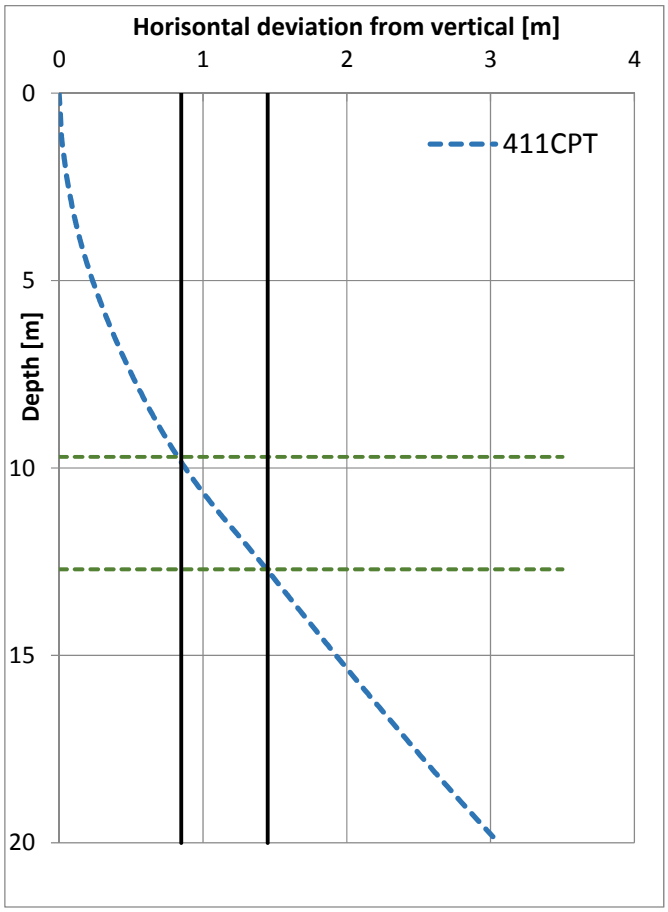

Figure 3. Calculated horizontal deviation of 411CPT using measured inclination data.

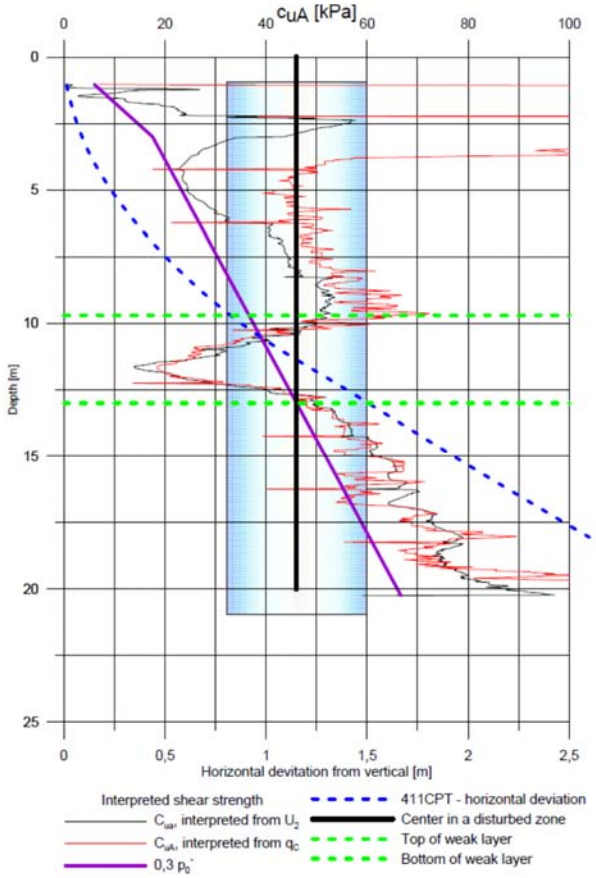

Figure 4. Interpreted shear strength, weak layer and the path of the CPT in the ground, from borehole 411CPT

5 ESTIMATING THE WIDTH OF THE DISTURBED ZONE

To estimate the width of the disturbed zone around the previous sounding one look at the horizontal distance that the CPT travels within the disturbed layer. In sounding 411, the CPT travelled 60 cm horizontally within the disturbed layer. This suggest that the disturbed zone is close to this width, and this indicates a disturbed zone of 8 – 12 times the diameter of the sounding that was done before the CPT.

Through assuming that the disturbed zone around a total sounding in clay is mostly the same width as the size of the drill bit always is the same, and that the total/rotary pressure soundings are vertical, the only unknown in each location will be the distance between the CPT and the previous sounding, as this is normally not known. It is common practise when surveying borehole locations that the least advanced test represents the borehole location, and that the other tests at the same locations are given the same coordinates.

The horizontal distance between the previous sounding and the CPT can be estimated by varying the horizontal distance between the previous sounding and the CPT in each of the cases where this anomaly presents itself on a plot where the following is plotted:

- The horizontal distance travelled by the CPT.
- The top and bottom of the disturbed layer from the shear strength interpretation
- Lines representing the zone of disturbance in the soil around the previous sounding In all these cases a 60 cm wide zone of disturbance fits well with the available data.

6 RESULTS

Figures 4 – 6 show 3 examples of borehole locations where the CPT, in the author's opinion, has crossed the previous total sounding/rotary pressure sounding. The red and black curves are the interpreted shear strength using the correlations for N_{kt} and $N_{\Delta u}$ from Karlsrud et. Al. 2005, for q_c and u_2 respectively. The purple curve is an evaluation of the shear strength of a normally consolidated clay using $S_u = 0{,}3p_0`$. The blue dotted line is the horizontal deviation of the sounding that is calculated using the measured inclination angle during the sounding. Also marked on the plot is the thickness of the disturbed layer, and the assumed placement of a previous borehole/ sounding the disturbed zone around it.

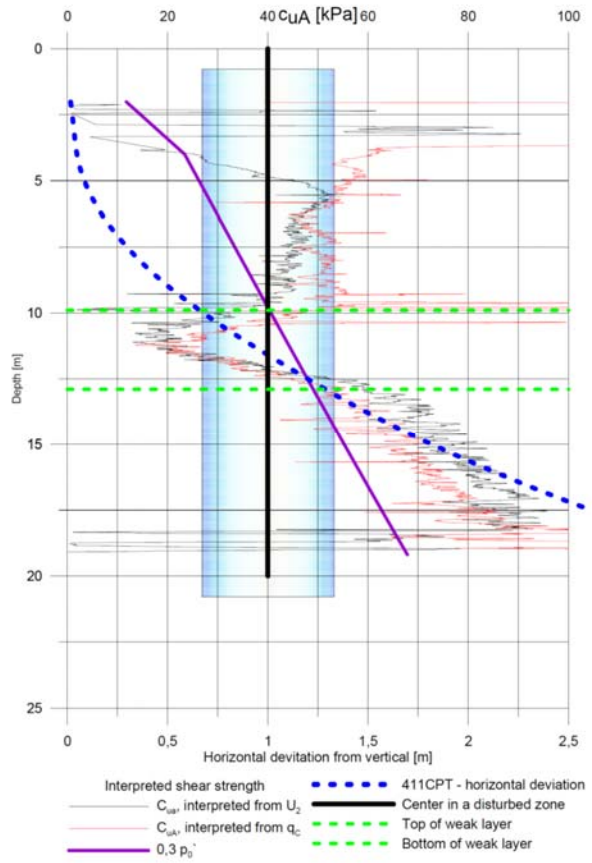

Figure 5. Interpreted shear strength, weak layer and the path of the CPT in the ground, from borehole 5 Stasjonsveien in Oslo

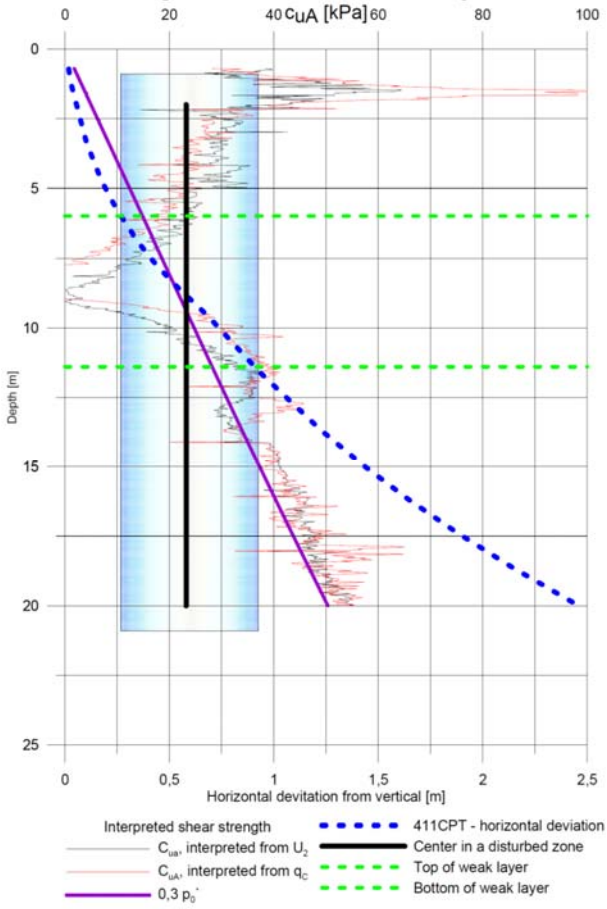

Figure 6. Interpreted shear strength, weak layer and the path of the CPT in the ground, from borehole V-NB-018 in Nykirke in Norway

7 DISCUSSION

In the estimation of the width of the disturbed or remoulded zone there is a couple of assumptions. Firstly, there is the assumption that the total soundings are vertical in the case where we see that the CPTs deviate strongly from verticality. However as the total soundings are rotating while penetrating the ground, they are less likely to deviate from the strait line, and as they are started from the terrain level, where the verticality of the drill string can be checked, the assumption of verticality of the total/rotary pressure sounding is not unreasonable for relatively short boreholes. The three examples in figure 4 – 6 shows that the CPT crosses the previous soundings at 9.8-13 m in figure 4, at 10-13 m in figure 5, and 6 -11 m in figure 6, and the width of the disturbed zone is the same, around 0,6 m, in all of them.

The second assumption is that the width of the disturbed zone is the same in all of the boreholes. The width of these may very well vary by several factors, some of which are listed below:

- Strength of the soil
- OCR of the soil
- Sensitivity of the soil
- Time in between the CPT and the previous sounding.
- Plasticity of the soil.
- Design of the drill bit/tool that generates the soil disturbance

However, there has not been enough data available to make any investigations into these factors and their impact, if any. It is the authors suggestion that further work are focused into collecting more data to look into which of these or other factors contribute to the generation of this type of anomaly and to look into what influences the width of the disturbed zone.

8 CONCLUSIONS

It is the author's opinion that the low values encountered in the presented soundings, cannot represent faulty equipment or low strength in the ground.
The geology in the area well known and the strength of the soil should not be as low as the measured values indicate. Moreover, since the low values cannot be reproduced by other CPTs or by sampling the most logical explanation for the low values is that the CPT has crossed a disturbed zone around a previous sounding.

The examples presented in the paper show that the path of the CPT can go through previous soundings in the ground near the CPT, even if the drilling rig is moved 1 m or more to the side, as the CPT can deviate several meters to the side during the sounding, as the horizontal deviations calculated from the measured inclinations. The zone of disturbance created by

total soundings, which are performed with as seem to be the around 60 cm, and this is around 10 times the diameter of the drill bit used for total soundings.

REFERENCES

Rambøll 2009, Report to Jernbaneverket Utbygging, Nytt dobbelstpor Oslo-Ski, Grunnundersøkelser, Datarapport, Innføring til Oslo S, report 4, project 6080030, dated 2009-11-11.

Karlsrud, K., Lunne, T., Kort, D.A. & Strandvik, S. 2005, CPTU Correlations for Clays. International Conference on Soil Mechanics and Foundation Engineering, 16. Osaka 2005. Proceedings, Vol. 2, pp. 693-702.

NGF 2010, NGF melding nr. 5 Veiledning for utførelse av trykksonderinger

Kåsin, K. 2011, Avvikende CPTU – 20110094 - 00-1 – R, Norges geotekniske institutt

Geotechnical and Geophysical Site Characterisation 5 – Lehane, Acosta-Martínez & Kelly (Eds)

Effect of inter-particle strength on K_0 correlation for granular materials

J. Lee, G. Kim, I. Kim, D. Kim, & B. Byun
Yonsei University, Seoul, South Korea

ABSTRACT: The coefficient of lateral earth pressure at rest K_0 is an important state soil variable that is necessary to characterize the in-situ stress state of natural soil deposits. In this study, the values of K_0 measured for various granular materials were analyzed and the effect of inter-particle strength on the K_0-ϕ' correlation was presented. The inter-particle strength was referred to as the surficial frictional resistance mobilized on the contact areas of adjacent soil particles. The measured K_0 values indicated that denser and more angular materials tend to produce lower K_0 values, likely due to the interlocking effect as postulated by the Jaky's K_0 equation. It was also seen that neither the critical-state friction angle nor the peak friction angle for the Jaky's K_0 equation produced close match to the measured K_0 values. The use of peak friction angle in fact underestimated the values of K_0. A new K_0 correlation model based on the inter-particle strength analysis was presented. The effect of interlocking on the lateral effective stress was taken into account for the inter-particle strength K_0 correlation model. It was shown that the inter-particle strength model well described the dependency of K_0, a state variable, on the internal friction angle of soil, a strength parameter.

1 INTRODUCTION

The well-known K_0 equation by Jaky (1944, 1948) is commonly adopted in practice to estimate the values of K_0 that is given as a sole function of the internal friction angle (ϕ') of soils. It was established and analyzed based on the stress distribution and equilibrium condition assumed within the wedge-shaped sand pile (Mesri and Hayat 1993, Michalowski 2005). While the Jaky's K_0 equation has been widely used for various purposes in geotechnical engineering, the close correlation of K_0 to ϕ' is still interesting in that a pre-failure state parameter is well related to the failure-state parameter of the friction angle. It is indicated that the appropriate quantification of the friction angle is crucial for the K_0–strength correlation to be valid.

The peak friction angle (ϕ'_p) is composed of the critical-state friction angle ϕ'_c and the dilatancy angle ψ_p (Bolton 1986). While ψ_p is a state variable, ϕ'_c is an intrinsic variable that would give a unique K_0 value. According to the original Jaky's K_0 equation, the friction angle for the correlation should be ϕ'_c. However, it has been observed and reported that K_0 is not unique but varies with the relative density (Ishihara 1993, Wanatowski and Chu 2007, Lee et al. 2013). It was also reported that the calculated K_0 values using ϕ'_p are not in good agreement with measured values. All these implies that the K_0 correlation to ϕ' is still subject to some uncertainties in particular in regard to the value of friction angle that is to be adopted into the correlation.

In this study, the values of K_0 for granular materials are analyzed by focusing on the correlation of K_0 to the strength parameter of soils. Based on the work given in Lee et al. (2013, 2014), a new correlation of K_0 based on the inter-particle strength is explored and presented. The mobilized stress state between soil particles and inherent particle characteristics are considered in the K_0 correlation.

2 COEFFICIENT OF LATERAL EARTH PRESSURE AT REST

The coefficient of lateral earth pressure at rest (K_0) is an important state variable that is given by the ratio of lateral to vertical effective principal stresses. It specifies the geostatic stress state of soils and the following correlation proposed by Jaky is commonly used in practice (Jaky 1944, 1948):

$$K_0 = 1 - \sin\phi' \tag{1}$$

where ϕ' = internal friction angle of soils. While Eq. (1) has been re-visited and confirmed by several authors (Mesri and Hayat 1993, Michalowski 2005, Pipatpongsa et al. 2009), it is still interesting that the

pre-failure state soil variable K_0 is well correlated to the strength parameter ϕ' that indicates failure.

In Eq. (1), the friction angle ϕ' corresponds to the repose angle of the sand wedge formed by pouring sand particles and thus is close to the critical-state friction angle ϕ'_c as discussed by Mesri and Hayat (1993). This then implies that K_0 is always unique for a given sand, which is however not the case of what is usually observed on actual sands. It is often observed that K_0 varies with the density condition showing increases with decreasing relative density (D_R).

3 EXPERIMENTAL TESTS

3.1 *Oedometer Tests*

To analyze the values of K_0 for various materials and stress conditions, thin-walled oedometer tests were conducted using three granular materials: Jumumjin sand, smooth glass beads and rough-surfaced etched glass beads (Lee et al. 2013). Triaxial (TX) tests were conducted on the test materials. The values of critical-state friction angle ϕ'_c were 37.8°, 27.1°, and 30.8° for Jumunjin sand, glass beads and etched glass beads, respectively. The peak friction angles ϕ'_p were also evaluated for different relative densities and confining stress levels.

The thin-walled oedoemeter test system was set-up and used to measure K_0 assuming that the K_0 condition is satisfied for the radial strain limit smaller than around 5×10^{-5} (Kolymbas and Bauer 1993). The thin-walled oedometer was made of aluminum with 0.13-mm thickness and 66-mm diameter. Strain gauges were installed on the surface of thin-walled cylinder. The height of samples prepared for thin-walled oedometer tests was 40 mm.

Test materials were placed in the thin-walled mold and compacted to achieve the target relative density. The test specimen was then subjected to loading-unloading-reloading process. Different relative densities were considered for the test specimens, D_R = 33% and 84% for Jumunjin sand and D_R = 56% and 80% and D_R = 55% and 81% for glass beads and etched glass beads, respectively.

3.2 *Measured K_0 Values*

Fig. 1 shows the values of K_0 with applied vertical effective stress (σ'_v) measured for different test materials at different relative densities. Note that the differences of maximum and minimum void ratios (e_{max} and e_{min}) was around 0.3 for Jumunjin sand while those for glass beads and etched glass beads were 0.1 and 0.2, respectively. The K_0 values of the dense sand were lower than of loose sand throughout the entire stress range for the tests. The results from dense sand showed the lower limit range of K_0 measured from all the test materials. The values of K_0 were higher during unloading while those for reloading were between loading and unloading stages. Note that, when unloaded, the horizontal stress tends to be locked and less released while unloading process makes the vertical stress entirely released.

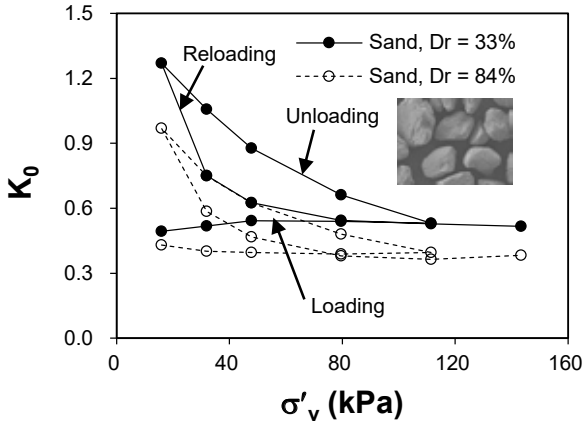

(a)

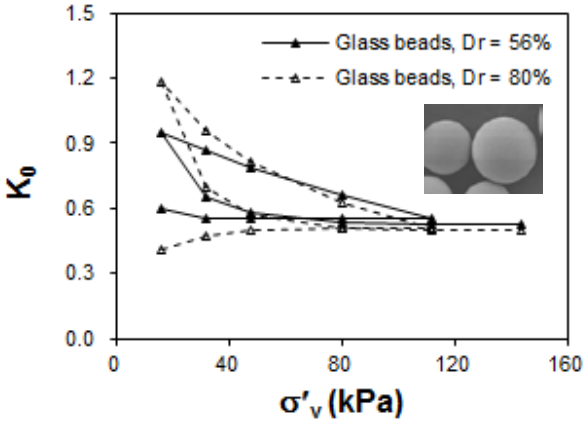

(b)

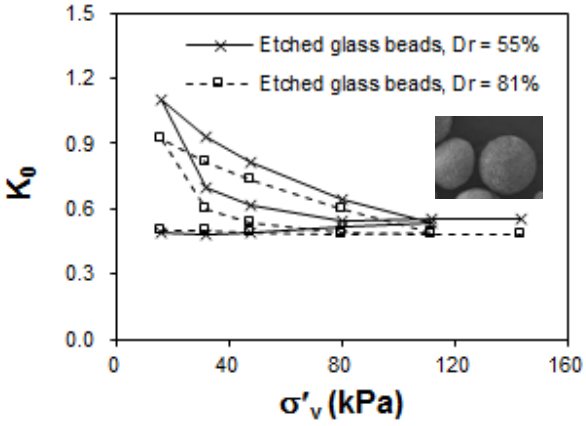

(c)

Figure 1. Values of K_0 for (a) Jumunjin sand; (b) glass beads and (c) etched glass beads.

The values of K_0 for dense sand were lower than for glass beads indicating the effect of angularity

and interlocking. The difference of glass beads and etched glass beads, on the other hand, indicated the degree of surface roughness. As compared from Figs. 1(b) and (c), the values of K_0 between untreated and etched glass beads were not significantly different.

Fig. 2 shows the measured versus calculated values of K_0 using the peak (ϕ'_p), critical-state (ϕ'_c) and inter-particle (ϕ'_s) friction angles obtained for the test materials. The values of ϕ'_s were estimated as equal to 26°, 17° and 21° for Jumunjin sand (JS), glass beads (GB) and etched glass beads (EGB), respectively, from the previously reported results in Procter and Barton (1974) and Andrawes and El-Sohby (1973). The values of K_0 obtained from ϕ'_c and ϕ'_s were constant as these friction angles were unique and constant. The calculated K_0 values with ϕ'_p showed the lowest range, while those using ϕ'_s were in the upper bound range. From Fig. 2, it is seen that the correlation of K_0 to ϕ'_c is approximately valid for uniformly round materials, whereas the particle interlocking affects the correlation for irregularly-shaped natural sands. It was also indicated that the correlation to ϕ'_p tends to underestimate K_0 values.

4 INTERPARTICLE STRENGTH MODEL

4.1 *Stress State*

Fig. 3 shows the mobilized stress state for the K_0 condition compared with those of active (σ'_a) and passive (σ'_p) stress states. For the mobilized friction angle ϕ'_{mob} in Fig. 3, K_0 can be given as the following relationship:

$$K_0 = \frac{\sigma'_{h0}}{\sigma'_{v0}} = \frac{1-\sin\phi'_{mob}}{1+\sin\phi'_{mob}} \qquad (2)$$

Eqs. (1) and (2) both represent the correlation between K_0 and strength characteristics. Eq. (2) may be however more straightforward as ϕ'_{mob} indicates the mobilized strength, which is difficult to quantify (Mesri and Hayat 1993).

Although the in-situ K_0 vertical and horizontal stresses of σ'_{v0} and σ'_{h0} given by ϕ'_{mob} exist within the zone below failure envelop, the inter-particle stresses acting on particle contacts would be at the limit stress states that is just about to initiate particle slips. The limit stresses are then related to the frictional resistance of particle surfaces, which can be characterized using the inter-particle friction angle ϕ'_s.

Fig. 4 shows the K_0 stress state [Fig. 4(a)] and the inter-particle stress states at particle contact [Fig. 4(b)]. The inter-particle stresses σ'_{np} and τ_p in Fig. 4(b) represent the limit stress state given by the inter-particle friction angle ϕ'_s. The inter-particle stresses will continuously develop until particle slip occurs until the global geostatic condition is reached. For the

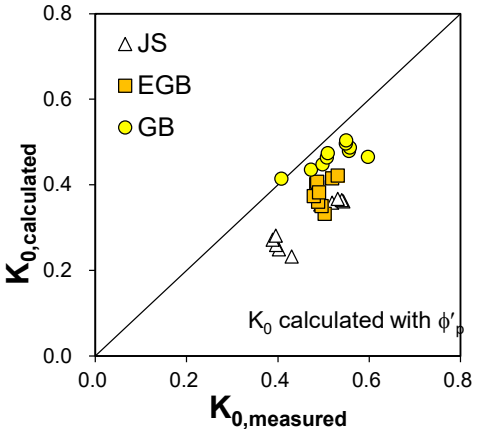

(a)

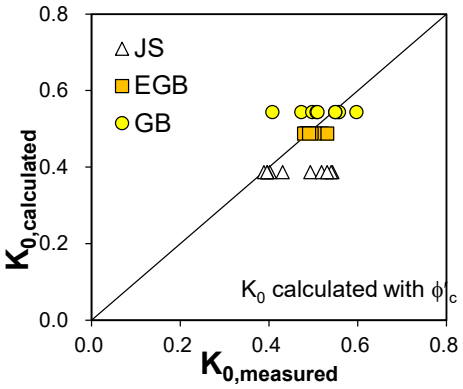

(b)

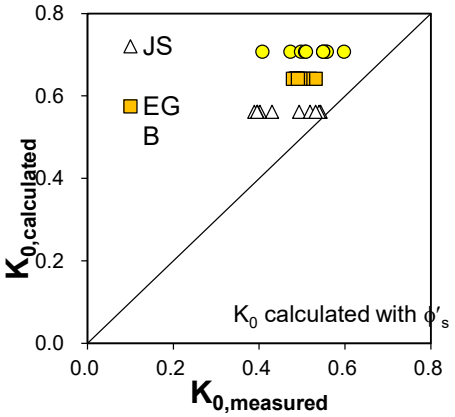

(c)

Figure 2. Measured versus estimated K_0 values of all materials for (a) ϕ'_p; (b) ϕ'_c and (c) ϕ'_s.

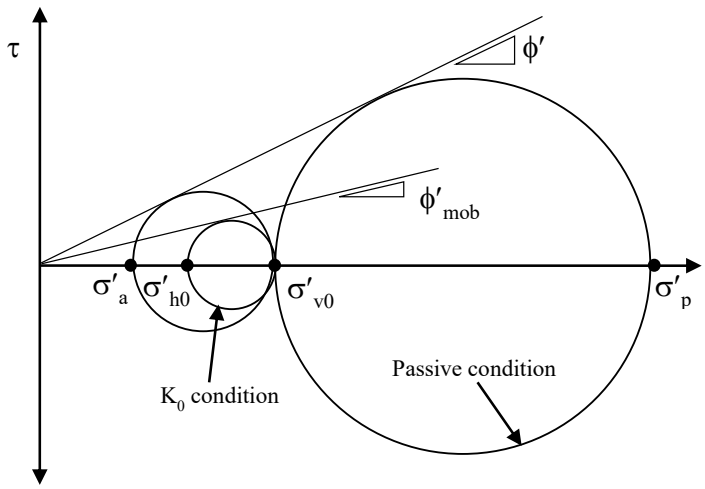

Figure 3. Stress states for K_0 condition.

inter-particle stresses acting on particle surfaces shown in Fig. 4(b), the local stress ratio K_{0p} between the local principal stresses of σ'_{vp} and σ'_{hp} can be given as follows:

$$K_{0p} = \frac{\sigma'_{hp}}{\sigma'_{vp}} = \frac{1-\sin\phi'_s}{1+\sin\phi'_s} \tag{3}$$

where K_{0p} = inter-particle stress ratio; σ'_{vp} and σ'_{hp} = vertical and horizontal principal stresses at particle contacts, respectively; and ϕ'_s = inter-particle friction angle. Due the stress concentration at contact areas, σ'_{hp} and σ'_{vp} are larger than σ'_{h0} and σ'_{v0}. However, the ratios of σ'_{hp} to σ'_{vp} and σ'_{h0} to σ'_{v0} would be similar as equilibrium conditions hold for both local and global stress states, implying that K_{0p} would also be similar to K_0.

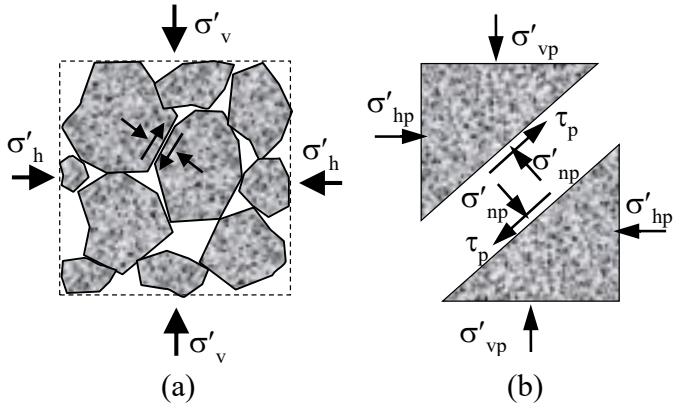

Figure 4. Stress states for (a) K_0 condition and (b) inter-particle state.

The particle interlocking is another factor that should be considered for K_{0p} of Eq. (3) and K_0 as ϕ'_s only represents the frictional resistance of particle surfaces. The particle interlocking affects the strength mobilization, stress propagation and thus the stress ratio. The mobilized friction angle ϕ'_{mob}, which defines the global stress state, in fact includes the effect of particle interlocking. This can be evaluated by combing the effect of particle interlocking and the inherent frictional resistance of the inter-particle friction angle ϕ'_s or critical-state friction angle ϕ'_c.

While both ϕ'_s and ϕ'_c can be adopted, ϕ'_c would be better option as it is more commonly used for soil characterization in practice. The K_0 correlation of Eq. (3) can then be modified in terms of ϕ'_c introducing a certain correlation parameter to consider the effect of particle interlocking given as follows:

$$K_0 = \frac{1-\sin(\beta\cdot\phi'_c)}{1+\sin(\beta\cdot\phi'_c)} \tag{4}$$

where β = correlation parameter that represents the effect of particle interlocking on K_0. As the strength characteristics of soil was logically included in Eq. (4), it justifies and explains well the sequence and validity of the K_0 correlation to strength.

In order to evaluate the values of β, back-analysis was performed using the measured K_0 values and Eq. (4). The back-calculated values of β are shown in Fig. 4 as a function of relative density (D_R). It is seen that β increases with increasing D_R showing a reasonably tight correlation. These results are reasonable as β indicates the effect of particle interlocking on the values of K_0. The correlation of β to D_R obtained from the results given in Fig. 14(b) is given as follows:

$$\beta = a\cdot\left[D_R(\%)\right]^b \tag{5}$$

where a and b = correlation parameters. The values of *a* and *b* were 0.1 and 0.44, respectively, for the test results adopted in this study.

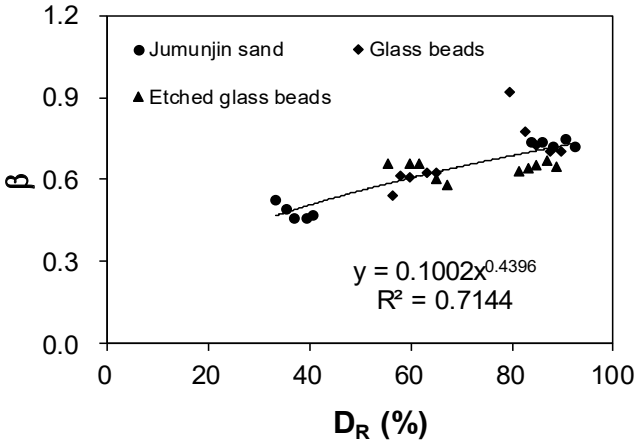

Figure 5. Values of β for test materials.

5 SUMMARY AND CONCLUSIONS

In this study, the correlation of K_0 to strength was explored focusing on the effect of inter-particle strength. Test results from thin-walled oedometer tests were adopted to analyze the values of K_0. Different granular materials of clean sand, glass beads and etched glass beads were used in the tests.

The values of K_0 were lower for higher relative densities for all test materials. Jumunjin sand showed higher K_0 values than glass beads, which was attributed to higher angularity and interlocking effects. The measured K_0 values indicated that denser and more angular materials tend to produce lower K_0 values. It was found that the Jaky's K_0 equation using the critical-state friction angle ϕ'_c produces satisfactory results for granular soil with uniform particles while did not match well for irregularly angular particles. The application of ϕ'_p underestimated K_0 values.

The inter-particle strength model was presented to describe the correlation of K_0 to strength characteristics of sand. It was explained that the mobilized strength at particle contacts plays key role for the mobilized K_0 stress state. The inherent particle strength was introduced to establish a modified K_0 correlation with consideration of interlocking effect. The correlation parameter was evaluated, which was given as a function of relative density.

6 REFERENCES

Andrawes, K. Z. and El-Sobby, M. A. 1973. "Factors affecting coefficient of earth pressure K_0." *Journal of the Soil Mechanics and Foundations Division*, 99(SM7), 527-539.

Bolton, M.D. 1986. "The strength and dilatancy of sands." *Geotechnique*, 36(1), 65-78.

Ishihara, K. 1993. "At-rest and compaction-induced lateral earth pressures of mosit soils." Ph.D Thesis, Virginia Polytechnic Institute and State University.

Jaky, J. 1944. "The coefficient of earth pressure at rest. In Hungarian (A nyugalmi nyomas tenyezoje)." *Journal of the Society of Hungarian Architects and Engineering*, 355–358.

Jaky, J. 1948. "Pressure in silos." *Proceedings of 2nd International Conference on Soil Mechanics and Foundation Engineering*. 1: 103-107

Kolymbas, D. and Bauer, E. 1993. "Soft oedometer: A new testing device and its application for the calibration of hypoplastic constitutive laws." *Geotechnical Testing Journal*, 16(2): 263–270.

Lee, J., Lee, D. and Park, D. 2014. "Experimental investigation on the coefficient of lateral earth pressure at rest of silty sands: effect of fines." *Geotechnical Testing Journal*. 37(6): 967 - 979.

Lee, J., Yun, T., Lee, D., and Lee, J. 2013. "Assessment of K_0 correlation to strength for granular materials." *Soils and Foundations*. 53(4): 584 – 595.

Mesri, G. and Hayat, T. M. 1993. "Coefficient of earth pressure at rest." *Canadian Geotechnical Journal*, 30(4): 647-666.

Michalowski, R. L. 2005. "Coefficient of earth pressure at rest." *Journal of Geotechnical and Geoenvronmental Engineering*, 131(11): 1429-1433.

Pipatpongsa, T., Heng, S., Iizuka, A., and Ohta, H. 2009. "Rationale for coefficient of earth pressure at rest derived from prismatic sand heap." *Journal of Applied Mechanics*, 12: 383 – 394.

Procter, D. C. and Barton, R. R. 1974. "Measurements of the angle of interparticle friction." *Geotechnique*, 24(4): 581 – 604.

Wanatowski, D. and Chu, J. 2007. "K_0 of sand measured by a plane-strain apparatus." *Canadian Geotechnical Journal*, 44: 1006 – 1012.

Geotechnical and Geophysical Site Characterisation 5 – Lehane, Acosta-Martínez & Kelly (Eds)

Soil Behaviour Type of the Sarapuí II Test Site

P. F. Nejaim
Insitutek Consultores Ltda, Rio de Janeiro, Brazil

G. M. F. Jannuzzi & F. A. B. Danziger
Federal University of Rio de Janeiro, Brazil

ABSTRACT: One of the major applications of the CPTU test has been the determination of soil stratigraphy and the identification of soil behaviour type. The present paper uses piezocone data from Sarapuí II soft clay test site to evaluate the soil behaviour type charts that have been suggested by Robertson and coauthors from a long time (Robertson et al. 1986, Robertson, 1990), and recently updated (Robertson, 2012). Two lightly overconsolidated clay layers, 3.0-7.5m, and 7.5-10m, for which detailed geotechnical data are available, have been used as references. The trend of both layers to be lightly overconsolidated was properly identified in the Q_{tn} versus F_r chart, which did not occur in the Q_{tn} versus B_q chart. Both layers fall into the undrained behaviour, which is consistent with their behaviour. However, layer 1 was classified as contractive and layer 2 as dilative, which is not right. It is suggested to move the limit between dilative and contractive behaviour towards the top of SBTn 4.

1 INTRODUCTION

One of the major applications of the piezocone test (CPTU) has been the determination of soil stratigraphy and the identification of soil type. This has typically been accomplished using charts that link cone parameters to soil type. The trend of a normally consolidated behaviour can also be obtained from some of those charts (e.g. Robertson 1990). Recently, Robertson (2012) proposed a chart where a more generous behaviour, i.e a dilative – contractive and drained –undrained behaviour can be obtained from the Normalized cone resistance versus Normalized friction ratio chart.

A number of very good quality piezocone tests have been performed in a soft clay test site and have been used to verify the reliability of the most common identification methods, by using the software CPeT-IT.

2 SOIL CLASSIFICATION FROM CPT AND CPTU

2.1 *Historical*

To the authors´ knowledge, Begemann (1965) proposed the first chart that link soil type to the cone parameters cone resistance (q_c) and sleeve friction (f_s), which was based on the mechanical cone. Other suggestions have been presented, based both on the mechanical CPT (e.g., Sanglerat et al. 1974, Schmertmann, 1978) and the electrical CPT (e.g. Douglas and Olsen, 1981).

The measurement of the pore pressure in the CPTU allowed the appearance of classification charts where the sleeve friction – considered a less reliable parameter, with respect to the cone resistance and the pore pressure – was replaced by the pore pressure (e.g., Jones et al. 1981, Jones & Rust, 1982, Senneset & Janbu, 1984).

The combination on the three piezocone parameters was first introduced by Robertson et al. (1986), through the use of two charts, the first one relating the corrected cone resistance q_t with pore pressure parameter B_q (equation 1), and the second q_t with friction ratio, R_f=f_s/q_t.

The Robertson et al. (1986) method has become very popular. Normalized parameters suggested by Wroth (1984), were used (Q_t and F_r, equations 2 and 3, in addition to B_q) in 1990 (Robertson, 1990), to take into account the soil stress state.

$$B_q = \frac{u_2 - u_o}{q_t - \sigma_{vo}} \quad (1)$$

$$Q_t = \frac{q_t - \sigma_{vo}}{\sigma'_{vo}} \quad (2)$$

$$F_r = \frac{f_s}{q_t - \sigma_{vo}} \quad (3)$$

Occasionally, soils will fall within different zones on each chart; in these cases, judgement is required to properly classify the soil (Lunne et al. 1997).

Robertson et al (1986) and Robertson (1990) stressed that the CPT-based charts were predictive of soil behaviour, and suggested the term 'soil behaviour type', because the cone responds to the in-situ mechanical behavior of the soil and not directly to soil classification criteria.

Twelve ´soil behaviour type` (SBT) zones were proposed by Robertson et al. (1986) and nine (SBTn) by Robertson (1990). Later, Robertson (2010) updated the early Robertson et al.´s (1986) method including a dimensionless cone resistance (q_c/p_a, where p_a=atmospheric pressure) and reducing the number of SBT zones from 12 to 9 in order to match the SBTn zones.

According to Robertson (2009), the normalized charts provide more reliable identification than the non-normalized charts, although when the in situ vertical stress is between 50 and 150 kPa the difference is very small.

It is interesting to note a change of hierarchy on the use of the pore pressure with respect to friction sleeve. In fact, Table 1, adapted from Liao (2005), provides a list of several soil classification charts found in literature. They are divided into three groups: a) charts based on cone resistance and sleeve friction; b) charts based on cone resistance and pore pressure; c) charts based on all three quantities of CPTU data. The trend of using the three CPTU quantities more recently can be seen from the table.

Table 1. Soil classification charts found in the literature (adapted from Liao, 2005)

Methods based on:
a) cone resistance and sleeve friction: Begemann (1965), Sanglerat et al (1974), Schmertmann (1978), Douglas & Olsen (1981), Vos (1982), Robertson & Campanella (1983), Erwing (1988), Olsen & Malone (1988), Olsen & Mitchell (1995), Zhang & Tumay (1999), Eslami & Fellenius (1997)
b) cone resistance and porewater pressure: Jones et al (1981), Jones & Rust (1982), Senneset & Janbu (1984), Parez & Fauriel (1988), Senneset et al (1989), Chang-hou et al (1990), Jian et al (1992) and Schneider et al (2008)
c) all three quantities of CPTU data: Robertson et al. (1986), Robertson (1990, 1991), Larsson & Mulabdic (1991), Jefferies & Davies (1991, 1993) and Ramsey (2002)

However, the trend of going back to the use of a single chart cone resistance versus sleeve friction (through normalized parameters) was justified in detail by Robertson (2012), based on the following (simplified) reasons:

i) In the case of onshore tests, the penetration is carried out through unsaturated soils before reaching saturated soil. The use of viscous liquids, like silicon oil, has minimized the loss of saturation but has not completely solved the problem. Also, few commercial CPT operators pre-drill the sounding and fill it with water.

ii) Although it has been documented (e.g., Lunne et al. 1986) that the sleeve friction is less accurate than the cone resistance, a number of measures on the cone design can provide reliable f_s measurements.

This chart is shown in Figure 1 below, where a more generalized cone parameter Q_{tn}, defined in Equation (4), is suggested. The chart is particularly useful, because a direct dilative-contractive and drained-undrained behaviour can be obtained.

$$Q_{tn} = \frac{q_t - \sigma_{vo}}{p_a} \cdot \frac{p_a}{\sigma'_{vo}} \quad (4)$$

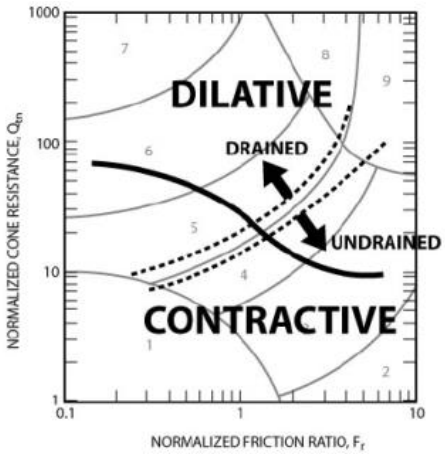

Figure 1. Approximate boundaries between dilative-contractive behaviour and drained-undrained CPT response on normalized SBTn Q_{tn} – F_r chart (after Robertson 2012).

3 THE TEST SITE

3.1 *General*

The early studies on the very soft clay of the region where the Sarapuí test site is located were conducted by Pacheco Silva (1953). The Sarapuí test site is situated in a flat swampy area, around Guanabara Bay, on the left bank of Sarapuí river, some 7km from Rio de Janeiro City, with average coordinates 22°44'41'' (S) and 43°17'23'' (W). It was established in the mid-1970s as a research site by the Transportation Research Institute of the Brazilian Federal Highway Department (IPR-DNER), with focus on the study of embankments on soft soils, an issue faced by this Department throughout Brazil (Ortigão & Lacerda 1979). A number of in situ and laboratory tests have been performed (e.g., Lacerda et al. 1977). A comprehensive report about the deposit has been provided by Almeida and Marques (2002).

In the last fifteen years, however, security reasons have prevented the use of the test site. A new area (named Sarapuí II) in the same deposit, 1.5 km from the previous area and inside of a Navy Facility, has been used since then. Two studies on pile behaviour

have been carried out at Sarapuí II site (Alves 2004, Francisco 2004). The initial tests with the torpedo piezocone (Porto et al. 2010) have also been performed at Sarapuí II test site. A number of in situ tests have been performed in this new area, which is being used by the Research Center of the Brazilian Oil Company (CENPES/PETROBRAS) and Federal University of Rio de Janeiro as a state-of-the-art test site on very soft organic clay. The very soft clay in the test area is around 8 m deep, and a clayey-silt layer underlies the very soft clay. A comprehensive study about the deposit of Sarapuí II was undertaken by Jannuzzi (2009, 2013) and Jannuzzi et al. (2015).

The liquid limit, plastic limit and natural water content, specific gravity, total unit weight, initial void ratio, activity versus depth are included in Figure 2. The grain size distribution, organic content, total salt content and NaCl content, relative percentage of clay minerals versus depth are shown in Figure 3.

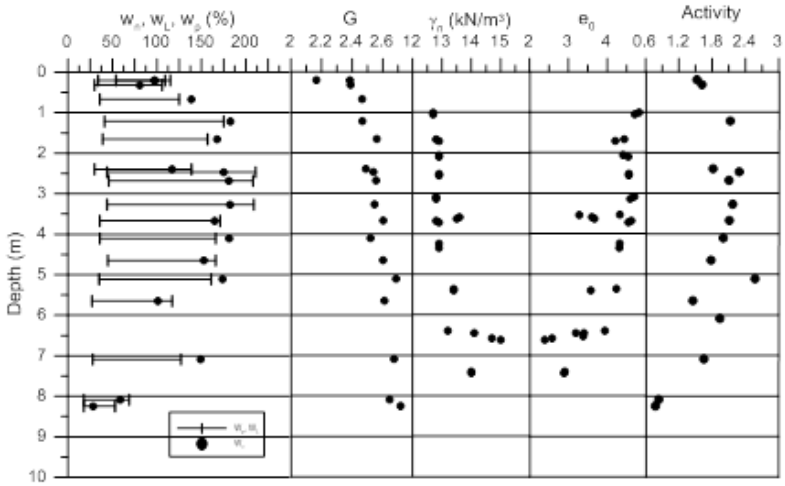

Figure 2. Liquid limit, plastic limit and natural water content; specific gravity; total unit weight; initial void ratio; activity versus depth (adapted from Jannuzzi 2013, Jannuzzi et al. 2015).

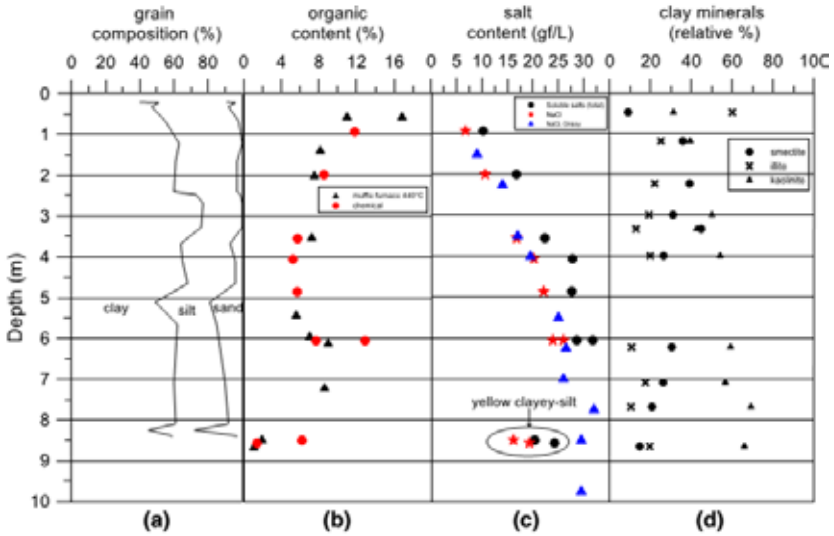

Figure 3. (a) Grain size distribution; (b) organic content; (c) total salt content and NaCl content (data from Onsøy clay also included); (d) relative percentage of clay minerals versus depth (Jannuzzi et al. 2015).

The overconsolidation ratio (OCR) versus depth, from 24h incremental loading tests performed in very good quality samples, is shown in Figure 4. The specimens in the depth range 4.0 – 5.5 presented a significant number of shells, providing meaningless results. It can be observed that the deposit is lightly overconsolidated below 3 m depth, approximately, with OCR around 2.

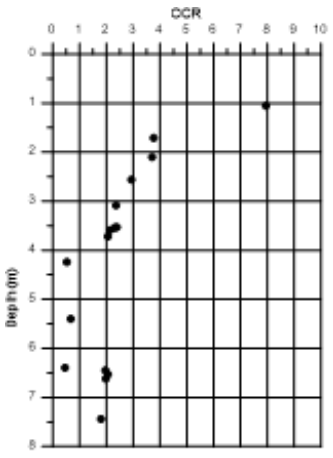

Figure 4. OCR versus depth, Sarapuí II test site.

3.2 *Piezocone tests*

Seven CPTU tests have been performed, one of them under an existing embankment. The standard rate of 20 mm/s has been used in all tests. The equipment used has been developed by COPPE – Federal University of Rio de Janeiro (UFRJ) and Grom Eng., and is able to measure cone resistance, q_c, sleeve friction, f_s and pore pressure at cone face, u_1, and cone shoulder, u_2. The advantages of measuring pore pressure at 2 positions have been recognized throughout the last 15 years at COPPE/UFRJ and have been reported by e.g. Danziger (2007).

Calibration has been carried out before and after every test series in the range of load /pressure values expected in the field. Water was used – as COPPE/UFRJ regular practice – as saturation fluid.

A typical result is shown in Figure 5.

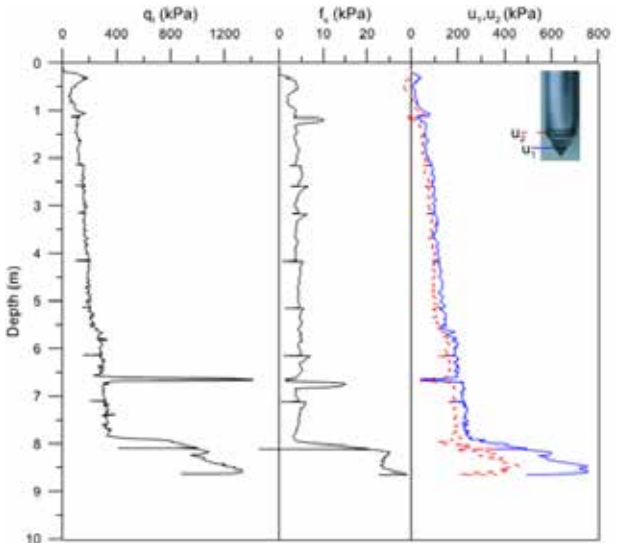

Figure 5. Corrected cone resistance (q_t), friction sleeve (f_s) and pore pressures at cone face (u_1) and cone shoulder (u_2) from a typical piezocone test at Sarapuí II site (Jannuzzi et al. 2015).

4 SBT FROM SARAPUÍ II TEST SITE

The analysis herein performed is related to two layers, the first 3 - 7.5 m (layer 1) and the second 7.5 - 9 m (layer 2). This choice was due to the fact that the upper 3 m of the deposit is overconsolidated, and the purpose of the paper is to analyze the material which can be said to be lightly overconsolidated. It must be pointed out that geological evidences show that the whole deposit was formed underwater. In other words, the OCR values of the material below 3 m has been attributed to secondary consolidation (Martins et al. 2009). Also, no reasons are known so far to justify the OCR values obtained in the upper 3 m of the deposit.

The data from six piezocone tests, with excellent repeatability, were plotted in the Robertson et al. (1990) chart, using the the software CPeT-IT, and the results are found in Figure 6. Layer 1 (organic clay), in grey, is mostly included in SBTn 3 – clays: clay to silty clay, in both charts, which is consistent with the tested material, although one should expect that the high organic content would indicate At least part of the data in SBTn 2 - clay-organic soil. Layer 2 (clayey silt), in green, falls mostly in the SBTn 4 in the case of the Q_{tn} x F_r chart, whereas the data spread in SBTn 3, 4 and 5 in the case of Q_{tn} x B_q chart. The SBTn 4 is consistent with the expected behaviour of the material, and the classification in different SBTn categories may be explained by the fact that the friction sleeve (and consequently F_r) is a value obtained over a certain length, and the pore pressure (and consequently B_q) is more localized, reflecting sudden changes in the soil profile.

The OCR trend is consistent with the data plotted in the Q_{tn} versus F_r chart, indicating approximately that both layers are lightly overconsolidated. The data plotted in the Q_{tn} versus B_q chart, however, do not reflect properly the differences between the two layers, because it indicates a higher OCR in the case of layer 2.

The data have also been plotted in the Robertson´s (2012) chart, where the drained-undrained and dilative-contractive behaviour are shown (Figure 7), with limits that have been included in the chart provided by the software CPeT-IT.

A quite interesting picture can be observed. Both layers fall into the undrained behaviour, which would be expected, because the separation between the two types of behaviour is approximately the line between SBTn 4 and 5, i.e. the separation between the clay type of behaviour and the sand type of behaviour. The results are consistent with the soil behaviour of both layers.

However, layer 1 was classified as contractive and layer 2 as dilative, which is not true. Both layers are contractive, as found in DSS tests carried out in samples reconstituted for the in situ stresses. Also, the geological evidences indicate that the whole deposit was formed underwater, and there are no evidences of significant layers that have been removed to justify a high OCR. Therefore, the limit between dilative and contractive behaviour should be moved towards the top of SBTn 4, as also indicated in Figure 7.

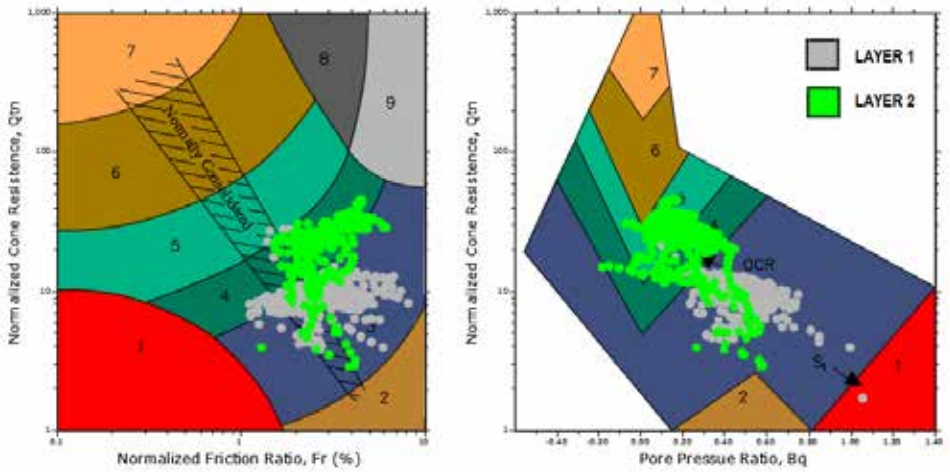

Figure 6. Two clay layers' data plotted at Robertson´s (1990) normalized charts.

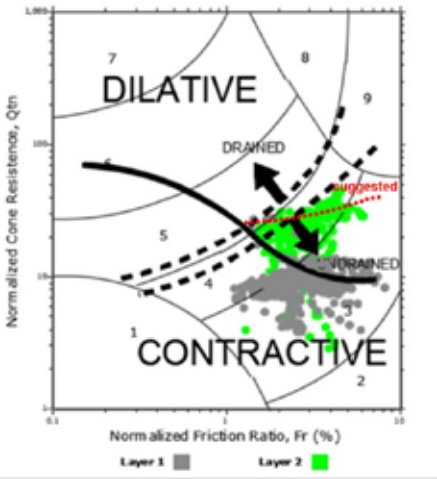

Figure 7. Two clay layers' data plotted at Robertson´s (2012) chart; suggested trend for dilative-contractive behaviour.

5 CONCLUSIONS

The results of six piezocone tests, carefully performed in a clay test site, were used to evaluate the reliability of the soil behaviour type which have been suggested by Robertson and coauthors from a long time (Robertson et al. 1986, Robertson 1990), recently updated (Robertson, 2012).

Two lightly overconsolidated layers were chosen to be used as references, the first one a dark grey very soft, very plastic, organic (layer 1), and the second one a yellow clayey-silt, stiffer, with a smaller organic content and plasticity index (layer 2). Both layers were properly classified as SBTn 3 (layer 1) and SBTn 4 (layer 2) in both normalized charts Q_{tn} versus F_r and Q_{tn} versus B_q. In fact, one would expect that layer 1 would have been classified as SBTn 2, because it presents a high organic content, which was not the case.

The trend of both layers to be lightly overconsolidated was properly identified in the Q_{tn} versus F_r chart, which did not occur in the Q_{tn} versus B_q chart. In fact, in this case there was an indication that layer 2 has a higher OCR than layer 1, which is not the case.

Both layers fall into the undrained behaviour, which is consistent with their behaviour. However, layer 1 was classified as contractive and layer 2 as dilative, which is not right. It is suggested to move the limit between dilative and contractive behaviour towards the top of SBTn 4.

6 REFERENCES

Almeida, M.S.S. & Marques, M.E.S. 2002. The behaviour of Sarapuí soft clay. *Proc. Workshop on the Characterisation and Engineering Properties of Natural Soils*, Singapore, 1: 477–504.

Alves, A.M.L. 2004. A influência da viscosidade do solo e do tempo após a cravação na interação dinâmica estaca-solo em argilas. PhD Thesis, COPPE/UFRJ, Rio de Janeiro.

Begemann, H. K. S. 1965. The friction jacket cone as an aid in determining the soil profile. *Proc. 6th ICSMFE*, Montreal, 2: 17-20.

Erwig, H. 1988. The Fugro guide for estimating soil type from CPT Data. *Penetration Testing in the UK*, Thomas Telford, London, 261-263.

Eslami, A. & Fellenius, B.H. 1997. Pile capacity by direct CPT and CPTu methods applied to 102 Case Histories. *Can. Geot. Journal*, 34(6): 880-898.

Cheng-Hou, Z., Greeuw, G., Jekel, J., Rosenbrand, W. 1990. A New Classification Chart for Soft Soils using the Piezocone Test. *Engineering Geology*, 29: 31-47.

Danziger, F. A. B. 2007. In situ testing of soft Brazilian soils. *Studia Geotechnica et Mechanica*, XXIX (1-2): 5-22.

Douglas, B.J. & Olsen, R.S. 1981. Soil classification using electric cone penetrometer. *Proc. Symp. on Cone Penetration Testing and Experience*, ASCE, St. Louis: 209-227.

Francisco, G.M., 2004. Estudo dos efeitos do tempo em estacas de fundação em solos argilosos. PhD Thesis, COPPE/UFRJ, Rio de Janeiro.

Jannuzzi, G.M.F. 2009. Caracterização do depósito de solo mole de Sarapuí II através de ensaios de campo. MSc Dissertation, COPPE/UFRJ, Rio de Janeiro.

Jannuzzi, G.M.F. 2013. Inovadoras, modernas e tradicionais metodologias para a caracterização geológico-geotécnica da argila mole de Sarapuí II. PhD Thesis, COPPE/UFRJ, Rio de Janeiro.

Jannuzzi, G.M.F., Danziger, F.A.B., Martins, I.S.M., 2015. Geological-geotechnical characterisation of Sarapuí II clay. *Engineering Geology*, 190: 77-86.

Jefferies, M. G. & Davies, M. P. 1991. Soil classification using the cone penetration test. *Can. Geot. Journal*, 28(1): 173-176.

Jefferies, M.G. & Davies, M.P. 1993. Use of CPTU to Estimate Equivalent SPT N60, *Geotechnical Testing Journal*, ASTM, 16(4): 458-468.

Jian, D., Xiaoling, Z., Longgen, Z., Lianyang, Z. 1992. Some in-situ and laboratory geotechnical test techniques used in China, *U.S. – China Workshop on Cooperative Research in Geotechnical Engineering*, Tongji University, Shanghai and The Ohio State University, Columbus, Ohio.

Jones, G.A., Van Zyl, D., Rust, E. 1981. Mine tailings characterization by piezometer cone. *Proc. Symp. on Cone Penetration Testing and Experience*, ASCE, St. Louis: 303-324.

Jones G. A. & Rust, E. 1982. Piezometer penetration testing, CPTU. *Proc. ESOPT-2*, Amsterdam, 2: 607-614.

Lacerda, W.A., Costa Filho, L.M., Coutinho, R.Q., Duarte, E.R. 1977. Consolidation characteristics of Rio de Janeiro soft clay. *Proc. Conf. on Geotechnical Aspects of Soft Clays*, Bangkok: 231-243.

Larsson, R. & Mulabdic, M. 1991. Piezocone Tests in Clay, *Swedish Geotechnical Institute*, SGI (42): 240.

Liao, T. 2005. Post Processing of Cone Penetration Data for Assessing Seismic Ground Hazards, with Application to the New Madrid Seismic Zone. PhD Thesis, Georgia Institute of Technology, Georgia.

Lunne, T., Eidsmoen, T., Gillespie, D., Howland, J.D., 1986. Laboratory and field evaluation on cone penetrometers. *Proc. In Situ'86: Use of In Situ Tests in Geotechnical Practice*, Blacksburg, 6: 714-729

Lunne, T., Robertson, P.K., Powell, J.J.M. 1997. *Cone penetration testing in geotechnical practice*. London: Blackie Academic & Professional.

Martins, I.S.M., Santa Maria, P.E.L., Santa Maria, F.C.M. 2009. Laboratory behaviour of Rio de Janeiro soft clays. Part 1: Index and compression properties. *Soils and Rocks* 32(2): 100-103.

Olsen, R. S., & Malone, P. G. 1988. Soil Classification and Site Characterization using the Cone Penetrometer Test. *Proc. ISOPT-1*, Orlando, 2: 887-893.

Olsen, R.S. & Mitchell, J.K. 1995. CPT Stress Normalization and Predication of Soil Classification. *Proc. CPT 95*, Linkoping, Swedish Geotechnical Society, 2: 257-262.

Ortigão, J.A.R. & Lacerda, W.A. 1979, Propriedades geotécnicas da argila cinza do Rio de Janeiro. IPR/DNER 2.019-03.01-2/14/42.

Parez & Fauriel 1988. Le Piezocone Ameliorations Apportees a la Reconnaissance de Sols. *Revue Francaise de Geotech*, 44: 13-27.

Pacheco Silva, F. 1953. Shearing strenght of a soft clay deposit near Rio de Janeiro. *Géotechnique*, 3: 300-305.

Porto, E.C., Medeiros Jr., C.J., Henriques Jr., P.R.D., Foppa, D., Ferreira, A.C.P., Costa, R.G.B., Fernandes, J.V.V., Danziger, F.A.B., Jannuzzi, G.M.F., Guimarães, G.V.M., Silva Jr., S.P., Alves, A.M.L. 2010. The development of the torpedo-piezocone. *Proc. OMAE 2010*, American Society of Mechanical Engineers, New York.

Ramsey, N. 2002. A Calibrated Model for the Interpretation of Cone Pentration Tests CPTs in North Sea Quaternary Soils. *Proc. SUT Conf.*, London

Robertson, P. K. & Campanella, R. G. 1983. Interpretation of Cone Penetrometer Tests, Part I Sand. *Can. Geot. Journal*, 20(4): 718-733.

Robertson. P.K., Campanella, R.G., Gillespie, D., Greig, J. 1986. Use of piezometer cone data; *Proc. In-Situ'86*, GSP 6, ASCE: 1263-1280.

Robertson, P.K. 1990. Soil classification using the cone penetration test. *Can. Geot. Journal*, 27(1): 151-158.

Robertson, P.K. 1991. Soil Classification using the Cone Penetration Test. *Can. Geot. Journal*, 28: 176-178.

Robertson, P.K. 2009. Interpretation of cone penetration tests – a unified approach. *Can. Geot. Journal*, 46: 1337-1355.

Robertson, P.K. 2010. Soil behaviour type from the CPT: an update. *Proc. CPT'10*, Huntington Beach, CA, USA.

Robertson, P.K. 2012. Interpretation of in-situ tests – some insights. *Proc. ISC'4*, Recife, Vol. 1, 3-24.

Sanglerat, G., Nhim, T. V., Sejourne, M., Andina, R. 1974. Direct soil classification by static penetrometer with special friction sleeve. *Proc. ESOPT-1*, Stockholm, 2: 337 - 344.

Schmertmann, J.H. 1978, Guidelines for Cone Penetration Test, Performance and Design. Federal Highway Administration Report FHWA-TS-78-209, Washington, D.C.

Schneider, J.A., Randolph, M.F., Mayne, P.W., Ramsey, N.R. 2008. Analysis of Factors Influencing Soil Classification using Normalized Piezocone Tip Resistance and Pore Pressure Parameters. *Journal of Geotechnical and Geoenvironmental Engineering*, 134(11): 1569-1586.

Senneset, K., & Janbu, N. 1984. Shear strength parameters obtained from static cone penetration tests. *Proc. Symp. on Strength Testing of Marine Sediments: Laboratory and In-Situ Measurements.* ASTM 04-883000-38, San Diego: 41-54.

Senneset, K., Sandven, R., Janbu, N. 1989, Evaluation of Soil Parameters from Piezocone Test. *In-situ Testing of Soil Properties for Transportation*, Transportation Research Record, Washington, D.C., (1235): 24 - 37.

Vos, J. D. 1982. The Practical Use of CPT in Soil Profiling; *Proc. ESOPT-2*, Amsterdam, 2: 933-939.

Wroth, C.P. 1984. The Interpretation of In-Situ Soil Tests, *Rankine Lecture, Geotechnique (4)*.

Zhang, Z. & Tumay, M.T 1999. Statistical to Fuzzy Approach toward CPT Soil Classification. *Journal of Geotechnical and Geoenvironmental Engineering*, ASCE, 125(3): 179-186.

Geotechnical and Geophysical Site Characterisation 5 – Lehane, Acosta-Martínez & Kelly (Eds)

Geophysical and *in situ* testing applied to site characterisation for non-engineered structures in developing regions

S. Ortiz-Palacio, S. Ibáñez García, A.V. López & J.B. Porres

University of Burgos, Burgos Castile and Leon, Spain

ABSTRACT: Residential dwellings have been estimated to represent more than three quarters of the building stock around the globe, most of which are not believed to have been properly engineered (that is, designed by architects or engineers and constructed by skilful workers with adequate materials). Narrowing the scope to developing countries, over a 90 percent of the population is deemed to be living, working or studying in non-engineered buildings. In earthquake-prone regions, these weak structures can become deathtraps for their occupants, forlornly adding to the casualty lists of recent and past seismic events. Thus, improving seismic resilience for vernacular housing has increasingly become a main theme for researchers. Also, other geotechnical issues, such as subsidences, slope instabilities, excessive settlement on soft soils, groundwater, inadequate designs, etc., are responsible for substantial risk of structural damages, ranging from small structural pathologies to major disasters. One of the keys to develop new safe and efficient foundation designs, or to retrofit existing ones, is to make available portable and low-budget ground probing techniques. This document will describe some of the most feasible *in situ* devices available, as well as discuss how seismic and electric methods can be used as portable and powerful tools to characterise both the strength and the stiffness of soils thanks to recent developments in stablishing the relationship between geophysical results and traditional geotechnical parameters (such as the SPT, the angle of internal friction, shear strength, etc.), with the help of statistical methods and dimensional analysis techniques.

1 INTRODUCTION

1.1 *The role of engineering in a sustainable development frame*

Among the seventeen Sustainable Development Goals declared by the United Nations (UN General Assembly, 2015), some key targets should benefit from the combined effort of engineers and researchers in the field of ground engineering in the least developed and developing countries, especially:

- Providing technical education (targets 4.c and 9.5) through the contribution of qualified trainers and researchers
- Developing resilient infrastructures (target 9.1), building stock (target 11.1) and historical sites (11.4), while promoting the use of local resources (target 11.c)
- Protection of population and the physical environment against catastrophic phenomena (target 11.5), implementing integrated risk management policies

Thus, two main themes should walk hand in hand in order to attain those goals:

- Education: specific technical and psycho-environmental training should be provided not only for those engineers living in the developing regions, but also for those coming from more developed countries, as they are seldom given the specific training to solve the complex earth system problems involved in those regions (Amadei, 2004; Francisca, 2011). Experiences such as those related by Fukubayashi and Kimura (2014) or by Sandekian et al. (2014), emphasise the prominence of good communication with local communities as a key for success in implementing new engineering techniques
- Development of sustainable novel solutions to new or preexisting problems

1.2 *Population growth and non-engineered building stock*

While there has been a reduction in the population living in slums in most regions of the world in the last 15 years (Way, 2015), thus achieving a meaningful life quality improvement for millions of people, there is still a long road ahead: as far as almost a 30 percent of the urban population in developing countries (as in 2014) still dwells in slums. Although that percentage was much higher twenty five years

ago, the number or people living in those slums is increasing in absolute numbers due to population growth, as described in table 1:

Table 1. Slum residents in urban areas (Way, 2015)

Year	Absolute number of residents (Millions)	Percentage of total urban population
1990	689	46.2
2000	830	39.4
2014	881	29.7

If we combine the slum building stock with the vernacular housing in rural areas, according to Oliver (2007), nine out of ten buildings around the world are estimated to be non-engineered structures, accommodating over a 90 percent of the population in developing or underdeveloped countries (Arya, 2000). Judging from recent population growth projections, and examining the extremes of the growth tendencies, although during the present century Europe will experiment a population decrease, Africa will contribute with over 3.2 billion people to the total world increase (which is projected to grow from 7.3 billion to over 11 billion people), as shown comparatively in figure 1:

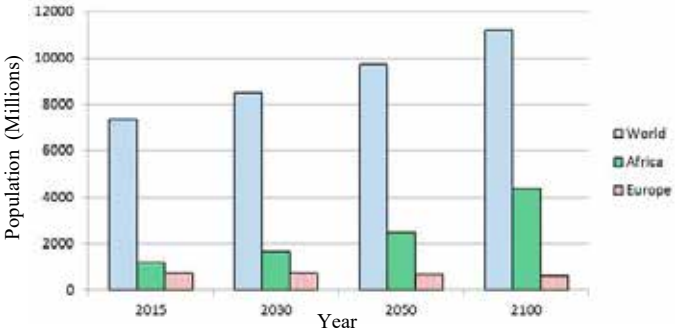

Figure 1. Increase in population between 2015 and 2100 in the world compared to Africa and Europe, adapted from United Nations (2015).

These figures only emphasise the importance of upgrading the building stock in the least developed countries, as the population living or working in non-engineered buildings subject to natural or artificial risks of collapse will grow otherwise in the next decades. In this context, several prominent engineering institutions have already acknowledged the crucial task in our hands, as the recent *"Madrid Declaration (...) for sustainable development and action for the climate"* (SICE, 2016) or the *"ASCE Vision for Civil Engineering in 2025"* (ASCE, 2007). These are paradigms that stress the necessary active role of the engineering global community in the future of developing countries.

1.3 *Geotechnical hazards and risks*

To understand our role in this scenario, we must first fathom the magnitude of the challenge. While sometimes both *hazard* and *risk* have been interchangeably used (Gkoumas, 2008; Renzi, 2009; Wang, 2008), it is important to acknowledge the difference between both terms in engineering: a hazard must be seen as an event that may originate a potential harm over a natural or artificial system, while a risk measures the probability of that hazardous event to have a negative consequence on such system. For instance, while the hazard of an earthquake in a sector of a city in which slums coexist with adjacent high-rise districts may be the same, the risk of structural damages and life losses is greater in the poorer, non-engineered part of that urban settlement.
Thus, the task of geotechnical engineers should be that of risk assessment and management of foundation design and ground structure interaction. On that regard, ground characterisation should be among the most important tools.

1.4 *Lost lessons after infrequent hazardous phenomena*

In many developing countries, catastrophic infrequent events (such as earthquakes, landslides, etc.) do not permeate into the traditional building traditions (McWilliams and Griffin, 2013), as opposed to those countries used to frequent low-magnitude events. As a consequence, the lessons that should have been acquired by the community are washed out soon after the event.

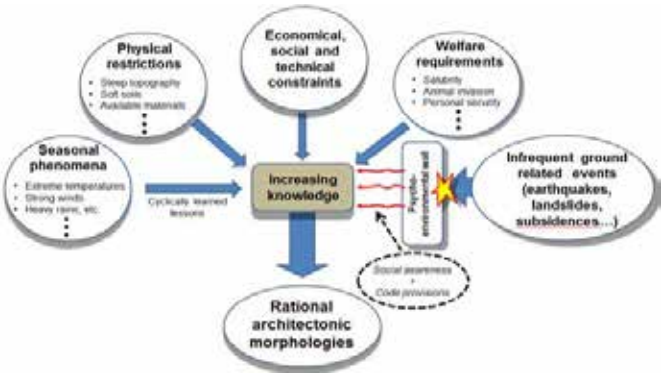

Figure 2. The mechanisms behind building morphologies, adapted from Ortiz-Palacio et al. (2015)

While other factor slowly help to shape vernacular housing architecture, infrequent but catastrophic events collide with psycho-environmental walls, which are built by lack of awareness, institutional indifference, superstition, etc. In figure 2 it is represented how building morphologies are reshaped by the environment.
For example, during the 20th century, around a 75% of deaths during or in the aftermath of earthquakes are believed to have been caused by the collapse of non-engineered masonry buildings (Mallick, 2015), which would mean that those structures claimed over 1.3 million casualties, according to the seismic-related total death toll described by Chowdhury and

Flentje (2007). Ground characterisation should be a stepping stone on which to support the means to demolish that psycho-environmental wall.

2 GROUND CHARACTERISATION IN DEVELOPING REGIONS

Financial access and technical restraints are two of the main obstacles pointed out by many experienced practitioners to undertake a proper ground characterisation for foundation design in developing communities. In the budgetary respect, paradoxically, a good prior characterisation of the soil conditions should always mean a lesser range of variability of the budgetary uncertainty involved in any project. For instance, MacDonald (1994) compiled some UK Highway Projects budget deviations due to geotechnical issues. In the report, the uncertainty in geotechnically related problems is proved to increase as the ground investigation cost/construction tender cost ratio decreases: when the ground investigation represented less than 1% of the construction tender cost, increases could reach in some cases almost a 100%, while ground investigation over a 5% reduced maximum increases down to a 15% (Whyte, 1995). Therefore, probing techniques should always be considered as an investment. Adapting to geotechnical site characterisation the effort curve described by MacLeamy (2004), in figure 3 we can compare the traditional building process against the ideal project scheme that should be adopted, in tune with new Building Information Modelling approaches to traditional engineering problems (Morin et al., 2014):

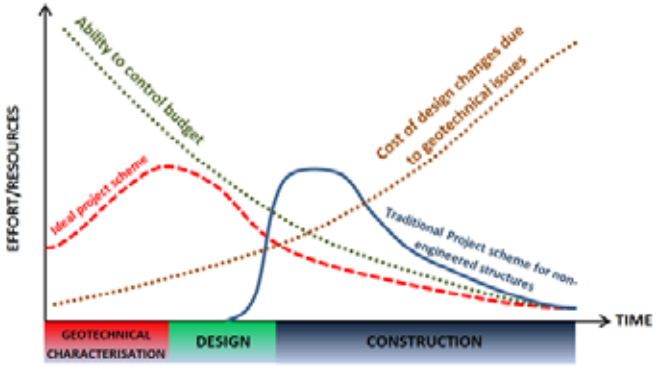

Figure 3. Effort curves in non-engineered buildings projects, adapted from MacLeamy (2004)

Once the construction has started, any geotechnical issue will consume far more resources if ground characterisation has not been properly performed. The problem is how to implement the site characterisation phase in complex environments. Nowadays, a wide range of *in situ* tests are available (Monnet, 2015), and as practitioners around the globe share their results in the engineering community, the interpretation of these results gives wider possibilities every day. However, these techniques are not widely available in developing countries, which render their use as very restricted in many occasions. Availability of specialised devices and trained personnel to use them is critical to define the potential use of these techniques (Robertson, 1986). Many experiences on these matter have been described (e.g.: the difficulty of finding a pressuremeter device in Pakistan summarized by Rehman (2010), or the unavailability of operative *in situ* and lab equipment described by Orsmond (2007) in Jamaica).

3 IN SITU TESTING: SOME FEASIBLE TECHNIQUES

As drilling rigs are not always available to perform boreholes in which not only samples of the soil are retrieved, but also where a wide variety of other of mechanical tests can be carried out –such as the Standard Penetration Test or the Pressuremeter Test, to name two of the most common ones-, during the last decades many researchers have been developing new portable low-budget devices, such as:

– *Dynamic Cone Penetrometers (DCP)*: this type of light testing devices were first designed in a primitive fashion at the end of the 17th century (Burnham and Johnson, 1993), but the first *modern* implementation was made by Scala (1956). Soon, many researchers started developing correlations between this technique and several other tests (CBR in pavements, unconfined compressive strength, shear strength, etc.) until our days (Jones and Harvey, 2005; Luo et al., 1998; Scala, 1956). While it can be easily transported and is relatively inexpensive, it requires a lot of physical resistance and its manual-operation nature introduces uncertainty in the results as penetration energy can vary from one blow to another. Also, this method has analogous limitations for use in cohesive soils as other dynamic penetration equipment.

– *Swedish Weight Sounding (SWS):* this light penetration equipment was developed by the Geotechnical Committee of the State Railways of Sweden as a multipurpose, low-cost *in situ* testing device (Habibi et al., 2007). It consists of a screw-pointed rod, manually driven to different depths under several static weights (Orense et al., 2014). During the test, the static penetration under such weights and the necessary torque after the static phase to further penetrate into the soil 25 cm is then measured. These parameters are then converted into SPT or CPT equivalent results. Although this equipment can perform low-cost and rapid tests (including approximate liquefaction assessment), there are some significant disadvantages, as the deviations in soil characterisation

due to rod friction or the low resolution for soft soils (Orense et al., 2014; Tanaka et al., 2012)
- *Screw Driving Sounding (SDS)*: recently devised in Japan (Orense et al., 2014), this enhanced version of the SWS overcomes some of its previously mentioned disadvantages, automatizing the test (thus, minimising the influence of operator deviations) and implementing rod friction measure systems
- Other devices: some good comprehensive list of other light and portable equipment, as the Airfield Cone Penetrometer, the Trafficability Cone Penetrometer, the Rapid Compaction Control Device, etc., can be found in Kianirad (2011). Some other recently developed equipments, such as the Rapid Soil Characterisation System (RapSochs), are being extensively reported, quickly widening their feasibility for ground characterisation (Gamache et al., 2009; Kianirad et al., 2011).

Many of these techniques incorporate man-portable, low-cost devices which allow us to classify them as potentially useful tools for geotechnical site characterisation in developing regions. However, as most of the time they could be used as stand-alone tests, efforts on expanding the available data and correlations should be carried out by the experts, in order to increase their possibilities.

4 GEOPHYSICS: EXPANDING POSSIBILITIES

The potential of geophysical techniques is growing each year, as testing devices are being continuously enhanced, decreasing in volume and weight while their versatility and possibilities are increasing. In parallel, the interpretation algorithms and the software that implements those are improving the resolution of these tests, even amplifying their possibilities.

The pieces of equipment can be easily carried as baggage by a reduced team of researchers to any place in the world, as the authors have verified on many occasions: just three people are enough to easily carry to different countries one seismograph, one resistivity meter, 24 geophones, 36 electrodes, and over 300 m of cables, along with auxiliary devices (laptops, batteries, etc.) in just four checked pieces of luggage and three cabin bags. The authors have successfully transported equipment in this fashion to Mexico, Bolivia, Nigeria, Jamaica, Uruguay, Costa Rica, etc. without ever encountering any problem.

Although this kind of systems are not usually inexpensive, through the collaboration of governmental institutions, non-profit organisations and researchers, these techniques can travel to places where other probing machinery has been proved to be unaffordable or unable to be transported, and their use can mean a significant difference to enhance the design process for traditionally non-engineered housing environments, as was shown in figure 3.

4.1 *Seismic methods*

Seismic surveys are known to offer many possibilities through the direct analysis of their resulting data: strata disposition (Milsom and Eriksen, 2011), detection of water or gas (Begay et al., 2000; Dai et al., 2004; Grelle et al., 2013), definition of subsoil cavities (Grandjean and Leparoux, 2004; Sheehan et al., 2005), landslide risk assessment (Hagedorn, 2014), etc.

Seismic refraction and surface wave tests are increasingly becoming very popular both as stand-alone field tests or as combined tools using several strategies: as pseudo joint P-wave refraction and surface wave 2-D inversion analysis (Ivanov et al., 2000), combined SH-wave refraction an MASW explorations (Yordkayhun et al., 2014), joint MASW and ReMi methods (Yordkayhun et al., 2014) or integrated study of Rayleigh-wave and Love-wave surveys (Dal Moro, 2014), to name only few.

One of the additional potential uses of seismic techniques in developing communities is to relate seismic results (namely, wave propagation velocities) with other geotechnical parameters traditionally used in foundation design, slope stability estimations, etc. Recent tendencies have tried to establish the relationship between the SPT-N blow count in Standard Penetration Tests with the s-wave propagation velocities, with good determination coefficients (see Thaker and Rao (2011) for a complete compilation of such correlations). However, s-wave analysis through surface waves recording can be quite difficult sometimes, and it can lead to inaccurate estimations of those velocities (Dal Moro et al., 2015). On the other hand, usually p-wave profiles can be more adjusted to the real underground properties of a site, if no hidden stiff layers are close to the surface.

With this idea in mind, the authors have crossed p-wave propagation data with SPT continuous profiling in several alluvial deposits in Mexico, discovering that while direct SPT-N vs. p-wave velocity present low determination coefficients, under the light of dimensional analysis (Butterfield, 1999), this approach renders good regression results. After the introduction in the dimensional analysis of other parameters such as the effective overburden stress, the unit weight, the void ratio or the saturation degree of the soil –consistent with the geotechnical dependencies described by Foti (2012)-, the determination coefficient increases over 0.9. As many methods used to estimate bearing capacity of foundations, settlement potential, etc., are formulated over SPT-N dependant expressions, this kind of dimensional analysis approaches could be quite useful in the near future to fill the void in previously non-engineered construction initiatives to estimate foundation design parameters.

4.2 *Electric tomography*

Some recent efforts in creating regression models relating electrical resistivity with soil properties such as water content, unit weight, cohesion, angle of internal friction, etc. (Akinlabi and Adeyemi, 2014; Cosenza et al., 2006; Siddiqui and Osman, 2013), have produced wide dispersions, quantified by low determination coefficients. Other approaches (Akinlabi and Adeyemi, 2014; Sudha et al., 2009) have however shown good linear correlations between transverse resistance and average SPT-N, that allow us to be confident on the development of its potential as predictive non-intrusive techniques in the future. On this regard, the authors are currently analysing the predictive character of these techniques. For instance, several tests on alluvial strata in Burgos (Spain) have been carried out to correlate DPSH (Deep Probe Super Heavy) penetration resistance in comparison with inverted resistivity, with results that show encouraging predictive possibilities.

Also, ERT is known a powerful tool to assess the potential existence of sinkholes in karstic systems, as those explored by the authors in Jamaica, as illustrated in figure 4:

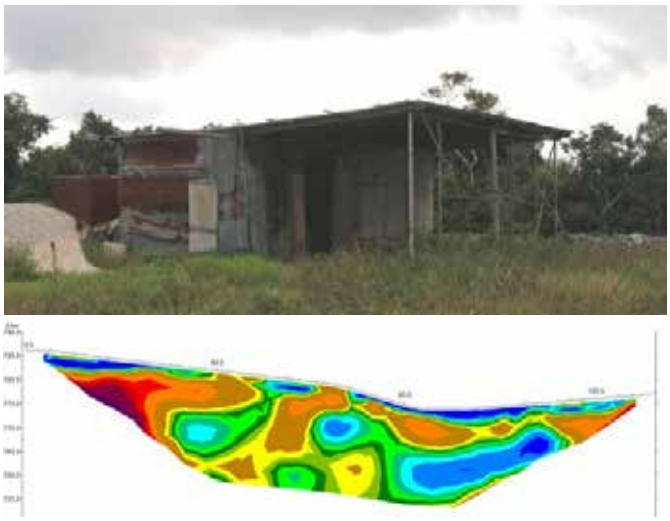

Figure 4. Electric tomography on karstified limestones next to a non-engineer shack in Mandeville (Jamaica)

4.3 *Joint seismic-electric methods*

If geophysical methods as stand-alone techniques have a wide variety of possibilities on the field of site characterisation, recent studies have pointed out the potential behind joint interpretations, using seismic and ERT methods on the same site (Driad-Lebeau et al., 2008; Johnson et al., 2002; Riddle et al., 2010; Sudha et al., 2009).

5 CONCLUSIONS

Devising new geotechnical site characterisation techniques and equipment specifically designed for underdeveloped and developing countries is a responsibility for the ground engineering practitioners and researchers, as the projections of the population living in non-engineered dwellings in hazardous parts of the world along this century is quite alarming. Several possibilities have been described, which outline the lines of research and development that will be required during the next decades.

6 REFERENCES

Akinlabi, I., Adeyemi, G., 2014. Determination of Empirical Relations between Geoelectrical Data and Geotechnical Parameters in Foundation Studies for a proposed Earth Dam. T*he Pacific Journal of Science and Technology* 15.

Amadei, B., 2004. Engineering for the developing world. *Bridge* 34.

Arya, A.S., 2000. Non-engineered construction in developing countries-an approach toward earthquake risk prediction. *Bulletin of the New Zealand Society for Earthquake Engineering* 33, 187-208.

ASCE (American Society of Civil Engineers), 2007. The ACSE vision for civil engineering in 2025. Reston, VA: *American Society of Civil Engineers* 15.

Begay, D.K., Miller, R.D., Watney, W.L., Xia, J., 2000. High-resolution P-and S-wave reflection to detect a shallow gas sand in southeast Kansas, *2000 SEG Annual Meeting. Society of Exploration Geophysicists*.

Burnham, T., Johnson, D., 1993. In situ foundation characterization using the dynamic cone penetrometer. Minnesota Department of Transportation. St. Paul, Minnesota.

Butterfield, R., 1999. Dimensional analysis for geotechnical engineers. *Geotechnique* 49, 357-366.

Cosenza, P., Marmet, E., Rejiba, F., Cui, Y.J., Tabbagh, A., Charlery, Y., 2006. Correlations between geotechnical and electrical data: A case study at Garchy in France. *Journal of Applied Geophysics* 60, 165-178.

Chowdhury, R., Flentje, P., 2007. Perspectives for the future of Geotechnical Engineering. *Proceedings of the International Conference on Civil Engineering For the New Millennium: Opportunities and Challenges*, India.

Dai, J., Xu, H., Snyder, F., Dutta, N., 2004. Detection and estimation of gas hydrates using rock physics and seismic inversion: Examples from the northern deepwater Gulf of Mexico. *The Leading Edge* 23, 60-66.

Dal Moro, G., 2014. Surface Wave Analysis for Near Surface Applications. *Elsevier Science*.

Dal Moro, G., Moura, R.M.M., Moustafa, S.S.R., 2015. Multi-component joint analysis of surface waves. *Journal of Applied Geophysics* 119, 128-138.

Driad-Lebeau, L., Piwakowski, B., Styles, P., Bourgeois, B., Contrucci, I., 2008. Geophysical detection of underground cavities, *Post-Mining Symposium*. Nancy, France.

Foti, S., 2012. Combined use of geophysical methods in site characterization. *Geotechnical and Geophysical Site Characterization (ISC-4, Brazil)*, 43-61.

Francisca, F., 2011. About the future of geotechnical engineering: a view from South America, *Proc. of the 2011 Pan-Am CGS Geotechnical Conference.*

Fukubayashi, Y., Kimura, M., 2014. Improvement of rural access roads in developing countries with initiative for self-reliance of communities. *Soils and Foundations* 54, 23-35.

Gamache, R.W., Kianirad, E., Pluta, S.E., Jersey, S., Alshawabkeh, A.N., 2009. Rapid Field Soil Characterization System for Construction Control. *Transportation Research Record: Journal of the Transportation Research Board* 617

Gkoumas, K., 2008. Basic aspects of risk-analysis for civil engineering structures. *Handling Exceptions in Structural*

Engineering: Robustezza Strutturale, Scenari Accidentali, Complessità di Progetto, Roma.

Grandjean, G., Leparoux, D., 2004. The potential of seismic methods for detecting cavities and buried objects: experimentation at a test site. *Journal of Applied Geophysics,* 56.

Grelle, G., Revellino, P., Guerriero, L., Soriano, M., Donnarumma, A., Guadagno, F.M., 2013. Water table detection with Water Seismic Index. *Rendiconti online Società Geologica Italiana*, Roma 24, 172-174.

Habibi, M., Cheshomi, A., Fakher, A., 2007. Advantages and disadvantages of using Swedish Weight Sounding for liquefaction assesment. *4th International Conference on Earthquake Geotechnical Engineering*, Thessaloniki (Greece).

Hagedorn, S., 2014. Landslide investigation using seismic refraction techniques. Delft University of Technology *IDEA League Joint Master's in Applied Geophysics*.

Ivanov, J., Park, C., Miller, R., Xia, J., Hunter, J., Good, R., Burns, R., 2000. Joint analysis of surface-wave and refraction events from river-bottom sediments. *70th Annual International Meeting, SEG*, pp. 1307-1310.

Johnson, W.J., Snow, R., Clark, J.C., 2002. Surface geophysical methods for dedection of underground mine workings. *Symposium on Geotechnical Methods for Mine Mapping Verifications*, Charleston, West Virginia.

Jones, D., Harvey, J.T., 2005. Relationship between DCP, Stiffness, Shear Strength, and R-value. *Research Report UCPRC-TM-2005-12*. Institute of Transportation Studies. University of California, Davis.

Kianirad, E., 2011. Development and testing of a portable in-situ near-surface soil characterization system. Northeastern University. Boston, Massachusetts

Kianirad, E., Gamache, R.W., Brady, D., Alshawabkeh, A.N., 2011. Equivalent quasi-static estimation of dynamic penetration force for near surface soil characterization, *Geo-Frontiers* in *Advances in Geotechnical Engineering*. ASCE, pp. 2325-2334.

Luo, X., Salgado, R., Altschaeffl, A., 1998. Dynamic cone penetration test to assess the mechanical properties of the subgrade soil. *FHWA/IN/JTRO-98/13*. Joint Transportation Research Program, Indiana Department of Transportation and Purdue University, West Lafayette, Indiana

MacDonald, M., 1994. Study of the efficiency of site investigation practices. Bridges and Ground Engineering Resource Centre, Transport Research Laboratory.

MacLeamy, P., 2004. The future of the building industry: The effort curve. *HOK Network, www.youtube.com/watch* vol.9.

Mallick, D.V., 2015. Protection against earthquakes of non-engineered construction. *WG7 Workshop*, Geneva.

McWilliams, H., Griffin, C., 2013. A critical assessment of concrete and masonry structures for reconstruction after seismic events in developing countries. Department of Architecture, Portland State University, Portland, Oregon, United States.

Milsom, J., Eriksen, A., 2011. Field geophysics. John Wiley & Sons.

Monnet, J., 2015. In Situ Tests in Geotechnical Engineering. John Wiley & Sons.

Morin, G., Hassall, S., Chandler, R., 2014. Case study–The real life benefits of Geotechnical Building Information Modelling. *Information Technology in Geo-Engineering: Proceedings of the 2nd International Conference (ICITG,)* Durham, UK. IOS Press, p. 95.

Oliver, P., 2007. Dwellings:: The Vernacular House World Wide. Phaidon Press.

Orense, R., Mirjafari, Y., Suemasa, N., 2014. Geotechnical site characterisation using Screw Driving Sounding method. *Soil Liquefaction during Recent Large-Scale Earthquakes*, 13.

Orsmond, W., 2007. The investigation of mud tailings and a comparison of different test methods with 3rd world constraints, *Proceedings of the Fourth International Conference on Soft Soil Engineering*. Taylor & Francis Group, London, Vancouver (Canada).

Ortiz-Palacio, S., Ibáñez, S., López-Ausín, V., Porres, J., 2015. Earthquake Vulnerability and the State-of-the-Art of Hybrid Structural Reinforcement and Soil Improvement Methods for Non-Engineered Structures. *6th Int. Conference on Earthquake Geotechnical Engineering, Christchurch*

Rehman, Z.U., 2010. Development of a Pressuremeter to Operate in Alluvial Soils of Punjab. University of Engineering & Technology, Lahore.

Renzi, S., 2009. Influence of dynamic soil-structure interaction analyses on shear buildings. University of Florence.

Riddle, G.I., Riddle, C.J., Schmitt, D.R., 2010. ERT and Seismic Tomography in Identifying Subsurface Cavities. *GeoConvention 2010*, Calgary, Alberta, Canada.

Robertson, P.K., 1986. In situ testing and its application to foundation engineering. *Canadian Geotechnical Journal* 23, 573-594.

Sandekian, R., Chinowsky, P., Amadei, B., 2014. Engineering for Developing Communities at the University of Colorado Boulder: A Ten Year Retrospective. *International Journal for Service Learning in Engineering, Humanitarian Engineering and Social Entrepreneurship*, 62-77.

Scala, A., 1956. Simple methods of flexible pavement design using cone penetrometers. *New Zealand Engineering* 11.

Sheehan, J.R., Doll, W.E., Watson, D.B., Mandell, W.A., 2005. Application of seismic refraction tomography to karst cavities. *US Geological Survey Karst Interest Group Proceedings*, Rapid City, South Dakota, 12-15.

SICI (Spanish Institution of Civil Engineers), 2016. Declaración de Madrid, Spain.

Siddiqui, F.I., Osman, S.B.A.B.S., 2013. Simple and multiple regression models for relationship between electrical resistivity and various soil properties for soil characterization. *Environmental earth sciences* 70, 259-267.

Sudha, K., Israil, M., Mittal, S., Rai, J., 2009. Soil characterization using electrical resistivity tomography and geotechnical investigations. *Journal of Applied Geophysics* 67, 74-79.

Tanaka, T., Suemasa, N., Ikegame, A., Yamato, S., 2012. Classification of strata using screwdriver sounding test. T*he 22nd International Offshore and Polar Engineering Conference*. International Society of Offshore and Polar Engineers.

Thaker, T., Rao, K., 2011. Development of statistical correlations between shear wave velocity and penetration resistance using MASW technique, *Pan-am CGS Geotechnical Conference*. Delhi, India.

United Nations, 2015. World Population Prospects: The 2015 Revision. Department of Economic and Social Affairs, Population Division. New York: United Nations.

United Nations General Assembly, 2015. Transforming Our World: The 2030 Agenda for Sustainable Development. *Resolution adopted by the General Assembly on 25 September 2015*. New York: United Nations.

Wang, Z., 2008. Understanding seismic hazard and risk: a gap between engineers and seismologists, *The 14th world conference on earthquake engineering*.

Way, C., 2015. The Millennium Development Goals Report 2015. New York: United Nations.

Whyte, I., 1995. The financial benefit from a site investigation strategy. *Ground engineering* 28, 33-36.

Yordkayhun, S., Sujitapan, C., Chalermyanont, T., 2014. Joint analysis of shear wave velocity from SH-wave refraction and MASW techniques for SPT-N estimation. *Journal of Science and Technology* 36.

Geotechnical and Geophysical Site Characterisation 5 – Lehane, Acosta-Martínez & Kelly (Eds)

Geotechnical characterization of Ballina clay

J.A. Pineda & R.B. Kelly
ARC Centre of Excellence for Geotechnical Science and Engineering, the University of Newcastle, Newcastle, NSW, Australia

L. Suwal, L. Bates & S.W. Sloan
ARC Centre of Excellence for Geotechnical Science and Engineering, University of Newcastle, Australia

ABSTRACT: Australia's first National Soft Soil Field Testing Facility has been established near Ballina in northern New South Wales. A detailed site characterization study has been performed to determine the site stratigraphy, material properties and engineering parameters. The results of combined *in situ* and laboratory campaigns are summarized in this paper. The Ballina clay can be characterized as a conductive, high plasticity, structured, high compressibility, low strength, low permeability, near-isotropic and lightly overconsolidated material.

1 INTRODUCTION

Geotechnical design relies very much on the accurate determination of soil parameters, as these affect the accuracy of the associated numerical analysis. *In situ* and laboratory characterization campaigns are the key to the development of safe and cost-effective designs for much of civil infrastructure. The intrinsic features of natural soft estuarine clays (low *in situ* stresses and undrained shear strength, a high compressibility, the presence of electrolytes in the pore fluid, the presence of organic matter and expansive minerals, as well as weak cementation) pose a number of challenges for proper geotechnical characterization, either *in situ* or in the laboratory.

This paper summarizes the results of *in situ* and laboratory characterization programs carried out on the materials composing the soil profile at the Ballina site (NSW, Australia), where a National Soft Soil Field Testing Facility (NFTF) has been established (Kelly, 2013) with the goal of improving engineering design methods via fundamental and basic characterization of a typical Australian estuarine soft clay. This facility is managed by the ARC Centre of Excellence for Geotechnical Science and Engineering (CGSE). Index properties as well as mechanical parameters have been interpreted from *in situ* and laboratory testing campaigns aimed at developing a geotechnical model for Ballina clay.

2 GEOLOGICAL ENVIRONMENT

The geological profile at the Ballina site comprises infill materials of the Richmond River valley, particularly estuarine Quaternary sediments (Figure 1a). According to Bishop (2004) three stages of Quaternary deposition for the soils in the area may be identified as follows. Stage 1 corresponds to deeper deposits of dense, heavily altered fluvial sandy-gravels (South Casino Gravel) accompanied by very stiff clays heavily oxidized and eroded (Dungarubba Clay). Stage 2 and 3 are composed of gravels and sandy clays (lower levels), combined with grey shelly muds which are dominant along the strata. Clays from the lower levels refer to the Gundarimba Clay. The upper estuarine clays, including Ballina soft soils, form the Pimlico Clay unit which displays variable thickness from 10 m - 40 m. South Casino Gravel, Dungarubba clay and Gundarimba clay are dated to be of Pleistocene age whereas the deposition of the Pimlico Clay is related to Holocene age. The absence of sands above RL -10 m AHD within the Pimlico Clay deposit correspond with the formation of a coastal barrier that created a low energy estuarine deposition environment behind it. The clays above 4 m depth were deposited in a tidal flat environment where a stable structure evolved. Clays below this depth are considered to be deposited in the less dynamic deeper water environment which allowed an open structure to be formed (Bishop & Fityus, 2006).

3 *IN SITU* CHARACTERIZATION

The *in situ* testing program included geophysics (electrical resistivity imaging –ERI- and multi-channel analysis of surface wave –MASW-), cone penetrometer, seismic dilatometer, shear vane and permeability tests carried out at different locations within the NFTF. Selected tests are indicated in Figure 1(b). Key results are presented below. For a detailed description of the *in situ* characterization campaign the reader is referred to Kelly et al. (2016a).

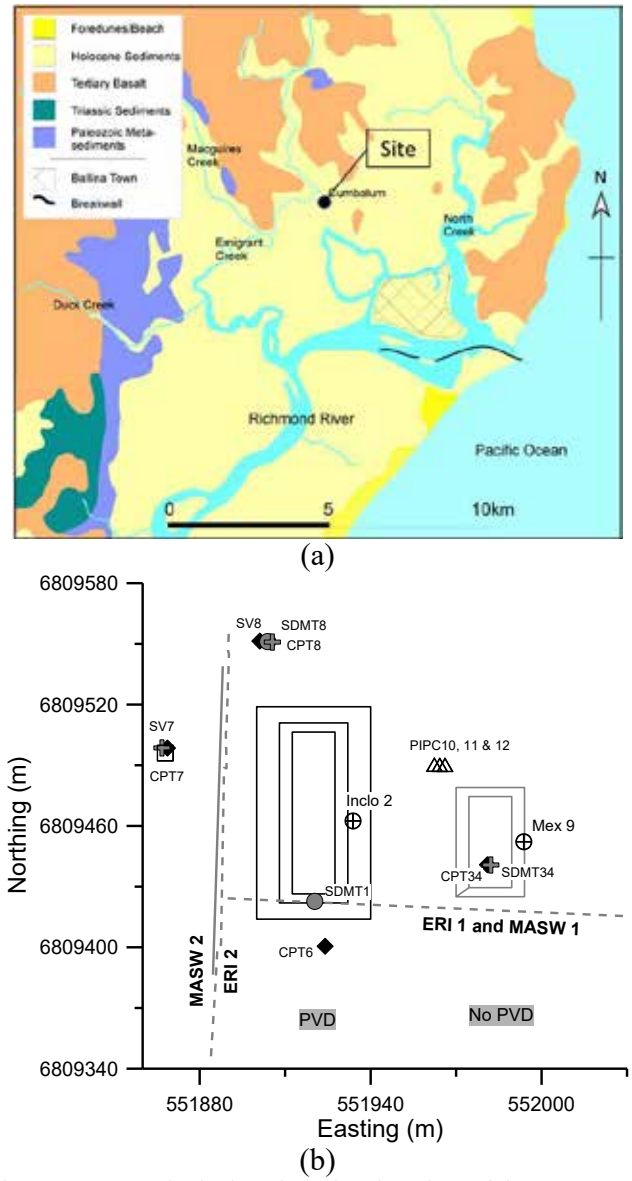

Figure 1. (a) Geological setting (b) Plan view of the NFTF.

The groundwater at the Ballina site is hydrostratic as estimated from vibrating wire piezometer measurements. *In situ* stresses were computed using bulk unit weight and water levels. Bulk unit weights were calculated in laboratory from moisture content and volume measurements. These data were then used to calculate the total vertical stress with depth. Effective vertical stresses were calculated by subtracting the hydrostatic pressure from the total stress. Total stresses, hydrostatic water pressures and effective stresses calculated at the location of cone penetration test CPT6 are shown in Figure 2(a).

Horizontal stresses and the associated K_0 values were estimated using push-in pressure cells (PIPC), which measures total horizontal pressure and water pressure. No correction has been made to the PIPC data for installation effects. SDMT and CPTu data have been used to estimate K_0. The SMDT has been interpreted using Marchetti (1980), Powell and Uglow (1988) and the recent proposal by Kouretzis *et al.* (2015) in which the relationship between K_D and K_0 is given by $K_0=0.36e^{0.11K_D}$. Profiles of K_0 obtained from dilatometer test SDMT1 are shown in Figure 2(b). The interpretation of Kouretzis *et al* (2015) is closest to the PIPC data while Powell and Uglow (1988) and Marchetti (1980) are 28% and 70% higher than Kouretzis *et al* (2015), respectively. The procedure for estimating values of K_0 using CPTu data is discussed in Kelly *et al*. (2016a).

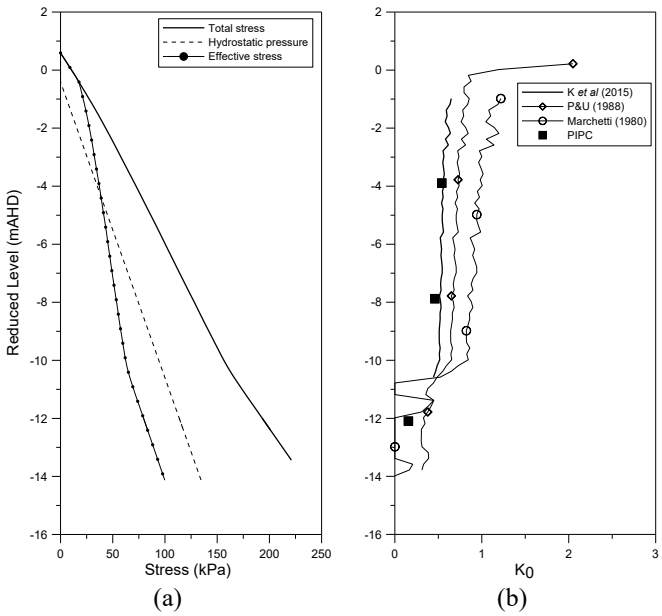

Figure 2.(a) Water pressure, total and effective vertical stresses at the location of test CPT6. (b) K_0 estimations from PIPC and SDMT data.

Figure 3 shows profiles of shear wave velocity, V_s, obtained from the test MASW-1 which followed East-West direction (Figure 1(b)). Values of V_s higher than 70 m/s are observed for depths above 2 m which corresponds to the overconsolidated alluvial crust. This layer is underlain by the Ballina clay between 2 m – 11 m, where V_s ranges from 60 m/s to 110 m/s. The analysis of ERI (not presented here) and MASW data shows a transition zone below the soft clay strata composed by sandy materials and stiff clay. The various layers are relatively uniform with depth along north-south direction. In contrast, the thickness of the soft clay layer increases towards the east whereas the sand layer decreases in thickness. The MASW defines the boundary between the soft clay and sand at a shear wave velocity between about 80 m/s and100 m/s in the north-south direction

and between about 90 m/s and 100 m/s in the east-west direction. Resistivity values are low, which is indicative of a highly conductive medium such as saline groundwater. The CPT data included in Figure 3 show clearly the stratigraphic boundaries across the site due to the high density of measurements in the vertical direction. A consistent stratigraphy in the horizontal direction, albeit for widely spaced tests, is also observed from the CPT results.

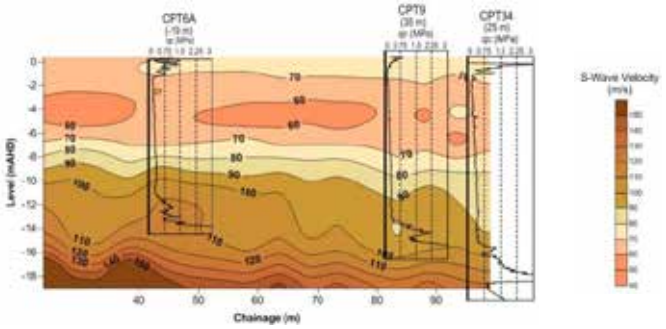

Figure 3.Shear wave velocity profiles obtained from MASW1 alongside East-West direction.

4 LABORATORY CHARACTERIZATION

Specimens obtained from two continuous boreholes (Inclo 2 and Mex 9; see Figure 1(b)) drilled up to 13 m depth were used in the laboratory characterization. A hydraulic fixed-piston sampler (89 mm in external diameter) was used for the sampling campaign. The laboratory study combined index characterization tests with one-dimensional and stress-path testing to evaluate compressibility, stiffness, permeability and strength parameters. Key results are discussed below. More details are given in Pineda et al. (2016).

4.1 *Index properties and natural state*

Figure 4 shows the results from classification and index tests performed on the Alluvium and Ballina clay. The natural water content is slightly lower than the liquid limit which ranges from 80% to 130%. Plastic limit and plasticity index vary between 40% and 50% and from 34 to 80%, respectively. The dry density reduces from 1.50 Mg/m^3 to 0.70 Mg/m^3 at 3 m depth which correspond to a void ratio of about 3. The minimum variation in ρ_d is observed between 3 m and 11 m. Clay content ranges from 60% to 80% by size with an organic content of 1% to 3% by mass. Density of solid particles lies around 2.63 Mg/m^3 - 2.71 Mg/m^3.

Geochemical analysis of the pore fluid indicates that the most abundant cations and anions are sodium (0.93 – 8.23 g/L) and chloride (2.5 – 15.4 g/L), respectively. Additional relevant cations are magnesium and calcium (<1 g/L). The presence of salts in the pore fluid is one of the fingerprints of marine clays which also play a key role on their mechanical response. Bulk (fluid+ solids) and the pore fluid salinity measurements were carried out on Ballina clay. A similar trend is observed between EC_{bulk} and EC_{fluid} with depth. The bulk measurements vary with depth from 4 mS/cm to 15 mS/cm. The values of EC_{fluid} are larger than EC_{bulk}, and vary from 7 mS/cm up to 36 mS/cm (the average below 5 m). The lower values measured at shallow depths may be due to dilution by fresh water from the ground surface. A comparison between *in situ* and laboratory electrical conductivity measurements and its use in the estimation of soil porosity is discussed in a companion paper (Kelly et al., 2016b).

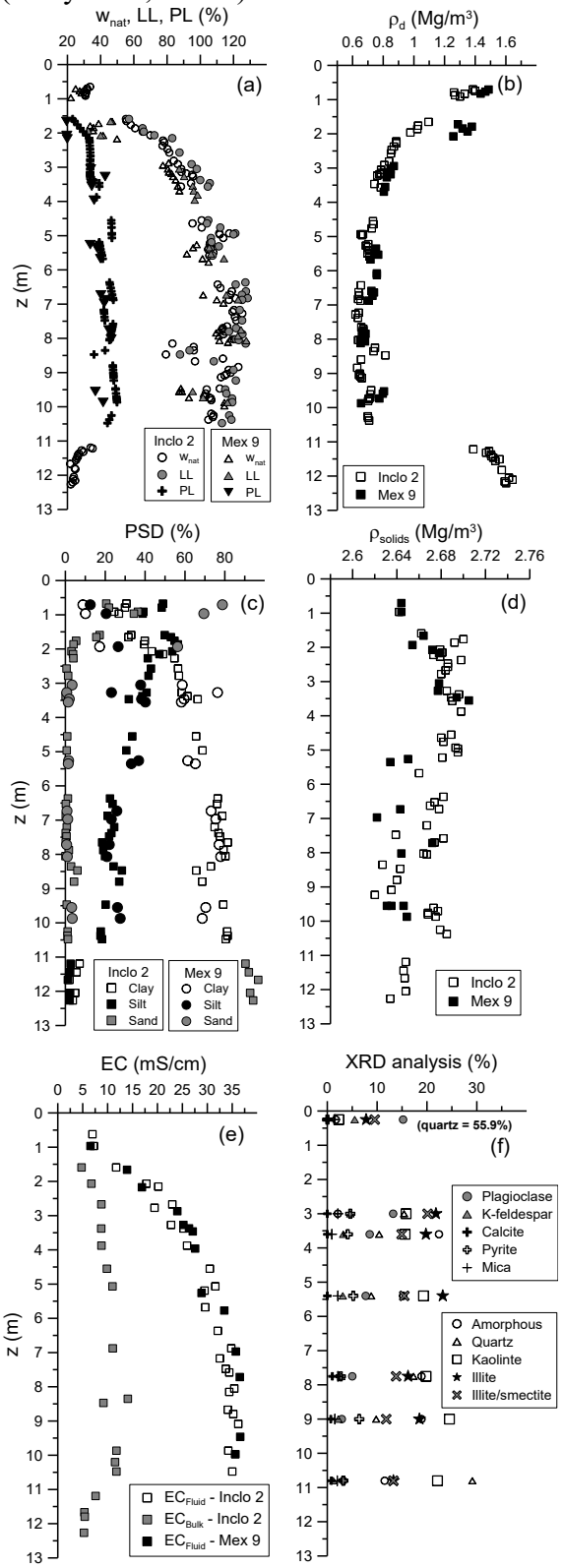

Figure 4.Index characterization tests.

Quantitative X-Ray diffraction analyses showed that the mineralogical composition of the clay varies down the soil profile. The specimens are composed of: amorphous minerals (1.7 – 22.4%), kaolinite (2.3 – 24.5%), illite (7.8 – 23.3%), quartz (8.8 – 55.9%), interstratified illite/smectite (9.5 – 20.1%), plagioclase (2.9 – 15.2%), pyrite (0 – 6.4%), K-feldspar (1.2 – 5.5%), mica (0.9 – 2.1%) and calcite (0 – 1.0%).

The fabric of the natural Ballina clay has been studied by means of microscope images obtained from scanning electron microscope (SEM) analysis on high-quality block specimens. As observed in Figure 5 the structural arrangement of the natural clay shows an open configuration with no preferential orientation. Macro-voids of around 1 – 2 μm size are detected. This behaviour is in agreement with the non-oriented fabric of soft marine illitic clays described by Mitchell (1976).

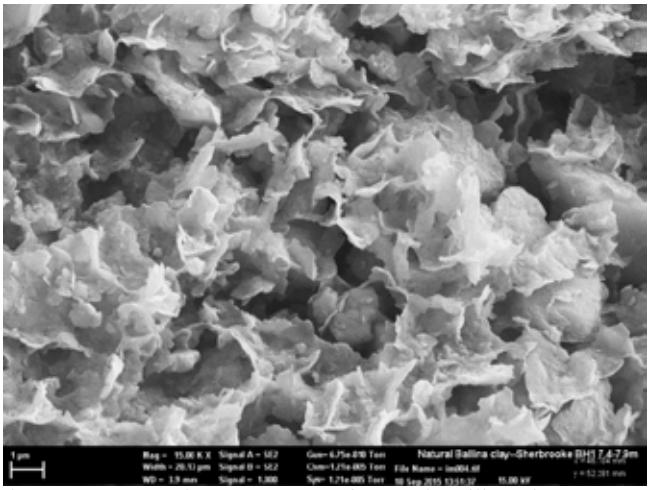

Figure 5.Structural arrangement of natural Ballina clay.

4.2 *Compressibility tests*

Figure 6 shows the compression curves obtained from constant rate of strain (CRS) tests. Synthetic pore fluid at the same EC as the natural clay was used in the tests. Curves have been normalized using the void index concept, $I_v=(e-e^*_{100})/C_c^*$, introduced by Burland (1990). Only loading paths are included in this figure for clarity. Curves for specimens from borehole Inclo 2 are represented by solid lines whereas dotted lines refer to specimens from borehole Mex 9. The Intrinsic Compression Line (ICL) and the Sedimentary Compression Line (SCL), determined by Burland (1990), are also included. The I_v-log σ'_v curves (natural soil) all lie above the ICL which is indicative of the natural structure of the clay. As the stress level increases beyond σ'_{yield}, destructuration takes place and the curves tend to converge to the ICL. Two destructuration rates are observed in Figure 6, depending on the specimen depth. Specimens from borehole Inclo 2 located below 5 m (black solid lines) shows larger destructuration than shallow specimens (grey solid lines). For stresses higher than 300 kPa, all the curves tend toward the ICL showing a gently destructuration rate. The curve represented by open circles corresponds to a specimen from 4.93m, which displays large destructuration beyond σ'_{yield}. This leads to earlier convergence with the curves from shallow specimens, and seems to indicate a change in the level of structure in the clay. At large stresses, the slope of the compressibility curves tend to the one of the reconstituted soil.

An important feature of Ballina clay is the strong stress-strain non-linearity observed in one-dimensional compression tests. Due to that, estimating a single representative value for the compression index, C_c, requires considerable judgement as it may change dramatically with the stress level. Figure 7 shows an example of the strong variation of C_c with the stress level in Ballina clay. Results for specimens from boreholes Inclo 2 and Mex 9 located between 6.50 m and 6.80m depth are included in this figure. Values of C_c have been estimated by deriving the e – log(σ'_v) relationship as $C_c= -\partial e/\partial \log(\sigma'_v)$. A second estimation procedure (discrete approach) has been also employed here for comparison. In the later, $C_c= -\Delta e/\Delta \log(\sigma'_v)$. It can be noted that C_c reachs a peak value at stresses around 1.3 - 1.5 times σ'_{yield} and then decreases progressively with stress. For $\sigma'_v/\sigma'_{yield}$ >5, values of C_c are similar to those for reconstituted specimens. Values of C_c up to 3.4 have been estimated for specimens between 6 m - 10m which reduces with depth to 0.9 – 1.2.

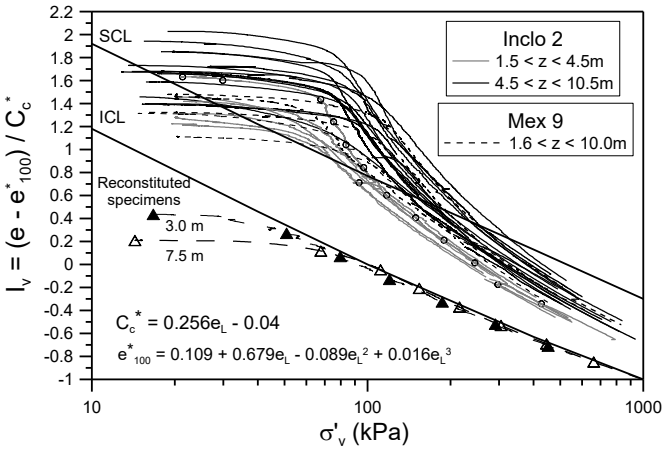

Figure 6.Compressibility curves obtained from CRS tests.

The results from CRS tests have been used to estimate the evolution of the consolidation coefficient, (c_v) and water permeability (k_w) following the procedure suggested by ASTM D4186. Results of representative specimens from borehole Inclo 2 are plotted in Figure 8. It can be seen that: (i) c_v tends to decrease with depth, and (ii) c_v reduces as the stress level increases, mainly in the overconsolidated range ($\sigma'_v < \sigma'_{yield}$) as a consequence of the progressive destructuration. For specimens located below 2m, c_v reduces from around 15 m^2/year to values ranging

between 0.3 to 0.85 m^2/year. The minimum variation is observed in the normally consolidated range. A similar response was observed for borehole Mex 9. This variation in c_v implies a variation in water permeability, k_w, between 10^{-8} - 10^{-11} m/s. Clear differences are observed between specimens below and above 5 m depth which confirms a change in soil structure at this level.

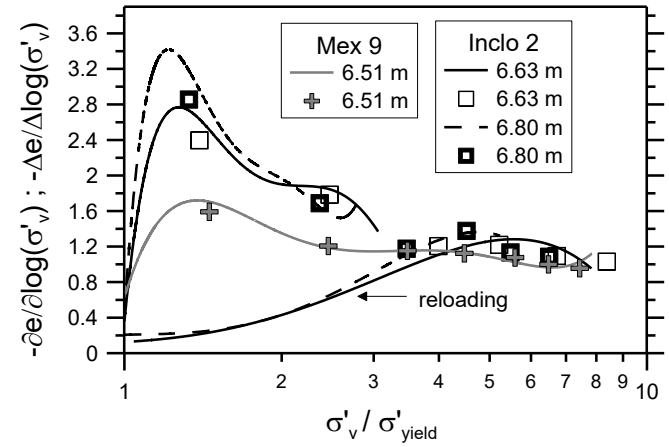

Figure 7.Variation of C_c with the stress level

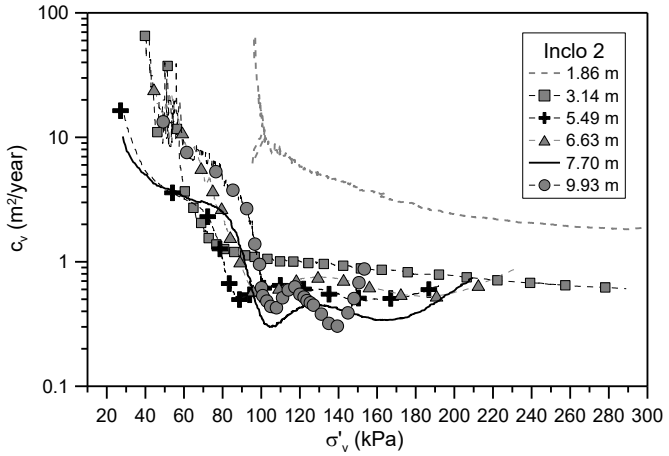

Figure 8.Variation of c_v with the stress level for specimens from borehole Inclo 2.

The secondary compression behaviour of Ballina clay was studied by means of Incremental loading (IL) tests in which long-term loading steps (five days) were applied. Specimens were compressed in steps by doubling the previous load increment according to ASTM D2435. The analysis of the displacement vs log(t) plots showed that primary consolidation was predominant only for stresses above σ'_{yield} whereas secondary compression was observed for all loading increments. Figure 9 shows that, except for stresses closer to yielding, the values of C_α/C_c vary in a narrow band between 0.025-0.05. This response is in agreement with the variation of C_α/C_c found by Mesri & Godlewski (1977).

4.3 *Shear tests*

Undrained triaxial (compression and extension) tests were carried out to estimate the undrained shear strength of Ballina clay deposits. Synthetic pore fluid at the same EC as the natural clay was used in the tests. Each triaxial test consisted of three stages: (i) saturation, (ii) consolidation, and (iii) shearing under undrained conditions. After getting a value for the Skempton's parameter B higher than 0.96, specimens were subjected to anisotropic consolidation, using the estimated K_0 values from SDMT tests, until σ'_{v0} was reached. The consolidation criterion followed in the triaxial tests was based on the dissipation of at least 90% of the excess pore water pressure.

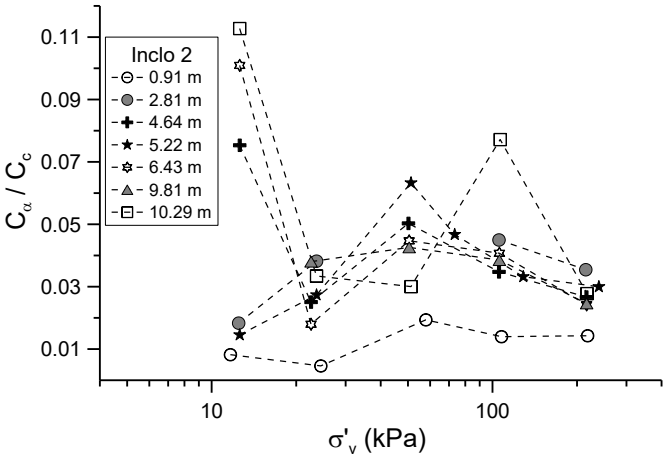

Figure 9.Variation of Cα/Cc ratio estimated from Incremental Loading tests for specimens from borehole Inclo 2.

Figure 10 shows the stress path followed in the q-p′ plane for specimens from borehole Mex 9 tested in triaxial conditions. The brittleness of the soil under shearing is observed in the effective stress paths presented in this figure. It is worth noting the marked difference between the friction angles in compression and extension for borehole Mex 9, where peak friction angles of up to 42º and 53º have been estimated in triaxial compression and triaxial extension, respectively. The effective stress paths shown in Figure 10 seem to indicate asymmetry of the yield locus about the isotropic line.

In addition to the undrained triaxial tests described above, drained direct shear tests were carried out to evaluate the strength parameters of sandy materials located above 1.5 m and between 11.1 and 12.3 m depth. Shear strength envelopes were estimated using three specimens consolidated prior to shearing under vertical stresses of 25, 50 and 100 kPa. The cconsolidation time was controlled via software and targeted to achieve 95% of soil compression. Finally, each specimen was subjected to shearing under a low shearing rate ($7x10^{-3}$ mm/min) until a maximum horizontal displacement of 20 mm was reached. The peak states plotted in Figure 11 suggest that, for three soil levels in borehole Inclo 2, a linear Mohr-Coulomb failure criterion seems to represent the peak conditions over the stress range tested. Shallow materials show a peak friction angle of $\phi'_{peak} \approx 34º$ whereas deep specimens display a peak

friction angle of $\phi'_{peak} \approx 38^o$. The effective cohesion for the shallow specimens is 15 kPa but is close to zero for the deep specimens. Due to the non-linearity of the failure locus at low stress levels, the values of the effective cohesion reported above should be treated with caution.

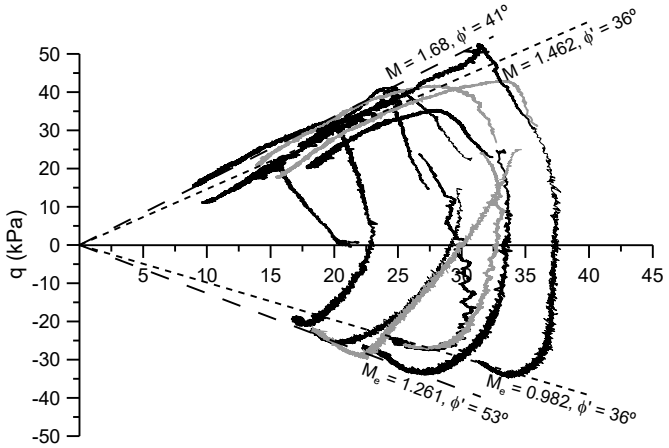

Figure 10.Stress-paths obtained from undrained compression and extension triaxial tests for specimens from borehole Mex 9.

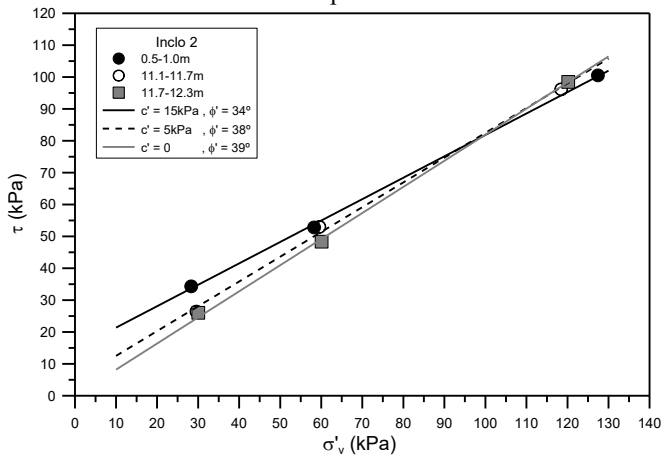

Figure 11.Direct shear test results for sandy specimens from borehole Inclo 2.

5 GEOTECHNICAL PROFILES

The results of the laboratory tests described above have been used to estimate the evolution of geotechnical parameters along the soil profile. The variation of σ'_{yield} with depth is shown in Figure 12(a). Values of σ'_{yield} were estimated using the energy method proposed by Becker et al. (1987). No correction for strain rate effects has been applied. The yield stress is higher than σ'_{v0} although a parallel variation with depth is observed below 3 m. The yield stress ratio reduces from around 3 (at shallow depths) towards a quasi-constant value of around 1.5 – 1.6 for borehole Inclo 2. Larger values are observed for borehole Mex 9, which is consistent with the differences in the water content (void ratio) reported in Figure 4. The shear wave velocity, V_s, estimated from *in situ* and laboratory tests is shown in Figure 13(a). Seismic dilatometer tests were performed at locations SDMT-1 and SDMT-34 (see Figure 1a). Laboratory values of V_s at σ'_{v0} were obtained during CRS tests using bender elements transducers. A good match is observed between the laboratory and *in situ* data along the soil profile. The shear wave velocity appears to vary linearly with depth between 3 m and 10.5 m. The laboratory data also capture the increase in V_s detected in SDMT-1 at depths below 11 m, where a sand layer appears.

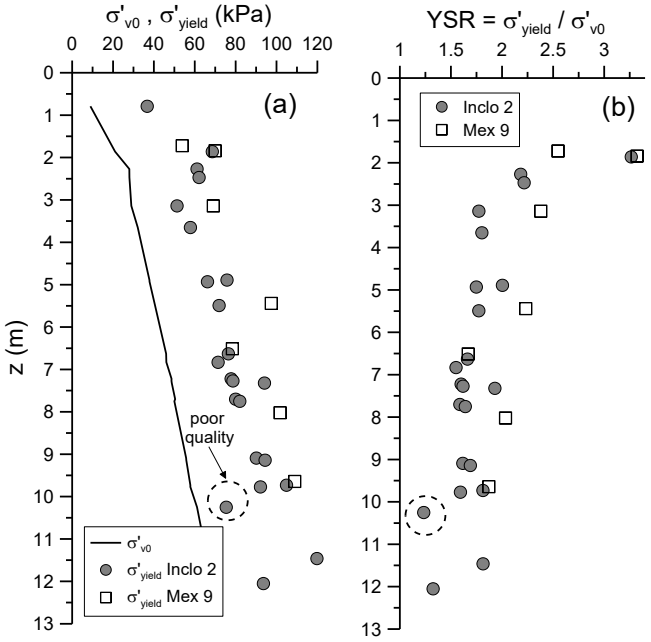

Figure 12.(a) *In situ* and yield effective stresses at Ballina site. (b) Yield stress ratio.

Coefficients of horizontal consolidation, c_h, have been interpreted from the results of CPTu dissipation testing. Interpretation of the dissipation tests has been performed using a curve fit to Teh and Houlsby's (1991) method provided by Mayne (personal communication) using values of rigidity index of 85 ($z < 7$m) and 125 ($z > 7$m) (see also Figure 14(c)). Figure 13(b) shows a comparison of c_h values from CPTu and piezoball (Colreavy *et al*, 2016) dissipation tests with c_v values estimated from CRS tests at σ'_{yield}. Very good agreement is observed between laboratory and the dissipation test results. For the materials from RL 2 to RL 10 m $c_{v\text{-}yield}$ lie between 2 to 10 m^2/yr whereas the c_h varies from 1.5 to 15 m^2/yr. The small differences between c_h and c_v suggest a low permeability anisotropy for Ballina clay as also recognized by Leroueil et al. (1990) for homogeneous marine clays.

Figure 14(a) shows the variation of the undrained shear strength, s_u, with depth for boreholes Inclo 2 and Mex 9. Results from the triaxial compression and triaxial extension tests are indicated by filled and empty symbols, respectively. The undrained shear strength increases with depth, not only in compression but also under extension shearing conditions. The strength s_u lies around 12.5 kPa at 1.8 m depth, and increases up to 27.5 kPa at a depth of 9.75 m. It increases almost linearly with depth in triaxial extension from 10.5 kPa to 17.5 kPa between a

depth of 3.5 m and 10 m. The results from triaxial tests reported in Figure 10 shows that Ballina clay displays a strength ratio $s_{u\text{-extension}}$ /$s_{u\text{-compression}}$ around 0.66, which seems to be insensitive to the soil plasticity.

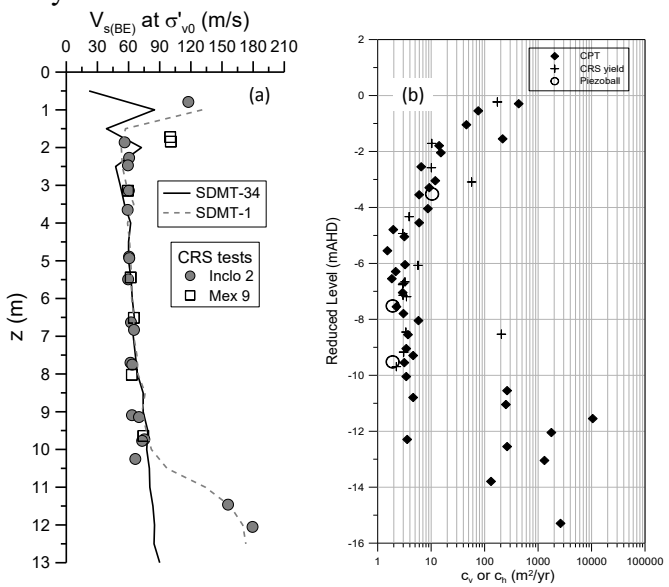

Figure 13.(a) V_s from SDMT and bender elements. (b) Comparison between c_h and c_v

Results from *in situ* tests are also reported in Figure 14(a). These include CPTu, SDMT and field vane (FVS) tests performed at the locations indicated in Figure 1(a). Values of $s_{u(CPTU)}$ were calibrated to the shear vane data using N_{kt} = 13.2. A comparison of peak undrained strengths from vane tests and triaxial compression and extension tests shows that, as would expected, s_u is greatest in triaxial compression, intermediate in vane shear and least in triaxial extension. The variations with depth are 8.4kPa + 2z for depths between 1.5m and 8m for triaxial compression and 10.7kPa + 1.2z (3.5 < z < 10 m) for triaxial extension. Soil sensitivity, estimated from field vane shear tests, reduces from around 10 at shallow depth towards an average value of around 3 between 2 – 11 m (Figure 14(b)). The rigidity index $I_r=G_{u50}/s_u$ was estimated from the triaxial data described above. Secant undrained shear moduli, G_{u50}, were computed at the 50% of the maximum deviatoric stress increment measured during the shearing stage. The rigidity index increases with depth from 25 to 150 although most of the data lie in the range 65-150. The fragile post-peak behaviour observed in undrained triaxial tests, associated with progressive soil destructuration, suggest that soil brittleness has to be considered. Figure 14(d) shows the variation of the brittleness index (Bishop, 1971) for specimens from boreholes Inclo 2 and Mex 9 subjected to triaxial compression. The brittleness index has been estimated as $I_B=[(q_{peak}-q_{post\text{-}peak})/q_{peak}]*100$, where $q_{post\text{-}peak}$ has been defined here as the deviatoric stress obtained at shear strains larger than 15%. It can be noted that up to 50% of the maximum deviatoric stress is lost if the clay is subjected to further straining. This aspect should be evaluated in practice due to its implication in stability analysis.

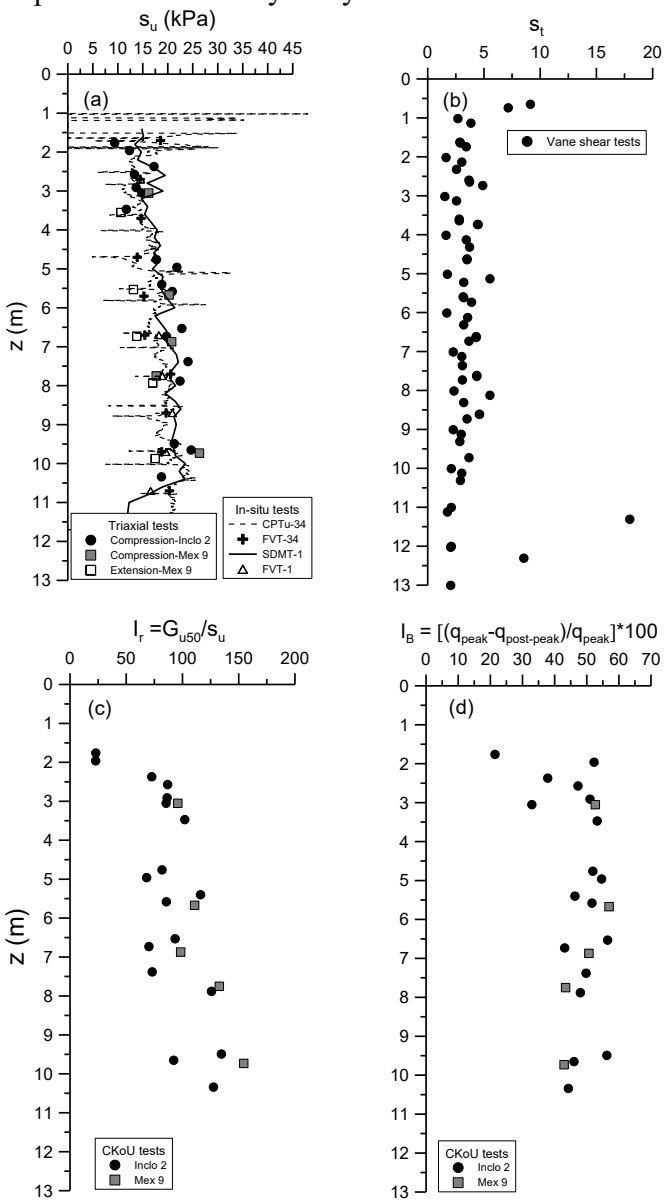

Figure 14.(a) s_u vs depth. (b) Sensitivity vs depth. (c) Rigidity index vs depth. (d) Brittleness index vs depth.

6 CONCLUDING REMARKS

Key results obtained from *in situ* and laboratory characterization campaigns carried out on the deposits that compose the soil profile at Ballina site have been described in this paper. Emphasis has been made to highlight aspects of the soil response relevant to practical problems aimed at providing geotechnical profiles of index and mechanical properties for the site. The site stratigraphy determined from the geophysical and *in situ* tests is reasonably uniform with depth alongside the north-south direction. In contrast, the thickness of the soft clay layer increases towards the east whereas the sand layer decreases in thickness.

Laboratory results show that these deposits display very high compressibility and a low undrained

shear strength which is larger in triaxial compression. The sensitivity of the clay is low according to *in situ* test results. Ballina clay shows a non-linear stress-strain response either in one-dimensional compression or undrained shearing. Results from undrained triaxial tests suggest asymmetry of the yield locus about the isotropic line. The consolidation coefficient, and consequently the water permeability, reduces dramatically with the stress level in the overconsolidated zone, mainly due to soil destructuration. A brittle response has been observed during shearing that reduces the undrained shear strength by around 50% after peak. Laboratory results show very good agreement with *in situ* estimations of shear wave velocity (small strain stiffness), consolidation coefficient and undrained shear strength.

7 ACKNOWLEDGEMENTS

The authors wish to acknowledge the support of the Australian Research Council Centre of Excellence for Geotechnical Science and Engineering and its industry partners Advanced Geomechanics (now Fugro), Coffey and Douglas Partners.

8 REFERENCES

ASTM D2435 (2011) Standard Test Methods for One-Dimensional Consolidation properties of Soils Using Incremental Loading.

ASTM D4186 (2006) Standard test method for on-dimensional consolidation properties of saturated cohesive soils using controlled-strain loading.

Becker, D.E., Crooks, J.H.A., Ben, K. & Jefferies, M.G. (1987) Work as a criterion for determining in situ and yield stresses in clays. Canadian Geotechnical Journal, Vol 24, 549-564.

Bishop, A. W. (1971). Shear strength parameters for undisturbed and remoulded soil specimens. In Stress–strain behaviour of soils: Proceedings of the Roscoe memorial symposium, Cambridge (ed. R. H. G. Parry), pp. 3–58. Henley on Thames, UK: G. T. Foulis.

Bishop, D.T. (2004) A proposed geological model and geotechnical properties of a NSW estuarine valley: a case study. Proc. 9th ANZ conference, Auckland, 261-267.

Bishop, D.T. and Fityus, S. (2006) The sensitivity framework: Behaviour of Richmond River estuarine clays, Australian Geomechanics Society, Sydney Chapter mini-symposium, 167-178.

Burland, J.B. (1990) On the compressibility and shear strength of natural clays. Geotechnique, 40(3), 329-378.

Colreavy C, O'Loughin C. & Randolph M. (2016) Estimating consolidation parameters from field piezoball tests. Géotechnique, doi: 10.1680/jgeot.15.P.106

Kelly R.B. (2013) Australia's first national facility for soft soils testing. Civil Engineers Australia, June, 76-78.

Kelly R.B., Pineda J.A., Bates L., Suwal, L.& Fitzallen I. (2016a). In situ Site Characterization for the Ballina Field Testing Facility. Geotechnique (in-print).

Kelly R.B., Pineda J.A. & Suwal L. (2016b) A comparison of in situ and laboratory resistivity measurements in soft clay. ISC'5 (this conference).

Kouretzis G., Ansari Y., Pineda J.A., Kelly R. & Sheng D. (2015) Numerical evaluation of clay disturbance during blade penetration, considering the effect of stress history. Geotechnique Letters, 5(3), 91-95.

Leroueil, S., Magnan, J-P and Tavenas, F. (1990), Embankments on soft clays, Ellis Horwood Series in Civil Engineering, Chichester, West Sussex

Mesri, G. & Godlewski, P.M. (1977) Time–stress-compressibility interrelationship. Proc. Geoch. Div. American Society of Civil Engineers. Civ. Eng., 22, GT5, 417-430.

Marchetti, S. (1980) In situ Tests by Flat Dilatometer. ASCE Jnl GED, Vol. 106, No. GT3, Mar., 299-321

Mitchell, J.K. (1976) Fundamentals of soil behaviour. Wiley & Sons.

Pineda, J.A., Suwal, L., Kelly, R.B., Bates, L. & Sloan, S.W. (2016) Characterization of Ballina clay. Geotechnique, 66(7), 556-577.

Powell, J.J.M and Uglow, I.M (1988) The interpretation of Marchetti dilatometer tests in UK clays. Proc. ICE Penetration Testing in the UK, Birmingham, 269-273

Geotechnical and Geophysical Site Characterisation 5 – Lehane, Acosta-Martínez & Kelly (Eds)

Geotechnical Parameters of Soft Soil in Macaé – Rio de Janeiro

L.M.M. Povoa, P.N.C. Nascimento, P.C.A. Maia & V.S. Singui

State University of Norte Fluminense Darcy Ribeiro, Brazil

ABSTRACT: This study aims to present strength parameters, compressibility and stress history through a campaign of surveys, piezocone and laboratory tests carried out at two sites in lowland area in Macaé, State of Rio de Janeiro. In this region, there is an extensive deposit of soft soil that mainly due to the development of the oil and gas industry, created a need for new buildings, causing the use of these areas. Moreover, particularly in Macaé, there is little or no information published on the geotechnical parameters. In total 22 holes of SPT, 4 vertical piezocone tests, 2 triaxial tests of unconsolidated undrained type and 5 laboratory oedometer tests were performed. Thus, a set of geotechnical parameters of the deposit was obtained. Additionally, the ratio of overconsolidation are also compared with values from laboratory oedometer tests. The results found showed a reasonable approach between field and laboratory parameters.

1 INTRODUCTION

Along the Brazilian coast it is common to find soft soils in sedimentary deposits formed in the Quaternary period of high compressibility, low permeability, high organic matter content, low bearing capacity and low resistance to penetration. In these deposits piezocone tests have been performed (Danziger and Schnaid, 2000; Coutinho, 2008) as well as in the state of Rio de Janeiro (Almeida & Marques, 2003; Almeida et al 2008a).

This paper presents field test data and laboratory tests carried out in sedimentary deposit in lowland area of Macaé, Rio de Janeiro.

2 DESCRIPTION OF THE AREA OF STUDY

The area of study is the sedimentary deposit of the lowland region located in the North Fluminense, in the city of Macae, Rio de Janeiro . The coastal region in which Macae was raised is intensely urbanized. The traffic flow causes major congestion in addition to the environmental issues generated by the lack of basic sanitation, garbage collection and sewage. Due to this urban saturation, the tendency is that the expansion of the city will happen towards the interior, where the soft soil deposit is found.

3 LOCATION OF RESEARCH POINTS

The research points were points of the deposit called: Imburo, Linha Verde and Virgem Santa. Typical stratigraphies of these three sites were obtained from 22 survey holes and are shown in Figure 1. The water table in general is quite shallow, at about 0.3 m depth. As these sites are surrounded by rivers or lagoons, the upper layer in many cases is either peat, dredged material, or uncontrolled fills.

Laboratory samples were collected with the help of a stationary piston Shelby tube, following the recommendations of the Brazilian code NBR-9820/1994.

The characterization and laboratory oedometer tests were performed in the region called Imburo. The particle size analysis revealed that the analyzed soil consists mainly of fine particles and tested points have similar granulometric charateristics.

The results of the characterization tests are shown in Table 1 while laboratory oedometer tests are shown in Table 2. High values of compression ratio CR observed in Table 2 indicate that the soil is quite compressible and, according to Almeida & Marques (2002), the moisture content of the soil is sensitive in most cases, superior to W_L. This behavior is found in most analyzed samples.

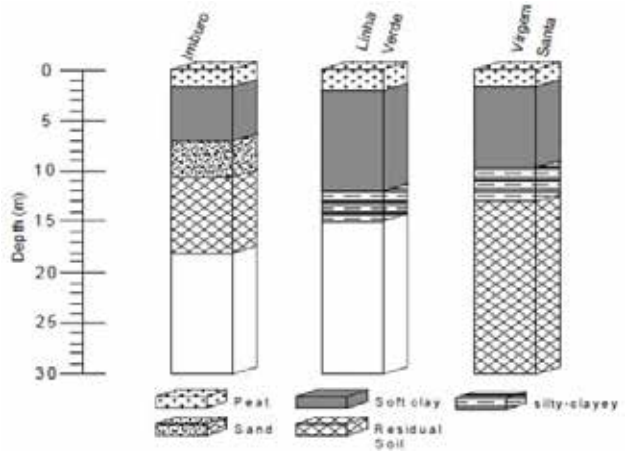

Figure 1. Stratigraphic profile of the investigated points

Table 1. Results of the characterization tests in Imburo

Depth (m)	G_s	W_0 (%)	γ (kN/m³)	e_0
0.15 – 0.75	2.56	80.8	14.9	2.07
1.0 – 1.6	2.56	187.68	12.62	4.84
1.3 – 1.9	2.56	212.47	12.48	5.41
1.5 – 2.1	2.6	189.95	12.74	4.83
2.1 – 2.70	2.62	217.6	12.41	5.7

Depth (m)	W_L(%)	W_P (%)	I_P (%)
0.15 – 0.75	102.5	44.3	58.2
1.0 – 1.6	194	78.4	115.6
1.3 – 1.9	192.9	56.8	136.1
1.5 – 2.1	191.4	62.3	129.1
2.1 – 2.70	165.1	60.2	105

Table 2. Results of the oedometric tests in Imburo.

Depth (m)	e_0	C_s	C_c	CR= Cc / 1 + e_0
1 .0 – 1.5	4.84	0.2	2.6	0.44
1.5 - 2	4.92	0.3	3.1	0.52
2.1 – 2.7	5.70	0.2	3.0	0.44
2.1 – 2.7	5.65	0.3	3.2	0.48
2.1 – 2.7	5.65	0.2	2.8	0.42
1.3 – 1.9	4.93	0.2	3.0	0.50

4 UNDRAINED RESISTANCE

Unconsolidated undrained triaxial tests were performed in the depths of 1.5 meters and 2 meters in Imburo, which resulted in undrained resistance values between 5 and 7,6 kPa. The comparison between the undrained resistance obtained from UU tests in this study and the undrained resistance found by other authors in sedimentary deposits with similar characteristics in Rio de Janeiro were very similar. It can be mentioned to the values found by Lima & Campos (2014) for the region of Guaratiba - RJ.

5 N_{KT} FACTOR

CPTu tests were performed, two in Linha Verde and 2 in Virgem Santa. Therefore, the data obtained through piezocone tests were used in combination with the results of triaxial undrained tests for the cone factor N_{KT} . The factor N_{kt} is obtained by using the corrected tip resistance (q_t) of CPTu testing and the resistance values of undrained UU triaxial tests, as follows:

$$N_{kt}= (q_t - \sigma_{v0})/S_u \quad (1)$$

Where σ_{v0} is the total vertical stress.

Since during this work two UU triaxial test were performed in Imburo, with 1.5 and 2 meters of depth, they will be used as reference. Therefore, Nkt values were calculated in these two depths for every test except piezocone CPT-02, which started at a depth of 2.4 meters. All of the total vertical stress calculations were made by considering the average specific weight.

Figure 2 presents the Nkt values calculated in this study and a comparison with N_{kt} values found in other studies. It can be noticed that the found values are consistent with those established in other studies.

6 STRESS HISTORY

A common way to estimate the stress history is through field tests. Among the field tests, the CPTU test can be used to promote an approximation through the equations proposed by Chen and Mayne (1996):

$$OCR= 0.305\ (q_t - \sigma_{v0})/\sigma'_{v0} \quad (2)$$

$$OCR=0.53\ (q_t-u_2)/\sigma'_{v0} \quad (3)$$

It is notable that the equations proposed by Chen and Mayne (1996) estimate much larger OCR values than the expected ones for slightly pre-consolidated clays and significantly greater than the OCR variation found through laterally confined consolidation tests performed in the first experimental program. As the proposed expressions are statistical by nature and for local soils, it is necessary to adjust the results of the expressions with respect to the reference values by correcting the multiplying factor. Therefore, in this work the equations 4 and 5 below were used:

$$OCR = 0.17\ (q_t - \sigma_{v0})/\sigma'_{v0} \quad (4)$$

$$OCR = 0.29\ (q_t - u_2)/\sigma'_{v0} \quad (5)$$

Figure 3 shows the OCR variation with depth for both of the equations above. It is noted that the OCR determined values show little variation when compared to laboratory results of the experimental program in Imburo.

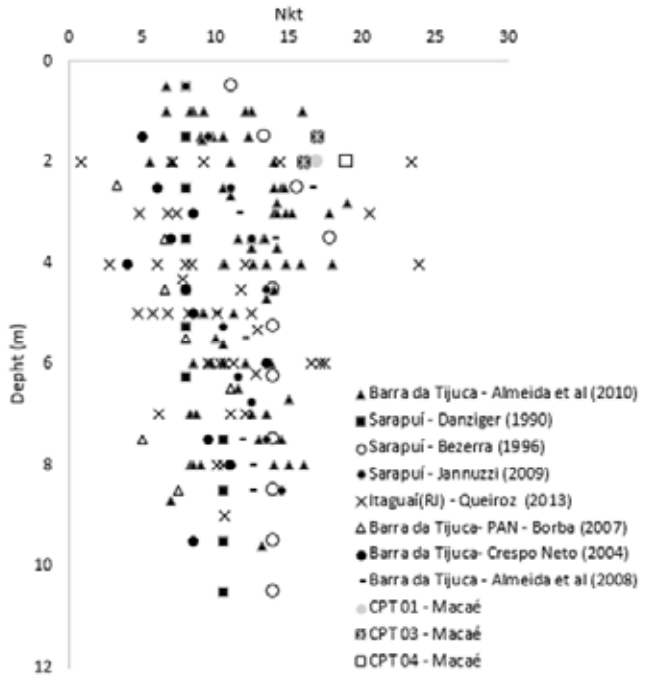

Figure 1 - Factor N_{KT} for the soft soil deposits in Rio de Janeiro

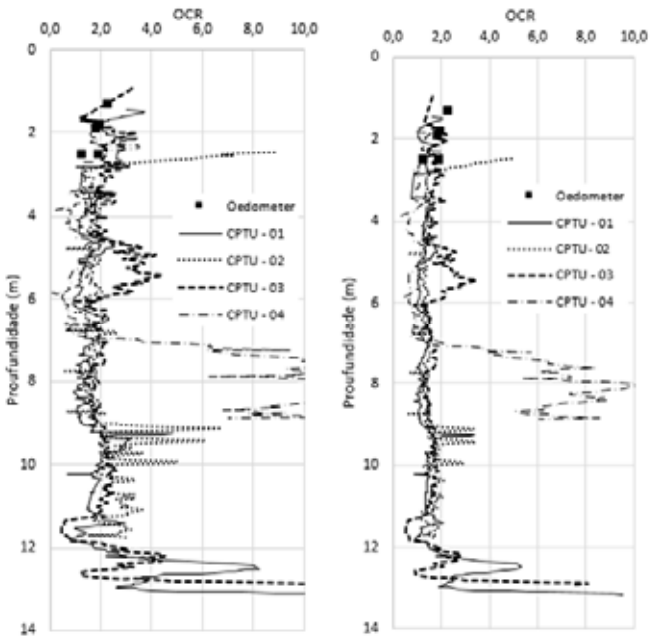

Figure 2. Approximation of vertical consolidation coefficient, CPT 01 and CPT 03.

7 CONCLUSION

The results of laboratory and field tests conducted in sedimentary deposits along the Brazilian coast have been widely used as a reference for geotechnical projects in areas with similar characteristics. However, it seems that due to the high variability of parameters, they are fundamentally guiding and do not eliminate the need for geotechnical field and/or laboratory research in analysis of cases related to specific edifications.

The SPT boreholes profiles, stratigraphy and compression parameters are similar, as simple as Atterberg limits are a bit different. The average value of the empirical factor Nkt of cone (17) obtained through the CPTu tests revealed values that are similar to those soft soil deposits found in Rio de Janeiro. The OCR values indicated that the deposit is slightly pre-consolidate.

8 ACKOWLEDGEMENTS

Rio de Janeiro Foundation for the Support of Research, FAPERJ.

9 REFERENCES

Almeida, M.S.S., & Marques, M.E.S. 2002. "The behaviour of Sarapuí soft organic clay". International Workshop on Characterisation and Engineering Properties of Natural Soils, Singapore. Editors: T.S. Tan, K.K. Phoon, D.W. Hight, & S. Leroueil, vol. 1, pp. 477–504.

Almeida, M.S.S., Marques, M.E.S., Alves, F., & Lima B. T. 2008. "Failure of a reinforced embankment on an extremely very soft peat clay layer". 4th European Geosynthetics Conference, Edinburgh.

Almeida, M.S.S., Marques, M.E.S., Baroni, M. (2010 a). Geotechnical parameters of very soft clays obtained with CPTU compared with other site investigation tools. 2nd International Symposium on Cone Penetration Testing, CPT'10, Huntington Beach, California, USA.

Almeida, M.S.S., Marques, M.E.S., Miranda, T.C., & Nascimento, C.M.C. 2008a. "Lowland reclamation in urban areas, Proc". TC 41 International Workshop on Urban Infrastructure, Búzios.

Bezerra, R.L. (1996), "Piezocone development COPPE / UFRJ third generation and its use in determining the parameters 'in situ' of shear strength and compressibility of soft clay". D. Sc. Thesis (in Portuguese), COPPE/UFRJ: Rio de Janeiro, Brazil.

Borba, A.M. 2007. "Analysis of performance of experimental embankment on Vila Panamericana". MSc. Dissertation (in Portuguese), COPPE/UFRJ: Rio de Janeiro, Brazil.

Chen, B.S., Mayne, P.W. (1996), " Statistical relationships between piezocone measurements and stress history of clays". Canadian Geotechnical Journal, Vol. 33, pp. 488-498.

Coutinho, R.Q. 2008. "In situ tests in geotechnical practice and advances". Proc. XIV Brazilian Congress on Soil Mechanics and Geotechnical Engineering, Búzios, pp. 201–230.

Crespo Neto, F.N. (2004). "Strain rate effect on shear stress from vane tests". MSc Dissertation (in Portuguese), COPPE/UFRJ: Rio de Janeiro, Brazil.

Danziger, F.A.B. (1990), “Development equipment to perform piezocone test: application to soft clays”. D. Sc. Thesis (in Portuguese), COPPE/UFRJ: Rio de Janeiro, Brazil.

Danziger, F.A.B., & Schnaid, F. 2000. “Piezocone Tests: Procedures, recomendatios and interpretation” (in Portuguese). In: Anais do Seminário Brasileiro de Investigação de Campo, BIC. São Paulo: ABMS.

Jannuzzi G.M.F (2009). “Characterization of soft soil deposit of Sarapuí II Field Testing Through”. MSc. Dissertation (in Portuguese), COPPE/UFRJ: Rio de Janeiro, Brazil.

Lima, I.S., Campos, T.M.P. (2014). “Characterization of a soft clay deposit Guaratiba- Rio de Janeiro – RJ” (in Portuguese). In: COBRAMSEG - XVII Congresso Brasileira de Mecânica dos Solos e Engenharia Geotécnica.

Queiroz. C.M. (2013). “Geotechnical properties of A Soft clay deposit of Itaguai-RJ”. MSc Dissertation (in Portuguese),UFMG/BH: Belo Horizonte, Brazil.

Geotechnical and Geophysical Site Characterisation 5 – Lehane, Acosta-Martínez & Kelly (Eds)

Geophysical and Geotechnical Characterisation of the Saltwater Creek Bridge Site, Morten Bay Rail Project, Queensland, Australia

A. Purwodihardjo, T. Rahiman & M. Parsons
Golder Associates

J. Kruger
EIC Activities/Thiess

ABSTRACT: This paper describes how surface geophysical techniques have supplemented intrusive geotechnical methods for the geotechnical investigation and driven pile design for Saltwater Creek Rail Bridge (BR270) and Saltwater Creek Shared Path Bridge (BR1240) on the Moreton Bay Rail Project, north of Brisbane. The geophysical methods included seismic refraction (SR) for imaging subsurface P-wave velocity and multichannel analysis of surface waves (MASW) for imaging subsurface S-wave velocity. The SR method is used to determine the depth of the bedrock and its lateral variation. The MASW method models S-wave velocity which is used to identify the variable strata above the bedrock. Due to inherent limitations of geophysical methods, a strict criteria was followed when interpreting geophysical data. This included site specific correlation to data from geotechnical drilling. Features that were cross checked included changes in depth of stratigraphic layers against corresponding changes in geometry of seismic velocity contours; correlation of P wave and S wave velocity values against material types and properties given in borehole logs; and S wave velocities were used to assess the inferred N-SPT values and subsurface strata. A comprehensive geotechnical model of interpreted ground conditions along the Saltwater Creek Bridge alignment was developed using borehole information and the results of surface geophysical surveys. As-built pile information indicate that the as-built pile toe elevations are reasonably close to design pile toe elevations at each pier location for each bridge.

1 INTRODUCTION

The Moreton Bay Rail Project (MBR) consists of a new rail passenger line due to open in mid to late 2016, which will link Brisbane's main northbound rail line to the suburbs in the Moreton Bay region north of Brisbane. The upgrade involves a 12.6 km heavy gauge dual-track to be built between Petrie and Kippa-Ring and the construction of six new rail stations including an upgrade of the existing Petrie Station. The upgrade will include the construction of 11 rail bridges, 2 shared path bridges and 7 road bridges. Bulk earthworks along the proposed alignment will comprise both cuttings and fill embankments.

This rail link passes over three waterways, including low lying saltmarsh land around Saltwater Creek at Rothwell (Figure 1). The design of the Saltwater Creek Bridge consists of 22 piers, is 325 m long and carries the MBR alignment across Saltwater Creek at Hays Inlet. The rail alignment is constrained by land availability and flood levels in the creek and the bridge configuration is defined by the environmental regulatory requirement to keep embankment construction above Highest Astronomical Tide (HAT) of 1.36 m, with the bridge soffit being above Q1000 and Q2000 flood levels.

This eastern section of the rail alignment through the Saltwater Creek / Hays Inlet area includes soft ground favouring an embankment height that is kept as low as possible to minimise settlement, however with the top of formation above 100 year ARI flood level. This leads to a bridge form with shallow depth and therefore fairly short spans.

The adjacent Saltwater Creek Shared Path Bridge (Figure 1) runs parallel to the rail bridge with approximately 3 m clear separation between the structures and adopts the same span configuration. It has a separate superstructure and foundations however shares the approach embankment and abutment spill-through.

The bridges are formed from standard 15 m Queensland Rail Prestressed Concrete (PSC) slabs with a single span of standard 25 m Queensland Rail PSC girders provided across the low flow channel of Saltwater Creek to minimise disturbance to the creek habitat.

The rail bridge piers are formed from eight 550 mm driven prestressed octagonal piles, arranged in two rows of four in order to resist the braking loads, which extend directly to a 3 m wide reinforced concrete headstock. The abutments are formed from four 550 mm driven prestressed octagonal piles with a reinforced concrete headstock.

The shared path bridge piers and abutments are formed from three 550 mm driven prestressed octagonal piles extending directly to a reinforced concrete headstock.

The design and construct contractors for the MBR was CPB Contractors (formerly Thiess) and Golder Associates (Golder) was the geotechnical designer. Aurecon AECOM Joint Venture (AAJV) was the structural designer.

Figure 1. Saltwater Creek Rail Bridge and Shared Path Bridge - Plan View

2 SITE GEOLOGY

The geology of the bridge site comprised alluvial, estuarine and coastal plain deposits, and residual soils underlain by various rocks of Tertiary, Jurassic, Triassic and Devonian aged formations as indicated in the Geological Map of Brisbane and Caboolture scale 1:100,000 series (Sheet No. 9543, Year 1986, and Sheet No. 9443, Year 1979) published by the Department of Mines.

The available borehole information indicates that the subsurface conditions within the proposed bridge location comprises up to 12.8 m thick of very soft to firm alluvial silty clay and loose to medium dense sands. The alluvial materials overlie stiff to hard residual sandy clay and sandy silt materials derived from the weathering of underlying sedimentary rock. The sedimentary rocks consist of sandstone, claystone, mudstone and interbedded sandstone and mudstone. The rock strength generally increases with depth from distinctly weathered (DW) of extremely low to low strength rock to slightly weathered (SW) of medium to high strength rock.

3 GEOTECHNICAL DESIGN & CHALLENGES

The main geotechnical challenge for the Saltwater Creek Bridges was the environmental constraints for the site investigation to obtain geotechnical data for the pile design. As shown in Figure 1, the Saltwater Creek Bridges were located within a tidal environment within the marine park area; which includes environmentally sensitive marine species such as salt couch across the majority of the site and pockets of mangroves near the lowest lying areas. Within this area, the approval process for environmental permits for the full construction works required about 3 to 4 months. During the detailed design, the available environmental permit only allowed minimum disturbance of the area, i.e. maximum of one metre width disturbance of the marine park vegetation (mainly saltwater couch with some pockets of mangroves) along the proposed bridge alignment.

Based on the Scope of Works and Technical Criteria (SWTC) requirement and AS 5100.3-2004 Bridge design - Foundations and soil supporting structures, the minimum number of boreholes shall be one per pier and abutment for each bridge.

A pre-investigation reconnaissance walkover of the bridge site revealed that drill rig access into the areas of the abutments was going to be difficult for various reasons including environmental constraints i.e. mangroves, marine park habitats, saltwater couch grass and thick vegetation areas which require clearing. To obtain all the permits for the intrusive site investigation activities was going to take months, and was not compliable with the time deadlines for the project.

For this reason a relaxation to the SWTC and AS5100 requirements for a borehole at each pier and abutment location was requested. To satisfy the intent of the clause and in order to progress the design and considering the environmental permit restriction, an innovative site investigation method, i.e. geophysical survey investigations using Seismic Refraction (SR) and Multichannel Analysis of Surface Waves (MASW) methods were adopted. The objective of the MASW survey was to understand the soil consistency for material above rock level (mainly for soft to firm soils), while the objective of the SR survey was to understand the top of rock level. Figure 2 illustrates the geophysical survey undertaken with minimal disturbance to the sensitive marine park environment.

Figure 2. Minimal ground disturbance to marine environment during the geophysical surveys at Saltwater Creek Bridges

4 METHODOLOGY OVERVIEW

In order to assess and to interpret the ground conditions, as well as to develop the geotechnical model along the proposed bridge alignments, the following methodology was adopted during the design process:

- For the DD (detailed design) 15% to 80%, available information from previous investigations, namely two boreholes (BH62 and BH20), six variable dynamic cone penetrometer tests (VDCP02 to VDCP07), and one piezocone penetration test (CPTu08) were used;
- For the DD 85%, four additional Stage 2 investigation boreholes (BH1240-01, BH1240-07, BH1240-13 and BH270-22) and geophysical surveys (i.e. Seismic Refraction (SR) and Multichannel Analysis of Surface Waves (MASW) surveys) were carried out along the BR270/BR1240 alignments. The main objective of the additional geophysical survey is to fill the gaps between the available geotechnical information and also to refine the initial ground model.

The following additional measures were also undertaken as part of risk mitigations:

- End of Drive Pile Driving Analyser (PDA) testing – which involves measuring dynamic response of pile to driving for every hammer blow during installation - was carried out at selected piles to assess pile toe levels, pile capacity, pile driving criteria for adjacent piles (i.e. drop height and final sets) and induced stresses in the piles during the pile driving. End of Drive PDA testing was carried out during pile driving on a minimum of one pile at every third pier of each bridge;
- Restrike PDA testing was carried out on a minimum of 1 pile per pier, for all piers that were not selected for End of Drive testing. Additional Restrike testing was also carried out at pier locations where piles effectively "refused" at shallower depth than predicted;
- Signal matching analyses using the "CAPWAP" program was carried out for each PDA test;
- All the piles were observed by a qualified geotechnical engineer;
- Ultimate bearing capacity of piles were assessed using Hiley pile driving formula which has been calibrated with the Restrike PDA test and CAPWAP analysis to provide a higher degree of QA/QC certainty;
- By referring to AS2159-2009 and using the PDA, a geotechnical reduction factor of 0.76 can be adopted. However for the ultimate bearing capacity analyses, the geotechnical reduction factor was limited to 0.6; and
- Sensitivity analysis for pile design has been undertaken to consider possible variation in the rock surface level from that interpreted from the geophysical survey. A variation in which the rock surface level may vary by 2 m has been considered. (i.e. rock surface being shallower or deeper by 2 m from the current adopted interpretation).

5 SEISMIC REFRACTION SURVEY

The Seismic Refraction (SR) method is the most widely applied geophysical methodology to assist in geotechnical investigations particularly for measuring depth to bedrock and identifying weathered zones. The main objective of the SR method is to measure the P wave velocity (primary wave or compression wave or V_p). The key limitations of the SR method are:

- Unable to detect a weak layer below a stiffer layer;
- Unable to be done over pavement; and
- Affected by external noises such as traffic, rigs, rain, wind, and electrical radiation of high voltage powerlines.

The seismic refraction survey was conducted using a Geometrics Geode, 24 channel engineering seismograph. The following acquisition parameters were used with the seismograph:

- Sampling interval 0.125 ms; and
- Record length: 0.25 to 0.3 s.

In each seismic spread, twenty-four 4.5 Hz geophones, fixed to a "land streamer" Kevlar Band, were positioned at 2 m intervals and connected together via a 24 channel multi-core "take out" cable. All geophones were mounted on a specially designed base plate to best couple the geophones with the ground. Five seismic source positions were used for each 24 channel spread. Seismic energy was provided using a 9 kg sledge hammer striking a square metallic plate at every shot location.

The digitally acquired seismic data was processed using the commercially available SeisImager 2D software package by Geometrics.

6 MASW SURVEY

The MASW method measures variations in surface wave velocity (V_s) with increasing distance and wavelength and can be used to infer the rock/soil types, stratigraphy and soil conditions. The key limitations of the SR method are:

- The 2D sections are developed based on interpolation of 1D data; and
- Reliability of 2D data highly depends on spacing of the 1D profiles.

MASW data was collected using the same equipment as the SR survey (i.e. geophones mounted on a Kevlar Band "land streamer"). Data were collected at 6 m intervals, with the equipment being dragged after each data point location. The following acquisition parameters were used with the seismograph:

- Sampling interval 0.15 ms; and
- Record length: 2 to 4 s.

A 10 m offset was generally found to produce the "cleanest" looking dispersion spectra and was used during the MASW survey. MASW data was analyzed using SeisImager SW software by Geometrics.

7 BENEFITS OF A COMBINED SR/MASW APPROACH

The main advantage to use the two different investigation methods is that each method can constrain the other and each method is specially designed to measure different properties of the subsurface material:

- The SR will give information about the topography of the bedrock as well as provide an indication of the strength of bedrock.
- The MASW will provide information on the condition of the alluvium or any other surficial material overlying the bedrock. Moreover the MASW profile can directly be correlated to the stiffness properties of the subsurface material.
- Additionally, surveying using SR and MASW techniques together can be used to calculate small strain Young's and shear moduli, together with Poisson's ratio. These can be calculated by assumed density values for subsurface materials and using theoretical equations; and correlated with laboratory results from recovered core.
- As the data is captured continuously, a continuous profile of the rock level along the alignment can be produced by both methods. This is a benefit when compared to boreholes, as boreholes alone can often miss undulating rock levels.
- Additionally, to better capture the data along the bridge alignments, we proposed carrying out the geophysics survey prior to the borehole investigation, so that the borehole locations could be targeted based on any critical locations as interpreted from the geophysics results.

8 LIMITATIONS OF GEOPHYSICAL TECHIQUES

The limitations in SR are that the transition/difference between "sandy gravel" and "rock" can be difficult to interpret based on the P waves alone. To mitigate this, the SR readings are interpreted in combination with the field descriptions of the material on borehole logs and the MASW S waves to establish the soil and rock interface.

Both methods of geophysics require spread over-lap to capture continuous data, as such at the edge of the investigation (where overlapping data is no longer available); there will be some loss in information. To mitigate this, the geophysics investigations were extended at least 30 m beyond the bridge abutments where accessible to ensure no key information is lost.

9 GEOPHYSICS RESULTS

In general, the quality of the recorded seismic traces was good and allowed picking of first breaks with little ambiguity. The reciprocal times differences, as a result, were generally low. Depth of penetration below ground surface of 15 to 40 m was achieved. Modelled P-wave velocities of subsurface material within this depth ranged from 300 m/s to 4000 m/s.

The measured S-wave velocities range from about 10 to 750 m/s. The S-wave velocity cross section is interpolated from 6 m spaced 1D profiles. Reliable measurements of S-wave velocity were obtained to a depth ranging from 15 to 25 m below ground level. The shaded area at the bottom of the cross section limits the effective depth of penetration of the MASW data.

Understanding of the site geology, correlations with borehole data, and past experience on relationship between P-wave velocity and proprieties rock have been used to best infer what the seismic P-wave velocities may represent in terms of rock properties along the survey line. The inferred rock level is plotted on the sections in Figure 3.

Rock level is defined as distinctly to slightly weathered, low to medium strength mudstone, sandstone and interbedded mudstone and sandstone. The top of this layer coincides approximately with the 2100 to 2300 m/s P wave velocity contour. The SR results indicated that the top of rock level undulates across the length of the site. On the southern side of the main creek channel, the rock level drops gradually from about RL -10 m at the southwest end to about RL -20 m towards the

northeast. North of the main creek channel, the rock level is much lower and is inferred to be at about RL -20 m. As also illustrated in Figure 3, the SR results can provide a better accuracy of the inferred top of rock.

The MASW data is most effective at characterising the nature of the soils. Understanding of the site geology, correlations with borehole data, and past experience on the relationship between S-wave velocity and proprieties soils have been used to best infer what the seismic S-wave velocities may represent in terms of soil properties along the survey line. Inferred subsurface layers and their approximate positions are plotted on the section in Figure 4.

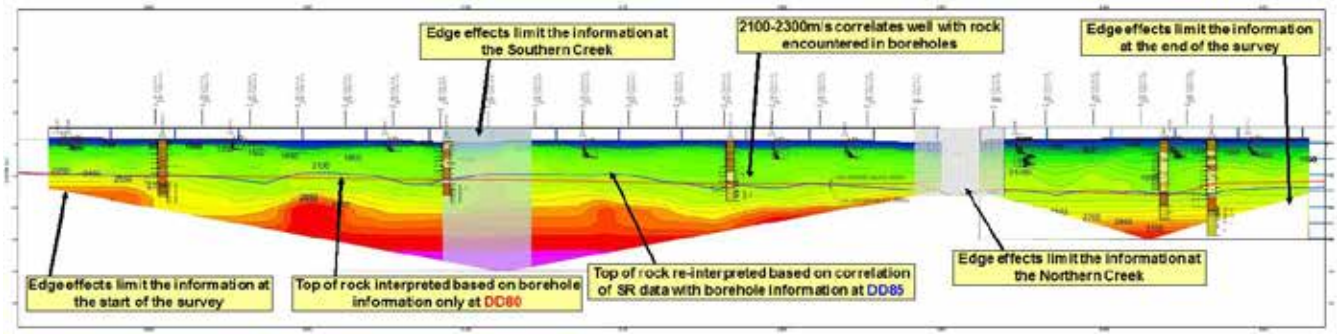

Figure 3. Saltwater Creek Rail Bridge - Top of rock interpreted based on borehole information only (DD 80) and re-interpreted based on correlation of SR results with borehole information (DD85)

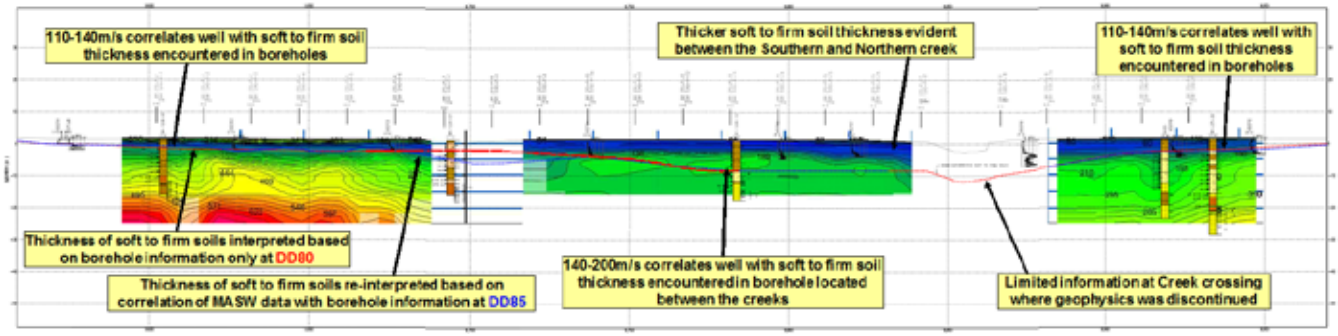

Figure 4. Saltwater Creek Rail Bridge - Inferred subsurface layers based on borehole information only (DD80) and re-interpreted based on correlation of MASW results with borehole information (DD85)

10 CORRELATIONS BETWEEN V_S AND N-SPT VALUES

Correlations between V_s and N-SPT values have been developed for the last half of century. Most of the researchers including Anbazhagan et al. (2012) utilised uncorrected N-SPT values in developing the correlation while Sitharam and Anbazhagan (2008) developed using corrected N-SPT values and obtained great correlation pattern. However, Uma Maheswari et al. (2010) reported that V_s predicted the corrected and uncorrected N-SPT values with comparable accuracy.

This paper evaluates the uncorrected N-SPT values obtained from available site investigations within the proximity of the MASW lines. The hypothesised empirical relationship used is a power-law relationship between the uncorrected N-SPT values and V_s as:

$$NSPT = (V_s/Y)^X \quad (1)$$

where NSPT = inferred N-SPT values; V_s = measured S wave velocity; and X and Y = site specific parameters.

As described in Equation 1, X and Y are site specific parameters which can be assessed from a regression analysis. The regression analysis and the inferred N-SPT value results are illustrated in Figure 5 and 6 respectively.

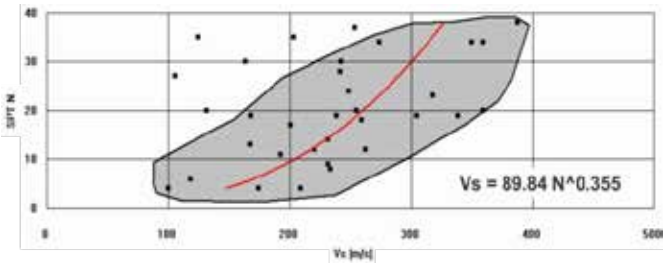

Figure 5. Regression Analysis

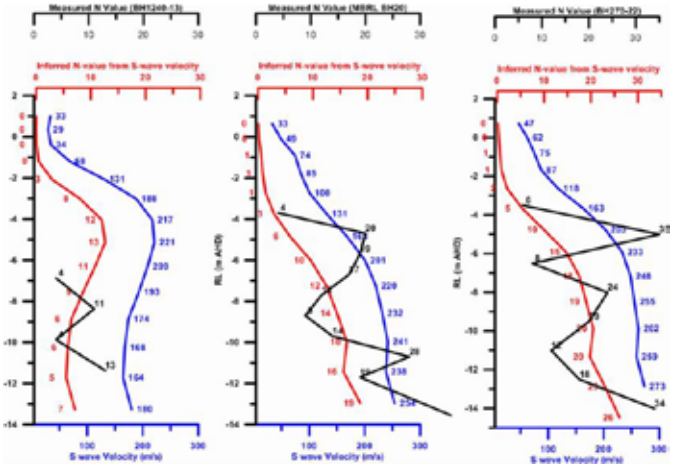

Figure 6. Inferred N-SPT values for Boreholes BH1240-13, BH20 and BH270-22

11 AS CONTRUCTED PILE TOE ELEVATIONS

The design considered that variations in founding level between predicted and as-built of around 2 m were possible, due to localised ground variations across the pier footprint. An overdrive allowance of 2 m was therefore provided for in pile lengths to account for this potential variation.

In general terms the as-built pile toe elevations were close to design pile toe elevations. Piers with a borehole at the pier location displayed a similar range of variation between design and as-built toe elevations, compared to those assessed using geophysical surveys.

Increased (however not significant) pile depth discrepancies were mainly noted in piles installed around the Saltwater Creek watercourse (Figure 7), where both conventional geotechnical boreholes and geophysical investigations were necessarily limited due to the presence of mangrove vegetation and narrow creek access.

The as-built pile records indicated that the actual pile toe levels are generally within ± 2 m of the design pile toe levels. Only at some pier locations, the actual pile toe levels deviate up to – 4 m. Considering the actual pile records, it is considered that the interpretation of geophysical surveys was quite successful and could provide meaningful geotechnical information for the design purposes.

12 CONCLUSIONS

The adopted site investigation technique using geophysical surveys and minimum borehole for the 325 m long Saltwater Creek bridges is the first site investigation approach undertaken in Queensland and probably in Australia. The use of geophysical investigation techniques in combination with a reduced number of 'conventional' geotechnical boreholes was effective in confirming ground conditions that allowed a satisfactory assessment of design pile toe elevations and pile capacity, for the ground conditions present at this site. As-built pile toe elevations were close to design pile toe elevations at each pier location for each bridge.

Figure 7. Saltwater Creek Rail Bridge and Shared Path Bridge - Piling.

The proposed site investigation methodology in combination with the proposed risk mitigations have been applied and have demonstrated the following key project aspects:

- A robust design process for the bridge driven pile foundation;
- A successful methodology to avoid the construction delay due the access issues; and
- A successful methodology to be more cost effective for the site investigation.

13 REFERENCES

Anbazhagan P., A. Kumar and T.G. Sitharam (2012) "Seismic Site Classification and Correlation between Standard Penetration Test N Value and Shear Wave Velocity for Lucknow City". *Indo-Gangetic Basin. Pure and Applied Geophysics*.

Golder Associates Pty Ltd (2014), "BR270/BR1240 – Saltwater Creek Rail Bridge/Shared Path Bridge Geotechnical Design for Bridge Pile foundation and Spill-Through Embankments", Technical Memorandum No. 137632134-02-50-70-311-TM-Rev0.

Golder Associates Pty Ltd (2015), "Geotechnical Close Out Report - BR270/BR1240 – Saltwater Creek Rail Bridge and Shared Path Bridges", Technical Memorandum No. 137632134-02-50-70-024-TM-Rev3.

Sitharam T.G. and P. Anbazhagan (2008) "Seismic Microzonation: Principles, Practices and Experiments". *Electronic Journal of Geotechnical Engineering*. Special Volume Bouquet 08, 1-61.

Uma Maheswari R., A. Boominathan and G.R. Dodagoudar (2010) "Use of Surface Waves in Statistical Correlations of Shear Wave Velocity and Penetration Resistance of Chennai soils", *Geotechnical and Geology Engineering*, 28(2),119-137.

Geotechnical and Geophysical Site Characterisation 5 – Lehane, Acosta-Martínez & Kelly (Eds)

CPT, DMT and MASW allowing economic design of a large residential project over soft soils

N.B. Schofield & R.W. Burke
Black Geotechnical Pty Ltd, Melbourne, Victoria, Australia

ABSTRACT: A three hectare medium density residential development in Melbourne located within the Yarra Delta overlies a complex sequence of compressible Quaternary sediments covered with 1-3 m of uncontrolled contaminated fill with a near surface water table. The development consisting of nearly three hundred triple storey townhouses required site levels to be raised by up to 1.5 m. Deep piled footings were an option but, due to significant cost savings, a high level footing option was pursued. A detailed geotechnical investigation, with Cone Penetration Tests (CPT) and Marchetti Dilatometer Tests (DMT), was conducted to characterise the sediments, which allowed a detailed finite element settlement analysis to be conducted. Ground improvement with impact compaction and preloading was conducted to reduce modelled differential settlements to acceptable levels for high level footing construction. The ground improvement verification was conducted with a combination of CPT and Multi-channel Analysis of Surface Waves (MASW). Design of preloading also required the use of dissipation tests to estimate the coefficient of consolidation, which was verified with a test preload pad and later confirmed with a preload monitoring program. This case history demonstrates how a combination of high quality in-situ tests (CPT, DMT and MASW) can provide high quality data at a sufficient frequency and economic cost for assessment of high level footings on a challenging soft soil site. The savings by adopting high level footings over deep footings is estimated to be in the order of $10M.

1 INTRODUCTION

1.1 *The development*

This case study details geotechnical investigation and monitoring during construction conducted for a 3.5 hectare medium density residential development in Melbourne located within the Yarra Delta Quaternary sediments. The site, previously a single large industrial premises, was developed with nearly three hundred triple storey townhouses with roof top terraces. The local authority required site levels to be raised by 1-1.5 m to protect the development from flooding.

1.2 *Geotechnical challenges*

Based on local experience and information from the client, the site presented significant geotechnical challenges. The water table was within 0.5 m of the ground surface. During demolition the existing fill was disturbed, up to a depth of 1.5 m, by the removal of footings, which introduced difficulties in recompaction of the fill. Below the fill, thick compressible Yarra Delta sediments were expected to lead to large load-induced settlements. Deep footings for industrial structures that had been left in the ground after building demolition were expected to exacerbate differential settlements.

2 PRELIMINARY GEOTECHNICAL ASSESSMENT

A preliminary geotechnical assessment of the site with nine Cone Penetration Tests with pore pressure measurement at u2 (CPTu) was conducted. The CPTs encountered a sequence of fill, Unnamed Recent Alluvium (URA), Port Melbourne Sand (PMS), Coode Island Silt (CIS) and Fishermens Bend Silt (FBS). Approximate thicknesses of the units encountered are as follows.

Table 1. Sub-surface conditions encountered

Unit	Description	Thickness (metres)
Fill	Loose sand and gravel, no clay	2.4 – 3.0
URA	Soft to firm silty clay	0.0 – 4.0
PMS	Loose to dense sand	0.0 – 5.5
CIS	Soft to firm silty clay	8.0 – 13.0
FBS	Stiff to very stiff clay	1.5 – 9.0

Below the FBS, around 10 m, or so, of Moray Street Gravel was expected based on local geological

maps. This unit was not fully penetrated by the CPT due to refusal of the cone.

Deep piled footings were considered, with piles founded at a depth of 25-30 m. Differential settlements between the rigid structure and the surrounding ground would be controlled by ground improvement by impact compaction of the fill and preloading to reduce settlements in the deep compressible sediments.

High level footings were also considered, with stiffened slab footings for the buildings, after impact compaction of the fill and preloading of the deep compressible sediments over the building footprints, where necessary, subject to a detailed assessment of differential settlements.

The high level footing option presented significant cost savings when compared to the deep footing option, and was the preferred option. However, pursuing this option necessitated a much more detailed geotechnical assessment to ensure the project could be constructed and maintain the required limit of post-construction differential settlement gradients of 1/500 over a 50-year period.

3 DETAILED GEOTECHNICAL ASSESSMENT

3.1 *Geotechnical investigation design*

The aim of the detailed geotechnical investigation was to measure the sub-surface variation under each building block sufficiently to allow prediction of post-construction differential settlements. It was known from the preliminary geotechnical assessment that the depth and consistency of the compressible sediments varied significantly so an intensive grid of testing would be required. CPTu was the obvious choice for the site as it provides continuous measurement of the sub-surface profile, is quick, economic, and provides more accurate information than boreholes with standard penetration tests. On average, the proposed testing frequency was one CPTu every 400 m^2 and one Marchetti Dilatometer Test (DMT) every 2000 m^2, targeted within the building footprints.

Recognising that preloading may be required, the coefficient of consolidation (c_v) needed to be estimated in order to determine the likely time required for preloading. To obtain this, a series of rapid-dissipation profiles (RDP) were performed, where CPT dissipations were run for 10 minutes each, every 0.5 m depth within the weak alluvium. Most dissipations reached t_{50} within 10 minutes and for those that did not, t_{50} was estimated by extrapolation.

The presence of old deep footings was investigated via a desktop study of historical aerial photographs, discussions with the demolition contractor, and a search through old construction drawings found on site. A preload test pad was required to verify calculated settlements and rate of consolidation.

3.2 *Geotechnical interpretation*

The CPT results provided excellent information on the stratigraphy of the site, which is complex. They showed the site spans a geological boundary of the PMS (Figure 1) that is present over two thirds of the site and overlies the CIS (Figure 2) that is present over the entire site. Above these units is a varying thickness of URA (Figure 3). The presence of the URA within the Yarra Delta is discussed by Neilson (Neilson 1996).

Figure 1. Geological boundary of Port Melbourne Sand. Note the absence of this unit towards the top the figure.

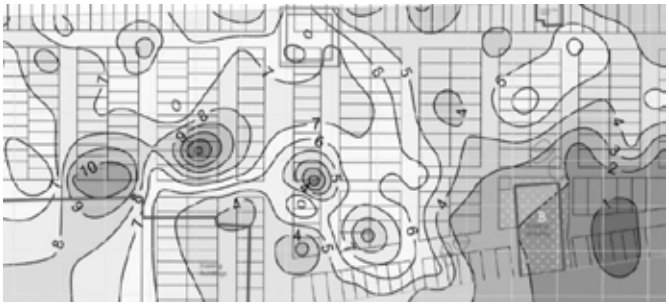

Figure 2. Thickness (m) of CIS with CPT qt < 1 MPa

Figure 3. Thickness (m) of Unnamed Recent Alluvium

The CIS and URA are slightly overconsolidated, compressible, silty clays. The PMS is relatively incompressible with the modulus highly dependent on the thickness of this unit.

The most important parameter to consider for the project was the stress-strain moduli of the soil. CPTs allow the estimation of constrained modulus in fine-grained soil by the empirical relationship $M = \alpha_m qt$, where M = constrained modulus; qt = corrected cone tip resistance; and α_m is a factor between 1 and 8 which depends on soil type and qc, the cone tip resistance (after Lunne, et al. 1997). Given the wide range of α_m, the estimation of constrained modulus is not well defined and to provide a better

measurement Marchetti Dilatometer Tests (DMTs) were conducted, at a lower frequency of one every 2200 m^2. DMTs provide a more direct measurement of modulus by the relationships $M_{DMT} = R_M E_D$, where E_D = dilatometer modulus. R_M is a factor based on K_D and I_D where I_D = material index (soil type) and K_D = Horizontal stress index, which can be considered as K_0 amplified by the penetration of the DMT blade (Marchetti, 2001). The vertical drained constrained modulus obtained from DMT is considered to be superior to laboratory testing for the following reasons. As it is an in-situ test it inherently accounts for effective stress. Sample disturbance for oedometer or triaxial testing leads to the underestimation of soil moduli (Bowles, 1997, Marchetti, 2001). For use in a 2D Finite Element Analysis, M is converted to drained Young's modulus, E', via drained Poisson's ratio, ν', in Equation 1, below.

$$E' = \frac{(1+\nu)(1-2\nu)}{(1-\nu)} M \quad (1)$$

Wroth (1975, cited in Kulhawy and Mayne, 1990) present data for ν' versus plasticity index for "several lightly overconsolidated soils", which results in an ν' of about 0.3 for the CIS and URA. Subsequent analysis of the preload test pad (see Section 3.4) indicated that using the constrained modulus directly in the 2D FEA was conservative. Simplified 1D settlement calculations using M gave very similar results to the 2D FEA using the same moduli and a ν' of 0.3. For this reason, the use of constrained modulus without conversion to Young's modulus was adopted for settlement analysis. Using a relatively small number of DMTs (15) allowed the determination of appropriate α_m values and therefore M from the CPT data across the different soil types at the site without sacrificing the efficiency of the testing program.

3.3 *Settlement analyses*

2-D finite element analyses (FEA) were performed on critical sections of the site to determine the likely total and differential settlements. Using moduli obtained from the DMT and from CPT correlated to the DMT results, the maximum post-construction primary settlement (immediate and consolidation) was about 110 mm.

The CIS is reported to undergo significant secondary consolidation, and in relatively thick deposits with high applied stresses this consolidation can become linear with time, at 5 mm to 10 mm per year for sites with 15 m to 20 m of CIS (Neilson, 1996, Srithar, 2010, and Ervin, 1992). It appears the behavior of the secondary consolidation trend is dependent on the applied stress. Donald (1976, cited in Ervin, 1992) suggests at stress levels below the preconsolidation pressure, secondary consolidation decreases linearly with log time, and presents data for the coefficient of secondary compression C_α, versus the log of the ratio of applied stress to effective stress, which shows a general trend of C_α increasing with an increase in the applied stress ratio. At log stress ratios greater than 1.0, the data becomes very scattered, but below this the relationship appears reasonable. The mechanisms behind a constant rate of secondary consolidation are not clear, and Srithar (2010) points to previous construction activity and/or groundwater drawdowns as a potential contributor to the observed settlements. For this development the stress ratio was between 0.3 and 0.5, and a stress-dependent approach was adopted. A C_α of 0.005 and 0.001 was adopted for the URA and CIS, respectively, which lead to a predicted total secondary consolidation of about 30 mm over 50 years.

Without preloading the site, the maximum total settlement including immediate, consolidation, and secondary consolidation computed in the FEA was 140 mm. Although large in total, the differential settlement gradient remained within the limit of 1/500.

The modelling of buried deep footings increased the differential settlements greatly and led to the conclusion that high level footings would not be appropriate without preloading of the building footprints, where deep footings were present. The required surcharge, determined by the FEA, was 7.5 kPa. This included an allowance for recompression after preload removal of 8% of the predicted primary consolidation.

3.4 *Preload test pad*

A preload test pad was constructed in part of the site where there was no PMS and where there was thought to be no deep footings. The preload test pad was about 3 m high over a 20 m by 20 m square area with 1H:1V batters and imposed a 50 kPa surcharge on pre demolition levels.

Four settlement plates and four Vibrating Wire Piezometers (VWP) were installed before the test pad was constructed. A CPTu, DMT and RDP were also conducted at the centre of the test pad location.

Over a period of one month the settlement plates recorded about 30 mm of settlement. However, the full settlement was not measured as the preload test pad was constructed over three days and the first survey base reading was only measured on the fifth day.

Based on the piezometer/dissipation data, it is estimated that a total primary settlement of the test pad was about 50-60 mm, which is about one third of that predicted in the FEA. Although not identified initially, a subsequent desktop study identified buried deep piles along two sides of the pad. The unexpectly low settlement is likely due to the piles taking a large proportion of the applied stress. Another possibility is historical preloading of the area. Not knowing the exact historical footing and loading details it was not possible to verify the predicted set-

tlements from the geotechnical investigation for the site. However, by comparing the response of the VWPs to the preload test pad, it was possible to verify the predicted time of consolidation, discussed in the following section.

3.5 *Consolidation time analysis*

From the preliminary geotechnical assessment, time estimates to reach 90% consolidation (t_{90}), varied widely from 6 months to 20 years. The greatest uncertainty was the length of drainage paths and the RDP test was designed to help provide this information and coefficients of consolidation. The preload test pad was also conducted to provide a field measurement of the consolidation time.

The RDP test results are shown in Figure 4 with horizontal coefficient of consolidation (c_h) estimated using the method recommended by Lunne et al. (1997). The figure shows four RDP profiles that were conducted within the area of the site where there is URA over CIS and no PMS.

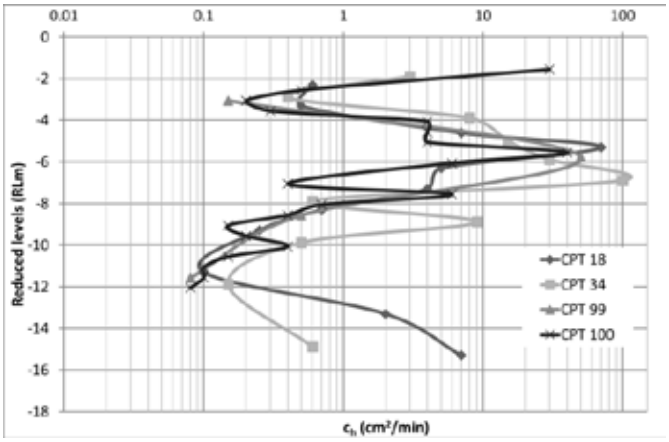

Figure 4. c_h estimates from RDP tests

Based on the lower bound values of c_h estimated from the RDP results a t_{90} of 2 years was adopted, prior to the results of the preload test pad becoming available. The VWP data from the preload test pad initially indicated t_{90} would occur after about 3 months, however, given the presence of buried piles t_{90} is likely to be somewhat longer, but still shorter than the estimated 2 years. The interpretation of the RDP was re-analysed in light of the preload test pad results. A large uncertainty was the ratio of c_h to c_v. As c_v is required for calculation of the consolidation time, a conversion from the RDP interpreted c_h to c_v is required. To convert the c_h to c_v, an estimate of the ratio of permeabilities (k_h/k_v) is required. Considering the formation of the URA/CIS and the CPT/RDP results, there are many sand, clayey sand and sandy clay layers that may be interconnected. If these layers are horizontal and are not connected then the k_h/k_v ratio could be high. However, if the layers are interconnected vertically the k_h/k_v ratio may be close to unity. Day and Woods (2007) suggest k_h/k_v ratio of CIS of 3-5. The initial interpretation, prior to the preload test pad results, used a c_h/c_v ratio of 4 being the mean ratio used by Day and Woods. In light of the preload test pad results and the above mentioned knowledge of the regular high permeability layers, a c_h/c_v ratio of 2 was used, which provided a t_{90} of 9 months for the lower-bound values of c_v. Even considering the presence of some deep footings under the preload test pad, the new consolidation time estimate was considered reasonable and was used for design of the preloading.

4 GEOTECHNICAL RECOMMENDATIONS

4.1 *Proposed ground improvement and monitoring*

The results of the geotechnical investigation showed that the high level footing option is feasible subject to the following recommendations. The demolition fill and loose PMS should be improved by High Energy Impact Compaction (HEIC). Preloading is required on building footprints over about three quarters of the site that may have deep footings present.

4.2 *Ground improvement by High Energy Impact Compaction (HEIC)*

Due to varying site surface levels, the groundwater (at about RL 0.3 m) was within 0.5 m to 1.5 m of the site surface at the time of ground improvement.

Trials were conducted in the lowest part of the site (groundwater within 0.5 m) to check the effectiveness of the impact compaction on saturated loose demolition fill and sand. Initial coverages of the HEIC caused water to flow rapidly from the surface at two locations, producing several sand boils and a large ponded area. The impact response of the ground was very low with significant heaving and mattressing. After resting the ground for 24 hours, the water had disappeared and further impact compaction showed a high response initially before water began to flow again and the impact response became low. This sequence of HEIC and resting was continued for several days and noticeable improvement of the impact response was evident, both visually and from subsequent test results.

The trials showed HEIC adequately improved the demolition fill and PMS to a depth of 3-4 m. The remainder of the site was successfully HEIC and the increase in stiffness over the site was verified with before and after CPTs and Multi-channel Analysis of Surface Waves (MASW).

The before and after CPTs showed a significant increase in the qc of the demolition fill and the PMS, and, as expected, no increase in the stiffness of the soft clay (URA). Two example before and after CPT comparisons are shown in Figure 5.

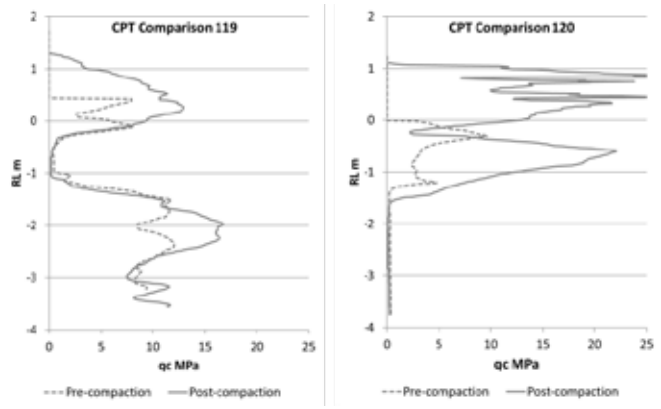

Figure 5. Before and after CPT cone tip resistances

The before and after MASW showed an increase in the shear wave velocity over the top 3-4 m of 20-75 m/s. A target shear wave velocity of 125 m/s was reached and confirmed with the MASW survey. An example before and after MASW comparison, with shear wave velocity contours in m/s, is shown in Figure 6.

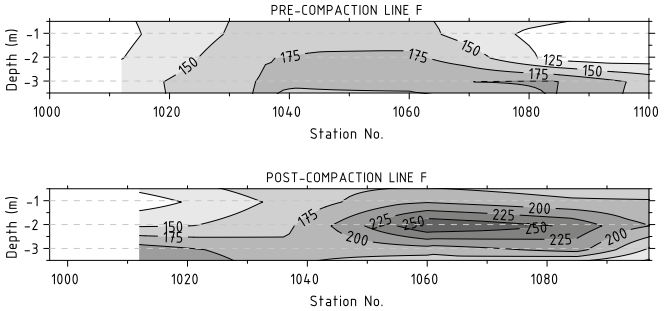

Figure 6. Before and after MASW shear wave velocities

In addition to the CPT and MASW testing, the Continuous Impact Response (CIR) and Continuous Induced Settlement (CIS) data recorded by the impact compactor was analysed. The CIS surveys use differential GPS measurements taken at each drop of the impact roller to produce a detailed level survey of the site. CIS surveys during and after HEIC give an indication of reducing site levels vs HEIC coverages, which helped determine when HEIC was complete. The results of the CIS showed an average settlement over the site of about 90 mm.

The CIR system measures the deceleration of the drums at each drop of the impact roller. The results of the CIR were used to assess potential soft spots and to locate post compaction CPTs in low impact response areas. All of the CIR surveys showed a significant improvement of the soil dynamic response, which indicates the ground improvement was very effective.

Two wet clay soft spots were identified and remediated by removal and replacement with drier site won fill subsequently improved by HEIC.

HEIC was conducted successfully at the site using a combination of CPT, MASW, CIS and CIR results to confirm the required stiffness had been achieved in the demolition fill and PMS over the proposed development area.

4.3 *Preloading building footprints*

A preload height of 1-1.3 m (about 20 kPa) over three months was recommended. The earthworks contractor had enough material on site to increase the surcharge further, typically about 2.5 m high, which increased the surcharge to about 45 kPa, reducing predicted times to reach required settlements to less than one month.

The preloading was conducted in stages to allow placement of engineered fill up to design levels to proceed at the same time. The different stress distributions caused by partial preloading compared to the full preloading were assessed in the FEA model and were found to have negligible effect provided whole blocks of building footprints were preloaded.

The monitoring was conducted with multiple settlement plates within each preloaded building footprint and four sets of VWPs installed at the centre of four preload pads across the site. The VWPs were installed at various depths, targeting low permeability compressible clays, mostly over the top 12 m and one installed at 22 m in the FBS. The VWPs were installed using a CPT rig with sacrificial tips, which was very quick and efficient, allowing eight VWPs to be installed per day. The alternative of installation by boreholes would have required casing and would have been much more time consuming and costly.

At the time of writing this paper three of the four VWPs sets had experienced the preloading.

The response of the VWPs was generally good with a measured increase in pore water pressure (PWP) of 50-100% of the modelled preload induced stress at a depth <5 m and 20-50% at a depth >5 m. The missing PWP response is thought to be due to the limit of the VWP sensitivity to rapid changes in PWP conditions during the construction of the preload.

The VWP measured PWP dissipations show there is, at least, a two stage rate of consolidation (an initial fast stage and following slow stage). This was observed when the expected logarithmic response was compared to the PWP dissipation measurements. The two stage response was also observed in the preload test pad measurements. It is thought the two stage rate of consolidation response is caused by the compressible clays being slightly overconsolidated, with the initial fast stage consolidating along the recompression curve, and the second slow stage, in the normally consolidated range stress range, consolidating along the virgin compression curve. Provided the preload induced stress covers the overconsolidated and normally consolidated range of stress, this would explain the observed measurements.

The Over Consolidation Ratio (OCR) of the compressible clay was estimated from CPT data us-

ing the following equation recommended by Lunne, et al. (1997).

$$OCR = k\frac{qt - \sigma_{v0}}{\sigma'_{v0}} \quad (2)$$

where k = 0.2 – 0.6, qt = corrected cone tip resistance. In this instance a k of 0.3 was chosen, and the resulting OCR was between 1.5 and 2.5 (generally closer to 2.0), which agreed generally with the DMT derived OCRs.

The interpreted OCR indicates that the stress range of the preload covers the overconsolidated and normally consolidated range.

The detailed results of the VWPs vary as expected with different c_v and drainage path lengths. The four preload pads with VWP measurements show that after one month on average 50% consolidation was reached on two preload pads and 80% consolidation was reached on the other two preload pads. Considering the two rates of consolidation, this extrapolates to 14 months and 4 months for t_{90}. The variation in the rate of consolidation times may be explained by the presence of deep footings under the preload pads with a lower predicted t_{90}. One of these pads is the preload test pad, which is known to have some deep footing present. Deep footings under a preload pad will attract stress reducing the imposed stress on the soil. Less stress will result in less consolidation and if the effect of the piles is not considered the percentage consolidation, based on remaining excess pore pressures, will be overestimated. One of the pads with 50% consolidation after one month was in an area known to be without deep footings. Therefore, the rate of consolidation of the compressible clay is more likely to be 50% over one month and 90% over 14 months. It should be noted that this assessment of t_{90} is based on a limited number of point tests (VWPs) which may not represent the average degree of pore pressure dissipation within a particular layer. This shows the initial predicted t_{90} of 9 months was shorter but close to that measured. It should also be noted that with larger preload surcharge, a greater proportion of the applied stress will be within the normally consolidated range which will increase the apparent t_{90}.

The measured settlements were typically about 50% of the predicted settlements. A lot of the settlement is likely to have occurred during and just after construction, which was missed by the timing of the first survey reading. Tracing logarithmic curves back from the measured data suggests settlements to within 20 mm of the predicted settlements.

It any case, the recorded settlement was in excess of that required for the proposed building loads and so the questionable extrapolated data did not have to be relied upon.

The majority of the preload pads required a one month period to achieve the required settlement.

5 CONCLUSIONS

The site characterisation was successfully conducted by high quality in-situ testing techniques (CPT, DMT and RDP), without the use of more conventional boreholes and laboratory testing, and they provided more relevant data for significantly lower fees.

Interpretation and analysis of the in-situ test data allowed the use of economic stiffened slab footings instead of the more expensive option of deep footings. The stiffened slab option is estimated to have reduced projects costs by about $10M.

Ground improvement monitoring with various in-situ tests (CPT, MASW, VWP and settlement plates) allowed the confirmation of geotechnical design and the efficient progress of ground improvement alongside construction earthworks.

In summary, there are significant project cost savings by using the above mentioned in-situ testing and monitoring techniques, making development of inner city areas on difficult ground more viable. This type of development is likely to become more common as inner city industrial sites are rezoned as residential.

6 REFERENCES

Neilson, J.L. 1996. The Geological Setting of the Coode Island Silt. *Building on Coode Island Silt Seminar,* Australian Geomechanics Society and the Structural Branch, Victoria Division.

Day, R.A. & Woods, P. 2007. Verification of Consolidation Parameters of a Near-Normally Consolidated Clay by Back-Analysis of and Instrumented, Wick-Drained Reclamation. *Proc. 10th ANZ Conf. on Geomech*. 2: 54-58.

Srithar, S.T. 2010. Settlement characteristics of Coode Island Silt. *Australian Geomechanics* 45(1): 55-64.

Ervin, M.C. 1992. Engineering properties of Quaternary age sediments of the Yarra Delta. In W.A. Peck, J.L. Neilson, R.J. Olds & K.D. Seddon (eds) *Engineering Geology of Melbourne*: 245-259. Rotterdam: Balkema.

Bowles, J.E. 1997. *Foundation Analysis and Design*. 5th International Ed. Singapore: McGraw-Hill.

Lunne, T., Robertson, P.K. & Powell, J.J.M. 1997. *Cone Penetration Testing in Geotechnical Practice.* New York: Spon Press.

Marchetti, S., Monaco, P., Totani, G. & Calabrese, M. 2001. The Flat Dilatometer Test (DMT) in soil investigations. A Report by the ISSMGE Committee TC16. In *Proceedings of the International Conference on In Situ Measurement of Soil Properties and Case Histories*: Bali, Indonesia 21-24 May 2001.

Kulhawy, F.H. & Mayne, P.W. 1990. *Manual on Estimating Properties for Foundation Design.* EPRI Report EL-6800. New York: Cornell University.

Geotechnical and Geophysical Site Characterisation 5 – Lehane, Acosta-Martínez & Kelly (Eds)

A 2016 case for public geotechnical databases

T. Thompson
Arup, Brisbane, Australia
The University of Queensland

ABSTRACT: In his 1973 book 'Cities and Geology', the Canadian-English Engineer Robert Legget presented a detailed case for creating and maintaining public geotechnical databases (Legget 1973). The book summarises several public and mostly paper-based databases of the time and outlines the challenges for implementation. The viability of a modern public geotechnical database is influenced by many factors including the availability of data, an area's population density, and seismic risk. Where a city, region or country has sustained the use of a geotechnical database or databases through evolving technology and generational change, no case needs to be made. Elsewhere the creation of a database may be constrained by questions of liability and intellectual property, or by consultants who view a public database as working to their competitive disadvantage. The paper summarises several public geotechnical databases around the world in the interest of highlighting their benefits and potential to advance the profession.

1 INTRODUCTION

For the development of urban areas there is great value in the data generated by geotechnical investigations. Some cities and even countries have understood the value of this information for many decades. Most geotechnical consultancies certainly do to inform preliminary studies, design development and the assessment of risk for a particular site. Like library books, individual investigation records may be filed away and seldom or never used again. But collectively, the records of a geotechnical database play a critical role in the practice of geotechnical engineers.

The English-Canadian Engineer Robert Legget outlined the reasons for establishing and maintaining public geotechnical databases in his 1973 book 'Cities and Geology'. Legget served as the Director of the Division of Building Research at the National Research Council of Canada for 22 years following experience teaching and working in private practice. In the concluding chapter of the book entitled 'What Every City Should Do', Legget argued with a logic shared by most geotechnical practitioners that the greater the availability of geotechnical information to inform design and construction, the more efficient and less wasteful design and construction can be. He summarised the benefits of data for informing what today would be referred to as 'geotechnical risk'. And he detailed the advantages of access to that data for urban planning, research, geology mapping, and public education.

Despite living in a world with 'too much information', geotechnical engineers still generally favour more data over less and spend significant amounts of time with clients justifying the cost of investigations. In short, data remains good for geotechnical engineers. And what is good for the private practice and what motivates it to invest its resources into a geotechnical database is also good for the engineering community as a whole and warrants some form of parallel investment and attention.

2 GEOTECHNICAL DATABASES

2.1 *Canada*

For various reasons including economic growth, increasing environmental awareness, glacial geology, and the influence of Legget and many of his colleagues, both contemporary and preceding, Canada in the early 1970s invested significantly in 'urban geology' and geotechnical data. In 1971 the Geological Survey of Canada (GSC) developed a national urban geology program through which geotechnical data from 27 cities was collected and collated (Scott 1998). Almost in parallel for a separate project, the GSC identified the benefits of automated databanks and nationally launched the Urban Geotechnical Automated Information System (UGAIS) (Karrow & White 1998). The primary objective of the UGAIS

was 'to develop methods of compiling, evaluating and presenting geological information to meet the needs of planners, administrators and engineers' (Belanger 1974). These initiatives funded the creation of geotechnical databases for the 27 cities involving records from over 110,000 boreholes.

A 1998 volume entitled 'The Urban Geology of Canadian Cities' (dedicated to the memory of Robert Legget who passed away in 1994) includes contributions on the geology of 23 of the 27 cities targeted by the 1971 GSC initiative, with discussion on the status of each database (Karrow & White 1998). To the frustration of several of the authors, 11 of the 23 databases were no longer in use. Investigation noted that the original databases required proficiency with and access to mainframe computers that effectively excluded some engineering firms, planners and regional governments (Belanger 1998). Through the evolution of computer data storage and the retirement of key personnel, the databases weren't universally updated. Of those databases that survive today, the Ontario borehole database is maintained by the Ontario Ministry of Northern Development and Mines (MNDM) and includes data from over 90,000 boreholes. Most of the original borehole logs are no longer available but a Google Earth interface (i.e. kml file) was created for the public in 2012 and includes stratigraphic, material consistency, and groundwater information from the boreholes. In 2015 the database was accessed on 3078 occasions, or almost twelve times every work day (correspondence with the MNDM).

2.2 *Great Britain*

Where geotechnical databases are well established and have been maintained through generational and technological change, a justification of their purpose isn't necessary. British interest in geological databases can probably be traced in part to William Smith's 1799 geological map of Bath, England which emerged from research and his meticulous observations as a surveyor. Detailed and persistent geological and later geotechnical record keeping in England from paper through several forms of computerised data management begat the British National Geotechnical Properties Database launched by the British Geological Survey (BGS) in 1992. This database now includes information from over 100,000 boreholes. Scans of original borehole logs can be accessed for free online by anyone through a 'Geology of Britain' web viewer that is opened approximately 60,000 times a month by what is presumably a wide community of engineering and scientific professionals as well as students (correspondence with the BGS). Ground models generated from standardized digital data and available records accompanying borehole logs (eg. reports and lab results) are available for purchase.

The BGS is to be credited with what is possibly the most comprehensive and beneficial geotechnical database to be found in the English language. While professional traditions and organisation are no doubt among the major reasons for the BGS database, the population density and limited geographical extent of England have certainly contributed as well. The professional cohesion afforded by a proximity of urban centres is not as easily achieved in a younger country of Canada's size.

2.3 *Perth, Australia*

A database for the Perth, Australia Central Business District (CBD) was created in 2004 and made available through the Australian Geomechnics Society (AGS-a) website where it remains (Stewart 2004). Information from 649 boreholes compiled in the 1970s was transferred to Excel format by members of the AGS-a. The database comprises a pdf location plan of the boreholes and supporting Excel spreadsheets including stratigraphic, groundwater, and Standard Penetration Test (SPT) data. Among those databases considered here, its organisation stands out for durability. Although the database includes no information collected after 1980 and has not been updated since its creation in 2004, it remains in use and demonstrates an important point in relation to the Canadian experience: with the internet a database can be used and survive without any significant maintenance for over a 10 year period.

2.4 *Japan*

The rapid urbanisation of Japan in the mid 20th century and the presence of several large cities set on coastal plains overlying Holocene deposits instigated creation of the country's first geotechnical databases (Todo et al, 2013). Analytical methods to predict seismic liquefaction and amplification were either non-existent or in their infancy when data collection in Japan commenced. From the 1960s regional databases developed with different formats, access restrictions (i.e. open vs. restricted) and emphases. Some databases focused on geological conditions with a view towards engineering design, while others focused on disaster mitigation following earthquakes (Todo et al, 2013). The collection of data for public use was aided in 2001 when 'the Act on Access to Information Held by Administrative Organs' came into effect. The act resulted in a release of geotechnical information collected for public works undertaken at various levels of government (Todo et al, 2013). A total of almost 200,000 boreholes are included in nine regional geotechnical databases of Japan. In 2010 these nine databases were related (but not connected) through the creation of national geotechnical ground models by the Japanese Geotechnical Society for open access by the public.

2.5 *Canterbury, New Zealand*

The Canterbury Geotechnical Database (CGD) was created following the earthquakes of 2010 and 2011 around Christchurch, New Zealand. Approximately 80% of the buildings in the city's CBD were damaged by the earthquakes beyond repair (French 2014). The database emerged following a widespread recognition of the value that geotechnical data could have in the process of re-building. As the database emerged from tragedy, perhaps it is not surprising that calls for its creation originated not just from within the technical community but from activists frustrated by the insurance claim process (Miles 2012). The Google Earth interface can be configured to access data from boreholes, CPTs, and trial pits among other investigation techniques. The icons link directly to pdf copies of the original logs and a separate text interface is available to query data, including liquefaction susceptibility studies.

While conventional geotechnical design cannot not be isolated from seismic considerations, use of the CGD will not stop with the determination of a seismic risk classification. The database will inform foundation and earthworks designs and before that may assist in the planning of new investigations. The CGD website includes a stated purpose of the database that doesn't mention earthquakes:

The CGD is for technical professionals to share data they have collected with other professionals. The collective set of information gives a much better understanding of a particular site. This can reduce the need for new investigations and helps all technical professionals develop the best design solutions for their clients (CGD 2016).

Unlike the previous systems, the CGD is limited to the use of registered engineers, scientists, and insurers 'to assist with the cost of maintenance and avoid the mis-use of highly technical information' (CGD 2016). The registration is also intended to ensure that consultants using data also contribute data. Perhaps a sign of the degree to which cross-agency collaboration can be achieved in the wake of a natural disaster, the database is supported by the New Zealand Ministry of Business, Innovation and Employment (MBIE), the Canterbury Earthquake Recovery Authority (CERA), Christchurch City Council, Selwyn District Council, and Waimakiriri District Council. Based on the CGD, in June 2016 the national New Zealand Geotechnical Database (NZGD) was launched.

2.6 *Summary*

A summary of the databases discussed above in addition to one from the Geological Survey of Ireland (GSI) is included in Tables 1 and 2 below.

Table 1: Geotechnical Database Summary 1

Database	Initial year(s)	Access	Interface
Ontario	1972	Open	Google Earth
BGS	1992	Open	Web-viewer
Perth CBD	2004	Open	Pdf/Excel
Japan	1950s/1960s	Open	Web-viewer
CGD	2013	Restricted	Google Earth
Ireland	2012	Open	Web-viewer

Table 2: Geotechnical Database Summary 2

Database	Approximate number of boreholes	Approximate monthly use
Ontario	>90,000	256
BGS	>100,000	60,000
Perth CBD	649	Not known
Japan	200,000	Not known
CGD	4,600 (CPTs>22,000)	2,500
Ireland	27,800	1,550

3 CONTENT

The systems summarised above include at their root information from borehole logs, whether a scan of those logs is available or not. Some of the systems provide online or in-person access to further information including laboratory data, geophysical surveys and foundation or interpretative reports. Where the right to use a borehole or other exploratory log is established (see discussion of ownership below), a pdf scan of that log with coordinates is enough to start what might be Phase 1 of a database. Given the potential complexity in identifying an ideal data format or in securing agreement for a specific format between major public and private entities, digitising exploratory hole and test data might be ideal Phase 2 objectives. Similarly, the incorporation of test data and additional information need not delay making scans of logs available to the public.

4 MANAGEMENT

While possibly based in a public entity such as a City Council, Department of Transportation, university or professional society, public database systems should be setup to accommodate the on-going inclusion of data from multiple agencies. A government-backed geological entity or professional society may be the ideal host to foster interaction between various public entities.

5 INDUSTRY TRENDS

5.1 *Standardised Data*

Beyond the benefits summarized earlier, the transition to digitised data by a public database could

serve as a catalyst for the standardisation of data to a format such as the Association of Geotechnical and Geo-environmental Specialists (AGS-b) or Data Interchange for Geotechnical & Geoenvironmental Specialists (DIGGS). Standardisation by a Department of Transportation or similar public entity can also act as a catalyst but the effect will be limited if other large public agencies in the same area don't agree/follow. While standardized data formats are currently limited in their representation of interpreted data, they still have the benefit of facilitating the transfer of data between organisations. With the increased sharing of factual data, there will be greater opportunities for the sharing of interpreted data, which should foster an increased use of Building Information Modelling (BIM) by geotechnical engineers (Morin 2015).

5.2 *Building Information Modelling*

The use of BIM for Geotechnical engineering is obviously not dependent upon the existence of a public geotechnical database. But the above suggestion of a link or potential for a link between public geotechnical databases and opportunities for BIM is probably less of a suggestion and more an observation of the influence that the BGS now has in Great Britain. To some degree the CGD is attempting to achieve the same influence with its adoption of the AGS-b data format. While geotechnical BIM with advanced 3 dimensional ground models is now being used on many projects around the world, those places with public geotechnical databases using standardized data are probably in the best position to advance.

5.3 *Data Analytics ('Big Data')*

Geotechnical databases present unique opportunities for data analytics. These opportunities encourage a shift in focus from 'who has data' towards 'what can be done with available data' (correspondence with the NZ MBIE).

5.4 *Geotechnical Baseline Reports*

While not appropriate for every project or contract, geotechnical baseline reports for large infrastructure projects, and especially tunnels, have become common in the last decade. As such reports aim to assess and assign geotechnical risk, their preparation (or preceding decision to prepare or not) benefit from the availability of historical data.

6 CHALLENGES TO IMPLEMENTATION

Many of the challenges to implementing a public geotechnical database have not changed since 1973. Robert Legget summarised issues of a) responsibility (liability), b) privacy (ownership of data), c) unwillingness by any local entity, d) the perception of a public database as not representing a civic responsibility, e) cost, and f) lack of local geological interest. He possibly did not envision in 1973 the extent to which consultants would be able to develop and digitise their own internal data, thus reducing the motivation for any parallel public system. Some of these issues are discussed below.

6.1 *Liability*

It is understandable that practicing geotechnical engineers and investigation contractors will not want to be held liable by any third party who uses data for purposes not envisioned. The databases discussed above all address this with several example statements included below.

The Ontario borehole database is limited to stratigraphic information and doesn't reveal the sources of borehole logs. It notes:

Ontario's Ministry of Northern Development, Mines and Forestry (MNDMF), Mines and Minerals Division, Ontario Geological Survey (OGS) and the Ministry of Natural Resources (MNR) shall not be liable in any way for the use of, or reliance upon, any information in this database (Ontario Borehole 2016).

The Canterbury Geotechnical Database which includes scans of original logs notes:

The Terms of Use set out the limitations regarding warranty. In short, data providers do not accept any liability associated with use of the data by a third party (CGD 2016).

The BGS notes:

The use of information provided by the British Geological Survey (BGS) is at your own risk.[5]

Of all the databases discussed, only the Perth CBD system stipulates that the information 'not be used to reduce the scope of any geotechnical investigation' (Stewart 2004). This may be related to the age of the source data used in the Perth system, but it is considered that the option of reducing investigation scope should be at the discretion of a designer. Designers should of course consider variations to groundwater levels over time as well as any plausible changes to the ground materials themselves. The BGS System addresses this matter as follows:

Data, information and related records, which have been donated to BGS have been produced for a specific purpose, and that may affect the type and completeness of the data recorded and any interpretation. The nature and purpose of data collection,

and the age of the resultant material may render it unsuitable for certain applications/uses. You must verify the suitability of the material for their intended usage.

Where 'historical' information warrants either a reduction in proposed investigation scope, or the execution of an investigation that aims in part to verify historical logs prior to finalizing a scope, this should be considered. The reality is that designers already make this judgment in reference to the data they maintain internally as a matter of normal practice.

6.2 *Ownership*

Exploratory data collected for the design and construction of public infrastructure is usually owned by a public entity and ideally should be transferred to the public domain at a reasonable time following construction of an asset. Exploratory data collected for the design and construction of a private asset is normally privately owned and cannot be directed to the public domain without formal agreement.

When a private client ceases to exist, an entity that possesses a geotechnical report financed by that client might become a de facto owner of the information subject to local legal review. The number of geotechnical investigation reports that have been lost or destroyed over the last century cannot easily be estimated. Geotechnical practitioners in particular are to be credited with saving many reports that otherwise would no longer exist. The contribution of such reports (or the investigation logs within) to a public geotechnical database is usually at the discretion of the consultancy. When a private client survives, they normally maintain the decision as to whether or not data can be contributed to the public. It is considered that most developers and other clients in their own financial interest should share the objectives of more efficient geotechnical design and construction (with less waste) and improved identification of geotechnical risk. A focus on reducing waste in particular aligns well with contemporary objectives for 'sustainable' infrastructure (correspondence with the NZ MBIE).

In all circumstances, data should not be transferred to the public domain in advance of a project's conclusion without full consideration by stakeholders. The BGS has a deposition form that accompanies contributed data:

If specified on the BGS standard deposition form, data can be held as commercial-in-confidence for 4 years before it becomes open-file. Special arrangements need to be made with the BGS for longer periods (AGS-b 2016).

No public database system will ever be complete, but the more data available, the better for all users. If only the exploratory logs associated with the design and construction of public infrastructure were made available for professional use, efficiencies in the normal practice of the profession would be found. In some areas including the UK, Japan and Ontario, data has become available or been maintained through governmental open data agreements or freedom of information laws. While not often practiced, it is certainly within the power of a government to make transfer of geotechnical data to a public database part of the building approval process. It can also become part of a professional culture to encourage the contribution of logs. To promote the contribution of data in Ireland, the GSI highlights its role as providing a repository for geotechnical information: *'The investigations are very expensive to undertake and should not be lost for posterity, and GSI provides a national repository for these reports'* (GSI 2016).

6.3 *Cost*

In 1973, Legget estimated $50,000 (Canadian dollar was roughly equivalent to US at the time) for the annual maintenance of a non-computer database (Legget 1973). This database would be available at a centralised location such as a city council office or public library and would require staff to maintain. Accounting for inflation, the figure is now roughly equivalent to US$260,000 (Inflationdata.com 2016).

Given agreement to use data, the relative ease with which that data can be compiled and made available through a web-viewer or Google Earth is in stark contrast to 1973. With the assistance of a professional society, it is considered that the Phase 1 database introduced earlier comprising the organisation of access to pdf exploratory logs could be accomplished for less than US$20,000. The cost of a Phase 2 database comprising an efficient user interface and the digitisation of data will necessarily include more programming, organisation and resources. An estimate is not easily made, and obviously depends upon the magnitude of the task.

6.4 *Inertia of Private Systems*

In the location of every geotechnical database noted above, many consultants maintain their own parallel databases. These private databases are most commonly sustained for the foundation reports and geotechnical interpretation that are not often included or available from public databases. Additionally, some firms have already digitised their data and call upon it regularly for the efficient generation of ground models and sections to support design. A public database with exploratory logs at its core will not supersede the value of these private databases. Separate to the fact that all consultancies should benefit from access to more information, the firms that have already digitised their data may be the most prepared to take advantage of data standardization.

Noteworthy is that the CGD ties those who use data to the future contribution of data: *The Terms of Use require that professional engineers will only use data from the database for a project if they are also prepared to upload any data they hold (or will procure in the future) for that project* (CGD 2016).

7 THE EXCEPTION OF SMALL TOWNS

In small towns where one or two drilling consultants or contractors work in harmony with a local or regional council, the value of a public geotechnical database is probably not as significant as for larger towns and cities with broader competition and construction activity. In these situations, the individual consultants may effectively act as the trusted manager of a database that other parties regularly rely upon.

8 CONCLUSION

In large towns and cities where public geotechnical databases do not currently exist, their creation could facilitate design efficiencies, reduce costs, and accelerate the adoption of new technologies and practices. While considered slightly peripheral to narrow professional motivations, public access to geotechnical data could encourage research, refined geological mapping with contemporary computational tools, and geology education at all levels. The act of creating a public geotechnical database will not likely be driven by individual consultants but rather by a public organisation or professional society.

9 COMMENTS

The author thanks John Scott, Geotechnical Advisor to the New Zealand Ministry of Business, Innovation and Employment (MBIE) for providing comments on the paper and insights from the process of establishing the CGD and later NZGD. Thanks are also extended to Chris Browitt and Alice Walker of the BGS, Stephen Buttling of NGC, and Peter Burnton and Mike Straughton of Arup for comments.

Landslide and Earthquake Strong Motion databases are forms of geotechnical databases that have not been considered here. The paper has also unavoidably missed some excellent work done in various places for the creation and maintenance of geotechnical databases. In 'Cities and Geology', Robert Legget discussed geological record keeping in Prague, and also summarised national or local databases in France, Zurich, Moscow, Warsaw, Boston and Johannesburg.

As a final note, "Cities and Geology" is considered to be among the few out-of-print books that should probably be in every geotechnical consultancy's library. It is highly recommended to anyone with an interest in urban geology and/or the history of 'ground' engineering. The author thanks Nik Sokol for having a copy of the book in his car one afternoon in 2003 after inspecting boreholes for the Second Avenue Subway in New York.

10 REFERENCES

Australian Geomechanics Society (AGS-a): www.autraliangeomechanics.org

Association of Geotechnical and Geo-environmental Specialists (AGS-b): ags.org.uk

Belanger J.R. 1974. Urban Geology Automated Information Systems (UGAIS) in Computer use in projects of the Geological Survey of Canada: Geological Survey of Canada, Paper 74-60, p.95-98.

Belanger J.R. 1998. Urban Geology of Canada's National Capital Area. In Karrow P.F. & White, O.L. (eds.), Urban Geology of Canadian Cities, Geological Association of Canada Special Paper 42, p. 365-384.

British Geological Survey: http://www.bgs.ac.uk/data/mapViewers/home.html correspondence with Rob Smith.

The Canterbury Geotechnical Database (NZ MBIE): https://canterburygeotechnicaldatabase.projectorbit.com/ correspondence with John Scott

French, Laura. 2014. Christchurch Bites Back After Devastat ing 2011 Earthquake. Business Destinations. 11 Nov 2014.

Geological Society of Ireland: https://www.gsi.ie/Mapping.htm correspondence with John Butler

Karrow, P.F., White O.L. 1998. A Summary of Canadian Ur ban Geology. In Karrow P.F. & White, O.L. (eds.), Urban Geology of Canadian Cities, Geological Association of Canada Special Paper 42, p. 11-20.

Legget, Robert F. 1973. Cities and Geology. McGraw-Hill. USA.

Miles, Sarah. 2012. The Christchurch Fiasco: The Insurance After-shock and its implications for New Zealand and Beyond. Dunmore Publishing. Canterbury, New Zealand.

Morin, Gary. 2015. The Benefits of Geotechnical BIM. Engineers Australia. Vol 87 No. 5: June 2015, p.78-79.

Ontario Ministry of Northern Development and Mines: https://www.ontario.ca/data/geotechnical-boreholes correspondence with Alphons Evers & Jon Webb.

Scott, J.S. 1998. Urban Geology in Canada - a Perspective. In Karrow P.F. & White, O.L. (eds.), Urban Geology of Canadian Cities, Geological Association of Canada Special Paper 42, p. 1-9.

Stewart, Doug (2003). Geotechnical Borehole Database for the Perth CBD. Australian Geomechanics Society Journal. Vol 38 No 4.

Todo, H. & Yamamoto, K. & Mimura, M. & Yasuda, S. 2013. Japan's Nation-wide Electronic Geotechnical Database Systems by Japanese Geotechnical Society. Geotechnical and Geological Engineering. Volume 31: p. 941-963.

Geotechnical and Geophysical Site Characterisation 5 – Lehane, Acosta-Martínez & Kelly (Eds)

Site characterization and seismic response analysis in the area of Collemaggio, L'Aquila (Italy)

G. Totani & P. Monaco
University of L'Aquila, DICEAA, L'Aquila, Italy
F. Totani
Consultant, L'Aquila, Italy
G. Lanzo
University of Rome Sapienza, DISG, Rome, Italy
A. Pagliaroli
University of Chieti-Pescara, INGEO, Pescara, Italy
S. Amoroso
Istituto Nazionale di Geofisica e Vulcanologia, L'Aquila, Italy
D. Marchetti
Studio Prof. Marchetti Srl, Rome, Italy

ABSTRACT: The paper describes the geotechnical investigations and analyses carried out for the restoration of the ancient Basilica di Collemaggio, L'Aquila (Italy), severely damaged by the 2009 earthquake. The subsoil model was defined based on a comprehensive investigation including boreholes, measurements of shear wave velocity V_S by seismic dilatometer (SDMT) in backfilled boreholes (non-penetrable soils) to 93 m depth and laboratory cyclic tests (double specimen direct simple shear, DSDSS). An "enhanced" seismic source was designed to improve the interpretation of V_S at large depths. Site response analyses were carried out with 2D FLAC finite difference code. Literature data and DSDSS test results were used for non linear cyclic characterization of soils. The input motions were seven real accelerograms compatible with reference response spectra on outcropping rock from the Italian code. The results, expressed in terms of free-field acceleration response spectra, showed amplification up to 2.5 s with maximum values > 2 in the period range 0.1-0.4 s.

1 INTRODUCTION

The Basilica Santa Maria di Collemaggio, located in L'Aquila (central Italy), is an important catholic church founded in the XIII century. It contains the most ancient Holy Door in the world and hosts every year a unique Jubilee (Perdonanza Celestiniana), a penitential observation devised by Pope Celestine V, who is buried here. Parts of the structure of the Basilica were severely damaged by the magnitude M_w = 6.3 April 6, 2009 L'Aquila earthquake. While the beautiful Romanesque façade is intact, the cupola, the transept vaults and the arches have collapsed.

The geotechnical investigations and seismic response analyses described in this paper were carried out as part of the project for the restoration of the Basilica, funded by Eni S.p.A. and currently under construction (scheduled end: 2017). Additional ground response analyses that cross the Basilica can be found in Amoroso et al. (2013, 2015).

2 BASIC GEOLOGICAL SETTING

The complex geological setting of the L'Aquila basin is extensively described e.g. in MS–AQ Working Group (2010). In the city centre, where the Basilica di Collemaggio is located, the upper portion of the subsoil is constituted by the deposit known as "Brecce dell'Aquila", composed of fine to coarse calcareous fragments of variable size (mostly of some centimetres) embedded in sandy or silty matrix, characterized by highly variable cementation and mechanical properties. The breccias, about 80-100 m thick, lay on fine- to medium-grained, mostly silty lacustrine deposits of average thickness ≈ 250-270 m, placed on the limestone bedrock. Gravimetric investigations (MS–AQ Working Group 2010), confirmed by deep boreholes (Amoroso et al. 2010), have indicated that in the city centre the bedrock is located below 300 m depth.

3 SITE INVESTIGATION

A comprehensive site investigation was carried out in the area of the Basilica di Collemaggio, including deep boreholes, measurements of the shear wave velocity V_S by seismic dilatometer SDMT (Marchetti et al. 2008) and active/passive seismic surface measurements (tomography, ambient noise, 2D array, AA.VV. 2013, Milana et al. 2011), as well as short

vertical/inclined boreholes across the existing church foundations.

Three boreholes (S1, S2, S3, Fig. 1) were drilled respectively to a depth of 80 m, 120 m and 275 m from the ground surface, with Standard Penetration Tests and retrieval of samples. The deepest borehole (S3), drilled partly with core recovery and partly as core-destructive, was aimed at detecting the top surface of the bedrock, which however was not reached within the investigated depth.

After completion the boreholes S1, S2, S3, plus an additional auxiliary borehole S3 bis b, were backfilled with clean fine-medium gravel (grain size 5-15 mm, no fines) in order to obtain V_S measurements by SDMT according to the procedure devised by Totani et al. (2009) for non-penetrable soils, largely employed in the L'Aquila area in post-earthquake investigations (Monaco et al. 2013). In this procedure the SDMT is inserted and advanced into a pre-drilled backfilled borehole by use of a penetrometer rig and V_S measurements are taken every 0.50 m of depth as usual, but without DMT measurements (meaningless in the backfill). In this case the SDMT acts only as a vehicle for inserting the seismic module. Such technique is based on the assumption that the S-wave travel path from the surface to the upper and lower receiver in the SDMT seismic module includes a short path in the backfill approximately of the same length, i.e. the time delay between the two seismograms and the interpreted V_S do not change (Totani et al. 2009). Comparative tests carried out at sites where both the usual penetration procedure and the backfilling procedure were adoptable indicated that the V_S obtained in the backfilled borehole are nearly coincident with the V_S obtained by penetrating the soil.

The site investigation included V_S measurements by SDMT (Fig. 1) in four backfilled boreholes (SDMT 1, SDMT 2, SDMT 3, SDMT 3bis b) to a maximum depth of 93 m from the ground surface (SDMT 3), and a limited number of SDMT measurements by penetration in the virgin soil (SDMT 3bis a, SDMT 4).

An "enhanced" seismic source was specifically designed and tested at the University of L'Aquila to tentatively improve the quality of the signals and reduce the uncertainty in the interpretation of V_S measurements by SDMT in deep backfilled boreholes. The "enhanced" seismic source ("Tirino Hammer", Fig. 2) is composed of a pendulum hammer having a mass of 130 kg, with a drop height of 2 m, which hits horizontally a ballasted steel anvil placed along one side of the truck, with the impact line parallel to the axes of the receivers. The "enhanced" seismic source was used only in SDMT 3, while all the other tests were carried out using the "standard" seismic source.

Figure 3 shows the superimposed V_S profiles obtained by SDMT (plotted in terms of elevation above the sea level) and the schematic soil profile.

Figure 1. Location of boreholes and V_S measurements by SDMT (in backfilled boreholes and in virgin soil).

Figure 2. "Enhanced" seismic source ("Tirino Hammer").

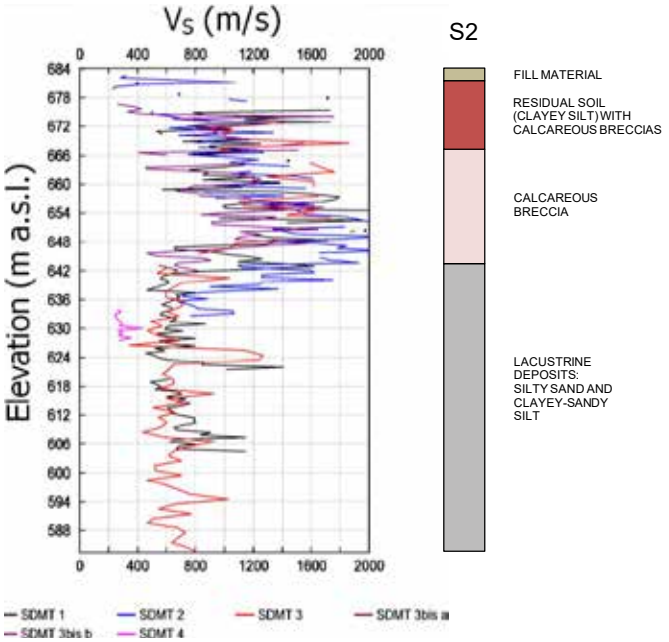

Figure 3. Superimposed profiles of V_S measured by SDMT in backfilled boreholes and schematic soil profile.

4 SUBSOIL MODEL FOR SITE RESPONSE ANALYSIS

The subsoil model was based on the site investigation carried out in the area of the Basilica di Collemaggio, and it was used for the site response analysis, as illustrated in Figure 4. Table 1 summarizes the geotechnical parameters of the materials introduced into the analysis, in terms of unit weight γ, shear wave velocity V_S, Poisson's ratio υ, normalized shear modulus G/G_0 and damping D curves. In particular V_S values refer to the SDMTs performed in the four backfilled boreholes, while υ values were estimated considering cross-hole tests carried out in similar soils. For the lacustrine deposits "L" and "LS", the G/G_0 and D curves were derived from simple shear tests carried out at University of Rome "La Sapienza" with DSDSS apparatus (D'Elia et al. 2003). Literature curves (Vucetic & Dobry 1991, with plasticity index PI = 15) were assumed for the fill material "R" and the residual soils "LAC1" and "LAC2". A visco-elastic linear behavior was assumed for the calcareous breccias "Ba" and "B".

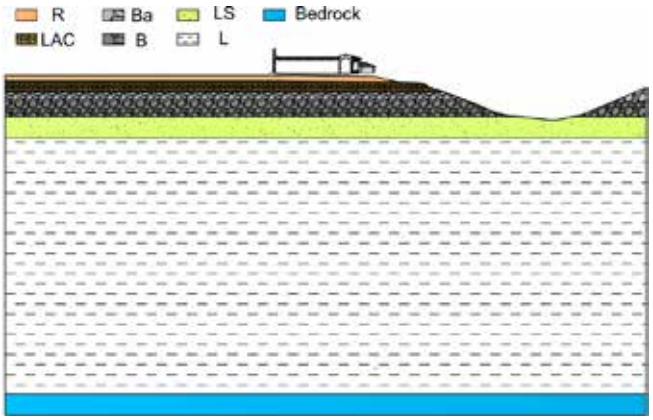

Figure 4. Subsoil model adopted for site response analyses.

Table 1. Subsoil model adopted for site response analyses (* = linear variation with depth).

Depth (m)	Material	γ (kN/m^3)	V_S (m/s)	υ (-)	G/G_0 and D curves
0-5	R	18.0	160	0.30	Vucetic & Dobry 1991 PI=15
5-10	LAC1	19.5	700	0.30	
10-16	LAC2	19.5	1000	0.30	Linear
16-24	Ba	20.0	1000	0.33	
24-40	B	21.0	1000-1800*	0.38	
40-60	LS	20.5	600	0.40	DSDSS tests
60-300	L	20.5	650-850*	0.40	
> 300	Bedrock	23.0	1250	0.33	-

5 SELECTION OF INPUT MOTION

The acceleration response spectrum with a return period of 475 years suggested by the Italian National Building Code (NTC-08) for flat outcropping rock condition (class A subsoil and topography category T1) was assumed as reference for input motion definition. Seven recordings, compatible on average with the reference spectrum, were selected as input for numerical analyses. The following procedure for selecting and scaling natural accelerograms was adopted (Pagliaroli & Lanzo 2008).

1. Candidate ground motion time-histories were extracted from the ITACA database (ITalian ACcelerometric Archive available at itaca.mi.ingv.it) on the base of magnitude M, source-to-site distance d and site classification. Based on the main active seismogenic structures in the region, reference was made to a magnitude-distance window defined by M = 5.9-6.9 and d < 25 km, representative of the L'Aquila Upper Aterno valley and Ovindoli-Pezza-Campo Felice fault systems (Akinci et al. 2009). Recordings at stations of class B with $V_{S,30}$ > 650 m/s were included in the selection because accelerograms at rock outcropping conditions (class A subsoil) are very few in the national database, especially for M_w > 6 and near-field conditions. Focal mechanism was not included in the search, even if preference was given to recordings of normal fault events dominating the activity in central Apennines.
2. All candidate records were scaled to target peak ground acceleration PGA (0.26 g) by using a scaling factor F.
3. Records characterized by F > 4.5 were rejected; the limit value of scaling factor was assumed higher than in previous studies (Pagliaroli & Lanzo 2008) to include available class A recordings from the 2009 L'Aquila earthquake. Parameters measuring spectral matching of single recordings with target spectrum (for example D_{rms}) were not considered because a large period range (0.2-2.5 s) was considered for the spectral compatibility with reference spectrum.
4. A selection of 7 recordings was finally made by comparing the average response spectrum with the reference one in the 0.2-2.5 s range; maximum underestimation of 10% with respect to target spectral amplitudes was assumed as requirement for spectral compatibility.

Basic characteristics of selected input motions are reported in Table 2, while single and average response spectra of input motion accelerograms are reported and compared with target spectrum in Figure 5.

6 NUMERICAL ANALYSES

6.1 *Numerical code*

The numerical analyses were carried out using FLAC 2D finite difference computer code (Itasca 2011). The code incorporates a dynamic option allowing 2D full dynamic analysis. The mesh employed for the analyses, with a detail of the Basilica area, is shown in

Figure 6. In order to achieve satisfactory accuracy, the height of the elements of the mesh was chosen as lower than $V_S/(10f_{max})$, where f_{max} is equal to the maximum frequency to be transmitted, assumed equal to 15 Hz. The aspect ratio of the elements is about 1. The radiation damping was simulated by employing a viscous boundary at the bottom and free-field boundary conditions at the lateral edges of the model. The input motions were applied at the base of the model in terms of shear stress time histories in order to simulate a transmitting base (Itasca 2011). The LAC2-Ba-B materials (Table 1) were assumed to be linear with damping properties modeled by the full Rayleigh damping formulation with a single control frequency, set at 2 Hz. This latter was assumed to be in the range between the fundamental frequency of vibration of the deposit (about 0.6 Hz, see later in the text) and the predominant frequencies of the input motions (generally 3-8 Hz, as shown in Fig. 5a). The target damping ratio for LAC2-Ba-B materials was set at 0.5% considering that a slight numerical overestimation occurs in the frequency range of interest.

For non-linear materials (R-LAC1-LS-L in Table 1), the Sigmoidal 4 hysteretic damping formulation, available in the FLAC library, was adopted. The model parameters were calibrated by using standard G/G_0 and D vs shear strain amplitude curves listed in Table 1. A small amount (0.5%) of Rayleigh damping was also added to provide a non-zero damping at very small strains.

6.2 *Linear analyses*

In order to validate the subsoil model assumed for the numerical study, linear analyses were initially carried out to compare the horizontal-to-vertical

Table 2. Main characteristics of the recordings selected as input motion: M_w = moment magnitude, d = epicentral distance, a_{max} = peak acceleration; Cat = subsoil class according to Italian Seismic code NTC-08, F = scaling factor.
All accelerograms are referred to normal fault events with exception of Friuli 4th shock.

ID	Earthquake	M_w	d (km)	a_{max} (g)	Cat	F
SRC0	Friuli 4th shock 15.09.1976	5.9	16	0.25	A	1.04
ARQ	Val Nerina 19.09.1979	5.8	21	0.08	A	3.44
ATN	Val Comino 07.05.1984	5.9	10	0.10	A	2.60
BSC	Irpinia 23.11.1980	6.9	28	0.10	A	2.70
AQG	L'Aquila 06.04.2009	6.3	4	0.45	B	0.58
MTR	L'Aquila 06.04.2009	6.3	22	0.06	A	4.17
PNT	Val Comino 07.05.1984	5.9	27	0.06	A	4.00

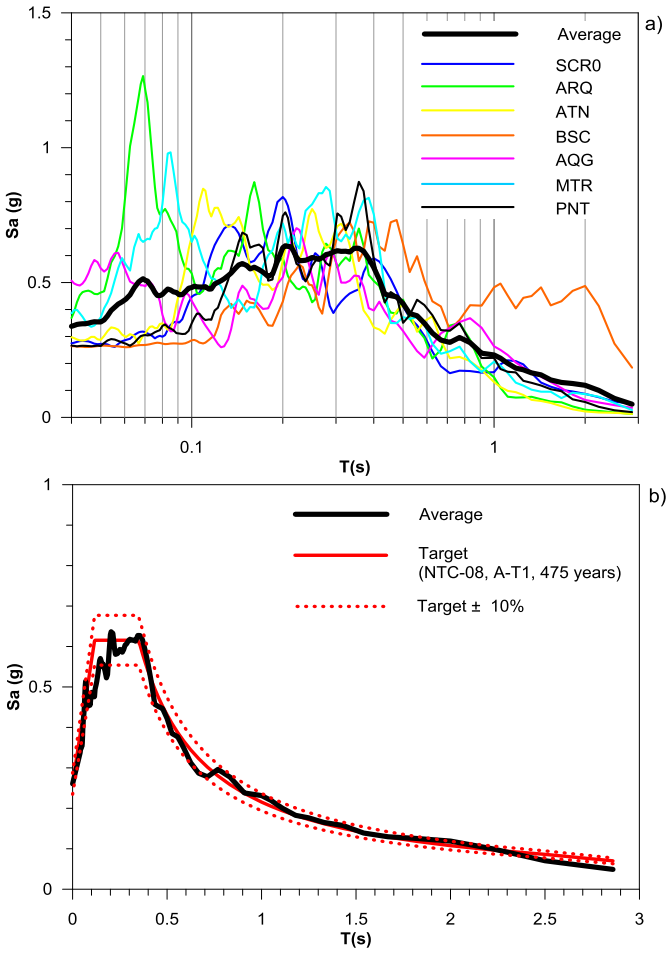

Figure 5. (a) Response spectra (5% structural damping) of accelerograms selected as input for site response analyses in semi-log scale. (b) Comparison between average input spectrum and target spectrum, linear scale (dashed lines represent target spectral amplitudes ± 10%).

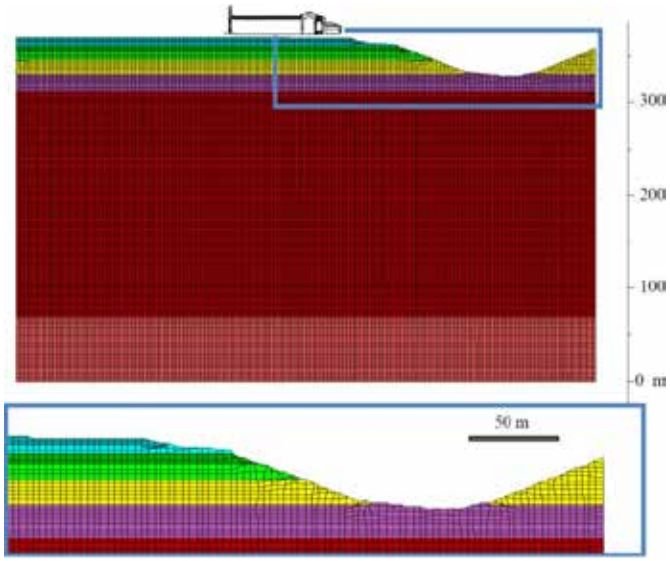

Figure 6. Mesh employed for the analyses, with a detail of the area of the Basilica.

spectral ratio (HVSR) obtained experimentally in the Basilica area from noise measurements (Milana et al. 2011) to numerical transfer functions; these latter were computed as the ratio between the smoothed Fourier spectrum in the node of interest and the corresponding spectrum of input motion. Soil behavior was assumed to be visco-elastic with mechanical properties characterized by their small strain values.

Figure 7 shows the comparisons between the numerical transfer functions at 4 representative nodes in the Basilica area (A, B, C and D) and a typical HVSR computed from microtremors (cmg11). Noise measurements highlight two resonance frequencies: the first one at about 0.6 Hz is related to the deep impedance contrast between the overall deposit and the bedrock; at about 7-8 Hz a further resonance, related to presence of the anthropic backfill over underlying LAC deposits, appears. The transfer functions computed via numerical analyses generally show a good qualitative agreement with the H/V curve; both resonance frequencies measured experimentally are properly reproduced.

The overall good match between experimental and numerical transfer functions therefore corroborates the subsoil model employed for the site response analyses, at least in the linear range.

For comparison, 1D visco-elastic analyses were carried out with STRATA computer code (Kottke & Rathje 2008). A good qualitative and quantitative matching between 1D and 2D transfer functions can be observed, thus indicating that moderate 2D effects take place in the Basilica area. In particular 2D effects appear for frequencies higher than 3 Hz, where some differences between 2D and 1D functions as well as between the 2D response at the 4 selected nodes do exist. As expected, behind the slope crest the moderate-to-high frequency motion presents a significant spatial variation. In the 6-10 Hz range, maximum amplification takes place at node C even if the aggravation with respect to 1D simulations is moderate.

6.3 *Non linear analyses*

The seismic action to be used for the analysis of the structure has been provided in terms of acceleration response spectra (5% of structural damping) at free-field. The spectra were computed as average over all 7 input signals. Results at representative nodes (A-D) are reported in Figure 8a. Significant amplification can be observed in the range 0.1-0.4 s (2.5-10 Hz), in agreement with information obtained from linear transfer functions (Fig. 7). The same spectra were regularized using the procedure proposed in the Italian guidelines for Seismic Microzonation (ICMS 2008) to be directly compared with NTC-08 code seismic action.

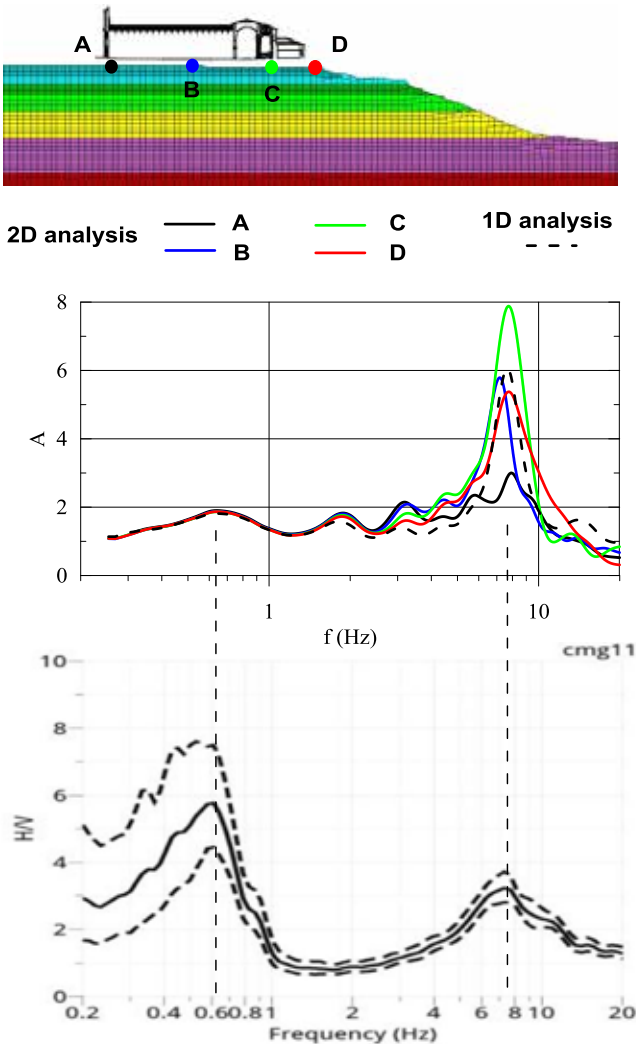

Figure 7. Comparison between transfer functions computed by 1D and 2D visco-elastic linear analyses and representative H/V ratio from noise measurements carried out in the Basilica area.

In Figure 8b the regularized spectra are compared with the response spectrum for subsoil class B corresponding to geotechnical profile in the upper 30 m of Basilica subsoil. Topographic amplification factor T2 (= 1.2) was also applied to consider the effect of superficial morphology. The comparison shows that the NTC-08 B-T2 spectrum leads to a significant underestimation of seismic action for period less than 0.5 s.

7 CONCLUSIONS

A comprehensive geotechnical investigation carried out in the area of the Basilica di Collemaggio, including deep boreholes, measurements of the shear wave velocity V_S by seismic dilatometer SDMT, active/passive seismic surface measurements, cyclic laboratory tests, allowed to provide an accurate subsoil model for 2D site response analyses.

Preliminary visco-elastic linear analyses were carried out to compare the numerical transfer functions with the H/V curve from noise measurements, thus corroborating the subsoil model.

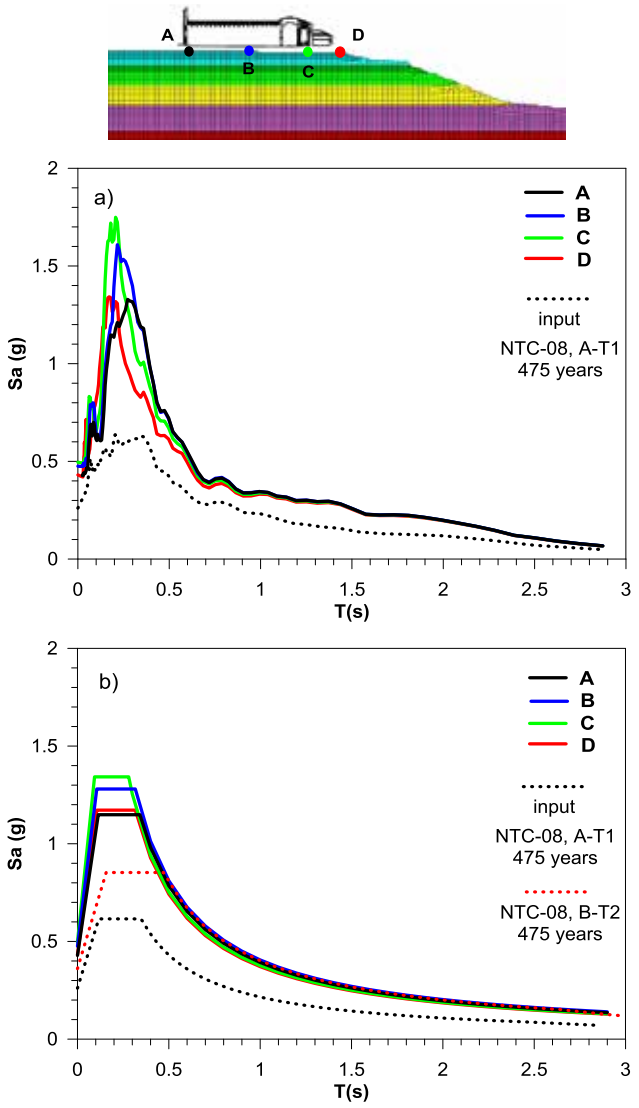

Figure 8. (a) Average response spectra computed in the Basilica area at nodes A-D. (b) The same spectra are reported in regularized form to be directly compared with NTC-08 code seismic action.

Moreover, linear 1D vs 2D results highlighted that behind the slope crest where Basilica is founded, the moderate-to-high frequency motion presents a noteworthy spatial variation. However the aggravation of motion amplification predicted by 2D model with respect to 1D simulations is moderate.

Non linear site response analyses were then executed to quantify the seismic action for the restoration project of the Basilica. Significant amplification can be observed in the range 0.1-0.4 s (2.5-10 Hz), where site response analyses give spectral acceleration considerably higher than those provided by Italian National Seismic code.

8 ACKNOWLEDGEMENTS

Eni S.p.A. (www.eni.com) is gratefully acknowledged for funding this study, as part of the project for the restoration of the Basilica di Collemaggio.

9 REFERENCES

AA.VV. 2013. Caratterizzazione geologica, geofisica e geotecnica del sito della basilica di Collemaggio. Consorzio Sperimentazione Edilizia, University of L'Aquila, Internal Report (in Italian).

Amoroso, S., Del Monaco, F., Di Eusebio, F., Monaco, P., Taddei, B., Tallini, M., Totani, F.& Totani, G. 2010. Campagna di indagini geologiche, geotecniche e geofisiche per lo studio della risposta sismica locale della città dell'Aquila: la stratigrafia dei sondaggi giugno-agosto 2010. University of L'Aquila, Report CERFIS 1/10 (in Italian).

Amoroso, S., Gaudiosi, I., Milana, G. & Tallini, M. (2013). Preliminary results of seismic response analyses at "Santa Maria di Collemaggio" Basilica (L'Aquila, Italy). *Proc. 32nd Conf. Gruppo Nazionale di Geofisica della Terra Solida (GNGTS), Trieste,* 2: 172-178.

Amoroso, S., Gaudiosi, I., Milana, G. & Tallini, M. 2015. Experimental analysis and numerical modeling of the seismic site response at Santa Maria di Collemaggio Basilica in L'Aquila. *Proc. 3rd Int. Workshop on Dynamic Interaction between Soil, Monuments and Built Environment, Rome,* 295-309. DISS_Edition.

Akinci, A., Galadini, F., Pantosti, D., Petersen, M., Malagnini, L. & Perkins, D. 2009. Effect of time dependence on probabilistic seismic-hazard maps and deaggregation for the central Apennines, Italy. *Bull. Seism. Soc. Am.,* 99(2A): 585-610.

D'Elia, B., Lanzo, G. & Pagliaroli, A. 2003. Small-strain stiffness and damping of soils in a direct simple shear device. *Proc. 7th Pacific Conf. on Earthquake Eng.,* University of Canterbury, Christchurch, New Zealand.

ICMS 2008. Indirizzi e Criteri per la Microzonazione Sismica. ICMS Working Group. Conferenza delle Regioni e Province autonome – Dipartimento Protezione Civile (in Italian).

Itasca 2011. FLAC – Fast Lagrangian Analysis of Continua – Version 7.0. User's Guide. Itasca Consulting Group, Minneapolis, USA.

Kottke, A.R. & Rathje, E.M. 2008. Technical manual for Strata. University of California, Berkeley.

Marchetti, S., Monaco, P., Totani, G. & Marchetti, D. 2008. In Situ Tests by Seismic Dilatometer (SDMT). *From Research to Practice in Geotechnical Engineering*, *Geotech. Spec. Publ. No. 180*, ASCE, 292-311.

Milana, G., Azzara, R.M., Bergamaschi, F., Bertrand, E., Bordoni, P., Cara, F., Cogliano, R., Cultrera, G., Di Giulio, G., Duval, A.M., Fodarella, A., Marcucci, S., Pucillo, S., Régnier, J. & Riccio, G. 2011. The contribution of seismic data in microzonation studies for downtown L'Aquila. *Bull. Earthquake Eng.,* 9(3): 741-759.

Monaco, P., Totani, G., Amoroso, S., Totani, F. & Marchetti, D. 2013. Site characterization by seismic dilatometer (SDMT) in the city of L'Aquila. *Rivista Italiana di Geotecnica,* XLVII(3): 8-22.

MS–AQ Working Group 2010. Microzonazione sismica per la ricostruzione dell'area aquilana. Regione Abruzzo – Dip. Protezione Civile, L'Aquila, 3 vol. & Cd-rom (in Italian).

Pagliaroli, A. & Lanzo, G. 2008. Selection of real accelerograms for the seismic response analysis of the historical town of Nicastro (Southern Italy) during the March 1638 Calabria earthquake. *Engineering Structures,* 30: 2211-2222.

Totani, G., Monaco, P., Marchetti, S. & Marchetti, D. (2009). V_S measurements by seismic dilatometer (SDMT) in non-penetrable soils. *Proc. 17th ICSMGE, Alexandria,* 2: 977-980.

Vucetic, M. & Dobry, R. 1991. Effects of the soil plasticity on cyclic response. *J. Geotech. Eng. Div.,* 117(1): 89-107.

Geotechnical and Geophysical Site Characterisation 5 – Lehane, Acosta-Martínez & Kelly (Eds)

Geotechnical and geophysical site characterization of a nuclear power plant site in United Arab Emirates

S. Parashar, R. Rice, P. Asprouda & H. Al Hammadi
Emirates Nuclear Energy Corporation (ENEC), Abu Dhabi, UAE

J.D. Lee
KEPCO Engineering & Construction (KEPCO E&C), Republic of Korea

ABSTRACT: This paper presents the various geotechnical and geophysical site characterization techniques utilized and typical results obtained during the site characterization of the selected site for the civil nuclear energy power generating project in Barakah, Western Region, Emirate of Abu Dhabi, UAE. The techniques adopted included conventional rotary drilling and testing in overburden soils followed by rock coring and conventional and advanced laboratory testing. In-situ testing of subsurface rocks included pressuremeter testing, and hydraulic conductivity testing. Geophysical testing included on-shore and offshore surface seismic reflection surveys, and down-hole shear wave velocity measurements using P-S suspension logging cross-hole logging techniques as well as acoustic televiewer surveys. Non-seismic geophysical testing surveys consisted of induction logging, natural gamma measurements, fluid conductivity and temperature measurements. The paper also presents typical estimated engineering properties using various techniques and the resulting estimated foundation performance as compared to actual observed behavior at site.

1 INTRODUCTION

In support of its long term sustainable growth vision, the government of the United Arab Emirates has embarked on the development of very large multi-billion dollar infrastructure projects relating to water, wastewater and energy sectors. These projects generally involve extensive site characterization programs tailored to the specific requirements of each project's unique characteristics. One major project being developed by Emirates Nuclear Energy Corporation (ENEC) in the Western Region of the Emirate of Abu Dhabi is the Barakah Nuclear Power Plant (BNPP) project, a large civil nuclear energy power generating project with a total planned capacity of 5600 MWe.

This paper presents an overview of the various geotechnical and geophysical site characterization techniques utilized through the initial stages of the project. A summary of the typical results from in-situ and laboratory tests and geophysical investigations is presented for the BNPP project.

A suite of site characterization techniques, ranging from conventional geotechnical rotary drilling and rock coring, to advanced geotechnical in-situ and laboratory testing was conducted. Surface and down-hole geophysical surveys, both seismic and non-seismic, were carried out to obtain geologic information on lithology and pore fluid characteristics. These are described in more detail in the following sections of this paper.

2 SITE CHARACTERIZATION PROGRAM

2.1 Geotechnical Investigation

The extensive geotechnical site investigation program carried out at BNPP was specifically designed to investigate the subsurface conditions by gathering ground characteristics relevant to the project's design and construction requirements. The site investigation comprised of drilling of exploratory boreholes with disturbed sampling of soils, rock coring, and suites of in-situ and laboratory testing.

A total of 223 exploratory geotechnical borings were completed over three phases drilled to a maximum depth of 184 meters below ground surface (m bgs). A representative typical subsurface profile at BNPP site is shown in Figure 1. Ground surface elevation at the site was an average of ~ 2m according to the Abu Dhabi Datum.

Boreholes were advanced through soil and rock using mud rotary drilling techniques, with the use of a temporary steel casing and water or drilling mud circulation for removal of cuttings. Standard penetration tests (SPT) were performed in the majority of boreholes through the unconsolidated overburden soils at typical intervals of 1m.

Additionally, Cone Penetration Tests (CPT) were conducted in selected boreholes advancing through the soil to the top of rock.

Rock coring was performed using mostly PQ size core barrels and bits, with a typical run of 1.5m long, starting from the top of rock, continuously to the final designated borehole depths. In order to enhance recovery and the quality of the core samples, double tube core barrels and wireline equipment was used when appropriate.

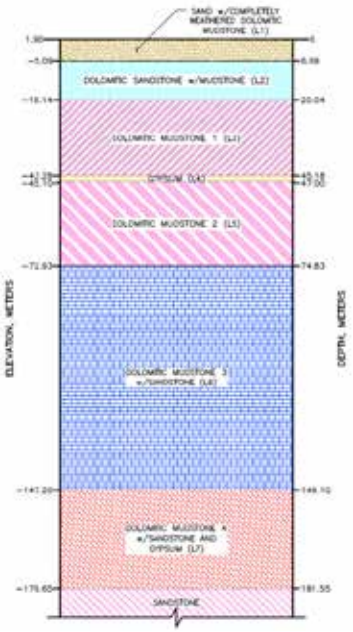

Figure 1. Typical Subsurface Profile (Parashar 2013).

In-situ testing included borehole pressuremeter tests, and hydraulic conductivity tests (packer) at selected intervals. Pressuremeter tests were used to measure the in situ rock mass modulus which was used for evaluation of the anticipated settlement of structures and the behavior of foundations. The test intervals focused on the primary foundation influence zone extending to depths approximately 1.5 times the foundation width. Other areas were also selected if weaker layers or layers of interest were encountered.

Packer testing was conducted in selected borehole locations, in order to obtain direct measurements of in-situ hydraulic conductivity of distinct geologic layers. Tests conducted within the same layer in adjacent boreholes aimed to evaluate lateral variability of hydraulic conductivity within the same layer.

Piezometers or monitoring wells were installed in certain boreholes for continuous monitoring of the groundwater levels. Upon completion of drilling, in-situ testing, and piezometer installation where applicable, the boreholes were grouted with a cement bentonite grout.

Soil and rock core samples were visually characterized in the field following conventional field classification methods. Rock core samples were placed in wooden boxes, depths recorded, and photographs of the core boxes taken. The samples were stored in a temperature controlled area for the duration of the site characterization program.

2.2 Geophysical Investigation

A suite of surface and borehole geophysical surveys were conducted during the site characterization stage in three Phases. Overall, these included:

- On-shore P-wave and S-wave surface seismic reflection surveys, and offshore geophysical profiles,
- P-S suspension logging, downhole seismic velocity surveys, AT surveys, and induction/natural gamma logging,
- Combined P-S suspension logging, borehole deviation, dual induction, caliper, natural gamma, and acoustic televiewer surveys in depths varying from 30 m to 175 m in boreholes across the site.
- Crosshole seismic logging conducted in the two pairs of boreholes near the reactor center points, to a total depth of approximately 100 m while maintaining test intervals of 1.5 m.
- Downhole seismic surveys were conducted within two boreholes near the reactor center points, to depths of approximately 150 m and at 1.5 m vertical test intervals.

Considering that the upper sections of the boreholes through the surficial sand deposits and upper weak or sloughing rock layers, the surveys were only conducted in the stable rock, therefore excluding the overburden soil layers.

The purpose of the geophysical surveys was to determine rock dynamic and geophysical properties that were in turn used to evaluate the site's seismic response, subsurface layer continuity, and identify any potential weak zones in the subsurface profile. An example geophysical profile from a randomly selected borehole is shown in Figure 2.

2.3 Laboratory Testing

The field site investigation techniques were supplemented by an array of soil and rock sample laboratory testing program.

The laboratory tests on soil samples consisted mostly of soil index property tests conducted on specimens recovered from SPT samples. These included particle-size analysis of soils, Atterberg limits, and Unified Soil Classification System (USCS).

Rock core samples were tested for index and static properties, dynamic properties, chemical and mineral properties. Index and static properties included unit weight, natural moisture content, specific gravity, permeability, unconfined compressive strength (UCS), UU triaxial compression, one-dimensional swell test on a limited number of samples, and classification based on Unified Rock Classification System (URCS). Dynamic property testing included Resonant Column Torsional Shear (RCTS), and Free-Free Resonant Column test. Laboratory tests for chemical properties included sulfate ion and chloride ion content, pH, and resistivity tests. Finally, petrographic and X-ray Diffraction (XRD) and Fluorescence (XRF) tests were carried out for determination of the mineral properties of selected rock core samples.

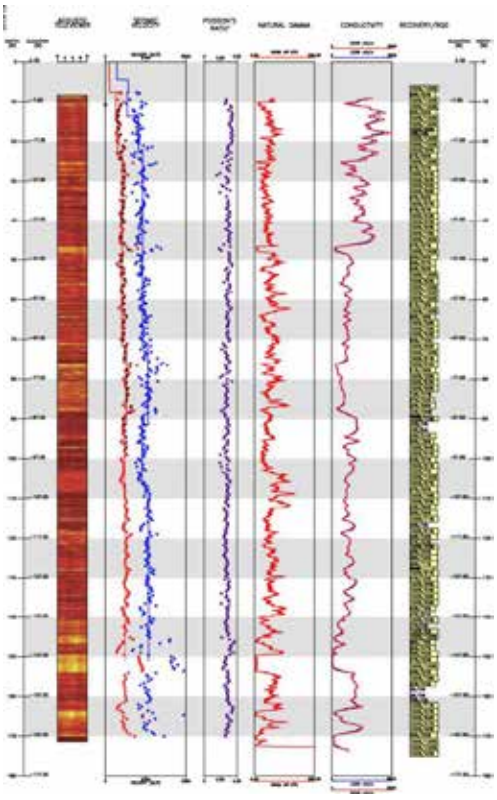

Figure 2. Example Geophysical Profile (Parashar 2013).

3 TYPICAL PROFILE AND ENGINEERING PROPERTIES

3.1 General Site Stratigraphy

The results of the geotechnical and geophysical surveys carried out during all phases of the site investigation indicated a generally homogeneous site profile. The site is a coastal site in the Western Region of Abu Dhabi, and the ground surface elevations range from El. 0 m to El. +3.0 m.

The site generally consists of a layer of an unconsolidated carbonate sand – silty sand layer, up to 8 m thick, underlain by sedimentary rock deposits consisting of dolomitic mudstone, siltstone, and sandstone locally interlayered with crystalline gypsum lenses or nodules. A simplified generic subsurface profile is shown in Figure 1. The subsurface profile and geotechnical properties have also been reported by Parashar et al (UAE, 2013) and Parashar et al (Singapore, 2013).

3.2 Overburden Soils

The overburden soils generally consist of fine to medium grained native silty sand deposits and low to non-plastic silt. A thin layer of completely weathered mudstone encountered at the top of the rock layer was also considered as part of the overburden soil layer.

The SPT N-values of the overburden sand layer ranged from 1 to 100 with an average of ~ 30. The peak friction angle was approximately 33 degrees.

3.3 Underlying Rock

3.3.1 *General*

The underlying sedimentary rock deposits encountered generally comprised very weak to weak rocks, with the exception of the crystalline gypsum. The rock deposits predominantly consist of dolomite, mostly encountered as dolomitic mudstone, dolomitic sandstone. The mudstone encountered on site is typically very weak to weak, light yellowish gray, slightly to moderately weathered, and is often encountered with inclusions of crystalline gypsum (Fig. 3).

Dolomitic sandstone is generally very weak to weak, yellowish gray, slightly to moderately weathered with bands of weakly cemented sand.

The crystalline gypsum, characterized by a fine to coarse grained crystalline structure, is mostly encountered as inclusions or distinct nodules within the dolomitic mudstone or sandstone, and also in layers of up to 4 m thick.

The average unconfined compressive strength (UCS) values of the rock column ranged between 2.4 MPa and 7.3 MPa, with the exception of the crystalline gypsum layer with an average UCS value of 9.8 MPa. Average UCS, Core Recovery and Rock Quality Designation (RQD) values for the typical rock profile are shown in Table 1.

Table 1. Rock Profile and Average Unconfined Compressive Strength Properties

Layer	Rock Type	Rock Strength Classification	UCS	Recovery	RQD
			MPa	%	%
1	Sand	Soil	-	-	-
2	Dolomitic Sandstone with Mudstone	Very Weak Rock	2.38	93	84
3	Dolomitic Mudstone 1	Very Weak Rock	3.72	91	77
4	Gypsum	Weak Rock	9.78	96	91
5	Dolomitic Mudstone 2	Very Weak Rock	3.68	91	77
6	Dolomitic Mudstone 3 with Sandstone	Very Weak Rock	4.19	80	57
7	Dolomitic Mudstone 4 with Sandstone and Gypsum	Weak Rock	7.25	91	78
8	Sandstone	N/A	N/A	100	92

Rock mass strength parameters, including Rock Mass Rating (RMR) and Geological Strength Index (GSI) were used to estimate shear strength properties of the foundation materials. Table 2 presents the average Rock Mass and Shear Strength properties of the rock column.

Table 2. Average Rock Mass Properties.

Rock Layer	RMR	GSI	m_i	D	φ'	c'
	Ave	Ave			deg	MPa
1	-	-	-	-	-	-
2	47	50	7	0.5	32	0.042
3	46	49	4	0.3	26	0.079
4	52	55	8	0.1	40	0.231
5	45	48	4	0.1	23	0.118
6	41	43	7	0	23	0.202
7	48	51	7	0	26	0.372
8	N/A	N/A	N/A	N/A	32	0.042

Figure 3. Example core box – Dolomitic Mudstone

3.3.2 *Elastic Properties*

The elastic modulus (E) and the rock mass modulus (E_{rm}) of the encountered rock layers were estimated based on data from pressuremeter tests, UCS tests, consolidation tests, and geophysical surveys (borehole geophysical tests and Resonant Column Torsional Shear and Free-Free Resonant Column Test).

The results of the in-situ pressuremeter tests were used to estimate G_p and E_p, as well as unload/reload modulus ($E_{u/r}$). UCS test results were used to obtain an estimate of E_{rm} based on the GSI, Disturbance factor, and RMR. The modulus of volumetric compressibility (m_v) obtained from consolidation tests conducted in the laboratory, was used to calculate the constraint modulus (E_c). Shear wave velocities and poisson's ratios from borehole geophysical tests were used to estimate the shear modulus (G_{max}) and the maximum elastic modulus (E_{max}). Shear wave velocities from Resonant Column tests were also used to calculate E_{max}.

Elastic moduli based on geophysical tests generally gave higher values than the rock mass modulus based on the pressuremeter test and the UCS. The unload/reload modulus ranged from 1.1 to 3.1 times the initial elastic modulus from pressuremeter tests, and between 3 and 13 times the E_{rm} from UCS results and RMR. Due to the significant difference between the different moduli, the estimated in situ strain in the rock is important in order to use the most appropriately representative values of elastic modulus. Table 3a and Table 3b present the average Elastic Moduli values based on the different methods described above.

Table 3a. Average Elastic Modulus Values Based on Geophysical Tests and qu (Units: MPa)

Layer	E (from Vs profiles and dynamic lab test results)				E_{rm}
	Geophysical	RCTS	UFRCT	Avg.	(from qu)
2	500	291	248	346	350
3	1046	690	376	704	380
4	1852	-	-	1403	1001
5	1075	1135	473	894	388
6	1633	537	581	917	332
7	1580	2962	-	2271	638
8	-	-	-	-	-

Table 3b. Average Elastic Modulus Values Based on Pressuremeter and Consolidation Tests (Units MPa)

Layer	E (from Pressuremeter Tests)			Ec (from Consolidation Test)	Erm, (recommended)
	Initial, Ei	Unload/ Reload E_{ur}	E_{ur} / E_i		
2	398	1235	3.1	58	500
3	646	1600	2.5	65	1046
4	2876	3089	1.1	-	1852
5	794	1989	2.5	54	1075
6	1892	4211	2.2	-	1633
7	1599	2567	1.6	107	1580

Considering that the elastic moduli obtained from in situ shear wave velocity measurements are less likely to be affected by drilling disturbances, these values are considered more appropriate for use in settlement analysis.

4 ESTIMATED ENGINEERING PERFORMANCE

One of the representative engineering performance assessment comes from analysis of the static stability of structures, involving the estimation of both the bearing capacity and settlement, calculated using established soil mechanics theories.

4.1 Bearing Capacity

The bearing capacity of major safety-related structures at BNPP required that foundation materials shall have the capacity to support the bearing pressure with a Factor of Safety (FOS) of 3.0 for static conditions, and FOS of 2.0 for dynamic and seismic loads.

The geometry and loading on the structures foundations were considered, along with the geotechnical profile and material strength properties presented in Table 1, and global and local shear failure modes were considered in the analysis. The resultant FOS against bearing capacity failure consistently exceeded the minimum required FOS of 3.0 for static and 2.0 for dynamic conditions, for all structures.

4.2 Settlement

Settlement analysis for the major safety related structures at BNPP was performed using a widely used finite element software (PLAXIS), considering the elastic material properties and subsurface profile presented above.

Two different soil models were used in the finite element software to represent the subsurface profile, both of which utilized the recommended elastic modulus values presented in Table 3a and Table 3b above. The first approach utilized the Mohr-Coulomb soil model, which assumes a linear-elastic, perfectly plastic behavior of the subsurface profile. The second approach utilized the Hardening Soil approach, which accounts for stress-dependency of the stiffness moduli, which represents the stiffening soil behavior as a function of depth and thus increased pressure. In the Hardening Soil model, the stiffness is described using the initial stiffness E_{50}, the unloading stiffness E_{ur}, and the oedometer loading stiffness E_{oed} which serves to represent the stress dependency of the elastic moduli.

The maximum estimated settlement under each NPP unit ranged from 54 mm when the Hardening Soil model was used, to a maximum of 78 mm when the Mohr-Coulomb model was used.

The foundation settlement monitoring program that commenced from the time of placement of base raft of major safety-related structure, and is continuing throughout the construction of the structures and installation of equipment, indicated a maximum of 4.9 mm settlement in September 2015 when construction of Unit 1 is nearly completed. The measured settlements is approximately 10 times less than the estimated settlement, indicating that the estimated elastic modulus properties are significantly lower than the actual properties of the in-situ rock. A potential justification for the substantial underestimation of the predicted settlements would be the intrinsic conservatism within all parameters, most importantly the elastic modulus parameters. Further studies and back-analyses would be required to examine the degree of the underestimation of the engineering properties that result in significantly larger estimated settlement as compared to observed behavior at site.

5 CONCLUSIONS

Geotechnical site characterization adopting conventional drilling, in-situ tests, lab tests and geophysical testing were conducted at the civil nuclear power plant site in Barakah, Western Region, Emirates of Abu Dhabi, UAE. Using the input data obtained in the geotechnical site characterization, engineering performance was estimated. The estimated engineering parameters show that the site has sufficient capacity to support the bearing pressures under static and dynamic conditions, and that the anticipated settlement was

well within the acceptable limits. Settlement monitoring results are in the order of 10 times less than the estimated settlements, indicating that the site was conservatively characterized, and the site characterization meets the safety goal for nuclear power plant.

6 REFERENCES

Emirates Nuclear Energy Corporation website *www.enec.gov.ae*

Parashar, S., Asprouda, P., Al Hammadi, H. & Lee, J.D., 2013, Geological, geotechnical, and geophysical conditions encountered at three distant sites across Abu Dhabi Emirate, UAE, 2nd International Conference of Engineering Geophysics, Al Ain, UAE.

Parashar, S., Rice, R. L., and Lee, J., 'Design, Construction and Performance of an on-shore cum off-shore cut-off wall adjacent to Arabian Gulf,' Advances in Geotechnical Infrastructure, 18th Southeast Asian Geotechnical Conference cum Inaugural AGSSEA Conference Singapore 2013, Leung, Goh & Shen ed., p.269-274

Theme 10. Characterisation in Rock and Residual Soil

Geotechnical and Geophysical Site Characterisation 5 – Lehane, Acosta-Martínez & Kelly (Eds)

Continuous-interval seismic piezocone testing in Piedmont residuum

S.S. Agaiby
Geosystems Engineering, Georgia Institute of Technology, Atlanta, GA, USA

E. Cargill
ConeTec Investigations, Charles City, VA, USA

T. Ku
Civil & Environmental Engineering, National University of Singapore, Singapore

P.W. Mayne
Civil & Environmental Engineering, Georgia Institute of Technology, Atlanta, GA, USA

ABSTRACT: Results from continuous-interval seismic piezocone testing (CiSCPTu) are reported for a test site located on the Georgia Tech campus that is situated in the Appalachian Piedmont geologic province and underlain by residual fine sandy silts to silty fine sands weathered from gneiss, schist, and granite. The CiS-CPTu uses an electro-mechanical auto hammer to deliver repeated impact-type seismic waves that are picked up while the penetrometer is advancing. Filtering and post-processing of signals and waves are required for the interpretation of wavelets. The derived profile of shear wave velocity is found to be in good agreement with conventional seismic cone tests (SCPT) and Rayleigh wave (e.g., MASW) measurements performed at the site.

1 INTRODUCTION

1.1 *Shear Wave Velocity*

A fundamental parameter of the ground is the shear wave velocity (V_s) which can be measured in the field using either invasive and/or non-invasive geophysics, as well as obtained on small lab specimens. Shear waves can be measured in all geomaterials ranging from clays and silts to sands and gravels and mixed soil types, as well as fractured to intact rocks, and man-made ground (e.g., compacted fills, mine tailings). Thus, it serves as an excellent benchmark in comparing stiffness and stress state in most geotechnical applications. In-situ V_s profiling can provide a preliminary means to evaluate soil properties, such as unit weight (Moon et al. 2015), stress history (Mayne 2005), and undrained shear strength of clays (Agaiby & Mayne 2015). The shear wave profile is a necessary input for static and dynamic geotechnical analyses since it directly provides the small-strain shear modulus:

$$G_{\max} = G_0 = \rho_t \cdot V_s^2 \quad (1)$$

where ρ_t is total mass density that is evaluated from:

$$\rho_t = \frac{\gamma_{sat}}{g_a} \quad (2)$$

and the saturated unit weight is evaluated from:

$$\gamma_{sat} = \frac{G_s + e_0}{1 + e_0}\gamma_w \quad (3)$$

where G_s is soil's specific gravity, e_0 is void ratio, γ_w is the unit weight of water = 9.81 kN/m^3 and g_a is acceleration due to gravity = 9.81 m/sec^2. The initial shear modulus (G_{max} or G_0) represents the fundamental stiffness and the beginning of the stress-strain-strength curve of the geomaterial under study. While its magnitude can be determined on small laboratory specimens from undisturbed samples (e.g., resonant column, ultrasonics, bender elements, and/or triaxial tests with local strain sensors), these approaches have several issues, specifically: sampling disturbance difficulties (Tatsuoka 1992), loss of ageing and diagenesis effects (Anderson & Stokoe 1978), and stress relief (Landon et al. 2004). Hence, V_s is best measured in-situ rather than in the laboratory.

1.2 *Shear Wave Velocity Measurement Techniques*

In-situ methods for the measurement of shear wave velocity can be classified into two main categories: invasive and non-invasive methods (Wightman et al. 2003). Invasive methods include cased borehole methods such as: crosshole test (CHT), downhole test (DHT), uphole test (UHT), and P-S suspension logger, as well as direct push methods: seismic cone penetra-

tion test (SCPT) and seismic flat dilatometer test (SDMT) that are efficient versions of the DHT mode, in addition to continuous-interval seismic piezocone testing (CiSCPTu) which is discussed in this paper.

Non-invasive methods include refraction survey, reflection survey, and surface wave methods that use either active sources to measure Rayleigh waves, including: spectral analyses of surface waves (SASW), multi-channel analyses of surface waves (MASW), and continuous surface wave method (CSW), or passive source techniques, such as passive surface waves (PSW)/microtremor array measurements (MAM) or reflection microseis (ReMi).

2 CONTINUOUS SHEAR WAVE GENERATION

2.1 *Introducing the Rotoautoseis*

The conventional geophysical techniques carried out in boreholes such as crosshole and downhole tests are relatively slow and sometimes inconvenient as they require a number of procedures including: rotary drilling, installation of plastic casing, grouting, slope inclinometer, and positioning of geophones for seismic readings. Many of these obstacles are overcome using direct-push technologies such as SCPT or SDMT where the vertically-propagating horizontally-polarized shear wave velocity, or V_{sVH} mode, is measured at regular intervals of 1m without the need for drilled-cased-grouted boreholes. However, direct-push techniques usually generate the V_s profile at 1-m intervals as the advancing probe stops at the rod breaks which can affect the resolution and the quality of the measured shear wavelets. To obtain a more detailed clear successive continuous shear wave velocity profile with a higher resolution and expedited shorter field testing time, a portable automated triggering system named “rotoautoseis” has been developed and introduced by Mayne and McGillivray (2008). Together with an enhanced data acquisition system, the automatic seismic surface source can generate consistent repeatable strikes via an electromechanical gear system per every 1 to 10 seconds. Additional details with basic schematic and diagrams of the rotoautoseis are presented by McGillivray and Mayne (2008).

The automated impulse source system can be used with conventional piezocone testing to generate continuous shear waves during the standard penetration rate of 20 mm/sec. Thus, all readings (q_t, f_s, u_2, V_s) are collected during non-stopping cone pushing and the test is called continuous-interval seismic piezocone test (CiSCPTu).

Since a significantly larger number of shear wavelets are generated and measured, a consequence is that more sophisticated and elaborate techniques are needed for interpreting the signals and evaluating the shear wave velocity profile data. Careful post-processing analyses are required to handle errors from noisy signals, overlapping refracted and reflected wavelets, and readings taken over very short distance intervals. A brief description of the post processing procedure for continuous shear wave profiling is presented in this paper with fuller details presented elsewhere (Ku & Mayne 2012; Ku et al., 2013a, 2013b).

3 SITE DESCRIPTION

3.1 *Georgia Tech W21 Test Site*

The test site is located in the middle of the Georgia Tech campus at parking lot W21 near the intersection of Hemphill Street and Ferst Drive in Atlanta, Georgia, USA. The state of Georgia is composed of four separate geologic areas, as illustrated in Figure 1: Piedmont; Blue Ridge, Coastal Plain, and Valley & Ridge /Plateau. As such, the natural soils and rocks, as well as compacted fills made from native geomaterials in these regions, can behave somewhat differently from each other because of their geologic origins. Atlanta is located in upper northwestern part of the state.

We can group the Appalachian Piedmont and Blue Ridge together due to their similarity. At one time, a range of mountains over 12 km in height dominated the region but have since essentially vanished due to extensive erosion, weathering, decomposition, and exposure to the elements over many millennia (Chew 1993). Parent bedrock is comprised primarily of gneiss and schist of Pre-Cambrian Z-age, with lesser amounts of igneous intrusives (granites) that appeared in Paleozoic times. The remaining terrain and ground conditions are underlain by residua that were derived by the in-place weathering of the metamorphic and igneous bedrock. The residual soils are often found to be silty, ranging from micaceous fine sandy silts to silty fine sands, that transition with depth to saprolites, partially-weathered rocks, and bedrock refusal. Locally, the layman's term for the upper few centimeters of native soils are called "Georgia red clay" due to the red-orange-tan colors due to iron oxides.

4 IN SITU TESTING PROCEDURE

Both invasive and non-invasive techniques were conducted at the W21 parking lot test site at the Georgia Tech campus for quantifying the shear wave velocity profile with depth. Figure 2 presents the schematics of the 3 geophysical methods conducted at the test site: (a) downhole test (DHT) via ASTM D 7400 using seismic piezocone testing with a large 25-tonne cone truck, (b) non-invasive multi-channel analyses of sur-

face waves (MASW) test measuring Rayleigh waves; and (c) continuous-interval seismic piezocone test (CiSCPTu) with an autosource.

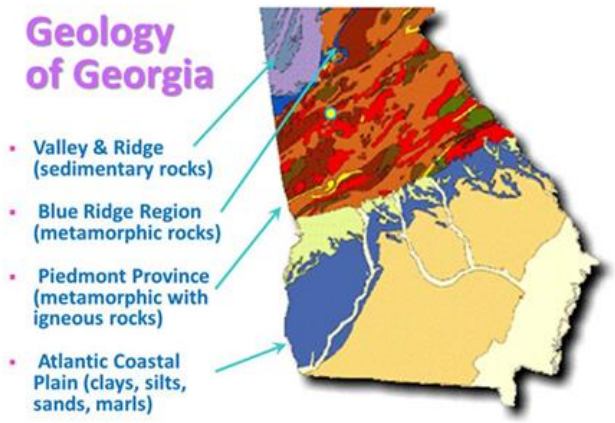

Figure 1. Geology of the state of Georgia.

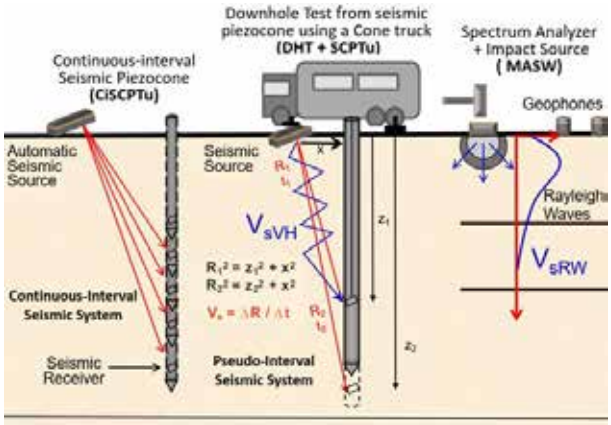

Figure 2. Schematic of different geophysical methods measuring V_s: Continuous-interval seismic piezocone test, Pseudo-interval seismic piezocone test, and non-invasive multi-channel analyses of surface waves test.

For the CiSCPTu carried out in 2015, a series of successive shear wave measurements were obtained using a rotoautoseis, a 15 cm^2 cone with a biaxial geophone positioned 0.2 m above the cone tip, and an equipped cone truck. The automated triggering system

provided uni-directional strikes for the series of continuous shear waves where it was situated at ground level with a horizontal offset of about 1m from the CPT rod string axis. Figure 3 presents successive raw shear wave signals recorded from special continuous-push where with the continuous pushing and advancement of the piezocone, shear wavelets are generated at the ground surface every 5 seconds.

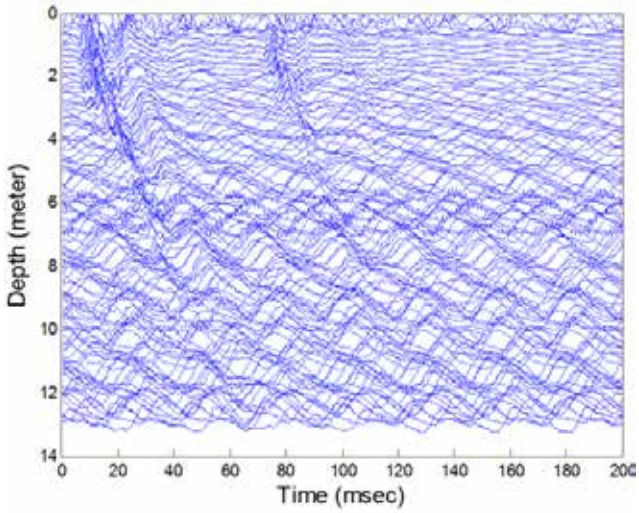

Figure 3. Successive raw continuous shear wave data from automatic seismic source at the Georgia Tech W21 test site.

The same cone truck and cone were used in conducting two standard seismic piezocone soundings (SCPTu-01 and SCPTu-02) with pseudo-interval arrays at 1-m depth intervals where paired sets of left and right strikes were accomplished using a sledge hammer and beam arrangement. Figure 4 presents the filtered 1-m interval paired left and right strike raw shear wave signals from SCPTu-01 that are used in evaluating the shear wave velocity profile. Downhole-type shear wave velocities can be calculated using the path length difference over a known time interval as shown in Figure 2. The results of the seismic piezocone readings (q_t, f_s, u_2, and 1-m interval V_s) from both soundings are presented in Figure 5 with a great agreement between the two soundings. Of additional note, SCPTu-01 was conducted in 2014 while SCPTu-02 performed in 2015.

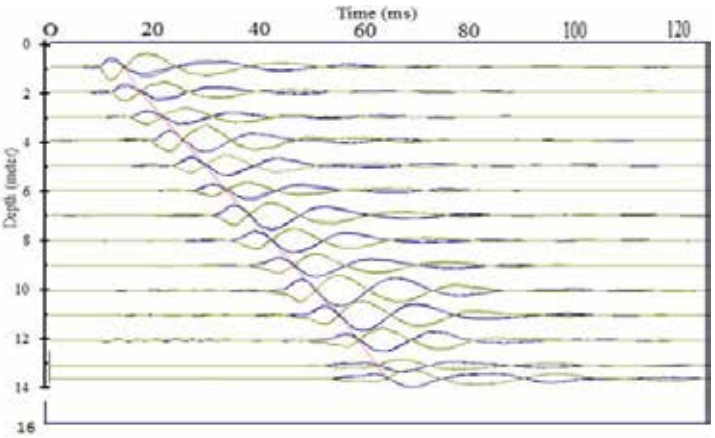

Figure 4. Filtered 1 m interval paired (left and right strike) shear wave signals from SCPTu-01 at the Georgia Tech W21 test site.

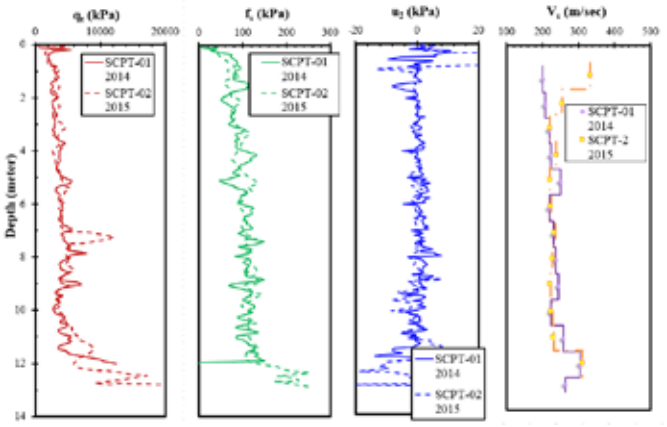

Figure 5. Results from conventional SCPTu soundings at Georgia Tech W21 test site: (a) cone tip resistance, (b) sleeve friction, (c) porewater pressure, and (d) shear wave velocity.

For the non-invasive MASW carried out in 2014, a spectrum analyzer with an impact source provided with 24 geophones were used in conducting the test. The geophones were equidistant at the ground surface and a sledge hammer was used to produce the surface wave and in seconds the wavelets were sensed using the geophones and recorded onto an on-site computer. The downhole shear wave velocity profile derived from the MASW test is plotted in Figure 6. This is shown in comparison with the conventional V_s profile from downhole testing at 1-m intervals from both soundings SCPTu-01 carried out in 2014 and SCPTu-02 carried out in 2015. It can be seen that the profiles of tests carried out in 2014 (i.e., MASW and SCPTu-01) show very good agreement, with values generally increasing from 200 m/s to about 300 m/s in the interval from the ground surface to about 13 meters. While for SCPTu-02, a clear increase in the magnitude of downhole shear wave velocity can be observed within the crust top 4 meters that can be attributed to the possibility of capillarity, desaturation, or effective stress changes in the vadose zone (soil above water table which was found to be at a depth of 12.5 meters in the location under study) where soils in unsaturated states may have an increase in the V_s at shallow depths (Cho & Santamarina, 2001).

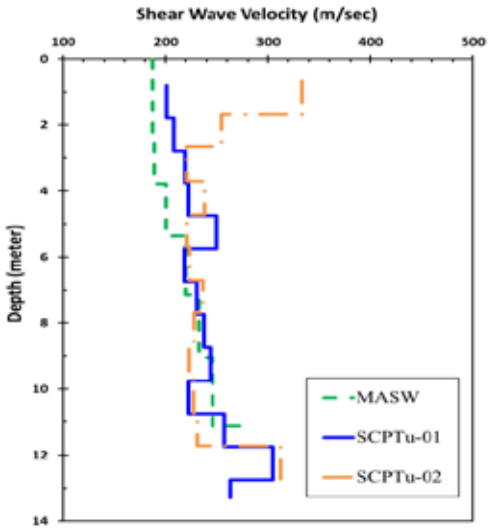

Figure 6. Downhole results showing a comparison of invasive (SCPTu) and non-invasive (MASW) shear wave velocity measuring techniques at the Georgia Tech W21 test site.

4 CONTINOUS SHEAR WAVE VELOCITY EVALUATION

4.1 *Signal Processing*

Shear wave time series signals should first be detrended and then filtered in order to eliminate any noise or interference in the measured wavelets. Detrending is a statistical operation for removing abnormal unexpected trends or any signal distortion such that the detrended raw data signals approach a baseline value. Filtering should be carefully conducted at the lowest possible level in both time and frequency domains to reduce the noise level (Santamarina & Fratta 1998, Ku et al. 2013a). In the current study, noise levels were mitigated using a band-pass filter to capture the desired frequency range of interest as presented in Figure 7 where a low- and high-cutoff frequency filter ranging from 150Hz to 350Hz was applied on the basis of visual examinations of fluctuations in signals.

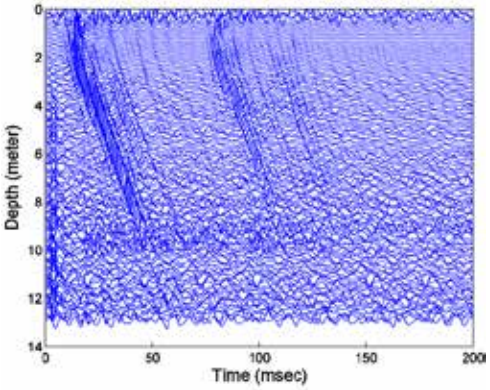

Figure 7. Successive continuous shear wave data after applying a band filter ranging from 150Hz to 350Hz.

After applying a band-pass filter to the raw wavelets, windowing was used to minimize the effect of spectral leakage of the data (Santamarina & Fratta 1998) and to provide better V_s evaluations for the cross correlation method (Liao & Mayne 2006). Figure 8 shows the filtered successive continuous shear wavelets after windowing where only the zone of interest for the expected main shear wave remains. Typically, a combined window using both a rectangular window for the majority of the signal and a hamming window for the tailing areas is applied.

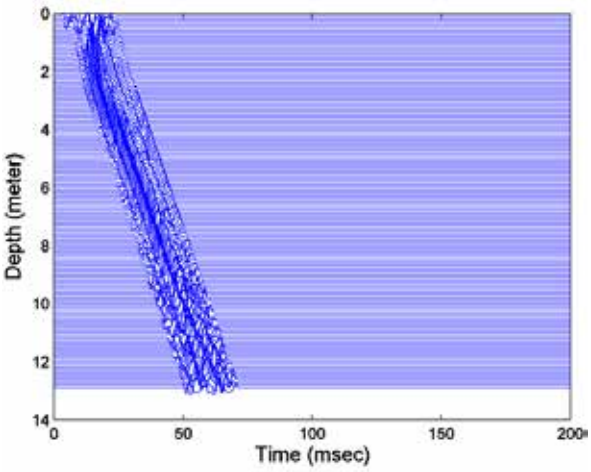

Figure 8. Successive continuous filtered shear wave data with window

After detrending, filtering, and windowing are completed, the cascaded continuous shear waves are evident and can be used for evaluating the shear wave velocity profile with depth. The simplest method in signal post processing and evaluation involve manually choosing the first arrival, first peak, and/or first crossover point. However, these manual methods are time consuming in the field work where paired opposite strikes are needed for the crossover and also time consuming in the evaluation process where the points are visually picked. Accordingly, cross correlation in the time domain and cross-spectral analysis in the frequency domain can be adopted using coded software packages such as MATLAB which is convenient in handling large amounts of data and can provide finer higher quality results.

4.2 *Cross Correlation Analysis in the Frequency and Time Domain*

This technique is usually recommended when successive wavelets have the same nature and characteristics, such as those that are generated with the rotoautoseis. The cross correlation function is used to evaluate the time shift between two independent wavelets by finding the lag time corresponding to the maximum covariance or maximum cross correlation in the time domain. The function reaches a maximum value when two consecutive signals that have similar shapes either overlap or coincide (Ku et al., 2013b).

The cross-spectral analysis is a technique used to identify the correlation between two time series at given frequencies (e.g., peak frequency). The analysis provides a phase spectrum in the frequency domain allowing the calculation of time shifts and phase velocities between two different wavelets. More details on the analysis technique can be found in Ku et al. (2013a, 2013b).

4.3 *Obtaining Final Corrected Continuous V_s Profile*

After applying both the cross-correlation and cross-spectral analyses on the filtered successive continuous shear wavelets, the results were somewhat sensitive and scattered. This can be attributed to different factors and issues that arise during the in-situ testing procedure, or also in the post-processing analyses such as the extremely short time lapse, cone penetration test rate variants, unfiltered noise, and the possibility of refracted and reflected signals. Hence, to obtain a representative corrected V_s profile with depth, a running-mean filter coefficient vector for the time interval (Δt) is applied for the V_s profiles obtained from both analyzing techniques. A special zero-phase forward and reverse digital filtering technique is used following the recommendations of Trauth (2010). By increasing the order of the running-mean filter (10^{th} in the presented study), a more accurate and a less scattered V_s profile with depth is obtained.

4.4 *Comparison of V_s Evaluation Methods*

Figure 9 shows the evaluated V_s profiles with depth for the different testing techniques carried out at the Georgia Tech test site. Both of the derived continuous V_s profiles using cross-correlation and spectral analysis seem to match well with the reference downhole test using the SCPTu and the MASW test data when adopting the 10^{th} order running mean filter. By comparing the different methods, a slight difference in the shear wave velocity magnitude can be observed which be attributed to time effects causing possible desaturation or water level fluctuations that can cause an increase in the shear wave velocity magnitude over time. Despite the presence of some minor deviations, all four evaluation methods show overall good agreement in the V_s profiles.

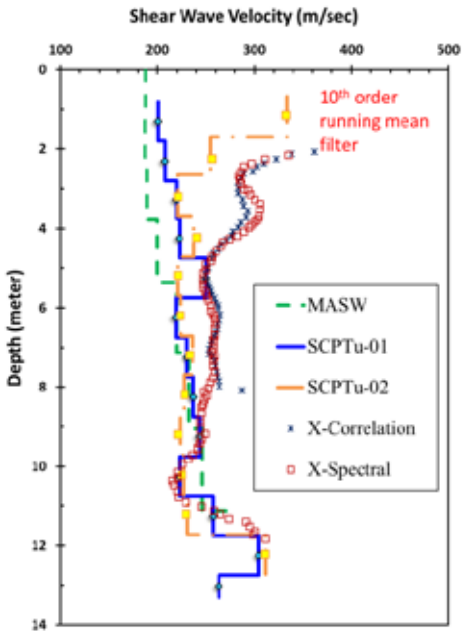

Figure 9. Downhole results showing a comparison of various shear wave velocity measuring techniques: MASW, SCPTu, and CiSCPTu using x-correlation and x-spectral methods.

5 SUMMARY AND CONCLUSIONS

A new W21 test site at the Georgia Tech campus was used to compare different geophysical techniques for measuring shear wave velocity profiles with depth in residual sandy silts to silty sands of the Appalachian Piedmont geology. The non-invasive technique of MASW test was carried out using 24 geophones measuring shear wave velocity from Rayleigh wave measurement with depth. Invasive techniques carried out at the test site included 2 conventional downhole tests (DHT) via SCPTu soundings (conducted two years apart) using a large cone truck and a pseudo-interval seismic system. In addition, a continuous-interval seismic piezocone test (CiSCPTu) using the electromechanical rotoautoseis to provide repeatable strikes approximately every 5 seconds.

The successive raw shear wavelets were detrended, filtered, and windowed. The filtered shear waves were analyzed using both the cross correlation method in the time domain and the cross-spectral analysis in the frequency domain, followed by the application of a high order running-mean filter. Both methods provided very comparable and consistent results when compared to the conventional 1-m interval downhole data and the non-invasive MASW data.

The successive signals generated by the continuous-push seismic system every 0.1 m are finer and more accurate with lower scatter, providing better more detailed resolution that can be used in geologic profiling.

6 REFERENCES

Agaiby, S.S. & Mayne, P.W. 2015. Relationship between undrained shear strength and shear wave velocity for clays., Proceedings of the 6th International Symposium on Deformation Characteristics of Geomaterials, Buenos Aires, Argentina), Vol. 6, IOS Press, Rotterdam: 358-364.

Anderson, D. G., & Stokoe, K. H., 1978. Shear modulus: A time-dependent soil property. *Dynamic Geotechnical Testing*, Special Technical Publication 654, American Society for Testing & Materials, West Conshohocken, PA: 66-90.

Chew, V.C. (1993). Underfoot: a geologic guide to the Appalachian Trail. second edition, *Proc. Appalachian Trail Conference*, Harpers Ferry, West Virginia, 237 p.

Cho, G.C. & Santamarina, J.C. 2001. Unsaturated particulate materials-particle-level studies. *Journal of Geotechnical and GeoEnvironmental Engineering*, 127(1): 84-96.

Ku, T. & Mayne, P.W. 2012. Frequent-interval SDMT and continuous SCPTu for detailed shear wave velocity profiling in soils. *Geotechnical Engineering Journal*, 43(4), South East Asian Geotechnical Society: 34-40.

Ku, T., Mayne, P.W & Cargill, E. 2013a. Continuous-interval shear wave velocity profiling by auto-source and seismic piezocone tests. *Canadian Geotechnical J.* 50(1): 382–390.

Ku, T., Weemees, I., Cargill, E., Mayne, P.W. & Woeller, D. 2013b. Post-processing continuous shear wave signals taken during cone penetrometer testing. ASTM *Geotechnical Testing J.* 36(4): 543-553.

Landon, M.M., DeGroot, D.J. & Jakubowski, J. 2004. Comparison of shear wave velocity measurements in-situ and on block samples of a marine clay. *Proceedings of the 57th Canadian Geotechnical Conference (GeoQuebec 2004):* Session 4E: 22-28.

Liao, T. & Mayne, P.W. 2006. Automated post-processing of shear wave signals, *Proc. 8th US National Conference on Earthquake Engineering*, San Francisco, pp. 460.1-460.10

Mayne, P.W. & McGillivray, A.V. 2008. Improved shear wave measurements using autoseis sources. *Deformational Characteristics of Geomaterials*, Vol. 2 (Proc. 4th ISDCG, Atlanta), Millpress/IOS Press, Amsterdam: 853-860.

Mayne, P.W. 2005. Invited keynote: Integrated ground behavior: in-situ and lab Tests, *Deformation Characteristics of Geomaterials*, Vol. 2 (Proc. IS Lyon'03). Taylor & Francis Group, London, UK: 155-177

McGillivray, A.V. & Mayne, P.W. 2008. An automated seismic source for continuous shear wave profiling. *Geotechnical & Geophysical Site Characterization,* (Proc. ISC-3, Taipei), Taylor & Francis Group, London: 1347-1352.

Moon, S.W., Khan, Q., & Ku, T. 2015. Shear wave velocity based estimation of soil unit weight and undrained shear strength on soft ground. *Proc. International Conference on Soft Ground Engineering (ICSGE2015)*, Research Publishing, Singapore: 853-861.

Santamarina, J.C. & Fratta, D. 1998. *Introduction to Discrete Signals and Inverse Problems in Civil Engineering*, ASCE, Reston, VA.

Tatsuoka, F., 1992. Deformation characteristics of soils and rocks from field and laboratory tests. *Proc. 9th Asian Regional Conf. Soil Mechanics and Foundation Engrg.*, 2, 101-170.

Trauth, M.H. 2010. *MATLAB Recipes for Earth Sciences*, 3rd ed., Springer, New York.

Wightman, W., Jalinoos, F., Sirles, P., & Hanna, K., 2003. Application of geophysical methods to highway related problems, *Report No. FHWA-IF-04-021*, Federal Highway Admin., Washington, DC: 742 pp.

Geotechnical and Geophysical Site Characterisation 5 – Lehane, Acosta-Martínez & Kelly (Eds)

Assessment of Results of CPT Tests in Porous Lateritic Unsaturated Soil from Campinas, Brazil

P.J.R. Albuquerque
University of Campinas, Campinas, Brazil

T.G. Rodriguez
Geoprova Engineering Testing and Monitoring, Campinas, Brazil

ABSTRACT: This work is an analysis of the results obtained by means of mechanical (Begemann Cone) and electric cone penetration tests (CPT) performed in porous, unsaturated lateritic soil from the subsoil of the Experimental Site of Soil Mechanics and Foundations of the University of Campinas (Unicamp), State of São Paulo, Brazil. To this goal, a campaign of three mechanical and three electric CPTs was performed down to the depth of 10 m, which is the limit to get to the rocky massif. The local subsoil is characterized by a 2 m thick surface layer of silty-clayey sand, followed by a layer of silty sand. The average porosity of the local subsoil is approximately 62% and the index of voids is 1.64. Readings of the parameters of both tests indicated low dispersion (q_c, f_s, R_f) in the section between 2 m and 8 m. Variability in the initial section was high. The application of the abacus to classify the soil behavior by means of mechanical cone displayed some dispersion in the results. However, in the electric cone tests, the abacus displayed a good classification. All propositions that were used identified the transition from the surface soil to the residual soil between 7 and 8 m.

1 INTRODUCTION

Over the last few years, the scenario of national engineering, in Brazil, has changed significantly. Expressive investments have been made both in infrastructure works and in civil works. Economic stability and the growing confidence in the Brazilian market led to a massive injection of foreign capital. In this scenario, interchange of methods and technologies has found greater acceptance in the field of engineering, with a strong marketing appeal. This is different from the scenario of some years ago when only the academic community was interested in geotechnical tests, except for SPT.

The presence of foreign companies and investments has led to co-participation of designers and consultants both from Brazil and from abroad. This has brought about technical enrichment and the Brazilian market needed to meet these new expectations. In this context, geotechnical tests such as CPT and particularly CPTU have gained strength nationwide, following the global trend.

In this context, there is lack of information on the possibility of using these tests as safe tools to produce stratigraphic and geotechnical parameters either directly or indirectly by means of correlations, particularly when dealing with tropical lateritic porous unsaturated soils. Pournaghiazar, et al (2013), Collins & Miller (2014) and Yang & Russel (2016) pointed this problem, concerning the suction influence in CPT parameters, specially concerning the correlations with soil parameters.

Therefore, the intent of this work is to analyze the results obtained from mechanical and electric CPT tests conducted at the Experimental Site of Mechanics of Soils and Foundations of the School of Civil Engineering of Unicamp, in Campinas city.

Another purpose of this work is to check, for the Campinas typical tropical lateritic soil, the adequacy of stratigraphic characterization standard methods, despite their potential problems regarding the unsaturated condition, once the methods were created for the saturated and/or dry soil conditions, as noted by Pournaghiazar, et al (2013).

2 GEOTECHNICAL CHARACTERISTICS

The Experimental Site is located within the city of Campinas, State of São Paulo, Brazil. It measures approximately 600 m², being composed of soils in an unsaturated and "porous", tropical condition with collapsible characteristics. The first studies developed in this

site were performed by Gon (2011), followed by Rodriguez (2013), who performed geotechnical characterization tests of the area both in laboratory and in situ tests. Figure 1 shows a simplified geological profile of the Experimental Site obtained from an in situ testing program of Standard Penetration Test (SPT) performed by Rodriguez (2013). This figure shows that the range of results increase below 8 m, perhaps as a function of the proximity of the mother rock strata (with variable depth within the site). This figure briefly summarizes the results from laboratory tests conducted by Gon (2011). The water table level was not found down to the impenetrable lawyer (approximately 10 m). It must be noted that the values of the fraction of sand, silt and clay were obtained by means of joint granulometry tests with no use of deflocculant.

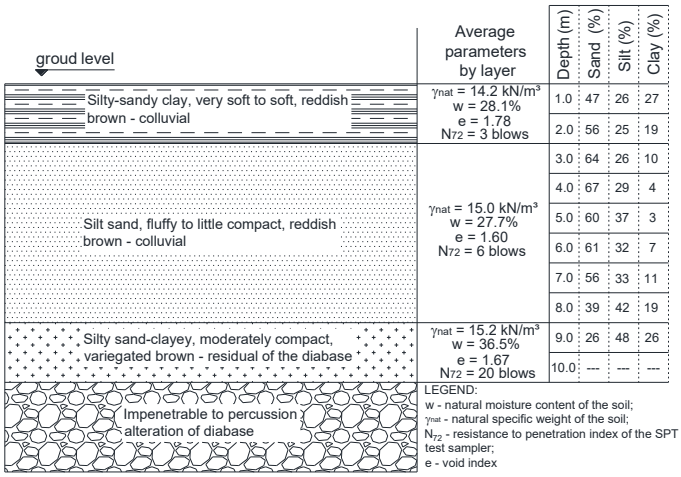

Figure 1. Simplified typical geological profile of the FEC – Unicamp Experimental Site.

2 CPT TESTS

In order to build the database of this work, three CPT-M (mechanical) tests were performed using the Begemann cone per recommendations of ASTM D3441-05 and three CPT-E (electric) tests with the use of Geoprobe instrumented cone per recommendations of ASTM D5778-12. The test site at the Experimental Filed of the School of Civil Engineering, Architecture and Urbanism (FEC) is shown in Figure 2.

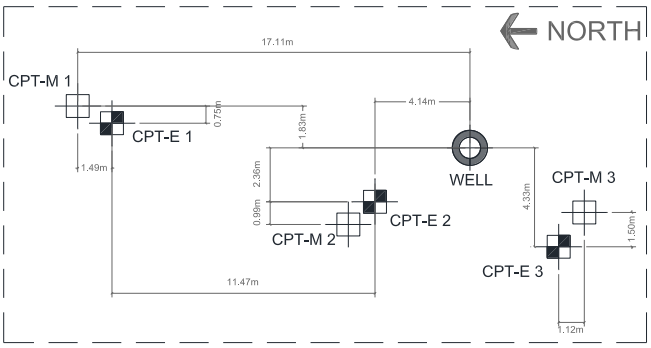

Figure 2. Location of the tests performed in the Experimental Field (Rodriguez, 2013).

2.1 *Results*

Based on the results of the tests, it is possible to observe the variation in resistance of the cone, of lateral friction and of the fact of friction (Figures 3, 4 and 5). The results indicated low dispersion in the readings of the parameters qc, fs and RF (%), particularly at the depths between 2 m and 8 m. The first meter displayed high variability, probably as a function of the dryness of the surface layer. This fact was also observed in the section below 8 m, where the values indicated greater dispersion as a function of the proximity to the rocky top, which had various depths.

Considering that qt = qc (due to u2 = 0), via Figure 3 it is possible to see that the mean values of cone resistance obtained both in mechanical and in electric tests displayed little variation among them. The qc (CPT–M) / qt (CPT – E) ratio was approximately 1.0, with variation coefficient (CV) in the order of 16 %.

As to the values of unit lateral friction, fs, shown in Figure 4, it was noted that the values obtained via CPT–M produced higher values than CPT–E. It must be noted that down to the depth of 6 m, a high value between the fs (CPT–M) / fs (CPT–E) ratio was recorded, i.e., a value in the order of 16, with variation coefficient (CV) of 80%, which indicated high dispersion. From 6 m down to the maximum depth of the tests (9.6 m), the mean value of the ratio was approximately 2.0 with a variation coefficient (CV) of the order of 40%. As the values of lateral friction displayed different trends for each test procedure, the values of RF also varied, as shown in Figure 5.

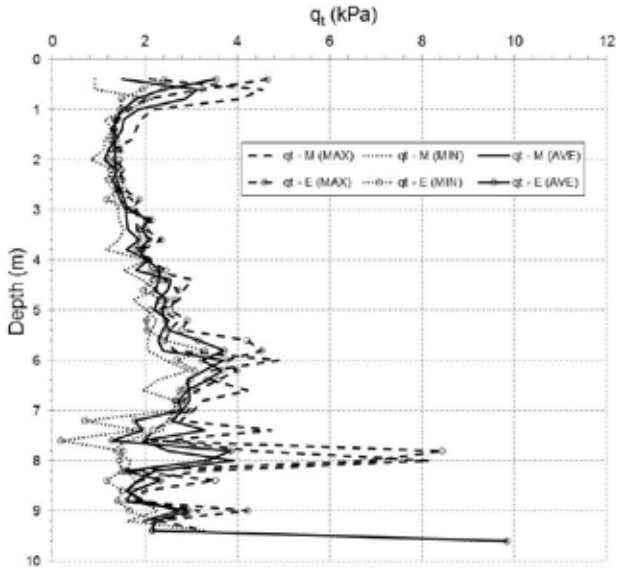

Figure 3. Variation of qt in depth.

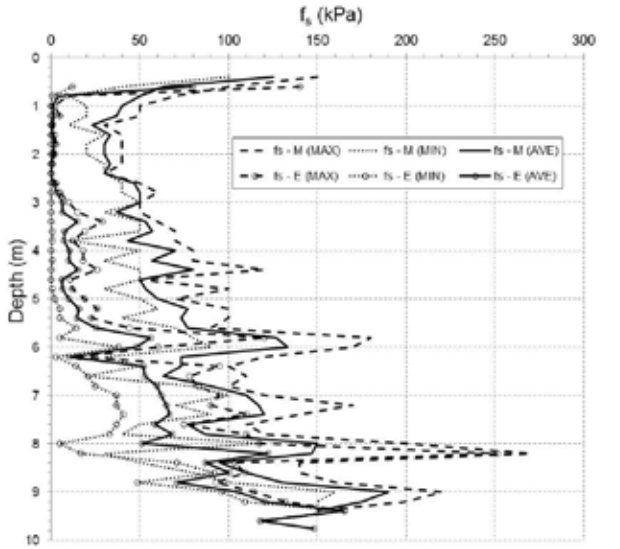

Figure 4. Variation of fs in depth.

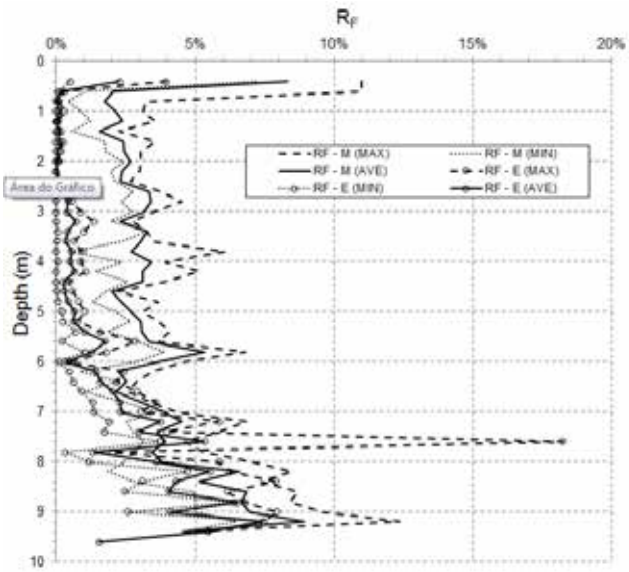

Figure 5. Variation of R_F in depth.

3 SOIL PROFILING

One of the possibilities of the use of CPT tests is to identify the horizons of the stratigraphic profile through the mechanical behavior of the soil when the cone is driven. The proposals of Begemann (1965) and Schmertmann (1969) were used to get the data from CPT-M. The proposals of Douglas & Olsen (1981), Robertson et al. (1986), Eslami & Fellenius (1997) and Robertson (1990) were used to get the data from CPT-E.

Figure 6 shows a summary of the results obtained with the application of the abacus of Begemann (1965). It must be pointed that, when using this abacus, a high concentration of points in the area of low accuracy of the graph was observed and this made it impossible to make the stratigraphic definition of the soil under study.

As to the abacus of Schmertann (1969), it was found that the points were distributed in a manner that made it possible to identify the horizons more clearly and classify the soil. Table 1 shows the results obtained with the use of the abacus of Schmertmann (1969). It was also found that the results showed mostly soil with silty behavior down to the depth of 6 m. Below this depth, the soil displayed clayey characteristics. It was possible to identify the transition of the behavior of the layers in the mean depth of 7-8 m in agreement with the granulometric analyses without Gon deflocculant (2011).

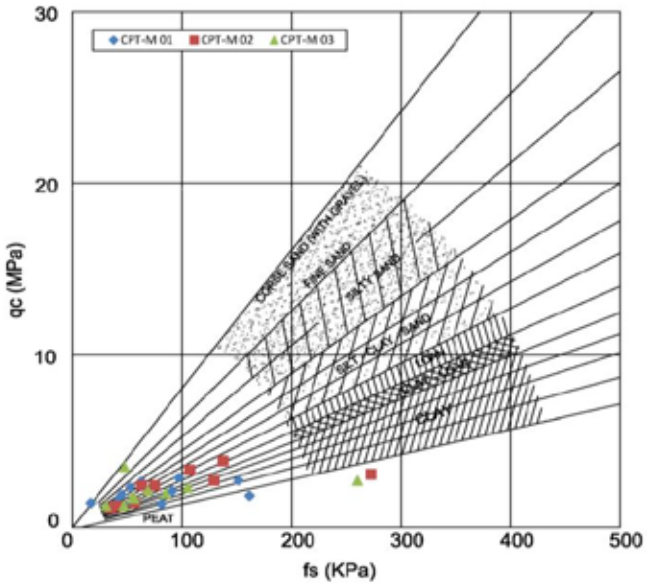

Figure 6. Soil classification by Begemann (1965).

Table 1. Soil classification by Schmertmann (1969).

Depth (m)	CPT-M 1	CPT-M 2	CPT-M 3
1	3	3	1
2	3	2	3
3	3	2	2
4	2	2	2
5	4	3	2
6	3	2	2
7	2	2	2
8	1	3	1
9	1	-	1
10	-	-	-
SBT	Description		
1	Clay		
2	Sandy and Silty Clay		
3	Clayey Sand and Silt		
4	Sand		

Using the data of the CPT-E tests, it was possible to apply the abacus of Doulgas & Olsen (1981), Robertson et al. (1986), Eslami & Fellenius (1997) and Robertson (1990) (Tables 2, 3, 4 and 5).

Table 2. Soil classification by Doulgas & Olsen (1981)

Depth (m)	CPT-E 1	CPT-E 2	CPT-E 3
1	3	3	3-2
2	3	3	3
3	3	3	3
4	3	3	3-2
5	3	3	3
6	3-2	3	3
7	3-2	3	3-2
8	2-1	2	3-2
9	3-2	2-1	2-1
10	-	1	2
SBT	Description		
1	Clay		
2	Silt		
3	Sand		

Table 3. Soil classification by Robertson et al. (1986)

Depth (m)	CPT-E 1	CPT-E 2	CPT-E 3
1	7	7	7
2	6	7-6	7-6
3	7-6	6	6
4	7-6	7-6	6
5	7	7	7-6
6	7-6	7	7-6
7	7-5	7-6	7-6
8	5-4	6-4	6-5
9	8-7	3	6-3
10	-	3	3

SBT	Description
3	Clay
4	Clay to Silty Clays
5	Silty Clays to Clayey Silt
6	Clayey Silt to Sandy Silt
7	Sandy Silt to Silty Sand
8	Silty Sand to Sand

According to the abacus proposed by Douglas & Olsen (1981), CPT-E 1 found two different layers: one from 0 to 5 m with sandy behavior and the second one 6 m down with sandy silty behavior. CPT-E 2 found three layers: the first one from 0 to 7 m with sandy behavior; the second one from 8 to 9 meters with silty to silty-clayey behavior, and the third one 10 m down with clayey behavior. The CPT-E 3 test found two layers: the first one from 0 to 8 m with sandy to silty sandy behavior and the second from 9 m down with silty behavior. The proposition of Douglas & Olsen (1981) led to identification of the behavior of sandy to silty-clayed layers at the mean depth of 7 to 8 m in CPTE-02 and CPTE-03 tests in agreement with the granulometric analyses without Gon deflocculant (2011). In the CPTE-01 test, the interface of the layers was seen at 5 m. The behavior of the second layer detected by the proposition was dispersed among the tests, and the result of the application of CPT-E 1 and CPT-E 3 was closer to the one obtained by Gon (2011).

Table 4. Soil classification by Eslami & Fellenius (1997)

Depth (m)	CPT-E 1	CPT-E 2	CPT-E 3
1	5-3	5-4	5-4
2	5	5-4	5-4
3	5	4	5-4
4	5	4	4-3
5	5	4	4
6	5-4	4	4
7	4-3	4	4
8	3	4-3	4
9	4	3-2	3
10	-	3	3
SBT	Description		
2	Soft Clay - Soft Silt		
3	Silty Clay - Hard Clay		
4	Silty Sand - Sandy Silt		
5	Sand - Gravel		

Table 5. Soil classification by Robertson (1990)

Depth (m)	CPT-E 1	CPT-E 2	CPT-E 3
1	6	7	8-6
2	-	6	6
3	-	6-5	6-5
4	-	5	5
5	6	5	5
6	5-4	5	5
7	5-4	5	5
8	4-3	4-3	4-3
9	5-4	3	4-3
10	-	3	3
SBT	DESCRIPTION		
3	Clays to Silty Clays		
4	Clayey Silts to Silty Clays		
5	Silty Sand to Sandy Silt		
6	Clean Sand to Silty Sand		
7	Stony Sand to Sand		

Table 5 is a summary of the classifications produced by the application of the abacus of Robertson et al. (1986). According to the methodology proposed by the authors, CPT-E 1 displayed three different layers: the first one from 0 to 7 m with silty behavior, the second one at 8 m with clayey to silty-clayey behavior, and the third one from 9 m down, with sandy behavior. CPT-E 2 displayed three layers: the first one from 0 to 7 m with silty behavior, the second from 8 to 9 m with silty to clayey behavior and the third one from 10 m down, with clayey behavior. CPT-E 3 displayed three layers: the first one from 0 to 7 m with silty behavior, the second one from 8 to 9 m with silty to clayey behavior, and the layer from 10 m down with clayey behavior. With the use of the abacus of Robertson et al. (1986), it was possible to differentiate the behavior of two layers interfacing at 7 m, in agreement with the indications of Gon (2011) in the granulometric analyses without deflocculant. The behavior of the first layer was that of sandy-silty to silty soils and the second layer was classified as silty-clayey to clayey soils.

Table 6 shows the results obtained according to the abacus of Eslami & Fellenius (1997). It was found that the CPT-E 1 test detected two different layers: the first one from 0 to 6 m with sandy to silty-sandy behavior, and the second one from 7 m down, with silty-sandy to silty clayey behavior. CPT-E 2 test displayed two layers: the first one from 0 to 7 m with sandy to silty sandy behavior, and the second one from 8 m down with silty-clayey to clayey behavior. CPT-E 3 test displayed two layers: the first one from 0 to 8 m with sandy to silty sandy behavior, and the second one from 9 m down, with silty clayey to clayey behavior. In general, the method of Eslami & Fellenius (1997) detected behaviors close to the one obtained by Gon (2011). It also distinguished the behavior of two layers, with interface at 7 m in average.

Table 7 shows the results of the application of the abacus of Robertson (1990). It was possible to observe that it was difficult for CPT-E 1 test to classify between 0 and 4 m due to the low values of RF obtained; silty and clayey behavior was seen from 6 to 9 m. In the CPT-E 2 test, the analyses indicated two layers: the first one from 0 to 7 m with sandy to silty behavior, and the second one from 8 m down, with silty to clayey behavior. CPT-E 3 test found two layers: the first one from 0 to 7 m with sandy to silty behavior, and the second one from 8 m down, with silty to clayey behavior. In general, the first layer, as characterized by the proposition of Robertson (1990), was similar to the results obtained by Gon (2011); however, the lower layers displayed clayey soils, contrary to the results of Gon (2011), same as the methodology of Robertson et al. (1986). It must be pointed out that these two methods presented the SBT (Soil Behavior Type) of the soils under analysis. It is advisable to assess several aspects such as soil fractions, clay contents, LL, LP, among other aspects to produce a more accurate diagnosis of the behavior of the material.

5 CONCLUSION

No differences were detected among the values found in the mechanical and electric tests for the values obtained via cone resistance (qt). This demonstrates the reliability of both methods.

A significant difference was observed in the behavior of lateral friction (fs) of the cone when the two types of tests (mechanical and electrical) are assessed. Down to the depth of 6 m (the layer with the highest index of voids and also with marked laterization), the differences were of the order of 16 times, whereas in the lower section, the differences were of the order of 2 times. This shows that this parameter is sensitive to the type of soil formation found. Therefore, attention must be paid to indiscriminate use of this parameter.

As for the data obtained from the mechanical cone test, it was difficult to use the abacus of Begemann (1965). This fact was not observed in the abacus of Schmertmann (1969). However, these abacuses were used only so that the results obtained with the mechanical cone could be applied, thus making it possible to make a comparison with those obtained with the electric cone.

The use of the CPT test to identify horizons of the stratigraphic profile by means of the mechanical behavior of the soil when the cone is driven proved to be ap-

propriate when the electric cone was used. The stratigraphic profiles obtained were very close to those obtained by means of the joint granulometric test without use of deflocculant. As the massif is composed of unsaturated porous lateritic soil, the test without the use of deflocculant is the most suitable method to indicate the soil behavior. The only point to be noted is the abacus of Robertson (1990) in which stratigraphic discretization of values of Rf is very impacted, as pointed out in CPT-E 1.

Despite the most popular abacus, and/or charts, used for soil characterization were developed for saturated and/or dry conditions, it presented good relation with the laboratory results for the unsaturated lateritic Campinas soil. The results obtained made it possible to clearly identify the transition of layers between the depths of 7 m and 8 m.

It's necessary to extend this research, using a calibration chamber, to check if the suction would affect the soil characterization using the abacus (or charts) used here in.

6 REFERENCES

ASTM-D3441. 2005. *Standard test method for mechanical cone penetration tests of soil*

ASTM-D5778. 2012. *Standard test method for electronic friction cone and piezocone penetration testing of soils*

Begemann, H.K.S.P. 1965. The friction Jacket Cone as an aid in determining the soil profile. *6th International Conference of Soil Mechanics and Foundation Engineering, Proc., Montreal, Quebec, Canada*, v.1, 17-20.

Collins, R., & Miller, G.A. 2014. Cone penetration testing in unsaturated soils at two Instrumented test sites. In Proceedings of the 6th international conference on unsaturated soils, UNSAT, Sydney, Australia, Balkema, Lisse, Vol. 2, 1489-1494.

Douglas, B.J. & Olsen, R.S. 1981. Soil classification using electric cone penetrometer. *Symposium of Cone Penetration Testing and Experience, Proc., ASCE. New York*, 209-227

Eslami, A. & Fellenius, B. H. 1997. Pile capacity by direct CPT and CPTu methods applied to 102 case histories. *Canadian Geotechnical Journal*, 34 (6), 880 - 898.

Gon, F.S. 2011. *Caracterização Geotécnica Através de Ensaios de Laboratório de um Solo de Diabásio da Região de Campinas*. FEC-UNICAMP. Dissertação de Mestrado, 153pp.

Pournaghiazar, M., Russell, A.R., & Khalili, N. 2013. The cone penetration test in unsaturated sands. Geotechnique 63(14): 1209-1220.

Robertson, P.K, Campanella, R.G., Gillespie. D. & Greig, J. 1986. Use of piezometer cone data". *In-Situ 86, Specialty Conference, Proc., ASCE, Blacksburg*, 1263-1280.

Robertson, P.K. 1990. Soil classification using the cone penetration test. *Canadian Geotechnical Journal*, 27, 151-158.

Rodriguez, T.G. 2013. *Caracterização geotécnica de um solo de diabásio por meio de ensaios de SPT e CPT*. FEC-UNICAMP. Dissertação de Mestrado, 167pp.

Schmertmann J. H. 1969. *Dutch Friction Cone Penetration Exploration of Research Area at Field 5, Eglin Air Force Base, Florida, US Army Waterways Experimental Station*, *Vicksburg, Mississippi*, Contract Report S-69-4

Yang, H. & Russell, A.R. 2016. The cone penetration test in an unsaturated silty sand. Canadian Geotechnical Journal. 53(3): 431-444.

Geotechnical and Geophysical Site Characterisation 5 – Lehane, Acosta-Martínez & Kelly (Eds)

Piezocone tests in residual soils: A Portuguese experience in granitic soils.

N. Cruz, J. Cruz & F. Martins
Direção de Coordenação Técnica Rodoviária da Mota-Engil, Porto, Portugal

C. Rodrigues
Polytechnic Institute of Guarda, Department of Civil Engineering, Portugal

M. Cruz
LEMA, Mathematical Engineering Lab, ISEP, School of Engineering, Polytechnic of Porto, Portugal

ABSTRACT: The general mechanical evolution of massifs throughout weathering is mainly governed by an increasing porosity of rock material, the weakening of mineral grains and the existing bonding between grains is progressively loss. In this process, weathering degrees W_1 to W_3 are represented by sound rock where the macro-fabric plays the major influence, W_4 and W_5 represent the transition behaviour, where micro and macro fabrics have similar influence, towards a residual soil-mass where the relict macrofabric is no longer present (residual soil), with a residual interparticle cementation structure always remaining, sometimes mixed with suction effects commonly present in natural profiles. Due to this structure these materials cannot be modelled by the classical theories of Soils Mechanics, which creates several difficulties on the interpretation of in-situ test results. In the last two decades several Portuguese institutions dedicated specific frameworks to study and characterize this kind of residual massifs (in granitic environments), which are quite common in the North and Centre of Portugal. In this paper, CPTu tests performed in the granitic formations of Porto and Guarda metropolitan areas are analyzed and compared with other geotechnical tests available in Porto Geotechnical Map, which were then calibrated by the results obtained in IPG experimental site (Guarda, Portugal). In this process more than 20,000 tests were involved, including laboratory (triaxial, shear box and oedometers) and in-situ (PMT, DMT, CH and permeability) techniques

1 INTRODUCTION

Residual soils strength characterization it is not an easy task, due to its cohesive-frictional nature as well as disturbance effects related with both sampling and installation of in-situ devices. The sampling problems and the discontinuous information related to laboratory tests leave an important role to in-situ testing on routine analysis. Piezocone penetration tests are among the most widely used in in-situ characterization, offering obvious advantages over other routine in-situ tests, such as sustainable correlations with geotechnical parameters at low cost, rapid procedures, continuous recording, high accuracy, repeatability and possibility of automatic data logging. References on the subject applied to transported sedimentary soils are widely known. However, the application of these current correlations to obtain parameters of residual soils usually leads to erroneous estimations of strength and stiffness parameters. In fact, one of the main characteristics of residual soils is related to the presence of a bonding structure, which generates a cohesive intercept in Mohr-Coulomb failure criterion and the development of more than one yield stress locus and when the sedimentary procedures are applied to residual environments, certain available correlations overestimate the respective geotechnical parameter, as a result of the bonding structure influence in final determinations (Rodrigues 2003, Viana da Fonseca 1996, Cruz 2010). As a consequence of this, it is fundamental to be sure that any correlations with in-situ test parameters respond properly in these soils. The study presented herein aims to contribute to the evaluation of adequacy of CPTu current correlations to determine the geotechnical design parameters, following the path crossed with DMT tests in these soils (Cruz 2010).

In this context, Porto and Guarda regions are perfect for this purpose due to the intensive research promoted and developed by FEUP (in Porto) and IPG (in Guarda), creating a fundamental knowledge of the behaviour of these granitic soils. Furthermore, the existence of Porto Geotechnical Map (COBA 2003), here designated as PGM, provides reliable and important geotechnical information on Porto Granitic Formation, which is very useful in defining trends and supporting characterization needs. This information was analyzed by Cruz (2010) and prepared under the perspective of mechanical evolution through the weathering (Cruz et al. 2015), which is particularly

useful in the present context. Furthermore, the calibration work of Cruz (2010) with DMT tests in residual soils, based in Porto and Guarda residual soils, created a very important in-situ reference base for comparing CPTu results. In that work, after a calibration experiment performed in the high quality experimental site of Polytechnic Institut of Guarda (IPG) (Rodrigues 2003, Cruz, 2010), adaptations, corrections and new correlations were settled to derive geotechnical parameters of these soils by DMT tests. The experimental work was performed in a calibration box where DMT tests were performed in artificially cemented soils (remoulded from Guarda granitic soils), followed by triaxial testing in both artificially and naturally cemented soils, leading to a specific set of correlations with the main geotechnical parameters of residual soils. To close the cycle, DMT tests were performed in the natural massif from where the experimental samples were retrieved, which confirmed the adequacy of established correlations.

As a consequence, information obtained by MOTA-ENGIL and IPG in granitic residual environments of the North and Center of Portugal, where pairs of CPTu and DMT tests were available, was gathered to generate the present study. At the end, 8 locations were selected, where 20 pairs of tests were performed, including the well characterized experimental site of IPG that served the calibration work of Cruz (2010), mentioned above. Data arising from these tests were firstly compared and analyzed together with PGM data, at a macro-level, allowing to recognize CPTu patterns of behaviour in residual soils and evaluating the adequacy of current correlations to obtain geotechnical parameters for design. On the other hand, due to its previous calibrations DMT tests were used to compare and control, being used as a reference for representing the mechanical properties of each experimental site.

2 CHARACTERIZATION OF PORTO AND GUARDA GRANITES

In Porto, the fundamental geological unit (Porto Granitic Formation) was installed at around 10 km depth at the end of Hercinic orogeny and can be described (COBA, 2003) as a leucocratic alkaline rock, comprising quartz, biotite and muscovite with the latter prevailing, white alkali-feldspar often in mega-crystals, white sodic plagioclase, and minor amounts of dark minerals. The alkali feldspar usually presents the higher grain size and is mostly orthoclase, sometimes microcline. As for plagioclases, oligoclase-albite and albite are commonly present. Guarda granitic formation is constituted by a leucomesocratic granite with quartz, sodic and potassic feldspars commonly in mega crystals, biotite and muscovite, as well as kaolin, sericite and clorite as secondary minerals (Rodrigues 2003).

The residual soils arising from both formations are the result of mechanical and chemical weathering, respectively by means of grain dismantling and hydrolysis of K-feldspar and Na-feldspar, which lead to the formation of kaolinite clay. Biotite (and amphibole, if present) are affected by oxidation to form iron oxides and quartz and muscovite remain stable due to their high weathering resistance. The consequent soil is described as sand evolved by a kaolin matrix with frequent less-weathered rock boulders (Cruz 2010). From mechanical point of view, these granitic masses are very complex and mostly characterized by its gradation from upper levels to lower (W2) sound rock, improving its behaviour with depth. Typically, after a thin layer of top soil (usually < 3.0 m thick) the residual profile starts with a thick layer of medium compact residual soil, referenced by NSPT ranging between 10 and 30 blows (G2), which is sometimes followed by a compact transition layer corresponding to NSPT between 30 and 60 (G3). According to PGM data (COBA, 2003), the medium compact layer can reach 15 to 20m of thickness and it is common to find boulders within this soil mass. The transition layer is generally thinner than 5m. In few areas (just 3 main spots in Porto) or in small pockets dispersed in the weathered mass, more intensively kaolinized soils can be found, corresponding to NSPT lower than 10 (G1). These residual units evolve in depth to decomposed (W5) to highly weathered (W4) rock massif represented by NSPT values typically higher than 60 and further to medium (W3) to slightly weathered (W2) granite. Although this may suggests a homogeneous evolution with depth, these formations show erratic profiles, either horizontally or with depth as a consequence of variations in climate conditions, composition of the parent rock and intensity of joint systems with its influence in water penetration level. CPTu and DMT tests are only feasible in residual soils, since in the transition materials (W4 and W5) are typically characterized by NSPT higher than 60, which means that is very difficult to push-in any of the equipments into the ground.

As already referred Porto Geotechnical Map (PGM) offers a huge quantity and variety of data that was used to compare field data. This data was prepared and organized in a sense of mechanical evolution with weathering and may be consulted for more detailed analysis in Cruz (2010) and Cruz et al. (2015). In this paper, we will only refer to the intervals of parameters that can be deduced by CPTu tests and only within the geotechnical unit where the tests were performed (G2, 10<NSPT<30).

3 PRESENTATION AND DISCUSSION OF RESULTS

In terms of soil identification, PGM data reveals an expected increase of fine content and plasticity with weathering, as a result of the chemical weathering of feldspars into kaolinitic clay. According to ASTM Unified Classification, UC (D2487 1998) soils are mainly represented by silty sands (SM), while soils with high kaolin content are represented by clayey sands (SC) and silts of low plasticity (ML). Physical ranges reveal an also expected increase of void ratio (e) and porosity (n) and decreasing unit weights (γ), while permeability is not greatly influenced by the weathering degree. On its turn, strength is characterized by the presence of an effective cohesion that is due to the cemented structure, as well as a shear resistance angle arising from the granular condition of these soils. Stiffness is compatible with the ranges of strength results. In the following tables a summary of the basic, intermediate and classification CPTu parameter ranges (Table 1) is presented and the resulting geotechnical CPTu deduced parameters are compared with DMT and PGM (Tables 2 and 3).

Table 1.Basic, intermediate and classification CPTu parameters

q_t (MPa)	f_s (kPa)	u_2 (kPa)	Q_T	F_R (%)	B_q	I_c
2.5-10	100-300	-75-50	25-150	<10	-0.05-0.05	1.5-3

Table 2. Comparison CPTu, DMT and PGM results (general)

Test	γ(kN/m^3)	k (m/s)	N_{SPT}	v_s (m/s)
CPTu	17-20	10^{-6}-10^{-8}	10-30	150-250
DMT	17-20	--	--	--
PGM	17-20	10^{-6}-10^{-7}	--	--

Table 3.Comparison CPTu, DMT and PGM results (strength and stiffness)

Test	c' (kPa)	ϕ (º)	Ψ	M (MPa)
CPTu	--	34-42	-0.2 – 0.0	40-150
DMT	4 -20*	31-37*	--	40-150
PGM	< 15	33-37	--	< 25

* Obtained by applying residual correlations (Cruz, 2010)

The CPTu field data was treated and interpreted using GEOLOGICISMIKI software. As it can be observed, the corrected point resistance varies from 2.5 to 10 MPa, slightly increasing with depth, which corresponds to the expected evolution with vertical effective strength, unit skin friction ranges within 50 and 300 kPa also increasing with depth and pore water pressure decreases with depth attaining significant negative values explained for the dilatant behaviour exhibit by these soils (Fig. 1). In the plots, the residual mass lies below 3m depth, being the upper part constituted by sedimentary cover. As a consequence of this, Q_T ranges within 25 and 150, F_R is always smaller than 10% and B_q is around zero.

From classification point of view, DMT accordance with local soils has been previously revealed by Cruz and Viana da Fonseca (2006), later confirmed by PGM data (Cruz 2010). If I_c classification (Robertson 2010) is used CPTu results are very consistent with these findings, as shown in Figure 2. In the same figure unit weights obtained by DMT (Marchetti & Crapps 1980) and CPTu (Robertson 2010) are also represented, since this is a parameter with direct influence in the determination of vertical in-situ stresses and consequently in deriving strength and stiffness parameters. The plot represents the comparison between DMT, CPTu and, which reveal a high level of accuracy of both tests. The same consistency is found with the permeability (Robertson 2010) that is coincident with the in situ permeability ranges represented in PGM (Table 2). As a consequence of these findings, it can be concluded that CPTu derived results for identification and physical characterization are representative of the main residual units of Porto and Guarda granites.

On the other hand, once residual and sedimentary soils do not follow the same pattern of behaviour, it turns to be relevant detecting the presence of cementation, in order to select the adequate methodologies for obtaining the best geotechnical approaches. For this purpose, interpreted charts to detect cementation have been proposed for SPT and (S)CPTu (Schnaid et al. 2004) and (S)DMT (Cruz 2010) tests. These charts were previously applied with success to CPTu (Schnaid et al. 2004; Viana da Fonseca et al. 2007) and DMT results (Cruz 2010) obtained in the experimental sites in granitic formations nearby the Portuguese cities of Porto and Guarda. Being so, the actual data was plotted in the CPT diagram presented in Figure 3, which revealed not strongly structured soils, lying near the lower bound line for cemented materials and converging to the previous findings. Previous CPTu data from Porto granites is also plotted. It should be stressed that between the two straight lines the level of cementation is variable, increasing as one goes up in the plot. In the context of strength behaviour, the range of N_{SPT} deduced from CPTu (Robertson 2010) match perfectly with the results obtained in the field, indicating that the established correlation between the two tests is also valid in residual soils, at least in this specific environment.

The shear resistance angles deduced from CPTu data (Robertson 2010) point out to 35º to 42º, which are convergent with DMT results obtained by applying the correlation for granular sedimentary soils (Marchetti 1997) but quite divergent from the results of PGM within 33º to 37º, as revealed by Table 2 and Figure 4. In the right hand side plot of the same figure, are also represented the shear resistance profiles, obtained by applying the correction proposed for DMT tests (Cruz 2010, Cruz et al. 2014). The gap is related to the cemented structure of these soils that creates an overall resistance assumed to be purely frictional when sedimentary approaches are followed (Cruz 2010).

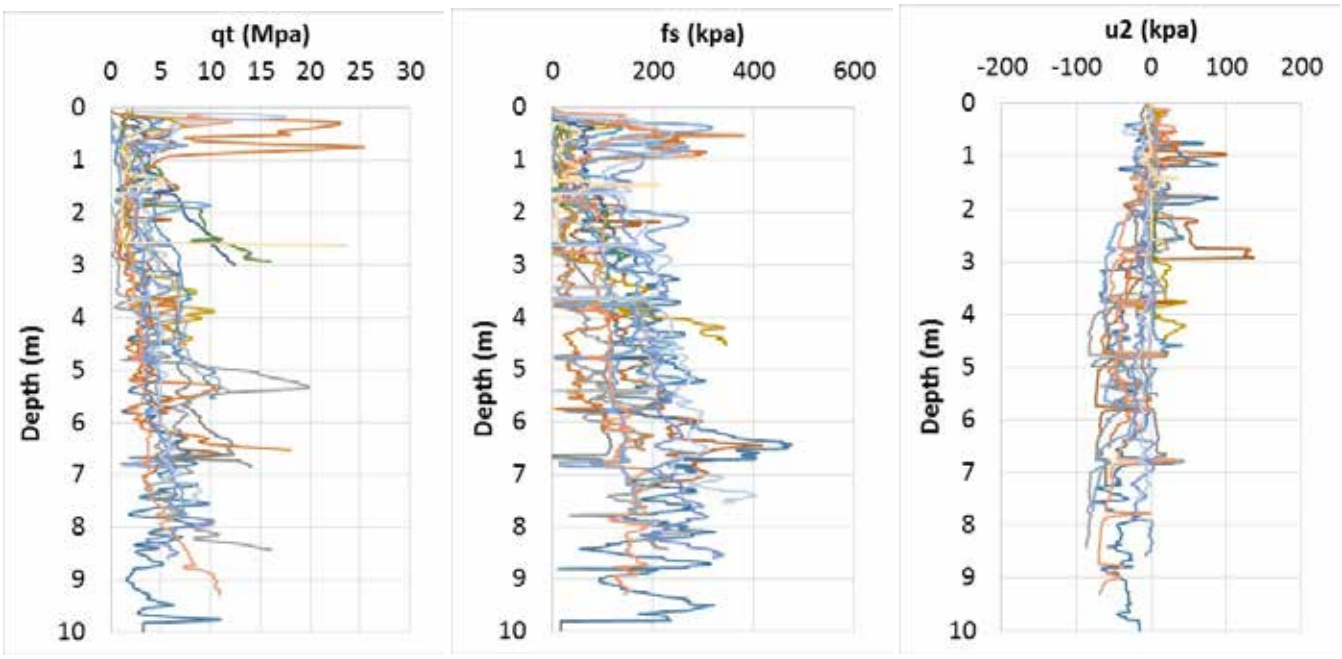

Figure 1. Evolution of CPTu basic parameters in the whole set of experiments

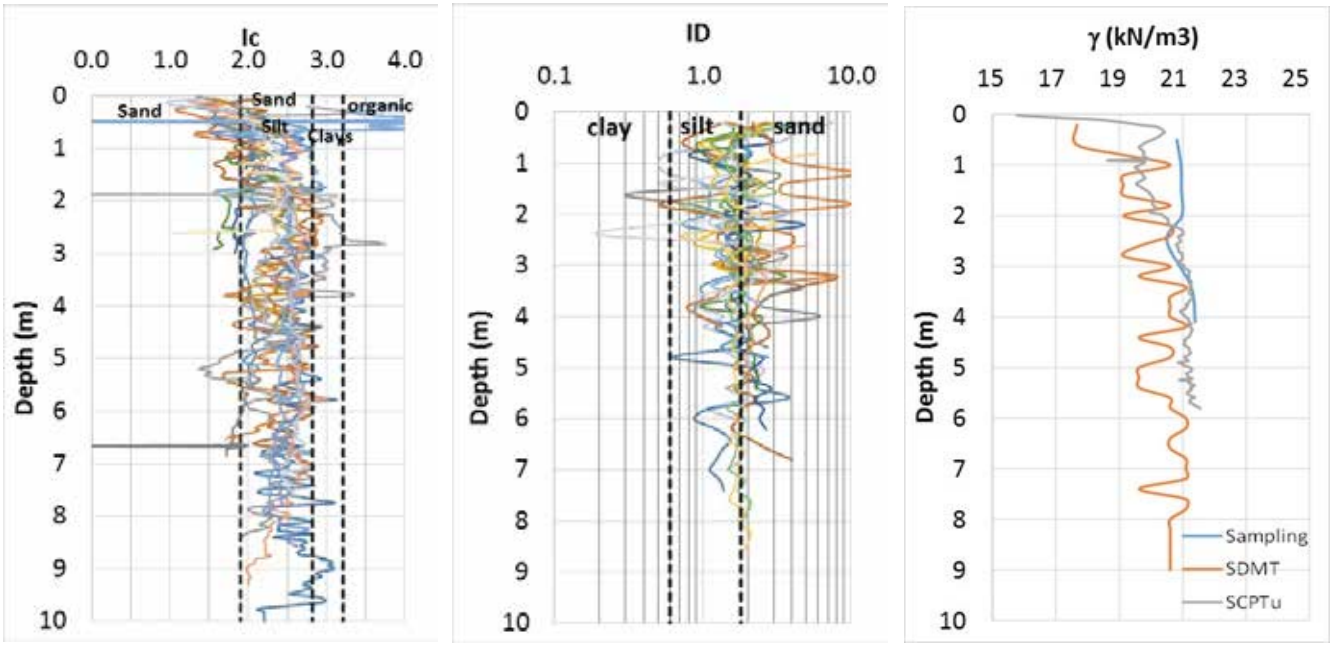

Figure 2. Identification and unit weights

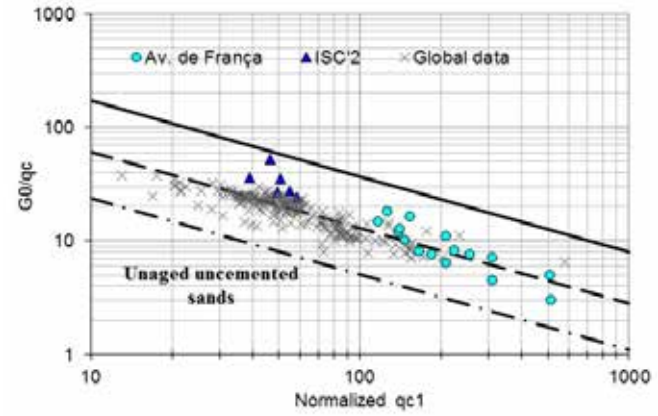

Figure 3. Cementation plot (Viana da Fonseca et al., 2007)

In terms of stiffness, the comparison is made through the constrained modulus (M), but similar behaviour can be observed when using G_0. Primarily, it is important to recognize that DMT is better suited for deducing deformability parameters, since they are based in stress and displacement measurements, while CPTu is mainly a strength test. Nonetheless, at least in the present study differences between M obtained by CPTu (Robertson 2009) and DMT (Marchetti 1980) are not significant, as shown in Figure 5. The plot on the right hand side represents an illustrative example of the convergence level between DMT and CPTu, found in this study.

On its turn, shear wave velocities deduced from CPTu data (Robertson 2010) fall within 150 and

250m/s, which fits the common register found in these soils (Fig. 6). In the central plot of same Figure, deduced velocities from CPTu results are directly compared with the velocities obtained from seismic devices incorporated in DMT and CPTu, revealing a good convergence between deduced and
real values, although the earlier are slightly higher. Another important issue in the detection of cementation can be established by using the ratio M/q_t, as proved by Cruz & Viana da Fonseca (2006) and Cruz (2010). Marchetti (1997), synthesizing the work of different authors, suggested that in sedimentary soils values of between 5 and 10 correspond to normally consolidated soils, whereas values of M/q_c between 12 and 24 would represent overconsolidated soils. In the plot on the right hand side of Figure 6, the great majority of residual values are within 10 and 15 falling in the overconsolidated interval. In this case, this ratio is somehow related with the cementation magnitude, in the same manner identified by Cruz (2010) in DMT case. A specific research framework was settled and has been carried out by MOTA-ENGIL and IPG, in the IPG experimental site (Rodrigues 2003, Cruz 2010) aiming to establish correlations to derive effective cohesion and angles for shearing resistance of these soils.

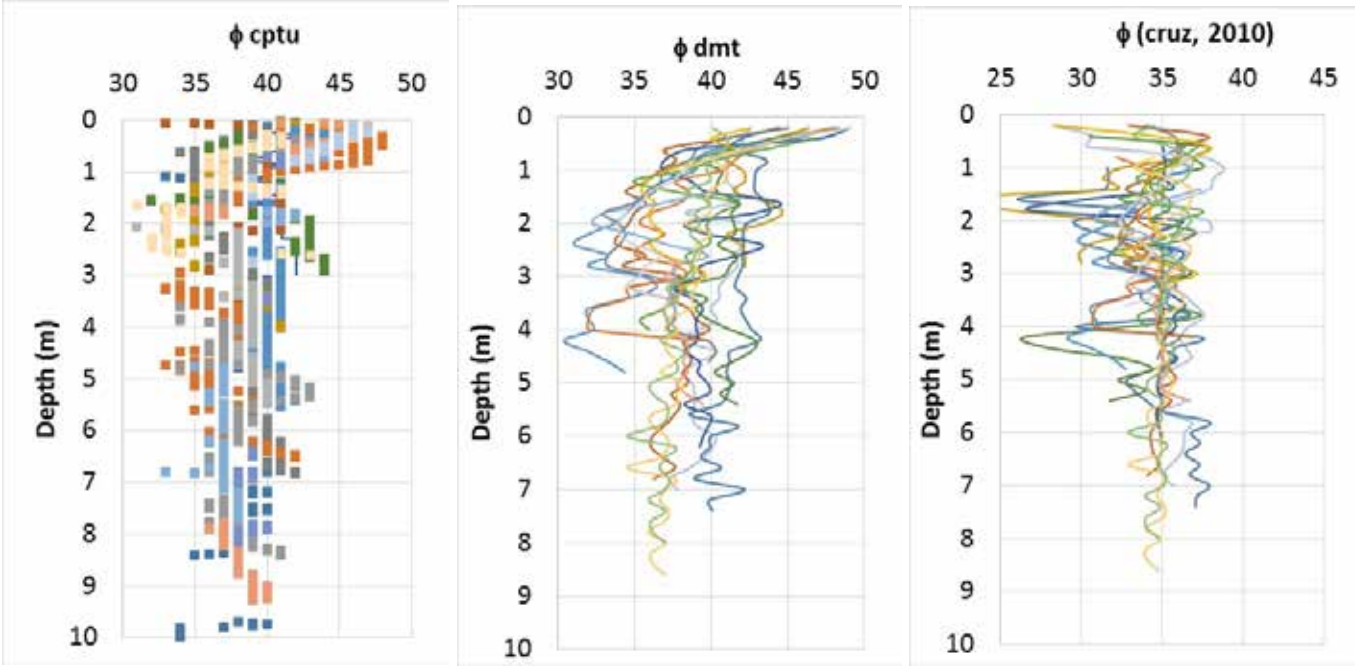

Figure 4. Strength parameters obtained from DMT and CPTu results

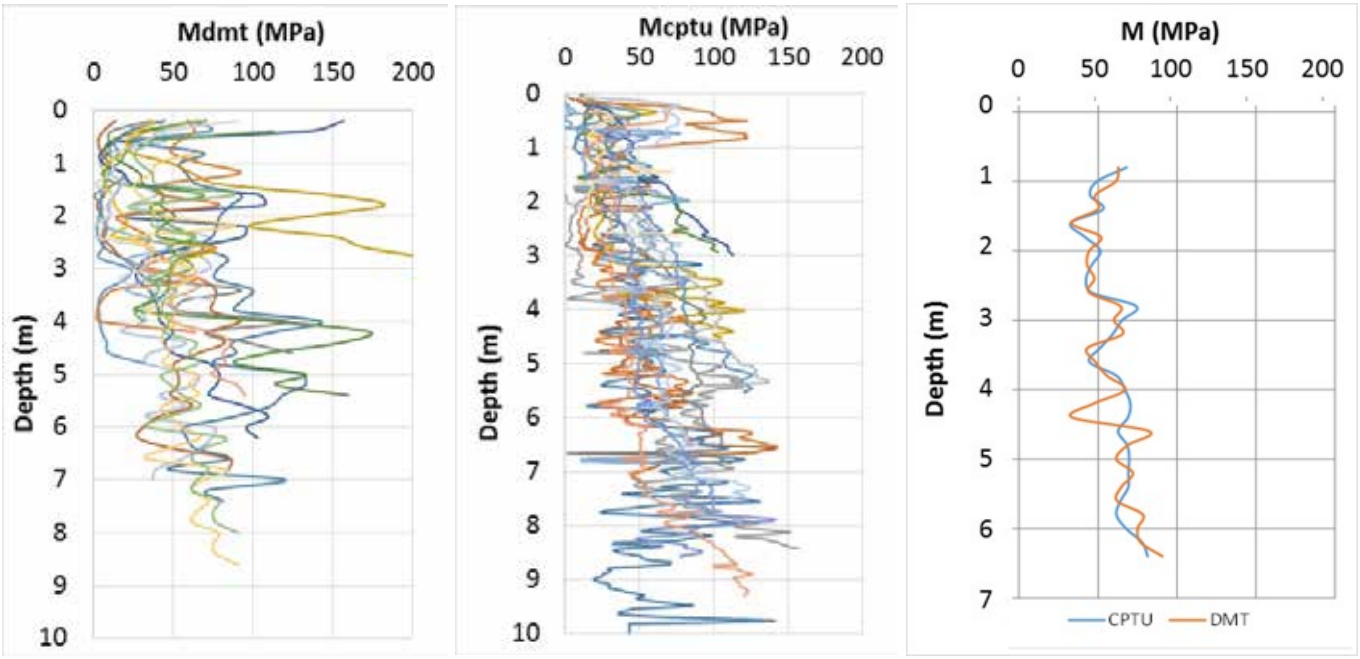

Figure 5 – Constrained modulus obtained from CPTu and DMT results

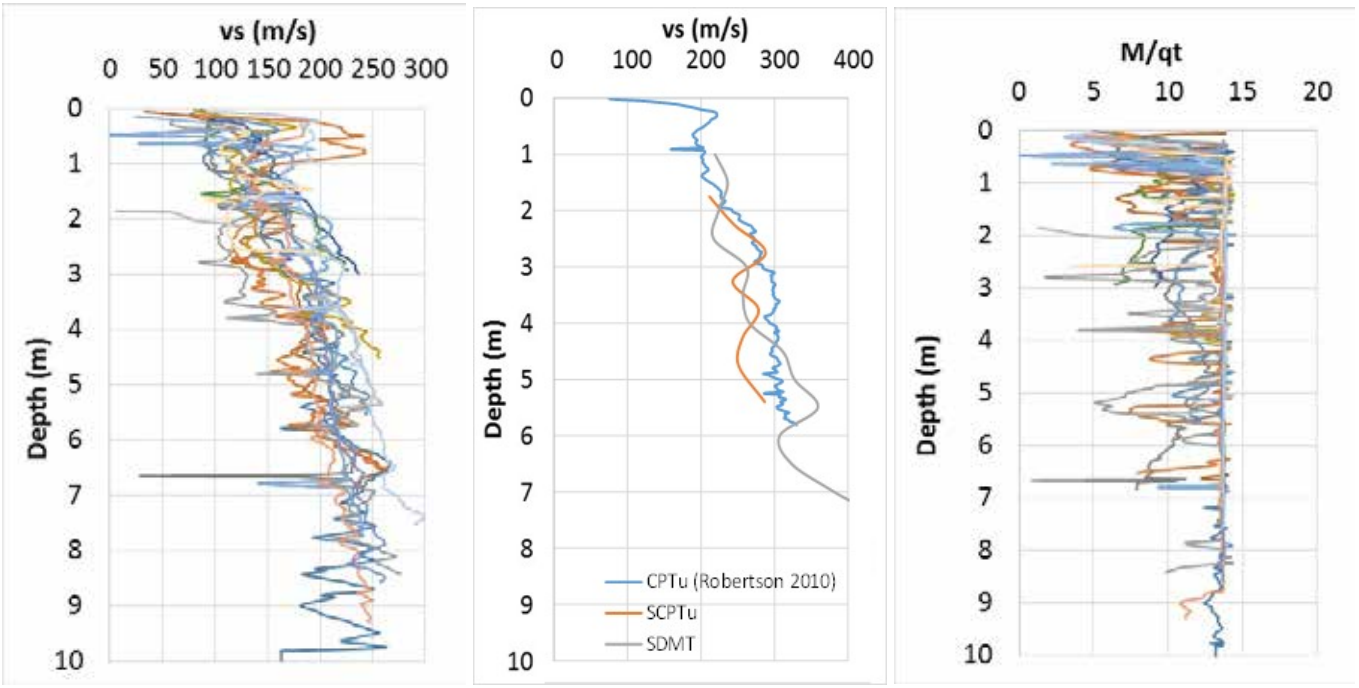

Figure 6 – Shear wave velocity and M/qt profiles

4 CONCLUSIONS

A significant volume of analyzed and treated CPTu data was compared with Porto Geotechnical Map geotechnical ranges and with DMT results obtained by following the proposals of Cruz (2010), in tests performed in pair with CPTu. The results prove that CPTu tests correctly predict most part of the main geotechnical parameter ranges, with the exception of the deduction of cohesive strength (a correlation has to be settled) and the angle of shear strength that is over predicted when sedimentary approaches are followed. The ratio M/qt seems to be an interesting parameter to solve this problem, thus a specific research program is under development in IPG experimental site.

REFERENCES

ASTM D 2487. 1998. Classification of soil for engineering purposes. *American Society for Testing Materials*.

COBA. 2003. Porto Geotechnical Map. COBA and Faculty of Sciences of University of Porto. Porto City Hall.

Cruz, N. 2010. *Modelling geomechanics of residual soils by DMT tests*. PhD thesis, University of Porto (*www.nbdfcruz.drupalgardens.com).*

Cruz, N., Gomes, C., Rodrigues, C. & Viana da Fonseca, A. 2015. An approach for improving Wesley Engineering Classification. The case of Porto Granites. *XVI European Conf. on Soil Mec. and Geot. Eng*, Edimburgh, UK

Cruz, N., Rodrigues, C. & Viana da Fonseca, A. 2014. An approach to Derive Strength Parameters of Residual Soils from DMT Results. *Soils & Rocks*, Vol.37, nº3,pp. 195-209.

Cruz, N. & Viana da Fonseca, A. 2006. Portuguese experience in residual soil characterization by DMT tests. R.A. Failmezger &and J.B. Anderson (eds), Flat Dilatometer Testing, Proc. *2nd International Conference on the Flat Dilatometer*, Washington D.C. pp. 359-364.

Marchetti, S. 1980. In-situ tests by flat dilatometer. *J. Geotechnical, Eng. Div.* ASCE, Vol. 106, No. GT3,pp. 299-321.

Marchetti, S. 1997. The flat dilatometer design applications. III *Geotechnical Engineering Conference*, Cairo University. Keynote Lecture. Vol.1, pp. 421-448.

Marchetti, S. & Crapps, D.K. 1981. Flat dilatometer manual. Internal report of GPE Inc., distributed to DMT users.

Robertson, P. K. 2009. Performance based earthquake design using the CPT. Keynote Lecture at *International Conference on Performance-based design in Earthquake Geotechnical Engineering*, IS Tokyo, Tsukuba, Japan.

Robertson, P. K. & Cabal, K.L. 2010. *Guide to Cone Penetration Test*. Gregg Drilling and testing, Inc. 4th edition.

Rodrigues, C. 2003. *Geotechnical Characterization and geomechanical behaviour analysis of a saprolite from Guarda granites*. PhD Thesis, University of Coimbra.

Schnaid, F., Lehane, B. & Fahey, M. 2004. In-situ test characterization of unusual geomaterial. *Geotechnical and Geophysical Site Characterization, ISC'2*. Viana da Fonseca, A. and Mayne, P.W. Millpress, Rotterdam, pp. 49–74.

Viana da Fonseca, A. 1996. *Geomechanics of Porto residual soil from granite. Design criteria for direct foundations*. PhD thesis presented to Porto University. (in Portuguese).

Viana da Fonseca, A., Silva, S. & Cruz, N. 2007. Retro-analysis of a supported excavation on a saprolitic soil from granite in Porto for design optimisation. *First Sri Lankan Geotechnical Society. International Conference on Soil and Rock Engineering*. Colombo, Sri Lanka.

Geotechnical and Geophysical Site Characterisation 5 – Lehane, Acosta-Martínez & Kelly (Eds)

A method to assess rock strength and excavatability of diamondiferous kimberlite ore through in situ rock testing.

S. Elbaz
School of Engineering and Information Technology, Federation University, Ballarat, Victoria, Australia
D. Crawford
Merlin Diamonds, Southbank, Victoria, Australia
M. Tuck
School of Engineering and Information Technology, Federation University, Ballarat, Victoria, Australia

ABSTRACT: This investigation considers the excavatability of diamondiferous kimberlite pipes of the Merlin field in the Northern Territory, Australia, through the use of in situ rock testing to assess hardness and subsequently excavatability. Historical diamond mining of the Merlin kimberlite pipes identified variable ore hardness both aerially and at depth within the pipe, which was attributed to the preferential weathering of the kimberlite. This variation in hardness presents a problem when determining the best method of excavation and hence can significantly influence production rates. This paper provides a relationship that can be used to relate field testing of rock hardness with rock strength. The results of the hardness to strength relationship are used in established empirical equations to confirm excavatability of the kimberlite ore. The relationships developed in this investigation enable in situ rock hardness testing to be directly related to rock strength for assessment of ore excavatability.

1 BACKGROUND

1.1 *Site Location*

The Merlin Diamond mine is situated in the North-ern Territory, Australia, approximately 80 km due south by air from the town of Borroloola and 720 km southeast of Darwin (see Figure 1). The Merlin dia-mond mine was started by Ashton Mining with trial mining of ore beginning in late 1998 and the first di-amonds being produced in February 1999. Rio Tinto acquired the mine in 2000 and continued operations until April 2003. Merlin Diamonds Limited (ASX:MED) are cur

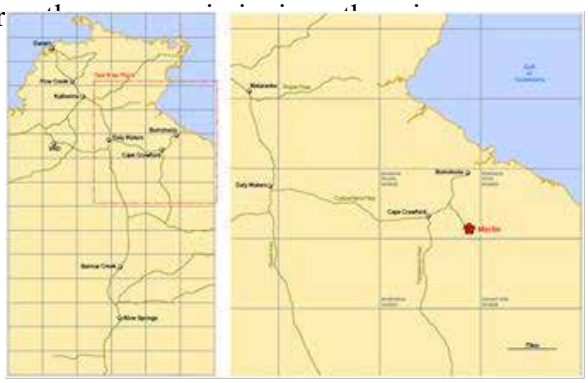

Figure 1. Location of Merlin Diamond Mine

1.2 *Geological Setting*

The Merlin Diamond field is located in the McArthur Basin which consists of Proterozoic (545 to 2,500 million years ago) marine and continental sediments and volcanics (1,000 to 2,500 million years old). The Batten Trough, also known as the Batten Fault Zone, is a 70 km wide zone of extensive faulting, trending north-northwest that occurs within the southern McArthur Basin. The Batten Trough, bounded on the east by the Emu Fault and covered to the west by the Roper Group of sedimentary rocks, is a synsedimentary graben containing up to 10 km of McArthur Basin sediments. Associated with the Batten Trough are the Mallapunyah and Calvert Faults, two northwest trending regional faults, approximately 50 km apart. The kimberlite pipes of the Merlin field are regionally located on the eastern shoulder of the Batten trough, some 6 km east of the Emu Fault and on the projected trace of the northwest trending Calvert Fault. All of the pipes in the field have intruded the Cambrian aged Bukalara sandstone, which is flat lying and unconformably overlies Proterozoic sediments in this area.

The typical geology of the Merlin kimberlite pipes is schematically depicted in Figure 2. The kimberlite has been preferentially eroded from the general regional surface expression and infilled with Cretaceous sediments. These Cretaceous sediments have

been subsequently mined during the open pit operations in order to access the underlying Kimberlite. The side walls of the existing pits are flanked by the stable, horizontally bedded Cambrian Bukalara Sandstone unit.

Ten of the fifteen known kimberlite pipe vents of the Merlin field have been mined from nine open cut pits. The mined pits are orientated north-south in three distinct clusters with the northern cluster of Gareth, Kaye and Ector; central cluster of Gawain and Ywain; and southern cluster of Excalibur, Launfal, Sacramore and Palomides. The regional groundwater level is approximately 20 metres below natural surface and the open pits were continuously dewatered during mining. Consequently, groundwater ingress since the end of mining has formed pit lakes in the remnant pits (see Figure 2).

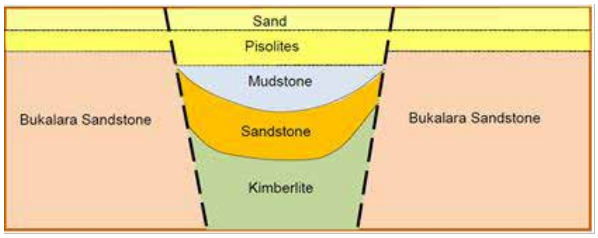

Figure 2. Generalised cross section of the typical kimberlite geometry

1.3 *Proposed Mining*

Historical records show that the open pit mine plans for Kaye and Ector kimberlite pipes in the northern cluster (see Figure 3) were never completed when Rio Tinto ceased operation at Merlin Diamond Mine in 2003. The current mine plan for these pits is to dewater and complete open pit mining using a D7 dozer to rip and push up ore for loading into dump trucks by excavator. For the completed open pits, a mechanical clamshell grab dredge mining is proposed from a barge floating on the pit lake (see Figure 3).

Figure 3. Open pits of the Northern Cluster: Kaye (left), Ector (right) and Gareth (background)

Even though ripping and excavation field tests are planned to be undertaken on the kimberlite before mining commences, Merlin Diamonds Limited were keen to determine a suitable in situ test to determine rock strength and excavatability for use during operations.

Pettifer and Fookes (1994) established that a D7 dozer can easily rip rock with small to medium discontinuities (100 to 300 mm) and a Point Load Index around 1.0 MPa (0.6 to 2.0 MPa). A Point Load Index (Is_{50}) can be directly approximated to Uniaxial Compressive Strength (UCS) whereby an Is_{50} of 1.0 MPa relates to a UCS of 24 MPa. Accordingly, 'easy ripping' of kimberlite with small to medium discontinuities as observed at Merlin can be completed with a D7 dozer up to a UCS of approximately 25 MPa. Similarly established empirical equations (Goktan & Gune, 2005) indicate the heavy clamshell grab selected for dredge mining at Merlin has a 'working' operational limit of 25MPa.

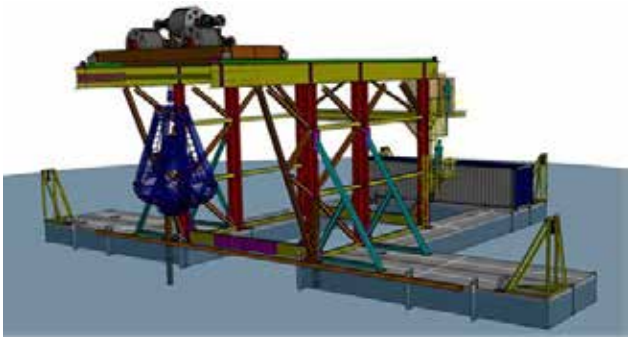

Figure 4. Mechanical Clamshell Grab Dredge Mining

2 TESTING

The Schmidt Hammer was selected for in situ rock strength testing. The Schmidt Hammer tests were performed on kimberlite diamond drill core and these results were compared to UCS values derived using standard destructive compression testing of the cores in the laboratory.

A review of Merlin's exploration database identified cores from eight diamond drillholes commencing in the pit floor of Gawain pit in the central cluster at Merlin. NQ and HQ diamond drill core with diameters of 47.6 mm and 63.5 mm, respectively, were available. Between three and nine core samples (average six) were prepared from each drillhole with a focus on selecting an equal spread of samples over the weathered zone (0 to 60 m depth). Two samples in the fresh zone at approximately 92m to 94m were also selected for testing, primarily for another study. The samples for UCS testing were prepared in accordance with *AS 4133.4.2.2* (Standards Australia, 2013) which stipulates a core length 3 times the diameter. This requirement results in *selection bias* when choosing core samples as only relatively long and intact sections of core, which consequently exhibit higher strength, are selected. Accordingly the results from core testing will represent the upper limit of rock strength for the orebody. Over 50 diamond drill core samples were prepared at Merlin mine and dispatched to the geotechnical laboratory at Federation University, Ballarat.

The Schmidt Hammer uses rebound hardness (Q-value) to approximate rock strength. The Schmidt Hammer testing was completed in accordance with the recommended procedure of the International Society of Rock Mechanics (Aydin, 2008), whereby 20 recordings are taken on a single sample. All care was taken to position the Schmidt Hammer over the cementitious material within the kimberlite core given this is acknowledged as the weaker component of the breccia. The median of the twenty Q-values for each core sample was taken prior to destructive UCS testing in the laboratory. Of the 43 samples that arrived to the laboratory intact, only 14 were considered sufficiently competent to withstand testing with the Schmidt Hammer prior to destructive UCS testing in the laboratory.

The prepared core samples were measured with Vernier callipers as described in *AS 4133.4.2.2* (Standards Australia, 2013). An average cross-sectional area (mm²) was derived for each core sample. The destructive compression testing was undertaken using a Shimadzu Autograph AG-Xplus Series machine in accordance with *AS 4133.4.2.2* (Standards Australia, 2013). Figure 5 shows a core sample that has failed in a single shear plane, which was typical of the failures observed. The force (N) at failure of each core sample was recorded and divided by the cross sectional area (mm²) to determine the UCS (N/mm² = MPa).

Figure 5. Failed Core Sample

Copy the template file B2ProcA4.dot (if you print on A4 size paper) or B2ProcLe.dot (for Letter size paper) to the template directory. This directory can be found by selecting the Tools menu, Options and then by tabbing the File Locations. When the Word programme has been started open the File menu and choose New. Now select the template B2ProcA4.dot or B2ProcLe.dot (see above). Start by renaming the document by clicking Save As in the menu Files. Name your file as follows: First three letters of the file name should be the first three letters of the last name of the first author, the second three letters should be the first letter of the first three words of the title of the paper (e.g. this paper: balpcc.doc). Now you can type your paper, or copy the old version of your paper onto this new formated file.

3 RESULTS

3.1 *Schmidt Hammer Field Test*

The graph in Figure 6 shows Schmidt Hammer Q-values relative to drill core depth which shows a weakly positive regression fitted by the method of least squares. The standard deviation of the twenty Q-values recorded for each core sample has been used to derive 95% confidence intervals for the data set. The upper and lower confidence interval bounds.

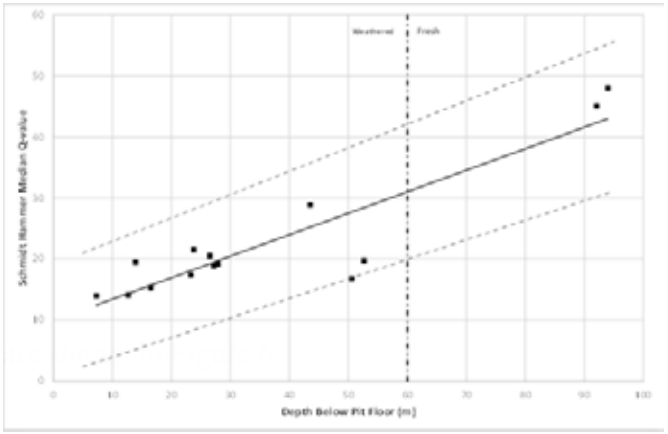

Figure 6. Schmidt Hammer Test Results Relative to Drill Core Depth

3.2 *Laboratory Test*

All 43 intact diamond drill core samples were subjected to destructive UCS tests in the laboratory. The laboratory UCS test results shown in Figure 7 depict a weakly positive least squares regression between the depth of kimberlite and UCS. Of the 43 samples tested, all but one of the weathered core samples (0 to 60 m depth) were within the upper limit of excavatability (25 MPa). The two samples of fresh kimberlite (deeper than 60 m) tested were beyond the upper limit of excavatability.

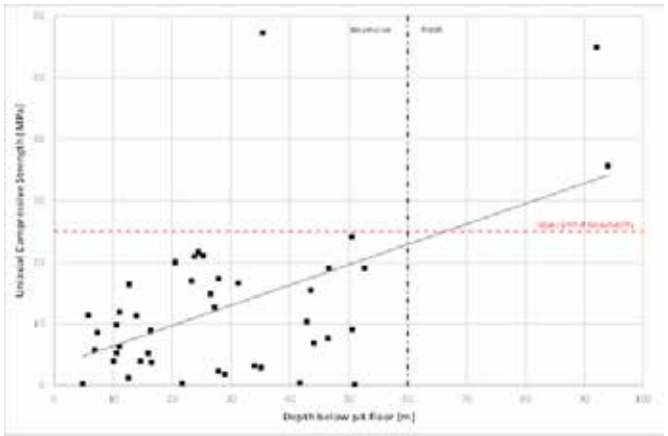

Figure 7. Laboratory UCS Test Results Relative to Drill Core Depth

3.3 *Field Vs Laboratory Test*

Figure 8 shows the regression of Schmidt Hammer Q-values against laboratory UCS test results. The least squares regression line shows a near direct

(1:1) relationship. The standard deviation of the twenty Schmidt Hammer Q-values recorded for each core samples was used to derive upper and lower 95% confidence intervals which are shown on Figure 8.

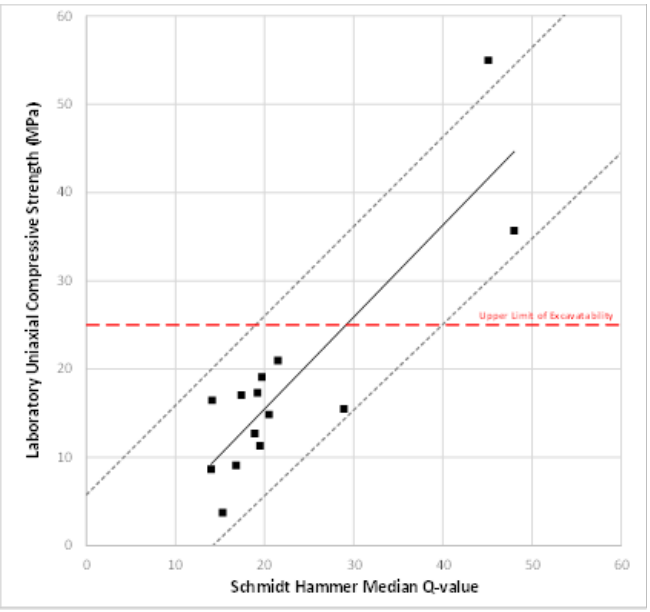

Figure 8. Schmidt Hammer Test Results Relative to Laboratory UCS

4 CONCLUSIONS AND RECOMMENDATIONS

The Schmidt Hammer, an in situ measuring device, was used to estimate rock strength of kimberlite core samples. This was followed by destructive compressive testing of the core samples to determine Uniaxial Compressive Strength (UCS). The Schmidt Hammer rock strength (Q-value) showed a near direct relationship to the UCS where UCS = 1.04 Q – 5.31. The results confirm the use of the Schmidt Hammer as a suitable device for in situ measuring of kimberlite and UCS estimation.

The UCS testing also showed that the weathered kimberlite in Gawain pit is below the upper limit of excavatability for ripping using a D7 dozer and excavation using a heavy dredging clamshell grab.

Ripping and dredging are tensile failures and the use of laboratory or field estimated UCS to predict excavatability assumes a direct relationship between compressive and tensile strength. Data presented by Morkel and Saydam (2008) show that the UCS to Brazilian Tensile Strength (UTB) ratio for a South African kimberlite breccia is 6.84 compared to that for most brittle rocks of approximately 10. A core sample adjacent to each UCS core sample from Merlin has been prepared for UTB testing to determine the UCS to UTB ratio for Merlin kimberlite breccia.

Hoek (1977) observed that rocks subjected to Point Load Index tests fail in tension and therefore the Is_{50} to UCS assumption adopted in this paper will depend on confirming the UCS to Brazilian Tensile Strength (UTB) relationship observed in South African kimberlite breccias.

The testing conducted used a Type (N) Schmidt Hammer which is better suited to higher strength rock. The Type (L) Schmidt Hammer is recommended for future assessment as this will enable testing of lower strength kimberlite as well as ore beyond the upper limit of excavatability.

5 ACKNOWLEDGEMENTS

The authors wish to acknowledge the assistance provided by Mr Peter Snook and Mr Justin Norgaard of Merlin Diamonds Limited in preparing the diamond drill core samples; Mr Vannu Khounphakdee of Merlin Diamonds Limited for assistance in drill core database and modelling, and Mr Paul Bennett, Laboratory Manager, Federation University for assistance during laboratory testing.

6 REFERENCES

Aydin, A. 2008. ISRM suggested method for deterination of the schmidt hammer rebound hardness: Revised version. (). Elsevier Ltd. Doi:10.1007/978-3-319-07713-0

Goktan, R.M. and Gunes, N. 2005. A semi-empirical approach to cutting force prediction for point-attack picks, The Journal of The South African Institute of Mining and Metallurgy VOLUME 105, REFEREED PAPER, APRIL 2005

Hoek, E. 1977. Rock Mechanics Laboratory Testing in the Context of a Consulting Engineering Organization. Int. J. Rock Mech. Min. Sci. and Geomech, Abstract 14, 1977. 93-101

Morkel, J., and Saydam, S. 2008. The influence of potassium on the weathering properties of kimberlite and the information provided by different testing methods.

Pettifer, G.S., and Fookes, P.G. 1994. A revision of graphical method for assessing the excavability of rock. Q J Eng Geol 27:145-164

Standards Australia. 2013. Rock strength test – determination of uniaxial compressive strength – rock strength less than 50 MPa (AS 4133.4.2.2). Retrieved from https://www-saiglobal-com.ezproxy.federation.edu.au/online/autologin.asp

Geotechnical and Geophysical Site Characterisation 5 – Lehane, Acosta-Martínez & Kelly (Eds)

Evaluation of the vulnerability of rock weathering based on monitoring using photogrammetry

D.H. Kim, I. Gratchev, E. Oh & A.S. Balasubramaniam
Griffith School of Engineering, Griffith University, Gold Coast, Australia

ABSTRACT: This article describes a methodology to identify a relationship between spatial topographic changes and the brightness of the 3D images for the assessment of the vulnerability of rock slopes to weathering. In this study, photogrammetry surveys were carried out at a rock slope over a two year interval. The strength properties of the rock material were also investigated under laboratory conditions. The obtained 3D images were employed to the identity of topographic changes and also for image analysis using the intensity of their greyscale images. By comparing the annual photogrammetric 3D images, the data of roughness heights were processed with relative brightness integers obtained from time considered greyscale images using a MATLAB image analysis tool. The results show that the loss of roughness height of the exposed surfaces appeared to be strongly related to the changes of integers of the greyscale images. This study suggests a methodology with regard to the sensitivity of weathering based on annual photogrammetry surveys.

1 INTRODUCTION

As an indication of weathering, surface recession of rocks has been used to investigate the rate of weathering (Meierding 1993, McCarrorll and Nesje 1996, White et al. 1998, Pope et al. 2002, Sancho et al. 2003). In attempting to quantify the recession of rocks, the alteration of rock surface was investigated by simulating the change of the curvatures. McCarrorll and Nesje (1996) used a profile gauge to investigate the roughness profiles and relevant parameters on a boulder of a cliff. In a similar way, Sancho et al. (2003) measured the depth of rock surface using steel pins linked in a specially designed guide frame and compared the surface recession with an original sandstone wall in the Alberuela castle site. However, roughness is solely insufficient to explain the aspect of weathering because the products of weathering appear in different ways due to their geological formation.

In a different way, various surface features were investigated using two dimensional images with image analysis techniques. In order to determine the mineral composition of rocks and to identify individual grain sizes of deposits, 2D images were successfully employed (McEwan et al. 2000, Trauth 2010). Recently, Filin et al. (2013) used an image analysis method to investigate on ground erosion. Similarly, Saito et al. (2010) investigated rock surface roughness by means of local roughness patterns using downscaled topography data. It was suggested from these studies that the image analyses effectively expressed the localized differences on the surface of earth using the information on the adjacent pixels of images.

Digital photogrammetry benefits both the creation of high density spatial data and the obtaining of realistic images of objects. The technique has enabled 3D images to be created at a distance of time as a record of rock surface investigations. Recently, it has been suggested that photogrammetry could provide a satisfactory level of accuracy with high density images in rock surface roughness investigations (Poropat 2008, Kim et al. 2015a). In creating realistic images of surfaces of objects, photogrammetry also enables the pixels of 3D images to be placed in positions for the real surfaces in any orientations. On the basis of the benefits, this study attempts to use the image information of photogrammetric 3D models to investigate roughness characteristics as well as the 3D data.

In this study, photogrammetry surveys were carried out for two years using the same camera positions in order to obtain 3D surface models of a study slope. To investigate the vulnerability of weathering, roughness heights were obtained from sample areas of the 3D models and the differences of roughness were analysed over a two year period. Greyscale images were transformed from the original 3D images and the relevant intensity of the greyscale images to the roughness profiles were analysed combined with the data.

2 METHODOLOGY

2.1 *Assessment of weathering based on alteration of roughness*

Two dimensional roughness of rock surfaces has been used to investigate the degree of rock surface weathering (McCarrorll and Nesje 1996, Sancho et al. 2003). In these previous studies, representative roughness parameters (RMS and maximum height of surface recession) were employed to indicate the recession of a rock surface. In addition, the joint roughness coefficient (JRC) has been employed to study the influence of weathering for jointed rock masses. Based on the weathering process, the change of recession on exposed rock surfaces in jointed rock masses can be observed at the intersections of the exposed joints within the surface areas. In this case, some changes of roughness can be detected along the exposed joints and the recessions can be quantified by using the various roughness parameters.

The aspect of roughness changes may differ according to its geological characteristics. For example, sandstones which are comprised of granular textures may tend to be eroded with rounded edges. On the other hand, laminated structured rocks such as shales and mudstone, exfoliations with a shape of flakes are more dominant than other types of breaks (Merriman et al. 2003). In the previous study using a sandstone and a shale (Kim et al. 2016), it was observed that partial exfoliations with the shapes of shale flakes could cause a significant increase in JRC values of rock surfaces due to the step-like profiles on the altered surfaces near joint intersections. JRC values should be thus carefully interpreted with other complementary investigation.

In this study, heights of surface recession and JRC values are obtained using photogrammetric roughness profiles. The values are compared between the data of 2012 and 2014. As a representative roughness parameter, Z_2, has been employed to estimate JRC values based on digitized roughness data. A regression equation using Z_2 to estimate the JRC values is employed to estimate JRC values as shown in Eq. (1).

$$JRC = 32.2 + 32.47 \log Z_2 \text{ (Tse and Cruden, 1979)} \quad (1)$$

2.2 *Image analysis for the characterization of roughness*

Various geological features have been investigated by two-dimensional images using image analysis techniques. Converting a RGB image to a greyscale image discards colour information and the adjacent colours to the exact same shade of grey. Each pixel of a grey scale image stores a luminance value which can be measured on a scale from black (0 intensity) to white (255 intensity, if the image is 8 bit). Using the differences of brightness, the variation of roughness can be analysed using a MATLAB image analysis tool box (Mathworks 2014). For example, simplified greyscale images successfully analysed roughness variations for the results of direct shear tests (Kim et al. 2014).

As a distinct advantage of 3-D images, extended meshes which cover all the areas of interest in orthogonal directions to the sections, can be obtained as shown in Fig. 1 (b) and (c). This enables an analysis of the integer values of pixels combined with the 3-D roughness data. In this study, the changes of intensity values of greyscale 3D images are interpreted with the changes of asperity heights obtained from photogrammetric profiles. The results are used to estimate the recession areas during the time interval.

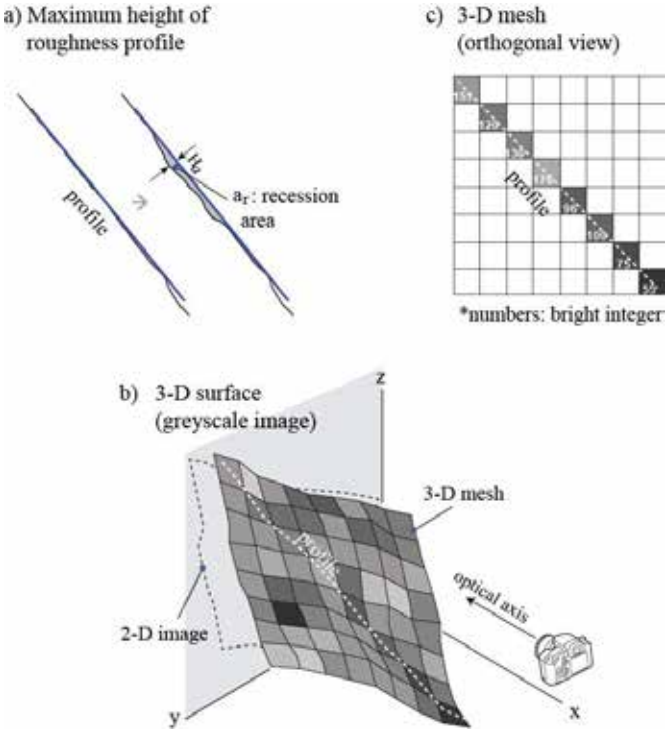

Figure 1. The use of a greyscale 3-D rock surface model to investigate surface recession by weathering

3 SITE INVESTIGATION AND PHOTOGRAMMETRY SURVEYS

3.1 *Geological conditions of the study area*

The study slope is located on the Gold Coast in Australia. The geological condition is composed of the alternate bedding structures of sandstone and shale in the Nerangleigh-Fernvale beds. The texture of the sandstone is medium to coarse grained and joint sets are frequently found from the slope surface. The texture of the shale is fine and has a laminated structure, and the orientations of the beddings are steeply inclined. The textures were observed using digital images taken by an 8 megapixel microscope camera from collected samples, as demonstrated in Fig. 2.

With regard to the strength characteristics, point load tests and slake durability tests were carried out

and the results are well reported in the authors' previous publication (Kim et al. 2015b). In this study, the unconfined compressive strengths (UCS) reported in the previous study have been reanalysed using the conversion factor 11 based on the study of Brisbane sandstone (Look & Griffith, 2001). The average values of UCS are 7.4 MPa and 32.4 MPa for the sandstone and the shale respectively. Using the estimated UCS values, the intact rock samples of sandstone and shale can be classified in 'slightly to moderately weathered' and 'fresh to slightly weathered' ranges respectively in accordance with the classification suggested by Bertuzzi & Pells (2002). The slake durability of sandstone samples varied with their strength. Low strength samples, which are classified as medium strength in point strength classification, showed low durability with a loss in weight of 50% (Gratchev & Kim 2016). The sandstone of this area is more vulnerable to physical weathering than the shale as indicated by the damages to the sandstone from the slake process which is more dominant than the loss of weight in the shale.

3.2 *Records of rock surface models using photogrammetry surveys*

Photogrammetry surveys were performed for the study slope within a two year time period (2012 and 2014). A normal digital DSLR camera, which is equipped with a sensor of 16.2 million effective pixels, was employed with a fixed focal length lens (FL = 24 mm). Stereo photographs were taken at two camera positions with 2.5 metres of baseline distances and the camera-to-object distance was around 17 metres. The study regions of the slope was a boundary region between sandstone and shale and the location of the overlapped camera footprint was adjusted to include both rock types together, keeping the same camera positions at a distance of time.

Sirovision (CSIRO, 2012) was used for the post-process of the photogrammetry surveys. Fig. 2 presents geo-referenced 3D models for both shale and sandstone areas of the models created in 2012. Two sections of both shale and sandstone were selected for a detailed investigation of roughness variation over two years. The selected areas were extracted from the both years' 3D models. The dimensions of the selected areas and the density of the 3D image pixels are summarized in Table. 1. The 3D image pixel scale, which indicates the measurement scales and the extent of accuracy of image analysis varied in accordance with the locations of sample sections. However, the range of variation is negligible.

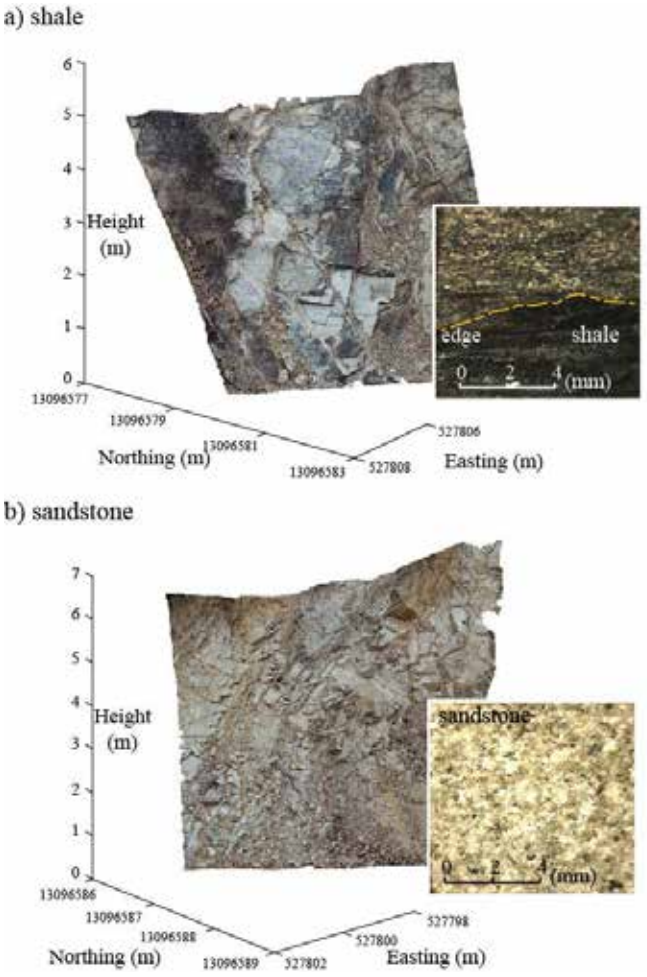

Figure 2. Photogrammetry 3D models of the study area and details of rock surface textures surveyed in 2012; Shale (a), Sandstone (b)

Table 1. Details of 3D images in sampling areas.

Rock types	Shale		Sandstone	
	Section 1	Section 2	Section 1	Section 2
1. Image size (mm)				
Width	331.5	666.6	407.0	523.0
Height	678.3	1123.4	427.2	512.6
2. Image scale (mm/pixel)				
Width	3.9	3.3	3.7	6.8
Height	5.1	4.1	4.8	7.6
3. Profiles (mm)				
Length	430~540	850~1,050	550~680	480~710
Point intervals	2.0	2.0	2.0	2.0

4 RESULTS AND DISCUSSION

4.1 *Variation of roughness profiles and JRC values*

By comparing of the 3D images of 2012 and 2014, the sample areas were selected because they show noticeable changes on the exposed surfaces, especially on the periphery of exposed joints. Using the extracted 3D images of the selected sections, JRC values were then estimated for the sample areas in four radial directions (steepest, 45˚, 90˚, 135˚). The variations of JRC values in the radial directions are

presented in Fig. 3. The overall undulations of the extracted profiles approximately simulated the locations of the loss of roughness and the positions of joint sets (see Fig. 4). The shapes of profile variations helped to detect the ranges for the correlation between the loss of height and the intensities of the greyscale images. The JRC values change over time according to the rock types. For example, for the given two year period, the JRC values for shale increased, as indicated in the graphs. Alternatively, in sandstone regions, the JRC values diminished slightly.

The accuracy of photogrammetric JRC values is influenced by various factors. It is generally accepted that high resolution images are required to simulate small scale roughness (Poropat 2008). As presented in Table 1, the point intervals of the extracted profiles are large to simulate small scale roughness in detail. This possibly results in an underestimation of JRC values (Kim et al. 2015a). However, the accuracy of photogrammetric JRC values is beyond the scope of this paper. The use of the estimated JRCs is limited in this study so as to compare the 3D surface models under the same photogrammetry setups.

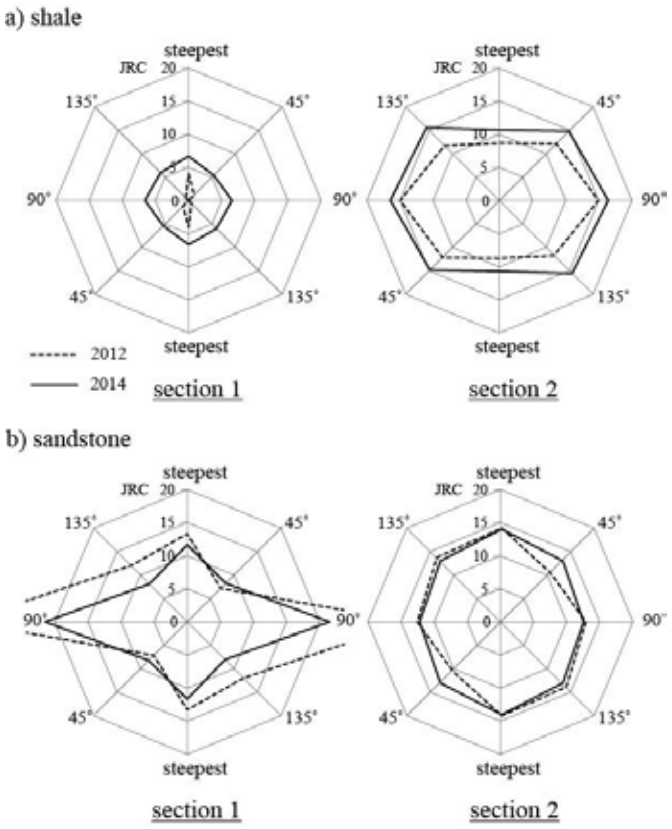

Figure 3. Alteration of photogrammetric JRC values in radial directions (0˚, 45˚, 90˚, 135˚) over the two year interval in the shale area (a) and sandstone area (b)

4.2 *The use of greyscale intensity of 3D images*

The original RGB 3D images were converted to greyscale with 8 bit pixel depth to simplify the image data. Fig. 4 demonstrates the brightness integers and the variation of asperity heights at the same positions along the profiles located in the centre lines extracted from the 3D models of the sandstone section 2. The variations of brightness integers (I) obtained from greyscale 3D images are correlated with the changes of asperity height. In the sandstone area, it is obvious that large variations of (I) values occurred at the same regions where the asperities are lost by weathering. Also, there is an extraneous increment range of (I) values caused by the different luminance between the photographing in 2012 and 2014. It can be also explained by the fact that there is no considerable roughness change in the range. In the shale area, however, it was observed that the ranges of brightness integers considerably varied by a discoloration along the exposed surface as a result of chemical weathering. Due to the various changes in colours, it was difficult to define the correlation between the roughness changes and the integers of greyscale images in the shale area. In addition, the difference of luminous intensity at the moment of photographing also disrupted the image analysis using the brightness integers.

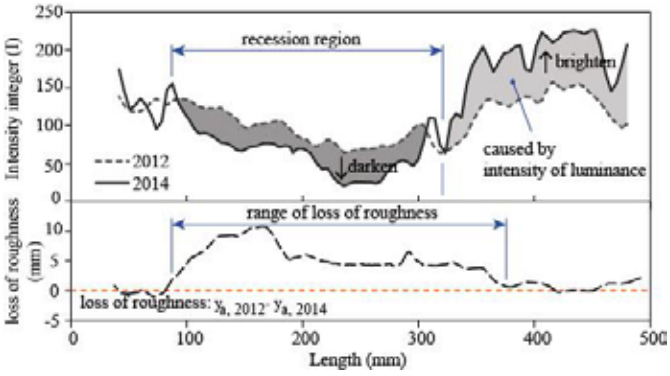

Figure 4. Changes of brightness integers (I) and the loss of roughness of the profile along the centre line of sandstone 2 section

This study also tried to detect the damaged area by weathering over the two year period. Using an image thresholding technique of MATLAB, the pixels of the greyscale images were filtered within the obtained guide ranges of (I) values from the profile analysis as described in Fig. 4. The obtained threshold images are demonstrated in Fig. 5. The percentages of the detected areas to the total areas were also calculated using the corresponding numbers of the pixels. The filtered areas of the sandstone are appeared to be reasonable as an indicator of the products of weathering as the ranges of brightness is relatively simple. As the sandstone in the study area is more vulnerable than the shales as shown by the results of slake durability tests, the recession areas were markedly increased (from 8.1% to 17.6%: section 1, from 8.6 % to 25.4 %: section 2). On the contrary, the recession areas analysed by using the guided integer range are inconsistently distributed on the

surfaces of the shale. This result can be explained by the responses of chemical weathering along the laminations of the shale surface.

Through this investigation, it is concluded that the image analysis using the colour information in the pixels of 3D images can be used to investigate the progress of weathering for the rock mass combined with the 3D roughness data. However, the limitations of this technique are related to the differences of luminance and the level of accuracy of photogrammetry models. It is noted that brightness of a rock surface may be inconsistent to be used as the indicator of weathering in accordance with its geological condition.

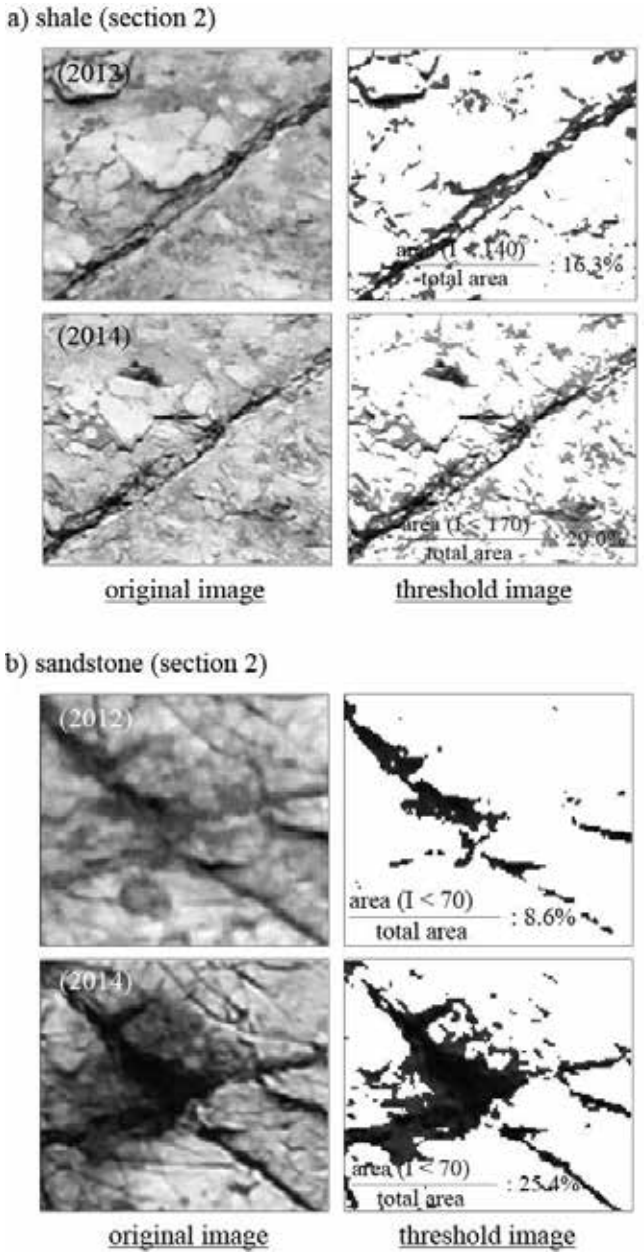

Figure 5. Original images of altered areas by weathering and detected areas by using MATLAB image analysis; for shale section 2 (a) and sandstone section 2 (b)

5 CONCLUSION

This study proposes a methodology to study the progress of weathering using 3D models. By comparing photogrammetric 3D models over a two year period, the recession of weathering for shale and sandstone slopes was investigated. The photogrammetric 3D models provided two dimensional roughness profiles and the 3D RGB image was converted to greyscale images and used as a source of an image analysis. The ranges of the brightness intensity obtained from MATLAB image analysis were compared with the changes of roughness profiles to detect the recession of weathering. The combined image analysis with photogrammetric roughness data could compensate the limitations of both the use of the 2D roughness data and the use of the integer values of 2D images. In the case of sandstone, which showed a simple color variation over the two year period, the recession area can be quantified by using an image threshold technique as changed from 8.6% to 25.4%.

This study suggests that the obtained area can be used to indicate the vulnerability of weathering. However, the intensity of images should be also carefully interpreted by considering both luminance conditions for photographing and the geological characteristics of rock mass.

6 ACKNOWLEDGEMENTS

This research was performed with the financial support of the Griffith University Postgraduate Research Scholarship (GUPRS) program. The authors would like to express their appreciation to CSIRO for providing the program SIROVISION for this study and to thank Mr. George Poropat for valuable helps.

7 REFERENCES

Bertuzzi, R. & Pells, P. J. N. 2002. Geotechnical parameters of Sydney sandstone and shale. *Australian Geomechanics* 37(5): 41-54.

Bureau of Meteorology in Australia Government. 2015. Summary statistics Gold Coast seaway. Website, www.bom.gov.au/climate/average/tables/cw_040764.shtml

CSIRO. 2012. Siro3D-3D imaging system manual version 5.0. CSIRO Exploration & Mining, 198 pp.

Filin, S., Goldshleger, N., Abergel, S., Aray, R. 2013. Robust erosion measurement in agricultural fields by colour image processing and image measurement. *European Journal of Soil Science* 64: 80-91.

Gratchev, I., Kim, D. H. 2016. On the reliability of the strength retention ratio for estimating the strength of weathered rocks. *Engineering Geology* 201: 1-5.

Kim, D. H., Chung, M., Gratchev, I. 2014. Assessment of rock joint roughness using image analysis of damaged area in direct shear tests. In *the 23rd Australasian Conference on the Mechanics of Structures and Materials (ACMSM23); Proc. Intern. Symp., Byron Bay, 2015.* 745-750.

Kim, D. H., Poropat, G., Gratchev, I., Balasubramaniam, A. S. 2015a. Improvement of photogrammetric JRC data distribution based on parabolic error models. *International Journal of Rock Mechanics & Mining Sciences* 80: 19-30.

Kim, D. H., Gratchev, I., Balasubramaniam, A. S. 2015b. A photogrammetric approach for stability analysis of weathered rock slopes. *Geotechnical and Geological Engineering*, 33: 443-454.

Kim, D. H., Gratchev, I., E. Oh., Balasubramaniam, A. S. 2016. Assessment of rock slope weathering based on the alteration of photogrammetric roughness data. In *the 19th Southeast Asian geotechnical conference & 2nd AGSSEA conference; Proc. Intern. Symp.,Kuala Lumpur, 2016*, 901-906.

Look, B. G., Griffith, S. G. 2001. An engineering assessment of the strength and deformation properties of Brisbane rocks. *Australian Geomechnics* 36(3): 17-30.

McCarroll, D., Nesje, A. 1996. Rock surface roughness as an indicator of degree of rock surface weathering. *Earth Surface Processes and Landforms* 21: 963-977.

McEwan, I. K., Sheen, T. M., Cunningham, G. J., Allen, A. R. 2000. Estimating the size composition of sediment surfaces through image analysis. *ICE-Water and Maritime Engineering* 142 (4): 189-195.

Meierding, T. C. 1993. Inscription legibility method for estimating rock weathering rates. *Geomorphology* 6: 273-286.

Merriman, R. J., Highley, D. E., Cameron, D. G. 2003. Definition and characteristics of very-fine grained sedimentary rocks: clay, mudstone, shale and slate. British Geological Survey Commissioned report, CR/03/281N, 20pp.

Pope, G. A., Meierding, T. C., Paradise, T. R. 2002. Geomorphology's role in the study of weathering of cultural stone. *Geomorphology* 47: 211-225.

Poropat, G. V. 2008. Remote characterisation of surface roughness of rock discontinuities. In *the 1st Southern Hemisphere International rock mechanics symposium; Proc. Intern. Symp., Perth, 2008*, 447-458.

Saito, H., Grasselli, G. 2010. Geostatistical downscaling of fracture surface topography accounting for local roughness. *Acta Geotechnica* 5: 127-138.

Sancho, C., Fort, R., Belmonte, A. 2003. Weathering rates of historic sandstone structures in semiarid environments (Ebro basin, NE Spain). *CATENA* 53: 53-64.

Trauth, M. H. 2010. MATLAB® Recipes for earth sciences. the 3rd edition, Verlag Berlin Heidelberg, Germany: Springer

Tse, R., Cruden, D. M. 1979. Estimating joint roughness coefficients. *International Journal of Rock Mechanics and Mining Sciences & Geomechanics Abstracts* 16: 303-307.

White, K., Bryant, R., Drake, N. 1998. Techniques for measuring rock weathering: Application to a dated fan segment sequence in Southern Tunisia. *Earth Surface Processes and Landforms* 23: 1031-1043.

Geotechnical and Geophysical Site Characterisation 5 – Lehane, Acosta-Martínez & Kelly (Eds)

In Situ Rock Stress Determined by Hydraulic Fracturing Test in Singapore

K. Kimura & T. Yasuda
Kiso-Jiban Consultants Co., Ltd. Singapore Branch, Singapore

S. L. Chiam & K. H. Goay
Building and Construction Authority, Singapore

ABSTRACT: The paper presents results of a series of hydraulic fracturing tests conducted in the Bukit Timah Granite, which belongs to the Triassic granite similarly found in the eastern Malaysian Peninsula and the Jurong Formation of Singapore comprising of the Triassic to Jurassic sedimentary rocks. The tests were carried out in vertical boreholes ranging in depth from 90 to 170 m. mostly in Classes I and II of Rock Mass Rating (RMR). Singapore is situated approximately 750 km northeast of the subduction zone between the Eurasian plate and the Indo-Australian plate. The general tectonic stress acts in NNE-SSW to NE-SW in the region. The results are interpreted and assessed in terms of the regional tectonics. The magnitude, horizontal-vertical ratio and orientation of in situ rock stress results are also discussed. The ratios of maximum horizontal stress to vertical stress are approximately 3 and 2, in the Bukit Timah Granite and the Jurong Formation, respectively. The relationship of maximum (S_H) and minimum (S_h) horizontal stresses, and vertical stress (S_v) is $S_H > S_h > S_v$, and indicates a thrust faulting stress regime that is characteristics of a compressional tectonic environment. The stress regime agrees with the regional geological setting and interpretation of seismic reflection surveys conducted in this study area. The orientations of maximum horizontal stresses generally show N-S to NE-SW and are consistent with the general compressive stress in the region.

1 INTRODUCTION

In situ rock stresses are commonly measured by hydraulic fracturing tests. A series of hydraulic fracturing tests was conducted in the Bukit Timah Granite and the Jurong Formation, which are the main bedrocks of Singapore. Seismic reflection surveys were also conducted to investigate geological structures in this study area. In this paper, the results are interpreted and assessed in terms of the regional tectonics. The magnitude, horizontal-vertical ratio and orientation of in situ rock stress results are also discussed, and are compared with the regional geological setting and interpretation of seismic reflection surveys.

2 GEOLOGICAL SETTING OF THE AREA

The Bukit Timah Granite is generally located in the centre of Singapore Island and the outcrops are exposed on the ground surface on the hills and lies underneath recent deposits in valleys. The Bukit Timah Granite is composed mainly of acid igneous rocks of granite and granodiorite. Quartz monzonite is also observed in part. The results of the U-Pb zircon geochronological study reveal that the Bukit Timah Granite has been dated at 244 ± 1 Myrs at Dairy Farm Quarry and 237.5 ± 1.3 to 239.2 ± 2.1 Myrs at Mandai Quarry (Oliver et al. 2014).

The Jurong Formation, which was formed in the period of Late Triassic to Early Jurassic, is distributed in the western part of the Island and is normally composed of series of sedimentary rocks such as sandstone, mudstone, shale, tuff, conglomerate, limestone, etc. The formation has been severely folded and faulted in the past as a result of tectonic movements. A general strike of the formation is NW-SE. Dips of the formation vary over a short distance from a few degrees to vertical or overturned. There are a number of faults in the Jurong Formation varying from major to minor with displacement ranging from unknown distance to a few decimetres.

3 IN SITU STRESS MEASUREMENT

3.1 *Method*

To perform hydraulic fracturing tests, the hydraulic straddle packers are positioned in the borehole at the interval selected, based on the rock cores and borehole wall images obtained by an optical televiewer. The straddle packers are inflated to a pressure of about 4 MPa. After the slug test, the test interval is

pressurized at a faster flow rate until fractures are induced in the borehole wall at the breakdown pressure (P_b). Upon reaching the breakdown pressure the pump should be turned off to obtain the shut-in curve from which the shut-in pressure (P_s) can be derived. The tests are followed by several re-opening tests cycles to determine the pressure required to reopen the induced fracture i.e. reopening pressure (P_r). It should be noted that all pressure records are derived from pressure sensor placed on the ground surface, thus, the in situ pressure should be determined by adding the hydrostatic pressure (P_H) to the recorded pressure. Data processing is conducted according to the ISRM Suggested Methods (Haimson and Cornet 2003) and the magnitude of the in situ stress is thus calculated according to the following equations:

$$S_H = T + 3S_h - P_b - P_0 \quad (1)$$

$$T = P_b - P_r \quad (2)$$

$$S_h = P_s \quad (3)$$

$$S_v = \Sigma \gamma_i D_i \quad (4)$$

where, S_H and S_h are the maximum and minimum horizontal principal stresses, respectively; T is hydraulic fracturing rock tensile strength; And P_0 is pore pressure, which is usually equal to the static water pressure. The vertical principal stress (S_v) is calculated based on the bulk density of overlying materials (γ_i) and their thicknesses (D_i).

After completion of all hydraulic fracturing tests in the borehole, the orientations of induced/reopened fractures are determined by using an impression packer with an orientator. The outer layer of the impression packer is made of semi-vulcanized rubber possessing a certain plasticity, which can give a geometrical copy of the induced fracture by the hydraulic fracturing test. The impression packer is usually pressurized to a pressure higher than the reopening pressure recorded in the hydraulic fracturing test. The pressure is maintained for about thirty to sixty minutes. The orientation and inclination of the fracture impressions are determined with respect to the marked line (baseline) and geometrical traces of the fracture. The orientation of the marked line is recorded by the orientator while the impressions being obtained.

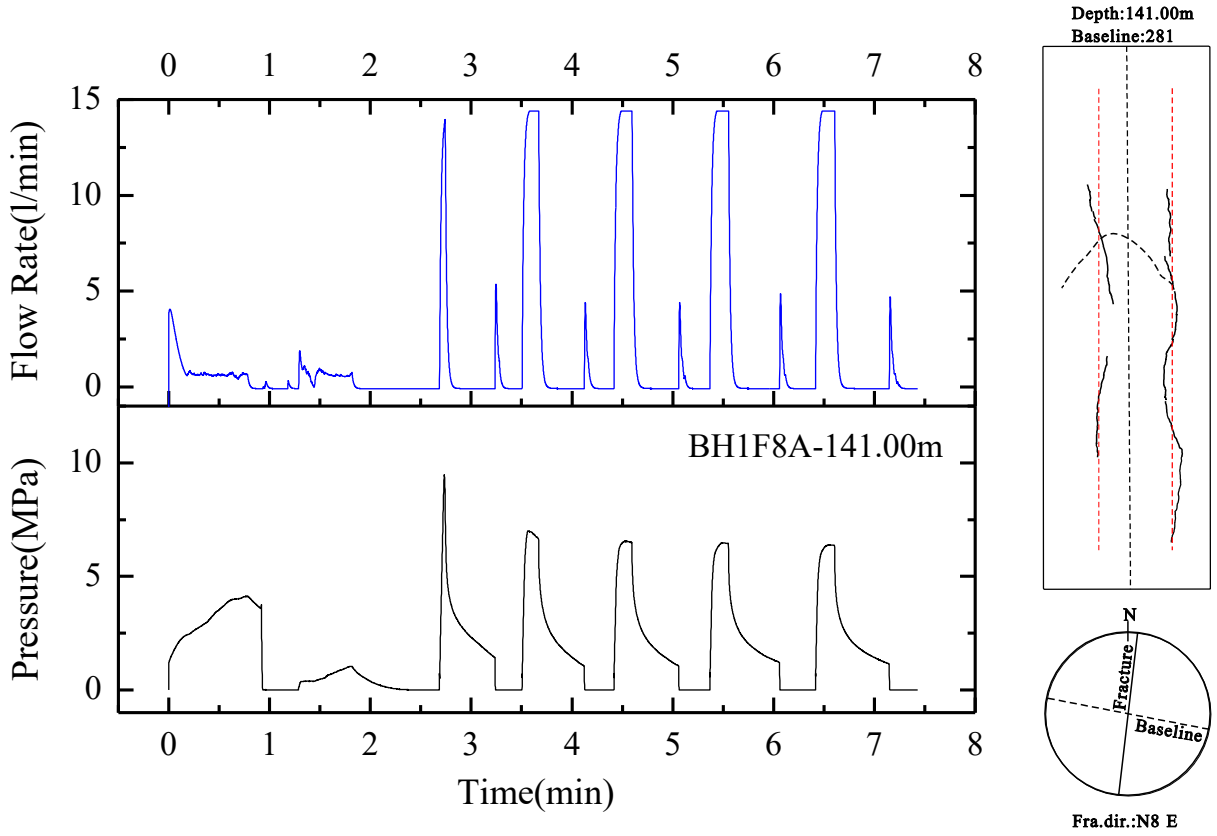

Figure 1. A typical set of pressure and flow rate history records of a hydraulic fracturing test (left) and orientations of the induced fractures (right) in the Jurong Formation.

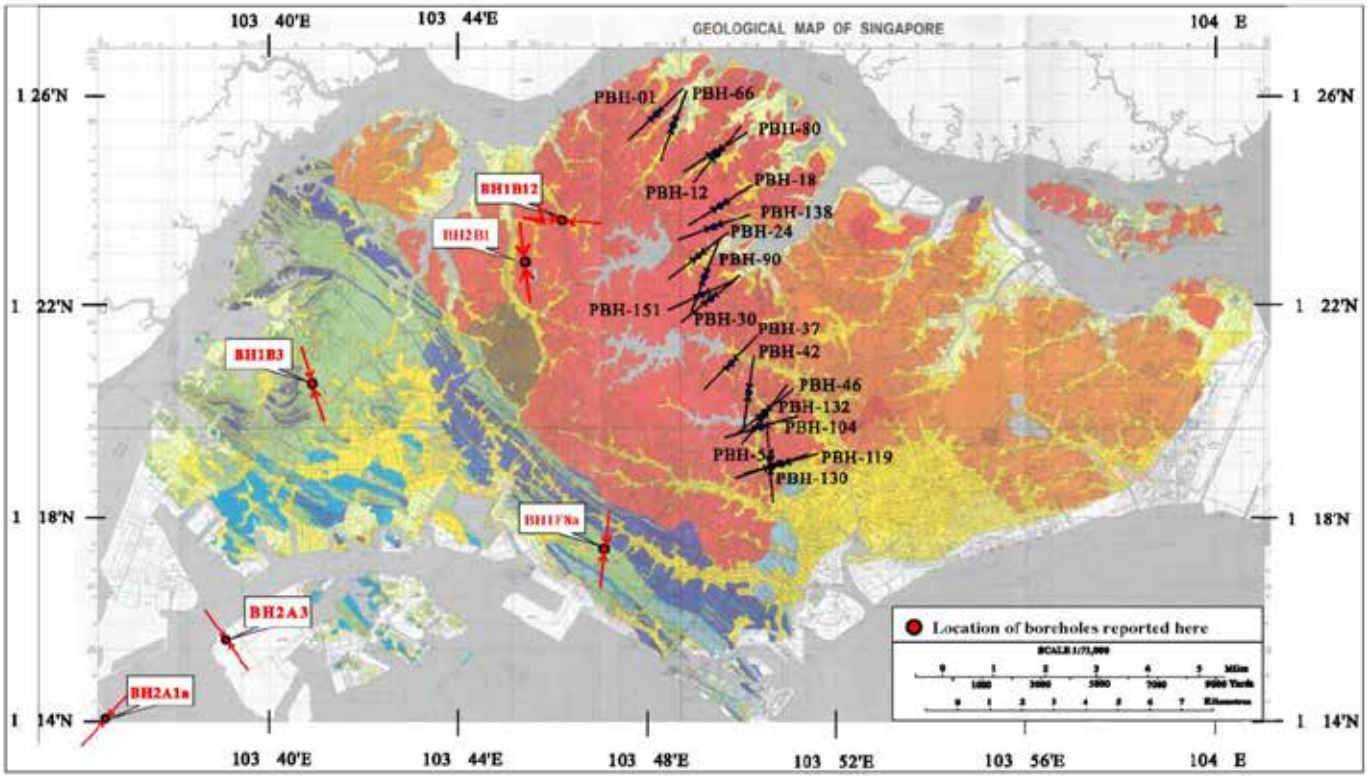

Figure 2. Orientations of S_H in Singapore Island (modified from Meng et al. 2012)

Table 1: Results of in situ stress

Bore-hole No.	Centre of test depth (m)	S_H [a] (MPa)	S_h [b] (MPa)	S_v [c] (MPa)	T_{hf} [d] (MPa)	S_H/S_v	S_h/S_v	S_H/S_h	Direction of S_H (°)	Rock Types
Bukit Timah Granite (BT)										
BH1B12	92.50	8.73	6.15	2.52	6.33	3.46	2.44	1.42	N62°W	gr [e]
BH1B12	117.10	8.69	5.91	3.19	6.17	2.72	1.85	1.47	N80°W	gr
BH1B12	150.50	9.40	6.25	4.10	5.98	2.29	1.52	1.50	N83°W	gr
BH2B1	91.30	7.84	5.77	2.38	5.89	3.30	2.43	1.36	N33°W	gr
BH2B1	101.20	9.10	6.06	2.64	4.67	3.45	2.30	1.50	N11°W	gr
BH2B1	121.20	9.80	6.37	3.16	4.51	3.10	2.02	1.54	N19°E	gr
Average	-	8.93	6.09	3.00	5.59	3.05	2.09	1.47	-	-
Jurong Formation (JF)										
BH2A1a	96.50	5.22	3.84	2.61	5.81	2.00	1.47	1.36	N64°E	li [f]
BH2A1a	116.50	6.39	3.99	3.14	6.57	2.04	1.27	1.60	N21°-47°E	si [g]
BH2A3	104.10	5.43	4.32	2.76	4.64	1.97	1.57	1.26	N23°W	tuffsa [h]
BH2A3	109.10	6.09	4.06	2.77	8.69	2.20	1.47	1.50	N51°W	si / tuffsa
BH1B3	140.00	6.93	5.26	3.75	5.86	1.85	1.40	1.32	N30°W	tuffsa
BH1B3	168.50	4.72	4.54	4.51	8.27	1.05	1.01	1.04	N18°W	tuffsa
BH1F8a	104.80	7.77	5.31	2.81	2.95	2.77	1.89	1.46	N15°E	cng [i]
BH1F8a	141.00	6.40	4.75	3.77	4.40	1.70	1.26	1.35	N8°E	sa
BH1F8a	159.90	7.60	5.08	4.28	3.71	1.78	1.19	1.50	N25°E	sa
Average	-	6.28	4.57	3.38	5.66	1.93	1.39	1.38	-	-

[a] S_H: maximum horizontal stress

[b] S_h: minimum horizontal stress

[c] S_v: vertical stress

[d] T_{hf}: rock tensile strength

[e] gr: granite

[f] li: limestone

[g] si: siltstone

[h] tuffsa: tuffaceous sandstone

[i] cng: conglomerate

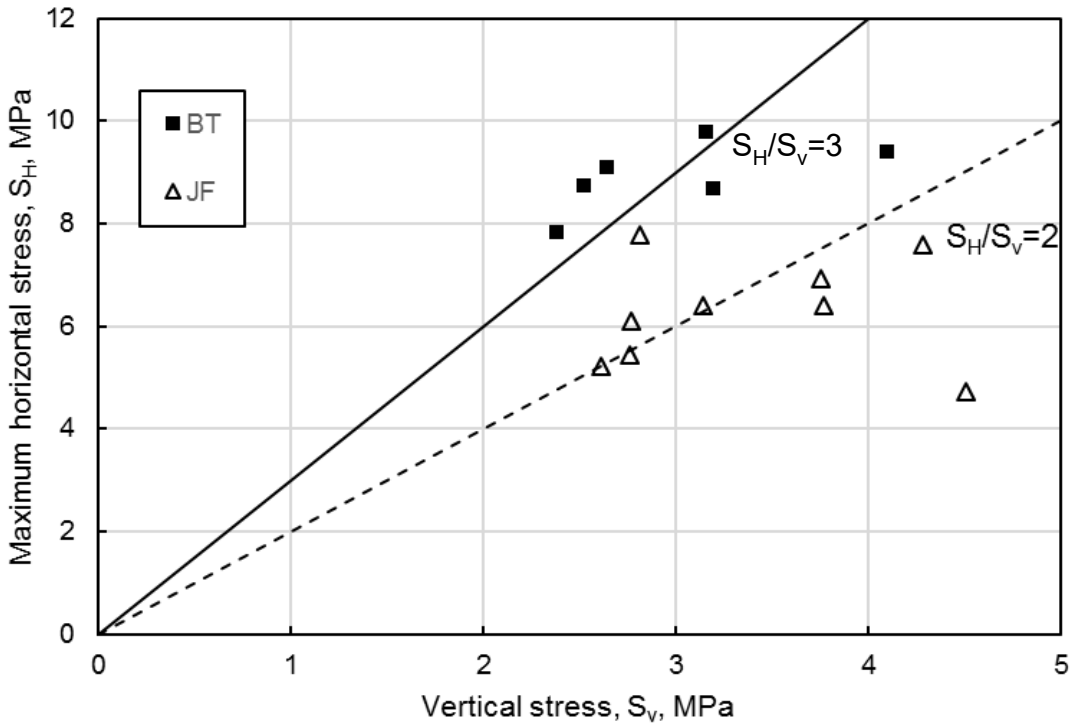

Figure 3. Stress ratios of S_H/S_V in Bukit Timah Granite (BT) and Jurong Formation (JF)

3.2 *Test Results*

The hydraulic fracturing tests had been conducted in two boreholes (BH1B12 and BH2B1) and four boreholes (BH2A1a, BH2A3, BH1B3 and BH1F8a) at the areas of Bukit Timah Granite and the Jurong Formation, respectively. The test sections were intact in rock core and their depths were ranging from 90 to 170 meters mostly in Classes I and II of Rock Mass Rating (RMR).

Figure 1 shows an example of hydraulic fracturing test result which includes a set of pressure, flow-rate records and orientations of the induced fractures performed in the borehole at the Jurong Formation area. The magnitudes of maximum and minimum horizontal stresses and the directions of S_H are summarised in Table 1. The maximum horizontal principal stresses are 7.8 to 9.8 MPa and the minimum horizontal stresses are 5.9 to 6.4 MPa in the Bukit Timah Granite. In the Jurong Formation, the maximum horizontal principal stresses are 4.7 to 7.7 MPa and the minimum horizontal stresses are 3.8 to 5.3 MPa. The orientations of the maximum horizontal principal stress in the boreholes are illustrated in Figure 2 with arrow indications. In the Bukit Timah Granite, the orientations of maximum horizontal stresses show approximately N-S and E-W in boreholes BH2B1 and BH1B12, respectively. In the Jurong Formation, the orientations of maximum horizontal stresses generally show NE-SW in boreholes BH2A1a and BH1B8a and NW-SE in boreholes BH2A3 and BH1B3. Figure 3 shows the ratios of maximum horizontal stress to vertical stress. The figure indicates that the ratios are generally higher in the Bukit Timah Granite in which the ratio is approximately 3, whilst 2 in the Jurong Formation.

4 DISCUSSION

4.1 *Ratio of principal stresses*

The test results indicate that ratio of S_H: S_h: S_v is approximately 3: 2: 1 and 2: 1.5: 1 in the Bukit Timah Granite and the Jurong Formation, respectively. The ratio of S_H: S_h: S_v in the Bukit Timah Granite is the same ratio as Zhao et al. (2005) reported based on the results of hydraulic fracturing tests conducted at depth ranging between 60 and 120 m below the ground in the Bukit Timah Granite. The in situ rock stresses were also measured at depth shallower than 60 m in the eastern part of the Bukit Timah Granite and the ratio of S_H: S_h: S_v is approximately 5: 3: 1 (Meng et al. 2012). This stress ratio is higher than the ratio determined in this paper and that may arise from the lower vertical stress at the shallower depth.

As to the Jurong Formation, the proposed ratio of S_H: S_h: S_v is similar to the ratio of 2.2: 1.3: 1 to 1.9: 1.4: 1 measured at 100 to 160 m depth in the Jurong Formation at Jurong Island (Winn and Ng 2013).

4.2 *Relationship between principal stresses*

From the available results of in situ rock stress measurement, the relationship between principal stresses is expressed as $S_H > S_h > S_v$. This relationship indicates a thrust faulting stress regime which is

characteristics of a compressional tectonic environment.

Oliver et al. (2014) propose a tectonic model of Singapore and the southern Malaysian Peninsula. The model presents that Sibumasu continental lithosphere was rifted from Pangea and the Palaeo Tethys Ocean was subducted under the eastern Malaysian Peninsula from the Early Permian to the Middle Triassic. In the Late Triassic, Sibumasu was collided with the eastern Malaysian Peninsula and that caused the Jurong Formation to be folded and thrusted.

At present, Singapore is situated at approximately 750 km northeast of the subduction zone between the Eurasian plate and the Indo-Australian plate.

In the interpretation of seismic reflection surveys carried out in the present study, folds, thrusts and reverse faults are identified in the Jurong Formation. The orientations of those axes and strikes generally show NW-SE.

The proposed stress regime agrees with the regional geological setting and interpretation of seismic reflection surveys.

4.3 *Orientation of maximum horizontal stresses*

From the results of impression packer tests, the orientations of maximum horizontal stresses generally show N-S to NE-SW whilst some test results present discrepant orientations, e.g., NW-SE oriented maximum horizontal stresses are recorded in BH2A3 and BH1B3. In these boreholes, the strikes of bedding are generally NE-SW which deviates from the general trends in the Jurong Formation. The deviation of bedding may imply that the discrepancy of orientations of maximum horizontal stresses arises from the local stress field differing from the dominant stress in the region.

The World Stress Map (Heidbach et al. 2008) presents that the general tectonic stress acts in NNE-SSW to NE-SW in the region. The interpreted orientations of maximum horizontal stresses are consistent with the general compressive stress in the region and perpendicular to the fold axes and fault strikes interpreted from the results of seismic reflection surveys.

4.4 *Application of in situ stresses*

In situ stresses are important in the design and stability analysis of underground structures such as tunnels, caverns, and shafts to identify zones of compression, tension and stress concentrations. For this purpose, the in situ stresses are required in the analytical/numerical approach for the design of underground structures. In the empirical design approach, in situ stresses are used for the determination of rock mass quality of Tunnelling Quality Index (Norwegian Q System) by Barton et al. (1974). In the Q system, in situ stresses are taken into account for the calculation of stress reduction factor. In situ stress field such as the direction of maximum horizontal stress is also important to determine the orientation of cavern long axis. In general, aligning caverns with their long axis parallel to the maximum horizontal stress is favourable so as to prevent overstressed zones.

5 CONCLUSIONS

The horizontal-vertical ratio and orientation of in situ rock stress are discussed based on the results of hydraulic fracturing tests conducted in Singapore. Our findings are summarised as follows:

The ratios of maximum horizontal stress to vertical stress are approximately 3 and 2, in the Bukit Timah Granite and the Jurong Formation, respectively. These results are consistent with the ratios found in the past.

The relationship of maximum (S_H) and minimum (S_h) horizontal stresses, and vertical stress (S_v) is $S_H > S_h > S_v$, and indicates a thrust faulting stress regime that is characteristics of a compressional tectonic environment. The stress regime agrees with the regional geological setting and interpretation of seismic reflection surveys conducted in this study area.

The orientations of the maximum horizontal stresses generally N-S to NE-SW and are consistent with the general compressive stress in the region, being perpendicular to the fold axes and fault strikes interpreted from the results of seismic reflection surveys.

In order to better interpret the stress conditions and geological structures in Singapore, further hydraulic fracturing tests shall be conducted. It is extremely important as an aid to the interpretation of the hydraulic fracturing test results to conduct reconnaissance survey, seismic reflection survey and borehole televiewer.

6 REFERENCES

Barton, N., Lien, R., Lunde, J. (1974) “Engineering classification of rockmasses for the design of tunnel support.” Rock Mechanics, 6(4), 189-239.

Haimson, B. C., Cornet, F. H. (2003) “ISRM Suggested Methods for rock stress estimation-Part 3: hydraulic fracturing (HF) and/or hydraulic testing of pre-existing fractures (HTPF).” International Journal of Rock Mechanics & Mining Sciences, 40, 1011-1020.

Heidbach, O., Tingay, M., Barth, A., Reinecker, J., Kurfeß, D., and Müller, B. (2008). “The World Stress Map database release 2008.” doi:10.1594/GFZ.WSM.Rel2008

Meng, W., Chen, Q. C., Du, J. J., Feng, C. J., Qin, X. H., and An, Q. M. (2012). “In situ stress measurements in Singapore.” Chinese Journal of Geophysics, 55(4), 429-437.

Oliver, G., Zaw, K., Hotson, M., Meffre, S., and Manka, T. (2014) "U-Pb zircon geochronology of Early Permian to Late Triassic rocks from Singapore and Johor: A plate tectonic reinterpretation" Gondwana Research, 26 (1), 132-143.

Winn, K. and Ng, M. (2013). "In situ stress measurement in Singapore." Advances in Geotechnical Infrastructure, 747-752.

Zhao, J., Hefny, A. M., and Zhou, Y. X. (2005). "Hydrofracturing in situ stress measurements in Singapore granite." International Journal of Rock Mechanics & Mining Sciences, 42, 577-583.

Geotechnical and Geophysical Site Characterisation 5 – Lehane, Acosta-Martínez & Kelly (Eds)

Use of the Light Falling Weight Deflectometer (LFWD) as a site investigation tool for residual soils and weak rock

D. Lacey & B. Look
Foundation Specialists Pty Ltd, Brisbane Queensland Australia
D. Marks
Department of Transport and Main Roads, Brisbane, Queensland, Australia

ABSTRACT: The Light Falling Weight Deflectometer (LFWD) is a surface based, dynamic plate load test that provides quick and direct measurement of the *insitu* modulus parameter of the near-surface. The LFWD's direct measurement of modulus negates the need to indirectly estimate the parameter via penetration or density testing, both of which have significant transformation errors associated with them. To demonstrate the potential use of the LFWD as an effective site investigation tool, two brands of LFWD were employed to assess the *insitu* modulus of a residual soil and weak sedimentary rock profile present along a significant infrastructure project in Queensland, Australia. The performance of both LFWDs was assessed and compared to other 'traditional' site characterisation techniques, including DCP profiling and laboratory (soaked) CBR testing. Characteristic *insitu* modulus parameters are presented, and variation thereof, for the range of material units that exist across the traditionally difficult to characterise residual soil to weak rock transition zone.

1 INTRODUCTION

The Light Falling Weight Deflectometer (LFWD) is a surface based, dynamic plate load test that provides quick and direct measurement of a near-surface, composite *insitu* modulus parameter. The direct measurement of modulus by the LFWD negates the need to indirectly estimate the parameter – which is currently frequently achieved by using the results of penetration (e.g. Dynamic Cone Penetrometers, DCPs) or density test techniques. Such methods may have significant transformation errors associated with them, especially if "universal" correlations are blindly applied to field test results.

Previous focus on the LFWD development has primarily related to its use as a Quality Assurance (QA) tool; for example, the verification that design parameters are met for base, sub-base and pavement layers (e.g. Vennapusa and White, 2009; Nazzal et. al., 2007; Fleming et. al, 2000). In this paper, the use of the LFWD as an effective site investigation tool for subgrade assessment is demonstrated.

Unlike processed pavement materials, which usually exhibit uniform or controlled Particle Size Distributions (PSDs), the materials that typically exist *insitu* across the residual soil to weak rock transition zone are non-homogenous. Often a gradational increase in the gravel (or larger) sized component of rock fragment / parent rock material also occurs across the weathering profile. Such properties may cause many site investigation techniques to become ineffective within such material profiles.

2 LIGHT FALLING WEIGHT DEFLECTOMETERS (LFWDs)

Insitu testing to determine the Young's Modulus of the composite material can be achieved by the use of LFWDs. Such instruments, as shown in Figure 1, are quasi-static plate load tests (PLTs), in which a sliding 10kg weight is manually raised along a vertical guide rod and dropped onto a rigid base plate. The load pulse – generated when the weight is dropped upon the rubber dampers – passes through the rigid plate and into the ground as a uniform stress. Depending on the LFWD manufacturer (refer Table 1), the imparted load can either be measured with a load cell or simply assumed to be a standard magnitude. An accelerometer or geophone measures the resulting deflection of the ground below the plate centre.

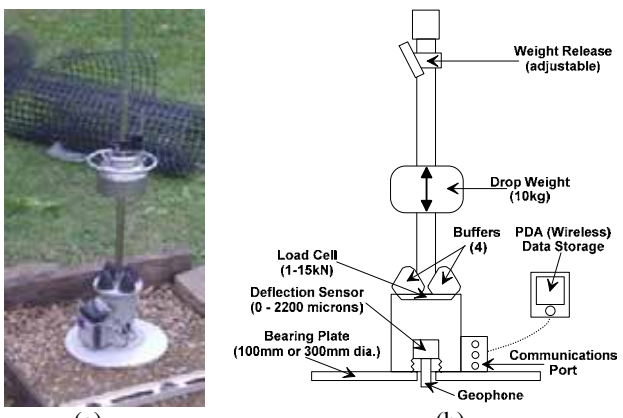

(a) (b)

Figure 1. Prima 100 LFWD (a) during fieldwork and (b) in cross-section in cross-section (after Fleming et. al., 2007)

Table 1. Comparative manufacturer details of LFWDs studied

Aspect of Equipment	ZFG 2000	Prima 100
Manufacturer	Zorn	Sweco (formerly Grontmij A/S)
Test Stress	All test loads assumed fixed at 7.07kN = 100kPa	Independently measured for each weight drop via loadcell
Plate Diameter	300mm	100mm, 300mm
Plate Material	Steel	Aluminum
Plate Thickness / Weight	20mm / 13.9kg	15 - 20mm / 5.9kg
Deflection Measure	Accelerometer mounted on plate	Geophone in contact with ground
Poisson's Ratio (ν) and Stress Reduction Factor (S)	(S, ν) fixed such that $S(1 - \nu^2) = 1.5$	Fully editable by user based on tested material

As both force and deflection values are measured over the duration of the load pulse, the composite Young's Modulus (E_{LFWD}) over the zone of test influence can thus be derived by the classic static elastic theory (Boussinesq elastic half-space) equation, as shown in Equation 1. Previously identified limitations relating to the application of static elastic theory for interpretation of LFWD results are detailed in Fleming et. al. (2007), and include a phase lag between the timing of the observed peak force and maximum deflection values.

$$E_{LFWD} = [A \times P \times R \times (1 - \nu^2)] / d_0 \quad (1)$$

Where: A = Plate rigidity factor ($\pi/2$ for rigid plate); P = Maximum Contact Pressure; R = Radius of plate ν = Poisson's Ratio; d_0 = Peak deflection

Lacey et. al. (2012, 2013) have previously compared the LFWD measured modulus parameter with the results of PLT and DCP tests, for fieldwork completed upon both processed and natural materials. Lacey (2016) also demonstrated that the E_{LFWD} parameter required standardisation to a 'reference' stress state. As the modulus parameter is stress-dependent, it is thus affected by the weight of hammer, drop height and plate diameter utilised. A value of 100kPa was used as the 'reference' stress to compare results for this study ($E_{LFWD\text{-}100kPa}$).

For this study, two (2) types of LFWD were used for the side-by-side testing completed in order to assess the differences in the reported E_{LFWD} parameter. The LFWDs utilised for this study were (a) the Prima 100 (built to ASTM E2835-07) and (b) the Zorn ZFG-2000 (built to ASTM E2583-11). Table 1 details the key variations between these two (2) types of LFWD.

3 FIELD AND LABORATORY TESTING PROGRAM

The completed *insitu* testing program formed a subset of a larger site investigation undertaken for a major highway project in South East Queensland, Australia. A number of *insitu* testing techniques were completed at side-by-side locations within 14 individual test pits at near surface depths of up to 1.2m. The field tests techniques employed included LFWD (2 types), density (sand replacement and nuclear gauge) and DCP profiling. At all locations a residual soil to weak rock profile was encountered (i.e. no alluvial material units). Laboratory testing of representative samples was also completed, allowing classification of the studied materials to Australian Standards (AS1726) and in terms of soaked CBR.

Typical material unit compositions are shown in Table 2. Although no PSD testing was completed on Extremely Weathered (XW) rock materials, a general trend of fines content reduction / gravel content increase of the materials was observed over the full 'Residual Soil' to Highly Weathered (HW) rock weathering interval. A similar trend for the Weighted Plasticity Index (WPI) was also observed, with all values suggesting that the studied materials had 'very low' potential for volume change. These

Table 2. Summary of laboratory determined classification tests, categorised by material unit

Material Unit		Moisture Content (%)	Atterberg Limits (%)				Particle Size Distribution (%)			Weighted Plasticity Index (WPI)
			Liquid Limit	Plastic Limit	Plasticity Index	Linear Shrink.	Gravel / Cobbles	Sand	Fines	
Residual	Granular	10.0 (7 – 13)	16.8	15.8	1.0	0.6	40	48	12	43
	Cohesive	19.1 (14 – 25)	44.5 (39 – 51)	23.4 (19 – 27)	21.0 (18 – 27)	10 (8 – 11)	24	11	65	1232
XW Rock		11.3 (5 – 18)	50.8 (50 – 51)	23.6 (21 – 26)	27.2 (25 – 29)	12.8 (11 – 14)	–	–	–	–
XW / HW Rock		16.5 (13 – 20)	39.5 (34 – 45)	23.9 (21 – 27)	15.6 (13 – 18)	6.4	54.5 (49 – 60)	12.5 (11 – 14)	33 (26 – 40)	612 (442 – 783)
HW Rock		9.0 (3 – 14)	30.6 (23 – 36)	20.2 (19 – 23)	10.5 (4 – 16)	5.4 (3 – 8)	64.3 (61 – 70)	20.3 (15 – 25)	15.5 (12 – 22)	195 (116 – 312)

Table 3. Summary of *insitu* modulus values determined by LFWD testing, categorised by material unit

Material Unit	$E_{LFWD\text{-}100kPa}$ (MPa) – ZFG 2000 LFWD				$E_{LFWD\text{-}100kPa}$ (MPa) – Prima 100 LFWD			
	Interquartile Range	Mean	Median	CoV (%)	Interquartile Range	Mean	Median	CoV (%)
Fill	10.7 – 13.7	11.9	13.2	27%	16.6 – 22.1	20.0	17.3	30%
Residual Soil - Granular	23.9 – 24.0	24.0	24.0	1%	31.7 – 50.8	41.2	41.2	66%
Residual Soil - Cohesive	13.6 – 20.4	16.6	14.5	35%	19.2 – 50.0	37.2	34.5	64%
XW Rock	23.2 – 37.7	31.1	28.5	47%	64.6 – 76.2	69.8	72.0	17%
XW / HW Rock	28.6 – 41.7	35.0	35.6	37%	70.9 – 96.7	85.1	79.8	31%
HW Rock	38.7 – 46.5	40.9	44.4	29%	119 – 152	134	139	25%

trends were considered typical of the gradational transition between residual soil and weak rock materials commonly encountered within QLD, Australia (Lacey, 2016).

4 INSITU MODULUS INCREASE ACROSS SOIL – WEAK ROCK TRANSITION

The *insitu* modulus (E_{LFWD}) parameter determined from each of the two (2) LFWD equipment types utilised in this study are summarised in Table 3. All results were standardised to the E_{LFWD} parameter observed under the application of a 100kPa test stress. A total of 23 side-by-side tests – using both ZFG-2000 and Prima 100 – were completed, with both LFWDs utilising 300mm diameter plates. After data processing via previously published standard methodologies (Lacey, 2016), three (3) datapoints were excluded, resulting in a dataset of 20 E_{LFWD} pairs (n = 20) being used to investigate the correlation between the two (2) LFWD instruments. Table 3 summarises the variation in the E_{LFWD} parameter categorised by both material unit and LFWD equipment.

It is clear that an increase in *insitu* modulus (i.e. decrease in measured LFWD plate deflection) can be strongly associated with the logged decrease of weathering effects within the rockmass. As shown in Figure 2 (for the Prima 100 LFWD results), when 'characteristic' E_{LFWD} values are calculated for each of the weathering classes tested, a near linear relationship is produced across the full 'residual soil' to 'HW rock' weathering interval. This general trend of E_{LFWD} parameter increase was observed regardless of the LFWD equipment utilised, although the magnitude of the reported modulus parameter differed significantly. Over the range of tested materials, the measured E_{LFWD} parameter increased by between 225% (Zorn LFWD) to 350% (Prima LFWD). The magnitude of this modulus increase is approximately the same as the increase observed within typical Shear Wave Velocities of SEQ materials over the same weathering profile interval, whereby an equivalent increase of between 270% and 320% has been observed (e.g. Lacey, 2016).

The surface based LFWD test was successfully applied across the full spectrum of tested 'residual soil' to 'soft rock' material. This finding demonstrates the suitability of the LFWD as a test technique that can be used to investigate the variation in material parameters across the full soil to rock transition. By contrast, the increase in the gravel and the large particle content across the transition between 'residual soil' and significantly weathered, 'soft' rock (refer Table 2) limits the applicability of many traditional site investigation test techniques. As identified by Lacey (2016) CPT tests have been found to typically refuse within residual soil materials within South East Queensland, whilst hammer driven penetration tests (i.e. DCP and SPT) can be expected to refuse within, or provide erroneous results for, XW-HW (or better) rock materials. For competent rock materials (i.e less weathered than Highly Weathered (HW) materials), it would be expected that rock coring site investigation techniques and rock strength testing would become suitable to characterise material parameters.

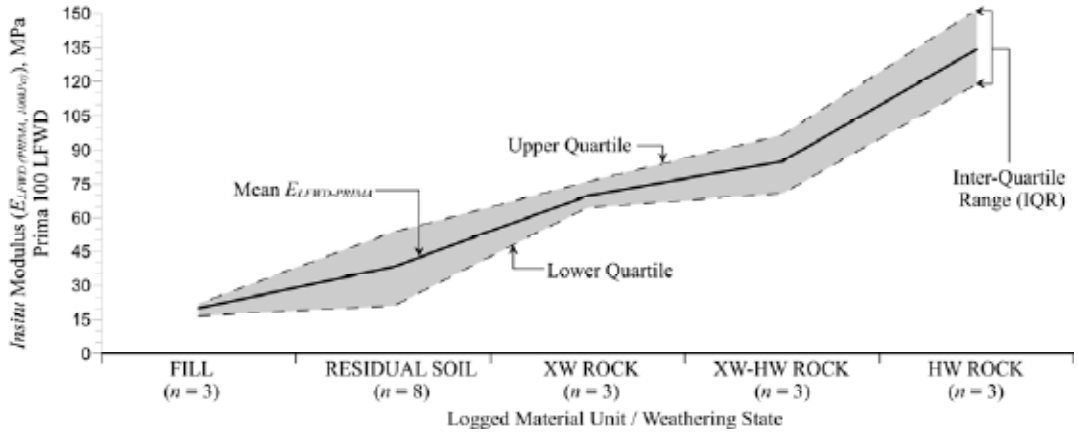

Figure 2. *Insitu* modulus measured by Prima 100 at 100kPa test stress ($E_{LFWD\text{-}PRIMA}$) categorised by weathering state of material

Figure 3. Comparison of *insitu* modulus parameter (E_{LFWD}) measured by Prima 100 and ZFG-2000 LFWD

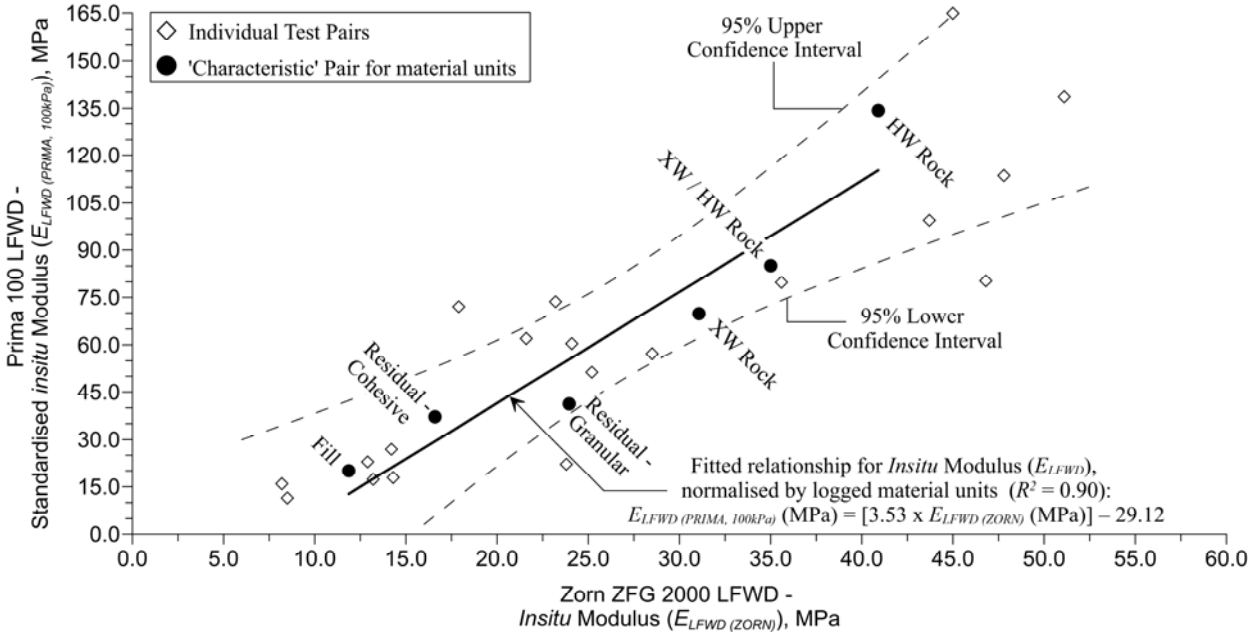

5 COMPARISON OF RESULTS OBTAINED BY LFWD EQUIPMENT VARIATIONS

Having identified that the LFWD test equipment was suitable for use to assess the comparative stiffness of material units across the weathering profile between 'residual soil' and 'HW rock', the difference in the Young's Modulus (E) between the two (2) variants of LFWD equipment used for the site testing was also assessed.

A regression analysis was completed for both the individual LFWD test pair data and using the characteristic E_{LFWD} values determined for each material unit. In both cases, a strong, positive linear relationship between the Zorn and Prima 100 *insitu* modulus values (E_{LFWD}) was demonstrated ($R^2 > 0.75$). Equation 2 and Figure 3 present the relationship between the characteristic E_{LFWD} values determined for each material unit.

$$E_{LFWD\ (PRIMA\ 100)} = [3.53 \times E_{LFWD\ (ZFG\text{-}2000)}] - 29.12 \quad (R^2 = 0.90,\ p < .05) \qquad (2)$$

Where all E_{LFWD} values are in MPa.

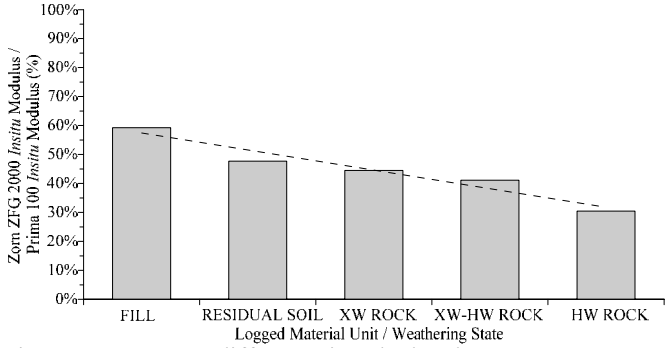

Figure 4.Percentage difference in calculated E_{LFWD} parameter between Prima 100 LFWD and ZFG-2000 LFWDs

By comparison of the average E_{LFWD} values determined by each LFWD instrument and for each of the weathering classes tested, the varying relationship between the two (2) E_{LFWD} values was again demonstrated. As presented in Figure 4, the difference between the comparable E_{LFWD} values linearly decreases as the stiffness of the tested material increases. The E_{LFWD} value determined by the ZFG-2000 equipment decreases from 48% to 30% of the Prima 100 value over the 'Residual Soil' to 'HW Rock' weathering interval.

The range of deflections produced by the Prima 100 LFWD at a 100kPa test stress ($\bar{x}$ = 0.6mm, σ = 0.4mm) were lower than comparative values observed with the ZFG-2000 LFWD ($\bar{x}$ = 1.2mm, σ = 0.6mm). As the calculated '*insitu* modulus' is a deflection dependent parameter (refer Equation 1), then the higher deflections recorded by the ZFG-2000 instrument resulted in consistently lower '*insitu* modulus' (E_{FLWD}) values being determined (for all other variables being standardised).

Previous studies (e.g. Lacey et. al., 2012; Nazzal et. al., 2007) have identified that the E_{LFWD} values produced using the Prima 100 LFWD equipment equate approximately to modulus values produced by traditional test methods, such as full scale Falling Weight Deflectometers (FWDs) and static Plate Load Tests (PLTs). Accordingly, it is recommended that the E_{LFWD} parameter produced by the ZFG-2000 instrument are not directly adopted as 'subgrade modulus' values or use in applications as a direct replacement for parameters determined by 'traditional' *insitu* modulus measurement techniques. As shown by the results of the current study and Figure 4, the additional factor that is required to be applied to the ZFG-2000 results varies based on the stiffness of the material.

Table 4. Typical DCP and *insitu* modulus material properties for range of material units investigated

Dynamic Cone Penetrometer (DCP)		*Insitu* Modulus, $E_{LFWD\text{-}100kPa}$ (MPa)		Material Unit / Weathering State
Blows / 100mm rod penetration (no.)	Rod penetration / Hammer Blow (mm)	Prima 100 LFWD[1]	ZFG-2000 LFWD[2]	
3	33	16	8	SOIL (Fill / Residual Soil)
4	25	20	10	
5	20	24	12	
10	10	43	21	Residual Soil to XW/HW Rock
20	5	76	36	XW / HW Rock
25	4	92	42	
33	3	116	53	HW Rock

[1] Modulus calculated assuming a total value of 1.5 for the Stress Reduction Factor and Poisson's Ratio pair (S, *v*)
[2] Additional conversion required to produce a design 'subgrade modulus' value from ZFG-2000 results

6 SUMMARY OF INSITU PARAMETERS FOR RESIDUAL SOILS AND WEAK ROCK

Of the 23 sites where comparative LFWD testing was completed, a Dynamic Cone Penetrometer (DCP) test profile extended to a depth below the level of LFWD testing for 22 sites. A correlation that related the penetration rate (PR) of the DCP test and the E_{LFWD} relationship was determined for the range of materials tested. This relationship builds on previously published DCP:E_{LFWD} correlations (e.g. Lacey, 2016; Nazzal 2007) and extends such relationships to the stiffer materials (i.e. lower PR values) investigated by this study.

Table 4 summarises the relationship between the typical DCP penetration rates and comparative *insitu* modulus (E_{LFWD}) values that were determined based on the data collected by this study. These results are anticipated to be generally applicable to residual soil and soft rock profiles found throughout SEQ, and general material and weathering state descriptors expected to be associated with each result are also provided in Table 4.

7 SOAKED vs. INSITU CBR VALUES

California Bearing Ratio (CBR) values are traditionally used to estimate the design modulus for embankment and pavement projects. Examples of this include CBR:*E* relationships included in standard design guidelines such as NAASRA (1987) or ASSHTO (2002).

In the study undertaken, both *insitu* and laboratory CBR values were determined. *Insitu* CBR values were determined via (a) direct measurement using a specialised CBR attachment for the ZFG-2000 LFWD equipment; (b) inferred from the results of DCP testing (adopting the NAASRA defined DCP_{PR}:CBR relationship). Laboratory determined CBR values were calculated as per AS1289.6.1.1; using samples soaked for four (4) days and prepared using standard compaction techniques.

For the dataset of soaked CBR values ($n = 14$), correlations were attempted to be made between the individual data pairs of *insitu* CBR values. Regardless of the method of *insitu* CBR calculation, no statistically significant relationships were found that related *insitu* to laboratory determined CBR values. This result (i.e. non-correlation between soaked CBR and *insitu* test pairs) was expected, as the soaked CBR test involves a fundamental change in both material state and composition – the removal of the oversize fraction of the sample and the subsequent compaction of material. The applied compactive effort would be expected to break inter-particle bonds present within the residual soil and weathered rock, and thus remove the structure that the relict rock structure provides to such materials.

When characteristic *insitu* and soaked CBR values were determined for each material unit, a strong, positive linear relationship could be demonstrated that related the results of the *insitu* and laboratory based tests ($R^2 > 0.85$). Figure 5a presents the relationship derived for the direct (ZFG-2000) and indirect (DCP via NAASRA relationship) estimation of *insitu* CBR respectively. However, due to the small dataset used ($n = 5$), the values produced via this relationship should be interpreted cautiously.

The laboratory determined, soaked CBR results displayed a plateauing across the XW to HW rock materials (12% < Soaked CBR < 13%) compared to the continually increasing CBR values produced by the results of *insitu* testing. As conceptually shown in Figure 5b, this observation has been interpreted to indicate the effect of the relict rock structure and oversize particles present within the weathered rockmasses. This finding also shows the highly conservative nature of adopting soaked CBR test results as representative of *insitu* conditions material properties associated with residual soils and weak rock materials. It should be noted that the CBR test is not applicable for samples with greater than 20% oversize materials (as per AS1289), yet continues to be used for such materials, due to the absence of a more reliable or convenient test.

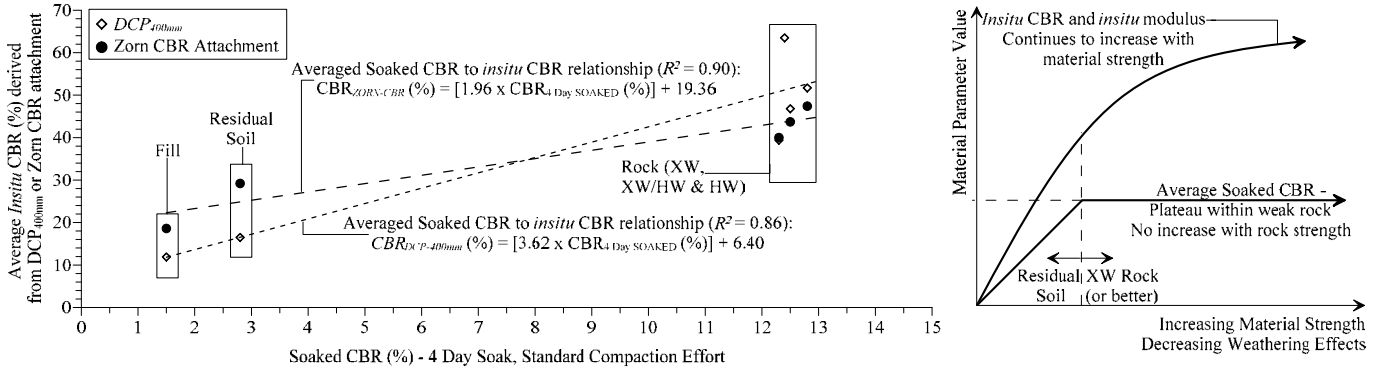

(a) (b)

Figure 5. (a) Soaked CBR (%) compared to *insitu* measured CBR (%) values, categorised by weathering state of material (b) conceptual difference between *insitu* and soaked CBR values over residual soil / weak rock profile.

8 CONCLUSIONS

The methodology and analyses detailed within this study demonstrates the successful use of LFWD equipment to characterise the *insitu* modulus parameter (E_{LFWD}) across a wide range of comparatively incompressible materials; from stiff residual soils to highly weathered, low strength rock. The suitability of the LFWD to be used for subgrade assessment across the full residual soil / weak rock interface has been demonstrated.

Other conclusions that can be observed based on the side-by-side testing completed and correlation of test results include:

- Although strongly correlated, the Zorn ZFG 2000 LFWD instrument will routinely produce deflections of higher magnitude than the Prima 100 LFWD instrument, and that the relationship between the Zorn ZFG 2000 and Prima 100 determined E_{LFWD} values varies based on the stiffness of the material undergoing testing;
- The strongest relationship between LFWD and DCP test results occurred when the DCP profile over the 400mm depth interval below the LFWD test was considered (i.e. zone of influence of LFWD equates to 1.33 x Plate Diameter);
- Strong relationships between characteristic *insitu* modulus, *insitu* CBR and soaked CBR values were developed when the data was normalised for weathering state of the tested material. Significant variations in laboratory determined (soaked) CBR values – likely due to material grading and the varying proportion of oversize materials – prevented direct comparison of test results for individual samples; and
- *Insitu* CBR values reflect the field conditions at the time of testing, whilst soaked CBR values are based on remoulded samples and applying 'flood' conditions. For the site investigated, soaked CBR values appeared to plateau at 12 – 13% across the full rock profile assessed (regardless of weathering state), whilst the *insitu* CBR values continued to increase as per the weathering grade.

9 REFERENCES

Australian Standards (2014). *AS 1289 – Methods of testing soils for engineering Purposes – Method 6.1.1*, SAI Global

Australian Standards (1993). *AS 1726 – Geotechnical Site Investigations*, SAI Global

AASHTO (2002). *Guide for Design of Pavement Structures* American Association of State Highway and Transportation Officials, Washington, DC

ASTM E2583-07 (2011). *Standard Test Method for Measuring Deflections with a Light Weight Deflectometer (LWD)*, ASTM International, West Conshohocken, PA.

ASTM E2835-11, (2011). *Standard Test Method for Measuring Deflections Using a Portable Impulse Plate Load Test Device*, ASTM International, West Conshohocken, PA.

Fleming, P. R., Frost, M. W. & Rogers, C. D. F. (2000). A comparison of devices for measuring stiffness insitu, *Proc., 5th Int. Conf. on Unbound Aggregate in Roads*, Nottingham, UK

Fleming P.R., Frost, M.W. & Lambert, J.P. (2007). "Review of Lightweight Deflectometer for Routine In Situ Assessment of Pavement Material Stiffness," *Journal of the Transportation Research Board*, No. 2004: 80–87.

Lacey, D., Look, B. & Williams, D. (2012). "Assessment of the compatibility between, and zone of influence of, PLT and LWFD tests", *9th ANZ Young Geotechnical Professionals Conference (9YGPC)*, Melbourne, Australia, 11th – 14th July

Lacey, D., Look, B. & Williams, D. (2013). "Assessment of Relationship between insitu modulus derived from DCP and LFWD testing" in Cui, Y-J., Emeriault, F. & Cuira, F. (eds.) *Proceedings of the 5th International Young Geotechnical Engineers' Conference: 5th IYGEC*, Paris, France, 31st August – 2nd September, IOS Press. 379–382

Lacey, D. (2016). *Assessment of some engineering properties and testing methods of residual soil and highly weathered rock materials in QLD, Australia*, Ph.D. Thesis, The University of Queensland, Brisbane, Australia

NAASRA (1987). *Pavement design: a guide to the structural design of road pavements*, National Association of Australian State Road Authorities, Sydney, NSW

Nazzal, M.D., Abu-Farsakh, M.Y., Alshibli, K. & Mohammad, L. (2007). "Evaluating the light falling weight deflectometer device for in situ measurement of elastic modulus of pavement layers", *Journal of the Transportation Research Board*, No. 2016. 13–22

Vennapusa, P. & White. D.J. (2009). "Comparison of Light Weight Deflectometer Measurements for Pavement Foundation Materials", *Geotechnical Testing Journal*, 32 (3): 239–25.

Geotechnical and Geophysical Site Characterisation 5 – Lehane, Acosta-Martínez & Kelly (Eds)

Morphology and geotechnical characterization of a phyllite weathering profile developed under tropical climate

M.F. Leão
Ph.D. Student, Geology Department, Universidade Federal do Rio de Janeiro, Rio de Janeiro (RJ), Brazil
E.A.G. Marques
Professor, Civil Engineering Department, Universidade Federal de Viçosa, Viçosa (MG), Brazil

ABSTRACT: Weathering profiles have been studied in several parts of the world in an attempt to better understand geotechnical and geomechanical behaviour of the different materials occurring along these profiles, specially transitional materials, formed by different portions of soil and weathered and sound rock. To this behaviour one can also add anisotropy and heterogeneity, making the problem even more complex. In order to evaluate such phenomena under tropical climate, a phyllite weathering profile located at Iron Quadrangle, Minas Gerais State, Southeast Brazil was selected. The cut slope in which the rock outcrops was detailed described and material from W1 to W4 weathering class materials were recognised. A detailed morphology description was performed in order to identify the contacts between those different weathering materials and to evaluate the result of weathering on rock matrix and on rock mass. This manuscript presents the results of this morphological description, as well as results from Schmidt hammer field and lab tests performed in all weathered materials recognised within the profile. Weathering profile morphology shows the presence of more weathered terms intercalated with sound ones. Schmidt hammer results proved to be an easy and useful way to differ weathering materials along the profile.

1 INTRODUCTION

The esclerometer or Schmidt hammer is a non-destructive physical method, through which it is possible to analyze the rock quality, in terms of the parameter obtained R (Rebound). This parameter allows, through mathematical correlations, empirical obtaining of rock uniaxial compressive strength (UCS) and deformability (Young's modulus). The sclerometry is considered a practical, fast, cheap way to mechanically characterize in situ rock.
Given these advantages the authors have sought to use the above test as a way of preliminary assessment of the rocks resistance and how it varies with weathering. The study is justified by the lack of information in the scientific literature on geomechanical parameters of altered rocks, mainly for lower degree metamorphic, such as phyllites. Through the characterization of a sericitic phyllite rock alteration profile and performing in situ assays, the authors demonstrate the variability of constitutive parameters of the rock due to the evolution of the degree of alteration.

2 REGIONAL GEOLOGY

The Quadrilátero Ferrífero is located in the South Central region of the state of Minas Gerais, between the cities of Belo Horizonte and Ouro Preto. At present, the rocks in the region are grouped into three main geological units: the complex granite-gneiss, the Rio das Velhas Supergroup (of Archean age) and the Minas Supergroup (Paleoproterozoic), where the latter include the rocks studied in this article, which belong to the Piracicaba Group - Batatal Formation, characterized by phyllites sericitic sometimes carbonaceous or ferruginous.

3 METHODOLOGY

The methodology can be divided into two steps. The first concerns the characterization of the alteration profile, identification of mechanical classes (according to ISRM, 2007), collection of representative samples and implementation of sclerometry in situ; a second stage comprised the repetition of the sclerometry, but in the rock blocks, in order to evaluate the influence of the in situ condition for this assay.

3.1 *Field Geological mapping and definition of geomechanical degrees*

The geological surface mapping took place in the Mariana city region, near the km 140 of BR-356, the

highway that connects the cities of Mariana (MG) and Ouro Preto (MG), Brazil, in a road cut where there exposing a phyllite sericitic weathering profile with some levels of localized quartzite and quartz pebbles (up to 10 cm), are spread on the ground surface. At this stage of mapping and recognition of the profile, at each point, the identification of the degree of change in sericitic phyllite was held, as well as structural data (fractures and foliation) from measurements with geological compass.

Figure 1. Weathering profile of phyllite rocks, in BR-356, MG – Brazil.

At the studied site (Figure 1) it was possible to identify five weathering levels, W1 to W4 and W5 (not included in the article), according to the ISRM (2007) classification criteria presented in the Table 1. 600 kg of sericitic phyllite samples were collected to characterize geological and geotechnical-geomechanical tests.

The characterization was performed throughout macroscopic analysis of mineralogy and mineralogical changes, color and variations thereof, grain size, rock matrix tests (evaluation of the degree of coherence), evaluation of fracture families, including characteristics such as spacing, openness and persistence and estimating RQD based on Jv ratio (number of cracks/m³). Disturbed and undisturbed samples (Figure 2) were collected directly from outcrops in road cuts. Note that due to the phyllites characteristics, such as the existence of clear parallels foliation plans, samples could not be molded in the form of standard blocks (30 cm x 30 cm x 30 cm), since during the extraction process, samples tend to suffer spalling.

3.2 *The Schmidt Hammer*

The rebound hammer or Schmidt hammer is a very useful device to get in situ compressive strength, as it is a simple and non-destructive test. It must be pointed out that the use of this test does not replace uniaxial compression tests in the laboratory, for example, but allows an estimate of that property.

Figure 2. Separation of samples collected for packaging in shipping boxes.

Table 1. Weathering rock classes (ISRM, 2015).

Term	*Description*	*Class*
Fresh rock	The rock material isn´t discolored and has its original aspect. The point of geological pick scratches the surface with many difficulties. When the hammer strikes the rock material a ringing sound is emitted	W1
Slightly weathered rock	Discoloration is present only near joint surface. The original mass structure is perfectly preserved. The point of geological pick scratches the surface with difficulty. When the hammer strikes the rock material a ringing sound is emitted.	W2
Moderately slightly weathered rock	The rock material is discolored, but locally the original color is present. The original mass structure is well preserved. The point of geological pick produces a scratch on the surface. The rock material makes a regular sound when is struck by a hammer.	W3
Highly slightly weathered rock	All rock material is discolored. The original mass structure is still present and largely intact. The point of geological pick not easily indents. When the hammer strikes the rock material a dull sound is emitted.	W4
Completely slightly weathered rock	All rock material is completely discolored and converted to soil, but the original mass structure is still visible. The point of geological pick not easily indents. When the hammer strikes the rock material a dull sound is emitted.	W5
Residual and colluvial soils	All rock material is converted to soil. The original rock structure is completely destroyed. The point of geological pick easily indents in depth. When the hammer strikes the rock material no sound is produced.	W6

Its operation is caused by the compression of a hammer rod through a spring, located inside the equipment. The hammer will stem retracts until it

reaches the end of its course. At this time the rod is released instantly, being projected onto the surface, which is being applied. This impact generates a shock wave transmitted to the application surface, causing a kind of rebound, causing a mass shift, which is subsequently transmitted to the device, registering a dimensionless value (R, rebound) or rebound hammer index. This value varies depending on the hardness of the material, the higher the R value, the greater the hardness of the rock.

Questions concerning the influence of the anisotropy of the material can be evaluated by conducting the test in different directions. Basu and Aydin (2004), reports that in non-horizontal conditions the test may be influenced by gravity in the test.

Likewise, Day and Goudie (1977) suggest that for effectiveness of the test application points should be far from the border samples, avoiding much lower values due to energy dissipation. The ISRM standard (1978a) recommends that the dimensions of the samples tested should have edges with a length of 6 cm, while ASTM (2001) recommends a minimum length of 15 cm. For analysis on cylindrical specimens, both standards agree with a minimum diameter NX (54.7 mm). The impact application surface should be free of cracks up to 6 cm deep, leading to influence the propagation of the shock wave. The influence of the surface smoothness must also be evaluated as it may influence the value of R, as the impact hammer can crush asperities or irregularities on the surface, resulting in an additional loss of energy (Hucha, 1965). Katz, et al. (2000) noted that the degree of rock polishing could influence the magnitude and frequency of R values obtained in the tests. Other aspects that should also be considered are the presence of families of fractures or foliation plans, excluding loose surfaces for conducting the test, the penetration of the tip in very altered and friable materials, the presence of heterogeneous materials, and the stability of the sample when test is performed in the laboratory. For igneous rocks, also the evolution of weathering processes should be considered, as it can produce microstructural changes from discoloration to the collapse of the crystal structure (Aydin and Duzgoren-Aydin, 2002). Several methods of classification weathering are well known, in general based on subjective criteria, providing differentiation among weathering degrees. An index-based classification tests have great advantages, mainly related to sensitivity and consistency in classification. Aydin and Duzgoren-Aydin (2002) have cited many important studies related to Schmidt Hammer used for this purpose.

To obtain the rebound hammer index for phyllites, the authors have used a digital Proceq rebound hammer, N type (Figure 3), recommended for obtaining hardness in the field, and, based on the results, a prediction of the weathering degree, as well as to obtain the uniaxial compression strength (UCS) and Young's modulus, by using correlations presented in the literature.

Figure 3. Rebound hammer N type used in the field (Source: www.proceq.com).

Twenty hits were recorded for each area of 20 cm x 20 cm, providing an estimate of JCS based on Brazilian Standard (NBR 7584 - ABNT, 1995), always respecting the same inclination for the test. After preparation of the rock surface the head of the Schmidt hammer was performed both vertically and horizontally, when possible, i.e. perpendicular to foliation and parallel to it, in order to estimate the anisotropy behavior of the rock.

In a second step, lab tests were performed on rock samples (thickness greater than 100 mm) in the laboratory in order to compare the variation of in situ tests. It was used a rebound hammer N type, analogical, also from Proceq manufacturer (Figures 4 and 5).

Figure 4. Analogical rebound hammer N type used in lab tests.

Figure 5. Sclerometry test on W4 class samples in the laboratory –(LEMETRO – UFRJ).

4 RESULTS

Based on field observations, Table 2 presents a summary of the characteristics observed.
It is possible to note that there is a variation in the characteristics and properties as there is a progressive degree of rock weathering, such as a reduction of the brightness and coherence and an increase in aperture and spacing of fractures, as well as in Jv.
The R values obtained from Schmidt hammer, also shows good relationship with weathering, presenting a decrease with weathering, both for in situ and lab tests, as shown in Figure 6 and Figure 7, respectively. Schmidt hammer results for tests performed perpendicularly and parallel to foliation were just representative for sound materials, as shown on Figure 6. These results are in line with those from Marques and Williams (2015) for phyllites from Australia.

Table 2. Weathering profile characterization of phyllite rocks.

Weathering Degree	W1	W2	W3	W4
Mineralogy	Rock, in general, has a very thin mineralogy, practically aphanitic, brightness silver intense in W1 samples reducing the same, to matte, more altered degrees W4, silky appearance, with detachment of fine clay and sand residues the fragments centimeters in W4 levels through laminar spalling, following the natural foliation of the rock. Displays cleavages are more evident crenulation level in positions orthogonal to each other. Despite clear gradation of rock conditions change, you cannot see, macroscopically mineralogical variations, and this is most evident feature through color and mechanical variations thereof.			
Coherence	Coherent rock	Coherent a low coherent rock	Low coherent rock	Very low coherent rock
Color	Silver grey	Silver grey with reddish passages	Dark silver grey with yellow passages	Dark grey of variegated color, with dull luster portions
Fractures	The rock has fractures families, nearly orthogonal and parallel to the foliation.			
Aperture /Spacing	0 to 0,2 cm/6 cm - 2 m	0,2 to 0,5 cm 6 cm - 2 m	0,5 cm to 0,8 cm/6 cm - 2 m	0,8 mm to 2,0 cm/6 cm - 2 m
Jv	1 -3		3 -10	

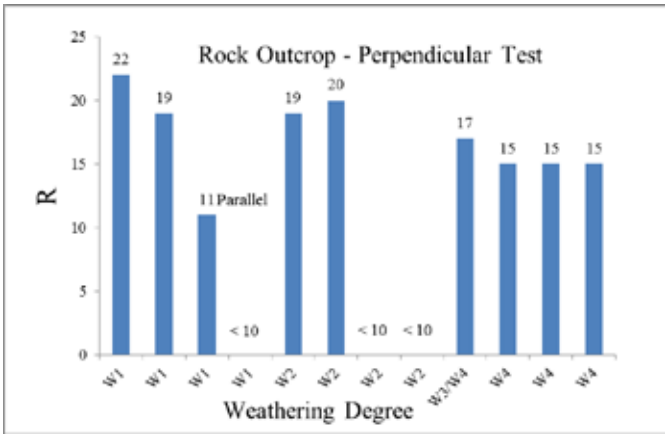

Figure 6. Schmidt Hammer in situ test.

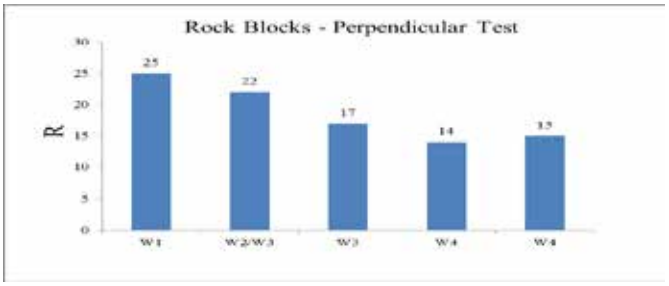

Figure 7. Schmidt Hammer test in rock blocks.

5 CONCLUSION

The results shows that the proposed methods used were able to produce data that can differentiate weathering materials for the phyllite under study, as it was possible to identify the variation of basic features such as color, brightness, physical properties of fractures, coherence and Jv. Also, Schmidt hammer results have proved to be used as an index parameter for the differentiation of weathering phyllite grades.

6 ACKNOWLEDGMENTS

The authors thank FAPEMIG for the financial support to attend the conference and to the Universidade Federal de Viçosa e Universidade Federal do Rio de Janeiro, Brazil, for funding and providing laboratory support.

7 REFERENCES

ABNT - NBR 7584. 1995. Concreto endurecido – Avaliação da dureza superficial pelo esclerômetro de reflexão. Rio de Janeiro. (In Portuguese)

ASTM, 2001. Standard test method for determination of rock-hardness by rebound hammer method. *ASTM Stand*. 04.09 (D 5873-00).

Aydin, A., Duzgoren-Aydin, N.S., 2002. Indices for scaling and predicting weathering-induced changes in rock properties. *Environ. Eng. Geosci.* VIII, 121–135.

Basu, A, Aydin, A. 2004. A method for normalization of Schmidt hammer rebound values. International Journal of Rock Mechanics & Mining Sciences 41 (2004) 1211–1214

Day, M.J., Goudie, A.S., 1977. Field assessment of rock hardness using the Schmidt test hammer. *Br. Geomorphol. Res. Group Tech. Bull.* 18, 19–29.

Hucka, V.A., 1965. A rapid method for determining the strength of rocks in situ. *Int. J. Rock Mech. Min. Sci., Geomech. Abstr*. 2, 127– 134.

Katz, O., Reches, Z., Roegiers, J.-C., 2000. Evaluation of mechanical rock properties using a Schmidt Hammer. *Int. J. Rock Mech. Min. Sci.* 37, 723–728.

Marques, E. A. G; Williams, D. J. (2015). Weathering of Bunya phyllites in Southwest Brisbane – a geotechnical approach. In: ANZ 2015 – 12th Australia New Zealand Conference on Geomechanics. Proceedings…New Zealand Geotechnical Society Inc. Wellington (NZ). p. 1-8.

ISRM. 2015. The ISRM Suggested Methods for Rock Characterization, Testing and Monitoring: 2007-2014 2015th Edition by R. Ulusay (Editor).

ISRM, 1978a. Suggested methods for determining hardness and abrasiveness of rocks. *Int. J. Rock Mech. Min. Sci., Geomech. Abstr.* 15, 89– 97.

Geotechnical and Geophysical Site Characterisation 5 – Lehane, Acosta-Martínez & Kelly (Eds)

Evaluation of the engineering properties of the weathered layer in Korea

S. H. Lee, B. H. Jo, C. Chung
Department of Civil and Environmental Engineering, Seoul National University, Republic of Korea

ABSTRACT: Nearly 80% of the ground surface in Korea is covered with weathered residual soils or weathered rocks, which can be classified into very dense coarse soil and weak and highly decomposed rock. As such, many geotechnical structures have been constructed on this weathered layer. These geomaterials, however, have not been mechanically distinguished from each other in a clear way, and as such, the boundary between the two layers has often been inconsistently and erratically determined. In this study, the strength and stiffness of the geomaterials of the weathered layer in Korea were investigated as design values using the investigation site database. The recommendations from the existing literature were examined, and quantitative assessment based on test results of SPT-N values was attempted. As a result, a more useful way of classifying the weathered layer and estimating the bearing capcity of pile including resistance of dense weathered residual soil were suggested and applyed it to the bearing capacity estimation of the pile resting on the weathered layer.

1 INTRODUCTION

Nearly 80% of the ground surface in Korea is covered with weathered residual soils or weathered rocks, which can be classified into very dense coarse soil and weak and highly decomposed rock. As such, many geotechnical structures have been constructed on the weathered layer. Especially, about 52% of the cast-in-place concrete piles in Korea have been installed in weathered rocks (KICT 2008), which means that the weathered layer is the main bearing stratum where side friction and end bearing resistance are mobilized. Therefore, assessment of the characteristics based on quantitative test results such as the strength and stiffness of the weathered layer as design values, and establishment of clear classification criteria, are very important.

Engineering properties such as the SPT-N value, RQD (rock quality designation), and UCS (unconfined compressive strength) are generally used to assess the characteristics of weathered layers. The relationship between the relative density of coarse soil and the SPT-N value was suggested by Terzaghi and Peck (1967), and the criterion of SPT-N value for classifying weathered rock was developed by Clayton (1995). RQD, originally proposed by Deere et al. (1976), is an indirect measure of the number of fractures within a rock mass, which is defined as the ratio of the summation of the core pieces longer than 10 cm to the total length of the core. As RQD is most useful when combined with other properties for evaluating rock strength, deformability, and discontinuity, many rock mass classification systems include RQD as a major parameter for assessing the rock mass characteristics. It is generally known that the rock mass consists of many intact rocks and discontinuities, and as such, the UCS of the intact rock is an important property for assessing the rock mass characteristics and grade. Hoek and Brown (1997) suggested rock mass classifications using UCS, which consist of seven grades, from extremely weak to extremely strong.

Geomaterials have been conventionally classified as soil and rock, but many of the geomaterials that are encountered in reality exhibit the properties of both soils and rocks. As such, it is very difficult to clearly define a geomaterial as soil or rock. O'Neil et al. (1996) defined a geomaterial that is in between soil and rock as an intermediate geomaterial (IGM), and applied it to the design of drilled shafts. The IGMs are divided into the cohesionless IGMs and the cohesive IGMs, which exhibit an SPT-N value within the 50-100 range and have 0.5-5 MPa unconfined strength, respectively. Especially, the cohesionless IGMs are similar to the relatively dense weathered residual soil in Korea.

In this study, the strength and stiffness of the geomaterials of the weathered layer in Korea were investigated as design values using the investigation site database. The recommendations from the existing literature were examined, and quantitative

assessment based on test results of SPT-N values was attempted. As a result, more useful classification criteria and estimating the bearing capcity of pile including resistance of dense weathered residual soil were suggested and applyed them to the bearing capacity estimation of the pile resting on weathered layer.

2 ANALYSIS OF THE CURRENT STATE IN KOREA

2.1 *Classification criteria of the weathered layer*

The weathered layer is divided into weathered residual soil and weathered rock in Korea. To determine the boundary of the two layers, engineers use quantitative information obtained from laboratory and *in-situ* test results. Several institutions have suggested a criterion for the weathered layer based on its engineering properties to assist engineers in classifying the weathered layer. In this study, the criteria recorded in the specifications of four major institutions in Korea were examined. These are summarized in Table 1 and 2.

As shown in Table 1 and 2, the types of engineering properties that are used to classify the weathered layer are not unified. Furthermore, even if the type of engineering property is the same, the suggested values are not equal to one another. In other words, no standard classification criterion has been established in Korea to date, which means that the depth and thickness of the weathered layer are variable according to the criterion selected by engineers. In addition, the weathered residual soil is not subdivided based on the degree of density. As described in the introduction part of this paper, relatively dense weathered residual soil is very similar to the cohesionless IGM, which exhibits an SPT-N value within the range of 50-100 blows. Although the strength of IGMs is as high as that of weathered rock, and although researches on the applicability of the IGM theory with relatively dense weathered residual soil for estimating the pile capacity have been conducted in South Korea, criteria for IGMs have yet to be established Therefore, when designers estimate the bearing capacity of a cast-in-place concrete pile embedded in a weathered rock, the side resistance of the dense weathered residual soil is usually not considered.

Table 1. Classification criteria of weathered residual soil

Institution	N-value[1)]	Elastic wave velocity	UCS
	blows/cm	km/s	MPa
Korea Expressway Corporation	≤ 50/15	≤ 3.0	≤ 25
Korea Rail Network Authority	≤ 50/15	-[2)]	-[2)]
Seoul Metropolitan Government	≤ 50/10	≤ 1.2	-[2)]
Korea Geotechnical Society	-[2)]	-[2)]	-[2)]

[1)] N-value is the number of blows when the penetration depth is 30 cm, but it is expressed with 50 blows/penetration depth for more than 50 blows in Korea.
[2)] No criterion is suggested.

Table 2. Classification criteria of weathered rock

Institution	N-value	Elastic wave velocity	UCS	RQD
	blows/cm	km/s	MPa	%
Korea Expressway Corporation	≥ 50/15	3.0 ~ 3.5	≤ 60	≤ 20
Korea Rail Network Authority	≥ 50/15	≤ 3.5	≤ 5	-
Seoul Metropolitan Government	≥ 50/10	1.0 ~ 2.5	≤ 10	≤ 10
Korea Geotechnical Society	-	0.7 ~ 1.2	30~70	-

2.2 *Distributions of the engineering properties*

To obtain the distributions of the weathered layer, 600 boring logs recorded with the engineering properties were randomly selected from the Geotechnical Information Database System of the Ministry of Land, Infrastructure, and Transport of the Republic of Korea. All the boring logs included the SPT-N values of the weathered layer, whereas the information on the UCS and RQD of the weathered layer was rarely recorded. Therefore, only the SPT-N values were analyzed in this study. The total number of SPT-N values that were analyzed for weathered residual soil was 742, and that for weathered rock was 432.

As the SPT-N value is expressed in two ways in South Korea (the number of blows/30 cm or 50 blows/penetration depth), every SPT-N value was converted to the ratio of blows to the unit penetration depth in this study for convenient analysis. Figure 1 and 2 show the distribution of the SPT-N values of weathered residual soil and weathered rock, respectively.

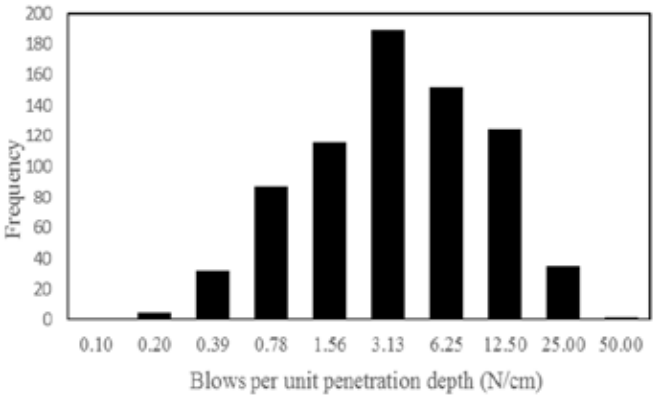

Figure 1. Distribution of the SPT-N values of weathered residual soil.

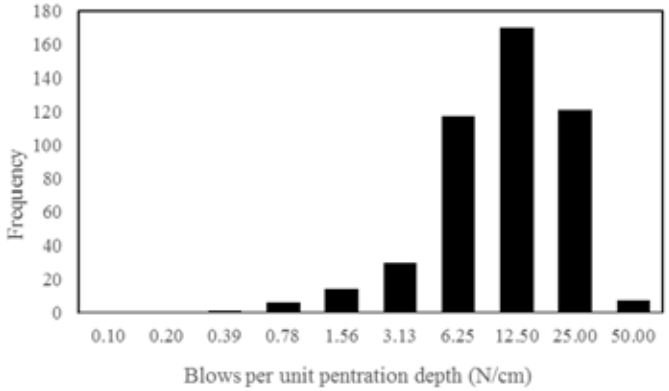

Figure 2. Distribution of the SPT-N values of weathered rock.

As shown in Figure 1, the range of blows per unit penetration depth of the weathered residual soil was from 0.07 (2 blows/30 cm) to 50 (50 blows/1 cm), which means that the degree of density of the soil is varied, from very loose to very dense. The frequencies and percentages of the major class intervals that are used to classify the weathered layer are shown in Table 3. Relatively loose weathered residual soil, which exhibited an SPT-N value of 0 blows/30 cm to 50 blows/30 cm, accounted for about 34%. Also, as the percentage of relatively dense weathered residual soil corresponding to the cohesionless IGM criterion was 24%, the weathered residual soil has to be subdivided based on the density. Although the boundary specified with the SPT-N value between the weathered residual soil and the weathered rock is 50 blows/15 cm or 50 blows/10 cm, 42% and 28% of the weathered residual soil that was analyzed in this study exhibited an SPT-N value with more than the boundary, which means that many investigators still determine the type of a weathered layer not with the quantitative engineering property but based only on their own empirical judgment.

Figure 2 and Table 4 show the distribution of the SPT-N values of weathered rock. Almost the whole weathered rock that was analyzed in this study exhibited higher than 3.33 blows per unit penetration depth (50 blows/15 cm), which corresponds with the boundary criterion between weathered residual soil and weathered rock. Using only the SPT-N value, however, limits the investigation to the characteristics of weathered rock. As such, a more detailed investigation using a triple-core barrel is needed to get the rock properties such as the UCS and RQD.

Table 3. Frequencies and percentages of the SPT-N values of weathered residual soil

Range of N value	Frequency	Percentage
Blows/cm		%
$0 \leq N < 50/30$	248	34
$50/30 \leq N < 50/15$	181	24
$50/15 \leq N < 50/10$	106	14
$50/10 \leq N$	207	28
Total	742	100

Table 4. Frequencies and percentages of the SPT-N values of weathered rock

Range of N value	Frequency	Percentage
Blows/cm		%
$N < 50/15$	16	4
$50/15 \leq N < 50/10$	56	13
$50/10 \leq N$	360	83
Total	432	100

2.3 *Inconsistent decision of boundary*

Only the SPT-N values have generally been used to investigate the weathered layer in Korea, but as the classification criteria of the weathered residual soil and weathered rock are not unified, as shown in Table 1 and 2, the boundary between the two layers has been determined according to the criterion used by the investigator. In addition, as a standard penetration test is performed at every 1 or 1.5 m depth spacing, which means that the SPT-N value is discrete information, the criterion between the two weathered layers, such as 50 blows/15 cm, could not be exactly measured. Therefore, the investigators usually determine the boundary based on their own judgment. For example, as shown in Figure 3, if the SPT-N value is measured as 50 blows/19 cm at a depth of 5 m, and as 50 blows/13 cm at a depth of 6 m, the investigator can decide the boundary between the two weathered layers as (1) a depth of 6 m for a conservative estimation or (2) a middle depth of 6 and 5 m or 3 m, a depth where the SPT-N value is predicted as 50 blows/15 cm by linear interpolation. Therefore, a specific method of arriving at a decision regarding this matter is needed to prevent the boundary from becoming variable.

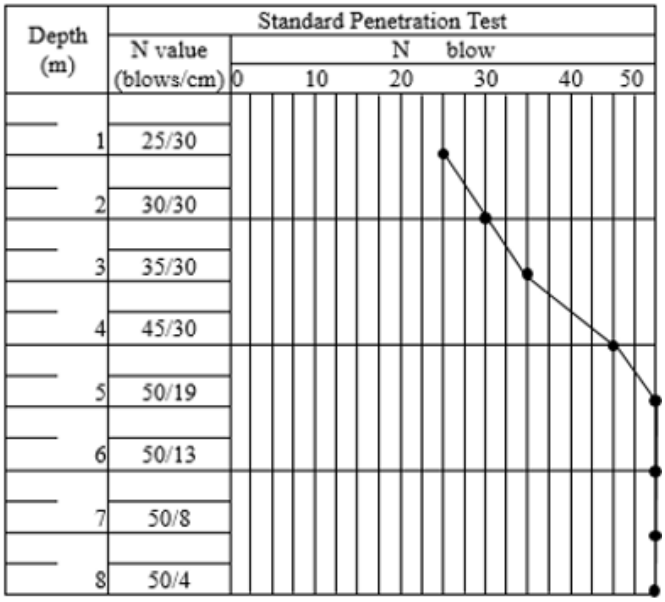

Figure 3. Example of a standard penetration test result.

3 MODIFIED CLASSIFICATION METHOD

3.1 *Modified classification method suggestion*

The modified classification method, which is more suitable for reflecting the characteristics of layers and is a more consistent way of classifying weathered layers, was suggested. Below is the detailed method of classifying weathered layers.

1) The boundary between weathered residual soil and weathered rock should be determined by using the SPT-N value of 50 blows/15 cm.
2) Weathered residual soil should be divided into loose weathered residual soil and dense weathered residual soil based on the SPT-N value, whose ranges are less than 50 blows/30 cm and 50 blows/30 cm to 50 blows/15 cm, respectively. The range of the dense weathered residual soil is the same as that of cohesionless IGMs.
3) The SPT-N value of the boundary between the two weathered layers should be consistently decided by applying linear interpolation.

3.2 *Application of the modified classification method*

The modified classification method is applied to the ultimate bearing capacity estimation of cast-in-place concrete piles embedded in weathered rock. Data on the piles and subsurface, including the pile diameter, load test result, boring log, and engineering properties, were collected from Jeon (2000) and Kwon (2004). The detailed data are summarized in Table 5.

Table 5. Data on the piles and engineering properties of weathered layers

Pile No.	Diameter	Socket Depth[2)]	UCS[1)]		RQD		Measured capacity
	m	m	MPa		%		kN
			Side	Base	Side	Base	
1	1	2.3	47.8	47.8	0	0	16700
2	1	2	47.8	47.8	0	0	13000
3	1	2.15	47.8	47.8	0	0	12000
4	1	1.9	47.8	47.8	42	40	18500
5	1	1.7	47.8	47.8	50	52	21330[3)]
6	0.4	6	20.2	12.3	0	0	2550
7	0.4	3	15.6	36.1	0	0	2130
8	0.4	3	15.7	17.3	0	0	1070
9	0.4	3	15.7	15.7	0	0	1100
10	0.4	6	30.4	12.0	0	0	3100[4)]
11	0.4	9	11.7	12.2	0	0	2950

1) The socket depth was determined from the boring log.
2) The UCS was measured by performing a uniaxial load test or a point load test.
3) The capacity was evaluated using the hyperbolic extrapolation method because the load test was completed before the ultimate state was reached.

The ultimate bearing capacities of all the piles were estimated through the conventional and modified methods, which are explained below.

Conventional method

(i) The thickness of the weathered layer is decided from the original boring logs recorded in the references.
(ii) The average value of the engineering properties in weathered residual soil and weathered rock is used, respectively.
(iii) The bearing capacity of the weathered rock layer is estimated by applying the specifications recommended in AASHTO (2010). The side resistance (q_s) and tip resistance (q_p) can be estimated using the equations below.

$$q_s = 0.6\alpha_E p_a(q_u/p_a)0.5 < 7.8p_a(f_c'/p_a)^{0.5}, \quad (1)$$
$$q_p = [s^{0.5} + (m \cdot s^{0.5} + s)^{0.5}]q_u, \quad (2)$$

where q_u is the unconfined compressive strength of the rock, p_a is the atmospheric pressure, α_E is the reduction factor specified in the reference, f_c' is the concrete compressive strength, and s, m is the fractured rock mass parameter specified in the reference.
(iv) The side resistance of weathered residual soil is not included in the bearing capacity of the pile.

Modified method

(i) The thickness of the weathered layer is decided through the modified classification method suggested in section 3.1.
(ii) The average value of the engineering properties in weathered residual soil and weathered rock is used, respectively.
(iii) The bearing capacity of the weathered rock layer is estimated by applying the specifications recommended in AASHTO (2010).
(iv) The side resistance of dense weathered residual soil is evaluated through the IGM theory and is included in the bearing capacity of the pile. The side resistance (q_s) can be estimated using the equation below.

$$q_s = \sigma_v' K_0 \tan\phi, \quad (3)$$

where σ_v' is the vertical effective stress, K_0 is the coefficient of earth pressure stress at rest, and ϕ is the internal friction angle.

The bearing capacities that were estimated using the two methods were compared with each other. As shown in Figure 4, the capacity estimated with the modified method was generally higher than that estimated with the conventional method. This tendency was caused by an increase of the side resistance, which resulted from an increase of the weathered rock socket depth and the additional resistance of the dense weathered residual soil. The weathered rock socket depth defined as the length from the boundary between the weathered residual soil and the weathered rock to the pile tip increased because the boundary was determined upwards by applying the unified criterion of 50 blows/15 cm and linear interpolation.

Also, as the characteristics of the dense weathered residual soil are very similar to those of the cohesionless IGMs, the resistance of dense weathered residual soil, which is conventionally ignored, was estimated and added using the cohesionless IGM theory. Therefore, the bearing capacity determined by applying the modified method was estimated to be higher than that obtained using the conventional method.

All the bearing capacities that were estimated using the conventional and modified methods were compared with the bearing capacity that was measured in the pile load test. The ratio of the measured capacity to the estimated capacity was defined as a K value to determine which method is more proper. The closer the K value is to 1, the more accurate the estimated capacity is. Figure 5 shows all the K values of each pile. Most of the K values that were evaluated using the modified method decreased and were closer to 1 compared to those that were evaluated using the conventional method. Therefore, the modified method, including the decision of the weathered layer and the application of the IGM theory, is more reasonable to use for estimating bearing capacity of the piles embedded in weathered rock.

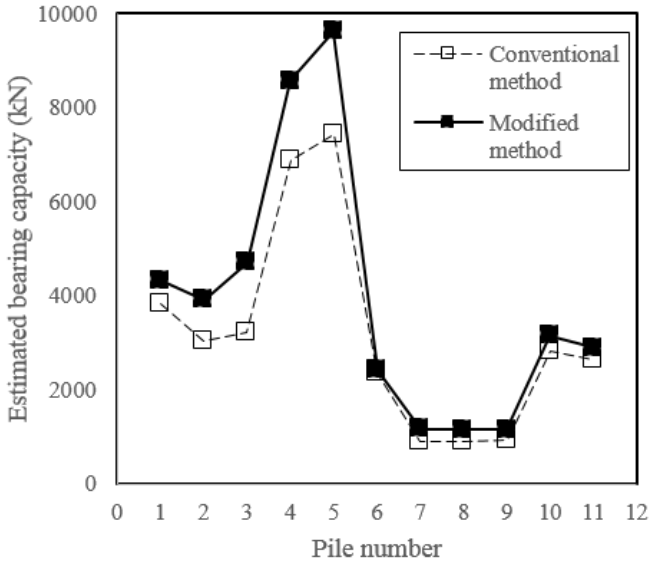

Figure 4. Ultimate bearing capacity estimated with the conventional method and the suggested method.

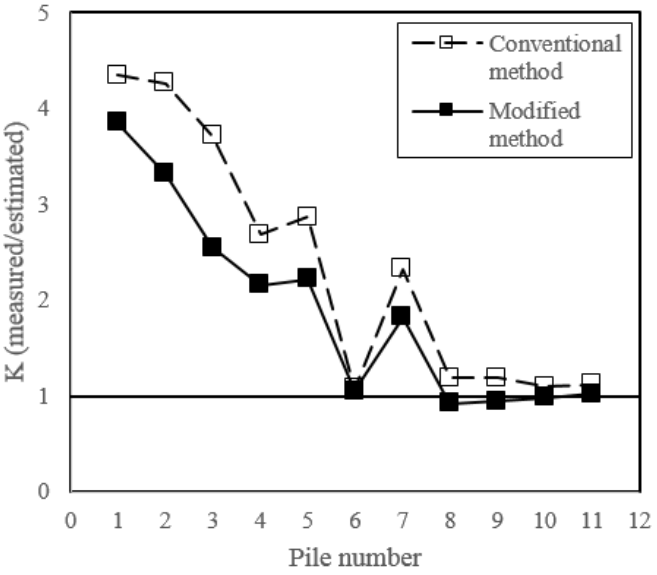

Figure 5. Ratio of the bearing capacity measured in the load test to the capacity estimated with the conventional and suggested methods.

4 CONCLUSIONS

In this study, the geomaterials of the weathered layer in Korea were investigated using the investigation site database to determine a more reasonable way of classifying the weathered layer. The recommendations for classifying the weathered layer from the existing literature were examined, and quantitative assessment based on test results of SPT-N values was attempted. Then a modified classification method for the weathered layer was suggested and applied it to the bearing capacity estimation of the pile resting on the weathered layers. The following conclusions were drawn from this study:

1) Several institutions in South Korea recommend engineering property types such as SPT-N value, UCS, and RQD for classifying the weathered layer, but the types of engineering properties are not unified, and even if the engineering property type is the same, the suggested values are not equal to each other. Also, although researches on the applicability of the IGM theory to the weathered residual soil have been conducted in South Korea, criteria for IGM have yet to be reflected.

2) To obtain the distributions of the weathered layer, the SPT-N values recorded in 600 boring logs were analyzed. The total number of SPT-N values that were used for weathered residual soil was 742, and that for weathered rock was 432. The SPT-N value from 0 blows/30 cm to 50 blows/30 cm accounted for about 34%, and 24% of the dense weathered residual soil corresponded to the cohesionless IGM criterion. Also, 42% had an SPT-N value larger than the upper boundary (50 blows/15 cm).

3) A modified classification method was suggested. The boundary between the two weathered layers had an SPT-N value of 50 blows/15 cm, and dense weathered residual soil was defined using the cohesionless IGMs. Also, linear interpolation was suggested for consistent decision making on the boundary between the two weathered layers.

4) The ultimate bearing capacities of the piles resting on the weathered rock were estimated to verify the feasibility of use of the modified method. The capacities that were estimated using the modified method were higher than those that were estimated using the conventional method, and were closer to the capacity measured in the load test.

5 ACKNOWLEGMENTS

This research was supported by a National Research Foundation of Korea grant funded by the South Korean government's MSIP (No.2015R1A5A7037372).

6 REFERENCES

AASHTO. 2010. "*AASHTO LRFD Brideg construction specifications, AASHTO,* Washington DC.

Clayton, C. R. I. & Matthews, M. C. Simons, N. E. 1995. "*Site Investigation, 2nd ed.* New York, Halstead Press.

Deere, D. U. & Hendron, A. J. & Patton, F. D. & Cording, E. J. 1967. "Design of surface and near surface construction in rock," *In Eight US Symposium on Rock Mechanics, Minneapolis*: 237-303.

Hoek, E. & Brown, E. T. 1997. "Practical estimates or rock mass strength," International Journal of Rock Mechanics and Mining Sciences 34(8): 1165-1186.

Jeon, K. S. 2000. "Analysis of vertical and horizontal resistance behavior of cast-in-situ concrete piles in completely weathered granite gneiss," PhD thesis, Seoul national university, Seoul.

Korea Expressway Corporation. 2009. "*Design method of expressway 4th tunnel*," Seoul, Korea Road & Transportation Association.

Korea geotechnical society 2009. "Structure f*oundation design specification,"* Seoul, Kummibook.

Korea rail network authority. 2011. *"Rail road construction specifications,"* Seoul, Korea rail network authority.

Kwak, K. S. 2008. "Determination of resistance factors for foundation structure design by LRFD," construction & transportation report.

Kwon, O. S. 2004. "Effect of rock mass weathering on resistant behavior of drilled shaft socketed into weathered rock," PhD thesis, Seoul national university, Seoul.

O'Neil, M. W & Townsend, F. C. & Hassan, K. M, & Buller, A. & Chan, P. S. 1996. "Load transfer for drilled shafts in intermediate geomaterials." FHWA-RD-95-171.

Seoul metropolitan government. 2006. "*Guide to site investigation,* Seoul.

Terzaghi, K. & Peck R. B. 1948. "*Soil Mechanics in Engineering Practice*," New York, John Wiley and Sons.

Geotechnical and Geophysical Site Characterisation 5 – Lehane, Acosta-Martínez & Kelly (Eds)

Impact of Rock Mass Strength Parameters on Lowwall Stability Assessment Outcomes in Open-cut Coal Mines

J. Li & N. Tucker
Strategy, Development and Planning, BHP Billiton – Coal

J. K. Todd
Caval Ridge Mine, BHP Billiton Mitsubishi Alliance

ABSTRACT: Many open cut coal mines have their own set of default mechanical properties used in modelling the behaviours of rock mass and waste materials, built from back analysis of historical low wall and highwall instability events. Among them, the strength parameters of fresh Permian rock masses in the cases of Queensland Bowen Basin mines, such as siltstones, sandstones, are related to low wall stability as they comprise the low wall dump foundation, especially when a clay-like weak plane (Shear) also exists below a coal seam floor. In practice these default strength parameters sometimes result in either over conservative or overly optimistic low wall designs. This paper presents methodologies of rock mass strength estimation using laboratory intact rock testing data & rock mass classifications systems, and provides examples of optimised designs and related stability assessment results using the estimated rock mass strength parameters. It is expected that utilising the rock mass strength estimation processes presented in this paper, which have been applied in underground hard rock mining for years, can be beneficial to all open cut coal mines.

1 INTRODUCTION

Optimal geotechnical design for *in situ* highwall rock mass and dragline disposed low wall spoil in coal strip mines becomes more and more critical under current economic conditions through increasing cost reduction and efficiency without compromising safety. To approach this objective, more effort is required to understand the nature of the rock mass, including lithology, jointing conditions (spacing, infill, roughness), as well as intact rock strength values. A set of localised and realistic rock mass strength parameters can then be developed and applied to slope stability analysis, particularly for low wall stability analysis.

For the sites with a long mining history, a set of default strength values has been established from back analysing previous failures which occurred due to unfavourable ground conditions. In reality it is more likely that better ground conditions exist over much of the mining area. Use of the default strength values can lead to a geotechnical floor design that has under-estimated the actual conditions when ground conditions differ unfavourably to the default values applied. On the other hand a slope design may be overly conservative when the actual ground is stronger than the default even in the presence of a thin band of weak material (Shear) below the pit floor. In both cases, optimal designs for safety and cost saving cannot be achieved.

This paper presents the rock mass strength estimation process applied to underground stope stability assessment (Li, 2004; Villeascusa and Li, 2004); and its application to an open cut coal mine over a two year period.

2 INTACT ROCK STRENGTH

An intact rock is a continuum of polycrystalline solid between continuities composed of mineral grains or aggregate. Properties of an intact rock are governed by the minerals and bonding nature between the grains. In reality, particularly in coal mine sedimentary rock, bedding planes and/or closed joints are present in the rock core samples used for laboratory intact rock strength testing. The presence of these defects is not an obstacle for obtaining intact rock strength estimation, but it is the angle between the defect and axis of loading applied on the sample that determines if the tested rock has failed along the defect plane or through intact rock, the continuum of polycrystalline solids.

In coal mines, the dip angle of bedding planes generally ranges from 0° to 20°. The intercepting angle between the rock core axis and the bedding plane would differ if an inclined hole is drilled; then the tested sample may be more prone to break along the structure than through the intact rock. Failure along any defect in a test sample results in a lower

strength value; therefore, this result should not be treated as the intact rock strength. As shown in Figure 1, in general there are five (5) failure modes for intact rock samples under uniaxial compressive strength testing: shear along defect, shear through intact rock, axial splitting, conical or hour glassing and multiple cracking. Except for the first failure mode (shear along defect) the testing results for all other failure modes can be treated as intact rock strength and used for rock mass strength estimation. In addition, it is important to record the angle between the shear plane and the loading axis in laboratory reports.

Figure 1. Examples of failure modes of laboratory intact rock testing: shear along defect, shear through rock, axial splitting, conical or hour glassing and multiple cracking.

3 ROCK MASS CLASSIFICATION AND ROCK MASS STRENGTH IN THE PIT FLOOR

Development of rock mass classification schemes commenced approximately 140 years ago (Hoek et al., 1998). Among the multi-parameter classification schemes, the RMR, Q-value and GSI (Bieniawski, 1989; Barton et al., 1974; Hoek et al., 1995) are more widely applied in the mining industry.

Estimating rock mass strength has been a difficult task in both underground stope and open pit/cut slope stability assessments. Rock mass characterisation requires a lot of information to represent the ground conditions for the area of concern. Over the last 20 to 30 years efforts have been placed into developing empirical relationships between laboratory intact rock strength data and the rock mass classification values for rock mass strength estimation by numerous researchers (Hoek and Brown, 1997; Kalamaras and Bieniawski, 1995; Ramamurthy, 1986; Singh, 1993; Hoek, 1998; Sheorey, 1997). Li (2004) and Villeascusa and Li (2004) reviewed these empirical relationships and recommended the process and equations established by Hoek and Brown, 1997; Kalamaras and Bieniawski, 1995 and Hoek, 1998 for application to the mining industry. Since 2004 these methods have been successfully applied to numerical modelling for underground open stope stability in numerous operations. The authors of this paper have started applying these rock mass strength estimation techniques to open cut coal mining since 2014.

The recommended empirical relationships for estimating rock mass strength values are the Hoek-Brown method (Hoek and Brown, 1997), which provides the friction angle and cohesion of rock mass (Figure 2), and Eq.1 (Kalamaras et al., 1995) and Eq.2 (Hoek, 1998), result in a rock mass compressive strength. However, if the friction angle value is used together with the compressive strength values from Eqs.1 and 2, the related cohesion values can be calculated by using Eq.3.

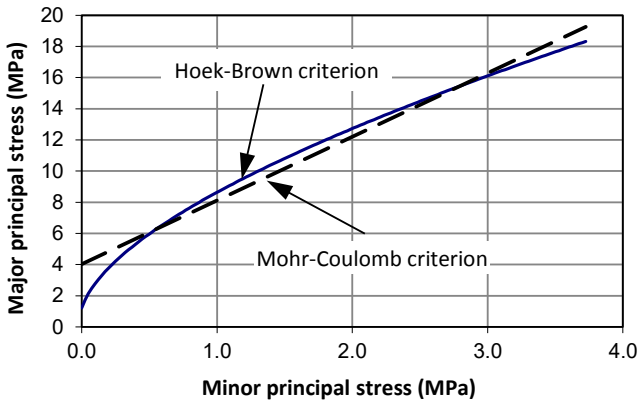

Figure 2. Using the Mohr-Coulomb criterion to fit the Hoek-Brown criterion – the Hoek-Brown method.

$$\sigma_{cm} = 0.5 \times \frac{RMR_{89} - 15}{85} \sigma_{ci} \quad (1)$$

$$\sigma_{cm} = 0.022 \sigma_{ci} e^{0.038 GSI} \quad (2)$$

where σ_{ci} is the uniaxial compressive strength of intact rock, σ_{cm} is the rock mass uniaxial compressive strength; RMR_{89} is the 1989 version of Rock Mass Rating (Bieniawski, 1989) and *GSI* is the Geological Strength Index (Hoek *et al.*, 1995).

The Hoek-Brown method and Eq.2 were established from a database of civil and mining, surface and underground projects, whilst Eq.1 was established from underground coal mining conditions. In addition, the impact of blasting damage on rock mass strength is not included in Eqs.1 and 2 with the exception being the Hoek-Brown method. Generally, the pit floor rock mass in open cut coal mines is not subjected to blasting damage. Therefore, these rock mass strength estimation methods could be applied to low wall stability analysis.

$$c = \frac{\sigma_{cm}(1-\sin\phi_m)}{2\cos\phi_m} \quad (3)$$

where ϕ_m is the rock mass friction angle. In application, the Rocscience's RocData or RocLab programs can be used to obtain the rock mass shear strength values for the Hoek-Brown method.

4 APPLICATION OF ROCK MASS STRENGTH ESTIMATION FOR LOWWALL STABILITY ASSESSMENT

4.1 *Example of an over designed low wall using default rock mass strength values*

A total of five (5) trenches at least 5m wide and 10m long were excavated after completion of coal mining in Strip 5 (S05) of a pit. Figure 3 shows the ground condition in the northern three trenches (T1 to T3), and suggests reasonable ground conditions in T1, very poor conditions in T2 and competent ground in T3.

Figure 3. Pit floor conditions revealed from trenches. Very poor ground shown in the trench T2.

Additional floor trenching around T2 confirmed that the weak ground was approximately 20m wide. No indications of faulting or weak rock mass had been identified in exploration holes due to sparse spacing. However, a fault was mapped in exploration boreholes north of block line 1 (BL1) shown in Figure 4. Projection of the fault and identified weak ground indicates potential Strip 6 low wall instability approximately 100m long around BL8, shown on the right-hand side plot in Figure 4.

The default strength values for fresh Permian rock mass are 256kPa cohesion and a 50° friction angle. Assuming $\sigma_{ci} = 0.6$ MPa, $GSI = 25$, $m_i = 9$, the estimated rock mass values using the Hoek-Brown method are 18kPa for cohesion and 22° for friction angle. When applied to stability analysis, the factor of safety (FoS) using the Sarma method was 1.18 for a general dragline spoil profile resulting in a failure surface through the dragline spoil (Figures 5 and 6). Therefore, no floor preparation was completed in S05 and no instability experienced for the S06 low wall.

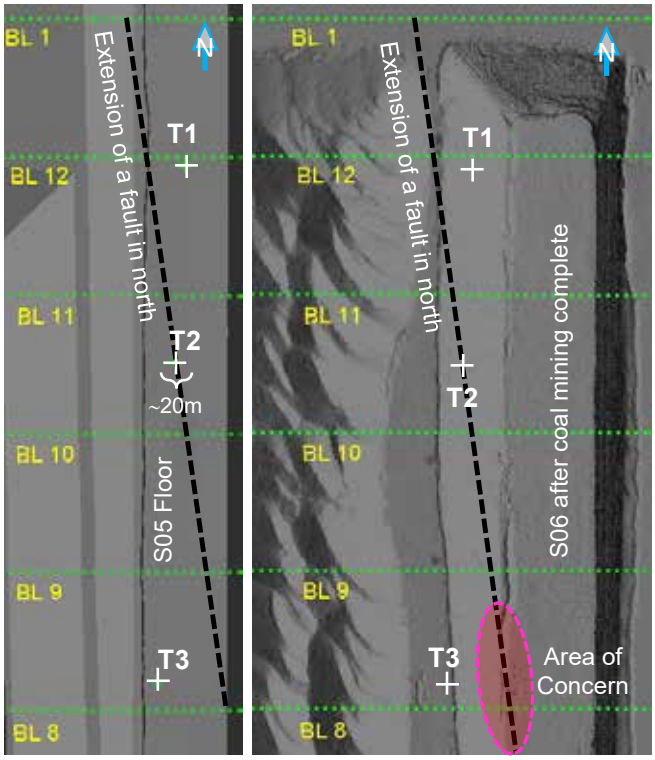

Figure 4. Location of trenches, extension of a fault from north and its relation to S06 low wall.

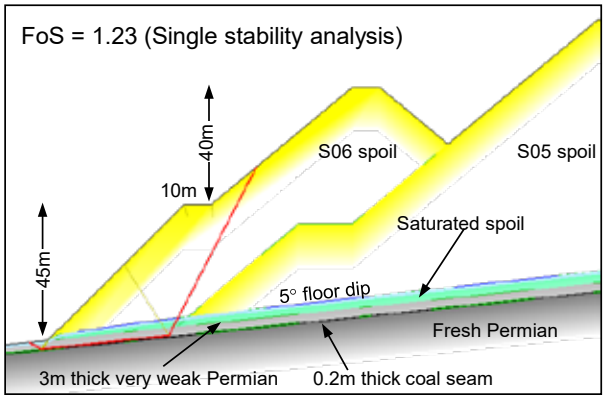

Figure 5. Single search using Galena® suggests no instability is expected through the weak rock mass below pit floor.

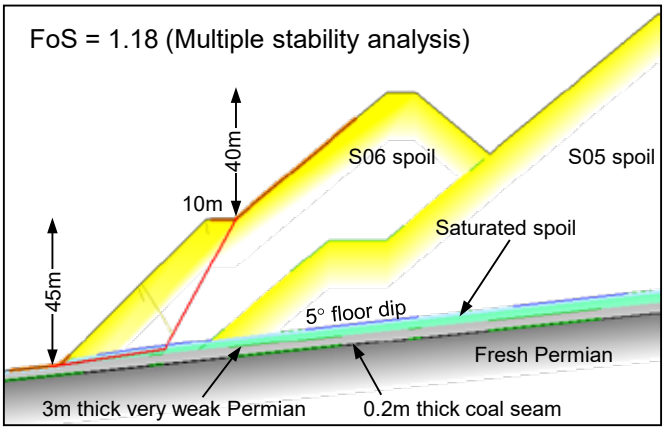

Figure 6. Multiple search analysis using Galena® suggests a potential failure surface above the pit floor.

From this case study we learnt that the default material strength values cannot be applied to any ground conditions; and a weak rock mass in the pit floor does not necessarily mean that floor preparation must be implemented. Sound engineering assessment can save operational costs reducing the need to spend time and resources dozer ripping or blasting the floor for slope stability.

4.2 *Example of an over conservative design*

When the floor rock mass is weak and / or a shear plane exists, floor preparation, either by dozer rip or blasting, are inevitable for low wall stability. However, in many cases the floor rock masses are stronger than the default strength parameters specified. As a result, floor preparation may not be required dependent on the strength values reflecting the actual rock mass conditions. Floor trenches in combinations of rock core photographs from coal quality holes have been used to identify the existence of a floor shear. Figure 7 shows a shear approximately 20mm thick, 1m below the coal seam floor. Two uniaxial compressive strength (UCS) tests were carried out failing through axial splitting resulting in a UCS of 14.9MPa.

Figure 7. Shear structure at 44.10m depth or 1.0m below the coal seam.

With σ_{ci} = 14.9MPa, *RQD* = 75 - 90, > 0.3m joint spacing with > 5mm gouge and dry conditions the *GSI* = *49* and RMR_{89} = 44. Assuming m_i = 19 for sandstone, the estimated rock mass friction angle is 35.6° using the Hoek-Brown method. Figure 8 shows the estimated pit floor rock mass strength values and the default strength. The cohesion values from Eq. 1 and Eq.2 are similar, but Eq.2 results in the lowest cohesion value among the three methods.

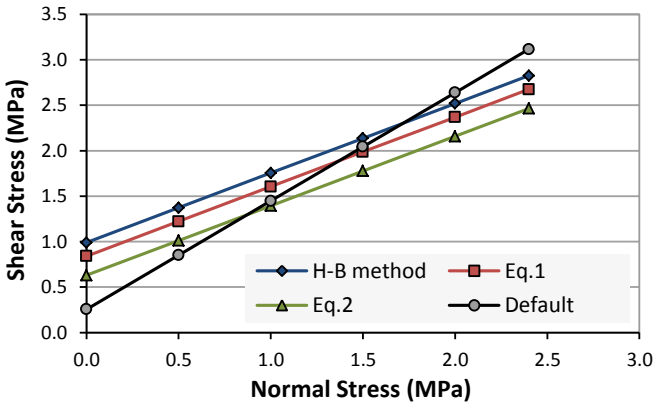

Figure 8. Comparison between the estimated and default pit floor rock mass strength values.

Low wall stability analyses were carried out using the GLE/Morgenstern-Price (GLE/MP) method incorporated in Rocscience Slide® software by applying the strength values shown in Figure 8. As standard practice at design stage a general dragline spoil profile is used in the assessment. The FoS results using each method are presented in Table 1. Figures 9 and 10 show the stability analysis results using the average of estimated strength values and the default rock mass strength.

Table 1. Stability analysis results using different strength values.

Strength values used	FoS
Hoek-Brown method	1.29
Eq.1	1.22
Eq.2	1.18
Average of above 3 methods	1.23
Default strength values	1.13

Based on the results from the stability analysis and the FoS greater than 1.2, it was decided that no floor preparation (dozer rip or floor shot) was to be required. Nevertheless, close observation of the low wall performance was completed throughout mining. The strip was successfully mined with no low wall instability issues experienced.

The rock mass strength estimation methods were also applied to a few strips in another pit of the mine, where the floor dip was < 5° with an interburden thickness of 0.3 – 0.5m to an uneconomic coal band below the pit floor. No shears were observed in

the floor trenches; however the coal band was highly brittle and broken. No floor preparation was required due to very competent interburden with much higher strength parameters than the default values calculated by using the rock mass strength estimation methods. No low wall instability was experienced even with 40% of the low wall consisting of weak Tertiary and weathered Permian materials.

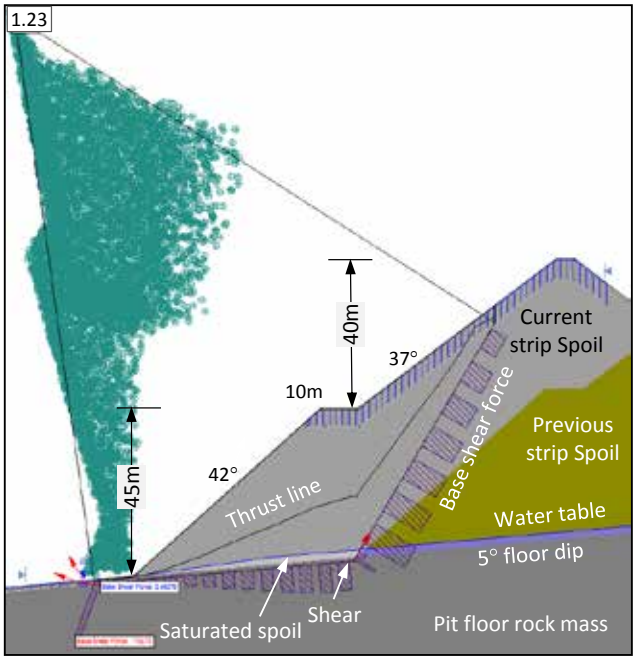

Figure 9. Stability analyses for a dragline low wall using average strength values from the Hoek-Brown meth and Eqs.1 & 2 (GLE/Morgenstern-Price method).

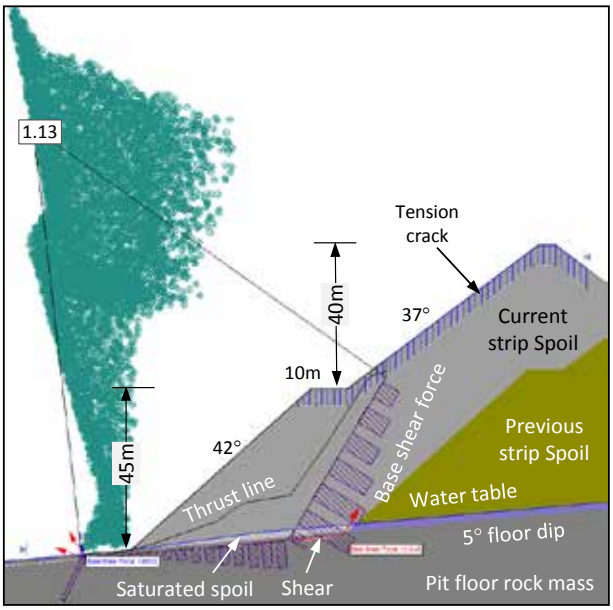

Figure 10. Dragline low wall stability analyses with the default strength values (GLE/Morgenstern-Price method).

5 DISCUSSION AND CONCLUSIONS

The rock mass strength estimation methods have been used in the mining industry for many years, particularly in underground open stoping mines. Considering the nature of strip mining, these methods may only be suitable for low wall stability assessment, where the pit floor rock mass is not subject to damage from blasting and no rating adjustment is required for joint orientation (for RMR). Examples presented in this paper have confirmed the applicability of empirical rock mass strength estimation methods in open cut coal mining.

Reviewing the failure mode of laboratory testing samples and using the real intact rock uniaxial compressive strength value is the first step for properly applying these empirical methods. Understanding the pit floor rock mass characterisation is the most critical and challenging step for rock mass strength estimation. Identification of floor shear and weak ground can be easily missed due to sparsely spaced exploration holes and limited floor trenches in coal mines. In a word, the default material strength values should not be blindly applied to any rock mass condition from aspects of either safety or cost reduction and productivity increase.

6 ACKNOWLEDGEMENTS

The authors would like to acknowledge BHP Billiton – Coal and BHP Billiton Mitsubishi Alliance for their permission to publish this paper.

7 REFERENCES

Barton, N. R., Lien, R. and Lunde, J. 1974. Engineering classification of rock masses for the design of tunnel support. In *Rock Mechanics, vol.6, 189 – 236.*

Bieniawski, Z. T. 1989. *Engineering Rock mass Classifications*. Wiley, New York.

Hoek, E., Kaiser, P. K and Bawden, W. F. 1995. *Support of Underground Excavations in Hard Rock*. Rotterdam: Balkema.

Hoek, E. and Brown, E. T. 1997. Practical estimates of rock mass strength. In Int. *Journal of Rock Mechanics & Mining Sciences, vol.34, no.8, 1165–1186.*

Hoek, E. 1998. Practical Rock Engineering. <http://www.rocscience.com/roc/Hoek/Hoek.htm> (Oct. 2, 2000).

Hoek, E., Kaiser, P.K. and Bawden, WF 1998. *Support of underground excavations in Hard Rock.* Rotterdam: Balkema

Kalamaras, G. S. and Bieniawski, Z. T. 1995. A rock mass strength concept for coal seams incorporating the effect of time. In Fujii T. (ed.), *Proc. 8th Int. Congress on Rock Mechanics, ISRM, vol.1, 295 – 302.* Rotterdam: Balkema.

Li, J. 2004. *Critical Strain of Intact Rock and Rock Masses.* PhD Thesis, Western Australian School of Mines, Curtin University of Technology.

Ramamurthy, T. 1986. Stability of rock mass. In I*ndian Geomechanics Journal, vol.16, no.1, 1 – 74.*

Sheorey, P. R. 1997. *Empirical Rock Failure Criteria*. A A Balkema, Rotterdam, 176p.

Singh, B. 1993. Indian case studies of squeezing grounds and experiences of application of Barton's Q-system. In *Workshop on Norwegian Method of Tunnelling, CSMRS*, New Delhi.

Villeascusa, E. and Li, J. 2004. A review of empirical methods used to estimate rock mass compressive strength and deformability in mining industry. In *Massmin 2004, 59-68, Santiago, Chile.*

Geotechnical and Geophysical Site Characterisation 5 – Lehane, Acosta-Martínez & Kelly (Eds)

Investigation the results of Plate Load Test using rigid plates in weak rock masses (Case study)

M. G. Nik
School of Railway Engineering, IUST University, Iran

B. Abrah & E.G. Samani
MSc, Rock Mechanics, Azmune Fulad Consulting Engineering Co., Iran

ABSTRACT: The most important parameters for designing and numerical modelling are deformability modulus, cohesion, friction angle, poison's ration and stress ratio, among which the modulus of deformation is of paramount importance. Plate loading test using rigid plates is one of the large scale tests for determining de-formability modulus of rock masses. This test has been used for measuring the aforementioned modulus of low quality rock mass at the left abutment of Karun2 dam in Iran. Care should be taken in interpretation of test results due to existence of fractures and porosities in weak rock masses. In this paper, analysing the re-sults of the experiments has been performed with three methods, i.e., ASTM, ISRM and UNAL and there has been a big difference between the out coming results of ASTM and ISRM methods with UNAL method.

1 INTRODUCTION

Plate load test is one of the in-situ rock mechanics experiments for determining deformation modulus of rock masses. In this test, for measuring the deformability characteristics of rock mass, loads are applied through a flexible jack or a pair of circular and rigid steel plates on the reciprocal surfaces in a small gallery or access tunnels. The induced deformation due to loading are measured in the boreholes behind the loading plates. The required data for calculating deformation modulus in loading-unloading cycles are achieved with increasing and decreasing the loads. Figure 1 shows schematic view of the method of conducting a flexible plate load test.

2 GEOLOGY OF KARUN 2 DAM SITE

The dam site is locating about 70 km far from Izeh city in Khuzestan province and has laid on the north eastern crest of Pabdeh anticline. Pabdeh and Asmari formation have been investigated in the vicinity of dam location. Engineering geological profile of dam axis has been shown in figure 2.

3 EQUIPMENT FOR CONDUCTING PLATE LOADING TESTS

This equipment consists of a pair of rigid plate having a weight of 750 kg and external diameter of 100 cm with a 14 cm central hole, steel spacers with different lengths for filling the gaps between rigid plates, 12 MPBX with related sensors, hydraulic jacks with the capacity of 250 tons and related pumps, data logger system, mechanical packers and related aluminum rods. Figure 3 shows the equipment for this tests in set up procedure. Two boreholes are drilled at behind the plates with the length and diameters of 6 m and 76 mm, in each 5 extensometers are installed.

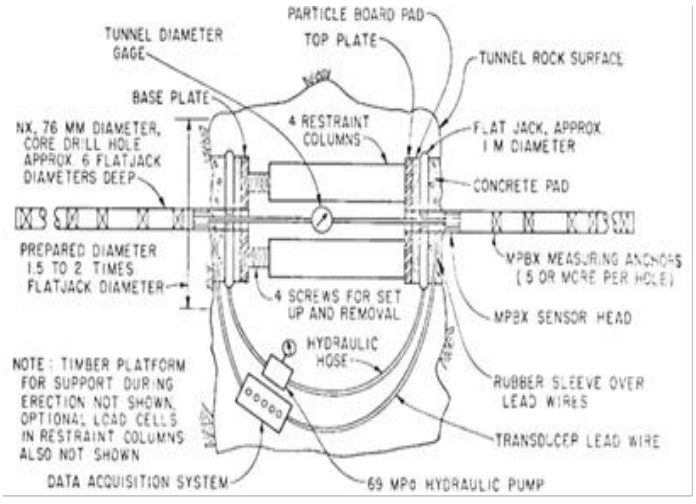

Figure 1. Typical setup for flexible plate loading test [4].

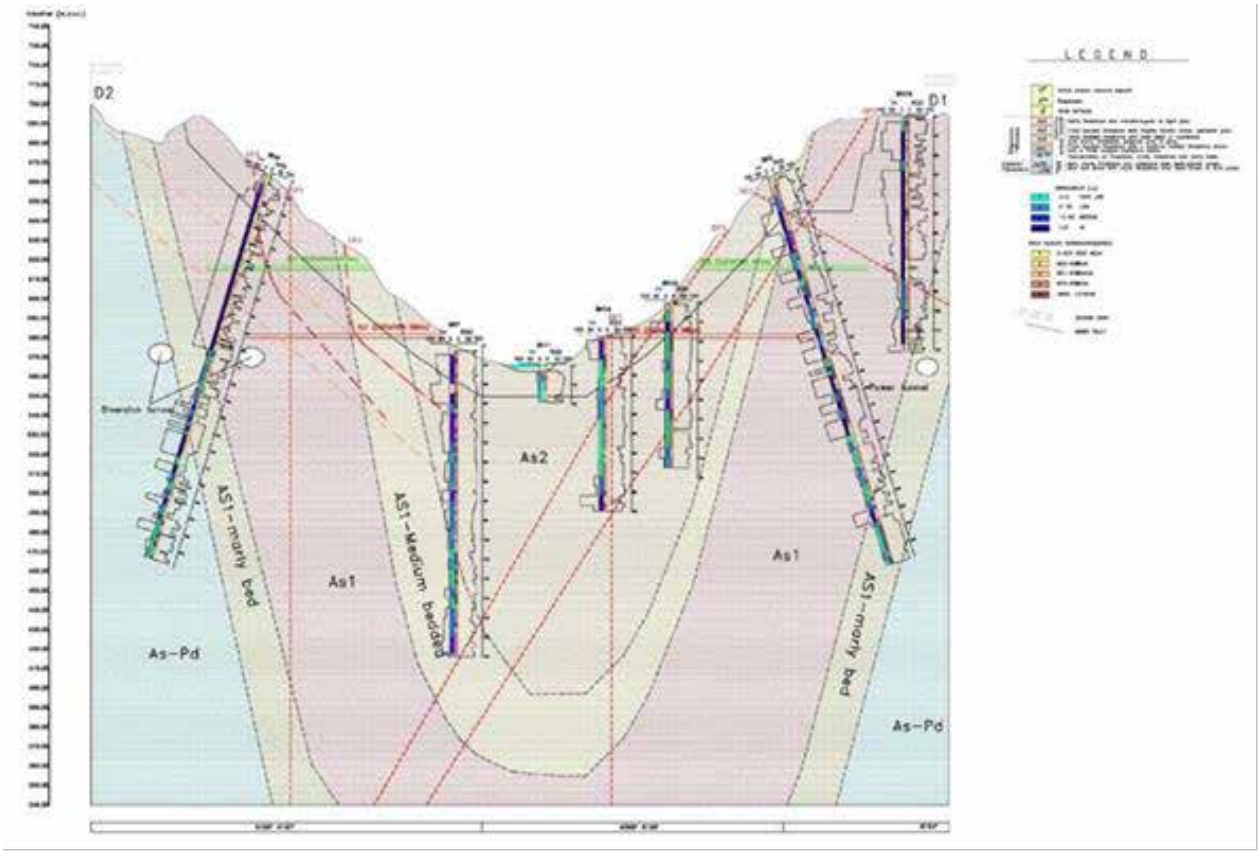

Figure 2. Engineering geological profile of Karun 2 dam axis [4].

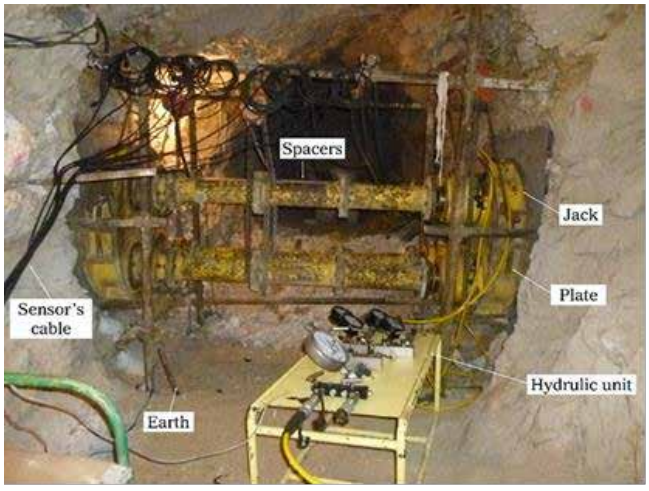

Figure 3. Equipment for conducting Plate Load Test [4].

4 GEOLOGICAL DATA ACQUISITION

Before placing rigid plates on the rock surface, chipped and smoothened surfaces have been mapped precisely (figure 4). These surfaces have then been paved with a layer of cement and a borehole has been drilled at the centre of each surface. Figure 5 shows a series of cores brought out of one of the boreholes.file.

5 SOLVING THE PROBLEMS AND INSTRUMENT INSTALLATION

One of the problems encountered in this project was the method of installing instruments in boreholes. Existing numerous voids and cavities of small (tens of cm) to large (more than 1 m) types, open discontinuities and fractured rocks enhanced the possibility for instruments to be stuck so that in one of the tests there was not possible to install the extensometers due to existing of voids up to 2 m wide. Also positioning the packers in points such as joints or other discontinuities in the rock mass could create doubts in validity of data. For these reasons, a borehole camera was used for determining the true position of the voids, open joints, fractured zones and appropriate location for extensometers to be installed. Since the camera showed a number of cavities, voids and weakness points in most of the boreholes, it was decided the voids in boreholes to be filled with soil and plaster grout (figure 6) and re-drilled with a single core barrel through the plaster grout which has filled the voids and cavities at the borehole walls and therefore resulted in making a smooth surface for installing the packers of extensometers. The merit of filling the voids with soil and plaster grout is that the

modulus of deformability is not changed accordingly.

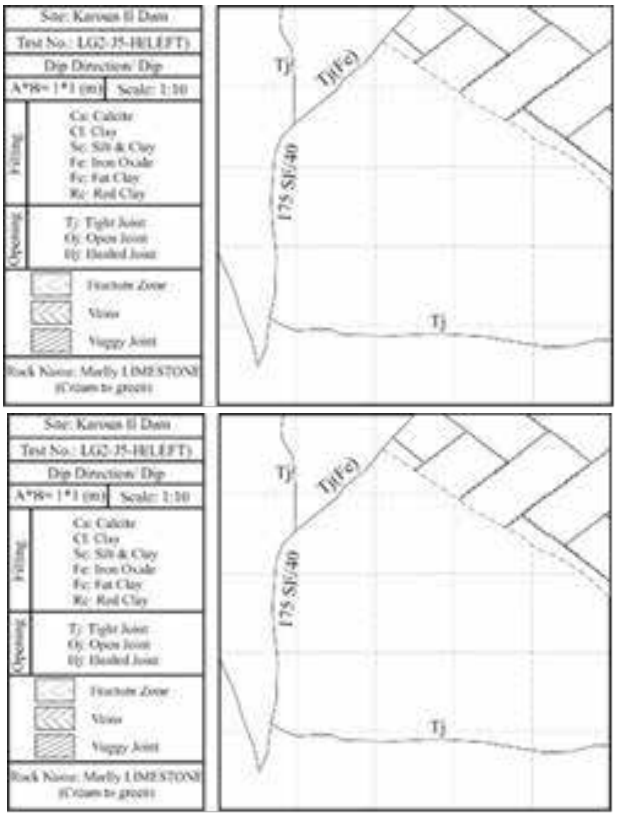

Figure 4. Mapping left and right chipped and smoothened surfaces before a test [4].

Figure 5. a sample box containing cores of a borehole in one of the tests [4].

As an example of encountered problem due to defects of rock mass in this project, the test number LG2-J5-H may be referred as a witness. The test has to be conducted in 5 cycles with maximum pressures of 2, 4, 6, 8 and 10 MPa. Due to the voids and clayey interlayers in the rock mass, the prepared rock surface could not bear the full pressure of the test and was deformed in 8 MPa obliquely (figure 7). With regard to the deformation on the right edge of loading plate and horizontal set up of the test, it was stopped at the end of the forth cycle to prevent the risk of injuries due to falling a very heavy steel column (figures 8 and 9).

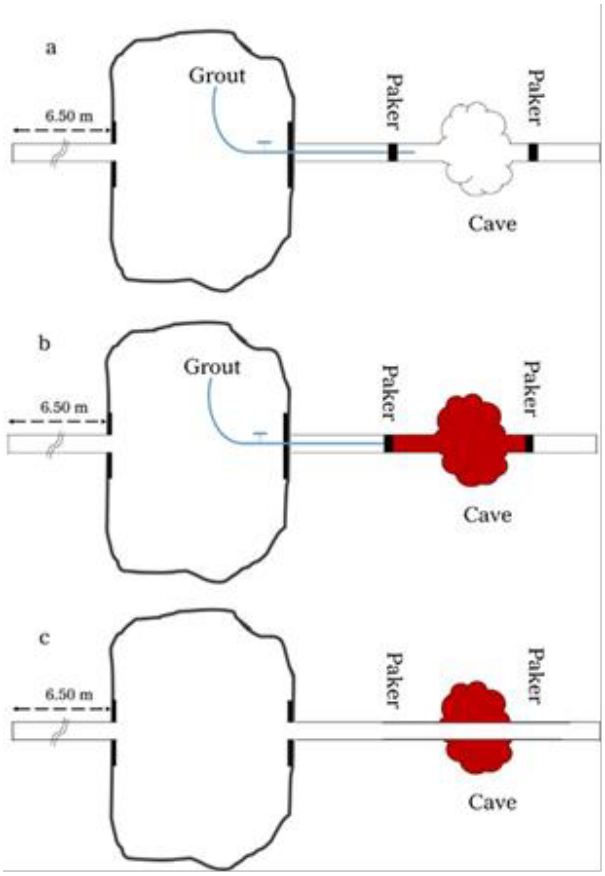

Figure 6. The procedure of filling voids and cavities in extensometer holes [4].


Figure 7. Dis-harmonic deformation in loading surface in a test [4].

6 CALCULATIONS

Three methods of calculations modulus of deformability, i.e., ISRM, 1981, ASTM, 2008 D4394-08 and UNAL, 1997, have been used in this project in order to compare the results obtained from these methods of calculations.

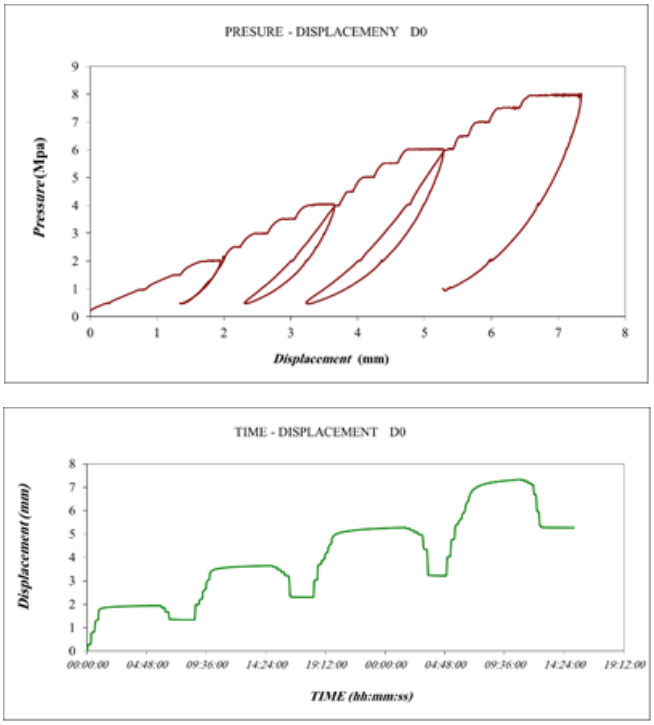

Figure 8. Pressure-displacement and Displacement-time curves [4].

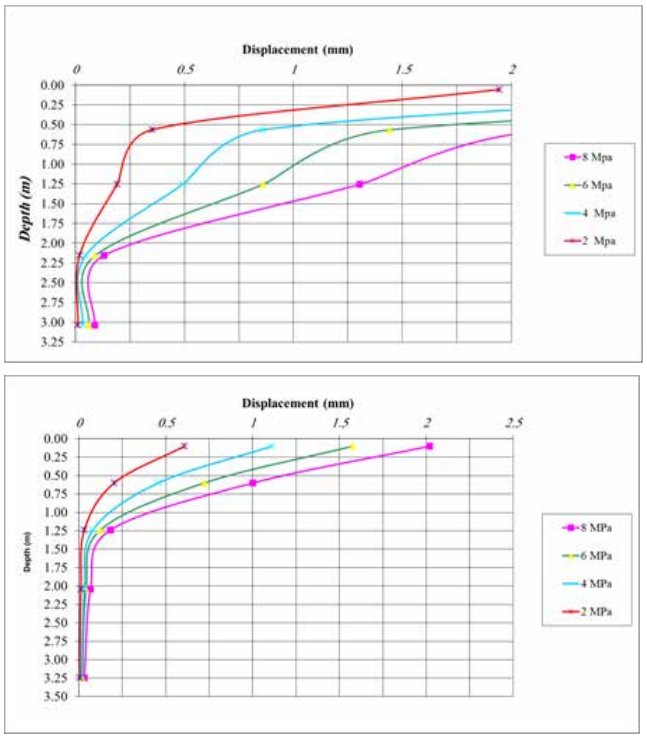

Figure 9. Displacement –depth for left and right plates [4].

6.1 *ISRM, 1981*

The relations used in this method are based on elastic solution for uniform loading (constant stress) on a circular surface of isotropic elastic semi-infinite media. As the rock mass under pressure has not conformity with these assumptions, the structural specifications of the rock mass and the parameters effective on the results should be considered in using the results of the tests. The Poisson's ratio used for calculation of deformability modulus in all the tests has been obtained from laboratory experiments on the cores came out from the related boreholes and has been equal to 0.25.

In the case of using flexible flat jack and having displacement amount in depth of Z in relative to loading surface, instantaneous deformability modulus is determined from relation 1:

$$E = \frac{2Q(1-\nu^2)}{W_z}[(R_2^2+Z^2)^{0.5} - (R_1^2+Z^2)^{0.5}] + \frac{QZ^2(1+\nu)}{W_z}[(R_1^2+Z^2)^{-0.5} - (R_2^2+Z^2)^{-0.5}] \quad (1)$$

Where, E is deformability modulus (MPa), Q is the pressure applied on loading surface (MPa), υ is Poisson's ratio of the rock mass, R_1 is the diameter of central hole of loading plate (m), Z is depth of the measuring point to loading surface (m), R_2 is the diameter of loading plate (m) and W_z is displacement of depth of Z (mm).

It should be mentioned that despite the extensive use of the relation proposed by ISRM for analysing plate load test results, this equation has been presented for experiments with flexible type of loading surfaces.

6.2 *ASTM, 2008*

Calculation the deformability moduli of rock mass in this method has been done based on proposed relation of ASTM, 2008 standard. This relation for determining deformability modulus of rock mass at the points in the extensometer borehole behind the rigid circular loading plates is as relation 2:

$$E = \frac{(1+\nu)P.R}{2W_Z}\left[(2-2\nu)arcSin\left(\frac{R}{(R^2+Z^2)^{0.5}}\right) + \frac{R.Z}{(R^2+Z^2)}\right] \quad (2)$$

Where, E is deformability modulus of rock mass (MPa), P is the pressure applied on loading surface (MPa), υ is Poisson's ratio of the rock mass, R is the diameter of loading plate (m), Z is depth of the measuring point to loading surface (m) and Wz is displacement of depth of Z (mm).

6.3 *UNAL, 1997*

Determination of instantaneous, average and total deformability modulus of rock mass is possible by means of the relation proposed by UNAL. Engineering judgment is required for selection of appropriate modulus. The relation is as:

$$E = \frac{Q_{ave}.R}{2W_Z}[2(1-v^2)arcCot\ Z + (1+v)\frac{Z}{Z^2+1}]$$

If: (3)

$$K = \frac{R}{2}[2(1-v^2)arcCot\ Z + (1+v)\frac{Z}{Z^2+1}]$$

Then:

$$E = K.\frac{\Delta Q_{ave}}{\Delta W_Z}$$

Where, Q_{ave} is average stress applied on loading plate (MPa) and R is the diameter of loading plate (m). It should be mentioned that instantaneous moduli has been used in this project. The calculated results from the above mentioned methods have been shown in table 1.

Table 1. Calculated results from three methods

Test Results Summary

Project: Karoun II Dam	Test No: LG2 - J5 - H	Test orientation: Horizontal	Date: 2014	By: B. Abrah

RIGHT Plate

			Anchor Depth (m)														
			3.035			2.155			1.255			0.565			0.055		
	Anchor No :		D4			D3			D2			D1			D0		
	Pressure (Mpa)		Modolus (GPa)			Modolus (GPa)			Modolus (GPa)			Modolus (GPa)			Modolus (GPa)		
	From	To	ISRM	ASTM	UNAL	ISRM	ASTM	UNAL	ISRM	ASTM	UNAL	ISRM	ASTM	UNAL	ISRM	ASTM	UNAL
Laoding (MPa)	0.5	2	16.6	16.5	32.1	14.9	14.8	27.7	2.5	2.4	4.0	2.4	2.3	2.9	0.7	0.6	0.6
	0.5	4	14.2	14.1	27.5	13.9	13.8	25.8	2.3	2.3	3.8	2.4	2.2	2.9	1.2	1.1	1.1
	0.5	6	13.0	12.9	25.1	11.6	11.6	21.6	2.1	2.1	3.5	2.3	2.1	2.8	1.5	1.3	1.3
	0.5	8	12.3	12.3	23.9	11.1	11.0	20.6	2.0	1.9	3.2	2.1	1.9	2.5	1.4	1.2	1.3
	0.5	10															
Unloading (MPa)	0.5	2	21.6	21.5	41.8	20.0	19.9	37.2	3.6	3.5	5.9	3.4	3.1	4.0	2.4	2.1	2.2
	0.5	4	18.3	18.2	35.4	16.7	16.6	31.0	2.9	2.8	4.7	2.9	2.7	3.5	2.3	2.0	2.1
	0.5	6	14.9	14.8	28.9	13.2	13.0	24.4	2.6	2.5	4.2	2.7	2.5	3.2	2.4	2.1	2.1
	0.5	8	12.8	12.7	24.8	11.5	11.4	21.4	2.4	2.3	3.9	2.5	2.4	3.0	2.7	2.3	2.4
	0.5	10															

LEFT Plate

			Anchor Depth (m)														
			3.25			2.04			1.24			0.6			0.1		
	Anchor No :		D9			D8			D7			D6			D5		
	Pressure (Mpa)		Modolus (GPa)			Modolus (GPa)			Modolus (GPa)			Modolus (GPa)			Modolus (GPa)		
	From	To	ISRM	ASTM	UNAL	ISRM	ASTM	UNAL	ISRM	ASTM	UNAL	ISRM	ASTM	UNAL	ISRM	ASTM	UNAL
Laoding (MPa)	0.5	2	56.9	56.7	110.9	29.7	29.5	54.7	16.2	15.9	26.4	4.1	3.8	5.0	2.3	1.9	2.0
	0.5	4	31.6	31.5	61.6	22.2	22.0	40.9	13.7	13.4	22.3	4.8	4.5	5.9	3.8	3.2	3.4
	0.5	6	37.8	37.6	73.6	28.0	27.7	51.4	14.4	14.1	23.4	5.1	4.8	6.3	4.4	3.8	3.9
	0.5	8	22.8	22.7	44.4	17.4	17.2	32.0	11.8	11.6	19.2	5.0	4.7	6.1	4.7	4.0	4.2
	0.5	10															
Unloading (MPa)	0.5	2	31.6	53.6	104.9	31.6	31.4	58.2	19.0	18.6	30.9	7.8	7.3	9.5	6.3	5.4	5.6
	0.5	4	22.8	30.1	58.9	22.8	22.6	42.0	14.9	14.6	24.3	6.8	6.4	8.4	5.9	5.1	5.3
	0.5	6	26.1	26.0	51.0	20.1	19.9	36.9	13.4	13.1	21.7	6.4	6.0	7.9	6.0	5.2	5.4
	1	8	23.9	23.9	46.7	18.2	18.1	33.5	12.3	12.1	20.1	6.3	5.9	7.8	6.5	5.6	5.8
	0.5	10															

7 CONCLUSIONS

Conducting experiments in weak rock needs special measures such as:

• In order to prevent the instruments to be installed on the voids, cavities, open joints, etc., the location of installation should be precisely controlled. It is achieved by means of a borehole camera.

• In this kind of rock mass the wall of the extensometers borehole is likely full of voids, cavities, open joints and crushed rocks. Therefore, various types of extensometers is difficult to be used. A method of treatment the walls suggested in this work is filling the voids with mixture of soil and plaster grout.

• With regard to the calculations and achieved results using three proposed methods, it was decided to use the data from sensors number 2 and 3 for calculation the deformability modulus as design parameter in all tests using ISRM 1981 and ASTM 2008 standards. In the meantime, the data obtained from one of the experiments has been used for calculating deformability modulus of rock mass with two aforementioned plus UNAL methods. Big discrepancies have been observed from comparison of the results of ISRM and ASTM with UNAL method

8 REFERENCES

ISRM, 1979 “Suggested methods for determining in situ deformability of rock – Part 1: Suggested method for deformability determination using a plate loading test (superficial loading)”, Int. J. Rock Mech. Min. Sci. & Geomech. 16: 197-202.

ASTM, 1998 "Flexible Plate Loading Method" [D 4395 – 04].

ASTM, 2008 “Standard Test Method for Determining In Situ Modulus of Deformation of Rock Mass Using Rigid Plate Loading Method”, Annual Book of ASTM. 04.08.

Report of geology of Karun 2 dam site, 2005.

Geotechnical and Geophysical Site Characterisation 5 – Lehane, Acosta-Martínez & Kelly (Eds)

Characterization of unsaturated tropical soil site by in situ tests

B. P. Rocha & R. A. dos Santos
USP, São Carlos – SP – Brazil

R. C. Bezerra, R. A. Rodrigues & H. L. Giacheti
Unesp, Bauru – SP – Brazil

ABSTRACT: Geotechnical site characterization consists in determining the stratigraphical profile, the groundwater level and the estimative of geo-mechanical designs parameters required for each project. In situ tests techniques can offer the best available and most economical way to achieve this characterization for different site conditions. This paper presents and discusses CPT, DMT, seismic (down-hole) and laboratory tests carried out in an unsaturated tropical sandy soil site, which the top 13 m is a colluvium overlaying a residual soil from sandstone. The results showed that the CPT and DMT tests were efficient for detailed stratigraphic logging, estimative of geotechnical parameters, however, temporal variability should be considered for proper site characterization of unsaturated tropical soils.

1 INTRODUCTION

The main objective of site characterization is to define the stratigraphical profile, which consists in identifying the soil layers, thickness, soil type, groundwater level and physical and mechanical properties. For this purpose, in situ and laboratory tests can be used. Some in-situ testing methods (e.g., CPT and DMT) can be used as an alternative to the traditional approach of drilling, sampling and laboratory testing, mainly in cohesionless soils, where reliable soil samples cannot be retrieved. Combining stratigraphic logging with a specific measurement at the some in situ test is a modern approach available for site characterization.

The cone penetration test (CPT) and the flat plate dilatometer test (DMT) are simple, remarkably operator-independent, rapid and they have been used more and more in geotechnical engineering practice. Both tests provide information about strength-stiffness soil behavior.

Tropical soils are predominantly formed by chemical-physical weathering of the rock. It is includes two classes: lateritic and saprolitic soils. Unsaturated tropical soil profiles have a cohesive-frictional behavior, where factors such as macro and microstructure, cementing, nonlinearity of stiffness, anisotropy, genesis and disintegration show greater influence on their behavior than the stress history (Vaughan et al. 1988). These factors have to be considered in the site characterization of this unusual geomaterial.

CPT, DMT and seismic test data from an unsaturated tropical soil are presented and discussed in this paper. The estimated soil parameters are compared to the available reference values determined by laboratory and others in situ tests. The seasonal site variability is considered and discussed from CPT tests carried out in two different weather conditions (wet season and dry season).

2 STUDY SITE

The study site is located at the experimental research area of the Research Group on Geotechnical Engineering from São Paulo State University - Bauru Campus. It is located on the central part of São Paulo State on the vicinities of the scarps of "cuestas" at the Paulista Central Plateau. The geographical coordinates are: 22º05' to 22º26' latitude south and 49º to 49º16'3 longitude west. The schematic position of São Paulo State, Bauru city, the Unesp campus and the research site in Brazil is shown on Figure 1.

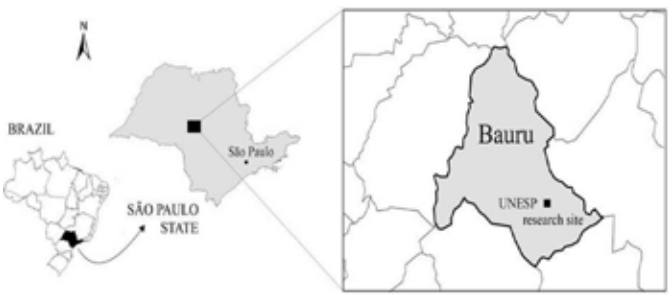

Figure 1: The location of the study site.

The Bauru city is located in the Bauru Group, which is formed by Marília and Adamantina Formation. In general, Marília Formation is composed by coarse and fine-grained sandstones. This rock mass also presents massive banks among tenues cross-stratifications, including layers of siltstones, mudstones and plane parallel-stratified sandstones. Moreover, sandstones present disseminated carbonate cementation configured by nodules and concretions. The Adamantina Formation consists of fluvial deposits with predominance of fine sandstones with lenses of sandy siltstones and mudstones. It presents cementation in the form of carbonate nodules. The studied profiles are generally unsaturated porous sandy soils with a high saturated hydraulic conductivity. An important geotechnical problem in this area is the soil collapsibility caused by wetting.

The climate of the region is subtropical with the concentration of rainfall in summer (between December to March). Total annual average rainfall in the Bauru city, varies in range from 870 mm to 1,720 mm. Figure 2 presents the average month water precipitation between 1981 to 2015. It is also possible to observe that the months of June, July and August present low average month precipitation value when compared to other months.

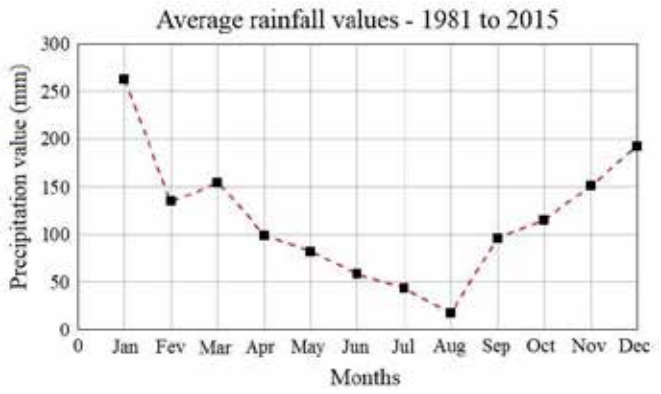

Figure 2: Average monthly precipitation values along 1981 and 2015 (IPMet, 2016)

3 SITE CHARACTERIZATION

SPT, SPT-T and different types of laboratory test were carried out to determine reference values for defining geotechnical soil parameters for the study site. Relevant geotechnical characteristics are summarized in Figure 3.

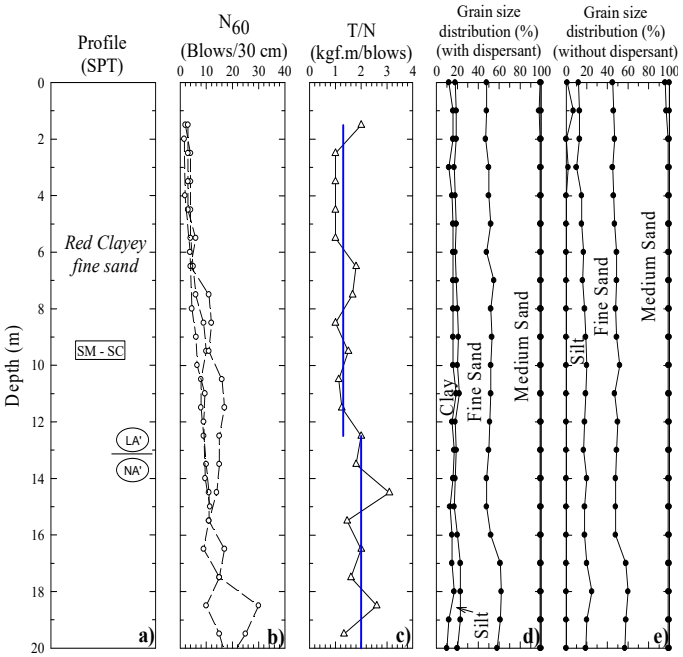

Figure 3: In situ and laboratory tests data (Rocha et al., 2015).

The soil profile is a red clayey fine sand identified based on SPT data. MCT Classification System (Nogami & Villibor 1981) classified the top 13 m as lateritic soil behavior (LA') followed by a non-lateritic soil behavior (NA'). N SPT values from SPT increase almost linearly with depth, up to 13 m depth (Fig. 3b). One SPT-T (Ranzine 1988) was carried out at the site and the T/N ratio profile is presented on Figure 3c. Figure 3c shows two different trends for the T/N ratio with average values of 1.3 for the top 12.5 m and 2.0 bellow this depth.

Grain size distribution for the soil samples retrieved every meter from one of the SPT were determined using dispersant (Fig. 3d) and without dispersant (Fig. 3e) as suggested for site characterization of tropical soils. It can be observed that clay and silt particles are naturally aggregated by oxides and hydroxides of iron and aluminium, which is typical in tropical soils.

The soil retention curve is an important information since the soil suction affects strength and stiffness parameters. Figure 4 shows the retention curves (drying method) for the soil samples collected at 1.5, 3.0 and 5.0 m depth from the study site.

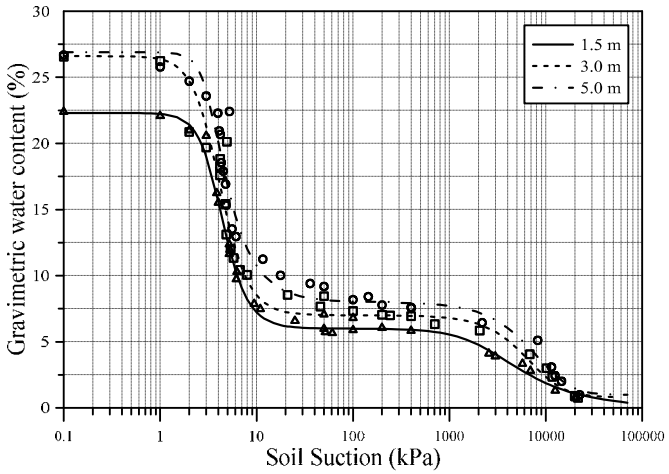

Figure 4: Soil-water retention curves (drying method) for 1.5, 3.0 and 5.0 m depth (after Fernandes et al. 2016).

4 TEST RESULTS AND ANALYSIS

4.1 *DMT*

Two DMTs were carried out at the study site and Fig 5 presents the tests data in terms of p_o, p_1, I_D, K_D and E_D where I_D, K_D and E_D calculated by Marchetti's (1980) equations. The soil behavior type was identified based on the I_D parameter (Fig. 5b) and the total unit weight was estimated by using the Marchetti & Crapps (1981) chart, which relates I_D and E_D values (Fig. 6).

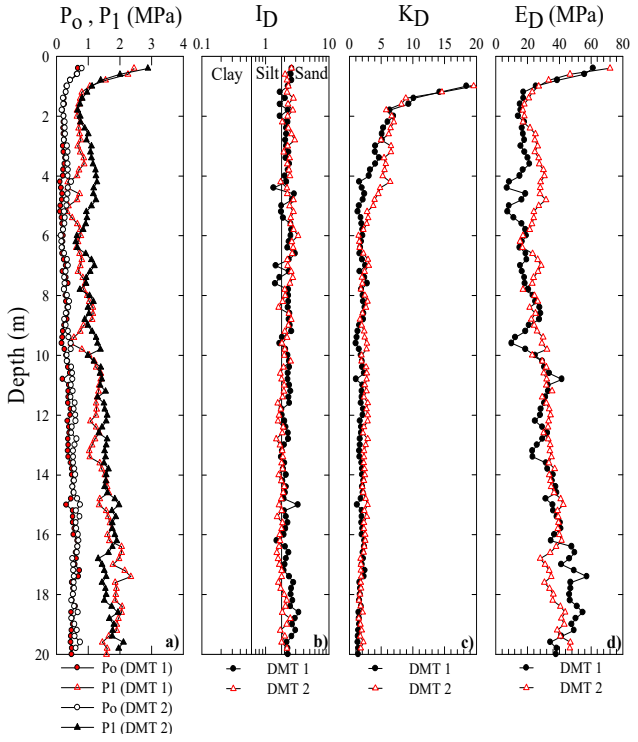

Figure 5: DMT tests data for the study site (adapted from Rocha et al., 2015)

4.1.1 *Soil Classification*

It can be observed in Figure 5b that the soil from the study site behaves like a silty sand. The grain size distribution determined in laboratory using dispersant according to the Brazilian standard (ABNT NBR-7181, 1988) classifies this soil as a clayey fine sand (Fig. 3.d). According to Marchetti et al. (2001), Material index (I_D) is not a result of a sieve analysis; instead it reflects the mechanical response of the soil to the DMT membrane expansion. Usually this index indicates that a mixture of clay and sand would generally be described as silt, which was obtained from grain size distribution without dispersant (Fig. 3e).

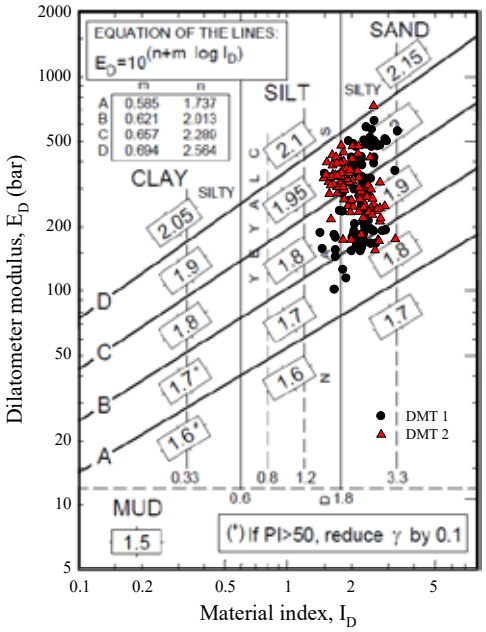

Figure 6: Study site testing data on the schematic DMT soil classification chart proposed by Marchetti & Crapps (1981).

4.1.2 *Geotechnical parameters*

One of the most important information for geotechnical projects are the strength parameters. Classical Soil Mechanics considers that sands are frictional geomaterials (ϕ') while unsaturated tropical soils have a cohesive-friccional behavior, so soil suction should be considered to proper represent their behavior. Fagundes & Rodrigues (2015) studied the influence of soil suction (s) on the shear strength of an undisturbed sample extracted from 1.5 m depth from the study site. They concluded that the friction angle (ϕ') values varied from 26.8º for the saturated condition and 32.7º for the higher suction value with an average value equal to 29.3º (Fig. 7a). The intercept of cohesion increased with suction from zero on the saturated condition to 3 kPa (s = 50 kPa), to 11 (s = 200 kPa) 16 kPa (s = 400 kPa) and to 34 (s = 33 MPa). The same study was carried by Fernandes et al. (2016) on undisturbed samples collected at 3 and 5 m depth. The authors also observed the increase on shear strength with soil suction. For 3 m depth the friction angle (ϕ') values varied from 32.6º for saturated condition and 33.8º for 400 kPa suction value, with an average value equal to 33.4º as shown on

Figure 7a. The intercept of cohesion increased with suction from 1.2 kPa on the saturated condition to 6.5 kPa (s = 50 kPa), to 13.4 kPa (s = 200 kPa) and 21.5 kPa (s = 400 kPa). The friction angle (ϕ') values varied from 32.4º for the saturated condition and 34.9º for the 400 kPa suction value with an average value equal to 33.8º for the sample collected at 5 m depth (Fig. 7a). The intercept of cohesion increased with suction from 5.3 kPa on the saturated condition to 10.3 kPa (s = 50 kPa), to 24.2 kPa (s = 200 kPa) and 28.7 kPa (s = 400 kPa).

Giacheti et al. (2006) presented reference friction angle determined using direct shear tests under consolidated drained condition (CD) on undisturbed soil samples up to 19 m depth at its natural soil condition for this site, as show in Figure 7a. The ϕ' angle varied from 30.1º to the soil from 1 m depth to 34.4º to the one from 19 m depth, with average value equal to 32.8º. The reference values were compared with friction angle based on Marchetti (1997) equation, which is depended of K_D values (Fig. 8a).

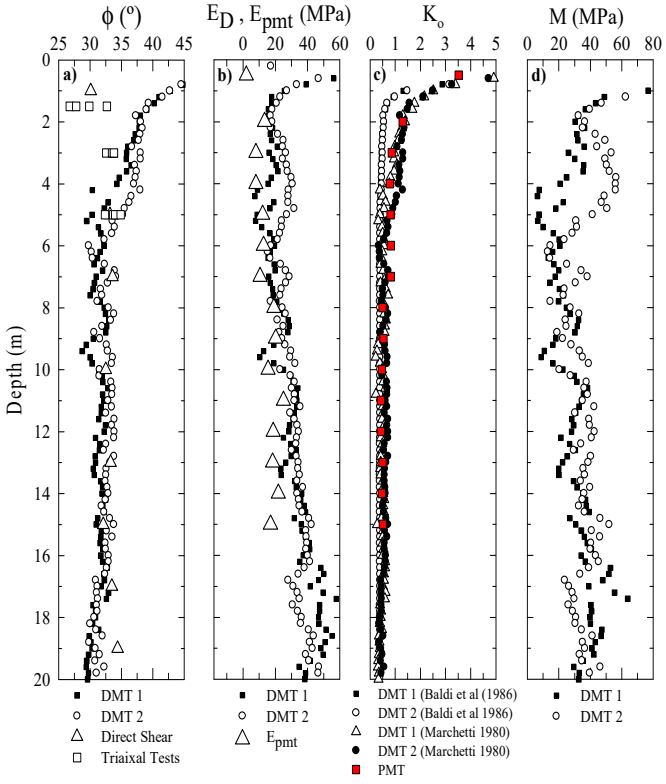

Figure 7: Estimated parameters from DMT tests data

It can be observed in Figure 7a that the estimated DMT friction angle values were reasonable below 5 m depth, with an average value of about 33º. However, the estimated DMT ϕ' values are much higher than the reference ones for the 5 m topsoil. This difference are caused by the influence of soil suction, which provides mainly an increase on the intercept of cohesion. Moreover, the estimated DMT ϕ' values incorporates the component of cohesion as a friction angle, since it assumes the soil behaves like sands.

Pressuremeter modulus (E_{pmt}) and coefficient of earth pressure at rest (K_o) obtained from Ménard pressuremeter tests (PMT) carried out by Cavalcante et al (2005) in this site will be used to evaluate the K_o and E_D determined using DMT correlations. Figure 7b shows E_D plotted together with Ménard PMT modulus (E_{pmt}). It can be observed that DMT data are produced reasonable estimates for deformability parameters, however, the E_D is always higher than E_{pmt} values. It can be explained by soil disturbance due to penetrations of DMT and PMT (Ortigão et al. 1996 and Giacheti et al. 2006).

Figure 7c presents K_o values estimated based on DMT data using Marchetti (1980) and Baldi et al. (1986) correlations plotted together with the K_o values interpreted based on PMT data. K_o from PMT is equal to 3.5 at 0.5 m depth, 1.3 at 1.5 m depth and it assumes an almost constant value equal to 0.8 up to about 8 m depth. For this part of the soil profile K_o predicted using Marchetti (1980) correlation better matched PMT K_o values. Below 8 m depth, the estimated K_o values from Baldi et al. (1986) correlation are closer to the PMT K_o values, which assumed almost a constant value equal to about 0.5 from 8 to 20 m depth.

One of the major application of the DMT is prediction settlements by use of Constrained Modulus (M_{DMT}). Figure 7d presents the constrained modulus estimated based on DMT data. The average M_{DMT} is equal 36.2 MPa between 1 to 6 m depth, 23 MPa between 6 to 10 m depth and 35.8 MPa below 10 m depth. Unfortunately, there are no oedometer tests for this site to provide reference constrained modulus values.

4.2 *CPT*

Figure 8 shows the average profiles from two CPTs campaigns carried out at the study site in a dry and in a wet season. The water content profiles for each of these seasons are also presented on this figure. They were measured based on soil samples collect using mechanical helical auger. These profiles are very different above 4 m depth (Figure 8). Considering the information from the water retention curves presented on Figure 4 it can be assumed that the soil suction values along all the soil profile is low during the wet season. In the other hand, during the dry season, soil suction values are much higher from 0 to 4 m depth.

It can also be observed in Figure 8 that the CPT data were affected by soil suction up to 4 m depth, since the other relevant characteristics of the soil profile did no significantly varied (relative density, grain size and stress history). As a result, q_c and f_s increased due to a higher suction during the dry season. The q_c and f_s profiles presented similar behavior below this depth (4 m) during the wet and the dry

season, since soil suction varied very little. It is important to point out that the range of variation on the water content in the field at the study site corresponds to the end of desaturation of the soil-water retention curves (Fig. 4). Changes on water content values reflected high changes in soil suction up to for 4 depth. It can explain significant differences on suction values up to this depth, which caused differences on q_c and f_s profiles determined in the different seasons up to the same 4 m depth.

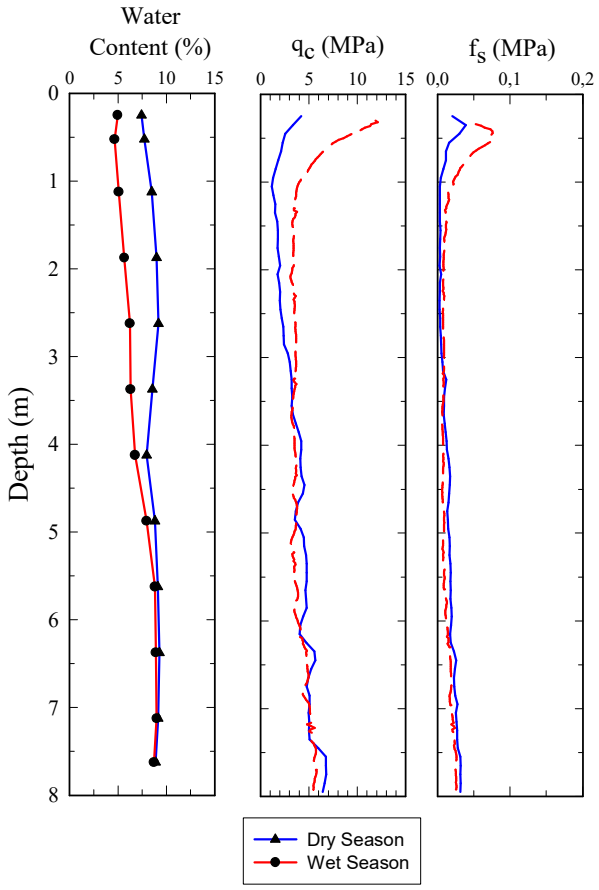

Figure 8. Water content, suction and two CPTs carried out in a dry and in a wet season at the study site (After Bezerra 2016).

4.2.1 *Soil Classification*

Robertson (2012) chart was used to show the influence of soil suction on the interpretation of CPT data. Figure 9 shows the two CPT data up to just 4 depth during the wet and the dry seasons. It can be observed in this figure a predominant contractive soil behavior for the CPT carried out in the wet season and a dilative behavior for the CPT from the dry season.

Fagundes & Rodrigues (2015) carried out suction-controlled triaxial drained shear tests (CD) to evaluate the influence of suction of the mechanical behavior of the 1.5 m depth soils of the study site. Figure 10 shows stress-strain and volume change curves obtained by CD tests at five different suctions (0, 50, 200, 400 kPa and 33 MPa) for 50 kPa confining pressure, which corresponds to mean effective stress for first meters of the study site.

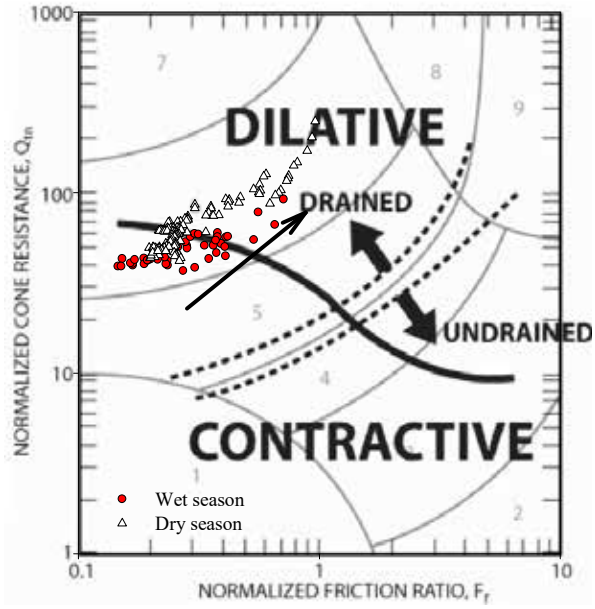

Figure 9: Q_{tn} vs F_t average values for wet and dry seasons I the Robertson (2012) chart.

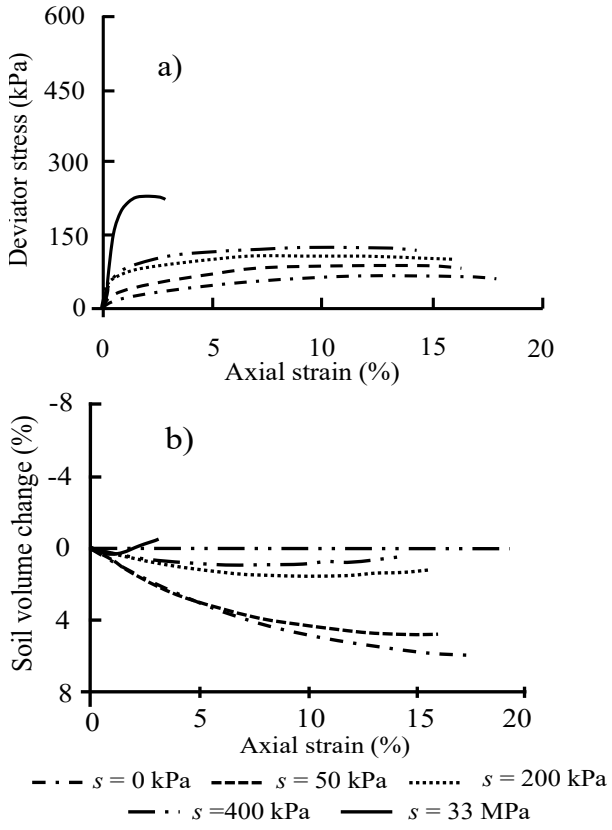

Figure 10: Stress-strain and volume change for unsaturated soil from 1 m depth (adapted from Fagundes & Rodrigues, 2015).

It can be observed in this figure a tendency for dilation during shear with increasing suction. Similar behavior was observed on the CPTs carried out in the dry season, due to higher values soil suction up to 4 m depth, which brought the points on Robertson (2012) chart from a contractive to a dilative behavior during the plastic deformation of the soil.

Considering the fact that the tests were carried out at the same position (to neglect the spatial variability), it is possible to consider the importance of the temporal variability (caused by water content and consequently the soil suction) which affects the soil behavior of unsaturated tropical soils.

4.2.2 *Geotechnical Parameters*

There are several correlations to estimate strength-strain properties of soils based on CPT. The estimative of geotechnical parameters from unsaturated soils is affected by soil suction, as previously discussed. Figure 11 shows the profiles of frictional angle (ϕ'), Young's modulus (E) and constrained modulus (M) estimated respectively by Robertson & Campanella (1983), Robertson (2009), Lunne & Christoffersen (1983) correlations, based on CPT carried out at the wet and dry seasons at the study site.

It can be seen in Figure 11 that the values of ϕ', E and M for dry season are higher than those estimated for wet season mainly in the upper part of the soil profile (4 m depth) where major influence of soil suction occurs. The tip resistance (q_c) and lateral friction (f_s) from CPT should be normalize to a reference suction value (zero suction) in order to proper take into account the influence of soil suction on the soil behavior, both in terms of soil classification, and geotechnical parameters estimative.

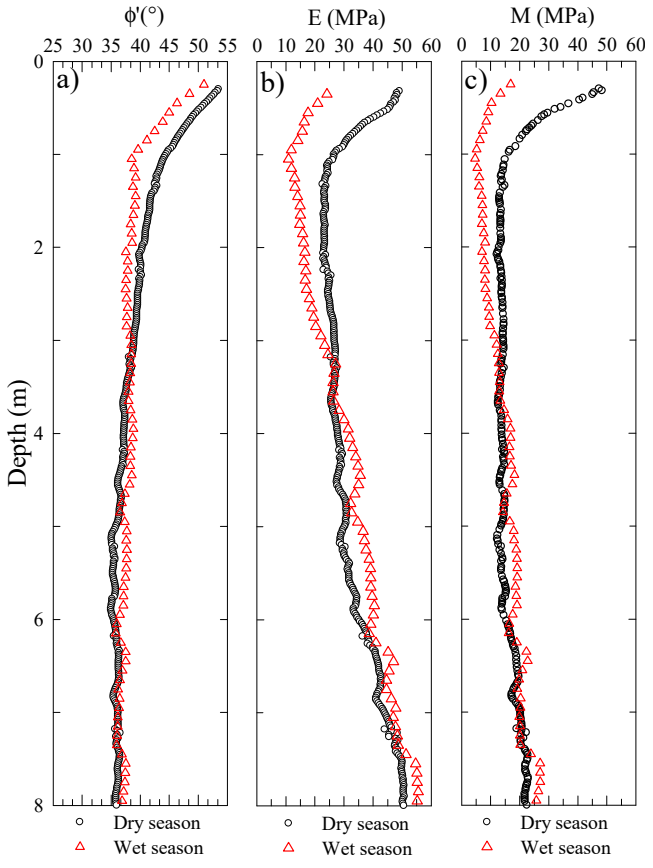

Figure 11: (a) Friction angle (ϕ'), (b) Young's modulus (E), and (c) constrained modulus (M) based on CPT data from the wet and the dry season for the study site.

5 SEISMIC TEST

Robertson et al. (1995), Schnaid et al. (2004), Schnaid & Yu (2007) and Cruz (2010 and 2012) demonstrate that the maximum shear modulus (G_o) together with SPT, CPT or DMT data is a useful tool to identify unusual geomaterials, such as the tropical soils. The G_o/q_c, G_o/M_{DMT} and G_o/E_D ratios allow evaluating the peculiar behavior of these soils (e.g. sensibility, age, cementation, etc.).

Schnaid et al. (2004) suggest that the G_o/q_c ratio provides a measure of the elastic stiffness to ultimate strength and may hence be expected to increase with sand age and cementation, primarily because the effect of these on G_o are stronger than on q_c. Schnaid et al. (2004) use the G_o/q_c *versus* q_{c1} chart, where q_{c1} is dimensionless normalized parameter defined as:

$$qc_1 = \left(\frac{q_c}{p_a}\right).\sqrt{\frac{P_a}{\sigma'_v}} \qquad (1)$$

where p_a = atmospheric pressure and σ'_v = vertical effective stress. According to Eslaamizaad & Robertson (1996) this relationship can be used to evaluate possible effects of stress history, degree of cementation and ageing for a given soil profile.

Cruz (2010) interpreted DMT data and suggested two charts and their boundaries to identify cemented structures in residual soils. The author used the G_o/E_D *vs* I_D and G_o/M_{DMT} *vs* K_D charts.

Six down-hole tests were carried out at the study site. Figure 12 presents the shear wave velocity (V_S) and maximum shear modulus (G_o) profiles.

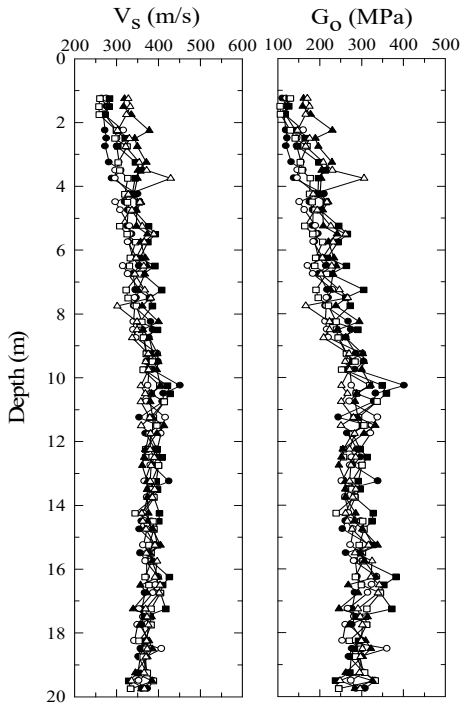

Figure 12: V_S and G_o profiles from downhole tests carried out at the study site.

The maximum shear modulus was calculated by the equation 2:

$$G_O = \rho . V_S^2 \quad (2)$$

where V_S is shear wave velocity, and ρ is the soil density, which was determined from undisturbed soil samples collected in sample pits excavated at the site.

Figure 13 e Figure 14 show the G_o/E_D *vs* I_D and G_o/M_{DMT} *vs* K_D charts, respectively, obtained from average values of G_o, I_D, K_D, E_D and M_{DMT}. Three lines and one equation are shown in each chart (Fig. 13 and Fig. 14) to define the limits for the DMT sedimentary international database and upper bounds for cemented structured soils (Cruz, 2010).

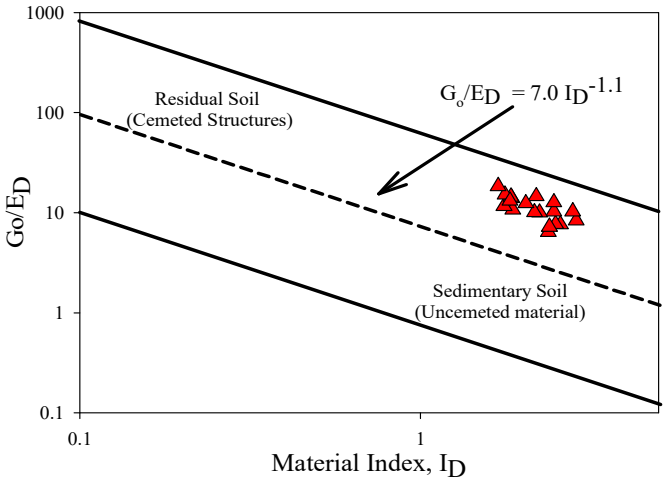

Figure 13: Seismic and DMT data plotted on G_o/E_D vs I_D chart for the study site (adapted from Cruz 2010).

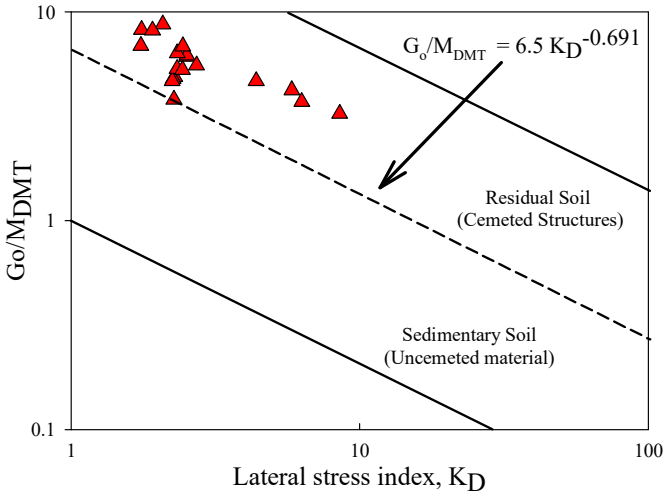

Figure 14: Seismic and DMT data plotted on G_o/M_{DMT} vs K_D chart for the study site (adapted from Cruz 2010).

In both charts the plotted data from the study site are above the equation line which separates the DMT sedimentary international database and nearby to the residual soil (cemented structures). It indicates that the bonded structure of the studied unsaturated tropical sandy soils produces G_o/E_D as well as G_o/M_{DMT} that are systematically higher than those measured in sedimentary soils.

The average values of q_c and G_o are plotted in the Schnaid et al. (2004) chart (Fig. 15) based on the data from both CPTs and all seismic tests. It shows that the G_o/q_c ratio for all soils from the study site are higher than those measured in cohesionless soils. In addition, it can be observed in this figure that the lateritic soils present a higher G_o/q_c than the saprolitic soils, which is in accordance with the findings from Giacheti & De Mio (2008).

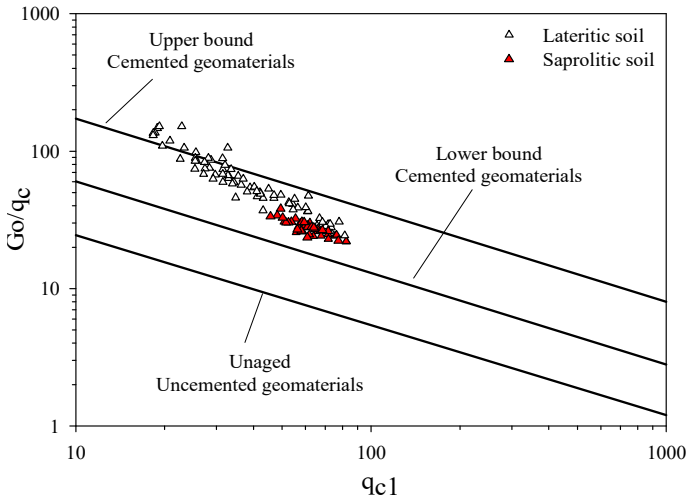

Figure 15: G_o/q_c for lateritic and saprolitic soils from the study site in the Schnaid et al. (2004) chart.

6 CONCLUSIONS

- The I_D parameter classified sand and clay mixtures from the study site as silty soils. This behavior is similar to which were found in the in situ grain size distribution determined without dispersant.
- The estimated geotechnical soil parameters based on classical DMT correlations worked well for the soil below 5 m depth for the study site. The friction angle estimative was much higher for topsoil. The unsaturated soil from the study site has a cohesive-friction behavior, which depends on soil suction. This estimative try to represent it just in terms of the friction angle.
- The average profiles from two CPTs campaings carried out in different seasons indicated that soil suction affected q_c and f_s values up to 4 m depth for the study site.
- The interpretation of CPTs carried out in the different seasons brought the points on Robertson (2012) chart from a contractive (wet season) to a dilative (dry season) behavior, which is in accordance to what was found in unsaturated triaxial tests carried out on undisturbed soil samples from the study site.
- The mechanical behavior of unsaturated tropical soils is directly influenced by soil suction. As a result, in situ soil index and estimated geotechnical parameters based these indexes should con-

sider the influence of soil suction. So, the moisture content profile together with the soil-water retention curve are relevant information for a proper site characterization for the study site.

- The charts from Cruz (2010) and Schnaid et al (2004) indicate that the soil from the study site has an unusual behavior. The bonded structure of unsaturated tropical sandy soils produced G_o/E_D, G_o/M_{DMT} and G_o/q_c, which are systematically higher than those measured in sedimentary soils.
- The test data and their interpretation pointed out the importance of using hybrid tests, like SCPT and SDMT, for the site characterization of unsaturated tropical soils as well as the importance of considering the temporal variability caused by soil suction, since it affects the soil behavior of unsaturated tropical soils.

ACKNOWLEDGMENTS

The authors gratefully acknowledge the support provided by the São Paulo Research Foundation - FAPESP (Grants # 2015/16270-0, # 2014/23767-8 and # 2010/50650-3).

REFERENCES

ABNT/NBR – 7181 1981. Soil – Grain size distribution. 13 p. (*in Portuguese*).

Baldi, G., Bellotti, R., Ghionna, V., Jamiolkowski, M., Marchetti, S. & Pasqualini, E. 1986. Flat Dilatometer Tests in Calibration Chambers. *Proc. In Situ '86, ASCE Spec. Conf. on Use of In Situ Tests in Geotechn. Eng*., USA, ASCE GSP. No. 6, 431-446.

Bezerra, R.C. 2016. CPT data interpretation considering the influence of unsaturated condition. *Undergraduate Research Report, FAPESP*. 47 p (*in Portuguese*).

Cavalcante, E.H.; Giacheti, H. L. & Bezerra, R. L. 2005. Parâmetros Geotécnicos e Previsão da Capacidade de Carga de Estacas Apiloadas em Solo Tropical, *Solos e Rochas, São Paulo*, 28, (1): pp.115-129.

Cruz, N. 2010. *Modelling Geomechanics of residual Soils with DMT Tests*. Ph.D. thesis. Porto: Porto University.

Cruz, N.; Rodrigues, C. & Fonseca A.V. 2012. Detecting the presence of cementation structures in soils, based in DMT interpreted charts. *In.: 4th International Conference on Site Characterization (ISC4)*. V. 1, p. 1723 – 1728.

De Mio, G. 2005. *Geological conditioning aspects for piezocone test interpretation for stratigraphical identification in geotechnical and geo-environmental site investigation*. Ph.D. Thesis. University of São Paulo, p. 354. (*in Portuguese*).

Eslaamizaad, S. & Robertson, P.K. 1996. A framework for in-situ determination of sand compressibility. *Proc. 49th Canadian Geotechnical Conference*, St John's, Newfoundland.

Fagundes, L.S. & Rodrigues, R.A. 2015. Shear strength of a natural and compacted tropical soil. *Electronic Journal of Geotechnical Engineering*, v. 20, p. 47-58.

Fernandes, J.B; Saab, A.L.; Rocha, B.P.; Rodrigues, R.A. & Giacheti, H.L. 2016. Shear strength of an unsaturated tropical soil. *Proc. XVIII Brazilian Conference on Soil Mechanics and Geotechnical Engineering*. p. 1 – 8.

Giacheti, H.L.; Peixoto, A.S.P.; De Mio, G. & Carvalho, D. 2006. Flat Dilatometer Testing in Brazilian Tropical Soils. *Proc. Second International Conference on the Flat Dilatometer, Washington. ASCE: R A Failmezger and J B Anderson Editors*. v. 1. p. 103-110.

Giacheti, H.L. & De Mio, G. 2008. Seismic cone penetration tests on tropical soils and the ratio G_o/q_c. *Proc. 3rd Geotechnical and Geophysical Site Characterization Conference, ISC'3*, Taiwain, v.1. p. 1289- 1295.

Luune, T. & Christophersen, H.P. 1983. Interpretation of cone penetrometer data for offshore sands. *Proc. of Offshore Technol. Conf*., Richardson, Texas, Paper No. 4464, pp. 1–12.

Marchetti, S. 1980. In Situ Tests by Flat Dilatometer, *Journal of the Geotechnical Engineering Division, ASCE*, V-106, nº GT3, pp. 299-321.

Marchetti, S. & Crapps, D.K. 1981. "Flat Dilatometer Manual". *Internal Report of G.P.E. Inc.*

Marchetti, S., Monaco, P., Totani, G. & Calabrese, M. 2001. The Flat Dilatometer Test (DMT) in Soil Investigations, TC 16 Report. *Proc. IN SITU 2001, International Conference on In situ Measurement of Soil Properties, Indonesia*, 41 pp.

Nogami, J.S. & Villibor, D.F. 1981. A new soil classification for highway purposes. *Proc. Symposium on Tropical Soils in Engineering, Brazil*, v. 1, p. 30-41 (*in Portuguese*).

Ortigão, J.A.R., Cunha, R.P. & Alves, L.S. 1996. In Situ Tests in Brasília Porous Clay. *Canadian Geotechnical Journal*. V. 33. p. 189-198.

Robertson, P.K. 2009. CPT interpretation – a unified approach. *Canadian Geotechnical Journal* 46, 11, 1337–1355.

Robertson, P.K. & Campanella, R.G., 1983. Interpretation of cone penetration tests part I: Sand. *Canadian Geotechnical Journal*. 20 (4), 718–733.

Robertson, P.K., Fear, C.E., Woeller, D.J. & Weemees, I.A. 1995. Estimation of Sand Compressibility from Seismic CPT." *Proc. 48th Canadian Geotechnical Conference*, Canada, p. 441-448, 1995.

Rocha, B.P.; Castro, B.A.C. & Giacheti, H.L. 2015 Seismic DMT Test in a Non-Text Book Type Geomaterial. *Proc. The 3rd International Conference on the Flat Dilatometer*, Roma. DMT 15, 2015. v. 1. p. 505-512.

Schnaid, F., Lehane, B.M. & Fahey, M. 2004. In situ test characterization of unusual geomaterials. *Proc. 2º Geotechnical and Geophysical Site Characterization*. Rotterdam: Edited by Viana da Fonseca e Mayne, v.1, p. 49-74.

Schnaid, F. & Yu, H.S. 2007. Interpretation of the Seismic cone test in granular soils. *Geotechnique*, 57, No. 3, 265 – 272.

Vaughan, P.R.; Maccarini, M. & Mokhtar, S.M. 1988. Indexing the engineering properties of residual soils. *Quarterly Journal of Eng. Geology*, 21, pp. 69- 84.

Geotechnical and Geophysical Site Characterisation 5 – Lehane, Acosta-Martínez & Kelly (Eds)

G-γ decay curves in granitic residual soils by seismic dilatometer

C. Rodrigues
Polytechnic Institute of Guarda, Department of Civil Engineering

S. Amoroso
Istituto Nazionale di Geofisica e Vulcanologia, Via dell'Arcivescovado

N. Cruz & J. Cruz
Direção de Coordenação Técnica Rodoviária da Mota-Engil – Engenharia e Construção

ABSTRACT: Due to stiffness non-linearity direct application of small-strain shear modulus to evaluate deformations in most practical problems is not possible, which gave rise to the development of modulus (E_0 or G_0) degradation curves. This has been applied with success to sedimentary soils, but in residual soils the experience and available information in the international community is still scarce. Those soils are considered as structured soils, often classified as problematic soils as they do not fit into the behaviour that of remoulded or unstructured soils. In reality the role of bonding and fabric enhances the strength and stiffness of the soil. In this paper, the use of the seismic dilatometer test (SDMT) for the determination of in situ decay curves of stiffness with strain level (G-γ curves or similar) in a granitic residual soil, located in NE region of Portugal (Guarda) is illustrated, revealing its adequacy to solve this kind of problems. In situ tests and laboratory tests were performed in those granitic residual soils. The results were used for this investigation. The approach adopted relies on the ability of SDMT to provide a small strain modulus G_0 (from the shear wave velocity V_s) and a "working strain" modulus G_{DMT} (from the constrained modulus M_{DMT} by elasticity theory). Thus in situ G-γ decay curves are tentatively constructed by fitting curves through these two points. At this site the working strain modulus and the operational strain modulus are compared with same depth reference stiffness decay curves obtained by triaxial tests.

1 INTRODUCTION

The design of geotechnical structures requires knowledge of the stiffness characteristics of soils, often expressed in terms of shear moduli. However, due to stiffness non-linearity direct application of small-strain shear modulus to evaluate deformations in most practical problems is not possible, which gave rise to the development of modulus (E_0 or G_0) degradation curves. Available studies reveal that the decay in sands is much less than in silts and clays decay curves, which are very similar and in all cases the decay is maximum in the NC or lightly OC region. This has been applied with success to sedimentary soils, but in residual soils the experience and available information in the international community is still scarce.

The SDMT testing is widely used in evaluating these deformational properties, due to its ability to provide the small-strain shear modulus G_0 and a working strain modulus at a medium strain level, G_{DMT} (derived from the constrained modulus M_{DMT} by elasticity theory). Monaco et al. (2009) argued that since M_{DMT} is a working strain modulus, G_{DMT}/G_0 could be regarded as the shear modulus decay factor at working strains. The possibility of having two independent measurements of stiffness in only one test, opens a way to attempt deriving in-situ decay curves of soil stiffness with strain, as suggested by Monaco et al. (2009). To do so, it is important to locate, even if roughly, the shear strain γ_{DMT} corresponding to G_{DMT}.

2 SITE CHARACTERIZATION

2.1 *Geological background*

The climate in the studied area (Guarda, northeast of Portugal) is moist moderate, which favours the weathering of the granitic rock mass that dominates the region, turning the granite masses into a permeable sandy frame. The fluctuations of water level that go from a submerged stage in the wet season followed by drying up to depths of 5 to 6 meters during the summer, create the conditions to favour the constant weathering of the rocky substrate. As weathering progresses, the primary interparticle bonds between the grains are broken and a series of intergranular voids are created. Afterwards, weathering makes the feldspars and micas unstable, allowing leaching to occur, with the creation of a network of

intragranular voids. In addition, the more stable minerals, mostly quartz grains, are bonded by highly weathered (and therefore unstable) grains of feldspars and micas to form a solid skeleton that is sometimes quite open.

2.2 *Testing program*

The testing program consisted of 6 SDMT tests, 6 SCPTu tests and 18 PMT tests distributed by 6 boreholes, as well as 3 triaxial tests with internal instrumentation performed in undisturbed and reconstituted samples, as represented in Figure 1. In this framework, emphasis is given to SDMT and triaxial tests carried out on selected samples as discussed hereafter.

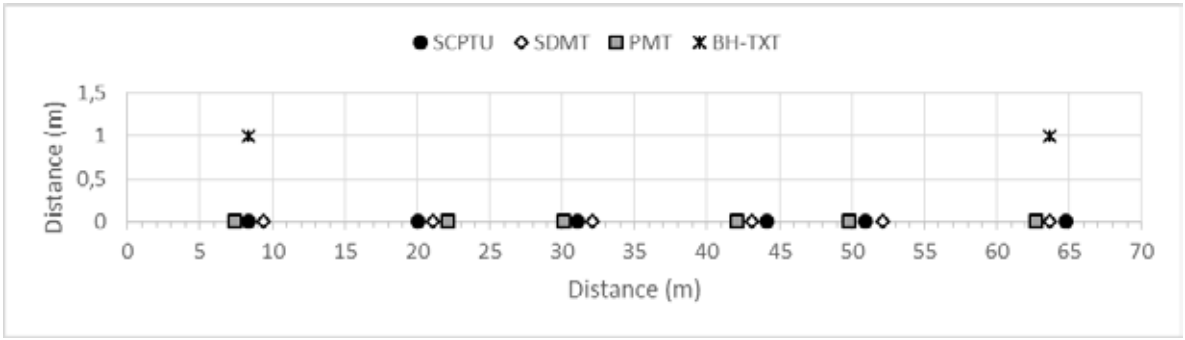

Figure 1. Spatial localization of the tests

2.3 *SDMT tests*

The seismic dilatometer (SDMT) is the combination of the mechanical flat dilatometer (DMT), introduced by Marchetti (1980), with a seismic module for measuring the shear wave velocity, V_s. From V_s the small strain shear modulus G_0 may be determined using the theory of elasticity. A new SDMT system has been recently developed in Italy (Marchetti 2008), where the seismic module (Fig. 2) is a cylindrical element placed above the DMT blade, provided with two receivers spaced 0.5 m apart. The signal is amplified and digitalized at depth. The true-interval test configuration with two receivers avoids possible inaccuracy in the determination of the "zero time" at the hammer impact, sometimes observed in the pseudo-interval one-receiver configuration. Moreover, the couple of seismograms recorded by the two receivers at a given test depth corresponds to the same hammer blow and not to different blows in sequence, which are not necessarily identical. Hence the repeatability of V_s measurements is considerably improved. V_s is obtained (Figure 2b) as the ratio between the delay of the arrival of the impulse from the first to the second receiver (Δt) and the difference in distance between the source and the two receivers (S2−S1). V_S measurements are obtained every 0.5 m of depth, while the mechanical DMT readings are taken every 0.20 m.

The SDMT test results obtained on site are summarized in Figure 3. From the soil identification point of view material index I_D is fully consistent with grain size of these granitic residual soils, revealing once more the adequacy of the parameter to correctly identify these soils (Cruz, 2010). On its turn, horizontal stress index K_D ranges between 10 and 40, clearly pointing out to a significant cementation structure present in the soil, which seems to be confirmed by the particularly high values of the constrained modulus M_{DMT} with a mean value of 200MPa in the upper part of profile and 325MPa after 4m depth, clearly corresponding to a different weathering level. Finally, the shear modulus G_0 profile shows a linear increasing with the depth.

2.4 *Triaxial tests*

A set of three triaxial tests (CID), with internal instrumentation, were performed in samples taken with a Shelby sampler 1m away from SDMT1 and SDMT6. In Figure 4 the secant stiffness-strain behaviour is presented, obtained from 3 samples collected at different depths and consolidated at 50 kPa, where three discontinuities can be identified and may be considered as yield points. The first was established in $\log E_{sec}$:$\log \varepsilon_a$ space and relates to the point where the initial horizontal stretch ends, defined as first yield. This yield corresponds to the end of the linear elastic behaviour, reached for very small strains (less than ε_a=0.005%). The second discontinuity, located nearby 0.07% of axial strain, corresponds to the second yield, where it is observed an increase in the volumetric deformation in relation to the triaxial distortion. This yield was set according to Alvarado et al. (2012) and corresponds to the initial change in the relation between the volumetric deformation ε_v and the distortion ε_s. The behaviour between the first and the second yields should be elastic, but close to the second yield plastic strains and permanent deformations occur. These first two yields correspond to Y_1 and Y_2 defined by Jardine (1992). The last yield (ε_a=1% to 2%), established in

logE_{sec}:logε_a space, corresponds to a point in which the structure is dramatically destroyed close to the maximum shear resistance. At this point, soils reveal large plastic strains and correspond to the Gross Yield of Coop & Wilson (2003) or the Bond Yield of Malandraki & Toll (2001).

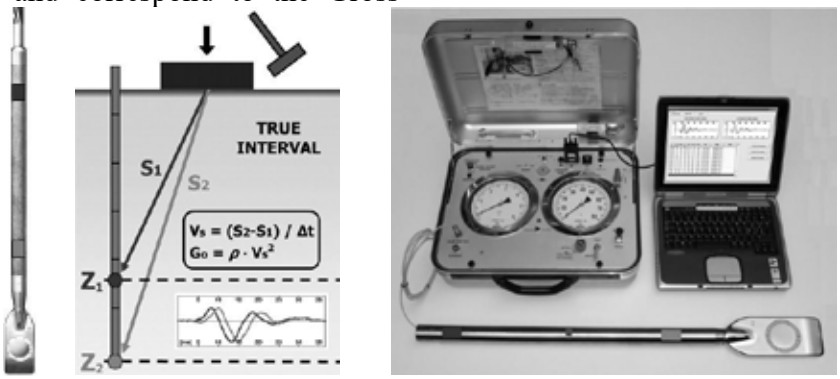

a) b) c)

Figure 2 - Seismic dilatometer test (Marchetti et al. 2008): DMT blade and seismic module (a); schematic test layout (b); seismic dilatometer equipment (c).

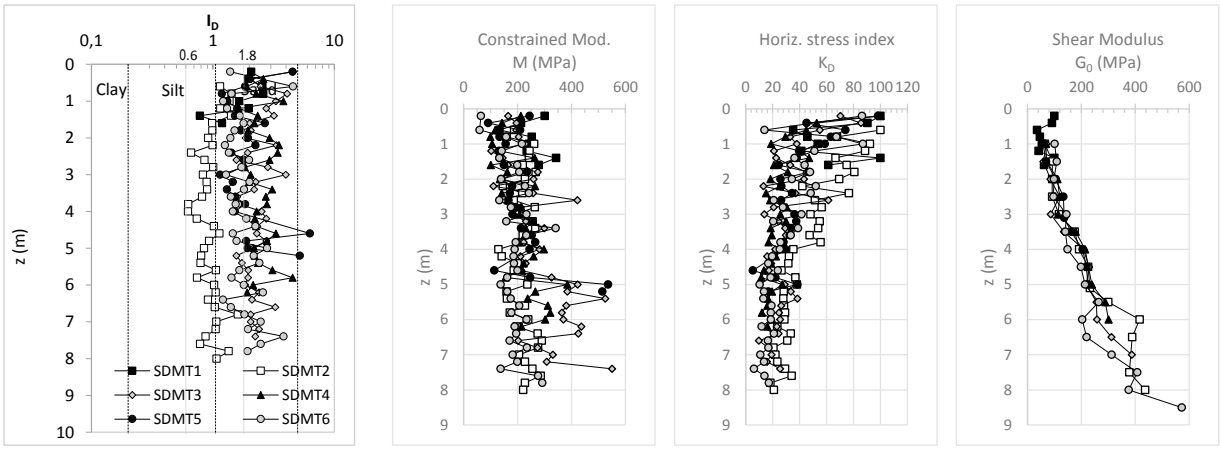

a) b) c) d)

Figure 3. SDMT test results

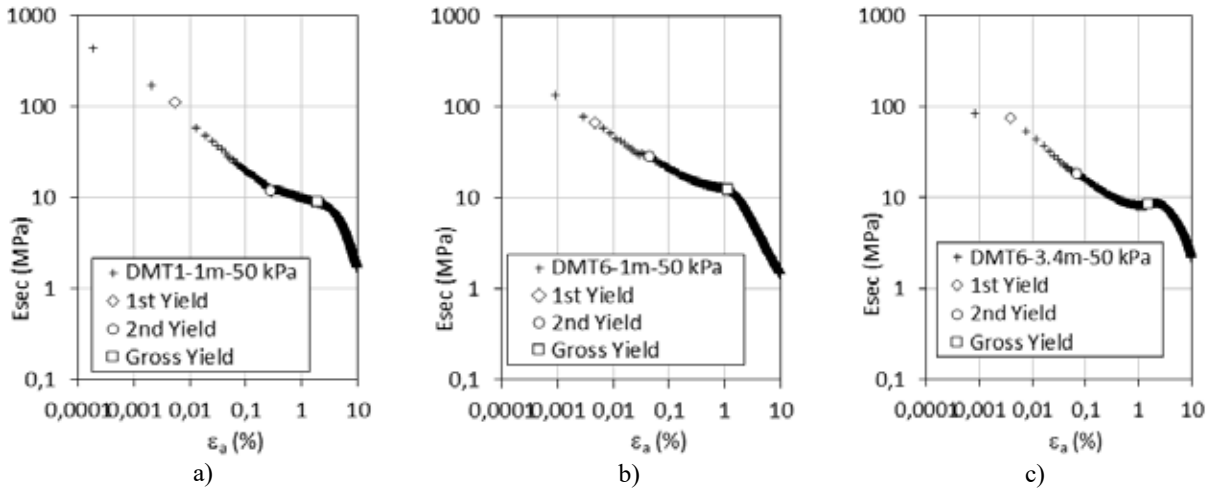

a) b) c)

Figure 4. Stiffness and yield points obtained by CID triaxial tests; a) BH 1, depth 1m, consolidation pressure 50 kPa; b) a) BH 6, depth 1m, consolidation pressure 50 kPa; a) BH 6, depth 3.4m, consolidation pressure 50 kPa.

3 IN SITU G-γ DECAY CURVES

3.1 *Seismic dilatometer*

The adopted approach relies on the ability of SDMT to provide routinely in sand at each depth both a small strain modulus (G_0 from V_S) and a "working strain" modulus (G_{DMT} from M_{DMT}) that could be tentatively used to fit in situ decay curves. The small shear strain modulus was evaluated by the SDMT ($G_0 = \rho V_s^2$) by using the shear wave velocity V_S obtained at the same depth of triaxial retrieved samples and the total mass density γ estimated by DMT unit weight results. On its turn, the working strain modulus G_{DMT} can be derived from the constrained modulus M_{DMT}, obtained from the flat dilatometer DMT (Marchetti et al. 2001) using the linear elastic formula (Eq. 1), as supported by Monaco et al. (2006) and Marchetti et al. (2008):

$$G_{DMT} = \frac{M_{DMT}}{2(1-\nu)/(1-2\nu)} \quad (1)$$

where ν = Poisson's ratio (taken equal to 0.2 in sand).

However, to use this G_{DMT} it is necessary to know the correspondent elemental shear strain, here designated as γ_{DMT}. Mayne (2001) indicates a range for γ_{DMT} within 0.05–0.1%, while Ishihara (2001) suggests that the range can be much higher, varying from 0.01% to 1%. Marchetti et al. (2006) reconstructed soil stiffness decay curves for the Treporti case history from local vertical strains measured at the centre of the embankment under each load increment. The intersection of the DMT data points with the observed in-situ decay curves indicated that γ_{DMT} was in the range 0.01–0.1% in sand and between 0.1% and 1% in silt. More recently, Amoroso et al. (2014) in a wider study concluded that γ_{DMT} varied from 0.015 % to 0.30 % in sand, 0.23 % to 1.75 % in silt/clay and higher than 2 % in soft clay.

3.2 *Tentative method for deriving in situ G-γ decay curves from SDMT*

The use of the SDMT to assess the in situ decay of stiffness at various test sites is explored using data obtained in granitic residual soils of Guarda and where both SDMT data and "reference" stiffness decay curves, obtained by triaxial tests, were available. The procedure adopted correspond to the proposed by Amoroso et al. (2014):

a) Using SDMT data obtained at the same depth of each available reference stiffness decay curve, a working strain modulus G_{DMT} is derived from M_{DMT} and normalized by its small strain value G_0 derived from V_S.
b) The G_{DMT}/G_0 horizontal ordinate line is superimposed to the same-depth experimental stiffness
c) decay curve, in such a way that the data point ordinate matches the curve;
d) The "intersection" of the G_{DMT}/G_0 (or E_{DMT}/E_0 in terms of Young's moduli) horizontal ordinate line with the stiffness decay curve provides a shear strain value referred to here as γ_{DMT}.

This methodology was applied in the present case, by using two SDMT and triaxial tests executed over samples retrieved at the same depth and subjected to same confinement observed in the DMT depths of determination. The respective results are presented in Figure 5, from where it is possible to draw the following considerations:

a) G_{DMT} results are within the same locus of the 1st yield, suggesting that installation of the equipment does not affect deeply the cementation structure, which was also noted by Cruz (2010);
b) The maximum stiffness obtained at small strain in triaxial tests are in the same order of magnitude that the obtained via shear wave velocities, which demonstrates the high quality achieved in the sampling processes;
c) Correspondent γ_{DMT} falls within 0.0025 % and 0.003 %, which are one order magnitude lower than those proposed by Amoroso et al. (2014) for sedimentary soils with similar grain size (0.015 % to 0.30 %), illustrating very well the influence of cementation structure on the mechanical behaviour of these soils.

4 PROPOSED NUMERICAL G- γ DECAY CURVES

Several authors (Hardin & Drnevich 1972, Bellotti et al. 1989, Byrne et al. 1990, Fahey and Carter 1993, Fahey 1998) introduced a hyperbolic model to represent the non-linear stress-strain behaviour of soil in pressuremeter tests. In this respect, the SDMT experimental data determined in the two triaxial tests were used to assist the construction of a hyperbolic stress-strain equation (Eq. 1), that confirm the formulation already found by Amoroso et al. (2014):

$$\frac{G}{G_0} = \frac{1}{1+\left(\frac{G_0}{G_{DMT}}-1\right)\frac{\gamma}{\gamma_{DMT}}} \quad (2)$$

Thus, the ratio G_{DMT}/G_0 obtained from SDMT and the estimated shear strain γ_{DMT} were used to plot the corresponding hyperbolic curve to both test. The results shown in Figure 6 plotted together with the curves obtained from SDMT using Eq. 2 and the coupled values of G_{DMT}/G_0-γ_{DMT}, and they provide a reasonable fit to the "measured" stiffness decay

curves in medium to high strains, while at low strain levels the match with hyperbolic model is poor. Amoroso et al. (2014) reported identical behaviour in the Shenton Park sands (Australia).

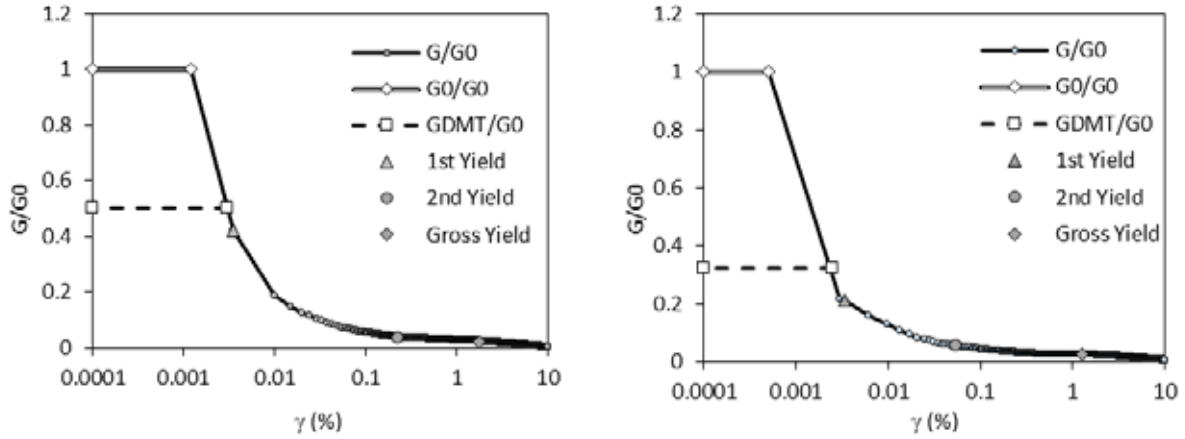

Figure 5 - Laboratory G/G_0-γ curves and superimposed G_{DMT}/G_0 data points at granitic residual soils of Guarda of: a) SDMT1, depth=1 m and b) SDMT6, depth =3.4 m.

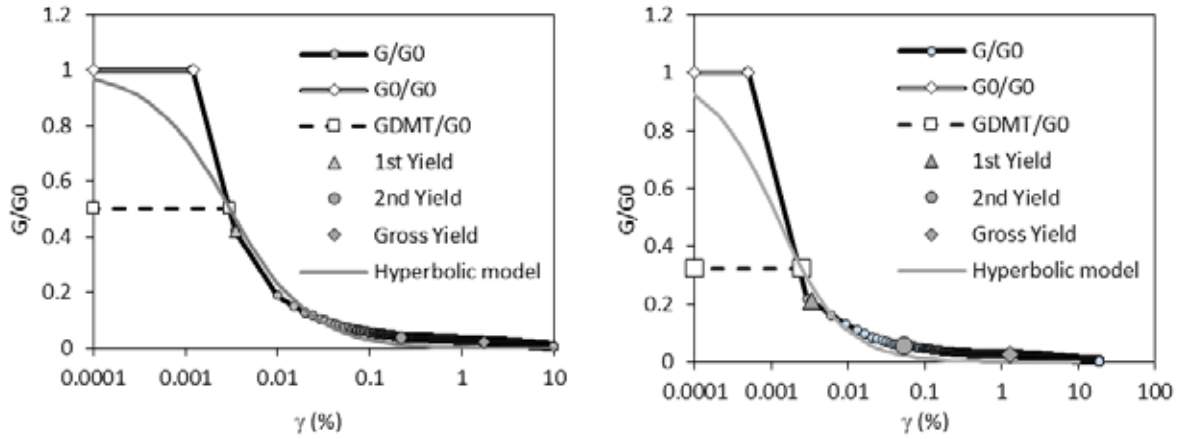

Figure 6 - Laboratory G/G_0-γ curves and superimposed G_{DMT}/G_0 data points at granitic residual soils of Guarda of: a) SDMT1, depth=1 m and b) SDMT6, depth =3.4 m.

5 CONCLUSIONS

The presented experimental work was based in a high quality characterization program constituted by DMT and triaxial testing performed in a granitic residual environment. Degradation curves (G/G_0-γ) were plotted considering triaxial and DMT results, which were then compared with hyperbolic model resulting curves. The results show that G_{DMT} results are within the same locus of the 1st yield, the maximum stiffness obtained at small strain in triaxial tests are in the same order of magnitude that the obtained via shear wave velocities (reflecting the high quality achieved in the sampling processes) and that correspondent strains (γ_{DMT}) falls within 0.0025% and 0.003%, substantially lower than those proposed by Amoroso et al. (2014) for sedimentary soils with similar grain size (0.015 % to 0.30 %), Hyperbolic model generally fits at medium to high strains, while at low strain levels the match is poor.

6 REFERENCES

Alvarado, G.; Coop, M.R. and Willson, S.M. 2012. On the role of bond breakage due to unloading in the behaviour of weak sandstones. *Géotechnique*, 62(4), 303–316.

Amoroso S., Monaco P., Lehane B. and Marchetti, D. 2014. Examination of the potential of the seismic dilatometer (SDMT) to estimate in situ stiffness decay curves in various soil types. *Soils and Rocks*, Vol. 37, No. 3, 177-194. ISSN: 1980-9743. Brazilian Association for Soil Mechanics and Geotechnical Engineering (ABMS) and Portuguese Geotechnical Society (SPG). São Paulo, Brazil. http://www.soilsandrocks.com.br/soils-androcks/SR37-3_177-194.pdf

Coop, M.R., Willson, S.M. 2003. Behavior of Hydrocarbon Reservoir Sands and Sandstones. *Journal of Geotechnical and Geoenvironmental Engineering*, 129(11), 1010-1019.

Cruz, N. 2010. *Modelling geomechanics of residual soils by DMT tests*. PhD thesis, Porto University, (*www.nbdfcruz.drupalgardens.com*).

Jardine, R.J. 1992. Observations on the kinematic nature of soil stiffness at small strains. *Soils and Foundations*, (32), 111-124.

Lehane, B.M. and Fahey, M. 2004. Using SCPT and DMT data for settlement prediction in sand. *Proc. 2nd Int. Conf. on Site Characterization ISC'2*. Porto: 2, 1673–1679.

Malandraki, V. and Toll, D. (2001). "Triaxial tests on a weakly bonded soil with changes in stress path". Journal of Geotechnical and Geoenvironmental Engineering, 27(3), 282-291.

Marchetti, S. 1980. In Situ Tests by Flat Dilatometer. *J. Geotech. Engrg. Div.*, ASCE, 106(GT3), 299-321.

Marchetti, S., Monaco, P., Calabrese, M. and Totani, G. 2006. Comparison of moduli determined by DMT and backfigured from local strain measurements under a 40 m diameter circular test load in the Venice area. Proc. *2nd Int. Conf. on the Flat Dilatometer*. Washington D.C. R.A. Failmezger and J.B. Anderson (eds), 220–230.

Marchetti, S., Monaco, P., Totani, G. and Marchetti, D. 2008. In Situ Tests by Seismic Dilatometer (SDMT). *ASCE Geot. Special Publication* GSP 170 honoring Dr. J.H. Schmertmann. New Orleans March 9–12.

Marchetti, S., Monaco, P., Totani, G., and Calabrese, M. 2001. The flat dilatometer test (DMT) in soil investigations—A report by the ISSMGE Committee TC16. *Proc., 2nd Int. Conf. on the Flat Dilatometer*, R. A. Failmezger and J. B. Anderson, eds., In-Situ Soil Testing, Lancaster, VA, 7–48.TC16 (2001).

Mayne, P.W. 2001. Stress-strain-strength-flow parameters from enhanced in-situ tests. *Proc. Int. Conf. on In Situ Measurement of Soil Properties and Case Histories*. Bali, 27–47.

Monaco, P., Marchetti, S., Totani, G., Marchetti, D. 2009. Interrelationship between small strain modulus G_0 and operative modulus. Proc. of *International Conference on Performance-Based Design in Earthquake Geotechnical Engineering* (IS-Tokyo 2009), Tsukuba, Japan. 1315-1323.

Monaco, P., Totani, G., Calabrese, M. 2006. DMT-predicted vs observed settlements: a review of the available experience. In R.A. Failmezger and J.B. Anderson (eds), Flat Dilatometer Testing, Proc. *2nd International Conference on the Flat Dilatometer*, Washington D.C. 244–252.

Geotechnical and Geophysical Site Characterisation 5 – Lehane, Acosta-Martínez & Kelly (Eds)

A consideration on the shear strength characteristics of unsaturated volcanic soils

A. S. Samim & M. Sugiyama
Tokai University

ABSTRACT: An increasing number of cases of fill failure due to an earthquake or heavy rain have been reported. Therefore, the mechanical properties of compacted soils (unsaturated soils) have been situated a focus of attention. Constitutive equations were proposed concerning saturated and dry soils. Some models have been applied for practical purposes. In this research the consolidated undrained shear test using statically compacted Kanto loam and Koroboku with varying degrees of saturation was conducted with a tri-axial compression test apparatus for saturated soils. To compare the test results with analytical data, an elasto-plastic finite element analysis is carried out to define the shear test result by unsaturated soil which is composed of three phases, namely soil particle, water and air was regarded as a two-phase system of soil particle and pore fluid (water and air) while considering compressibility.

1 INTRODUCTION

Compacted soils comprise a large part of the earth structures designed by engineers. Examples include the roads, airfields, earth dams and many other structures comprising an important part of society's infrastructure. Swelling clays, collapsing soils and residual soils are all examples of unsaturated soils encountered in engineering practice. Recently, an increasing number of cases of fill failure due to an earthquake or heavy rain have been reported. Therefore, the mechanical properties of compacted soils (unsaturated soils) deserve close attention. Whenever embankment height exceeds 100m, the stability of the slope during and after construction is a crucial issue. Many geotechnical problems such as bearing capacity, lateral earth pressures, and slope stability are related to the shear strength of a soil, and shear strength of a soil can be related to the stress state in the soil. The strain constant generally used for an unsaturated soil are the net normal stress, and the matrix suction. Under normal conditions, Japanese soils exist in a highly humid climate and are therefore close to saturation even in a formally unsaturated state. It is therefore of great practical significance to understand the strength and deformation parameters of highly saturated yet not fully saturated soils. We suggest a set of constructive hypothetical equations to describe saturated and dry soils. Several mathematical models have been applied for practical purposes. For unsaturated soils, Alonso, Kohgo, Karube and others have proposed a number of models. These studies are still in process, moving toward practical applications. Discussing the strength and deformation characteristics of unsaturated soils requires consideration of the degree of saturation and matrix suction affecting those soils. These two parameters are known to have a great impact on the mechanical behavior of unsaturated soils and this mechanical behavior is directly related to the strength and deformation characteristics of soils. In order to investigate these behaviors, an experimental program based on a three-dimensional setting is performed. Examining the strength and deformation characteristic of unsaturated soils requires a testing apparatus that is capable of controlling suction and air emission. In this research the tri-axial compression test (UU, CU, CD test) using statically compacted Kanto loam and Koroboku with varying degrees of saturation was conducted with a tri-axial compression test apparatus for saturated soils. To compare the test results with analytical data, an elasto-plastic finite element analysis is carried out to define the shear test results of unsaturated soil composed of three phases, namely, soil particles, water, and air was regarded as a two-phase system of soil particles and porous fluid (water and air) while evaluating compressibility.

2 SAMPLE CREATION AND TEST METHOD

Samples of Kanto loam and Kuroboku were collected in Hiratsuka City, Kanagawa Prefecture (natural water content: 100 to 112%). A sample with an initial degree of saturation S_r of 50% or higher was made by drying the soil for two days in a 110°C drying furnace, passing it through a 2 mm sieve and adding a designated amount of water. The physical properties of the samples are listed in Table 1. The unsaturated 5 cm diameter and 10 cm height soil

sample was placed in three layers in a 5 cm diameter, 12.5 cm high mold. An overburden pressure of 200 kPa was applied to each layer gradually, with the excess being trimmed away and used to check water content. To prepare a saturated sample, initial moisture ratio of 160% of the samples is prepared. The sample was then placed in a 21.5cm diameter mold to which a static load of 50 kPa was applied, gradually, for about 10 days.

After creation of a given specimen, the specimen was placed in a triaxial compression apparatus for saturated soils (pore pressure was measured at the lower pedestal at the bottom of the sample). The case of UU test, first cell pressure applied then sheared with the shearing rate of 1mm/min. The case of CU and CD tests, its consolidated at a designated isotropic consolidation pressure σ for 24 hours and a cell pressure increment $\Delta\sigma$ was applied in stages to measure the pore pressure coefficient B (= $\Delta u/\Delta\sigma$, referred to as the B value). Subsequently, triaxial consolidated shear tests were conducted both under drained and undrained conditions. The undrained shear rate was 0.08 mm/min and drained shear rate was 0.004 mm/min, respectively. Table 2 shows the initial condition of samples which used for the triaxial experiments.

Table1 Physical property of Kanto Loam and Kuroboku

Sample	ρs	w_L	w_P	Grading (%)		
	(g/cm^3)	(%)	(%)	Clay	Silt	Sand
Kanto Loam	2.589	104.9	72	20.9	42	37.1
Kuroboku	2.349	NP	NP	7	47	46

Figure 1 Procedure of sample creation

Table 2. Initial saturation of sample for both UU and CU tests

Soil used	UU Test Sr(%)	CU Test Sr(%)
Kuroboku	51-57	52-53
	61-67	58-64
	71-78	83-87
	94-95	94-99
Kanto-Loam	44-46	54-56
	56-59	62-64
	71-85	87-88
	91-93	94-100

3 EXPERIMENTAL RESULT AND CALCULATION

3.1 Results of UU test

Figure 2 shows the relationship between a deviator stress q and an axial strain ε of Kanto loam and Kuroboku; the results are classified by color and shown by the different confining pressure p. The deviator stress q increases monotonically with increasing strain. There is no result which shows obvious peak strength, even at 15% of axial strain. Thus, strength increases with an increase in the confining pressure. Figure 3 compares stress-strain relationships versus the difference in the degree of saturation as, for example, a confining pressure of 100 kPa of Kuroboku is shown. Because the axial strain indicates approximately equal behavior to within 1% independent of the degree of saturation, the overall stiffness is approximately equal. It turns out that a difference arises in both, after that and strength differs by almost 2 times when there is a difference of 40 % in the degree of saturation. Figure 3 compares Mohr's stress circle under different degrees of saturation. Generally, as for the strength constant of the saturated soil in a UU test, φ_u is set to 0. In the case of unsaturated soil, the failure envelope expressed in terms of total stress is nonlinear, and values of c_u and φ_u can be quoted only for specific ranges of normal stress. These figures show that the angle of shear resistance, the inclination of the failure envelope of two samples, decreases with an increase in the degree of saturation. Figure 5 shows variations in c_u and φ_u against a degree of saturation. Although the cohesion c_u of Kanto loam under 25-35 kPa remains intact, without seeing an obvious variation with degree of saturation, the cohesion c_u of Kuroboku increases with an increase in the degree of sat-

uration, and φ_u decreases as well, similar to Kanto loam. For reference, according to the UU test that Odaka et al. performed for the mixed soil which prepared dry density, c_u and φ_u showed decrease with an increase in the degree of saturation.

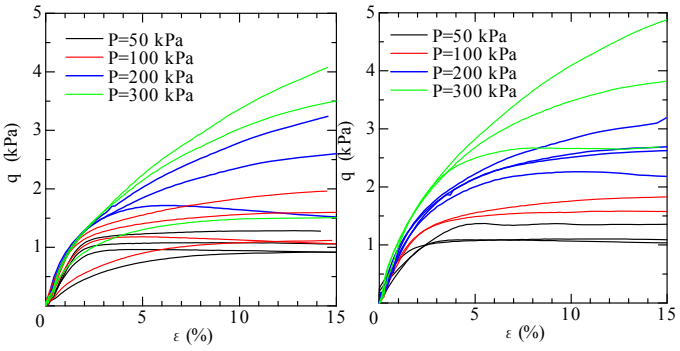

(a)Kanto-Loam (b) Kuroboku

Figure 2. Stress-Strain result of Unconsolidated Undrain (UU) Experiment (Y-axis/10)

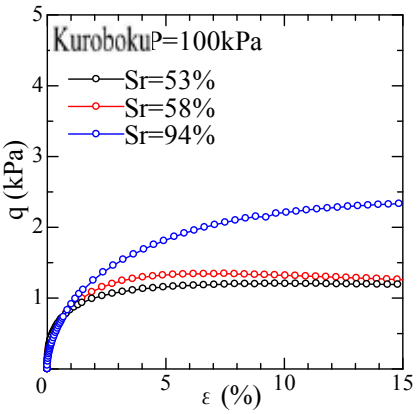

Figure 3. Compares stress-strain relationships versus the difference in the degree of saturation (Y-axis/10)

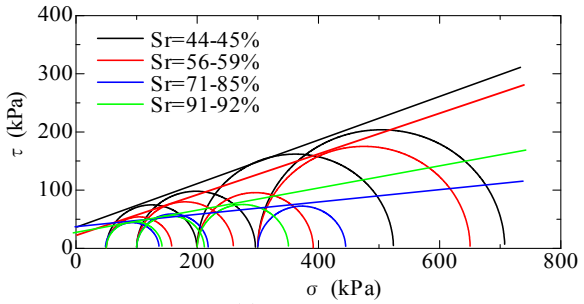

(a) Kanto-Loam

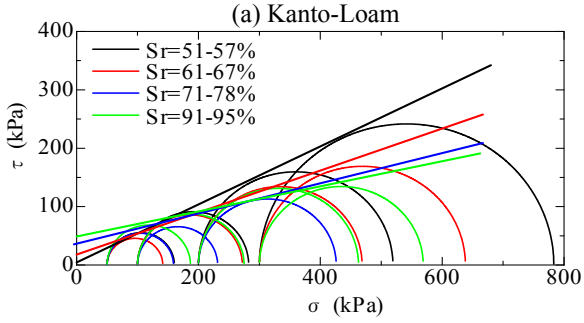

(b) Kuroboku

Figure 4. Mohr circle diagram for different degree of saturation（UU Test）

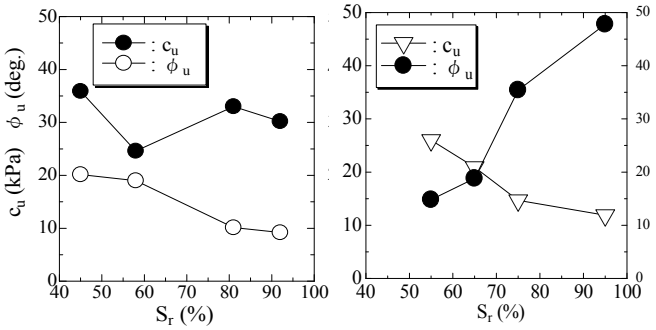

(a) Kanto Loam (b) Kuroboku

Figure 5 c_u andφ_u against a degree of saturation（UU Test）

3.2 Results of triaxial CU test

Figure 6 shows experimentally derived effective stress paths using specimens with an initial degree of saturation of 100, 95 and 85% of Kanto loam. The degree of saturation Sr shown in Figure 6 is the value before consolidation. The effective stress paths with a degree of saturation of 100% in Figure 6(a) shows that dilatancy changed from negative to positive near the critical state line (CSL) and deviator stress increased subsequently along the CSL. Figure 6(b) and (c) were obtained from unsaturated specimens with Sr of 97 through 94% ($\Delta u/\Delta\sigma$ = 0.54 to 0.48) and Sr of 89 through 85% ($\Delta u/\Delta\sigma$ = 0.15 to 0.1).

It is evident that the angle of shear resistance ϕ' decreased with the degree of saturation. When the initial degree of saturation is approximately equal, the shape of the effective stress paths indicate similar shapes independent of consolidation pressure. In both figures, pore pressure increases with the increase in deviator stress and the effective stress path converges on the CSL. Figure 6 shows the effective stress paths using specimens with an initial degree of saturation of 94.4~99.4%, 58~63.6% and 51.5~53.3% of Kuroboku

These results also show the effective stress paths with saturation from 94.4~99.4% and demonstrate that dilatancy changed from negative to positive near the CSL

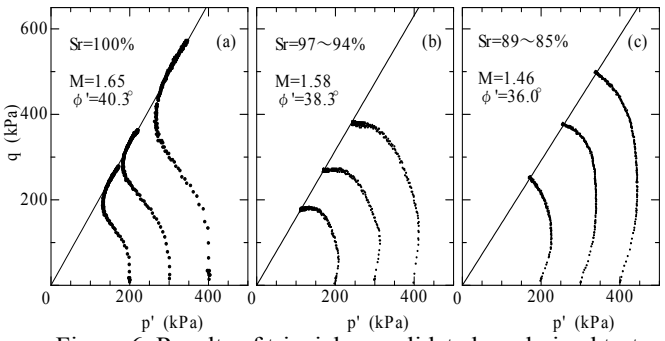

Figure 6. Results of triaxial consolidated un-drained test

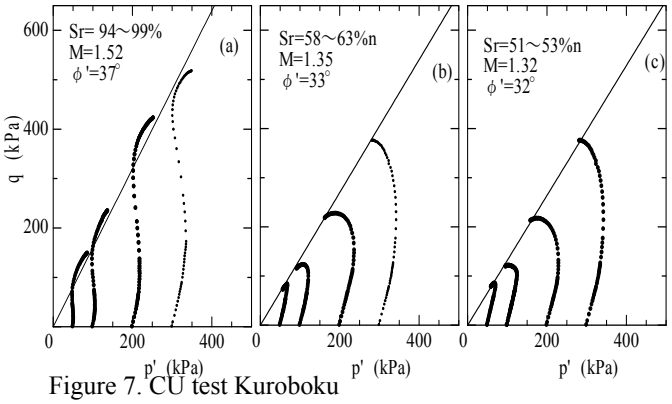

Figure 7. CU test Kuroboku

3.3 Effect of initial Sr, on ϕ, and c.

In this section the effect of initial Sr on ϕ and c are discussed. To determine the effect of saturation on cohesive shear strength, the angle of internal friction, c_{cu}, and ϕ_{cu} a series of samples with different degrees of saturation and confining pressure was performed and shown in Figure 8. Figure 9 shows the effective stress paths (total stress paths) obtained in a tri-axial consolidated drained test. As in the consolidated undrained test, ϕ_d decreased as Sr decreased. At Sr = 100%, ϕ_d was in agreement with ϕ' in the consolidated undrained test. The experimental result shows that increased saturation increases the cohesive shear strength and angle of internal friction.

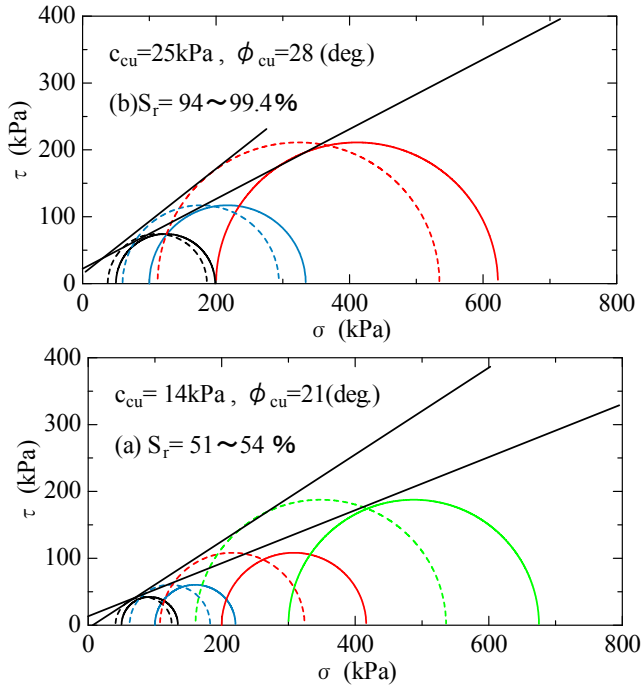

Figure 8. Results of triaxial consolidated undrained (CU) test Mohr circle result of Kuroboku

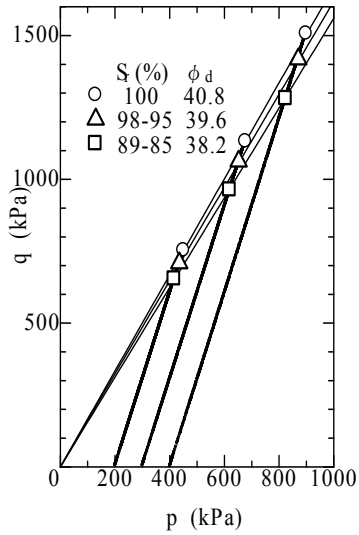

Figure 9. Results of consolidated drained (CD) test

4 VALUE OF B FOR UNSATURATED KANTO LOAM

Specimens with different degrees of saturation were consolidated at 200 kPa. Then, a cell pressure increment of $\Delta\sigma$ was applied gradually under the undrained condition. The relationship between $\Delta\sigma$ and measured pore pressure increment Δu is shown in Figure 10. Pore pressure identical with cell pressure increment occurred from the initial stages of loading at S_r =100 %. Pore pressure that was generated in the early stages of loading decreased with the decrease in S_r. In unsaturated specimens, the incidence of pore pressure increases with increasing$\Delta\sigma$. Then, the value of B after the cell pressure exceeds 100 kPa is closer to 1. It is thus evident that the value of B in unsaturated soils would vary due to the increase of cell pressure at the time of measurement. Figure 11 shows the relationship between the $\Delta\sigma$ obtained from Figure 10 and the value of B. The value of B under the undrained condition is expressed by equation (1) according to Naylor [2]. Equation (1) is transformed into (2), where K_f is the volumetric modulus of elasticity of the saturated soil element, K' is the volumetric modulus of elasticity for effective stress, and α is a coefficient indicating the compressibility of a porous fluid.

$$\left(B = \frac{K_f}{K' + K_f} \right) \tag{1}$$

$$K_f = \frac{B}{1 - B} K' = \alpha K \quad \left(\alpha = \frac{B}{1 - B} \right) \tag{2}$$

Figure 12 shows the relationship between the value of B and the coefficient α in equation (2). In Figure 12, the value of B in Figure 10 was replaced with the coefficient α using equation (2). The coefficient α increased rapidly with a smaller stress increment at a greater degree of saturation. We assume that the relationship shown in Figure 12 was applicable to the increase in the value of B due to the increase of mean stress p during the shearing process, and calculations were made to reproduce the results of the tri-axial consolidated undrained test.

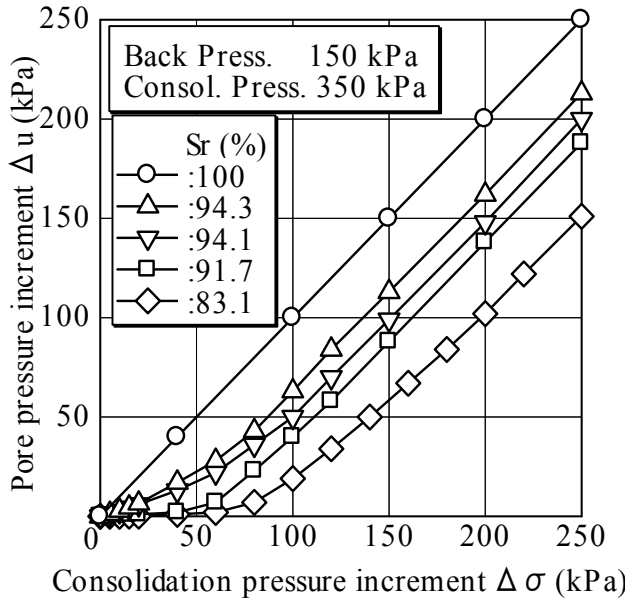

Figure 10. Cell pressure increment and pore pressure increment

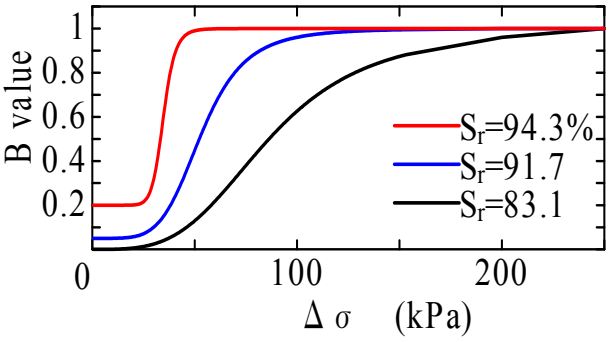

Figure 11. Cell pressure increment and B value

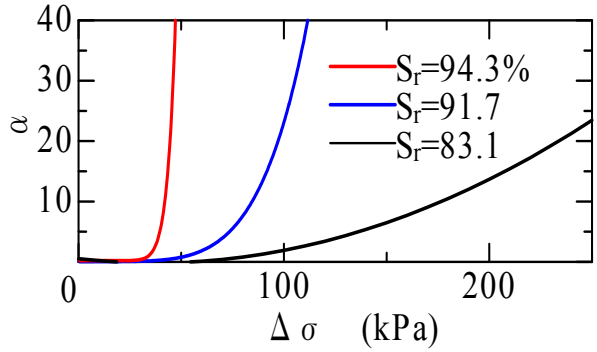

Figure 12. α and B value

5 CALCULATION TO REPRODUCE THE RESULTS OF TRIAXTIAL CU TEST

Calculations were made by incorporating the relationship shown in Figure 12 into CRISP, an elasto-plastic finite element analysis program for a modified Cam Clay model. The constants required for calculation are listed in Table 3

Poisson's ratio was estimated from the coefficient of earth pressure at rest K_0, which was estimated from the angle of shear resistance ϕ'. The results of calculations to reproduce effective stress paths using CRISP are shown in Figure 13 by solid lines. The modified Cam Clay model demonstrated no reversal of dilatancy, as observed in Figure 13(a) under the saturated condition. Calculations, however, reproduced test results in cases with varying degrees of saturation and effective stress up to the critical sate line.

Table 3 Constants for calculation

λ	κ	Γ-1	K_0	ν
0.169	0.021	3.307	0.42	0.261

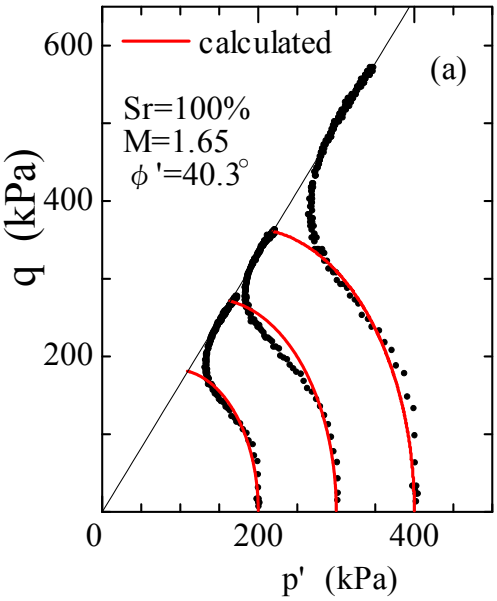

Figure 13. Comparison of the test results and calculations result triaxial consolidated undrained test

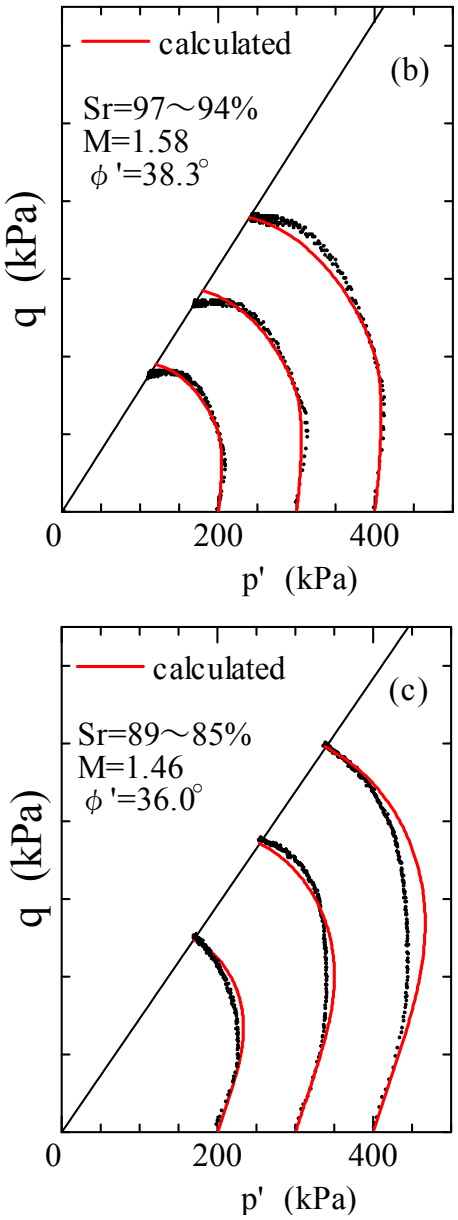

Figure 13. Comparison of the test results and calculations result triaxial consolidated undrained test

6 CLOSING REMARKS

In this study, unsaturated soil was assumed to be a two-phase system of a porous fluid (water and air), with compressibility taken into consideration, and soil particles. A triaxial apparatus for assessing saturated soil was used to examine the mechanical behavior of unsaturated soil. Calculating the value of B while varying the degree of saturation and shearing processes, it could be simulated the behavior of unsaturated stress paths. Further examination of stress-strain relationships is necessary in the future to better understand these properties.

7 REFERENCES

Alonso, E.E, et al.: Constitute Model for Partially Saturated Soils, Geotechnique, Vol. 40, No.43, pp.405-430, 1990.

Britto, A. M. and Gunn, M.J. : Critical State Soil Mechanics via Finite Elements, Eliss Horwood. , 1987.

Daizo, K. et. al. : The Relationship between the Mechanical Behaviour and the State of Porewater in Unsaturated Soil, J. of JSCE, No.535, Ⅲ-34, 83-92, 1996

Kohgo, Y., et. al : Verification of the Generalized Elastoplastic Model for Unsaturated Soils, Soils and Foundations, Vol.33, No.4, pp.83-92,1993.

Kodaka et al. : Strength and deformation characteristic of unsturated soils mixed with bentonite and sand, 49th anual meeting of JGS,pp.2115-2116.

Geotechnical and Geophysical Site Characterisation 5 – Lehane, Acosta-Martínez & Kelly (Eds)

Characterisation of a lateritic soil using laboratory and in-situ tests

W. Shi

Changzhou Key Laboratory of Structure Engineering &Material Properties, Changzhou Institute of Technology, Changzhou, China

B.M. Lehane

School of Civil, Environmental and Mining Engineering, University of Western Australia

A. Gower

Water Corporation, Western Australia

S. Terzaghi

Arup Pty Ltd, Sydney

ABSTRACT: This paper extends our understanding of the characterisation of residual soils by presenting results from a field and laboratory investigation of a laterite soil from the site of Millstream Dam in southern West Australia (WA). The laboratory tests were conducted on intact (block) and reconstituted samples to allow the effects of structure on the mechanical characteristics of the soil to be examined. It is shown that structural effects contributing to the strength of the intact soil are relatively small but that this soil has a more open, permeable structure than equivalent reconstituted soil. Cone Penetration Tests are shown to provide a reasonable means of assessing the undrained strength of this particular soil (which is close to full saturation), despite the permeability being about 10 times higher than a typical sedimentary clay.

1 INTRODUCTION

Residual soil is typically found between the tropics of Cancer and Capricorn and is the weathered material remaining in-situ after soluble parent rock constituents have been removed. Recent large infrastructure developments in Northern Australia have revealed significant shortcomings in the characterisation and assessment of geotechnical design parameters for the residual soils present at these developments. Such shortcomings provide the motivation for this paper which aims to illustrate particular distinguishing features of one residual soil type and to examine the impact of these features on the derivation of parameters from the Cone Penetration Test (CPT).

Having formed in-situ, residual soils possess characteristics which are distinct from soils produced by erosion, transport and deposition. Laterites are residual soils formed by intensive and long lasting tropical weathering of the underlying parent rock. This tropical weathering is a prolonged process of chemical weathering which produces a wide variety in the thickness, grade, chemistry and ore mineralogy of the resulting soils (e.g. Geological Society 1997). The leaching and re-deposition of ions also causes a change in mineralogy and often produces a high void ratio and permeability. The high sensitivity to sample disturbance is a well known characteristic of residual soils (e.g. Leroueil & Vaughan 1990, Wesley 1990, 2010) and has been a significant impasse to the development of parameter interpretation techniques by geotechnical practitioners. The bonded structure of residual soils, which essentially provides a highly important c' component of strength, is damaged to varying degrees by conventional sampling techniques (i.e. tube and rotary cored sampling). As a consequence, correlations drawn between the laboratory test results on samples and in-situ test data (from CPTs and Standard Penetration Tests, SPTs) are poor and unreliable. Such poor reliability has discouraged Industry from specifying laboratory tests and has led to a reliance on design correlations for residual soils with in-situ test results. However, the (only available) correlations in use are those derived for un-structured soil, which are clearly not appropriate for residual soils.

This paper extends our understanding of the characterisation of residual soils by presenting results from a field and laboratory investigation of a laterite soil from the site of Millstream Dam in southern West Australia (WA). The laboratory tests were conducted on intact (block) and reconstituted samples to allow the effects of structure on the mechanical characteristics of the soil to be examined.

2 SOIL CHARACTERISATION

2.1 *Site conditions and sampling*

The first phase of the study involved the retrieval in 2012 of block samples of residual (lateritic) soil from the site of Millstream Dam, WA. The samples were obtained from a 9m deep benched excavation that had been created by the WA Water Corporation as part of its activities to increase the height of the dam (which was originally constructed in 1962). The block samples were cut from a depth of 4.5m below original ground level into 250×250×250mm cubes, which were subsequently wrapped in polythene and waxed (with the location and orientation clearly labelled). The samples were stored in specially fabricated wooden boxes and in a temperature and humidity controlled room at the University of Western Australia (UWA). A CPT had been performed in 2008 prior to any excavation at the location of the block samples.

The regional geology of the Millstream dam area is discussed in detail by Gordon (1984), and others. Weathering during the Tertiary period led to extensive laterisation of the in-situ quartz meta-gabbro and gneissic parent bedrock resulting in a well developed laterite soil profile (regolith). The CPT end resistance (q_c) and friction ratio profile at the block sample location is provided in Figure 1 along with the interpreted soil profile. The upper part of the profile comprises pisolitic or nodular gravel clasts in a sandy matrix and indurated pisolitic or massive ferricrete horizons.The block samples were obtained from the underlying, pale coloured (grey) lower pallid zone, which had neither the relic fabric of the underlying saprolite nor the significant development of secondary segregations such as mottles, nodules or pisoliths typical of other mottled zones within the profile. The maximum previous overburden pressure at this location is unknown.

2.2 *General soil classification tests*

The Robertson (2009) soil behaviour type (SBT) deduced form the CPT data at 4.5m on Figure 1 classifies the soil as a 'silty clay to clay' with a SBT index (I_c) of approximately 3. This classification is a little at variance with the hydrometer and sieve particle size distribution (psd) analyses which indicated that the material has a fines content of only 52% and a clay fraction (CF) of 18%. Liquid and plastic limits of the material are 62% and 35% respectively and these limits plot just below the A-line on Casagrande's plasticity chart in the high plasticity region (plasticity index, I_p=27%). The mean bulk density, specific gravity and degree of saturation of material from the block samples were 1560 kg/m^3, 2.65 and 84% respectively. The in-situ water content was 44 % (implying a liquidity index of 0.67) and the in-situ void ratio was 1.4.

The groundwater regime at the dam site is complex and influenced by both the reservoir water and water infiltration from the abutments. Based upon the available information, it is assumed that total and effective stresses are approximately the same at a depth of 4.5m (i.e. ambient pore pressure close to zero); the high degree of saturation of the block samples suggests that this is a reasonable assessment.

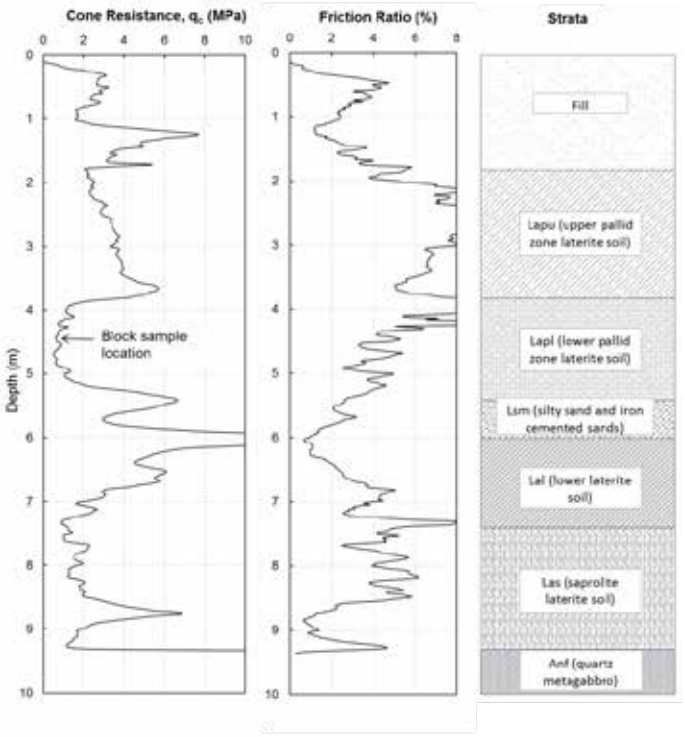

Figure 1. The in-situ CPT test results and soil profile.

2.3 *General soil classification tests*

X-ray diffraction analyses indicated that approximately 50% of the clay particles were kaolinite with some halloysite. Microcline and Muscovite (directly from the parent rock) made up 15% and quartz contributed another 15%. The material has evidently been leached of much of its iron content with only 4% of the clay fraction comprising iron rich compounds (ilmenite was dominant). The analyses could not distinguish about 15% of the constituents, labelling this component as 'amorphous content'.

The psd and Atterberg data imply a relatively high activity (I_p/CF) of about 1.5 which is more consistent with a clay mineral with higher activity than kaolinite; this may be due to the presence of particularly fine kaolinite crystals such as those described by Drummond *et al*. (2001).

2.4 *Behaviour in 1D compression*

Following on from the work of Burland (1990), and others, structural effects in the intact block samples were investigated by comparing the response of the intact soil in 1-D compression to the response of reconstituted soil. Reconstituted soil slurry with a water content of 62% (equal to the liquid limit) was prepared by adding water to oven dried soil that was ground down using a mortar and pestle. After de-airing using a vacuum, the slurry was consolidated one-dimensionally over a period of 10 days in 72mm diameter, 200mm high tubes (with top and bottom drainage) to a vertical effective stress of 56 kPa.

63.5mm diameter specimens for oedometer tests were extracted from the block samples and reconstituted tube samples using a cutting ring. The water bath was filled after application of the anticipated in-situ vertical effective stress of ~60 kPa. A comparison of the void ratio (e) - vertical effective stress (σ'_v) relationship obtained for both specimen types in standard oedometer tests (load increments held for 24 hours with a load increment ratio of 1) is provided on Figure 2. As is typical of structured soils (e.g. see Leroueil & Vaughan 1990), it is seen that the curve for the intact soil falls above that of the reconstituted soil (i.e. it exists at a higher void ratio at a given σ'_v). The intact sample indicates a vertical yield stress (σ'_{vy}) of about 125 kPa, which is 3 to 4 times the estimated in-situ effective stress at the block sample location. The compression index (C_c) for the reconstituted soil is 0.33 and significantly lower than the post-yield C_c value of 0.55 shown by the intact sample.

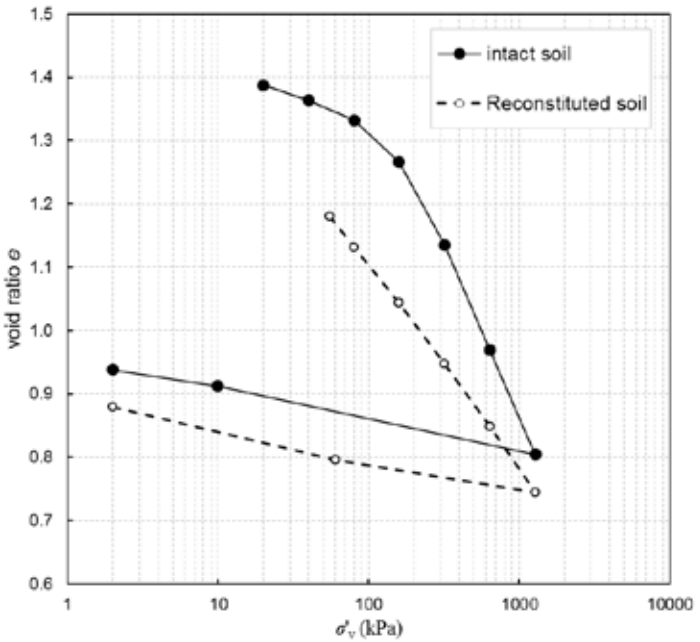

Figure 2. 1D compression curves for the intact & reconstituted soil.

The oedometer tests revealed far more rapid rates of consolidation for the intact sample. The coefficients of consolidation (c_v) derived from the settlement data are plotted against σ'_v on Figure 3 and indicate c_v values for the intact soil at the in-situ stress level over 100 times greater those for the reconstituted soil. The difference between the respective c_v values reduces as the stress level increases above the yield stress with c_v for the intact soil being 10 times the reconstituted value at σ'_v ~1 MPa. The values of vertical permeability (k) inferred from these c_v values around the in-situ stress range are 5×10^{-8} m/s and 5×10^{-10} m/s for the intact and reconstituted soil respectively. The relatively high c_v and k values for the intact soil are typical of residual soils and arise due to their distinctive formation process.

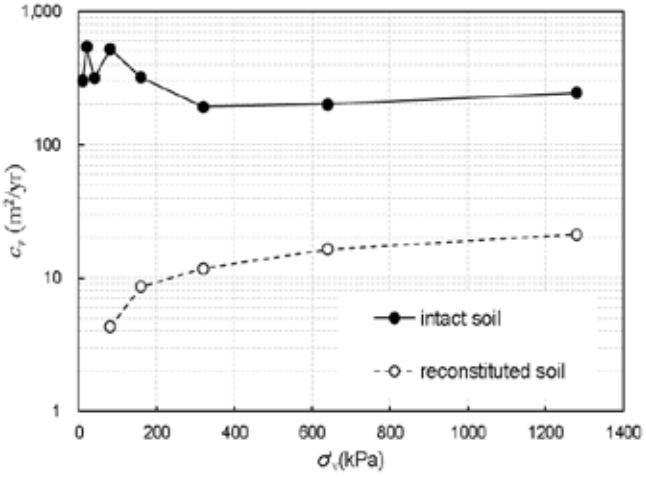

Figure 3. c_v values for intact and reconstituted samples

2.5 *Behaviour in triaxial compression*

Specimens for triaxial testing with a diameter of 72 mm and length of 150 mm were carved from the block samples and from samples extruded from the tubes used to prepare reconstituted samples for oedometer tests (discussed previously). The specimens were saturated and consolidated isotropically to mean effective stresses (p'_0) of 60 kPa, 120 kPa and 300 kPa before being sheared undrained. The variations of the deviator stress (q) with p' measured during the undrained shearing phase are shown on Figure 4.

These show a marked contrast between the stress paths recorded by the intact and reconstituted soil after consolidation to 60 kPa but generally similar paths after consolidation to the higher stress levels of 120 kPa and 300 kPa. The mean undrained strength ratio (s_u/p'_0) of the three tests on the (normally consolidated) reconstituted soil is 0.44. This relatively high ratio (compared to a more typical value of 0.25 to 0.3

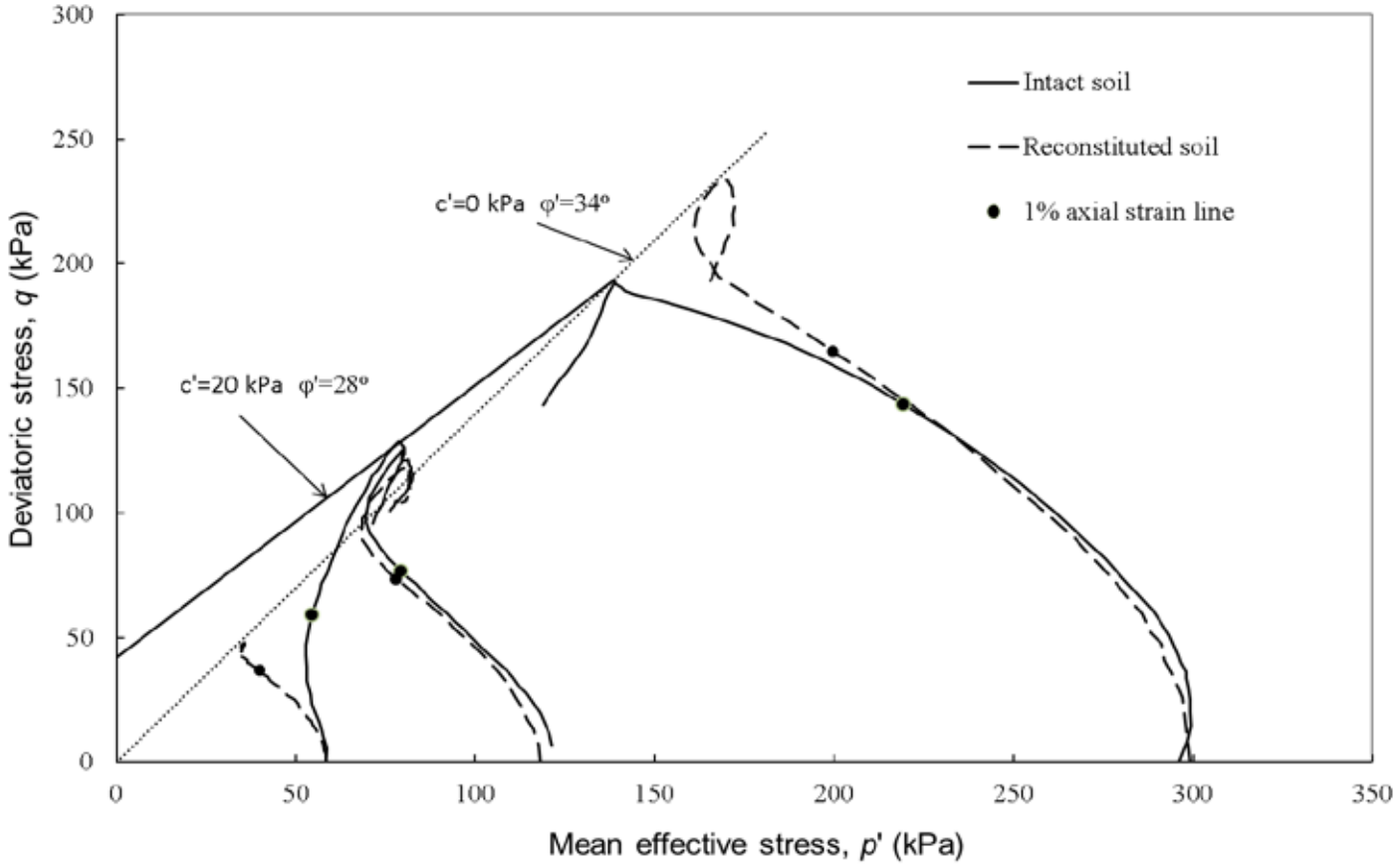

Figure 4. Stress paths in q-p' space during undrained triaxial compression tests on intact samples and reconstituted (normally consolidated) samples.

for alluvial clays) is attributed to the large coarse fraction and consequent tendency for a reduced level of contraction (or greater dilation) under shear compared to more fine grained deposits.

The high undrained strength developed by the sample consolidated to 60 kPa (s_u/p'_0 ~1.2) cannot be explained solely by overconsolidation (given that the other stress paths suggest that the maximum pre-consolidation isotropic stress is about 120 kPa) and must also reflect some structural effects which appear to be progressively destroyed with the imposition of high stresses. Although the behaviour of the intact specimens with the reconstituted specimens for $p'_0 \geq 120$ kPa is comparable, the effects of structure are clearly still important as the intact samples are at a considerably higher void ratio than their reconstituted equivalents (e.g. see Figure 2).

Mohr Coulomb parameters of c'=20 kPa and φ'=28° provide the best fit to the peak strength envelope for the intact soil. The best-fit friction angle of 34° for the reconstituted soil (for which c'=0) is relatively high compared to that of the intact soil and possibly reflects differences in the way the respective soil fabrics were created.

2.6 *Small strain stiffness*

Small strain shear moduli (G_{max}) were derived from the shear wave velocities deduced from bender elements located at the top and bottom of the triaxial specimens. Surprisingly, G_{max} values for the reconstituted soil were found to the greater than those of the intact soil. When G_{max} values are normalised by the void ratio (e) function, $F(e)=e^{-1.3}$, proposed by Lo Presti (1994), intact and reconstituted values exhibit the same relationship with mean effective stress, as shown on Figure 5. The best fit equation for G_{max}, which uses atmospheric pressure (p_{atm}) as a reference stress, is as follows. This reveals a square root dependence of G_{max} on the effective stress level, which is typical of coarse grained soils (Tatsuoka et al 1997):

$$\frac{G_{max}}{e^{-1.3}p_{atm}} = 900\left(\frac{p'}{p_{atm}}\right)^{0.5} \quad (1)$$

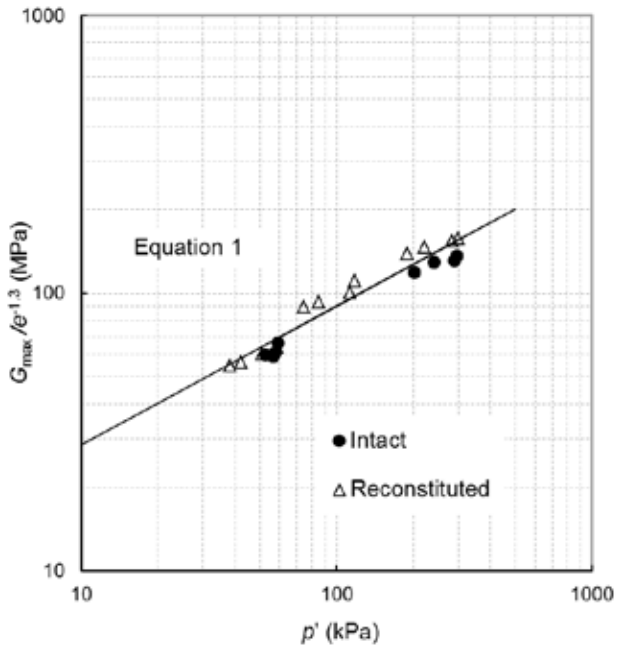

Figure 5. Relationship between maximum small strain shear modulus and mean effective pressure.

The applicability of Equation (1) to both the intact and reconstituted soils suggests that bonding within the intact soil is not significant.

3 DISCUSSION

The soil recovered in the block samples from 4.5m depth at Millstream classifies as 'silty clay to clay', according to the CPT soil behaviour type classification system with an I_c index of approximately 3. However, like many residual soils, the void space and permeability of the samples was relatively high compared with equivalent sedimentary soils (e.g. see Figure 2) with the consequence that there is a high chance of errors associated with conventional in-situ test interpretation due to effects of partial drainage.

Research on the effects of partial drainage during CPT penetration summarised by Suzuki (2014) indicate that the in-situ's material's coarse fraction of 48 % as well as its coefficient of consolidation (Figure 3) and interpreted k value (~5 $\times 10^{-8}$ m/s) imply that standard cone penetration (at 2cm/s) is essentially undrained with a likelihood of a small degree of partial drainage.

The laboratory tests have indicated that the undrained strength of in-situ material in triaxial compression (with an estimated K_0 value of ~0.8) is approximately 60 kPa. The average CPT end resistance (q_t) at the depth of the block samples was 730 kPa, leading to a backfigured cone factor, N_k, of approximately 11. This N_k value is similar to that inferred in many clays (Lunne *et al.* 1997) suggesting that partial drainage and suction effects are not significant. It is concluded, therefore, that the CPT is a reasonable means of assessing the in-situ undrained strength of the type of laterite encountered at the Millstream site.

4 CONCLUSIONS

Triaxial tests on high quality block samples from the lower pallid zone of a lateritic profile have shown a relatively low level of structure (consistent with a c' value of about 20 kPa) and a comparable friction angle to reconstituted material. The void ratio of the in-situ material, which is close to full saturation, is higher than equivalent reconstituted samples consolidated to the same effective stress level. The very small strain (elastic) shear stiffness of the intact and reconstituted soil are the same if the void ratio differences are accounted for; this observation also indicates that structural effects in the intact soil are not significant. The more open fabric in the intact soil gives rise to permeabilities and coefficients of consolidation which are an order of magnitude higher than the reconstituted material. Despite this characteristic and an estimated in-situ permeability of 5 × 10^{-8} m/s, standard cone penetration (at 2cm/s) in the material led to resistances consistent with undrained penetration. The CPT is shown to provide a reasonable means of assessing the in-situ undrained strength of the type of laterite encountered at the Millstream site.

5 ACKNOWLEDGMENTS

The support provided by Arup and Water Corporation, WA is gratefully acknowledged. Sponsorship of the first author by the Jiangsu Overseas Research & Training Program for University Prominent Young & Middle-aged Teachers and Presidents is also acknowledged. The project is also supported by National Natural Science Foundation of China (Grant No. 41302226). The authors acknowledge the excellent assistance provided by the laboratory staff at The University of Western Australia.

6 REFERENCES

Burland J.B. (1990) On the compressibility and shear strength of natural clays. *Geotechnique*, 1990, 40(3): 329-378.

Drummond A.F., Varagão C., Gilkes R.J. and Hart R.D. (2001). The relationships between kaolinite crystal properties and the origin of materials for a Brazilian kaolin deposit. *Clays and minerals*, 49(1),44-59.

Geological Society (1997).Tropical Residual Soils. A Geological Society Engineering report, edited by P.J. Fookes, Published by the Geologiocal Society of London, pp184.

Gordon F. R., 1984, The Laterite weathering profiles of precambrian igneous rocks at the Worsley Alumina Refinery site, South West Division, Western Australia. *Proc 4th Australia-New Zealand conference on geomechanics*, Perth, Western Australia, V1, P261-266.

Leroueil S. & Vaughan P.R. (1990). The general and congruent effect of structure in natural soils and weak rocks. *Geotechnique*, 40(3), 467-488.

Lo Presti (1994). Measurement of shear deformation of geomaterials in the laboratory. *Proc. 1st Int. Conf. Pre-failure deformation of geomaterials*, Sapporo, Japan, 2, 1067-1088

Lunne, T., Robertson, P. & Powell, J. (1997). Cone penetration testing in geotechnical practice. London: Blackie Academic & Professional.

Robertson, P. K. (2009). Interpretation of cone penetration tests - a unified approach. *Canadian Geotechnical Journal*, 46(11), 1337-1355.

Wesley L.D. (1990). Influence of structure and composition on residual soils. *J. Geotechnical Engineering Division*, ASCE, 116(4), 589-603.

Wesley L.D. (2010). Geotechnical Engineering in residual soils. Wiley, pp272.

Theme 11. Characterisation of Non-standard soils

Geotechnical and Geophysical Site Characterisation 5 – Lehane, Acosta-Martínez & Kelly (Eds)

Estimation of undrained shear strength for peat using CPT

H. Hayashi & T. Hayashi
Civil Engineering Research Institute for Cold Region (CERI), Sapporo, Japan

ABSTRACT: Fibrous and high organic peat is distributed widely in Hokkaido, the northernmost island of Japan. Peat ground is extremely soft and has strange engineering properties. Since behavior of peat ground differs greatly from that of ordinary soft ground, it is classified as a problematic soil. Peat ground is a significant hindrance to infrastructure construction. Electric cone penetration tests (CPT) for peat deposit were conducted at several sites on peat ground in Hokkaido, Japan and K_0 consolidated-undrained triaxial compression test on undisturbed peat collected from the same sites, to clarify the undrained shear strength (S_u) of such ground. This paper presents that results of the tests, and proposes a method for determining S_u for peat using CPT.

1 INTRODUCTION

When embankment such as road and river levee is constructed over soft ground, the stability of the ground is commonly evaluated by the safety factor obtained from circular slip analysis. In this analysis, it is very important to determine the undrained shear strength (S_u) of the ground. As peat, which is a widely distributed soft and problematic soil in Hokkaido, Japan, is accumulated heterogeneously (Noto, 1991), unconfined compression tests, vane shear tests and other tests performed for only a few samples lack validity. The electric cone penetration test (CPT) is more reasonable and valid than these, in that CPT can estimate average S_u from in-situ tests, which continuously provide information. Therefore, the aim of this study is to establish a method for estimating the S_u of peat ground by performing CPT.

A series of K_0 consolidated-undrained triaxial compression tests (K_0CUC tests) on undisturbed peat soil collected at several sites in Hokkaido was conducted. Also the CPT was performed at the same sites. This report describes the relationship between S_u obtained from the K_0CUC tests and CPT cone resistance (q_t), and a method for estimating S_u in peat soil from q_t.

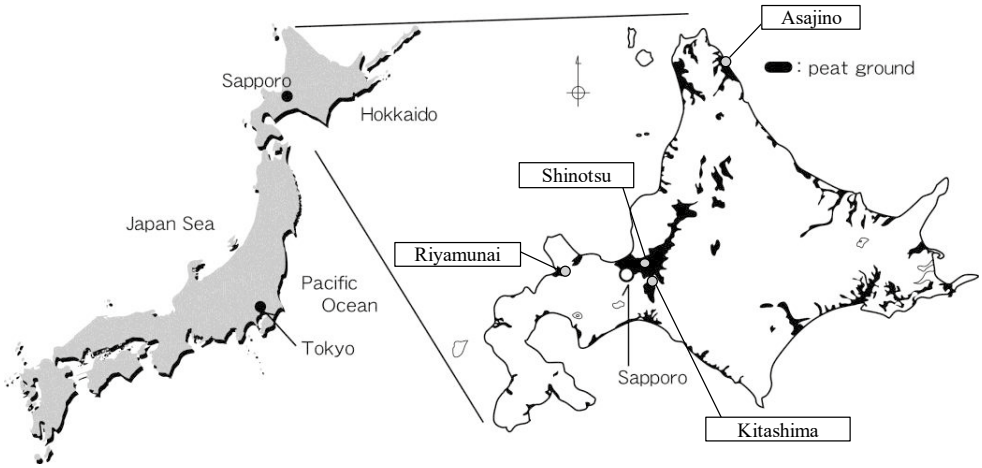

Figure 1. Location of the investigation sites (Peat distribution in Hokkaido; Noto, 1991)

Table 1. Engineering properties of the soil samples

Site	Soil type	Number of samples for K0-consolidated triaxial compression test	Natural water content W_n (%)	Ignition loss L_i (%)	Degree of decomposition von Post	In-situ void ratio e_0	Conmpression index C_c
Shinotsu	Peat	3	323～459	37～66	H5	7.9	5.1
Asajino	Fibrous peat	1	860	92	H2	14.8	9.3
Riyamunai	Fibrous peat	3	724～945	82～94	H3	13.5	10.0
Kitashima	Peat	1	387	55	—	—	—

2 INVESTIGATION METHOD

2.1 *Investigation site*

A series of CPT and collection of undisturbed samples for the laboratory tests were conducted at the four sites (Shinotsu, Ebetsu city; Asajino, Sarufutsu village; Riyamunai, Kyowa town and Kitashima, Eniwa city) in peat ground in Hokkaido, Japan (Fig. 1). The undisturbed samples were collected using a thin-wall sampler with a fixed piston (JGS 1221; JGS, 2015). Table 1 shows the soil types and the engineering properties of the sampling soils at the investigation sites. The sampling soils at the Asajino site and the Riyamunai site were classified as fibrous peat.

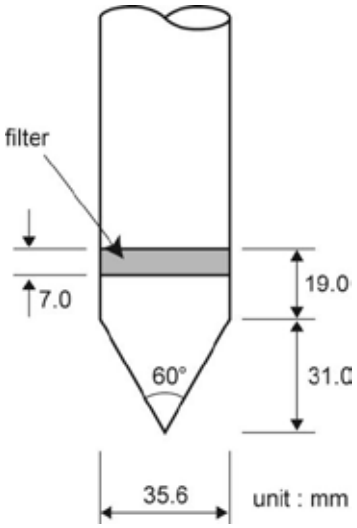

Figure 2. Dimension of the CPTU cone used in this study

2.2 *CPT*

Figure 2 shows the dimension of the CPT cone used. The penetration velocity was set at 2 cm/s, and q_t, skin friction (f_s) and pore water pressure (u) were continuously measured at each 1 cm of penetration. The cone resistance (q_t) obtained from the CPT is a value that takes into account the influence of water pressure at the filter, as determined by Equation (1), where q_{ce} is the measured cone resistance (kN/m^2), A_e is the effective cross-sectional area of the cone (m^2), A_p is the area of the base of the cone (m^2) and u is the pore water pressure (kN/m^2).

$$q_t = q_{ce} + (1 - A_e/A_p)\, u \quad (1)$$

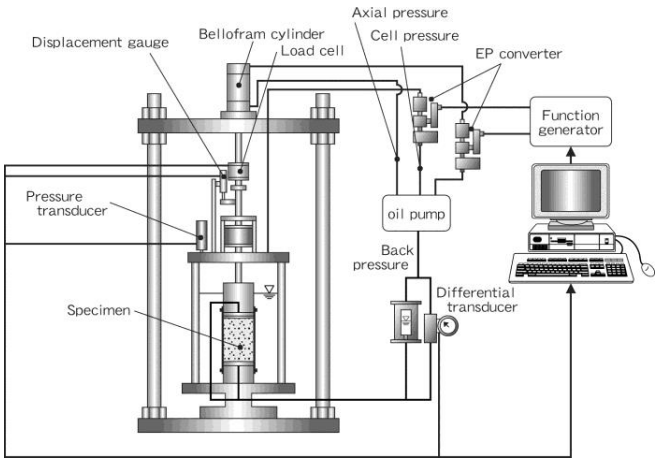

Figure 3. Set up of the K_0 consolidated-undrained triaxial compression test used in this study

2.3 *K_0 Consolidated-Undrained Triaxial Compression Test*

To calculate the undrained shear strength of peat, the K_0CUC test (JGS0525: JGS, 2011) was performed for undisturbed soil samples (Fig. 3). Each sample was 75 mm in diameter and 150 mm in height. The samples were carefully trimmed and set on the test device to avoid unnecessary disturbance. As the S_u of the soil is significantly affected by the confining pressure, K_0 consolidation was conducted with a

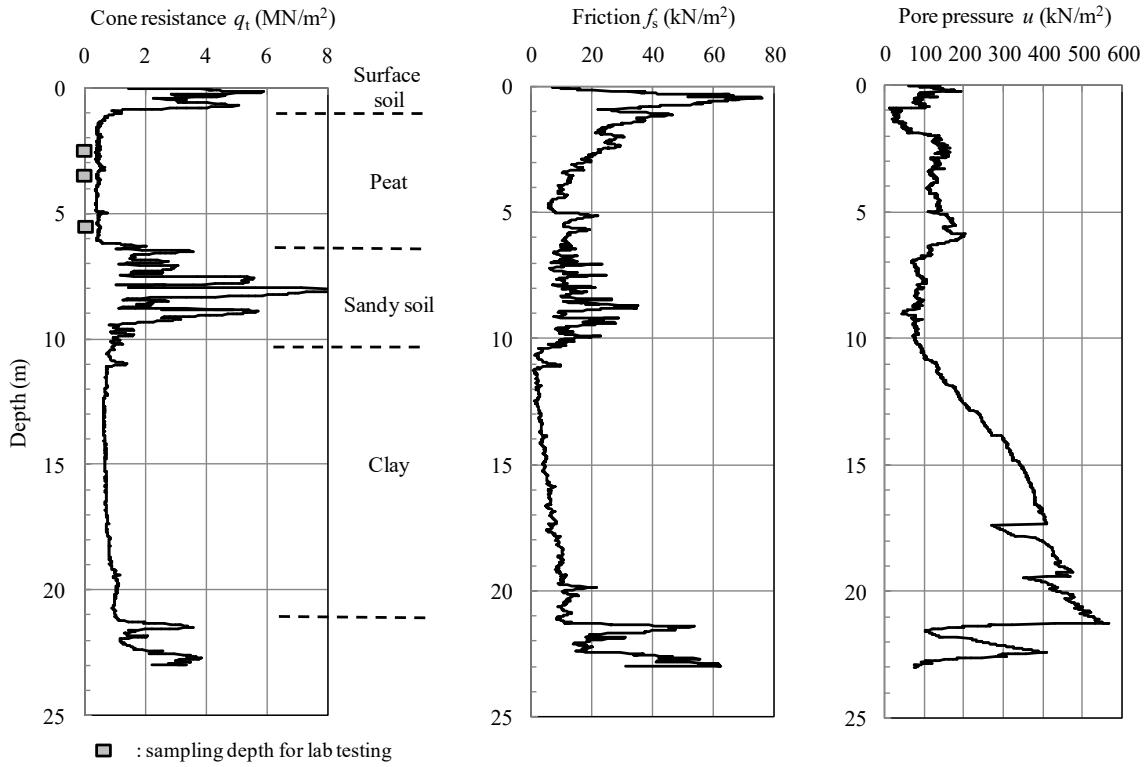

Figure 4. Depth distribution results of the CPT at the Shinotsu site

pressure equivalent to the in-situ stress. This means that the in-situ anisotropic consolidation was reproduced in the laboratory. After the K_0 consolidation, compression (0.1%/min of strain rate) under an undrained condition was done. Additionally, an oedometer test and physical index tests were conducted.

3 RESULTS AND DISCUSSION

3.1 *CPT Profile*

Figure 4 shows the depth distribution results of the CPT at the Shinotsu site. This is the typical CPT profile (q_t, f_s and u) of this study. The geologic columnar section obtained from drilling at the Shinotsu site was added to the figure. The q_t in the peat layer (q_t = 0.33-0.71 MN/m²) was lower than that in the other soil types, which indicates that the peat layer is very soft. Great excess pore water pressure, which was caused by the cone penetration, was generated in the peat layer and the clay layer.

3.2 *Relationship between Cone Resistance and Undrained Shear Strength*

To calculate the S_u of the ground from CPT, Equation (2) is commonly applied. Where, the S_u and q_t are both expressed in units of kN/m², σ_{v0} is the total overburden pressure (kN/m²), and N_k is a correction coefficient called the cone coefficient.

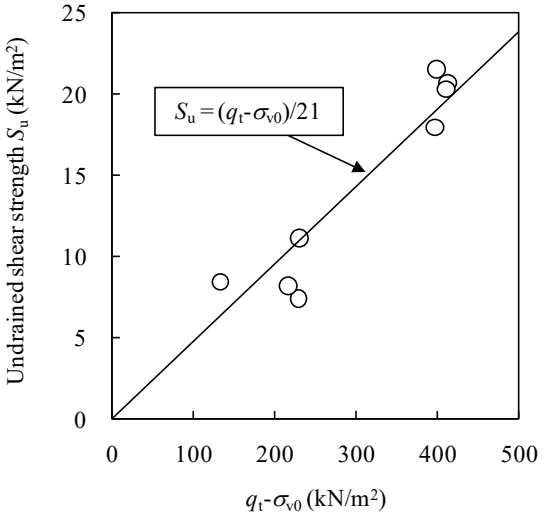

Figure 5. Relationship between (q_t-σ_{v0}) and undrained shear strength for peat

$$S_u = (q_t - \sigma_{v0}) / N_k \quad (2)$$

Konrad & Lan (1987) reported that N_k in Equation (2) greatly varies by soil property. Figure 5 shows the relation between (q_t - σ_{v0}) and S_u obtained from the K_0CUC test, to reveal the N_k of peat. As shear strength does not peak in the K_0CUC test on peat, S_u was assessed by assuming 15% of the shear-

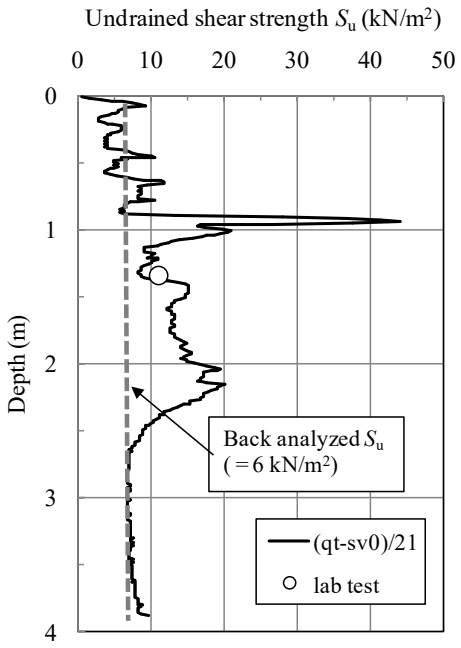

Figure 6. Undrained shear strength calculated using N_k = 21 and Eq. (2), and obtained from the K_0 consolidated-undrained triaxial compression test at the Asajino site

ing strain as failure. Overall, the S_u in peat was only between 5 - 20 kN/m^2, and S_u increased linearly with increase in (q_t - σ_{v0}). This relation proves that N_k value in Equation (2) of peat is 21.

Noto (1991) reported that the N_k of peat is 20, based on the cone resistance obtained from a mechanical cone penetration test. Konrad & Lan (1987) reported that the N_k of clay is between 10 and 20. In this study, the N_k of peat was found to be similar to that reported by Noto (1991), and was found to be greater than that of clay.

Figure 6 shows the depth distribution of S_u, calculated by the q_t measured at the Asajino site and N_k = 21 for Equation (2). At Asajino, sliding failure happened during embankment construction. Back circular slip analysis was performed based on this fact of the sliding failure, which led S_u of the peat layer to be 6kN/m^2. This roughly corresponds with the S_u calculated by N_k = 21 for Equation (2). This indicates that it is possible for Equation (2) and N_k = 21 to estimate S_u in peat ground.

4 CONCLUSIONS

To clarify the estimation method of undrained shear strength (S_u) for peat ground, a series of electric cone penetration tests (CPT) and laboratory tests were conducted for peat ground in Japan. The main results can be summarized as follows:

(1) The S_u value for peat ground increases linearly with the increase in cone resistance (q_t) of CPT.

(2) The relationship between q_t and S_u in peat ground can be approximated by "$S_u = (q_t - \sigma_{v0})/21$", where σ_{v0} is whole overburden pressure. It is possible to estimate of S_u value for peat ground using this relationship.

5 REFERENCES

Japanese Geotechnical Society. 2015. *Japanese Geotechnical Society Standards – Geotechnical and Geoenvironmental Investigation methods -*

Japanese Geotechnical Society. 2009. *Japanese Geotechnical Society Standards – Laboratory Testing Standards of Geomaterials -*

Konrad, J. M. and Lan, K. T. 1987. Undrained shear strength from piezocone tests, *Canadian Geotechnical Journal*, 24(3), pp.392-402

Noto, S. 1991. *Peat Engineering Handbook,* pp.24-66

Geotechnical and Geophysical Site Characterisation 5 – Lehane, Acosta-Martínez & Kelly (Eds)

A review of the unconfined compressive strength of microbial induced calcite precipitation treated soils

R. N. Hora, M. M. Rahman, S. Beecham & R. Karim
School of Natural and Built Environments, University of South Australia, Adelaide, Australia

ABSTRACT: Microbial induced calcite precipitation (MICP) is an enhanced and accelerated natural process where bacteria precipitate calcite and bind soil particles together and thereby increase its strength. This is an environmentally friendly approach for ground improvement which has attracted significant research interest. Since 2005, there have been approximately 70 journal articles published on MICP in the field of engineering geology and civil engineering. A critical scrutiny reveals that only some of these articles focus on the engineering properties of soil e.g. unconfined compressive strength (UCS) with total calcite precipitation in a MICP treated soil. This article examines UCS data with relating to calcite precipitation and finds there is a wide range of results. It is hypothesised that soil grading significantly affects the throat-size of soil particles which influences the bonding created by calcite precipitation. Therefore, soil grading properties such as Cu, D_{10} and Cc were considered to find a suitable relationship for UCS. The lack of data was overcome with the use of the Inverse Distance to a Power (IDP) gridding method. The contour plot of UCS in the space of total calcite precipitation and grading properties such as D_{10} and Cc provided a general trend for estimating the UCS of MICP treated soils.

1 INTRODUCTION

Substantial increases in infrastructure development have led to the need to develop new and feasible soil improvement methods. In the past, many soil enhancement techniques have been developed which have a different degree of effectiveness in improving strength of soil over time. One of these techniques is mixing artificial cement with soil to bind soil particles together to enhance its strength. Artificial cement requires a large amount of energy for manufacturing and application, produces carbon, utilizes large volume of natural resources combined with land deterioration. Therefore, mixing cement with soil is not considered as an environment friendly approach. However, soil cementation occurs naturally at a slow rate which can be enhanced and accelerated as an alternative via an engineering process. This process is claimed as sustainable and environment friendly and referred to as microbial induced calcite precipitation (MICP). MICP uses naturally occurring bacteria to bind soil particles together (cementation) through calcium carbonate ($CaCO_3$) precipitation, thereby increasing the strength and stiffness of soil. The expected life of MICP treated soil is more than 50 years, which is compatible with the expected service life of many geotechnical structures (DeJong*, et al.*, 2013).

The interest on MICP treated soil triggered when Mitchell and Santamarina (2005) and US National Research Council (NRC, 2006) identified biological processes as an important research topic for the 21st century. Since then more than 100 technical conference and journal papers have been published dedicated to this field (DeJong*, et al.*, 2013). These works include identifying microorganisms (Mitchell and Santamarina, 2005), geometric compatibility between bacteria and pore space (DeJong*, et al.*, 2010) and survivability (Rebata-Landa and Santamarina, 2006), $CaCO_3$ precipitation and its efficiency in MICP (Al Qabany*, et al.*, 2012, Cheng*, et al.*, 2013) and ultimate soil strength improvement (Whiffin*, et al.*, 2007, Burbank*, et al.*, 2011, Burbank*, et al.*, 2013). Only a part of these articles was specific to MICP technique. A search for "MICP" in web of science finds 70 articles in relation to the field of engineering geology and civil engineering. Many of these articles are focused on optimizing MICP in relation to soil bio-chemistry and application processes; however, a part of these literatures studied calcite precipitation and improved soil strength behaviour such as unconfined compressive strength (UCS). The $CaCO_3$ precipitation in MICP treated soils depends on many factors of MICP treatment process such as chemistry and concentrations. Even for the same MICP process, the engineering properties of

treated soils depends on soil characteristic and it's states such as particle sizes and their distribution, density, stress etc. The nature and contribution of soil characteristic to UCS for a similar MICP treated soil are not clear as most of the earlier studies were focused on a particular soil. Therefore, this article critically reviewed previously published articles for similar MICP process and put an effort to develop cohesive understanding of soil grading on UCS of MICP treated soil. The demographic statistic of these 70 publications also provided interesting information about the leading institutions and countries for MICP technique and future research direction of this new evolving technique.

2 GENERAL REVIEW OF MICP

2.1 *Methods for MICP*

MICP can be achieved in many ways such as through urea hydrolysis, denitrification, as well as iron and sulphate reduction. However urea hydrolysis is the most energy efficient and ubiquitous method for natural soils.

Sporosarcina pasteurii, which is an alkalophillic soil bacteria with a highly active urease enzyme, is the most commonly used in urea hydrolysis. In the process, urea is hydrolysed to carbamate (NH_2COOH) and ammonia (NH_3) as in Eqn.1. Carbamate is then spontaneously hydrolysed to give carbonic acid (H_2CO_3) and ammonia (NH_3) as in Eqn. 2 which then undergoes hydrolysis according to Eqn. 3 and 4. In the presence of dissolved calcium, this process precipitates $CaCO_3$ (Eqn. 5).

$$CO(NH_2)_2 + H_2O \xrightarrow{\text{urease}} NH_3 + NH_2COOH \quad (1)$$

$$NH_2COOH + H_2O \leftrightarrow H_2CO_3 + NH_3 \quad (2)$$

$$H_2CO_3 \leftrightarrow H^+ + HCO_3^- \quad (3)$$

$$NH_3 + H_2O \leftrightarrow NH_4^+ + OH^- \quad (4)$$

$$Ca^{2+} + HCO_3^- + OH^- \leftrightarrow CaCO_3 \downarrow + H_2O \quad (5)$$

The negative charge on the bacteria cell wall attracts the soil particle. Physiochemical properties of the cell and soil particle further help in binding them together where $CaCO_3$ precipitates.

Since 2006, the studies have been focused on treating soil using different MICP application methods. These methods can be broadly classified in two groups: (1) bio-augmentation and, (2) biostimulation. In bio-augmentation, external microbes are either injected or percolated into the soil along with nutrient medium to help in their growth and $CaCO_3$ precipitation (DeJong, *et al.*, 2006). In biostimulation, indigenous microbes of the soil are stimulated with external nutrient medium thereby inducing growth and $CaCO_3$ precipitation (Burbank, *et al.*, 2013).

2.2 *Demographic statistics of the literature*

Mitchell and Santamariana (2005) was arguably the first publication in main stream geotechnical engineering journals that explicitly discussed the application of biological processes. Then, the US National Research Council (NRC, 2006) identified biological processes as an important research topic for the 21st century. DeJong, *et al.* (2006) was the first publication that was focused on undrained behaviour of MICP treated sand. Since then about 70 journal articles published on MICP. The trajectory of the number of publications by years shows an exponential trend up to 2013 and then remained steady for last 3 years, as shown in Fig. 1. The source countries of these publications are shown in Fig. 2. USA, China, England, Canada, Netherlands and Australia are the source of 26%, 11%, 6%, 5%, 5% and 5% of these publications, respectively. The top two leading institutions for MICP research are University of California, Davis and North Carolina State University and their contribution were 14.29% and 7.14% to these publications. These indicate their leadership and strong research focus on MICP treated soil.

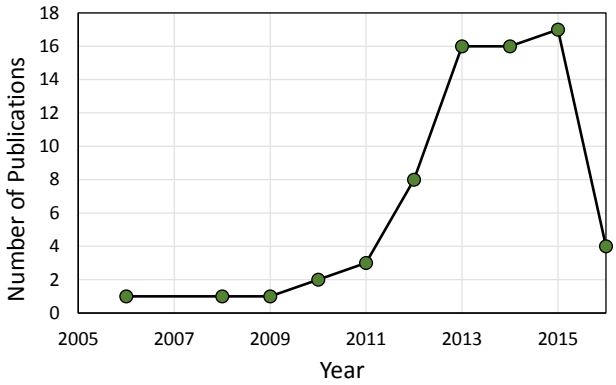

Figure 1. Increasing trend of number of publications for MICP in treating soil (up to March 2016).

3 CRITICAL REVIEW OF IMPROVEMENT OF MICP TREATED SOILS

3.1 *Data selection*

The MICP processes use different chemistry and concentrations for treatment solutions, different application techniques (saturation/unsaturation), different environments, different specimen sizes and soil characteristics which makes it difficult to compare results from different studies. To minimize the influence of the factors that affect $CaCO_3$ precipitation, the amount of precipitate $CaCO_3$ was used, directly, as a parameter in this study. However, the crystal structure of $CaCO_3$ and their formation around the soil particles can also be affected by environment, specimen size, degree of saturation etc. This study only considered small specimens (typical size of 100mm height and 50mm diameter) that was treated with MICP process under laboratory condi-

tion in saturated soil and $CaCO_3$ precipitated as calcite crystal structure. Despite the scrutiny of the literature, it may not be possible to eliminate all the influences of the above factors. However, accepting this limitation, this study compile a larger dataset from around the world which was synthesized with statistical analysis to reveal a qualitative trend.

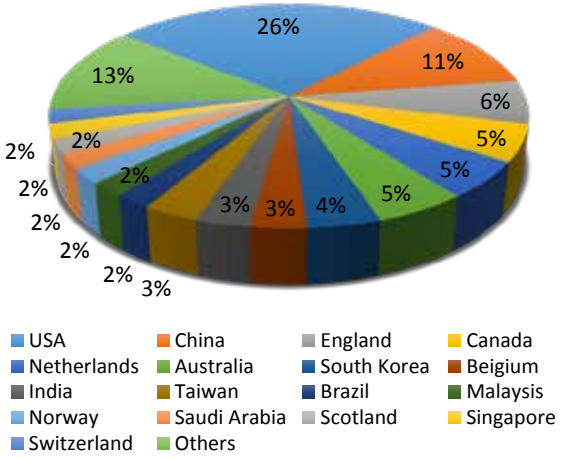

Figure 2. Distribution of source countries of MICP related journal articles (up to March 2016).

3.2 *Soil used for MICP treatment*

A total of 12 different silica sands were found in the literature that were used for the study of unconfined compressive strength, UCS of MICP treated soil. 19 data points for UCS and $CaCO_3$ of these silica sands are extracted from the literature. The distribution of UCS data points with respect to soil types are shown in Fig. 3. Soil particle size and their grading are important for particle arrangement and the void space (throat size) between particles of a soil specimen. Both the arrangement and void space between particles are important for MICP treatment for fluid flow, geometric compatibility between bacteria and pore space and $CaCO_3$ precipitation (DeJong, *et al.*, 2010). Rahman and co-workers (Rahman and Lo, 2008, Rahman, *et al.*, 2008), by analysing a wide range of grading for soil and spherical steel balls, identified that D_{10} (10% or finer on a particle size distribution curve) is a characteristic particle size that has a significant influence on particle arrangement, particularly for the gap (throat size) between particles. Therefore, D_{10} of these soils are also noted in Fig. 3 and will be used in subsequent analyses.

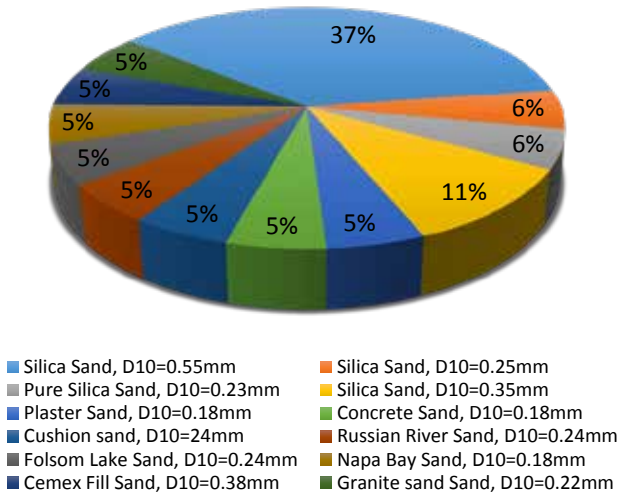

Figure 3. Distribution of UCS data points with respect to their soil type.

3.3 *Unconfined compressive strength of MICP treated soil*

Extreme MICP treatment can turn a soil into a brick-like material (UCS ≈ 20MPa) by applying repeated treatment under very stringent controlled laboratory condition (Cheng and Cord-Ruwisch, 2012) where as a light treatment can have a lower UCS of 0.80MPa (Cheng, *et al.*, 2013). Therefore, the UCS of MICP treated soil cannot be directly comparable without considering fundamental changes in the bonding between soil particles. A crude way of quantifying these bonding would be comparing them with the total percentage $CaCO_3$ precipitation (by mass) during MICP treatment. A comparison of UCS for MICP treated soil with total $CaCO_3$ is presented in Fig. 4. The scatter of the data points does not allow an interpretation of the contribution of $CaCO_3$ to UCS i.e. there is no unique relation. Note how the total $CaCO_3$ precipitates and how it contributes to the effective bonding, depends on particle arrangement and gap between host sand particles for a particular MICP application process. Therefore, it is envisaged that a characteristic parameter for particle size distribution (PSD) curve combined with $CaCO_3$ may give a better correlation

3.4 *Challenges and discussion*

The data points in Fig. 4 were obtained by different testing methods. 15 out of 19 data points were obtained by UCS tests of cylindrical specimens (Cheng, *et al.*, 2013, Gomez, *et al.*, 2014). However, other 4 data points by Cheng and Cord-Ruwisch (2012), Al-Thawadi (2008) and Cheng, *et al.* (2014) were obtained from treated larger sand column into a polyvinyl chloride (PVC) column. These data points were outlier of the scattered data points and there-

fore, neglected for subsequent analysis. Note that removing these 4 outliers did not improve the interpretation of the contribution of $CaCO_3$ to UCS.

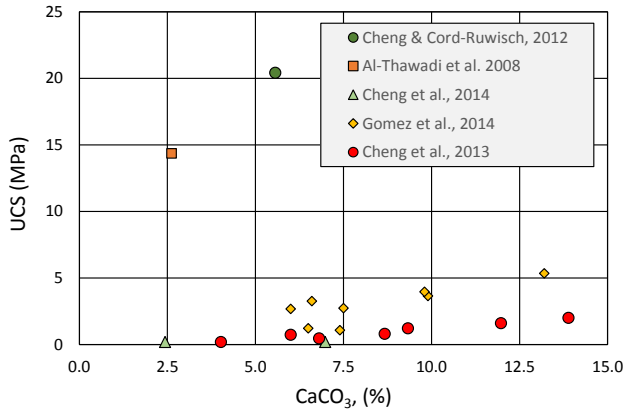

Figure 4. Distribution of UCS vs $CaCO_3$ data points with respect to their soil type.

A 2D plot (UCS vs $CaCO_3$) is not suitable for observing the contribution of MICP treatment on UCS, knowing that the particle arrangement and gap between them significantly influences the bond created by $CaCO_3$. Therefore, the characteristic parameter of PSD curve is added with UCS and $CaCO_3$ in a 3D plot (contour plot) to reveal an observational trend between them. Since the extracted data points were irregular in the grid space, an Inverse Distance to a Power (IDP) gridding method was used for interpolation. In this method data are weighted during interpolation such that the influence of one point relative to another declines with distance from the grid node. Weighting is assigned to the data through the use of a weighting power that controls how the weighting factors drop off as distance from a grid node increases. As the power increases, the grid node value approaches the value of the nearest point. For a smaller power, the weights are more evenly distributed among the neighboring data points. The interpolated value for grid node "j" can be calculated by the following equation:

$$\hat{C}_j = \frac{\sum_{i=1}^{n} \frac{C_i}{(h_{ij})^{\beta}}}{\sum_{i=1}^{n} \frac{1}{(h_{ij})^{\beta}}} \qquad (6)$$

where h_{ij} is the effective separation difference between grid node "j" and the neighboring point "i", $\hat{C}_j$ is the interpolated value for grid node "j", C_i are the neighboring points and β is the weighting power (the Power parameter). The details of the statistical method can be found in Davis (2002) and Franke (1982). Normally, Inverse Distance to a Power behaves as an exact interpolator. When calculating a grid node, the weights assigned to the data points are fractions, and the sum of all the weights are equal to 1.0. When a particular observation is coincident with a grid node, the distance between that observation and the grid node is 0.0, and that observation is given a weight of 1.0, while all other observations are given weights of 0.0. Thus, the grid node is assigned the value of the coincident observation. Contour maps were then plotted through these grid points.

3.5 *UCS of MICP and soil grading*

The uniformity coefficient, $Cu=D_{60}/D_{10}$ is often considered to represent soil grading; where D_{60} is particle size at 60% finer on PSD curve. For example, Cu > 4 is well graded sand and Cu < 4 poorly graded sand. The Cu and $CaCO_3$ of the extracted data points are plotted in x and y axis, respectively, in Fig. 5. The UCS is presented by colour contour (z-axis) for an interval of 1MPa. The grid points for this plot were generated by 50 rows and 35 columns i.e. 1750 grid points. Note that a large number of grid points are required for smaller contour interval. For the contour interval of 1MPa, the Fig. 5 would remain same for as low as 360 grid points i.e. contour map is not affected by the finer gird points. However, it may affect by the methods to generate grid points.

Fig. 5 also shows the UCS data points and their values. The contours plot captured the zone of high UCS (in blue) and low UCS (in red). However, this plot shows that Cu does not correlate with UCS and $CaCO_3$.

Since Rahman and coworkers (Rahman, *et al.*, 2008, Rahman, *et al.*, 2014) identified D_{10} as a characteristic particle size for particle arrangement, particularly the gap between particles which influence effective bonding, the contour plotted with D_{10} instead of Cu is presented in Fig. 6. For the same amount of $CaCO_3$, a specimen with smaller D_{10} had higher UCS. The rate of increasing UCS is higher with $CaCO_3$ at lower D_{10}. A mild trend of increasing UCS can be observed with $CaCO_3$ at higher D_{10}.

The coefficient of curvature, $Cc = (D_{30})^2/(D_{10}xD_{60})$ is a characteristic parameter that consider wider range of particle size, including D_{10} for soil grading; where D_{30} is particle size at 30% finer. The contour plot for UCS with $CaCO_3$ and Cc is presented in Fig. 7. Although it shows a general trend of increasing UCS with the increase of $CaCO_3$ and Cc, a maximum increase was obtained at Cc=0.8. This is due to the missing data points in the zone of higher $CaCO_3$ and Cc (0.8 to 1.6). Similar limitation was observed in Fig. 6 with D_{10}, perhaps little vague than in Fig. 7. The Inverse Distance to a Power (IDP) gridding method is suitable to develop an unforeseeable relation among three parameters. However the certainty of the inferred trend is also

dependent on the spread of data points in the x-y space.

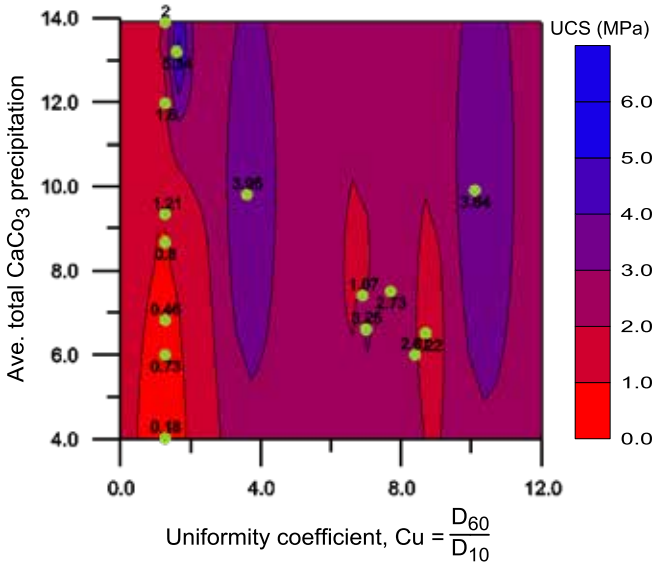

Figure 5. Contour plot for UCS with Cu and $CaCO_3$.

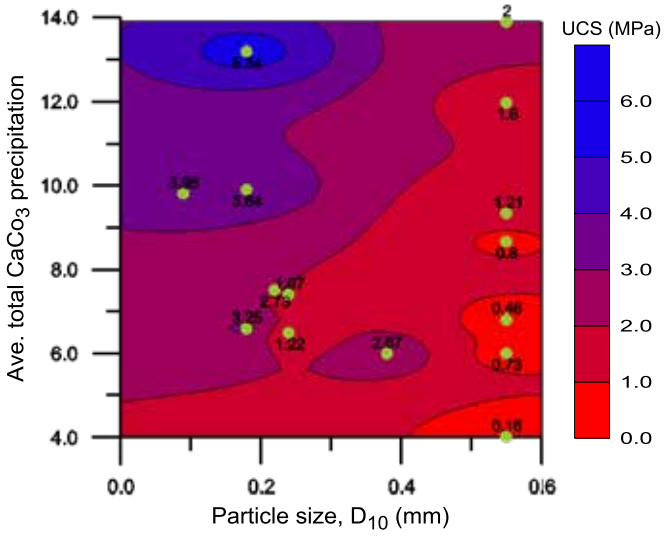

Figure 6. Contour plot of UCS with D_{10} and $CaCO_3$.

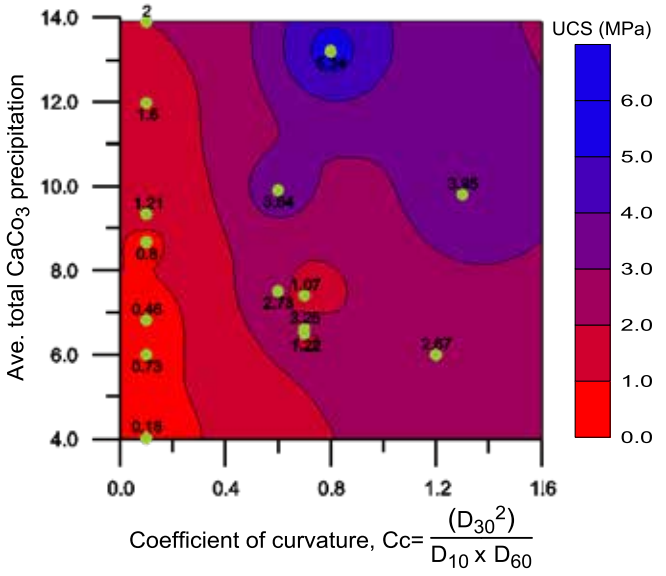

Figure 7. Distribution of UCS vs $CaCO_3$ data points with respect to their soil type.

4 CONCLUSIONS

Microbial induced calcite precipitation (MICP) technique utilizes naturally occurring bacteria to precipitate $CaCO_3$ to bind soil particles together and this increases soil strength. This article reviewed 70 journal articles that have used MICP in the field of civil engineering and engineering geology. A scrutiny of literature revealed that only a few articles reported total $CaCO_3$ precipitation for similar MICP process and engineering properties such as the unconfined compressive strength (UCS) of soil. The major findings are:

- The demographic statistics of those publications showed that the research and publications on MICP increased exponentially from 2005. USA, China, England, Canada, the Netherlands and Australia are the leading countries in terms of MICP research. The University of California, Davis and North Carolina State University are two universities that have particularly focused on MICP techniques.
- A total of 12 different silica sands have been used to compare total $CaCO_3$ with UCS. A compilation of these data points displays a large scatter in terms of the contribution of $CaCO_3$ on UCS. The scatter is due to whether $CaCO_3$ creates an effective bonding between particles. The particle arrangement and gap between host sand particles were considered as major influencing factors for effective bonding.
- Three parameters, namely Cu, D_{10} and Cc, were considered as characteristic parameters which influence particle arrangement and the gaps between them and therefore the effective bonding of $CaCO_3$. A statistical tool known as the Inverse Distance to a Power (IDP) gridding method was used to describe the relation between UCS with $CaCO_3$ and these three parameters. While contour plots with Cu did not produce an inferable trend, other contour plots with D_{10} and Cc did show general trends. D_{10} is embedded in the Cc calculation which indicates a strong influence of D_{10} on overall behaviour. This is consistent with Rahman's earlier work that D_{10} is a characteristic size for the gap between particles.

The missing data points in the x-y space influence the contour plot in the IDP gridding method which does not provide absolute certainty of the inferred trend. However it does give an overall understanding of the trend.

5 ACKNOWLEDGEMENTS

The first author, Reena Hora, would like to acknowledge the Australian Department of Education's Australian Postgraduate Award (APA) at the University of South Australia which has allowed her to conduct research on MICP techniques as part of her PhD dissertation. Dr Mizanur Rahman acknowledges the Early Career and New Appointee Researcher Development Award, ITEE, UniSA, 2013 which also supports this research.

6 REFERENCES

Al-Thawadi, S. M. 2008. "High strength in-situ biocementationof soil by calcite precipitating locally isolated ureolytic bacteria." PhD Thesis, Murdoch University.

Al Qabany, A., Soga, K., and Santamarina, C. 2012. "Factors Affecting Efficiency of Microbially Induced Calcite Precipitation." *Journal of Geotechnical and Geoenvironmental Engineering*, 138(8), 992-1001. doi:doi:10.1061/(ASCE)GT.1943-5606.0000666.

Burbank, M., Weaver, T., Lewis, R., Williams, T., Williams, B., and Crawford, R. 2013. "Geotechnical Tests of Sands Following Bioinduced Calcite Precipitation Catalyzed by Indigenous Bacteria." *Journal of Geotechnical and Geoenvironmental Engineering*, 139(6), 928-936. doi:10.1061/(ASCE)GT.1943-5606.0000781.

Burbank, M. B., Weaver, T. J., Green, T. L., Williams, B. C., and Crawford, R. L. 2011. "Precipitation of Calcite by Indigenous Microorganisms to Strengthen Liquefiable Soils." *Geomicrobiology Journal*, 28(4), 301-312. doi:10.1080/01490451.2010.499929.

Cheng, L., and Cord-Ruwisch, R. 2012. "In situ soil cementation with ureolytic bacteria by surface percolation." *Ecological Engineering*, 42, 64-72. doi:http://dx.doi.org/10.1016/j.ecoleng.2012.01.013.

Cheng, L., Cord-Ruwisch, R., and Shahin, M. A. 2013. "Cementation of sand soil by microbially induced calcite precipitation at various degrees of saturation." *Canadian Geotechnical Journal*, 50(1), 81-90. doi:10.1139/cgj-2012-0023.

Cheng, L., Shahin, M. A., and Cord-Ruwisch, R. 2014. "Bio-cementation of sandy soil using microbially induced carbonate precipitation for marine environments." *Géotechnique*, 64(12), 1010-1013. doi:10.1680/geot.14.T.025.

Davis, J. C. 2002. *Statistics and Data Analysis in Geology*, Wiley, New York, United States.

DeJong, J. T., Fritzges, M. B., and Nusslein, K. 2006. "Microbially Induced Cementation to Control Sand Response to Undrained Shear." *Journal of Geotechnical and Geoenvironmental Engineering*, 132(11), 1381-1392.

DeJong, J. T., Mortensen, B. M., Martinez, B. C., and Nelson, D. C. 2010. "Bio-mediated soil improvement." *Ecological Engineering*, 36(2), 197-210. doi:http://dx.doi.org/10.1016/j.ecoleng.2008.12.029.

DeJong, J. T., Soga, K., Ian, K., Burns, S., Paassen, l. A. V., Qabany, A. A., Aydilek, A., Bang, S. S., Burbank, M., Caslake, l. F., Chen, C. Y., Cheng, X., Chu, J., Ciurli, S., Esnault-filet, A., Fauriel, S., Hamdan, N., Hata, T., Inagaki, Y., Jefferis, S., Kuo, M., Laloui, l., Larrahondo, J., Manning, D. A. C., B. Martinez, Montoya, B. M., Nelson, D. C., Palomino, A., Renforth, P., J. C. Santamarina4 , Seagren, E. A., Tanyu, B., Tsesarsky, M., and Weaver, T. 2013. "Biogeochemical processes and geotechnical applications: progress, opportunities and challenges." *Géotechnique*, 63(4), 287–301. doi:10.1680/geot.SIP13.P.017.

Franke, R. 1982. "Scattered data interpolation: tests of some methods." *Mathematics of Computtation*, 38(157), 181-200. doi:10.1090/S0025-5718-1982-0637296-4.

Gomez, M., Anderson, C., DeJong, J., Nelson, D., and Lau, X. 2014. "Stimulating In Situ Soil Bacteria for Bio-Cementation of Sands." *Geo-Congress 2014 Technical Papers*, 1674-1682.

James. K. Mitchell, and J. Carlos Santamarina 2005. "Biological Considerations in Geotechnical Engineering." *Journal of Geotechnical and Geoenvironmental Engineering*, 131(10), 1222-1233. doi:10.1061/(ASCE)1090-0241(2005)131:10(1222).

Mitchell, J. K., and Santamarina, J. C. 2005. "Biological Considerations in Geotechnical Engineering." *Journal of Geotechnical and Geoenvironmental Engineering*, 131(10), 1222-1233.

NRC 2006. *Geological and geotechnical engineering in the new millennium: Opportunities for research and technological innovation*, National Research Council, Washington, DC, USA.

Rahman, M., Baki, M., and Lo, S. 2014. "Prediction of Undrained Monotonic and Cyclic Liquefaction Behavior of Sand with Fines Based on the Equivalent Granular State Parameter." *International Journal of Geomechanics*, 14(2), 254-266. doi:10.1061/(ASCE)GM.1943-5622.0000316.

Rahman, M. M., and Lo, S. R. 2008. "The prediction of equivalent granular steady state line of loose sand with fines." *Geomechanics and Geoengineering*, 3(3), 179 - 190. doi:10.1080/17486020802206867

Rahman, M. M., Lo, S. R., and Gnanendran, C. T. 2008. "On equivalent granular void ratio and steady state behaviour of loose sand with fines." *Canadian Geotechnical Journal*, 45(10), 1439-1455. doi:10.1139/T08-064.

Rebata-Landa, V., and Santamarina, J. C. 2006. "Mechanical limits to microbial activity in deep sediments." *Geochemestry, Geophysics, Geosystem*, 7(11), 1-12. doi:10.1029/2006GC001355.

Whiffin, V. S., van Paassen, L. A., and Harkes, M. P. 2007. "Microbial Carbonate Precipitation as a Soil Improvement Technique." *Geomicrobiology Journal*, 24(5), 417-423. doi:10.1080/01490450701436505.

Geotechnical and Geophysical Site Characterisation 5 – Lehane, Acosta-Martínez & Kelly (Eds)

Challenges with sampling coarse-grained permafrost: an experience in Svalbard

T. M. H. Le
Sustainable Arctic Marine and Coastal Technology (SAMCoT), Centre for Research-based Innovation (CRI), Norwegian University of Science and Technology, Trondheim, NORWAY

M. Wold & M. G. Bærverfjord
Sweco, Trondheim, Norway

ABSTRACT: The need for better understanding about permafrost (i.e. frozen soils) has grown recently due to increasing interest from oil companies in the potential oil and gas reserve in the Arctic regions. Building sustainable infrastructures along the Arctic coasts for the exploration and exploitation of oil and gas requires reliable data on permafrost properties. However, retrieving samples of permafrost is a challenging task particularly for coarse-grained soils, due to their low water content. In this study, tests of four sampling methods (permafrost corer, commercial core barrel, percussion sampler and conventional auger) have been conducted with coarse-grained coastal permafrost on Svalbard. The tests show that none of the four methods were able to cut and retrieved undisturbed cores in the low water content, coarse-grained permafrosts found at several locations on Svalbard. Even though the permafrost corer and the conventional core barrel have been shown to be efficient in fine-grained permafrost, they failed to cut through the large grains in the soils on Svalbard. The percussion sampler and the conventional auger can only retrieved heavily remoulded samples which can be used for some index tests but are unsuitable for strength testing. Although no satisfactory methods were found, the tests reveal some specific issues with sampling in coarse-grained permafrosts including low water content and heat generated by friction. These issues are discussed which will provide a useful reference for future work on developing sampling method for coarse-grained permafrost.

1 INTRODUCTION

The potential reserve of oil and gas resources in the high Arctic regions has led to an increased interest from oil companies and contractors in investigation of permafrost (i.e. frozen soil that remains frozen for more than two consecutive years). Particularly, the demand for development of sustainable and adapted infrastructure in Arctic regions sets new challenges for geotechnical engineering with regard to retrieving reliable permafrost samples for measuring properties and strength parameters. Reliable samples require first and foremost that the samples are undisturbed during the sampling process. Undisturbed samples would reduce uncertainties regarding soil strength parameters and improve the accuracy of geotechnical assessment for the site.

Up to the 70s a large amount of work on permafrost sampling was conducted in Alaska and Canada. Early attempts of core drilling in coarse-grained permafrost reported in Lange (1963) and Hvorslev & Goode (1963) were successful. A number of studies in the 80s conducted at the Cold Regions Research and Engineering Laboratory, United States (CRREL) have led to development of a drill system which can be used for fine-grained frozen soils (Brockett & Lawson 1985; Sellmann & Brockett 1986a; Sellmann & Brockett 1986b, Sellmann & Brockett, 1987). More recently, a small portable earth drill system for permafrost studies has been developed at the Laval University, Canada (Calmels et al. 2005). The system is however limited to shallow samples (within 7 m depth), and also requires an ice volumetric content of minimum 5 – 10 % and fine soil materials for the drilling to be successful. Very few studies have reported development in drilling equipment that can handle coarse-grained frozen soils. Saito & Yoshikava (2008) tested a small portable drilling system for coarse-grained permafrost. The system can work but require the pore spaces among the coarse grains to be filled with clayey and silty materials to be able to operate effectively (Saito & Yoshikava 2008)

Cooling the drilling system to protect the equipment and maintain the sample quality is also an important issue to be considered. Past work normally used a cooled flushing liquid which had a tempera-

ture below the actual ground temperature (Lange 1963; Hvorslev & Goode 1963). The low temperature of the fluid preserved the freezing bonds in the soil and made it possible to keep the cores intact during sampling. In the past, diesel was commonly used as drilling fluid. However, there have been concerns about the interference of these liquid media with the water/ice content of the sample, and thereby altering the strength properties of the soil. Since both ice and pore water chemistry are important features of permafrost, core drilling equipment using a liquid as coolant and borehole fluid should be used with caution, as brine or antifreeze liquids may contaminate the retrieved cores and influence the results (Agergaard et al. 2012). In addition, environmental regulations in many Arctic regions now strictly forbid the use to liquid that could contaminate the environment. The use of oil/diesel flushing liquids is therefore not possible in many Arctic regions nowadays.

Geotechnical fieldwork and fieldwork in general in Arctic regions sets high demands to both equipment and personnel. Operating in cold climate, with limited access to workshops and spare parts, combined with the environmental challenges related to fieldwork in the fragile Arctic nature impose additional challenges for conducting soil investigations. Collecting cores with sufficient quality has proven challenging in fine-grained permafrost, and even more so in coarse-grained permafrost. This paper presents some test attempts to retrieve permafrost samples with four different methods (permafrost corer, conventional core barrels, percussion sampler and conventional auger). The tests were performed in coarse-grained coastal permafrost on Svalbard.

2 SITE DESCRIPTION

The tests were conducted on Svalbard which is an island north of the mainland Europe, midway between continental Norway and the North Pole (Figure 1 - right). Many scientific activities are being conducted on the island which provides a well-supported base for this research operation. The temperature regime in the area is well-documented. The main test site is located at Hotellneset, close to the airport in Longyearbyen on Svalbard. Most of the tests were performed at Vestpynten which is a point west on Hotellneset (Figure 1 – right).

Observation of the bluff front at Vestpynten clearly shows stratification of the permafrost profile with many layers dominated by gravels/pebbles (Figure 2). Earlier attempts to collect samples in Vestpynten relied on conventional auger which was the only available methods to the research group in spring 2012. This resulted in heavily remoulded bag samples which were used for observation of basic properties such as grain size distribution. The storing and protection of the bag samples taken in 2012 were not good enough for accurate measurement of water/ice content.

Figure 1. Location of Vestpynten study site on Svalbard.

The samples show that soils at the Vestpynten site consist of a well-graded material with particles varying between gravel and silt. The gravels/pebbles fraction varies considerably in sizes, but is dominated by particle range from 1-3 cm. The soil is covered with an organic top layer at most locations. The soil materials appear very dry and loose indicating very low ice/water content (Guegan & Christiansen, 2016).

Figure 2. Stratification observed in the bluff at Vestpynten

3 DRILLING EQUIPMENT AND METHODS

3.1 *Drilling rig*

The investigations described in this paper were conducted by using a geotechnical 504 drilling rig which has been specially equipped to cope with the harsh climatic condition on Svalbard. The drill rig is owned by SINTEF and stationed on Svalbard (Figure 3). The rig can be divided into four sections, each weighing less than 1300 kg, which enable them

to be transported by helicopter to sampling locations. The rig has a rotation speed up to 180 rpm which can reduce the drilling time in hard soils and bedrocks. This is especially important when cutting cores in very hard permafrosts and bedrocks.

Figure 3. Geotech 504 drilling rig for Arctic condition

During cutting, the system is ventilated with a cooled air flow which is delivered at 27 m^3/min by an air compressor (Atlas Copco XRVS 476). The air cooling is important in permafrost drilling since it reduces the problem with thawing. Compared with a liquid flushing system, it has an advantage because it does not introduce a foreign liquid into the soil, which can alter the water content and hence the strength of permafrost.

3.2 *Sampling methods*

3.2.1 *Permafrost corer*

The permafrost corer is a sampling equipment, developed internally by the SINTEF/NTNU workshop in Trondheim during autumn 2012 (Figure 4). Over many years, SINTEF has worked on several projects in Svalbard, gathered experience and modified the equipment in order to adapt it to different applications in permafrost investigation. The corer consists of a cutting bit attached to a thick-walled hollow core collecting auger (Figure 4a), similar to the modified CRREL core barrel for ice-drilling (Veillette, 1974). The permafrost corer uses a highly durable poly-crystalline diamond composite (PCD) inserts to increase it cutting capacity into specially hard materials such as cobbles and rocks (Figure 4d). The corer has proven to be efficient in collecting cores in fine-grained frozen soils and can produce intact samples of high quality.

The tested version of the corer in this investigation is a modification of a previous version which was built in 2007. This first version has the ability of cutting cores with a diameter of 70 mm. This gives the possibility of trimming cores down to 54 mm for standard strength testing in Norwegian geotechnical laboratories. For this new modified version, the rotation direction, the diameter and the wall thickness are modified to increase its capacity to penetrate into hard materials. The new corer has reduced diameter to reduce resistance during drilling and produces cores with a diameter of 45 mm. This also reduces the required effort for pre-drilling,

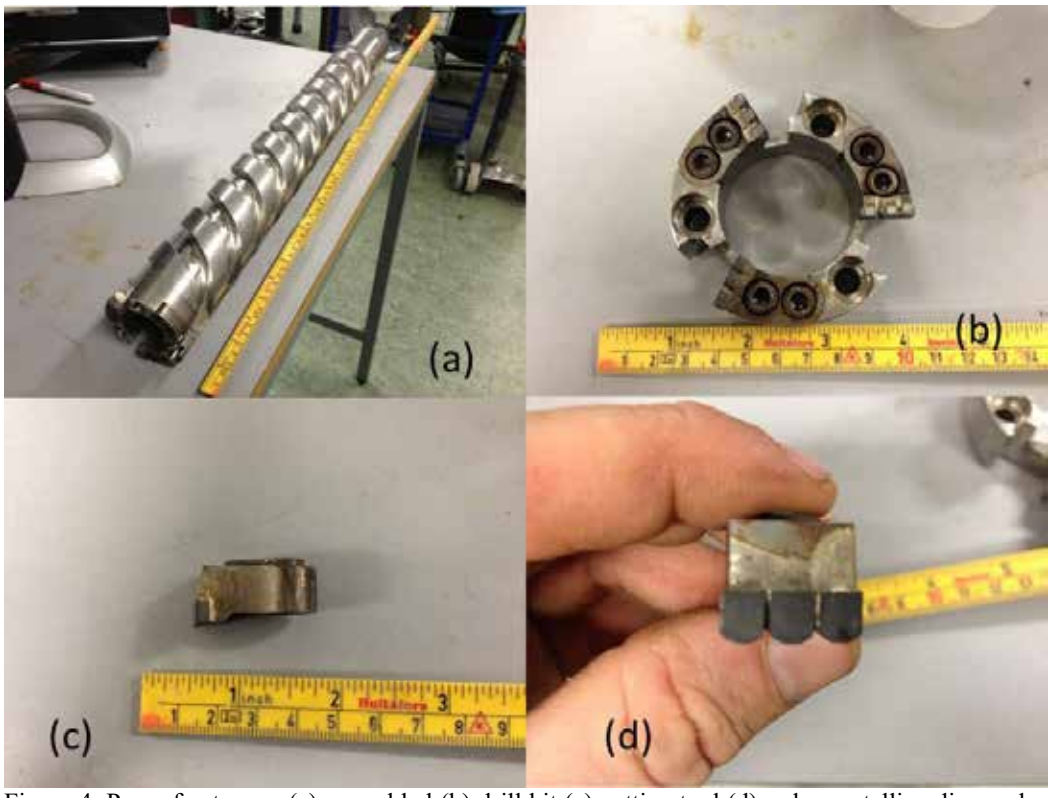

Figure 4. Permafrost corer (a) assembled (b) drill bit (c) cutting tool (d) poly-crystalline diamond composite inserts

which can decrease the total drilling time considerably. The wall thickness of the corer is also reduced to approximately 15 mm to reduce resistance and the heat generated. The modified corer rotates left which makes it compatible to use in the rock drilling rod system normally employed in Norwegian geotechnical drilling rigs.

When operating in cold climate, environmentally unfriendly additives often have to be used in order to prevent the cooling liquids from freezing. These additives are prohibited by the strict environmental regulations in Svalbard. Therefore, the coring barrels are used without drilling fluids in the tests presented in this paper. In principle, the corer can be fitted with a bit holder which is compatible with the rock drilling rod system with possibility for flushing with air. This would be an advantage in coarse and dry gravels in order to remove the cutting and cool down the drilling bit, but was not available at the time of this study.

3.2.2 *Atlas Copco 76 T2 Core barrel*

The Atlas Copco 76 T2 corer is a standard double-walled core barrel with the ability of cutting 1.5 m long cores having a diameter of 61.7 mm. Figure 5a shows the different parts of the core barrel. This corer has previously been used to collect cores in bedrock and coal deposits in Svalbard but has not been thoroughly tested in coarse-grained permafrost prior to this study. This type of core barrel is very versatile and can be fitted with a variety of drill bits depending on the materials. This system can also use both air and water as drilling coolants. In this system the flushing is released through the bit throat. The use of face discharge drill bits is recommended for coring in permafrost (Hvorslev & Goode 1963), but it is not possible to attach face discharge bits to this system.

Two different drill bits were tested. The surface set diamond coring bit which has previously been used for cutting cores in bedrock and coal deposits in Svalbard (Figure 5b). This bit is oversized to allow airflow up in the hole. To ensure the performance of this drill bit, the material has to be hard and abrasive enough to wear down the bit so that the surface set diamonds remains sharp. The tungsten carbide drill bit has a more aggressive cutting surface with large tungsten carbide inserts (Figure 5c). This bit is built to give high penetration in soft rock formations. This bit is not oversized, but could be combined with a reaming shell to ensure good airflow. Reaming shell was not used in this study.

3.2.3 *Moraine percussion sampler*

The moraine percussion sampler consists of a conventional destructive drilling bit (Figure 6) which is attached to an open thick-walled cylinder. This bit ensures penetration in almost any soil or rock and has previously been used to collect samples in moraine areas both on land and offshore in the Norwegian mainland. The method is efficient when collecting samples in soils where a conventional piston corer cannot be used. The moraine percussion sampler is rotated and hammered down with flushing to the actual depth where the sample is to be collected. The flushing is then shut off and the sampler is hammered down to fill the cylinder. The hammering energy fills and packs the cylinder tightly which allows sample retrieval. However, this method can only produces disturbed samples.

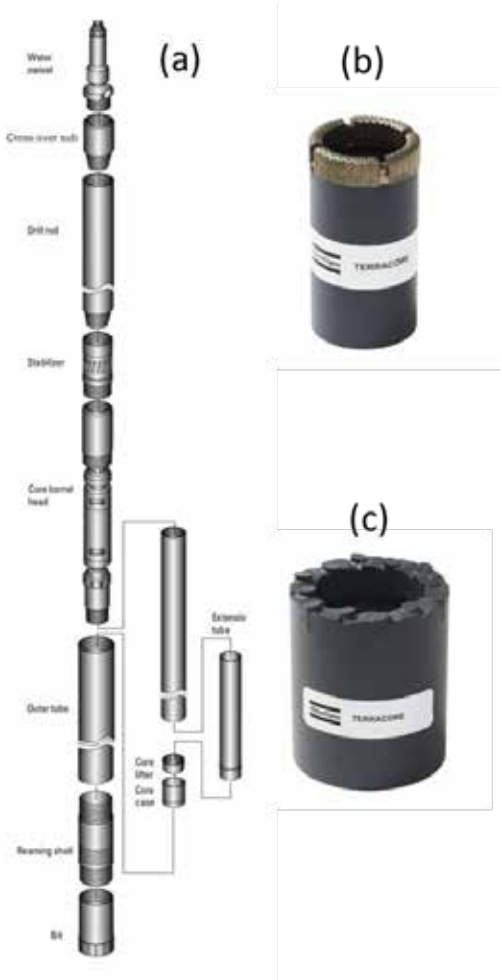

Figure 5. Atlas Copco 76 T2 core barrel (a) split drawing (b) surface set diamond drill bit (c) tungsten carbide drill bit (Source: Atlas Copco).

Figure 6. Moraine percussion sample drill bit (a) top view (b) side view

3.2.4 *Conventional auger sampler*

Tests of permafrost sampling are also conducted with conventional auger which is rotated and hammered down. The materials rotated up or stuck to the auger flightings are collected in bags. The main drawback with this method is that it remoulds the soil before it can be collected and also crushes rocks during penetrating. It is also important to note that this method of sampling generates heat, especially in coarse-grained soils. This heat melts the ice in the permafrost and this may influence the measured water content in the samples. The moraine percussion sampler, described in the previous section, seems to retrieve less remoulded material and more depth specific than the auger sampling.

4 RESULTS AND DISCUSSION

4.1 *Permafrost corer*

One test was attempted by starting the coring process from the surface (Figure 7). The permafrost corer penetrated easily through the frozen organic peat at the top of the soil profile. However the drilling must be stopped when the drill bit hit a rock. When restarting after the stop, the problem became evident. Due to the low water-content of the permafrost at the test site, the coarse materials had no freezing bonds to hold the soil materials together. Therefore, the forces exerting by the drilling system mixed and remoulded the permafrost instead of cutting through it. The large rocks which were not cut through were pushed and became wedged between the core barrel and the sidewalls of the borehole. In order to prevent damage to the equipment, the test was aborted when the problem was discovered.

Another test with the permafrost corer was conducted in a borehole where a new thermistor was going to be placed. At this location the active layer contains large rocks and exists in unfrozen condition which can cause significant challenge for drilling. The hole was therefore predrilled down to 1.8 m. The permafrost is expected to start close to this depth. The core barrel was attached to the rod system and lowered down to the bottom of the hole. The corer immediately hit large rocks and encountered the same problem as described in the previous attempt. It became evident that this attempt failed and must be aborted.

The causes for the failure become apparent after these two attempts. The main problem with drilling in coarse-grained permafrost was the low water content of the soils. There are therefore few freezing bonds to hold the grains together to exist as large strong mass, similar to rock mass or permafrost with high water content. Therefore, the grains move easily under forces exerted by the drilling system, which lead to remoulding of the materials instead of cutting. In addition, even though the barrel of the permafrost corer has reduced wall thickness compared with its earlier version, the core barrel still needs to remove quite a significant amount of soil materials during cutting cores. It was observed in the tests that the permafrost corer generated a lot of heat due to lack of an adequate cooling system. Therefore, even if the drilling bit was able to cut the material, the heat would have destroyed the samples in these tests.

Figure 7. The drilling system with the permafrost corer set-up for sampling

4.2 *Atlas Copco 76 T2 core barrel*

Figure 8. The drilling system with the Atlas Copco core barrel set-up for sampling

Two attempts were conducted with the Atlas Copco 76 T2 core barrel (Figure 8). The tests were started from the ground surface and showed that this system could also cut through the frozen organic peat at the top. At the beginning of the tests, it was observed that the air flushing exited up the hole and blew away the cuttings. As the drilling progressed, the flow of air up the drilling hole stopped. It seemed that the large cavities (or pores) among the dry and loose gravel allowed the air to disperse in all directions easily which reduced the air pressure in front of

the drill bit. After penetrating approximately 1 meter in depth, the corer was retrieved, but the core barrel was found to be empty. This happened in both attempts. The temperature of the barrel was checked and it seemed that the cooled air used for flushing managed to reduce the influence of the friction heat generated during drilling.

The failure of these tests can also be attributed to the low water content of this coarse-grained permafrost, similar to the failure of the permafrost corer. With little presence ice, there was almost no bond to hold the soil materials together. The materials ended up being remoulded and blown away during drilling.

4.3 *The moraine percussion sampler*

The moraine percussion sampler was tested in coarse permafrost at an old coal quay in Hotellneset. The soil conditions in this area are similar to those found in Vestpynten with the exception of the water content. This area is below the sea level, hence the material is assumed to be fully saturated.

The sampler was drilled down to the desired depth with constant flushing to prevent material from entering the cylinder. The flushing was shut off and the sampler rammed down without rotation. The sample was taken at 28 m depth. To ensure that the sampler would be sufficiently filled, the sampler was rammed further than the cylinder length. This process compacted the materials which made it remain inside the cylinder instead of falling out. The sampler was then retrieved. The content was emptied into bags. The material retrieved with the moraine percussion sampler is remoulded. However, its ability to collect coarse materials at relatively large depths still makes it a useful tool in permafrost sampling.

4.4 *Conventional auger*

Figure 9. Sampling with auger

This method has been used in many different soil conditions earlier and is considered so far the most efficient method for material retrieval in Vestpynten (Figure 9). The soil materials, even with low ice/water content, can be quite effectively trapped between auger flightings and hence brought up to the ground surface. This methods and retrieve permafrost from quite large depths. However it remoulds the material, crushes and larger rocks and ice. Also the heat generated melts ice which can alter the water/ice content. The method does not give samples suitable for strength testing but can be used for some other tests (e.g. simple index tests).

5 CONCLUSIONS

None of the methods tested were able to cut or retrieved undisturbed cores in the low water/ice content and coarse-grained permafrost found in Svalbard. The following two main challenges are identified for sampling in coarse-grained permafrost (i) The low water content of coarse-grained soils means that there are few freezing bonds to hold the soil materials together. The soils therefore end up being remoulded rather than being cut under the forces exerted by the drilling system, and (ii) A large amount of heat is generated during cutting coarse-grained samples, therefore an efficient cooling system is essential and must be in place for sampling.

The permafrost corer and the Atlas Copco core barrels could not cut through coarse-grained loose permafrost in Svalbard. The moraine percussion sampler and the conventional auger can be used for sampling bag samples at a specific large depth, but the samples are highly remoulded.

6 ACKNOWLEDGEMENTS

The authors would like to acknowledge the financial support from the SAMCoT through the Research Council of Norway and all the SAMCoT partners.

7 REFERENCES

Brockett, B. E. & Lawson, D. E. 1985. Prototype drill for sampling fine-grained perennially frozen ground. CRREL Report 85-1. Hanover, NH: U.S. Army Engineer.

Calmels, F., Gagnon, O. & Allard, M. 2005. A portable earth-drill system for permafrost studies. *Permafrost and Periglacial Processes* 16(3): 311-315.

Guégan, E. B. M. & Christiansen, H. H. 2016. Seasonal Arctic Coastal Bluff Dynamics in Adventfjorden, Svalbard. *Permafrost and Periglacial Processes* 27(1).

Hvorslev, M. J. & Goode, T. B. 1963. Core drilling in frozen soils. In *Int. Conf. on Permafrost*, Lafayette, Ind. Publ,No. 1287, Washington, DC: National Academy of Sciences, National Research Council: 364-371.

Lange, G. R. 1963. Investigation of sampling per-ennially frozen alluvial gravel by core drilling. In *2nd Int. Conf. on Permafrost*, Yakutsk, USSR: National Academy of Sciences, Washington, DC.

Saito, T. & Yoshikava, K. 2008. Portable shallow for frozen coarse-grained material. *Proc. 9th Int. Conf. on Permafrost*, Fairbanks: 1561-1566.

Sellmann, P. V. & Brockett, B. E. 1986a. Auger bit for frozen fine-grained soils. CRREL Special Report 86-36. Hanover, NH: U.S. Army Engineer

Sellmann, P. V. & Brockett, B. E. 1986b. Drill bits for frozen fine-grained soils. CRREL Special Report 86-27. Hanover, NH: U.S. Army Engineer

Sellmann, P. V. & Brockett, B. E. 1987. Bit design improves augers. *The Military Engineer, VA* 79(516): 453-54.

Veilette, J. 1974. Modified CRREL ice coring augers. *Geological survey of Canada* Paper 75-1: 425-26.

Geotechnical and Geophysical Site Characterisation 5 – Lehane, Acosta-Martínez & Kelly (Eds)

Collapse settlement and strength characteristics of unsaturated soils with different degrees of compaction

A.M. Shahnoory & M. Sugiyama
Tokai University, Kanagawa, Japan

ABSTRACT: From a practical viewpoint, collapse settlement due to water infiltration into the soil affects fills or road bases that are developed by compacted unsaturated soils. The compacted soil is frequently assessed based on the degree of compaction (ratio of dry density to maximum dry density). Furthermore, no consideration has yet been given to the mechanical properties of compacted soils as a criterion for determining the effect of compaction, or to the condition of soil immersed in water which is the most dangerous state of soil. This paper presents the results of collapse settlement test and direct shear tests of four different types of Japanese soils. The influence of initial degree of saturation, initial dry density and overburden pressure have chosen as parameters. In addition, in this research, the influence of water content on unconfined compressive strength were investigated.

1 INTRODUCTION

In the field of geotechnical engineering, it is well known that several soil problems are caused by a surplus of water in the soil. There are various ways which soil can adsorb water such as rising of water table in the rainy seasons, reservoir in case of earth dams, leakage or damage of underground water supply system, flooding and etc. These problems generally can be caused to loss shear strength and excessive deformation, (Basma et al. 1992), therefore, it is imperative that engineers consider and control the deformation or settlement which occurs by wetting-induced (collapse) in compacted fills, including foundation of structures, embankments of transportation infrastructures such as roads, highways, railways, runways, parking-lots, and other compacted fills. The collapse can occur in engineered fills, has been demonstrated in both the field and laboratory (Booth et al. 1977).

This paper involves an extensive experimental investigation of collapse settlement and strength characteristics of unsaturated soils with different degrees of compaction. The work focuses particularly on collapse settlement and shear strength parameters to examine the influence of dry density, degree of compaction, and overburden pressures using four types of unsaturated soils (Kanto loam, DL clay, Kaolin clay and Kuroboku) which are silty loam, silt, clay and sandy loam respectively.

The work also investigated the effect of water content on unconfined compressive strength of aforementioned soils. Because the strength of fills that are constructed after compaction is considered to be reduced while the water content increases with no changes in density, especially in the rainy seasons.

2 SAMPLES AND TEST PROCEDURE OF COLLAPSE TEST

2.1 *Sample preparation*

Table 1 Physical property of the tested soils

Sample	ρ_s (g/cm^3)	WL (%)	Wp (%)	Grading (%)		
				Clay	Silt	Sand
DL clay	2.65	NP	NP	4.7	95.3	0
Kanto loam	2.65	NP	NP	4	51	45
Kaolin clay	2.67	73.1	36.7	96.8	3.2	0
Kurobuko	2.39	NP	NP	7	47	46

This research was conducted on four types of soils. Of these, Kanto loam, which was taken directly from a construction field inside Tokai University in Hiratsuka city, and the Kuroboku, collected from Ibaraki prefecture. Both soils, after being dried in an oven, were sieved by a 2 mm sieve. Thus, the maximum grain size was 2 mm. DL clay was prepared from Showa Chemical Co., Ltd and Kaolin clay was provided from Takehara Chemical Industries, Ltd.

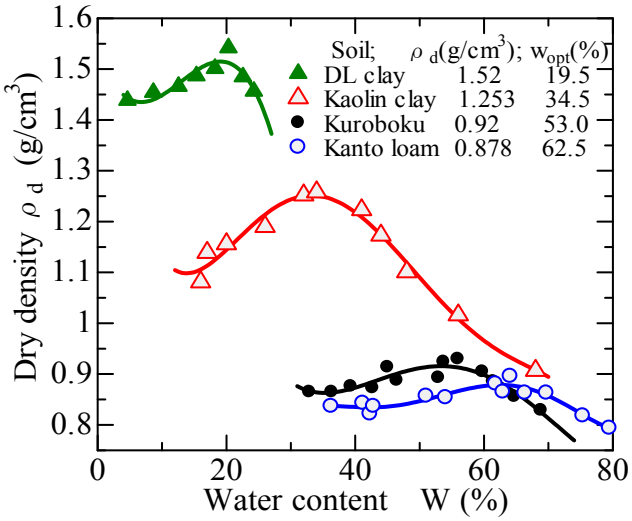

Figure 1 Compaction curves of tested soils

Table 1 shows the physical properties of the tested soils and Figure 1 shows the compaction curves, tests which were obtained from the results of compaction test (JIS A1210). According to the results of compaction tests, the amount of soil and water for both collapse and shear test specimens were calculated, and after mixing the soil with water and placing it in an oedometer ring or shear box, static compaction was used to make the specimens.

2.2 *Sample preparation*

The specimens for all types of soils were developed based on the method of (Kamei et al. 1994) in order to investigate collapse settlement. The collapse settlement tests were performed using an odometer apparatus (JIS A1217). Eight different overburden pressures (p=5~640kPa) as shown in Table 2, were applied on unsaturated specimens which were 6cm in diameter and 2 cm in height. Following this, the amount of compressive deformation was measured for 24 hours. Then, keeping the same overburden pressure, water was absorbed through the bottom surface of the specimen and the influence of water on collapse settlement was monitored for another 24 hours. A total of 232 collapse tests were conducted on the four types of soils with the initial conditions shown in Table 2.

Under the same initial conditions as the collapse tests, direct shear tests (JGS 0561) were performed to investigate the shear parameters (c and ϕ). For each test condition, two specimens were tested separately to compare the results of unsubmerged specimen with submerged one. After the specimens were made, the designated vertical pressure was applied to one of them and an one hour of wait time was provisioned; while settlement occurred, the specimen was sheared. The same procedure followed for the second specimen, but after settlement, the specimen was soaked with water via its bottom surface. This soaking period depended on the permeability of each soil. Typically for clayey soils, a period of more than one hour was necessary to observe water appearing on the top surface of the vertical loading pedestal of the shear box. While collapse settlement occurred, shear stress was applied to compare the influence of water on shear parameters of soil.

Table 2. Initial conditions of collapse tests

Type of soil	Dry density ρ_d (g/cm^3)	Degree of saturation S_r (%)	Pressure p (kPa)
DL clay	1.1, 1.2, 1.3, 1.36	20, 40	5, 10, 20, 40, 80, 160, 320, 640
Kanto loam	0.5, 0.6, 0.65	25, 40	
Kaolin clay	1, 1.1, 1.2	30, 60	
Kuroboku	0.555, 0.694, 0.74, 0.786	35, 45	

3 TEST RESULTS AND DISCUSSIONS

3.1 *Result of collapse settlement test*

A literature review has shown that nearly all types of compacted soils are subjected to collapse under certain conditions (Booth A.R 1977). It is important to note that even clean sand, pure clays (including pure montmorillonite), and soils containing substantial gravel fractions can also collapse (Dakshanamurthy, V. 1979).

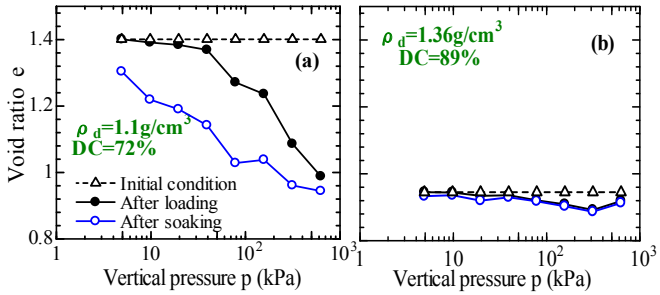

Figure 2 e– log p relation of DL clay at S_r=20%

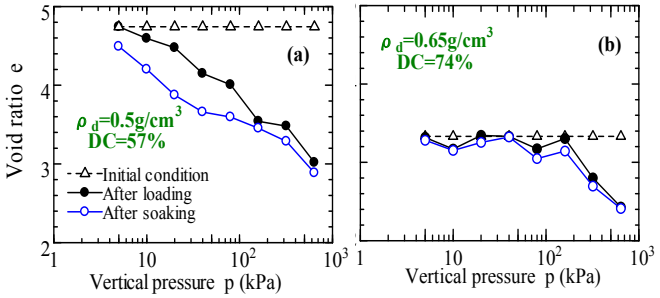

Figure 3 e– log p relation of Kanto loam at S_r=25%

Figure 2 through Figure 5 show the relationships between void ratio e and overburden pressure p. For all types of soils, the filled circles indicate the deformation of specimens before soaking, and opened circles show the deformation process after specimens were soaked with water. Figure 2 indicates the result of DL clay at S_r=20 %, and ρ_{d0} =1.1 and 1.36 g/cm^3; it shows that, with increase of overburden pressure,

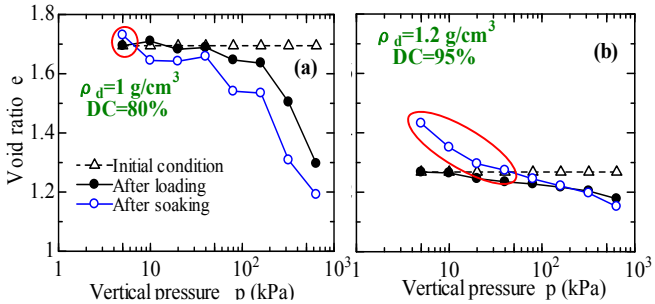

Figure 4 *e*–log *p* relation of Kaolin clay at S_r=30%

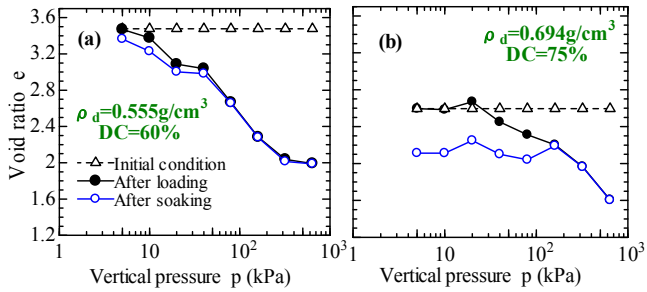

Figure 5 *e*–log *p* relation of Kuroboku at S_r=35%

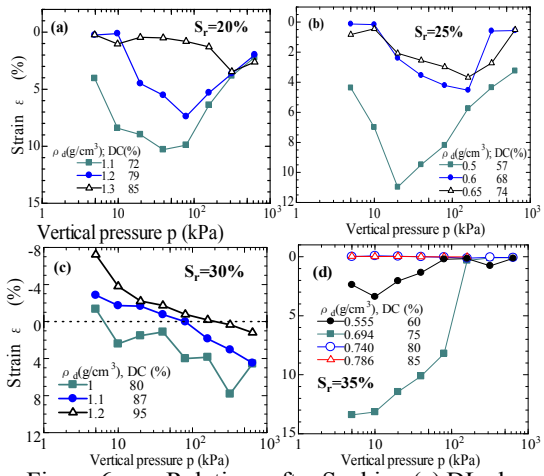

Figure 6. ε–p Relations after Soaking (a) DL clay, (b) Kanto loam, (c) Kaolin clay, (d) Kuroboku

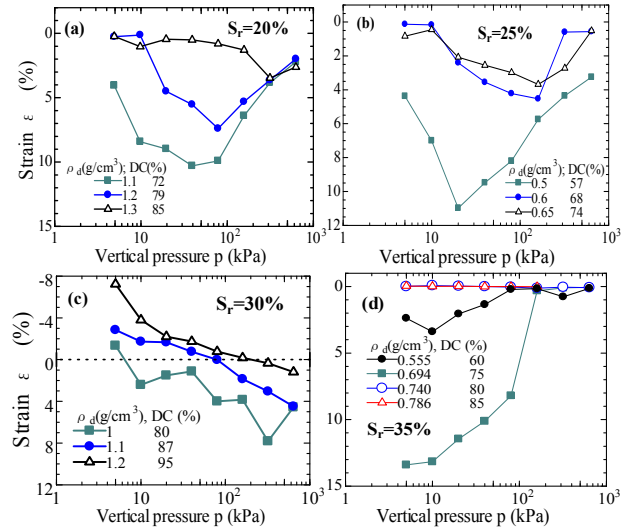

Figure 6 *ε–p* relations after soaking, (a) DL clay, (b) Kanto loam, (c) Kaolin clay, (d) Kuroboku

the void ratio decreased and collapse settlement has occurred Figure 2(a). At ρ_{d0} =1.36g/cm^3 in Figure 2(b), hardly any settlement occurred. Figure 3 presents the result of Kanto loam; collapse settlement occurred immediately when water absorption started as shown in Figure 3 (a), whereas in higher dry density in Figure 3 (a), little collapse occurred.

The Kaolin clay results (Figure 4) indicated both collapse and swelling, depending on vertical pressures and dry densities. In the case of high density in Figure 4 (b), the collapse only occurred at the higher pressures, p=320 and 640 kPa. Figure 5 expresses the results of Kuroboku. Although 72 collapse tests were conducted with various initial densities, ρ_{d0}=(0.463, 0.555, 0.601, 0.694, 0.74, 0.786) g/cm^3, and initial degrees of saturation, S_r=(15, 20, 25, 35, 40, 45)%, collapsed only occurred at lower densities and pressures, (p<80kPa) at S_r=35% in Figure 5 (b). Comparing all results, except Kuroboku, at lower dry densities, the changes of void ratios after soaking are much larger than the initial condition of the tests.

Figure 6 shows the relations between axial strain ε and vertical pressure p. The DL clay result in Figure 6 (a) is near the result of Kanto loam in Figure 6 (b). Both results indicated that, strain increased with p peaked and then gradually decreased at lower dry densities (ρ_{d0}=1.1, and 1.2g/cm^3 for DL clay, and 0.5, and 0.6g/cm^3 for Kanto loam). Results from Kaolin clay in Figure 6 (c) show that swelling (increase in volume) gradually increased with increment of dry densities at overburden pressures lower than 320 kPa. Negative strain indicates that, after soaking, the specimen has a bigger volume than its initial volume. This result can be matched with the mechanism of collapse within which, for any given set of conditions, the amount of collapse generally decreases with increasing initial moisture content, increasing initial dry density, and decreasing overburden pressure (Lawton et al. 1991b). Figure 6 (d) shows the *ε-p* relation of Kuroboku soil. Strain constantly reduced only at ρ_{d0} = 0.555, 0.694 g/cm^3. Unlike DL Clay or Kanto loam, no increments of strain were shown.

3.2 *Result of direct shear test*

To investigate the influence of dry density and water content on shear parameters of soils (c and ϕ), the strain-controlled test method of direct shear test (JGS 0561) was performed. Therefore, shear stress was applied to one-half of the shear box, and the rate of shear displacement was measured by the horizontal dial gauge.

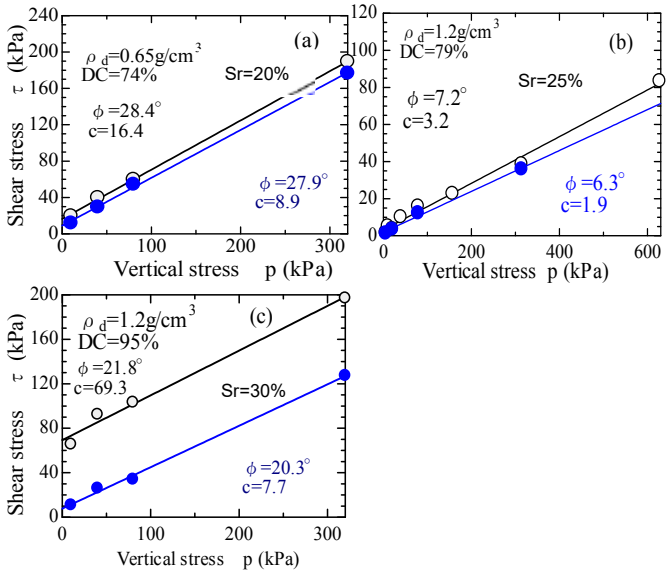

Figure 7 τ-p Relations, (a) Kanto loam, (b) DL clay and (c) Kaolin clay

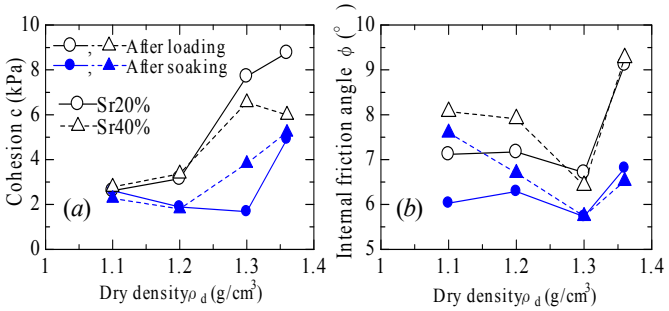

Figure 8 ρ_d-c,φ relations of DL clay

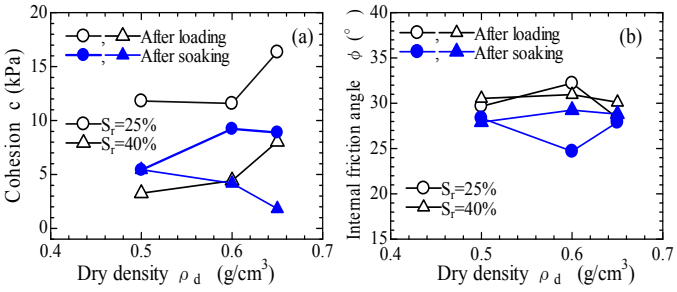

Figure 9 ρ_d-c,φ relations of Kanto loam

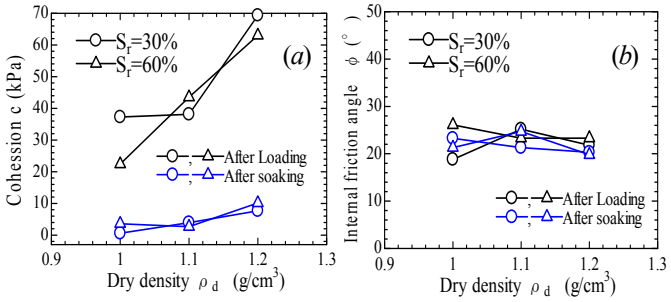

Figure 10 ρ_d-c,φ relations of Kaolin clay

Figures 7 (a) ~ (c) indicates the relationships between shear stress τ and vertical stress p of DL clay, Kanto loam and Kaolin clay at S_r=20%, 25% and 30%, respectively. The results indicated that after specimens were soaked with water, small changes occurred in ϕ (decreased), but c has significantly moved downward, especially for larger dry density condition of Kaolin clay in Figure 10 (a). Regardless of S_r, c has decreased after soaking all soils in Figure 8(a), 9 (a) and 10 (a). The results of Kanto loam show both decrease and increase of ϕ after the specimens was soaked, but the changes of ϕ in Kaolin clay is greater than the others.

The tests result shows that in the submerged specimens, the changes of cohesion c is larger than unsubmerged specimens. The changes in c of Kaolin clay are greater than Kanto loam and the changes of c in Kanto loam are greater than DL clay. The result is that whether the practical size of soil is smaller, the shear parameters will change more after the specimens are soaked. The increasing of dry density did not significantly affect the changing of cohesion c.

4 UNCONFINED COMPRESSION TEST

4.1 *Sample and Test Procedure*

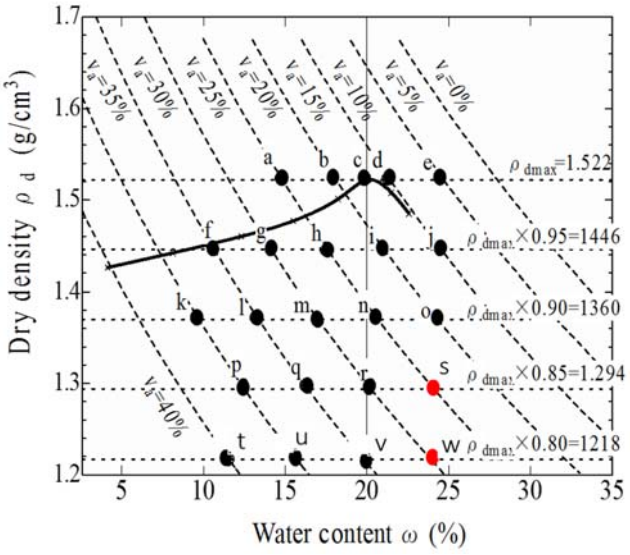

Figure 11. Initial positions of tested samples in compaction curve of DL clay

The initial conditions of specimens were selected based on the results of compaction tests (JIS A1210)

According to five different degrees of compaction (DC = 80, 85, 90, 95, 100 %), the initial densities were calculated ($\rho_d = \rho_{d\,\mathrm{dmax}} * DC$). Then the intersection points of dry densities with void ratios were selected for conducting the tests. After, based on the locations of points, the initial dry densities and water contents were measured for each specimen. A total of 21 specimens of DL clay (except point s and w, due

to being so loose that they failed when they were removed from the mold), 23 specimens of Kaolin clay, 26 specimens of Kanto loam, and 24 specimens of Kuroboku were tested. Figure 11 (point a~w) is a sample of this method which belongs to the DL clay compaction result. The specimens prepared were with a height of 10 cm and a diameter of 5 cm, which was made by the static compaction method.

4.2 *Result of unconfined compression test and discussions*

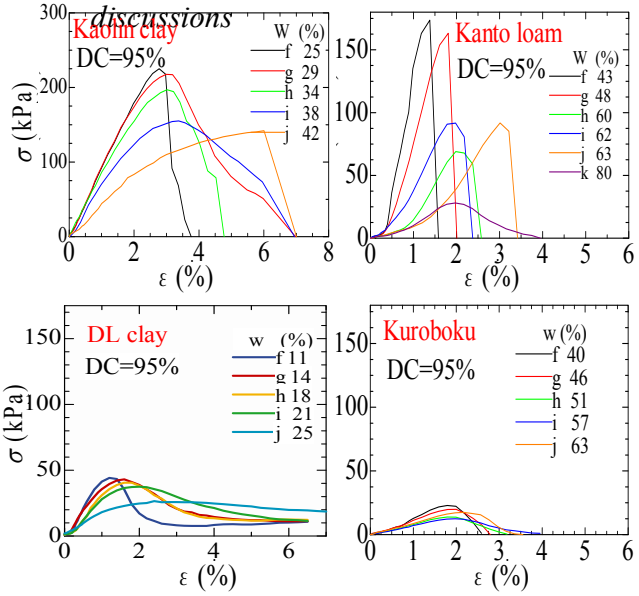

Figure 12. Stress-strain relations

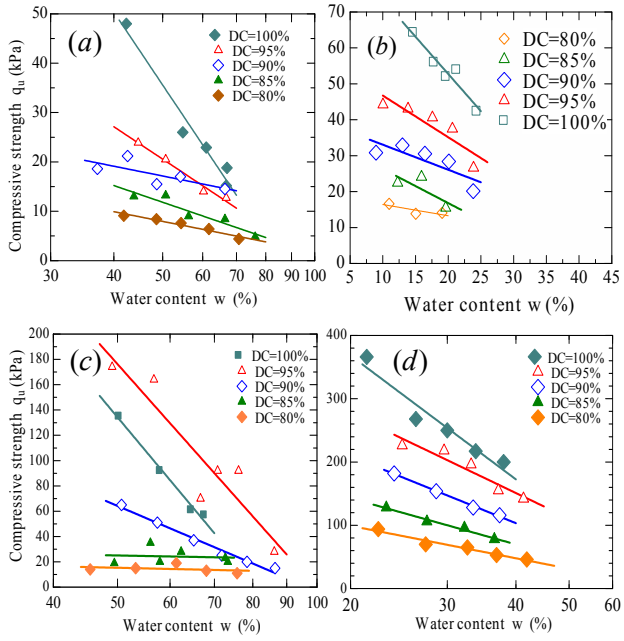

Figure 13 q_u-w relations, (a) Kuroboku, (b) DL clay, (c) Kanto loam and (d) Kaolin clay

sign. This analysis becomes increasingly important when embankments are built over weak soils, which are normally consolidated cohesive soils. The variation of this strength caused by rain can be changed in embankments when water content changes. Therefore, unconfined compression tests (JIS 1216) were conducted to investigate the effect of water contents on unconfined compressive strength q_u.

One result from each types of soil with the degree of compactions (DC=95%) have been shown to compare the stress-strain relations in Figure 12. The results indicated that by increasing water content, strain also increased. To compare these results, strain in Kuroboku is much less than Kaolin clay.

Generally clayey soil has shown higher strength than silty or sandy soils. Figures 13 (a)~(d) shows the relationship between water content w and compressive strength q_u, which are the results for Kuroboku, DL clay, Kanto loam and Kaolin clay, respectively. Data analysis indicated significant trends of unconfined compressive strength reduction with the increasing of water content; the degree of strength reduction is more outstanding at higher degrees of compaction. By decreasing water content, q_u has gradually increased and vice versa. Abe et al. conducted the same test using silty sand collected in the field. The test results in this study are similar to their results. In the silty sand used by Abe et al, unlike the sample in this study, q_u can be obtained even at with water content exceeding the optimum level.

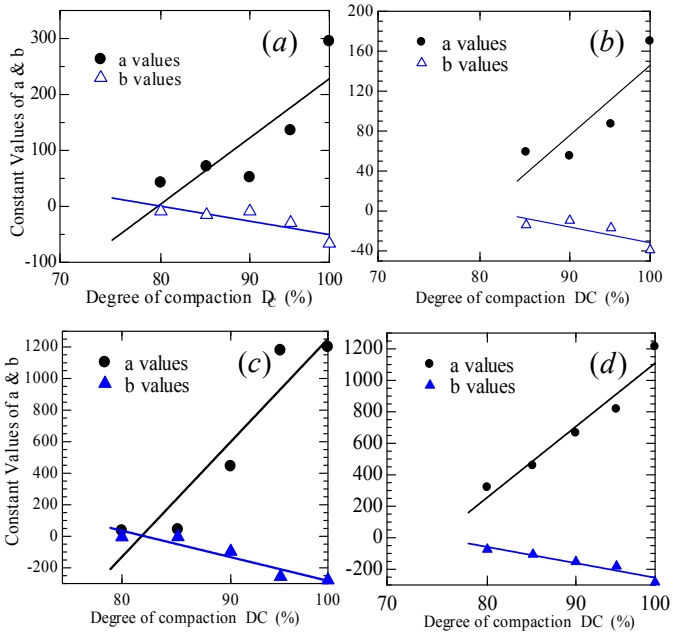

Figure 14 Constants of a and b relations with DC, (a) Kuroboku, (b) DL clay, (c) Kanto loam and (d) Kaolin clay

The strength of fills that are constructed after compaction is considered to be reduced, while there are no changes in density in the case where water content increases due to rainfall after construction (Abe et al. 2014). Therefore, it is important to prevent water from entering the fills as much as possible.

Based on the relation of q_u-w in Figure 13, and using least-square method, the following equation is proposed to determine the compressive strength of soils without performing unconfined compression test:

$$q_u = a + b \ln w \quad (1)$$

The constant a was found from the relationship of constants c and d with degree of compaction. Additionally, the coefficient. b was obtained from the relation of constants g and f with degree of compaction DC for each type of soil in Figure 14. It is worth mentioning that constant a and coefficient b have variable values according to DC.

$$a = c + d \ln DC \quad (2)$$

$$b = g + f \ln DC \quad (3)$$

It is mentionable that these equations are applicable for (JIS A 1210) standard compaction method whereas for other methods due to various compaction energies, the values of constants a, c and g and coefficients b, d and f will be varied.

5 CONCLUSIONS

The collapse tests results indicated that silty loam (Kanto loam) tends to collapse even at a higher degree of compaction, but silty soil (DL clay) shows no collapse at a higher degree of compaction or higher density. Clayey soils (Kaolin clay) shows both collapse and swelling, depending on overburden pressures and dry densities. Mostly soils containing montmorillonite tend to swell at higher density when the water content increase. However many experiments with various dry density and degree of saturation have been done on Kuroboku soil, but it has collapsed only at DC= 60% and 75% at lower overburden pressures. This soil which is an organic soil consist of small parts of plants and roots, difficult to determine its collapse behavior.

The result of direct shear tests indicated that changes of cohesion c are more outstanding than ϕ in submerged specimens for all types of soils. Cohesion c is willing to decrease more in clayey soils than silty or sandy soils, and the largest reduction of c appeared on the result of Kaolin clay, and this reduction has increased with increase of dry density, whereas for silty and sandy loam, the increase of dry density didn't significantly affect on cohesion.

The results of unconfined compression tests presented that, with the increasing of water content, the compressive strength of tested soils were decreased, and the degree of strength reduction is more outstanding at higher degrees of compaction. Therefore it is imperative to prevent the embankments or other compacted fill as much as possible from water infiltration. The main outcome of this part of research is the three proposed equations that in the future without conduction the unconfined compression test, the unconfined compressive strength of soils can be calculated.

6 ACKNOWLEDGEMENTS

The writer wish to express their appreciation to Mr. Yuki KAWANA and Mr. Koki HIRATA for their assistance in performing the laboratory tests.

7 REFERENCES

Basma, A.A and Tuncer, E.R 1992: Evaluation and Control of Col lapsible Soils, *Proc. ASCE*, Vol.118, No.GT 10, pp.1491-1504.

Booth, A. R 1977:Collapse settlement in compacted soils, CSIR Res. Report 324, Council for scientific and industrial Research, Pretoria, South Africa.

Cox, D.W. 1978:Volume changes of compacted clay fill Proc., Conf. on Clay fill, Inst. of Civil Ingres., London, 79-87.

Dakshanamurthy, V. 1979:A stress-controlled study of swelling characteristic of compacted expansive clays, *Geotech. Test.J.,* 2(1), 57-60.

Goro K.1985: Design and construction considerations 7. Soil compaction, *Soils and Foundations*, Vol.33, No.7, pp.57-64.

Japan Road Association: Highway Earthworks Series - Manual for Fill Works (fiscal 2010), 2010.

Kamei, T. and Enomoto, M. 1994:Wetting-induced Collapse Behavior of Compacted Silty Soil,J. of JSCE, No.505,Ⅲ-29,pp.97-103.

Lawton, E. C., Fragaszy, R J., and Hetherington, M. D. 1991: Review of wetting-induced collapse in compacted soil, Tech. Report No.9101, Univ. of Utah, Salt Lake City, Utah.

Lawton, E.C. fragaszy,r,j., and hardcastle.j,h.1989: Collapse of compacted clayey sand, *J.geotech. engrg.* ASCE. 115 (9) .1252-1267.

Tetsuo Abe et al. 2014: Strength characteristics of compacted fill dependent on changes in water content, *Proceedings of the 49th Japan National Conference on Geotechnical Engineering*, pp. 1013-1014.

Geotechnical and Geophysical Site Characterisation 5 – Lehane, Acosta-Martínez & Kelly (Eds)

Prediction of swelling potential of Sudanese clayey sand (SC) soils

H. Shammat
Dar Al Riyadh Consultants, Riyadh, Saudi Arabia

M. A. Osman
ESD Company, Khartoum, Sudan

ABSTRACT: Although some Clayey sand soils were classified as (SC) soil still have appreciable high values of Atterberg limits, swelling pressure (SP) and/or settlement as change in their moisture content. Many structures in Sudan were situated in areas dominated by (SC) soil reported damages. Consolidation test was conducted on clay-sand and sand-bentonite mixtures having different sand contents to study the expansive behavior of such (SC) soils. Soil parameters were calculated to study the impact of expansiveness on sandy soil structure and fabric. Test results were analyzed and presented in MS excel charts and verified by SPSS package to obtain simple prediction methods between soil parameters. Soil samples showed decreasing in volume change characteristics with increase of sand fraction. New prediction methods with good correlation coefficients, near to 1.0, were obtained between sand content, Atterberg limits and (SP) for clay-sand and sand-bentonite mixtures to predict the swelling potential of (SC) soils.

1 INTRODUCTION

Unified Soil Classification System (USCS) describes clayey sand (SC) soils varying to great extent in percentages of clay fraction and consistency limit (i.e. LL, PL and PI). These Soils of sand content greater than 50% and percentage finer less than 50% can have very high values of Liquid Limit (LL) and Plasticity Index (PI). Clayey sand (SC) soils are known to exist in different areas in Sudan, especially in the eastern and center of Sudan. These soils tend to have relatively high values of Atterberg limits and noticeable variations of volume change when its moisture content varied. The expansive clay in (SC) soil tends to increase with the increase of its colloidal contents. Although these soils are identified as clayey sand (SC) they can have considerable volume change characteristics that will affect the safety of the foundations and the floors of the buildings. The specifications for fill material under foundations and floors of building must comply with the requirement of strength and settlement limits. It's well known that expansive clay soil swells when wetted and shrinks when dry and usually results in ground movement and depending on its severity, swelling can cause structural damage to low-rise buildings (e.g. foundation movement, cracks in walls…etc.). Upon expansion, the soil exerts an upward pressure on foundation and structures founded on it.

The interaction between coarser and finer grain matrices affects the overall stress–strain behavior of (SC) soils (Monkula, Ozdenb, 2005). Soils that contain platy particles are more compressible than those composed entirely of bulky grains. In some models proposed for compression behavior of cohesionless soils such as those by Hardin (1987) and Pestana and Whittle (1995); effects of initial void ratio, relative density, particle shape, mineralogy, structure and applied stress conditions were mentioned. These factors were also prominent in the experimental researches related to the compression of sands (Yamamuro et al. 1996, Chuhan et al. 2003). Skempton (1985) indicated for the clayey soils that if the clay fraction is less than about 25%, the soil behaves much like a sand or silt, whereas residual strength is controlled almost entirely by sliding friction of the clay minerals when the fraction is above 50%. Georgiannou et al. (1990) concluded that up to a fraction of 20%, clay does not significantly reduce the angle of shearing resistance of the granular component.

Several factors can influence the swelling potential of clay soils; these factors include the amount and type of clay minerals, cation exchange capacities of clay minerals, availability of moisture, initial water content and other factors related to clay deposition history such as fabric and overburden pressures. Both gradation and grain shape affect the compressibility of a cohesionless soil (United States (US) Army 1992 - Field Manual FM 5-410). Therefore, gradation and grain shape are main factors in swelling behavior of a clayey sand soil.

2 MATERIALS AND SAMPLES PREPARATION

Sand-bentonite mixtures (i.e. artificial soil samples and clay-sand mixtures (i.e. natural soil samples) were used to clarify the effect of sand fraction on the volume change behavior of sand-clay mixture. Artificial soil samples were made by combining sodium bentonite with different standard sand contents. Natural soil samples are clayey soils mixed with standard sand in various ratios. The effect of increasing sand fraction on soil was determined on different types of clay minerals, i.e. sodium bentonite (pure montmorillonite) and highly expansive natural soil, and various mixing ratios.

Relatively high plastic clay soils were obtained from (Soba) district, south of Khartoum, Sudan. Tests pits were excavated, disturbed soil samples were obtained. Field moisture content and field density were recorded using the standard procedures. The samples have relatively high natural moisture contents (NMC) (ranging from 17% to 23%). Standard sand was washed and passed through #40 sieve (0.425 mm) and retained in #200 sieve (0.075 mm).

Percentage of bentonite in artificial samples by weight was varied from 10%, 15%, 20%, 25%, and 30% by weight. On the other hand, natural samples were mixed with standard sand in percentage of the total weight of mixture. Sand percentages varied from 17 % (as origin sample), 25%, 40%, 55%, 60%, and 65% from the total weight. Classification, compaction, Consolidation and swelling tests were performed. Laboratory testing carried out according to the BS 1337 - 1990 and classification of soil samples results were established in accordance to Unified Soil Classification System (USCS).

Table 1. Physical properties of testing materials

Material	LL	PL	PI	Specific Gravity
	(%)	(%)	(%)	
Standard Sand		None plastic		2.59
Sodium betonies	395	45	350	2.86

3 EXPERIMENTAL WORK RESULTS

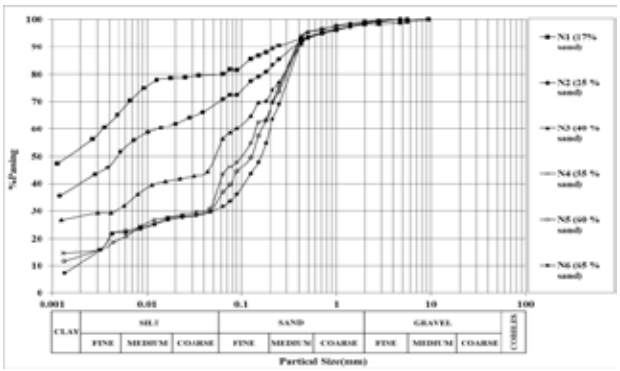

Figure 1. Grain size distribution curves for natural soils samples

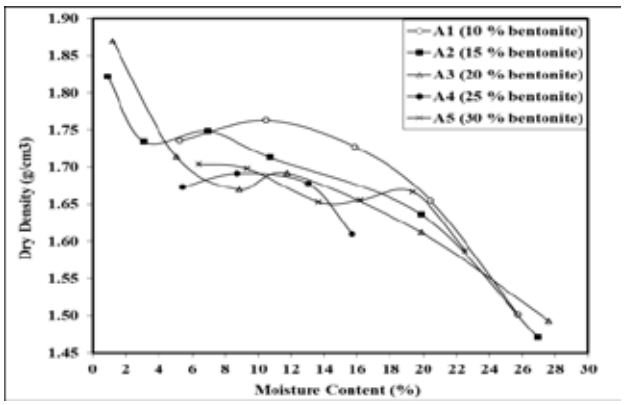

Figure 2. Moisture-density relationships (artificial soil samples)

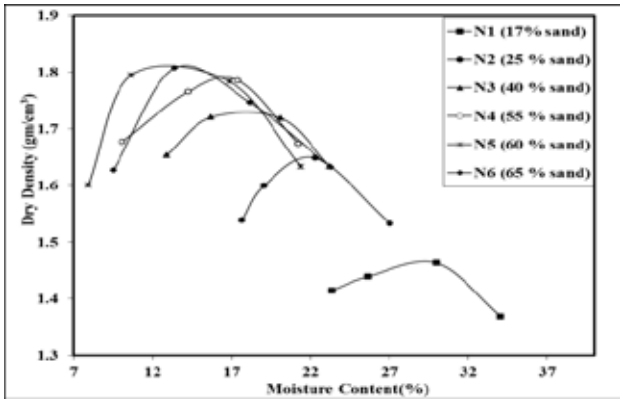

Figure 3. Moisture-density relationships (natural soil samples)

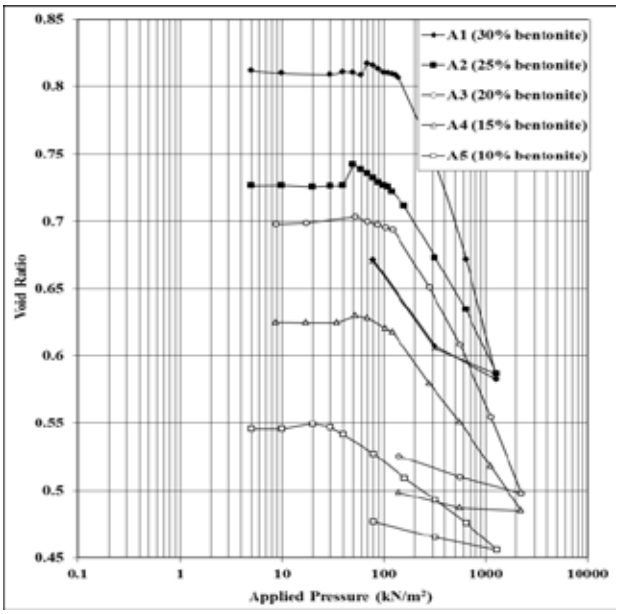

Figure 4. Consolidation curve results (artificial soil samples)

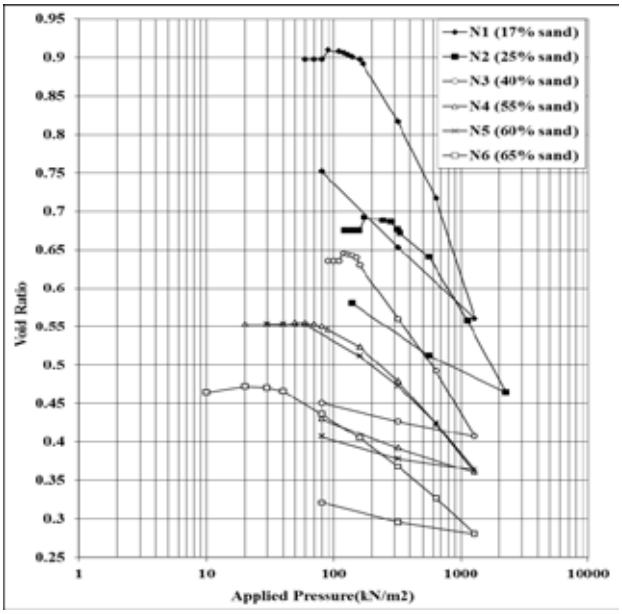

Figure 5. Consolidation curve results (natural soil samples)

Table 2: Index properties for artificial and natural soil samples

Soil code	Sand content	LL	PL	PI	LS*	Clay fraction (< 2μm)	Activity
(%)	(%)	(%)	(%)	(%)	(%)	(%)	
A1	70	115	21	94	19.3	30	3.13
A2	75	95	17	78	15.7	25	3.12
A3	80	78	20	58	12.4	20	3.0
A4	85	64	19	45	8.6	15	2.9
A5	90	46	21	25	5.0	10	2.5
N1	17	78	23	54	14.7	53	1.02
N2	25	77	25	52	13.6	40	1.30
N3	40	66	19	40	10.6	28	1.43
N4	55	52	18	34	7.9	16	2.13
N5	60	37	14	23	7.1	13	1.77
N6	65	35	14	21	6.2	11	1.91

* LS= Linear Shrinkage

Table 3: Compaction & swelling test results for artificial and natural soil samples

Soil code	Sand content	MDD*	OMC**	Free swelling	Swelling pressure
(%)	(%)	(g/cm^3)	(%)	(%)	(kN/m^2)
A1	70	0.48	0.81	0.296	0.079
A2	75	0.33	0.72	0.158	0.069
A3	80	0.24	0.70	0.188	0.023
A4	85	0.14	0.62	0.110	0.012
A5	90	0.06	0.54	0.066	0.018
N1	17	0.35	0.89	0.517	0.154
N2	25	0.32	0.67	0.309	0.079
N3	40	0.27	0.63	0.282	0.052
N4	55	0.18	0.55	0.210	0.033
N5	60	0.16	0.55	0.199	0.025
N6	65	0.14	0.47	0.154	0.024

* MDD = Max. Dry Density
** OMC = Optimum Moisture Content

Table 4: Consolidation test results for artificial and natural soil samples

Soil code	Sand content	Swelling potential	Initial void ratio	C_c	C_r
	(%)	(%)	(e_o)		
A1	70	0.48	0.81	0.296	0.079
A2	75	0.33	0.72	0.158	0.069
A3	80	0.24	0.70	0.188	0.023
A4	85	0.14	0.62	0.110	0.012
A5	90	0.06	0.54	0.066	0.018
N1	17	0.35	0.89	0.517	0.154
N2	25	0.32	0.67	0.309	0.079
N3	40	0.27	0.63	0.282	0.052
N4	55	0.18	0.55	0.210	0.033
N5	60	0.16	0.55	0.199	0.025
N6	65	0.14	0.47	0.154	0.024

4 ANALYSIS AND DISCUSSIONS

4.1 *Atterberge Limits*

Increasing bentonite content from 10% to 30% made LL and PI to increase from 46% to 115% and from 25% to 94% respectively (see Table 2). This is due to the mineralogy of sodium bentonite having physical properties almost dictated by the smectite minerals (Grim and Guven, 1978). In natural samples, Atterberg limits results showed that LL decreased from 78% to 35% and PI decreased from 54% to 21% (see Table 2). Soil sample designated (N4) showed high values of LL and PI despite the sand fraction is more than 50%. This soil sample presents the object of this study.

4.2 *Classification and identification of expansiveness*

Sand-bentonite mixtures were classified as having very high swelling potential, except samples (A4) and (A5) which showed high and medium swelling behavior, respectively. Four samples were classified as (CH) according to (USCS) and one sample classified as (CL) (i.e. A5 sample). Classification and identification of expansiveness for natural samples results were shown in table (5). Soil samples (N1) and (N2) were classified as having very high swelling potential soils and sample (N3) was classified as having high to very high swelling soil. Soil samples (N4), (N5) and (N6) with sand contents greater than 50%, represent (SC) soils. These were noted to have medium to high swelling behaviour. From Table (5), sample (N4) exhibits expansive soil with medium to high swelling potential from several classifications. Although soil sample (N4) contains sand content more than 50%, but significantly it has an expansive behaviour. This behavior attributed to mineralogy composition, particles shape, texture and particles size distribution of the sand-clay mixture.

Table 5: Classification and identification of expansiveness for natural soil samples

→ Soil Code / ↓ Classification	N1	N2	N3	N4	N5	N6
USCS classification	CH	CH	CH	SC	SC	SC
Skempton's method (1953)	N	N	A	A	A	A
Swelling potential (Chen, 1975)	VH	VH	VH	M	M	M
Potential expansiveness (Dakshanamurthy & Raman, 1973)	CV	CV	CH	CH	CI	CI
Swelling potential (Snethen, 1980)	VH	VH	VH	H	Mo	Mo
Potential expansiveness (Van der Merwe,1964)	VH	VH	VH	M	L	L
Degree of expansion (Holtz & Gibbs,1956)	VH	VH	H	M	M	M
Swelling potential (Seed,1962)	VH	VH	H	M	L	L

*Where:
CH = High plasticity clay
SC = Clayey Sand
N = Normal
A = Active
VH = Very high
H = High
M = Medium
CV = Very high swelling
CH = High swelling
CI = Medium swelling
L = Low swelling
Mo = Moderate

4.3 *Compaction test results*

Artificial soil samples results for compaction tests are shown in Table 3 and Figure 2. They showed increasing in OMC with increase of bentonite content. Santucci de Magistris (1998) was working with relatively low bentonite contents and reported that a general tendency for OMC to increase with high contents of bentonite.

Natural soil samples results present increasing in MDD with the increasing of sand fraction (see Table 3 and Fig. 3). It's postulated that the sand will fill the voids between soil grains and that will result increasing dry density. Many authors (Sorochan, 1991; Elarabi, 2004; Nelson and Miller, 1992) were conducted many experiments and concluded that the swelling rate increases when the density of soil is increased. From density results and conclusions of the mentioned authors it can be extracted that the problem of (SC) soil will come bigger when it is dense because this will increase the swelling rate of soil.

4.4 *Consolidation and swelling test results*

Swelling pressure (SP) results, of artificial soil samples, are directly proportional to PI and gave correlation coefficient value of 1.0 (see Fig. 6). This correlation indicated that a new equation can be derived to predict SP of sand-bentonite mixtures from PI. Good relationship was presented for PI results with C_c with correlation coefficient of 0.88 (see Fig. 7).

Generally, natural soil samples showed reduction in swelling and compressibility characteristics as the percentage of sand fraction was increased (see Tables 3, 5 and Fig. 5). The initial void ratio (e_o) decreased from 0.89 for sample (N1) to 0.47 for (N6) which indicated that sand grains fill the void of the clay (see Table 4). Very good correlation coefficient was obtained between LL, PI with SP (R^2= 0.96) (see Fig. 8). Samples (N4) and (N5) have almost the same values of initial void ratio, swell potential and (C_c) (see Table 4).

In expansive soils, larger change in moisture implies higher degree of volume change (swelling and settling) in soil structure. The influence of volume change on the consolidation characteristics of expansive soil is not similar to non-expansive clay soils. In non-expansive clays, it shows flatter e-log P curves (Mesfin Kassa, 2005). Whereas, the laboratory test results of artificial samples and some natural samples including soil sample (N4) have shown that the soil exhibit a steeper e-log P plot (see Figs 4 and 5). Consolidation is the property of the soil mass that is highly dependent on permeability which depends on the structural arrangement of soil particles. On the other hand, swelling is the property of the soil particle, which depends on the mineralogy of soil particle. In effect, both phenomena bring about volume change in the soil mass. As can be seen from the test results, the factors that affect the swelling characteristics of expansive soils (i.e. moisture content variation and density) have also affected the consolidation characteristics of expansive soil and consequently affect the characteristics of expansive (SC) soils.

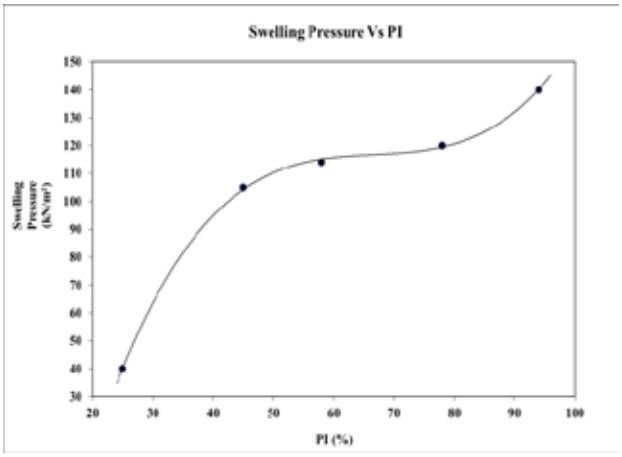

Figure 6. Relationship between SP and PI (artificial soil samples)

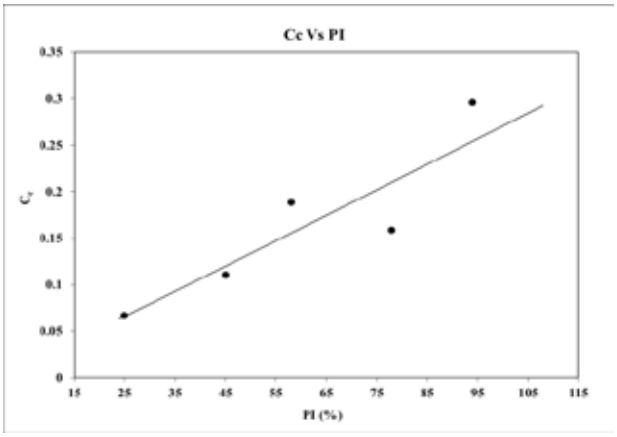

Figure 7. Relationship between C_c and PI (artificial soil samples)

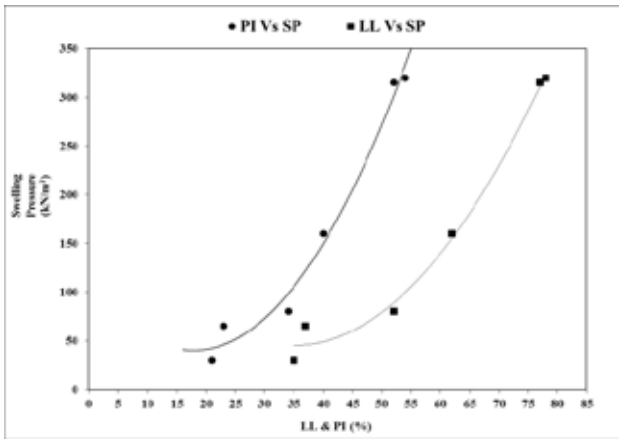

Figure 8. Relationship between SP, PI and LL (natural soil samples)

5 CONCLUSIONS

Mineralogy and density of clay are essential parameters to predict the behavior of (SC) soils and to classify its expansiveness. New methods were derived to predict the expansiveness of the clay-sand mixtures. All soil samples showed decreasing in volume change characteristics with increase of sand fraction. Increasing sand fraction from 7% to 10% for (SC) soil will give considerable strength and low volume change materials to use in construction.

6 REFERENCES

BS 1377 (1990), "Soils for civil engineering purposes: part 2: classification tests".

Chuhan, F.A., Kjeldstad, A., Bjorlykke, K., Hoeg, K. (2003), "Experimental compression of loose sands: relevance to porosity reduction during burial in sedimentary basins", *Canadian Geotechnical Journal* 40, 995–1011.

Chen, F.H. (1975), "Foundations on Expansive soils", *American Elsevier publ.*, New York, pp. 280.

Dakshanamanthy,V. & Rahman,V. (1973), "A simple method of identifying an expansive soil", *Japanese society of soil mech. and foundation engineering,* Vol. 13, pp. 97-104.

Elarabi, H (2004), "Factors influencing swelling behavior of expansive soils", *BRRI journal*, BRRI, University of Khartoum, Vol.6.

El turabi, M.A.D. (1985), "A study on expansive clay soil in Sudan", thesis submitted for the degree of M.Sc in civil engineering, Building and Road Research institute (BRRI), University of Khartoum.

Georgiannou, V.N., Burland, J.B., Hight, D.W. (1990), "The undrained behaviour of clayey sands in triaxial compression and extension", *Geotechnique*, Vol. 40 (3), pp. 431–449.

Grim, R. E. & Guven N. (1978), "Bentonites: Geology, Mineralogy, Properties and Uses", Elsevier Scientific Publishing Company, New York, pp. 256.

Hardin, B.O. (1987), "1-D Strain in Normally Consolidated Cohesionless Soils", *Journal of Geotechnical Engineering, ASCE*. Vol. 113, No. 12. pg 1449 – 1467.

Holtz, W. & Gibbs, J.J (1956), "Engineering properties of Expansive Clays", *Journal of the Soil Mech. and Foundation Div.*, American Society for Civil Engineers (ASCE), Transactions paper No. 2814, Vol. 121, pp. 641- 663.

Julio Esteban (2002), "Suction and volume changes of compacted sand-bentonite mixtures", thesis submitted for the degree of Doctor of philosophy (Ph.D) in Faculty of engineering, Imperial College of Science and Medicine, London University.

Monkul, M.M., Ozden, G. (2005), "Effect of intergranular void ratio on one-dimensional compression behavior", *Proceedings of International Conference on Problematic Soils*, International Society of Soil Mechanics and Geotechnical Engineering, Famagusta, Turkish Republic of Northern Cyprus, 3, pp. 1203–1209.

Nelson, J.D. & Miller, D.J. (1992), "Expansive soils: *Problem and practice in foundation and pavement engineering*", John Wiley & Sons, Inc, New York.

Pestana, J.M. & Whittle, A.J. (1995), "Compression Model for Cohessionless Soils" *Géotechnique*, Vol. 45 (4), pp. 611-631.

Osman, M.A. & Ali, E.M. (1984), "Construction expansive soils in Sudan", *Journal of construction Engineering and Management*, Vol. 110, pp. 359– 374.

Osman, M.A. & Hamadto, M.E.M (1987), "Identification & classification of expansive soils in arid and semi-arid regions", *Proceeding of the 9th Regional conference for Africa on soil Mechanics and Foundation Engineering, Lagos*, Vol. 9, pp. 113-116.

Skempton, A.W. (1953), "The colloidal "activity" of clays", *Proceedings the 3rd International conference on Soil Mechanics and Foundation Engineering, Zurich*, Vol. 1, pp 57-61.

Skempton, A.W. (1985), "Residual strength of clays in landslides, folded strata and the laboratory", *Geotechnique* Vol. 35 (1), 3–18.

Snethen, D. R. (1980), "Characterization of expansive soils using soil suction data", *Proceeding 4th International Conference on Expansive Soils*, American Society for Civil Engineers (ASCE), Vol. 1, pp. 54-75.

Sorochan, E.A. (1991), "*Construction of Buildings on Expansive Soils*", Publisher: Taylor and Francis.

United States (US) Army - Engineering school (1992), "Military soils engineering", *Field Manual FM 5-410*.

Van Der Merwe, D .H. (1964), "Prediction of heave from the plasticity index and percentage clay fraction of soils", *South African Institute of civil Engineers*, Vol. 6, pp. 103-107.

Yamamuro, J.A., Bopp, P.A., Lade, P.V. (1996), "One dimensional compression of sands at high pressures", *Journal of Geotechnical Engineering, ASCE*, Vol. 122 (2), pp. 147–154.

Theme 12. Design Using In-situ tests

Geotechnical and Geophysical Site Characterisation 5 – Lehane, Acosta-Martínez & Kelly (Eds)

Evaluation of Tip Resistance to Auger Drilling

G.G. Boldyrev & G.A. Novichkov
Penza State University of Architecture and Construction, Russia

ABSTRACT: Analytical solution for auger tip resistance in soils is presented. It involves several drilling parameters: torque, axial force, rotation speed, linear velocity. Tip resistance to auger drilling can be used to soil strata identification and to interpretation mechanical properties of soils in the same way as is done for cone penetration test.

1 INTRODUCTION

Cone penetration test (CPT) method is broadly applied to both soil strata identification and to evaluation of soil strength and deformation parameters. In the latter case correlation equations are applied between CPT data and laboratory test data (Robertson, 1983).

Drilling penetration method is, in our view, a more attractive method. Firstly, this method differs from CPT in that it is applicable both in clays and in sands as well as in coarse-grain and in frozen soils. Secondly, the method enables determination of soil Young modulus and shear force with no correlations applied. Also other soil parameters can be found by application of correlation equations.

2 EVALUATE THE TIP RESISTENCE

In order to evaluate the down-hole tip resistance to penetration F we applied solutions from published papers on auger soil cutting of soil or displacement of loose materials with auger conveyors (Zacny, 2007).

Figure 1 shows main parameters, measured during drilling tests. As is evident from Figure 1, unlike CPT drilling enables measuring penetration force (vertical load) Q (N), torque M_{rot} (Nm), drilling column weight G_1 (H) and soil weight on flanges G_2 (N), flanges tilt angle α (degrees), vertical displacement V (m) and angular frequency of revolution ω (rad/s).

Auger drilling efficiency depends on M_{rot}, Q and ω. Drilling practical experience prompts that rotation speed shall be roughly 100-300 rpm or 1.67-5 rad/s for different soils. The lower limit of rotation frequency is limited by soil lower displacement rate. Low frequencies allow drilling while viscous dense clays may require frequencies up to 300 rpm and higher. Sand can be drilled through at relatively low frequencies while viscous dense clays may need up to 300 rpm and more. In order to displace soil from the bits with smooth interface between cutting blades and auger spiral it is necessary to reciprocate the drill bit and to pour water in the hole. Maximum rpm is limited by the drill bit vibrations i.e., by purely technical drilling rig parameters in general.

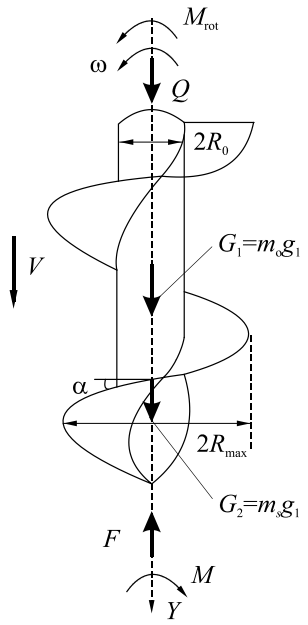

Figure 1. Parameters, measured during drilling penetration

Depending on geometrical parameters of the bit and its friction ratio over soil there exists a minimum drill bit rotation rate that ensures non-stop soil movement up to the surface. This critical rotation speed can be found as follows.

As is known soil moves against the auger. The drilled soil moves to the auger flanges and due to centrifugal forces presses against the borehole cylindrical wall. The friction and gravity forces somewhat slow down a soil particle movement against the auger surface i.e. it rotates with lower angular speed than that of the auger.

The final equation for minimum auger rotation frequency, required to lift soil is as follows (Zacny, 2007):

$$\omega_{\text{rot}} \geq \sqrt{\frac{g\left(\sin\alpha + \tan\varphi_{ag}\cos\alpha\right)}{K_1 R_{\max}\tan\varphi_s\left(\cos\alpha - \tan\varphi_{ag}\sin\alpha\right)}} \quad (1)$$

or in rotations per second (Hz):

$$N_{\text{rot}} \geq \sqrt{\frac{g\left(\sin\alpha + \tan\varphi_{ag}\cos\alpha\right)}{4\pi^2 K_1 R_{\max}\tan\varphi_s\left(\cos\alpha - \tan\varphi_{ag}\sin\alpha\right)}} \quad (2)$$

where $\tan\varphi_s$ = friction coefficient soil-against-soil; $\tan\varphi_{ag}$ = friction coefficient soil-against-steel; and K_1 = soil-against-soil friction ratios.

In order to analyze the above equations there were staged field tests. The hole was drilled by a continuous 135 mm external diameter auger, equipped with a 151 mm diameter three-piece bit. The drilling parameters were measured with a automatic measuring system.

The analyses borrow parameters: K_1, $\tan\varphi_s$ and $\tan\varphi_{ag}$ were assumed constant, the latter were determined from tests in flat shear conditions. Unit weight of soil γ_s is accepted as average value for the borehole from results of laboratory tests. Auger geometrical parameters $R_{\max}$ and R_0, α and mass auger m_0 and the soil m_s were directly measured.

Figure 2 shows two graphs: bit rotation frequency versus depth dependence and the dependence, calculated as per equation (2), of minimum necessary rotation frequency for successful delivery of soil to the surface.

In order to determine tip resistance F to descent into the borehole use the schematic on Figure 1.

The sum of all forces projections on vertical axis $\sum Y = 0$:

$$Q + m_s g + m_0 g + \\ + \left(\tan\varphi_{ag} m_s g\cos\alpha + \tan\varphi_{ag}\tan\varphi_s m_s R\omega^2\sin\alpha\right)\times \\ \times\sin\alpha K_1 - F = 0. \quad (3)$$

Only for F:

$$F = Q + g\left(m_s + m_0\right) + \tan\varphi_{ag} m_s \times \\ \times\left(g\cos\alpha + \tan\varphi_s R\omega^2\sin\alpha\right)K_1\sin\alpha. \quad (4)$$

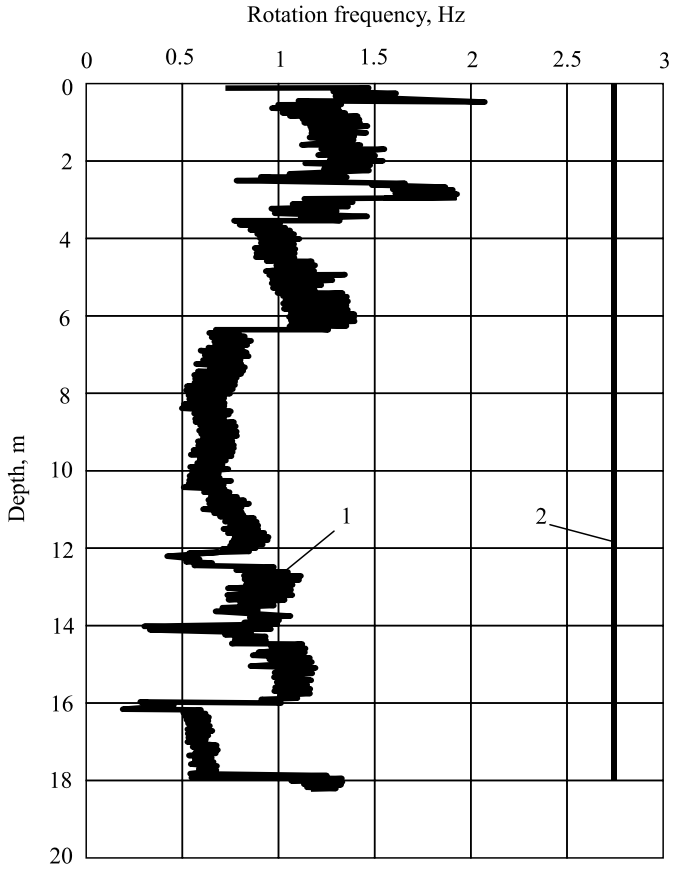

Figure 2. Bit rotation frequency profile: 1 – measured rotation frequency; 2 – minimal analytic rotation frequency

Substitution of test data in equation (3) yielded the graph of dependence (Figure 3) of the third term share in equation (3) in the overall sum for F.

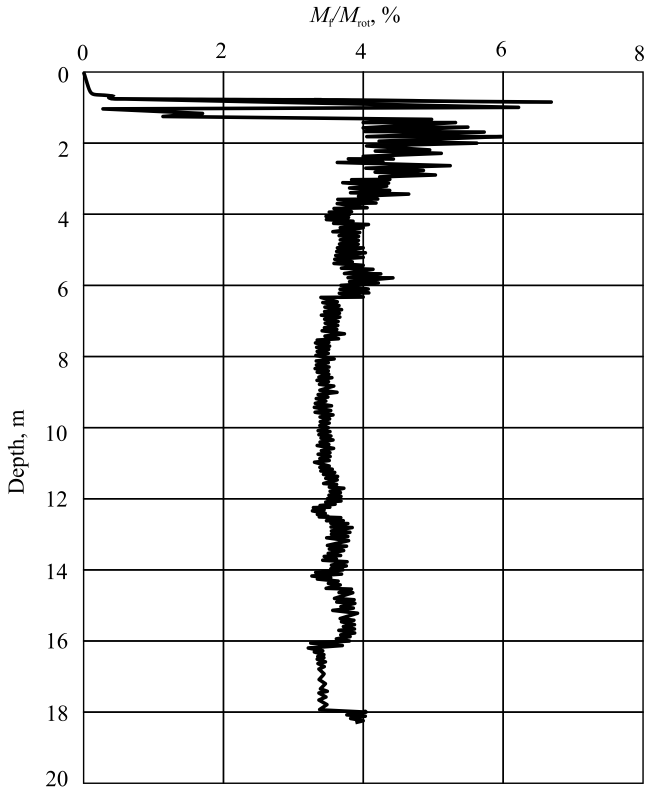

Figure 3. Share of the third term in equation (4) in the total sum at rotation frequency 0.5÷1.5 rps

Diagram on Figure 3 shows that the share of the third term at rotation frequency up to 1.5 rps is not essential and does not exceed 4% at most for coarse sand while frequency 3 rps this share would have been greater than 50 %. However, because of small share of the vertical load work in the total work of drilling the soil (see Figure 4), the contribution of coefficients selection is negligible with plotting full power, spent on drilling.

In view of this it is not correct to compare the value of tip specific soil resistance under CPT probe with the specific downhole soil resistance under the cone, because we have a different soil destruction type here. In the first case the probe is sunk without rotation while in the second case it mainly sunk due to auger rotation with practically no axial force. It is illustrated by Figure 4, showing that drilling of soil is mostly effected by torque. During drilling operation soil is "cut'' by the bit teeth at a certain value of the vertical bit pressure on soil. The bit sinks downhole per one rotation while the value of the applied torque depends on the soil properties and the bit geometry.

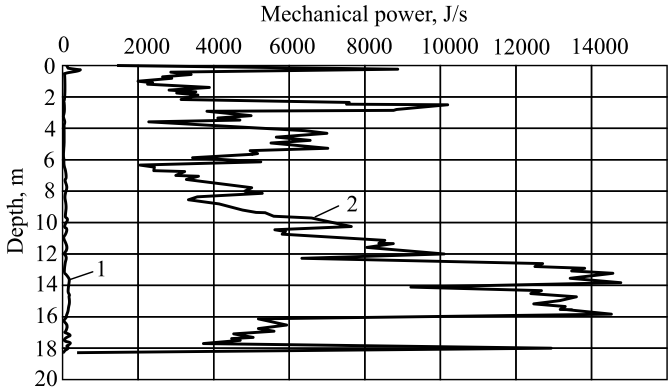

Figure 4. Vertical load power for drilling soil by the vertical load (1) and torque (2)

The dependence of the tip resistance (pressure) is more universal for augers of all dimensions:

$$P = \frac{F}{\pi R_{\max}^2} = \frac{Q + g\left(m_s + m_0\right)}{\pi R_{\max}^2} + \\ + \frac{\tan\varphi_{ag} m_s \left(g\cos\alpha + 4\pi^2 N^2 \tan\varphi_s R_{\max} \sin\alpha\right) K_1 \sin\alpha}{\pi R_{\max}^2} \quad (5)$$

Figure 5 shows two relationships: the first (1) one was obtained by direct measurements while the second (2) one was calculated as per equation (5). With the exception of the initial stage, the borehole was drilled with no applied axial load from the drilling rig but just under the weight of the bit and soil on it and also due to reaction force from soil displacement upward.

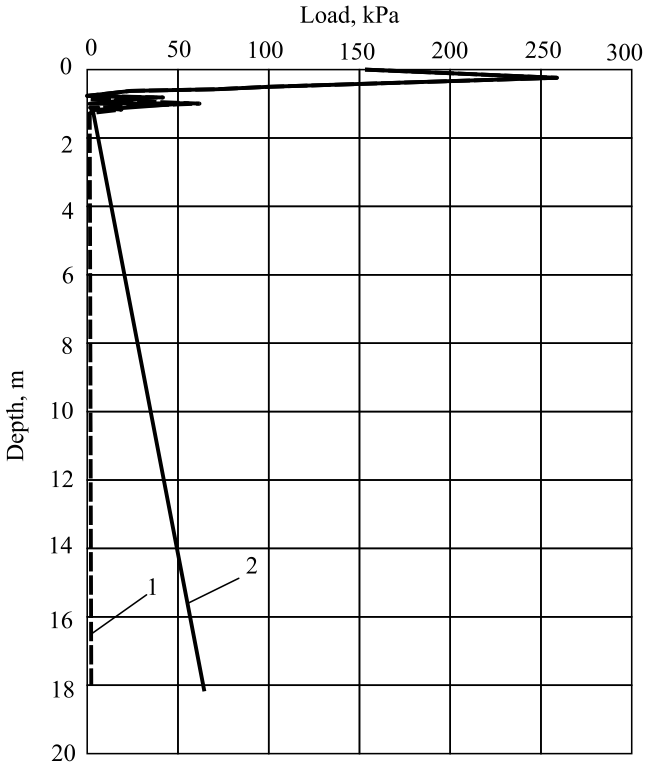

Figure 5. Vertical load Q (1) and tip resistance P (2) profile

The value of the downhole torque M can be found from the moments equilibrium condition:

$$\sum M = M_{\text{rot}} - M_f - M = 0, \quad (6)$$

where M_{rot} = measured torque, created by the drilling rig; M = torque share for soil destruction downhole; M_f = drilling bit friction force moment against borehole wall, which is found from the following expression:

$$M_f = \tan\varphi_{ag} m_s \left(g\cos\alpha + \tan\varphi_s R_{\max}\omega^2 \sin\alpha\right) \times \\ \times K_1 \cos\alpha R_{\max}. \quad (7)$$

Thereby the torque M can be calculated from equation:

$$M = M_{\text{rot}} - \tan\varphi_{ag} m_s \times \\ \times\left(g\cos\alpha + \tan\varphi_s R\omega^2 \sin\alpha\right) K_1 \cos\alpha R_{\max} \quad (8)$$

By inserting data in equation (7) there was found the dependence of the soil friction torque against the borehole wall M_f over the torque, generated by the drilling rig M_{rot}. The main conclusion from this equation consists in that if soil is lifted to the surface along the auger then drilling parameters measurement on the surface yield results close (2-3% at Figure 1.5 rps and 8-10% at 3 rps) to the values, measured downhole (Figure 6). Hence, drilling parameters measured on the surface are identical with just a minor error.

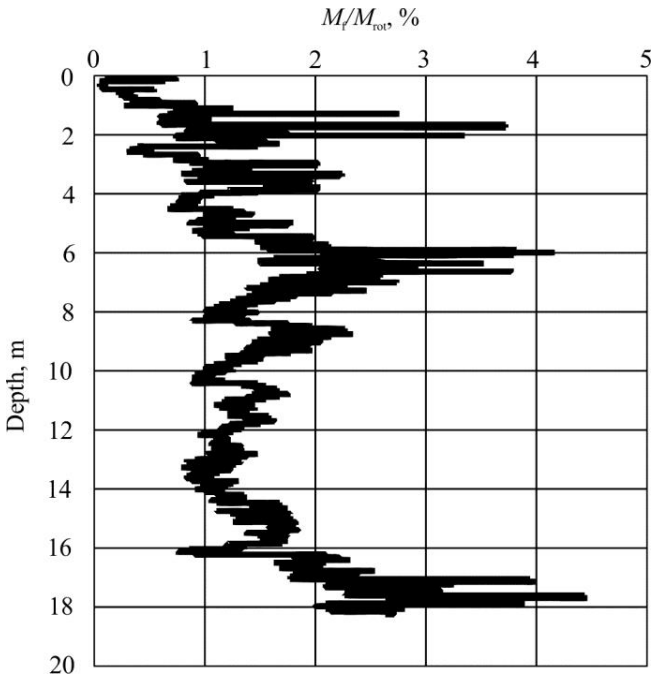

Figure 6. Ratio of soil borehole friction torque M_f against borehole wall to drilling machine torque M_{rot}

One of the parameters, measured in drilling probing, is a mechanical power of the rotating load at the current drilling depth, kJ/s:

$$A = 2\pi M\omega, \tag{9}$$

where M= current torque; ω= drill bit rotation frequency.

This parameter relates to work per second (power), and is called specific work. Analysis of test results showed formation of "gaskets" i.e., uncontrollable deviations of profiles of work, spent on soil drill-outs. As is seen on the torque work profile (Figure 7, curve 1), the torque increases during submersion of the current auger (intervals AB and CD, and after its cleaning it drops down (intervals BC and DE). Evidently, it is not just a coincidence, and these "false" spikes of readings are caused by formations of "gaskets" and soil transportation stops. Torque work profiles calibration enables accounting for these deviations. The true value of work are the values, obtained at the beginning of the auger submersion after cleaning (Figure 7, curve 2).

Deep drilling parameters are listed at the beginning of this paper. They are used to determine specific energy, which is the amount of work, necessary for drilling unit volume of soil (Teale, 1965):

$$E = \frac{Q}{A} + \frac{M\omega}{Av} \tag{10}$$

where Q = axial force, applied to the tool in the downhole, including weight of the drilling string, weight of tool and rotating head together, axial force, applied to the drill string; v = drill tool translation movement velocity.

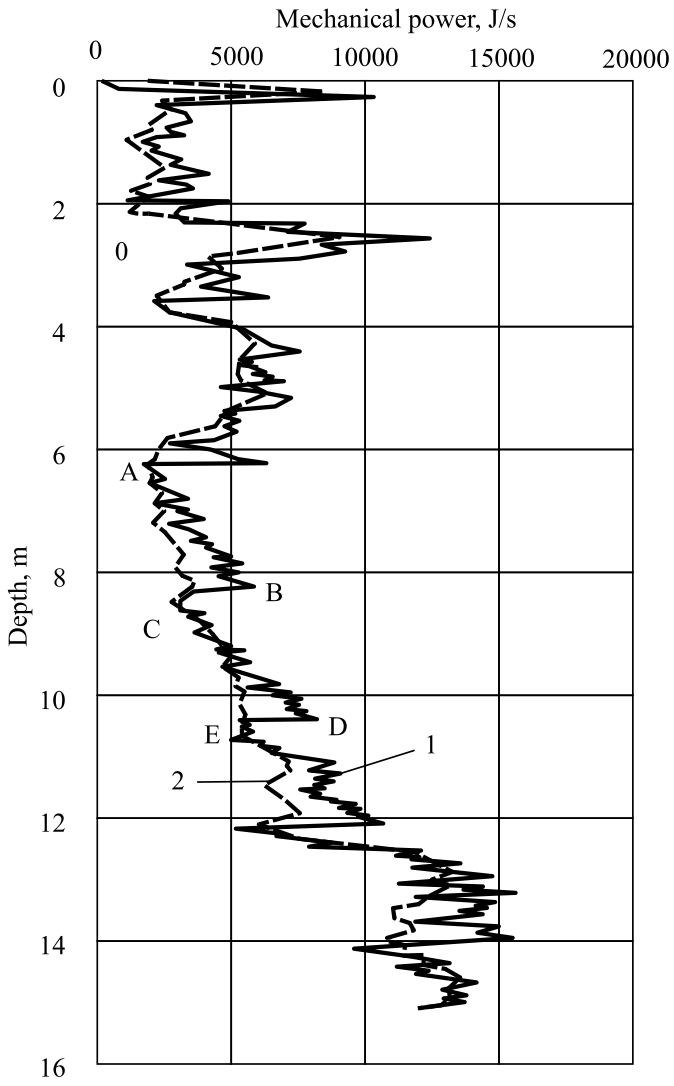

Figure 7. Mechanical power

Specific energy index is used to optimize drilling of deep vertical, slated and horizontal holes. Penetration rate depends on several factors, including the load on the tool, rotation rate, pressure gradient in the bottom hole, drilling mud, rock strength, etc. However, specific energy index is not used in engineering geology in spite of the fact that the similar holes are drilled, but not so deep.

Figures 4 and 5 show that the role of the first addend in equation (10) on auger hole drilling is negligible as compared with the work, produced by torque. In this case equations (9) and (10) coincide. On the Figure 8 there are shown two curves, characterizing dependence of the specific work dependence on specific energy versus depth. Both graphs are almost identical and could be applied to determine the thicknesses of strata of different strengths.

Drilling parameters variation are due to soil properties. For the given type of soil or rock variations of just one of the recorded parameters are decisive. However, although it helps interpretation it is possible that two different types of soils would have a similar domineering parameters. Therefore, it is very important to do initial calibration after completion at

least one hole near sampling holes, and then to compare the values of parameters with lithology, obtained from holes for sampling monoliths. In the absence of holes for sampling it is more difficult to identify the formation nature. This problem is solved easily for hole drilling with hollow full-bore augers with sampling monoliths with a thin-wall sampler.

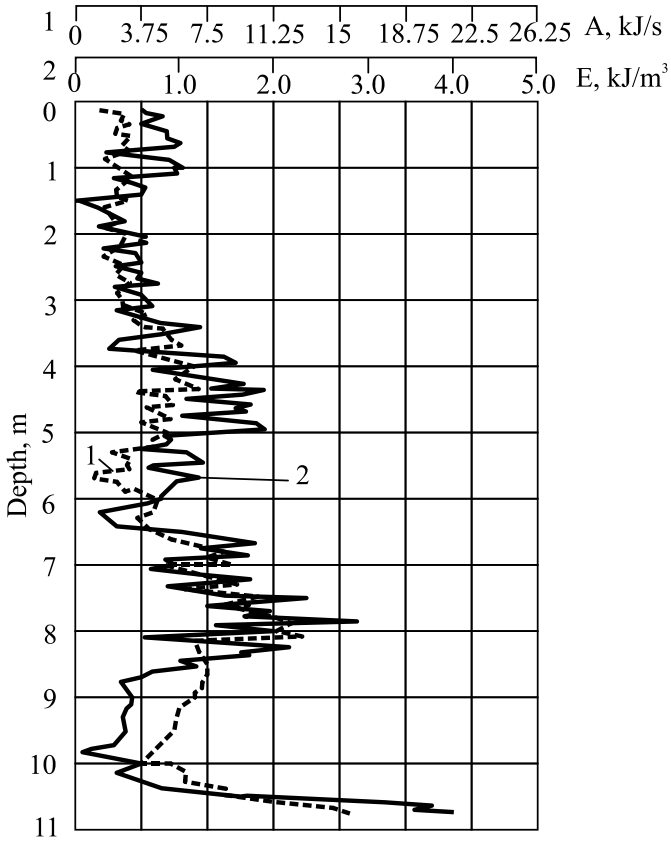

Figure 8. Specific work (1) and specific energy (2) in the course of hole drilling

3 CONCLUSION

Down-hole tip resistance is the sum (1) of the vertical load on the bit from the machine, weight of auger with the captured soil (2) and the reactive force due to soil transportation that depends on soil-soil and soil-auger materials interaction, flanges inclination angle (3). The third term can be from 1 to 30 % and more, depending on friction ratio, rotation frequency and inter-flange space filling ratio.

If soil is successfully displaced along the auger with no “gaskets” formed, then it can be assumed with less than 10% error that drilling parameters surface measurement produce realistic data on work, spent on soil drilling in the down-hole.

The portion of work for soil drilling per unit time, performed by the vertical load is much less than that by the torque (less than 5 % of the total sum).

Specific work or specific energy indices can be applied to determine soil layers thicknesses, having different strengths.

Tip resistance to auger drilling can be used to interpret mechanical properties of soils in the same way as is done for CPT. In order to do it available correlation relationships between tip resistance and soil stiffness/strength parameters can be applied.

4 REFERENCES

Robertson, K.E. & Campanella R.G. 1983. Interpretation of cone penetration test. Part 2. Clay. *Canadian Geotechnical Journal* 20(4): 734–745.

Zacny K.A. & Cooper G.A. 2007. Methods for cuttings removal from holes drilled on Mars. *The International Journal of Mars Science and Exploration* (3): 42-56.

Teale, R. 1965. The Concept of Specific Energy in Rock Drilling. *International Journal of Rock Mechanics* (2): 57-73.

Geotechnical and Geophysical Site Characterisation 5 – Lehane, Acosta-Martínez & Kelly (Eds)

Characterisation of a Norwegian Quick Clay using a Piezoball Penetrometer

N.P. Boylan
Norwegian Geotechnical Institute (NGI), Perth, Australia (formerly of COFS, UWA)

A. Bihs
Department of Civil and Transport Engineering, Norwegian University of Science and Technology (NTNU), Trondheim, Norway

M. Long
School of Civil Engineering, University College Dublin (UCD), Dublin, Ireland

M.F. Randolph
Centre for Offshore Foundation Systems (COFS), University of Western Australia (UWA), Perth, Australia

S. Nordal
Department of Civil and Transport Engineering, Norwegian University of Science and Technology (NTNU), Trondheim, Norway

ABSTRACT: The piezoball, or ball penetrometer with pore pressure measurement, was developed for assessing the geotechnical properties of soft soils, particularly soft seabed sediments where the traditional cone penetrometer can have limitations. The measurement of pore pressure during this test can be beneficial for understanding the soil drainage conditions during penetration and thus assist the interpretation of the soil type and in-situ state. In addition, dissipation tests, where the pore pressure decay with time is monitored during a pause in penetration, can be used to assess the consolidation properties of the soil. In order to add to the experience base of piezoball testing in different soil types, testing was conducted at the Tiller quick clay site near Trondheim, mid-Norway. This paper presented the results of this testing with particular focus on the pore pressure response during penetration and the interpretation of consolidation properties from dissipation tests.

1 INTRODUCTION

The spherical ball penetrometer is increasingly being used for characterising soft seabed sediments, particularly the upper metres of the seabed, where the traditional cone penetrometer may prove inadequate. An enhancement of this device, referred to as a piezoball, incorporates a single or multiple pore pressure sensors on the surface of the ball to obtain parameters in addition to the penetration resistance, thus enabling estimation of the consolidation properties of soil. In recent years, research has focused on the interpretation of pore pressure measurements during ball penetration and the relationship with geotechnical parameters. Multiple experimentally based studies (e.g. Boylan et al. (2007, 2010), Colreavy et al (2016), DeJong et al (2008) and Low et al. (2007)) and numerical based studies (Mahmoodzadeh et al., 2015) have been carried out examining this topic. Experience to date has predominantly been in soft clays and silts of low to medium sensitivity. This paper describes research carried out using the UWA piezoball at the Tiller quick clay site, near Trondheim, Norway. The material at this site is characterised by its high shear strength sensitivity, and thus provides useful insight into the measured piezoball response in these soils and its relationship to geotechnical parameters. The paper examines the performance of the piezoball at this site and with particular focus on the pore pressure response during testing.

2 UWA PIEZOBALL PENETROMETER

For this research, a piezoball penetrometer was developed in-house at The University of Western Australia (UWA) (see Fig. 1). The ball has a diameter (D_b) of 60 mm and is connected to a reduced shaft section (d) of 20 mm diameter which results in shaft to penetrometer area ratio (A_s/A_p) of 0.11. The reduced shaft section is 185 mm long before tapering out to the standard rod diameter of 35.7 mm. This reduced shaft length is to minimise the migration of the excess pore pressures generated by the taper to the pore pressure field around the ball.

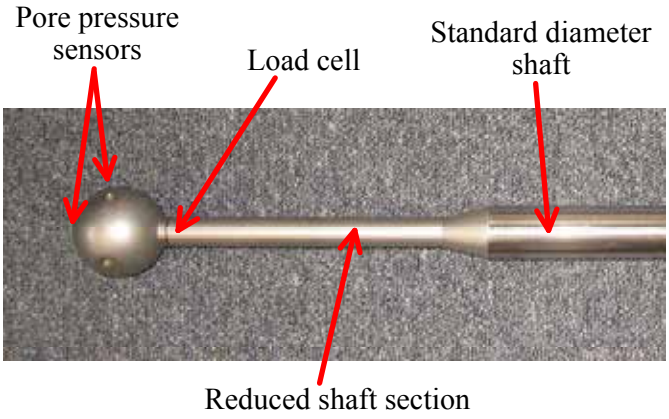

Figure 1. UWA piezoball penetrometer

On the ball, the pore pressure is measured simultaneously at both the tip (u_{tip}) and the mid-height (u_m), or equator of the ball. At the tip position there is a single pore pressure filter while at the mid-height there are four filter position located at 90° to each other. At each filter position, the pore pressure is measured by miniature total stress transducers (Kyowa PS-10KD) which are located in a recess close to the surface of the ball. The recess allows for a small fluid filled cavity covered by a porous high-density polyethylene (HDPE) filter which is flush with the surface of the ball. The locating of the sensor close to the surface of the ball is to minimize problems saturating the ball and ensures fast response times at the pore pressure filter locations.

The penetration and extraction resistance of the ball is measured by a load cell located directly behind the ball within the reduced shaft section. The load cell is a strain gauged section, fitted with a double full bridge of strain gauges and includes temperature compensation. The ambient temperature is also measured by a thermistor located alongside the load cell. The inclination of the ball during testing is monitored by an inclinometer within the standard diameter shaft section above the ball.

3 TILLER SITE

The Tiller site, which is locally referred to as Kvenild, is located to the south-east of Trondheim on the west coast of Norway. The site has been a research site of the Norwegian University of Science and Technology (NTNU) since the early 1980s due to the presence of a uniform deposit of highly sensitive clay and has been the subject of several soil characterization studies (see Table 1 of Gylland et al (2013) for a summary). Gylland et al. (2013) provide a detailed description of site and the geotechnical properties of the Tiller clay. Thus, only a brief description is provided in this paper.

Tiller clay is a marine clay having previously been below sea level during the last glaciation. The melting of the glaciers led to a post-glacial rebound of the land such that the site is now + 125 m above the present sea level. Since that time, the leaching of salt in the pore water of the clay has led to a situation whereby the clay has a high shear strength sensitivity and upon disturbance can transform to a fluid-like state.

Figure 2 shows the soil profile alongside data for the fall cone sensitivity (S_t) with depth. The fall cone sensitivity data has been obtained from a number of investigations since the early 1980's and the details are reported in Gylland et al (2013). Above 2 m, which is the lowest recorded level of the water table, the soil consists of a stiff clay crust layer. This is underlain by a predominantly lightly over-consolidated sensitive clay which transitions at a depth of approximately 8 m from a low to high sensitivity (i.e. $S_t > 30$) clay, into a quick clay. The definition of a quick clay is according to NGF (1982), which classifies it for conditions where the remoulded strength ($s_{u\text{-}rem}$) < 0.5 kPa. Within the quick clay deposit, sensitivity values of many hundreds are recorded, which indicate that the clay can transform dramatically into a near liquid state when disturbed. In all layers, the soil, which has an average clay content of 38%, is described as a low plasticity clay, having an average plasticity index (I_P) of 6.3%. Liquidity indices (I_L) are an average of 2 in the low-high sensitivity clay layer above 8 m, increasing to an average of 4 in the quick clay layer. The water content averages 38% and is relatively uniform with depth for the clay between 2 m and 20 m b.g.l.

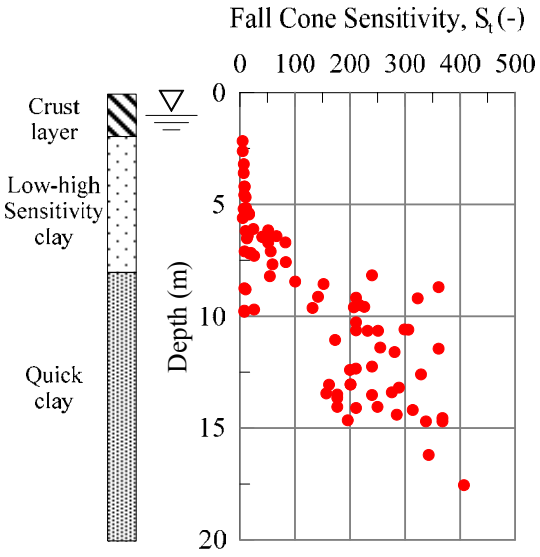

Figure 2. Soil profile and fall cone sensitivity

4 PENETROMETER TESTING

4.1 Equipment and Procedures

In-situ testing was carried out at the Tiller site using both a standard 10 cm^2 piezocone (CPTU) and the

piezoball penetrometer described in Section 2. Prior to each test, the test locations were predrilled to between 1 m and 2 m b.g.l. through the surficial material. From examination of the predrilled holes, the water table was found to be within 1 m of the surface.

For the piezocone testing, the procedures and results have been reported by Bihs et al. (2012). For the piezoball tests, the ball was saturated by immersing the ball in a container of glycerine. A syringe was used to ensure no air bubbles remained in the fluid cavities on the surface of the ball and the filters were then inserted. A latex membrane was placed over the ball to maintain saturation prior to each test commencing. At the beginning of each test, the penetrometer was lowered into the borehole and allowed to equilibrate in the ground water. When the sensor readings reached equilibrium, zero readings were taken and the test commenced. Penetration and extraction were conducted at the standard rate of 20 mm/sec throughout. In a number of tests, dissipation tests were performed, whereby the penetration of the ball was halted at a particular depth, the rods clamped, and the decay of the pore pressures recorded. During each piezoball test, at least one cyclic penetrometer test was carried out to evaluate the symmetry of penetration and extraction resistance and allow the data to be re-zeroed if necessary. At the end of each test, zero readings of all sensors were taken for comparison to the readings taken at the beginning of the test.

4.2 Data Interpretation

For the piezocone tests, the net resistance (q_{net}) was calculated by correcting the measured cone resistance (q_c) for unequal pore pressure effects and overburden resistance using (Lunne et al, 1997):

$$q_{net} = q_t - \sigma_{v0} = q_c + (1-\alpha)u_2 - \sigma_{v0} \quad (1)$$

where q_t = corrected cone resistance, α = unequal area ratio of the cone (0.61 in this case) and u_2 = total pore pressure measured at the shoulder position behind the cone. The pore pressure parameter from piezocone tests (B_q) was calculated from:

$$B_q = \frac{u_2 - u_0}{q_{net}} = \frac{\Delta u}{q_{net}} \quad (2)$$

where u_0 = ambient pore pressure. For the piezoball tests, the net ball resistance (q_{ball}) was calculated by correcting the measured resistance (q_m) using the following expression (Chung & Randolph, 2004):

$$q_{ball} = q_m - [\sigma_{v0} - (1-\alpha)u_0]\frac{A_s}{A_p} \quad (3)$$

where α = unequal area ratio of the piezoball (0.85 in this case). The pore pressure parameter from piezoball tests (B_{ball}) was calculated for the pore pressure measured at the mid-height (u_m) and the pore pressure measured at the tip (u_{tip}) using the following expressions:

$$B_{ball-m} = \frac{u_m - u_0}{q_{ball}} = \frac{\Delta u_m}{q_{ball}} \quad (4)$$

$$B_{ball-tip} = \frac{u_{tip} - u_0}{q_{ball}} = \frac{\Delta u_{tip}}{q_{ball}} \quad (5)$$

For the mid-height pore pressure, u_m represents the average pore pressure measured by mid-height sensors.

5 RESULTS AND DISCUSSION

5.1 Piezocone – Penetration Response

Figure 3 shows a typical piezocone test conducted at the Tiller site, in terms of both the corrected (q_t) and net cone resistance (q_{net}), excess pore pressure (Δu) and the pore pressure parameter (B_q). The net cone resistance initially reduces after penetration through the base of the crust. It then reaches a relatively uniform value of 400 kPa in the sensitive clay layer above 8 m, before increasing with depth at an average rate of ~ 40 kPa/m in the quick clay layer. Through penetration in the sensitive clay and quick clay layers, the excess pore pressure increases relatively linearly with depth from ~ 200 kPa at 2 m b.g.l. at a rate of ~ 25 kPa/m. B_q values increase from 0.5 to 0.9 in the sensitive clay layer and relatively uniform in the quick clay layer lying between 0.9 to 1. The trend of an increasing B_q with the soil sensitivity is consistent with the trends reported by Karlsrud et al (2005). A B_q ~ 1 is commonly used to identify quick clay layers in Norway.

5.2 Piezoball – Penetration Response

Figure 4 shows the results of four piezoball tests conducted at the Tiller site. The results are shown in terms of the net ball resistance (q_{ball}), the excess pore pressures at the mid-height and tip (Δu_m & Δu_{tip}) and the pore pressure parameter at these positions ($B_{ball\text{-}m}$ & $B_{ball\text{-}tip}$). Examining the results, the net ball resistance initially reduces from ~ 500 kPa in the crust layer to ~ 200 kPa in the upper portion of the sensitive clay layer and tends to reduce further towards the base of the layer where the soil sensitivity increases. The lowest ball resistance of ~ 140 kPa at the top of the quick layer before increasing at a rate of ~ 15 kPa/m. Overall, the ratio of ball to

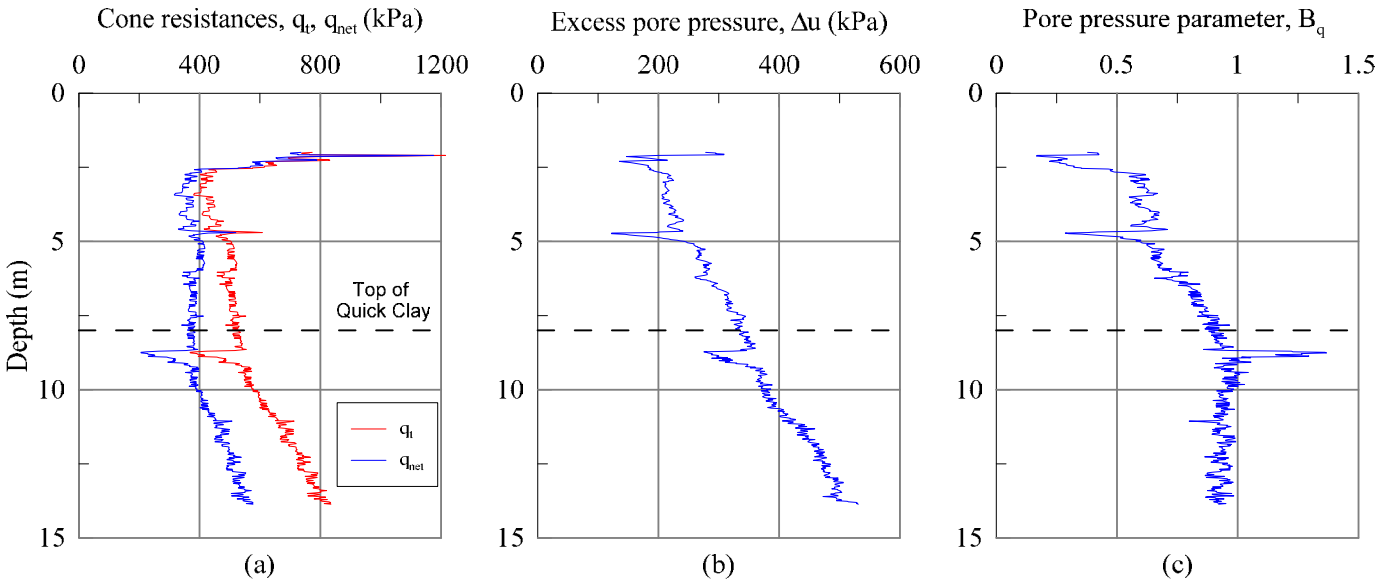

Figure 3. Piezocone test result (a) Cone resistances (b) Excess pore pressure (c) Pore pressure parameter

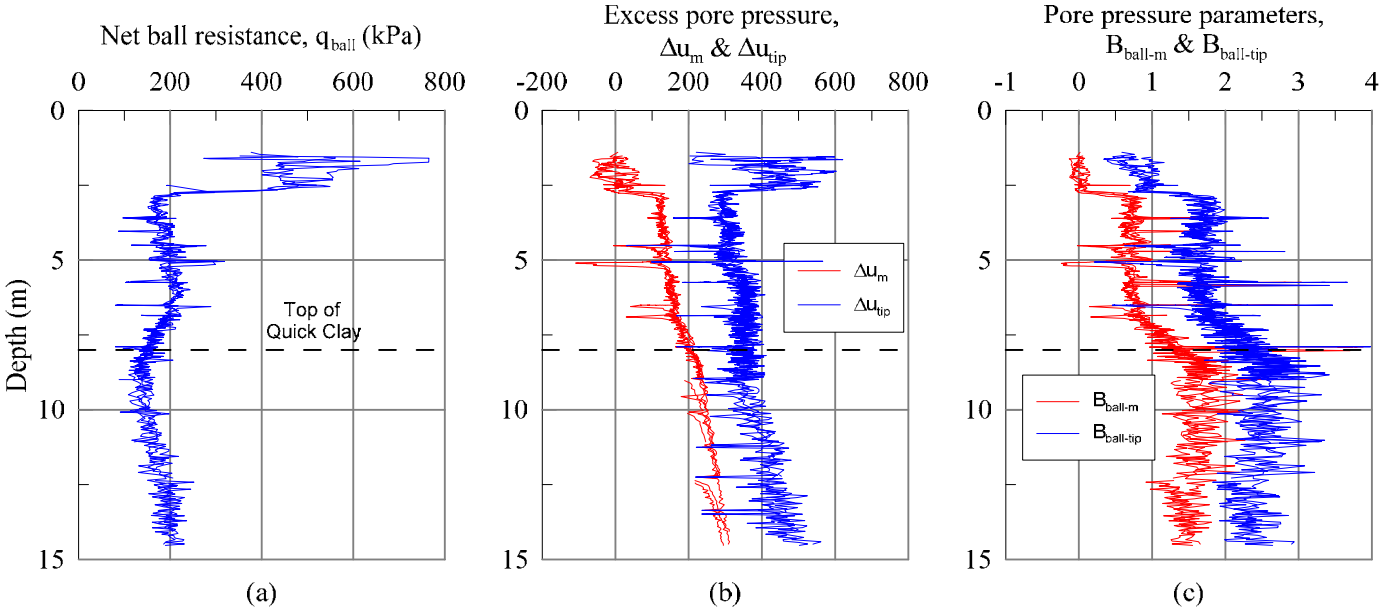

Figure 4. Piezoball test results (a) Net ball resistance (b) Excess pore pressures (c) Pore pressure parameters

cone net resistance (q_{ball}/q_{net}) is between 0.3 to 0.5 in the sensitive clay and quick clay layers. The low q_{ball}/q_{net} ratio is perhaps surprising, but consistent with previous studies in high sensitivity clays. DeJong et al. (2012) report q_{ball}/q_{net} ratios of 0.5 to 0.7 in sensitive Canadian clays (S_t range of 33 to 85). The lowest ratios here are for the zone of quick clay, with S_t between 100 and 350, so showing a consistent trend. The main reason for such low ratios is the greater degree of remoulding, and hence lower average shear strength during initial penetration, for full-flow penetrometers compared with a cone penetrometer (Osman & Randolph, 2014). In addition, the insertion of the ball results in lower resistances being generated as the soil is able to flow around the penetrometer, while in the case of the cone this does not occur.

During penetration the excess pore pressure at the mid-height position (Δu_m) is close to zero and slightly negative in the crust layer while the tip position (Δu_{tip}) is strongly positive. As the ball penetrates into the sensitive clay layer, positive excess pore pressures are measured at both the mid-height and tip positions and increase linearly with penetration. In the sensitive clay layer, the ratio of mid-height to tip pore pressure ($\Delta u_m/\Delta u_{tip}$) is in the range 0.4 to 0.5 and increases to 0.6 to 0.7 in the quick clay layer. The difference between the response in the crust layer and the sensitive/quick clay layers at the two filter locations reflects the soil in-situ state, its sensitivity and the stress changes that occur at the relevant positions on the ball during penetration. At the tip position, the soil is in compression at all times and thus positive pore pressures are measured in all layers. At the mid-height position, the soil is subjected to shear stresses and the response depends on the state of the soil and the shear stress level. In the crust layer, the heavily overconsolidated nature of the soil causes the soil to dilate when sheared and thus low and negative excess pore pressures are in-

duced. In contrast, in the sensitive and quick clay layers, the normally to lightly overconsolidated nature of the soil results in positive excess pore pressures during penetration in these layers.

The corresponding pore pressure parameters for the piezoball are shown on Figure 4c. Values of $B_{ball\text{-}m}$ are close to zero in the crust layer, lie between 0.5 and 1 in the sensitive clay layer and increase to between 1 and 2 in the quick clay layer. In contrast, $B_{ball\text{-}tip}$ values are between 0.5 and 1 in the crust layer, between 1.3 and 2 in the sensitive clay layer and between 2 to 3 in the quick clay layers. Thus compared to the cone, ratios of $B_{ball\text{-}m}/B_q$ are between 0.8 and 1.7 throughout the sensitive and quick clay layers. Ratios of $B_{ball\text{-}tip}/B_q$ are between 2 to 3 in the same layers.

5.3 Piezoball – Dissipation Tests

To assess the consolidation properties of the Tiller clay, a number of dissipation tests were performed at different depths in the soil profile. In total, four dissipation tests were performed in the sensitive clay layer at depths of 4.5 m and 6.5 m, and a single test in the quick clay layer at 9.5 m. The interpretation of the soil consolidation properties from piezoball tests requires the use of a theoretical/numerical dissipation curve to relate the recorded profile of pore pressure decay with time to the soil consolidation properties. To provide this relationship, Mahmoodzahed et al (2015) performed large deformation finite element analyses (LDFE) of the excess pore pressure dissipation process around shafted ball penetrometers with various shaft to ball diameter ratios (d/D_b) and considering a range of soil properties. These analyses showed that a unique dissipation response for different locations on the ball could be obtained by calculating the non-dimensional dissipation time (T_b) as follows:

$$T_b = \frac{c_h t}{D_b d I_r^{0.25}} \qquad (6)$$

where c_h is the operative coefficient of consolidation, t is the time from the commencement of the dissipation test and I_r is the soil rigidity index. Combining all the results of the LDFE assessments, Mahmoodzadeh et al. (2015) developed a unique dissipation profile for the piezoall, which is given by:

$$\frac{\Delta u}{\Delta u_i} \approx \frac{1}{1+T_b/T_{b50}} \quad for \quad \frac{\Delta u}{\Delta u_i} < 0.7 \qquad (7)$$

where $\Delta u/\Delta u_i$ is the normalised excess pore pressure and T_{b50} is the non-dimensional piezoball dissipation time for 50% dissipation. For the case of dissipation at the mid-height position on the ball, T_{b50} is 0.18.

Figure 5 compares the dissipation curves recorded in the five piezoball dissipation tests conducted at the Tiller site. In each case, c_h has been adjusted to match the backbone profile generated using Equation 7 and $T_b = 0.18$ in the region of $\Delta u/\Delta u_i \approx 0.5$. For $\Delta u/\Delta u_i < 0.6$, the gradient of the piezoball tests matches very well with the profile suggested by the backbone curve. For $\Delta u/\Delta u_i > 0.6$, the match between the piezoball tests and the backbone curve is less good but this can be attributed to the simplicity of the formulation of Equation 7, which is at the expense of obtaining close matches in that region.

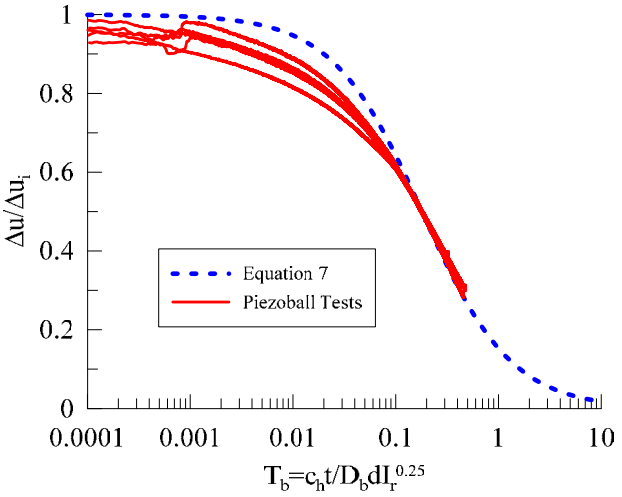

Figure 5. Piezoball mid-height position dissipation profiles at Tiller clay site

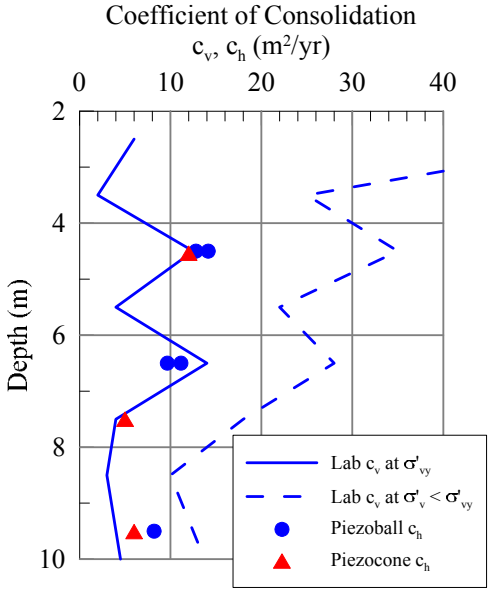

Figure 6. Comparison of consolidation properties of Tiller clay from both lab and field tests

Figure 6 compares the consolidation properties determined from the piezoball dissipation tests with values determined from piezocone dissipation tests reported by Bihs et al. (2012) and laboratory tests data reported by Sandven (1990). In the case of the piezocone dissipation tests, the consolidation properties are the values determined using the method proposed by Teh and Houlsby (1991). The laboratory test data was determined from continuous rate of

strain (CRS) oedometer tests on the Tiller clay and coefficient of consolidation (c_v) profiles are shown for vertical effective stresses (σ'_v) equal to the yield stress (σ'_{vy}) and for stresses below this value. Based on comparison of the results, it can be see that there is reasonably good agreement between the c_h values determined from the piezoball and piezocone tests, with ratios between the two ($c_{h\text{-}Ball}/c_{h\text{-}Cone}$) ranging between 1.06 and 1.36. Compared to the laboratory test data, the measure c_h values for both penetrometers lie closest to the c_v values measured at the yield stress, thus corresponding to normally consolidated conditions.

6 CONCLUSIONS

This paper has examined the performance of a ball penetrometer with pore pressure measurements, termed piezoball, in sensitive and quick clay layers of the Tiller clay site near Trondheim, Norway. Particular focus has been on the pore pressure response during penetration and the dissipation of pore pressures during intended pauses in the penetration. Examination of the pore pressure response during penetration and comparison with the response obtained from the longer established piezocone tests, is useful for gaining reference test data and will ultimately assist in the development of soil classification charts for this test. Interpretation of piezoball dissipation tests using recently established methods has shown good agreement with the soil consolidation parameter determined from both in-situ piezocone tests and the results of laboratory tests on soil samples.

7 ACKNOWLEDGEMENTS

This work forms part of the activities of the Centre for Offshore Foundation System at UWA, currently supported as a node of the Australian Research Council Centre of Excellence for Geotechnical Science and Engineering. At the time of the work it was supported by the State Government of Western Australia through the Centre of Excellence in Science and Innovation program, and also by the CSIRO Flagship Collaboration Cluster on Subsea Pipelines. The various support is gratefully acknowledged. The first author is also grateful to the Australian Academy of Science for their support under the Scientific Visit to Europe scheme.

8 REFERENCES

Boylan, N., Long, M., Ward, D., Barwise, A. & Georgious, B. 2007. Full-flow penetrometer testing in Bothkennar clay. *Proc. of 6th Int. Conf. on offshore site investigation and geotechnics conference*, London: 177–186

Boylan, N., Randolph, M. F. & Low, H. E. 2010. Enhancement of the ball penetrometer test with pore pressure measurements. *Proc. of 2nd Int. Symp. on Frontiers in Offshore Geotechnics (ISFOG '10)*, Perth: 259–264.

Bihs, A., Nordal, S., Boylan, N. & Long, M. 2012. Interpretation of consolidation parameters from CPTU results in sensitive clays. *Proc. Int. Conf. on Geotechnical and Geophysical Site Characterisation (ISC'4)*, Brasil: 227-234.

Chung, S. F. & Randolph, M. F. 2004. Penetration resistances in soft clay for different shaped penetrometers. *Proc. of 2nd Int. Conf. on Geotechnical and Geophysical Site Characterization (ISC'2)*. Porto, 1: 671-677.

Colreavy. C., O'Loughlin, C.D. & Randolph, M.F. 2016. Estimating consolidation parameters from field piezoball tests. *Géotechnique*, 66(4): 333–343.

DeJong, J.T., Yafrate, N.J. & DeGroot, D.J. 2011. Evaluation of undrained shear strength using full flow penetrometers. *J. Geotech. Geoenviron. Eng.*, ASCE, 137(1): 14-26.

DeJong, J. T., Yafrate, N. J. & Randolph, M. F. 2008. Use of pore pressure measurements in a ball full-flow penetrome-ter. *Proc. of 3rd Int. Conf. on Geotechnical and Geophysi-cal Site Characterization (ISC'3)*. Taipei: 1269-1275.

Gylland, A., Long, M., Emdal, A., & Sandven, R. 2013. Characterisation and engineering properties of Tiller clay. *Engineering Geology*, 164: 86-100.

Karlsrud, K., Lunne, T., Kort, D.A. and Strandvik, S. 2005 CPT correlations for clays. *XVI ICSMGE*, Osaka: 693-702.

Low, H. E., Randolph, M. F. & Kelleher, P. J. 2007. Compari-son of pore pressure generation and disipation from cone and ball penetrometers. *Proc. of 6th Int. Conf., Society for Underwater Technology, Offshore Site Investigation and Geotechnics (SUT-OSIG)*. London: 547-556.

Lunne, T., Robertson, P. K. & Powell, J. J. M. 1997. *Cone Penetration Testing in Geotechnical Practice*, Blackie Academic and Professional, London.

Mahmoodzadeh, H., Wang, D. & Randolph, M. F. 2015. Interpretation of piezoball dissipation testing in clay. *Géotechnique*, 65(10): 831-842.

NGF, 1982. Veilding for symboler og definisjoner i goetenikk - presentasjon avgeotekniske undersøkelser. Norwegian Geotechnical Society (Norsk Geoteknisk Forening), Oslo (In Norwegian).

Osman, A. & Randolph, M.F. 2014. On the calculation of cumulative strain around full-flow penetrometers in steady-state conditions. *Int. J. Num. and Anal. Methods in Geomechanics*, 39(4): 368-387.

Sandven, R., 1990. Strength and Deformation Properties of Fine Grained Soils Obtained from Piezocone Tests. Norges Tekniske Høgskole (now NTNU), Trondheim.

Teh, C. I. & Houlsby, G. T. (1991). An analytical study of the cone penetration test in clay. *Géotechnique*, 41(1): 17–34.

Geotechnical and Geophysical Site Characterisation 5 – Lehane, Acosta-Martínez & Kelly (Eds)

Observing Friction Fatigue on Calcareous Material

D. Denes
Foundation Specialists Group, Victoria, Australia.

ABSTRACT: This case study describes the results of dynamic testing and CAPWAP® analysis on open ended steel tubular piles driven into calcareous material. PDA monitoring of the complete driving process has enabled observation of a progressive breakdown in shaft friction, otherwise known as friction fatigue. A series of CAPWAP® analyses, undertaken at varying penetrations, demonstrate the progressive loss of pile shaft resistance during driving to a residual strength value. Previous research has demonstrated that friction fatigue is associated with pile length, and more recent investigations show that it is more likely associated with cyclic motion. The mechanism involved is discussed that provides an explanation for this loss of shaft resistance which is thought to be attributed to the progressive degradation of localised materials at the pile/soil interface due to the continuous shearing that is generated as the pile is driven. Using CAPWAP® to evaluate the progressive changes in the distribution of shaft resistance provides important insight into the phenomenon of this break down in shaft resistance at a macro level. Nevertheless, it appears that shaft resistance degrades to a residual value.

1 INTRODUCTION

The behaviour where a soil loses resistance around the shaft during driving or cyclic loading is termed friction fatigue. This phenomenon was first observed with piles installed in calcareous sands as described in literature since 1973 (Angemeer et al) and has since then been the subject of academic study (e.g. Murff 1985, Poulos 1989, White and Bolton 2002). By using dynamic testing methods to measure the complete installation of a pile, the variation of shaft resistance distribution as a function of pile penetration can be inferred.

This case study focuses on a project off the northwest coast of Australia. The first dynamic test pile occurred at a penetration of 23.5m and several days later at a penetration of 43.5m. At both penetrations, the driving set was 4mm per blow using the same hammer and drop height. It is this difference in penetration and the similar set per blow that raised issues with the shaft frictional resistance. Therefore a particular pile (F1) was chosen for detailed assessment to be monitored over an installation length of 39 meters. The aim of the study is to observe friction fatigue using PDA and undertake CAPWAP® modelling to determine if there is a reduction/fatigue of shaft resistance around the pile.

The pile tested is a 508mm outside diameter open ended steel tube with a 12.7mm wall thickness with no toe thickening or plate. A 1.3t hydraulic drop hammer with a maximum drop height of 1.3m was used for installation for the entire pile penetration (LP) length of 39 meters.

2 BACKGROUND

2.1 *PDA-CAPWAP®*

Dynamic pile testing, also known as Pile Driving Analyzer (PDA) testing, is a technology which was developed in 1960 (Smith) and commercially available in the 1970's by Pile Dynamics, Inc. (PDI). Strain and accelerometers gauges are attached to a pile and capture strain/acceleration time records for each hammer/pile impact. The information recorded is both the stress-wave from the hammer and the reflected stress-waves generated along the pile length as well as from the pile toe. These stress-waves can be interpreted using wave analysis programs such as CAPWAP®, in order to determine the total capacity and the distribution of the capacity along the shaft length and at the pile toe. The program CAPWAP®, developed by Goble and Rausche (1979), is generally accepted to be the definitive method on interpret-

ing dynamic pile records. It is based on modelling the pile as an elastic body, with both mass and stiffness, and the surrounding soil as a series of elasto-plastic static resistance springs and linear dashpots. Actual soils do not follow simple elasto-plastic behaviour and are more typically non-linear, but CAPWAP® in most cases has shown proven reliability providing that a sensible and realistic model has been applied. To make a rational and valid CAPWAP® model, the engineer should have all information at hand, including hammer details, driving records, set measurements, geotechnical conditions and pile details. The theory of PDA and CAPWAP® will not be further discussed within this paper.

2.2 *Pile Design*

Prior to the realisation that calcareous sands behave differently to terrigenous sands, determination of shaft resistance was based on standard or 'conventional' methods which are still currently used today. These methods were initially applied to all types of sands, both silica and calcareous. It was not until the 1970's (Angemeer 1973) and the 1980's (i.e. North Rankine A – Senders et al. 2013) that pile test results observed shaft resistance values well below the 'conventional' design.

The standard conventional methods involve the use of overburden stress and a frictional co-efficient between the pile type, soil and the earth pressure co-efficient, K. (Johannessen and Bjerrum 1965, Chandler 1968 adopted slightly different approach). Other methods involve correlations between collected in-situ testing (such as SPT). A number of foundation textbook even advise to limit the maximum skin friction, which is proven incorrect (Kulhawy 1984). More modern methods for shaft resistance are based on CPT (Kelly and Wong 2005) and on the expansion cavity expansion theory where there is an increase in radial stress related to dilation effects. Using the cavity expansion approach removes the 'K' value and the overburden stress, both being replaced with the effective radial stress acting on the shaft at failure and the critical state sand interface angle of friction, which is developed when the soil at the interface has ceased dilating or contracting (i.e. zero volume change).

2.3 *Friction Fatigue*

Friction fatigue is the destruction of the surrounding material due to excessive shear stresses, thought to be related to the following:
the 'h/D' effect (Randolph et al 1994). (Figure 1). This is associated with the decrease of horizontal effective stress (radial/normal stress) as the pile penetrates deeper. Hence the higher the h/D ratio below a nominated depth, the larger the decrease in shaft resistance;
a repetition of shearing the soil at the pile/soil interface produced by movement of the pile (this is referred to as a cycle – i.e. a pile hammer blow);

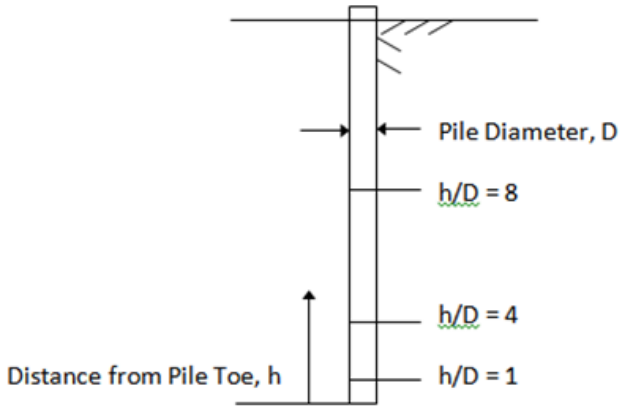

Figure 1. h/D Effect


Figure 2. Hollow Structure – Coralline Rock

3 CALCAREOUS SANDS

3.1 *What is it?*

Calcareous material is a generic description given to granular soil composed of calcium carbonate. It is formed from shells and skeletal remains from benthos organisms (bottom dwelling) such as coral, molluscs and calcareous algae. Closer inspections of these biogenous sediments reveal a porous hollow structure, with a rough surface (Figure 2).

3.2 *Engineering Properties*

Calcareous sands are special because they do not behave like normal sands. They have a higher void ratio due to the hollow structure and therefore tend to crush more readily compared to lithogenous sediments (quartz sand). These sands may be found in cemented or uncemented states. At first there is some strength to the grain due to the material and potential cementation effects. But once a certain pressure is exceeded, it crushes quickly. Trying to determine the initial nature of calcareous materials is quite difficult. For example, undertaking SPT testing involves damaging the possible cementation bonds.

The friction angle is generally quite high, typically above 35 degrees and often exceeding 50 degrees (Murff 1987). It is noted that even partial cementation can cause 'arching' around the pile, hence the sand can effectively self-support itself, not applying a great deal of lateral pressure to a pile. Poulos (1989) showed that under a series on monotonic loading on calcarenite core samples, that the normal stress reduces as shear displacement increases. These tests are quite important as they demonstrate the volume change characteristics for calcareous material where initial contraction leads to a continued reduction in the post peak strength at the interface.

3.3 *Friction Fatigue and Calcareous Material*

White and Bolton (2002) discuss that friction fatigue is related to pile movement. Experiments observed the decrease in horizontal stress at a nominated depth below ground level as the pile toe passes this nominated point and continues further beyond. They observed that a zone of sand beside the pile underwent volume reduction reducing the normal stress. White and Lehane (2004) undertook laboratory experiments using instrumented piles to determine if friction fatigue is related to the h/D ratio. The piles were installed in one of three ways: 1. Monotonic; 2. Jacked – cycles of fixed downward displacement and 3. Pseudo-dynamic – comprising of a downward then upward displacement. Results from the Monotonic loading showed only a minor decrease in shaft resistance with increasing depth. However, the jacked and pseudo-dynamic showed significant degradation of shaft friction with the results showing that it is related to the number of cycles that had occurred beyond the soil horizon, not the h/D ratio. This observation is quite unique because it eliminates the h/D effect alone based on the monotonically installed piles. However, for piles that are installed under cyclic condition, it is shown that it is the number of cycles that influences the reduction in shaft reduction.

3.4 *Shear Resistance Values for Calcareous Material*

Observations (Angemeer et al 1973) from a series of load tests on driven piles showed the capacities were approximately 20% of those predicted by conventional methods. Murff (1985) listed a number of test results from 1973 to 1985 and observed mean peak values ranging between 13.4 to 20.3 kPa. Aggarwal et al (1997) further defined skin friction resistance relating to percentage of calcium carbonate, where above 45% shaft resistance is approximately 28kPa. Poulos (1989) provided peak skin friction values ranging between 10 to 20kPa for uncemented material. Residual friction values ranged between 5-20kPa for various cementation levels. Ghazali et al (1990) discussed limiting skin friction to 20kPa.

4 FULL MONITORING OF PILE F1

The final penetration for Pile F1 was 39m below sea bed level. PDA monitoring commenced from 6m. Data collected was of good quality and four strain gauges were used for the last 33m of driving due to slight hammer alignment issues. There was a total of 7226 hammer hits (or cycles) from the start of driving. The set vs penetration is shown in Figure 3. As the hammer drop height is consistent, the set per blow variation gives an indication of the strength of the material at the toe of the pile. Hence a smaller set may indicate stronger material, or higher cementation.

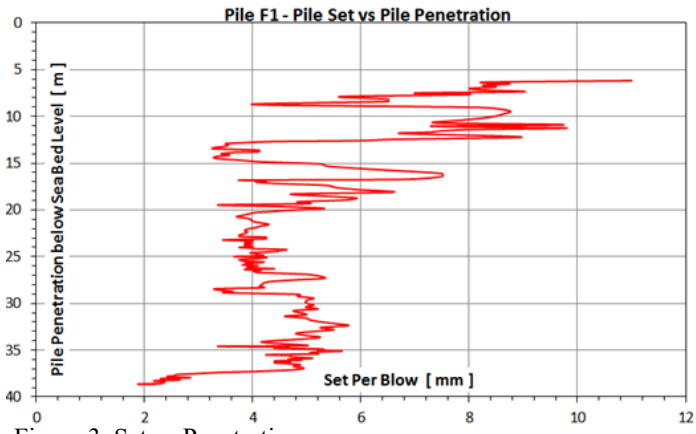

Figure 3. Set vs Penetration

4.1 *Site Geotechnical Model*

Due to the remote location of the work site, a geotechnical investigation was not undertaken at the work site location. Therefore the geological environment is based on a desktop study, local observations and geotechnical reports in similar environments. The geological age is Late Quaternary to Recent. It is composed of bedded marine calcarenite, thick reefs, calcareous sand and talus (limestone) deposits. The generalised profile for the test site is as follows: Upper 15m comprising of calcareous sandy sediments, carbonate sands, coral, phosphate sediments, and talus. Areas may be cemented. Below 15m – porous limestone layers, varying degrees of cemented sand layers, sand layers composed of coral, coralline limestone, shells, carbonate sands and silts.

4.2 *PDA Observations of Pile F1*

PDA testing captures the downward generated compressive stress wave (from the hammer impact) and the subsequent reflections. The data is generally presented by viewing force/velocity time records, or more commonly used view of Wave-Up (WU) and Wave-Down (WD). The WU trace gives a visual guide of the dynamic soil resistance around the shaft of the pile. As the wave travels down (WD) the pile, the pile moves downwards and displaces the soil around which 'slips' past the pile around the perime-

ter. This slipping is referred to as mobilisation, which is displacement vs shear resistance. This soil resistance is partially reflected as compression waves where these reflected waves are cumulative added together to generate the WU response. To further demonstrate this, Figure 4 shows the WU response and an indication of the shaft resistance on the pile. As the WU line increases, the shaft resistance on the pile increases. Therefore if the pile is PDA monitored for the full penetration, then by comparing the WU response, we are able to visually assess how the shaft resistance around the pile behaves.

The Wave-Up response for various penetrations of pile F1 is shown in Figure 5. The response has been modified to only show length of penetration (i.e. the pile toe response has been removed). The changes in the response are quite dramatic at certain locations. For example the response at LP 13.7 and 17m are much higher compared to the other response. This correlates with the sets being lower per blow indicating harder ground conditions. Once the pile penetrated beyond 17m, the response drops of significantly. This example demonstrates that the shaft resistance is reducing as the penetration is increasing due to driving. At the final penetration, it is noted that the WU response seems to come to a final 'residual' line following the same trend for 33m.

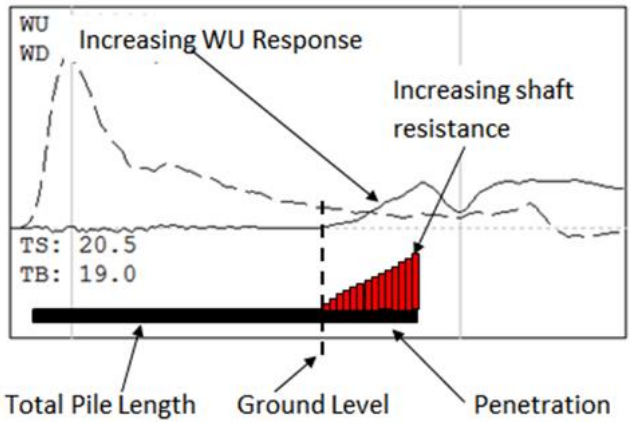

Figure 4. Interpretation of Wave-Up Response

The WU response eventually becomes a downward slope once the penetration reaches 25-30m and beyond. Generally, the WU increases with respect to increasing skin friction resistance which represents that the shaft resistance is increasing with depth. When the WU starts to 'flatten' or even reduce this may indicate that the shaft resistance is decreasing in strength or it is associated with pile unloading (an upward movement of the gauges as the pile bottom is still moving downwards), or a combination of both. When there is unloading in PDA data, a CAPWAP® analysis is required to model the effects of unloading on the WU response to determine if the decrease in the response is caused by lower shaft resistance values. Therefore, the straight forward visual approach of using WU to indicate the shaft resistance model is not applicable from when the unloading section begins. Therefore, if there is a weaker layer, CAPWAP® will model this.

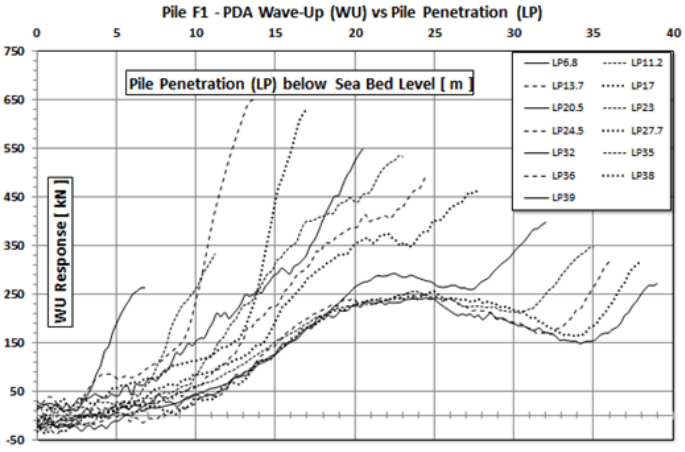

Figure 5. Wave-Up Response for Various Penetrations

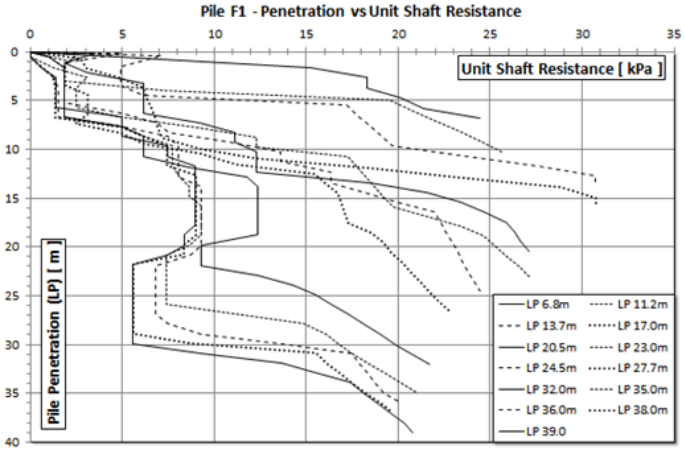

Figure 6. Shaft Resistance Values Vs Pile Penetration

4.3 *CAPWAP® Analysis and Observations for Pile F1*

A CAPWAP® Analysis was undertaken for each of the penetrations as shown in the PDA Wave Up response. The total unit shaft resistance at each meter of shaft vs penetration is shown in Figure 6. The results are representative of the PDA data, which show similar trends to the WU responses. Using the depth at 13m as an example, the modelled total unit shaft resistance based on the data from LP13.7m is 30.7kPa. At the same depth location but looking at the results from the CAPWAP® at LP38m, the total shaft resistance is 7.8kPa. This is a decrease of approximately 75%.

In all CAPWAP® analysis, it is the bottom 1-2meters of the pile that has the highest unit shaft resistance. This may be expected because the pile has just been driven into virgin material, where the surrounding soil is trying to be 'pushed' to the side of the pile. As the calcareous sand particles are trying to dilate, there is an increase in horizontal stress

which increases the shear stress which initiates collapse of the sand. Associated with this collapse is volume reduction. This is also evident, as the unit shaft resistances 4m above the toe (or an approximate h/D ratio of 8) are up to 40% lower compared to the initial value.

From the CAPWAP analysis, the values below are given as total kPa values acting on the external section of the pile. Therefore, depending on what percentage is acting internally, the values may be less: Peak: 20.7-35kPa, Residual (LP3-7): 1.3kPa, (LP15-20) 9kPa, (LP22-30) 5.5kPa, Average 5kPa, which is similar to what has been observed in literature.

To determine if friction fatigue is related to penetration (the h/D ratio) or to the number of cycles, further investigation is required using the CAPWAP results. The following depth locations below sea bed level will be used for this analysis, which are: 5, 15 and 25m depths. For this, the total external shaft resistance values have been converted to percentage decrease from peak shaft values using the initial first peak shaft value determined at each depth.

Figure 7 compares the % shaft resistance decrease vs the number of blows encountered below each nominated depth location. This shows that at each of the 3 penetrations, there is a break down in shaft resistance ranging from 70 to 90% from its initial shaft resistance value over a period of 3000 to 4000 cycles. All three depths show an approximate linear decrease starting at 100% which flattens out to a potential 'residual' value. Figure 8 shows the % shaft resistance decrease vs the h/D ratio. This now shows that the decrease in unit shaft resistance ranges from 70-90% for an h/D ratio ranging from 21 to 33, an average ratio of 27. It is noted for both that a trend begins to appear where the unit shaft resistances show a similar degradation/fatigue pattern for both.

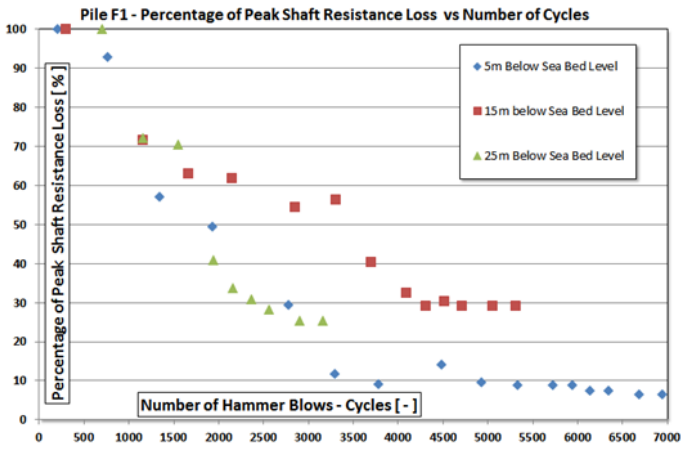

Figure 7. Percentage Shaft Loss vs No. of Cycles

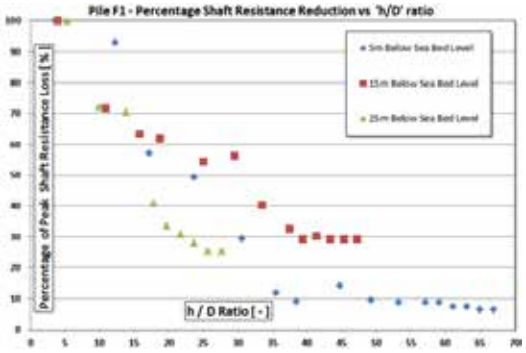

Figure 8. Percentage Shaft Loss vs h/D Ratio

Summarising the above information, the best visual trend is seen in Figure 7 (Percentage Peak shaft loss Vs Cycles) where all 3 penetrations seem to align to approximately 60% (a 40% decrease). After that, the 5 and 25m locations follow each other, while the 15m location takes a slightly different path. Figure 8 (Peak Shaft loss compared to h/D ratio) still shows a visual trend for all 3 locations, but is more scattered. It appears that friction fatigue is better associated with the number of cycles applied compared to h/D ratio based on visual assessment of trending data. It is also interesting to note that both methods observe a 'residual' value, which is a loss in shaft resistance from 70 to 90% of its original peak value.

The above review is quite unique to observe a pile with over 7200 cycles. These observations seem to correlate with the data observed from White and Lehane (2004). Unfortunately, laboratory models cannot reproduce this type of analysis due to scaling effects and model size limitations, with respect to pile displacements per blow.

5 CONCLUSION

This case study focused on the observation of friction fatigue in calcareous material using Pile Dynamic Testing (PDA) to observe the changing nature of the shaft resistance by recording the response wave for every cycle. The response wave is generated by in situ shaft resistance and the cycles are generated from a driving hammer. Results from Pile F1 showed that PDA is an interesting and suitable vehicle for observations of friction fatigue and provides an insight to what is occurring in real time. CAPWAP® modelling of the pile at various penetrations allowed the determination of peak and residual shaft resistance which correlated quite well to existing literature from the past 40 years. The shaft resistance values allowed further analysis by comparing the fatigue in the shaft resistance values to be compared to the number of cycles as well as the penetration, or h/D ratio, to observe if there is a relationship with either method. Overall, the number of cycles compared to shaft degradation seemed to best represent

friction fatigue which was based on the observation of 3 different penetrations and comparing the unit shaft resistance which showed better trends compared to h/D. This case study has provided a direct and unique insight into the phenomenon of friction fatigue.

6 ACKNOWLEDGEMENTS / INFORMATION

I would like to thank Dr. Julian Seidel for his time, support and encouragement. A great mentor. This paper is based on my Masters Specialists subject, referenced below.

7 REFERENCES

Angemeer, J., Carlson, E. and Klick, J.H. (1973). Techniques and results of offshore pile load testing in calcareous soils. Proceedings, Fifth Annual Offshore Technology Conference, Houston, Texas, 677-692.

Denes, D. (2015). Observing Friction Fatigue on Calcareous Material: A Progressive Breakdown of Shaft Resistance for Piles driven into Calcareous Material as observed during Dynamic Pile Testing. Masters Subject. UNSW.

Ghazali, F.M., Baghdadi, Z.A. and Mansur, O.A. (1990). A comparative study of pile foundations in coral formations and calcareous sediments. JKAU Eng. Vol 2. pp. 3-17.

Goble, G.G. and Rausche, F. (1979). Pile driveability predictions by CAPWAP®. Proc. Int. Conf. on numerical Methods in Offshore Piling, ICE, London, pp. 29-36.

Johannessen, I. J. and Bjerrum, L (1965). Measurement of the compression of a steel pile to rock due to settlement of the surround clay. Proceedings of the 6th International conference on Soil Mechanics and Foundation Engineering, Montreal, 2, pp. 261 to 264.

Kelly, R. B. and Wong, P.K. (2005). Case Study: Assessment of the shaft capacity of a driven pile in sand using CPT based methods. Australian Geomechanics. Vol 40, No. 4. December. pp.73-80.

Kulhawy, F. (1984). Limiting tip and side resistance: Fact of fallacy, analysis and design of pile foundations, ASCE, 1984, pp. 80-98.

Murff, J.D. (1987). Pile capacity in calcareous sands: State of the art. Journal of Geotechnical Engineering, Vol 113, No5, May. pp. 490-507.

Nauroy, J.F. and LeTirant, P. (1983). Model tests of piles in calcareous sands. Offshore Engineering Practice, ASCE, pp356-369.

Nauroy, J.F. and LeTirant, P. (1985). Driven piles and drilled and grouted piles in calcareous sands. Proceedings Seventeenth Annual Offshore Technology Conference, Houston, Texas. pp. 83-91.

Pile Dynamics, Inc. (2015). Manual for the PDA 8G and PDA-S Software.

Poulos, H.G. (1989). The mechanics of calcareous sediments, John Jaeger Memorial Address. Australian Geomechanics. pp. 8-40.

Randolph, M.F., Dolwin, J. and Beck, R. (1994). Design of driven piles in Sand. Geotechnique, 44, No3, pp. 427-448.

Senders, M., Banimahd, T., Zhang, T., Lane, A. (2013). Piled Foundations on the North West Shelf. Australian Geomechanics, Vol 48, No4. December. pp149-160.

Smith, E.A.L. (1960). Pile driving analysis by the wave equation. Journal Soil Mechanics and Foundations, ASCE, 86 (SM4). pp. 35-41.

White, D.J., Bolton, M.D., (2002). Observing Friction fatigue on a jacked pile. Centrifuge and Constitutive Modelling: Two extremes. Springman S.M. (ed) pub Balkema, Rotterdam.

White, D.J., Lehane, B.M. (2004), 'Friction fatigue on displacement piles in sand', Geotechnique, 54, 10, pp. 645-658

Geotechnical and Geophysical Site Characterisation 5 – Lehane, Acosta-Martínez & Kelly (Eds)

Data driven design- a vision for an automated approach

J.P. Doherty & B.M. Lehane
School of Civil, Environmental & Mining Engineering, University of Western Australia, Australia

ABSTRACT: Geotechnical calculation procedures require engineers to assign values to a number of input parameters. Usually there are a number of well-defined input parameters with clear guidance on how values should be assigned. However, there are also often a small number of less well defined parameters with little, if any, guidance given on how values should be selected; "engineering judgment" is required. It should, there-fore, not be surprising that there is strong evidence to demonstrate that geotechnical engineers given the same data and same design task will interpret the data in very different ways and ultimately produce vastly different design calculations. This is clearly unsatisfactory as a vital step in producing reliable and cost effective geo-infrastructure is to develop design procedures that can be applied with consistency. This paper will discuss a web based application that uses CPT or CPTu data directly as an input and performs a lateral analysis of pile foundation. The application interprets that CPT data and automatically assigns appropriate *p-y* curves for sands, silts or clays. In principle, the application requires no engineering judgment to analyse a pile founda-tion, other than to decide if the CPT data is appropriate for the task. This is likely to lead to more consistent and ultimately reliable designs.

1 INTRODUCTION

Many aspects of modern society have been automated, with machines processing data and making decisions. Commercial passenger planes all but fly themselves and self-driving vehicles are now a reality and are expected to be common place on public roads over the next 5-10 years. Yet, engineering design is still a labour intensive and highly subjective process. The subjective nature of engineering design has been demonstrated through a number of design or prediction competitions. For example, Lehane *et al.* (2009) conducted a foundation settlement prediction competition, involving vertical load tests on four square concrete footings. Prior to the load tests, engineers from around the world were invited to submit settlement predictions and were provided with high quality in-situ and laboratory data to use in their calculations. Figure 1 shows a comparison of predictions along with the actual measured settlement for a typical case.

What is arguably most alarming in the results from 26 group submissions is that the predictions varied by more than two orders of magnitude (from less than 1mm to up to100mm). Remarkably, many of the groups used the same calculation method, but came up with vastly different results. The differences clearly arise in the way engineers interpret the available data for use in their design calculations.

Codes of practice exist to try and standardise engineering design. However if engineers interpret data differently and end up with different design calculations, what genuine use is a code of practice?

If it is universally accepted that we should, as far as possible, remove subjectivity in design, then it logically follows that we should remove, as far as possible, engineering judgment from design tasks. This paper presents a "proof of concept" web based application that uses CPT or CPTu data directly as an input and performs analysis of pile foundation subjected to lateral loads. The application interprets the CPT/CPTu data and automatically assigns *p-y* curves for sands, silts or clays. In principal, the application requires no engineering judgment to analyse a pile foundation, other than to decide if the CPT data is appropriate for the task. Using the same data and the same design approach, engineers will almost certainly produce the same calculation result. This "data driven design" approach will lead to more consistent designs. Ultimately, as subjectivity is re-

moved from the calculations, uncertainties related to specific formulations embodied within the automated procedure can be determined. Such a measure of method uncertainty can be incorporated in the procedures and lead to greater design reliability. Formulations with reduced method uncertainty will inevitably emerge.

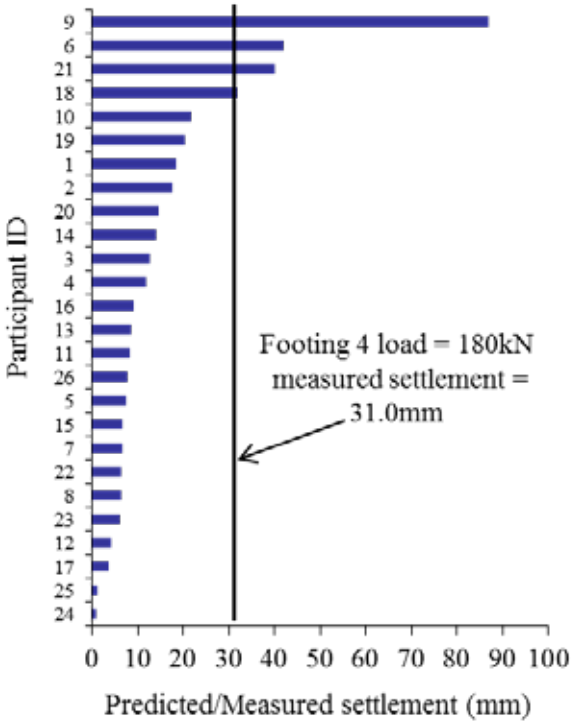

Figure 1: Lateral load test set up at Shenton Park

2 A PROOF OF CONCEPT APPLICATION FOR LATERALLY LOADED PILES

2.1 *The web app*

LAP: (Lateral Analysis of Piles) is a web-based application for calculating the behaviour of vertically orientated piles subjected to lateral loads. The pile is modelled with structural beam elements and can be assigned either linear elastic or elastic-perfectly plastic material properties. Up to five different pile sections can be included in a single analysis. The soil is modelled as a collection of independent (Winkler) springs. The load-displacement behaviour of the springs can be specified using parameters for common *p-y* load transfer functions. Load transfer functions can also be generated by directly pasting in Cone Penetration Test (CPT) data. Users can also specify their own *p-y* curves. Pile loads can be specified as a combination of horizontal forces, applied moments, prescribed horizontal displacements and prescribed rotations at any location on the pile. Horizontal and rotational reaction springs can also be included and a surcharge load adjacent to the pile can be included. The program solves for the pile response using non-linear finite element analysis. The calculations are performed on a cloud server. This means the programs run efficiently on all devices that can connect to the internet.

LAP was developed by James P. Doherty at the University of Western Australia. The program is made freely available for use as a research and teaching tool and can be accessed at www.geocalcs.com/lap

2.2 *The p-y method for laterally loaded piles*

The so called "*p-y* method" is the standard approach for the analysis and design of laterally loaded piles. It is popular due to its simplicity and long established record in Industry. The method uses non-linear independent (Winkler) springs to define a relationship between the net soil resistance at any depth per unit length of soil adjacent to a pile (p) and the lateral deflection of the pile at that depth (y).

There are a number of *p-y* formulations but all use some measure of soil strength to determine the relationship between p and y. For example, for soft clay, the American Petroleum Institute (API, 2011), recommends a formulation based on Matlock (1970), which requires an estimate of the unconsolidated undrained triaxial compression shear strength (s_u). The API method for piles in sand is also derived empirically from full-scale tests on free-headed piles and only requires specification of the soil's friction angle (ϕ') to determine the relationship between p and y.

Both API methods for clays and sands are highly sensitive to the choice of the material strength (s_u for clay and ϕ' for sand). This sensitivity is exacerbated by the need to employ empirical correlations with in-situ test results to estimate the strength parameters.

To address these limitations, researchers proposed using the cone penetration test (CPT) end resistance (q_c) as the measure of soil strength to determine the relationship between p and y for carbonate (Novello 1999, Dyson and Randolph 2001) and silica (Suryasentana and Lehane 2014) sand. Truong and Lehane (2014) present q_c-based *p-y* curves for clays. The primary advantage of these methods is that they utilise measurements directly and are therefore not susceptible to the subjectivity associated with estimating strength parameters.

These methods provide an opportunity to develop a "data driven design" pile application, where test data are used directly as an input into the calculation procedure.

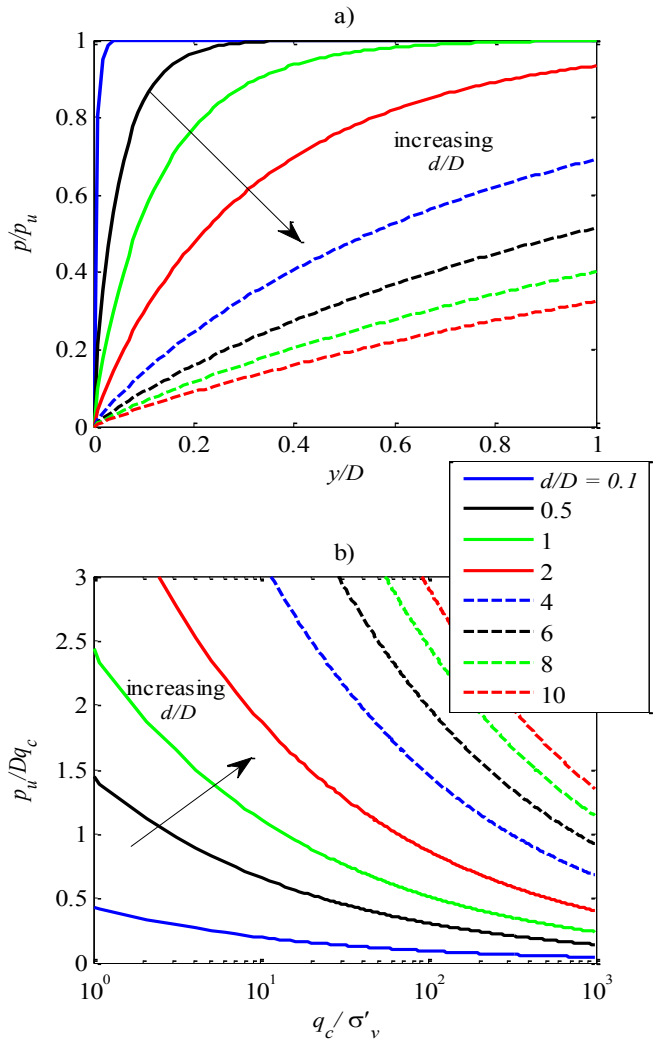

Figure 2: CPT sand *p-y* models a) normalised p-y response; b) normalised pu with normalised qc

2.3 *CPT based p-y curves in LAP*

LAP has a number of popular *p-y* models built in. It also has the option to select "CPT Auto" as a *p-y* type. The user must then specify if (u_2) pore pressure measurements are included (i.e. piezocone). A method for classifying the soil is then selected. The following four methods are considered in LAP:

1. Robertson F_r; Robertson (1990)
2. Robertson B_q; Robertson (1990)
3. The I_c method; Robertson (2009)
4. u_2 method; Schneider et al. (2008)

The cone area ratio is specified (if CPTu is selected) and then CPT data is pasted into a table.

When the analysis is executed, the program first classifies the soil using the CPT data according to one of the methods selected from the four options listed above.

At a particular depth, if the material is classified as sand (or a coarser grained material) then the q_c value at that depth is used as an input into the Suryasentana and Lehane (2014), which assumes:

$$p = p_u\left(1 - \exp\left(-6.2\left(\frac{d}{D}\right)^{-1.2}\left(\frac{y}{D}\right)^{0.89}\right)\right) \quad (1)$$

where d is the depth, D is the pile diameter and p_u is the ultimate lateral resistance (p_u) given as:

$$p_u = 2.4\sigma'_v D\left(\frac{q_c}{\sigma'_v}\right)^{0.67}\left(\frac{d}{D}\right)^{0.75} \quad (2)$$

The normalised shape of the *p-y* curves for a range of *d/D* values is plotted in Fig. 2a. It can be seen for low *d/D* ratios, the ultimate lateral resistance is mobilised after very small normalised displacements.

Equation 2 can be rearranged to explore the relationship between q_c and the ultimate lateral resistance pressure p_u/D,

$$\frac{p_u}{q_c D} = \left(\frac{q_c}{\sigma'_v}\right)^{-0.33}\left(\frac{d}{D}\right)^{0.75} \quad (3)$$

q_c values normalised in this way are is plotted against normalised p_u in Fig. 2b for a range of *d/D* ratios.

If the material is classified as a silt (or a finer grained material), lateral loading is assumed to lead to an undrained response. The q_c value at that depth is used as an input into the Truong and Lehane (2014) method, which assumes:

$$\frac{p}{p_u} = \begin{cases} \tanh\left((0.26I_r + 3.98)\left(\frac{y}{D}\right)^{0.85}\left(\frac{d}{D}\right)^{-0.5}\right) & \text{for } \frac{d}{D} < 3 \\ \tanh\left((0.15I_r + 2.3)\left(\frac{y}{D}\right)^{0.85}\right) & \text{for } \frac{d}{D} \geq 3 \end{cases} \quad (4)$$

where I_r is rigidity index and the ultimate lateral resistance is given by

$$\frac{p_u}{D} = q_{net}\left(\left(\frac{3}{4.7 + 1.6\ln I_r}\right) + (1.5 - 0.14\ln I_r)\tanh\left(\frac{0.65d}{D}\right)\right) \quad (5)$$

The general nature of this *p-y* formulation is illustrated in Fig. 3 which shows the ultimate pressure normalised by q_{net} ($=q_t-\sigma_{v0}$) plotted against rigidity index in Fig 3a and the normalised *p-y* response plotted in Fig 3b.

3 EXAMPLE APPLICATION

To demonstrate the application of *LAP* using CPT data as an input, a case history by Robertson *et al.* (1985) was examined. This case history provided the CPT traced presented in Fig. 4 which was digitized and entered into LAP. The pile was 0.915m in diameter with an 18mm wall thickness and a length of 90m. A lateral load was applied in increments of ap-

proximately 100kN until a lateral displacement of 150mm was measured.

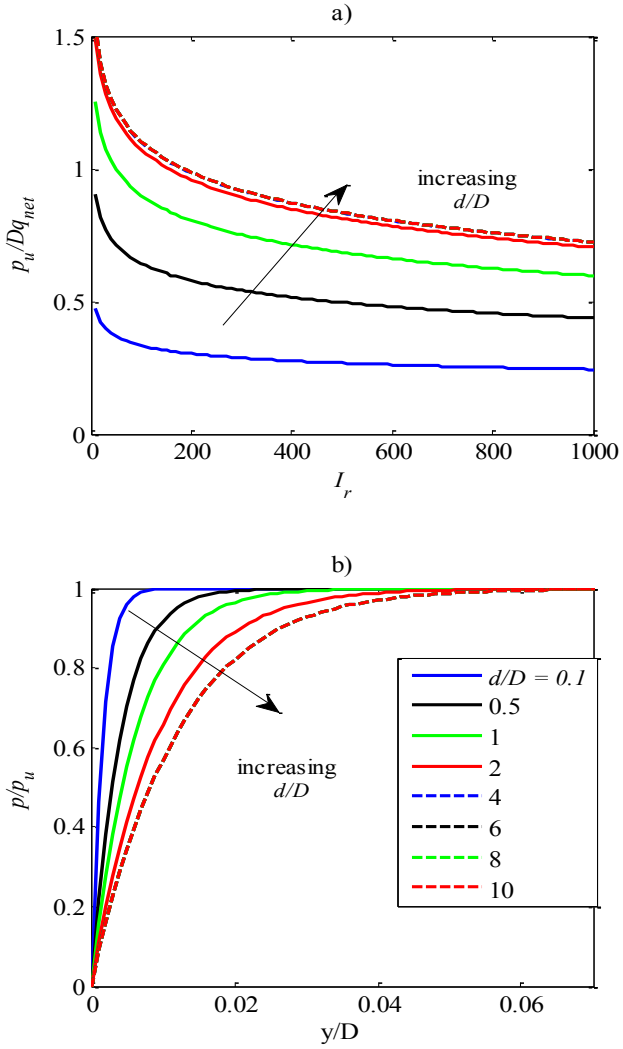

Figure 3: CPT clay *p-y* models (a) normalised p_u variation with rigidity index; (b) normalised *p-y* response

Prior to the pile testing, the upper 4m of rubble was removed and replaced with loose sand fill. No test data are presented for this upper layer and therefore a q_c profile had to be adopted in order to use this case history. The following relationship between q_c, relative density (D_r) and vertical effective stress was used, based on Lunne and Christoffersen (1983)

$$D_r = 1/2.91 \ln\left(\frac{q_c}{\sigma'^{0.71}_v}\right) \quad (6)$$

where σ'_v is the vertical effective stress and both q_c and σ'_v are expressed in kPa.

The relative density was assumed to be 40% and the vertical effective stress variation with depth was estimated assuming a total unit weight of 17kN/m^3. Fig 5 shows the classification chart produced by LAP after running the analysis (and selecting Robertson F_r method of classification).

The computed load displacement response from *LAP* is compared with the measured load-displacement response presented by Robertson *et al*. (1985) in Fig. 6. While there is a reasonable agreement between the measured and computed response, it is difficult to draw any firm conclusions about the performance of the model *p-y* curves used as the response of the pile is largely dominated by the material in the upper 4m, where there was an absence of actual data. However, this example does demonstrate the possibility of analysing pile foundations using CPT data directly as an input. This approach paves the way for potential automation in engineering analysis and design.

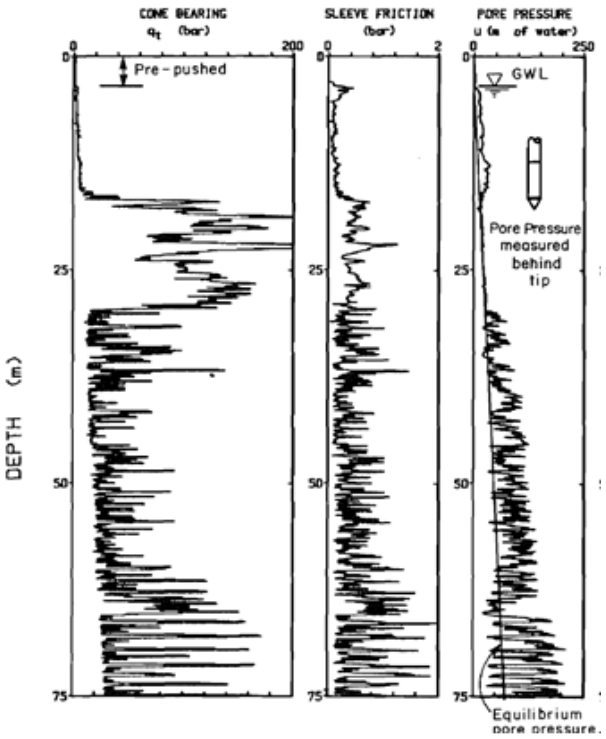

Figure 4: In-situ data (after Robertson et al (1985)

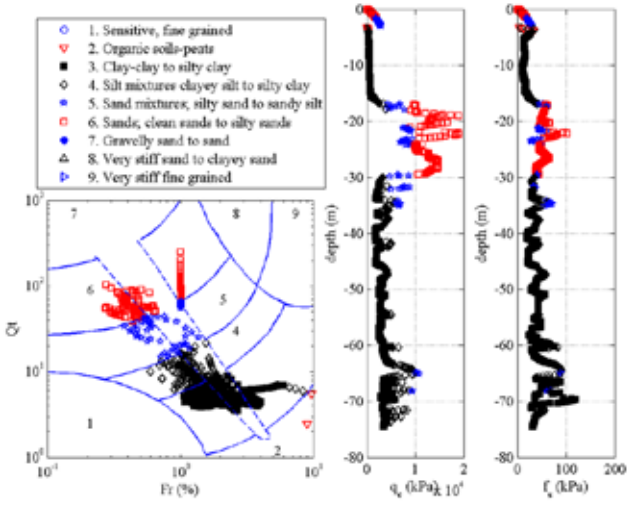

Figure 5: Robertson Q_t vs F_r classification chart from LAP

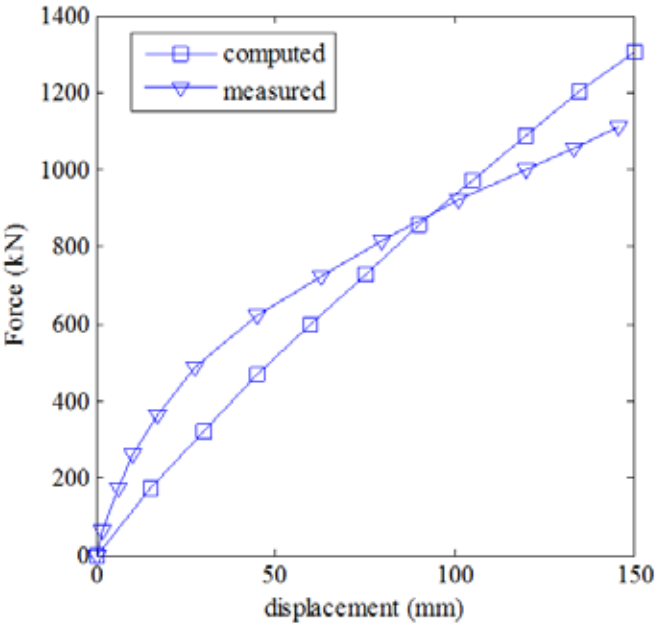

Figure 6: Comparison between measure caste history results and computed results from LAP

4 CONCLUSIONS

Engineering calculation procedures that require judgement to assign material parameter values introduce a significant issue with regard to reliability, as it has been shown that engineers with the same data and calculation tasks judge the data in different ways and ultimately produce vastly different calculation results. A proof of concept web based application was presented that uses CPT or CPTu data directly as an input and performs a lateral analysis of pile foundation. The application interprets that CPT data and automatically assigns appropriate *p-y* curves for sands, silts or clays. In principle, the application requires no engineering judgment to analyse a pile foundation, other than to decide if the CPT data is appropriate for the task. This is likely to lead to more consistent and ultimately more reliable designs. The case history presented was not ideal given some key data was missing. However, the basic principle of using in-situ data directly to conducted geotechnical analysis was demonstrated. This approach is one illustration of the automation of engineering analysis and removal of subjectivity in design.

5 REFERENCES

Doherty, J. (2016). User manual for LAP, Laterally loaded pile analysis. School of Civil, Environmental & Mining Engineering, University of Western Australia, Perth WA 6009. www.geocalcs.com/lap

Dyson, G. & Randolph, M. (2001). Monotonic lateral loading of piles in calcareous sand. *Journal of Geotechnical and Geoenvironmental Engineering* **50**, No. 1, 346–352.

Lehane B.M., Doherty J.P. and Schneider J.A. (2008). Settlement prediction for footings on sand. Keynote Lecture, Proc. 4th International Symposium on deformation characteristics of Geomaterials, Atlanta, 1, 133-152, IOS press, The Netherlands.

Lunne, T. and Christoffersen, H.P (1983). Interpretation of cone penetrometer data for offshore sands. OCT, 4464 Huston, Texas.

Novello, E. A. (1999). From static to cyclic p–y data in calcareous sediments. In *Engineering for calcareous sediments* (ed. K. Al-Shafei), vol. 1, pp. 17–24. Rotterdam, the Netherlands: Balkema.

Robertson, P.K., Campanella, R.G. and Brown, P.T. (1985). "Design of axial and laterally loaded piles using in-situ tests, A case history. Canadian Geotechnical Journal, Vol 22, 518–527.

Robertson, P.K. (1990). Soil classification using the cone penetration test. Canadian Geotechnical Journal, Vol 27(1).

Robertson, P.K. (2009). Interpretation of cone penetration tests – a unified approach. *Canadian Geotechnical Journal*, 46, 1337-1355

Schneider, J., Randolph, M., Mayne, P., and Ramsey, N. (2008). Analysis of Factors Influencing Soil Classification Using Normalized Piezocone Tip Resistance and Pore Pressure Parameters. Journal of Geotechnical and Geoenvironmental Engineering, Volume 134, Issue 11

Suryasentana, S. K., & Lehane, B. M. (2014). Numerical derivation of CPT-based p-y curves for piles in sand. Géotechnique, 64(3), 186-194.

Truong, P., & Lehane, B.M. (2014). Numerically derived CPT-based p-y curves for a soft clay modeled as an elastic perfectly plastic material. Proc. 3rd International Symposium on Cone Penetration Testing, Las Vegas, Nevada, USA.

Geotechnical and Geophysical Site Characterisation 5 – Lehane, Acosta-Martínez & Kelly (Eds)

The Smithfield Bypass Project – Justifiable Need for a Second Stage Piezocone Testing.

L.E. Ezeajugh
Queensland Department of Transport and Main Roads, Australia

ABSTRACT: The proposed Smithfield Bypass is a 4.15 km long dual carriageway spanning between Yorkeys Knob Road and Reed Road Roundabout in Cairns, Australia. On completion, the project will reduce traffic bottle necks currently experienced on the Captain Cook Highway and improve on the overall level of service of the highway. The proposed bypass will consist of two (2) new bridge structures over Avondale Creek, North and South, two (2) overpass bridge structures over Captain Cook Highway, five (5) major culverts, some retaining walls and associated motorway on and off ramps. Embankments heights are variable at the site reaching up to 9m at the approaches to the overpass structures. The project site traverses relatively flat alluvial coastal flood plain with thick sequence of alluvial deposits including up to 18m thick organic silty clays of high compressibility and low bearing strength. At the site, due to flooding concerns, there is only a 5-month window for ground improvement works. Using the coefficient of consolidation (Cv) values obtained from the first stage piezocone testing, the installation of perforated vertical drains (PVDs) and preload plus surcharge will have to be carried out to 100% of the southern section of the site with the exception of the at-grade sections. With improved c_v values obtained from a more careful and prolonged (occasionally overnight) second stage testing which ensured that 50% dissipations were reached, even on the basis of a low bound Cv value of $3m^2/yr.$, only 22% of the site would require surcharge and would meet the required 5-month target window for ground improvement.

1 INTRODUCTION

The proposed Smithfield Bypass is a 4.15km long dual carriageway spanning between Yorkeys Knob Road and Reed Road Roundabout in Cairns, Australia. On completion, the project will reduce traffic bottle necks currently experienced on the Captain Cook Highway and improve on the overall level of service of the highway.

The proposed bypass will consist of the following elements:

- overhead bridge structures, high embankments and retaining walls at McGregor roundabout and McGregor bypass connection road;
- two bridge structures and approach embankments over Avondale Creek;
- five major culvert structures;
- associated motorway on and off ramps; and
- at-grade and grade separated sections with variable embankment fill heights.

Based on existing information on the constructed Avondale Creek Bridge on the Captain Cook Highway located about 200m from the Smithfield Bypass site, the project area is on the Barron River flood plain with thick sequences of alluvial deposits. Soft to firm organic silty clays of up to 18m thick constitute a reasonable proportion of the alluvial deposits on the southern section between chainages 0m and 1650m (Ch. 0m and Ch. 1650m) of the alignment. These soft soils present potential stability and settlement risks to the project and need to be catered for in design as a means of ensuring that the strict in-service performance criteria on the project are met. Ground improvement has been identified as a viable option that could be used to manage long-term in-service settlement issues on the project but it has to be limited to a 5-month window due to flooding concerns. The flooding concerns and poor subsoil characteristics presented two major challenges to the project namely:

a) a reliable assessment of the properties of the subsoil such as in-situ shear strength, consolidation parameters such as compression and recompression indices, coefficient of consolidation, drainage path length, pre-consolidation pressure as well as thicknesses of the poor subsoil layers. A reliable estimate of these parameters will assist in the design of a competitive earthworks scheme;
b) how to construct the southern end of the bypass between Ch. 0m and Ch. 1650m, within the flood plain, as quickly as possible. The client had indi-

cated that should preloading due its cost competitiveness and proven efficiency compared to other ground improvement techniques be adopted as a means of ground improvement scheme on the project, that only preload can be left in place during periods of flooding. Should surcharge be required, as a means of facilitating settlement, they will be limited to a maximum duration of about 5 months during the non-flooding season (i.e. nominally May to October). With the formation level on the southern end of the project kept as low as possible in order to act as a weir to cater for flooding concerns and with poor subsoil thicknesses in the order of 18m to 20m the need for surcharge on the site becomes inevitable. This implies that early works (preload + surcharge construction) is anticipated to be carried out during the wet season.

Data obtained from the first stage piezocone testing at the site were considered unrealistic to enable a reasonable assessment of the consolidation characteristics of the compressible clay layer at the site. A second stage piezocone testing was embarked upon. The results of the second stage testing were very useful for the design of the ground improvement works and have been discussed in this paper.

2 SITE DESCRIPTION AND INVESTIGATION

2.1 *Site Description*

The locality and site plan showing the alignment of the proposed Smithfield Bypass is shown in Figures 1 and 2. It is located to the East of the Captain Cook Highway in the coastal plain. The coastal plain is mainly flat terrain, with alluvial deposits.

Figure 1. Google image of the site area with the proposed bypass alignment shown in broken line.

Figure 2. Site plan showing the extent of the project.

Figure 3. Site photo showing the relatively low elevation of the southern end of the site

The southern segment of the road alignment (Figure 2) from Yorkeys Knob roundabout (Ch. 0m) passes over Avondale Creek and continues to about Katana Road (Ch. 1600m) traversing the low lying Barron River delta, flood plain as shown in Figure 3. The ground elevation levels in this low lying area vary from RL 2m to RL 4m approximately. Vegetation in the flood plain consists mostly of grasses and commercially grown sugarcane.

Further to the north, the road alignment traverses gently undulating ground of elevation generally increasing from RL 4m to around RL 13m at the McGregor

Roundabout. The section of the site generally covered by moderate vegetation with medium to large sized trees, shrubs and grass and is outside the subject of this paper.

2.1 *Site Investigation*

The field investigation for this project was carried out in two (2) stages – Stages 1 and 2. The Stage 1 investigation consisted of the drilling of eight (8) number of boreholes at the proposed bridge structures, thirteen (13) number soil profiling using piezocones (CPTu) soundings and four (4) dissipation tests, the excavation of test pits and the execution of dynamic cone penetrometer (DCP) probing. The Stage 2 investigation consisted of ten (10) CPTu soundings and four (4) pore pressure dissipation tests to fill in the gaps in the Stage 1 investigation and most importantly, to re-evaluate the drainage characteristics of the clay layer due to perceived shortcomings in the results derived from the Stage 1 investigation.

The boreholes were drilled using a track mounted rig under the supervision of geotechnical staff from the Department of Transport and Main Roads (TMR) and generally involved the augering and casing of the first 3m followed by wash boring to completion of the hole. SPTs were undertaken at intervals of one metre for the first 5m and then at an intervals of 1.5m up to a maximum of 32m. From there onwards SPTs were undertaken at 3m intervals to termination depth. In one of the boreholes, field shear vane tests were alternated with U50 thin wall push tube undisturbed samples at 1.5m intervals.

The CPT's and CPTu's were undertaken mainly to establish the thickness of the soft to firm clay layer as well as the in-situ consolidation properties of the layer. The second stage CPTu was necessitated by the poorly executed dissipation tests in Stage 1 which led to drainage characteristics which were considered erroneous. A combined piezocone (CPTu) plot which gives an indication of the soft clay profile at the site is given in Figure 4. Plotted on the figure is also the over-consolidation ratio (OCR) as proposed by Chen and Mayne (1994):

$$OCR = 0.32 \left(\frac{q_c - \sigma_0}{\sigma'_0} \right) \quad \text{..... (1)}$$

where q_c = uncorrected cone resistance; σ_0 = total overburden stress; σ_0'= effective overburden stress.

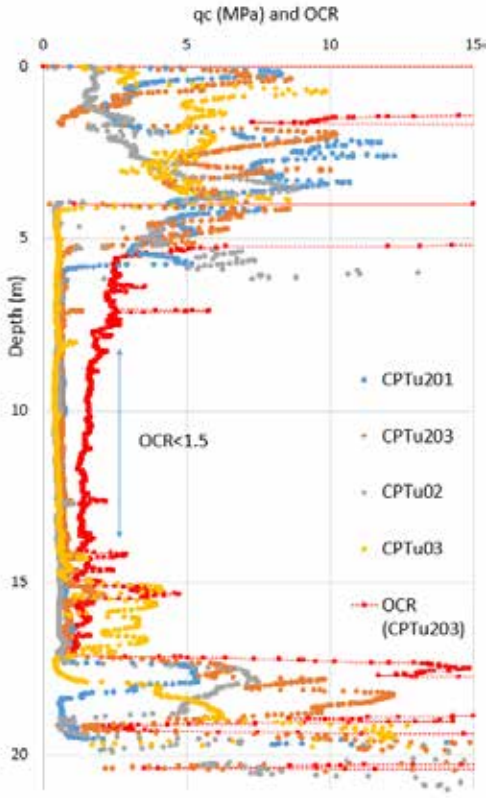

Figure 4. Combined plot of piezocone profiles between chainages 300m and 500m showing typical thickness of soft to firm clay at the Smithfield Project site.

Typical dissipation test results re-plotted in excel format from Stages 1 and 2 tests are shown in Fig. 5.

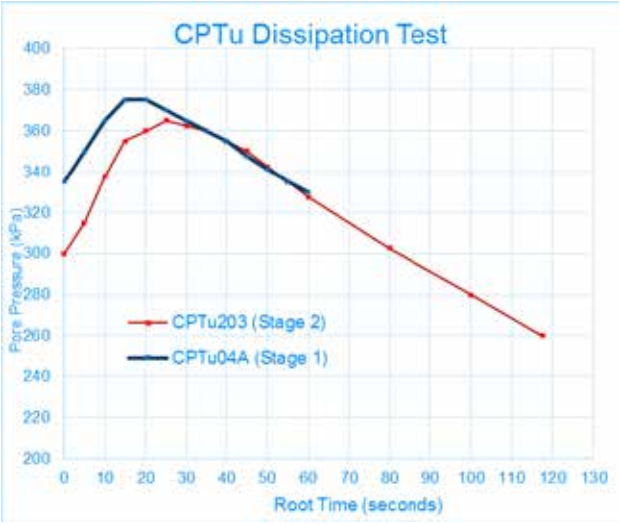

Figure 5. Typical dissipation test results from Stages 1 and 2 investigations.

3 GEOTECHNICAL MODEL AND KEY DESIGN PARAMETERS

The subsoil profile at the southern section of the project between Ch. 0m and Ch. 1650m consist mainly of deep deposits of alluvium. The maximum depth of the drilled holes during the investigation was 50m.

Even up to this depth, no bedrock was encountered. The top layer at the site consists of variable thickness of crustal layer which comprise of silty clay and loose sand mixtures. Underlying this layer is a soft to firm clay layer of variable thickness ranging from 9.5m to 18m with Standard Penetration Test (SPT) blow count generally less than 1 (SPT N <1). Within this thick clay layer a continuous sand lens with variable thickness (generally <1.5m) was encountered, especially between Ch. 550m and Ch. 700m. Underlying the consolidating clay layer is interbedded sand and silt of medium dense consistency but occasionally frim to stiff clay.

The consolidation characteristics of the clay layer namely, void ratio (e_0), compression index (Cc), recompression index (Cr), pre-consolidation pressure (Pc') and coefficient of consolidation (Cv) were established based on laboratory test results backed by correlations with published data. The coefficient of secondary compression (ε_α) was based on published correlation by Mesri (1973). Apart from the Cv values, the values of the other parameters from the two stages of investigations were in agreement. Given in Table 1 is a summary of the interpreted Cv values from Stages 1 and 2 investigations.

Table 1. Interpreted coefficient of consolidation (Cv) from Stages 1 and 2 investigations

S/No.	Test Location	Depth (m)	C_h (m^2/yr)	C_v (m^2/yr)	
				k_h/k_v=2	Average
	STAGE 1				
1	CPTu2A	12.3	1.92	0.96	1.03
2	CPTu3A	9.6	2.54	1.27	
3	CPTu4A	10.9	1.25	0.63	
4	CPTu7A	5.9	2.49	1.25	
	STAGE 2				
5	CPTu201a	7.0	8.4	4.2	2.58
6	CPTu203a	6.0	5.4	2.7	
7	CPTu203a	11.0	2.1	1.05	
8	CPTu209a	8.0	4.7	2.4	

As indicated earlier, the estimated value of Cv based on Stage 1 investigations were considered to be too low. The values were even lower than laboratory test values (1.42 to 2.46 m^2/yr) that were carried out on 50mm samples. They were deemed to be erroneous. As shown in Figure 5, the estimated Cv values were based on poorly conducted dissipation tests that never reached t50 values. Stage 2 tests were carried out to fill some gaps left in the first stage investigation and as a verification tool and were continued to ensure that t50 pore pressure dissipations were reached. In some cases, the dissipation continued overnight. The results were generally higher than the laboratory values without accounting for scale effect. Generally, it is widely accepted that actual (field operating) Cv values could be as high as 5 to 10 times those of laboratory values. The adopted Cv values based on Stage 1 test was 1.4m^2/yr, a median value of the test results from piezocone and laboratory test results. For the Stage 2, values ranging between 3m^2/yr and 5m^2/yr were adopted. The 3m^2/yr was considered lower bound in recognition of the sand lenses observed from the field data.

Summarized in Table 2 are the design parameters adopted for the consolidating clay layer for the Smithfield Project.

Table 2. Adopted design parameters for consolidating clay layer

Material	Unit Weight (kN/m^3)	Moisture Content (%)	Liquid Limit (%)	e_o	c_c
Soft to firm clay	18.0	*60 to 77	*60 to 97	1.82	0.7
	c_r	P_c' (kPa)	$\varepsilon_{\alpha\,(\%)}$	Cv (m^2/yr)	
				Stage 1	Stage 2
	0.07	100 to 110	0.008	1.4	3 to 5

Note: * Based on results from BH01

3 DESIGN CRITERIA FOR SETTLEMENT

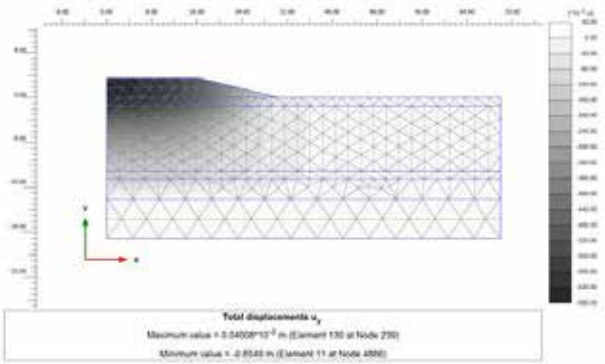

Figure 6. Estimated primary consolidation settlement between Ch. 550m and Ch. 700m.

4.1 Design Criteria

As per the Queensland Department of Transport and Main Roads Geotechnical Design Standard (GDS) - Minimum Requirements (2015), the following settlement criteria should be met to ensure minimisation of whole-of-life costs and maximise whole-of-life benefits for road pavements:

- maximum total in-service permissible settlement within 40 years of construction (post construction settlement – PCS) shall not be more than 50mm within

The structure zone and 200mm away from structure-zone. The structure zone is a length not less than 25m within the approach to any structure;

- the structure zone shall be constructed to the requirement of the GDS;
- design change in grade due to the differential settlement over any 5m length of pavement must be limited to 0.3% to 0.5%, depending on pavement type; and
- post-construction in-service movements must not impair or compromise pavement support.

3.1 *Design for Settlement*

3.1.1 *Construction Program*

Critical to the delivery of this project is the need to cater for hydraulic (afflux) issues that may arise due to embankment placement. The Smithfield Bypass project is located in the Barron River floodplain and strict controls are required to be put in place to minimise any impacts due to afflux.

To cater for hydraulic concerns, the vertical alignment between Ch. 0m and Ch. 550m has been lowered to enable this section of the bypass act as a "weir" and is overtopped in a flood event equal to or greater than an annual exceedance probability (AEP) = 20% (5yr ARI). Further to this, it is a requirement on the project to construct the southern end of the bypass (Ch. 0m to Ch. 1650m), within the flood plain, as quickly as possible. Any preload works can be left in place during periods of flooding, however, surcharge works are limited to a maximum duration of approximately 5 months (i.e. nominally May to October). To meet the May to October target, it implies that early works construction (preload + surcharge) has to be carried out in wet season and the surcharge removed before the flooding season.

3.1.2 *Design and Design Outcomes*

Initial estimates of the settlement magnitude and degree of consolidation were carried out using Terzaghi's I-Dimensional consolidation theory implemented using excel spread sheet. The calculations were optimized in order to accommodate multiple soil layers efficiently as well as simulate staged construction procedure using Plaxis 2D (2014) and Settle 3D v. 3.0 (2009) softwares. Both the Mohr-Coulomb and soft soil creep advanced model in Plaxis were used in settlement estimates. The Mohr-Coulomb model was used to model the behavior of the embankment and sandy layers whereas the soft soil creep model was used to model the behavior of the compressible clay layer. The results of the analyses are summarized in Table 3 and Figures 6 and 7.

Table 3. Summary of the results of the analyses

Chainage (m)	**Max. Embankment Height (m)**	**Stress History (Expected Settlement)**	**Estimated total settlement Primary (Creep*)**
0 to 300	At - Grade	-	-
300 to 550	2.5	POP << ΔP (High)	470 (153)
550 to 700	3.5	POP << ΔP (High)	605 (191)
700 to 800	Bridge over Avondale Creek		
800 to 1060	1.6	POP < ΔP (Low)	157 (211)
1060 to 1550	1.3	POP > ΔP (Negligible)	-
1550 to 1650	At - Grade	-	-

Chainage (m)	Maximum Embankment Height (m)	Time in months to achieve 90% consolidation under preload $Cv\ (\frac{m^2}{year})$			Time (months to achieve 90% consolidation under preload + PVD $Cv\ (\frac{m^2}{year})$		
		1.4	3	5	1.4	3	5
0 to 300	At - Grade		-	-	-	-	-
300 to 550	2.5	>5	>5	>5	>5	<5	<5
550 to 700	3.5	>5	>5	>5	>5	>5	<5
700 to 800	Bridge over Avondale Creek						
800 to 1060	1.6	>5	>5	>5	>5	<5	<5
1060 to 1550	1.3	-	-	-	-	-	-
1550 to 1650	At - Grade	-	-	-	-	-	-

Note: *Creep settlement within 40 year service life.

In the light of the client request to limit surcharge on the project to no more than 5 months and considering the settlement criterion on the project, the following deductions are made from the results of the analyses.

a) In order to satisfy the permissible post construction settlement criterion on the project, ground improvement is required;

b) With only the preload in place, 90% consolidation settlement will not be achieved within 5 months;
c) On the basis of the adopted c_v value obtained from the 1st Stage site investigation, to meet the 5 months window allowed for ground improvements, surcharge in addition to the use of PVD and preload will be required for a 660m length section of the site with embankment heights ranging from 1.6m to 3.5m;
d) On the basis of the revised Cv that was obtained from a more realistic dissipation test in the Stage 2 investigation, the use of surcharge is limited to the 150m length between Ch. 550m and Ch. 700m for a lower bound Cv of $3m^2/yr$. This equates to about 22% of the 660m length of the site that are not at-grade. Should the operating c_v be up to $5m^2/yr$, the 90% consolidation target will be achieved without the need for surcharge for the 660m length of the project;
e) Considering the cost of re-mobilizing and carrying out additional testing at the site for the second stage testing and the cost implication of limiting the area to be surcharged that resulted from the revised Cv values, there is significant cost benefit to the project. The second stage testing is therefore justifiable;
f) As part of a validation tool on the project, the use of observational approach is recommended to be implemented and monitored before, during and after construction.

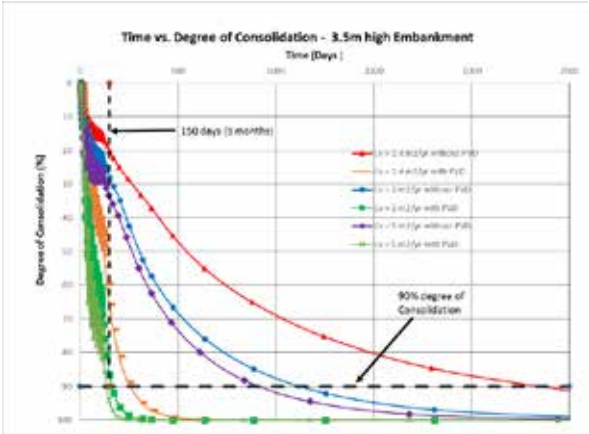

Figure 7. Estimated degree of consolidation with and without PVD for varying coefficient of consolidation (Cv) between Ch. 550m and Ch. 700m.

4 CONCLUSIONS

Due to other competing demands in government spending, funding for road projects do not come so easily in recent times. Where poor subsoils of low bearing capacity and compressibility are encountered and stringent settlement criteria are to be met, cost of ground improvement works add on to the overall cost of the project. The Smithfield Bypass project falls into this category due to additional cost imposed on the project by poor subsoil consisting of 9.5m to 18m thick very soft to firm compressible clays.

A re-appraisal of the coefficient of consolidation (Cv) obtained from the 1st Stage investigation carried out on this project and used in the initial estimates of the ground improvement works was carried out due to perceived inconsistencies in the test results. A 2nd Stage investigation aimed at establishing a more realistic Cv was carried out and the obtained values used in further analyses.

Based on the 1st Stage Cv = $1.4m^2/yr$, the recommended ground improvement works at the project site will consist of the installation of PVDs, preload plus surcharge and would have been carried out to 100% of the southern section of the site except for the at-grade sections. The total length of the southern section requiring ground improvement is equal to 660m. Using the revised Cv values, on the basis of a lower bound Cv of $3m^2/yr$, only 22% section of the 660m length would require surcharge. With a Cv of $5m^2/yr$, only the PVD and preload is required without surcharge to achieve a 90% consolidation within the required 5 month period imposed on the project by flooding risks.

The revised Cv on the basis of the 2nd Stage investigation has significant cost benefit for the project.

5 ACKNOWLEDGEMENTS

The author would like to express his gratitude to his colleagues in the Geotechnical Engineering Section of the Department of Transport and Main Roads, especially the Director Lalith Welikala and Engineers Siva Sivakumar and Dr Preba Nadarajah who reviewed the geotechnical design report from which the contents of this paper were largely drawn from. Likewise my thanks also goes to Engineers Devinder Pal, Jeremy Kirjan, Mali Yagama, Michael Sun and Vernon Pereira, Regional Geologist, TMR, Far North, Region for their assistance in the preparation of the technical report and this paper.

6 REFERENCES

Brinkgreve, R.B.J (2013), Plaxis 2D Manual, A.A. Balkema Publishers, Netherlands.
Chen, B. S. C and Mayne, P. W. (1994), Profiling the overconsolidation ratio of clays by piezocone tests. NSF Grant No. MSS-9108234, Georgia Institute of Technology, Atlanta.
Mesri, G. (1973), Coefficient of secondary compression. Proc. ASCE, 99, S.M.1, pp. 123-137.
Queensland Department of Transport and Main Roads (2015), Geotechnical Report No. R3540, Smithfield Bypass Project, Yorkeys Knob Roundabout to Reed Road Roundabout.
Queensland Department of Transport and Main Roads. 2015. Geotechnical Design Standard – Minimum Requirements.
Rocscience Inc. (2009), Settle3D-Settlement and consolidation analysis.

Geotechnical and Geophysical Site Characterisation 5 – Lehane, Acosta-Martínez & Kelly (Eds)

Soil strength in the Murray River determined from a free falling penetrometer

A. Fawaz, A. Teoh & D.W. Airey
School of Civil Engineering, University of Sydney, Australia
T. Hubble
School of Geosciences, University of Sydney, Australia

ABSTRACT: The paper describes briefly the design of a new free fall penetrometer developed at the University of Sydney. The motion of the device is captured using a low cost inertial measurement sensor unit, miniature processor and open source software. The device has been used to investigate the soil strength of the upper 2 m of sediment in the Lower Murray River. The results from the free falling penetrometer have been compared with data from conventional CPT tests performed at several points along a 100 km stretch along the Lower Murray River. These data have allowed an assessment of rate effects associated with the free falling device. The rapidity and ease of use of the free falling device has then enabled a complete description of the soil strength across the width of the river at several locations. The paper will present summary data from this investigation and highlight the benefits of free falling penetrometers.

1 INTRODUCTION

Characterisation of surface sediments in rivers, estuaries and offshore can be challenging because the sediments are often very soft, and special and costly equipment is needed to obtain undisturbed samples. In-situ testing, for example using cone penetration tests, can provide useful information, however because of the cost and time associated with deployment this is often impractical for all but major projects. An alternative is to make use of simple and relatively lightweight free falling penetrometers (FFP). These provide an indication of soil strength and in some cases additional sensors enable soil type and state to be evaluated. For most free falling penetrometers accelerometers are used to track the motion and this data is used in simple force balanced equations to determine the soil strength. Evaluation of soil strength is not straightforward because of uncertainties in the magnitude of rate effects and the effects of soil drag associated with the rapid penetration.

There are two main types of FFP; full-shafted that have identical shaft and tip diameters, and thin-shafted that have tip diameters larger than the shaft. Full shafted penetrometers are similar to standard CPT devices and can provide similar data. However, the different shaft and tip responses, and differences in rate effects complicate interpretation of the dynamic response. Thin-shafted penetrometers are generally only instrumented with a single accelerometer so that their ability to distinguish soil type is limited, however, the absence of shaft resistance (Hurst & Murdoch 1991), makes interpretation of the data much simpler. This paper describes the development and application of a new thin-shafted device. The new device builds on experience from an extensive series of laboratory model scale tests of a miniature FFP (Chow and Airey, 2014) and the method of interpretation developed in that study (Chow and Airey, 2013).

An important goal of this project was also to demonstrate the ability of cheap and widely available components and open source software to be utilized to create the instrumentation package (Surjadinata and Airey, 2015). The instrumentation package makes use of a low cost inertial measurement unit (IMU). These units contain multiple sensors including a three axis accelerometer and a three axis gyroscope that generate measurements of linear acceleration and angular velocity, respectively. To date applications of IMUs in geotechnical applications are rare, however, they have also been used by Blake et al (2016) in other types of dynamic penetration test.

The newly designed thin-shafted penetrometer has been used to investigate the soil strength of the Lower Murray River. Between 2008 and 2011, 68 bank failures were recorded by the South Australian Department of Water, Environment and Natural Resources (2016) between Blanchetown and Wellington on the Lower Murray River. These riverbank collapses are believed to be due to historically low river levels and the presence of soft clays. Back

analyses of the failures have been based on soil strength data primarily obtained from CPT measurements obtained on the river banks. The FFP tests will allow the strength profile across the river to be explored and will assist in constraining the back analysis of the failures and improve understanding of the failure mechanisms.

2 APPARATUS AND PROCEDURE

2.1 *Free Falling Penetrometer Apparatus*

Figure 1 shows the configuration of the FFP device. The design of the penetrometer required consideration of weight, geometry, internal member strength, instrumentation and provision of a waterproof module to allow underwater use. The mass of the penetrometer determines the momentum of the penetrometer at impact, and as a result determines the penetration depth. However, there are limits to the mass as if it is too high the ease of deployment and recovery from the riverbed would require special equipment and also any increase in size could increase fluid drag. The mass of the penetrometer was made variable with the addition of slots on the shaft for additional weights. The maximum mass of the penetrometer used was 11.5kg, although this could be increased by adding further weights.

The tip shape and size have been found to have negligible effect on the interpreted soil resistance (Chow and Airey, 2014), but increasing tip size increases the resistance and thus reduces the depth of penetration. Tip diameters which varied between 30 mm and 50 mm have been used in the current tests.

A shaft diameter of 20 mm was used. The diameter needed to be sufficient to: resist buckling on impact into a hard soil; damage during handling, and to be broken down into sections for ease of transport. It was also required that the device had sufficient strength to be extracted from the soil.

The instrumentation was contained in a thin-walled aluminium cylindrical module, 80 mm in diameter and 130 mm long. The module was mass balanced about the axis of the cylinder and four small fins were attached to the outside of the module to prevent rotation when falling under gravity. The instrumentation module housed a Razor IMU, a breakout board, a Raspberry Pi microcomputer, a microSD data card, a WiFi dongle and a battery pack. These components are all widely available and had a total cost of A$190. The IMU incorporates three sensors, a triple axis gyroscope, a triple axis accelerometer and a triple axis magnetometer producing 9 degrees of inertial measurement. The three sensors are all processed through an on-board microcontroller and data output over a serial interface. The sensor chip responsible for the triple axis accelerometer is the ADXL345. The ADXL345 is a

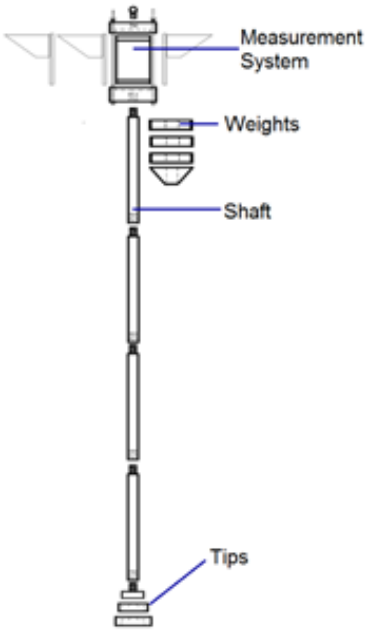

Figure 1. Schematic diagram of the FFP device

small, thin, low power, 3-axis accelerometer with range of ±16g and a resolution of 13 bits. The IMU was controlled from the microcomputer and data stored on the microSD card. Software provided with the IMU allowed all 9 channels to be logged at a rate of 50 Hz, which was not considered sufficient. The control software was modified to allow either the 3 accelerometers to be logged at a rate of 250 Hz or just the vertical acceleration to be logged at a rate of 750 Hz. Preliminary tests showed that the device fell vertically and without rotation and in the tests reported below only the vertical acceleration has been recorded at the maximum logging rate.

2.2 *Test procedure*

The measurement of the undrained shear strength along the Lower Murray River required equipment for deployment and retrieval of the penetrometer, as well as transportation upstream and downstream the river.

A small motor boat was used as the main penetrometer deployment vessel. To retrieve the penetrometer nylon rope with 300 kg tensile capacity was attached to the motor boat and the top of the FFP device. To start a test the FFP device was lowered into the water, as shown in Figure 2, and held vertically on the side of the motor boat. The data logging program was then initiated from a laptop on the motor boat that sent control commands wirelessly to the module's microcomputer. The logging program was set to run for 2 minutes and then the penetrometer was released and allowed to fall freely. After a test the penetrometer was retrieved using the rope and when it was out of the water the data could be downloaded wirelessly. The data could also be transmitted

Figure 2. Deployment of the Free Falling Penetrometer

through a wired connection but this required breaking the seal on the instrumentation module, which was undesirable in the small craft used for deployment. The battery and data storage were sufficient to allow several drops to be performed each day.

2.3 *Data Interpretation*

The motion of the FFP can be described by:

$$ma = W - F_d - F_t \quad (1)$$

where m is the mass, a the measured acceleration, W the submerged weight, F_d the drag force, and F_t the soil tip resistance.

Laboratory studies reported by Chow and Airey (2013) have shown that the tip resistance can be determined using:

$$F_t = s_u A N R \quad (2)$$

where s_u is the undrained strength at the reference penetration rate, A is the cross-sectional area of the tip, N is a bearing capacity factor taken as 10.8, and R is a rate factor given by

$$R = 1 + (1.926 - 0.023\, s_u)\left(1 - e^{-0.01 v / v_{ref}}\right) \quad (3)$$

where v is the velocity of penetration, and v_{ref} the reference penetration rate.

Combination of equations 1 to 3 enables the undrained strength to be evaluated. It should be noted that the drag force, which arises mainly from the motion of the instrumentation module through the water, is also a function of velocity. This force has been estimated from the initial stage of the test where the device is falling through water.

3 RESULTS

The Lower Murray River test sites are located in reaches of the channel that are incised into an extensive layer of soft lacustrine clay deposited between 6,000 and 2,000 years before the present day (Hubble and De Carli 2015). CPTs conducted on the river banks have indicated that a 10 to 20 m thick soft clay layer is present with undrained strength varying from 10 ± 5 kPa at river level increasing with depth at a rate of about 1 kPa/m (Liang et al, 2012). Water depths in the centre of the 200 m wide channel typically vary from 10 to 20 m.

A typical CPT result is shown in Figure 3 (from Hubble et al, 2014). The CPT test was performed from a stable platform situated about 3 m out from the waterline of this regulated river's channel margin. There is some sand at the soil surface, derived from fill on the riverbank and then a uniform clay deposit with q_c increasing linearly with depth. There is a suggestion of softening in the upper 5 m as for these depths q_c values drop below the linear trend that is evident in Figure 3 for depths greater than 7.5 m. CPT results at various locations along a 50 km stretch of the river have shown practically identical responses. In several locations a very soft layer of recently sedimented clay, up to 2 m thick, overlies the older consolidated clay. The presence of a soft and possibly mobile upper layer and softening in the

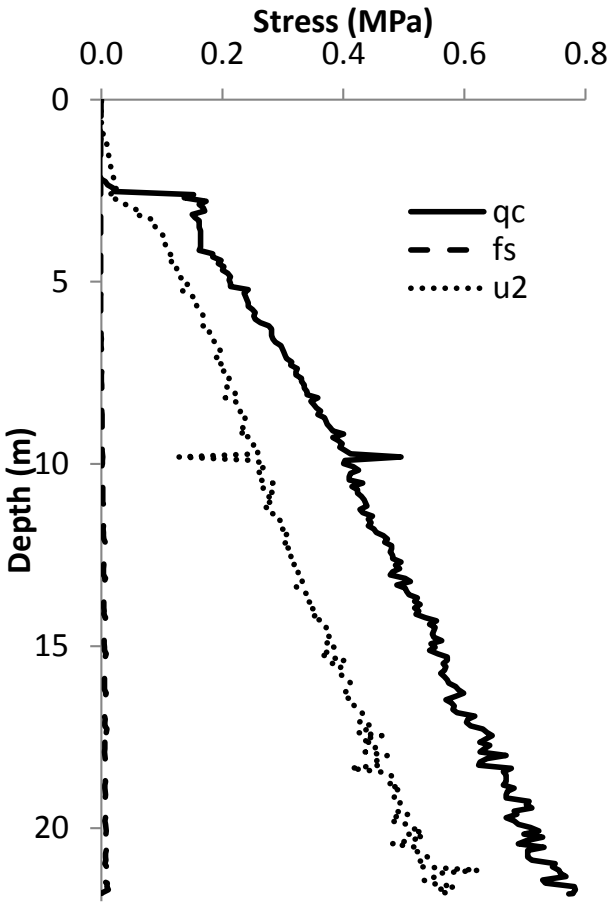

Figure 3. Typical CPT response (after Hubble et al, 2014)

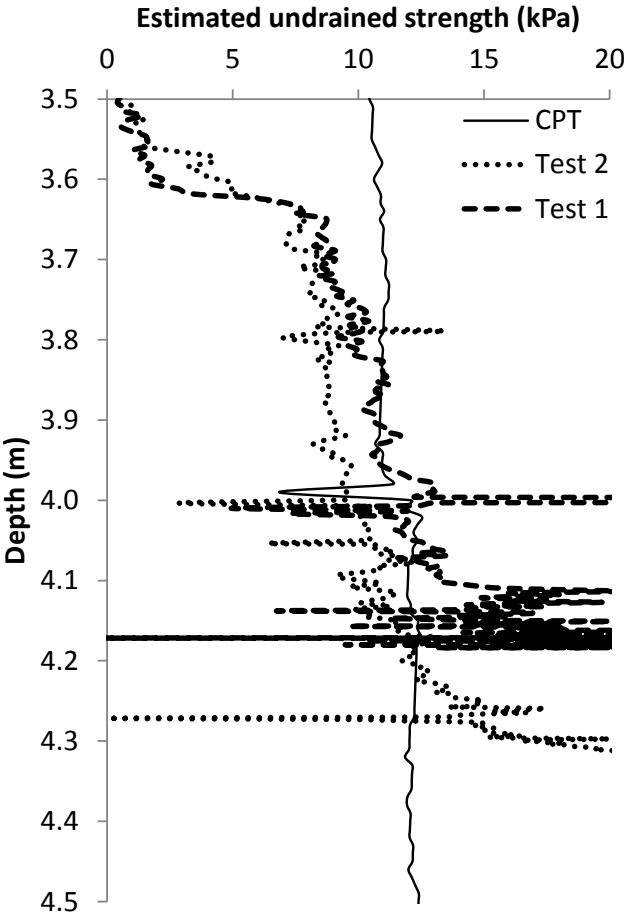

Figure 4. Comparison of strengths from FFP and CPT

clay associated with river incision has important implications for river bank stability. The FFP is an ideal tool to investigate these aspects which primarily influence the surficial layers.

To enable comparison of the FFP and CPT responses two FFP drops were conducted within 20 m of the location (Riverglen marina) of the CPT shown in Fig 3. They could not be performed closer because the FFP tests had to be performed in water depths of about 4 m to allow the device to reach close to its terminal velocity.

A comparison of the undrained strengths estimated from the static and dynamic penetrometers is shown in Figure 4. This figure shows the undrained strength as a function of depth below the water level in the river. The two FFP drops showed similar responses and penetrated on average 0.75 m after impacting the soil at a similar water depth of 3.5 m. The FFP drops show that there is a soft layer, about 0.1 m thick, over the consolidated clay, and that from 3.65 m to 4.2 m the strengths are similar, or slightly lower, than that estimated from the adjacent CPT, for which the mean q_{net} was 0.13 MPa. The similarity of the responses suggests that the method of interpretation of the dynamic loading is providing reasonable values of the undrained strength. However, the tests were performed at different points down the slope and although the undrained strength is expected to vary linearly with depth from the original clay surface, some softening of the clay would be expected near the surface associated with the stress reduction from the erosion of overburden caused by the river. If the FFP data are correctly indicating the strength then at this location, close to the bank, there is apparently little softening of the clay. It can also be seen from Figure 4 that the dynamic FFP responses are more sensitive to slight variations in soil characteristics and it is notable that all three tests pick up a weak layer at 4 m. In the final 0.1 m of penetration both FFP responses indicate a rapid increase in soil strength. This is believed to be a consequence of equation (3), which accounts for the rate effects associated with the rapid penetration, not responding correctly as the penetrometer is slowing rapidly to a halt, a response which has also been observed in laboratory tests (Chow and Airey, 2014). To allow for this effect would significantly increase the complexity of the equations and detract from the simplicity of the method of interpretation.

An alternative method of assessing the reliability of the FFP strength interpretation is to compare the results of a series of drops with different sized tip diameters. Results are presented for FFP drops at two locations, Woodlane Reserve in Figure 5 and Theile Reserve in Figure 6. In both locations the tests were performed about 50 m from the river bank in water depths of about 9 m. Because the boat was not anchored the exact locations of the drops varied,

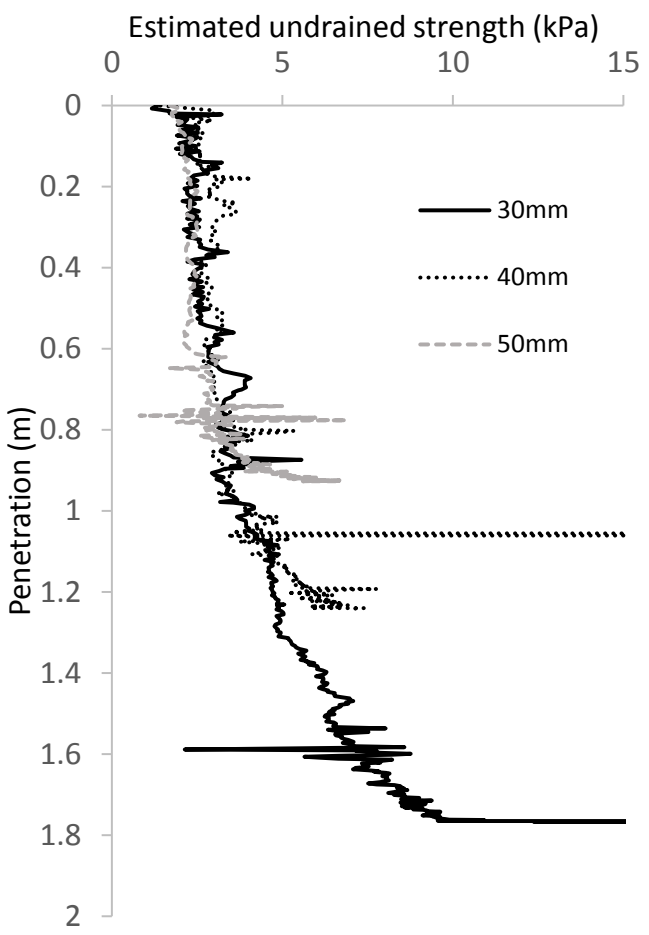

Figure 5. Effect of tip diameter, Woodlane Reserve

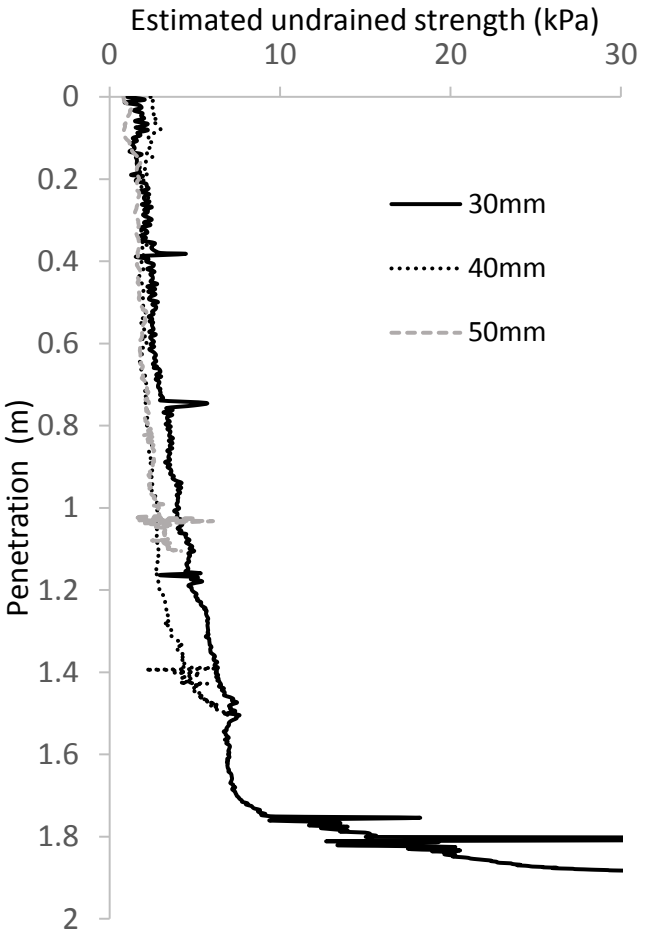

Figure 6. Effect of tip diameter, Theile Reserve

but were estimated to be within 20 m of one another. Figure 5 shows that essentially the same strength profile is obtained, which is independent of the tip diameter. However, the resistance to penetration increases with tip diameter and the penetration reduces from 1.8 m with a 30 mm tip to 1.25 m with a 40 mm tip and 0.95 m with the 50 mm tip. Figure 6 shows a very similar picture with penetrations of 1.9 m, 1.5 m and 1.1 m for the 30 mm, 40 mm and 50 mm tips respectively. Figure 6 shows that the 30 mm tip indicates slightly higher soil strengths from 0.4 m on, but this is probably a consequence of a slightly different FFP position, as across the river water depths and the strength of the soft clay layer varied. It should also be noted that for penetrations greater than 1.9 m, as at Theile Reserve with the 30 mm tip, the instrumentation module contacts the soil and after this the interpreted strength is meaningless.

It is also evident from the low strengths in both Figures 5 and 6 that a layer of soft and relatively recent sediment overlies the consolidated clay deposit. At depths of 9 m an undrained strength of between 15 kPa and 20 kPa was expected from the measurements on the river margins. However, this consolidated layer cannot be observed at either site. The Theile Reserve results suggest higher strengths beyond depths of 1.8 m, but as discussed above these may be unreliable because of problems with interpreting the strength in the final 0.1 m of penetration and because of the impact of the instrumentation module with the soil surface.

4 DISCUSSION

One of the objectives of this project was to explore the capabilities of cheap and readily available IMUs, microcomputers, computer accessories, and associated open source software. One of the limitations of these low cost devices is their data processing speed. As explained by Blake et al (2016) to fully describe the motion of a falling penetrometer like device requires three accelerometers and three gyroscopes. However, the serial data rate of 50 Hz from the IMU was not considered sufficient to accurately capture the response of the penetrometer when it impacts the soil. It was decided to capture only the vertical acceleration as this allowed data to be captured at over 700 readings per second. Provided the device falls vertically the motion will be correctly captured, and to ensure this care was taken to balance the instrumentation module and provide fins to minimise any rotations. Typical acceleration and velocity data as a function of time are shown in Figure 7 for a drop with a 30 mm tip diameter. This figure shows that as the FFP falls through the water the acceleration ini-

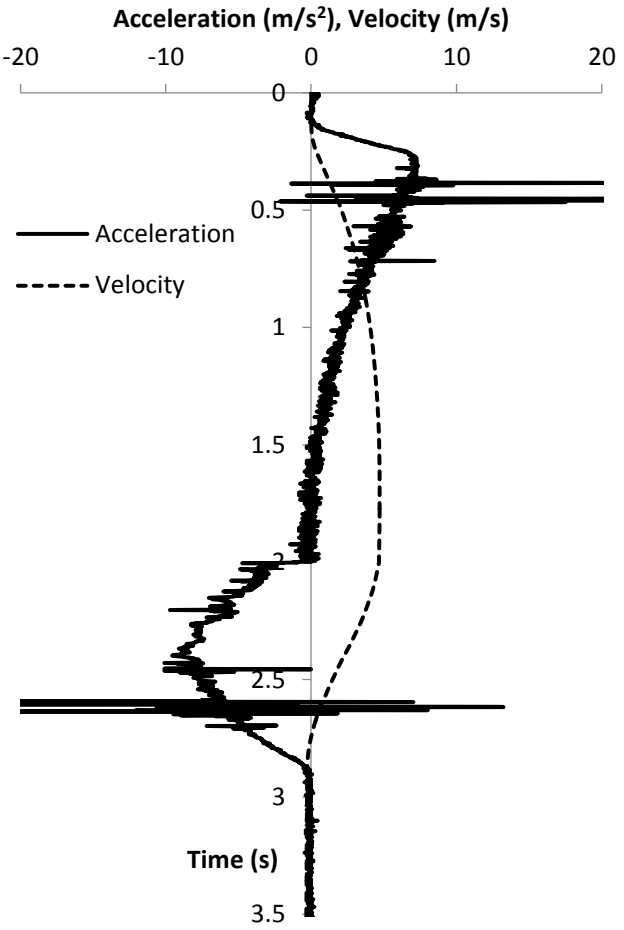

Figure 7. Typical acceleration and velocity records

tially increases rapidly and then slowly reduces to zero as a terminal velocity of about 4.7 ms^{-1} is reached. Slightly lower terminal velocities were attained with larger tips. The FFP needs to fall about 3.5 m to reach its terminal velocity and as the device is 2 m long, water depths of 5.5 m are required to reach this speed. The spikes in the response as the FFP falls through the water are believed to be caused by the retrieval rope, and occurred at similar times in all the tests. Impact with the soil can be clearly detected from the sudden deceleration at time of 2 seconds even though the strength of the soil was only of the order of 2 kPa. In the soft clay investigated the rate of data recording has provided a very detailed picture of the penetration which typically took 0.5 s to 1 s.

5 CONCLUSIONS

A low cost thin-shafted free falling penetrometer has been developed which is easy to use and can provide fast and accurate measurement of undrained shear strength in soil above or underwater. The method of interpretation developed from laboratory tests in kaolin has been shown to provide reasonable strength estimates in the field. Penetrations of up to 2 m have been obtained in soft clay and the time to drop and retrieve the penetrometer is typically 3 minutes.

More testing in a variety of soils is required to investigate the capabilities of the FFP. It has been demonstrated that the FFP is capable of producing repeatable results and these results are independent of the tip diameter and mass. However, to achieve the full penetration optimisation of tip diameter and FFP mass will be required.

The field study revealed that there were significant depths of soft, relatively recent deposits of clay overlying the original clay layer, the extent of which had not previously been realised. The results also suggested some softening of the surface clay has occurred, which could be significant for the analysis of the majority of the failures of the river banks which are relatively shallow.

6 ACKNOWLEDGMENT

The assistance of the support team of Ross Barker, Anna Helfensdorfer, Stuart Jamieson and Guien Miao for the field testing is gratefully recognized.

7 REFERENCES

Blake AP, O'Loughlin CD, Morton JM, O'Beirne C, Gaudin C, White DJ. (2016). In-situ measurement of the dynamic penetration of free-fall projectiles in soft soils using a low cost inertial measurement unit. Geotechnical Testing Journal, 39, 2,235-251

Chow SH and Airey DW (2013) Soil Strength Characterisation Using Free Falling Penetrometers, Géotechnique, 63,13, 1131-1143

Chow SH and Airey DW (2014) Free falling penetrometers: a laboratory investigation in clay, J. of Geotechnical and Geoenvironmental Engineering, 140, 1, 201-214

Hubble T, De Carli EV, Airey DW (2014). Geomechanical modelling of the Murray's Millennium Drought river bank failures: a case of the unexpected consequences of slow drawdown, soft bank materials and anthropogenic change. 7th Australian Stream Management Conference 278-284. Townsville, Queensland.

Hubble, T., and De Carli EV. (2015) Mechanisms and Processes of the Millennium Drought River Bank Failures: Lower Murray River, South Australia, Goyder Institute for Water Research Technical Report Series No. 15/5, Adelaide, South Australia.

Hurst, R.B. & Murdoch, S. (1991). Measurement of sediment shear strength for mine impact burial predictions. Report of the 18th Meeting of the mines and mine countermeasures technology panel GTP-13

Liang, C, Jaksa MB and Ostendorf B (2012) GIS-based back analysis of riverbank instability in the lower river Murray, Australian Geomechanics, 47, 4, 59-65

South Australian Government (2016) Riverbank collapse historical incident register, https://www.waterconnect .sa. gov. au / Systems/RCHIW/SitePages/Home.aspx

Surjadinata J and Airey DW (2015) Development and Applications of Mobile Applications in Geotechnical Engineering, 12th ANZ Conference on Geomechanics, 136-142

Geotechnical and Geophysical Site Characterisation 5 – Lehane, Acosta-Martínez & Kelly (Eds)

Correlations of Regional (Poland) Geotechnical Parameters on the Basis of CPTU and DMT Tests

T. Godlewski
Building Research Institute, Warsaw, Poland

ABSTRACT: The article presents the results of geotechnical in situ tests of different soil types for the Polish area. Static penetration tests (CPTU) and dilatometer tests (DMT) enabled to determine deformation and strength parameters of subsoil. Relationships between these two methods and measured basic parameters have been determined and analysed. The article presents some new, experimental correlations, for example: contours of normalized M_{DMT} chart obtained additionally for different types of soils, establishing more accurate dependences for Polish grounds conditions. Also some recommendations for the interpretation of the results from CPTU and DMT tests for analysed deposits have been proposed.

KEYWORDS: in situ tests, CPTU, DMT, regional correlation, types of soils.

1 INTRODUCTION

The requirements of the Eurocode 7 (PN-EN-1997-1 and PN-EN 1997-2) have caused the necessity of quantitative description of soils for geotechnical design. The in situ tests give this opportunity. Their main advantages are commonly known: continuous recording, decreasing the number of laboratory tests and drillings, reduction of total costs and time of investigations. They also allow for determining the soil parameters in natural conditions.

The correlations between sounding results and geotechnical parameters require regional determination or adaptation for local conditions. Additional difficulties refer to many other factors that have an influence on the soil behavior and which are still impossible to measure, or the measurements are not reliable enough (Wysokiński et al. 2009; Godlewski 2013).

The results obtained by means of new types of static probes with piezocone (CPTU) or flat dilatometer of Marchetti type (DMT) do not have Polish correlations for geotechnical parameters determination, or the existing ones have not been verified yet. The data obtained by foreign researchers refers to local soils and may not be applicable for Polish conditions. The results obtained from soundings are used mainly for geological profile investigations and determination of density or liquidity index of soils. Some geotechnical parameters necessary for design calculations are still assessed on the basis of the $q_{c(t)} \rightarrow I_D$, I_L correlation. Many institutions in Poland have started intensive research on interpretation methods of CPT/CPTU and DMT results for determination of geotechnical parameters (φ', c_u, E_{eod}) (i.e. Bałachowski et al. 2008; Wysokiński et. al. 2009; Wierzbicki 2010; Młynarek et al. 2013; Rabarijoely & Garbulewski 2013; Godlewski 2015). The aim of the research project (Grant Number 4 T07E 047 30, 2008) conducted by ITB (Building Research Institute in Warsaw) was to find these correlations.

2 INVESTIGATION METHODS

ITB has large experience in in-situ soil investigations by means of cone penetration test and dilatometer test. The huge amount of data, including different types of soils for different types of constructions, has been collected. In the research project (Grant Number 4 T07E 047 30, 2008) the new results were added to the database and statistical calculations were done. Wherever it was possible, the module obtained from in situ tests was compared to the one obtained by back-analysis based on the settlements measurements.

The correlations are based on the results from more than 30 test sites on different types of soils in Poland. Each test site was considered as a node, consisting of CPTU profile, DMT profile, geological profile, laboratory tests and settlement data. After extreme values elimination, the data was divided into litho-genetic groups from different test sites. The following litho-genetic groups were distinguished:

- alluvial deposits of River beds - alluvial sands,
- fluvioglacial deposits - fluvioglacial sands,
- tertiary clays,
- glacial deposits - glacial clays (tills from Middle Polish glaciation),
- eolian deposits - loess,
- silty hollow deposits - silty sands, silty clays, silts,
- organic deposits - gyttja, mud (alluvium silt), peat.

All the tests were conducted in accordance with Eurocode 7 and specification for the CPTU and DMT. The tests were carried out very close to each other (within a 2-3 m) on chosen test sites. Because the frequency of measurements for CPTU (each 2 cm) and DMT (each 20 cm), the results from CPTU were averaged (from upper and lower surrounding values) to obtain the mean value for each 20 cm. The measured values from these two types of soundings were compared to find correlations in interpretation of the profile and modulus.

3 FROM THE TESTS RESULTS TO CORRELATIONS

3.1 *Tests Results*

For each type of the soil the R_f ratio (for CPTU) → I_{DMT} (DMT material index) were compared. The results were plotted on existing nomograms. The best fitting was obtained on Schmertmann nomogram (Schmertmann 1986) and all further analyses were based on this graph (Figure 1).

The highest variability was observed for hollow and organic soils. The diversity for hollow soils may be explained by specific sedimentation mechanism which causes high variability in vertical and horizontal profile. The organic soils are represented by many lithological types of soils: organic sand, mud, peat and gyttja.

This group appears in the graph under the line marked along the value of q_c < 1-1.5 MPa. This value for Polish conditions may be considered as the border of "weak" soils (often considered for replacement or improvement). As it may be seen in the graph, clays and glacial clays (tills) are characterized by high variability. The interbeddings of more or less sandy or silty layers may be observed within clays and the group of clayey sands may be distinguished additionally. The influence of granulometry on q_c value in sandy soils was confirmed.

On the basis of the obtained data, a simple comparison has been made between the two analysed methods. Because each point on the graph (Figure 1) has the assigned value of the modulus, it was possible to interpolate curves (an approximation is applied on the basis of the contour map). In Figure 2, the interpolated curves of constrained modulus obtained from DMT tests with a Schmertmann classification diagram as a background are presented (Wysokiński et al. 2009). This simple correlation has its own drawback (a large dispersion of the collected data, over a wide range of effective vertical stress), but allows to make first approximation and has its support by practical experience. The dilatometer modulus correlates with settlements measurements (see next chapter), so the values of the modulus may be considered as a careful estimation of modulus for calculations according to Eurocode 7. The obtained values of modulus compared to those presented in PN-81/B-03020 standard for different types of soils are close to those obtained from oedometer tests (this was also confirmed for other types of soils by other authors (i. e. Marchetti 1980; Mayne 2001; Monaco et al. 2006).

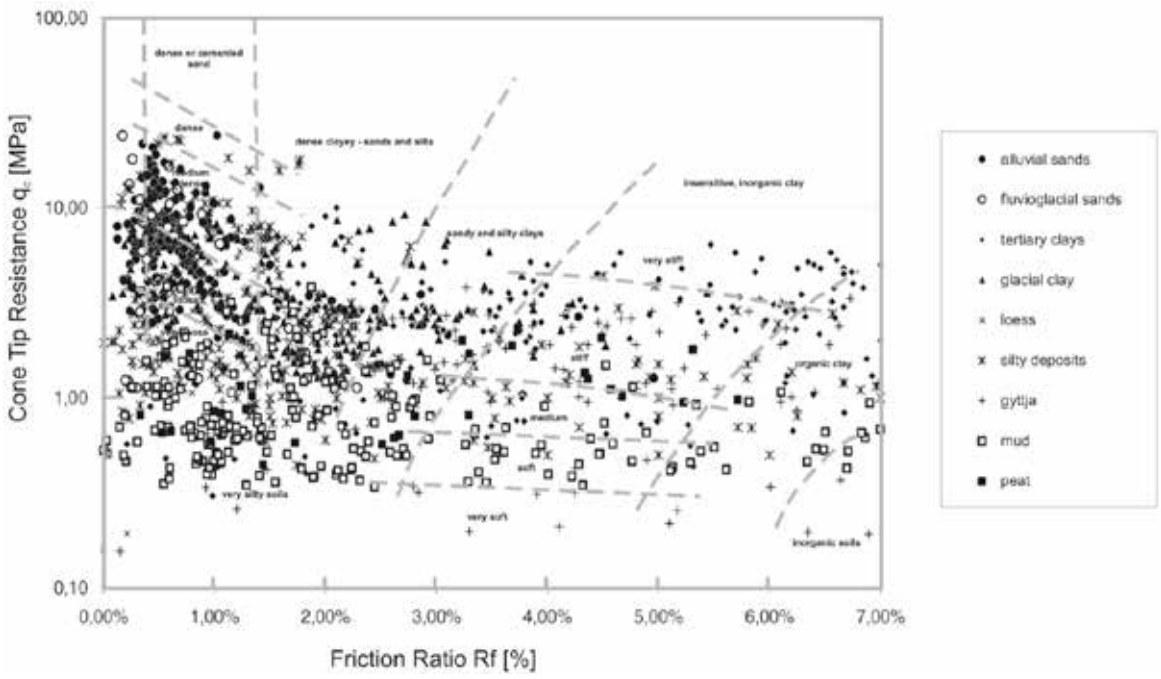

Figure 1. All results for different litho-genetic types of soils plotted on Schmertmann's nomogram (Grant Nr 4 T07E 047 30, 2008).

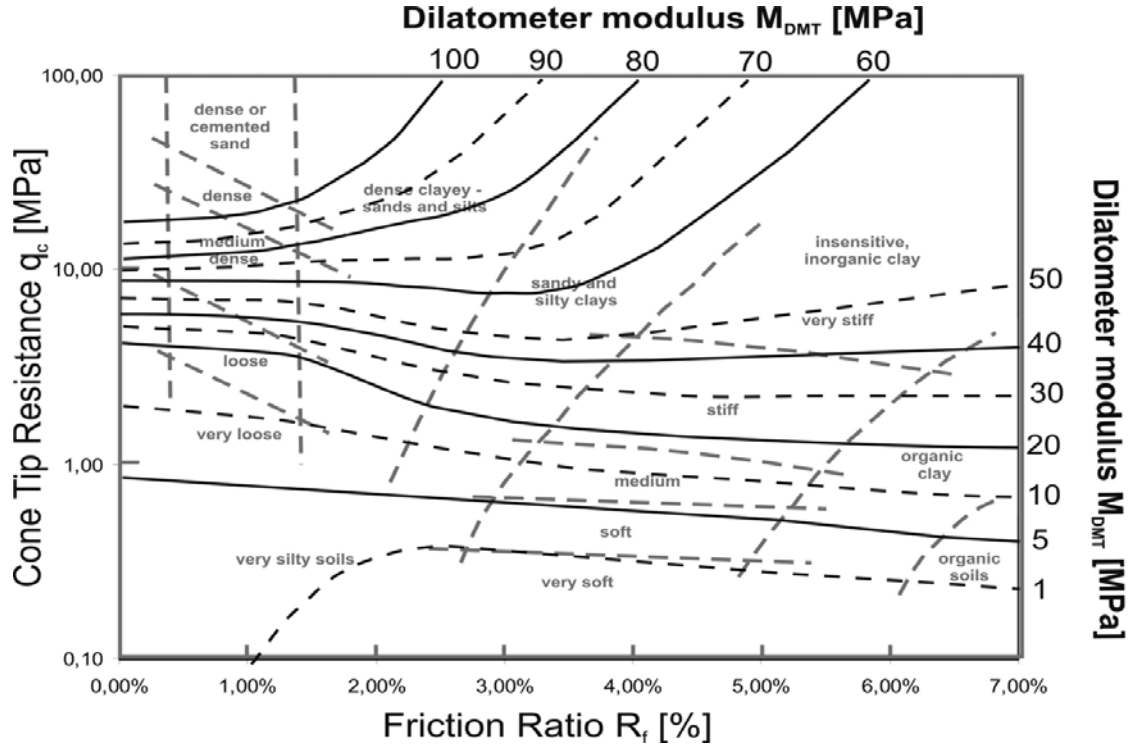

Figure 2. Experimental proposition of the nomogram of constrained modulus determination on the basis of static sounding (Wysokiński et al. 2009).

3.2 *Calibration of CPTU/DMT Probes*

The Marchetti flat dilatometer is a device dedicated to determine the deformation parameters of soils. This is supported by the specificity of measurement itself (Marchetti 1980). Expansion of a steel membrane in the soil is a controlled displacement test, i.e. measurement of pressure at desired displacement. This allows for the estimation of the deformation modulus directly in the soil (in situ), which is the basis for prediction of displacements of the designed structure. Determining the magnitude of settlement and foreseeing such settlement is, especially for any structure designed in difficult geotechnical conditions, an element which is crucial for the determination of foundation method. Depending on the type and importance of the structure, the difference between shallow founding with the necessity to execute soil improvement or "avoidance" of the problem by deep foundations is small. For typical buildings (up to 11 storey's) the value of permissible settlement is 5 cm (as per National Annex to Eurocode 7), Polish Standard (PN-81/B-03020) allowed for 7 cm. Direct evaluation of parameters (including modulus) of soil is possible only on the basis of test loads and by in situ methods.

The requirements of new European standards (PN-EN-1997-1 and PN-EN 1997-2) result in the necessity to carry out quantitative tests (mainly probing) when preparing the soil documentation. The correlations applied in practice between probing results and information on soil conditions of a founded structure require regional adjustments or adaptation to local conditions. This is very important because determination of soil-structure interaction demands that properly determined parameters be used with a particular design method (Mitew-Czajewska 2015).

For the new types of static penetration probes (such as: CPTU with a piezocone or dilatometer) sufficiently good (regional) Polish correlations for interpretation of results have not been issued yet or they are not sufficiently verified. The literature data (including that specified in the annexes to Eurocode 7) obtained abroad in other soils are often unsatisfactory under Polish conditions and sometimes lead to incorrect conclusions (Godlewski 2013).

Worldwide experience (Monaco et. al. 2006) indicates that DMT is highly useful in determination of soil deformation modulus. This method is reliable, provided that it is calibrated and validated (by other methods). In this case, the best method is to compare the settlement values measured at given structures or performance of test loads against the settlement values obtained from DMT. Comparison of settlement values measured at the structures with respect to those obtained by dilatometer and literature data (26 structures) (Monaco et. al. 2006) and own observations (23 structures) (Godlewski 2015) is presented in Figure 3. For a total of almost 50 structures, the type of foundation (pad, strip or slab foundation) and soils at the foundation level were indicated (sandy soil: Sa, cohesive: saSi, sasiCl, Cl

and organic: Or). These are mainly typical residential and industrial buildings not exceeding 11 storey's with the exception of 2 road structures (abutment and embankment). Additionally a set of measurements for improved soil was added, wherein the dilatometer was used to determine the deformation modulus of the "composite" – soil and soil improvement elements (Dynamic Replacement / sand and gravel / Controlled Modulus Columns / concrete columns).

The described set of buildings shows high correlation (R^2 = 0.92). It should be added that the given set of buildings was limited to structures with shallow foundation (including those on improved soil). For the purpose of evaluation and forecasting settlement, the dilatometer is a well-calibrated device for typical structures. In the cases of founding on very soft and organic soils in which the quality of drilling and collected samples is insufficient, only in situ probing allows for obtaining reliable parameters for design calculations.

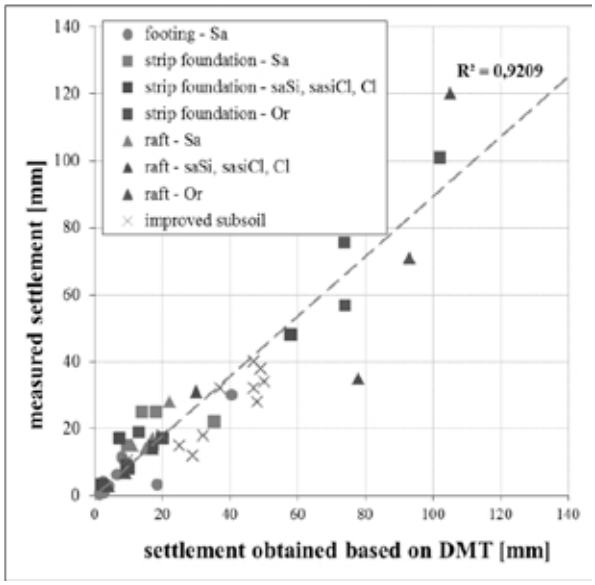

Figure 3. Calibration curve obtained for Polish conditions relating to measurements from literature (Godlewski 2015).

3.3 *Correlation of CPTU/DMT results*

Dilatometer modulus as a reference value allows for calibration of CPT/CPTU results (q_c i R_f) with modulus values. The results obtained at each test site by means of CPTU and DMT soundings were compared. The analysis was based on Mayne's experience (Mayne et al. 2004). Dilatometer modulus (E_D) were converted to confined modulus (M') by Marchetti method (Marchetti 1980).

In the first approach to data correlation, the graph of dilatometer modulus (M_{DMT}) versus net cone resistance (q_n, comprising vertical stress $q_n=q_c-\sigma_{vo}$) was drawn. The method of linear regression allowed for obtaining the calculation coefficient for each test site. Example graphs show in Figure 4-5.

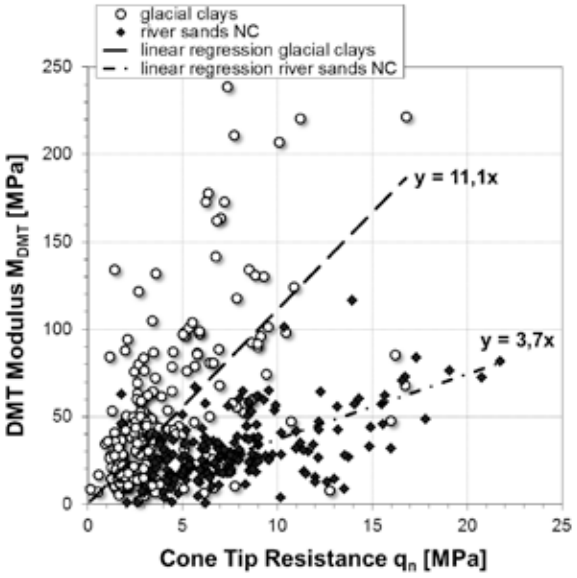

Figure 4. M_{DMT} versus q_n for glacial clays and river sands.

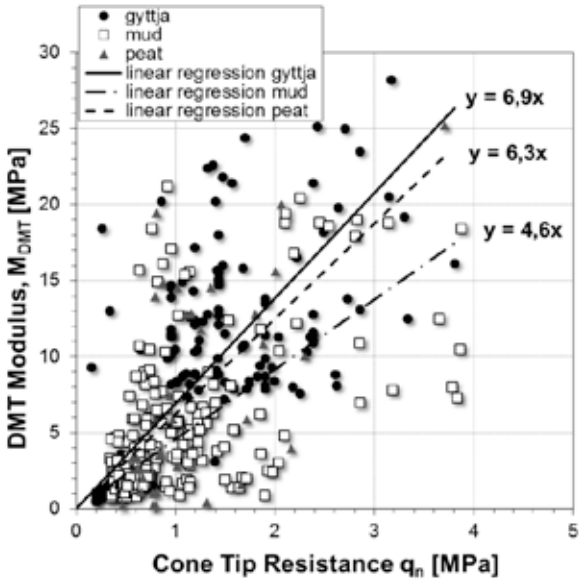

Figure 5. M_{DMT} versus q_n for all analysed organic soils.

The best validation was obtained for river sands and hollow silts ($R^2 \geq 0.6$). In case of glacial clays or organic (special muds) deposits the correlation was unsatisfactory ($R^2 \leq 0.3$). This is due to specific character of these soils. Glacial clays are a type of mixed material: from silty sands to clays, with large natural variability. The same situation is in the case of organic deposits.

The next step included the correlation determination for classifying parameters for each type of sounding. The R_f (sleeve friction / cone resistance ratio $100f_s/q_c$) from CPTU and material index I_D (in publications I_{DMT} or I_D, it should not be considered

as density index) from DMT were taken into correlations. Both the material index from DMT and sleeve friction from CPTU refer to particle size distribution. This correlation was described for each litho-genetic type (Table 1). It should be mentioned that for highly variable soils (for example hollow deposits) the obtained correlations are general.

Table 1 – Obtained correlations from CPTU and DMT tests

Litho-genetic type of soil:	E_D**= (a) *** q_n	I_D **= (b) +/_ (a) *** R_f
alluvial sands		
NC ($\alpha = M_{DMT}/q_c = 3 \div 10$)	**3.7** * q_n	**4.8 – 144.0** * R_f
OC ($\alpha > 10$)	**9.8** * q_n	**4.8 – 22.2** * R_f
fluvioglacial sands OC	**20.2** * q_n	**3.0 – 17.0** * R_f
tertiary clays:		
clays from Cracow	**3.4** * q_n	**0.7 + 5.3** * R_f
clays from Warsaw	**6.9** * q_n	**1.2 – 5.5** * R_f
glacial tills (Middle Polish glaciations)	**4.4** * q_n	**2.0 – 4.4** * R_f
loess deposits	**5.8** * q_n	**2.5 + 7.8** * R_f
hollow deposits:		
silty sands	**3.5** * q_n	**4.0 – 13.0** * R_f
slity clays and silts	**4.3** * q_n	**2.8 – 30.9** * R_f
organic soils: gyttja	**6.4** * q_n	**0.7 – 1.1** * R_f
mud	**3.1** * q_n	**0.7 – 1.0** * R_f
peat	**3.1** * q_n	**0.6 – 3.1** * R_f

On the basis of CPTU test results the values of the modulus were determined. The same calculations as for DMT were used, taking the correlations from table 1 for E_D and I_D. According to Marchetti instruction and proposed formulas (Marchetti 1980) the modulus may be obtained having R_M coefficient (R_M=M'/E_D), which is calculated from material index I_D and vertical strain coefficient K_D. Having E_D and K_D according to Marchetti correlations, R_M coefficient and constrained modulus were obtained. Example graphs show in Figure 6.

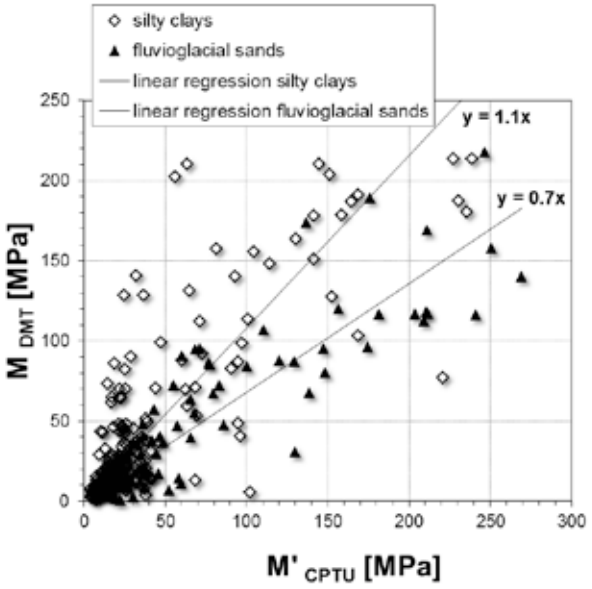

Figure 6. Validation of CPTU method for evaluating DMT Constrained modulus: for example in sands and hollow soils.

The mean values obtained from CPTU and DMT allow for correlation of these two methods. The average of regression line is about 0.7÷1.1. For all analysed litho-genetic type of soils, the best validation was obtained for glacial clays and silts. In the case of loess deposits and gyttja, all correlation results are placed below the theoretical curve (y=1.0x). This is due to specific character of these soils (loess is characterized by collapsing settlements and gyttja is very sensitive). For these types of soils the character of penetration (kinematic, static) and undisturbed sampling are very important. In the case of clays all correlation points are spread along vertical line. This refers to their anisotropy and the direction of penetration.

4 DISCUSSION

Of course, the author realize that given correlations and values require consideration of additional factors affecting insufficient correlation parameters. This requires further analysis with the use of more advanced statistical methods.

However, the coefficients for each soil type (i. e. empirical cone factor "α") very well characterised by specificities of Polish ground conditions were obtained. This is particularly evident in the case of glacial clay (tills) or tertiary clay, which are "very strong" soils (rated by soil consistency as hard to extremely hard). In this case, the values are several times higher than proposed in the literature. In Polish practice, in the interpretation of CPTU tests, three factors are most commonly used: α = 15 for non-cohesive soils, α = 8 for cohesive soils and α < 1.5 for organic soils. Sometimes, significant differences clearly indicate that it is not correct approach in all the cases.

Presented methods of interpretation are very simplified (Sanglerat 1972, Mayne 2001). In literature (Tanaka 1998; Sikora 2006; Wierzbicki 2010) more complex methods of determining the constrained modulus value from CPTU tests were presented - with regard to overburden stress (σ_{v0}) or stress history (OCR). But these methods, (based on general formula described by Sanglerat) are still more popular in geotechnical practice.

Presented results relate to large number of tests and have high statistical value because about 2500 results were used for the analysis.

Constrained modulus (M') taken for presented empirical cone factor (α) applies to range of effective vertical stress from 50 to 400kPa.

5 CONCLUSIONS

The development of interpretation methods of soundings is based mainly on statistical correlations which demand huge set of measurements. The examples of these sets are in PN-81/B-03020, geological and engineering atlas of Warsaw and ITB guidelines. The comparison of the results gave local correlations or allowed adjusting the classification from the literature to local conditions. All existing nomograms may be used only if the appropriate (according to standards) penetrator is used according to particular procedure. The correlations presented in the article are the example which may be used in the national annex to Eurocode 7. The obtained correlations may be compared to the data from literature as a background. It should be underlined that presented analyses support the Eurocode 7 implementation process. The main goal of these analyses was to intercorrelation between CPTU and DMT tests for Polish soils. However, some issues still need to be supplemented: loess, gravels and sand and gravel mixtures should be added to the database and overconsolidation and cementation processes should be taken into consideration for sands as well as anisotrophy of clays. These factors probably cause high scatter of the results (Bałachowski et al. 2008, Młynarek et al. 2013).

Because of the article size limit, not all issues have been presented. The author give only information about the problem which needs further investigations.

6 FUNDING

Part of this work was supported by the funds for science in the years 2006-2008 as a Research Project: „Regional correlations of geotechnical parameters on the basis of soundings, laboratory tests and settlements measurements" supported by KBN [grant number 4 T07E 047 30].

7 REFERENCES

Bałachowski L.; Kozak P.; Kurek N. 2008. Intercorrelation between CPTU-DMT test for sands on the Baltic coast. Proc. of 11th Baltic Sea Geotechnical Conference, Gdańsk. Geotechnics in Marintime Engineering. Z. Młynarek, Z. Sikora & E. Dembicki (ed.). Vol. 1. Printing-Office MISI-URO, Gdańsk: 359-366.

European/Polish Standard: PN-EN 1997:2008 Eurokod 7 – Geotechnical Design, part 1 and part 2.

Godlewski T. 2013. Interpretacja badań polowych a Eurokod 7. Acta Scientiarum Polonorum, Architektura-Budownictwo 12 (3): 61-72.

Godlewski T. 2015. Practical use of the dilatometer tests - some case studies from Poland. Proc. of The 3rd International Conference on the Flat Dilatometer DMT'15, Rome. Marchetti, Monaco & Viana da Fonseca (edit.): 99-106.

Marchetti S. 1980. In Situ Tests by Flat Dilatometer. Journal of the Geotechn. Engineering Division, ASCE, Vol. 106, No. GT3: 299-321.

Mayne P.W. 2001. Stress-strain-strength-flow parameters from enhanced In-situ tests. Proc. of International Conference on In Situ Measurement of Soil Properties & Case Histories (In Situ 2001), Bali: 27-48.

Mayne P.W. & Liao T. 2004. CPT-DMT interrelationships in Piedmont residuum. Proc. Intnl Site Characterization ISC'2 – Porto Portugal: 345-350.

Mitew-Czajewska M. 2015. Geotechnical investigation and static analysis of deep excavation walls – a case study of metro station construction in Warsaw. Annals of War-saw University of Life Sciences – SGGW. Land Reclamation No 47 (2): 163-170.

Młynarek Z., Gogolik S., Sanglerat G., 2013. Interrelationship between deformation moduli from CPTU and SDMT tests for overconsolidated soils. Proceedings of the 18th International Conference on Soil Mechanics and Geotechnical Engineering, Paris: 583-586.

Młynarek Z.; Stefaniak K..; Wierzbicki J. 2013. Evaluation of deformation parameters of organic subsoil by means of CPTU, DMT, SDMT. Architecture Civil Engineering Environment, vol. 6, no 4: 51-58.

Monaco P.; Totani G.; Calabrese M. 2006. DMT – predicted vs. observed settlements: a review of the available experience. Proc. from the Second International Flat Dilatometer Conference, Washington D.C.: 275-280.

Polish Standard: PN-81/B-03020.Building soils. Foundation bases. Static calculation and design.

Rabarijoely S., Garbulewski K. 2013. Simultaneous interpretation of CPT/DMT tests to ground characterization. Proceedings of the 18th International Conference on Soil Mechanics and Geotechnical Engineering, Paris, Vol. 1, p. 1337-1340.

Sanglerat G. 1972. The penetrometr and soil exploration. Elsevier, Amsterdam.

Sikora Z. 2006. Sondowanie statyczne – metody i zastosowanie w geoinżynierii. wyd. nauk-tech. Warszawa.

Schmertmann, J.H.et al. 1986. CPT/DMT Quality Control of Ground Modification at a Power Plant. Proc. In situ '86 ASCE Spec. Conf. Virginia Tech, Blacksburg, VA: 985-1001.

Tanaka H.; Tanaka M.; 1998. Characterization of Sandy Soils using CPT and DMT. Soils and Foundations, Japanese Geot. Soc.,Vol. 38, 3: 55-65.

Wierzbicki J. 2010. Ocena prekonsolidacji podłoża metodami in situ w aspekcie jego genezy. Rozprawy Naukowe nr 410. Wydawnictwo Uniwersytetu Przyrodniczego w Poznaniu.

Wysokiński L., Godlewski T., Wszędyrówny-Nast M. 2009. Zależności regionalne parametrów geotechnicznych na podstawie sondowań CPTU i DMT. XV KKMGiIG, Bydgoszcz, Wyd. Uczelniane UTP, 235-242.

Geotechnical and Geophysical Site Characterisation 5 – Lehane, Acosta-Martínez & Kelly (Eds)

Evaluating the OCR and permeability of Cutoff Wall using CPTU Results

X.P Li, G.J Cai, J. Lin & S.Y Liu
Institute of Geotechnical Engineering, Southeast University, Nanjing, China

A.J. Puppala
Department of Civil Engineering, The University of Texas at Arlington, Arlington

ABSTRACT: The technology of piezocone penetration test (CPTU) provides a unique opportunity to evaluate the hydraulic conductivity of in-situ backfills in soil-bentonite cutoff walls. The method of estimate the hydraulic conductivity depends on the type of pore pressure dissipation curve. The pore pressure dissipation curve shows a monotonic behavior when the soil is normally to lightly overconsolidated clay (low OCR), while it shows a dilatory dissipation behavior when the soil is heavily over consolidated soils (high OCR). So it is very necessary and important to determinate the OCR of soil. A landfill site with soil-bentonite cutoff walls is selected in this paper based on the CPTU investigation. A method of using laboratory test to extrapolate the OCR of CPTU is applied in a full-scale soil-bentonite cutoff wall located in Jiangsu, China. Several values of OCR of different depths are determined by laboratory one-dimensional consolidation test firstly. And the relationship between OCR from laboratory test and normalized cone tip resistance is explored. The obtained hydraulic conductivity of the in-situ soil-bentonite of the cutoff wall is lower than the design criteria (10^{-7} cm/s). Evaluating the OCR and permeability of Cutoff Wall using CPTU results is recommended for the soil.

1 INTRODUCTION

As a useful technique to evaluate the compressibility, strength and permeability of soil, the piezocone penetration test, is widely used in geotechnical engineering (Sully et al 1999, Chai et al. 2004, Cai et al. 2014). From the results of CPTU investigation, the pore pressure dissipation curve shows a monotonic type. However, for the test sites conducted in overconsolidated soil or dense sandy soil, the pore pressure dissipation curve shows a dilatory type with the pore pressure increasing from an initial value to a maximum first, and then decreasing to the hydrostatic value (Burns & Mayne 1998, Teh & Houlsby 1991, Chai et al. 2014). Therefore, it is worth to evaluate the OCR value firstly for estimating other parameters of soil (Mayne and Holtz 1988, Chen and Mayne 1996, Babanouri et al. 2011, Monaco et al. 2014).

Over-consolidation ratio (OCR) is defined as a ratio of the maximum pre-consolidation pressure and the present effective overburden stress. The published literature has been rich with different approaches to estimate OCR from cone penetration test data since 1978. Baligh et al. (1980) proposed the pore pressure measured during the undrained cone penetration test may reflect the stress history of soil deposit and then OCR. Sully et al. (1988) stated that the normalized pore pressure difference have a relationship to OCR. Based on the combination of cavity expansion and critical state theory, Mayne (1991) presented a method to evaluate OCR, the correlation is:

$$OCR = 2\left[\frac{1}{1.95M+1}\left(\frac{q_t - u_2}{\sigma'_{v0}}\right)\right] \quad (1)$$

where M is the slope of the critical state line, q_t is corrected cone resistance; u_2 is the pore water pressure with filter element located on shoulder of cone; σ'_{v0} is the effective overburden stress. The general assumption of the influence of OCR on the normalized cone resistance (Q_t) was found by Sugawara in 1988. Lunne et al. (1997) shows that the relationship between the shape of cone resistance profile and the value of OCR. Based on the approach and comments of geotechnical literature, using CPT or CPTU data to evaluate OCR is recommended. Evaluating the value of OCR based on Q_t when little experience is available is suggested. This relationship can be expressed as:

$$OCR = kQ_t = k\left(\frac{q_t - \sigma_{v0}}{\sigma'_{v0}}\right) \quad (2)$$

where k is the parameter (with a range of 0.2 to 0.5); σ_{v0} is the overburden stress. The use of only one val-

ue of the *k* parameter is a simplification for OCR.

The evaluation of isolating effect of cutoff wall with bentonite in the terms of hydraulic conductivity in the landfill site is most important. (Manassero 1994, Yeo et al. 2005, Krage et al. 2015). Low hydraulic conductivity helps improving the durability and resistance of cutoff wall to chemical attack (Robertson et al. 1992, Cai et al. 2010).

In this paper, the piezocone dissipation tests are performed in a full-scale soil-bentonite slurry trench cutoff wall of landfill site in China. A mixture with 5% bentonite and 95% in-situ natural soil were selected to produce a mixture with slump of 100 to 150 mm for the desired hydraulic conductivity of cutoff wall. The relationship between OCR from oedometer test and normalized cone resistance of cutoff wall from CPTU data has been established. And then the values of OCR with different depths for soil-bentonite backfill of cutoff wall are obtained. The OCR values are useful to calculate the coefficients of consolidation and hydraulic conductivities of cutoff wall.

2 LABORATORY TESTS

The used bentonite is hydrogel from Wyo-Ben of Inc with a bentonite content of 5% by dry weight for the cutoff wall. Table 1 lists the properties of bentonite. According to the laboratory tests using a standard 300 mm slump cone, the water content of soil-bentonite is 50% corresponding to a slump of 125 mm.

Table 1. Properties of bentonite used in cutoff wall

Soil type	G_s	w_L/%	w_P/%	I_P
Bentonite	2.50	200.8	39.8	161.0

Several Boreholes were drilled and high quality soil samples were taken for the one-dimensional consolidation tests. The soil samples were collected by a stationary piston sampler with the 76mm diameter. Several one-dimensional consolidation tests were conducted to evaluate the properties of natural soil particle used in cutoff wall (see Table 2). The stress of one-dimensional consolidation is 50kPa, 100kPa, 150kPa and 200kPa. The compression coefficient (a_v) and compression modulus (E_s) can be obtained.

Table 2.The properties of natural soil particle used in cutoff wall

Depth /m	w	ρ	G_s	w_L /%	w_p /%	a_v /MPa	E_s /MPa
4.7	30.8	1.84	2.70	35.3	27.2	0.38	5.05
6.7	31.7	1.89	2.69	35.8	28.9	0.29	6.46
8.0	35.4	1.82	2.68	36.4	30.9	0.52	3.83

After the one-dimensional consolidation of soil-bentonite, the over-consolidation ratios of several depths are calculated by the following expression:

$$OCR = \frac{q_c}{\sigma_{v0}} \tag{3}$$

where p_c is the pre-consolidation pressure. The value of pre-consolidation pressure can be obtained from the curve of e~lg$p$ based on the Cassagrande method (Fig. 1). And Table 3 shows the OCR value of soil-bentonite estimated from the laboratory tests with the undisturbed soil.

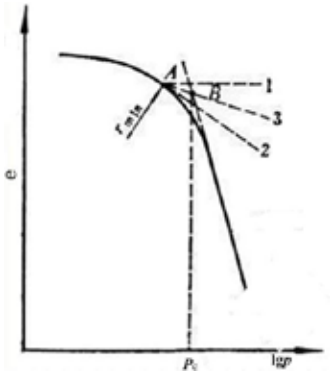

Figure 1. The determination of pre-consolidation pressure (p_c) from Cassagrande method

Table 3. The OCR value of soil-bentonite from laboratory test

Depth /m	2	3	4	5	6
OCR	4.23	6.42	2.34	1.71	1.04

3 CPTU TESTS

The piezocone penetration test uses a cone with 10cm^2 cross sectional area, 150cm^2 sleeve friction surface area and 35.6mm cone diameter. Penetration device are controlled at a constant speed of 20 mm/s by hydraulic piston. Figure 2 shows the in-situ piezocone penetration test in cutoff wall of landfill site. The soil-bentonite cutoff wall has the properties of 0.6m width, 15m length, and 10m depth. Each penetration depths are larger than the depths of cutoff wall.

Figure 2. The in-situ piezocone penetration test in cutoff wall of landfill site

The filter elements of measuring pore water pressure can be located on different locations: the middle face of the tip, the shoulder (u_2 position) or the shaft of a cone. However, the u_2 position is now considered to be the standard location (Lunne et al. 1986). Figure 3 shows the piezocone used in this test site.

4 RESULTS AND ANALYSIS

4.1 *Evaluation of OCR*

Figure 4 shows the typical results in soil-bentonite cutoff wall by piezocone penetration test. The groundwater is about 1.0 m below the ground surface at this test site. The site soil can be simply divided as soil mixed with bentonite layer and silty sand layer. In the layer of soil mixed with bentonite, the corrected cone tip resistance (q_t) is lower (less than 0.2 MPa) than the value of natural soil without bentonite (about 1 MPa). And the sleeve friction (f_s) is less than 10 kPa. Both the corrected cone tip resistance and sleeve friction values of soil mixed with bentonite layer are much smaller than those of silty sand layer. The pore pressure remains increasing with depths in the soil mixed with bentonite layer, while there have a very small even no pore pressure in silty sand layer.

Figure 3. The piezocone used in this test site

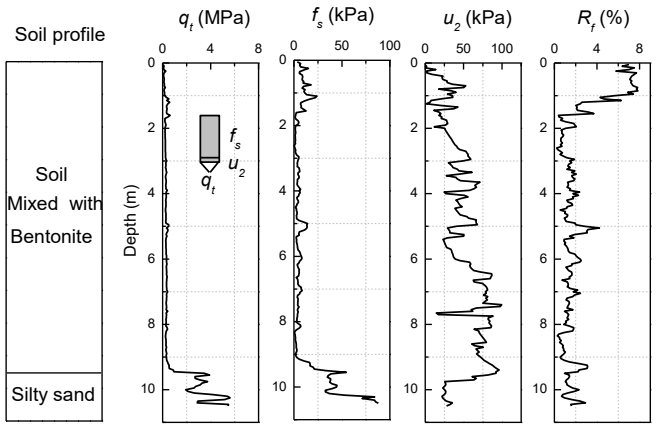

Figure 4. CPTU results in soil-bentonite cutoff wall

Table 4 shows the collected cone tip resistance of soil-bentonite and natural soil without bentonite. The value of collected cone tip resistance of soil-bentonite (q_{t2}) is only 0.07 to 0.44 times of natural soil (q_{t1}) without bentonite.

Table.4 The collected cone tip resistance of soil-bentonite and natural soil

Depth /m	q_{t1} of natural soil /MPa	q_{t2} of soil-bentonite /MPa	q_{t2} / q_{t1}
1	1.93	0.14	0.07
2	1.00	0.20	0.20
3	0.98	0.43	0.44
4	0.85	0.25	0.29
5	0.65	0.25	0.38
6	1.38	0.22	0.16
7	1.48	0.23	0.16

The normalized cone tip resistance (Q_t) can be expressed by the following simple equation:

$$Q_t = \left(q_t - \sigma_{v0}\right) / \sigma'_{v0} \tag{4}$$

A method of using laboratory test to extrapolate the OCR of CPTU is applied in this full-scale soil-bentonite cutoff wall located in Jiangsu, China. In order to evaluate the value of OCR, the parameter k in equation 2 should be estimated firstly. Then the relationship of OCR from laboratory test and the normalized cone tip resistance (Q_t) from CPTU can be established. The value of Q_t can be calculated by equation 4. The highest q_t value is 0.43 MPa at the depth of 3m, where the Q_t value is 20.58 (σ_{v0} = 39 kPa, σ'_{v0} = 39 kPa). Figure 5 shows the fit results of OCR value in cutoff wall. The OCR can be expressed as:

$$OCR = 0.32\left(q_t - \sigma_{v0}\right) / \sigma'_{v0} \tag{5}$$

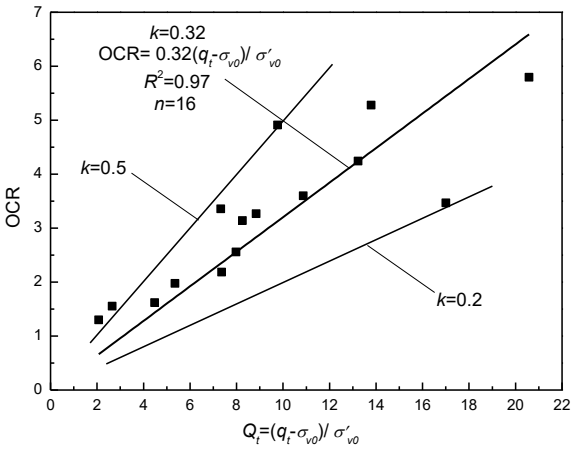

Figure 5. The relationship between OCR from laboratory test and normalized cone resistance

Equation 5 shows the relationship between OCR and normalized cone resistance by the CPTU technical. Then the OCR value of different depths can be calculated at last depend on the normalized cone resistance. Figure 6 shows the OCR value with depths from CPTU investigation. In the depth of 2m to 3m,

the OCR value is about 3 to 6, which shows the soil is overconsolidated. However, the soil is normally to lightly overconsolidated with the depth of 5m to 8m.

The OCR value of soil with depth of 3m is 6.4, which shows the soil is overconsolidated. The pore pressure dissipation curve should be dilatory behavior. Figure 7 shows the dilatory dissipation behavior of high OCR from CPTU data with depth of 6m. A good agreement of the relationship between OCR and the pore pressure dissipation behavior demonstrates the high quality of the testing data and the effectiveness of the analysis method. Figure 8 shows the dilatory dissipation behavior of high OCR from CPTU data with depth of 3m. The OCR value of soil with depth of 6m is 1.04, which shows the soil is normally consolidated. The pore pressure dissipation curve should be monotonic behavior.

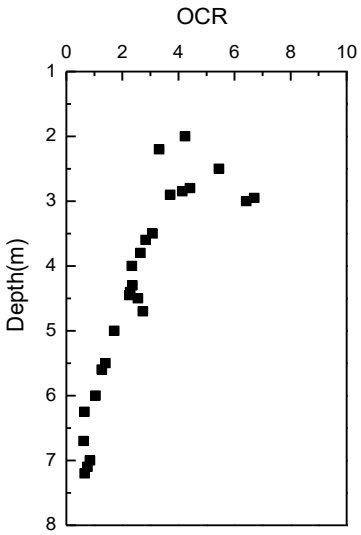

Figure.6 The value of OCR varied with depths

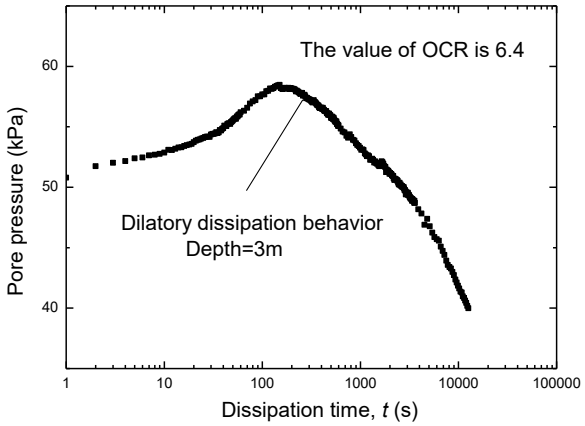

Figure 7. Dilatory dissipation behavior of high OCR from CPTU data

4.2 *Evaluation of hydraulic conductivity*

Teh and Houlsby (1991) proposed an Equation to evaluate coefficient of consolidation c_h in monotonic dissipation behavior:

$$c_h = \frac{T_{50}}{t_{50}} r^2 \tag{6}$$

where r is cone radius, t_{50} is the time for 50% dissipation, T_{50} is related to location of the filter element and the size of the cone (T_{50}=0.245).

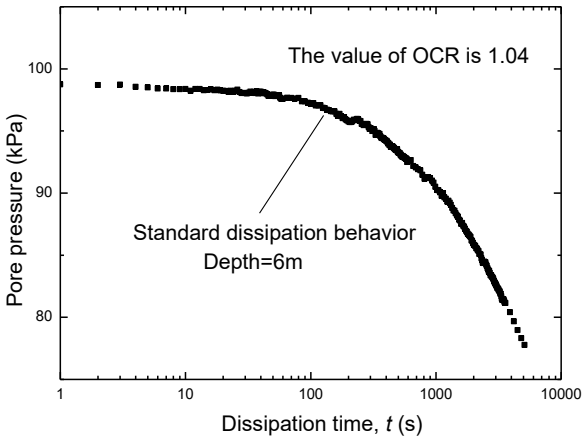

Figure 8. Monotonic dissipation behavior of low OCR from CPTU data

In dilatory dissipation behavior, Chai et al. (2004) used cylindrical cavity expansion theory and developed an empirical equation to correct t_{50}.

$$t_{50m} = \frac{t_{50}}{1+18.5\left(\frac{t_{u\max}}{t_{50}}\right)^{0.67}\left(\frac{I_r}{200}\right)^{0.3}} \tag{7}$$

where t_{50m} is corrected time for 50% excess pore pressure dissipation, t_{50} is time difference between the maximum and 50% of the maximum excess pore pressure, t_{umax} is time for the measured excess pore pressure to reach its maximum value. Then the c_h value can be calculated with the following equation

$$c_h = \frac{c_p r^2 \sqrt{I_r}}{t_{50m}} \tag{8}$$

where c_p is a factor related to the size of the cone and the location of the filter element. c_p = 0.245 (for the u_2 location). I_r is the rigidity index.

The k_h values can be obtained by substituting c_h values in following Equation (Baligh and Levadoux 1986):

$$k_h = \frac{\gamma_w}{2.3\sigma'_{v0}} RRc_h \tag{9}$$

where γ_w is the unit weight of the water, γ_w = 10kN/m^3; σ'_{v0} is initial vertical effective stress in the wall, and RR is recompression ratio, which can be determined from laboratory consolidation test (RR=0.5×10^{-2} to 2.0×10^{-2}).

Figure 9 shows the k_h values of cutoff wall from CPTU data. The k_h values obtained from c_h values depend on the pore pressure dissipation behavior. It shows that the k_h values of cutoff wall are in the range from 0.4×10^{-8} cm/s to 3.8×10^{-8}cm/s, which is lower than the design criteria of 1×10^{-7} cm/s.

5 CONCLUSIONS

It is suitable to evaluate the over consolidated ratio by piezocone penetration test technology. A method of using laboratory test to extrapolate the OCR of CPTU is applied successfully in a full-scale soil-bentonite cutoff wall located in Jiangsu, China. The relationship between OCR and normalized cone resistance of the test site is explored. The value of OCR is 0.32 time of normalized cone resistance in the cutoff wall. A good agreement of the relationship between OCR and the pore pressure dissipation behavior demonstrates the high quality of the testing data and the effectiveness of the analysis method. The OCR values obtained by CPTU are very useful to evaluate the coefficients of consolidation and hydraulic conductivities of cutoff wall. And the k_h values of cutoff wall obtained from c_h value are in the range from 0.4×10^{-8} cm/s to 3.8×10^{-8}cm/s, which is lower than the design criteria of 1×10^{-7} cm/s

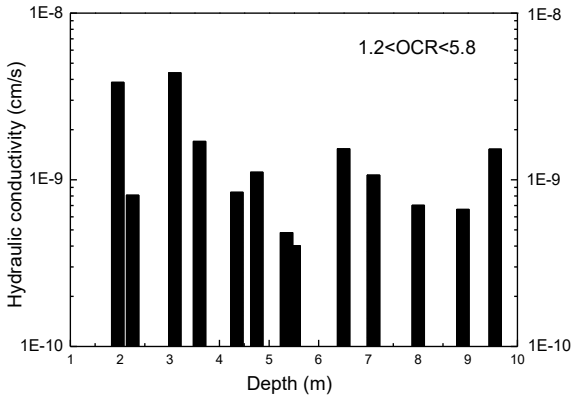

Figure 9.The hydraulic conductivity of cutoff wall from CPTU data

6 ACKNOWLEDGEMENTS

Majority of the work presented in this paper was funded by the the Foundation for the New Century Excellent Talents of China (NCET-13-0118), the Foundation of Jiangsu Province Outstanding Youth (Grant No. BK20140027), the Foundation for the Author of National Excellent Doctoral Dissertation of PR China (Grant No. 201353), and the High Level Talent Project of Peak of Six Talents in Jiangsu Province (Grant No. 2015-ZBZZ-001). These financial supports are gratefully acknowledged.

7 REFERENCES

Babanouri, N. Nasab, S.K. Baghbanan, A. & Mohamadi, H.R. 2011. Over-consolidation effect on shear behavior of rock joints. *International Journal of Rock Mechanics & Mining Sciences*. 48: 1283-1291.

Baligh, M.M. Vivatrat, V. & Ladd, C,C. 1980. Cone penetration in soil profiling. *Journal of the Geotechnical Engineering Division* 106(GT4): 447-61.

Baligh, M. M. & Levadoux, J. N. 1986. Consolidation after undrained piezocone penetration. II: interpretation. *Journal of Geotechnical and Geoenvironmental Engineering* 112 (7): 727-745.

Burns S.E. & Mayne P.W. 1998. Monotonic and dilatory pore pressure decay during piezocone tests in clay. *Canadian Geotechnical Journal* 35:1063-1073.

Cai, G.J. Liu, S.Y. Tong, L.Y. et al. 2010. Predictions of the OCR from Piezocone Tests in Quaternary Clays. *Marine Georesources and Geotechnology* 28:91-104.

Cai, G.J. Puppala, A.J. & Liu, S.Y. 2014. Characterization on the correlation between shear wave velocity and piezocone tip resistance of Jiangsu soft clays. *Engineering Geology* 171:96-103.

Chai, J.C. Carter, J.P. Miura, N. & Hino, T. 2004. Coefficient of consolidation from piezocone dissipation tests. *Proc. of Int. Symposium on Lowland Technology*, Bangkok, Thailand, 1-6.

Chai, J.C. Hossain, M.J. Carter, J. & Shen, S. L. 2014. Cone penetration- induced pore pressure distribution and dissipation. *Computers and Geotechnics* 57: 105-113.

Chen, B.S.Y. & Mayne, P.W. 1996. Statistical relationships between piezocone measurements and stress history of clays. *Canadian Geotechnical Journal* 33: 488-498.

Krage, C. P. DeJong, J. P. & Schnaid, F. 2015. Estimation of the coefficient of consolidation from incomplete cone penetration test dissipation test. *Journal of Geotechnical and Geoenvironmental Engineering* 141(2): 06014016.

Lunne, T. Eidsmoen, T.E. Gillespie, D. & Howland, J. 1986. Laboratory and field calibration of cone penetrometers. *In Use of In-situ Tests in Geotechnical engineering. Edited by S. P. Clemence. Geotechnical Special Publication* 6: 714-729.

Lunne, T. Robertson, P. K. &Powell, J.J.M. 1997. *Cone penetration testing in geotechnical practice*. Blackie Academic and Professional, London.

Manassero, M. 1994. Hydraulic conductivity assessment of slurry wall using peizocone test. *Journal of Geotechnical and Geoenvironmental Engineering* 120:1725-1730.

Mayne, P.W. & Holtz. R.D. 1988. Profiling stress history from piezocone soundings. *Soils and Foundations* 28: 1–13.

Mayne, P.W. 1991. Determination of OCR in clays by piezocone tests using cavity expansion and critical state concepts. *Soils and Foundations* 31(2): 65-76.

Monaco, P. Amoroso, S. Marchetti. S. et al. 2014. Overconsolidation and Stiffness of Venice LagoonSands and Silts from SDMT and CPTU. *Journal of Geotechnical and Geoenvironmental Engineering* 140(1): 215-227.

Robertson, P. K. Sully, J. P. Woeller, D. J. & Campanella, R. G. 1992. Estimating coefficient of consolidation from piezocone tests. *Canadian Geotechnical Journal* 29(4): 539-550.

Sugarawa, N. 1988. On the possibility of estimating in-situ OCR using the piezocone. *Penetration testing* 2: 985-991.

Sully, J.P. Campanella, R.G. & Roberstson, P.K. 1988. Overconsolidation ratio of clays from penetration pore water pressures. *Journal of Geotechnical Engineering* 114(2):209-215.

Sully, J.P. Roberstson, P.K. Campanella, R.G. & Woeller, D.J. 1999. An approach to evaluation of field CPTU dissipation data in overconsolidated fine-grained soils. *Canadian Geotechnical Journal* 36:369-380.

Teh, C.I. & Houlsby, G.T. 1991. An analytical study of the cone penetration test in clay. *Geotechnique* 41(1):17-34.

Yeo, S.S. Shackelford, C.D. & Evans, J.C. 2005. Consolidation and hydraulic conductivity of nine model soil-bentonite backfills. *Journal of Geotechnical and Geoenvironmental Engineering* 131(10):1189-1198.

Geotechnical and Geophysical Site Characterisation 5 – Lehane, Acosta-Martínez & Kelly (Eds)

Evaluation of relative density and liquefaction potential with CPT in reclaimed calcareous sand

P. Mengé, K. Vinck & M. Van den Broeck
DEME N.V., Zwijndrecht, Belgium

P.O. Van Impe & W.F. Van Impe
AGE bvba Geotechnical Consultants, Erpe-Mere, Belgium

ABSTRACT: Land reclamation works in the Middle East often are realized with carbonate sands. Compaction of such underwater and above water hydraulic granular fills is generally realized by means of vibroflotation and/or dynamic compaction, resulting in an inhomogeneous fill of more compacted and less compacted zones. The aim of compaction should be to guarantee performance requirements of the fill, such as maximum long term residual (differential) settlements, minimum bearing capacity and liquefaction resistance during seismic events. Quality control of such fill is often realized by means of the CPT, however the quality assessment procedure is often ambiguous with regard to how to deal with the heterogeneity of the fill and with regard to the effect of crushing of the calcareous sand. In this paper the problem is illustrated and the approach used for a land reclamation project with calcareous sand is discussed.

1 INTRODUCTION

Land reclamation works in the Middle East often have to be realised with carbonate sands which are abundantly present in the region. Depending on the goal of the reclamation works, several performance requirements may apply: maximum long term residual (differential) settlements (under static loads and post-earthquake); minimum bearing capacity for foundation systems and liquefaction potential under seismic events. This often is translated into a minimum relative density or, derived thereof, a target CPT-q_c line.

Compaction of such underwater and above water hydraulic granular fills is generally realised by means of vibroflotation and/or dynamic compaction. Such operations are grid-oriented and inevitably result in an inhomogeneous fill of more compacted and less compacted zones. The quality control of the fill is mainly realized by means of the Cone Penetration Test (CPT). The quality assessment procedure to follow is often ambiguous and is mainly focused on point measurements while the real performance of the fill should be of main importance.

Compaction of calcareous sand and, even more, CPT testing of such sand causes crushing of the grains which influences the results. Evaluation of relative density of the compacted fill from CPT resistance by means of literature correlation formulas cannot longer be applied as these formulas are valid for dry silica sand. As a simplified approach, often a 'Shell Correction Factor' (SCF) is used, which allows to derive an equivalent 'silica sand cone resistance' which is used for evaluation of relative density and assessment of liquefaction potential. The SCF is not a unique figure and depends on many factors, among which sand type, density and stress state. In order to overcome this problem for the case study, calibration chamber (CC) tests were performed on the saturated and dry calcareous sand used in order to define a site-specific correlation formula.

The working method for the quality control (QC) of the compacted hydraulic fill with regard to required (relative) density and liquefaction assessment is discussed in following sections, based on a case study of land reclamation work in the Middle East.

2 HYDRAULIC FILL

A general discussion on hydraulic fills is beyond the scope of this paper, but reference can be made to Chu et al. (2009) and van 't Hoff & van der Kolff (2012) where hydraulic fills for land reclamation works are discussed. One of the typical effects of underwater and above water hydraulic fills is the variation in density obtained depending on sand installation methods: under water by dumping, rainbowing, spraying or outflow of land pipe lines; above water by rainbowing or land pipe lines.

Table 1 gives an overview of the expected relative densities (D_r) taking into account the hydraulic installation method. As a result of this variation,

compaction may be required depending on the project functional requirements.

Table 1. Typical relative densities as a result of hydraulic fill.

Placement method	D_r (%)
Spraying (discharge under water)	20-40
Dumping (discharge under water)	30-50
Land pipelines (discharge Under water)	20-40
Rainbowing (discharge under water)	40-60
Land pipelines (discharge Above water)	60-70
Rainbowing (discharge Above water)	60-80

3 LANDFILL REQUIREMENTS

In the Specifications, project functional requirements are translated into performance requirements or even further in more detailed technical specifications. The level of detail of such requirements differs depending on the type of contract. Typical landfill requirements for granular fill will discuss following items:

Suitable fill material: mainly granular material with limited amount of stones and limited fines content (generally less than 10% to 15% of particles smaller than 63microns). Main reason for the fines content limitation is compactability under water.

Allowable residual settlements: such settlements may originate from deeper layers below sea bottom level as well, but for the sake of this paper, focus is on settlements originating from the fill material itself. Settlements related to granular fill may result from self-weight auto-compaction (ageing) and deformations under service loads. When the project location is to be considered as a seismic region, post earthquake settlements may apply as well. Differential settlements are very difficult to demonstrate in pre-project phase, but may be a requirement and be a point of attention for execution method selection, during execution and testing.

Bearing Capacity: bearing capacity requirements define the type of footing, size, depth of application, load to be carried and factor of safety to be applied to define the 'safe bearing capacity'. Normally no deformation requirement is linked to such specification.

Slope stability: this is mainly valid at the edges of the reclamation and results in slope stability calculations based on the method of slices from which maximum slopes combined with a certain minimum friction angle will follow. In seismic regions, the slope stability will usually be realized with the pseudo-static method

Liquefaction resistance: when peak Ground Acceleration (PGA) and the Magnitude (M) are defined, the liquefaction assessment can be based on one of the many methods described in literature. Most commonly used is the NCEER method starting from CPT's performed after compaction.

It is clear from the above discussion that the compaction of the hydraulically deposited fill material may be necessary. The above discussed performance requirements are often translated into technical requirements such as minimum friction angle and a minimum relative density or relative compaction.

After deep compaction, the most practical means of QC over the full height of the fill is the CPT. At this stage, the evaluation method needs to be defined clearly, so as to be able to conclude whether or not the compaction is sufficient and the project functional requirements will be achieved.

4 CALCAREOUS SAND

Carbonate soils are defined as soils in which carbonate minerals predominate. They are widely distributed in the warm and shallow seas and oceans of the world's tropical and sub-tropical regions covering almost 40% of the ocean floor. Carbonate deposits are usually formed by accumulation of skeletal remains of small marine organisms from the upper waters of the ocean (bioclastic deposits), but may also have a non-organic origin, for instance, as a result of chemical precipitation from carbonate-rich water (oolites) (van 't Hoff & van der Kolff 2012).

Calcareous sand and its geotechnical engineering behavior is much discussed in literature (e.g. Coop & Airey 2003). For land reclamation QC, main issues are the crushability leading to different behavior during testing, high angularity leading to high shear strength and liquefaction resistance, cementation and load-deformation behavior depending strongly on stress history.

In the field of QC of land reclamation works, the focus will be on the influence of crushing on cone penetration testing and maximum density testing. For CPT this phenomenon has been covered since many years by several authors (Almeida et al. 1991; Wehr 2005, Mayne 2014, Van Impe et al. 2015). The cone resistance in calcareous sand for the same D_r and stress state is lower compared to silica sand. Consequently, typical correlations between q_c and D_r are no longer valid. Ideally, a site specific correlation should be derived through calibration chamber (CC) testing. As a simplified approach, sometimes the use of a 'Shell Correction Factor' (SCF = $q_{c,silica}/q_{c,calc}$ >1) is used.

However, when the q_c-value to be expected in calcareous sand is known, it must be considered unlikely that other correlations with the relative density parameter D_r (liquefaction susceptibility, compressibility, …) still hold. New correlations will have to be determined that should directly link in-situ measurements with the relevant soil parameters.

Maximum Dry Density (MDD) testing, needed to define relative density or relative compaction, is often performed by means of dynamic laboratory tests

such as proctor compaction (to define the moisture-density relationship) or vibrating hammer compaction. Such techniques cause crushing of carbonate sand particles, resulting in a different particle size distribution and higher densities than can be reached in the field. To avoid such effect, authors have demonstrated by comparative testing that the vibratory table test (ASTM D4253) causes least crushing and is hence the recommended test to define the MDD of calcareous sand.

5 RELATIVE DENSITY CONSIDERATIONS

The use of relative density in geotechnics is widely spread because of the influence of degree of compaction on many parameters. However, often D_r proves to be an unreliable parameter. It is a calculated value depending on particle density, bulk density, minimum and maximum density. Especially the two latter are notoriously difficult to pin down as they depend strongly on the method with which they are determined. Moreover, each small error in the measurement of the above parameters has a larger than proportional effect on the final value of D_r.

6 CASE STUDY

6.1 *Project description*

The project considers off-shore land reclamation for the construction of oil drilling islands in the Persian Gulf. Typically for this region, the main soil material was a calcareous sand of biogenic origin (shells and coral).

Technical requirements stated that the fill had to be compacted to 90% MDD and that the reclaimed material had to resist an earthquake with PGA=0.15g and M=6. Additionally, a higher compaction requirement was valid to the top 0.9m. Bearing capacity and settlement requirements were applicable as well, but will not be discussed here. In zones of 25m by 25m, the CPT had to be used to establish the degree of densification of the hydraulic fill. In situ density tests were required in the top 0.9m layer.

Deep densification of the hydraulic fill was realized by vibroflotation, aiming to reach values of D_r above 62% (equivalent to 90% MDD). It was decided to perform CC testing in order to establish a site specific correlation between q_c, D_r and vertical effective stress (σ'_v).

6.2 *Sand characteristics*

CC tests were done on samples taken from the borrow areas where later on the material of the reclamation would be excavated. Samples from these areas are further referred to as BAE (borrow area east) and BAW (borrow area west). The additional testing campaign was undertaken during the actual construction phase. Testing material for this second campaign was taken from one construction site, as soon as it surfaced. This material will be denoted as S1 in this paper.

All materials were analysed to determine standard reference parameters: particle size distribution (PSD), carbonate content and index densities. Figure 1 shows the results of the PSD. A significant difference was noted in the particle size distribution of the sands from the borrow areas (BAW and BAE). The material S1 closely resembles the BAW material. The results of this basic reference testing are given in Table 2. As reference, literature data from other typical testing materials is mentioned as well.

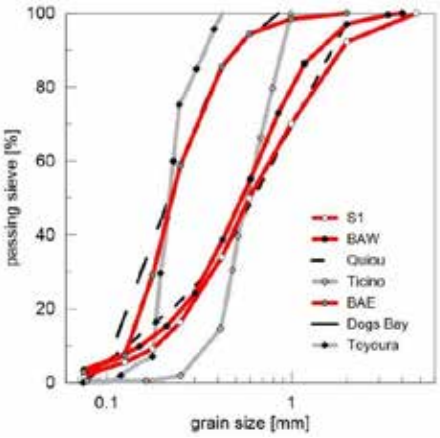

Figure 1. PSD of the BAE, BAW and S1 sands, with some literature reference testing sands.

Table 2. Overview of sand characteristics.

Sand	γ_s *[kN/m³]*	D_{50} *[mm]*	$CaCO_3$ *[%]*	e_{max} *[-]*	e_{min} *[-]*
BAE	2.84	0.23	93	1.551	0.979
BAW	2.84	0.57	98	1.392	0.843
S1	2.84	0.59	95	1.278	0.741
Dogs Bay	2.75	0.24	87-92	1.830	0.98
Quiou	2.72	0.71	77	1.281	0.831
Ticino	2.69	0.55	<	0.934	0.582
Toyoura	2.65	0.16	<	0.977	0.605

6.3 *Calibration chamber testing*

The calibration chamber tests have been performed in a centrifuge at ISMGEO, Bergamo, Italy. Thus, q_c-D_r relations could be established at a continuous range of overburden stresses, while the traditional calibration chamber tests only resulted in a single q_c-D_r-σ'_v data point for each test. In the centrifuge setup, due attention was paid to cone diameter to mean grainsize ratio and chamber diameter to cone diameter ratio in order to minimize size- and boundary effects. Details of the setup and testing are given in Van Impe et al. (2015).

Centrifuge CC tests have been performed on BAE and BAW samples, both in dry and wet conditions. A significant impact of the presence of water was found, leading to much lower values of $q_{c,wet}$ compared to $q_{c,dry}$ at similar relative density and

stress level. This effect has been noticed as well for silica sands, although to a (much) lesser extent. Jamiolkowski et al. (2001) states that the value of D_r would typically be underestimated by 7% to 10% for the sands considered in their research. For the BAE and BAW sand the error is rather 30% and the physical background of this phenomenon is unclear; possibly (micro-) cementation may occur in the dry sand which could not be proven. In the discussion below only the results of the wet CC tests will be discussed. Figure 2 shows the results of the tests on the wet BAW material.

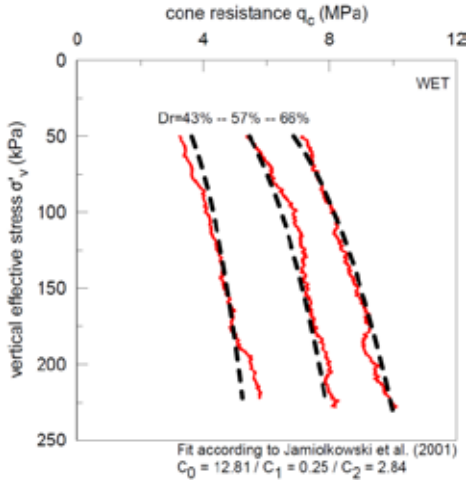

Figure 2. Results of the centrifuge CC tests on wet BAW material.

Jamiolkowski et al. (2001) proposed following form of q_c-D_r-σ'_v correlation:

$$\frac{q_c}{p_a} = exp^{D_r \cdot C_2} \cdot C_0 \cdot \left(\frac{\sigma'_v}{p_a}\right)^{C_1} \quad (1)$$

Where p_a is the atmospheric pressure in the same unit system of stress and penetration resistance (98.1 kPa); C_0, C_1 and C_2 are non-dimensional empirical correlation factors.

The data obtained from the CC testing was analyzed using the above correlation and the correlation factors defined. The correlation factors for BAW, BAE, for an average correlation and for typical research silica sands (Ticino-Toyoura-Hokksund; Jamiolkowski et al. 2001) are given in Table 3.

Table 3. Empirical coefficients for q_c-D_r correlation (1)

Coeff.	*BAE*	*BAW*	*Average*	*TS+TOS+HS*
C_0	13.09	12.81	12.95	17.68
C_1	0.29	0.25	0.27	0.50
C_2	2.68	2.84	2.76	3.10

Figure 3 shows the 4 correlations from Table 3 graphically. It can be noticed that, although both BAE and BAW sands have a clearly different PSD, they behave very similarly in the CC-tests. This indicates that PSD has less impact on the behavior of the material than its mineralogy. These correlations are valid for σ'_v > 50kPa; for lower stresses an adapted correlation applies (not further discussed here).

From these correlations a SCF can be derived. Figures 4 and 5 give the SCF in function of vertical effective stress and in function of D_r, also indicating SCF's as given in literature by Wehr (2009) and Mayne (2012). Figure 4 illustrates that the SCF is not a constant value, but differs with vertical effective stress. Figure 5 was derived for a vertical effective stress of 100kPa and demonstrates that the SCF which was proposed by Wehr perfectly matches the SCF derived here for a stress level of 100kPa. This proves that the sand found in the same region behaves similar under CPT testing. The SCF as suggested by Mayne seems not to correspond well and may be valid for other types of calcareous sands.

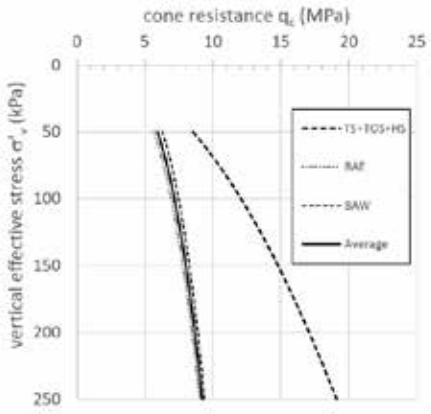

Figure 3. q_c-D_r-σ'_v correlations from Table 3 (D_r=62%).

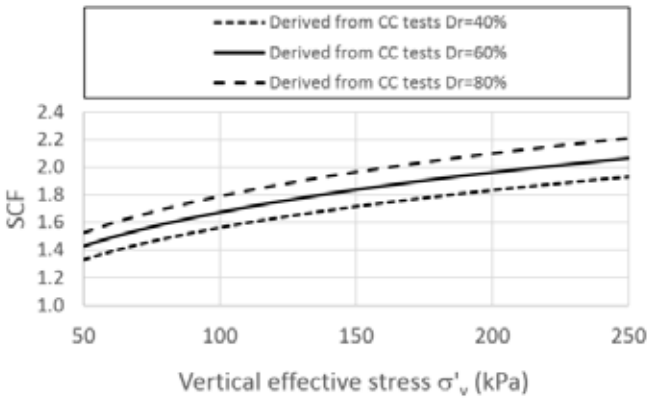

Figure 4. SCF in function of vertical effective stress and relative density.

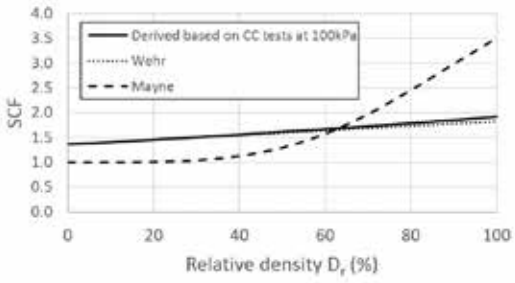

Figure 5. SCF in function of relative density.

Notwithstanding the findings with regard to SCF and its ease of use, authors prefer the more accurate scientific approach using the results of CC-tests to define the relative density of calcareous sands from CPT. Also note that for the calculation of the SCF the correlation (1) was used with the correlation factors as given in Jamiolkowski et al. (2001) for a series of silica sands (TS+TOS+HS) (also shown in Table 3). This correlation was selected because it is believed to be the most recent, well documented and fully corrected correlation. Should other correlations be used, other SCF's will be found.

6.4 *Relative density verification with CPT*

Deep compaction was performed by vibroflotation. Compaction is usually performed in a triangular grid with probe spacing between 3m and 5m. The zone of influence of each compaction point should overlap (Figure 6). However, there will be a gradient in degree of compaction when moving away from the compaction point and different levels of compaction will be found depending on the location of the CPT test. In Figure 7 two typical locations where CPT testing can be done are indicated: at the centroid of the compaction points and at 1/3 on the line between two compaction points. The first will theoretically give the lowest result while the second one is assumed to give the best result. To have a CPT diagram which is representative for the behavior of the whole fill, it is common practice to calculate an 'average' CPT curve from the two positions (i.e. at each level, the average of the two measured values is defined). This average curve is then used for evaluation.

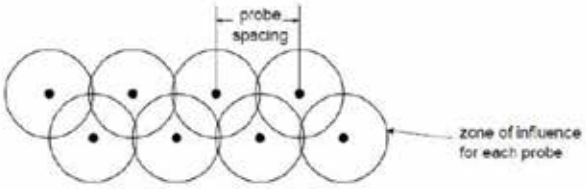

Figure 6. Zone of influence and probe spacing for vibroflotation.

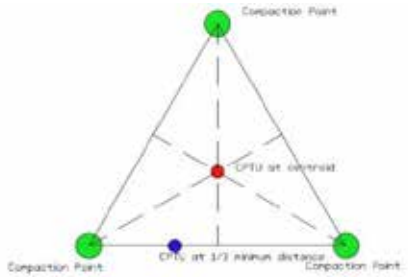

Figure 7. Post-vibroflotation testing locations related to a triangular compaction grid.

In Figures 8 and 9 the results of a pre- and post-compaction CPT's are given (the post compaction CPT is the average curve) for a zone where locally a layer with higher fines content is found. The target D_r is verified in the graph at the right of the figure. The D_r above the water table (horizontal line) clearly is very high while under water the expected low densities are found. In the post-compaction figure the D_r is verified again and should be above the target line. This is the case over most part of the figure, except for the zone with higher fines content (between -8m CD and -10.5m CD).

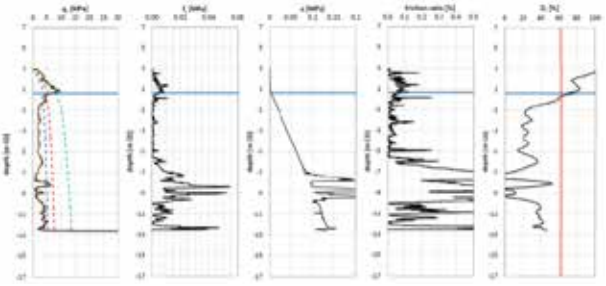

Figure 8. Pre-compaction CPT

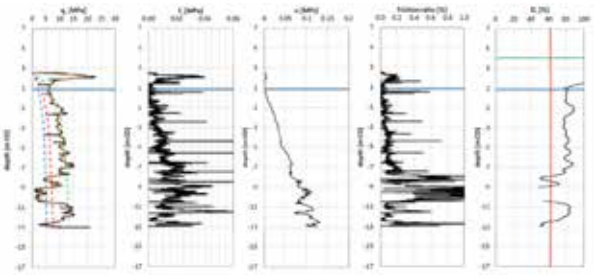

Figure 9. Post-compaction average CPT

In order to smoothen the result, a 'moving average' curve is calculated over 0.5m height (= average value calculated from all values 0.25m above and 0.25m below the considered level). When averaged q_c-results are below the target line, the total height over which the criterion fails is defined. For the CPT shown in Figure 9 this is the case for a height of 6.3%. Individual failing layer thickness has to be less than 0.5m and the total sum has to be less than 10% of the CPT height. More failure of the target line can only be accepted after 'Engineering Review' (ER). ER means that the effect of failing the target line is studied from a point of view of engineering behavior (static and post-earthquake settlements, bearing capacity, stability and liquefaction) and based on this evaluation it will be decided whether the realized fill can be accepted. When necessary, ER may include additional testing or boreholes with sampling and lab testing.

6.5 *Liquefaction analysis*

Apart from the relative density requirement, also liquefaction assessment is necessary. Hereto, the NCEER method is followed, based on the corrected CPT diagram. For correction, a SCF was calculated as described above and thus varied with compaction level and stress level. In order to take into account, the effect of the (limited) fines content, the proce-

dure based on the soil behavior type-index I_c is used. For these calculations, the above mentioned averaging cannot be allowed and individual CPT's are evaluated. This leads to the discussion whether each individual CPT is representative for the behavior of the whole fill or whether averaging of the obtained factors of safety against liquefaction ($FoS_L > 1.25$) can be done for final assessment.

Authors believe the overall behavior cannot be evaluated on basis of individual CPT's at the 'worst' and 'best' CPT-locations and suggests to use (weighted) averaged FoS_L. Similar situations with soil replacement columns in liquefiable soils have been studied numerically (Rayamajhi et al. 2013).

In Figure 10 the results of one of the post-compaction CPT's is shown. In this figure the SBT I_c and FoS_L are displayed. Where the higher fines content occurs, the CPT 'fails'. Decision has to be made by means of ER whether this location needs re-compaction or other remedial actions.

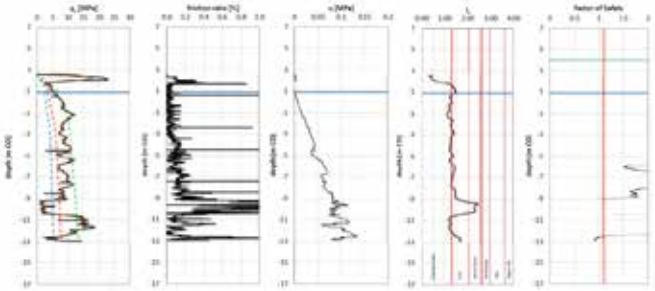

Figure 10. Post compaction CPT, liquefaction assessment

6.6 *Additional considerations*

The CPT's shown in Figures 8 to 10 have been chosen to show 'failing' CPT's. When performing hydraulic fill with crushable material under water, it is impossible to avoid locally sand with increased fines content to get included in the reclamation. The increased fines content was still rather limited as the material is classified as 'sand mixtures' based on I_c. In such cases ER is required to decide on what to do. Re-compaction, going through more than 10m of well compacted material is not an easy task and the final result may even be worse than the result obtained now. So when ER demonstrates that the 'performance requirements' of the fill and future structures are met, no further compaction is really necessary.

In case of failing layers, the Liquefaction Potential Index (LPI) (Li et al. 2006) may be an approach to estimate the probability of liquefaction to occur. Such LPI approach seems not to be globally accepted, but it would offer a systematic approach to evaluate a whole soil column instead of a soil element.

Ageing may be important in compacted sand; in general a time period of minimum 2 weeks is allowed between compaction and CPT testing.

Compaction quality testing as discussed above is focused on 'parameter testing', and not on the real engineering behavior, unless the concept of ER is applied. Direct testing of engineering behavior by means of large plate load tests (Zone Load Test) or in situ measurement of the shear wave velocity should be considered as preferable alternative approach.

Instead of using the NCEER method with corrected CPT values, cyclic triaxial and/or cyclic direct simple shear testing could be done to evaluate the liquefaction behavior of the calcareous sand. Such an approach avoids the need to use the NCEER correlations which may not be valid for this specific sand.

7 CONCLUSIONS

The problem of quality control of the compaction of large land reclamation works with calcareous sands is discussed and illustrated on basis of a case study. It is advised to perform CC tests at an early stage of the project. This approach allows to have an undisputable correlation between q_c, D_r and σ'_v. Liquefaction assessment is often performed according to the NCEER method, based on corrected CPT results. Because of the heterogeneity of the compacted fill, a specific approach was followed when evaluating the CPT's; this approach is illustrated in this paper.

8 REFERENCES

Almeida, M.S., Jamiolkowski, M. & Peterson, R. 1991. Preliminary results of CPT tests in calcareous Quiou sand. *First Int. Symp. on Calibration Chamber testing*. Potsdam, New York: 41-53.

Chu, J., Varaksin, S., Klotz, U. & Mengé, P. 2009. Construction processes. State-of-the-art report (TC17, ISSMGE). *Proc. 17th Int. conf. on SMGE*. Alexandria, Egypt.

Coop, M.R. & Airey, D.W. 2003. Carbonate sands. *Characterisation and Engineering properties of Natural Soils*, Tan et al. eds. Swets & Zeitlinger, Lisse, Netherlands: 1049-1086.

Jamiolkowski, M., Lo Presti, D.C.F. & Manassero, M. 2001. Evaluation of relative density and shear strength of sands from CPT and DMT, *ASCE Geotechnical Special Publication 119*:201-238.

Mayne, P.W. 2014. Interpretation of geotechnical parameters from seismic piezocone tests. *3rd Int. Symp. on Cone Penetration Testing*, Las Vegas, Nevada, USA: 47-73.

Li, D.K., Juang, C.H. & Andrus R.D. 2006. J*ournal of GeoEngineering*, Vol.1, No. 1: 11-24.

Rayamajhi D., Nguyen, T.V., Ashford S.A., Boulanger, R.W., Lu, J., Elgamal, A. & Shao, L. 2013. Numerical study of shear stress distribution for discrete columns in liquefiable soils. *J. Geotech. and Geoenviron. Eng*., ASCE.

Van Impe, P.O., Van Impe, W.F., Manzotti, A., Mengé, P., Van den Broeck, M., Vinck, K. 2015. Compaction control and related stress-strain behavior of off-shore land reclamations with calcareous sands, *Soils and Foundations*, 55(6):1474-1486.

van 't Hoff, J. & Nooy van der Kolff, A. 2012. Hydraulic Fill Manual. For dredging and reclamation works. *CUR/CIRIA Publication*. CRC Press/Balkema.

Wehr, W.J. 2005. Influence of the carbonate content of sand on vibrocompaction. *Proc. 6th Int. conf. on Ground Improvement techniques*, Coimbra, Portugal: 525-632.

Geotechnical and Geophysical Site Characterisation 5 – Lehane, Acosta-Martínez & Kelly (Eds)

Use of CPTU for the assessment of the stiffness model of subsoil of subsoil

Z. Młynarek
Poznań University of Life Sciences, Poznań, Poland

J. Wierzbicki
Institute of Geology, Adam Mickiewicz University, Poznań, Poland

W. Wołyński
Faculty of Mathematics and Computer Science, Adam Mickiewicz University, Poznań, Poland

ABSTRACT: The article presents the assessment of the stiffness model of the subsoil based on constrained moduli. Changes in the subsoil with depth of the model were determined on the basis of cone resistance changes profile from CPTU tests. The subsoil consisted of soils belonging to 3 geological formations: normally- and overconsolidated glacial tills formed by Pleistocene Scandinavian glaciers, and glacifluvial sands. Hierarchic method of functional cluster analysis was used to group profiles of changes in the M modulus with depth. The performed analysis indicated differences between the obtained stiffness model based only on the stratigraphic model of the subsoil and the model assess on the basis of the CPTU results with the use of the presented method of grouping data and the IDW statistical method.

1 INTRODUCTION

In case of many engineering structures with shallow foundations, a crucial role is played by determination of the degree of settlement of the foundations and, in particular, the non-uniformity of settlements. These factors are decisive to choice of foundation system, and frequently also of a static diagram of the structure. To calculate the degree of foundations settlement constrained oedometric modulus M is commonly used. As is universally recognized, this modulus can be determined by laboratory tests and several in-situ tests. A particularly expedient method is the CPTU static penetration method. Profile of cone resistance changes along with changes in geostatic stress σ_{v0}, obtained from CPTU tests, may be transformed into the equivalent profile of constrained modulus changes along with changes in depth, i.e. σ_{v0}. CPTU tests used for the purpose of this paper had been conducted in the area indented for construction of a multi-story building. These tests allowed for obtainment of a spatial change in constrained modulus and assessment of a spatial model of stiffness of the subsoil. Factors that justify the possibility to determine the profile of constrained modulus changes with change in σ_{v0} include numerous and well-recognized empirical relationships between cone resistance, and constrained modulus and overburden stress σ_{v0} (e.g. Lunne et al. 1997, Robertson 2009). Such a model makes it possible to assume a calculation model of the subsoil, and determine expected settlement of individual foundations of the structure. To assess the stiffness model of the subsoil and group statistically the most similar profiles of constrained modulus changes with changes in geostatic stress σ_{v0}, the cluσtering method of functional analyσis was applied. In turn, to determine the spatial model the Inverse Distance Weighting (IDW) method was used.

Utility of the clustering method in separating the statistically similar zones of the subsoil based on the cone resistance has been documented in several works, e.g. Młynarek & Lunne (1987). In these works, grouping was performed on fixed horizontal stress σ_{v0}. In the current paper, a new approach has been acquired that consists in clustering full curvilinear profiles, describing cone resistance or constrained moduli change with change in σ_{v0} stress in the tested points of the subsoil. This approach appeared to be a highly effective method of accurate assessment of the stiffness model of the subsoil.

First indications of the degree and expected non-uniformity of settlements may be obtained from the stratigraphic model that distinguishes lithological soil layers and the course of these layers, and defines the genesis of individual groups of soils. The interesting question then emerges of what is the adequacy of assessment of stiffness of the subsoil with use of the stratigraphic model and the model based on CPTU profiles, especially when the subsoil consists of deposits belonging to various geological formation. This issue constitutes the subject of this article.

2 SITE CHARACTERISATION

The test site has been previously used for the geotechnical investigations and its geology was described in details by Tumay et al. (2011). It is located in the middle west of Poland, within the area of the post glacial moraine plain formed by the Pleistocene Scandinavian glaciers. The glaciations yielded two layers of glacial till, interbedded with glacifluvial sands and gravels (Fig. 1). The upper tills can be generally divided into two parts: upper (soft) and lower (stiff). The lower tills are overconsolidated and stiff.

A total number of 9 CPTU were carried out at the test site, located not more than 35 m each other, and creating the triangular shaped grid. Simultaneously two borings were carried out, providing some information about lithology. Physical properties of the tested soil were determined via laboratory tests on samples collected from the borings. Soil classification to individual types of soil was investigated by Tumay et al. (2011) and is shown in Figure 2.

3 DATA PREPARATION AND ANALYSIS

3.1 *Assessment of constrained modulus from CPTU*

The main parameter used for assessment of the stiffness of the tested soil was constrained modulus during primary consolidation M, corresponding to oedometric modulus. Values of this modulus were calculated based on the CPTU test results according to the following formula (Lunne et al. 1997):

$$M = \alpha(q_t - \sigma_{v0}) \tag{1}$$

where α for soils with drained conditions depends on cone resistance (Lunne & Christophersen 1983), and in the case of soils with undrained conditions the values of 8.25 for overconsolidated soil and 13.13 for normally consolidated soil was assumed, according to Młynarek et al. (2016) investigations.

3.2 *Data preparation for statistical analysis*

The analysis included 9 profiles characterized by the M value in "z" function, which is illustrated by the equation and in Figure 3.

$$M = f(z) \tag{2}$$

The 'z' parameter assumed values within the range from 1.0 to the depth of the test, every 0.2. This way a set of 7720 M values, characterizing the stiffness of the tested subsoil, was obtained. These data were used for determination of function defining the equation (2), separately in each testing point. For this purpose the Ramsey & Silverman (2005) procedure was used. This method consists in smoothing of the function of the modulus depending on depth, in each of the testing point, providing the spline function $M_i(z)$, $z \in Z$, $i = 1,2,...,N$:

$$M_i(z) = \sum_{j=1}^{K} c_{ij}\phi_j(z) \tag{3}$$

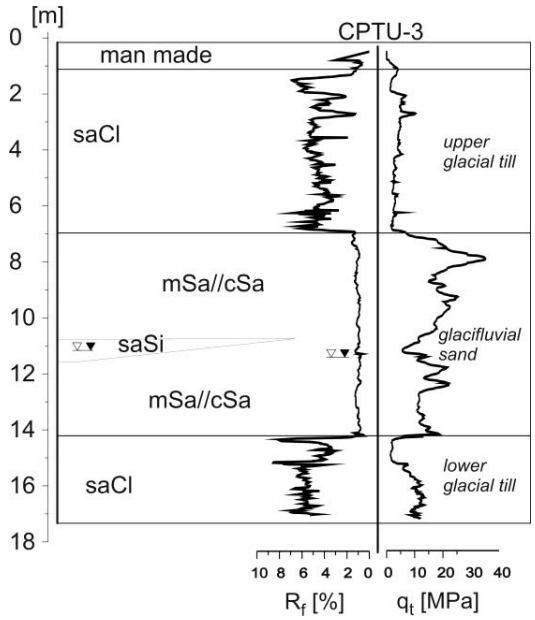

Figure 1. An example of CPTU results at the background of geological profile of the test site.

The coefficients c_{ij} are estimated by the least squares method.

For each i let $c_i = (c_{i1},...,c_{iK})'$, and

$$\boldsymbol{M}_i = \begin{bmatrix} M_i(z_1) \\ M_i(z_2) \\ \vdots \\ M_i(z_L) \end{bmatrix}, \quad \boldsymbol{\Phi} = \begin{bmatrix} \phi_1(z_1) & \cdots & \phi_K(z_1) \\ \phi_1(z_2) & \cdots & \phi_K(z_2) \\ \vdots & \cdots & \vdots \\ \phi_1(z_L) & \cdots & \phi_K(z_L) \end{bmatrix} \tag{4}$$

Then we obtain

$$\hat{\boldsymbol{c}}_i = (\boldsymbol{\Phi}'\boldsymbol{\Phi})^{-1}\boldsymbol{\Phi}'\boldsymbol{M}_i \tag{5}$$

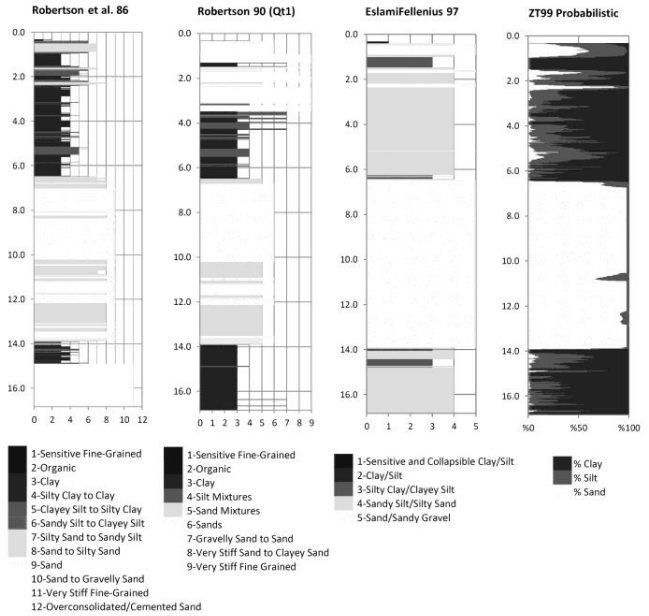

Figure 2. The soil classifications according the classification systems have been analyzed at the testing point CPTU-3 (after Tumay et al. 2011).

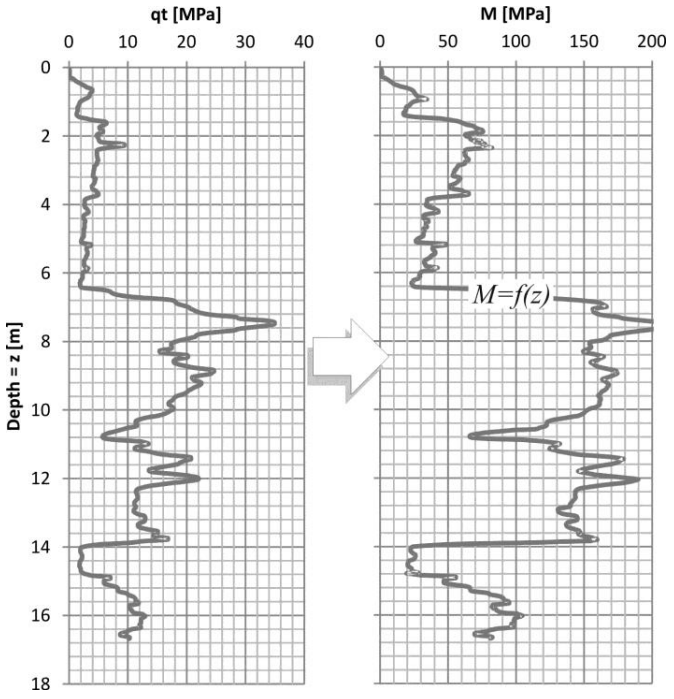

Figure 3. Transformation of corrected cone resistance in the form of function *M=f(z)*.

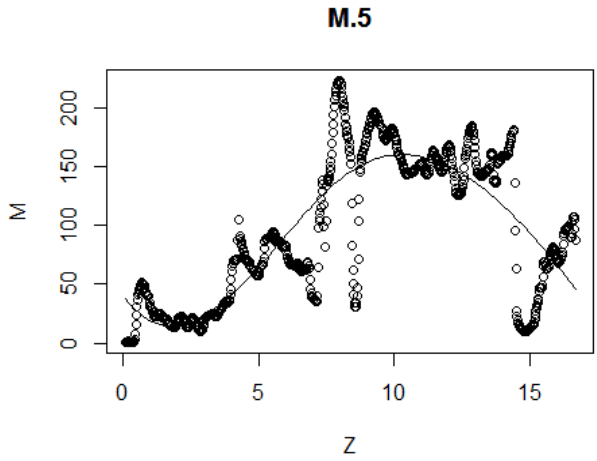

Figure 4. Graph of the smoothed M function in CPTU profile 5, in dependence on depth, assumed for coefficient *K*=5.

The degree of smoothness of the function $M_i(z)$ depends on the values of K (small values of K cause more smoothing of the curves). The criteria for the optimum K selection, applied in this analysis was the BIC (the Bayesian Information Criterion).

In the case of N functions $M_i(z)$ one common value of K is chosen, as a modal value of numbers $K_1,K_2,...,K_N$. After the smoothing processes we have:

$$M_i(z) = \mathbf{\Phi}(z)\hat{\boldsymbol{c}}_i \tag{6}$$

where:

$$\mathbf{\Phi}(z) = [\phi_1(z), \ldots, \phi_K(z)] \tag{7}$$

Calculations were performed for coefficient K=5 However significant the influence of the degree of spline function smoothing for the K=5 value may seem compared to the output (Figure 4), Młynarek et al. (2014) demonstrated that it hardly affected the obtained results. Spline functions were also determined along the profile, for coefficient K=100 and K=200, providing an almost ideal representation of changes in modulus values with depth, but do not influencing the final results of analysis.

3.3 *Analysis of similarity between data*

In the analyzed case, smoothed M functions were divided into 1 meter segments, between 1 to 16 meters of depth, in order to enhance accuracy of clustering. This way the database included 135 objects. In the determination of the scale of similarity between analyzed objects the following measure of distance between obtained objects is assumed:

$$d(M_{i,j}, M_{k,l}) = \sqrt{\int_0^1 |M_i(z+j) - M_k(z+l)|dz}, \quad (8)$$

$$i,k = 1,2,\ldots,9,\ j,l = 1,2,\ldots,15$$

where $M_{i,j}$, is the smoothed M function in the *i*-th testing point and the *j*-th depth interval.

After the distance have been established the hierarchic cluster analysis was conducted (Młynarek et al. 2007). The Ward method was applied in clustering of objects. The idea of analysis of similarities between individual smoothed M functions may be generally defined as the search for minimal differences between areas below the line graphs of individual functions (Fig. 5).

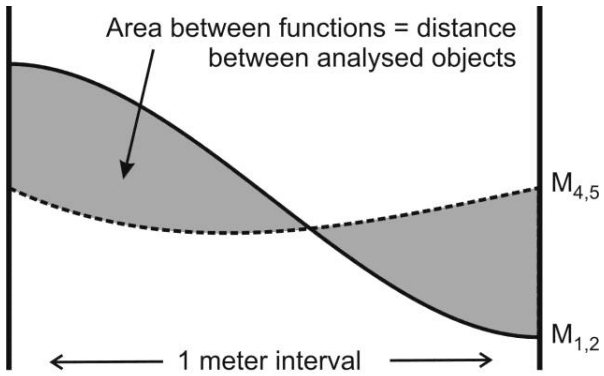

Figure 5. Ideogram of the assessment procedure of similarities between analyzed segments of spline functions of the M parameter ($M_{1,2}$ – function M in the first testing point and the second depth interval, $M_{4,5}$ – function M in the fourth testing point and the fifth depth interval.

As a result we obtain the hierarchy of object similarity, which may be presented most comprehensibly in the form of a dendrogram (Fig. 6).

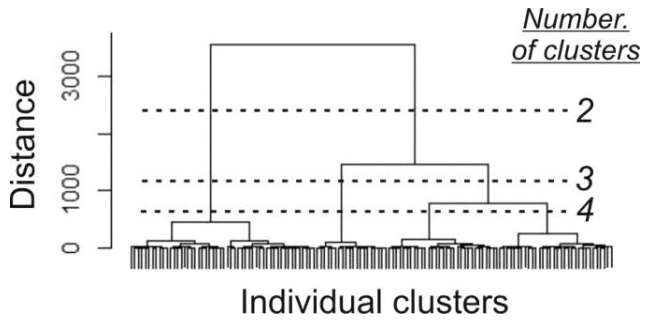

Figure 6. Dendrogram of clustering hierarchy of curves *M= f(z)* from CPTU testing sites for the strongly smoothed function (*K*=5).

Based on the obtained dendrograms an optimal division of the testing sites into homogeneous clusters was provided in accordance with the silhouette index criterion (Rousseeuw 1987).

Figure 7 indicates that the highest values of the silhouette index appear for 2 clusters. The silhouette value changes little for 3 or 4 clusters, and only for 5 clusters it considerably drops. This allows for assumption that solutions with 3 or 4 clusters are statistically almost equivalent.

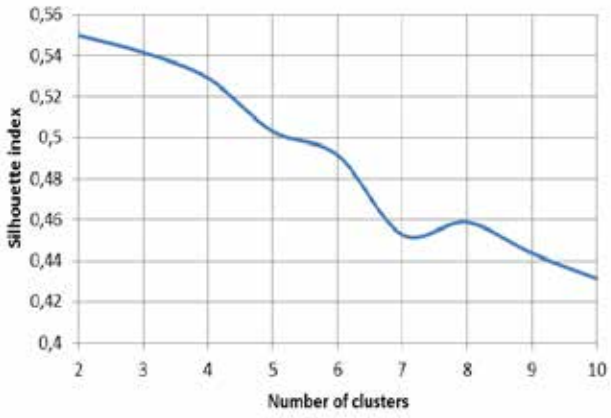

Figure 7. Line graph of changes in silhouette index for clusters obtained with the hierarchical analysis shown on a dendrogram in Figure 6.

3.4 *IDW statistical model*

In the construction of the 3-D model of subsoil stiffness the IDW method was applied (Młynarek et al. 2007). For this method the interpolation value - M in a given point with coordinates (x_0,y_0,z_0) is established on the basis of values defined by coordinates x_i,y_i,z_0. Each of these values affects the interpolated value of v_0 with the weight, which is inversely proportional to the distance between these points. The formula used in IDW takes the form:

$$v_0 = \frac{\sum_{i=1}^{|N(v_0)|} w_i v_i}{\sum_{i=1}^{|N(v_0)|} w_i} \quad (9)$$

where $|N(v_0)|$ denotes the number of included observations from the neighbourhood of v_0, and weight w_i takes the form:

$$w_i = \frac{1}{(d_i + s)^p}. \quad (10)$$

where the value of d_i denotes the Euclidean distance between points (x_0,y_0,z_0) and (x_i,y_i,z_0).

4 ASSUMPTION OF STIFFNESS MODEL

The results of the conducted clustering of constrained modulus M for the entire testing site were presented by placement of individual clusters in the analyzed profiles. Profiles 1,3,5 and 7 are shown in Figure 8 as examples.

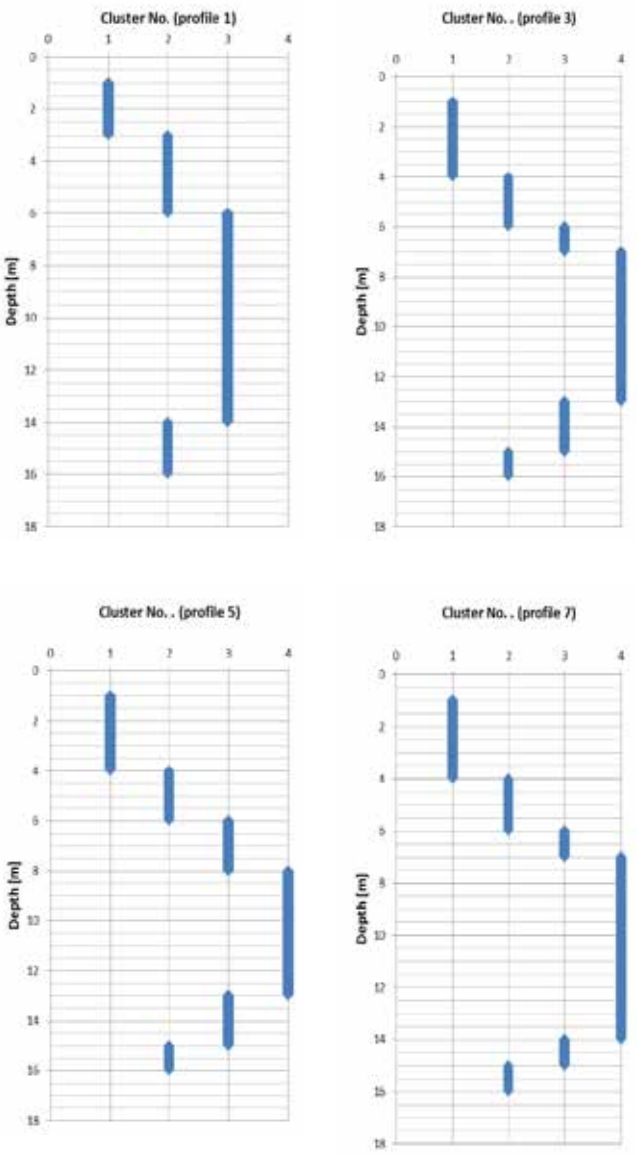

Figure 8. Localization of the obtained clusters along the profiles: 1,3,5 and 7.

Figure 8 indicates that the elements essential for separation of homogenous, in terms of M modulus, zones in the subsoil include both glacial tills stratigraphy and the presence of intermediate zone between individual geological layers. Comparison of Figures 1 and 8 reveals that in each case the surface layer of younger glacial tills (cluster 1) and the layer of glacifluvial sands (clusters 3 and 4) are distinct. Layer of older glacial tills statistically does not differ in stiffness from the contact zone between younger tills and glacifluvial sediments. This observation indicates considerable influence of a highly stiff layer on the less stiff layer directly above. For each analyzed case, this strengthened intermediate zone has thickness of about 2 m and it is entirely supported on the thill of younger tills..

The observation leads also to a conclusion that from a geological model of subsoil point of view, presumption of geological division into layers may lead to an invalid assessment of stiffness of subsoil. Figures 9 and 10 show the differences between the IDW model based on stratigraphy and the IDW model based on the results of functional analysis, in which cone resistance was applied in order to estimate changes in M modulus with depth.

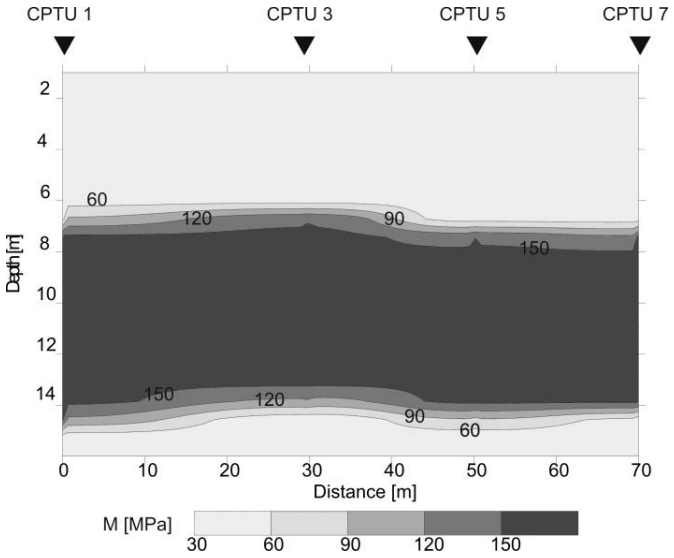

Figure 9. IDW stiffness model of the subsoil based on CPTU tests and subsoil stratigraphy in section between points 1, 3, 5 and 7.

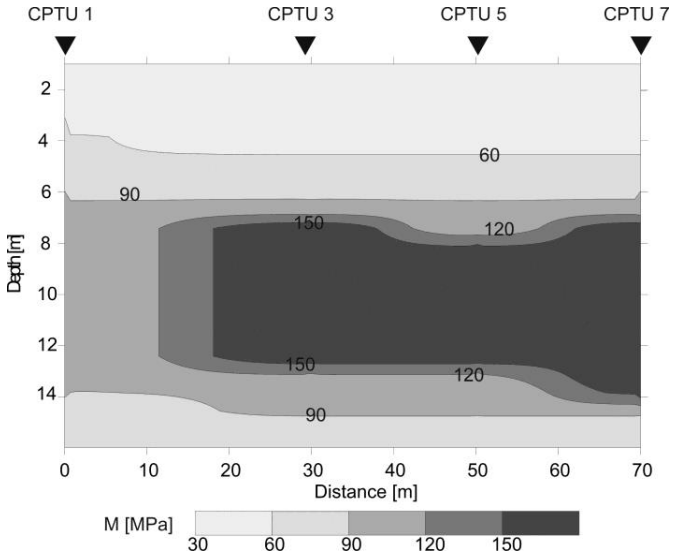

Figure 10. IDW stiffness model of the subsoil based on CPTU tests and functional analysis in the section between points 1, 3, 5 and 7.

5 CONCLUSIONS

CPTU penetration tests proved to be a notably convenient method of assessment of the stiffness model of the subsoil built of genetically and lithologically diversified soil layers. Accuracy of recording of cone resistance profiles with changes in the σ_{v0} stress in the subsoil allows for accurate determination of zones of strengthening and weakening of the subsoil with the use of constrained moduli M. The presented analyzed stiffness model may be assessed in various directions along one profile, depending on geometry and size of the construction project. The performed analysis also showed that in complex soil conditions, information drawn only from the stratigraphic model of subsoil may be insufficient for an accurate analysis of the expected degree and non-uniformity of settlements of the construction.

6 REFERENCES

Lunne T. & Christophersen H.P. 1983. Interpretation of cone penetrometer data for offshore sands. In *Proc. of the Offshore Technology Conference*. Richardson, Texas. Paper No. 4464.

Lunne T., Robertson P.K. & Powell J.J.M. 1997. Cone Penetration Testing in geotechnical practice. Reprint by *E & FN Spon*, London.

Młynarek Z. & Lunne T. 1987. Statistical estimation of homogeneity of a North Sea overconsolidated clay. *Proceedings of 5th International Conference on Application of Statistics and Probability in Soil and Structural Engineering, Vancouver:* 961–968.

Młynarek Z., Wierzbicki J. & Lunne T. 2016. Identification of the influence of overconsolidation effect on subsoil's stiffness by a CPTU method. In *Proc. of ISC'5 (in print)*.

Młynarek Z., Wierzbicki J. & Wołyński W. 2007. An approach to 3D subsoil model based on CPTU results. In V. Cuellar et. al (eds.) *Geotechnical Engineering in Urban Enviornment,*. Vol. 3, 1721-1726. Millpress, Rotterdam.

Młynarek Z., Wierzbicki J. & Wołyński W. 2014. Use of functional cluster analysis for grouping homogenous CPTU characteristics. *Proc. of CPT'14: International Symposium on Cone Penetration Testing, Las Vegas, Nevada, US*, *May 2014.*

Ramsey J.O. & Silverman B.W. 2005. Functional data analysis. 2nd Ed., Springer.

Robertson P. K. 2009. Interpretation of Cone Penetration Testing – a unified approach, Canadian Geotechnical Journal, 46 (11), 1337–1355

Rousseeuw P.J. 1987. Silhouettes: A graphical aid to the interpretation and validation of cluster analysis. *Journal of Computational and Applied Mathematics*, Vol. 20: 53-65.

Tumay M.T., Karasulu Y.H., Młynarek Z. & Wierzbicki J. 2011. Effectiveness of CPT-based classification charts for identification of subsoil stratigraphy. In A. Anagnostopoulos et al. (eds.), *Proc. of the 15th European Conference on Soil Mechanics and Geotechnical Engineering*: 91-98. IOS Press.

Geotechnical and Geophysical Site Characterisation 5 – Lehane, Acosta-Martínez & Kelly (Eds)

Empirical estimation of soil unit weight and undrained shear strength from shear wave velocity measurements

S.W. Moon & T. Ku
Department of Civil and Environmental Engineering, National University of Singapore, Singapore

ABSTRACT: The main objective of this study is to establish useful empirical relationships to estimate engineering properties of soil in terms of geotechnical applications of shear wave velocity (V_s). Based on each special database compiled from globally well-documented geotechnical test sites, site-specific stress-normalized V_s and downhole-type shear wave mode are utilized for estimating soil unit weight and undrained shear strength, respectively. In addition, the application of proposed global empirical relationships is examined at two test sites (i.e., Australia and China) as independent case studies. The geological setting and geotechnical characterization of the two test sites are summarized and further discussions are described in detail. Using the proposed correlations, it is shown that field shear wave velocity measurements can offer reasonable profiles of the soil unit weight and undrained shear strength at given sites.

1 INTRODUCTION

Shear wave velocity (V_s) of geo-materials such as soils and rocks is one of the fundamental engineering measurements for geotechnical design problems due to its direct relationship with initial shear modulus (G_0) at small strains. Indicating the beginning of all stress-strain-strength curves, the initial shear modulus is calculated using $G_0 = \rho \cdot V_s^{\ 2}$, where ρ is the bulk soil density. It is employed for performing site response analysis as well as ground deformation analysis with respect to foundation system.

For measuring shear wave velocity, borehole seismic methods (downhole test or crosshole test) and non-invasive geophysical techniques (surface wave survey or reflection test/refraction test) as well as laboratory testing methods (bender element test or resonant column test) have been developed. The utilization of in-situ V_s data for establishing several empirical relationships may lead to potential uncertainty coupled with scattered outliers attributed to inherent site conditions and sensitivity of applied test methods. Nevertheless, in-situ V_s measurement techniques are generally efficient and suitable for assessment of geotechnical engineering problems since V_s data can be obtained quickly and economically with minimum soil disturbance. Furthermore, G_0 calculated from in-situ V_s measurement is commonly considered to be more accurate and reliable than that determined from laboratory tests, which generally present lower G_0 due to sample disturbance, stress relief, and loss of ageing effect (Ghionna and Jamiolkowski 1991; Ku and Mayne 2014; Stokoe and Santamarina 2000; Tatsuoka and Shibuya 1992).

In several previous studies, the in-situ V_s measurements have been applied to establish empirical correlations with engineering properties of soils (e.g., soil unit weight, γ_t; peak friction angle, ϕ_p; and undrained shear strength, s_u) (Levesques et al. 2007a; Mayne 2007b; Uzielli et al. 2013). Using two special databases compiled worldwide, this paper describes two new global empirical relationships between: (1) soil unit weights (γ_t) and in-situ site-specific stress-normalized shear wave velocity, instead of conventional $V_s - \gamma_t$ models; (2) undrained shear strength (s_u) and shear wave velocity.

2 PROPOSED RELATIONSHIPS

2.1 Normalized shear wave velocity – unit weight

For this study, a special database (Mayne et al. 2009) is applied based on 120 well-documented test sites consisting of 61 clay sites, 6 fissured and calcareous sites, 8 silt sites, 35 sand sites, and 10 other sites. The ranges of compiled engineering properties of soils such as plasticity index (PI), void ratio (e), and total unit weight (γ_t) are summarized in Table 1.

For assessment of seismic liquefaction potential of soils, the in-situ measurements of V_s have been normalized by effective overburden pressure (σ'_{v0}) adopting a constant exponent of 0.25 at the reference

Table 1. Details of collected database: soil type, number of site and data, and range of soil properties (PI, e, γ_t, V_{s1}, V_{sn}) used for correlation between unit weight and normalized shear wave velocity (data from Mayne *et al.* 2009).

Soil Type	No. of Site	No. of Data	Range of					Symbol
			PI	e	γ_t (kN/m^3)	V_{s1} (m/s)	V_{sn} (m/s)	
Intact Clay	61	698	0-250	0.40-6.75	11.2-22.7	35-406	39-438	
Fissured Clay	3	21	12-55	0.43-0.84	18.8-21.3	178-313	187-306	
Calcareous Clay	3	18	0-11	0.95-1.38	16.2-19.7	186-400	182-535	
Silts	8	32	0-15	0.64-1.43	16.7-20.2	122-319	142-215	
Sands	35	200	0-11	0.43-2.15	14.9-22.2	106-621	88-728	
Gravels	7	43	-	0.27-0.70	19.6-22.5	120-366	263-280	
Clay Till	3	16	0-11	0.19-0.56	20.1-24.0	188-611	242-645	

stress of 1 atmospheric pressure (Kayen et al. 2013). On the other hand, a site-specific exponent that depends on actual geostatic stress condition at each site can be employed for the normalization of V_s instead of the constant exponent 0.25. In this study, stress-normalized shear wave velocity (V_{s1}) and site-specific stress-normalized shear wave velocity (V_{sn}) of various geo-materials are calculated from the following equations, respectively:

$$V_{s1} = V_s\,(m/s) / (\sigma'_{v0} / \sigma_{atm})^{0.25} \quad (1)$$

$$V_{sn} = V_s\,(m/s) / (\sigma'_{v0} / \sigma_{atm})^{n} \quad (2)$$

where σ'_{v0} = effective overburden pressure, σ_{atm} = 1 bar = 101.325 kPa = atmospheric pressure, n = site-specific stress exponent. As noted in Equation 1, the exponent 0.25 has been commonly determined as an empirical value based on laboratory tests with clean silica sands (Stokoe et al. 1985; Yu and Richart 1984). However, the exponent n in Equation 2 can be estimated to have various values because it is often significantly dependent on the site-specific conditions as noted by Ku *et al.* (2011).

In order to obtain better fitting models, involving an increase in coefficient of determination (R^2) and decrease in the standard error of the dependent variable (S.E.Y.), higher order regressions are examined using stress-normalized V_s and PI. Two empirical correlations for the estimation of total unit weight are observed in Figure 1 as a function of both PI and V_{s1} or V_{sn}:

$$\gamma_t = 11.27(V_{s1})^{0.147}(PI)^{-0.096} \quad (3)$$

$$\gamma_t = 7.91(V_{sn})^{0.194}(PI)^{-0.068} \quad (4)$$

As described in Figure 1, Equation 3 and 4 present improved γ_t relationships for clay and clay tills from the database collected. In addition, the proposed expression (N = 39; R^2 = 0.768; S.E.Y. = 0.069) using V_{sn}, Equation 4, is comparable with that (N = 53; R^2 = 0.726; S.E.Y. = 0.074) using V_{s1}, Equation 3. Based on the observed statistical information, the regression model using V_{sn} can be considered to be slightly more robust. Apparently, both normalized shear wave velocities are proven to have strong relationships with soil unit weight in spite of some scattered data.

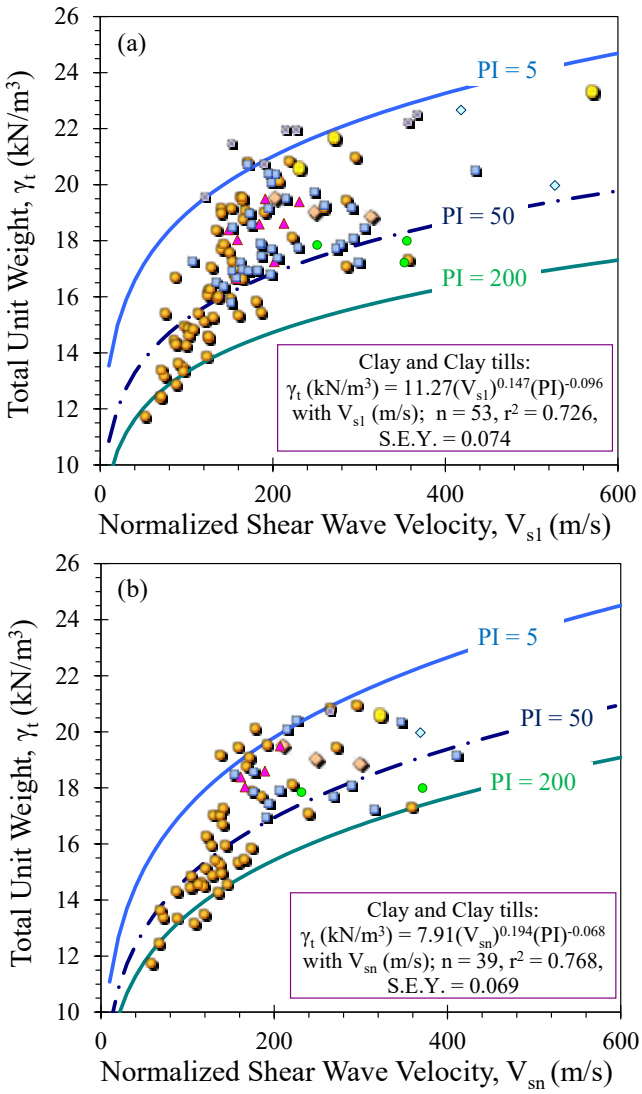

Figure 1. Total unit weight versus normalized shear wave velocity with prediction lines from multiple regression analysis: (a) V_{s1} and (b) V_{sn}.

From the proposed empirical relationships between γ_t and V_{s1} or V_{sn}, γ_t is determined with depth via following procedures: (1) determination of σ'_{v0} with depth based on assumed initial γ_t values; (2) calculation of V_{s1} and V_{sn}; (3) estimation of γ_t with depth using Equations 3 and/or 4; (4) re-calculation of σ'_{v0}

and n using γ_t with depth obtained from previous stage; (5) re-estimation of γ_t with depth using Equation 3 and/or 4; (6) iterations of stage 4 and 5 until convergence (e.g., 2-3 times). The assumed initial γ_t values in step 1 have a little effect on the results.

2.2 Shear wave velocity – undrained shear strength

A new worldwide database was compiled towards the intent of this study, including Australia, Canada, Greece, Ireland, Italy, Japan, Korea, Norway, Singapore, Taiwan, Thailand, and United States, Figure 2. It was observed that the collected clay database exhibits a wide range of overconsolidation ratios (OCR) and PIs.

In-situ V_s and/or G_0 values were collected from several geophysical tests such as cross-hole test (CHT), and down-hole type test (DHT or seismic cone penetrometer).

Figure 2. Worldwide site locations from the compiled database in this study.

On the other hand, s_u values were selected based on various in-situ tests, including field vane shear test (FV), cone penetration test (CPT), fall cone test (FCT), pressuremeter (PMT), standard penetration test (SPT), and plate load test (PLT). s_u values from different types of laboratory tests, including isotropic consolidated undrained compression (CIUC), K_0-consolidated undrained compression (CK_0UC), and unconsolidated undrained compression (UU) were also included.

$s_{u(FV)}$ values obtained from FV were used as a primary option for this study because it is generally considered to be a reference value and also correlated with other strength parameters. It should be noted that corrected $s_{u(FV)}$ values with PI (e.g., s_u multiplied by a correction factor (μ) which varies with PI) were collected for the database. For a few sites with unknown correction information, $s_{u(FV)}$ data were assumed to be corrected values. As a second option, $s_{u(TC)}$ values that were measured from laboratory CIUC or CK_0UC tests were also used for this study. In addition, some $s_{u(CPT)}$ values were compiled based on CPT at four test sites because no other reference s_u data were available.

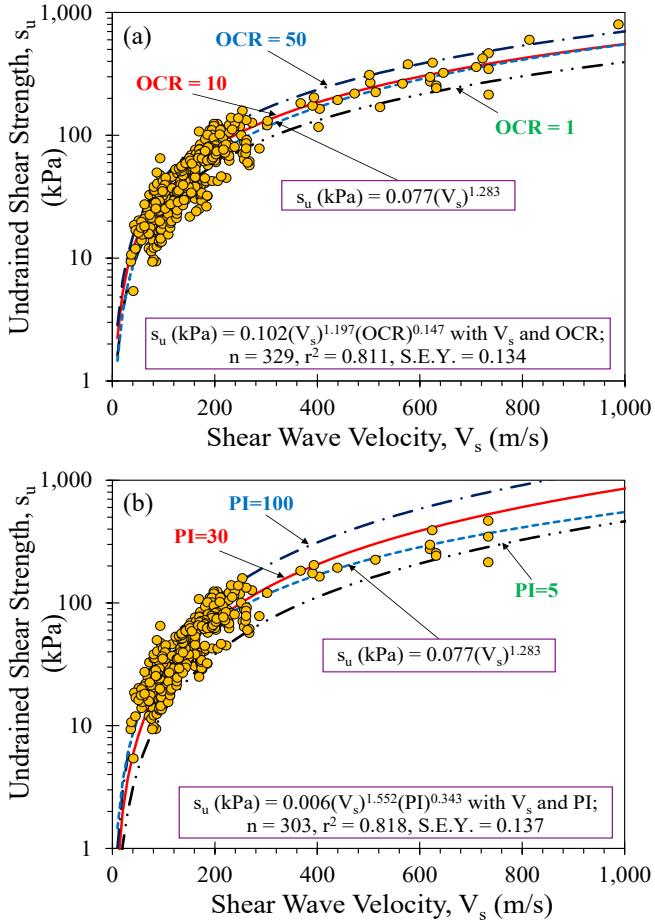

Figure 3. Trends between undrained shear strength and shear wave velocity with repect to (a) OCR, (b) PI.

Due to the dependency of the measured s_u on various factors (e.g., testing method, strain rate), it is unreasonable to compare the selected s_u values directly. Thus, several transformation methods have been proposed to convert undrained shear strength obtained from different types of tests to the reference (Bjerrum 1972; Kulhawy and Mayne 1990; Mesri and Huvaj 2007). In order to convert $s_{u(TC)}$ to the reference ($s_{u(FV)}$), this study employs a correction factor determined by comparing the ratio between $s_{u(TC)}$ and $s_{u(FV)}$. Based on the collected database, the average ratio (i.e., $s_{u(FV)}/s_{u(TC)}$=0.76) is used as the correction factor to convert the $s_{u(TC)}$ values.

Attempting to improve the fitting and statistics (e.g., R^2 and S.E.Y.), the higher order regressions are investigated by including PI or OCR with V_s in terms of s_u. Significant statistical trends relating undrained shear strength as a function of both V_s and PI or OCR are observed in Figure 3 and the multi-regressions are expressed as follows:

$$s_u = 0.102(V_s)^{1.197}(OCR)^{0.147} \quad (5)$$

$$s_u = 0.006(V_s)^{1.552}(PI)^{0.347} \quad (6)$$

3 CASE STUDIES

In order to investigate the applicability of the proposed new regression models for the estimation of γ_t and s_u, available geotechnical and geophysical data from the well-known Burswood clay in Australia and Huaiyan Expressway site in China are reviewed. These two sites were not included in each compiled database, thus independent case studies can be performed using the data from both sites.

3.1 Burswood site

Figure 4 shows the selected engineering properties of soils such as PI, OCR and V_s, based on a variety of site investigations performed for Burswood clay (Low 2009). The soil profile consisting of 3 m thick weathered crust (stiff and fine sand) and 12 m thick soft silt clay exhibits a lightly overconsolidated and sensitive silty clay, having high to uncommonly high plasticity. Shell fragments and silt lenses are frequently found in a depth of 12 m and tiny shell fragments are occasionally found at greater depth. In addtion, dessicated plants are found in a depth of 7 m (Low 2009). The profile of measured shear wave velocity is obtained from seismic cone tests, as shown in Figure 4(c).

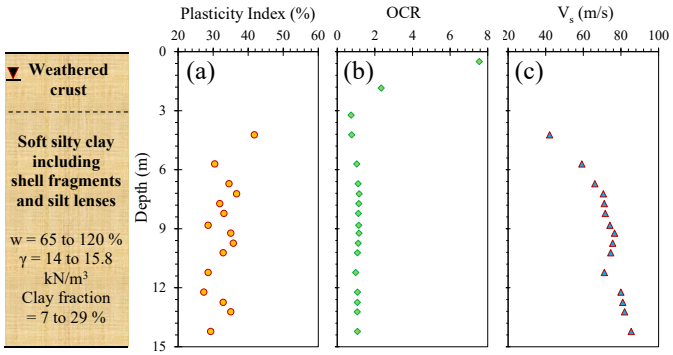

Figure 4. Case study for Burswood clay (data from Low (2009)): (a) PI, (b) OCR, and (c) V_s.

Table 2. Empirical correlations in previous studies

Empirical relationships	References
$\gamma_t\ (kN/m^3) = 30.4 \cdot PI^{-0.174}$	Mayne & Peuchen (2013)
$\gamma_t\ (kN/m^3) = 6.87(V_s\ m/s)^{0.227}/(\sigma'_{v0}\ kPa)^{0.057}$	Burns & Mayne (1996)
$\gamma_t\ (kN/m^3) = 8.32\log(V_s\ m/s) - 1.61\log(z\ m)$	Mayne (2001)
$\gamma_t\ (kN/m^3) = 4.17\ln(V_{s1}\ m/s) - 4.03$	Mayne (2007a)
$\log(s_u\ (kPa)) = (\log(V_s\ (m/s)/23)/0.475$	Ashford et al. (1996)
$s_u\ (kPa) = (V_s\ (m/s)/7.93)^{1.59}$	Levesques et al. (2007b)
$s_u\ (kPa) = 0.001 \cdot V_s^{\ 2}(m/s) + 0.016 \cdot V_s\ (m/s) + 60.8$	Long et al. (2013)

Figure 5(a) compares the measured γ_t profile with the estimated γ_t profiles from the Equation 3 and 4 described in this study. In addition, the predicted γ_t profiles are compared with four empirical correlations using 1) PI from Mayne and Peuchen (2013); 2) V_s from Burns and Mayne (1996) and Mayne (2001); and 3) V_{s1} from Mayne (2007a), as listed in Table 2. As shown in Figure 5(a), γ_t of 16 kN/m^3 was initially assumed. Eventually, the predicted γ_t profiles after three iterations from the equations using V_{s1} and V_{sn} derived in this study provide more reasonable agreements with the measured γ_t profile, compared with the estimated γ_t profiles from the existing correlations in previous studies.

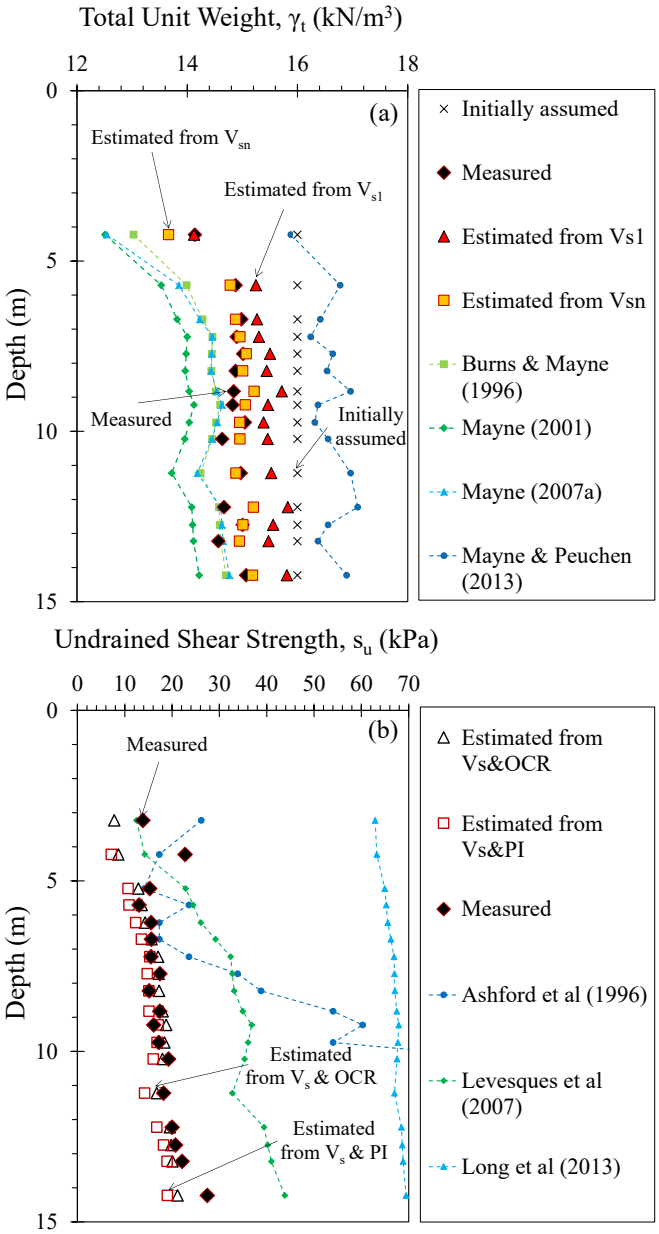

Figure 5. Comparison of estimated and measured (a) unit weight and (b) undrained shear strength at Burswood clay site.

Figure 5(b) presents the measured s_u profile from field vane shear tests, compared with the estimated s_u profiles from the Equation 5 and 6. Also, the reference s_u profile is compared with three existing empirical correlations using 1) Ashford et al. (1996); 2) Levesques et al. (2007b); and 3) Long et al. (2013), as illustrated in Table 2. Figure 5(b) shows that the predicted s_u profiles from the equations us-

ing PI and OCR derived in this study are closely matched to the measured s_u profile. Evidently, the predictions seem better matched than the other s_u profiles estimated from previous correlation studies.

3.2 *Huaiyan express site*

Huaiyan express site is located on the Lixia River area which is near the city of Yancheng in East Juangsu province, China. Figure 6 shows soil profiles determined from the geotechnical site investigations using samples from boreholes and the laboratory test results (Anand et al. 2011; Cai et al. 2015; Cai et al. 2010). The soil layers consist of a clay fill and slightly overconsolidated lacustrine clay deposit of the Holocene age. Also, the soil boundary between highly sensitive and moderately sensitive clay was found at approximate depth of 13 m. From Seismic Piezocone Test (SCPTu), it is noted that the generation of pore water pressure is remarkably increased with depth in the muck layer and dramatically decreased again (i.e., below 12 m). In addition, Figure 6(c) presents shear wave velocity measurements obtained from SCPTu.

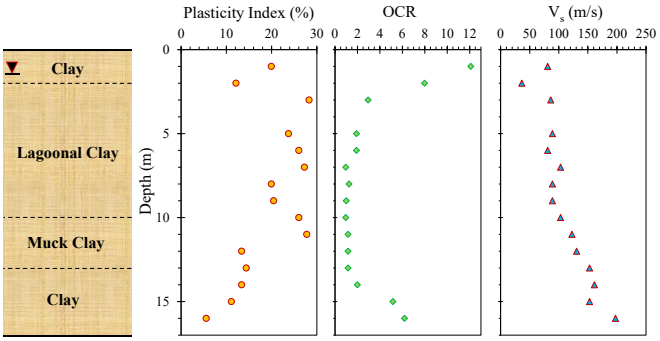

Figure 6. Case study for Hauiyan express site (data from Anand et al. (2011), Cai et al. (2015), Cai et al. (2010)): (a) PI, (b) OCR, and (c) V_s.

Figure 7(a) compares the measured γ_t profile with the estimated γ_t profiles from the Equation 3 and 4 in this study as well as other four empirical correlations. As presented in Figure 7(a), γ_t of 16 kN/m^3 was assumed in the initial stage and the evolved γ_t profiles are obtained after three iterations from the equations using V_{s1} and V_{sn} derived in this study. The final prediction profiles show more reasonable agreements with the measured γ_t profile than the estimated γ_t profiles from the existing correlations in the depth range of 3m to 12m. The underestimation of predicted γ_t at depths of below 13m can be attributed to the existence of the boundary changing from highly sensitive clay to moderate sensitive clay.

Figure 7(b) presents the measured s_u profile from field vane shear tests and the estimated s_u profiles from the Equation 5 and 6. Again, the reference s_u profile is compared with three existing empirical correlations. Figure 7(b) shows that the predicted s_u profiles from the equations using PI and OCR in this study provide relatively good agreements with the measured s_u profile.

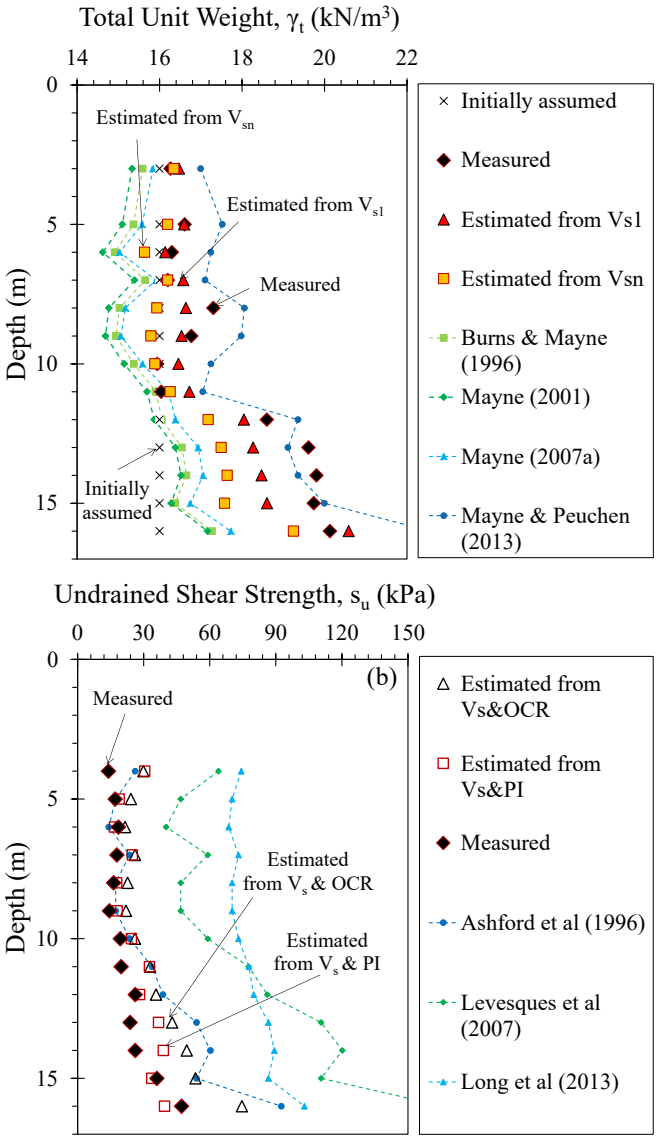

Figure 7. Comparison of estimated and measured (a) unit weight and (b) undrained shear strength at Huaiyan express site.

4 CONCLUSIONS

In this study, the global correlation models between: (1) soil unit weight and normalized shear wave velocities (V_{s1} and V_{sn}), and (2) undrained shear strength and shear wave velocity were investigated via each special database compiled worldwide. Two case studies (i.e., Burswood and Huaiyan Express) were examined for the estimation of γ_t and s_u. For estimating soil unit weight and undrained shear strength, consequently, newly developed V_s-based empirical expressions from multiple regression studies which are combined with OCR or PI are recommended beyond various previous empirical approaches.

5 REFERENCES

Anand, J.P., Guojun, C., Liyuan, T., Songyu, L., 2011. Assessment of the coefficient of lateral earth pressure at rest (K o) from in situ seismic tests. Geotechnical Testing Journal, 34(4), 1-11, doi: 10.1520/GTJ102520.

Ashford, S.A., Jakrapiyanum, W., Lukkanaprasit, P., 1996. Amplification of earthquake ground motions in Bangkok.

Bjerrum, L., 1972. Embankments on soft ground. ASCE Specialty Conference on Performance of Earth and Earth-Supported Structures. ASCE, Purdue University, Lafayette, Ind., 1-54.

Burns, S.E., Mayne, P.W., 1996. Small- and high-strain measurements of in-situ soil properties using the seismic cone penetrometer. National Academy Press, Washington, DC.

Cai, G., Liu, S., Puppala, A.J., 2015. Evaluation of geotechnical parameters of a lagoonal clay deposit in Jiangsu Lixia River area of China by seismic piezocone tests. KSCE Journal of Civil Engineering, 1-14.

Cai, G., Liu, S., Tong, L., 2010. Field evaluation of deformation characteristics of a lacustrine clay deposit using seismic piezocone tests. Engineering Geology, 116(3), 251-260.

Ghionna, V., Jamiolkowski, M., 1991. A critical appraisal of calibration chamber testing of sands. . 1st International Symposium on Calibration Chamber Testing (ISOCCTI). Elsevier, Potsdam, N.Y, 13-39.

Hight, D.W., Bond, A.J., Legge, J.D., 1992. Characterization of the Bothkennar clay : an overview. Geotechnique, 42(2), 303-347.

Kayen, R.E., Moss, R.E.S., Thompson, A.M., Seed, R.B., Cetin, K.O., Der Kiureghian, A., Tanaka, Y., Tokimatsu, K., 2013. Shear-Wave Velocity–Based Probabilistic and Deterministic Assessment of Seismic Soil Liquefaction Potential. Journal of Geotechnical and Geoenvironmental Engineering, ASCE, 139(3).

Ku, T., Mayne, P.W., 2014. Stress history profiling using OCD-G_0 anisotropy relationship. Geotechnical Engineering, Proceedings of the Institution of Civil Engineers (ICE) journal, 167(5), 476-490.

Ku, T., Mayne, P.W., Gutierrez, B.J., 2011. Hierachy of Vs modes and stress-dependency in geometerials. 5th International Symposium on Deformation Characteristics of Geometerials, Seoul, 533-540.

Kulhawy, F.H., Mayne, P.W., 1990. Manual on estimating soil properties for foundation design. Electric Power Research Inst., Palo Alto, CA (USA); Cornell Univ., Ithaca, NY (USA). Geotechnical Engineering Group.

Levesques, C.L., Locat, J., Leroueil, S., 2007a. Characterization of postglacial sediments of the Saguenay Fjord, Quebec. Characterization and Engineering Properties of Natural Soils. Taylor & Francis Group, London, 2645-2677.

Levesques, C.L., Locat, J., Leroueil, S., 2007b. Characterization of postglacial sediments of the Saguenay Fjord, Quebec. In: Tan, T.S., Phoon, K.K., HIght, D.W. & Leroueil, S. (eds.) Characterization and Engineering Properties of Natural Soils. Taylor & Francis Group, London, 2645-2677.

Long, M., Quigley, P., O'Connor, P., 2013. Undrained shear strength and stiffness of Irish glacial till from shear wave velocity. Ground Engineering, 26-27.

Low, H.E., 2009. Performance of Penetrometers in Deepwater Soft Soil Characterisation. Doctor of Philosophy, The University of Western Australia.

Mayne, P.W., 2001. Stress-strain-strength-flow parameters from seismic cone tests. Intl. Conf. on In-Situ Measurement of Soil Properties & Case Histories, Bali, Indonesia, 27-48.

Mayne, P.W., 2007a. In-situ test calibrations for evaluating soil parameters. . Characterization & Engineering Properties of Natural Soils. Taylor & Francis Group, London, 1602-1652.

Mayne, P.W., 2007b. Synthesis 368: Cone Penetration Testing. National Cooperative Highway Research Program (NCHRP).

Mayne, P.W., Peuchen, J., 2013. Unit weight trends with con resistance in soft to firm clays. Geotechnical and Geophysical Site Characterization 4. Taylor & Francis Group, London, 903-910.

Mesri, G., Huvaj, N., 2007. Shear strength mobilized in undrained failure of soft clay and silt deposits. Proceedings of Geo-Denver, 1-22.

Stokoe, K.H., Lee, S.H.H., Knox, D.P., 1985. Shear moduli under true triaxial stresses. Advances in the Art of Testing Soil Under Cyclic Conditions. ASCE Convention, Detroit.

Stokoe, K.H., Santamarina, J.C., 2000. Keynote: Seismic wave-based testing in geotechnical engineering. GeoEng 2000, Melbourne, Australia, 1490-1536.

Tatsuoka, F., Shibuya, S., 1992. Deformation characteristics of soil and rocks from field and laboratory tests, Keynote Lecture. IX Asian Conference on SMFE, Bangkok, 101-190.

Uzielli, M., Mayne, P.W., Cassidy, M.J., 2013. Probabilistic assessment of design strengths for sands from in-situ testing data. In: (series), A.i.S.M.G.-n.E. (ed.) Modern Geotechnical Design Codes of Practice. IOS-Millpress, Amsterdam, 214-227.

Yu, P., Richart, F.E., Jr., 1984. Stress ratio effects on shear modulus of dry sands. Journal of Geotechnical and Geoenvironmental Engineering, ASCE, 110(3), 331-345.

Geotechnical and Geophysical Site Characterisation 5 – Lehane, Acosta-Martínez & Kelly (Eds)

Small Strain Stiffness assessments from in situ tests – revisited

J.J.M Powell
Geolabs Limited, United Kingdom

L. Dhimitri & D. Ward
Insitu Site Investigation Ltd, United Kingdom

A.P. Butcher
Consultant, United Kingdom

ABSTRACT: The increasing trend to model the behaviour of the ground requires more detailed soil properties that include small strain data. These data can be obtained from both field and laboratory tests to measure shear wave velocities from which the shear modulus at small strains can be calculated. However, such measurements are only specified for large projects and so smaller projects have to rely on correlations from other in situ tests. In 2004 Powell & Butcher presented and discussed some correlations between the small strain stiffness of the ground in different orientations measured by geophysical tests and parameters measured by the Cone Penetrometer (CPT) and the Marchetti Dilatometer (DMT). Since that time the database of information has grown and this paper reviews and updates the findings of the earlier paper. Anisotropy of stiffness is shown to be a major factor in the correlations especially in 'aged' clays.

1 INTRODUCTION

Whilst there has always been a need to not only design to prevent failure but to control movements, the latter item has often only been given cursory attention and often satisfied by a very generous factor of safety on the ultimate or failure state. Increasingly through the Euro and other codes we have to also show that we can prove that we satisfy serviceability (movement) limit state. As a result of this and also the need to supply strength and stiffness parameters for geotechnical modelling the need for realistic stiffness parameters has gained increased interest. It has been shown by Simpson et al (1996) that in order to successfully predict lateral and vertical movements around excavations and tunnels in overconsolidated soils the anisotropy of stiffness and stress are the most important properties to quantify.

The shear modulus is largest at very low strains and decreases with increasing shear strain. It has been found that the initial maximum shear modulus is constant for strains less than 10^{-3}% although this may vary with plasticity index I_P (Vucetic & Dobry (1991). This initial, small strain modulus is often denoted G_0.

Stiffness varies with stress level and is generally non-linear for most soils. It is now well accepted that the change or decay of stiffness follows an 'S' shaped curve with the stiffness at very small strain being the starting plateau maximum which decays to a lower plateau at large strains. Great interest has developed in the measurement of stiffness at very small strains and its extrapolation to the larger strains typical of other in situ testing devices.

Butcher & Powell (2001) published data from laboratory and field testing on a series of established and well-characterised testbed sites which highlighted the stiffness anisotropy present in many soils especially heavily overconsolidated 'aged' clays. Their work and that from many other authors has tried to explain what controls this anisotropy in terms of the basic soil properties encountered and the stresses present in the ground. Powell & Butcher (2004) published the stiffness data from their testbed sites and related it to measured and derived parameters from various in situ tests trying to establish simple correlations between the data. Others have tried similar approaches but, as will be discussed later, introduced various additional parameters in equations to improve 'fit'. Powell & Butcher (2004) suggested that a major influence in the derivation of correlations was 'anisotropy', from both stresses and inherent or fabric influences.

This paper tries to build on the 2004 paper by including additional data not only from the original sites but also from a variety of additional sites and databases that are now available. These comprise 10 European testbed sites with high quality information and used for a Brite Euram study on semi empirical foundations design procedures from in situ tests (Shields et al 1999, Powell et al 2001), 3 heavily overconsolidated clay sites investigated by Hosseini Kamel (2012) and Brosse (2012), the heavily overconsolidated Boom clay, Piriyakul (2006) and 11

working sites covering a range fine grained deposits including some additional London clay sites.

This paper uses selected data from these sites where geophysical seismic wave measurements have taken place as well as CPT, CPTU and DMT.

The purpose of the paper is to suggest that increased confidence can be given to previously suggested relationships related to anisotropy of stiffness and realistic correlations related to in situ test devices.

2 THE SITES

To include a table of the sites and their basic geotechnical properties would take up too much space and so the interested reader is referred to references mentioned above for full details. To summarise some information in a brief form for the new sites with 'aged' clays in Table 1.

Table 1. Aged Clays.

Clay	Approx. Age	W_P	W_L	I_P	e
	10^6 years	%	%	%	
Oxford Clay	161-156	34	66	32	0.6
Kimmeridge Clay	156-151	23	49	26	0.46
Gault Clay	122-995	28	74	46	0.67
London Clay*	56-49	29	66	37	0.82
Boom Clay**	35	26	72	46	0.73

* See other LC info in Powell& Butcher 2005.
** from Piriyakul (2006)

The rest of the clays in the study tend to be considerably younger, either of late glacial origin or estuarine or marine clays of Holocene age.

Void ratios vary from around 1.7 for the young estuarine and marine clays to as low as 0.45 for some of the glacial clays. For the 'aged' clays void ratios vary from 0.8 to 0.45.

3 GEOPHYSICAL TESTING

The interest in geophysical testing has grown considerably in the last 20 years as a way of establishing the small strain stiffness of a soil (the highest or maximum stiffness) from which point the now stiffness against strain decay curve can be deduced, often referred to as the 'S' shaped decay curve. The value derived is often referred to as G_{max} or G_0 which can be misleading. It is strongly suggested that, when a value for small strain stiffness from geophysical testing is reported, then it should be quite obvious as to how and in what orientation it was derived. The various methods of geophysical testing tend to test the ground in different orientations and hence can be used to look at stiffness anisotropy.

The original field measurements of shear wave velocities were made using BRE equipment and

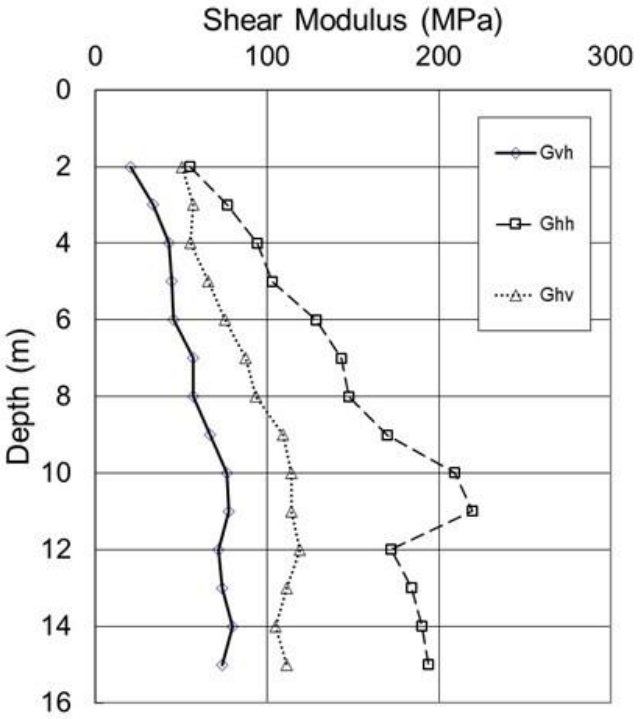

Figure 1. Typical G_{vh}, G_{hv}, and G_{hh} profiles for London Clay

techniques (Butcher & Powell, 1995a). Figure 1 shows a typical result from a London clay site.

For convenience in the following, subscripts will be added to G which will be related to the direction of polarization and propagation of the shear waves. For example, G_{vh} will denote the stiffness derived from vertically propagating, horizontally polarized (down- hole/seismic cone) shear waves.

It is generally to be expected that for a continuum medium $G_{vh} = G_{hv}$ and this has been shown by Stokoe et al (1991) and Bellotti et al (1996) for sands and Lo Presti et al (1999) and Pennington et al (1997) for reconstituted clays. However, Butcher & Powell (1995b) and Pennington et al (1997) showed that this may not be true for very stiff overconsolidated or layered clays and in fact differences can exist between G_{vh} and G_{hv} even in soft soils, but this may relate more to differences in testing methods in the two orientations, and others have found similar behaviour. In terms of stress anisotropy then it may be expected that G_{hh} is either close to or less than G_{vh} and G_{hv} in normally consolidated soils and greater in heavily overconsolidated soils. The situation is further complicated in the 'aged' clays or those showing significant fabric as there will be both stress and inherent anisotropy.

It must be remembered that there is a significant scale difference between field and laboratory shear waves used in the measurements. It is likely that fabric will affect field measurements more than laboratory measurements hence contributing to the differences between G_{vh} and G_{hv}.

Hardin (1978) suggested that for clays, the small strain shear modulus, G_0, depends on the applied stresses, void ratio and overconsolidation ratio

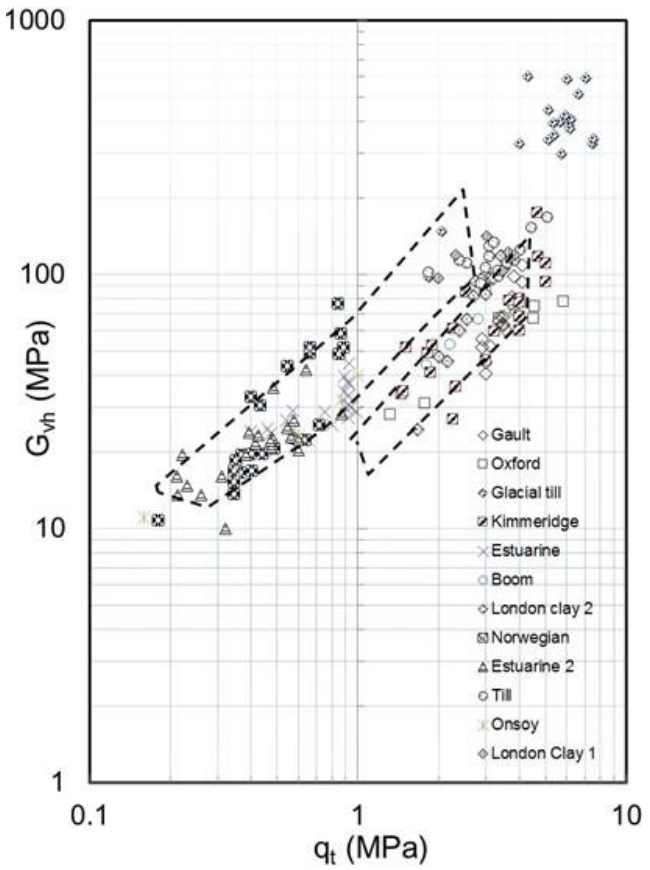

Figure 2a. Shear Modulus G_{vh} against q_t

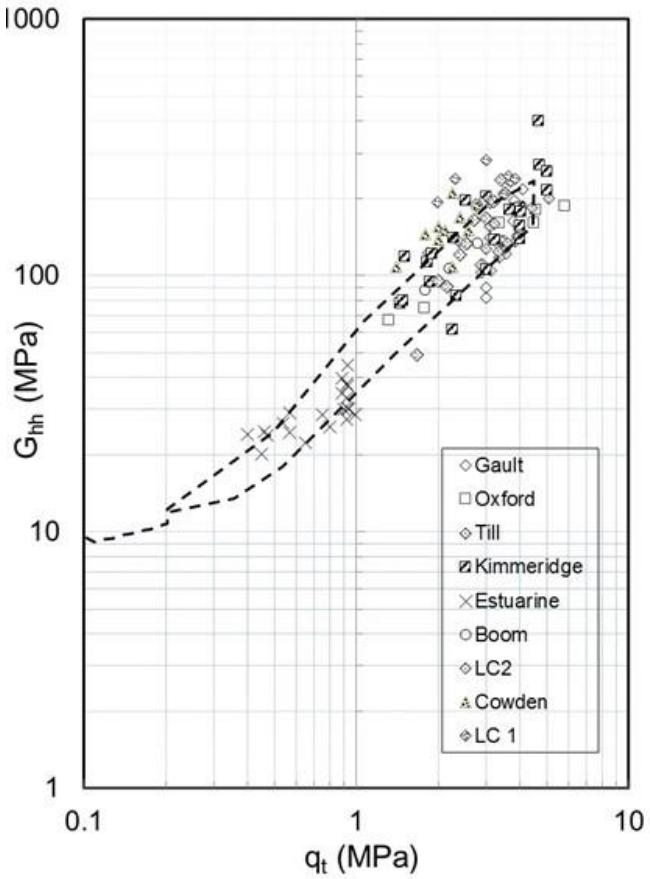

Figure 2b. Shear Modulus G_{hh} against q_t

(OCR). It has however been shown that the effect of OCR is, to a large extent, taken into account by the effect of void ratio and could be neglected. Butcher and Powell (1995b) had some success in relating shear modulus to the in situ stress anisotropy and its influence on the propagation and polarisation directions of the shear waves.

4 SMALL STRAIN STIFFNESS FROM CPT

Many authors have tried to correlate parameters from CPT and CPTu tests with small strain stiffness.

Various authors have tried to correlate q_c or q_t with G_0 with varying success. One of the first to do this, Mayne and Rix (1993), used an extensive database to try to correlate G_0 with measured cone resistance, q_c, with some success but also with some considerable scatter. They later suggested (Mayne and Rix, 1995), based on the original premise of Hardin mentioned above, that it might be better to relate the small strain shear modulus with a combination of void ratio (e) and cone penetration resistance q_c and suggested that it was valid for a wide range of clays. Variations of their equations can be found in the literature.

Simonini and Cola (2000) suggested that the pore pressure ratio from the piezocone (B_q) could be used as an additional parameter in the correlation to replace void ratio. They showed that when considering relatively lightly overconsolidated mixed deposits in Venice, then a better correlation between q_t and G_0 was obtained. Long & Donohue (2010) have tried this route for Norwegian soils and came up with a variation on the Simonini and Cola (2000) equations. Many authors seem to have some degree of success finding fits to their own data sets, but when used by others these often seem to fail (see Long and Donohue 2010 for some examples).

In Figure 2a the G_{vh} shear moduli derived from either standard downhole or SCPT testing, on the collection of sites mentioned earlier, are plotted against the corrected cone resistance q_t (on a log-log plot). For clarity only the boundary of the original data from Powell & Butcher (2004) is shown, simply by areas bounded by dotted lines. Also included are results from Norwegian clays presented by Long & Donohue (2010), but only for those sites with SCPT data (in their paper other sites used MASW results and these certainly increased the scatter of their data). It can be seen that all the new data fall either within or as extensions to the earlier data, with a reassuring result. The 'aged' clays (Table 1 + additional London and Gault clay sites) fall in a lower group and the younger clays tending to the upper group.

Because of a lack of availability of equipment, or a lack of understanding of its usefulness, field G_{hh} testing is seldom done. An alternative approach has been used to try and extend the earlier study, namely scaling the G_{vh} data by the use of laboratory assess

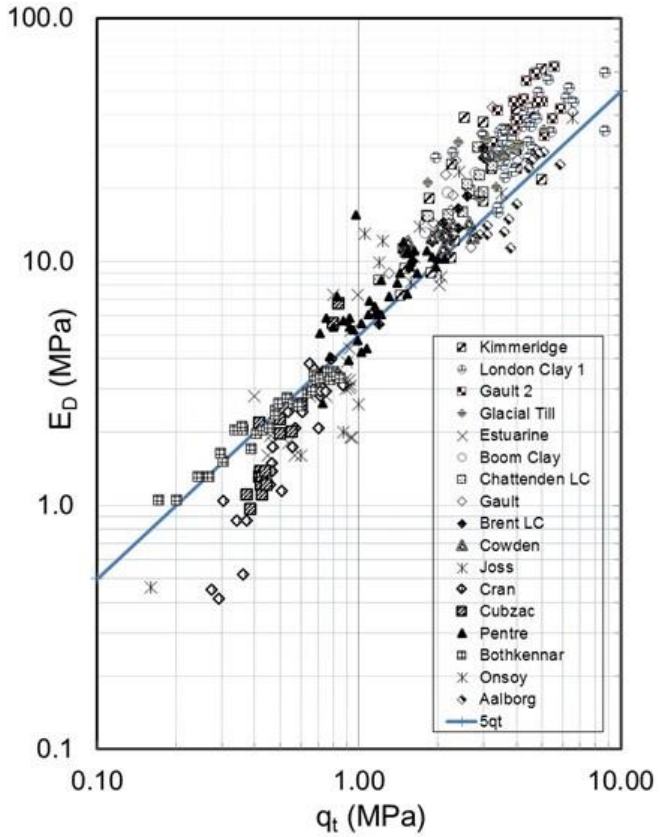

Figure 3. Dilatometer Modulus E_D against q_t

ments of the G_{hh}/G_{vh} ratio on high quality samples. In the earlier field work Powell & Butcher showed that typically for London clay G_{hh}/G_{vh} was between 2 and 2.5 and in the Gault clay around 2 (for the normally consolidated slightly cemented Bothkennar clay the ratio was 0.8 - 0.85; for Pentre 0.9 – 1.05). From Laboratory work Hosseini Kamel (2012) reports ratios based on G_{hh}/G_{hv} (note G_{hv} used here) of 1.8 for London clay (Gasparre 2005), 1.9 for Gault Clay, 1.7 for Kimmeridge Clay and 2.3 for the Oxford clay; he puts the higher values in the Oxford clay down to the prominent clay particle orientation and bedding. Piriyakul (2006) suggests a ratio of just over 2 for the Boom clay. In advanced commercial laboratory testing at Geolabs similar ratios to those above have been found for London and Gault clays.

Whilst in the field it is often found that G_{vh} and G_{hv} are not equal these differences are often not so marked in laboratory testing, given that G_{hv} is generally larger than G_{vh} this may explain the slightly lower values of G_{hh}/G_{hv} from Hosseini Kamel (2012) work compared to field test data. Piriyakul (2006) in fact does show differences and examines the potential role of the different stresses acting in the different planes. He investigates the effects of stress anisotropy as well as inherent anisotropy and this is an area mentioned by many including Butcher and Powell (1995b) when they tried the same approach. In Figure 2b the G_{vh} results for the stiff aged clays have been plotted as G_{hh} using the scaling factors above. A constant ratio has been used for each clay type and this may explain the larger scatter seen using this approach as compared to actual field measurements (see Butcher & Powell 2001) to see that ratios change with depth most probably related to changing inherent anisotropy). It is clearly seen in Figure 2b that the strong relationship suggested by Powell and Butcher (2004) between q_t and G_{hh} is further confirmed by these additional 'aged' soils as well as the stiff clay tills (Cowden field G_{hh} data is now also included).

In their earlier paper G_{hv} was also considered and showed an improvement over G_{vh} but only to a limited extent.

5 CORRELATIONS WITH DMT

The Marchetti Dilatometer is now widely used in many countries and its derived parameters are correlated with many soil properties (Marchetti 2015). Figure 3 shows data from many of the sites in the present and past studies plotted as E_D, the dilatometer modulus against q_t.

A very strong trend linking the two parameters can immediately be seen. Most recently Robertson (2009) showed this type of relationship with the use of normalized parameters. He suggested that the equation $E_D = 5q_n$ would fit most of the data where q_n is the net cone resistance (q_t minus the vertical total stress) but that 'site specific' values between 2 and 10 would be even better. It can be seen in Figure 3 that there could well be 'site specific' values available here especially at low values of q_t. Using net cone resistance in Figure 3 would generally simply tend to move the points with lower q_t values slightly to the left in the plot when tests are shallow. In the simple form shown here there is still a striking link between the two parameters which would not fully fit with Robertson's mean equation though.

In Figures 4a & b we see plots of E_D and small strain modulus G_{vh} and $G_{hh;}$ again with the previous data ranges from Powell and Butcher (2004) shown as boundaries marked with dotted lines. Once again we can see the data falling into two distinct groups in Figure 4a (young upper, 'aged' lower)' but in Figure 4b we see a strong potential single group correlation between E_D and G_{hh} rather than G_{vh}. It implies, as one might expect, that E_D is very much related to a horizontal stiffness.

Marchetti (1980) uses E_D to derive a constrained modulus from the test. This is done using

$$M_{DMT} = R_M.E_D$$

where $R_M = 0.14+2.36 \log K_D$; for clays

Good success has been reported using this approach in predicting settlements of foundations

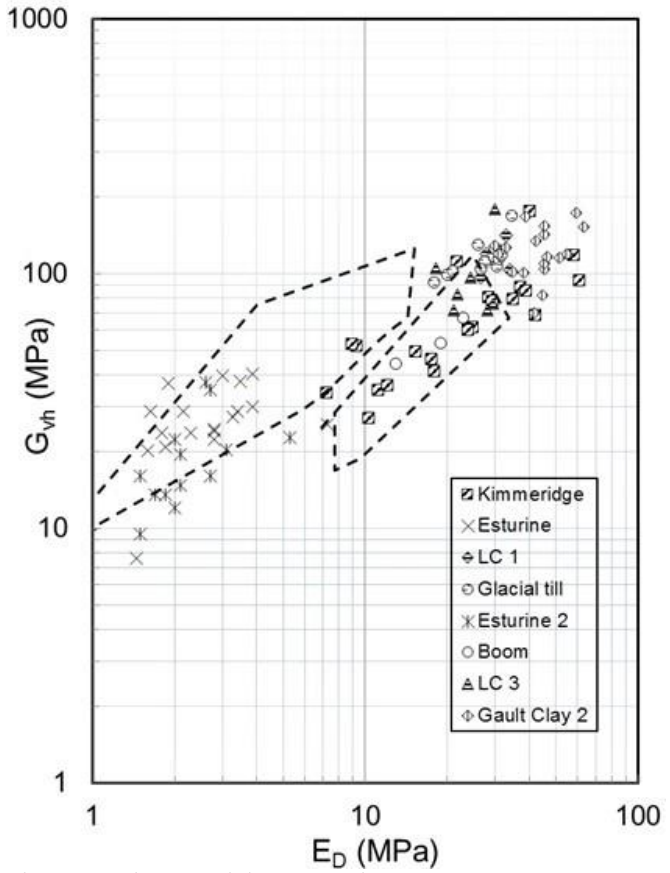

Figure 4a. Shear Modulus G_{vh} against E_D

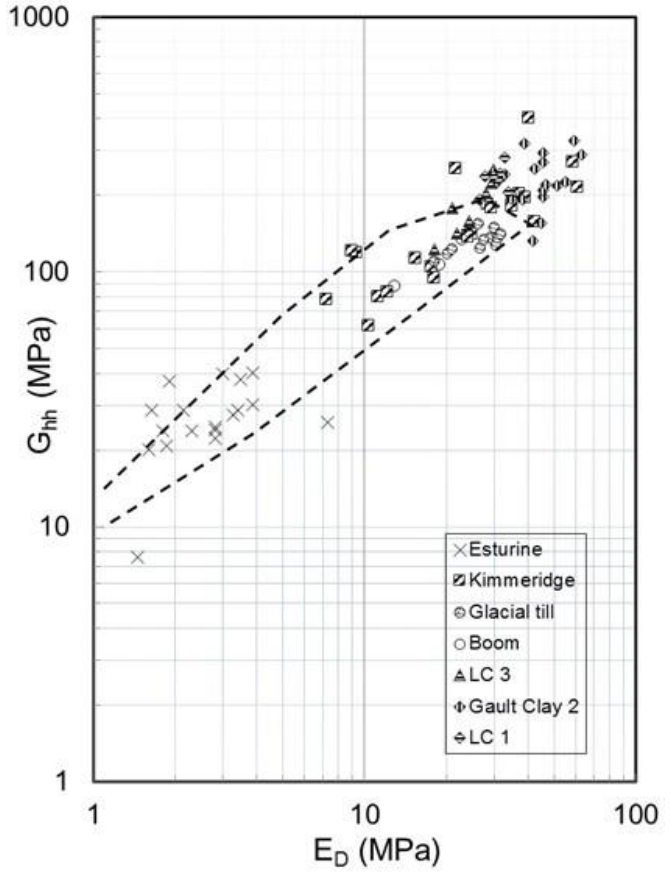

Figure 4b. Shear Modulus G_{hh} against E_D

however, the above seemingly strong correlation between E_D and G_{hh} opens up a question. The link between R_M and E_D. Marchetti (1980) shows K_D is linked to K_0 and OCR and an increasing K_D shows and increasing K_0 and OCR, however and increasing K_D also gives and increasing R_M in the above equation. This raises a question, should R_M really increase with increasing K_D? Surely if E_D is related to horizontal stiffness then, as K_0 increases the scaling horizontal to vertical should reduce. Using the above equation, R_M rises from 0.87 to typically 3 or so as K_D increases. Powell and Uglow (1988) suggested that R_M was around 0.5 for the 'aged' clays.

Monaco et al (2009) looked at links between G_0 and E_D and other dilatometer parameters. Consideration of the above matters may well influence their conclusions.

It is suggested that the topic of anisotropy of stiffness within the DMT framework needs further consideration and review.

6 DISCUSSION AND CONCLUSION

Data from a range of different soils have been presented in this paper that strongly supports the earlier work of Powell & Butcher (2004). This will give increased confidence to designers who rely on the correlations to get small strain behavior from in situ tests. It shows that the corrected cone resistance from the CPTu, q_t, and the Dilatometer Modulus, E_D, are strongly influenced by the horizontal stiffness and stresses in the ground. Both parameters correlate well with the in situ horizontal shear modulus G_{hh} and these correlations are very much stronger than with either G_{vh} or G_{hv}. To what extent the inherent anisotropy of very old 'aged' clays plays a role within this cannot be determined at this stage. It is only with the marked differences in directional stiffness in these aged clays that the picture becomes clearer.

Most of the correlations developed to date have tended to concentrate on data from younger clays and have often not been very successful when transferred to different soils. The presentation of the data in log-log is not ideal but does seem to indicate strong trends.

It is suggested that the correlation of constrained modulus (M_{DMT}) from E_D of the DMT test needs to be better understood.

7 ACKNOWLEDGEMENTS

The authors would like to thank their many colleagues who over the years have helped them gather the data that forms the basis of this work.

8 REFERENCES

Bellotti, R., Jamiolkowski, M., LoPresti, D.C.F. & O'Neill, D.A. 1996. Anisotropy of small strain stiffness in Ticino sand. *Géotechnique,* Vol. 46 (No 1):115-131.

Brosse, A. (2012). *Study on the anisotropy of British mudrocks using a Hollow Cylinder Apparatus*. Ph. D. thesis, Imperial College London

Butcher, A.P. & Powell, J.J.M. 1995a. Practical considerations for field geophysical techniques used to assess ground stiffness. *Proc. Int. Conf. on Advances in Site Investigation Practice*. ICE London, Thomas Telford: 701-714.

Butcher, A.P. & Powell, J.J.M. 1995b. The effects of geological history on the dynamic stiffness in soils. *Proceedings, 11th European Conference on Soil Mechanics and Foundation Engineering*. Vol. 1: 27-36.

Butcher, A.P. & Powell, J.J.M. 2001. Deformation properties of soil from in situ and laboratory tests. *Proc. XVth ICSMGE,* Istanbul. Vol 1 pp 51-54

Gasparre A 2005. *Advanced laboratory characterization of London clay.* Ph.D. thesis, Imperial College of Science, Technology and Medicine, University of London.

Hardin, B.O. 1978. The nature of stress strain behaviour of soils. *Proc. ASCE Geot. Div. Specialty Conf. on Earthquake Eng. and Soil Dynamic*s, Pasadena, Vol. 1: 3-90.

Hosseini Kamal, R. (2012). *Experimental study of the geotechnical properties of UK mudrocks*. Ph.D. thesis, Imperial College London.

Long, M. and Donohue, S. (2010) Characterization of Norwegian marine clays with combined shear wave velocity and piezocone cone penetration test (CPTU) data. *Can. Geotech. J*. 47: 709–718.

LoPresti, D.C.F., Pallara, O., Jamiolkowski, M., & Cavallaro, A. 1999. Anisotropy of small strain stiffness of undisturbed and reconstituted clays. *Proc.2nd Int. Symp. on Pre-failure Deformation Characteristics of Geomaterials*, IS- Torino. 99, Vol. 2: 11-18.

Lunne, T., Robertson, P.K. & Powell, J.J.M. 1997. *CPT in geotechnical practice*. Spon Press.

Marchetti, S. 1980 In situ tests by flat dilatometer. *J. Geot. Eng. Div. ASCE,* Vol. 106 (GT3): 299-321.

Marchetti, S. 2015. Some 2015 Updates to the TC16 DMT Report., DMT'15. Rome, Italy.

Mayne, P.W. & Rix, G.J. 1993. Gmax-q_c relationships for clays. *Geotechnical Testing Journal, Vol*. 16 (No 1): 54-60.

Mayne, P.W. & Rix, G.J. 1995. Correlations between shear wave velocity and cone tip resistance in natural clays. *Soils and Foundations,* Japanese Society of Soil Mechanics. Vol. 35 (No 2): 107-110.

Mengé, P. 2001. Soil Investigation results at Sint-Katelijne-Waver (Belgium). *In Screw Piles-Installation and Design in Stiff Clay*. Holyman (Ed). Swets & Zeitlinger. pp 19-62

Monaco, P., Marchetti, S., Totani, G. & Marchetti, D. 2009. Interrelationship between Small Strain Modulus G_0 and Operative Modulus. *International Symposium IS-Tokyo 2009 on Performance-Based Design in Earthquake Geotechnical Engineering*, 1315-1323.

Pennington, D.S., Nash, D.F.T., & Lings, M.I. 1997. Anisotropy of G_0 shear stiffness in Gault clay. *Symp. Pre-failure deformation behaviour of Geomaterials*. London: 5-12

Piriyakul, K. 2006. *Anisotropic Stress-Strain Behaviour of Belgian Boom Clay in the Small Strain Region*. PhD thesis Ghent.

Powell, J.J.M. & Butcher, A.P. 2004. Small Strain Stiffness assessments from in situ tests. *Proc. ISC2* Porto, September 2004. pp 1717- 1722.

Powell, J.J.M. & Uglow, I.M.1988. The interpretation of the Marchetti dilatometer test in UK clays. *Proc. Conf. on Penetration testing in the UK*, Birmingham, July 1988: 269-273.

Powell, J.J.M., Lunne, T. & Frank, R. 2001. Semi-Empirical Design Procedures for Piled Foundations. *Proc. XVth ICSMGE, Istanbul*. Vol 1, pp 991-994.

Robertson, P.K. 2009. CPT-DMT Correlations. *Journal of Geotechnical and Geoenvironmental Engineering*, Vol 135, No11, pp

Simonini, P. & Cola, S. 2000. Use of piezocone to predict maximum stiffness of Venetian soils. *Proc ASCE. Journal of Geotechnical and Geoenvironmental Engineering*. Vol.126 (No 4): 378-382.

Shields, C.H., Frank, R., Mokkelbost, K.H. & Denver, H. 1996. Design fourfold. *Ground Engineering*. Vol. 29 (No 2): 22-23.

Simpson B, Atkinson JH and Jovicic V 1996. The Influence of Anisotropy on Calculations of Ground Settlements above Tunnels. *Proc. Geotechnical Aspects of underground Construction in Soft Ground*, City Univ, London: 591-595.

Stokoe, K.H., Lee, J.N.K., and Lee, S.H.H. 1991. Characterisation of soil in calibration chambers with seismic waves. *Proc. 1st Int. Symp. Calibration Chamber Testing, Potsdam*.

Vucetic, M. and Dobry, R. 1991. Effect of Soil Plasticity on Cyclic Response. *Proc ASCE, JGED*. Vol. 117: 89-107.

Geotechnical and Geophysical Site Characterisation 5 – Lehane, Acosta-Martínez & Kelly (Eds)

Case Studies on Variability in Soils and Driven Pile Performance

W. A. Prakoso
Universitas Indonesia, Depok, Indonesia

ABSTRACT: In a pile foundation design, it is presumed that the pile performance variability could be related to the variability in the design soil parameters. The variability of these parameters is determined by considering the natural soil variability and the measurement errors, as well as the transformation uncertainty. The transformation uncertainty would theoretically increase the variability in the design parameters and therefore in the expected pile performance. The uncertainty of the calculation models would increase the expected foundation performance variability as well. To examine whether the variability increase is factual, the variability in actual pile performance is evaluated in relation to the variability in field test results. This paper focuses on the variability in driven pile performance, and three case studies in Jakarta are examined. The driven pile performance deduced from axial compressive pile load tests is evaluated, and the variability of pile settlement at different load levels is examined. The soil variability is deduced from the N-SPT values and the cone penetration resistance in the upper part of soil profiles. In general, the COV of soil profile is relatively comparable to the COV of pile settlement at different load levels. This trend is different from the results of the theoretical approach. The possible approaches to bridge this difference are subsequently discussed.

1 INTRODUCTION

In a foundation design, the expected foundation performance variability is determined by the variability in the design soil or rock parameters (eg, Prakoso and Kulhawy 2011a,b) and the uncertainty of the calculation models (eg, Prakoso & Kulhawy 2002). The design parameter variability is in turn determined by the natural soil or rock variability and the measurement errors, as well as the transformation uncertainty. This transformation uncertainty would theoretically increase the variability in the design parameters and therefore in the expected foundation performance. The uncertainty of the calculation models would increase the expected foundation performance variability as well. Therefore, it is of interest to understand whether this general theoretical approach would lead to an excessive or to a reasonable expected variability of foundation performance.

In this paper, to examine whether the variability increase is factual, the variability in actual foundation performance is evaluated in relation to the variability in field test results. The focus of this paper is on the variability in driven pile performance deduced from pile load tests. Three case studies in Jakarta are examined. The general observations of the case studies are than discussed in the relation to the expected results of that general approach.

2 SOURCES OF EXPECTED FOUNDATION PERFORMANCE VARIABILITY

The increase in design parameter variability due to transformation uncertainty is often can not be avoided. A calculation model for pile axial deformation (e.g., Fleming et al. 2009) employs a certain design parameter taken from a particular test (ie, shear modulus), which sometime may not be available due to field difficulties or sample quality issues. Consequently, simpler tests (eg, cone penetration tests, standard penetration tests) need to be performed, and the parameters from these tests (eg, cone resistance q_c, N-SPT values) have to be transformed into that certain design parameter using correlations (eg, Kulhawy & Mayne 1990). Therefore, in addition to the natural material variability and the measurement errors, the design parameter would contain the additional uncertainty coming from the use of the correlations. For example, Prakoso & Kulhawy (2011a) discuss parameters from different tests in relation to a model design parameter.

The calculation models could be developed from theoretical approaches and from empirical studies. For the former, the models ideally should be validated against actual field cases or other means to assess their uncertainty, while for the latter, the models would contain inherent uncertainties. In evaluating

model uncertainty, Prakoso & Kulhawy (2011b) use the Monte Carlo simulations for theoretical models, while Prakoso & Kulhawy (2002) discuss the inherent uncertainty of empirical models.

3 CASE STUDIES

3.1 *Case Study 1*

A series of seven (7) axial compression load tests of 400 mm square prestressed concrete piles was conducted in a construction site in the southern part of Jakarta. The piles were driven through a residual soil deposit, and the pile lengths vary from 20 m to 23 m. The piles tested were distributed relatively evenly within the construction site. The pile slenderness ratio was 50 or greater, and therefore more than 90% of the load would be resisted by the shaft (e.g., Fleming et al. 2009).

The load tests were conducted according to ASTM D1143 Standard Test Method for Deep Foundations Under Static Axial Compressive Load (2007) to a 200% load of 2 MN in four (4) cycles. The loading backbone curves of the seven load tests are shown in Figure 1. For a load of 1 MN (100%, Cycle No. 2), the mean, standard deviation (SD), and coefficient of variation (COV = SD / mean) of the pile head settlement are 5.19 mm, 1.30 mm, and 25.1%, respectively. For a load of 2 MN (200%, Cycle No. 4), the mean, SD, and COV of the pile head settlement are 12.90 mm, 2.86 mm, and 22.2%, respectively. For the zero load condition at the end of the first and the fourth cycles, the COV values of the pile head plastic settlement are 65.2% and 36.9%, respectively. The distribution of pile head settlement for loads of 1 MN (100%, Cycle No. 2) and 2 MN (200%, Cycle No. 4) is shown as Figure 2.

Five (5) mechanical cone penetration tests (MCPT) (D3441, ASTM 2005) were performed by a soil investigation company. The test locations were distributed relatively evenly within the construction site. The MCPT results are combined and shown as Figure 3. Based on the cone resistance q_c and friction ratio R_f, four (4) soil layers can be identified. The cone resistance q_c of 15 MPa were found at depths from 19.2 m to 22.4 m. These depths are relatively consistent with the lengths of the piles tested. The mean and SD of point cone resistance q_c values, as well as the mean and SD of point friction ratio R_f, are shown in Figure 3. Up to a depth of 18 m, most of the COV of q_c are within the range from 16% to 34%, with a mean value of 25.1%. Those of The COV of q_c and R_f is shown in Figure 3 as well. The statistics for each soil layer after the q_c layering and de-trending process are summarized in Table 1. It can be seen that the resulting COVs for both evaluation approaches are within the range of q_c inherent variability as observed by Phoon & Kulhawy (1999).

Table 1. Soil layers and associated statistics for Case Study 1.

Layer	Depth (m)	q_c (MPa)	SD	COV (%)
1	0 – 7.0	0.314·z + 0.831	0.489	54.7-16.1
2	7.0 – 17.0	2.077	0.560	27.0
3	17.0 – 22.2	1.175·z – 17.091	1.761	43.4-19.6
4	>22.2	> 15.0	-	-

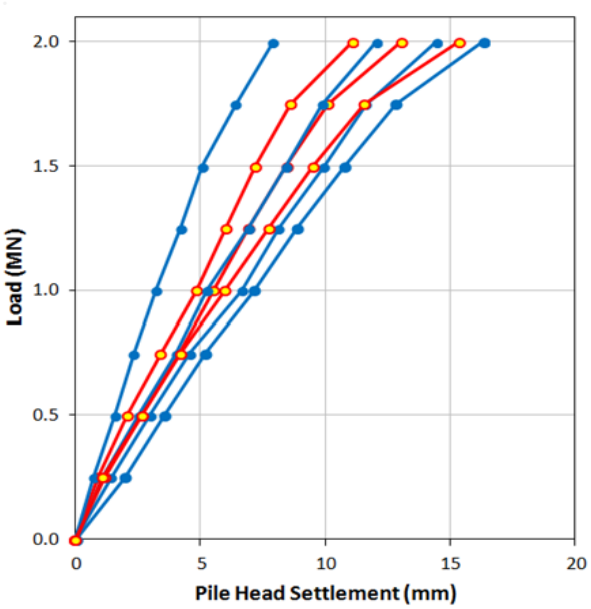

Figure 1. Pile load test results for Case 1.

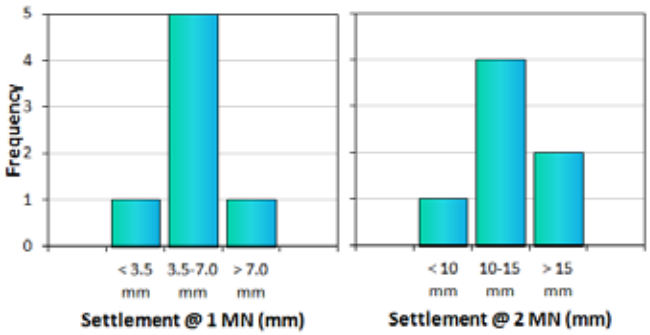

Figure 2. Distribution of pile head settlement at 100% load (cycle 2) and 200% (cycle 4) load for Case 1.

3.2 *Case Study 2*

A series of five (5) axial compression load tests of 500 mm square prestressed concrete piles was conducted in a construction site in the central part of Jakarta. The piles were driven through a soft soil deposit, and the pile lengths vary from 25 m to 39 m (mean = 32.5 m and SD = 5.7 m, median = 32.5 m). The piles tested were distributed relatively evenly within the construction site. The pile slenderness ratio was 50 or greater, and therefore more than 90% of the load would be resisted by the shaft (e.g., Fleming et al. 2009).

The load tests were conducted according to ASTM D1143 Standard Test Method for Deep Foundations Under Static Axial Compressive Load

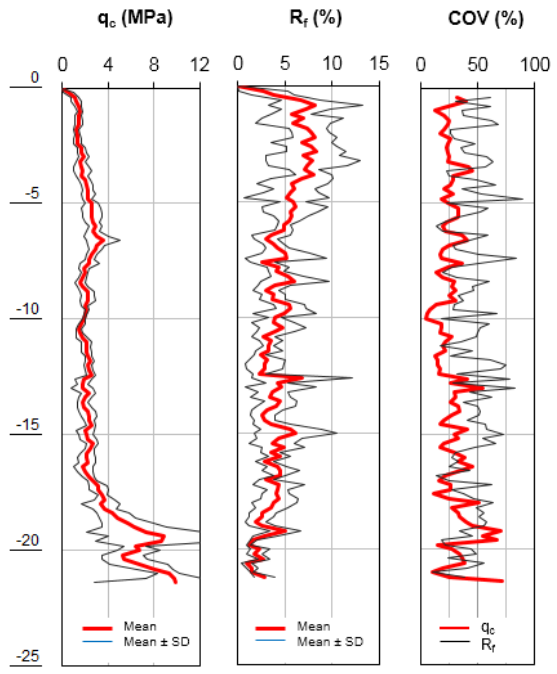

Figure 3. Mechanical cone penetration test results for Case 1.

Table 2. Soil layers and associated statistics for Case Study 2.

Layer	Depth (m)	N-SPT (blows/0.3m)	SD	COV (%)
1	0 – 18.0	2.08	1.20	57.4
2	18.0 – 27.0	1.05·z – 13.49	4.43	82.2-29.9
3	27.0 – 40.0	33.87	9.84	29.1
4	>40.0	>48	-	-

(2007) to a 200% load of 4 MN in four (4) cycles. The loading backbone curves of the five load tests are shown in Figure 4. For a load of 2 MN (100%, Cycle No. 2), the mean, SD, and COV of the pile head settlement are 7.26 mm, 2.95 mm, and 40.7%, respectively. For a load of 4 MN (200%, Cycle No. 4), the mean, SD, and COV of the pile head settlement are 22.44 mm, 7.03 mm, and 31.3%, respectively. For the zero load condition at the end of the first and the fourth cycles, the COV values of the pile head plastic settlement are 105.5% and 147.8%, respectively. The distribution of pile head settlement for loads of 2 MN (100%, Cycle No. 2) and 4 MN (200%, Cycle No. 4) is shown as Figure 5.

Seven (7) sets of standard penetration tests (SPT) (D1586, ASTM 2011) relevant to the pile length variation were performed by four soil investigation companies in different years. The test locations were distributed relatively evenly within the construction site. The SPT results are shown as Figure 6, and one can see that the ground conditions vary significantly. N-SPT values greater than 50 blows/0.3m were found in depths varying from about 14 m to 49 m. The mean and SD of N-SPT for 3 m intervals are shown in Figure 7. The COV of point N-SPT up to a depth of 39 m (about maximum length of tested piles) varies from 31% to 125%, with a mean value of 68% (solid line on Fig. 7). It is noted that the N-SPT values of greater than 50 blows/0.3m at a depth of 14 m were not considered in the mean and SD evaluation because there were no tested piles with a length of about 14 m. The COV values of point N-SPT performed by two companies were evaluated further. For a company with three data sets, the COV varies from 10% to 73%, with a mean value of 35% (dashed line on Fig. 7), while for the other with two data sets, the COV varies from about 0 to 128%, with a mean value of 49% (dashed-dotted line on Fig. 7). The statistical results of this company-based evaluation suggest that the contribution of the measurement error in COVs might be significant when the soil investigation is conducted by more than one party.

Based on the soil descriptions, four (4) soil layers can be identified as summarized in Table 2. It is noted that the depths are the median values. The statistics for each soil layer after the N-SPT layering and de-trending process are summarized in Table 2 as well. It appears that the layering and de-trending process could lower the COV upper bound value rather significantly, but not for the mean value.

The above COVs for N-SPT are not significantly different from the range of N-SPT inherent variability as observed by Phoon & Kulhawy (1999). The range for sands is between 19% and 62% with a mean value of 54%, and that for clays/loams is between 37% and 57% with a mean value of 44%.

3.3 *Case Study 3*

A series of eight (8) axial compression load tests of 450 mm circular prestressed concrete piles was conducted in a construction site in the northern part of Jakarta. The piles were driven through a soft soil deposit, and the pile lengths vary from 22.0 m to 34.5 m (mean = 25.5 m and SD = 3.8 m, median = 24.5 m). The piles tested were distributed relatively evenly within the construction site. The pile slenderness ratio was about 50 or greater, and therefore more than 90% of the load would be resisted by the shaft (e.g., Fleming et al. 2009).

The load tests were conducted according to ASTM D1143 Standard Test Method for Deep Foundations Under Static Axial Compressive Load (2007) to a 200% load of 2.28 MN in four (4) cycles. The loading backbone curves of the eight load tests are shown in Figure 8. For a load of 1.14 MN (100%, Cycle No. 2), the mean, SD, and COV of the pile head settlement are 4.81mm, 1.05 mm, and 21.9%, respectively. For a load of 2.28 MN (200%, Cycle No. 4), the mean, SD, and COV of the pile head settlement are 13.87 mm, 3.36 mm, and 24.2%, respectively. For the zero load condition at the end of the first and the fourth cycles, the COV values of the pile head plastic settlement are 92.7% and 44.2%, respectively. The distribution of pile head settlement for loads of 1.14 MN (100%, Cycle No. 2) and 2.28 MN (200%, Cycle No. 4) is shown as Figure 5.

Three (3) sets of standard penetration tests (SPT) (D1586, ASTM 2011) were performed by two soil investigation companies in different years. The test locations were distributed relatively evenly within the construction site. The SPT results (N-SPT) are combined and shown as Figure 10. N-SPT values greater than 50 blows/0.3m were found in only one of the SPT sets for a thickness of about 3 m at a depth of about 23 m. The mean and SD of for 3 m intervals of N-SPT are shown in Figure 10 as well. The COV of N-SPT up to a depth of 36 m (about maximum length of tested piles) varies from 13% to 97%, with a mean value of 43%. For a company with two data sets, the COV varies from 24% to 91%, with a mean value of 40% (dashed line on Fig. 10). In this case, the contribution of the measurement error in COVs appears to be rather minimum.

Based on the soil descriptions, four (4) soil layers can be identified as summarized in Table 3. It is noted that the depths are the median values. The statistics for each soil layer are summarized in Table 3 as well. It appears that the layering process could lower the COV value for the upper soil layer only.

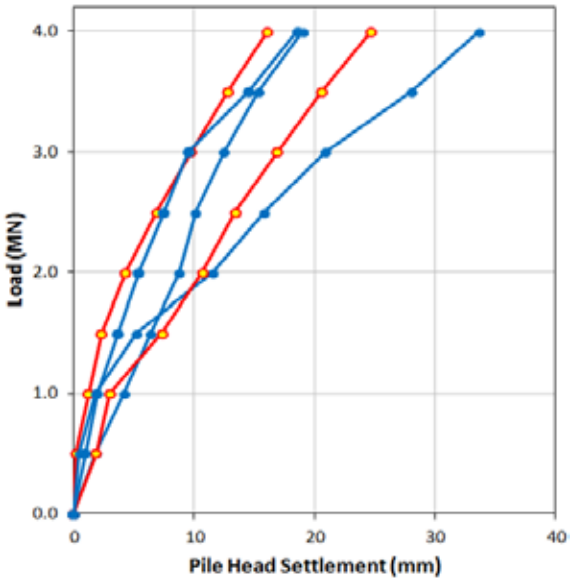

Figure 4. Pile load test results for Case 2.

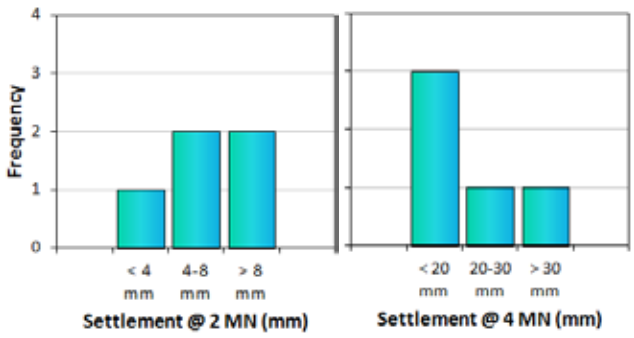

Figure 5. Distribution of pile head settlement at 100% load (cycle 2) and 200% (cycle 4) load for Case 2.

Table 3. Soil layers and associated statistics for Case Study 3.

Layer	Depth (m)	N-SPT (b/0.3m)	SD	COV (%)
1	0 – 10.0	1.92	0.64	33.3
2	10.0 – 23.0	16.24	7.40	45.6
3	23.0 – 28.0	36.57	10.24	28.0
4	>28.0	>48	-	-

Table 4. COV of soils and pile settlement.

Soil /	Coefficient of Variation (%)		
Pile Performance	No. 1	No. 2	No. 3
Soils			
All Data	25.1	67.8	43.0
Set #1	-	35.1	40.3
Set #2	-	48.8	-
Upper Layer	35.4	57.4	33.3
Pile Settlement (Peak)			
Cycle 1 (50%)	24.4	49.7	24.8
Cycle 2 (100%)	25.1	40.7	21.9
Cycle 3 (150%)	22.3	35.3	21.9
Cycle 4 (200%)	22.2	31.3	24.2
Pile Settlement (Plastic)			
Cycle 1 (0%)	65.2	105.5	92.7
Cycle 2 (0%)	51.9	141.8	80.0
Cycle 3 (0%)	51.0	199.8	55.0
Cycle 4 (0%)	36.9	147.8	44.2

4 DISCUSSIONS

The uncertainty of soils along respective pile lengths and the variability of pile settlement from all case studies are summarized in Table 4, represented by the coefficient of variation (COV). For the former, the COV values of all data, as well as those examined from data sets obtained from different companies, are given. There is a general trend that combining data sets (in these cases, N-SPT data sets) obtained by different companies tend to increase the soil variability. For Case Study No. 2, the increase is unexpectedly high, about 20% to 30%. The highly varied soil conditions might also contribute to this significant increase in COV. In addition, the COV value for the upper soil layer is given as most of the load would be resisted by the pile shaft.

The COV of pile settlement at different peak load levels was found to be relatively constant (Nos. 1 and 3) when the COV is relatively not too high, but also found to decrease with an increase in load levels (No. 2) when the initial COV is relatively high. For Case Study Nos. 1 and 2 (for data obtained from an individual company), the COV of pile settlement appears to be relatively in the same range of the COV of soils. However, for Case Study No. 3, the COV of pile settlement is much lower than the COV of soils, with a difference of about 15% to 20%.

The COV of pile plastic settlement after different peak load levels is much higher than the COV at peak load levels. Furthermore, the COV of pile plastic settlement appears to be higher for soils with higher COVs.

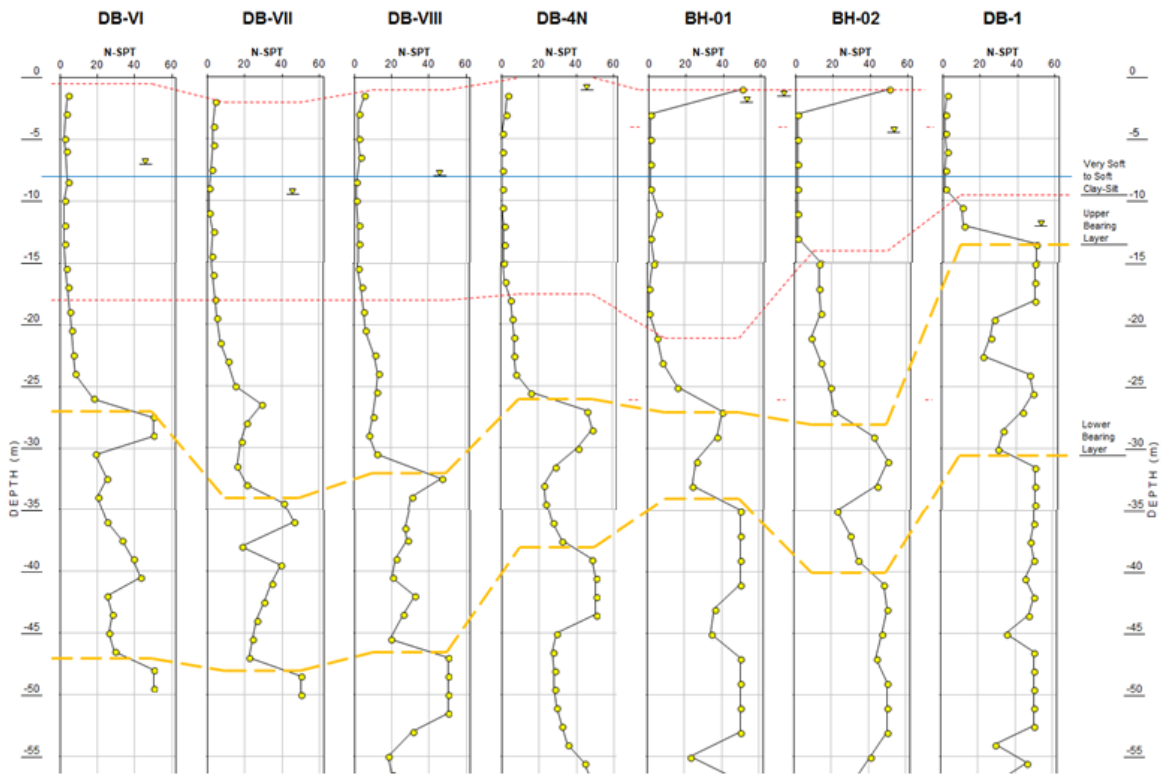

Figure 6. Standard penetration test results for Case 2.

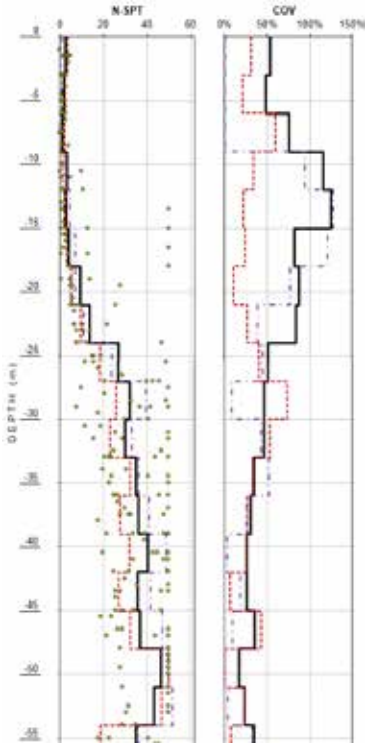

Figure 7. Mean and COV of standard penetration test results for Case 2.

The fact, that the COV of pile settlement at different peak load levels tends to be relatively constant with or lower than the COV of soils, is not in agreement with the theoretical approach in which the transformation uncertainty and the calculation model uncertainty would increase the expected foundation performance variability. Even after separating soil data obtained by different companies, the COV of

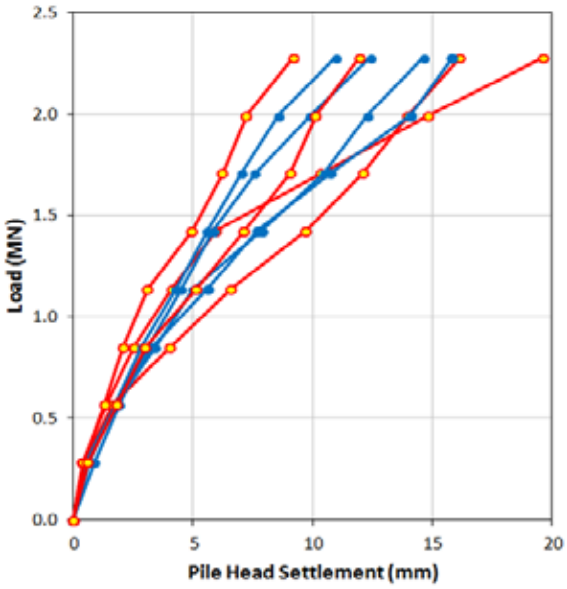

Figure 8. Pile load test results for Case 3.

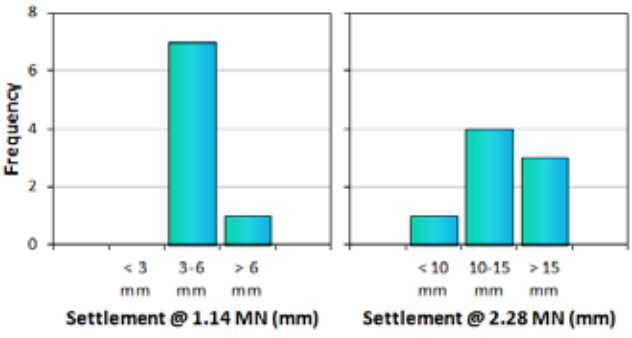

Figure 9 Distribution of pile head settlement at 100% load (cycle 2) and 200% (cycle 4) load for Case 3.

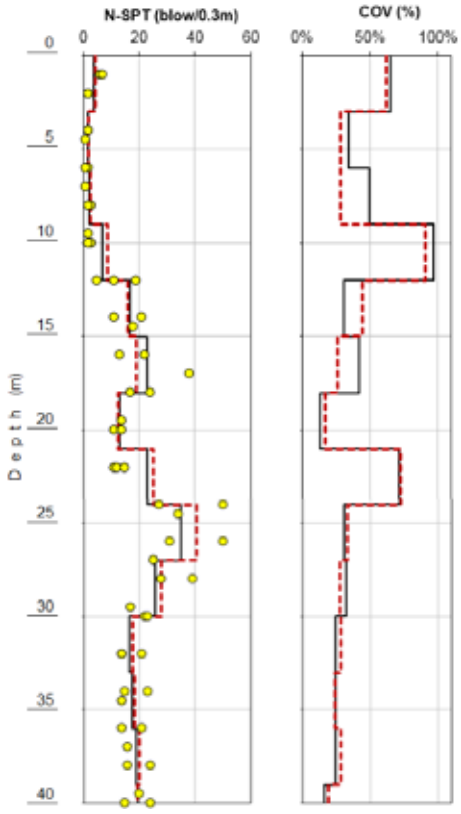

Figure 10. Standard penetration test results for Case 3.

pile settlement is not found to be greater than the COV of soils. One can then conclude that the use of theoretical approach in the current form would lead to an excessive expected foundation performance variability and therefore unnecessary conservatism in foundation design.

Ching & Phoon (2015), quoting Honjo & Otake, argue that the transformation uncertainty is one of the major sources of geotechnical performance uncertainty. Furthermore, they argue that the reduction of transformation uncertainty can lead to a more economical design in a reliability-based design framework. They offer the use of the multivariate probability distribution that models the correlations between the design values used and the values obtained using different tests. The important feature of this approach is that it accepts multiple practical test results, so the transformation uncertainty can be reduced further by incorporating more practical tests. As an example, they show that the COV of soil parameter can be more than 30% when no test result is known but can be reduced to less than 10% when multiple test results are known.

A similar approach may be applied to the estimation of calculation model uncertainty. The current practice is to correlate a large number of foundation resistance data to the respective soil or rock test results (eg, Prakoso & Kulhawy 2002). This practice actually introduces some uncertainties, including mixing different soil or rock behavior, mixing different resistance definitions. The use of multivariate probability distribution may separate different contributing factors in the correlation development, so that the resulting calculation models would have lower degree of uncertainty.

5 CONCLUSIONS

This paper discussed the variability in driven pile performance, and three case studies in Jakarta are examined. In two cases, piles were driven through soft soil deposits with relatively high variability, and the field tests conducted were standard penetration tests. In one case, piles were driven through residual soils with medium level of variability, and the field tests conducted were mechanical cone penetration tests. The driven pile performance was deduced from axial compressive pile load tests (5 to 8 tests for case study), and the variability of pile settlement at different peak load levels was examined. The soil variability was deduced from the N-SPT values and the cone penetration resistance q_c along the respective pile lengths. The variability was represented by the coefficient of variability COV, and it was found that the COV of soils was generally comparable to the COV of pile settlement at different load levels. This was not in agreement with the results of the theoretical approach, and possible strategies to bridge this difference were discussed subsequently.

6 REFERENCES

ASTM International 2005. *ASTM D3441 Standard Test Method for Mechanical Cone Penetration Tests of Soils*. ASTM International, West Conshohoken, PA, USA.

ASTM International. 2007. *ASTM D1143 Standard Test Method for Deep Foundations Under Static Axial Compressive Load*. ASTM International, West Conshohoken, PA, USA.

ASTM International 2011. *ASTM D1586 Standard Test Method for Standard Penetration Test (SPT) and Split-Barrel Sampling of Soils*. ASTM International, West Conshohoken, PA, USA.

Ching, J. & Phoon, K.K. 2015. Reducing the transformation uncertainty for the mobilized undrained shear strength of clays. *J. Geotech. Geoenviron. Eng.* 141(2): 04014103.

Fleming, K., Weltman, A. Randolph, M. and Elson, K. 2009. *Piling Engineering*, 3rd Ed. New York: Taylor & Francis.

Kulhawy, F.H. & Mayne, P.W. 1990. *Manual on Estimating Soil Properties for Foundation Design*, Report EL-6800. Palo Alto : EPRI.

Phoon, K.-K. & Kulhawy, F.H. 1999. Characterization of geotechnical variability. *Can. Geotech. J.* 36: 612–624

Prakoso, W.A. & Kulhawy, F.H. 2002. Uncertainty in capacity models for foundations in rock. *Proc. 5th North American Rock Mech. Symp*., Toronto.

Prakoso, W.A. & Kulhawy, F.H. 2011a. Effects of Testing Conditions on Intact Rock Strength and Variability. *Geotechnical and Geological Engineering*, Springer, 29: 101-111.

Prakoso, W.A. & Kulhawy, F.H. 2011b. Some Observations on Reliability-Based Design of Rock Footings. *Proc. ASCE GeoRisk2011*, Atlanta.

Geotechnical and Geophysical Site Characterisation 5 – Lehane, Acosta-Martínez & Kelly (Eds)

Evaluation of CPT- based ultimate lateral pile resistance in sand

H.Y. Qin
School of Computer Science, Engineering and Mathematics, Flinders University, Adelaide, Australia
W.D. Guo
School of Civil, Mining and Environmental Engineering, University of Wollongong, Wollongong, Australia

ABSTRACT: The CPT-q_c has been used quite successfully to estimate the shaft friction f_s along vertically loaded piles. This prompts the question of how to use the q_c to estimate the ultimate laterally loaded pile resistance p_u, as the correlation between q_c and p_u is not as strong as that between q_c and f_s. In this paper, modulus of subgrade reaction k and the p_u profile were deduced using closed-form solutions and measured response of eight laterally loaded rigid piles tested in-situ and in 1g model tank, respectively. A good comparison is made for each test using a constant k and linear increasing p_u. The deduced values of k and p_u are consistent with those gained previously for 57 lateral piles. Particularly, the gradient of p_u over $q_{c\_average}$ for the short piles is equal to (1.8 - 8.8)%, which is only a fraction of other suggestions. This difference necessitates further study on the correlation between q_c and p_u.

1 INTRODUCTION

Load transfer approaches using p ~ y curves are widely used to analyse the behaviour of laterally loaded piles. Several methods for the formulation of p ~ y curves for piles in sand have been put forward, in which the friction angle of the soil is generally required to estimate the ultimate soil resistance. Alternatively, the ultimate soil resistance profile may be deduced from the analysis of test results using closed-form solutions or numerical modelling. In previous study, Qin & Guo (2014a,b) investigated the nonlinear response of 57 laterally loaded rigid piles in sand. Measured response of each pile test was used to deduce input parameters of modulus of subgrade reaction and the ultimate lateral soil resistance using elastic-plastic solutions. Based on statistical analysis, an equation is presented to estimate the gradient of the ultimate lateral soil resistance with a linear variation with depth from the effective unit weight, square of the passive earth pressure coefficient and diameter of the pile.

In this paper, elasto-plastic solutions were used to analyse the response of laterally loaded rigid piles in sand obtained from new field tests, in which the cone penetration test (CPT) cone resistance q_c were measured. Results from these tests allow the ultimate soil resistance p_u profiles to be back calculated and then linked with CPT q_c values. Comparisons were also made between the back calculated p_u with those computed using the expression directly based on CPT q_c values.

2 ELASTO-PLASTIC SOLUTIONS FOR LATERALLY LOADED RIGID PILES

A pile is defined as rigid if the pile-soil relative stiffness, E_P/G_s exceeds a critical ratio, $(E_P/G_s)_c$, where $(E_P/G_s)_c = 0.052(l/r_0)^4$ and E_P is Young's modulus of an equivalent solid cylindrical pile of diameter d, G_s is the soil shear modulus, l is the pile embedded length, and r_0 is the outer radius of the pile. The elasto-plastic solutions were developed for laterally loaded rigid piles using a load transfer model (Guo 2008). As shown in Figure 1(a), the pile head is free with no constraints. The pile soil interaction is characterized by a series of springs distributed along the shaft. The spring has an elastic-plastic p ~ y (u) curve at each depth, where p is the soil lateral resistance per unit length, u is the pile deflection. The lateral resistance, p is proportional to the local pile displacement, u at that depth and the modulus of subgrade reaction, kd, i.e. p = kdu, where k is the gradient of the p ~ u curve and d is pile outer diameter. The gradient k may be written as k_0z^m, with m = 0 and 1 being referred to as constant k and Gibson k hereafter. Where the soil resistance reaches the limiting p_u, relative slip takes place along the pile-soil interface and extends to a depth z_0, which is called pre-tip yield state. With increasing load the pile-soil relative slip may also initiate from the pile tip (z = l) and expand upwards to another depth z_1 (see Figure 1(c)). The two plastic zones tend to

merge at which the pile reaches the ultimate state, i.e. yield at rotation point ($z_0=z_1=z_r$). It is assumed that the p_u varies linearly with depth z and is described by $p_u=A_rdz$, where A_rd is the gradient of the p_u profile. The solutions allow the nonlinear responses (e.g. load, displacement, rotation and maximum bending moment) to be readily estimated, using the two parameters k and A_r. Conversely, the two parameters can be deduced from the measured pile test results. The solutions have been implemented into a spreadsheet program to facilitate calculation.

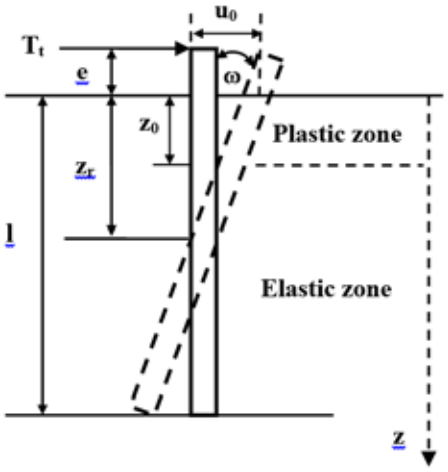

(a)

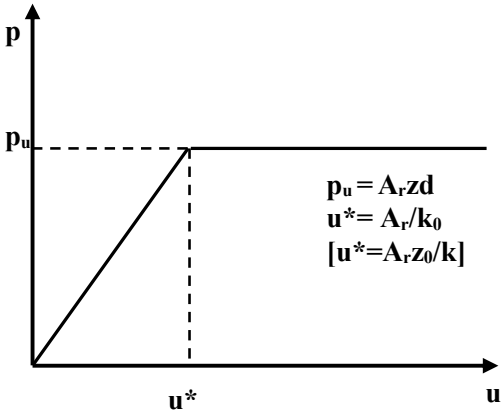

(b)

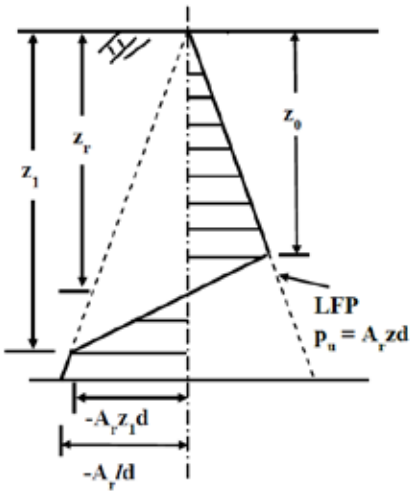

(c)

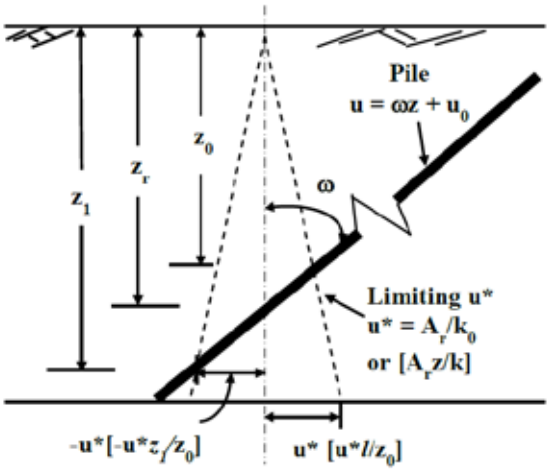

(d)

T_t = lateral load; e = eccentricity; z = depth from ground line; u_0= pile displacement at ground surface; ω = angle of rotation (in radian); u^* = local threshold u above which pile soil relative slip is initiated

Figure 1. Schematic analysis for a rigid pile (after Guo (2008)) (a) pile-soil system, (b) load transfer model, (c) p_u (LFP) profiles, (d) pile displacement characteristic

3 ANALYSIS OF MEASURED PILE RESPONSES

Using the spreadsheet program, responses of eight piles in sand with the CPT q_c profiles measured at the test sites were investigated, following the same approach in Qin & Guo (2014a, b). The q_c values vary approximately linearly with depth in these tests. The properties of the piles and soils are tabulated in Table 1. Each case study is presented below.

Table 1. Summary of pile and soil properties

Test	l (m)	d (m)	e (m)	γ_s' (kN/m^3)	ϕ_s' (°)	Reference
T1	1.2	0.4	2	14.5	35.4	Lee et al.
T2	2.4	0.4	2	14.5	35.4	(2010)
T3	2.4	0.4	0.15	14.5	35.4	
1	1.2	0.4	2	18	30	Choi et al.
2	2.4	0.4	2	18	30	(2013)
4	2.4	0.4	0.15	18	30	
PS2	2.2	0.34	0.4	20	37	Li et al. (2014)
1	0.915	0.165	0.99	9.3	35.5	Zhu et al. (2015)

3.1 *Bored pile tests in weathered clayey sand*

Lee et al. (2010) reported three field tests conducted on bored piles in weathered clayey sand at Iksan, South Korea. The piles (T1, T2 and T3) have a diameter of 0.4 m with embedded depth of 1.2 m, 2.4 m and 2.4 m, respectively. The lateral load was applied at 2 m for T1 and T2, and 0.15 m for T3 above

the ground level. The dry unit weight of the clayey sand is 14.5 kN/m^3 with a relative density of about 30~35 %. The peak friction angle of the soil was determined as 35.4° from triaxial tests. The measured CPT cone resistance q_c profile down the pile depth can be approximated by q_c = 4.2 +0.2z, where q_c is in MPa, z in m. The measured lateral load T_t ~ pile displacement at the ground level u_0 are plotted in Figure 2(a). Back calculations were made for the three tests and the calculated pile responses (T_t ~ u_0) by best matching the measured curves are also plotted in Figure 2(a). The deduced parameters A_r, k and k_0 are presented in Table 2. The calculated ultimate loading capacities T_u are 22.3, 52.4, and 220.0 kN for tests T1, T2 and T3, respectively. They compare well with the ultimate capacities of 22, 50 and 210 kN determined from the load ~ displacement curve using the criterion suggested by Meyerhof, which defines the T_u as the load from which the displacement increases approximately linearly with load.

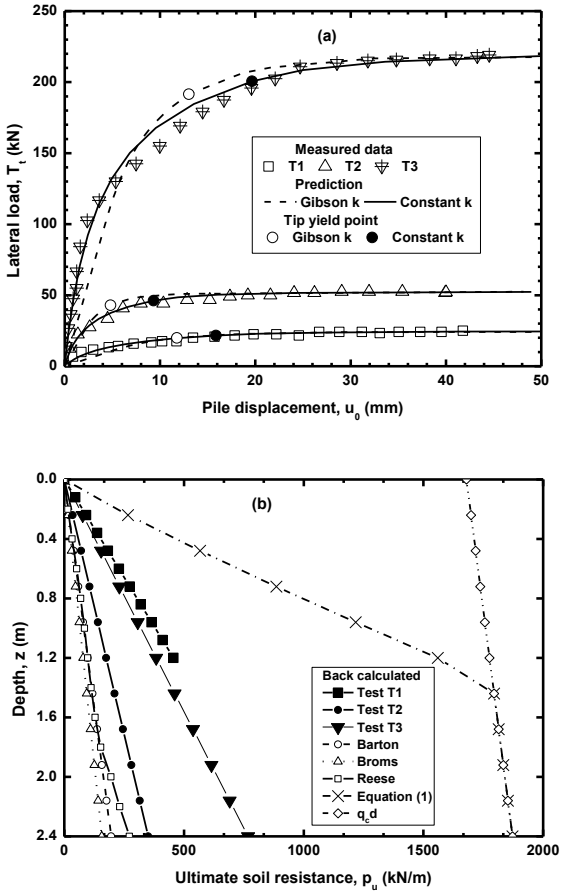

Figure 2. Predicted and measured responses of piles (Lee et al. 2010)

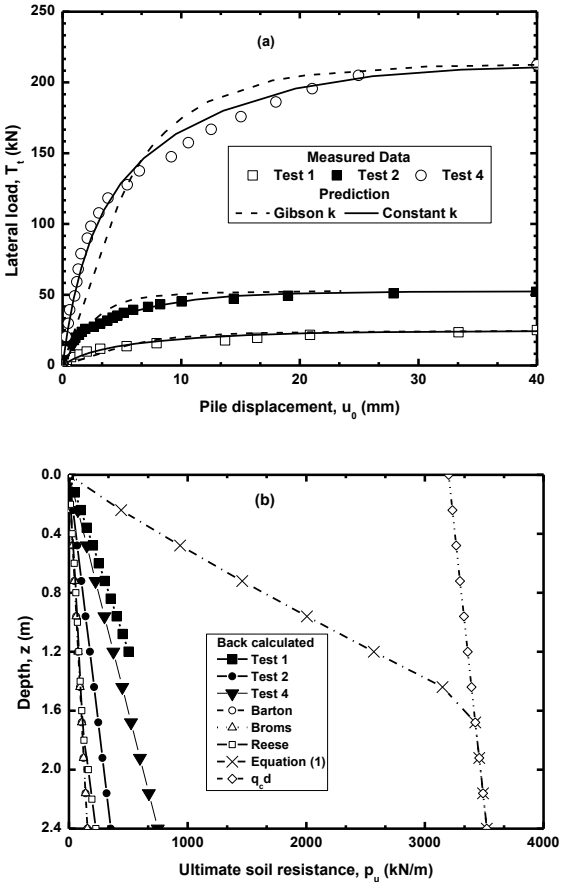

Figure 3. Predicted and measured responses of piles (Choi et al. 2013)

3.2 *Bored pile tests in weathered silty sand*

Choi et al. (2013) reported full scale field model tests of laterally loaded bored piles in weathered silty sand at Iksan city, South Korea. The model piles have the same diameter of 0.4 m and were installed to an embedded length of 1.2 m (Test 1), and 2.4 m (Test 2 and 4). The unit weight of the silty sand is 18 kN/m^3 corresponding to a relative density of 30~35 %. The internal friction angle and cohesion of the soil was evaluated as 30° and 20 kPa, respectively, from triaxial tests. The measured CPT cone resistance q_c profile along the embedded pile length can be estimated by q_c = 8 +0.335z, where q_c is in MPa, z in m. Load was applied at an eccentricity of 2 m for Tests 1 and 2, 0.15 m for Test 4. The measured lateral load T_t ~ pile displacement at the ground level u_0 are plotted in Figure 3(a). The A_r, k and k_0 were calculated by matching the predicted and measured T_t ~ u_0 relationship. They are summarised in Table 2. Interestingly, the range of the deduced A_r, k, k_0 and T_u are similar for the same pile dimensions, ratio of loading eccentricity to pile embedded length, and similar soil properties for the tests conducted in Iksan by Lee et al. (2010) & Choi et al. (2013).

3.3 *Driven pile tests in dense siliceous sand*

Li et al. (2014) presented a series of field lateral load tests performed on open-ended steel pipe piles driven in dense siliceous sand. The tests were conducted

at the University College Dublin geotechnical test site in Blessington, Ireland. The in situ relative density was close to 100% and the unit weight of the soil was 20 kN/m^3. A constant volume friction angle of 37° was determined from triaxial compression tests and the peak friction angle decrease from 54° at 1 m depth to 42° at about 5 m depth. The averaged cone resistance q_c obtained from multiple CPTs increases approximately linearly with depth and can be described by $q_c = 10 + 5z$ between ground level and 2 m depth, where q_c is in MPa, z in m. Among these tests, the pile PS2 was driven to an embedded depth of 2.2 m and the load eccentricity was 0.4 m. The measured $T_t \sim u_0$ and the moment at ground level M0 ~ pile rotation angle ω curves are plotted in Figure 4 (a) and (b). With A_r = 850 kN/m^3, k_0 = 100 MN/m^4, k = 108 MN/m^3, the predicted $T_t \sim u_0$ and $M_0 \sim \omega$ relationships compare well with the measured data. Nevertheless, the maximum bending moment was overestimated by about 35% at T_t =101 and 110 kN in Figure 4(c). The comparison also shows that the solution with a Gibson k offers a better estimation against measured $T_t \sim u_0$ curve (within u_0 of 5% of the pile diameter) than that based on constant k for the same A_r. This reveals that the assumption of Gibson k may suit very dense sands with very high relative density, for instance, close to 100% in this test.

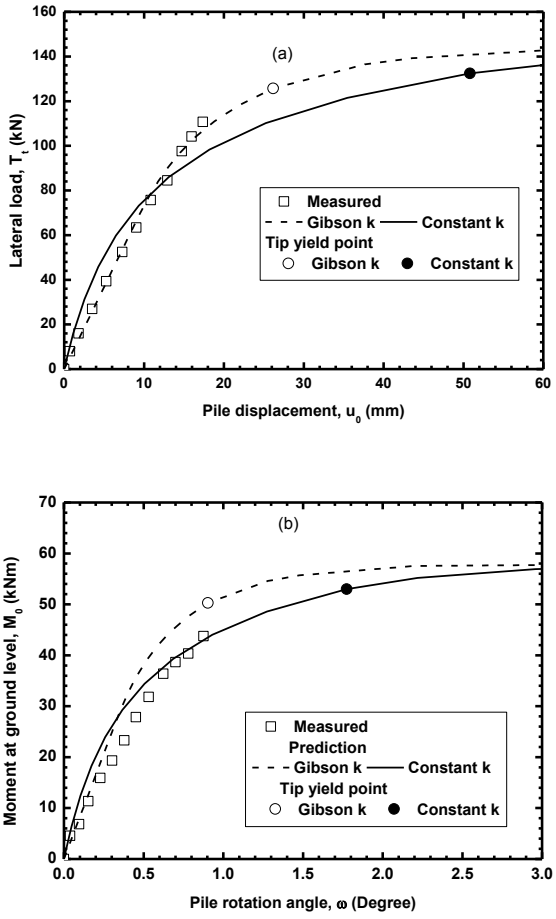

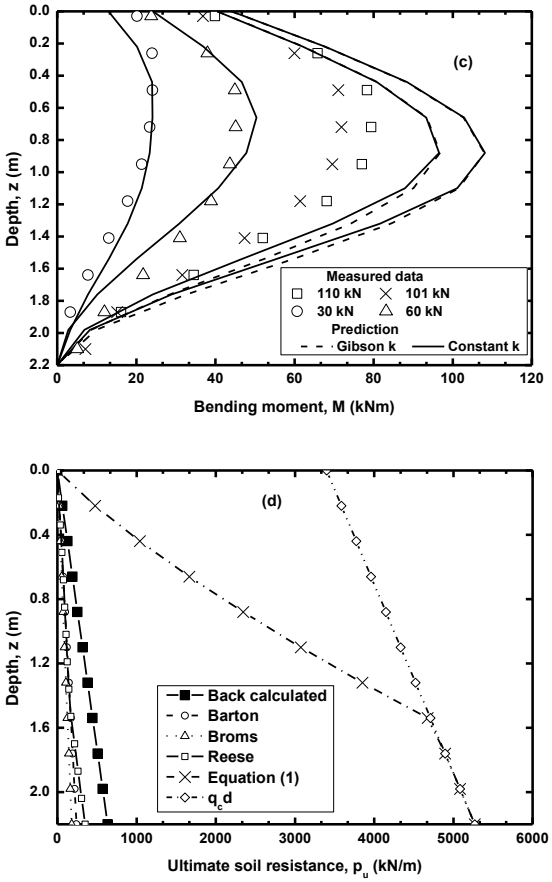

Figure 4. Predicted and measured responses of piles (Li et al. 2014)

3.4 *Laboratory model pile tests in sandy silt*

Zhu et al. (2015) reported a series of 1-g model tests on an instrumented rigid pile subjected to lateral loads. The response of their Test 1 was analysed in this study. The model steel pipe pile has an embedded length of 0.915 m and diameter of 0.165 m. The load eccentricity is 0.99 m (i.e. e = 5d). The tests were carried out in sandy silt under submerged condition. The soil has a saturated unit weight of 19.1 kN/m^3, relative density of 88%, effective peak and residual frictional angle of 41.5° and 35.5°, respectively. The measured CPT cone resistance q_c profile along the embedded pile length can be estimated by $q_c = 3.0z$, where q_c is in MPa, z in m. The measured $T_t \sim u_0$ curve is plotted in Figure 5 (a). The measured pile displacement under load T_t of 736, 992, 1452, 1522 N are plotted in Figure 5(b). The measured soil pressure on the pile using pressure transducers at T_t = 1522 kN is plotted in Figure 5(c). The back-calculated pile responses by best matching all the measured curves are also plotted in Figure 5 (a)-(c). This was achieved by taking A_r = 220 kN/m^3, k_0 = 26.5 MN/m^4, k = 16.5 MN/m^3. It is worth noting that the measured load T_t = 1452 N is close to the calculated T_t = 1435 N (constant k), but slightly (9%)

greater than T_t= 1330 N (Gibson k) at the tip yield state. This means that the pile may be in post-tip yield state at T_t = 1522 kN. The on-pile force profiles at T_t = 1522 N in Figure 5 (c) was obtained by using z_0/l = 0.59, z_r/l = 0.72, z_1/l = 0.93 for constant k and 0.56, 0.73 and 0.91, respectively, for Gibson k. Using the elastic-plastic model, the ultimate soil resistance increases linearly, following closely with measured soil pressure in Figure 5 (c), from zero at groundline to the maximum value at the slip depth z_0. Afterwards, the resistance decreases with depth and becomes zero at the pile rotation depth z_r. The soil pressure distribution proposed by Prasad & Chari (1999) was also included for comparison. The measured data fall within the zones enclosed by the individual soil pressure profile, indicating the pile was at tip yield state or post-tip yield state.

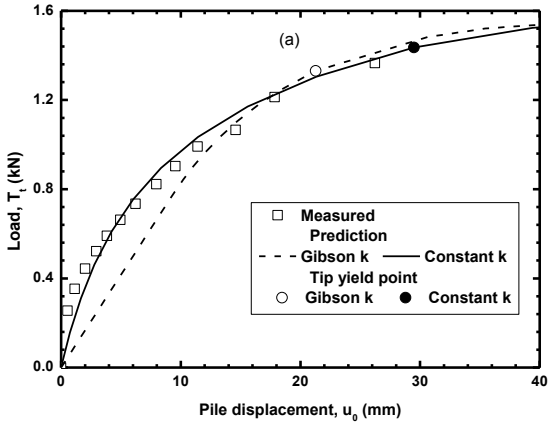

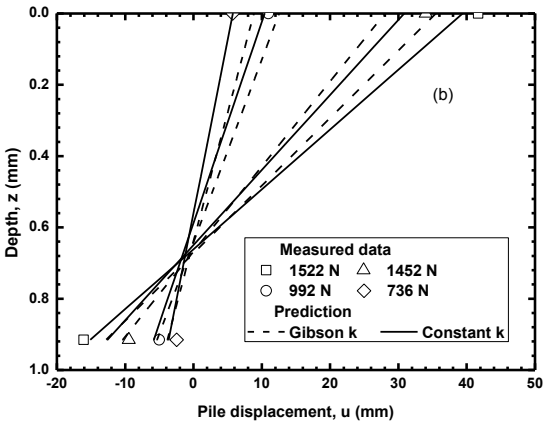

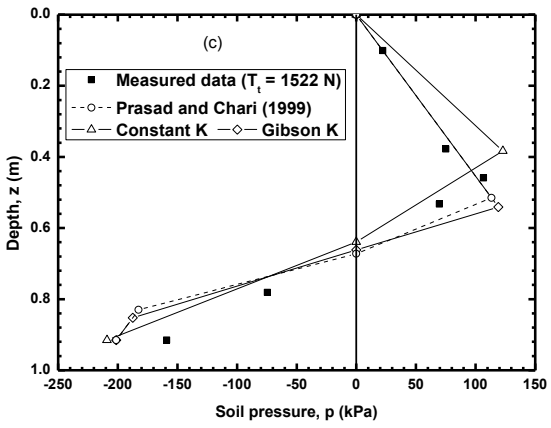

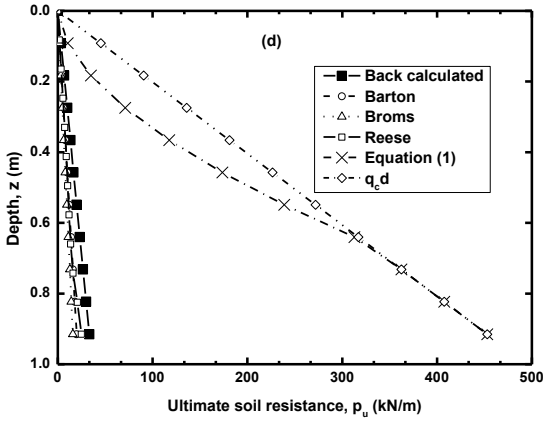

Figure 5. Predicted and measured responses of piles (Zhu et al. 2015)

Table 2. Summary of back calculated parameters

Test	A_r (kN/m^3)	N_g	k_0 (†)	k (*)	q_{c_ave} (kPa)	$A_r d/q_{c\_ave}$ (%)
T1	950	4.7	184	220	4320	8.8
T2	365	1.8	234	200	4440	3.3
T3	800	3.9	304	200	4440	7.2
1	1050	6.5	206.5	186	8201	5.1
2	368	2.3	206.5	197	8402	1.8
4	780	4.8	206.5	297	8402	3.7
PS2	850	2.6	108	100	12750	2.3
1	220	1.7	26.5	16.5	1372	2.6

† in MN/m^4, * in MN/m^3

4 ESTIMATION OF P_U PROFILE FROM CPT CONE RESISTANCE

To facilitate comparison, a non-dimensional parameter N_g is defined as $N_g = A_r/\gamma_s' K_p^2$, where γ_s' is the effective unit weight of the soil (dry unit weight above water table, and buoyant unit weight below); $K_p = \tan^2(45°+\phi_s'/2)$, is the coefficient of passive earth pressure; ϕ_s' is the effective frictional angle. The N_g was calculated for each pile test and tabulated in Table 2. Excluding the Test 1 by Choi et al. (2013), the values of N_g varies from 1.7 to 4.8, which is within the range determined previously by Qin & Guo (2014a,b) from the analysis of 57 pile test results.

The deduced p_u profiles are plotted in Figures 2(b), 3(b), 4(d), and 5(d), together with those using Broms' $p_u = 3\gamma_s' K_p dz$, (i.e. $N_g = 3/K_p$) (Broms 1964), Barton's $p_u = \gamma_s' K_p^2 dz$ (i.e. N_g = 1) (Barton 1982) and Reese's p_u profile (Reese et al. 1974). Recently, Suryasentana & Lehane (2014, 2016) proposed to estimate the p_u of a circular pile in cohesionless soils from the CPT cone resistance q_c by

$$p_u = 2.4\gamma_s' z d \left(\frac{q_c}{\gamma_s' z}\right)^{0.67} \left(\frac{z}{d}\right)^{0.75} \leq q_c d \qquad (1)$$

Using the q_c distribution, the ultimate soil resistance p_u was calculated and plotted in these figures as well. The comparison shows that the p_u calculated from equation (1) significantly overestimates those back calculated for all the tests as well as those calculated from Broms, Barton and Reese methods, thus resulting in over prediction of ultimate lateral capacity. Equation (1) is associated with hardening CPT-based p ~ y curves. Guo & Zhu (2005) investigated the effect of using different shapes of p ~ y curves on the difference in predicted pile response for static and cyclic laterally loaded piles in calcareous sand. Their results show that p ~ y curves from the two models, elastic-perfectly plastic as in Figure (1b) and hardening p ~ y curves like those proposed by Suryasentana & Lehane (2014, 2016), offer similar pile-head displacement, maximum bending moment, distribution of pile displacement and bending moment. However, the p ~ y models affect remarkably the distribution of soil reaction, especially within the upper few diameters of the pile. For the eight pile tests, the embedded length is relatively short (maximum 2.4 m), the average q_c along the embedded pile depth may be used to estimate the gradient of the linear p_u profile, A_rd. Using the calculated $q_{c\_average}$, this leads to A_rd = (1.8 - 8.8)% $q_{c\_average}$.

5 CONCLUSION

The responses of laterally loaded piles in sand were back calculated using elastic-plastic solutions against the results from field test, in which the CPT q_c were measured. Eight case studies demonstrate that, with elasto-plastic p ~ y curves, the pile responses can be well predicted. The assumption of Gibson k may be suitable for very dense sands. Comparison among the back calculated and existing p_u profiles indicates that the expression proposed by Suryasentana & Lehane (2014, 2016) may overestimate the ultimate lateral resistance. The analyses allow the gradient of the linear ultimate lateral resistance profile for sand to be calculated directly from the average cone resistance q_c along the pile embedded depth by A_rd = (1.8 - 8.8)% $q_{c\_average}$. However, this equation is obtained from relative short piles with small diameter. More case studies available will be helpful to refine this equation.

6 ACKNOWLEDGEMENTS

The authors thank Dr Weichao Li for providing the measured data in Figure 4(c).

7 REFERENCES

Broms, B.B. 1964. Lateral resistance of piles in cohesiveless soils. *Journal of Soil Mechanics and Foundation Engineering* 90(3): 123-156.

Barton, Y.O. 1982. Laterally loaded model piles in sand : centrifuge tests and finite element analysis. *Ph.D. thesis, University of Cambridge*.

Choi, H.Y., Lee, S.R., Park, H.I., & Kim, D.H. 2013. Evaluation of lateral load capacity of bored piles in weathered granite soil. *Journal Geotechnical and Geoenvironmental Engineering* 139(9): 1477-1489.

Guo, W.D. 2008. Laterally loaded rigid piles in cohesionless soil. *Canadian Geotechnical Journal* 45(5): 676-697.

Guo, W.D. & Zhu, B.T. 2004. Static and cyclic behaviour of laterally loaded piles in calcareous sand. In S. Gourvence & M. Cassidy (ed.), *Frontiers in Offshore Geotechnics*; *Proc. ISFOG, PERTH, 19-21 SEPTEMBER 2005*. London: CRC.

Lee, J.H., Park, H.I., Kim, M.K., & Kyung, D.Y. 2010. Estimation of lateral load capacity of rigid short piles in sands using CPT results. *Journal Geotechnical and Geoenvironmental Engineering* 136(1): 48-56.

Li, W., Igoe, D., & Gavin, K. 2014. Evaluation of CPT-based p-y models for laterally loaded piles in siliceous sand. *Geotechnique Letters* 4(2): 110-117.

Prasad, Y.V.S.N. & Chari, T.R. 1999. Lateral capacity of model rigid piles in cohesionless soils. *Soils and Foundations* 39(2): 21-29.

Qin, H.Y. & Guo, W.D. 2014a. Nonelinear response of laterally loaded rigid piles in sand. *Geomechanics and Engineering* 7(6): 679-703.

Qin, H.Y. & Guo, W.D. 2014b. Limiting force profile and laterally loaded rigid piles in sand. *Applied Mechanics and Materials* 553: 452-457.

Reese, L. C., Cox, W. R., & Koop, F. D. 1974. Analysis of laterally loaded piles in sand. *Proc., 6th Annual Offshore Technology Conf.,Vol.* 2: 473–483.

Suryasentana, S.K. & Lehane, B.M. 2014. Numerical derivation of CPT-based p-y curves for piles in sand. *Geotechnique* 64(3): 186-194.

Suryasentana, S.K. & Lehane, B.M. 2016. Updated CPT-based p-y formulation for laterally loaded piles in cohesionless soil under static loading. *Geotechnique* 66(6): 445-453.

Zhu, B., Sun, Y.X., Chen, R.P., Guo, W.D., & Yang, Y.Y. 2015. Experimental and analytical models of laterally loaded rigid monopoles with hardening p-y curves. *Journal Waterway, Port, Coastal, and Ocean Engineering* 141(6): 04015007-1-04015007-11.

Geotechnical and Geophysical Site Characterisation 5 – Lehane, Acosta-Martínez & Kelly (Eds)

Interpretation of CPT data for pile loading behavior - inverse estimation of void ratio over depth

K.-F. Seitz & E. Heins & A. Carstensen & J. Grabe
Institute for Geotechnical Engineering and Construction Management, Hamburg University of Technology, Harburger Schlossstr. 20, 21079 Hamburg, Germany

ABSTRACT: Cone penetration tests are often used for geotechnical site investigation before pile installation. Usually the measured data for cone and shaft resistance are roughly interpreted and applied for the design of the pile resistance. This paper presents an approach for soil modelling included in numerical simulations of pile loading behavior which employs the CPT data directly. Considering the material properties to be known, e.g. from laboratory tests which have been performed on bore hole excavations, state variables such as void ratio distribution and in situ stress state need to be determined to model an accurate initial state. This paper proposes an inverse determination of these unknown variables with mathematical optimization using an evolutionary algorithm to minimize the difference between measured CPT data and simulation results obtained from FEM. The obtained initial state variable distribution for void ratio for a given stress state may then be used to simulate the pile loading behavior without the need of prior interpretation of CPT data. The solution of the proposed inverse problem will be compared to the determination of state variables for a fictitious problem, in which the initial state is known.

1 INTRODUCTION

The cone penetration test (CPT) is a method of geotechnical sampling used for site investigation. This method is frequently applied to correlate relative density, friction angle or even stress state (Grabe and König, 2004; Grabe et al., 2005) with its output values, tip resistance and skin friction. Furthermore, Pucker et al. (2013) proposed a method to determine the foundation penetration directly from CPT measurements. For the design of geotechnical structures such as pile foundations these correlations as well as numerical simulations may be used.

For such a numerical simulation the soil has to be modelled realistically. The material properties are usually known from laboratory tests. State variables such as void ratio distribution and stress state need to be determined from CPT. An inverse determination method to determine the state dependent variables is developed using mathematical optimization with an evolutionary algorithm which minimizes the difference between measured CPT data and Finite Element Method (FEM) simulation results. This technique enables the determination of an initial state for a design process without prior interpretation of CPT data. Therefore, the overall error rate will be reduced.

This paper presents the developed technique and shows its applicability. Three fictitious problems with known state dependent variables are proposed. The solution of the proposed inverse technique for initial relative density as well as stress state will be calculated and compared to the known parameters of the fictitious problems.

2 NUMERICAL METHOD

2.1 *Evolutionary Algorithm*

The inverse parameter determination is conducted using a multicriterial evolutionary optimization algorithm according to Kinzler (2011). The evolutionary optimization method is used to determine parameter sets which minimize the deviation of model results from the measurements. This is done by analyzing arbitrary parameter variations with respect to the overall deviation. Each iteration considers a so called generation of various individuals. These individuals represent parameter sets. The objectives of the optimization are evaluated to identify the best individuals. The evaluation of the objective function comprises in this case of: the modification of material parameters e_0 and initial conditions K_0; the FE-analysis using Abaqus/Standard; the result readout and the evaluation of deviation. The best individuals persist and through recombination and mutation, ar-

bitrarily chosen individuals complete the generation for the next iteration. The iterative procedure of an evolutionary algorithm is shown in Figure 1.

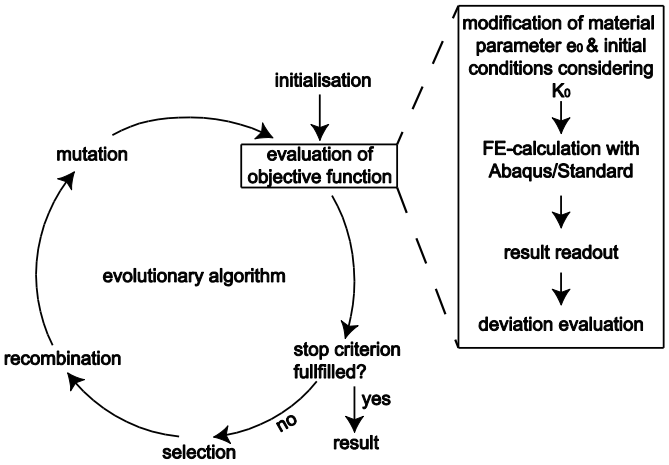

Figure 1. Iterative procedure of evolutionary multicriterial optimization algorithm

3 NUMERICAL MODEL

Numerical models for CPT need to be able to simulate large relative motions between cone and subsoil as well as large deformation of the subsoil. This can be done using axisymmetric models based on FEM including the 'zipper technique' (Cudmani, 2001). With this approach Grabe and König (2004) simulated a CPT in non-cohesive soil successfully and investigated the influence of stress state and relative density on sounding resistance. In this model, the cone is modelled as a rigid body and penetrates the soil displacement-controlled.

Geometries, dimensions and boundary conditions are shown in Figure 2. The penetration of the cone into a deeper soil layer is simulated by applying a stress boundary condition $\sigma'_v = \gamma' z$ according to the overburden stress.

The cone is modelled with a rigid tip to distinguish its contributions to the total resistance. At the beginning of the simulation the cone is preinstalled into the subsoil by approximately 5Dcone using the wished-in-place technique, i.e. the previous installation process is neglected. Penetration is modelled using the presented zipper technique (Cudmani, 2001).

The stress-strain behavior of the non-cohesive subsoil is modelled using the hypoplastic constitutive model according to von Wolffersdorff (1996) extended by small strain stiffness according to Niemunis & Herle (1997). By using this sophisticated soil model the stress paths in the subsoil during cone penetration can be simulated realistically, as it includes effective stresses and void ratios as state variables of the soil. The soil parameters for the non-cohesive soil layer are adapted from Cuxhavener Sand (fS, u'). Parameters for the hypoplastic constitutive model for Cuxhavener Sand have been determined and published in Bubel and Grabe (2013). Saturated and fully drained conditions are assumed during cone penetration, i.e. no excess pore pressure will occur.

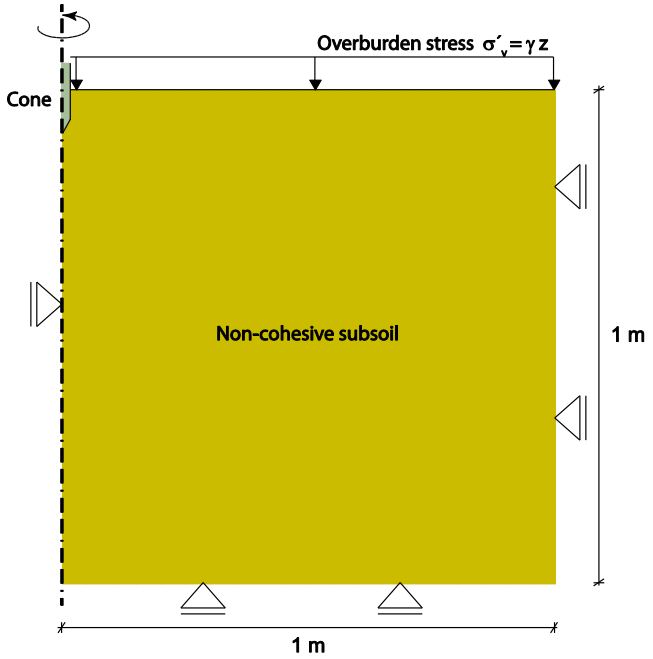

Figure 2. Geometry, dimensions and boundary conditions for the axi-symmetric CPT FE-model

Normal contact between the cone and the subsoil is transmitted as long as there are no tensile contact stresses. For the smooth surface of the cone, a stick-slip model for the contact in tangential direction is applied using an assumed low friction coefficient of $\mu = 0.1$.

Table 1. Parameter sets for the original fictitious problems

	A	B	C
K_0 [-]	0.5	0.5	0.5
e_0 [-]	0.724	0.724	0.972
σ'_v [kN/m²]	60.5	121	121

Three different combinations of initial K0-stress state, void ratio and overburden stress σ'v will be evaluated as fictitious problems. The prescribed value of the coefficient of earth pressure at rest of $K_0 = 1 - \sin(\varphi) = 0.5$ will be chosen for all simulations. The initial void ratio is either $e_0 = 0.724$ or $e_0 = 0.972$ corresponding to dense and medium dense material. The overburden stress is either 60.5 or 121 kN/m² which corresponds to a depth of 5.5, respective 11 m. The fictitious parameters are shown in Table 1. External loads for this initial state are gravity load and a pressure on the upper boundary of the soil column according to the overburden stress. Next, the cone penetrates downwards by prescribing its vertical constant velocity of 1 cm/s. The reaction forces for the tip are monitored.

4 OPTIMIZATION

For each fictitious problem A, B and C, an optimization is conducted using 30 iterations with each 10 parameter sets in order to determine the initial K0-stress state and void ratio. The optimization procedure offers the choice of an initial range and an overall range as well as an additional choice of initial parameter sets. For the first iteration it is possible to define initial parameters. For the present analysis one initial parameter set is chosen for the problems A, B and C. The remaining nine parameter sets are initialized using a random distribution within the range for the initial parameter sets, which matches the overall range for parameter sets used for further iterations. The chosen ranges and initial values are the same for the three optimization problems and are summarized in Table 2.

Table 2. Ranges for optimization concerning the initial parameter set and range of definition and initial parameter set

		A, B, C
range for parameter sets	e_0 [-]	0.6 to 1.22
	K_0 [-]	0.5 to 1.0
range for initial parameter sets	e_0 [-]	0.6 to 1.22
	K_0 [-]	0.5 to 1.0
initial parameter	e_0 [-]	0.97
	K_0 [-]	0.6

For each parameter set a FE-analysis will be conducted. The forces of tip resistance are evaluated and compared to the fictitious problem. The optimization's objective is to minimize the overall deviation summed over the penetration depth between the tip resistance of the original problem and the simulation with the optimized parameter set.

Figure 3 shows the original state variable and the tested parameter sets for the three original problems A, B and C. The original state variable is depicted as asterisk. The tested parameter sets are shown as crosses. The diagram in the lower row on the right depicts the maximum deviation from the original solution within during the course of iteration for the three original problems. During the iterative process the maximum deviation is reduced. The best optimization results are summarized in Table 3. They are in fairly good agreement with the original state variables. The optimization results differ maximum 2.3 % from the original fictitious problem.

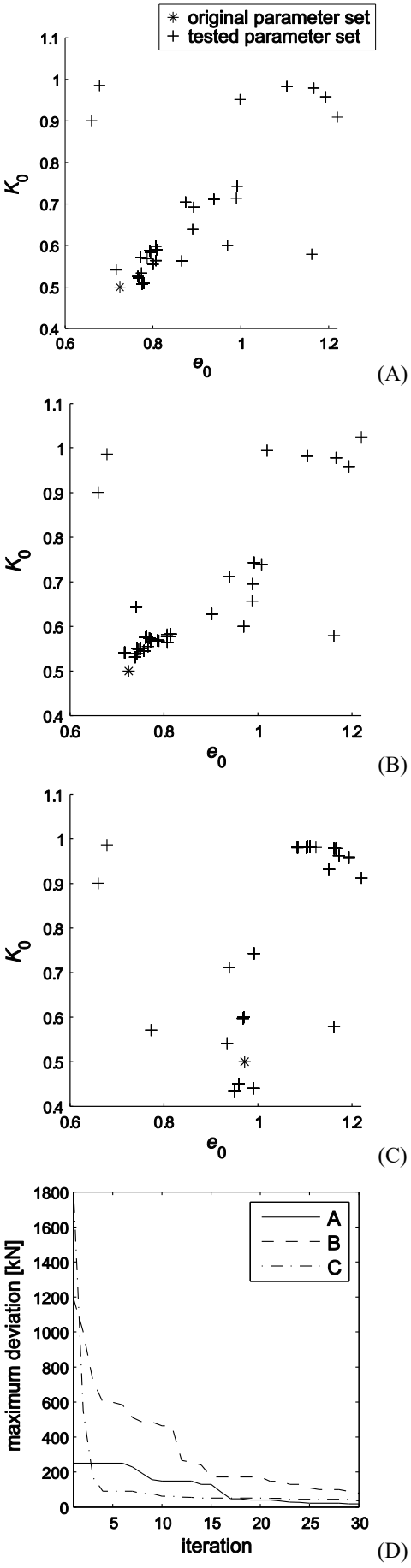

Figure 3. Optimization results for the original problems A, B and C; the maximum deviation for each iteration step is depicted (D)

Table 3. Best optimization results after 30 iterations, with corresponding e_0 and K_0-stress state

Parameter	A	B	C
K_0 [-]	0.5	0.5	0.5
e_0 [-]	0.724	0.724	0.972
σ'_v [kN/m²]	60.5	121	121
Deviation of tip force [kN]	7.5	11.3	8.0
Deviation normalized to overall sum [%]	1.3	1.1	2.3

5 CONCLUSION

The present paper shows that the proposed method for determination of state variables such as initial void ratio and K0-stress state is effective. With this method it is possible to determine the unknown state variables based only on the results of CPT-measurements. This technique enables the determination of an initial state for a design process without prior interpretation of CPT data. Therefore, the overall error rate will be reduced.

Since different initial state variables in different depths can be determined, the numerical model could be calibrated directly on the CPT-measurements. However, calibrating a whole numerical model for pile installation requires large amounts of computational resources. Each iteration step considers several parameter sets which all need to be evaluated through FE-analysis, e.g. using 10 parameter sets in 30 iterations 300 FE-analyses have to be carried out, which is, depending on the model size, an enormous computational effort. Consequently, the applicability of this method to more complex problems might be limited by computational resources.

6 REFERENCES

Bubel J. and Grabe J. 2013. Wave-induced bottom pressure on submarine slopes. *Proceedings of Conference on Maritime Energy (COME)*, Veröffentlichung des Instituts für Geotechnik und Baubetrieb der TU-Hamburg-Harburg, Heft 23 pp. 211-227.

Cudmani, R. O. 2001. Statische, alternierende und dynamische Penetration in nichtbindigen Böden. Dissertation. Veröffentlichungen des Instituts für Bodenmechanik und Felsmechanik der Universität Fridericiana in Karlsruhe, Heft 152.

Grabe, J. and F. König 2004. Zur aushubbedingten Reduktion des Drucksondierwiderstandes. *Bautechnik* 81 (7):569–577.

Grabe, J., F. König, and K.-P. Mahutka 2005. Zur indirekten Beurteilung der Lagerungsdichte nichtbindiger Böden auf der Grundlage von Drucksondierungen. Mitteilungen des Instituts für Geotechnik der TU Dresden, Heft 15. Dresden, pp. 1–18.

Kinzler S. 2011. Zur Parameteridentifikation, Entwurfs- und Strukturoptimierung in der Geotechnik mittels numerischer Verfahren. Veröffentlichung des Instituts für Geotechnik und Baubetrieb der TU-Hamburg-Harburg, Heft 23.

Niemunis, Herle 1997. Hypoplastic model for cohesionless soils with elastic strain range. *Mechanics of Cohesive-Frictional Materials* 2 (4): 279-299.

Pucker T., Bienen B. and Henke S. 2013. CPT based prediction of foundation penetration in siliceous sand. *Applied Ocean Research*, 41:9-18.

von Wolffersdorff 1996. A hypoplastic relation for granular materials with a predefined limit state surface. *Mechanics of Cohesive-Frictional Materials* 1 (3): 251-271.

Geotechnical and Geophysical Site Characterisation 5 – Lehane, Acosta-Martínez & Kelly (Eds)

Interpretation of shear strength data for construction on mine tailings deposits

D.J. Williams
The University of Queensland, Brisbane, Australia

ABSTRACT: The safety of an upstream embankment raise or final capping for a conventional surface slurried tailings storage requires that the existing tailings be desiccated and a geotechnical investigation to demonstrate adequate bearing capacity. Typical geotechnical investigation methods include in situ shear vane testing and cone penetration testing. Heavily desiccated tailings may allow direct access using a conventional rig. Otherwise, a rig with wide tracks may be required, or access roadways may have to be constructed over the tailings. The data from these tests are then interpreted to determine the shear strength profile for the desiccated tailings, to enable bearing capacity, geotechnical slope stability and settlement analyses of a proposed upstream embankment raise or capping. The paper describes two case studies of such geotechnical investigations, test data interpretation, and geotechnical analyses; one for an upstream embankment raise on heavily desiccated tailings and the other for the capping of variably desiccated tailings.

1 INTRODUCTION

For mine tailings conventionally deposited as a slurry in a surface tailings storage facility (TSF), in situ vane shear testing and cone penetration testing including pore water pressure measurement (CPTu) are typically employed to determine the shear strength profile with depth of the tailings. The shear strength profile is used to assess the feasibility and safety of upstream raising of the containment embankment on tailings or final capping of the tailings for rehabilitation purposes.

Two case studies of such geotechnical investigation, test data interpretation and geotechnical analyses are described. The first involves the proposed upstream embankment raise on heavily desiccated tailings at South23's Cannington Underground Mine in north-west Queensland, Australia. The second involves the capping of variably desiccated tailings at New Hope Group's New Acland Coal Mine in south-east Queensland. The focus of the paper is on test data interpretation, which is an area that is often deficient.

2 DESCRIPTION OF CANNINGTON SITE

South32's Cannington Underground Mine is located 250 km south-east of Mount Isa in north-west Queensland, Australia, and has produced silver, lead and zinc since 1997. The ore is ground to -180 micron, and processed to produce Sandy SILT to Silty SAND-sized tailings. The tailings are thickened in a high rate thickener and discharged at 65% solids by mass. Of the tailings produced by the processing of the ore, 60% is returned underground as cement paste backfill, and 40% reports to a surface tailings storage facility (TSF) comprising three cells. Tailings deposition into Cell 1 ceased about 4 years ago, and the embankment is proposed to be raised by the upstream method using borrow material located partially on heavily desiccated tailings to accommodate tailings from late 2017. The proposed 3 m high upstream raise of Cell 1 is the optimal solution to cost-effectively and safely provide additional tailings storage capacity beyond the filling of Cell 3.

2.1 *Tailings storage facility to be raised*

The surface TSF comprises three cells. Cell 1, with an area of 44 ha, and Cell 2, with an area of 44 ha, were constructed in the late 1990's, and have each been raised a number of times to reach their current embankment heights. Tailings deposition into Cell 1 ceased about four years ago and deposition into Cell 2 ceased about one year ago. Cell 3, with an area of 58 ha, was completed in May 2014 and is currently the active cell. Cell 3 is expected to be filled by August to October 2017. A 20 September 2013 aerial view of the Cannington surface TSF, with Cell 2 still operational and Cell 3 under construction, is shown

in Figure 1, and a view of the heavily desiccated surface of Cell 1 is shown in Figure 2.

Figure 1. Aerial view of Cannington's surface TSF (Google Earth, 20 September 2013).

Figure 2. View of heavily desiccated surface of Cannington's surface TSF Cell 1.

2.2 *Geotechnical investigation and testing*

The geotechnical investigations reported by SRK Consulting (2015) included Dynamic Cone Penetration Tests carried out in the desiccated Cell 1 and 2 tailings, which highlighted the far greater desiccation of the Cell 1 tailings that had been left to desiccate about four times as long as the Cell 2 tailings since the last deposition of tailings. Twelve Cone Penetration Tests with pore water pressure measurement (CPTu) and *in situ* vane shear testing were carried out in the heavily desiccated Cell 1 tailings. Laboratory characterisation and geotechnical parameter testing was carried out on tailings and borrow samples.

The Cannington tailings particle size distribution is Silty SAND to Sandy SILT-sized, with 40 to 70% sand-size (0.06 to 1.5 mm), 37 to 63% silt-size (0.002 to 0.06 mm), and 3 to 7% clay-size (<0.002 mm). The tailings are generally non-plastic, with a Liquid Limit of 14 to 16%. The specific gravity of the tailings is about 3.15, and the near surface settled and desiccated dry density is about 1.76 t/m^3 (SRK Consulting 2015).

2.3 *Interpretation of CPTu and vane shear data*

The consolidation state of a soil may simply be interpreted using the method of Schmertmann (1978), which was applied to all 12 CPTu cone resistance profiles with depth in the heavily desiccated Cell 1 tailings. The Schmertmann (1978) method involves extrapolating lines through the lower bounds of the cone resistance profiles to the surface. The lower bound line intersecting the surface to the right of the origin indicates under-consolidated tailings, passing through the origin indicates normally-consolidated tailings, and intersecting the surface to the right of the origin indicates over-consolidated (usually desiccated) tailings. In addition, the depth to the (presumed) perched water table within the tailings was estimated based on the measured pore water pressures. A typical interpretation is shown in Figure 3.

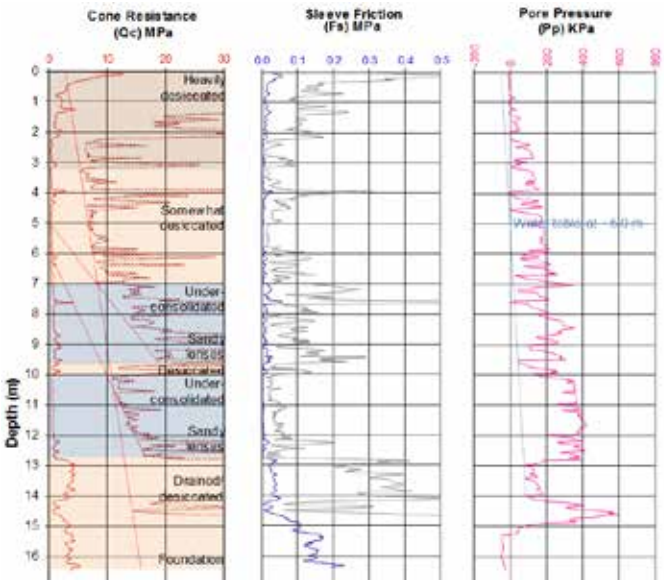

Figure 3. Typical interpreted consolidation state and depth to water table for a CPTu in heavily desiccated Cell 1 tailings.

The upper layer of the tailings in Cell 1 is seen in Figure 3 to have become heavily over-consolidated due to four years of desiccation since tailings deposition ceased. The layer below that is generally somewhat desiccated (over-consolidated) due to intermittent surface desiccation followed by re-wetting by fresh tailings, or normally-consolidated (maintained under water), and occasionally under-consolidated (unable to drain the self-weight-induced excess pore water pressures). The layer of tailings above the foundation is drained or desiccated. The spikes in cone resistance profile indicate sandy lenses. The range and average interpreted consolidation states and estimated perched water table depths estimated from all 12 CPTu profiles in Cell 1 tailings are summarised in Figure 6.

Vane shear strength testing carried out in the Cell 1 tailings gave the data shown in Figure 4 (SRK Consulting 2015). There is a lack of vane shear strength data in the upper 4 m constituting the desiccated crust since the crust was too stiff to test. Correlating the vane shear strengths S_u with the corresponding CPTu cone resistance values Q_c gives the bearing capacity factor N_c:

$$N_c = \frac{Q_c}{S_u} \tag{1}$$

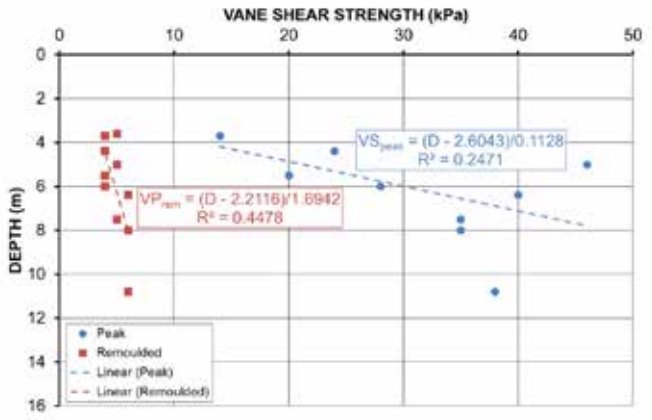

Figure 4. Peak and remoulded vane shear strengths with depth in Cell 1 tailings.

Values for the peak and remoulded bearing capacity factors are plotted in Figure 5. The reported vane shear strength data and the calculated bearing capacity factors are very scattered. The range of peak bearing capacity factors is 7.8 to 24.0, with an average value of 14.4, while the range of remoulded bearing capacity factors is 53 to 160, with an average value of 88.6.

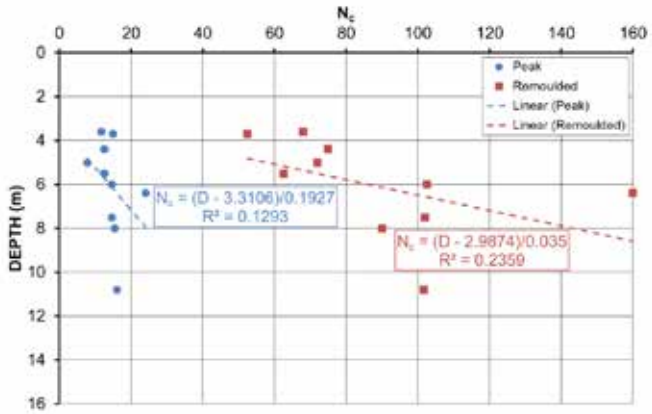

Figure 5. Calculated peak and remoulded bearing capacity factors with depth in Cell 1 tailings.

Conservative (lower bound) values of the peak vane shear strength are equivalent to 0.25 times the vertical effective stress, and conservative values of the remoulded vane shear strength are equivalent to 0.04 times the vertical effective stress. The average ratio of the remoulded to the peak vane shear strengths of 0.16 is low compared with ratios expected for tailings of about 0.5 below the water table and about 0.33 above the water table (Williams 2005). The remoulded vane shear strength is representative literally of the shear strength that applies on remoulding, such as that caused by loading the tailings so much and so rapidly as to cause "bow-wave" failure.

Skempton and Henkel (1953) were the first to suggest an empirical relationship between undrained shear strength S_u and vertical effective stress σ_v'. For normally-consolidated (nc) soils (in the context of tailings, those always stored below water):

$$\left(\frac{S_u}{\sigma_v'}\right)_{nc} = 0.11 + 0.37\left(\frac{I_P}{100}\right) \quad (2)$$

where I_P = Plasticity Index. For over-consolidated (oc) soils (in the context of tailings, those subjected to desiccation drying followed by re-wetting):

$$\left(\frac{S_u}{\sigma_v'}\right)_{oc} = \left(\frac{S_u}{\sigma_v'}\right)_{nc} OCR^m \quad (3)$$

where OCR = over-consolidation ratio, and m = an empirical exponent, generally taken as 0.8. Inputting the values of the parameters for Cannington Cell 1 tailings, Equation (2) gives $(s_u / \sigma_v')_{nc} = 0.17$, which is low compared with the value typical for normal soils of 0.25. It will subsequently be shown that a value for $(s_u / \sigma_v')_{nc}$ of 0.25 is consistent with the CPTu and vane shear data, and can be adopted. The upper Cannington Cell 1 tailings are clearly over-consolidated due to their heavy desiccation, leading to a higher value for $(s_u / \sigma_v')_{oc}$.

All 12 CPTu cone resistance profiles are plotted in Figure 6, together with the average profile. In Figure 7, the CPTu cone resistance data have been divided by the average peak bearing capacity factor of 14.4 to provide the estimated profiles of peak shear strength with depth, again including the average profile, plus the "smoothed" lower bound of the average profile, ignoring the peaks caused by the sandy lenses.

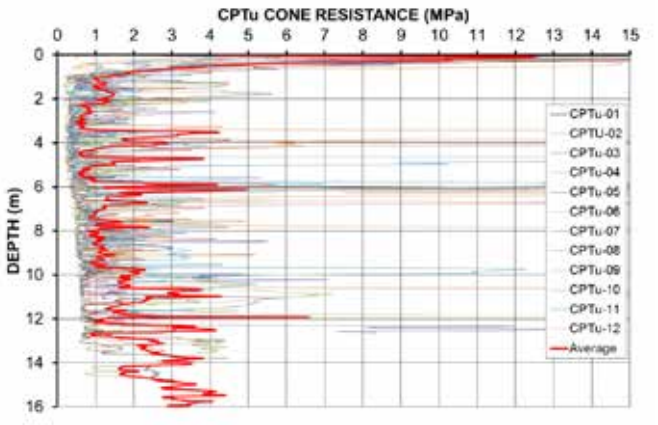

Figure 6. CPTu cone resistance versus depth profiles.

Also shown in Figure 7 are the approximate normally-consolidated, self-weight profile and the approximate over-consolidated profile, the latter made to match the smoothed average profile below the water table (from about 4.6 m depth). The average OCR is approximately 3.15 and, using Equation (3), $(s_u / \sigma_v')_{oc}$ is approximately 0.63, 2.5 times the adopted normally-consolidated value of 0.25. The

remoulded values are approximately 0.4 times these values, but will only be realised if remoulding is initiated.

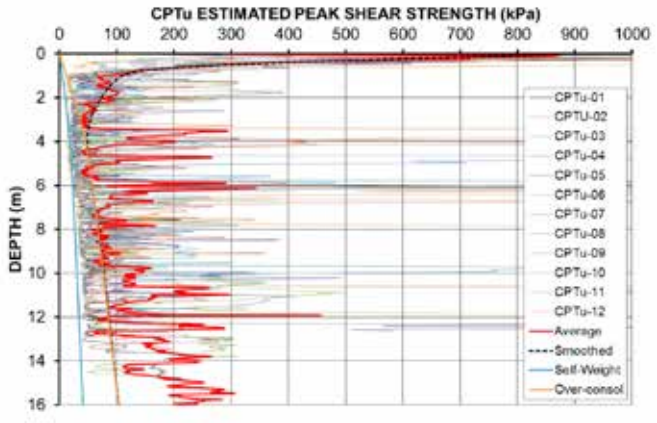

Figure 7. Estimated peak shear strength versus depth profiles.

3 DESCRIPTION OF NEW ACLAND SITE

New Acland Coal Mine in the Clarence Moreton Basin within the lower Walloon Coal Measures, is located north-west of Oakey in South East Queensland, Australia. Initially, New Acland discharged slurried tailings generated by their coal processing plant to a surface tailings storage facility (TSF1 and TSF1 Extension), before establishing in-pit TSFs (see Figure 8).

Figure 8. New Acland surface and in-pit TSFs (aerial photograph taken on 12 March 2013).

Sometime after the cessation of tailings deposition into TSF1, following surface crusting, spoil was dumped from haul trucks onto the surface of the tailings from the northern and eastern upper tailings beach. However, this resulted in 'bow-waving' of the crusted tailings. Spoil placement was stopped when a 1 to 1.5 m high bow-wave overtopped the bund dividing TSF1 from TSF1 Extension, and approached the southern external wall of TSF1. Subsequently, New Acland committed to more effectively capping the surface TSF.

3.1 *Method of capping of surface TSF*

The bow-waving that occurred on the placement of spoil on the upper northern tailings beach of TSF1 highlighted the need to select a less impacting capping method. Coarse reject from the coal preparation plant was proposed as the initial capping material due to its availability as a waste material that had to be disposed of, and it being better-draining than spoil, which degrades rapidly. The overall cover was to comprise and initial approximately 1 m thick capping layer of coarse reject, followed by a second 2 to 3 m thick layer of coarse reject, and finally a topsoil layer that was to be seeded with pasture grasses and fertilised.

Pushing coarse reject by D6 Swamp Dozer was adopted as the initial capping method. The D6 Swamp Dozer, with an operating mass of 21.7 t exerts an average track bearing pressure of 35 kPa, equivalent in bearing pressure to about 1 m height of fill. This needs to be taken into account in addition to the height of fill placed, to ensure safe operation on the crusted tailings.

3.2 *Assessing bearing capacity of tailings*

The bearing capacity of tailings is a function of their shear strength profile with depth. Given the difficulty of sampling and generally low shear strength of fine-grained coal tailings, in situ vane shear testing is the most appropriate and direct means of obtaining an estimate of the shear strength profile of the tailings with depth. Both the peak and remoulded vane shear strengths should be measured. The peak vane shear strength is the value obtained on initial shearing, while the remoulded vane shear strength is the value obtained on re-shearing after remoulding by rotating the vane a nominal three revolutions. The vane shear strength of the tailings S_v is estimated using:

$$S_v = T\ 10^6 / \left[\pi \left(\frac{D^2 H}{2} + \frac{D^3}{6} \right) \right] \quad (4)$$

where T = measured (peak or remoulded) torque in N.m, D = vane diameter in mm, and H = vane height in mm (typically twice the diameter, to limit the shear resistance on the ends of the vane to about 10% of the total shear resistance on the vane).

The fill height H in m that may safely be placed by pushing using a D6 Swamp Dozer over crusted tailings, without causing remoulding and bow-waving, is given by (adapted from Williams 2005):

$$H = \left(\frac{N_c\ S_v}{F\ \gamma} \right) - H_e \quad (5)$$

where N_c = bearing capacity factor = 5.14 assuming that a strip of fill is pushed over a broad front, F =

adopted factor of safety with a minimum value of say 1.5, γ = unit weight of the fill of about 18 kN/m³, and H_e = equivalent height of fill corresponding to the average bearing capacity of the D6 Swamp Dozer, which is about 1 m. Hence:

$$H \approx 0.190\, S_v - 1 \quad (6)$$

The peak shear strength of loaded tailings will increase as they drain, according to (Williams 2005):

$$\Delta\tau = \Delta\sigma_v' \tan\phi' \quad (7)$$

where $\Delta\tau$ = increase in the peak shear strength, $\Delta\sigma'$ = increase in the effective stress following loading by a height of fill H and drainage of the excess pore water pressures generated, and ϕ' = effective (drained) friction angle of the tailings of about 30°. Hence:

$$\Delta\tau \approx 10\, H \quad (8)$$

on full drainage (after about one to four weeks, depending on the hydraulic conductivity of the tailings).

Note that the peak vane shear strength is a measure of how much additional fill can be placed, since any fill previously placed and left for a sufficient time to dissipate all excess pore water pressures, is already supported.

3.3 *Vane shear strength testing of crusted tailings*

Ahead of the capping of TSF1, the peak and remoulded vane shear strengths, and hence bearing capacities, of the tailings were assessed. The vane shear testing was carried out using a hand-operated, 65 mm diameter by 130 mm high vane shear and torque wrench. The vane shear testing was carried out at depth intervals of 0.2 m, starting at 0.1 m depth and extending to between 0.9 m and 1.9 m depth. The test hole was advanced by hand augering between vane tests, which also enabled tailings samples to be collected for subsequent laboratory testing (not reported herein). The vane was connected to a central rod within an outer sleeve, so that the shear resistance on the vane alone was recorded by the torque wrench.

Note that self-weight consolidation of submerged coal tailings results in a linear increase in shear strength of only about 0.8 kPa/m depth. If desiccation crusting occurs, but the depth and shear strength of the surface crust are limited, and/or there has been no desiccation of previously deposited tailings layers, there will be increased risk of bearing capacity failure through the crust into the underlying soft tailings. This will result in remoulding and loss of shear strength, followed rapidly by the generation of a bow-wave failure. The excess pore water pressures generated by fill placement will dissipate relatively rapidly (over one to four weeks, depending on the hydraulic conductivity of the tailings, affected by their particle size distribution and clay mineral content), accompanied by an increase in shear strength given by Equation (8), after which fill placement can recommence.

Selected peak and remoulded vane shear strength profiles with depth for TSF1 tailings are shown in Figure 9. Included in Figure 9 is the shear strength profile expected for coal tailings maintained 'underwater', due to its self-weight alone. The tailings at the bow-wave induced by the previous placement of spoil is capable of safely supporting a fill height of up to 6 m, while the surface of the tailings towards the reeds can only support a maximum of 2 to 3 m of fill, from Equation (6). The average ratio of the remoulded:peak vane shear strength for TSF1 tailings is about 0.4, implying a corresponding drop in the fill height that can safely be supported on remoulding.

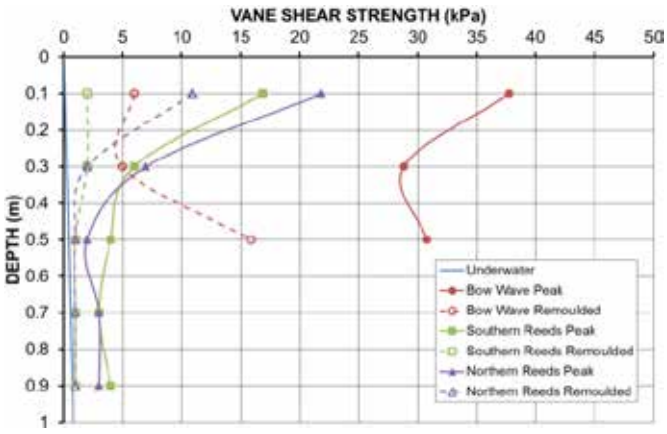

Figure 9. Selected peak and remoulded vane shear strength profiles with depth.

3.4 *Capping experience at TSF1*

Photographs of the early pushing of the initial capping of coarse reject over the raised crest of the old bow wave of TSF1 are shown in Figure 9. Fill placement caused the tailings to drain, often raising the water table to the surface of the tailings, as seen in Figure 10(a). The first sign of imminent bow-waving was the appearance of hydraulic fractures radiating out from the toe of the fill, as seen in Figure 10(b), with continued dozing leading to the formation of a bow-wave, as seen in Figure 10(c).

Figure 9. Early pushing of a capping of coarse reject over old bow-wave of surface TSF.

(a) (b) (c)

Figure 10. Fill placement causing: (a) water table rise to tailings surface, (b) hydraulic fractures radiating out from toe of fill, and (c) formation of a bow-wave on continued dozing.

On the placement of the initial capping layer (typically about 1 m high in an effort to avoid bow wave failure), excess pore water pressures are induced in the tailings, raising the water table (often to the surface). These excess pore water pressures dissipate through drainage to the surface, resulting in a general increase and greater uniformity of the peak vane shear strength profile with depth, as shown in Figure 11. The increased peak shear strength, averaging 15.3 kPa in Figure 11, corresponding to Equation (8), would allow an additional fill height of almost 2 m to be safely placed using the D6 Swamp Dozer.

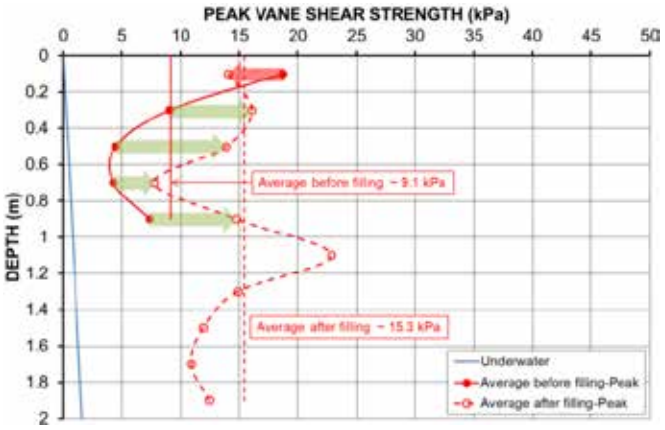

Figure 11. Increase in peak vane shear strength due to dissipation of excess pore water pressures.

Figure 12 shows the progress of capping TSF1 as at June 2015, with the initial 1 m thick layer and the follow-up 2 to 3 m thick layer of coarse reject.

4 CONCLUSIONS

The paper presents two case studies involving the interpretation of shear strength data for construction on mine tailings deposits. In the Cannington case study, heavily desiccated tailings are shown to provide adequate bearing capacity to cost-effectively and safely support a proposed 3 m high upstream embankment raise on a conventional surface slurried tailings storage facility. Data from cone penetration and vane shear testing of the tailings were interpreted to determine their shear strength profile, with an average peak cone factor of 14.4 being obtained.

The New Acland case study involves the successful capping of a conventional, surface slurried coal TSF, to facilitate rehabilitation of the crusted tailings surface for grazing purposes. The capping involved placing by D6 Swamp Dozer an initial 1 m thick layer of coarse reject, followed by a second 2 to 3 m thick layer of coarse reject placed by a D6 and D9 dozers. The shear strength and bearing capacity of the crusted coal tailings were first assessed using vane shear strength testing, backed-up by observations of the placement of the initial capping. As capping progressed, further vane shear testing was carried out to assess the shear strength of the tailings beyond the capping layer, and the strength gain over time in the already covered tailings, which enabled further capping material to be safely placed.

Figure 12. Progress of capping of TSF1 as at 25 June 2015, showing the initial 1 m thick layer and the follow-up 2 to 3 m thick layer of coarse reject.

5 ACKNOWLEDGEMENTS

The managements of South32's Cannington Mine and New Hope Group's New Acland Coal Mine are acknowledged for providing access and granting approval to publish the site and tailings data contained in this paper.

6 REFERENCES

Schmertmann, J.H. 1978. *Guidelines for cone penetration test, performance and design*. Federal Highway Administration, Report FHWA-TS-78-209, Washington, July 1978.

Skempton, A.W. and Henkel, D.J. 1953. The post-glacial clays of the Thames estuary at Tilbury and Shellhaven. In: *Proceedings of the 3rd International Conference on Soil Mechanics and Foundation Engineering, Zurich, Switzerland, 16-27 August 1953*, **I**, 302-308.

SRK Consulting. 2015. *Cannington TSFE2 Cell 1 Tailings and Embankment Investigation – Factual and Interpretive Report*. May 2015.

Williams, D.J. 2005. Chapter 17: Placing covers on soft tailings. In B. Indraratna and Chu Jian (eds), *Ground Improvement-Case Histories*, 491-512. Oxford, Elsevier.

Geotechnical and Geophysical Site Characterisation 5 – Lehane, Acosta-Martínez & Kelly (Eds)

Estimation of Shear Wave Velocity Based on SPT Profile Data

F. Yi
CHJ Consultants, Colton, USA

F.P. Yi
Highland, USA

ABSTRACT: In most of the early studies, researchers correlated shear wave velocity with Standard Penetration Test blowcounts (e.g., Kanai 1966 and Ohta & Goto 1976). Later correlations developed by various researchers (e.g., Ohta & Goto 1978; Andrus et al. 2004, Branderburg et al., 2010; and Wair et al., 2012) directly or indirectly took into account the effect of overburden pressure. The author of this paper found that the fines contents and the mean grain size of the soil also play an important role in the estimation of shear wave velocity based on SPT data. In this paper, a predictive equation for estimating shear wave velocity based on SPT profile data including SPT blowcounts (N_{60}), fines contents (FC) and normalized mean effective confining stress (σ'_m/P_a) are presented. The equation was developed based on a statistical analysis of 179 valid data sets obtained from northern to southern California with soil profiles predominately of clean sands, silty sands or sandy silts. The comparison of measured and calculated shear wave velocities yields a better prediction using the proposed equation than existing methods for soils which vary from clean sand to sandy silt with low plasticity.

1 INTRODUCTION

The importance of characterization of the initial (or small-strain) shear modulus (G_0) is recognized because of its applications in nonlinear seismic ground response analysis, such as site response analysis and soil-structure interaction (SSI) analysis. Required inputs for seismic ground response analysis include initial soil stiffness information for each soil layer of the site in question. Initial soil stiffness is usually represented by G_0. The direct measurement of G_0 is very difficult. Fortunately, it is directly related to small strain shear wave velocity, V_s, by

$$G_0 = \rho V_s^2 \quad (1)$$

where ρ = mass density of soil (total unit weight of the soil divided by the acceleration of gravity).

Another important role of V_s is its use in site classification. The Next Generation Attenuation ground motion prediction equations use the shear wave velocity of the top 30 m of the subsurface profile (V_{s30}) as the primary parameter for characterizing the effects of sediment stiffness on ground motions (Wair et al. 2012). This issue has captured the attentions of researchers in recent years.

Although less attention has been paid to it, V_s also plays a very important role in the estimation of dry sand seismic settlement. Dry sand seismic settlement is governed by 3 key factors, earthquake level, shear modulus ratio vs. shear strain relationship and the volumetric strain model. V_s is usually utilized to calculate G_0 and further to calculate the shear modulus ratio, G/G_0. Other than in ground motion prediction, the depth of soil profile is more focused on top approximately 20 m in dry sand seismic settlement estimation. Due to the sensitivity of estimated dry sand settlement to G/G_0, a more accurate V_s profile is preferred.

V_s can be directly measured by various methods such as crosshole seismic (CH), seismic cone penetrometer test (SCPT), multichannel analysis of surface waves (MASW) and refraction microtremor analysis (ReMi). However, not all projects can absorb the cost of direct measurement. This is especially true for small projects. In most cases, these projects must rely on shear wave velocity correlations with standard penetration test (SPT) data.

The earliest published studies comparing SPT N-value and V_s were performed by Japanese researchers in the 1960s and early 1970s. Wair et al. (2012) provided a relatively detailed review of those early studies. From that review, it is clear that in most of the early studies, V_s was solely correlated to SPT N-value. Ohta & Goto (1978) were the first to correlate V_s to N-value, depth, geologic age and soil type. They developed different empirical V_s correlation equations considering these four index

properties. Andrus & Stokoe (2000) pointed out that the state of stresses in the soil is also an important factor influencing V_s. They corrected V_s to a reference overburden stress using the following equation (Sykora 1987; Robertson et al. 1992),

$$V_{s1} = V_s \left(\frac{P_a}{\sigma_v'}\right)^{0.25} \quad (2)$$

where, P_a = the reference stress of 100 kPa or about atmospheric pressure and σ_v' = initial effective overburden stress (kPa). They developed a correlation between overburden stress-corrected shear-wave velocity V_{s1} and corrected blowcount $(N_1)_{60}$ based on liquefaction case history data. The correlation was later updated by Andrus et al. (2004).

A detailed discussion about the influence of σ_v' was made by Branderburg et al. (2010). To count for the influence of soil type, separate empirical equations were proposed for sand, silt and clay (e.g., Imai 1977, Ohta & Goto 1978, Branderburg et al. 2010, Wair et al. 2012). The author noted that it is difficult to apply those empirical equations to soils transiting from clean sand to sandy silt and fines contents (FC) exerts important influences on the measured shear wave velocity. No publications are available which discuss soil types that transit from silty sand to sandy silt.

In this study, the author utilized data sets collected at various sites from northern to southern California. Statistical analysis was performed in order to correlate V_s to blowcount (N_{60}), normalized mean effective confining stress (σ_m'/P_a) and FC.

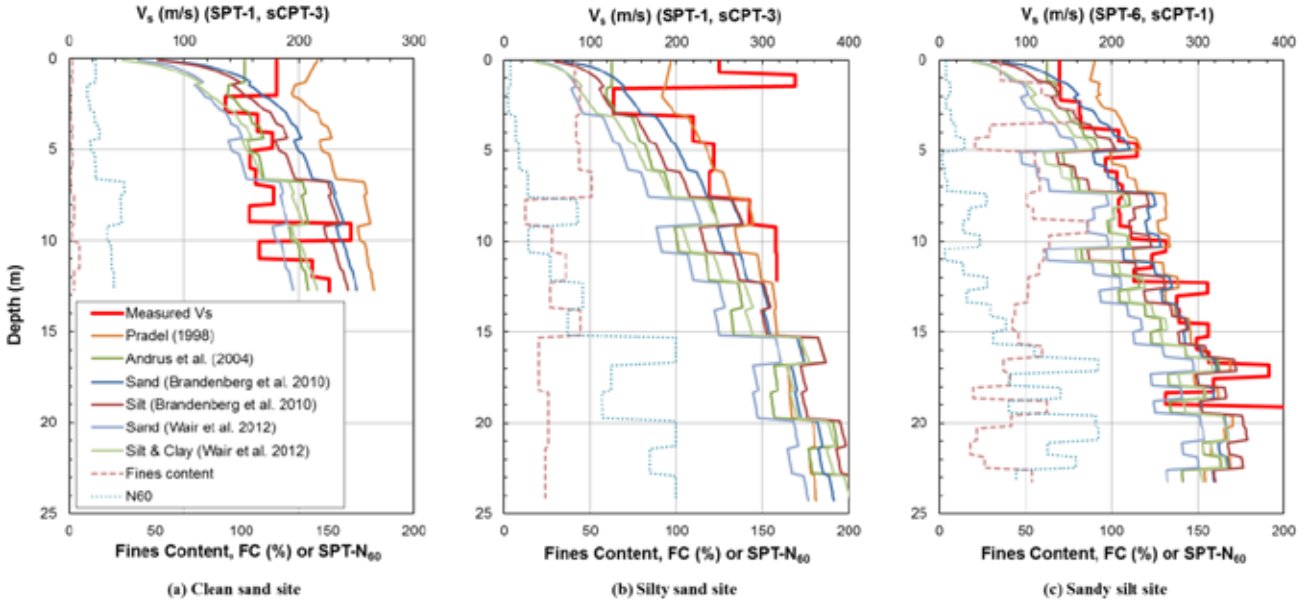

Figure 1. V_s profiles of sites predominated by clean sands, silty sands, and sandy silts.

2 EFFECT OF FINES CONTENTS

In previous studies, different correlation equations were developed by researchers for different soil types, such as sand, silt, clay, and/or gravel. The reason for this may have been that most of these equations were developed based on previous data which did not include detailed information for soil classification but relied on simple soil type classification. In daily practice, engineers can become confused when they encounter a transiting soil type such as silty sands and sandy silts as shown in Figure 1(b) and (c).

Figure 1 shows three typical soil profiles from sites predominately composites of (a) clean sands, (b) silty sands with FC varing from 12 to 50%, and (c) sandy silt with FC up to 90%. The measured V_s profiles are compared with those predicted using various methods (Pradel 1998, Andrus et al. 2004, Brandenberg et al. 2010, Wair et al. 2012). Pradel's equation does not provide a direct correlation between V_s and SPT-N, but an equation calculating G_0 as a function of mean effective confining stress σ_m' and corrected blowcounts $(N_1)_{60}$. This was originally proposed by Seed & Idriss (1970) and Seed et al. (1984). Andrus et al. (2004) utilized stress corrected shear wave velocity V_{s1} correlated to $(N_1)_{60}$. Both equations were utilized to calculate the uncorrected V_s values in Figure 1.

It can be seen from Figure 1 that if FC is very low (clean sand) and N_{60} is relatively high, most of current correlation equations tend to overestimate V_s (Figure 1(a)), while if FC is relatively high (silty sand or sandy silt) and N_{60} is relatively low, most of current correlation equations tend to underestimate V_s (Figures 1(b) and 1(c)),. The author believe that this inconsistency overwhelmingly demonstrates that FC is one of the critical factors influencing V_s.

3 DATA COLLECTION

In order to correlate various field measurements, a specially designed field investigation program was

set up and performed (Yi, 2014). Soil conditions underlying test site were explored by means of three groups of exploratory borings and SCPT soundings. Each of the three groups included two exploratory borings (using a standard SPT sampler and a modified California (MC) sampler, respectively) and one SCPT sounding, placed on vertexes of an approximately equilateral triangle forming a circumcircle approximately 3 m in diameter. The layout and distance were established so as to ensure the comparability of the soil profiles but at the same time not affect the adjacent SPT or SCPT results.

3.1 *Measurement of SPT-N values*

The soil borings were drilled with hollow-stem auger, per ASTM D6151, using a truck-mounted CME 75 drill rig equipped for soil sampling. Standard SPT blowcounts were obtained at approximately 0.75 m intervals. Relatively undisturbed samples were obtained at the same depth using a MC sampler in order to test field density. Samplers were driven with an automatic hammer that drops a 63.5-kg weight 76 cm for each blow. Blowcounts were recorded. Relatively undisturbed as well as bulk samples obtained were returned to the laboratory in sealed containers for filed density and FC tests.

3.2 *Measurement of V_s*

SCPT soundings were performed per ASTM D-5778, utilizing a 25-ton truck mounted CPT rig. A seismic pizeocone with tip surface area of 10 cm^2 and friction sleeve area of 150 cm^2 was used. A pore pressure transducer was also utilized. The CPT cone was pushed to practical refusal between 20 and 21 meters below existing ground surface. Shear wave velocity was measured at 0.75 m interval.

3.3 *Laboratory Testing*

Included in the laboratory testing program were field moisture content and field dry density tests on all of the relatively undisturbed samples. Fines content testing was performed on all samples obtained with the standard SPT sampler. Atterberg limit testing was conducted on selected silty soils as an aid to classification.

3.4 *Other data collection*

In order to provide a larger sample size, the author also collected measured *SPT-N*, V_s and FC from various sites spread from northern to southern California (Boulanger et al. 1995). For those sites, SPT borings were placed generally no more than 3 m from SCPT soundings. A total of 188 data sets were collected. 9 of those were considered extreme and were removed from this regression analysis.

4 STATISTICAL REGRESSION ANALYSIS

In the opinion of the author, for low plasticity sandy to silty soils, the factors influencing V_s include SPT blowcounts (N_{60}), fine contents (FC), normalized mean effective confining stress (σ'_m/P_a) and median grain size (D_{50}). The general expression of correlation is in following form:

$$V_{sc} = \beta_0 \cdot (N_{60})^{\beta_1} \cdot (FC)^{\beta_2} \cdot \left(\frac{\sigma'_m}{P_a}\right)^{\beta_3} \cdot (D_{50})^{\beta_4} \qquad (3)$$

where, $\sigma'_m = \left(\frac{1+2K_0}{3}\right)\sigma'_v$ and β_0, β_1, β_2, β_3, and β_4 are constants that were obtained by regression analysis. K_0 = coefficient of geostatic horizontal stress ($K_0 = \sigma'_h/\sigma'_v$). Due to the lack of available D_{50} data, β_4 was assumed to be 0 in this study. V_{sc} = calculated V_s in *m/s*.

Eq. (3) can be rewritten as a polynomial in *log - log* form. By using the Data Analysis tool in Microsoft Excel, a multiple regression analysis was performed for a total of 179 valid data sets. Table 1 shows the summary of the regression statistics.

Table 1. Summary of regression statistics

Regression Statistics	
Multiple R	0.859
R Square	0.737
Adjusted R Square	0.733
Standard Error	0.072
Observations	179

	Coef.	*Standard Error*	*t Stat*	*P-value*	*Lower 95%*	*Upper 95%*
Intercept	2.3102	0.0344	67.2137	0.0000	2.2423	2.3780
$LogN_{60}$	0.0195	0.0195	0.9994	0.3190	-0.0190	0.0580
LogFC(%)	0.0272	0.0105	2.5866	0.0105	0.0065	0.0480
$Log(\sigma_m'/P_a)$	0.3846	0.0289	13.3055	0.0000	0.3275	0.4416

The residuals are plotted in Figure 2 as functions of N_{60}, FC, and σ'_m/P_a, respectively. The ±1 standard deviation lines (±1σ) are also included in Figure 2. Figure 2 shows that the majority of the residuals fall within the ±1σ range. For ±1σ, the possible error in the predicted V_s using Eq. (3) is approximately 17.8%.

Figure 3 shows the line fit plots of measured and predicted V_s versus N_{60}, FC, and σ'_m/P_a, respectively. These plots show that the measured V_s exhibits more dispersion with respect to N_{60} and FC than to σ'_m/P_a.

Utilizing the constants obtained from the statistical regression analysis, measured shear wave velocity data could be normalized to other variables in order to demonstrate the influence of only one variable as shown in Figure 4. These figures indicate that the influence of fine contents in predicting V_s is as important as that of blowcounts but appears to be lower than that of mean effective confining stress.

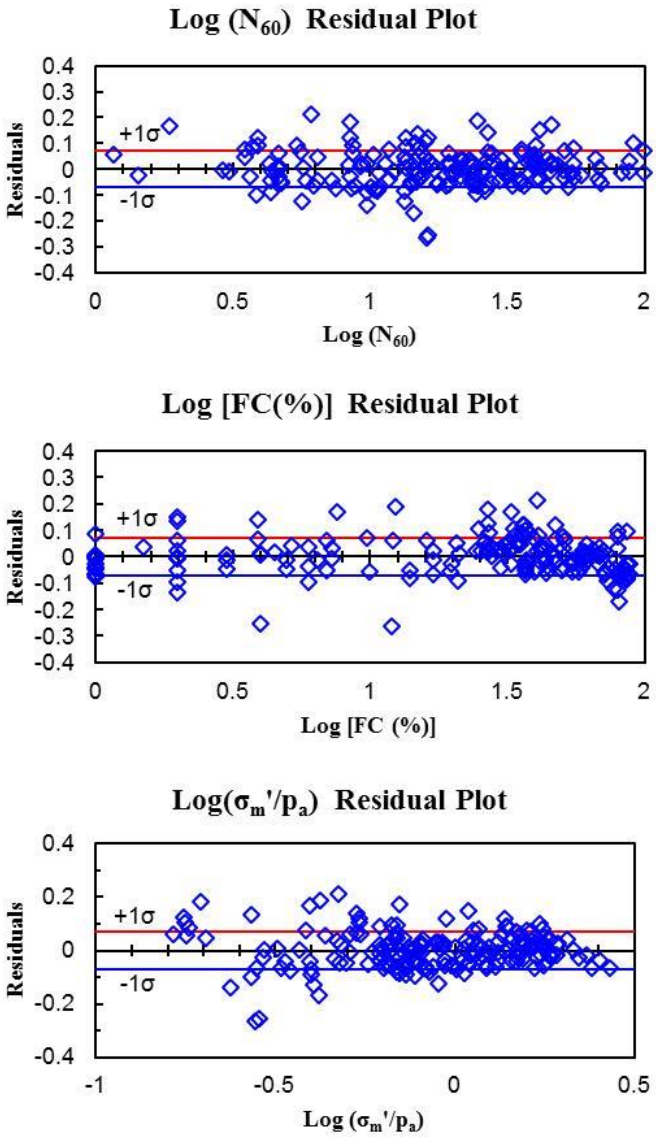

Figure 2. Residual plots

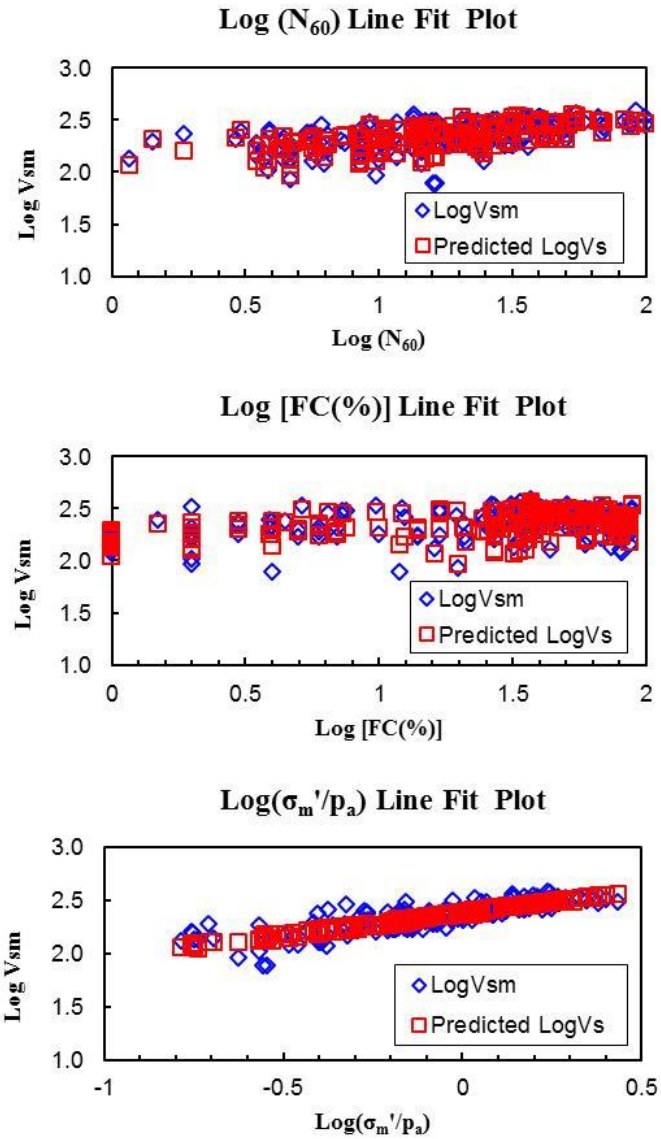

Figure 3. Line fit plots

This may be due in part to the small sample size used in this study. It is expected that with more measured data sets, N_{60} and FC may show more influence in predicting V_S.

The comparison of measured and calculated shear wave velocities is shown in Figure 5 in quantile-quantile plot. The circular marks show calculated V_S using the regression constants shown in Table 1. Ideally, the calculated and measured data should be of 1:1 regression line. However, the results indicate that the regression analysis constants underestimate the calculated V_S by approximate 3%. By adjusting the *intercept coefficient* shown in Table 1, this underestimation can be corrected as shown as diamond shaped marks in Figure 5. Table 2 shows the adjusted constants for Eq. (3) for low plasticity sandy to silty soils with a Holocene geologic epoch.

Table 2. Summary of regression constants (σ'_m/P_a)

Geologic epoch	β_0	β_1	β_2	β_3	β_4
Holocene	210.4	0.0195	0.0272	0.3846	0.0

4.1 *Correction for low confining stresses*

The σ'_m/P_a term in Eq. (3) tends to yield very low values near the surface where the stress ratio is very low. This may significantly deviate from actual site condition. In the simplified liquefaction calculation method, an overburden stress correction factor, C_N, is introduced to correct N_{60} to the equivalent value, $(N_1)_{60}$, that would have been obtained in sand if the vertical effective stress had been 1 atm. The C_N value is limited to a maximum value of 1.7 because of practical considerations and the fact that the equations in the method were not derived for very low effective stresses (Idriss & Boulanger, 2008).

$$C_N = \left(\frac{P_a}{\sigma'_v}\right)^{0.5} \leq 1.7 \quad (4)$$

With the same consideration and assuming K_0 of 0.5 for normally consolidated soils, the normalized mean effective confining stress in Eq. (3) should be taken as

$$\sigma'_m/P_a \geq 0.23 \quad (5)$$

when the calculated value is too small.

4.2 *Regression for overburden pressure, σ'_v*

In Eq. (3), the calculation of σ'_m requires a known K_0. In general, laboratory data on small triaxial specimens and instrumented oedometer tests indicate that the following relationship can be adopted in uncemented sands and well-behaved clays of low to medium sensitivity (Mayne 2007):

$$K_0 = (1 - sin\phi')OCR^{sin\phi'} \quad (6)$$

where OCR = over-consolidation ratio and ϕ' = effective frictional angle of soil. Various methods are available for the calculation of the OCR and ϕ' (Mayne 2007 and Yi 2015). For overconsolidated soils, some iteration is required in the calculation.

To avoid iterating calculations, regression can be performed directly on the effective overburden pressure.

$$V_{sc} = \beta_0 \cdot (N_{60})^{\beta_1} \cdot (FC)^{\beta_2} \cdot \left(\frac{\sigma'_v}{P_a}\right)^{\beta_3} \cdot (D_{50})^{\beta_4} \quad (7)$$

The regression results for Eq. (7) indicate a R^2 of 0.595 which is lower than R^2 of 0.737 when regressed with respect to σ'_m/P_a. Table 3 shows the summary of constants.

Table 3. Summary of regression constants (σ'_v/P_a)

Geologic epoch	β_0	β_1	β_2	β_3	β_4
Holocene	157.0	0.0831	0.0579	0.2385	0.0

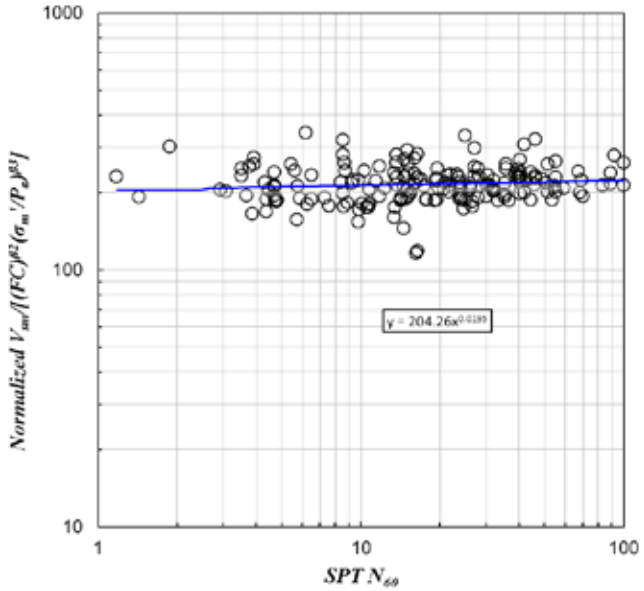

Figure 4(a). Relationship of normalized V_s versus SPT N_{60}

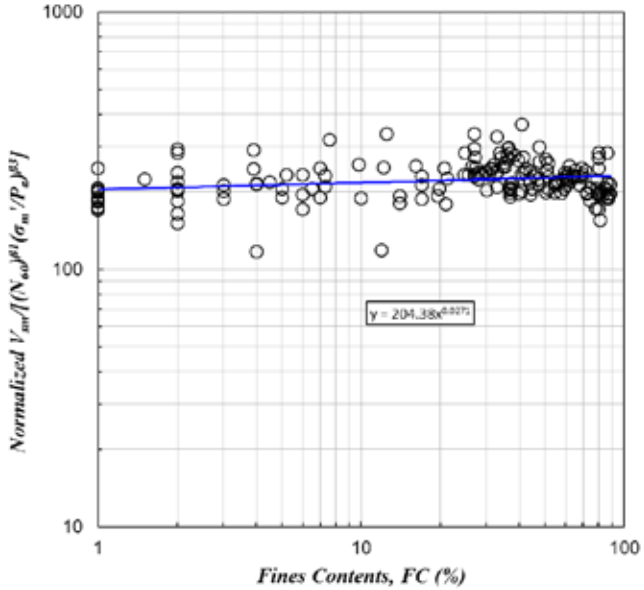

Figure 4(b). Relationship of normalized V_s versus FC

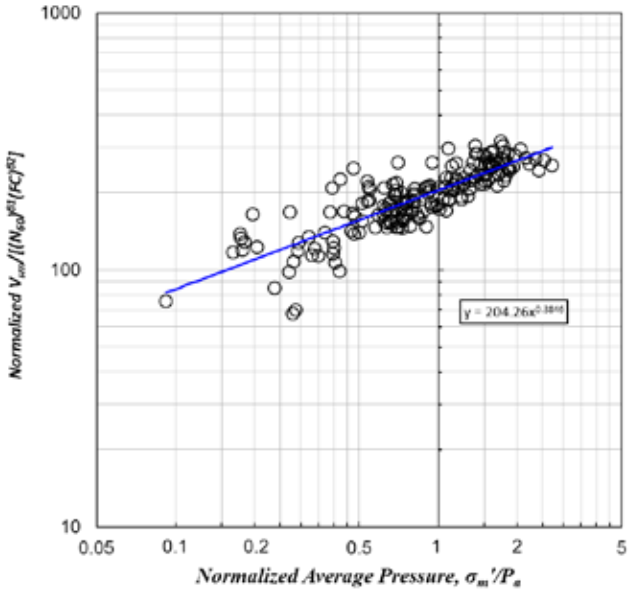

Figure 4(c). Relationship of normalized V_s versus σ'_m/P_a

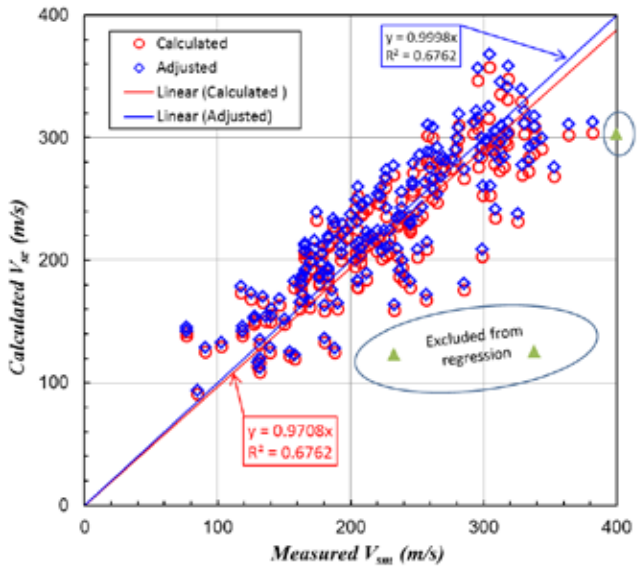

Figure 5. Quantile-quantile plot showing measured and calculated V_s

4.3 *Comparison of V_s Profiles*

Eq. (3) was used to predict V_s for the soil profiles shown in Figure 1. The results are shown in Figure 6 which indicates that in general, Eq. (3) provides a better prediction of V_s for soil profiles varying from clean sand to sandy silt.

5 CONCLUSIONS

A new empirical equation for shear wave velocity prediction based on SPT profile data was proposed in this paper using statistical regression method. Based upon recent studies by the author, the proposed new equation not only considers the influence of confining stresses or overburden stress but also the influence of fine contents. Comparison of V_s profiles show that the proposed equation provides better prediction of V_s for soil profiles which vary from clean sand to sandy silt.

6 ACKNOWLEDGEMENTS

The authors appreciate the support of Mr. Robert J. Johnson for this study and his review of the manuscript.

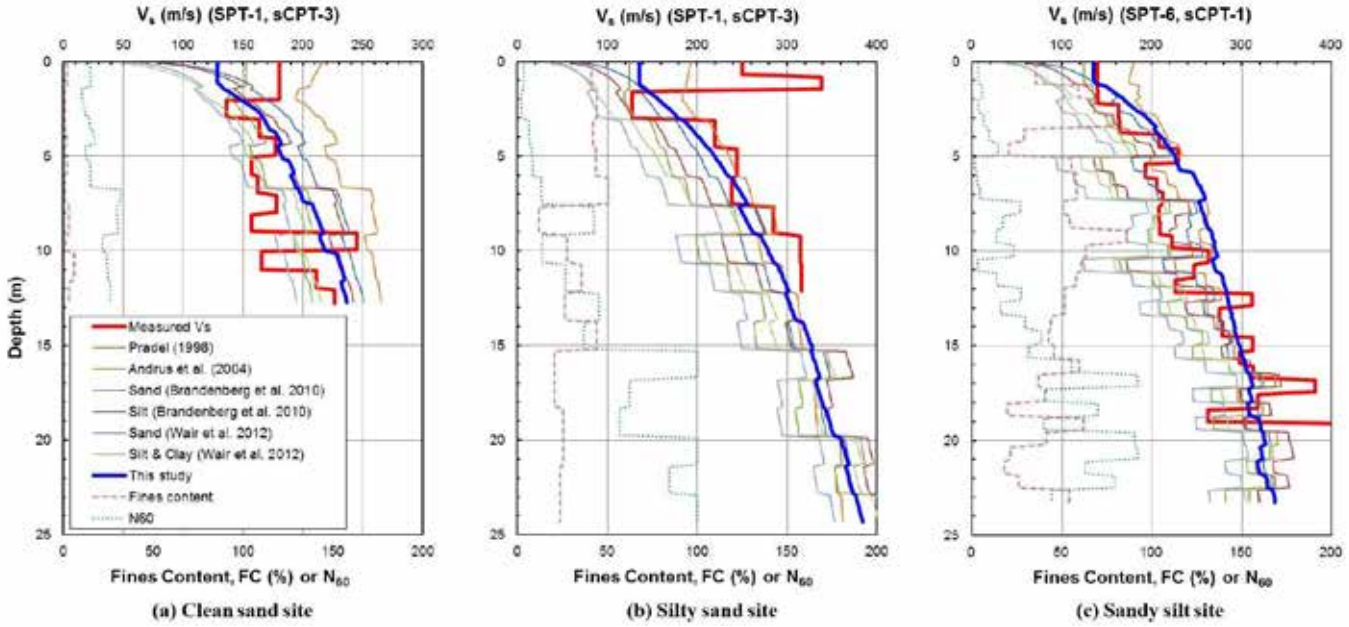

Figure 6. Comparison of measured and predicted V_s profiles of sites predominated by clean sands, silty sands, and sandy silts.

7 REFERENCES

Andrus, R.D., & Stokoe, K.H., II. 2000, Liquefaction resistance of soils from shear-wave velocity, *Journal of Geotechnical and Geoenvironmental Engineering, ASCE, 126(11)*: 1015-1025.

Andrus, D. A., et al., 2004, Comparing Liquefaction Evaluation Methods Using Penetration-V_S Relationships, *Soil Dynamics and Earthquake Engineering*, Volume 24, Issues 9-10, October 2004, Pages 713-721.

Boulanger, R. W., et al. 1995. Investigation and evaluation of liquefaction related ground displacements at Moss Landing during the 1989 Loma Prieta earthquake. *Rep. No. UCD/CGM-95/02*, Ctr. for Geotech., Modeling, UC Davis, Calif.

Brandenberg, S. J., et al. 2010, Shear wave velocity as function of standard penetration test resistance and vertical effective stress at California bridge sites, *Soil Dynamics and Earthquake Engineering* 30 (2010) 1026–1035

Imai, T. 1977. P-and S-wave velocities of the ground in Japan, *Proc. 9th Int. Conf. on Soil Mechanics and Foundation Engineering*, vol 2, 127–32.

Idriss, I. M., & Boulanger, R. W. 2008. *Soil Liquefaction During Earthquake*, EERI Publication MNO‐12.

Kanai, K. 1966. Observation of microtremors, XI: Matsushiro earthquake swarm areas, *Bull. Earthq. Res. Inst.*, Vol. XLIV, Part 3, University of Tokyo, Tokyo, Japan.

Mayne, P.W., 2007, *Cone Penetration Testing*, National Cooperative Highway Research Program Synthesis 368, Transportation Research Board, Washington, DC

Ohta, Y. & Goto, N. 1976. Estimation of S-wave Velocity in Terms of Characteristic Indices of Soil, *Butsuri-Tanko*, Vol. 29, No. 4, 1976, pp. 34-41 (in Japanese)

Ohta, Y. & Goto, N. 1978. Empirical shear wave velocity equations in terms of characteristic soil indexes, *Earthq. Eng. Struct. Dyn.*, 6:167–187

Pradel, D., 1998, Procedure to Evaluate Earthquake-Induced Settlement in Dry Sand Soils, *Journal of Geotechnical and Geoenvironmental Engineering*, Volume 124, No. 4.

Robertson, P. K., et al. 1992. Seismic cone penetration test for evaluating liquefaction potential under cyclic loading. *Can. Geotech. J.*, Ottawa, 29, 686–695.

Seed, H. B.·& Idriss, I. M. 1970. Soil Moduli and Damping Factors for Dynamic Response Analyses, *Report No. EERC 70-10*, UC Berkeley, Calif.

Seed, H. B., et al. 1986. Moduli and damping factors for dynamic analyses of cohesionless soils, *Report No. EERC UCB/EERC-84-14*, UC Berkeley, Calif.

Sykora, D. W. 1987. Creation of a data base of seismic shear wave velocities for correlation analysis. *Geotech. Lab. Miscellaneous Paper GL-87-26*, U.S. Army Engineer Waterways Experiment Station, Vicksburg, Miss.

Yi, F., 2014, Estimating soil fines contents from CPT data, *3rd International Symposium on Cone Penetration Testing,* May 12-14, 2014 - Las Vegas, Nevada

Yi, F., 2015, *GeoSuite©,* ‐ A Comprehensive Package for Geotechnical and Civil Engineers", http://geoadvanced.com/

Geotechnical and Geophysical Site Characterisation 5 – Lehane, Acosta-Martínez & Kelly (Eds)

Application of dynamic cone penetrometer for measuring active thaw layer depth

H-K.Yoon
Daejeon University, Daejeon, Korea
Y.S. Kim & S.S. Hong
Korea Institute of Civil Engineering and Building Technology, Gyonggi-do, Korea
Y-H. Byun
University of Illinois at Urbana-Champaign, IL, USA
J-S. Lee
Korea University, Seoul, Korea

ABSTRACT: The Dynamic Cone Penetrometer (DCP) has been widely applied to estimate the subsurface characterizations by using penetration resistance. The objective of this study is to enlarge the application of DCP for detecting the active layer in freezing and thawing region. The Arctic area, located in Ny-Alseund, Svalbard, is selected to investigate the thickness of active layer through DCP. The experiment is started from surface to a depth of 800mm. The penetration depth according to every blow by impacting hammer is recorded. The three layers are divided by DCP and the thickness of active layer is investigated to the depth of 200mm through the minimum value of DCP. The thickness of active layer is also estimated by using the maximum ground temperature profile and the thickness of active layer based on the two methods show the good agreement. This study suggests that the DCP is useful instrument for investigating the thickness of active layer.

1 INTRUCTION

The active layer is defined to the depth, which is subjected to freezing and thawing, and thus, it is generally estimated to the depth above permafrost (Associate Committee on Geotechnical Research 1988). The geotechnical structure in frozen soil may be easily affected by active layer and the characterization of active layer should be investigated to enhance the safety.

The experimental and numerical methods have been studied to detect the active layer. The experimental methods include mechanical probing, soil temperature monitoring, visual measurement, soil moisture measurement, and vertical movement monitoring (Byun et al. 2014). The numerical method has been developed to investigate the spatial characterization of active layer (Nelson et al. 2001; Oelke et al. 2003). However, the applications of previously suggested techniques are very few and thus, the Dynamic Cone Penetrometer (DCP) as an alternative technique is considered to estimate active layer in this study. This paper describes the selected instrument (DCP) and the characterizations of applied site are also explained. Finally, the active layer deduced by DCP is demonstrated and it is compared with that based on the profile of ground temperature.

2 DYNAMIC CONE PENETROMETER

The Dynamic Cone Penetrometer (DCP) has been generally applied to obtain the characterization of subgrade as an impacting method. The DCP consists of driving rod, anvil and hammer guide to enhance the efficiency of penetration with impact as shown in Figure 1. The impact is performed by a hammer with fixed height and force of 575mm and 78.8N, respectively. The diameters of DCP and driving rod are designed to 24mm and 16mm. And the apex angle of cone tip of DCP is 60°.

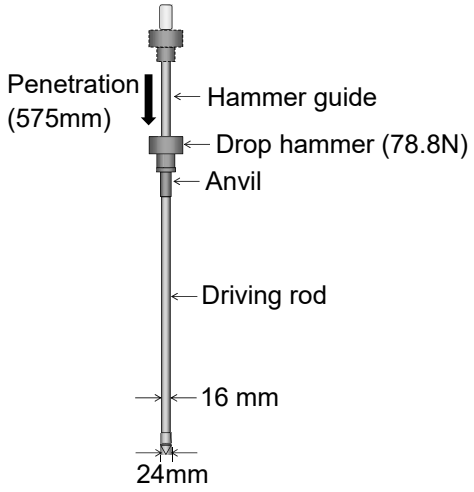

Figure 1. Schematic drawing of Dynamic Cone Penetrometer (DCP).

3 CHARACTERIZATION OF TESTING SITE

The Ny-Alseund in the northwestern part of Spitsbergen, Svalbard, Norway (latitude 78°55'N, longitude 11°56'E) was selected to carry out the penetration test

of DCP to find the active layer. In particular, the testing site is located at research station Dasan, which is a Korean Arctic Research Base as shown in Figure 2.

Figure 2. Photograph of testing site of DCP. The red circle denotes the research station Dasan.

4 APPLICATION TEST AND RESULT

The DCP test was performed from surface of ground at summer and the impacts were expired at the depth of 74cm due to the limitation of penetrated force. The penetration depth of DCP according to every blow was obtained and the differences between measured depths are plotted as shown in Figure 3. The penetration depth is recorded to 3cm at near the surface and the values decrease to average 0.8cm below the depth of 20cm. The three layers are divided through huge (between surface and 10cm), middle (between 10cm and 20cm) and constant (below 20cm) penetration depth. And thus, the active layer is determined to 20cm because it is estimated to permafrost zone below the depth of 20cm. Furthermore, after a depth of 20cm, the calculated values show the asymptotic trend with a depth of 740cm.

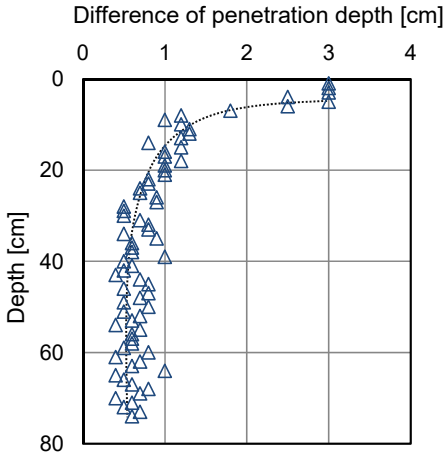

Figure 3. Result of DCP. The dotted line shows the trend line.

The temperature of ground has been continuously measured by using T-type thermocouples and the measured values were demonstrated in Figure 4. The solid and dotted lines show the temperature variation measured by summer and winter conditions. Even though the measured temperature shows different range according to season, the temperature shows nearly constant below the depth of approximately 20cm. Note that the active layer is estimated to about 20cm because the depth is above permafrost experienced by freezing and thawing.

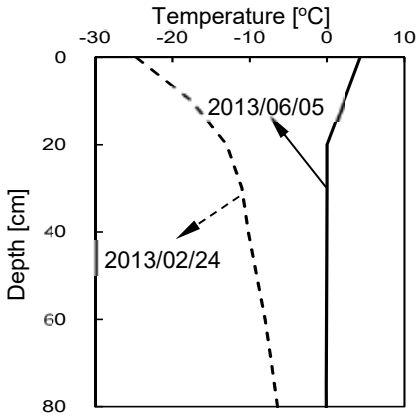

Figure 4. Measured temperature profiles under conditions of summer (2013/06/07) and winter (2013/02/24)

5 CONCLUSION

The active layer was investigated by using the Dynamic Cone Penetrometer (DCP) in Ny-Alesund, Svalbard, Norway. The DCP shows the active layer around 20cm in testing site and the active layer based on the temperature distribution in ground shows also similar values. This study denotes the DCP is an alternative technique for determining active layer in frozen soil.

6 ACKNOWLEDGEMENT

This research was supported by a grant (15IFIP-B067108-03) from Industrial Facilities & Infrastructure Research Program funded by the Ministry of Land, Infrastructure and Transport of Korean government.

7 REFERENCES

Associate Committee on Geotechnical Research. 1988. Glossary of permafrost and related ground-ice terms. Tech. Memo. 142, Natl. Res. Counc. Of Can., Ottawa, Ont., Can.

Nelson, F. E., N. I. Shiklomanov, G. R. & Mueller. 2001. Subsidence risk from thawing permafrost. Nature 410(6831): 889-890.

Oelke, C., T. Zhang, M. C. & Serreze, R. L. Armstrong. 2003. Regional-scale modeling of soil freeze/thaw over the Arctic drainage basin. Journal of Geophysics Research 108(D10): 4314.

Byun, Y. H., Yoon, H. K., Kim, Y. S., Hong, S. S., & Lee, J. S. (2014). Active layer characterization by instrumented dynamic cone penetrometer in Ny-Alesund, Svalbard. Cold Regions Science and Technology, 104: 45-53.

Theme 13. Case Histories

Geotechnical and Geophysical Site Characterisation 5 – Lehane, Acosta-Martínez & Kelly (Eds)

Two-Dimensional Non-linear Dynamic Response of a Heap Leach Pad Located in Peru

F.C. Perez
Amec Foster Wheeler Peru

J.D. Ale
Universidad San Ignacio de Loyola, Lima, Peru

ABSTRACT: In this research a dynamic characterization in function of mean stress of share wave velocities and his corresponding maximum shear modulus (V_s, G_{max}) of ROM (run of mine) ore stacking were carried out based on MASW survey. In addition a triaxial compression tests (consolidated undrained, CU of 6" diameter) have been carried out to determine the mechanical properties of the ROM ore stacking of sandstone crushed material. The study has focused on the understanding of the two-dimensional non-linear dynamic response of a heap leach pad located in a higher seismicity Andean region of Peru. This geostructure modeled in Finite Differences Method software (FLAC, Itasca) was subjected to an Operating Basis Earthquake (OBE) obtained from a spectral matching in the time domain (Abrahamson, 1993). A constitutive Mohr-Coulomb Model with stress-level dependent is used to simulate the stress-strain behavior of the ore material. The slope stability and the permanent deformations at the end of this excitation are evaluated. As well as, the development of the deformations during the earthquake are present here in.

1 INTRODUCTION

The current technology of lixiviation process has been widely developed since the last thirty years, becoming this in an efficient method to treat oxidized gold, silver and copper minerals and extract precious metals from small and shallow ore deposits. Important mining operations in regions with a higher seismic activity have the leaching process as their main mineral extraction method. This scenery have generated the necessity for further knowledge in dynamic analysis in order to understand the dynamic response and optimize safely the civil and geotechnical designs of these mining structures. This paper studies a real case of a heap leach facility which the ore stack is composed of quartz-sandstone material.

2 PROPERTIES OF THE QUARTZ-SANDSTONE ORE MATERIAL SPECIMENS

2.1 *Physical Properties and Parameters*

In order to characterize the ROM material was performed a laboratory test program on three samples of quartz-sandstone ore material from a heap leaching project located in the Andean region of Peru. Figure 1 shows the grain-size distribution of the samples analyzed, considering a sample fraction of maximum particle size of 3 inches. The characteristics of these materials, including USCS classification, dry unit weight, and effective Mohr-Coulomb parameters (obtained from triaxial compression tests consolidated undrained TX-CU in 6-inch-diameter samples) are presented in Table 1.

The grain-size distribution of these quartz-sandstone ore materials is very variable, and according to UCSC these samples are classified as: SP-SM, GM, and GP-GM. The Mohr-Coulomb strength parameters determined from the 6" TX-CU tests vary, in terms of effective internal friction angle (ϕ'), from 36.4 to 38.8°. They also vary, in terms of effective cohesion (c), from 7 to 9 kPa.

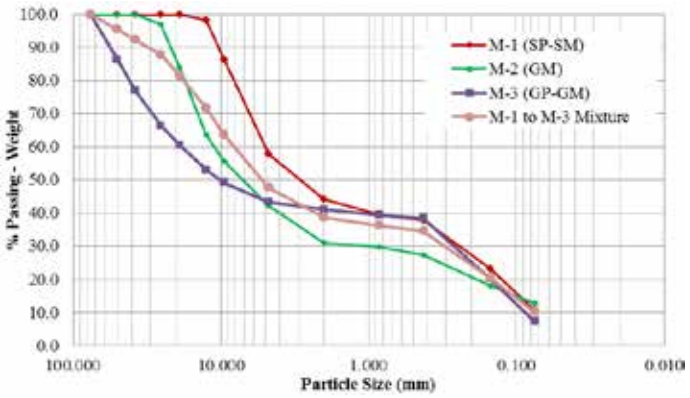

Figure 1. Grain-size distribution of angular quartz-sandstone ore material samples.

Table 1. Mechanical properties of the quartz-sandstone ore material.

Id	UCSC classification	Dry unit weight γ_d (kN/m^3)	Initial confining stresses, σ'_3 (kPa)	c' (kPa)	ϕ' (°)
M-1	SP-SM	17.1	600; 300; 150	7	36.4
M-2	GM	17.7	600; 300; 150	0	38.2
M-3	GP-GM	17.9	600; 300; 150	9	38.8

2.2 *Lithological Characterization*

The specimens tested were composed mainly of quartz-sandstone of fine to medium grain from the Chimu Formation in the northern Andes of Peru. This sedimentary formation is arranged in thick layers (over 0.50 m) and has great strength. It almost always is rough and steep. In some areas one can see the presence of silt-claystones and siltstones, which are sometimes interbedded with coal layers (Navarro et al., 2010). Loose materials from this formation usually have a granular nature with minimal fines content. They are primarily non plastic materials of angular to very angular shape, and with high resistance. Granular materials from the quartz-sandstones of the Chimu Formation are considered as competent material, potentially suitable for use as structural fill, drainage gravel, and rockfill.

2.3 *Multi-channel Analysis of Surface Waves (MASW) Survey*

Were estimated the maximum dynamic shear stress modulus (G_{max}) in *in-situ* conditions, shear-wave (V_s) velocities profiles were extracted from a geophysical investigation, based on a multi-channel analysis of surface waves (MASW) surveying performed on an *in-situ* M-3 sample. The MASW profile obtained from that area is shown in Figure 2.

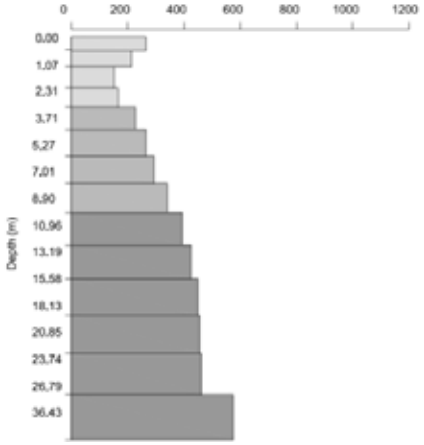

Figure 2. Profile of shear-wave velocity in depth over sample M-3 *in-situ* location.

3 GROUND-MOTION PARAMETERS

3.1 *Seismicity of the Region*

The Peruvian Andes, region where this geostructure is located, were formed as tectonic effect of the subduction of the Nazca Plate under the South American Plate. The rock mass in this region were subjected to strong deformations over 40 million years ago, during a period of intense volcanic activity 15 million years ago. The seismicity of this region is considered as higher, with registered data of about 110 epicenters of earthquakes of 4.0 M_w and epicentral depths <100 km located within 200 km. All historical earthquakes with magnitudes above 6.0 M_w have occurred over 100 km from the site.

3.2 *Earthquake Time History*

For the non-lineal dynamic analysis was selected an input signal considering an Operating Basis Earthquake (OBE), usually defined as the earthquake for which a structure is designed to remain its operational condition, with the damage being readily repairable following the event. Considering that the OBE is likely to occur during the design life of the structure and the seismicity of the region, was selected the seismic event of 5.7 M_w occurred in 01-03-2015 (according with the seismicity of the region), which location is presented in Figure 3.

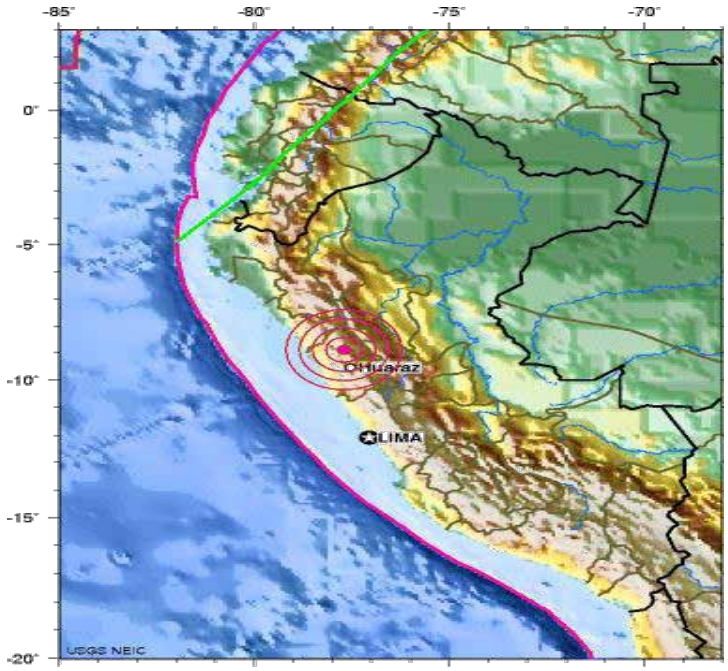

Figure 3. Location of earthquake 5.7 M_w occurred in 01-03-2015 (www.usgs.gov/).

3.3 *Site Response Spectrum for Design*

The design site response spectrum, presented in Figure 4, was previously calculated based on probabilistic methods, having a 2% probability of exceedance in 50 years.

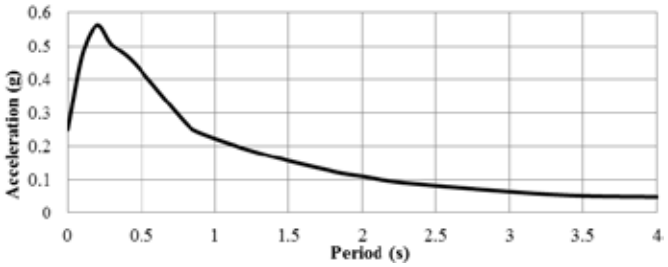

Figure 4. Design response spectrum.

3.4 *Shear Modulus for Granular Soils*

Most available data on maximum shear modulus (G_{max}) has been developed for either sand or gravelly soils. Because most soils have curvilinear stress-strain relationships, it will be appreciated that G_{max} is not constant but is usually expressed as the secant modulus determined for the specific value of shear strain. Seed and Idriss (1970) and Seed et al. (1986) have shown that G_{max} values for gravelly soils are strongly influenced by confining pressure (σ'_m, expressed in Equation 2), strain amplitude (γs), and void ratio (e), finding the relationship in Equation 1 that conveniently related G_{max} and σ'_m.

$$G_{\max} = 21.7 K_{2.\max} P_a \left(\frac{\sigma'_m}{P_a} \right)^{1/2} kPa \qquad (1)$$

$$\sigma'_m = \left(\frac{\sigma'_1 + \sigma'_2 + \sigma'3}{3} \right) \qquad (2)$$

where $G_{\max}$ = maximum shear modulus, $K_{2.\max}$ = shear modulus at small shear strains (10^{-4}%), σ'_{m} = mean effective confining stress, Pa = atmospheric pressure (100 kPa), and $\sigma'_{1,2,3}$ = maximum, intermediate and minimum effective stresses.

In order to obtain the main effective confining stress, a unit weight at moisture content of 5% was considered for M-3 embankment and at-rest earth pressure coefficient (k_0) of 0.5 was obtained considering the Equation 3 and ν=0.33 from TX-CU in the deformed sample at the end of the test. The $K_{2.\max}$ value presented was obtained from a parabolic function regression in a $\sigma'_m - V_s$ plot presented in Figure 5.

$$\nu = \frac{k_0}{1 + k_0} \qquad (3)$$

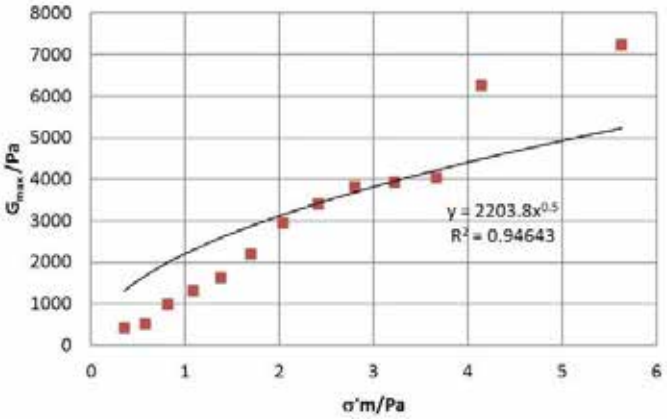

Figure 5. Determination of $K_{2.\max}$.

Where ν = poisson's ratio and k_0 = at-rest earth pressure coefficient.

The $K_{2.\max}$ value is obtained by the division of the x-coefficient of the adjusted parabolic equation in Figure 5 by 21.7 (Equation 1) obtaining a $K_{2.\max}$ = 101.55, as is shown in Table 2.

Table 2. Value of $K_{2.\max}$ in quartz-sandstone ore material.

ID	UCSC classification	MASW Depth (m)	G_{max}	
			$K_{2.\max}$	R^2*
M-3	GP-GM	0-36.43	101.55	0.94643

* R^2 is the adjusted R-squared value of the equation

3.5 *Internal Friction Angle*

The internal friction angles obtained from 6" CU-TX of the quartz-sandstone ore material were evaluated following the method proposed by Barton & Kjaersnly (1981) and expressed in Barton (2008). The estimated parameters used in Equation 4 are listed in Table 3, and are similar with those reported by Leps (1970) for similar frictional materials.

$$\phi = \phi_1 - \Delta\phi \log\left(\frac{\sigma'_3}{P_a} \right) \qquad (4)$$

where ϕ_1 and $\Delta\phi$ = reference friction angle (at $P'=P_a$) and friction angle reduction for every log cycle of stress level increase, respectively.

Table 3. Strength Parameters Used.

ID	UCSC classification	Average dry unit weight γ_d (kN/m^3)	Unit weight γ (kN/m^3)	ϕ (°)	$\Delta\phi$ (°)
M-1 to M-3 Mixture	GP-GM	17.5	19.0	37	5

3.6 *Finite Differences Element Model*

The 140-meter-high model conformed by heap leach stack (80 m high) and basement rock (60 m high) were discretized using a finite-differences grid composed of 35x170 regions in the vertical and horizontal directions, respectively. The special element size (Δl) of zones was 4 m according to Equation 5. The quartz-sandstone ore material was stacked in 1.5H:1V inter-bench slope (of benches of 8 m high and 9 m width) and 2.5H:1V global slope, placed above -3% slope surface of about 520 m over a total model length of 700 m.

$$\Delta l = \frac{\lambda}{8} \qquad (5)$$

where λ = wavelength associated with the highest frequency component that contains appreciable energy of the input wave.

Figure 6 shows the FLAC finite differences model along with the different material zones considered in the analysis and the history control points considered. A built-in Mohr-Coulomb model with stress-level dependent was implemented using the programming language FISH following the Equations 1, 2 and 4, this code was applied to quartz-sandstone ore material in order to obtain the distribution of G_{max} in function of σ'_m and the distribution of effective internal friction angle in function of σ'_3, as is shown in Figure 7 and 8, respectively.

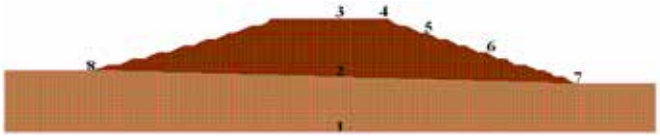

Figure 6. Profile FLAC finite differences model (with history points).

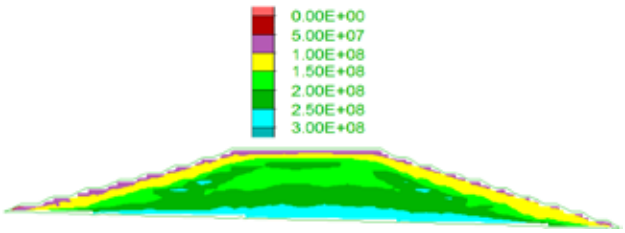

Figure 7. Distribution of G_{max} (Pa) in function of σ'_m

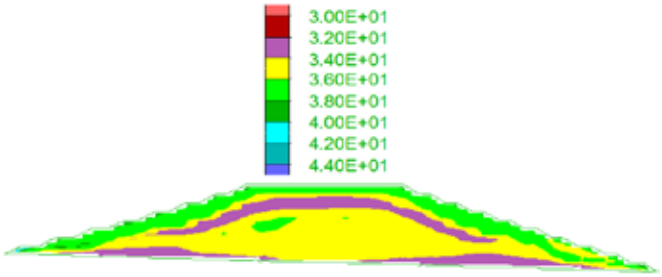

Figure 8. Distribution of effective internal friction angle (°) in function of σ'_3.

3.7 *Spectral Matching*

The time domain matching procedure was used to modify the historic OBE record and match its spectrum to the design spectrum at 5% damping, following the methodology proposed by Abrahamson (1992) and Hancock et al. (2006), Figure 9 present results of the

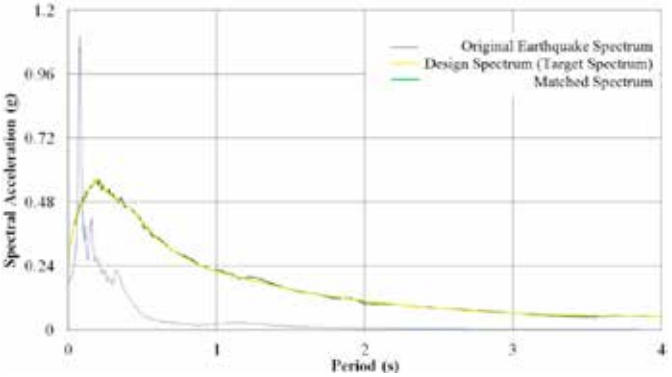

Figure 9. Spectral matching.

matching procedure application. Previously the original time history was corrected by baseline and filtering in order of the maximum frequency of 8 Hz, using the computer program EZ-Frisk (2011). Figure 10 (left) presents the component strong motion compatible with the site response spectrum, used in the dynamic analysis.

4 ANALYSIS RESULTS

4.1 *Acceleration Amplification*

The horizontal acceleration time history computed at the top of the leach pad (history point 3) due to OBE design imposition reached a maximum acceleration of about 0.5g, its value represents about 2 times the peak ground acceleration of the imposed signal (0.25g), as is shown in Figure 10a and 10b.

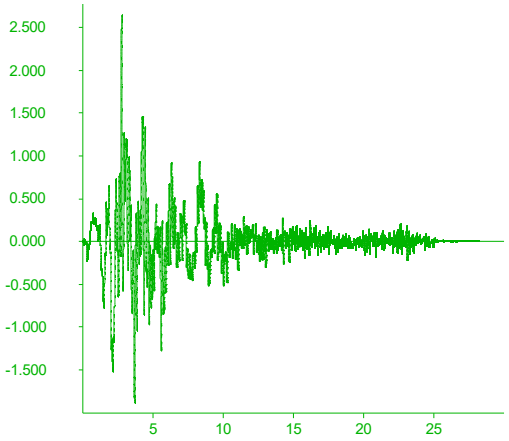

Figure 10a. Acceleration time history at the base of FLAC model a_x (m/s^2) vs t (s).

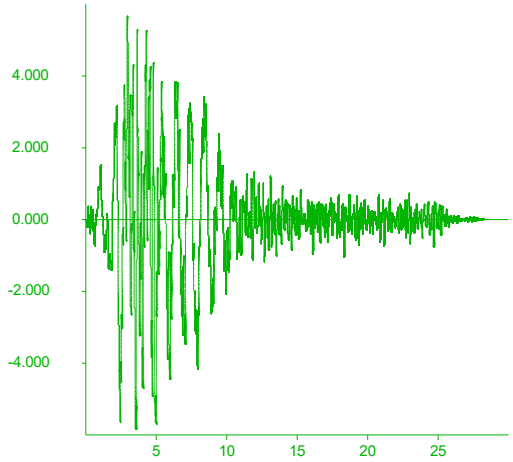

Figure 10b. Acceleration time history at the top of FLAC model a_x (m/s^2) vs t (s).

4.2 *Maximum Permanent Displacements*

Figure 11 and 12 shows the permanent horizontal and permanent displacements contours in the body of the leach pad, respectively, as obtained by applying the input motion at the base of the model. The horizontal displacements reach their maximum values near to the slope of the ore stack in the benches, obtaining deformations of 0.5 m, decreasing in magnitude deepening inside the slope at 0.1 m until null displacements.

The vertical reach their maximum values near to the slope of the ore stack in the benches, obtaining deformations of 0.25 m, decreasing in magnitude deepening inside the slope at 0.05 m until null displacements.

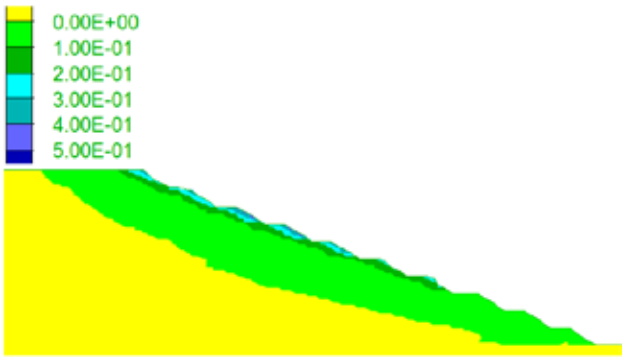

Figure 11. Horizontal displacements in meters.

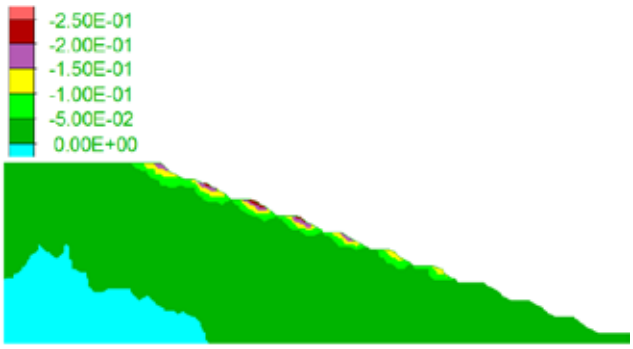

Figure 12. Vertical displacements in meters.

4.3 *Time History Displacement*

Figure 13a and 13b shows displacement time histories horizontal and vertical relatives to the model base, respectively. These relative displacements where computed in control points 4, 5 and 6 located over the downstream slope. The displacement time histories are very irregular and are plotted by sharp alternate peaks, as a result of the back and forth motion until the end of the excitation. The control point 5 reached the maximum permanent displacements about 0.5 m and 0.25 m in horizontal and vertical axes, respectively.

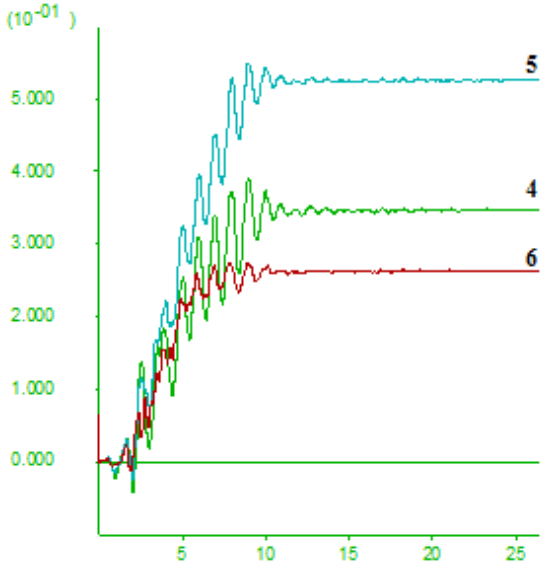

Figure 13a. Horizontal displacements in history points 4; 5 and 6 in meters.

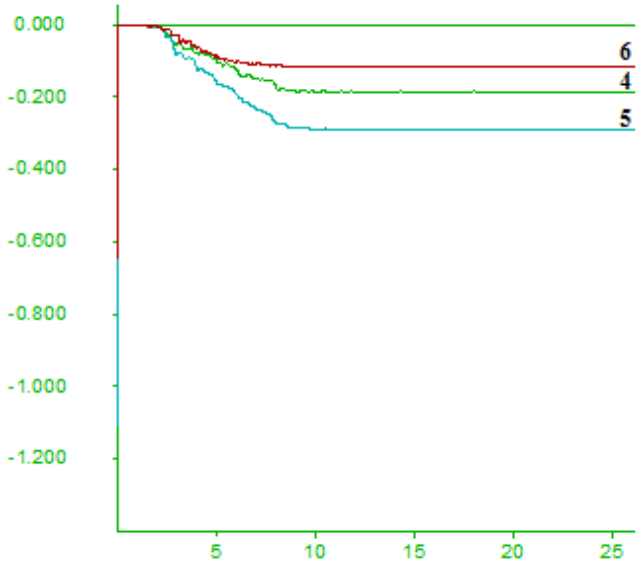

Figure 13b. Vertical displacements in history points 4; 5 and 6 in meters.

Horizontal time history displacements relative to the model base of control points located at the interface region 2, 7 and 8 are presented in Figure 14. The maximum deformation computed in this area reached values below 0.03 m in control points 7 and 8.

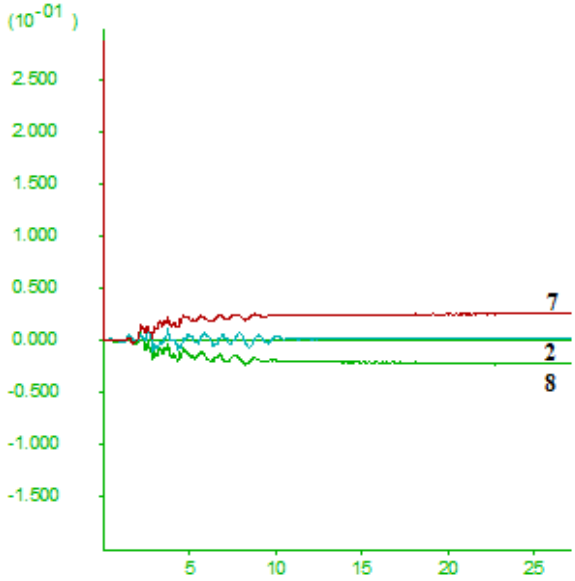

Figure 14. Horizontal displacements in interface history points 2; 7 and 8 in meters.

5 CONCLUSIONS

Using the finite differences method code FLAC, the dynamic behavior in operation-term of a leach pad was modeled and simulated. A built-in Mohr-Coulomb model with stress-level dependent was used for the ore material. From the results of the dynamic analysis it can be concluded that the geostructure will remain safely during an OBE design occurrence, with maximum permanent deformations at the upper region of the downstream benches of about 0.5 m in horizontal and 0.25 m in vertical, permanent deeper deformations in the downstream slope region of about 0.1 m in horizontal and 0.05 m in vertical were registered as well.

The acceleration time history obtained shows an amplification of about 2 times considering the history points located at the top and at the base of the model. The overall deformation pattern of the heap leach facility mainly consists in a slope compaction associated with lateral deformation. The main objective of this stability assessment was to quantify the permanent deformations product of the inertial forces induced by the imposition of an OBE design, the existence of a low permeability soil liner interface (liner system) between the ore stack and soil foundation was not considered for this analysis.

6 REFERENCES

Abrahamson, N. A. 1992. Non-stationary Spectral Matching, Seismological Research Letters 1992; 63(1), 30.

Barton, N., and Kjaernsli, B. 1981. Shear Strength of Rock-Fill, ASCE Journal of the Geotechnical Engineering Division, V. 107(GT7): 873-891.

Barton, N. 2008. Shear Strength of Rock-Fill, Interfaces and Rock Joints, and their Points of Contact in Rock Dump Design, Keynote Address, Rock Dump, Ed. A. Fourie, Perth, Australia.

Coulomb CA. 1976. Sur une application des règles maximis et minimis a quelques problèmes de statique, relatives a l'architecture. Acad Sci Paris Mem Math Phys; 7: 343–382.

Gazetas, G. and Dakoulas, P. 1992. Seismic Analysis and Design of rockfill Dams: State-of-the-Art, Soil Dynamics and Earthquake Engineering 1991; 11: 27-61.

Hancock, J., Watson-Lamprey, J., Abrahamson, N. A., Bommer, J. J., Markatis, A., McCoy, E. and Mendis, R. 2006. An improved method of matching response spectra of recorded earthquake ground motion using wavelets, J. of Earthquake Eng.; 10 (Special Issue 1), 67-89.

ITASCA. 2005. Fast Lagrangian Analysis of Continua (FLAC), Version 5, User's Guide. Itasca Consulting Group, Inc.

Janbu, N. 1963. Soil Compressibility as Determined by Oedometer and Triaxial Tests, European Conference on Soil Mechanics and Foundation Engineering, Wissbaden, Germany, 1: 19-25.

Leps, T.M. 1970. Review of Shear Strength of Rock-Fill, ASCE Journal of the Soil Mechanics andFoundation Engg. Division, V. 96 (SM4), pp. 1159-1170.

Mohr O. 1900. Welche Umstände bedingen die Elastizitätsgrenze und den Bruch eines Materials? Zeit des Ver Deut Ing.; 44: 1524–1530.

Navarro, P., Rivera, M., and Monge, R. 2010. Geología y Metalogenia del Grupo Calipuy (Volcanismo Cenozoico) Segmento Santiago de Chuco, Norte del Perú, Boletín N°28 Serie D; Estudios Regionales; INGEMMET.

Risk Engineering, Inc. 2011, EZ-FRISK™ Online User's Manual, EZ-FRISK™ Version 7.62, Boulder, Colorado.

Seed, H.B. and Idriss, I.M. 1970. Soil Moduli and Damping Factors for Dynamic Response Analysis[R]. U.C. Berkeley, Calif.: EERC.

Seed, H.B., Wong, R.T., Idriss, I.M. et al. 1986. Moduli and Damping Factors for Dynamic Analyses of Cohesionless Soils, Journal of Geotechnical Engineering; 112:11: 1016-1032.

Geotechnical and Geophysical Site Characterisation 5 – Lehane, Acosta-Martínez & Kelly (Eds)

Ultimate resistance and settlement of foundations using Ménard pressuremeter test results: case of bored piles

R. Bahar, N. Alimrina & L. Djerbal
University of Sciences and Technology Houari Boumediene, Laboratory of Enviromnent, Water, Geomechanics and Structures (LEEGO), Algiers, Algeria

ABSTRACT: Ménard pressuremeter test data are used for estimating the bearing capacity and settlement of bored piles. The Ménard pressuremeter tests carried out on soils in different regions of Algeria are analyzed by the numerical method called PRESSIDENT taking into account the Duncan and Chang model. Numerical calculations taking into account the rheological parameters derived from this method are performed in order to analyze the behaviour of a single bored pile subjected to a static axial load of some projects. The predictions are compared to the measured data, and show the applicability of the approach.

1 INTRODUCTION

The Ménard pressuremeter test can be performed in all kinds of grounds. It provides the measurement of in situ stress-strain response of soils, and the geotechnical engineer with both a failure parameter (the limit pressure p_{LM}) and a deformation parameter (the presssuremeter modulus E_M). It is a particularly good tool to analyze axial bearing capacity, pile settlement and behaviour under lateral loading (Briaud 1995). Direct correlations between the measured parameters and the design parameters are used for estimating the bearing capacity and settlement of piles, and for their behaviour under lateral loading (Ménard 1957, MELT 1993).

Another trend of interpretation of these tests consists of identifying the usual soil parameters required by simple constitutive models for soils in numerical calculations. This paper deals with the estimation of bearing capacity and settlement of bored piles using the results of Ménard pressuremeter tests. The interpretation of Menard pressuremeter test results is performed by the method PRESSIDENT which is a numerical program developed to analyze this test taking into account the Duncan and Chang model (Bahar et al., 1995). Then, numerical calculations taking into account the rheological parameters derived from this method are performed in order to predict the behaviour of a single bored pile subjected to a static axial load. The predictions are compared to the measured data, and the empirical methods.

2 INTERPRETATION OF MENARD PRESSUREMETER TESTS

2.1 *PRESSIDENT method*

PRESSIDENT (Pressuremeter Identification) computer program is developed at the Ecole Centrale de Lyon, France (Boubanga, 1990; Bahar 1992). The determination of the parameters of the non-viscous and viscous constitutive model from the pressuremeter test consists in solving the inverse problem to find a set of parameters which minimize the difference between the experimental data, the pressuremeter curve defined as the applied pressure versus the cavity wall deformation, and the simulated curve (Bahar et al., 1995). Only the non-linear elastic Duncan model [described in several papers is presented in this study (Duncan & Chang, 1970). The hyperbolic stress-strain relationship is developed for incremental analyzes of soil deformations where nonlinear behavior is modeled by a series of linear increments. It takes into account a tangent modulus E_t and a bulk modulus B in the following form:

$$E_t = \left[1 - \frac{R_f\left(1-\sin\varphi\right)\left(\sigma_1-\sigma_3\right)}{2c\cos\varphi + 2\sigma_3\sin\varphi}\right]^2 K_e P_a \left(\frac{\sigma_3}{P_a}\right)^n \quad (1)$$

$$B = K_b P_a \left(\frac{\sigma_3}{P_a}\right)^m \quad (2)$$

k_e , k_b, n, m, R_f, c, φ are the model parameters.

Using the PRESSIDENT approach, these parameters are identified as follows. For cohesive soils, the pressuremeter tests can be considered as undrained. In these cases, the internal friction angle can be considered equal to zero. Then, the optimization proce-

dure only leads to the definition of the parameter k_e and the undrained cohesion c_u. Figure 1 shows an identification example using the non linear elastic Duncan model. For cohesionless soils, the pressuremeter tests can be considered as drained tests. Moreover, the cohesion of these materials is equal to zero. The procedure optimization procedure only leads to the definition of k_e end φ. For cohesive-frictional soils (general case), it will not be possible to determine c and φ if only one test is available, so it will be necessary to make an assumption for one of the two parameters c or φ. If two tests at two different depths can be analyzed it would be possible to define the three parameters: k_e, c and φ. For each depth it is possible to calculate the value of c and k_e corresponding to different given values of φ (20°, 25°,30°,...), so it is possible to determine several acceptable couples of values for c and φ. A representation of these acceptable values can be drawn for different tests realized at different depths (Fig. 2). The values of c and φ which have to be taken into account are the values acceptable for all the tests: intersection point between the different curves corresponding to different depths.

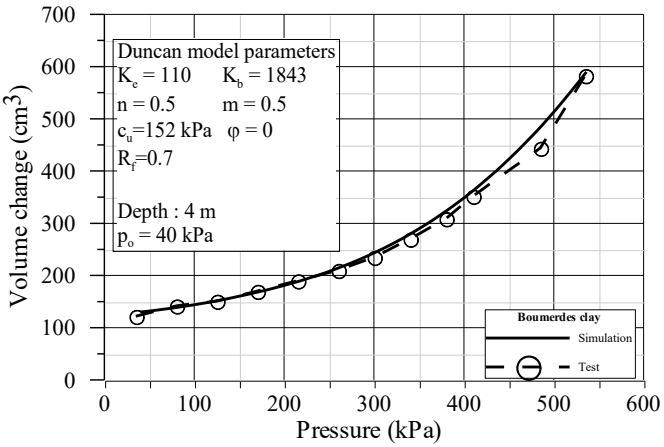

Figure 1. An example of identification for cohesive soil.

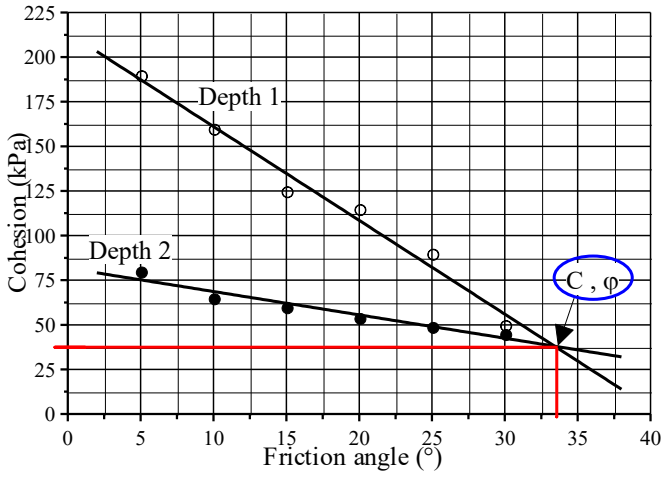

Figure 2. Identification of c and ϕ parameters for cohesive frictional soils.

2.2 *Site investigation*

The PRESSIDENT method has been used to identify the properties of Annaba sites, located in the east of Algeria. The soil stratigraphy encountered on the different sites consists of muddy soft to very soft brownish clay. The thickness of the clay layer is about 25 to 30 m. The ground water table was about 5 m depth from the ground surface. The clay is saturated. The natural water content w_n varies between 18% and 60%. The plasticity index varies between 26% and 35%. The shear strength parameters derived from consolidated undrained triaxial tests with pore pressure measurement range from 10° to 21° for the friction angle and from 11 kPa to 36 kPa for cohesion. Consolidation testing indicates that the soils are unconsolidated with a high compressibility index, C_c ranging from 0.11 to 0.41. Figure 3 shows geotechnical parameter profiles.

The undrained cohesion obtained using the PRESSIDENT method and empirical methods proposed by Menard (1957), and Amar & Jézéquel (1971) presented in Figure 4. In these figures, it can be noted that, for limit pressure less than 300 kPa, the undrained cohesion values deduced from the PRESSIDENT approach are close to those obtained from the empirical methods. For limit pressure higher than 300 kPa, the undrained cohesion values deduced from the PRESSIDENT approach were on the average 170% higher than those deduced from the empirical methods. There are a lot of factors that can explain the observed difference in the values of c_u obtained by different methods.

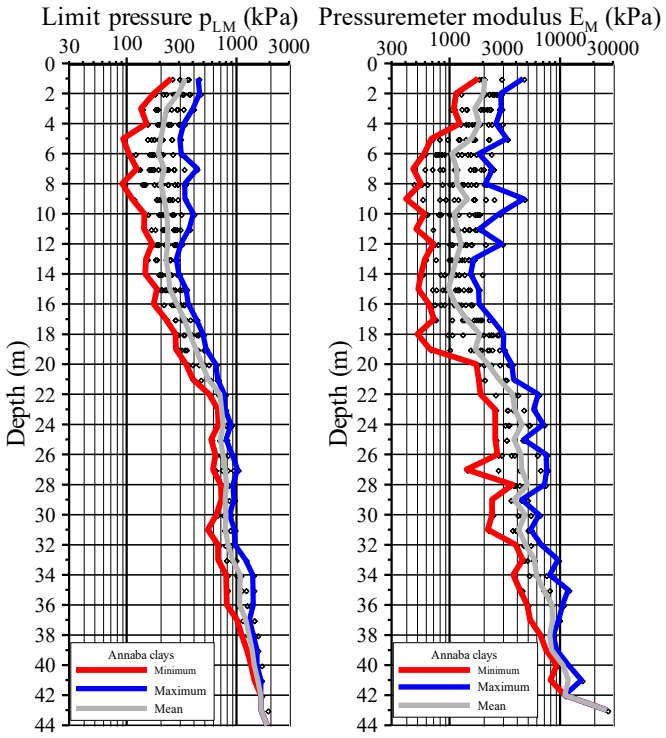

Figure 3. Soil insitu test profiles.

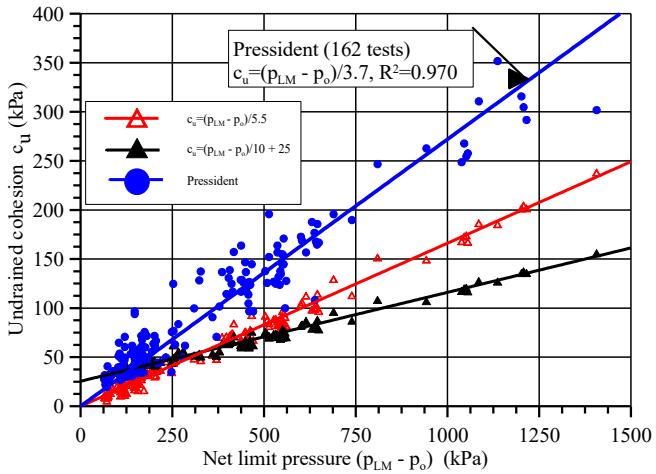

Figure 4. Undrained shear strength against net limit pressure.

The two empirical methods are established by correlation between limit pressure obtained from pressuremeter tests and undrained shear strength obtained from field vane and triaxial tests for soft soils. Very often, pressuremeter undrained shear strength obtained using cavity expansion methods are significantly higher than the values obtained using other in situ or laboratory tests. High undrained shear strengths from pressuremeter tests have been frequently observed. The measured c_u will be affected by the in situ or laboratory method used and the stress path followed during the test (Wroth, 1984). Wroth (1984) showed that the undrained shear strength derived from pressuremeter tests should be larger than the strengths derived from field vane tests due to the nature of the different stress paths.

3 LOAD-SETTLEMENT PREDICTION OF A BORED PILE

3.1 *El-Djazair Mosque project*

The building complex is situated in the central axis of the famous golf of Algiers, facing the Mediterranean Sea. The minaret is a very slender parallelepiped with a total height of 265 m above ground and a squared plane with the side of 26.5 m.

The Geotechnical investigation survey for the Minaret involved four pressuremeter boreholes down to 70 m depth, 3 boreholes to the same depth and 1 borehole to the 90 m depth for soil sampling and 28 SPT (Standard Penetration Test). The limit pressure and pressuremeter modulus profiles are shown in Figure 5. The soil stratigraphy encountered on the minaret site consists of 10 m thick silty clay layer, underlain by silty sand extending to a depth approximately 40 m, underlain by sandy marl to the maximum explored depth. The marl consistency increases with depth. Groundwater was encountered at a depth of approximately 6.50 m. The soils are saturated. The measured natural water content varies between 10 and 35%. The plasticity index varies between 10 and 30%. The shear strength parameters derived from consolidated undrained triaxial tests with pore pressure measurement range from 11° to 26° for the friction angle and 18 kPa to 212 kPa for the cohesion. Consolidation testing indicates that the soil is normally consolidated to overconsolidated with medium compressibility, C_c ranging from 10 to 14%.

In this case, for each layer, using PRESSIDENT, it would be possible to define the three parameters, k_e, c and φ using two pressuremeter tests performed at two different depths (Fig. 2). Table 1 summarizes the average values of Duncan model parameters for each layer. Figure 6 compares the simulations curves obtained using the average values and the experimental data for the silty clay layer.

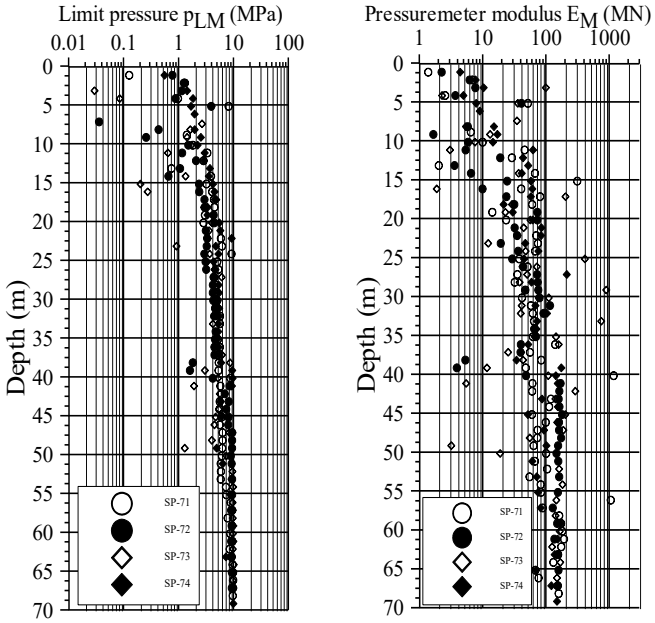

Figure 5. Limit pressure and pressuremeter modulus profiles.

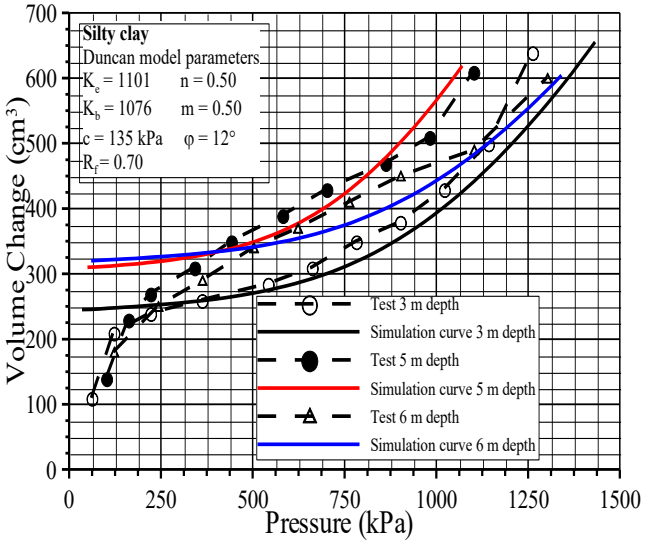

Figure 6. Simulation of pressuremeter curves by PRESSIDENT.

Table 1. Average values of identified model parameters using PRESSIDENT approach.

Soil layers	Depth	k_e	k_b	c	φ	E
	(m)			(kPa)	(°)	(MPa)
Silty clay	0 - 10	1104	1076	135	12	106
Silty sand	10 - 40	2297	2252	165	27	510
Sandy marl	40 - 70	5317	5213	200	35	1758

Two static vertical pile load tests, PV-01 and PV-02, are performed on non-working bored piles of 1000 mm diameters and 51.5 m lengths. For the bored pile construction, rotary drilling was employed for bored pile excavation under bentonite. The pile is instrumented by 27 extensometers over in entire length, defining a total of 9 measuring sections (3 extensometers by section at 120°) according to the project specifications. The piles are loaded up to 21.8 MN, 1.5 times the design working load (14.50 MN) of the foundation piles. The adopted loading cycle increments for the test piles are in according to the project specifications. Figure 7 shows the load-settlement curves.

3.1.1 *Ultimate resistance*

With a settlement value S_0 = 100 mm, using failure criteria of 1/10th of the pile diameter as the total settlement (MELT 1993), the ultimate resistance Q_{ult} of the pile was not achieved under the maximum load test of 21.8 MN (2180 t). At this loading, the average settlement was about 19.2 mm for the two piles. As the test load was released to 0.65 MN, the residual settlements measured were 5.00 mm and 6.00 mm. Various methods were used to assess the ultimate pile capacity, among them the Chin method (Chin 1970). By using this method, a plot is made between settlement divided by corresponding applied load and the settlement as shown in Figure 8. The slope of the best linear fit gives the ultimate load which is 34.4 MN and 31.4 MN for PV-01 and PV-02 respectively. According to EUROCODE 7, part 2, the ultimate load Q_{ult} can be calculated from Ménard pressuremeter tests using the equation:

$$Q_{ult} = Ak_p(p_{LM} - p_0) + P\sum(q_{si}\ z_i) \quad (3)$$

Q_{pu} and Q_{su} are the ultimate tip load and the ultimate skin friction respectively, where A is the pile section, kp a bearing factor based on soil type and pile type, p_{LM} is the limit pressure, p_0 is the horizontal earth pressure at rest, P is the pile perimeter and q_{si} is the unit shaft resistance at a depth z_i. By using these equations and the Ménard pressuremeter test results, it is possible to predict Q_{ult} given in Table 2 for the fourth limit pressure profiles. The bearing capacity values computed using Pressuremeter Menard Tests (PMT) direct design pressuremeter lie spread between 0.65 and 0.84 times that deduced from static axial load tests by extrapolating Chin's method. According to the French Design Code (MELT 1993), the creep bearing capacity Q_c corresponding to the end of the pseudo-elastic resistance for the pile can be obtained by $Q_c = 0.5Q_{pu} + 0.7Q_{su}$. The Q_c obtained values is ranging between 14.25 MN and 16.27 MN, which was conservative compared to vertical pile test results.

Table 2. Bearing capacity obtained using the French Design Code (MELT 1993).

Soil profile	Q_{pu}	Q_{su}	Q_{ult}	Q_c	Q_{ult} (PMT)/Q_{ult} (Chin)
	MN	MN	MN	MN	(%)
SP71	6.80	15.50	22.30	14.25	65
SP72	11.10	15.10	26.20	16.12	76
SP73	10.70	15.60	26.30	16.27	84
SP74	8.83	15.90	24.73	15.54	79

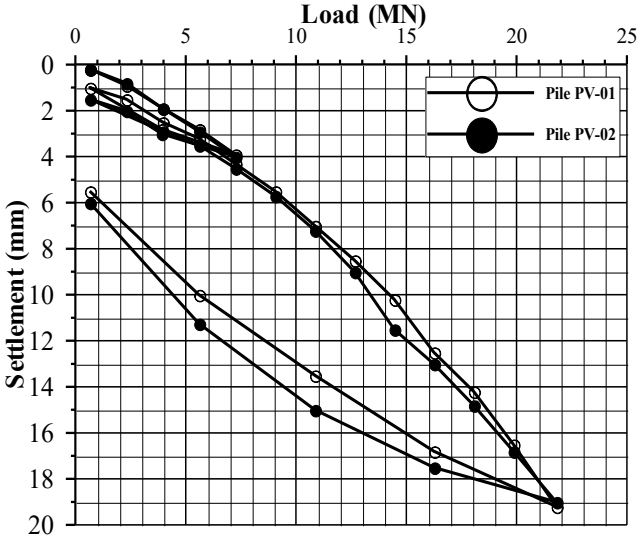

Figure 7. Static axial load settlement curves.

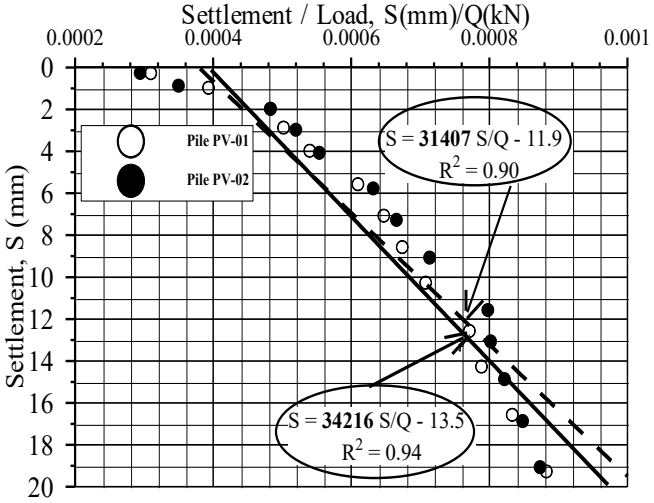

Figure 8. Ultimate pile capacity by Chin method.

3.1.2 *Settlement predictions*

In Fascicule 62-V (MELT 1993), two methods are proposed for settlement prediction of static vertical load pile. In the first the settlement is arbitrarily defined as a percentage of the pile diameter. The second method is a determination of load transfer q-z curves as a function of Ménard pressuremeter modulus as proposed by Frank and Zhao in 1982 (Gambin & Frank 2009). Numerical methods are also used for settlement prediction of piles. The axial response of static vertical bored piles is investigated using PLAXIS^{3D} FOUNDATION (Brinkgreve & Swolfs 2007), which is based on finite element method. Linear elastic behavior is assumed for the pile and the Mohr-Coulomb criterion is considered for soils. The 3D mesh consists of 26176 tetrahedral elements with 10 nodes. PLAXIS imposes a set of standard fixities to the boundaries of the geometry model. The 3D finite element simulation was performed considering the geostatistical stresses characterizing the initial state, automatically generated. The initial stresses within the soil mass are established assuming that they are characterized by an earth pressure coefficient k_o condition, according to the consolidation state of the soil layers. Numerical calculations were performed for the two static axial pile, 51.5 m deep and 1 m diameter, subject to maximum service load. The method of Frank and Zhao (Gambin & Frank 2009) was also used to find the mobilized vertical stress versus the tip displacement. Figure 9 shows the experimental load-settlement curves, the predicted by the Frank-Zhao method, the predicted by PLAXIS code taking into account PRESSIDENT approach and laboratory tests and the one predicted by Chin method. Frank and Zhao method and 3D calculation using parameters derived from laboratory tests give results quite close and provided ultimate resistance lower than those obtained by the PRESSIDENT approach and experimentally

3.2 *Exercise of ISP5*

The pile, 0.5 m in diameter and 12 m deep, was drilled using a continuous flight auger. The static pile loading test is carried out in accordance with European standard EN ISO 22477-1-1. It is a staged loading test, which consists in loading the pile by increments ΔQ equal to $0.1Q_{max}$ until Q_{max} is reached. The limit load Q_u is conventionally defined as the settlement at pile head equal to the higher of the two values: either 20 mm or B/10, which is here equal to 50 mm. The pile is embedded in a 9.6 m thick clay layer, below a 2.4 m thick silt layer. The water table is located 1.8 m below ground level. The laboratory tests carried out on soil samples extracted close to the pile location showed that the site physical properties were relatively homogeneous.

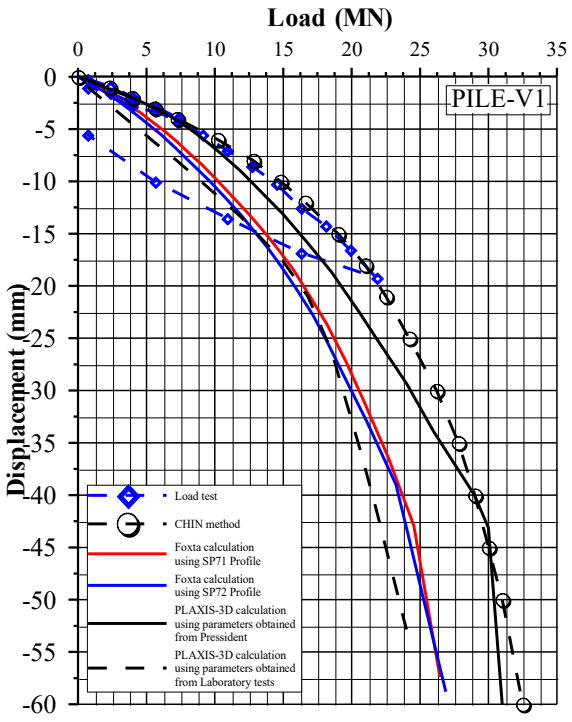

Figure 9. Comparison of measured and calculated load-settlement curves

The shear strength parameters derived from consolidated undrained triaxial tests with pore pressure measurements are c'=57 kPa and φ'=23°. The Young modulus at 0.2% strain derived from unconsolidated undrained triaxial tests is E=50 MPa. The results of three Menard pressuremeter boreholes, given in the exercise, are used to define the soil parameters by the PRESSIDENT approach. Figure 10 summarize the evolution of undrained cohesion evaluated by means of the approach and by the empirical relationships proposed by Ménard (1957) and Amar *and Jézéquel (1972)*, and by triaxial tests. On the basis of the results obtained by means the PRESSIDENT approach, a soil profile is proposed (Fig. 11). Then, each layer is characterized by an average value of the initial Young Modulus E, the undrained cohesion c_u and the parameter A.

The calculation of the bearing capacity and settlements of a bored pile using the parameters derived from the two methods are achieved using FLAC^{3D} software (Itasca, 2005) considering an elastoplastic model with Mohr Coulomb criterion. Figure 11 gives the parameters used for achieving the calculations. Figure 12 compares the results obtained from PRESSIDENT approach to the experimental data (Reiffsteck, 2006). For this case again, one can note that the method is in a fairly good agreement with the measured load-settlement curve on site.

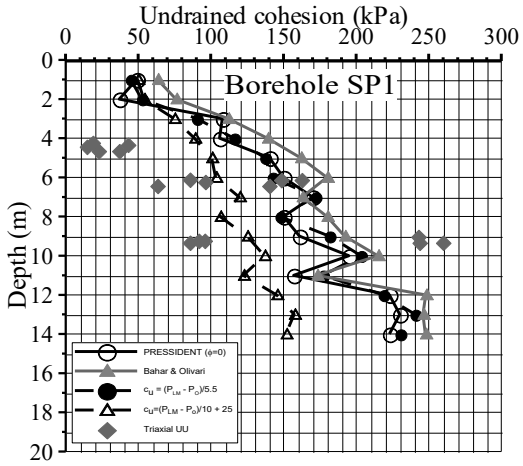

Figure 10. Undrained cohesion profiles.

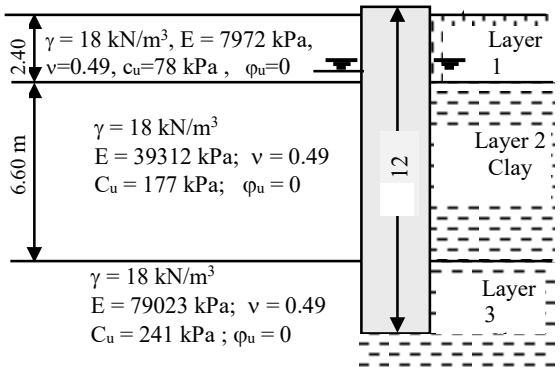

Figure 11. Pile and model parameters of soils.

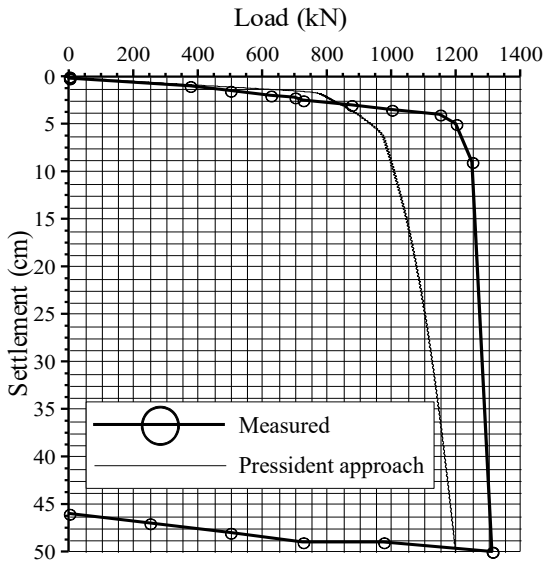

Figure 12. Measured and calculated load-settlement.

4 CONCLUSION

The usual soil parameters required by simple constitutive models for soils in numerical calculations are determined using PRESSIDENT method which is a numerical program developed to analyze pressuremeter tests. Numerical calculations taking into account these parameters are performed in order to predict the behaviour of a single bored pile subjected to a static axial load. For El-Djazair mosque site, the results show that the Frank and Zhao method and numerical calculations using laboratory tests give results quite close and provided ultimate resistance lower than those obtained by the PRESSIDENT approach and experimentally. For ISP5 site, the obtained results using the PRESSIDENT method are in a fairly good agreement with the measured load-settlement curve on site. The numerical calculation results compared to in situ measurements, show the applicability of the approach.

5 ACKNOWLEDGEMENT

The authors greatly appreciate the assistance of the technical staff of ANARGEMA, the project owner, especially for data available for scientific use.

6 REFERENCES

Amar, S., & Jézéquel, J.F. 1972. Essais en place et en laboratoire sur sols cohérents: comparaison des résultats. *Bulletin de Liaison des Ponts et Chaussées*, Vol. 58 : 97-108.

Bahar, R. 1992. Analyse numérique de l'essai pressiométrique: application à l'identification de paramètres de comportement des sols. *Thèse de doctorat,* E. C. de Lyon.

Bahar, R., Cambou, B., & Fry, J.J. 1995. Forecast of creep settlements of heavy structures using pressuremeter tests. *Computers and Geotechnics*, Vol. 17: 507-521.

Boubanga, A. 1990. Identification de paramètres de comportement des sols à partir de l'essai pressiométrique. *Thèse de doctorat.* Ecole Centrale de Lyon. France.

Brinkgreve, R.B.J. & Swolfs, W.M. 2007. Plaxis 3D Foundation. Finite element code for soil and rock analyses", *Users manual, 2007*, Netherlands

Briaud, J.L. 1992. The pressuremeter, *CRC Press*, p. 336.

Chin, F.K. 1970. Estimation of the ultimate load of piles not carried to failure, *Proceedings of the 2nd Southeast Asian Conference on Soil Engineering*, 81–90.

Duncan, J.M., & Chang, C.V. 1970. Non linear analysis of stress and strain in soils. *Journal of the Mechanics and Foundations Engineering Division*. 96 (SM5): 1629-1653.

Gambin, M. & Frank, R. 2009. Direct design rules for piles using Ménard pressuremeter. International Foundation Congress and Equipement Expo'09, ASCE Geotechnical Special Publication No. 186: 111-118

Itasca, FLAC^{3D}, 2005. Fast Lagrangian Analysis of Continua. Itasca Consulting Group, *User's manual*, Minneapolis.

MELT 1993. Règles techniques de calcul et de conception des fondations des ouvrages de génie civil, *CCTG Fascicule 62 Titre V," Ministère de l'Équipement, du Logement et des Transports*, Paris, Texte officiel N° 93-3, p. 182.

Ménard, L., 1957. Mesures in situ des propriétés physiques des sols. *Annales des Ponts et Chaussées*, Vol. l.3: 357-376.

Reiffsteck, P. 2006. Portance et tassements d'une fondation profonde - Présentation des résultats du concours de prévision. *Comptes rendus Symposium international 50 ans de pressiomètres (ISP 5)*, Marne-la-Vallée, Vol. 2:521-535.

Wroth C.P. 1984. The interpretation of in situ soil tests. 24th Rankine lecture, *Geotechnique* 34: 449-489.

Geotechnical and Geophysical Site Characterisation 5 – Lehane, Acosta-Martínez & Kelly (Eds)

Applicability of CPT to determine geotechnical properties of sand deposits to an Uruguyan gas plant

A.W. R. Barreto
Delta Geotechnics Ltd., Uberlândia, Brazil

B. L.C.G. Árabe
Delta Geotechnics Ltd., São Paulo, Brazil

ABSTRACT: Regasification project in Uruguay has been required geotechnical investigation. CPT demanded complex apparatus because of the tides and currents in offshore works. A Break Water construction called for a geometrical and mechanical sand deposit analysis. Initially it was performed five CPT's, then soil samples were taken by rotary drilling process. The top layer of the known points was between -6mCW to -9mCW of sand deposit allowing to estimate the depth of the test. The tests counted on an equipment and tools layout project, arranged in fixed auto lifting platform, called Jack-up. Its apparatus fought against the dynamic inter-ference of water. Across the deposit layer the qc results were from 10MPa to 15MPa, reaching above 20MPa in the layers next to impenetrable. Impenetrable materials were extracted to prove the impenetrability of CPT. Interference of the site and location of equipment were limiting for obtaining the results, and their previous knowledge determined the period of performance and data integrity.

1 INTRODUCTION

1.1 *Uruguayan Regasification Project*

In order to diversify the energy matrix of Uruguay the construction of GNL del Plata regasification terminal will promote the supply of natural gas in the country using clean resources.

The infrastructure will consist of a breakwater to remove the interference of currents and waves, a sea pipeline, a land-based pipeline and a terminal located on the breakwater itself, which will have 263,000 m³ capacity. The regasification project will also feature a permanent boat, containing gas with auxiliary port for smaller tankers, tugboats and supply ships. The heat source would be water from the Rio de la Plata. GNL del Plata will have a maximum capacity of 10Mm3/d and a stacking capacity of 263,000 m³. Vessels will carry about 170,000 m³ of GNL. The terminal will have a maximum capacity of 10 billion cubic meters of natural gas per day. The project will be connected to the pipeline Cruz del Sur. This one has a marine tranche, which will be placed under the ocean floor from the terminal to Punta Yeguas, and another on the ground. Except for two points, transfer station and pressure regulating station, the pipeline will be buried completely.

Currently, the project implementation has stopped, in part, by some administrative reasons, what includes the terminal construction. In its entirety, the project will cost around US$ 1.3bn.

1.2 *Project Location*

The implementation of the project will take place in Rio de la Plata, more precisely in Punta Sayago in the capital Montevideo, Uruguay (Fig.1). Estuary created by the rivers Parana and Uruguay, the Rio de la Plata form on the Atlantic coast of South America a triangular shape of 290 kilometers long. Their combined watershed and its affluent are the rivers Lujan, Matanza, Samborombón and South Salado, has approximately 3.2 million square kilometers of surface.

The Rio de la Plata is physically divided into three geographical regions. Its inner zone, which starts from Punta Gorda to Cologne line - La Plata, characterized by a substrate of sand, silt and clay. An intermediate zone in the interval between the line Cologne - La Plata to Montevideo line – Punta Piedras, where it can be observed the marine influence by increased importance of the tides. Already the outer zone, which starts on the line Montevideo – Punta Piedras to the outer boundary to meet the South Atlantic Ocean, where the waters are already brackish, with a varied salinity. The shores of the Rio de la Plata have many variable characteristics. The Uruguayan coast belongs to the geological formation of

Figure 1. Project Location. Source: google.com/maps.

the Massif of Brasilia, consisting of high coastlines and sandy beaches surrounded by dunes separated by rocky headlands. On the other hand, the Argentine coast, similar to sedimentary basin de la Pampa, the river is formed by plateaus of clay ranging between clay plains and marshy plains.

Over 57 million m³ of sediment coming from the northern provinces of Argentina and the states of southern Brazil are transported per year, and dragged to the estuary. The river channel is dominated by the presence of large banks with low depth which prevents navigation off draft vessels, which should be done following several natural and artificial channels, many of which, such as the route that communicates Buenos Aires to Atlantic Ocean, need constant dredging to avoid the accumulation of sediments and remain open navigation.

Uruguayan coast morphology is generally high, with sandy beaches, it comes from Martín García materials who are characterized by a river elevation of the canals and composed of gray-brown sediment, sand in the north, muddy sands and sandy sludge in the south. The main tributaries of the Uruguayan coast are the rivers San Juan, Rosario, Santa Lucía and Solís. The main ports in Rio de la Plata are Buenos Aires, in the southwest, and Montevideo, northwest.

1.3 *Geothecnical Tests for the Project*

Among the existing structures in this implementation of regasification terminal is called Break Water, which required a sensitive survey of geotechnical parameters in a constructive step. The structure, as showed in the Figure 2, is basically divided into three stages in its execution. Initially, a cleaning of muddy material present at the site was performed by a dredging vessel. The first stage consists of a sandy deposit of trapezoidal cross-section. Following the same way and with thinner thickness rock material is deposited as a reinforcement, and the third stage there will be an accretion of a layer made with

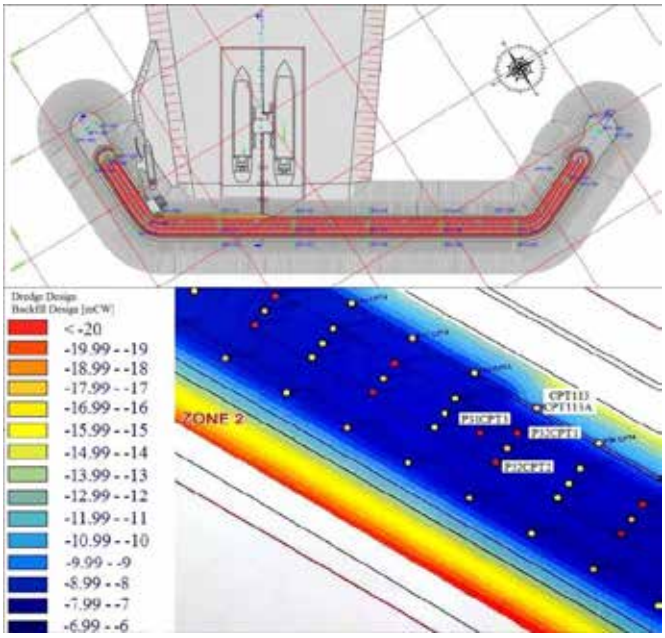

Figure 2. Structure of Break Water. Source: The Authors.

smaller structures of 3.0m³ made of precast reinforced concrete, called Accropodes. The latter has the function of conferring stability to the set of landfill under the liquid surface, which also delimits an area without interference of currents and waves.

In order to raise the geotechnical parameters, the first phase of work demanded Cone Penetration Test. The implementation plan of the in situ tests consisted in the division of a dozen sections with many points in the body of the landfill structure, which were presented by a location plan, divided by execution priority as the stage of dredging and sand deposition were advancing. Along with the location plan a sense of dredging and sand deposit format was given and the most important CPT points were in the center. The depths of the landfill were presented in a color scale in which red is the maximum depth of the landfill -20mCW and blue the top layer -6mCW (Fig.2). The unit of measurement adopted to these depths is called Meters Cero Warthon, an Uruguayan unit, which is the relationship between sea level to the local reading established.

An arrangement of equipment was designed and established to enable the acquisition of CPT data, which are the point of resistance (q_c), friction (f_s) and pore pressure (u_2). Several constructive adaptations to the standard methodology were evaluated and added so that the data obtained were not compromised as required in the magnitude of the project. The tests acquired a mobile platform (Jack-up) capable of supporting the equipment involved, probes for the sounding and blocking layers of waste, and other auxiliary equipment distributed to a layout which facilitates workability and production.

As the work was developed in aquatic environment, the natural interference of waves and currents and the local productive process created a big challenge for the acquisition of reliable data and its integrity. Although the acquisition has demanded longer time than the normal to CPT, it was possible to complete data from five different points before the work stoppage, which was given for some administrative reasons. The geotechnical tests to this project are presented and discussed in this paper.

2 EQUIPMENT LAYOUT

2.1 *Equipment and range*

To acquire geotechnical information from CPT data for the Break Water construction, how to obtain the parameters in the landfill has been questioned. The main question was which method to use for the required depth in the project, and in this case was beyond 30m. Not only the blade of water depth of approximately 10m in this site, but also the development of a construction site able to meet the specific needs, in this case both were the difficulties of this work. This investigation used conventional equipment for land soundings, adapted to off-shore environment. Thus, the main concern was to maintain the stability of the boundary conditions so the dynamic test would not suffer any interference. The option was to use robust equipment for greater ranges, thereby avoiding the influence of the stresses produced by ocean currents and waves.

For drilling activity, it was used a mobile platform Jack-up (Fig.3) of North American origin, scaled to shallow designs. The shelf had a length of 90ft, 50ft beam and depth of 7ft. With a spud length of 80ft it was possible to reach a maximum depth of 60ft.Positioned with aid of a trailer boat and GPS, Jack-up was able to keep in the river without interference from water and its drives, producing a static condition similar to investigations on land surfaces. A metal base grid format was replaced by the module that formed the basis of the Jack-up, called Moon Pool allowed a punctual probe visibility and the vertical positioning of the sounding objects. The structure of the platform was able to withstand all the located equipment, being chosen by developing a layout design of equipment and analysis of the stability at loading.

The execution of geotechnical tests demanded two hydraulic probes, one for crimping and for installation of metal casing tubes in accordance with the advance of the depth test, the other was required for crimping the CPT equipment. Although there are probes capable of performing both process, the project opted for economic viability, using both, since there was no negative interference in the production process. The rotating probe with engine powered diesel with 4 vacuumed cylinders and maximum power67CV and 2500 RPM, could move up to 300m deep, powered diesel with 4 vacuumed cylinders and maximum power 67CV and 2500 RPM, could move up to 300m deep, spiking was already strictly used for spiking of CPT equipment with competent power to beat the sandy soil deposit resistance to halt the test limits. As the CPT drilling probe has its own handling capacity, the places exchanges between the probe was facilitated during the tests.

Figure 3. Mobile Platform (Jack-up). Source: The Authors.

The CPT probe of Swedish origin, are equipped with individual sensors for point resistance $_{(qc)}$, sleeve friction $_{(fs)}$, pore pressure $_{(u2)}$. The data measured by the sensors is digitized, multiplexed and encrypted with an error detecting code in the probe before it is forwarded to the transmitter or cable adapter for transmission to the surface. To back up the data transmission, the cones can also be delivered with a back-up memory of 8 hours' capacity, with 18-bit resolution on all channels. In accordance with the probe calibration certificate, giving by the producer, the identification number is 3425 (Probe number), the ranges are point resistance of 50 MPa, lateral friction of 0.5MPa, area factor (b) of 0.014, pore pressure of 25MPa and tilt angle variable from 0 to 40 degrees. This equipment meets the requirements of the tests, managing to reach the impenetrable layers of soil.

2.2 *Loaded platform layout*

A layout of the equipment (Fig. 4), was designed thinking about the workability and loading of heavy equipment on the platform. In its distribution there were three maritime containers, two warehouses and one for dining and supporting materials to labor. They were leased symmetrically to the larger axis of

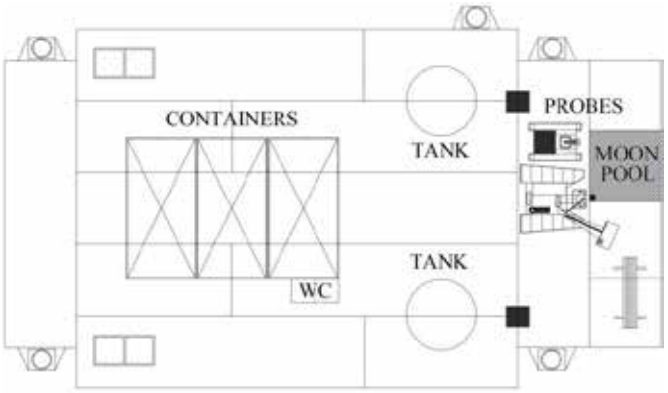

Figure 4. Equipment Layout. Source: The Authors.

the jack-up two water reservoirs to aid in the blockage of the holes and circulating water during rotary drilling, and the pumps for this process. The probes were located near the Moon Pool, for ease of exchange. In addition, collective protection equipment was installed, bathrooms, as well as access stairs to the platform and meeting point in case of emergency situations. In this location the weight of the equipment and its eccentricity were taken into account to a uniform distribution of loads involved. Table 1 indicates the located equipment and their weights.

Table 1. Equipment weights

Description	Amount	Unit weight	Total
		kg	kg
Loaded Containers	3	3,250	7,500
Pump	2	405	810
WC	2	78	156
Water Reservoir	2	5,000	10,000
Rotating Probe	1	2,200	2,200
CPT Probe	1	4,740	4,740
Coatings and roads	1	1,680	1,680
Total			27,086

* The maximum load of each container to the platform of stability analysis was considered.

3 METHODOLOGY AND RESULTS OF CPT

3.1 *Methodology of CPT*

CPT test is today one of the most important tools of geotechnical investigation, Schnaid, F. 2000 (ed.) Ensaios de Campo e suas aplicações à Engenharia de Fundações. São Paulo: Ofinia de Textos. Briefly the CPT test consists of slow static spiking of a mechanical or electrical cone that stores in a computer data with 2.0cm/s of speed, what does that each meter 50 lines of data are recorded. The cone allocated to this hydraulic pump is penetrated into the ground and its speed needs to be constant for data acquisition. The equipment, being hydraulic spikes the cone on the ground and acts as a press. After spiked it acquires the data automatically and the system itself captures the contents and makes the continuous recording of the same along the depth.

This method provides the point resistance $_{(qc)}$, the lateral friction resistance $_{(fs)}$ and the correlation between both (Rf measured in%) that enable identification of the type of soil. Characterization and Identification of Soil are one of the most important problems of soil mechanics, Melo, V.F.B.1953 (ed.) Mecânica dos Solos e Engenharia de Fundações. Revista de Engenharia Mackenzie.

According to ABNT NBR 12069: 1991 - Cone Penetration Test in situ (CPT), the cone tips can be mechanical or electrical. The electrical ferrule has one or more elements for measuring electrical within the tip of the penetration resistance components. Generally, it is necessary that the land has access conditions to receive the product. Within the team that accompanies this procedure it is necessary to have a geotechnical engineer.

In practice the implementation of the CPT tests in the first stage of the landfill construction was performed by coating the hole with metal pipes, then CPT readings were taken from the depth coated till get the test limits, sometimes stopped for getting high point resistance $_{(qc)}$, on the other hand by the high tilt angle. That is, it was first located the platform at the required point in your base distanced approximately 1.0m from the water level. The closer the top of the sand layer was to the Jack-Up surface (-6mCW to -9mCW), the less would be the dynamic water interference. CPT probe was also used to read the first layers, before coating the hole, and the test was finalized by standards recommendations. Because of the sand landfill compactness, it was necessary to weld the probe in the surface, to anchor the machine. For the hole coating a HW diameter and 50.0cm length liner pipes were installed one by one, this process granted that the unknown deposit layers were not dented or deformed by the drilling process. Once deformed, the CPT date should not be reliable and maintain its integrity was critical to the success. These procedures were alternated to the impenetrable soil limit. Thus, it was possible to limit deviations (Tilt Angle), so that the spiking ran vertically.

3.2 *CPT results*

Before the presentation of the results obtained in CPT tests is necessary to make a brief comment on the material used in the construction of the landfill. Some samples of the used sand were also analyzed in the laboratory of Delta Geotechnics Ltd. The

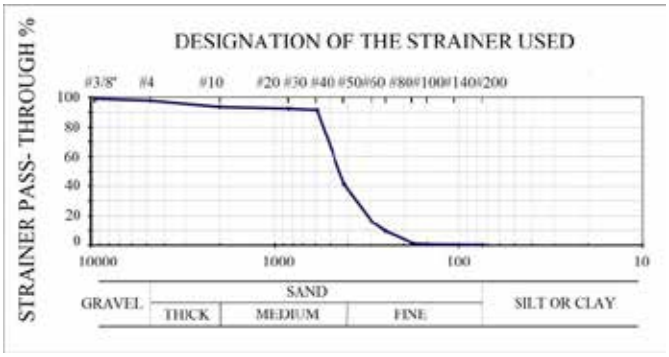

Figure 5. Arquimedes Bank Granulometry. Font: The Authors.

visual and tactile aspects, as well its particle size were previously raised.

The sand, taken from Bank Archimedes in Rio de la Plata, presented color variations, them were indentified as light gray, dark gray and dark brown gray. Continuous and open granulation and thick to medium granulometry. The material showed the presence of fine, medium and thick gravels and shells in its portion. Figure 5 shows the most commonly particle size found in the composition of bank loan. The sedimentation of higher density materials occurred as expected and small lenses of thick material were hard to obstruct by the rotating probe and CPT.

With this prior knowledge of the particle size, five different penetration tests were executed. The aim of this paper is to present the results and the classification of the material. It is known that the material investigated comes from a sedimentation process, in which over the years igneous and metamorphic rock became sedimentary rock. This process was given by the great waterways of the rivers, with the breaking of hard material on the impact of water. According to an abacus proposed by Robertson & Campanella, as this work treats of a sedimentary soil, the parameter used is the friction ratio Rf (%). It identifies the profile widely variable stratigraphy, composed of strata of sand, clay and silt-clay in the sand layers, deposited material, the resistance (qc) has relatively high values, for a ratio of the order of 1%. Robertson, P. K. & Campanella, R.G. (1988). Guidelines for using the CPT, CPTU and DMT for geotechnical design. Re-port PA 87-023, Federal Highway Administration, Washington. Equation 1 indicates how the frictional ratio is obtained (Rf%).

$$Rf = \frac{fs}{qc} \quad (1)$$

where Rf = friction ratio; qc = resistance; and fs = lateral friction.

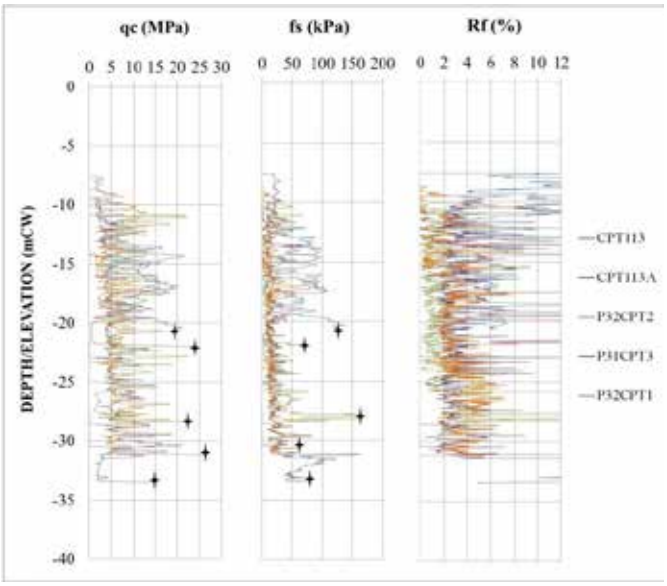

Figure 6. CPT data and interpretation. Source: The Authors.

The five CPT tests performed had a depth range of -33mCW to -7mCW, which included points in the middle of the landfill and its sides, with greater depth of approximately 40,00m from the deep of the test to the base of the Jack-up. In these penetration tests resistance (qc) gave a response in the range 5 to 10MPa, which corresponds to higher resistance to soils. The lateral friction (fs) responded with a range of 25 to 50 kPa. The complete result of these CPT's are showed in Figure 6, the value of friction ratio is expressed in percentage to the abacus analysis, (Fig.7), which each point of this cloud of points belongs to the sounding line of reading and the interpretation.

When the results are analyzed, it is very necessary to make some comparisons with the site information observed, which indicated the sensitivity of the operator to continue or end the test. During the penetration resistance lenses were observed which reached 20MPa home in a few depth advances. These lenses are explained by the sedimentation process, wherein after deposition of the granular material, those of higher density deposited first in the background. The strength gain intervals was justified by the steps of deposition, which were made on different days on the river. This fact was also confirmed after each CPT test, on the hole casing process, which demanded more power from the rotating probe and longer time of maneuver.

Although it is not important to consider the measurement of pore pressure (u2) for the type of analysis adopted, these data were collected for testing. It has been observed that the distribution of pore pressure was quite linear and ascending as far as the penetration was reaching greater depths. In this case there was no significant presence of lenses that were considered important for the interpretation of the results,

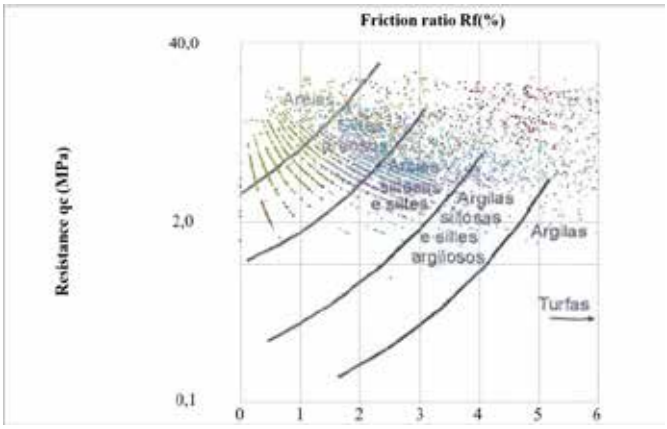

Figure 7. Cloud points on Robertson & Campanella abacus. Source: The Authors, Robertson & Campanella (1983).

except when the test came close to inscrutable layers. As the dredging of the previously existing muddy material was not able to eliminate it completely, a small layer demonstrates a much higher porepressure gain than the previous distribution. The granulometry size of the landfill layer, sometimes continuous or open, shows that in the acquired data there is no differential pressure that can overcome the water pressure. The voids in the soil operate as if the cone was immersed only in water to this kind of data.

Analyzing the abacus proposed by Robertson & Campanella (1983) it is possible to visualize a cloud of points tending to be close to the classification that involves the sandy soils. Most points filled in the interval lines demarcating as silty sands and silts, thus proving that the material had a coherent scatter at the time of deposition. This means that the examined points had not only been dredging of fine material and muddy, but also the deposition of the sandy layer and the construction of the first stage of Break Water was completely done.

After the closing of the soundings by CPT method some attempts to extract samples of the impenetrable layer of soil were conducted. Even if the test indicated imperviousness, for example increasing the point resistance $_{(qc)}$ immediately after a thin layer of soft material, the sampled materials confirmed the good quality of the tests. A sampler and a diamond impregnated crown, with NW diameter, was used for extraction. The material found was a sandstone substrate, covered by a silty clay layer with fine, medium and thick gravels and shells.

4 CONCLUSIONS

The application of geotechnical testing is of paramount importance to the lifting of information of a project. Major works have increasingly required execution control through penetration tests. The analysis of this equipment with the aim of investigation facilitates the viability of data acquisition of given location.

For the implementation of landfills in areas of water it is extremely important to consider the history of the construction site, as well as knowing the nature of the loan material. The previous study of these elements makes the decision and operation, reducing costs for the work and applying reliability to the final product. For tests and equipment involved, the layout of the project and its distribution in platform leveraged the productivity since the machines were commonly used in surveys of land surfaces. This analysis promoted constructive adjustments needed to acquire reliable CPT data, which can economically viable projects of such magnitude. CPT are used results not only for the projection of future construction, but also for the project foundations, as well as to control the execution of a work quality. Tying the landfill information, the lending bank, dredging and sand deposition was possible to determine the level of safety of the construction.

The results showed that the material was deposited by settling of particles on the lower density over the higher. The process of dredging and the construction of the landfill indicated that although it is known the loan material, to run it is impossible without influence of natural material, however small. This process causes very fine particles of soil are suspended in water for days, and that during construction of the embankment they mix forming an unknown artificial material.

5 REFERENCES

ABNT: MB 3406. 1991. *Ensaio de Penetração de Cone In Situ (CPT) – Método de Ensaio*. Associação Brasileira de Normas Técnicas.

ABNT: NBR 7217. 1987. *Determinação da Composição Granulométrica.* Associação Brasileira de Normas Técnicas.

ABNT: NBR 12284. 1991. *Áreas de vivência em canteiros de obras.* Associação Brasileira de Normas Técnicas.

Árabe, L.C.G. 1993. *Aplicabilidade de Ensaios In Situ Para a Determinação de Propriedades Geotécnicas de Depósitos Argilosos e Solos Residuais*. Rio de Janeiro: PUC.

ASTM: D3441 – 05. 2005. *Standard Test Method for Mechanical Cone Penetration Tests of Soil (With-drawn 2014)*. ASTM International:West Con-shohocken, PA.

ASTM: D5778-12. 2012. *Standard Test Method for Electronic Friction Cone and Piezocone Penetration Testing of Soils*. ASTM International:West Conshohocken, PA.

Melo, V.F.B. 1953. *Mecânica dos Solos e Engenharia de Fundações*. São Paulo: Revista de Engenharia Mackenzie.

Schnaid, F. 2000. *Ensaios de campo e suas aplicações à Engenharia de fundações*. São Paulo: Oficina de Textos.

Geotechnical and Geophysical Site Characterisation 5 – Lehane, Acosta-Martínez & Kelly (Eds)

Study on Seismic Response Analysis in "Vincenzo Bellini" Garden area by Seismic Dilatometer Marchetti Tests

A. Cavallaro
CNR-Ibam, Catania, Italy

S. Grasso & A. Ferraro
University of Catania, Department of Civil Engineering and Architecture, Catania, Italy

ABSTRACT: This paper deals with a research conducted at the Bellini Garden area in the city of Catania (Italy). The results of in situ and laboratory investigations are described and compared in order to provide a representative geotechnical model of soil conditions for a realistic seismic response analysis. In situ Seismic Dilatometer Marchetti Tests (SDMT) were carried out, with the aim to evaluate the soil profile of shear wave velocity (V_s). Moreover, laboratory tests were carried out on undisturbed samples. Among these Resonant Column Tests (RCT) were carried out. The Seismic Dilatometer Marchetti Tests were performed up to a depth of 30 meters. The seismic response analysis at the surface, in terms of time history and response spectra, has been obtained by linear equivalent 1-D codes.

1 INTRODUCTION

The city of Catania is located on the east coast of Sicily, which is one of the most seismically active areas of Italy. The east coast of Sicily has been struck by various disastrous earthquakes with an MKS intensity from IX to XI in the last 900 years. The earthquake of January, 11, 1693 is considered one of the biggest earthquakes which occurred in Italy. It is supposed that more than 1500 after shocks occurred along a period of more than two years after the main shock. This earthquake, with an intensity of XI degree of MKS scale in many centres, struck a vast territory of south-eastern Sicily and caused the partial, and in many cases total, destruction of 57 cities and 60000 casualties. In order to study the dynamic characteristics of soils in the Catania municipal area, laboratory and in situ investigations have been carried out to obtain soil profiles with special attention being paid to the variation of the shear modulus (G) and damping ratio (D) with depth (Cavallaro & Maugeri 2005, Cavallaro et al., 2006b, 2007). This paper tries to summarise this information in a comprehensive way for Bellini Garden area in order to provide a representative model of ground condition of different zones in the city for realistic seismic scenarios response analysis. Similar geotechnical study was successful performed for significant historical test sites (Cavallaro et al., 2003, 2004, 2013c, 2014)

2 THE BELLINI GARDEN

The Bellini Garden (or Villa Bellini) is one of four major public gardens in Catania. Locally it is often referred to simply "a Villa".

The oldest part of the garden dates back to the eighteenth century and belonged to the Prince Ignazio Paternò Castello of Biscari, who had wanted according to the types of the time with hedges structured to form mazes, decorating statues in the walkways and numerous fountains of various shapes to gush of water or waterfalls. This architectural conception had earned its name Labyrinth. The garden was entrusted to skilled gardeners among which the first was Pietro Paolo Arcidiacono and later Giuseppe Squillaci. After the death of the prince patron, which took place on 1 December 1786, the garden gradually declined due to the absence of the heirs. It was offered for sale since 1820 but only after a long period of negotiations, September 29, 1854 the Labyrinth was bought by the city of Catania by the owner Anna Moncada Paternò Castello, descendants of the Prince's heirs. The transformation of the garden to accommodate public use encountered numerous difficulties not least economic ones as to make it suitable for the intended purpose you had to solve related problems such as purchasing some adjacent private gardens. In 1858 the Marquis Antonio Paternò del Toscano, head of the city administration wrote a report on the "Project for a walking public".

The Bourbon government authorizes the financing of the work but arose rivalry between the experts responsible for blocking execution until, in the month of April 1863 was given the task of directing the execution to architect Landolina Ignatius (1822 - 1879). It was then that began the transformation of the private garden into a public garden whose works lasted until 1875.

In 1866 at the foot of the hill south, side Via Etnea, it was placed the bust of Vincenzo Bellini which is dedicated to the garden.

In 1875 the municipality of Catania buys by the Dominican Fathers the land adjacent to the southwest of the ancient Labyrinth, in 1877 the northern part of which belonged to the Prince Paterno di Manganelli and the vegetable garden of San Salvatore by Capuchin Fathers.

On October 4, 1877, under the new direction of engineer Filadelfo Fichera (Catania, 1850 - 1909), they began the unification efforts of the new funds acquired. The Fichera worked to make the use of the area more functional and easier through the resolution of the delicate technical aspects due to the terrain morphology, connecting the Biscari labyrinth garden with the land of San Salvatore. The Fichera - among the leading experts in the field of sanitary engineering of period - was able to remedy the said difficulties by an elegant and erudite use of stairways, bridges and avenues, giving the Garden Bellini the current setting. On the side facing Via Etnea were demolished, the Chiarenza house and stables of Majorana home.

Overall it was made a grove rather rent crossed along the perimeter by a promenade with pedestrian paths and connected a ring avenue for carriages; on the north hill it was built with a square in the middle by an elegant wooden kiosk (named Chinese Pavilion).

Figure 1. The Chinese Pavilion (Photo by Mirko Chessari).

The "Avenue of Illustrious Men" at West was completed in 1880 with busts on columns of the most famous characters of Italian and Catania history, but already in 1875 at the beginning of the avenue had been placed the bronze statue of Giuseppe Mazzini work of the sculptor Francesco Licata.

The monumental entrance of Via Etnea was built and opened in 1932 as part of the reorganization of the area and the construction of the overpass on the Via Sant'Euplio according to the project of architects Antore, Samonà and Gessigrande.

The following year, at the top of the staircase, in the square overlooking the Via Sant'Euplio tunnel at the center stands the large pool with fountain and swans were placed the four groups of monumental statues representing the arts, by the sculptor Domenico Maria Lazzaro and the Seasons, by the work of sculptor Perrotta. At the end of the fifties it was reordered the tunnel area of the Via Sant'Euplio and the adjacent ones. In those years it was extensively treated the floral aspect and expert gardeners created real drawings and inscriptions in the flower beds of the twin hills. A short time later it was increased the number of aviaries and exotic birds, then captured and reared aquatic birds such as ducks and swans, whose habitat had been equipped in large pools and fountains of which the garden was gifted. Around 1960 the garden also became a small zoo with wild birds and animals, such as various species of monkeys, and finally even elephants. Since the mid-seventies began a gradual downsizing of municipal funds allocated for routine maintenance and decay was not slow to manifest itself. The widely it rains ruined the flower beds on slopes of the southern part of the garden and the plants were badly treated. Seasonal ones actually disappeared. No better fate befell the animals that slowly reduced. The Indian elephant donated to the city by the Orfei circus, last survivor of the small but rich zoo of Bellini Garden, died in the mid-eighties.

During the last ninety years has been used for cultural and religious events, concerts to singing, even for traditional fairs. However it lost the old attendance of families with their children. After years of uncertainty and abandonment in 2001 an unknown origin fire totally destroyed the Chinese pavilion placed at the top of the north hill, together with its content of books and documents. For some years the usability was first reduced because of barriers and scaffolding that allowed only free transit along the length in the tree-lined avenue beside the Via Sant'Euplio and then completely denied. In 2007 he was tackled a functional recovery project much disputed because if it had been made would upset the overall architectural appearance and botanical garden. On September 23, 2010, the anniversary of the death of Vincenzo Bellini, with a pompous opening ceremony and a concert by the Carabinieri band held in the Chinese pavilion for long time inactive, after a rehabilitation, the garden was opened to the public.
For the diversity of views that it offers, the Bellini Garden is considered one of the most beautiful in Europe (Di Blasi & Lanza 2007, Galeazzi 2010).

3 INVESTIGATION PROGRAM AND BASIC SOIL PROPERTIES

The central area of Catania, deposits mainly consist of silty clay with a natural moisture content w_n from

between 20 and 27 % and a plasticity index of PI = 18 - 32 %. The soil unit weight γ is prevalently in the range between 19.2 to 20.5 kN/m^3, specific weight unit G_s is about 2.54 - 2.67, void index e is about 0.551 - 0.695, cohesion c' is about 43 kPa, angle of shear resistance ϕ' is about 24°. The angle of shear resistance was calculated from Direct Shear Test.

Shear modulus G and damping ratio D of Catania deposits were obtained in the laboratory by Resonant Column/Torsional shear apparatus (Cavallaro et al. 1999).

G is the unload-reload shear modulus evaluated from RCT, while G_o is the maximum value or also "plateau" value as observed in the G-log(γ) plot. Generally G is constant until a certain strain limit is exceeded. This limit is called elastic threshold shear strain (γ_t^e) and it is believed that soils behave elastically at strains smaller than γ_t^e. The elastic stiffness at $\gamma<\gamma_t^e$ is thus the already defined G_o.

For resonant column tests (RCTs) the damping ratio was determined, during the resonance condition, using the steady-state method.

Table 1. Test Condition for Saint Nicola alla Rena Church area.

Test No.	H [m]	σ'_{vc} [kPa]	e	PI [%]	RCT	G_o [MPa]
1	22.00	246	0.582	28.60	U	64
2	35.70	375	0.653	20.02	U	77
3	39.00	411	0.695	31.40	U	93

where: PI = Plasticity Index. U = Undrained. G_O from RCT.

The RCT conditions and the obtained small strain shear modulus G_o are listed in Table 1. The undisturbed specimens that have platens attached to each end were isotropically reconsolidated to the best estimate of the in situ mean effective stress. The specimen was subject to RCT after a rest period of 24 hrs with open drainage. The size of solid cylindrical specimens are Radius = 35 mm and Height = 140 mm. An electromagnetic sinusoidal torsional excitation is imposed to the top platen (free-end). The bottom platen is rigidly fixed (fixed-end). The frequency of the excitation is adjusted until the first mode resonance of the specimen is established. Measurements of the resonant frequency, acceleration and amplitude of the applied vibration excitation are made at the free-end. The measurements during torsional excitation are then combined with the apparatus characteristics to calculate the shear modulus G and shear damping ratio D of the soil.

Figure 2 shows the results of RCTs normalised by dividing the shear modulus G(γ) for the initial value G_o at very low strain.

The experimental results of specimens from Bellini Garden area were used to determine the empirical parameters of the eq. proposed by Yokota et al. (1981) to describe the shear modulus decay with shear strain level:

$$\frac{G(\gamma)}{G_o} = \frac{1}{1+\alpha\gamma(\%)^{\beta}} \quad (1)$$

in which:
G(γ) = strain dependent shear modulus;
γ = shear strain;
α, β = soil constants.
The expression (1) allows the complete shear modulus degradation to be considered with strain level.
The values of α = 11 and β = 1.119 were obtained for Bellini Garden area clay.

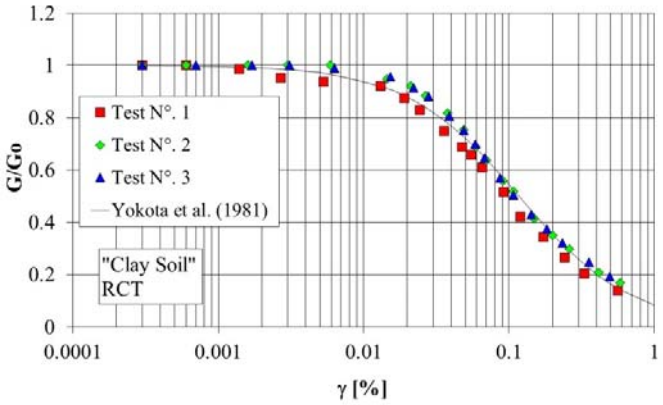

Figure 2. G/G_o-γ curves from RCT tests.

As suggested by Yokota et al. (1981), the inverse variation of damping ratio with respect to the normalised shear modulus has an exponential form as that reported in Figure 3 for the central area of Catania:

$$D(\gamma)(\%) = \eta \cdot \exp\left[-\lambda \cdot \frac{G(\gamma)}{G_o}\right] \quad (2)$$

in which:
D(γ) = strain dependent damping ratio;
γ = shear strain;
η, λ = soil constants.
The values of η = 31 and λ = 1.921 were obtained for Catania central area clay.
The equation (3) assume maximum value D_{max} = 31 % for $G(\gamma)/G_o$ = 0 and minimum value D_{min} = 4.54 % for $G(\gamma)/G_o$ = 1.
Therefore, eq. (2) can be re-written in the following normalised form:

$$\frac{D(\gamma)}{D(\gamma)_{max}} = \exp\left[-\lambda \cdot \frac{G(\gamma)}{G_o}\right] \quad (3)$$

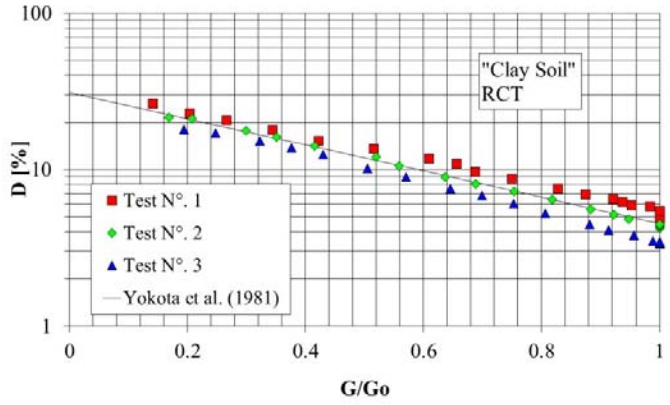

Figure 3. D-G/G_o curves from RCT tests.

4 THE SEISMIC DILATOMETER (SDMT)

The seismic dilatometer (SDMT) is the combination of the mechanical flat dilatometer (DMT), introduced by Marchetti in 1980, with a seismic module for measuring the shear wave velocity V_s.

A new SDMT system, described in Marchetti et al. (2008), has been recently developed in Italy. This apparatus was also used in offshore condition by Cavallaro et al. (2013a, 2013b).

The schematic layout of the seismic dilatometer test is shown in Figure 4. The seismic module is a cylindrical element placed above the DMT blade, provided with two receivers spaced 0.50 m. The shear wave source at the surface is a pendulum hammer (≈ 10 kg) which hits horizontally a steel rectangular plate, pressed vertically against the soil (by the weight of the truck) and oriented with its long axis parallel to the axis of the receivers, so that they can offer the highest sensitivity to the generated shear wave. The signal is amplified and digitized at depth.

The *true-interval* test configuration with two receivers avoids possible inaccuracy in the determination of the "zero time" at the hammer impact, sometimes observed in the *pseudo-interval* one-receiver configuration. Moreover, the couple of seismograms recorded by the two receivers at a given test depth corresponds to the same hammer blow and not to different blows in sequence, which are not necessarily identical.

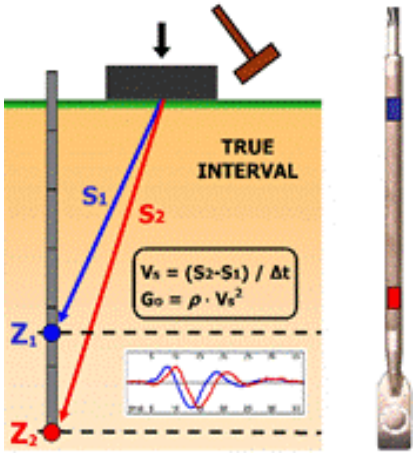

Figure 4. Schematic layout of the seismic dilatometer test.

Hence the repeatability of V_s measurements is considerably improved (observed V_s repeatability ≈ 1 - 2 %).

V_s is obtained (Figure 4) as the ratio between the difference in distance between the source and the two receivers (S_2 - S_1) and the delay of the arrival of the impulse from the first to the second receiver (interval time Δt). V_s measurements are typically obtained every 0.50 m of depth (while the mechanical DMT readings are taken every 0.20 m).

The determination of the delay from SDMT seismograms, normally obtained using a cross-correlation algorithm, is generally well conditioned, being based on the waveform analysis of the two seismograms rather than relying on the first arrival time or specific single points in the seismogram. Validations of V_s measurements by SDMT compared to V_s measurements by other in situ techniques at various research sites are reported in Marchetti et al. (2008).

Besides the shear wave velocity V_s, the seismic dilatometer provides the usual DMT parameters by use of common correlations Figure 5 (Marchetti 1980).

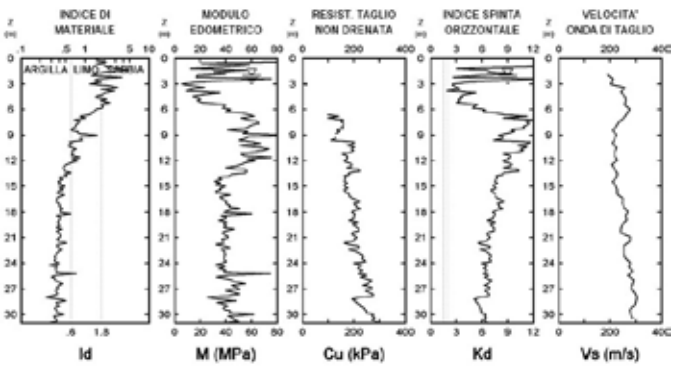

Figure 5. Summary of SDMTs in Bellini Garden area.

The measured arrival times at successive depths provide pseudo interval V_s profiles for horizontally polarized vertically propagating shear waves (Figure

4). V_s may be converted into the initial shear modulus G_o.

The combined knowledge of G_o and of the one dimensional modulus M (from DMT) may be helpful in the construction of the G-γ modulus degradation curves (Cavallaro et al., 2006a). A summary of SDMT parameters is shown in Figure 5 where,I_d: Material Index; gives information on soil type (sand, silt, clay); M: Vertical Drained Constrained Modulus; C_u: Undrained Shear Strength; ϕ' Angle of Shear Resistance; K_d: Horizontal Stress Index; V_s: Shear Waves Velocity. The profile of K_d is similar in shape to the profile of the overconsolidation ratio OCR. $K_d = 2$ indicates in clays OCR = 1, $K_d > 2$ indicates overconsolidation. A first glance at the K_d profile is helpful to define the deposit characteristics.

5 GROUND RESPONSE ANALYSIS

Since the areas studied here appear rather flat and characterized by lithological units trending subhorizontal, it was performed a one dimensional local seismic response analysis to assess the ground amplification due to local stratigraphic conditions. So, the analyses was performed using 1-D code, assuming a geometric and geological model of substrate as 1-D physical model. These analyses were carried out here with EERA (Bardet et al. 2000) and STRATA (Kottke & Rathje 2008), both linear equivalent codes operating in the frequency domain. The layers characteristic of the model have been carried out from geological surveys. The 16 1-D columns have a height of 35 m and are excited at the base by the synthetic scaled seismograms of 1693 earthquake, with a PGA of 0.200 - 0.225g corresponding to a return period of 475 years in the current Italian seismic code "seismic hazard and seismic classification criteria for the National territory" obtained by a probabilistic approach in the interactive seismic hazard maps. Further analyses have been performed using scaled accelerograms of 1990 earthquake in the Sortino recording station. Figures 6 - 8 show the results i.e. for site 1 respectively in terms of maximum accelerations with depth, in terms of amplification ratio and in terms of response spectra.

Similar studies have been performed for the zonation on seismic geotechnical hazards in the city of Catania (Italy) (Bonaccorso et al. 2005, Cavallaro et al. 2012, Grasso & Maugeri 2005, 2009a, 2009b; Maugeri & Grasso 2012) and for the Abruzzo Region (Italy) during L'Aquila earthquake (Maugeri et al. 2011a, 2011b; Monaco et al. 2011a, 2011b). Results of site response analysis are useful for soil-structure interaction behavior in the mitigation of seismic risk of buildings (Cavallaro et al. 2003).

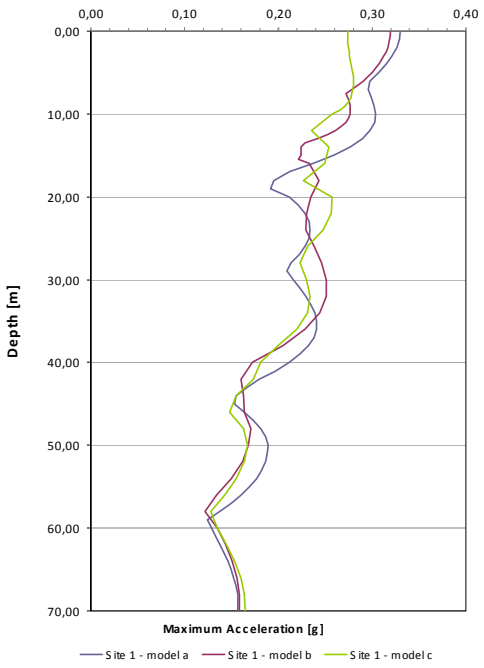

Figure 6. Maximum acceleration with depth.

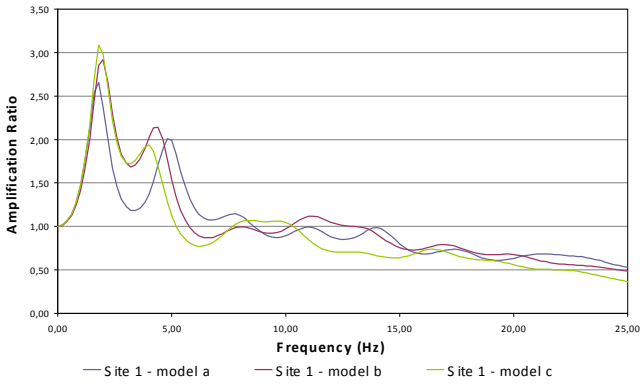

Figure 7. Fourier amplification ratio against Frequency.

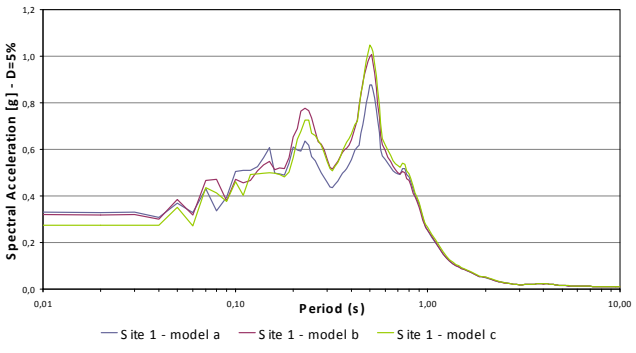

Figure 8. Response spectra against period.

6 CONCLUSIONS

A site characterization to evaluate the basic data for a seismic response analysis for Bellini Garden area in the city of Catania has been presented in this paper, with particular reference to SDMTs.

On the basis of the data shown it is possible to draw the following conclusions:
- SDMTs were performed up to a depth of 30 meters; the results show a very detailed soil characterization profiles of the more relevant soil properties, such as the material index (I_d), the constrained modulus M and the dilatometer modulus E_d, the angle of shear resistance φ' for sandy silty soil and undrained shear strength C_u for clayey soil, the shear wave velocity V_s, the horizontal stress index K_D.
- for the evaluation of shear modulus at small strain, Resonant Column tests have been performed;
- the results interpreted by the equations suggested by Yokota et al. (1988) describe the shear modulus decay with shear strain level and the inverse variation of damping ratio with respect to the normalized shear modulus. Results allowed also seismic geotechnical hazard evaluation in the city of Catania (Italy) also for soil-structure interaction and for the retrofitting of buildings.

7 REFERENCES

Bardet, J. P., Ichii, K. & Lin, C. H. 2000. EERA - A Computer Program for Equivalent-Linear Earthquake Site Response Analyses of layered Soil Deposits. *University of Southern California, Dept of Civil Eng*.

Bonaccorso, R., Grasso, S., Lo Giudice, E. & Maugeri, M. 2005. Cavities and Hypogeal Structures of the Historical Part of the City of Catania. *Advances in Earthquake Engineering*. 14: 197 - 223.

Capilleri, P., Cavallaro, A. & Maugeri, M. 2014. Static and Dynamic Characterization of Soils at Roio Piano (AQ). Italian Geotechnical Journal, Vol. XLVIII, N°. 2, Aprile – Giugno 2014, Patron Editore: 38 - 52.

Cavallaro, A., Maugeri, M., Lo Presti, D. C. F. & Pallara, O. 1999. Characterising Shear Modulus and Damping from in Situ and Laboratory Tests for the Seismic Area of Catania. Proceedings of the 2nd International Symposium on Prefailure Deformation Characteristics of Geomaterials, Torino, 28 - 30 September 1999.

Cavallaro, A., Massimino, M. R. & Maugeri, M. 2003. Noto Cathedral: Soil and Foundation Investigation. Construction and Building Materials, 17: 533 - 541.

Cavallaro, A., Maugeri, M. & Ragusa, A. 2004. Design Parameters of a Cohesive Soil from Laboratory Tests. Proceedings of A. W. Skempton Memorial Conference, London, 29 - 31 March 2004: 381 - 392.

Cavallaro, A. & Maugeri, M., 2005. Non Linear Behaviour of Sandy Soil for the City of Catania. Advanced in in Earthquake Engineering, Volume 14, 2005: 115 - 132.

Cavallaro, A., Grasso, S., Maugeri, M. 2006a. Clay Soil Characterisation by the New Seismic Dilatometer Marchetti Test (SDMT). Proceedings of the 2nd International Conference on the Flat Dilatometer, Washington, 2 - 5 April 2006: 261 - 268.

Cavallaro, A., Grasso, S. & Maugeri, M. 2006b. Volcanic Soil Characterisation and Site Response Analysis in the City of Catania. Proceedings of the 8th National Conference on Earthquake Engineering, San Francisco, 18 - 22 April 2006.

Cavallaro, A., Grasso, S. & Maugeri, M. 2007. Dynamic Clay Soils Behaviour by Different in Situ and Laboratory Tests. Solid Mechanics and its Applications, 146, 2007: 583 - 594.

Cavallaro, A., Ferraro, A., Grasso, S. & Maugeri, M. 2012. Topographic Effects of the Monte Po Hill in Catania. Soil Dynamics and Earthquake Engineering, Vol. 43, December 2012: 97 - 113.

Cavallaro, A., Grasso, S., Maugeri, M. & Motta, E. 2013a. An Innovative Low-Cost SDMT Marine Investigation for the Evaluation of the Liquefaction Potential in the Genova Harbour (Italy). Proceedings of the 4th International Conference on Geotechnical and Geophysical Site Characterization, ISC'4, Porto de Galinhas, 18 - 21 September 2012, pp. 415 - 422.

Cavallaro, A., Grasso, S., Maugeri, M. & Motta, E. 2013b. Site Characterisation by in Situ and Laboratory Tests of the Sea Bed in the Genova Harbour (Italy). Proc. 4th Int. Conf. on Geotechnical and Geophysical Site Characterization, ISC'4, Porto de Galinhas, 18 - 21 September 2012, pp. 637 - 644.

Cavallaro, A., Cessari, L. & Gigliarelli, E. 2013c. Site Characterization by in Situ and Laboratory Tests for the Structural & Architectural Restoration of Saint Nicholas Church, Nicosia, Cyprus. Proc. of the 2nd Int. Symposium on Geotech. Engng. for the Preservation of Monuments and Historic Sites, Napoli, 30 - 31 May 2013: 241 - 247.

Di Blasi, M. T. & Lanza, C. G. 2007. Il Cicerone. Storia, Itinerari, Leggende di Catania. Edizioni Greco, Catania, 2ª ed., 2007.

Galeazzi, M. 2010. Il Giardino Bellini di Catania. Tra storia e Progetto. Bonanno Editore, Acireale-Roma, 2ª ed., 2010.

Grasso, S. & Maugeri, M. 2005. Vulnerability of Physical Environment of the City of Catania Using GIS Technique. *Advances in Earthquake Engineering*. 14, 2005: 155 - 175.

Grasso, S. & Maugeri, M. 2009a. The Road Map for Seismic Risk Analysis in a Mediterranean City. *Soil Dynamics and Earthquake Engineering*. 29 (6): 1034 - 1045.

Grasso, S., Maugeri, M. 2009b. The Seismic Microzonation of the City of Catania (Italy) for the Maximum Expected Scenario Earthquake of January 11, 1693. Soil Dynamics and Earthquake Engineering. 29 (6): 953 - 962.

Kottke, A. R. & Rathje, E. M. 2008. Technical Manual for Strata. PEER Report. Pacific Earthquake. Engineering Research College of Engng. Univ. of California, Berkeley.

Marchetti, S. 1980. In Situ Tests by Flat Dilatometer. Journal of Geotechnical Engineering, ASCE, No. GT3.

Marchetti, S., Monaco, P., Totani, G. & Marchetti, D. 2008. In Situ Tests by Seismic Dilatometer (SDMT). From Research to Practice in Geotech Engng, ASCE Geotech. Spec. Publ. 180: 292 - 311.

Maugeri, M., Simonelli, A. L., Ferraro, A., Grasso, S. & Penna, A. 2011a. Recorded Ground Motion and Site Effects Evaluation for the April 6, 2009 L'Aquila Earthquake. Bullettin Earthquake Engineering 2011, 9: 157 - 179.

Maugeri, M., Totani, G., Monaco, P. & Grasso S. 2011b. Seismic Action to Withstand The Structures: The Case History of 2009 Abruzzo Earthquake.. Proc.8th Int. Conf. on Earthquake Resistant Engineering Structures. Chianciano Terme, 7 - 9 September 2011: 3 - 14.

Maugeri, M. & Grasso, S. 2012. The Seismic Microzonation of the City of Catania (Italy) for the Etna Scenario Earthquake (M = 6.2) Of February 20, 1818. Earthquake Spectra. February 2012.

Monaco, P., Santucci De Magistris, F., Grasso, S., Marchetti, S., Maugeri, M. & Totani, G. 2011a. Analysis of the Liquefaction Phenomena in the Village of Vittorito (L'Aquila). Bullettin Earthquake Engineering 2011, 9: 231 - 261.

Monaco, P., Totani, G., Totani, F., Grasso, S. & Maugeri, M. 2011b. Site Effects And Site Amplification due to the 2009 Abruzzo Earthquake. WIT Transactions on the Built Environment. Vol 120, pp. 29 - 40. In: Proc. of the Eight Int. Conf. on Earthquake Resistant Engineering Structures. Chianciano Terme, 7 - 9 September 2011: 29 - 40.

Yokota, K., Imai, T., Konno, M. 1981. Dynamic Deformation Characteristics of Soils Determined by Laboratory Tests. OYO Tec. Rep. 3: 13 - 37.

Geotechnical and Geophysical Site Characterisation 5 – Lehane, Acosta-Martínez & Kelly (Eds)

Predicted and measured behavior of a tall building in a lateritic clay

L. Décourt
Luciano Décourt Consultoria, São Paulo, Brazil

C. Grotta Jr.
Construtora Grotta & Salvetti Ltda, São Paulo, Brazil

A. S. D. Penna
Damasco Penna Engenheiros Associados, São Paulo, Brazil

G. C. Campos
Instituto de Pesquisas Tecnológicas – IPT, São Paulo, Brazil

ABSTRACT: For design purposes, SPT-Ts and in situ determinations of G_0, were carried out. The efficiency of the Brazilian SPT is, on average, 72%. Settlement rather than capacity governed the design. Later, with the building already under construction, other tests were performed, exclusively for research purposes. A load test was carried out on a square footing foundation, up to the conventional failure load, Q_{uc} (the load corresponding to a settlement of 10% of the equivalent width of the foundation, B_{eq}). Based on these test results, predictions of capacity and deformations of the foundations were made. And, what is unusual in any foundation experimental field, a 25 storey building was constructed, the settlements of its columns being measured. However, these settlement measurements started only when about 2/3 of the nominal column loads had already been applied. Computer programs were developed, for allowing correct assessments of column loads and settlements, since the very beginning of the loadings. The measured settlements, up to the end of construction were very small, less than 10.0 mm, no matter the stresses applied to the footings being very high, typically 1.2 MPa, confirming the high stiffness (load/settlement) of this lateritic clay.

1 INTRODUCTION

The Carmel Building was constructed by Grotta Company, owned by the second author. The foundation design was made by the first author. For design purposes SPT-Ts were carried out. The SPT-T is the traditional SPT complemented by torque measurements, T, Décourt & Quaresma Filho (1994).

The equivalent (N_{eq}) is defined: N_{eq} = T (kgf.m)/ 1.2. Considering that the boring results suggested that the clay layers were lateritic, Cross Hole and SDMT tests have also been carried out. The correlation $G_0 \times N_{SPT}$, established by Barros and Pinto (1997) was used for identifying this type of soil. Décourt (1994) demonstrated that lateritic clays present stiffness much higher (tipically 2 or more times) than other clays, with similar N_{SPT} values.

2 THE FOUNDATION DESIGN

In the area where the building was constructed, the bearing layer was a hard sandy silty clay, red and yellow.

The values of N_{SPT} and N_{eq} were 26 ± 15%, the lower bond value corresponding to the average of the N_{eq} values and the upper bond value, the average of the traditional penetration resistance, N_{SPT}.

Cross Hole and SDMT tests confirmed that these clays were lateritic. The design was based exclusively on settlement predictions, using the method proposed by the first author, Décourt (1999).

$$\log q/q_{uc} = C\ (1 + \log s/B_{eq})$$

where *s*= settlement and B_{eq} is the square root of the footing area. The two fundamental parameters in the above formula, the stress corresponding to the conventional bearing capacity, q_{uc} and the Coefficient of Intrinsic Compressibility, C, were much better for this lateritic clay than those for common soils.

For most of soils found in São Paulo city, whose grains are made of quartz, C values are 0.4 ± 10%, and q_{uc} is obtained using correlations with N_{SPT}, proposed in Décourt (1995). For partially saturated soils, other than sands, q_{uc} in kgf/cm² units is approximately, equal to the Brazilian N_{SPT} (average efficiency of 72%). Using the official SI units: q_{uc} (MPa) = N_{SPT} /10. For sands, q_{uc} is approximately 20% higher and for saturated clays, approximately 20% lower.

The average value of N_{SPT} considered was 26 and a majorating factor β_l, for lateritic clays, equal to 1.5 was adopted. Therefore, q_{uc} (MPa) = (0.8×1.5×26)/10 = 3.12 MPa (lateritic saturated clay).

The C value considered was the most adequate for São Paulo clays, 0.42. The maximum tension applied to the soil by the footings was 1.2MPa. The expected settlements were about 20.0mm.

3 LOADING TESTS

With the construction of the building under way, the first two authors decided to implement at this site a foundation experimental field.

In a region behind the building, here named Site I, a load test was carried out on a square block foundation with 78.0 cm in width. The average N_{SPT} value (efficiency of 72%) was 21, corresponding to $N_{60} \cong 25$.

The results of this loading test are presented in figures 1, 2 and 3.

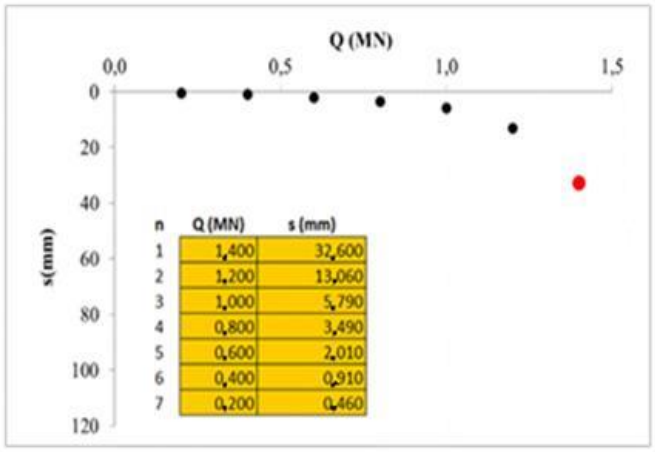

n	Q (MN)	s (mm)
1	1,400	32,600
2	1,200	13,060
3	1,000	5,790
4	0,800	3,490
5	0,600	2,010
6	0,400	0,910
7	0,200	0,460

Figure 1 - Load test data

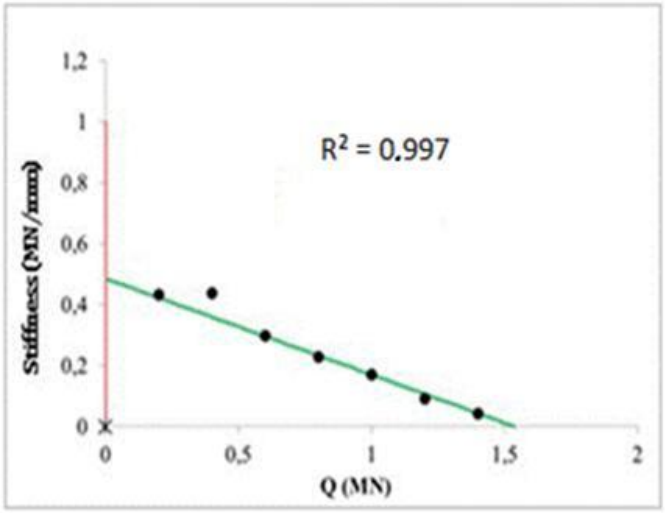

Figure 2 – The stiffness plot, Décourt (1999)

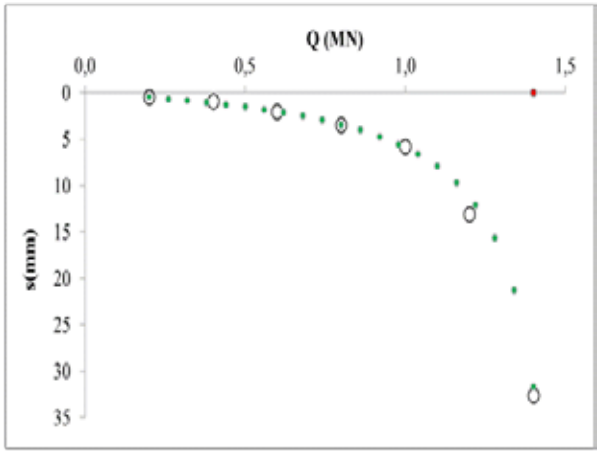

Figure 3 – Measured values and the regression curve that best fits the data

The results and the interpretation made using the stiffness plot, developed by the first author, Décourt (1999) are presented. The relation load x stiffness was a straight line; see Fgure 2.

The conventional bearing capacity, Quc, according to this method was 1.46MN and the corresponding stress, q_{uc}, was 2.40MPa. In Figure 4 relationships between $q/q_{uc} \times s/B_{eq}$ for common soil are presented, for different values of C. Observe that lateritic clays may follow, sometimes, a different pattern, as for example the cases of Carmel Building and Décourt (2003).

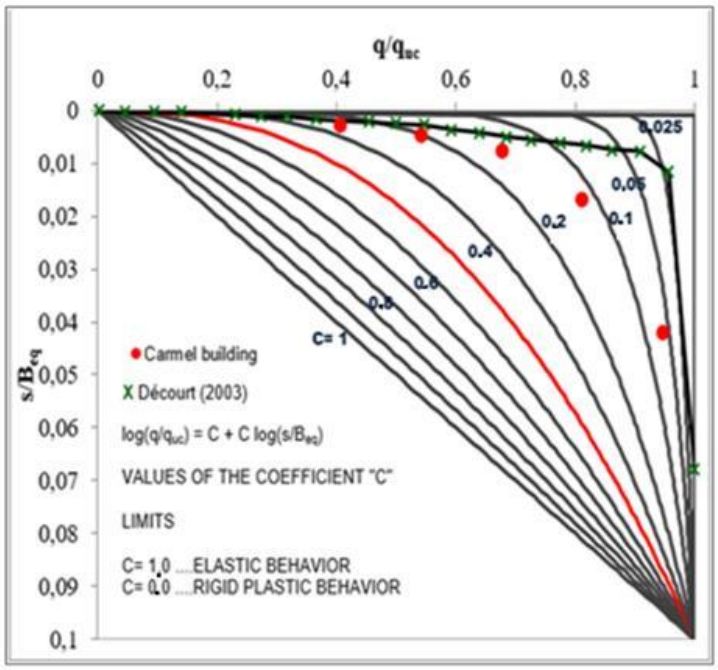

Figure 4 – Values of q/q_{uc} x s/B_{eq} as a function of C

4 SETTLEMENT MEASUREMENTS

4.1 *Measured values*

Column settlement measurements have been made by a team of the Technological Research Institute of São Paulo (IPT) under the guidance of the fourth au-

thor. Unfortunately, these measurements started only when about 60% of column loads had already been applied. However, the knowledge of the magnitude of these settlements, since the very beginning of the loadings, was considered fundamental.

4.2 *Correction method*

The second author developed a program in order to estimate the loads applied to the building columns, at any stage of the construction, taking into account the permanent static loads of the following elements, namely: structure, masonry (with built-in installation), subfloor, internal parget, external parget, floor and wall tiles.

As settlements were measured by IPT (Technological Research Institute), the loads applied by the above elements (according to the stage of execution at that moment) were estimated and distributed on the columns previously built. Accordingly, only live loads were considered. In order to obtain the settlement missing informations, a computer program was developed by the first author. The stiffness plot, Décourt (1999), was used. The program corrects the measured settlements of the columns. Using both programs, it was possible to simulate a loading test for each of these columns

4.3 *Checking the validity of the proposed correction method using load test data*

For checking the reliability of the proposed method for correcting the measured settlements, the loading test carried out on the square block was used.

For the load of 0.6MN, the measured settlement, in the load test, was 2.01mm. This value was subtracted from all other measured settlements. In figure 5 the plot stiffness x load is presented.

The coefficient of correlation, R^2 was very poor, 0.922 as compared with the one corresponding to the original load test, 0.997. The method for settlement correction was applied and a settlement of 2.06mm for the load of 0.6MN was obtained, a value that differs from the measured one (2.01mm) by only 2.48%, confirming its reliability.

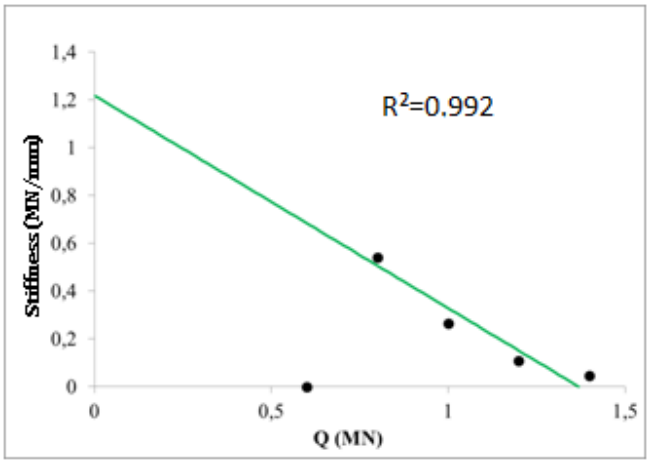

Figure 5 – Stiffness plot for the simulated curve

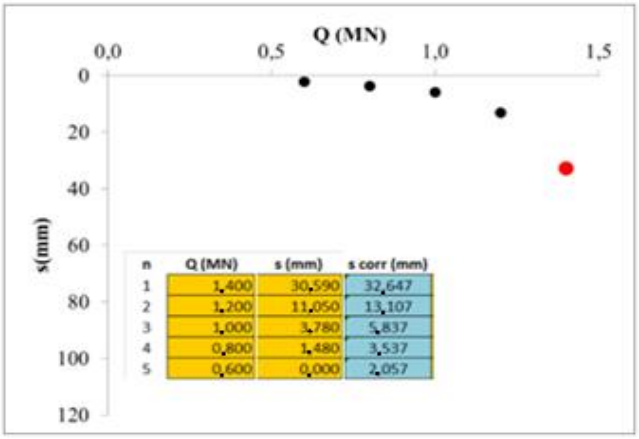

Figure 6 – Corrected load settlements curve

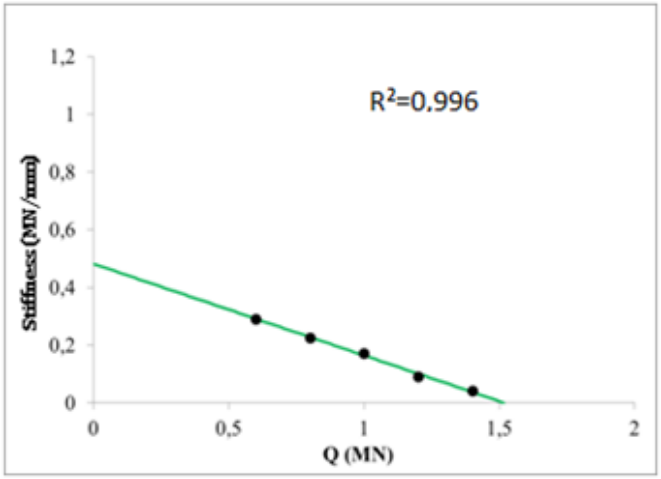

Figure 7 - Stiffness plot for the reconstituted curve

In the stiffness plot, with this value included, the coefficient of correlation was again very high, 0.996, a value practically identical to that corresponding to the original loading test, 0.997.

5 CORRECTED SETTLEMENT VALUES

In figures 8, 9 and 10 the corrected load-settlement curves are presented, for 3 columns.

These curves allowed not only the knowledge of the full range of settlement values, but also represent the best fit to the measured ones.

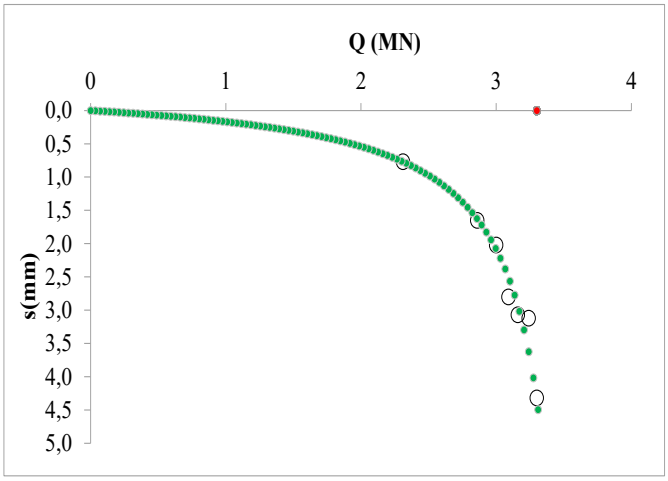

Figure 8 – Corrected load-settlement curve for P6A

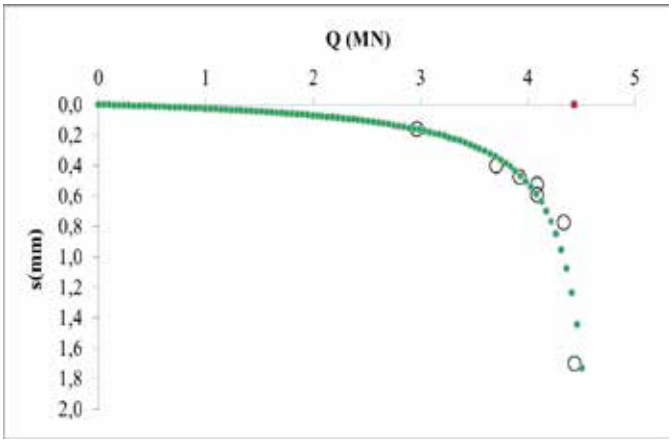

Figure 9 – Corrected load-settlement curve for P23A

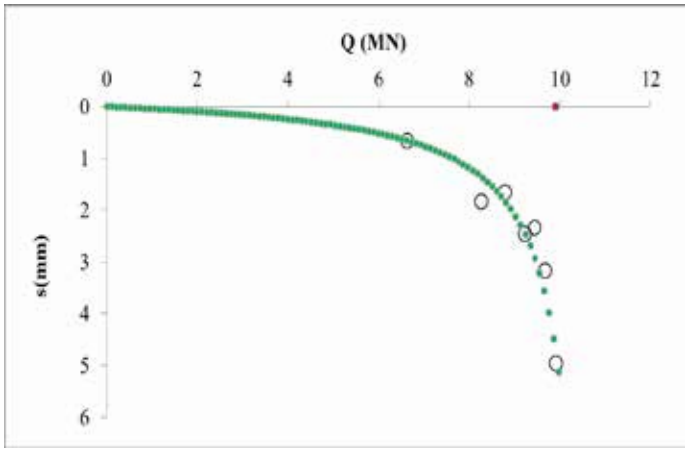

Figure 10 – Corrected load-settlement curve for P13B/P15B

In Table 2, for each column whose settlements were measured, estimates of q_{uc}, are presented, Décourt (1999). Knowing q_{uc}, the corresponding values of N_{SPT} could be derived, assuming valid for lateritic clays, Décourt (1995) proposals. Two soil conditions were considered, non saturated soil (type II) and saturated soil (type III).

Table 2. Soil parameters derived from settlement measurements

Column	s_c (mm)	q_{uc} (MPa)	C	N_{SPT}*
6A	4.320	2.470	0.210	25/31
21A	3.098	2.142	0.205	21/27
23A	1.701	2.277	0.177	23/28
12A/14A	1.225	2.520	0.229	25/31
13A/15A	1.837	xx	xx	xx
Average		2.352	0.205	23.50/29
3B	7.740	2.420	0.290	23/29
8B	7.901	1.950	0.223	19.5/24.5
20B	6.923	2.530	0.256	25/31
12B/14B	5.988	2.400	0.284	24/30
13B/15B	4.942	2.050	0.208	20.5/25.5
Average		2.270	0.252	22.5/28

* Lower values corresponding to non saturated soils (type II) and higher values corresponding to saturated soils, type III, Décourt (1995).

xx Results considered non reliable.

The range of values, for both, blocks A and B were more or less the same 23/29. The average values of C, however, varied substantially, from 0.205 for block A, to 0.252 for block B. The difference in C values is the main responsible for the differences in the measured settlements, much higher for block B, than for block A.

It is also interesting to observe that this range of values, 23/29, falls within the range of average values given by the borings 22/30, the lower value being average of N_{eq} and the higher value average of N_{SPT}.

6 CONCLUSIONS

The initial investigations, SPT-T, Cross-Hole and SDMT allowed correct assessment of capacity and confirmed the lateritic characteristics of the clay layers. But these tests gave no information on the compressibility of these layers which is fundamental for correct settlement predictions.

The load test on a square block, 0.78m in width, confirmed the predicted capacity of shallow footings on this clay. But, what is of paramount importance, is that the average Coefficient of Intrinsic Compressibility, C, was half the value considered in design. Besides, C values were not constant, as it usually happens for most of the soils, but decrease as the applied stresses increase. Such behavior is characteristic of some soils with cemented particles and have already been detected by Décourt (2003). The analysis of the settlement measurements, simulating load tests, suggested that characteristic N_{SPT} values and q_{uc} were about the same for both blocks A and B, but C values were higher for block B as compared to block A (0.252 and 0.205). The measured settlements for block B at the end of construction were, on average, less than half the values predicted in design and those for block A, on average, less than 50% of those corresponding to block B.

Notwithstanding the applied stresses being more than twice those currently considered in design, the settlements were less than half the expected values, demonstrating the outstanding importance of recognizing lateritic clays.

7 REFERENCES

Barros, J.M.C. & Pinto, C.S. 1997. Estimation of maximum shear modulus of Brazilian tropical soils from standard penetration test. XIV ICSMFE, Vol I, Hamburg, Germany.

Décourt, L. 1994. The Behavior of a Building with Shallow Foundations on a Stiff Lateritic Clay. Vertical and Horizontal Deformations of Foundations and Enbankments. ASCE, G.S.P. n. 40, Vol II, College Station, Texas, U.S.A.

Décourt, L. 1995. Prediction of Load-Settlement Relationships for Foundations on the Basis of the SPT- T. Ciclo de Conferencias Internationales, Leonardo Zeevaert, UNAM, Mexico.

Décourt, L. 1999. Behavior of foundations under working load conditions. Proceedings of the XI Panamerican Conference on Soil Mechanics and Foundation Engineering. Vol.IV. Foz do Iguaçu, Brazil.

Décourt, L. 2003. Behaviour of a CFA Pile in a Lateritic Clay. Proceedings of the 4th International Geotechnical Seminar on Deep Foundations on Bored and Auger Piles, BAP IV, Ghent, Belgium.

Décourt, L. ; Belincanta, A. ; Quaresma Filho, A. R. 1989. Brazilian Experience on SPT. XII ICSMFE, Rio de Janeiro. Suplementary Contributions by the Brazilian Society for Soil Mechanics.

Décourt, L. & Quaresma Filho, A R. 1994. Practical Applications of the Standard Penetration Test Complemented by Torque Measurements, SPT-T; Present Stage and Future Trends. XIII ICSMGE. New Delhi. India.

Geotechnical and Geophysical Site Characterisation 5 – Lehane, Acosta-Martínez & Kelly (Eds)

Remedial measures to facilitate the construction of stable bridge approach fills: A case study

V. Diyaljee

Gaea Engineering Ltd, Brampton, Ontario, Canada

ABSTRACT: The proposed construction of a north-south log haul road from Secondary Road (SR 686) to North of the Little Cadotte River was to form part of the roadway infrastructure requirements for the proposed Daishowa Pulp Mill in Peace River, Alberta. This paper deals primarily with stability issues associated with the Cadotte River crossing. After the construction of 5 m of the proposed 20 m high bridge approach fill in No-vember 1988 deep seated movements were noted at a depth of 22 m below the original ground from monitoring of slope indicators on the north approach. Remedial measures consisting of wick drains, stone columns, flatter approach fill head and sideslopes, and interceptor drains were then implemented. However, as a result of the movements that were taking place at depth it was decided to abandon the proposed 3-span bridge and construct a one-span Bailey bridge. This paper addresses the geotechnical investigation, evaluation and assessment of the bridge approach fills and the remedial measures implemented to minimize the movements.

1 INTRODUCTION

Roadway infrastructure to facilitate log haul to the Peace River Pulp Mill, a Division of the Daishowa-Marubeni International Ltd (DMI), situated sixteen (16) kilometres north of the Town of Peace River, Alberta, required the construction of a north-south log haul roadway from SH 686 to the Little Cadotte River. This route, which covers a distance of 50 km, required a bridge at the Cadotte River crossing shown in Figure 1.

Due to the projected fast paced schedule of the pulp mill project a geotechnical assessment of the ground conditions at the proposed crossing was initiated in July–August 1987 to meet the requirements for the design and construction of the bridge approach fills. The bridge structure was conceived as a three-span bridge and scheduled for construction in November 1988.

The schedule appeared realistic if everything went well, but could not be accomplished as a result of unforeseen ground conditions at the site of the bridge crossing. This paper outlines and discusses the problems encountered during the construction of the bridge approach fills which resulted in the abandonment of the proposed bridge. To overcome these setbacks which resulted from slope instability problems, a Bailey bridge had to be constructed at this site on a shifted alignment.

2 SITE DESCIPTION AND CHARACTERISTICS

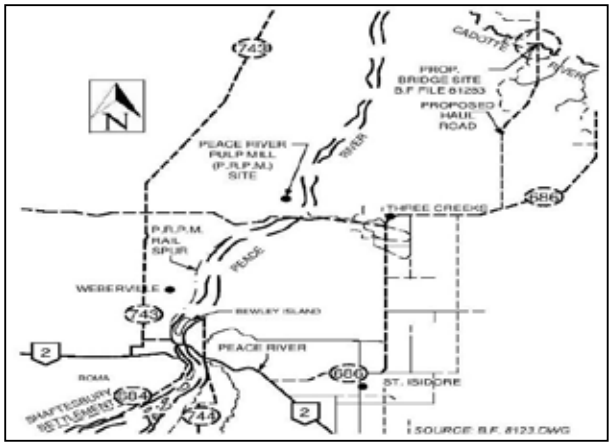

Figure 1. Location of Roadways, Bridge and Pulp Mil

At the proposed bridge location, the Cadotte River is a narrow, shallow east–west oriented stream contained in a deeply incised river valley. A width of 1 km between valley walls and an average elevation difference of about 65 m from streambed to the top of the valley walls are indicative of the extent of river activity and/or glacial activity on the topographic development of the Cadotte River in its geologic past. The topographic features of the north and south valley slopes appeared very similar except that the north valley slope was somewhat hummocky with evidence of slide scarps at the top of the valley immediately adjacent to the proposed alignment.

Limited aerial photography assessment during the alignment study did not indicate the presence of deep seated slide activity nor slide activity of recent origin. The aerial photos did, however, reveal some puzzling features which gave the impression that some ground displacement had occurred on the north side of the river or that a river channel once dissected the present flood plain. Similar river channel features were also present on the south side of the crossing.

Site reconnaissance of the alignment undertaken during the summer of 1988 showed waterlogged conditions from the river to almost 150 m on both north and south sides of the crossing. The water logged areas were observed to have resulted from beaver activity. From brief observations these stagnant sources were considered drainable towards the river. During this reconnaissance it was felt that the ground between the river and a beaver pond on the north side had undergone some previous displacement. This was deduced from the relief of the ground which showed an abrupt ridge 2 to 3 m in height merging into the beaver pond. No such abrupt relief was observed on the south side of the crossing. The puzzling nature of this ground relief along with adjacent ground features raised immediate geotechnical concerns of the site conditions.

3 SITE INVESTIGATION

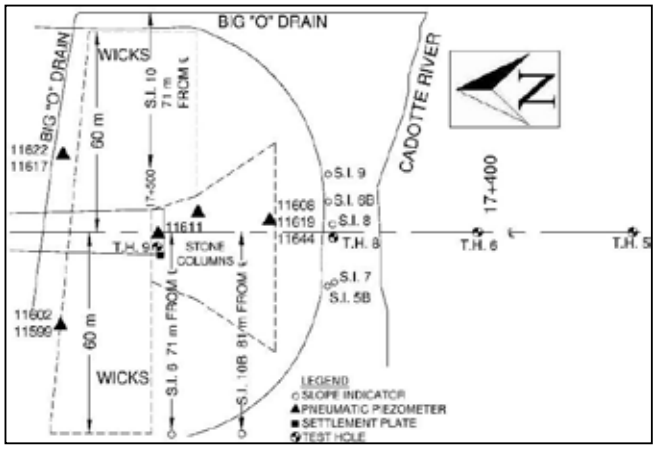

Figure 2. Testhole, Instrumentation & Trench Drain Loca-

Concerns of possible old slide activity coupled with the projected schedule for bridge construction in November 1988 and projected heights of approach fills in the order of 20 to 30 m above streambed prompted the undertaking of an early site investigation.

The site investigation was undertaken in July 1988. A total of twelve (12) testholes were drilled between Sta 16+650 and Sta 17+890 covering the river crossing and north and south valley walls.

For the bridge approach fills and foundation assessment four (4) testholes were drilled. These holes are referenced as TH 5, 6, 8, and 9 and located as shown in Figure2. Testhole drilling was undertaken using an auger rig with capabilities of coring using a wire line coring approach. Sampling by coring and standard penetration testing (SPT) was undertaken in the four (4) testholes.

4 SUBSURFACE CONDITIONS

In general, the soil stratigraphy in the vicinity of the approach fills consisted of 2 to 3 m of soft surficial alluvial deposits of sand, silt and clays overlying over consolidated clay shale varying in consistency from stiff to hard and extending to a depth of about 25 m where the drilling was terminated. Groundwater was observed within a metre of the ground surface at the testhole locations. In scrutinizing the testhole logs, it was observed that the SPT values were generally smaller at similar depths on the north side than on the south side. However, the SPT values showed the underlying shale to be reasonably competent with depth.

Laboratory visual description of the samples of clay shale revealed the material to be essentially silty clay containing silt varves, indicating a marine depositional environment. Laboratory testing for moisture content, index properties, and strength determinations indicated slickensided shear with strain softening behaviour at small strains. Variable unconfined compressive shear strengths were obtained from core samples within the clay shale. Moisture contents were generally below optimum moisture throughout with material classification being predominantly MH/CH. In one sample at a depth of 25 m in TH 8 a 50 to 100 mm thick piece of bentonite was reported in the laboratory visual description. This sample had a liquid limit of 135%, plastic limit of 31 % and a field moisture content of 22%.

5 ASSESSMENT OF SUBSURFACE CONDITIONS

Following the field testhole drilling and in consideration of the proposed fill heights along with soft and wet conditions in the top 2 to 3 m of ground it was decided to undertake stage construction of the approach fills. The construction of the fills was to be preceded by the excavation of soft surficial material.

A testpit investigation was undertaken to decide on the extent of removal of soft soil with depth throughout the site. This investigation was carried out in September 1988 and was concentrated on the south approach although it was originally proposed to undertake this investigation on both sides of the river. At this time the north side had only been cleared of treed vegetation and a drainage channel opened to the river to facilitate drainage of the beaver ponds/sloughs and no testpitting undertaken.

In light of the presence of water and the hard bottom within the excavated areas in the vicinity of the stub approach fill on the south side, it was recommended that the excavation should be backfilled with granular material to original ground before placement of the

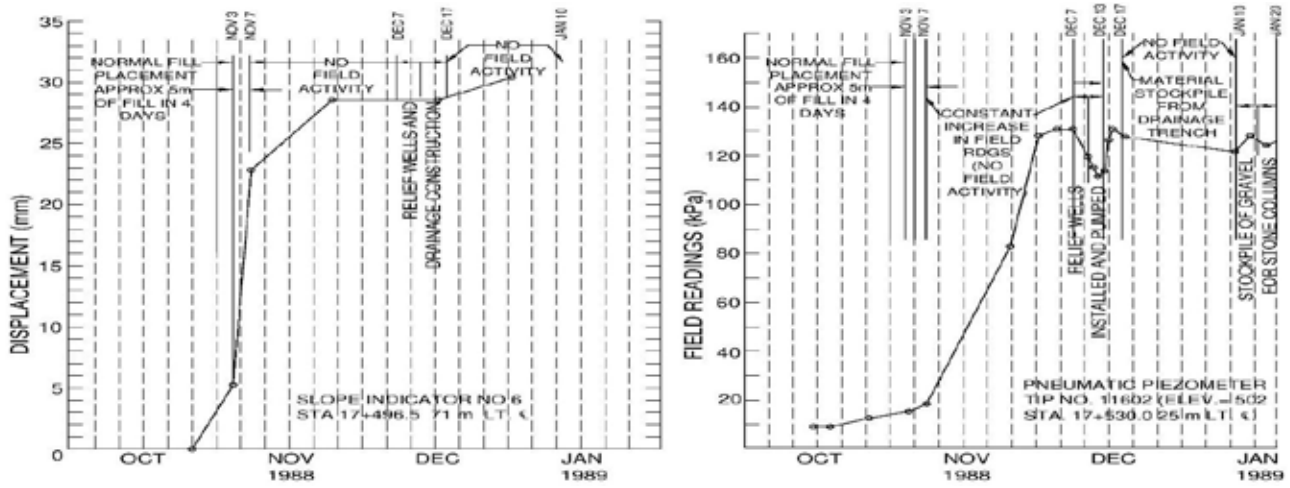

Figure 3. Porewater pressures and displacements versus time

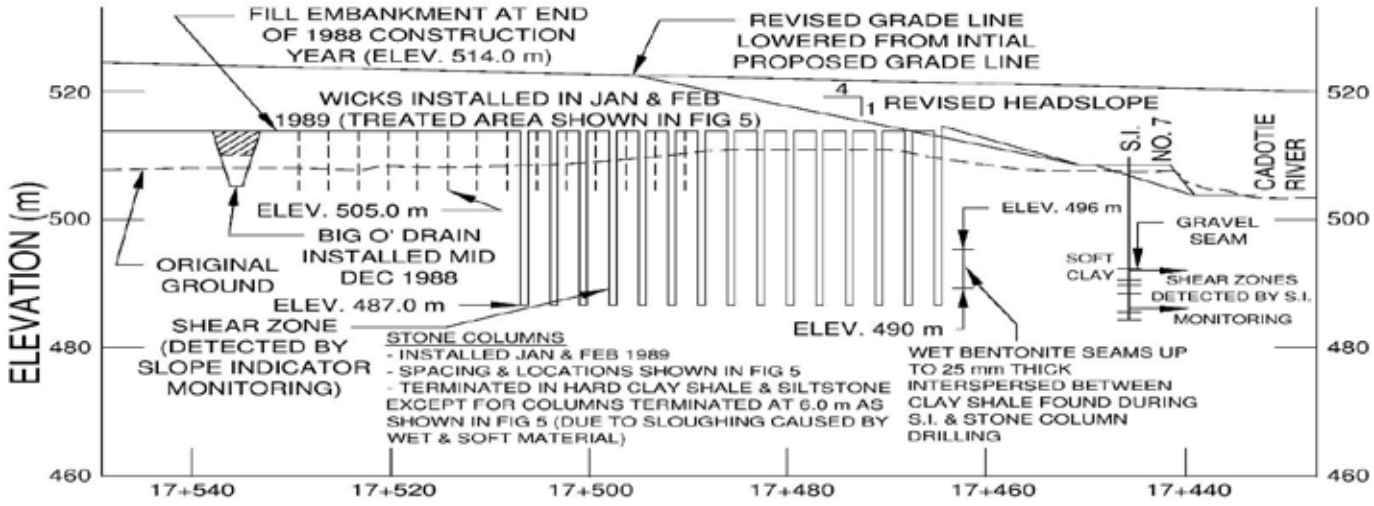

Figure 4. Cross section at North Approach Fill showing weak zones

approach fill. However, in consideration of the quantity of material required for both sides of the river, the non-availability of gravel within an economic haul distance and general restrictive site conditions at the time of truck hauling this proposal was abandoned in favour of backfilling with clay borrow and removing free water from the site through its displacement by the advancing fill.

The use of geotextiles beyond the stub fill area in a very silty and unstable section of the south side was also recommended. This was considered essential to facilitate earthworks hauling by scrapers. No geotextile was recommended for use on the north side although initial discussions considered its use in the slough areas if the bottoms of the sloughs were decidedly soft or weak. Testpitting was done subsequently on the north side and a similar sub-excavation was undertaken on this side as was done on the south side. In subsequent discussions of the project site characteristics with the Bridge Planning Engineers a 2.5:1 headslope was recommended for both the north and south approach fills instead of the traditional 2:1 headslopes used to minimize bridge length and hence overall structure costs.

6 INTRUMENTATION

Prior to the placement of the bridge approach fills slope indicators and pneumatic piezometers were installed to aid in the monitoring of fill construction. Piezometers were installed at locations shown in Figure 2 to a maximum depth of 9 m below existing ground. No deeper installation was undertaken at that time since it was not perceived that movements, if they were to occur, would be deep seated. Slope indicators were, however, installed to a depth of 26 m although the first installation (SI 2) on the south side was terminated around 13 m since very hard ground was encountered. The decision to install the inclinometers to 26 m was based on the observation of the variability of the clay shale with depth from the testhole logs.

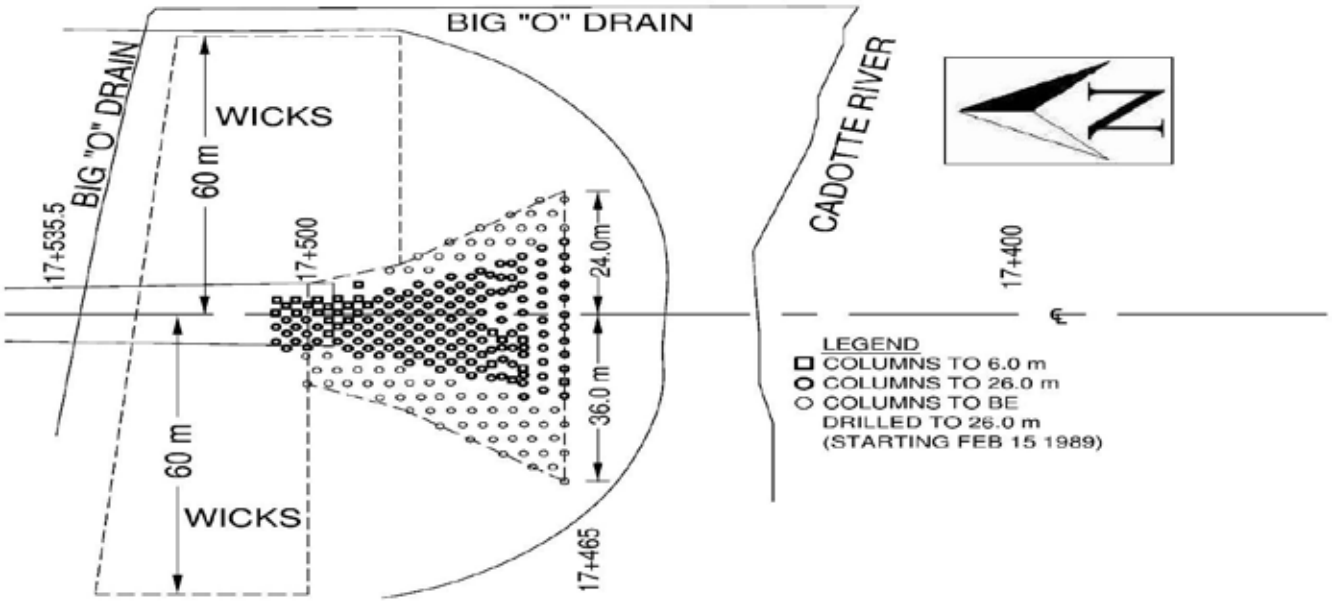

Figure 5. Layout of Stone columns and Wick Drains – North Approach zones

7 FILL CONSTRUCTION

Approach fill construction began around September 15, 1988. Slope indicators and pneumatic piezometers were monitored regularly as the fill was placed. The weather condition was generally good until October 20 when a temporary halt in construction was made due to snowfall. Heavy snowfall on November 7 signaled the onset of winter and resulted in a permanent halt to construction activity.

At this stage fill construction attained a height of about 5 to 6m on both sides of the river crossing. A third set of slope indicator readings was taken on November 7. The results of this monitoring showed movement to be occurring in all slope indicators on the north side to a depth of about 22 m. Except for SI 2 on the south side which was installed to a depth of 13 m and which showed movement around 12 m, the remaining SIs on the south side did not show any well defined zone of movement.

The observed depth of movement at 22 m led to many questions concerning the validity of the field measurements in relation to whether instrument error, poor installation techniques, etc., were responsible for the results attained. After much evaluation it was decided that movement was indeed occurring at that depth and that there was some correlation with the weak zones noted in TH 8 where blow counts had been observed to be variable. A decision was made to re-read the SIs with a different inclinometer probe to ensure that the depth of movement was indeed factual. The slope indicators were re-read on November 24, 1988 using a different probe. During this re-reading it was reported that the probe became stuck at the depth of 25 m recorded previously in SI 8, hence confirming the previous monitoring results. As well, the deformations recorded to the depth at which the probe became stuck were comparable to those obtained previously.

Piezometer readings showed substantial increases in porewater pressure than previously recorded during fill construction. On the basis of these field observations it was concluded that deep seated movements were indeed occurring at the site.

8 INVESTIGATION OF GROUND MOVEMENT

The determination of the cause of movement led to further drilling and site inspections during the period November 29 to December 18, 1988. Deep drilling using auger and rotary drilling were undertaken to ascertain the reasons for the high pore pressures as well as to ascertain whether weak material existed at the zone of movement. Auger drilling revealed water to be associated with the old beaver ponds/slough areas which was attributed to possible seepage from uphill of the flood plain or from water trapped during embankment construction. Testpits dug to a depth of 8 m uphill of Sta 17+585 proved to be dry and suggested that the slough areas resulted from beaver dam activity. However, the high piezometric pressures at a depth of 7 m below original ground suggested that downward seepage was possible and that piezometric pressures were caused by the weight
of fill. A check on the piezometric levels confirmed that these levels were as high as and becoming higher than the fill elevation. The steadily increasing pore pressures observed following fill construction were attributed to the poor drainability of the site.

Further field testing to reduce pore water pressures included installation of 300 mm diameter wells to about 9 m below fill elevation. These wells were located in the vicinity of Sta 17+585 to intercept the old slough areas and were pumped for 2 days. A total of

2200 gallons of water were pumped. During this period porewater pressures were monitored and from Figure 3 it can be seen that a drop of 27 kPa in piezometric pressure occurred. This observation along with the observation of large underground flow during testpitting opposite SI 6 outside of the fill slope led to the idea of installation of trench drains to aid in removal of trapped or seepage water.

Trench (French) drains with Big-O drainage pipe were installed as shown in Figure 2. During excavation of these trench drains seepage zones were observed along the walls of the trenches from gravel and sand layers. The majority of flow, however, was associated with a lower gravel layer which appeared to be co-incident with the base of the beaver ponds.

Almost opposite SI 6 a classic structural folding due to a geologic process was observed showing bentonite rich shale thrust into the gravel stratum resulting in an upward displacement of the gravel. This bentonite rich shale was very friable and crumpled instantly when handled without hardly any pressure.

This observation added credence to the belief that this site had undergone prior movements. The folding led to the belief that glacial thrusting, for lack of a better explanation had occurred. The presence of bentonite near the surface was also of valuable significance since it confirmed the laboratory visual observations. As well, the movements recorded by the slope indicators were becoming more reasonable to understand. In short there was now more evidence from field observations to conclude that this site presented some very complex ground conditions. A number of probe testholes were subsequently done to determine whether bentonitic zones could be defined and also to define the wet areas and seepage zones. As shown in Figure 4 soft wet zones about 1 m in thickness were observed to be sandwiched between very intact and competent shale material. At first it was felt that poor drilling methods might have caused this to occur but careful drilling and scrutiny of cores showed that these zones resulted from softening due to shearing action. The presheared zone was very soft with pocket penetrometer readings varying from 0.25 to 0.5 Tons/ft^2. Also shown in Figure 4 is the depth range at which bentonite was observed.

On the basis of the field observations and stability assessments several aspects were debated for the continuing construction of the fills. A culvert option was considered in lieu of a bridge but was scrapped a result of instability problems that would result from excavation along with associated costs for a proposed large reinforced concrete structure. In addition, environmental concerns would be a major problem. The idea of ground modification by deep soil mixing was pursued but this equipment could only be obtained from a Contractor in the USA, with a price tag of about $US1.5 million. This was considered too expensive and not pursued. Site relocation was also considered but not pursued since this idea had limitations in terms of overall roadway network logistics and the fact that there may not be a more desirable site. Instead it was finally decided that a combination of wick drains, stone columns along with flatter fill and head slopes would be the preferred approach to use to stabilize the site.

9 REMEDIAL MEASURES AND FIELD IMPLEMENTATION

The use of wick drains and stone columns in combination would provide a reduction of the pore water pressures by the wicks while the stone columns to be installed by augering and replacement of the excavated material with compacted gravel aggregate would provide for removal of the weak material and an increase in the shearing resistance of the ground. From stability assessments the combination of reduced porewater pressures, increased shearing resistance and flatter head and side slopes would result in the overall factor of safety of 1.2 to 1.3.

Field implementation of remedial measures began on January 10, 1989 with wicks and stone columns. The stone columns were installed using two Texoma Drill rigs equipped with a 1m diameter auger. Compaction of the stone columns was undertaken with the aid of a 750 mm diameter plate tamper attached to the end of the Kelly bar of the drill rig. The compactive effort was applied to small lifts of gravel backfill via the crowd force applied by the drill rig on the Kelly bar. Figure 5 shows the layout of stone columns and wick drain installations.

On January 16, 1989 stone column installations revealed the zones of bentonite to be contained between El 490 and El 496. A test drilling was done near to SI 8 to ascertain the material characteristics at the zone of movement. It was rewarding to find bentonite in a very wet and greasy condition in addition to free water between clay shale that portrayed a fissured appearance. The reason that water was present at great depths either via downward penetration through fissures or underground seepage was therefore substantiated and that instability resulted from excess porewater pressure at very low shearing resistance of the bentonitic seams. The fissured nature of the clay shale was attributed to valley rebound following glaciation.

10 SUMMARY AND CONCULUSIONS

The implementation of the remedial measures did not fully arrest the ground movements. As a result, the approach fill slope on the north headslope was modified from 2.5:1 to 4:1 with side slopes of 4:1. On the south side the initial design of the approach fill slopes of 2.5:1 headslope and 3:1 sideslopes were maintained. In addition, as a result of the movements it was decided to utilize a Bailey Bridge at the crossing location. This bridge is shown in Fig 6. Monitoring of

this bridge by survey hubs between June 2 and October 11, 1990 showed initial movements of 7 mm per day to July 4 and thereafter 1.2 mm per day. A recent site observation in August 2013 (Figure 7) shows that the bridge is still serviceable after 23 years.

Figure 6. Aerial Photo Showing Bridge

Figure 7. Site photo taken in August 2013

11 ACKNOWLEDGEMENTS

The writer appreciates the assistance of Mr. Jason Khan for drafting the figures contained in this paper and Mr. Roy Callioux, P.Eng, former Construction Manager, Alberta Transportation, Alberta, for his periodic post construction site reviews and providing the site photo (Fig,7).

Geotechnical and Geophysical Site Characterisation 5 – Lehane, Acosta-Martínez & Kelly (Eds)

Subsidence Characterisation for a proposed Concrete Shaft using a 250 m deep Inclinometer Borehole, Huntly East Coalmine, New Zealand

Z. Du
Curtin University, Perth, WA, Australia
M. Balks & V. Moon
The University of Waikato, New Zealand
P. Page, R. Winter & L. Cunningham
(Previously) Solid Energy, New Zealand.

ABSTRACT: This paper reports on inclinometer monitoring of a 250 m deep borehole to characterise strata movement that occurred as underground mining approached the borehole near Huntly East Coalmine, New Zealand. Thirteen inclinometer surveys were conducted, using one inclinometer probe, during 2 years from March 2009. This characterisation contributes to the design and installation of a proposed 300 m concrete shaft in the Huntly East coalmine. Three major movement zones were identified; two 'shear zones' and one 'creeping zone'. The borehole lateral movements were non-linear in time, and lateral movement trajectories varied with depth. Three equations were developed from regression and Phase2 modelling, indicating the relationship between extraction edge distance and the induced lateral movement at three separate depths of the three movement zones. Equations from both regression and modelling gave 'very strong' correlation at 1 m depth. At the other two depths investigated, 135 m and 166 m, correlations were 'strong' for equations from both the regresssion and the modelling methods. A 'movement trajectory of the borehole' was used for analysing and characterising the mine ground movement. There were a number of limitations in this research. Lateral movement has been analysed and characterised in this study, but vertical subsidence has only been identified to exist and is not discussed in detail.

1 HUNTLY EAST COALMINE

Huntly East Underground Mine is located north of Huntly Township, approximately 80 km south of Auckland, New Zealand. The Huntly East Mine geology consists of a sequence of mudstones and coal seams of the Te Kuiti Group with a thickness ranging from 25 m to 250 m, over a succession of saturated sands, silts, and gravels of the Tauranga Group with a thickness from 25 to 70 m. This sequence lies on greywacke basement rocks. Two economic coal seams, the Renown and Kupakupa Seams, lie near the base of the Te Kuiti Group. The coal seams have a typical total thickness of 20 m, and are normally 150 to 300 m below the surface (Solid Energy 2006; Solid Energy 2011).

Subsidence above the Huntly East Mine has occurred since initial production in early 1983 (Kelsey 1986). In 2006, the planned and managed subsidence over the north mine panels 51 and 52 ranged approximately from 1 to 1.2 m (Guy et al. 2006). Installation of a new 300 m deep concrete shaft was proposed to improve access to the western portions of the mine; strata movement surrounding this shaft may compromise the stability of the shaft opening. To assess likely movement amounts, Solid Energy installed a 250 m deep inclinometer borehole in the North 5 mining area in 2009 ahead of advancement of the mining operations at the time (Solid Energy 2009).

2 INCLINOMETER DATA AND BOREHOLE MOVEMENT

2.1 *Methods*

The Borehole (20091) for inclinometer monitoring was drilled by wash coring in February 2009, to a depth of 250 m. The borehole was watertight as it was enclosed by a PVC casing and grout sealing (Solid Energy 2009). Thirteen inclinometer surveys were conducted using the same inclinometer digital probe (Series Number 1678, Soil Instruments Limited 2010) on 13 separate days from March 2009 to February 2011. The first survey on 27 March 2009 is the reference or initial baseline for this research. The data errors in the 13 inclinometer datasets included the extreme checksum values (Machan & Bennett 2008; Mikkelsen 2007; Mikkelsen 2003; Cornforth 2005). After error corrections, two abnormal surveys were

discarded, and the 11 useful survey datasets were used for further analysis.

2.2 *Identification of movement zones*

Cumulative displacement graphs for both the A and B axes (Figure 1a and 1b) indicate the deviation from the shape of the borehole measured immediately after installation on 27/03/2009. Figure 1c presents the resultant cumulative displacement plots from summation of the A axis and B axis components in Figures 1a and 1b. Data are cumulated from the base of the borehole. This assumes zero deviation at the base (Stark & Choi 2008; Cornforth 2005).

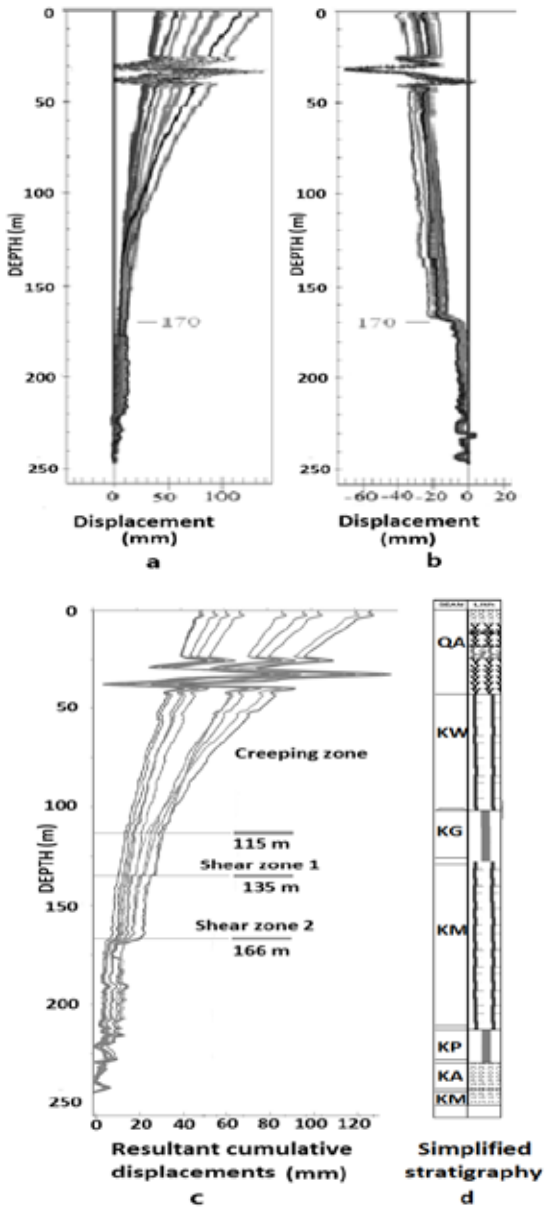

Figure 1. a, the A axis cumulative displacement after error correction. b, the B axis cumulative displacement after error correction. c, Resultant cumulative displacements showing three movement zones. d, The simplified stratigraphy of borehole 20091, QA: Quaternary age in Tauranga group; and KW: Whaingaro Formation, KG: Glen Massey Formation, KM: Mangakotuku Formation, KP: Mangakotuku – Pukemiro Mbr formation, and KA: Pukemiro – Glen Afton formation in Te Kuiti Group.

Several discrete zones can be seen in the resultant cumulative displacement plots (Figure 1c).

From 115 m to 0 m (surface) a progressive lean is observed in the resultant curves suggesting increased movement of the strata towards the surface. The top 115 m of the borehole may thus be a zone of creep (Figure 1c).

The creeping region includes a zone of extreme deviation between approximately 22 and 40 m which is inferred to represent suspending and floating of the casing due to poor grouting. This extreme displacement is considered artificial and does not represent strata movement so is not considered in this discussion.

Shear zone 1, from 135 to 135.5 m, is a narrow (0.5 m) shear zone (Figure 1c), largely due to movement in the B axis. Shear zone 2 at approximately 166 m – 170 m presents a sharp jump in the resultant curves, this is largely due to movement in the B axis (Figure 1b) and represents a dispersed shear zone approximately 4 m thick.

The three zones coincided well with the geological structures showing in geophysical Logs from the inclinometer borehole, provided by Solid Energy (2009).

2.3 *Direction of movement*

The plotted trajectories of borehole movement at 1 m, 135 m, and 166 m depths, show that: the movements were all non-linear; the trajectory at 1 m is quite consistent overall, with a trend of approximately 140°; movement patterns at 135 m and 166 m were very similar to each other.

2.4 *Rates of movement*

Patterns of movement rate were similar, with all three depths showing peak rates during measurements 5-6 and 9-10 (Figure 2). Movement was consistently fastest in the creeping zone, measured at 1 m depth, and generally slowest at 166 m.

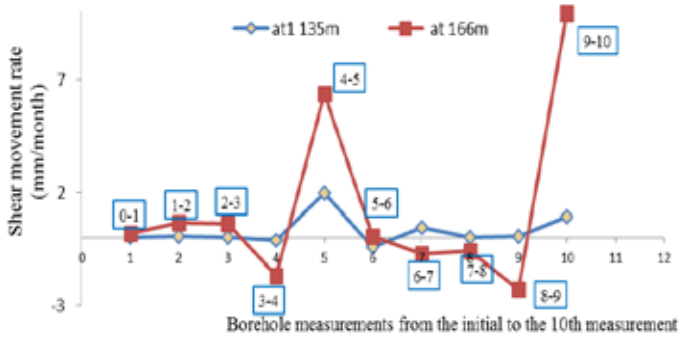

Figure 2. Strata movement rates along trajectory at 1m, 135 m and 166 m, all was showing a major trend of rising over time, and decreasing with depth. Here the digitals in squares, are measurement numbers, 1-2 means the movement measurement from 1st measurement to the 2nd measurement.

The shear movements of the two shear zones (at the depths of 135 m and 166 m) were different from one another (Figure 3). The movement at 166 m shows a short period of reverse movement prior to each of the periods of rapid movement. This may suggest tilting of rock blocks.

The shear movements of the two shear zones (at the depths of 135 m and 166 m) were different from one another (Figure 3). The movement at 166 m shows a short period of reverse movement prior to each of the periods of rapid movement. This may suggest tilting of rock blocks.

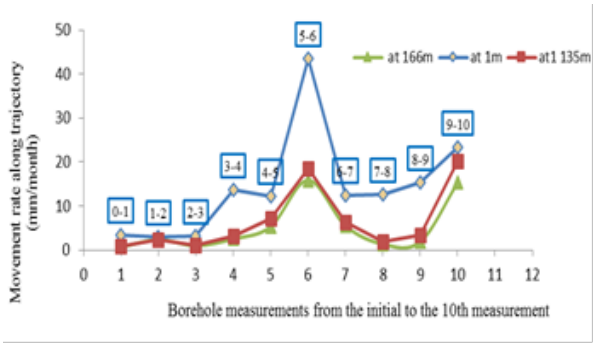

Figure 3. Comparison of the strata shear movement rates at 135 m and 166 m.

3 MODEL DEVELOPMENT OF STRATA MOVEMENT

It has been observed by several authors (Mitchell 2007; Solid Energy 2007) that 90% of the subsidence takes place during the first 6 months from the first observation to the finish of subsidence at the surface. Kelsey (1986), in a study of the Huntly East Coalmine around the NZED Hotel, commented on the total delay time between panel extraction completion and observed finish of surface subsidence, of approximately 1 to 2 years. The best estimate of the delay time from the completion of extraction to the completion of surface subsidence used in the modelling was determined as 18 months (Du 2012). The subsidence development was delineated as: surface subsidence began one year after completion of extraction, and developed during the following 6 months to reach the maximum subsidence.

The coal seam depth in the North 5 mining area was relatively stable. The coal roof from the ground surface at the Borehole was at an approximate depth of 295 m. The extraction seam height was relatively stable at approximately 7 m. The extraction volume could be simplified and represented by extraction area (m2) times 7 (m). One varying component: the distance from the extraction to the inclinometer borehole was used. Others were relatively consistent or assumed to be stable. Thus, the correlation study focused on the relationship between the magnitude of the borehole movement and the distance from the nearest edge of the extraction to the inclinometer borehole, and the direction relationship between lateral movement direction and the bearing of the extraction.

To simplify the analysis, the subsidence was approximated as 8 separate subsidence events, relating to the strata lateral displacement measurements in May, June, August, September, October, November, December 2010, and February 2011 (Table 1). Each monthly measurement was assumed to be the final static subsidence of the strata, which was induced by the 6 continuous months of extraction between 12 and 18 months prior to each measurement time, with weights from 6/6 to 1/6 respectively contributing to induction of a measured lateral movement.

Table 1. The horizontal displacement measured and distance from the nearest extraction edge to the measurement point of inclinometer borehole, in eight separate subsidence events.

No.	Depth	Distance from EDGE	Horiz. Displ. measured	No.	Depth	Distance from EDGE	Horiz. Displ. measured	No.	Depth	Distance from EDGE	Horiz. Displ. measured
	m	m	mm		m	m	mm		m	m	mm
1-1		238	-27.9	2-1		238	-12.3	3-1		238	-10.7
1-2		255	-12.5	2-2		255	-6.3	3-2		255	-5.5
1-3		263	-12.5	2-3		263	-1.9	3-3		263	-1.3
1-4	1	272	-19.2	2-4	135	272	-11.8	3-4	166	272	-8.5
1-5		336	-13.6	2-5		336	-3.1	3-5		336	-2.5
1-6		382	-3.1	2-6		382	-1.1	3-6		382	-1
1-7		448	-3.4	2-7		448	-0.8	3-7		448	-0.6
1-8		460	-2.9	2-8		460	-2.3	3-8		460	-2.3

Correlations between the lateral movement of strata and coal extraction for an 18 month delay pattern were sought by scatter chart and regressions (Figure 4).

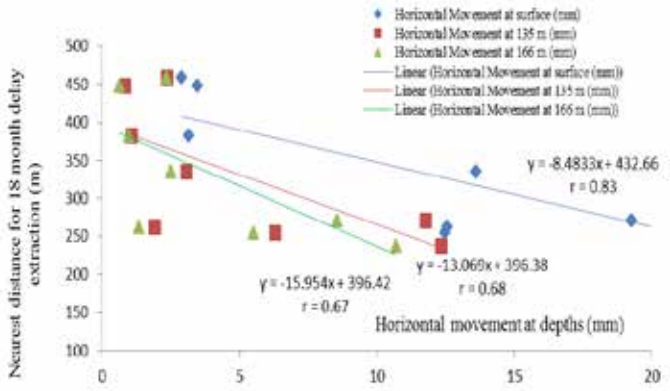

Figure 4 Scatter plot of the horizontal movement and nearest edge distance from extraction to the borehole for 18 month delay pattern.

According to Evans & Feltz (1996) for the absolute value of r, and the Scatter charts in Figure 4, the correlations between the horizontal movement and the nearest extraction distance at surface, 135 m and 166 m are 'very strong', 'strong' and 'strong' respectively.

Modelling using Phase2 (RockScience Inc. 2011), as detailed in Du (2012), gave the following numerical equations:

$$y = 0.0003x^2 - 0.3216x + 83.306 \quad \text{at 1 m} \quad (1)$$

$$y = 7E\text{-}05x^2 - 0.0759x + 23.284 \quad \text{at 135 m} \quad (2)$$

$$y = 2E\text{-}05x^2 - 0.0304x + 11.131 \quad \text{at 166 m} \quad (3)$$

where: x = the nearest distance from extraction edge to the Borehole, m; and y = the lateral movement distance of the Borehole at a depth over a month, mm.

Comparing the measured data and the modelled data, the correlations between the measured movement and the modeled movement had the r values of 0.855, 0.715, and 0.700. According to Evans & Feltz (1996) for the absolute value of r, the correlations between the horizontal movement modelled and measured at surface, 135 m and 166 m are 'very strong', 'strong' and 'strong' respectively.

4 CONCLUSIONS

Three movement zones were identified, two 'shear zones', and one 'creeping zone'. The trajectories of the borehole lateral movement show that the movement was non-linear, and the trajectories varied with depth, having a varying movement rate and direction. The two shear zones occurred on two separate strata bedding planes of the Te Kuiti Group. The creeping movement occurred in the soft Tauranga Group and within the upper Te Kuiti Group. The trajectory of the extraction advancing was not in a straight line. The trajectory of the borehole lateral movement was also a non-linear movement having a varying movement rate and direction.

The correlation between the extraction nearest edge distance and the lateral movement was initially represented by three equations. Of which Equation for movement at 1m (surface) gave the best correlation, 'very strong' correlation. At other two depths investigated (135 m and 166 m) correlations were 'strong', not as strong as for 1 m depth. The correlations between the horizontal movement modelled and measured at surface, 135 m and 166 m are 'very strong', 'strong' and 'strong' respectively.

Lateral movement has been analysed and characterised in this study, but vertical subsidence has only been identified to exist and was not discussed in detail due to the limited dataset available.

We found no reports in the literature of the installation of an inclinometer borehole deeper than 120 m. According to ASTM (2005), no standards are available yet for evaluation against precision and bias issues arising from the use of a borehole inclinometer (ASTM 2005). Therefore, the inclinometer borehole in this study may be one of the most complicated cases for monitoring and measurement of strata movement induced by underground extraction in New Zealand.

5 ACKNOWLEDGEMENTS

The authors would like to acknowledge Solid Energy who supported this work.

6 REFERENCES

ASTM, 2005. *Standard Test Method for Monitoring Ground Movement Using Probe - Type Inclinometers, ASTM D6230 - 98 (2005)*, American Society for Testing and Materials.

Cornforth, D.H., 2005. *Landslide in Practice: investigation, analysis and Remedial / preventative options in soil*, USA: John Wiley & Sons Inc.

Du, Z., 2012. *Strata Movement Study Using a 250 m Deep Inclinometer Borehole, Huntly East Coalmine, New Zealand*. The University of Waikato.

Evans, J.D. & Feltz, C. 1996. Straightforward Statistics for the Behavioral Sciences. *Perceptual and Motor Skills*, 81(1995), p.1391.

Guy, G. et al., 2006. An Investigation into Underground Mine Interaction with Overlying Aquifers, Huntly East Mine, New Zealand. In *Coal Operators' Conference, University of Wollongong & the Australasian Institute of Mining and Metallurgy, 2006*. Wollongong, Australia, pp. 164–174. Available at: http://ro.uow.edu.au/coal/44, 02 April 2011.

Kelsey, P.I., 1986. *An engineering geological investigation of ground subsidence above the Huntly East Mine area*. University of Canterbury. Available at: http://ir.canterbury.ac.nz/handle/10092/1659.

Machan, G. & Bennett, V., 2008. *Use of inclinometers for geotechnical unstrumentation on transportation projects*, Washington, DC. Available at: www.TRB.org.

Mikkelsen, P.E., 2003. Advances in Inclinometer Data Analysis. In *Symposium on Field Measurements in Geo-mechanics*. Norway, p. 13. Available at: www.slopeindicator.com/pdf/papers/advances-in-data-analysis.pdf.

Mikkelsen, P.E., 2007. Inclinometer Data & Recognition of System Errors. , pp.1–22. Available at: http://www.slopeindicator.com/pdf/papers/mikkelsen-inclinometer-errors.pdf.

Mitchell, G.K., 2007. *Huntly north project surface water management*, Auckland, New Zealand.

RockScience Inc., 2011. Phase2 Tutorials. *RockScience Inc.*, pp.32. Available at: http://www.rocscience.com/downloads/phase2/webhelp/tutorials/Phase2_tutorials.htm [Accessed October 14, 2011].

Soil Instruments Limited, 2010. Vertical Digital Bluetooth Inclinometer System MkII with Archer PDA User Manual (1), pp.1–34.

Solid Energy, 2006. *N55/57 Project Area Draft Geological Interpretation*, Huntly, New Zealand.

Solid Energy, 2007. *Huntly north project Huntly east mine assessment of environmental effects*, Huntly, New Zealand.

Solid Energy, 2009. *Borehole 20091 Driller logs, chip photographs and geophysical logs*, Huntly, New Zealand.

Solid Energy, 2011. The Waikato Coal Region - Solid Energy New Zealand Ltd Page 1 of 2. *Solid Energy New Zealand Ltd*, p.2. Available at: http://www.coalnz.com/index.cfm/1,198,0,49.html [Accessed September 4, 2011].

Stark, T. & Choi, H., 2008. Slope inclinometers for landslides. *Landslides, Springer-Verlag*, 5(3), pp.339–350.

Geotechnical and Geophysical Site Characterisation 5 – Lehane, Acosta-Martínez & Kelly (Eds)

Subsurface Compacted Rubble Raft technology for ground improvement

Z. Du & M. A. Shahin
Curtin University, Perth WA 6845, Australia

ABSTRACT: In this paper, a new promising ground improvement technology called Subsurface Compacted Rubble Raft (SCRR) is presented and described. The SCRR technology implies generating a solid bearing platform comprised of a number of rubble bulbs that displace the liquefiable soil to form a subsurface crust which can avoid the liquefaction occurrence, and also work as a subsurface raft to carry the building loads. It can also be used on non-liquefaction sites to remove problematical soil layers. The SCRR bulbs are formed from demolition and industrial wastes or construction materials. Traditional foundations such as piles and mats can be built on top of the SCRR, thus, the risk of potential future foundation settlements can be significantly reduced and differential settlements almost eliminated. The SCRR technology is suitable for most engineering and geological conditions.

1 INTRODUCTION

The abbreviation SCRR is used in this paper as a short name for a new ground improvement technology called Subsurface Compacted Rubble Raft. The SCRR technology was conceived in 2015 by the first author of this paper and was recorded through the New Zealand Patent Application (714011) for the primary purpose of eliminating the damage caused to foundations and above buildings due to soil liquefaction. In principle, the SCRR technology is based on the mature theory of CRUST developed by Ishihara (1985), and the following practices: FRANKI piles (Franki Foundations Group 2015), practical bearing base piles (State Intellectual Property Office of the PRC 1998) and commonly used compacted gravel raft foundations (NZGS 2015). The SCRR implies generating a solid bearing platform that is comprised of a number of rubble bulbs which are pushed down from the ground surface to displace and densify the surrounding liquefiable (or weak) soil for a thickness of up to 6 m deep so as to form a subsurface crust to avoid the liquefaction occurrence and work as a subsurface raft to carry the building loads. In the meanwhile, the generated SCRR can work as a bridge that separates any possible lower liquefiable soil layers. This paper describes the mechanism and constructing procedure of the SCRR technology and discusses its implying applications. Several critical suggestions are also recommended for further development.

2 SCRR STURCTURE AND FORMATION

2.1 *SCRR Structure*

Subsurface Compacted Rubble Raft (SCRR) is an integrity of bulbs (or units), which are primarily arranged in two layers. Every bulb is comprised of a compacted rubble zone and a densified neighbouring soil zone (see Fig. 1).

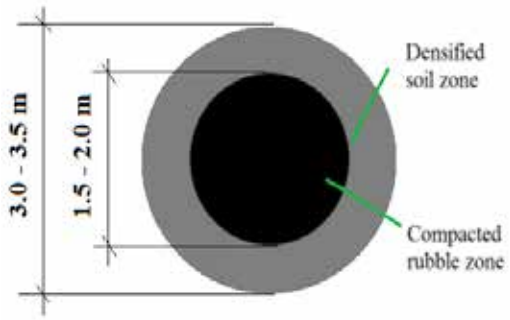

Figure 1. Subsurface compacted rubble raft bulb structure.

The bulbs are built next to each other, and are approximately 2 meters away center to center (see Fig. 2). Upon installation of two bulbs, a common compacted soil zone is generated between them (Fig. 2). The thickness of a single layer of jointed bulbs is generally 2-3 m, which may be not robust enough to form a consistent subsurface CRUST, because there may be a weak zone existing between the bulbs in the first layer, considering the normally substantial variation of common subsurface geological and geotechnical conditions. To build a robust SCRR, a

second layer, even a third layer may be required; however, a two-layer structure is the main formation of SCRR.

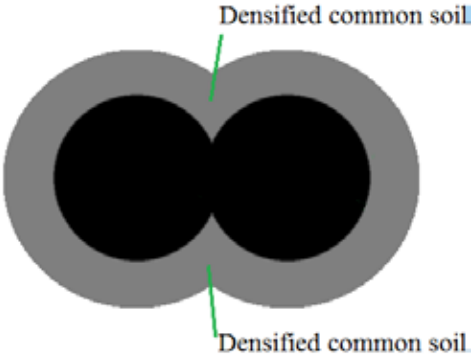

Figure 2. Cross section of two bulbs with compacted common soil zone.

Figure 3 is a cross sectional view of a functional structure of four SCRR bulbs, installed close to each other, in a four-bulb pyramid structure, three at the bottom to work as a base supporting the one on top and providing a stable and robust mechanism.

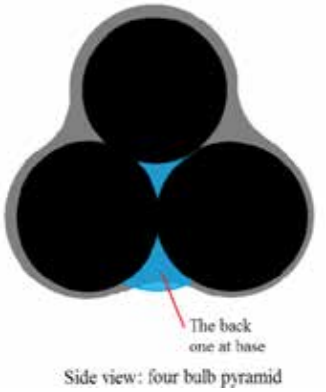

Figure 3. A four bulb pyramid structure in Subsurface compacted rubble raft.

Figure 4 shows a typical example of a SCRR comprised of a framework of locked two layers of bulbs of four-bulb pyramid structure. The upper layer bulb after compaction is firmly installed upon the three base bulbs, a joint interface or highly densified soil zone is then produced. Generally, two layers of bulbs will have a thickness of 5-6 m, substantial for forming a reliable raft and acting as a "subsurface CRUST of Ishihara". The liquefaction potential, not only in the bulb-worked layer but also in the lower liquefiable layer, is removed. Then the liquefaction damages to the above foundations and buildings will be eliminated or mitigated.

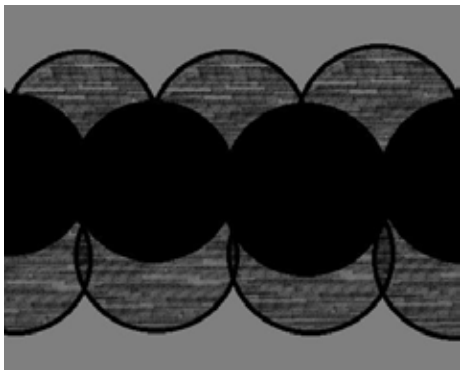

Figure 4. Bird view of the elementary two layer plan.

2.2 *SCRR formation*

The construction of SCRR is conducted by similar method to that used in Franki piling (Franki Foundations Group 2015) and base bearing piling (Qi 2007). The procedure consists of seven steps in three main stages (see Fig. 5).

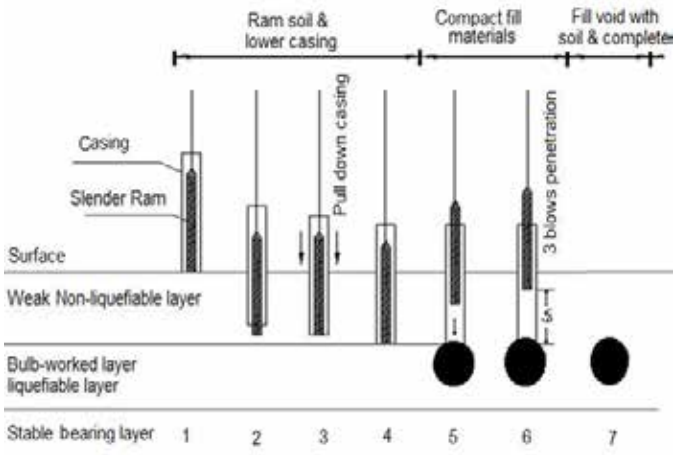

Figure 5. Procedure to create a SCRR bulb (adapted from Franki Foundations Group 2015, Qi 2007).

The three main stages include: (1) hammer soil and lower casing to the design depth; (2) repeatedly fill demolition rubble and compact to form a compacted rubble zone, meanwhile the surrounding soil is compacted to form a densified soil zone; and (3) withdraw the casing, fill the casing void with soil or engineering materials. At the end of step 6, when the volume of filling material is well compacted and approached the design value (i.e. 1.5 m^3), a 3.5 tonne hammer is then freely dropped three times with a 6.0 m drop distance. The technician records each penetration and sums up the three readings, and the three drive penetrations should not be larger than the design value. The second and third readings should not be larger than its previous one (Qi 2007, Wang 2008).

3 MECHANISM, QUALITY CONTROL AND ADVATNAGES

3.1 *Mechanism*

The mechanism of a single layer SCRR has similar function to that of the surface compacted raft and base bearing piling mass (NZGS 2015, Yang & Wang 2012). The compacted rubble materials, however, displace and densify the subsurface surrounding the liquefiable layer. According to Menard & Broise (1975 cited by Bo et al. 2009), the degree of granular soil improvement by the dynamic compaction of a ram increases with the applied energy, and the influence depth has a proportional correlation with the ram weight and drop height. Lukas (Bo et al. 2009) improved Menard and Broise formula, and proposed an equation that provides a more accurate estimation of the influence depth, *D*, in meters, as follows:

$$D = n \times (w \times h)^{1/2} \quad (1)$$

where; *w* = weight of ram (tones); *h* = ram free drop height (meters); and *n* = empirical coefficient factor that varies between 0.3 and 1.0.

For the SCRR compaction, *w* = 3.5 tonnes, *h* = 6 m and *n* = 0.5 (Leonards et al.1980), then, the influence depth of SCRR compaction is calculated as: $D = 0.5\ (3.5 \times 6)^{½} = 2.3$ m. That is, the 2.3 m thick soil layer below the compacted rubble base will be compacted. However, more accurate empirical coefficient factor, *n*, requires further study for RBB compaction, because the compaction power in SCRR piling is transferred by the compacted rubble to the below soil, it is an indirect compaction.

While the surrounding soil is now compacted and consolidated to form a densified soil zone, the surrounding compacted soil properties change dramatically. Field tests carried out on the base bearing piling have shown that the potential of soil liquefaction is eliminated in the 3-4 meters zone of the created single bearing base, which includes the compacted rubble and surrounding compacted soil (Zhu 2013, Yang & Wang 2012, Yang & Wang 2011). This means that the surrounding liquefiable soil, within 3-4 m of the bearing base, loses its liquefaction properties after one base is constructed. Similarly, in SCRR, the 5-6 meters of thick raft zone loses its liquefaction potential. More significantly, the 5-6 m of Ishihara CRUST also eliminates the liquefaction risk from the soil layer below the SCRR. All installed SCRR bulbs under one building work as one solid 3D subsurface framework (i.e. the subsurface compacted rubble RAFT), having a thickness of 5-6 m which removes the liquefaction potential in the bulb-worked layer.

The work carried out by both Ishihara (1985) and Youd & Garris (1995) showed that, for sites with any substantial thickness of liquefiable soil, the upper non-liquefiable soil typically possesses a critical thickness beyond which the "likelihood of ground surface manifestation of liquefaction does not increase" (Tonkin & Taylor 2013). The function of SCRR is to increase the upper non-liquefiable layer thickness to something larger than the critical crust thickness so as to remove or mitigate the manifestation of sand ejection and in turn the destructive effects to foundations and buildings. Therefore, the SCRR raft, not only eliminates the liquefaction potential on the bulb-worked zone but in the meanwhile also bridges and separates any possible lower liquefiable soil layers. Accordingly, the ground damage due to liquefaction can thus be avoided. Moreover, the conventional foundations, such as piles, raft slabs and waffle foundations can be safely built on or above the SCRR with much higher bearing capacity.

3.2 *Quality Control*

For quality control, SCRR uses 3-blow penetration of a ramp, which is 3.5 tonnes, having a 6 metres free falling distance. All bulbs under one building will have the same or smaller 3-blow penetration and provide the same or larger bearing capacity than the designed bearing capacity for one entire foundation. The building on one SCRR will thus have a small and even settlement (Yang et al. 2010). According to the Chinese Ministry of Construction (2007), the 3-blow penetration has a correlation with the efficient bearing area of the bulb in a certain soil. For instance, in fine sand, when the 3-blow penetration is controlled at 20 cm, in the slightly dense fine sand, the formed bearing bulb will have an effective bearing area of 2.5~2.9 m^2. On the Chinese Standards JGJ 135-2007，the characteristic value of the vertical bearing capacity per bulb, *Ra*, is calculated by empirical Equations 2 and 3, as follows:

$$R_a = f_a \times A_e \quad (2)$$

$$f_a = f_{ak} + \eta_d \times \gamma_m \times (d - 0.5) \quad (3)$$

where： f_a = characteristic bearing capacity of the bearing layer after depth correction (kPa); A_e = effective area of the bearing base for calculation (m^2), obtained from back calculated data from field piling project cases (Table 1); η_d= correction coefficient; γ_m = effective relative density (kN/m); and d = equivalent buried depth of foundation (m).

Verification of SCRR quality is to be undertaken using the cone penetration test (CPT) with high capacity tip resistance, examining its improvement of soil density, consistency and uniformity for quality assurance (Robertson & Cabal 2014). The CPT data obtained are inputted into the soil liquefaction software CLiq (Robertson & Cabal 2014, GeoLogismiki Software 2016), to analyse whether or not the liquefaction potential has been eliminated or mitigated in the SCRR and underneath soil. If a pile

foundation is seated on a SCRR, the two traditional pile testing methods including the static testing and small strain testing can be applied to verify the pile bearing capacity and quality (Yang et al. 2010, Franki Foundations Group 2015, Puissant Group Ltd. 2015). The consistency and integrity of the SCRR raft can be validated by the technique of multichannel analysis of surface waves (MASW), by profiling the depth, size, thickness and stiffness of SCRR. The material Young's modulus and load-bearing capacity of the raft can then be derived from the MASW results (Park et al. 2007).

Table 1. Effective bearing area of the SCRR bulb in sand (China Ministry of Construction 2007).

Strengthened layer		Three drive penetration, cm		
		10	20	30
Fine sand	Medium dense	2.4~2.8	2.1~2.5	1.8~2.2
	Slightly dense	2.8~3.2	2.5~2.9	2.2~2.6
Medium to coarse sand	Medium dense	2.7~3.1	2.4~2.8	1.9~2.4
	Slightly dense	3.1~3.5	2.8~3.2	2.4~2.8

3.3 *SCRR advantages*

The SCRR technology is an attractive and promising ground improvement technique and has the following advantages and benefits:

Wide application: SCRR is suitable for most engineering and geological conditions, especially for weak or liquefiable ground, and has an easy quality control.

Eliminating liquefaction damages: SCRR provides a robust way to solve the liquefaction problems, by displacing and densifying the liquefiable soil, and bridging and separating lower liquefiable soil layers. Building foundation damages due to liquefaction can thus be avoided. The use of SCRR can make the construction work realisable in some areas like the Red Zone (non-residential land) in Christchurch, where it can be transferred into TC2 and TC3, or even TC1 land for residential purposes.

Environmental and ecological benefits: each SCRR bulb uses around 1.5-2.0 m^3 of rubbles. SCRR engineering sites are tidy without mud, dewatering and excavation. No reverse impact on planting and underground service networks above the SCRR. The compacted rubbles comprise waste or rough fragments of brick, concrete, stone, etc., particularly as debris from demolition of buildings. This technology is thus compliant with many government wastes minimisation policies such as the ones applied in New Zealand (Ministry for the Environment New Zealand 2002) and Australia (Department of Environment Australia 2011).

Economic benefits: rubbles are easy to source and have low cost. The overall cost of a foundation using SCRR technology is approximately 30-60% of cost of other conventional engineering solutions.

4 DESCRIPTION OF IMPLIED APPLICATIONS

In this section, the practical implication of using SCRR is presented through a few examples in applications such as road foundations, underground services and residential buildings on liquefiable soil sites and/or weak soil layers. In such circumstances, the SCRR is used to increase the upper non-liquefiable layer thickness to be larger than the critical thickness. For sites of weak layers only, the SCRR is used to densify the weak layers to increase foundation bearing capacity and decrease the settlement and differential settlement.

Figure 6 shows a cross sectional view of a SCRR used for a road foundation in a liquefaction prone area in which the SCRR is constructed in the upper part of a liquefiable layer overlying a stable layer. In an earthquake event, this system can avoid the liquefaction damage to the above road, and otherwise prevents the road from slow deformation due to the daily ground creeping which is caused by the slow movement of the liquefiable soil underneath.

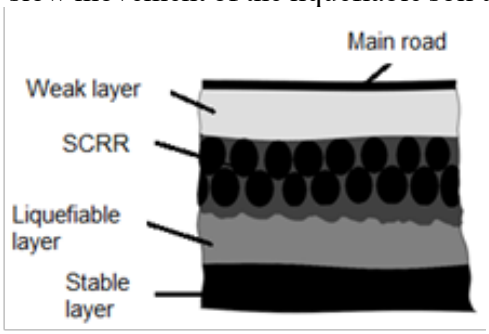

Figure 6. SCRR under a main road.

Figure 7 shows an example of the use of SCRR for an underground network of wastewater lines in which the SCRR is constructed along and below the underground network. The repair or the replacement work of the underground services (i.e. wastewater mains) can thus be avoided after any earthquake impact.

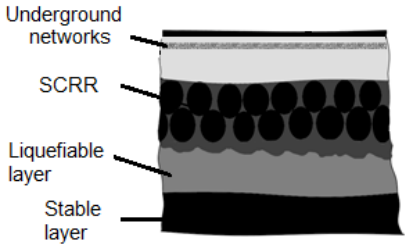

Figure 7. SCRR under an underground network.

For multi-storey buildings or normal houses with heavy cladding and roofing materials such as those in Christchurch TC2 and TC3 zones, the use of SCRR in addition to piles is an appropriate solution (Fig. 8). In such cases, SCRR can eliminate the liquefaction potential from the soil below, and also provides a reliable bearing capacity to the above foundation or building.

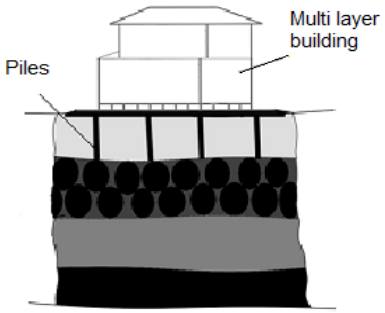

Figure 8. SCRR for multi-storey house with pile foundations.

5 DISCUSSION AND CONCLUSION

Implication of subsurface compacted rubble raft can eliminate the liquefaction risk and improve the bearing capacity of weak ground. It consumes quantities of demolition wastes, attributing it as an economical and environment-friendly technology. It is suitable for most engineering and geological conditions, where its quality control is easy to manage. The application of SCRR technology would provide notable benefits to the economy and the environment. Particularly speaking, minimizing the demolition wastes and eliminating the potential risk of liquefaction in cities such as Christchurch are important reasons for the imperative demand of this promising technology. For SCRR technology to gain a wide acceptance, it requires further advanced and rigorous analytical or numerical modelling studies and in-situ experiments, which will be carried out in a future development of the current study.

6 REFERENCES

Bo M. W., Na Y. M., Arulrajah A, & Chang M. F. 2009. "Densification of granular soil by dynamic compaction," Proc. ICE - Gr. Improv., vol. 162, no. 3, pp. 121–132.

Chinese Ministry of Construction 2007. *Chinese Professional Standards: Design Specification of Ram-compacted Piles with Base Bearing* (JGJ 135-2007), Construction Industry Publisher, Beijing, China, 2007 (in Mandarin).

Department of Environment Australia 2011. *Construction and demolition waste status report-management of construction and demolition waste in Australia*, retrieved from http://www.environment.gov.au/protection/national-waste-policy/publications/construction-and-demolition-waste-status-report on 20 Feb 2016.

Franki Foundations Group 2015. *FRANKI pile*, retrieved from http://www.franki.de/pdf_en/FRANKI_pile.pdf 2015.

GeoLogismiki Software 2016. *CLiq v.1.7 – Soil liquefaction software*, http://www.geologismiki.gr/products/cliq/2016.

Ishihara K. 1985. Stability of natural deposits during earthquakes, *Proceedings, 11th Int. Conf. on Soil Mechanics and Foundation Engineering.*, San Francisco, 1985, 12-16.

Leonards G. A., Cutter W. A. and Holtz R. D. 1980. Dynamic compaction of granular soils. Journal of the Geotechnical Engineering Division, ASCE, 106, No. 1, 35–44.

Ministry for the Environment New Zealand 2002. *The Guide to Managing Cleanfills: Acceptable cleanfill material*, Prepared by Beca Carter Hollings & Ferner Ltd, retrieved from https://www.mfe.govt.nz/sites/default/files/cleanfills-guide-jan02.pdf, 2016.

NZGS 2015. *Geotechnical earthquake engineering practice, MODULE 5A: Specification of ground improvement for residential properties in the Canterbury region*, New Zealand Geotechnical Society (NZGS), Ver. 1, http://www.nzgs.org/resources/pdfs/Geotechnical-Module%205A-PROOF6.pdf 2016.

Park C.B., Miller R.D., Xia J.H & Ivanov J. 2007. Multichannel analysis of surface waves (MASW)—active and passive methods, *The Leading Edge*, January 2007, http://library.seg.org.dbgw.lis.curtin.edu.au/doi/abs/10.1190/1.2431832.

Puissant Group Ltd. 2015. *The profile of Puissant Group Ltd*, Beijing, http://www.puissant.com.cn/zjpst/index.html, July 2015 (in Mandarin).

Qi, Y.SH. 2007. Application of Ram-compacted Pile with Base Bearing, *National Seminar for Enforcing the New Chinese National Standards JGJ 135-2007*. Beijing (in Mandarin).

Robertson P. K & Cabal K.L. (Robertson) 2014. *Guide to Cone Penetration Testing for Geotechnical Engineering*, Gregg Drilling & Testing, Inc. 6th Edition, December 2014, pp140. Retrieved from http://www.greggdrilling.com.

State Intellectual Property Office of the PRC. 1998. *Construction method for concrete pile*, CN 1052284 C, retrieved from http://www.sipo.gov.cn/ on 20 Feb 2016.

Tonkin & Taylor Ltd. 2013. *Liquefaction vulnerability study Report*, Earthquake Commission New Zealand, Report, Tonkin & Taylor Ltd, T&T Ref. 52020.0200/v1.0, pp59.

Wang, J.Z. 2008. Birth and development of the Ram-compacted Pile with Bearing Base, *Building and Structure*, Vol 38 (4), April 2008, Beijing, China (in Mandarin).

Yang, J., Zhang, B.L., & Chong, Y. 2010. Design Practice of the Ramp-compacted Pile with Bearing Base, *Engineering of Coal Industry*, 2010 (11) 21-22.

Yang, Q.A. & Wang, J.Z. 2011. Expansive Research of the Ram-compacted Piles with Bearing Base, *Eng. of Road and Foundations*, Vol 156 (3), 68-71, 2011 China (in Mandarin).

Yang, Q.A. & Wang, J.Z. 2012. Effect of Ramp-compacted Pile with Bearing Base to Nearby Soils, *J. of Foundation Technology Forum*, 2012, 22-33. China (in Mandarin).

Youd, T.L. & Garris, C.T. 1995. Liquefaction-induced ground surface disruption, *J. Geotech. Eng.* 121 (11), 805 – 809.
Zhu, X.F. 2013. Application of Bearing Base Pile Composite Foundation in Liquefied Soil Treatment in a High Speed Railway Project, *Guangdong Highway and Traffic*, Issue 124, 2013, Guangdong, China (in Mandarin).

Geotechnical and Geophysical Site Characterisation 5 – Lehane, Acosta-Martínez & Kelly (Eds)

A4 motorway operation in the area of linear discontinuous surface deformations

M. Grygierek

Silesian University of Technology, Poland.

J. Kawalec

Silesian University of Technology, Poland.

ABSTRACT: The A4 motorway is a very important element of transport network in Poland linking East with West. In a section a few dozen kilometers it passes through the Upper-Silesian Industrial Conurbation, where mining and post-mining areas exist. The A4 motorway section passing through the area of linear discontinuous surface deformations (LDSD) should be considered especially crucial. In this area, immediately after the construction of pavement (2003), damage emerged on the right-of-way surface in the form of steps and single cracks nearly perpendicular to the road axis. During more than decade of motorway use in this area the damage was reproducing despite performed repairs. A thorough reconstruction of the pavement and subgrade improvement started in 2015 provides an opportunity to sum up the carried out tests, analyses, and previously presented theses. An extremely significant advantage of the started construction works is a possibility to verify the actual condition of layers building the pavement and its subgrade and to compare it with previously made theses and expressed opinions. The observations and conclusions presented in the paper are based inter alia on results of drilling through the pavement and subgrade, geophysical tests, analyses of geological-mining situation, land surveying, measurements of pavement deflection by FWD and visual inspections.

1 INTRODUCTION

The section of A4 motorway passing through the area of Upper Silesia in the southern part of Poland (Fig. 3) is an example of difficult coexistence of the deep hard coal mining and the transport infrastructure operation. The road pavement durability is equally significant parameter determining its technical condition, depending on the stiffness of pavement structural layers and of the subsoil. Mining deformations have always a negative impact on the pavement. In the case of continuous deformations, described by a subsidence trough, high-speed roads may operate retaining permissible speeds, but subject to some restrictions in the mining operations, hereinafter referred to as the mining preventing actions. Also on the construction side it is required to apply construction prevention activities and of carrying out the roadway monitoring.

Significantly more complicated situation occurs in the case of discontinuous deformations. In such cases the ground surface continuity is broken and sudden changes in the ground profile originate, including the roadway (Pic. 1). Deformations are frequently accompanied by discontinuities of surface nature (Pic. 4). The case described in the paper is related to the motorway, on which linear discontinuous deformations have been appearing since the beginning of its use and which originated from the past mining operations and from impacts of the current mining. For the analysed motorway section the consecutive events have been presented chronologically, related to: the historical and current mining operations, the phase of construction, deformation development on the surface, the pavement repair, and tests.

Pic. 2-1. A linear-type discontinuous surface deformation (Grygierek 2010)

2 MINING OPERATIONS BEFORE THE MOTORWAY CONSTRUCTION

The past mining operations in the analysed area were carried out from 1947 in 15 seams, most frequently with caving. The mining depth ranged from 200 m to 900 m. The mining was concentrated west and east of existing there fault zones III and IV. The result of mining carried out this way was a large difference in subsidence, because in the section connecting the fault zones the subsidences were approx. 1.5 m and west and east of the fault zones they reached 10 m (Fig. 1). Papers (Kotyrba at al 2009) (Kotyrba at al 2015) (Kotyrba A. 2006) present a detailed analysis of mining conditions.

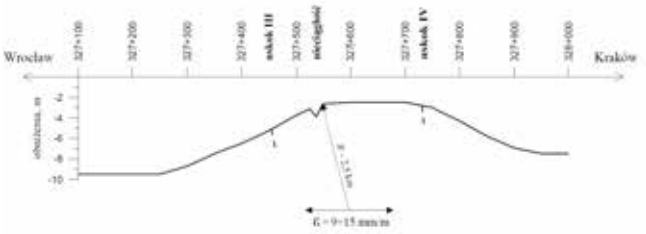

Figure 2-1. Surface subsidence in motorway axis, in the area of fault III and IV zone before the construction start, caused by the past mining operations (Kotyrba at al 2009). uskok = fault; obniżenia = subsidences

3. MOTORWAY CONSTRUCTION PERIOD

3.1 The Roadway Description And The Pavement Structure

The analysed area covers a strip of land corresponding to A4 motorway section from km 327+400 to km 328+400. The construction was carried out in the period 2002-2005. The Service Areas (MOPs), on the southern and northern side of the road, are characteristic facilities in this section. This section goes on the ground on the northern side and in an excavation on the southern side. The northern part of MOP is built of Quaternary sediments, which cover Carboniferous in layers from 0 to around 3 m thick. There are mainly clays.

Firm silty clays and sandy clays should be distinguished among them, with admixture of gravels and sand interlayers. The clays condition is specified as very stiff or stiff. In the southern part of MOP there are Carboniferous strata, which are covered by embankment layers 0 to 3 m thick. It should be stated that the geological structure of the whole area is inhomogeneous, affected by the course of Carboniferous formation roof. As mentioned earlier, in the MOP area there are two faults marked as III and IV, with throws of 20 m and 10 m, respectively.

Fig. 3-2. The course of fault III and IV in relation to MOP and A4 motorway (Kotyrba & Kowalski 2009)

A detailed description of the geological structure may be found in reports prepared under A. Kotyrba and A. Kowalski direction, research staff members of the Central Mining Institute in Katowice (Kotyrba at al 2009) (Kotyrba at al 2015) (Kotyrba 2006). The cross-section comprises two roadways (2x14.75m) with three lanes (3x3.75m) and an emergency lane (3.00m) each way with service areas on both sides. The pavement after commissioning (2003) featured the following arrangement of structural layers:

- 5 cm, wearing course SMA 0/12.8,
- 10cm, binding course BAWMS 0/25,
- 10cm, base course BAWMS 0/31.5,
- 22cm, aggregate base course 0/31.5,
- Tensar SS-40 stabilizing monolithic geogrid,
- 20cm, engineering course 0/63,
- 20cm, frost protection layer 0/63,
- Geotextile layer and foil layer,
- Approx. 40 cm, stabilised subgrade layer (slag + large aggregate).

Figure 4-3. Location of events in the motorway right-of-way and in the adjacent area (Google Earth)

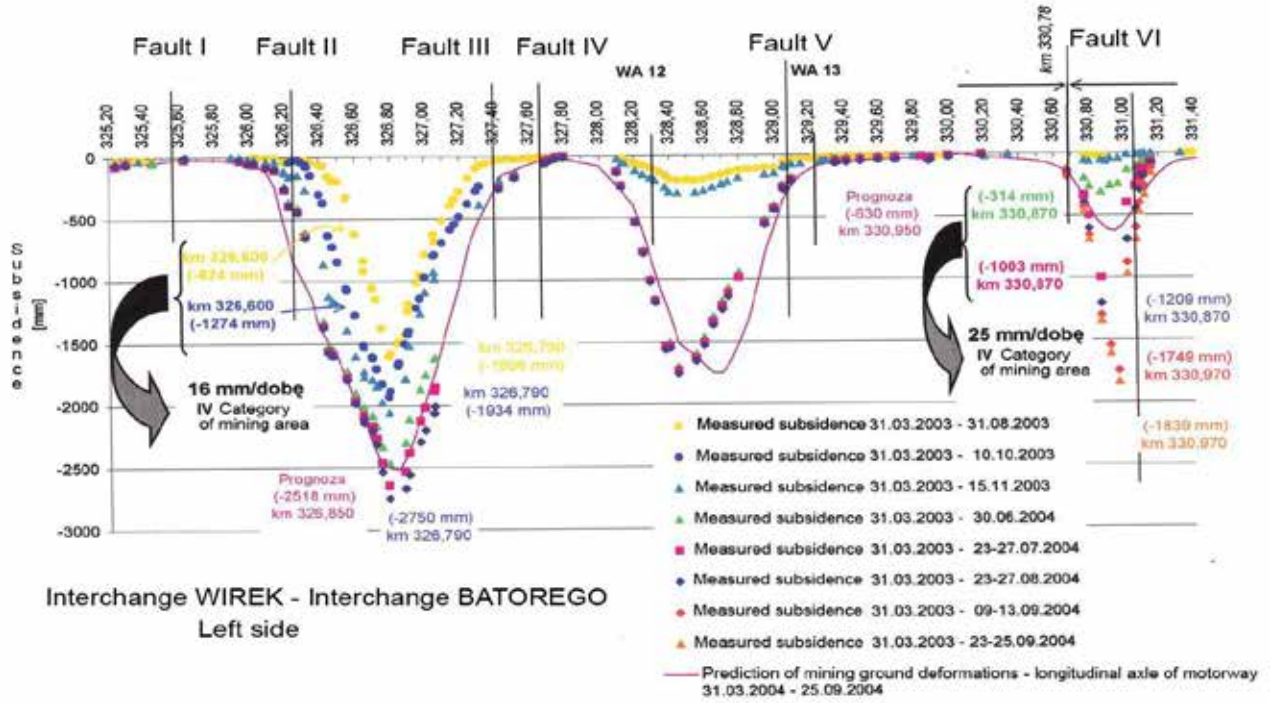

Fig. 6-3. Subsidence of A4 motorway right-of-way measured in the period Mar 2003 - Nov 2004 (Chlipalski at al 2010)

In fault zones (fault III and IV) in a section approx. 100 m long an additional reinforcement was applied in the form of a geomattress 50 cm thick, with inserts of uniaxial polypropylene geogrids of high short-term tensile strength at the bottom and at the top. The geomattress was built-in on a layer of so-called "sand pad" and was situated around 2 m deep from the road formation line.

3.2. Surveying Monitoring

A network of surveying monitoring points, mainly along the boundary of the motorway right-of-way, was designed and constructed due to the forecast impacts of mining operations. The idea of surveying monitoring consisted in cyclically made surveying measurements, based on which the forecast deformations were compared with the actual, i.e. measured, ones.

Conclusions from the comparative analysis were crucial, because they determined the further progress of works and the introduction of design changes, which were forced due to the adaptation of the motorway parameters (the formation line) to the required values.

3.3. The Mining Operations Impact On The Ground Surface. Measurement Data Analysis

During the carried out construction works the intensity of ground surface mining deformations, including the motorway right-of-way, was extremely high, nearly along the entire contract section (6 km). It is worth noticing that the greatest subsidence exceeded the value of 2.5 m (between 2002 and 2004).

Pic. 4-2. Survey of the next phase of discontinuous deformations development - 16 October 2003 (Strycharz B. at al 2005)

It is a characteristic fact that the analysed motorway section (from km 327.400 to 327.800) was situated on a ridge of two subsidence troughs, which originated on both sides of the fault zone (Fig. 3) and certainly by their reach covered this zone, resulting in subsidence from 17 mm to 27 mm. However, the most significant fact is the same nature of deformations distribution on the surface as that originating from previous mining operations (Fig. 1), i.e. from the period 1947 - 2002

Permanently superimposing tensions in the rock mass resulted in the origination in the fault zone of so-called linear discontinuous surface deformations, which first symptoms were visible as early as during the motorway construction in the forest area adjacent to the motorway right-of-way.

Till the construction works completion (2004), the discontinuous deformations emerged only in the ground strip adjacent to the motorway right side. No

discontinuities were recorded during the construction period, in the right lane and in the service areas.

4. MOTORWAY OPERATION AFTER CONSTRUCTION

4.1. Motorway Pavement Damage In 2005

The next discontinuities in the analysed area were recorded in May 2005, that is less than a year from the motorway commissioning. Deformations occurred on both roadways (Pic. 3) and in the area immediately adjacent to the roadway, including the area of MOP still under constructio.

Pic. 6-3. Pavement damage observed in May 2005 (Kowalski 2015).

The course of those deformations did not coincide with the course of earlier faults III and IV. Unfortunately, deformations occurred on the motorway section not protected against such mining impacts. On the roadways the deformations caused unevenness in the form of corrugations, accompanied by cracks of significant opening (fissures). The cracks were going in the NE direction. Corrugations that occurred on roadways were cold milled and the cracks sealed; afterwards a repair design preparation started. An unfavourable geological structure of the rock mass, the existence of faults III and IV zone in the area where no mining operations were carried out, the Carboniferous strata outcrops on the surface, the lack of younger strata overburden, as well as the past mining before the motorway construction west and east of the fault zone, which resulted in the origination of a zone with accumulations of horizontal tensile deformations, were considered causes of deformations observed in the motorway right-of-way at that time.

The mining operations carried out during the motorway construction resulted in increments of horizontal deformations on the ground surface of around 1.8mm/m, including 0.6 mm/m after the motorway construction. Also we should not forget the total values of deformations from the period before the motorway construction (1947 – 2003), when the deformations were estimated at +9 mm/m to +21.0 mm/m

The geophysical - electric resistance studies performed at that time allowed finding the existence of open cracks not filled with the soil at deeper parts, which confirmed a destructive nature of the carried out mining operations before the motorway construction start. Apart from electric resistance tests also a georadar measurement was applied, due to which an image of the road body and its immediate subsoil was obtained.

Because of the originated deformations, the pavement was repaired in a section approx. 20 m long - removing the pavement layers to the floor of broken aggregate subgrade 0/31.5 (bottom subgrade layer). Finally, in 2007 the following arrangement of layers was executed:

- 5 cm, wearing course SMA 0/12.8,
- 10cm, binding course BAWMS 0/25,
- 10cm, base course BAWMS 0/31.5,
- 22cm, aggregate base course 0/31.5

Flat biaxial geomesh of welded strips 40/40 (PP)

Taking into consideration the performed reinforcement it should be noted that it features a minimum reach (intervention) in the pavement, because to a depth of 47 cm, including 22 cm below the mineral-asphalt pavement.

4.2. Motorway Pavement Damage In The Years 2007 - 2015

The pavement repair described in section 4.1 was implemented in 2007. Shortly after in the area of discontinuity existing between faults III and IV the discontinuous deformations opened again. If for the first time (2004) the deformations occurred in a strip of around 20 m passing skew to the road axis, i.e. at an angle of approx. 66^{o} (SW-NE), then in the next years the deformations concentrated in a very narrow trail, i.e. in the form of a step passing in the central part of 20 m strip and with a course consistent with the direction of previous damage.

The cohesion of MMA (mix asphalt) layers was seldom disturbed due to a relatively slow deformation build-up. A small deformation increase with time and the asphalt mix flexibility (viscous properties) in the period of higher temperatures existence allowed the asphalt mix to adapt to the deforming subsoil on a current basis (Pic. 4).

Pic. 7-4. Deformation of the northern roadway of A4 motorway - 5 August 2010 (Grygierek at al. 2015)

In the analysed period the reproducing step caused restrictions in the traffic due to a limited speed and unevenness. This situation forced to make the next repairs, which took place in 2011 and in 2014. Both

repairs consisted only in the profiling of the longitudinal pavement profile, i.e. in cold milling and building in a levelling and the wearing course.

The durability of such treatments was only temporary, because after a short time the step was again felt by the drivers. It is worth adding that based on the collected surveying measurements data the subsidence in the fault zone in the period 2006 - 2012 amounted to approx. 75 mm, and the mining was carried out at a distance of more than 350 m (Kotyrba, Kowalski 2015)

5. 2015 DEMOLITION WORKS

As a result of frequently occurring difficulties a repair design was developed in 2012, which was implemented in the second part of 2015.

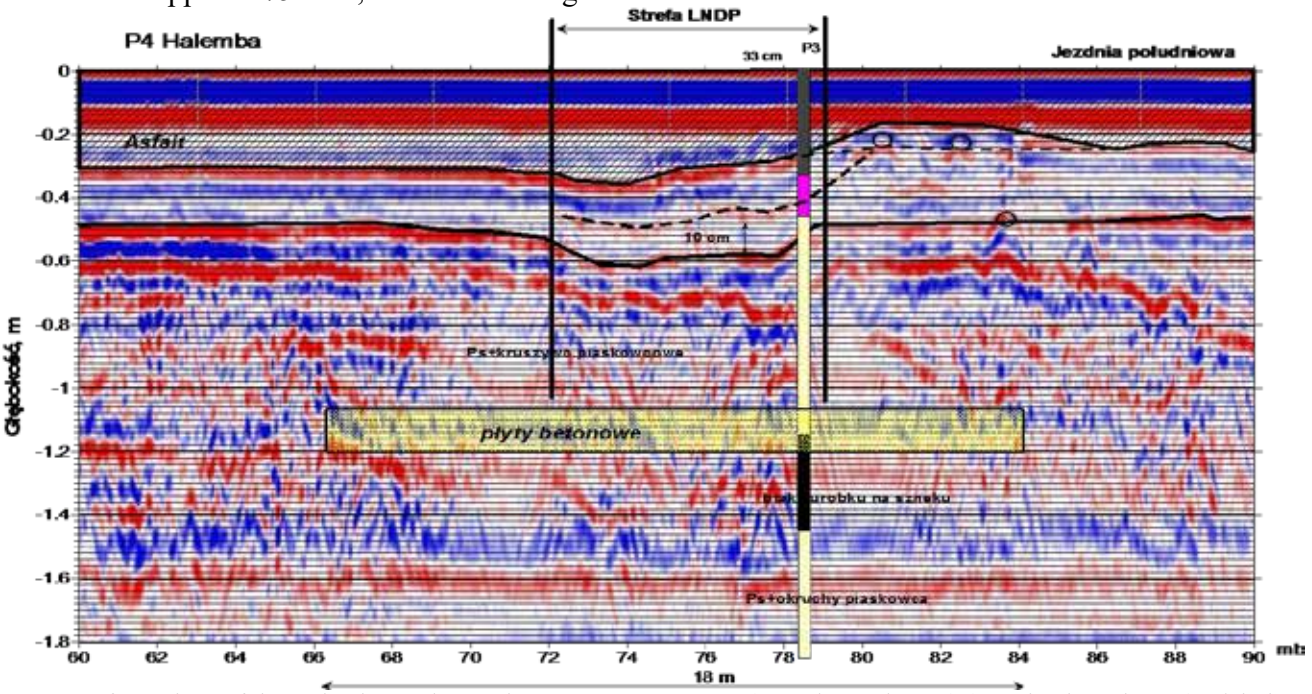

Fig. 7-4. Deformations of the embankment layers down to approx. 1.0 m. (Kotyrba at al 2015) (Grygierek at al 2015) Głębokość = Depth; Strefa = Zone; Jezdnia południowa = Southern roadway; kruszywo piaskowcowe = sandstone aggregate; płyty betonowe = concreto slabs; okruchy piaskowca = sandstone chips.

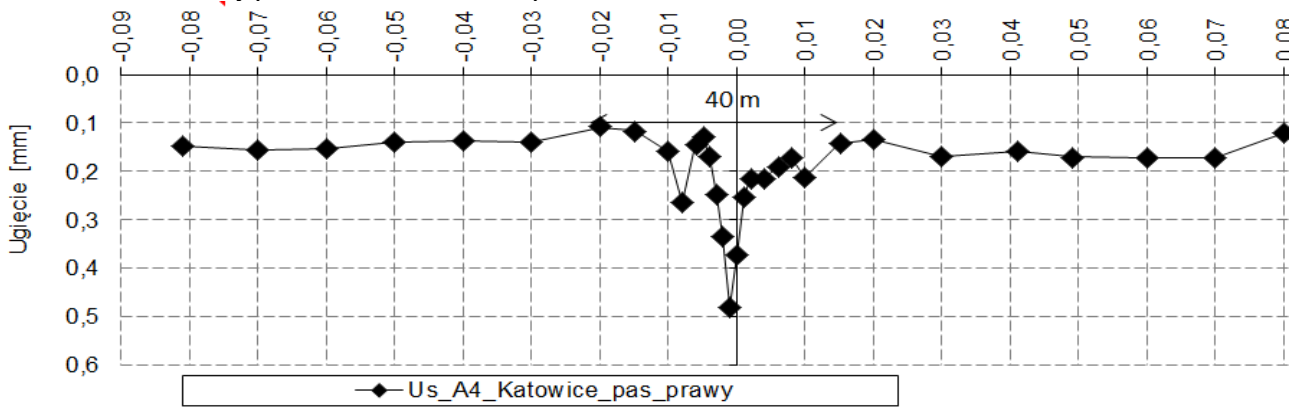

Fig. 8-5. Results of pavement deflections measured by an FWD (Falling Weight Deflecotmeter) (Grygierek M. & Kawalec J. & Kwiecień S. & Mencfel R. 2015). pas_prawy = right-hand_lane.

The design work included the performance of geophysical surveys and of geological-engineering boreholes, based on which the scope of construction works was planned.

The studies carried out at that time by the design entity indicated a possibility of voids existence in the rock mass, hence the treatment works (voids filling) were designed. The studies repeated by the works Contractor before taking over the right-of-way (geophysics, boreholes, probing) as well as the construction works themselves rejected the existence of any voids, and also the existence of significant cracks. Even more, based on georadar surveys it was found that the biggest anomalies, including profile deformations, existed in the embankment layers, i.e. situated at a depth of approx. 1.20 m between the native subsoil and the mineral-asphalt pavement.

This observation was one of arguments, based on which an alternative solution was suggested, which *inter alia* consisted building-in a reinforced concrete - pin jointed slab at a depth, at which the deformations disappear (Fig. 4). Attention was also paid to the subsidence, on the radarogramme, in the area of actual fault III outcrop. In fault III area, during the surveying work, a mild pavement deformation was

found, visible in particular on the edge line. The work preceding the construction works included the performance of pavement deflection measurements using an FWD instrument, to evaluate the impact of discontinuities on the pavement deflections distribution, and thus on the stiffness of the layer system building the pavement structure (Fig. 5). The test force of 90 kN was applied during the test for a better penetration of the pavement and subsoil layers. The obtained deflections distribution reflects well the results of georadar surveys. Zones of similar profile deformation length were obtained on both graphs - georadar and deflection increase (FWD). It is worth noting that beyond the discontinuities zone (approx. 30-40 m), the pavement featured very small deflections, i.e. below 0.20 mm at the MMA layers temperature of 20ºC and the test force of 90 kN.

Finally, the pavement subsoil structure consisting of a package of a few goegrid geomattresses featuring a very high long-term strength, a slip layer and other aggregate layers was made as a protection, in total 2.0 m thick. The pavement structure was build on the subsoil prepared this way.

6 SUMMARY

Selected events related to the motorway operation in a very difficult area, situated within the reach of deep mining operations, have been presented. The motorway was constructed in extremely difficult conditions, resulting from the necessity of construction works and mining operations - and related intense ground deformations - coexistence. The past mining in the area of the analysed section, carried out taking into account faults III and IV existing at a small distance, resulted in high tensions in the rock mass, which in effect led to the initiation of a discontinuous deformation phenomenon between these faults, in addition in the place, where no protections in the subsoil were applied. The next years of the motorway operation witnessed the next events, related to the origination and then the reproduction of discontinuous deformations in the same location. Studies carried out, in particular before this section reconstruction start, allowed to determine the length of this section weakening zone to approx. 30 m - 40 m. Also the geophysical surveys and the pavement deflection measurements by an FWD instrument turned out to be helpful to determine this scope. The adopted solution, based on a system of geomattresses, using among others a geogrid of high long-term strength, will allow to verify the implemented reinforcement concept. However, it is necessary to add, that this section will be situated beyond the area of main impacts.

7 REFERENCES

Chlipalski K. & Grygierek M. & Kliszczewicz B. & Strycharz B. 2010. The Experience of Monitoring A4 Motorawy Section In The Mining Areas (in Polish). Research Reports of Central Mining Institute. Mining & Environment no /1 pp. 31-42.

Grygierek M. 2010. Road Pavement Damage Caused By Discontinuous Mining Deformations Research Reports of Central Mining Institute. Mining & Environment no 4/1 pp: 72-82.

Grygierek M. & Kawalec J. & Kwiecień S. & Mencfel R. 2015. Evaluation Of Originated Discontinuous Deformations Impact, In The Area of Wirek and Halemba MOPs, On The Technical Condition Of A4 Motorway Pavements From km 327+450 To km 328+400 Including The Presentation Of Repair Solutions Concept - The Construction Part Technical University of Silesia. Gliwice, August 2015 (in Polish).

Kotyrba A. 2006. Analysis Of Tectonic Discontinuities Mapping In The Context Of Fault III Studies In The Subsoil Of A4 Motorway In The Area Of Kochłowice (Halemba Mine Field), Conference On Building Structures Safety In Mining Areas - Mining Damage/, Ustroń, 20-21 November 2006 (in Polish)

Kotyrba A. & Kowalski A. & Frolik A. & Gruchlik P. & Kortas Ł. & Siwek S. & Polanin P. 2015. Evaluation Of Originated Discontinuous Deformations Impact, In The Area of Wirek and Halemba MOPs, On The Technical Condition Of A4 Motorway Pavement From km 327+450 To km 328+400 And On The Subsoil Of Footbridge KP11 Between MPOs at km 327+650, Including The Presentation Of Repair Solutions Concept - The Geological And Mining Part. Central Mining Institute, Department of Geology and Geophysics, Department of Surface and Building Structures Protection, Katowice, July 2015. (in Polish).

Kotyrba A. & Kowalski A. 2009. Linear discontinuous deformation of A4 highway within mining area „Halemba". – Mineral Resources Management, Tom 25 book 3/2009.: 128 – 141,

Kowalski A. 2015. Surface deformations in in Upper Silesian Coal Basin. Monografia. Central Mining Institute Publishing, Katowice 2015: 130-136.

Strycharz B. & Chlipalski K. & Grygierek M. & Basiński T. 2005. Mining deformations and damage to the surface of A-4 motorway between junctions Wirek and Batory. XXII Conference on Structural Failures, Szczecin-Międzyzdroje, May 2005, Conference Proceedings pp. 625-634 (in Polish)

Geotechnical and Geophysical Site Characterisation 5 – Lehane, Acosta-Martínez & Kelly (Eds)

Effects of additional excavation on critical slip surface of stabilized walls with soil nailing

A. Hajiannia, M.T. Dorobati & S.B. Baghbadorani
Department of Civil Engineering, Najafabad Branch, Islamic Azad University, Najafabad, Iran.

S. Kasaeian
School of Engineering, University of Queensland, Australia

ABSTRACT: In recent years, soil nailing has been increasingly used, due to its low cost, high safety, workability and remarkable performance, to stabilize slopes and support excavations. Much research has been done on parameters affecting safety factor, stress, settlement and displacement. However, studies on the effects of additional excavation on excavation walls or, in other words, methods and mechanisms to preserve additional depth without compromising the whole wall stability while maintaining and controlling the initial slip surface are not many. Therefore, this paper aims at investigating the effects of 7m additional excavation on the 23m-deep excavation walls (totally 30 m) of the Twin Towers project in Shahr-e kord, Iran, retained by soil nailing systems. To retain the additional depth, use has been made of the 2D-FEM and anchorage method with in-situ concrete piles, and the results have been validated through a comparison between the calculated and measured wall displacements. The effects of seven key design factors (pile diameter, horizontal spacing, embedded length, anchor angle, prestressing force, bonded/unbonded length of the piles or anchors) have been discussed based on the results of FEM which is quite an efficient method for settlement predictions. Finally, a number of design charts have been prepared for in-situ concrete pile anchorage used in additional excavations.

1 INTRODUCTION

Nailing (started in mid 1980s in Hong Kong) has been widely used in deep excavations in recent years because of its safety, workability, and cost-effectiveness. In cases where excavation does not allow mere nailing walls, a combination with prestressed anchor cables can be quite effective. Nailed walls consisting of nailing and anchorage can be used effectively in reinforcing soil and controlling displacements in deep excavations. In recent decades, the combination has become a very popular method in Iran. So far, extensive research has been done on this method which is widely used in protecting deep excavations. Earlier, such research studies were based on limit equilibrium methods. Then, over time, and with the progress in FEM methods, many researchers used them to simulate nailed walls. Design and implementation of nailing is now several decades old and extensive research has been done.

Using the finite difference method for the analyses of composite nailed walls. Wang et al. concluded that the maximum horizontal displacement occurs mostly at the anchor tip and, then, it decreases from top to bottom. Tang et al (2008). analyzed the displacement and stress in prestressed anchor cables of the composite nailed structures and showed that the wall displacements (vertical and horizontal) are controlled better when use is made of prestressed anchor cables with the nailing system. Jin et al. (2010) concluded, in their research, that a combination of nailing and prestressed cables is more appropriate for the protection of the walls of deep excavations. Yan combined Drucker-Prager's and tensile slip models, carried out the finite element analysis of the composite nailing, and concluded that better results are found (compared to using only Drucker-Prager's model). Ma et al.'s research results showed that a composite nailed structure has a better seismic performance than a simple one.

A point common in all the related studies is a constant excavation depth, but if, for any reason, e.g. when the design parameters are not found at the drill-hole bed, the excavation depth is to be increased and,

therefore, its wall protection system (designed based on the former depth) will not work properly; the depth increase will cause an increase in displacements, settlements, forces in different anchoring members, and, hence, a decrease in the factor of safety. Therefore, it is necessary that proper measures be taken to stabilize the additional depth, maintain the position of the initial slip surface, prevent the displacements to exceed the allowable limits, and, finally, preserve the stability of the whole implemented system. To achieve these goals, use has been made, in the present research, of a combination of in-situ concrete piles and prestressed anchor cables as a stabilization system for the additional depth. The effects of such parameters as the pile diameter, horizontal spacing and embedded length, and the anchor angle, prestressing force, and bonded/unbonded length on the critical slip surface have been studied and the results discussed in full details in the sections that follow. In general, past researches have shown that composite soil anchorage methods (using steel profiles, concrete piles or concrete blocks) are quite efficient in controlling displacements in excavation walls. Krabbenhoft et al., (2005), Tan and Paikowsky, (2008), Niroumand and Kassim, (2010), Ghareh, (2011), and Ghareh and Saidi, (2011) are only a few among many researches carried out on the subject.

2 A BRIEF STUDY OF THE GEOTECHNICAL CONDITIONS OF THE PROJECT SITET

The project in question is situated in Shahr-e Kord, Iran, in a piece of land 7000 m2 in area facing streets from three sides and a 1-storey building from the fourth; the site lies in Zagros Zone. Our studies started through drilling three 25m, two 30m, and two 45m deep boreholes none of which met the underground water level. The SPTs performed at different depths needed more than 50 blows showing the soil layers' high compactness. In addition, some pressuremeter tests were also carried out in some boreholes on undisturbed samples to study the horizontal displacement module for the profile of the soil being studied (Table 1).

Table 1. Soil properties used in the FEM simulation

Depth(m)	SoilType	ϕ (deg)	C (kPa)	γ (kN/m^3)	E (kPa)	BS* (kPa)
0-4.5	GC	38	9.8	20	68600	250
4.5-12	SC	38	9.8	20	58860	250
12-16	GC	38	9.8	20	68600	250
16-21.5	GC	38	9.8	20	83380	250
21.5-45	SC	38	9.8	20	245250	250

* Bond stress.

The borehole depth was 23m, the excavation amounted close to 160000 m3, and stabilization was done by 11 rows of nails placed 2 meters apart (vertically and horizontally) at an angle of 150 (FIG. 1).

Fig. 1 A view of walls stabilized by nailing

3 THE ANALYSIS METHOD STABILITY ANALYSIS

To study the effects of different parameters on the slip surface, use was made of Slop/w section of Geostudio (a product of Geoslope Co.) which is based on the limit equilibrium relations and checks the safety factor and the condition of the slip surface.

4 DISCUSSION AND RESULTS

To validate the obtained results, a model was made based on the B. Xu et al.'s (2006) (Figure 2) and the safety factor and the slip surface conditions were studied. As shown in FIG. 3, the results conform to those of B. Xu et al.'s (2006) concluding that the proposed modeling has presented acceptable results.

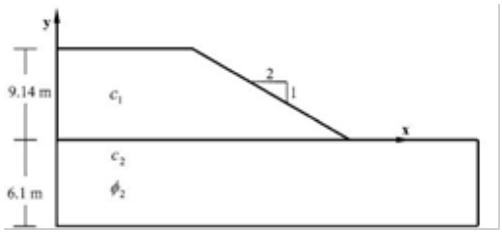

Fig. 2 Modeling for the validation of the results of Geoslope

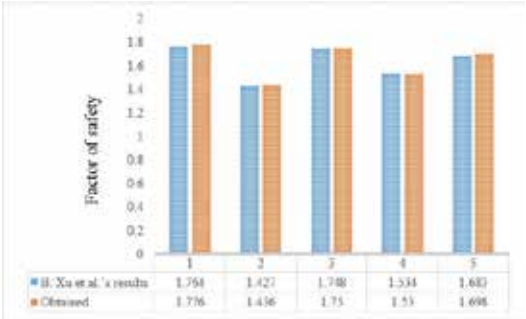

Fig. 3 Comparison of B. Xu et al.'s results with those obtained by the proposed modeling

If there is additional excavation, as shown in Figure 4, the initial slip surface will fundamentally change

and shift position to a lower level causing inefficient performance of the nails in previous levels and an increase in the displacements- hence the instability of the whole system.

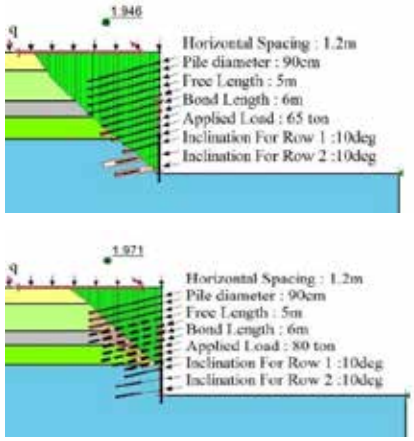

Fig. 4 The initial and secondary slip surfaces based on the limit equilibrium relations

Since the initial depth has been 23 m increasing to 30 m after 7 m of additional excavation, we are to take measures to anchor the additional depth and preserve the slip surface at its initial state and do not allow the displacements to exceed the permissible limits.

When the slip surface shifts position to a lower level, the nails in the first 23 m do not work efficiently and will not play a role in the stability of the system; therefore, effort has to be made to make the system work properly and, in the mean time, insure the stability of the additional depth. To achieve these goals, use was made, in this paper, of in-situ concrete piles with anchors, and the 7 key design parameters mentioned before were checked (results will be presented in the sections that follow). Figure 5 shows an overall picture of the wall after additional excavation.

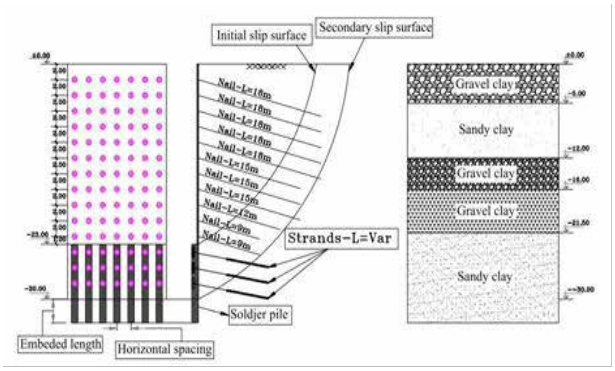

Fig. 5- An overview of the wall after additional

4.1 *Effects of anchor angle*

Effects of the anchor angle on the controlling situation of the initial slip surface were investigated for 2 and 3 rows of anchors at angles of 10, 15, 20, and 25˚ (and also combinatorial angles according to Tables 2).

Table 2. Combinatorial angles

Number of row	Angle(deg)	Angle(deg)
1	10	15
2	15	20
3	20	25
View	Mixed Angle:1	Mixed Angle:2

Number of row	Angle(deg)	Angle(deg)
1	10	15
2	25	20
View	Mixed Angle:1	Mixed Angle:2

To check the effects of the anchor angle on the position of the initial slip surface (3 rows of anchors) some models were made with 80 cm diameter piles, for a prestressing force of 50 tons and a horizontal spacing of 1.2 m for different anchor angles; the results are shown in Figure 6a.

For 2 rows of anchors too, some models were made with 120cm-diameter piles, for a prestressing force of 80 tons and a horizontal spacing of 1.5 m for different anchor angles; the results are shown in FIG. 6-b.

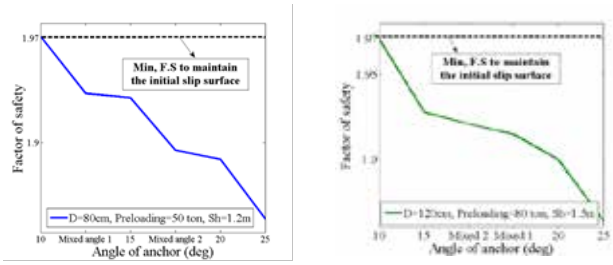

a) 2 rows of anchors b) 3 rows of anchors

Fig. 6 Effects of anchor angle on the F.S and the initial slip surface

Figure 6 shows that the angle increase from 10 to 25˚ generally causes a decrease in the F.S and a position shift of the initial slip surface; the use of combinatorial angles is, by far, better than using 20 and 25˚ angles.

4.2 *Horizontal spacing of piles and anchor members*

Any change in this spacing directly affects the performance of the stabilization system; this is clearly shown in Figures 7 and 8. The initial slip surface too was checked (as the displacements were). Figure 7 shows the effects of the increase in the horizontal spacing for different angles for both 2 and 3 rows of anchors; the pile diameter is 90 cm and the prestressing force is 80 tons. As shown, for 2 rows of anchors,

the initial slip surface is maintained only when the spacing is 1.2 m; if this is increased, the F.S is reduced considerably and the slip surface shifts position to a lower level. For 3 rows of anchors, the spacing can be increased up to 1.5 m.

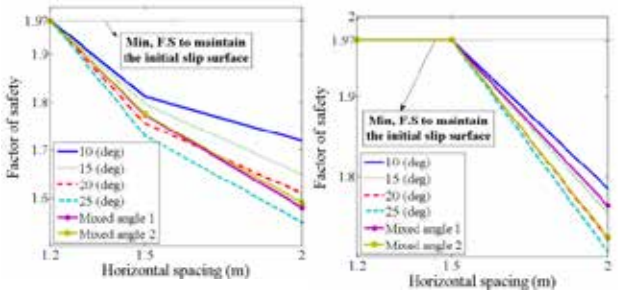

a) 2 rows of anchors b) 3 rows of anchors

Fig. 7 Effects of horizontal spacing on the F.S and the position of the initial slip surface

Figure 8 shows that if the stabilization system stiffness is increased and 120cm-diameter piles are used, in no case will the initial slip surface be maintained if the spacing is increased to 2 m; for 2 rows of anchors, the initial slip surface will be maintained only when the angle is 100 and the spacing is 1.5 m; therefore, it can be stated that the maximum possible horizontal spacing is 1.5 m (considering other conditions as well).

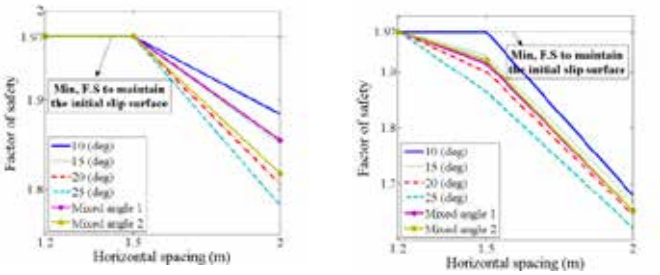

a) 2 rows of anchors b) 3 rows of anchors

Fig. 8- Effects of stiffness variations on the F.S and the position of the initial slip surface

4.3 *Effects of pile diameter on displacements*

One of the parameters that cause a change in the initial slip surface is a change in the pile diameter; such effects were studied once for 2 rows of anchors, 80 tons prestressing force, and 1.5 m spacing, and again for 3 rows of anchors, 65 tons prestressing force (same spacing). Results are shown in FIG. 9 for anchor angles of 10, 15, 20, and 25˚.

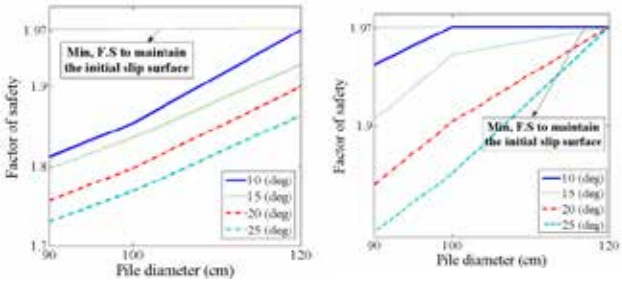

a) 2 rows of anchors b) 3 rows of anchors

Fig. 9- Effects of pile diameter on the F.S and the initial slip surface

Both figures show that the pile diameter increase can be an effective parameter in maintaining the position of the initial slip surface.

4.4 *Effects of prestressing force*

To check the effects of the anchors' prestressing force, different combinatorial forces were studied according to the values in Tables 3 and 4.

Table 3. Anchors' prestressing forces (2 rows of anchors)

Number of row	Preloading(ton)				
1	80	80	65	65	50
2	80	65	65	50	50
View	80,80	80,65	65,65	65,50	50,50

Table 4. Anchors' prestressing forces (3 rows of anchors)

Number of row	Preloading(ton)			
1	80	80	80	80
2	80	65	65	50
3	80	65	50	50
View	80,80,80	80,65,65	80,65,50	80,50,50

Regarding the relation between the prestressing force and the condition of the initial slip surface, FIG. 10 shows that it can be maintained with 3 rows of anchors, piles of 90 cm diameter, and a prestressing force of 65 tons (spacing and angle are considered to be constant); with 2 rows, the prestressing force is 80 tons.

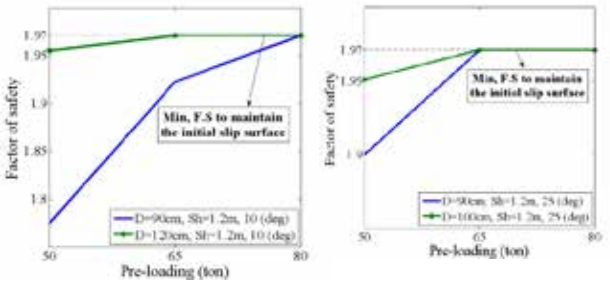

a) 2 rows of anchors b) 3 rows of anchors

Fig. 10 Effects of prestressing force on the F.S and the initial slip surface

4.5 *Effects of bonded and unbonded lengths*

Figure 11 shows that the bonded/unbonded anchor length does not affect the position of the initial slip surface.

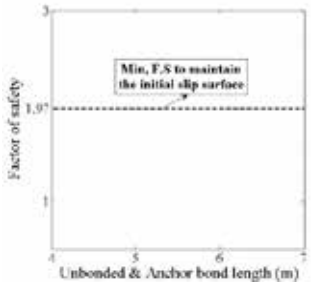

Fig. 11 Effects of bonded/unbonded anchor length on the F.S and the initial slip surface

4.6 *Effects of embedded pile length*

The embedded pile length, in this research, was found to have no considerable effects on the F.S and the position of the initial slip surface (Figure 12).

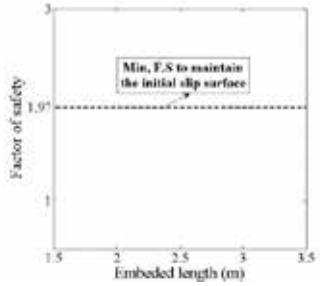

Fig. 12 Effects of the embedded pile length on the F.S and the position of the initial slip surface

Figure 13 shows the effects of pile spacing, pile diameter, anchor prestressing force, and anchor angle on the F.S and the position of the initial slip surface for 3 rows of anchors.

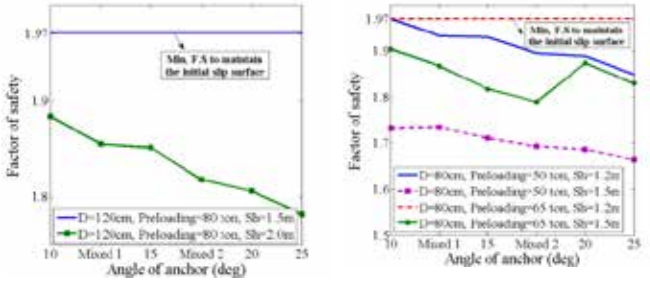

Fig. 13 Effects of pile spacing, pile diameter, anchor prestressing force, and anchor angle on the F.S and the position of the initial slip surface for 3 rows of anchors

As shown, an increase in the anchor angle from 10 to 25˚ will cause a decrease in the F.S and the position shift of the initial slip surface to lower levels; the use of combinatorial angles is by far better than 20 and 25˚ angles.

The use of 80cm-diameter piles with prestressing forces of 50 and 65 tons, and horizontal spacing of 1.2 and 1.5 m was also investigated; the position of the initial slip surface will be maintained when only 1.2 m spacing is used for piles. If the prestressing force decreases from 65 to 50 tons, the position of the initial slip surface will be lowered and, in this case, the position will be maintained only when the anchor angle is 10˚; if the prestressing force is 65 tons, the position will be maintained for all the angles. If the pile diameter and the prestressing force are increased to 120 cm and 80 tons respectively, the position will be maintained if the horizontal spacing is 1.5 m.

For 2 rows of anchors, if the spacing and the prestressing force are 1.2 m and 65 tons respectively, the position of the initial slip surface will change with an increase in the pile diameter. If the latter is 120 cm, the position will be maintained for all the defined angles, and if it decreases to 100 cm, the position will be maintained for anchor angles of 10, 15, and 20˚, and if it decreases to 90 cm, the F.S necessary to maintain the position will not be sufficient (for all the defined angles) and the initial slip surface will shift position to a lower level (FIG. 14).

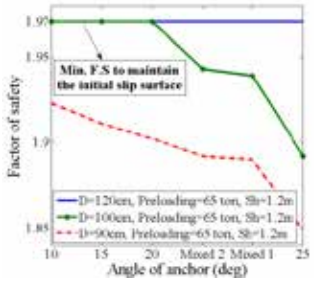

Fig. 14 Effects of pile diameter and anchor angle on the F.S and the position of the initial slip surface

Figure 15a shows (for constant pile diameter of 120 cm and prestressing force of 80 tons) the combined effects of the F.S and the position of the initial slip surface due to changes in the anchor angle and the horizontal pile spacing. Decreasing the pile diameter to 100 cm (other parameters remaining unchanged), the conditions will be more critical (compared to the previous case) if the spacing is increased (FIG. 15-b); the F.S will be reduced and the initial slip surface will shift position to lower levels for all the defined angles.

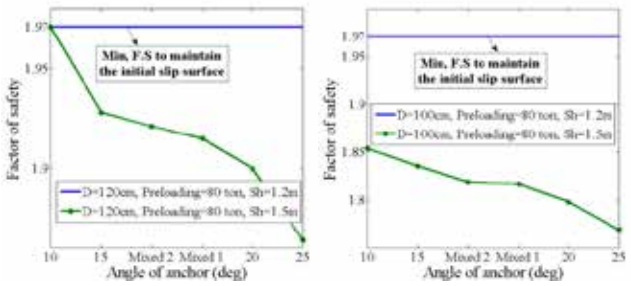

Fig. 15 Effects of anchor angle and horizontal pile spacing on the F.S and position of the initial slip surface

5 CONCLUSIONS

In this case study, we investigated a 23 m deep excavation wall stabilized by soil-nailing and a 7 m deep additional excavation stabilized by a combinatorial system of in-situ concrete piles and anchorage (based on the FEM) using limit equilibrium relations for the stability analyses; results are as follows:

- Effects of the 7 key design parameters (pile diameter, horizontal spacing, embedded length, bonded/unbonded length, anchor prestressing force, anchor angle) on the initial slip surface were studied and the results are as follows:

- It can be stated, considering the condition of the initial slip surface, that for both 2 and 3 rows of anchors, an angle of 10˚ can be optimal.

- Pile diameter variations affect the position of the initial slip surface; an increase in the pile diameter from 80 to 120 cm (for 3 rows of anchors) or from 90 to 120 cm (for 2 rows of anchors) increases the F.S and maintains the position of the initial slip surface.

- An increase in the anchors' prestressing force from 50 to 80 tons will lead to an increase in the F.S to maintain the position of the initial slip surface.

- An increase in the bonded/unbonded anchor length and the concrete piles' embedded length does not considerably affect the position of the initial slip surface.

- It is worth mentioning that the key design parameters studied in this research are somehow interrelated; a change in any one of them will affect the main conditions governing the design; hence, for an optimum design, use can be made of the graphs of this research to check the combined effects of the parameters that affect the design.

6 REFERENCES

Wang, J., Cao, J., Hu, J. and Liu, H. (2008). "Application of FLAC in foundation pit with compound soil nailing wall support." IEEE, Fourth International Conference on Natural Computation.

Tang, L., Song, M., Liau, H., Wu, Z. and Xu, T. (2008). "Analysis of stress and deformation of prestressed anchor cable composite soil nailing." Chinese J Rock Mech Eng, 27, 410.

Ma, T., Zhu, Y. and Meng, D. (2013). "Numerical analysis of composite soil nailing retaining wall under earthquake." Appl Mech Mater, Vols. 275-277, 1353-1358.

Jin, Q., Li, X. and Hu, B. (2010). "Application of composite soil nailing structure in foundation pit supporting." IEEE, Third International Conference on Information and Computing.

Yan, Z.G. (2012). "FEM analysis of composite soil-nailing considering tensile failure." Appl Mech Mater, Vols. 105-107, 1488-1491.

Brinkgreve, R.B.J. (1994). "Geomaterial models and numerical analysis of softening." Ph.D. dissertation, Delft University of Technology, Delft, the Netherlands.

Song, E.X. and Chen, Z.Y. (1996). "Soil nailing supported and finite element analysis." Engineering Investigation. 2:1-5. (in Chinese).

Yang, G.H. (2004). " Practical calculation method of retaining structures for deep excavations and its application. Beijing." Geological Press. (in Chinese).

Yang, J. and Song, E.X. (2004). "Analysis of an underground excavation and recommendation." Industry Architecture (Supp.):333-336. (in Chinese).

L. Ma, S.L. Shen, Y.J. Du and W.J. Sun. (2011). "A case study of the behavior of soil-nail supported deep mixed wall in the soft deposit of Shanghai." Lowland Technology Internation Vol. 13, No. 2, 1-8, International Association of Lowland Technology (IALT), ISSN 1344-9656.

B, Xu.and B, K. Low. (2006). "Probabilistic Stability Analyses of Embankments Based on Finite-Element Method." Journal of Geotechnical and Geoenvironmental Engineering, Vol. 132, No. 11, November 1, 2006. ©ASCE, ISSN 1090-0241/ 2006/11-1444–1454.

Soils Engineering Services Consulting Engineers Co. (2012). "Geotechnical Investigation Report, Construction of retaining walls for ShahrekordTwinTowers project." Shahrekord.

Niroumand, H., and Kassim, Kh.A. (2010). " Analytical and numerical studies of horizontal anchor plates in cohesion less soils." Electronic journal of geotechnical engineering (EJGE), Vol. 15, Page 281-292.

Ghareh. S. (2011). "Numerical Analysis of Behavior of Pile System under Lateral Loading." 6 th National Congress on Civil Engineering.

FHWA-0-IF-03-017. (2003). "Manual for Design and Construction Monitoring of Ground Anchors and Anchored Systems." U.S. Department of Transportation, Federal Highway Administration.

Cimponella, G.R. and Rubertsen, K.P. (1999). "Common problems with conventional testing." *J. Geotechnical & Geoenv. Engrg.*, Vol. 181 (9): 1193-1199.

FHWA. (1986). "Recommendations for Monitoring Applied Load During Permanent Anchor Testing Geotechnical Engineering Notebook, Geotechnical Guideline No. 12, Federal Highway Administration, Washington, D.C.

Cimponella, G.R. and Rubertsen, K.P. (1999). "Common problems with conventional testing." *J. Geotechnical & Geoenv. Engrg*, Vol. 181 (9): 1193-1199.

Ghareh, S. Saidi, M. (2011). "An Investigation on the Behavior of Retaining Structure of Excavation Wall Using Obtained Result from Numerical Modeling and Monitoring Approach. (A Case Study of International Narges Razavi 2 Hotel Mashhad)." Journal of Structural Engineering and Geotechnics, 1 (2), 17-23.

Geotechnical and Geophysical Site Characterisation 5 – Lehane, Acosta-Martínez & Kelly (Eds)

Field Investigation of the Performance of Soft Soil Reinforcement with Inclined Pile

A. T. Harianto & L. Samang
Geo-environmental Laboratory, Department of Civil Engineering, Hasanuddin University, Indonesia
B. Suheriyatna & Y.Sandyutama
Department of Public Works, Agatis, Tanjung Selor, Indonesia

ABSTRACT: A full-scale test of inclined timber pile was conducted to observe the effectiveness of this soil reinforcement in reducing the settlement with various types. A series of reinforcement method were applied in the field under a trial embankment with 4,5 m high. Field instrumentation was set up on the site to observe the movement and settlement behaviour of reinforced soil under embankment load. Pile reinforcement of soft soil made from galam timber with 6 m length and 10 cm in diameter. The settlement monitored by using settlement plate during the construction stage and the lateral displacement measured by using inclinometer. Piezometer was used in order to monitor the change of pore water pressure during the preloading test. It was concluded that construction of embankment using inclined pile as reinforcement on soft soil can reduce the settlement and lateral movement significantly and can be used as an alternative soil reinforcement material.

1 INTRODUCTION

Construction of road embankment over a soft soil poses challenging problems in its development. Generally, the strength of soft clay is not strong enough for supporting embankment stability. The problem of construction on soft clay is the low bearing capacity and differential settlement, therefore innovation in soil improvement is needed. Recently, many researchers conducted field observation of full-scale model (e.g. Falorca et al., 2011; Won and Kim, 2007; Hatami and Bathurst, 2005, 2006; Bergado et. al., 1995, 2000, 2003; Ling and Leshchinsky, 2003; Varuso et al., 2005). Nunes et al. (2013) reported that the settlement efficacy of pile-supported embankment is a reliable parameter to assess the overall performance of the rigid inclusion technique.

An experiment of full-scale trial embankment constructed on soft soil reinforced by several reinforcement methods is conducted in this study. Due to the limitations of construction materials especially in East Kalimantan Island (Indonesia), most of the construction materials for road construction were imported from outside the Kalimantan Island causing inefficiency (very high costs) in construction. Moreover, the trees (melalucea lencadendron linn/galam) are a local timber and easily found in Kalimantan and have long life if buried in the swamp. This timber is considered as an alternative material for soil reinforcement over soft clay. The performance of inclined pile compare to construction of conventional pile and geotextile reinforcement was observed.

Table 1. Soil properties

Soil Type		Layer 1 (0,00 - 4,00) m	Layer 2 (4,00 - 6,00) m	Layer 3 (6,00 - 12,00) m	Layer 4 (12,00 - 18,00) m	Layer 5 (18,00 - 25,00) m	Layer 6 (25,00 - 30,00) m	Fill
		Soft Clay					Sand	Slected Sand and Gravel
γ_{unsat}	[kN/m³]	12	12	13	15	16	16.5	19
γ_{sat}	[kN/m³]	14.5	14.5	15	16	18	20	20
k_x	[m/day]	6.89E-04	6.89E-04	6.89E-04	6.89E-04	6.89E-04	2	2
k_y	[m/day]	1.38E-03	1.38E-03	1.38E-03	1.38E-03	1.38E-03	1	1
E	[kN/m²]	-	-	-	-	-	8000	10000
v	[-]	-	-	-	-	-	0.35	0.35
Cc	[kN/m²]	0.9	0.9	0.85	0.6	0.4	-	-
Cs	[kN/m²]	0.13	0.11	0.13	0.09	0.09	-	-
e_0	[-]	2.2	2.2	2	1.8	1.5	-	-
φ	[°]	5	8	12	14	16.5	30	33
c	[kN/m²]	10	12	20	25	30	1	1

2 MATERIAL PROPERTIES AND METHODS

2.1 Soil and timber properties

In order to collect and determine the soil properties of experimental study location, deep borehole test was carried out. The soil properties are presented in Table 1. The general soil properties consist of very soft clay over the top 18 m. The silty sand is found between the depths of 18 and 30 m. This layer is underlain by medium stiff clay down to about 70 m depth. Moreover, the property of timber pile (galam) that is used in this study was presented in Table 2.

Table 2. Galam timber characteristics

Characteristic of Galam	Value
Water Content	22,95%
Compressive Strength //	23,3 Mpa
Compressive Strength ⊥	14,4 Mpa
Tensile Strength	17,9 Mpa
Bending Strength	101,4 Mpa

2.2 Instrumentation

A Full-scale test of trial embankment was constructed on 16.5 m width and 20 length of each type of reinforcement with 4.5 m of embankment high. The piles were installed with 6 m length and beneath the embankment a layer of geotextile was installed. The arrangement of pile reinforcement is shown in Figure 1. Typical cross section showing soft soil, piles and geotextile is shown schematically in Figure 2a. A series of instruments were installed on the embankment in order to monitor the deformation behavior such as settlement plate, inclinometer and piezometer. The instrumentation in the subsoil for each type of reinforcement {i.e. geotextile, conventional and inclined pile} was installed prior to the construction of the embankment as shown in Figure 2b.

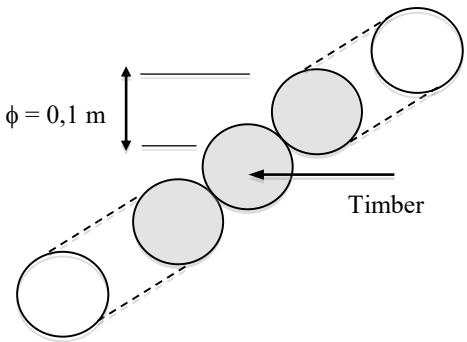

Figure 1. Inclined pile setting

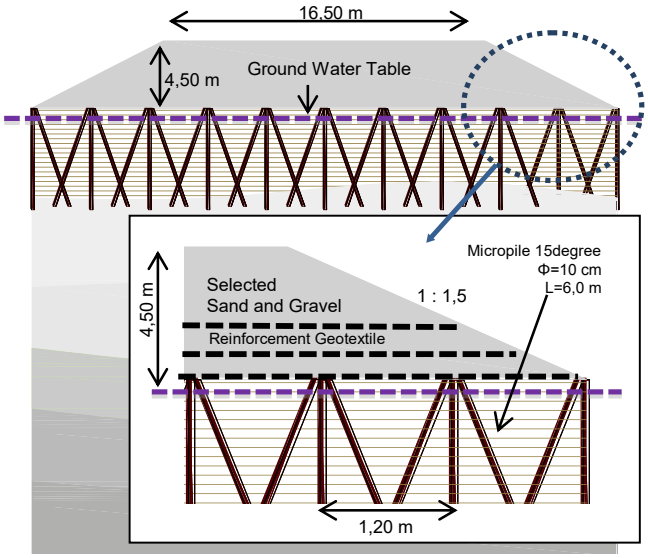

Figure 2a. Cross section of embankment

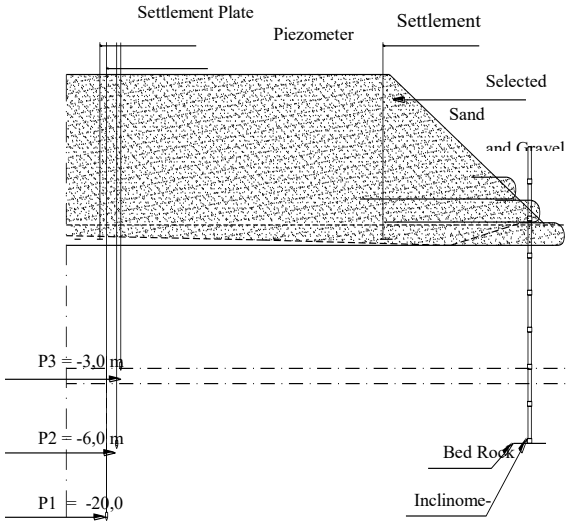

Figure 2b. Placement of instrumentation

3 RESULT AND DISCUSSION

The trial embankment observation was conducted in 3 months. Based on the observation results, the settlement of geotextile reinforcement was found about 1.1 m. It is indicated that the geotextile reinforcement inadequate in supporting the trial embankment with 4.5 m height. The bearing capacity also very low which indicate by huge amount of lateral displacement observed in the field.

For conventional pile reinforcement, the settlement was found lower than geotextile reinforcement. The total settlement reduces about 52%. It is indicated that the presence of piles tends to increase the bearing capacity of subsoil in supporting the embankment.

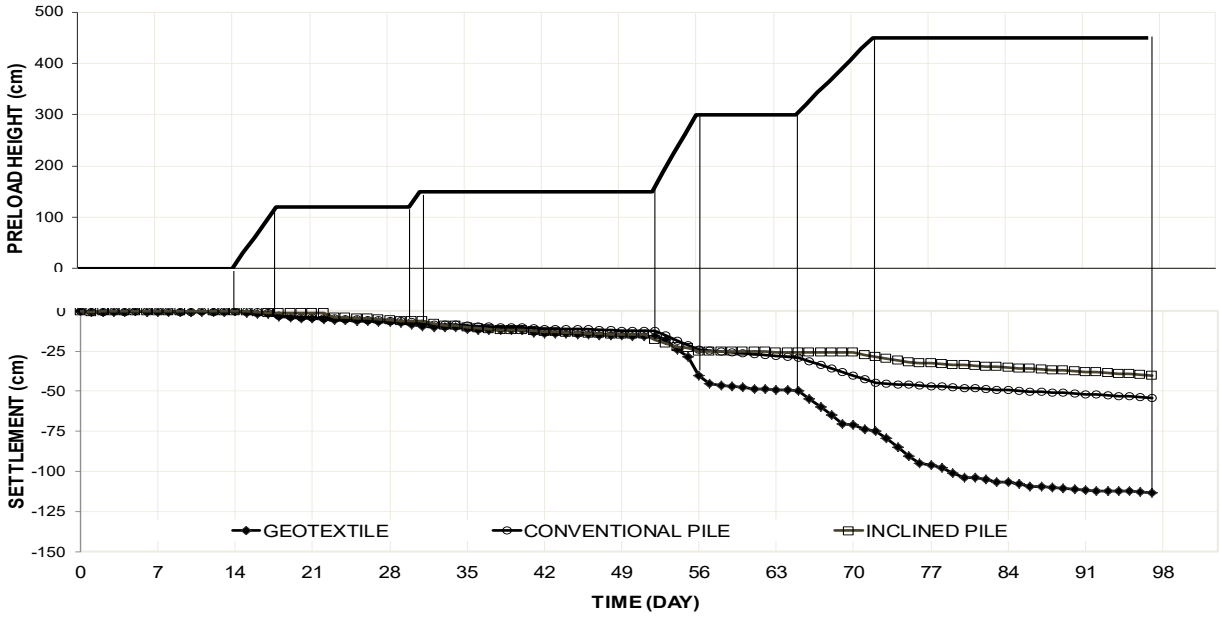

Figure 3. Summary of time versus settlement observations

Similar result obtained with the inclined pile reinforcement method. Reduction of settlement was found around 65% compare to geotextile reinforcement. The bearing capacity of this type of reinforcement has a highest value compare to other reinforcement method. The results of total settlement (3 months) are summarized in Table 3. The combination of all reinforcement method conducted in this study is shown in Figure. 3.

Table 3. Result of settlement plate observation

No	Construction Type	Settlement (cm)	Reduction of settlement compare to geotextile reinforcement (%)
1	Geotextile	113	-
2	Conventional Pile	54	52
3	Inclined Pile	40	65

Figure 4 shows the inclination pattern of three types reinforcement tested in this study. The displacement versus time at specific depth is useful to determine the rate of movement at that depth. It is found that the shear zone located near the surface (0-4 m depth). Installation of inclined pile significantly reduces the amount of lateral movement about 75% compared to geotextile reinforcement. This phenomenon mainly due to the presence of pile up to 6 m depth that provide the lateral resistance in the zone with pile reinforcement.

There were three piezometer points monitored in the field. Piezometer levels are shown plotted as a pore water pressure with various depth in Figure 5 (3, 6 and 20m). It was observed that with increasing height of embankment, the pore water pressure increase. The initial pore water pressure was increased to a depth of 20 m due to the stresses induced by the application of the embankment fill and construction equipment.

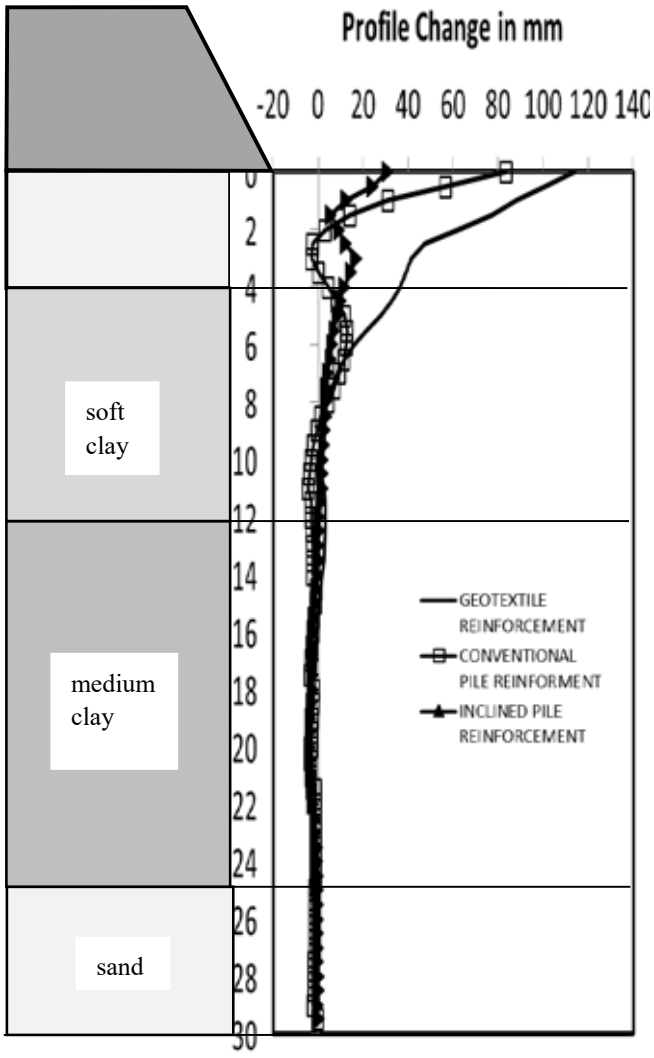

Figure 4. Inclination of various reinforcement

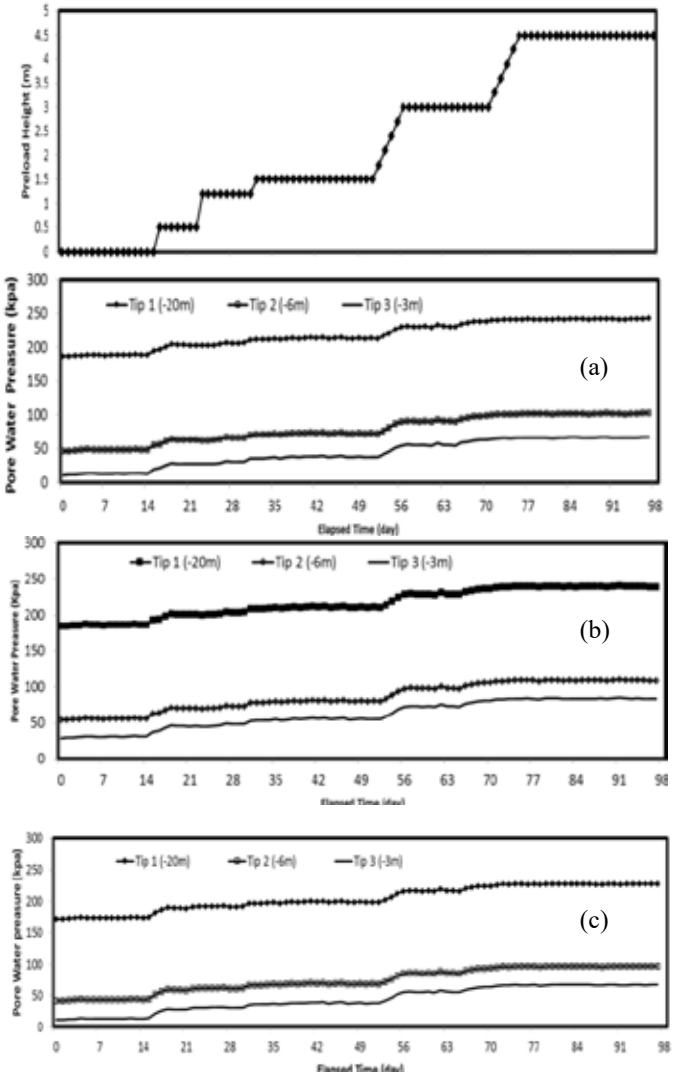

Figure 5. Pore water pressure profile (a) geotextile, (b) conventional pile, (c) inclined pile

4 CONCLUSIONS

The bearing capacity of reinforced soil with conventional and inclined pile is sufficient to support the trial embankment (4,5 m). The small amount of lateral movement was observed for both pile reinforcement, which is indicated that the sufficient slope stability of trial embankment, occur with the installation of pile reinforcement. The initial pore water pressure was increased to a depth of 20 m due to the stresses induced by the application of the embankment fill and construction equipment. The total settlement reduction for both conventional and inclined pile compared to geotextile reinforcement was found 52% and 65% respectively. Therefore, the inclined pile reinforcement has a potential application for road construction on soft soil as an alternative construction method.

5 REFERENCES

Bergado, D.T., Chai, J.C., Miura, N., 1995. FE analysis of grid reinforced embankment system on soft Bangkok clay. Computers and Geotechnics 17: 447-471

Bergado, D.T., Teerawattanasuk, C., Youwai, S., Voottipruex, P., 2000. FE modelling of hexagonal wire reinforced embankment on soft clay. Canadian Geotechnical Journal 37 (6): 1-18.

Bergado, D.T., Youwai, S., Teerawattanasuk, C., Teerawattanasuk, C., Visudmedanukul, P., 2003. The interaction mechanism and behaviour of hexagonal wire mesh reinforced embankment with silty sand backfill on soft clay. Computers and Geotechnics 30: 517-534.

Falorca, I., Gomes, L. and Pinto, M., 2011. A full-scale trial embankment construction with soil reinforced with short randomly distributed polypropylene microfibers. Geosynthetics International, 18(5) : 280.

Hatami, K., Bathurst, R.J., 2005. Development and verification of a numerical model for the analysis of geosynthetic-reinforced soil segmental walls under working stress conditions. Canadian Geotechnical Journal 42: 1066-1085.

Hatami, K., Bathurst., R.J., 2006. Numerical model for reinforced soil segmental walls under surcharge loading. Journal of Geotechnical and Geoenviromental Engineering, ASCE 136 (6): 673-684.

Ling, H.I., Leshchinsky, D., 2003. Finite element parametric study of the behaviour of segmental block reinforced – soil retaining walls. Geosynthetics International 10 (3): 77-94.

Nunez, M. A., Briancon, L. and Dias, D, 2013. Analyses of a pile-supported embankment over soft clay: Full-scale experiment, analytical ans numerical approaches. Engineering Geology, 153: 53-67.

Varuso, R.J., Grieshaber , J.B., Nataraj, M.S., 2005. Geosynthetic reinforced levee test section on soft normally consolidated clay. Geotextiles and Geomembranes 23 (4): 362-383.

Won, M.S., Kim, Y.S., 2007. Internal deformation behaviour of geosynthetics-reinforced soil walls. Geotextile and Geomembranes 25 (1): 10-22.

Geotechnical and Geophysical Site Characterisation 5 – Lehane, Acosta-Martínez & Kelly (Eds)

Static Load Testing of Concrete Free Reticulated Micropiles System

A.Mehdizadeh
Swinburne University of Technology, Australia

M.M. Disfani
University of Melbourne, Australia

R.Evans & E. Gad
Swinburne University of Technology, Australia

A.Escobar & W.Jennings
Pandoe Pty Ltd (sureforrt), Melbourne, Australia

ABSTRACT: Surefoot is a new steel micropile group footing system, light enough to be manually handled by a single operator and installed using very simple power tools. It does not require excavation, drilling or use of any concrete. Surefoot can be described as a "Braced Batter Micropile Group". It comprises an adjustable steel pile cap with 3 to 16 "inclined micropiles", depending on the nature and magnitude of loads and soil conditions. To evaluate the ultimate capacity of the new foundation system and assess the applicability of current pile design methods to this new system, a series of static pile load tests were performed. Testing regime covered a range of geometric configurations and embedment depths of the new footing system. All testing was conducted in an area with surface geology of quaternary basaltic clay deposits in Braybrook, Victoria. This paper presents results of site classification, in-situ strength tests, laboratory strength tests, along with the field static load tests on the new micropile footing system. The field test results were analysed using a range of methods to anticipate the failure load.

1 GENERAL INSTRUCTIONS

Micropiles are usually defined as small diameter piles of less than 300 mm. They can be driven or grouted depending on soil type, project aim and micropile material. Micropiles were first used in the early 1950s to underpin damaged historical buildings (Mason and Bruce, 2001). The ability to work in areas with limited access (i.e. a basement) without the need to disturb the existing structure was one of the main reasons for their development (FHWA, 2005). Micropiles are known as multi-rule retaining/foundation systems and have been used for other geotechnical problems such as ground reinforcement due to their flexibility in construction, dimension and layout (Bruce et al., 1997; Schlosser and Frank, 2004). Fernando Lizzi was one of the first engineers to provide this new concept to internally strengthen the existing unreinforced masonry structures using reticulated micropiles (Mason and Bruce, 2001).

Pre-1989, most of the available micropile design methods were only used to determine the total number of micropiles required. Cantoni et al. (1989) overcame this limitation by proposing a simple method for using micropiles in slope stabilization applications. At present, it is generally accepted that the geotechnical capacity of a micropile is mobilised by its skin friction. End bearing resistance can be disregarded in most cases due to the relatively small toe area of a micropile (Bruce and Yeung, 1984; Juran et al., 1999; Cadden et al., 2004). Field performance of micropiles has shown that the actual bearing capacity of micropiles is usually higher than predicted values, which has been attributed to high skin friction (Sharma and Hussain, 2011). Besides improving the frictional resistance, groups of micropiles also confine the soil by creating a geocomposite material with higher stiffness and resistance (Sadek et al., 2006).

The group effect of micropiles has been investigated by many researchers. For instance, Estephan and Frank (2002) showed that the interaction between soil and micropile group was mainly dependent on group geometry and individual micropiles, soil characteristics, and the installation method. Furthermore, from tests conducted on reticulated micropiles, Lizzi (1982) and Schlosser and Frank (2004) concluded that the network configuration of the micropiles had a positive effect and increased the soil stiffness.

The inclination of micropiles in a group is another parameter that has shown to influence the bearing capacity of a micropile network against various loading patterns. Sadek et al. (2006) performed 3D numerical modelling of a micropiles group to investigate this effect. The analysis indicated that the use of inclined micropiles improved foundation performance under vertical, inclined and lateral loads. They also concluded that axial and lateral stiffness of the micropile group increased by using inclined micropiles.

Recently, a new reticulated micropile system has been developed as an alternative to traditional footing systems. Its market name is Surefoot. Due to the quick and easy installation, lower overall cost and

minimum site disturbance of this new system, it is becoming more and more popular. The Surefoot system comprises of a steel pile cap that sits either on or above the ground and a number of inclined stainless steel or galvanised hollow micropiles (40 mm diameter), which are driven through the guiding sleeves and into the ground by a small jackhammer as shown in Figure 1. For instance, the SF100 consists of a square shape pile cap with a width of 263 mm and a thickness of 6 mm (Figure 1 (a)). Four hollow galvanised pipes (micropiles) with different embedment depth (depending on design loads and ground condition) are driven into the ground through the guiding sleeves connected to the pile cap and then fixed to the sleeves using screws (Figure 1 (b)). Installation typically takes 10 to 30 mins per Surefoot system with minimal disturbance to the surrounding ground. It is highly suitable for areas with limited access and can support a range of loading patterns.

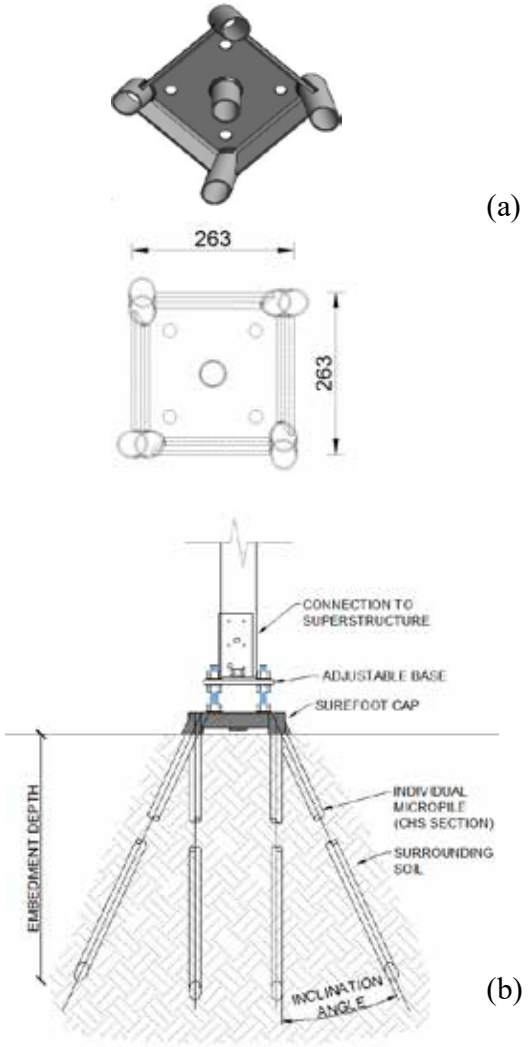

Figure 1. (a) Surefoot SF100 pile cap (dimensions in mm) (b) Surefoot system with surrounding soil.

To evaluate the performance of the Surefoot system in terms of ultimate load capacity under axial compression and tension, eight static field load tests (based on a modified quick load test method) were carried out. This paper addresses the geotechnical characteristics of the soil and presents the in-situ field tests results. The ultimate capacity of each Surefoot test system was initially determined using a range of available methods (from current literature), which has been discussed with some recommendations proposed.

2 SITE DESCRIPTION

The test site was located in Melbourne's western suburb of Braybrook in Victoria. The geological and geotechnical investigation revealed the presence of two distinct soil layers down to 2 m below the surface. The first layer was a fill material that varied in depth from 300 to 700 mm across the site. Underlying this layer was a soft highly plasticity clay (CH) according to AS 1726 (Standards Australia, 1993). Organic root matter was also noted in both layers down to a depth of 1000 mm.

Due to limited site access caused by existence of soil instrumentation for other research projects, it was not possible to remove the fill material or install the footings in a location free of fill material. Therefore, the footings were mounted at ground level and the effect of the fill material was later taken into account via back-analysis.

Drained and undrained shear strength parameters of the fill and clay layers were determined by Unconsolidated Undrained (UU) and Consolidated Undrained (CU) triaxial testing of undisturbed samples. The soil characteristics of both layers have been reported in Table 1. The average undrained shear strength (S_u) was found to be 12 kPa and 23 kPa for the fill material and clay, respectively. Due to the effect of the fill and organic material, it is plausible that the field soil strength is less than the measured values. In addition, Dynamic Cone Penetrometer (DPT) testing was performed in the centre of each Surefoot footing system, as well as at the midpoint of each two test footings as in accordance with AS 1289.6.3.2 (Standards Australia, 1997). The average measured penetration per blow was approximately 14 at a depth of 200 mm down to 1700 mm. No water table or adverse moisture conditions were observed to a depth of 2 m during the study.

In total, four Surefoot footings with different pile cap dimensions (SF100 and SF300), number of micropiles and embedment lengths were tested under compression and tensile loadings (Figure 2). To provide the required reaction forces, ten Surefoot footings (SF400) were installed as reaction piles in such way to satisfy the minimum required distance between the main test micropiles and reaction micropiles (Table 2).

Table 1. Geotechnical characteristics of Braybrook clay

Soil Type	z (mm)	LL (%)	PL (%)	w (%)	S_u (kPa)	c (kPa)	Internal Friction, φ (˚)	c' (kPa)	φ' (˚)	E_{50} (MPa)
Fill	450	75	28	13.5	8.5					
Fill	550				16					
Clay	750				27					
Clay	750					13	14	0	34	9-19
Clay	900	75	22	23	19					
Clay	1150				26					
Clay	1250				18.5					

Table 2: Specification and details of the installed reaction and test footings

Footing Type	Embedment Depth (mm)	Type of Footing	Surefoot Footing Details		
			Number of Micro-piles	Pile Cap Dimensions (mm)	Pile Cap Thickness (mm)
SF400-2000	2000	Reaction	9	482x482	10
SF100-1200	1200	Test	4	263x263	6
SF100-1500	1500	Test	4	263x263	6
SF300-1200	1200	Test	6	382x382	8
SF300-1500	1500	Test	6	382x382	8

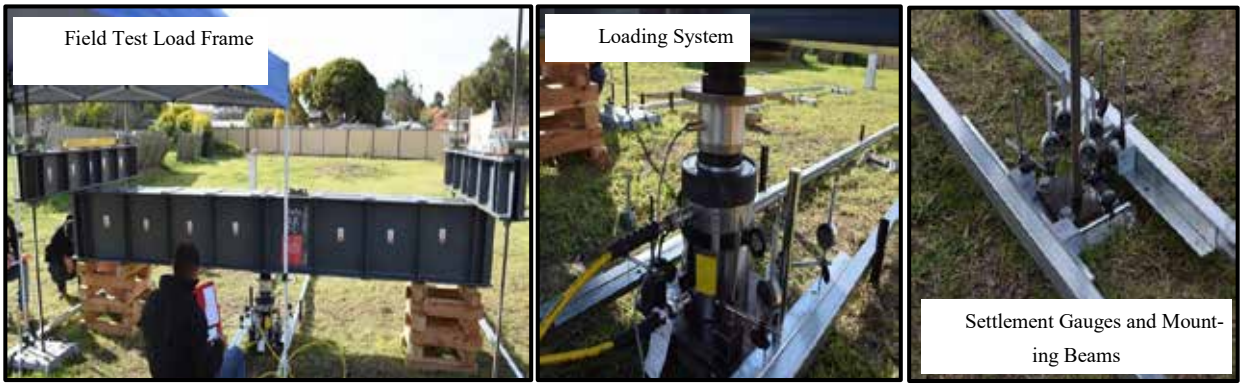

Figure 2. Field testing of Surefoot

3 TESTS RESULTS

The Quick Maintained Pile Load Test Method (ASTM D1143/D1143M-07, 2013) was selected to investigate the ultimate capacity of the Surefoot footings. Ten per cent of the anticipated ultimate capacity was selected as the load increment, which was maintained for 15 minutes for each increment. In addition, the potential of soil/system creep was assessed at the end of the final loading stage by holding the load for an extra 10 minutes. Creep-displacement criterion is usually defined as the allowable displacement of 2 mm per log of cycle of time. The footing was unloaded in three or four steps based on the achieved ultimate load. It is worth mentioning that the ultimate load was defined by continuous jacking to maintain the applied load. Figure 2 shows field testing set-up and Figure 3 illustrates the behaviour of the tested footings under the compression and tension loadings.

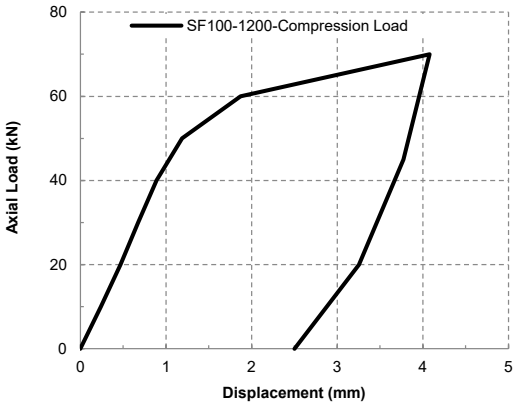

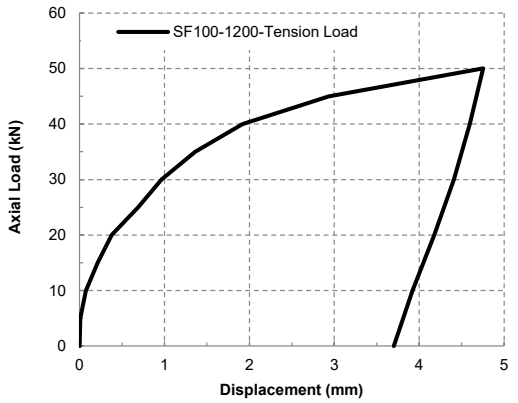

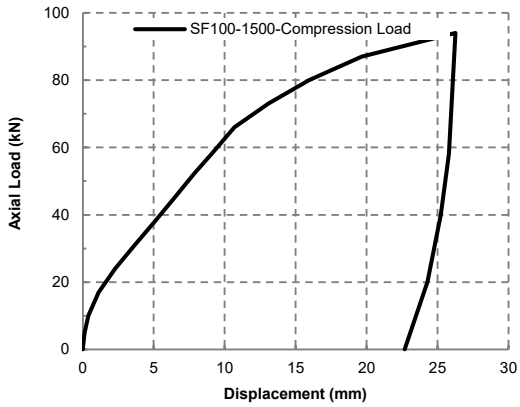

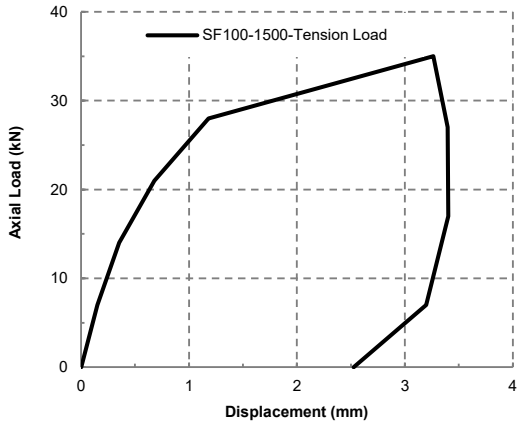

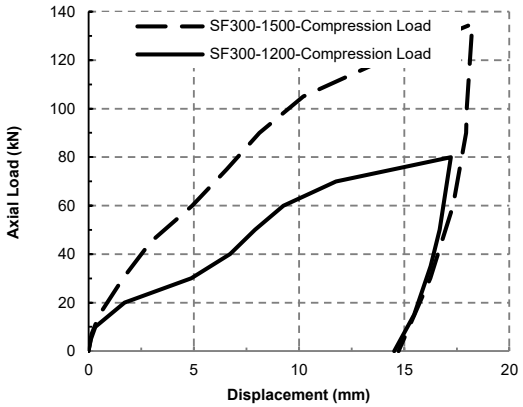

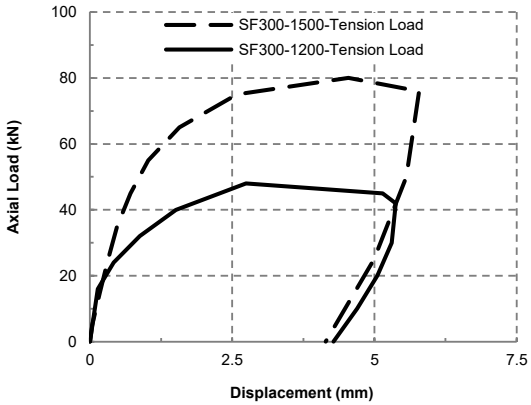

Figure 3. Load-settlement curves for the tested footings

The tensile load test on each footing was typically performed first, except for footing type SF100-1200 where the compressive load test was performed first. To allow the soil to relax and dissipate any possible induced excess pore pressures, a gap of 2 to 3 days was allowed between the tensile and compressive load tests. The results achieved in Figure suggest that the ultimate bearing and pullout capacities of the Surefoot system improve by an increase in length and number of micropiles (except for the SF300-1200). It is believed that the lower resistance of this footing was due to the deeper fill material at that location. This was even more obvious for bearing capacity. Comparing the test results of SF100-1200 and SF100-1500, suggests that although the bearing capacity of SF100-1500 was higher, the required micropile movement to activate this capacity was also much higher at 11 mm to reach the 65 kN compressive load. This was almost four times greater than the observed displacement for SF100-1200. It is also worth noting that all eight tests indicated that the creep settlement was negligible and well below the criteria (FHWA, 2005).

From current literature, there are various methods available to derive the ultimate capacity of a pile from a field load test. However, not all of these methods are always applicable. This depends on the type of pile or micropile. Figure 4 presents the calculated ultimate bearing and pullout capacities for the tested Surefoot system using a variety of methods. Some of

the determined values were out of the reasonable range and removed from the plot. Upon review of these values, there appears to be no specific trend that shows which method is the most accurate. However, from this study, the Brinch Hansen 80% Criterion (1963), Chin-Konder Extrapolation (1970) and Mazurkiewics (1972) all calculate higher values.

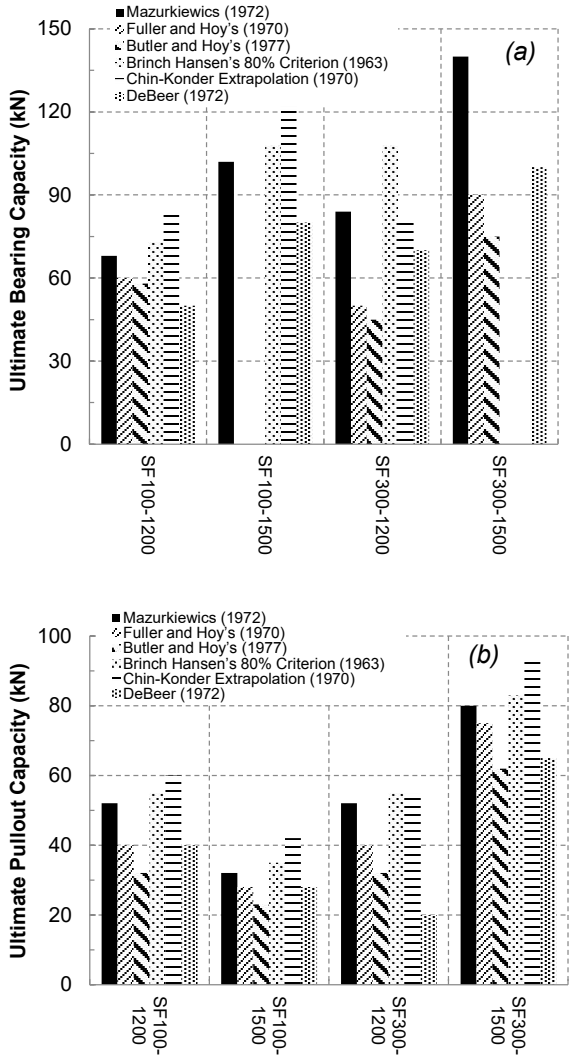

Figure 4. Calculated ultimate (a) bearing and (b) pullout capacities of the Surefoot footings using various methods

The measured ultimate capacities with respect to soil condition and footing dimension showed that this type of footing could be considered as an alternative for residential and industrial construction. However, impact of soil shrinkage, fluctuation of water table or load-unload conditions need to be considered further.

4 DISCUSSION

The current approach of designing a Surefoot system is based on the bearing capacity of shallow foundations, skin friction of deep foundations and lateral passive resistance forces. The combination of bearing capacity and skin friction is used to determine the allowable bearing capacity. However, the pullout forces are derived from mobilising the skin friction and passive forces acting on the micropiles. Only the skin friction acting on the outside of micropiles is considered in the analysis.

To investigate the accuracy of the current method, the ultimate bearing capacity of the SF300-1500 was calculated and compared with the field results (Table 3). The bearing capacity (Meyerhof method for shallow foundation), skin friction (λ method for deep foundation) and passive resistance of each micropile (Rankine method) were calculated considering the undrained shear strength of 12 and 23 kPa for the upper fill layer (0 to 400 mm) and for Braybrook clay (400 to 1500 mm), respectively.

Table 3. Ultimate bearing and pullout capacity of SF300-1500, field data and design approach

Bearing Capacity (kN)	Skin Friction (kN)	Passive Forces (kN)	Ultimate Bearing Capacity (kN)
36.18	27.7	17.62	63.88

Ultimate Pullout Capacity (kN)	Field Bearing Capacity (kN)	Field Pullout Capacity (kN)
45.32	101	76

The calculated values for ultimate bearing and pullout capacity are approximately 60 per cent of the observed field capacities. In this analysis, the ultimate capacity of the Surefoot footing system was determined based on the contribution of each micropile individually. However, it seems that the confining effect of the micropiles as a group should also be considered. Nevertheless, more field tests combined with numerical modelling is required to better determine the contribution of group effect or soil confinement on the system's capacity. Interaction of micropiles and soil and, stress distribution beneath the top cap and along the micropiles length can be investigated using a 3D numerical model.

5 CONCLUSION

A new footing system known as Surefoot was tested in the field to determine its ultimate bearing and pullout capacities. The results of the field load tests were used to back-analyse the design approach. It was noted that the current design method is conservative due to not considering the confining effect of the micropiles and soil arching. However, field capacity test results showed that this footing can be used as a cost-effective alternative of traditional footing to support residential and industrial loadings. The research achievements and recommendations are summarized below:

- The ultimate pullout capacity of the Surefoot system was measured at 50 to 70 per cent of ultimate bearing capacity in Braybrook clay.
- Regardless of the confining effect of micropiles, the contribution of every meter of each micropile in supporting the compressive and tensile loads was approximately 13 and 7 kN/m.
- Finite element modelling is required to study the influence of different parameters such pile cap thickness, length, inclination or diameter of micropiles on system's capacity.

6 ACKNOWLEDGEMENT

This research is funded by the State Government of Victoria, Department of Economic Development, Jobs, Transport and Resources. R&D Voucher Program IVP-BRD-264A.1. In addition, the authors would like to thank Pandoe Pty Ltd (Surefoot) for their financial and in-kind support.

7 REFERENCES

ASTM-D1143 (2013). Standard test method for piles under static axial compression load. ASTM International, DOI: 10.1520/D1143_D1143M

Brinch, H. and Hansen, J. (1963). "Discussion Hyperbolic Stress-Strain Response. Cohesive Soils." Journal of Soil Mechanic and Foundation, ASCE, 89 (4), 241-242.

Bruce, D. A., and Yeung, C. K. (1984). "A review of minipiling with particular regard to Hong Kong applications." Hong Kong Engineer, 12 (6), 31-54.

Bruce, D. A., Dimillio, A. F., and Juran, I. (1997) "Micropiles: the state of practice." Ground Improvement, 1 (1), 25–35.

Butler, H. D. and Hoy, H. E. (1977). "Users Manual for the Texas Quick-Load Method for Foundation Load Testing." Federal Highway Administration, Office of Development, Washington, DC.

Cadden, A., Gomez, J., Bruce, D., and Armour, T. (2004). "Micropiles: recent advances and future trends." In Current practices and future trends in deep foundations. ASCE, 140-165.

Cantoni, R., Collotta, T., Ghionna, V. N., and Moretti, P. C. (1989). "A design method for reticulated micropile structures in sliding slopes." Ground engineering, 22 (4).

Chin, F. K. (1970). "Estimation of the Ultimate Load of Piles not Carried to Failure." Proceedings 2th Southeast Asian Conference on Soil Engineering, Singapore, 81-90.

De Beer, E. E. and Wallays, M. (1972). "Franki Piles with Overexpanded Bases." La Technique des Travaux, 333, 48.

Estephan, R. and Frank, R. (2002). "Experimental and numerical approaches to the study of the behaviour of micropile groups and networks subjected to vertical or horizontal loading." International Workshop of Young Doctors in Geomechanics, Champs-sur-Marne, France, 63-64.

FHWA. (2005). "Micropiles design and construction." Federal Highway Administration (FHWA). Report No. FHWA NHI-05, 39.

Fuller, F. M. and Hoy, H. E. (1970). "Pile Load Tests Including Quick-load Test Method Conventional Methods and Interpretations." 333, 78-86.

Juran, I., Bruce, D. A., Dimillio, A., and Benslimane, A. (1999). "Micropiles: the state of practice. Part II: design of single micropiles and groups and networks of micropiles." Ground Improvement, 3 (3), 89-110.

Lizzi, F. (1982). "The pali radice (root pile): a state-of-the-art report." Proceedings of the Symposium on Recent Development in Ground Improvement Techniques, Bangkok, 417–432.

Mason, J., and Bruce, D. (2001). "Lizzi's structural system retrofit with reticulated internal reinforcement method." Transportation Research Record: Journal of the Transportation Research Board, (1772), 107-114.

Mazurkiewicz, B. K. (1972). "Test Loading of Piles According to Polish Regulations." Royal Swedish Academy of Engineering Sciences Commission on Pile Research, Report No. 35, Stockholm, 20

Sadek, M., Shahrour, I., and Mroueh, H. (2006). "Influence of micropile inclination on the performance of a micropile network." Proceedings of the ICE-Ground Improvement, 10 (4), 165-172.

Schlosser, F. and Frank, R. (2004). "FOREVER (FOndations REnforce´es VERticalement): Synthe`se des re´sultats et recommandations du Projet national sur les Micropieux." Presse de l'ENPC, Paris.

Sharma, B., and Hussain, Z. (2011). "A Model Study of Micropile Groups Subjected to Lateral Loading Condition." In Proceedings of Indian Geotechnical Conference.

Standards Australia. (1993). "Geotechnical Site Investigation". AS 1726-1993, ISBN: 0726278785, Standards Association of Australia, Homebush, NSW, Australia.

Standards Australia. (1997). "Methods of testing soil for engineering purposes - Soil strength and consolidation tests-Determination of the penetration resistance of a soil –9 kg dynamic cone penetrometer test". AS 1289.6.3.2-1997, ISBN: 0733710581, Standards Association of Australia, Homebush, NSW, Australia.

Geotechnical and Geophysical Site Characterisation 5 – Lehane, Acosta-Martínez & Kelly (Eds)

A comparative analysis of the stability of a slope in an overconsolidated clay pit based on CPT and DMT measurements

H. Peiffer
Laboratory of Geotechnics, Department of Civil Engineering, Ghent University, Ghent, Belgium

ABSTRACT: In Belgium the Boom Clay is a well know overconsolidated tertiary clay formation. In the period 2011-2014 small slidings occurred in the slopes of a pit with a depth of 30 m. Because more slidings could be expected, a monitoring was started including a series of DMT-tests and CPT-tests around the pit. In June 2014 a very large sliding (an area about 100 m by 50 m) occurred. In the present paper the results of the DMT-tests and the CPT-tests were discussed at different stages, before the sliding and after the remediation works. Although both CPT and DMT gives a clear image of the sliding surface, the measurement with the DMT gives a more pronounced result.

1 INTRODUCTION

The dilatometer as developed by Marchetti, gives the opportunity to evaluate stress changes in the soil. This opportunity resulted, besides other applications, in an experimental method for the evaluation of changes of the stress in the soil during pile installation (Peiffer, 1997). The DMT test allows also for the risk assessment for the stability of slopes (Peiffer, 2015). In this article a comparative analysis is made considering the results of the cone penetration test (CPT) and the dilatomer test (DMT) in order to evaluate the sensitivity of these test methods for the evaluation of slope stability. In order to make this evaluation, the tests were carried out in a clay pit in Flanders (Kruibeke). In the period 1963 – 2010 the pit was excavated in the Boom Clay till a depth of about 30 meters.The clay was used for the fabrication of expanded clay granulates.

In 2010, the exploitation of this pit stopped because the borders of the concession were reached. One year later, in 2011 a first (limited) instability of the slope of this pit occurred (sliding). Apparently, it became clear that more stability problems could be expected. In 2012 and 2013, new (limited) slidings occurred. In the beginning of 2014 it was decided to setup an extensive monitoring program in order to evaluate the risk of further instability of the slopes, site investigation was carried out (DMT and CPT). Besides the monitoring of the settlements and the pore water pressures in the environment, the in-situ-tests were carried out on a regular basis.

In the consecutive DMT-measurements one could clearly see an evolution towards instability (Peiffer, 2015) . After an important failure (sliding) in one zone in June 2014 (an area of 100 m by 50 m was affected), remediation works were done in the destabilized zone (October – November 2014). In 2015 and 2016 additional soil investigation was done, in order to evaluate the change in stress state after these remediation works. The results of the tests before the period of instability and after stabilization are discussed. More detailed results are presented in the general test report (Peiffer, 2015). In the future the tests will continue. Although the last measurements are about two years after the sliding, the measurements will continue in the futur, in order to monitor the evolution of the soil conditions.

2 SOIL PROFILE AND LAYOUT OF THE SITE

2.1 *Geology*

Based on the geological investigations and data maps, the upper layer consists out of a sandy silt (quaternary deposit). Under this layer the tertiary overconsolidated Boom Clay can be found. This can be seen also on the I_D-diagram as presented below. The profile confirms the results of the undisturbed sampling of the soil.

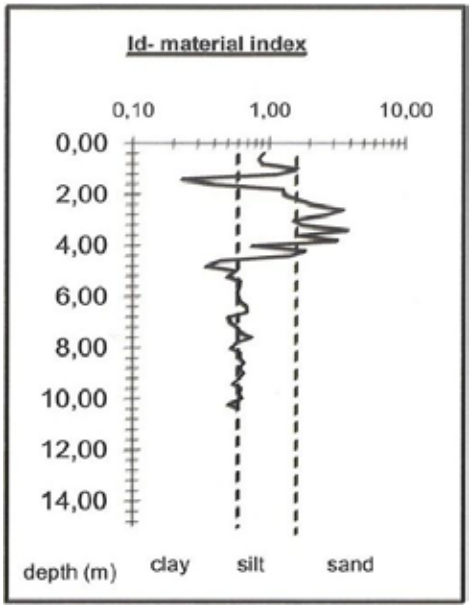

Figure 1. I_D (DMT1)

2.2 *Groundwater*

The phreatic level is at depth of about 1,5 m (before remediation). The thickness of the clay at the bottom of the pit is about 10 m. This thickness is sufficient in order to resist the upward artesian water pressures.

2.3 *Sliding (2014)*

In the next figures a general view of the main sliding is presented. After excavation of the clay pit till a depth of about 30 meters, in the Northern part of the pit instability (small slidings) of the walls started to occur after some years. The main raison for this was the lack of a sufficient resistance against horizontal stability. During the period of excavation the pit became the central dewatering point for the region. Unfortunately the surface between the upper quaternary layer and the underlying Boom clay was slightly declining towards the pit. The upper part (quaternary layer), with a thickness of about 4 to 5 m moved towards the pit, resulting in instability. Also the underlying Boom Clay was affected by this slide.

In the figures 2 and 3 a general impression of the sliding and the soil movement is presented. A zone of 100 m by 50 m started to move resulting in a downward movement of about 9 m in the corner of the pit. After the first sliding in the northwestern part of the pit a monitoring program was set up. The monitoring consisted out of the execution of CPT-tests and DMT-test. Besides these tests, also the water pressures were measured on a regular base

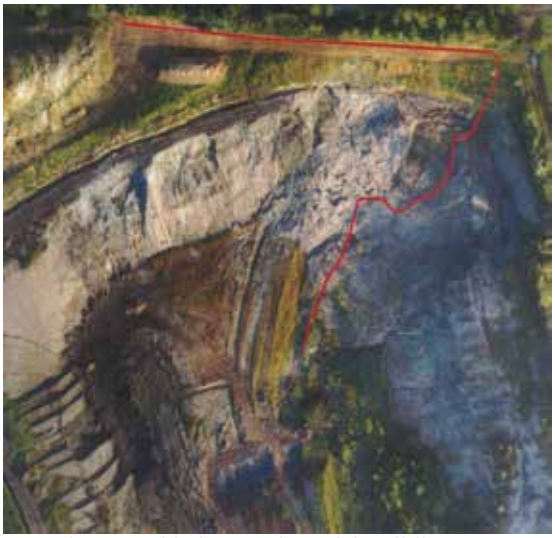
Figure 2. Photographic impression of the sliding


Figure 3. Detailed impression of the instable slope

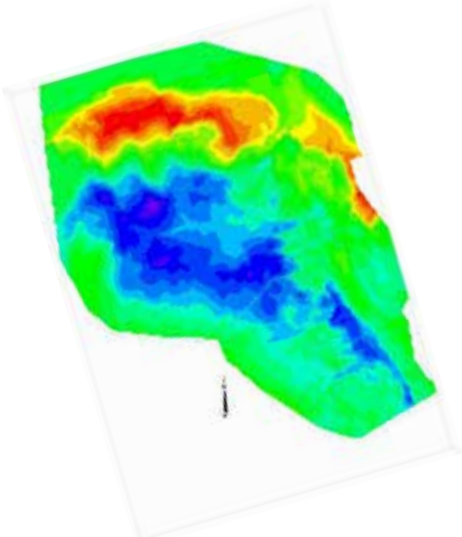
Figure 4. Topographic survey of the soil movement

An overview of the monitoring points is presented in figure 5.
Until now four campaigns were organized :

January 2014 – DMT 1 to 5 (before the important sliding)
July 2014 – DMTA to F (about 1 month after the sliding)
January 2015 – DMT I to IV (after stabilizing)
March 2016 - DMT1' to 5'

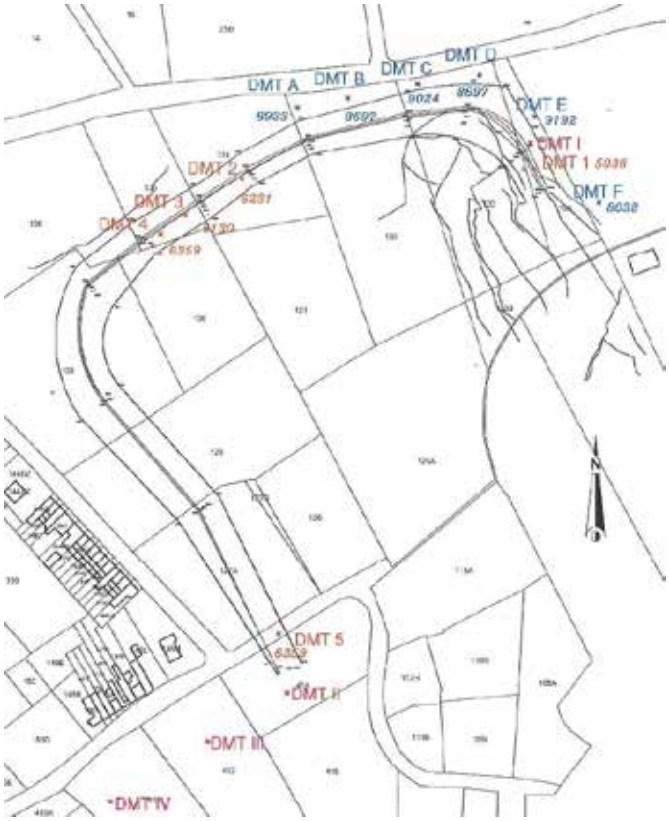

Figure 5. Overview in-situ tests

3 DMT AS A TOOL FOR THE DETECTION OF SLIP SURFACES

3.1 *DMT-K_D-method*

The principle of the DMT-K_D-method for the detection of slip surfaces can be shown as follows. (Marchetti, 1997). In many OC clay landslides, the sequence of sliding, remoulding and reconsolidation, leaves the clay in the slip zone in a normally consolidated (NC) or nearly NC state, with loss of structure, ageing or cementation effects.

Based on field data from different clay sites in various geographical areas correlations could be established (G. Totani et al., 1997, Lacassse & Lunne,1988).

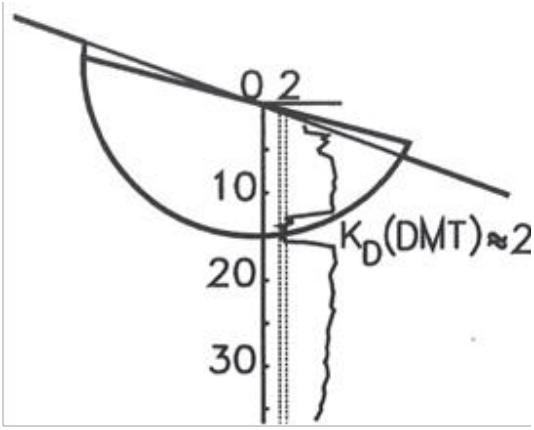

Figure 6. Principle of the DMT-K_D-method

In genuinely NC clays (no structure, ageing or cementation) the horizontal stress index K_D from the DMT is approximately equal to 2, while KD values in OC clays are considerably higher (for the Boom Clay about 8).

Therefore it is known that, if and OC clay slope contains clay layers with KD ≈ 2, these layers are highly likely to be part of a slip surface (active or quiescent).

The DMT-K_D-method method consists on identifying zones of NC-clay in a slope, using KD ≈ 2 as the identifier of the NC zones.

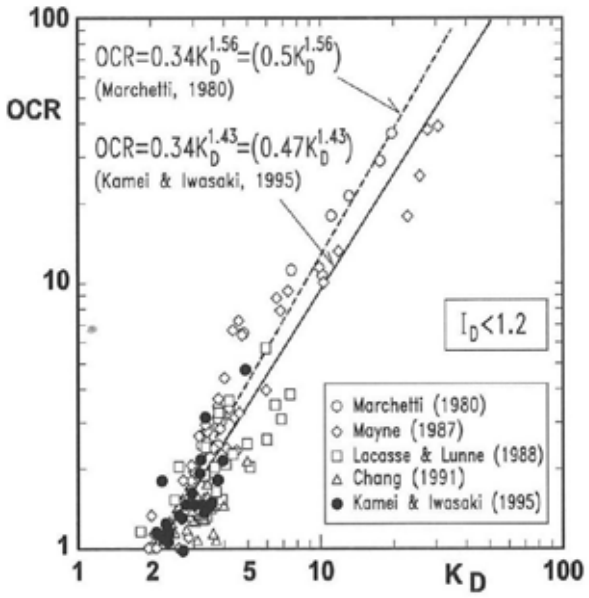

Figure 7. Correlation KD – OCR for cohesive soils (after Kamei & Iwasaki, 1995)

4 FIRST SLIDINGS

4.1 *Period 2011 and 2012*

The first instability occurred in 2011. The size of the sliding was limited. No DMT-measurements were done before or after this sliding.

In the second half of 2013 a more important slide occurred in the neighborhood of point 5 on figure 5. The number 5 refers to DMT 5 executed in the beginning of 2014 at a distance of 5 m from the top of the slope.

In the figure 8 a photo of the slide is presented. The sliding occurred in the quaternary layer until a depth of about 1.5 m in the Boom clay.

Figure 8. Photo of the unstable zone after sliding

5 MORE PRONOUNCED INSTABILITY OF THE SLOPE (2014)

5.1 *Instability problems in 2014 (period June-July)*

As discussed in 4.1., after the more pronounced sliding in 2013, a monitoring program was elaborated for different points at the top of the slope around the pit. Besides topographic surveys and the measurement of the phreatic waterlevel, DMT-tests were carried out. In this article the top of the slope in section AA' is discussed. The section itself is given in thefigure 9. The reference level in the figures 1 and 9 corresponds with the national reference (TAW) +/- +8 m TAW.

5.2 *Discussion of the results*

In the figure 10, the results are presented for the tests before (January 2014), immediately after (July 2014)

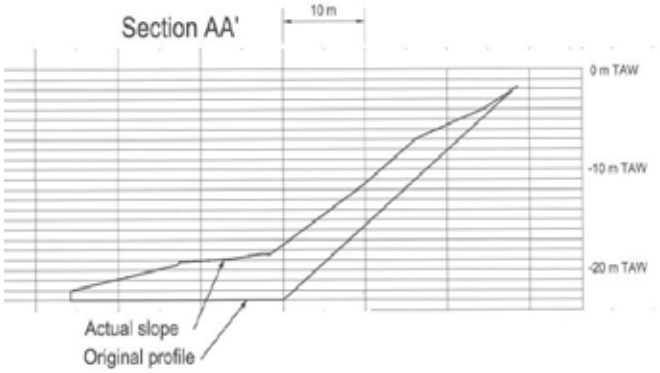

Figure 9. Section AA' (fig. 9)

and about two years after the sliding in point of section AA', corresponding with DMT1 in the figure 5.

In the test diagrams one can distinguish the upper quaternary sandy silt layer. In the K_D-graph one can see that two points (one in a weaker point in the quaternary deposit and one at the interface between the quaternary layer) show a lower value of K_D. The CPT diagram shows also the presence of a weaker layer at depth of about 2m. The DMT-results show a decrease in horizontal stress at these point.

The layer between these two points became unstable in June 2014, resulting in an important sliding. One can see on the diagrams of figure 10 (July 2014) that the K_D-value became lower than 1.8, referring to unstable soil conditions. The failure occurred in this zone and affected a slip layer with a thickness of about 1.5 m. Although the cone resistance decreased with a factor about 2, and a significant decrease of qc between 2 and 4 meter can be seen in this layer, the CPT-diagram doesn't give a clear reflection of the sliding. It is also important to notice that the KD-values below the sliding zone decreased till a depth of about 5 m below the sliding surface. It is interesting to see which way the stresses changed after the sliding. In the last column of figure 10, the results are presented for the measurements carried out in March 2016. Remediation works were done in October-November 2014 (see 6.).

The q_c-value did not change in an important way. Out of the K_D-diagram it become clear that the K_D-values exceeded the critical value 1.8. For the clayey layer the measurement reflects actually a normally consolidated soil. For the intermediate sandy silt layer, one can see a slightly overconsolidated soil condition. The difference between the measurements of July 2014 and March 2016 can be explained by the presence of excessive pore pressures, resulting in lower values of K_D in the sandy silt layer in the sliding layer.

After consolidation a residual part of the original overconsolidation did appear again. The soil conditions after sliding and reconsolidation can be measured more clearly using the dilatometer.

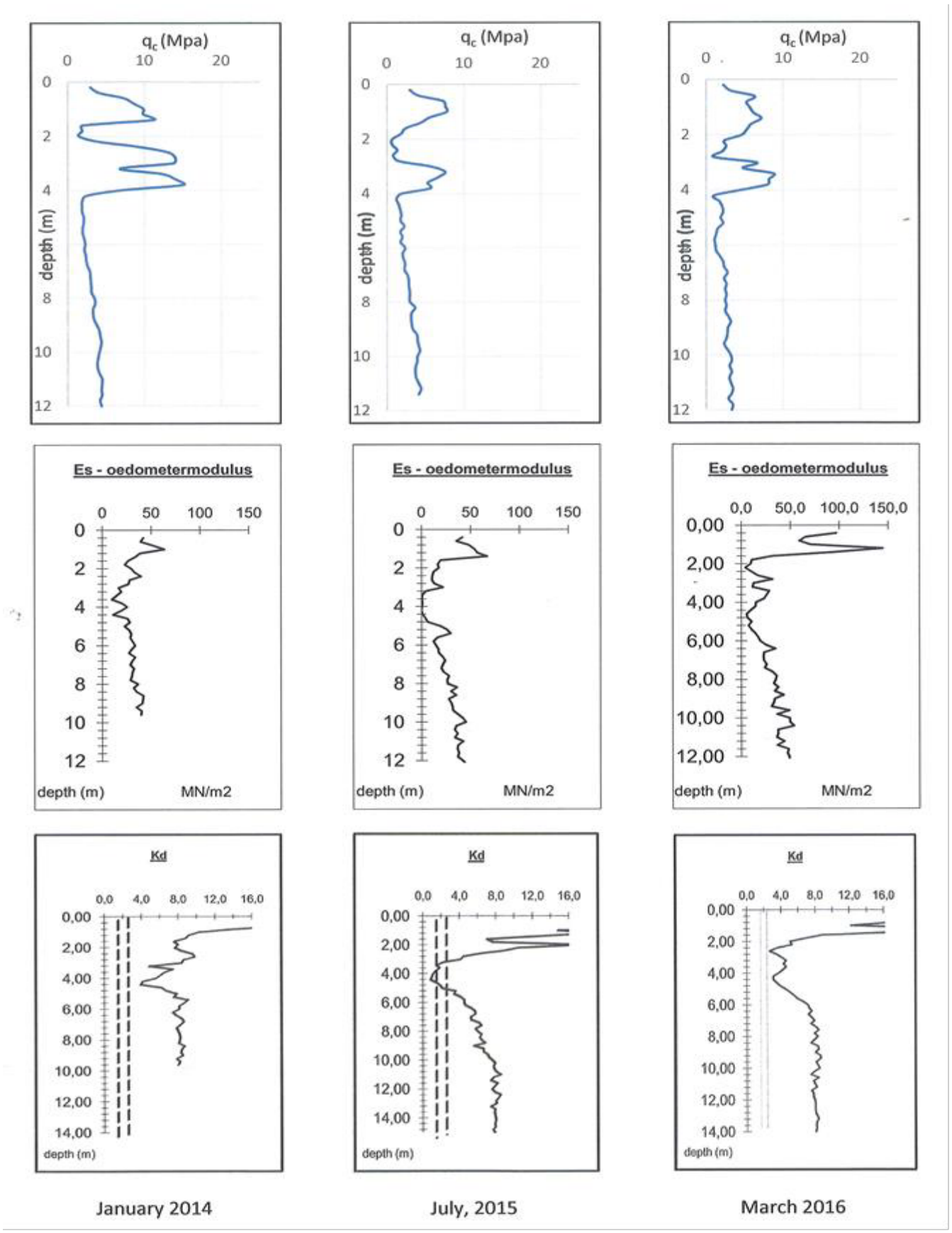

Figure 10. Results of CPT and DMT

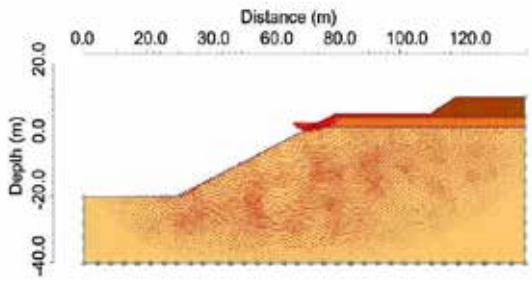

Figure 11 – PLAXIS-analysis

6 STABILITY ANALYSIS

In order to get a better understanding of the effects resulting in this instability and in order to design an appropriate remediation, additional investigation was done to determine the design soil characteristics (CPT-tests and laboratory tests (triaxial tests, oedometer tests)). This analytical and numerical analysis is not discussed in detail in this article. Out of the theoretical analysis it became clear that the effect of the groundwater pressures on the horizontal equilibrium was dominant.

The Fig. 11 presents the calculated critical horizontal disequilibrium due to the presence of the groundwater out of an equilibrium analysis the zone within the most critical global sliding surface. But in the upper part of this zone the equilibrium is broken in the upper layer (lower part of the quaternary deposit and top layer of the Boom clay (big red arrows)). In reality it could be seen that the sliding in the upper part of the Boom clay was more pronounced than in the analysis made with Plaxis.

The analysis resulted in a design where a deep drain has to be installed at a depth of 5 m., as shown in the Fig. 2. This drain was installed in November 2015. The red line in figure 2 is the position of the drain in plan view. After the installation of this drain, there was an immediate effect on the depth of the groundwater. The original depth of 1,5 m increased to a depth of about 4.5 m. The safety of the slope stability increased from 0,9 to 1.31.

7 CONCLUSIONS

In 2014 an important sliding occurred in the top layer of an excavation pit in the Boom Clay. Because previously small slidings occurred around the pit, an extensive monitoring program was started before this important sliding, based on the execution of DMT-tests and CPT-test.

This way the stability of the slope could be evaluated before, during and after sliding. Comparison between the DMT-test before and after the sliding shows clearly an important reduction of K_D (factor about 4) and E_D in the sliding zone (resulting in lower values of E_s). It is important to notice that the K_D-value also were reduced in the layer immediately below the sliding zone. The CPT-measurements showed a decreased strength (q_c reduced with a fac tor about 2) and stiffness in the soil, but the sliding zone could not be indicated that pronounced. After a period of about two years, the K_D-value in the sliding zone increased towards values corresponding with the state of normal consolidation. The CPT-diagram didn't show a remarkable change of q_c

8 REFERENCES

Kamei, T. & Iwasaki, K. (1995) "Evaluation of undrained shear strength of cohesive soils using a flat dilatometer.", *Soils and Foundations 35 (2)*, 111-116

Lacasse, S. and Lunne, T (1988). "Calibration of dilatometer correlations",*Proc. ISOPT-1 1*, 348-359

Marchetti, S. (1980) "In situ tests by flat dilatometer", *ASCE Jnl G.E. (106) (GT3)*, 299-321

Marchetti, S. (1997) "The Flat Dilatometer : Design Applications", *3rd International Geotechnical Eng. Conf. Cairo University*

Peiffer, H. (1997), "Interpretatie en aanpassing van de dilatometerproef, uitgebreid tot de beoordeling van de spanningstoestand naast schroefpalen" *Doctoral Thesis,* Ghent University

Peiffer, H. (2015), "Studierapport stabiliteit kleigroeve te Kruibeke", Antwerpen

Peiffer, H. (2015), "The Use of a DMT to Monitor the Stability of the Slopes of a Clay Exploitation Pit in the Boom Clay in Belgium *The 3rd International Conference on the Flat Dilatometer*, Rome, 127-133

Totani, G., Calabrese, M., Marchetti, S. and Monaco, P.(1997) "Use of in-situ flat dilatometer (DMT) for ground character ization in the stability analysis of slopes", *XV ICSMFE Hamburg*, vol 1, 607-610

Geotechnical and Geophysical Site Characterisation 5 – Lehane, Acosta-Martínez & Kelly (Eds)

How many drillings are necessary? A case study

M. Premstaller
Premstaller Geotechnik ZT-GmbH, Hallein, Salzburg, Austria

ABSTRACT: In Zell am See, Austria, an 8 m deep two floor underground parking was built next to the Grand Hotel. For the site-investigation the first plan was to carry out ten drillings. The study of existing geologic data show that the construction-site lies at the end of an alluvial delta, where homogeneous sand/gravel-sediments were expected. Based on this knowledge the geologic investigation could be reduced to only two CPT´s. The excavation pit was stabilized with jet-grouting walls and due to the high groundwater-level and the high permeability of the soil the bottom was sealed with a jet-grouting-plate. The soil conditions turned out as predicted, situated in the loose, homogeneous sand-gravel-ground the technically challenging jet-grouting work could be carried out without any problems.

1 INTRODUCTION

The Grand Hotel in Zell am See, Austria, is situated on the alluvial delta of the Schmittenbach right next to the lake of Zell am See. Due to the shortage of space in the dense covered area and the lack of parking places, a two-floor underground was planned. Because of the high groundwater-table near the lake and the high permeability of the soil, a dense excavation pit was necessary. A drawdown of the groundwater was not allowed.

A preliminary geologic analysis including mapping and the study of existing papers made it possible to reduce the costs of the site-investigation to a minimum.

2 LOCATION

Zell am See is a small but famous ski resort in Salzburg, Austria (Fig. 1)

Figure 1. Topographic map of Austria with location of the project

The small town is situated between the western bank of the lake and the rising mountains in the west. The topographic surface is formed by an alluvial delta and falls like a gentle slope to the lake (Fig. 2).

Figure 2. Location Zeller See

3 PROJECT

On the area of the Grand Hotel in the gap between the buildings, a tow-floor underground parking should solve the local parking problems. A construction with a length of 30 m, a width of 20 m and a depth of 8 m below the surface was planned (Fig. 3). The east side of the building reaches to the lakeshore and the north and south sides touch the basement of existing buildings.

Figure 3. Position of lower basement

4 GEOLOGY

As this project includes a geotechnical very deep and difficult excavation the first idea for the geologic investigation was to carry out ten drilling – a quit costly plan.

The alternative concept for the site-investigation was to make at first a geologic mapping including all existing papers and data and then decide in a second step the range of the soil exploration.

4.1 *Geologic overview*

Zell am See lies in a valley, which was deeply eroded in the ice-age and postglacial filled with sediments up to the present-day surface level. The valley-trough reaches down to a depth of about 500 m. The lake of Zell am See is a relict of this glacial basin.

4.2 *Local geologic situation*

The deposits of the alluvial delta of the Schmittenbach are the youngest sediments, which lies on the postglacial basin-sediments. The delta has its origin at the bottom of the mountains on the west side and continues with a uniform, small surface gradient down to the lake. The delta exists of sand-gravel material including stones and boulders. The permeability is generally very high.

On the project area the groundwater table is just below the surface and is corresponding with the water level of the lake.

5 GEOLOGICAL INVESTIGATION

The first step was to carry out a geological mapping and search for all existing investigation-points and data. According to the long history of Zell am See with the first settlements 3000 years ago, we found a lot of data including many drillings which are shown in Fig. 4.

Figure 4. Alluvial delta with existing investigation

The analysis of this basic data gave an interesting composition of the delta-sediments. These sediments are very inhomogeneous at the beginning of the delta with a matrix of sand and gravel and lots of stones and boulders (torrent-debris) up to a size of 10 meters. With an increasing haulage distance the material becomes more and more homogeneous resulting in a uniform sand-gravel-mixture. At the end of the delta there are no more stones or blocks; the energy of the river is too low and cannot transport these big parts, that's why they are deposited at the origin of the delta.

We knew from the first study that the soil at the construction site is homogeneous and can be penetrated with the CPT-equipment, that's why we decided to bring down just two CPT-sounding. The two outcrops showed pretty much the same CPT-profiles and confirmed the assumption of the geologic situation. In Fig. 5 the documentation of the CPT shows loose gravely sand with a high permeability.

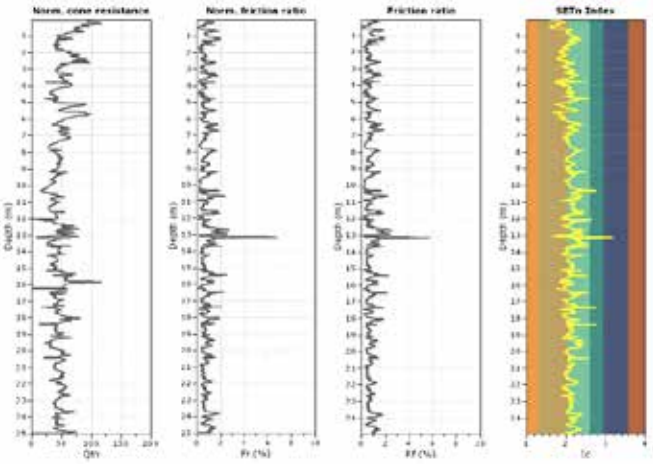
Figure 5. CPT Profile interpretation

6 EXCAVATION PIT

According to the results of the soil-investigation the fully sealing of the excavation-pit, with the jet-grouting system, was decided. At the front side, situated near the lake, sheet-piles were built in order to protect the lake from cement. This was a necessity, because the lake water has drinking water quality (Fig. 6 and 7).

Figure 6. Layout of Jet-Grouting and Pile Wall

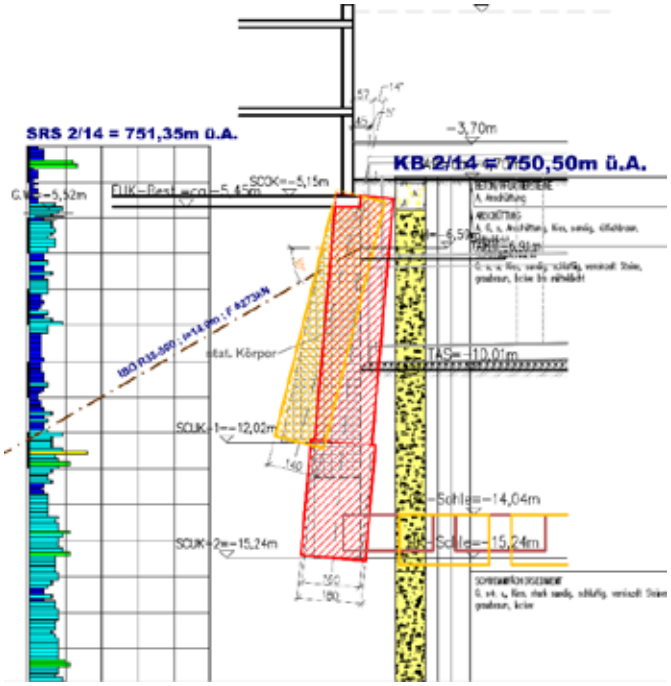

Figure 7. Sectional drawing of Jet-Grouting Columns

With the jet-grouting system the basements of the existing buildings on the north and south side could be underpinned and the jet-grouting walls stabilized the side bands.
To seal the bottom a jet-grouting-plate was injected, which had to be fixed in the ground with soil-nails due to the high water pressure.

The high-tech jet-grouting work was carried out according to the plan. For the bottom jet-grouting-plate, the direction of every drilling-point was measured by an inclinometer, in this way the deviation could be detected and the water tightness of the plate was guaranteed. Due to the short construction-time it was not possible to test the reseal the pit. The geologic conditions turned out as predicted and the grouting-work was carried out with no problems. Pictures of the jet-grouting-works and excavation near the lake are shown in Fig. 8 and 9.

Figure 8. Picture of Jet-Grouting-Works

Figure 9. Picture of excavation and soilcrete columns

7 CONCLUSION

This case study shows that even for a very difficult ground-operation a site-investigation with only two

CPT's was enough. The base for this low-budget program was an intensive preliminary geologic study with the understanding of the soil-genesis and the geotechnical interpretation. The mentioned example above shows that even a very complex undergroundwork does not automatically require a cost intensive site-investigation.

8 REFERENCES

Marchetti S., et al. (2001). "The flat Dilatometer Test (DMT) in Soil Investigations." Report of the ISSMGE Technical Committee 16 on Ground Property Characterisation form In-situ Testing.

Robertson P.K. and Cabal K.L. (2010). "Guide to Cone Penetration Testing for Geotechnical Engineering." Gregg Drilling & Testing, Inc.

Keller Holding GmbH (2014). "The Soilcrete – Jet Grouting Process." Brochure 67-03E

Geotechnical and Geophysical Site Characterisation 5 – Lehane, Acosta-Martínez & Kelly (Eds)

Elastic and Non-Elastic Response of Pile-Raft System Embedded in Soft Clay

M. V. Shah, A. R. Gandhi & D.V. Jakhodiya
Assistant Professor & Professor, Applied Mechanics, L. D. College of Engineering, India.

ABSTRACT: A pile-raft system is viable approach to carry heavy loads in clay soils. Very limited research work is available if a pile-raft system is used in soft clay. Present research aims to study the elastic and non-elastic response of integrated and non-integrated pile-raft system embedded in soft clay using a physical mod-elling approach. The pile-raft model system is fabricated using aluminium and piles employed had a slender-ness ratio, L/D, of 10. The behaviour was compared with responses of a flexible unpiled raft, single pile, and rigid pile groups. The effects of the numbers of piles on settlement, load sharing between pile and raft, load improvements ratio and settlement reduction ratio are some of the major issued that presented and discussed.

1 INTRODUCTION

For most piled raft foundation, the primary purpose of the piles is to act as settlement reducers. The proportion of load carried by the piles is considered as a secondary issue in the design. Over the past decades, extensive research work has been presented, aimed at improving the accuracy in the prediction of the behaviour of piled rafts. To carry the excessive loads that come from the superstructures like high-rise buildings, bridges, power plants or other civil structures and to prevent excessive settlements, piled foundations have been developed and widely used in recent decades. However, it is observed that the design of foundations considering only the pile or raft is not a feasible solution because of the load sharing mechanism of the pile-raft-soil. Therefore, the combination of two separate systems, namely "Piled Raft Foundations" has been developed (Clancy and Randolph (1993)).

The conventional approach of designing pile-raft foundation system generally results in the installation of more piles than that are necessary, which leads to uneconomical design practice. Different approaches, involving the use of piles as settlement reducers have been reported by Randolph (1994), Burland (1995), Sanctis et al. (2002), and Fioravante et al. (2008). The term 'settlement reducing piles' originates from Burland, Broms & de Mello (1977).

Bajad et al. (2008) conducted small scale model tests at 1 g-level to investigate the settlement behaviour of pile-raft system over soft clays having 4, 16, 36, 64 piles in group. Poulos 2001 gives the three stage progress to design the piled raft foundation system and compares his analysis with other analytical approaches available. Fioravate 2011 have studied the load transfer mechanisms between a pile and a raft with an interposed granular layer by means of centrifuge physical model tests.

2 EXPERIMENTAL WORK

A series of laboratory tests were performed on models of unpiled raft, single pile and central piled raft to examine the settlement behaviour of axially loaded pile-raft foundation system. Tests on 19 mm diameter aluminium piles with single pile has been carried out for centrally located pile and same thickness of raft. Details of piles configuration and model raft dimensions adopted in present research work is shown in Figure 1.

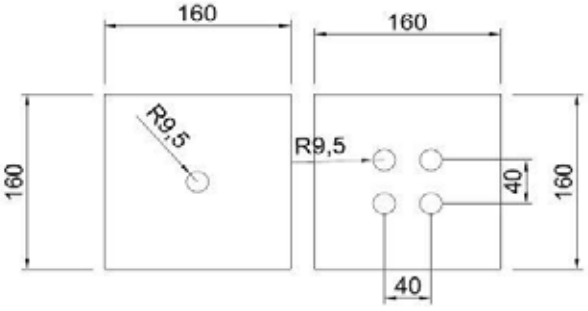

Figure 1. Details of piles arrangement (Dimensions in mm).

2.1 *Experimental set-up*

Tests were performed in a cylindrical mild steel vessel of 500 mm diameter and height of 500 mm. The mild steel base plate was also provided with four numbers of holes separated at 1200 angle and distanced at R/2, R/4, 2R/3 and at centre c/c for the drainage purpose. The loading frame consists of four vertical columns (C-Section) of 1 m height, two on each side and two horizontal beams (C-Section). The load was applied through a mechanical jack fixed at centre as shown in Figure 2. Two linear vertical displacement transducers (LVDTs) of 0.01 mm accuracy were located at the middle side of the raft, to measure vertical downward settlement.

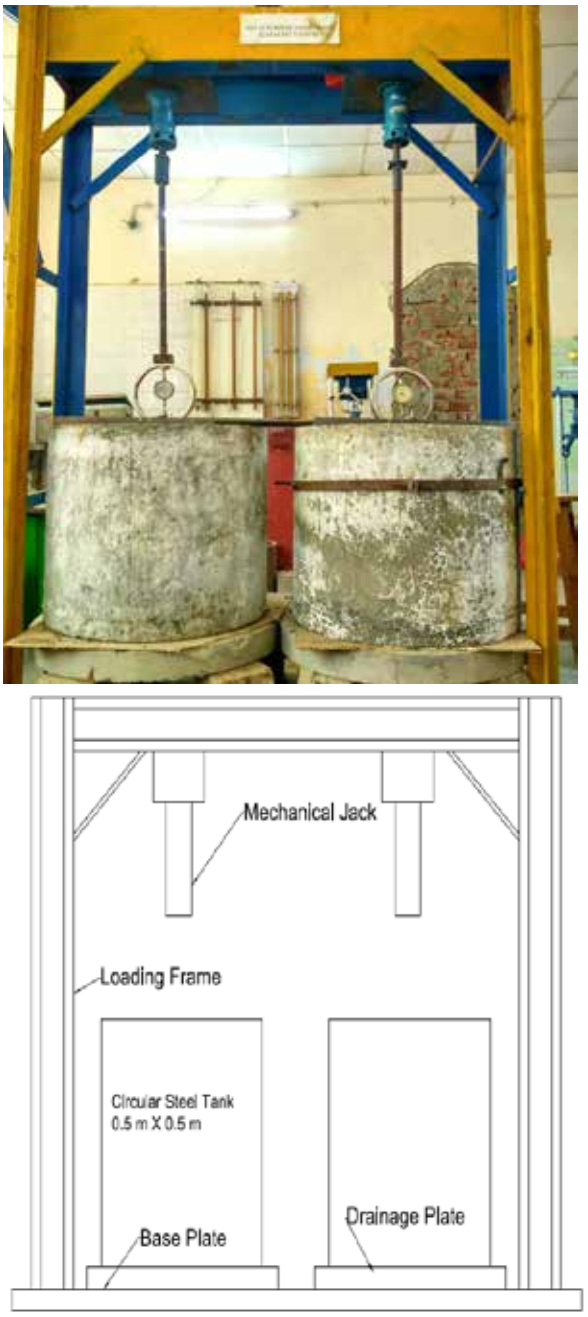

Figure 2. Schematic diagram and actual photograph of model test set-up.

2.2 *Properties of materials*

Marine soft clay is used to prepare soft clay bed. The index properties of soft clay are presented in Table 1

Table 1. Properties of soft marine clay

Index Property	Values
Specific gravity	2.47
Liquid limit	55
Plastic limit	21.31
Plasticity index	33.69
Shrinkage limit	17.16
Free swell index	30.77
Maximum dry density	16.7
Optimum water content	20.80

2.3 *Preparation of soft clay bed*

Soft marine clay available at Dahej, Gujarat having liquid limit and plastic limit as 55 % and 21.31 %, respectively was used in present research work. It was placed in the cylindrical vessel with water content equal to liquid limit and consolidated under the consolidation pressure of 80 kPa. After final consolidation, the water content of soil after model test was found to be between 35-40 %. Undrained shear strength of the consolidated clay as measured by unconfined compression tests after the model test was found to be 10 ±0.5 kPa. The angle of internal friction between pile and clay was found to be 11.910.

2.4 *Model of raft and piles*

Aluminium plates, with fixed thickness, served as model rafts. The dimensions of the raft was 160 mm ×160 mm × 4 mm. The modulus of elasticity and Poisson's ratio of aluminium plates were 70 GPa and 0.33, respectively. The model piles used in the experiments were aluminium hollow pipes of 19 mm in outside diameter and 1.5 mm in wall thickness. The modulus of elasticity and Poisson's ratio of the aluminium pipe were 70 GPa and 0.33, respectively. The embedded pile lengths of 200 mm was used in the experiments. The lengths represent L/D ratios of 10. Top head of each pile was provided with a bolt of 6 mm in diameter with a wooden piece of 20 mm length to connect the pile to the cap through two nuts to ensure a complete fixation between the pile and the cap as shown in Figure 3.

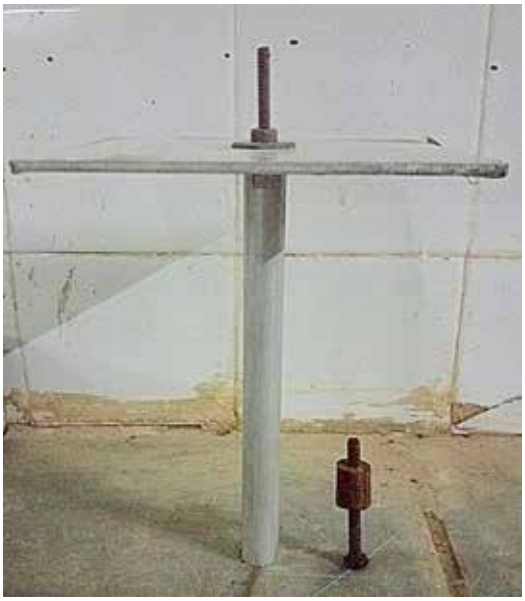

Figure 3. Connection between the pile and the raft.

2.5 *Test procedure*

– Each experiment started with placing the clayey soil in the cylindrical steel vessel in slurry state. The slurry was allowed to consolidate by its own for 24 hrs. Then artificial consolidation was carried out at 80 kPa.
– As the piles were driven, wooden templates were used to locate the piles in the correct positions, and then each pile was inserted vertically into the clay by driving with a steady succession of bellows on the top of the pile using a steel hammer weighting 2 kg. The sequence of piles installation started with the inner piles, then corner piles, and finally the edges piles.
– After the installation of piles to the required depth, the wooden templates were removed. Then, the raft model was placed on the clay surface and the horizontality of the raft model was adjusted by a level and each pile was connected to the raft model by two nuts.
– Two LVDTs were placed at the centre of the raft sides to measure the vertical downward settlement.
– A calibrated proving ring of 10 kN capacity was connected to mechanical jack. The model raft was loaded incrementally and at the end of each load increment vertical settlement was measured. The rate of loading was 0.1 kN/min. The loading was continued till the foundation system's settlement reaches 25 mm in case of unpiled raft, and piled raft. In case of pile group the test continued till the settlement reaches 20 mm.

3 RESULT AND DISCUSSION

The model tests results obtained from laboratory tests are analyzed and discussed in this section. The settlement equal to 10% of pile diameter or raft width is often adopted to define the ultimate load capacity in foundation design (Cerato et al. 2006, Lee et al. 1999, Lee et al.2005). In this model tests, loading was continued till the raft settlement reaches 25 mm and pile settlement reaches 20 mm.

3.1 *Effect of raft's thickness*

As seen in Fig. 4. the increase in raft's thickness improves load bearing capacity of unpiled raft. The thickness of raft is selected such as the stiffness varrying from very flexible raft to rigid raft. The load carrying capacity of unpiled increases by 6% and 13% at 10mm settlement going from 2mm thick raft to 4mm and 8mm thick raft respectively. Similarly the increment was 9% and 20% for 4mm and 8mm thick raft at 25mm settlement.

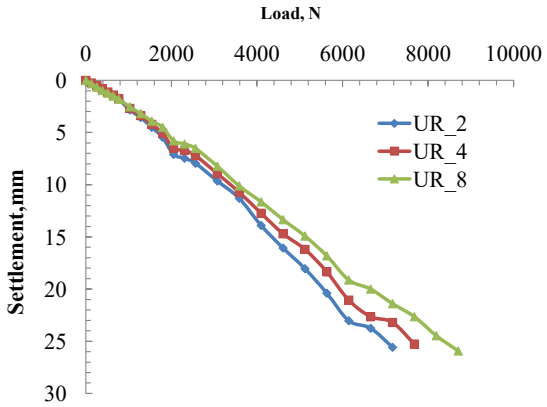

Figure 4. Load vs. Settlement for 2mm, 4mm and 8mm thickness of raft.

3.2 *Effect of number of pile*

Figure 5 shows the effect of number of piles in pile group and piled raft. The L/D ratio was 10, number of piles were 1 and 4 and raft of thickness 4 mm. It is seen that in case of pile group, increasing pile number from 1 to 4 increases load carrying capacity at 20 mm settlement by 6.45 %. While in case of piled raft system the load carrying capacity at 20 mm settlement increases by 39.57 % by replacing single pile by 4 piles. PG_1_10 means pile group with single pile of slenderness ratio 10, PR_4_1_10 means piled raft with 4mm thick raft and single pile of L/D 10.

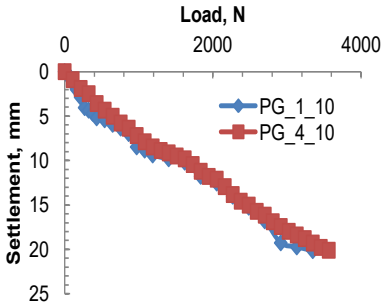

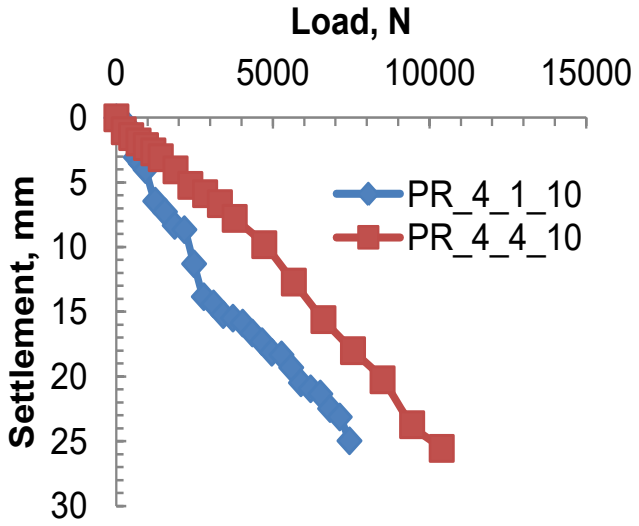

Figure 5. Load Vs Settlement for 1 and 4 numbers of piles in pile group and piled raft system .

3.3 *Piled raft system*

Figure 6 shows the load-settlement behaviour of piled raft foundation in soft clays compared to unpiled raft and pile group with 1 and 4 piles.

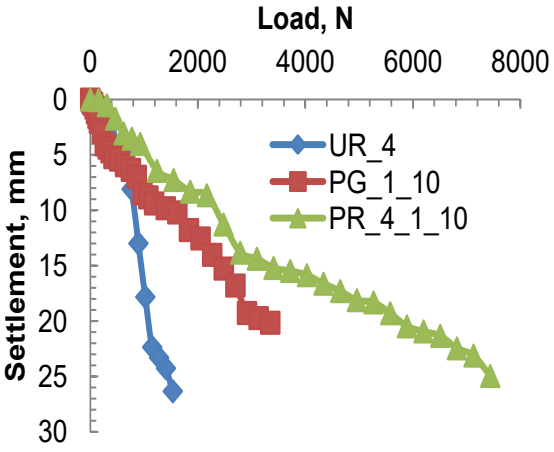

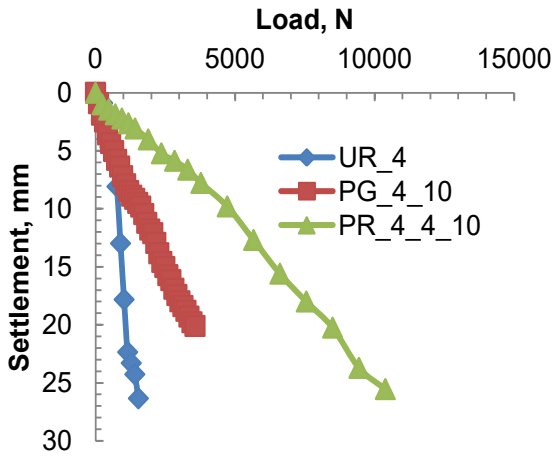

Figure 6. Load vs Settlement a) single pile b) four piles.

As seen in Figure 6a and Figure 6b the load carrying capacity of unpiled raft is higher than pile group for initial stage of loading but for at higher settlement the load carrying capacity of pile group is higher than unpiled raft. As seen in Figure 6a up to 7 mm settlement raft carries higher load than single pile then the single pile carries higher load. And in Figure 6b it has seen up to 5 mm settlement raft carries higher load after then pile carries higher load. The bearing capacity of piled raft is higher than both the unpiled raft and pile group.

(b)

3.4 *Settlement of pile-raft*

The theoretical settlement of pile-raft foundation was calculated using Burland's approach (1995).

$$s_{pr} = s_r * K_r / K_{pr} \quad (1)$$

Table 2. Theoretical and measured settlement

Theoretical Settlement, mm	10
Measured settlement for piledraft with 1 pile, mm	7
Measured settlement for piledraft with 1 pile, mm	3.15

Its seen that the measured settlement is lesser than the theoretical value of settlement. And it reduces as the number of pile increases.

3.5 *Load sharing behaviour*

The load sharing behaviour can be expressed using the load sharing ratio αp that represent the ratio of load carried by piles to the total load imposed on piled raft.

$$\alpha_p = Q_p / Q_{pr} = 1 - Q_r / Q_{pr} \quad (2)$$

Q_{pr} = load imposed on piled raft, Q_r and Q_p = load carried by piles and raft.

Clancy and Randolph proposed an equation of αp in terms of pile and raft stiffness as :

$$\alpha_p = 1 - [\{(1 - i_{rp})(K_r / K_p)\} / \{1 + (1 - 2i_{rp})(K_r / K_p)\}] \quad (3)$$

where K_r and K_p = raft and pile stiffness on load-settlement curves; i_{rp} = raft-pile interaction factor.

Using both the equations it is determined that in case of pile-raft system with single pile and four piles the load shared by pile is 45 % of total imposed load on pile-raft and raft is carrying is 55 % of it.

Figure 7a shows the variation of the proportions of loads carried by piles and raft with the number of settlement reducing piles for raft of relative stiffness 0.36. As seen from the graph, by adding four piles the load sharing ratio of raft reduces by 23.52 % and by same amount the load sharing ratio of pile increases for 4 number of piles. It can be noted from Figure 7b that at the same raft relative stiffness (0.36) and L/D ratio (10), the value of L/R increases as the number of piles increases. At 25 mm settlement, for 0.36 relative stiffness of raft, installing 4 settlement reducing piles with L/D=10 causes an increases in the raft load by 35.74 %.

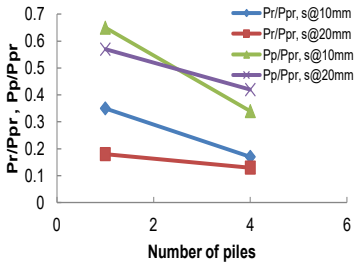

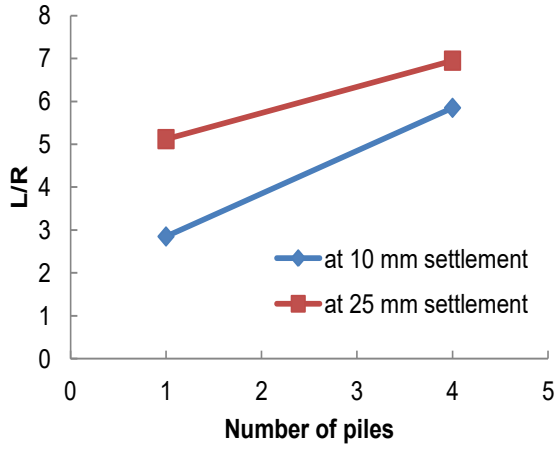

Figure 7. a) Load sharing between raft and piles for central piled raft, b) Load improvement ratio with number of piles at 10mm and 25mm settlement

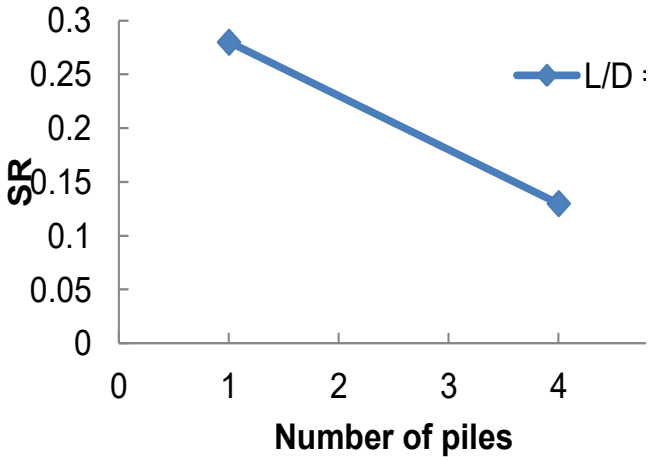

Figure 8. Settlement ratio, SR, with number of piles.

Figure 8 shows the variation of settlement ratio, SR, with the number of piles for raft with relative stiffness of 0.36. It is observed that the settlement ratio decreases as the number of piles increases i.e. installing 4 piles causes a decrease in the settlement of the raft by 53.57 %.

4 CONCLUSIONS

The paper has presented experimental results of load tests on model unpiled raft, pile group, and piled raft embedded in soft clays. The research work focuses on the load-settlement behaviour and load sharing between the pile and raft. From the result of this study following conclusion can be drawn:
From the result of this study, the following conclusions can be drawn:

- Increase in raft thickness shows higher increment in the load carrying capacity of unpiled raft for large settlment compared to small settlement.
- The addition of piles beneath the raft causes increase in raft's load bearing capacity. Addition of 1 and 4 piles causes 4 and 6 times increament in load carring capacity of unpiled raft.
- At 10 mm and 25 mm settlements, L/R, load improvement ratio increases as number of piles increases. There is 18.8 % increament in L/R for 4 numbers of piles from 10 mm to 25 mm settlement.
- Its also observed that as the number of piles increases the load shared by raft reduces and load shared by pile increases.
- There is also considerable amount of decrement in settlement ratio by going from 1 to 4 number of piles.
- The rate of increase of settlement reduction ratio decreases as the thickness of raft increases.With either increase in length of pile or number of piles the ultimate load carrying capacity of pile-raft system decreases.

- The influence of number of pile over settlement analysis shows that as the number of pile increases the % settlement reduction increases for the same load.
- In case of length of pile, the increase in pile length causes an increment in % settlement reduction of pile-raft system.
- It is observed from the research study that the amount of compressive load resisted by unpile raft is more than that of pile group with mono pile for the same settlement.
- It is also observed that even if there is increment in the length of the pile its resistance to compressive load is less than unpiled raft.
- In case of group piles it is observed that the compressive load resisted by pile group with four piles is more than that of unpiled raft for higher settlement.
- Initially the compressive load carried by raft is higher than that pile group but gradually as the compressive load increases the compressive load carried by pile group increases.

A raft may be adequate in terms of bearing capacity but calculated settlements may exceed the tolerable values. In such cases, piles may be introduced under the raft foundation. These piles are limited in number so that they are continuously at the limit state with factor of safety of one. This concept is known as settlement reducing piles. It is also concluded that pile-raft system flexible and rigid raft and 4 number of piles is efficient both in terms of compressive load capacity and settlement when embedded in soft clay. Out of many factors which affect the pile-raft system behaviour and its load transferring mechanism, the slenderness ratio (L/D), number of piles, thickness of raft, soil-pile interface angle (δ), stiffness of pile-raft system, moisture content of soil bed, joint between pile and raft are major factors which play a major role in estimating load capacity and settlement under axial compressive.

If a raft behaves as a flexible member with a pile the flexible approach of uniform compressibility under raft will govern the design or load carrying capacity. While assuming raft to be rigid like a pile cap, the design will be governed by type of pile and pile length. Thus from the above study the pile-raft system can be used successfully in clays with selection of suitable approach.

5 ACKNOWLEDGEMENT

The experimental works described in this paper are part of P.G. work of the third author. The test facilities provided by Applied Mechanics Department at L. D. College of Engineering, Ahmedabad, India to carry out this work are gratefully acknowledged.

6 REFERENCES

Arora, K.R., 1987. *Soil Mechanics and Foundation engineering*.Delhi, Standard Publishers Distributor.

Bajad, S.P., et al. 2008. pile-raft interaction in piled raft foundation on soft clay. *IGC,* Bangalore.

Bajad, S.P. and Sahu, R.B. 2009. Optimum design of piled raft in soft clay—a model study. *IGC*, Guntur.

El-Garhy, B., et al. 2013. Behaviour of raft on settlement reducing piles: experimental model study. *Journal of Rock Mechanics and Geotechnical Engineering*, Vol., 5, 389-399.

Gopinath, B., et al. 2010. Numerical modelling of piled raft foundation in soft clays. *Indian Geotechnical Conference*, Mumbai.

Lee, L., et al. 2014. Analysis of load sharing behaviour for piled rafts using normalized load response model. *Computers and Geotechnics*, Vol. 57, 65-74.

Nguyen, D., and Kim, S. 2013. Design method of piled-raft foundations under vertical load considering interaction effects. *Computers and Geotechnics*, Vol. 47, 16-27.

Patil, J. D., et al. 2014. An experimental investigation on behaviour of piled raft foundation. *International Journal of Geomatics and Geosciences*, Vol. 5, No. 2.

IS: 1904-1986: Code of practice for design and construction of foundations in soils: general requirements.

IS: 6403-1981: Code of practice for determination of breaking capacity of shallow foundations.

IS: 2911 (Part 1/Sec)-2010: Design and construction of pile foundations-code of practice.

IS: 2911 (Part 4)-1985: Code of practice for design and construction of pile foundations.

IS: 2950 (Part 1)-1981: Code of practice for design and construction of raft foundations.

Geotechnical and Geophysical Site Characterisation 5 – Lehane, Acosta-Martínez & Kelly (Eds)
© 2016 Australian Geomechanics Society, Sydney, Australia, ISBN 978-0-9946261-2-7

Geotechnical monitoring of in situ heater test

K. Sosna & J. Záruba
Arcadis CZ a.s., Prague, Czech Republic

ABSTRACT: In the frame of an in-situ experiment a study of heat stress of rock is carried out in underground laboratory Josef (central Europe). The rock massif is monitored in c. 10m perimeter around a heating borehole, being built by fractured granitic rocks crosscut by a swarm of quartz veinlets. The main objective of the study is to confirm or eliminate any possible changes in physical and chemical parameters of granitic rocks exposed to thermal load of maximum 95°C. Deformation modulus of rock massif which were used to calculate the stress changes was determined by Goodman Jack test. Geotechnical monitoring is focused on stress and strain changes in rock matrix, groundwater pressure and displacements induced along fractures. Present results indicate very rapid reaction of the rock massif to fluctuations in rock heating intensity and large extent of these artificially induced stress changes. The changes appear without any observable hysteresis.

1 INTRODUCTION

Efficient and inexpensive energy storage systems represent a crucial component in the modern sustainable energy strategy. The thermal energy storage, defined as the temporary storage of thermal energy at high or low temperatures (Ercan Ataer, 2006), seems to be the most suitable tool for balancing the mismatch arising sometimes between the energy production and demand (Dincer & Rosen, 2010). Except thermal energy storages, the thermo-mechanical response of a rock massif subjected to temperatures around 100°C is investigated also in the context of high level radioactive waste disposal. In this case, various in-situ heater tests were published from the KAERI Underground Research Tunnel (e.g. Kwon et al., 2013), the Stripa mine and Äspö in Sweden (e.g. Chan et al., 1981; Andersson & Martin, 2009), the Grimsel Test Site (e.g. Schneefuβ et al., 1989), and the Underground Research Laboratory of AECL (e.g. Berchenko et al., 2004).

Our in situ experiment has been set up in order to evaluate cyclic heating and cooling on the thermo-hydro-mechanical characteristics of granitic rock. The main objective of the experiment is to confirm or rule out any potential changes in physical and chemical parameters of granitic rocks due to the thermal load of maximum 95°C. Appropriate attention is also paid to changes in the flow and circulation of groundwater and to the deformation of the rock massif caused by cyclic heating. These are the key parameters necessary for the safe design and construction of underground structures intended for the storage of thermal energy or for radioactive waste disposal. Geotechnical monitoring is focused on stress and strain changes in rock matrix (stressmeters and strain gages), pore pressure (piezometers) and displacements induced along fractures (micro and 3D crackmeters).

2 EXPERIMENT AND METHODS

In the Underground Research Laboratory (URL) Josef, located in Central Bohemia, Czech Republic, granitic rock (tonalite) is being studied as a host rock of the underground thermal energy storage. The Josef URL is situated in the exploration gallery of Psí hory gold-bearing ore district. The rock massif is built by faulted/fractured granitic rocks of Sázava pluton which belongs to the Central Bohemian Plutonic Complex. It is penetrated by dense swarms of quartz gold-bearing veinlets and younger fissures filled with calcite. The crystallization age of the Sázava tonalite was determined by conventional zircon U–Pb method to 354.1±3.5 Ma (Janoušek et al, 2004). The Sázava pluton intruded into low metamorphosed rocks of neoproterozoic Teplá-Barrandien Unit (volcanosedimentary sequence of Jílove Zone) (Žák et al., 2005).

The experiment is located in an opening about 2.3km from the adit entrance and is covered by about

120m thick rock overburden. The rock massif is monitored in ca. 10m perimeter around horizontal heating borehole with diameter of 0.85m and length of 2.20m. Monitoring boreholes (0.4 to 10.5m long, ca. 130m total length) are used for application of non-destructive measurement methods, particularly for the monitoring of thermodynamic (temperature), geotechnical (straingage, position, rock stress, stressmeter), hydraulic (piezometer, hydrostatic pressure), and microseismic (seismo-acoustic) data. Boreholes VG-1 to VG-3 are oriented subparallel to the heating-cooling (main) borehole, VG-4 is perpendicular to it. Remote VG-5 trends 55° to the main borehole. The blue cylinder in the main borehole is an unwanted artifact of 3D texturing. The blue line at bottom represents an old prospection borehole, used presently for measurement of underground water pressure. The figure depicts a view from the rock massif to the experimental adit, while the brown 3D shaded body represents an outer shell of the adit (Figure 1). A cyclic thermal load of rocks is simulated by repeated heating and cooling. Duration of the first cycle of heating-cooling lasted eleven months, the second cycle took five months. Additional four shorter cycles (heating between six and thirty four days) followed to simulate the practical working regime of the system, which should cover energy production peaks. The heater/cooler consists of an electro boiler/heat pump and a tank, circulating pumps, and PEX-AL-PEX tubes. Temperature of the water, which is used as the heat medium, varies between 10°C and 95°C. The PEX-AL-PEX tubes are coiled in the horizontal heating borehole from the depth of 1.7m to 2.2m (Figure 2). The first 1.7m of the heating borehole is insulated against the heat exchange by the bags filled with cellular glass insulation (FOAMGLAS).

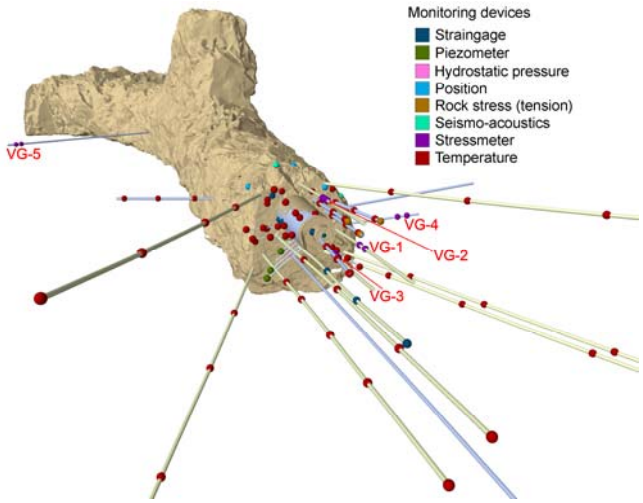

Figure 1. 3D laser scan model of the test site with monitoring boreholes and devices

Figure 2. The heating borehole with the heating water pipe

Deformation modulus of rock massif was determined by Goodman Jack test (Durham Geo Slope Indicator, Hard Rock Type) before and after the heating experiment. Ca. fifty tests were carried out in ten monitoring boreholes of 76mm diameter. Each test was comprised of two loading and unloading stages with the pressure step of 5MPa. The data from second loading stage, where the pressure level was stepwise increased from 20MPa to 40MPa, were selected to calculate the deformation modulus.

In situ stress changes induced by thermal loading were measured by vibrating wire stressmeters (Geokon, Model 4300BX Hard Rock). Each stressmeter is equipped with a thermistor, which enables to measure the temperature simultaneously. This value is used for correction caused by temperature changes of the sensor body. Three stressmeters, installed in the monitoring boreholes at 0°, 45°, and 90°orientations according to vertical direction, were required to completely evaluate stress changes in a given plane perpendicular to borehole axis. The stressmeters were installed in five boreholes with diameter of 60mm and preloaded to ca. 5MPa. Three of total fifteen stressmeters don't work due to cable cutting during installation. Distances of VG-1, VG-2, and VG-3 stressmeters are mentioned in the direction perpendicular to the heater borehole. Distances of VG-4, and VG-5 stressmeters were determined in the direction parallel to the heater borehole (Table 1).

Table 1. Stressmeters placement

Borehole label	Distance from the heater [m]	Stressmeter depth position in the borehole [m]	Stressmeter orientation according to vertical direction [°]
VG-1	0.78	2.00	0
		1.80	45*
		1.63	90
VG-2	0.24	2.03	-15
		1.85	30
		1.70	75
VG-3	0.32	2.00	0

Borehole label	Distance from the heater [m]	Stressmeter depth position in the borehole [m]	Stressmeter orientation according to vertical direction [°]
		1.64	45
		1.85	90
VG-4	3.80	1.85	0
		2.02	45*
		1.59	90
VG-5	12.60	5.79	0
		5.59	45
		5.39	90*

(*doesn't work due to cable cutting during installation)

Groundwater pressure in the rock massif was monitored by vibrating wire piezometers (Geokon, Model 4500SH). All sensors are equipped with thermistors, which enable temperature measurement and temperature correction for transducer thermal expansion. The piezometers were installed in three narrow boreholes drilled from horizontal heating borehole (Table 2). They were sealed up by mechanical packers.

Table 2. Piezometers placement

Borehole label	Strike [°]	Dip [°]	Borehole length [m]	Packer length [m]	Depth in heating borehole [m]
N-5	82	45	0.415	0.18	2.1
N-7	82	45	0.87	0.55	1.7
N-8	82	45	1.04	0.8	1.5

3 RESULTS AND DISCUSSION

Deformation modulus of rock massif calculated according to (Heuze, 1984; Heuze and Amadei, 1985) has an average value of 9.0 GPa. This value was used to calculate stress changes registered by stressmeters.

Thermally induced stress changes in borehole VG-2 (0.24m from heater) varies between 3.8MPa (subvertical position) and 6.0MPa (subhorizontal position) (Figure 3). Thermally induced stress changes in borehole VG-3 (0.32m from heater) varies between 2.4MPa (horizontal position) and 5.4MPa (vertical position) (Figure 4). As the short testing heating with subsequent passive cooling were performed before the actual start of the experiment, the initial state of the stress and temperature field at time zero was quite different from the unaffected state. Therefore the zero value for the measurement was set after the first heating/cooling cycle, assuming that the effect of any non-uniform thermal field at the beginning vanishes during this period. The vibrating wire stressmeter is a relatively stiff instrument which suggests that its output is insensitive to changes in the Young's modulus of the host rock (Spathis, 1990). If there would be used a value of deformation modulus of 75.0GPa (from laboratory uniaxial compression of rock specimen), the stress changes values would be only twice higher due to sensor sensitivity factor. The sudden drops of stress and temperatures near the 84., 129., 146., and 437. day of the experiment are caused by failure of power supply to the heater, lasting each time several hours. The related stress increase in VG-2 and VG-3 boreholes reach their steady values during following c. 60 days. The steady values are similar in the first and second heating cycle. Such a development of stress changes indicates reversible elastic behavior of the granitic massif. Due to the shorter duration of the additional cycles and thus lower achieved temperatures, there are also lower peak stress changes.

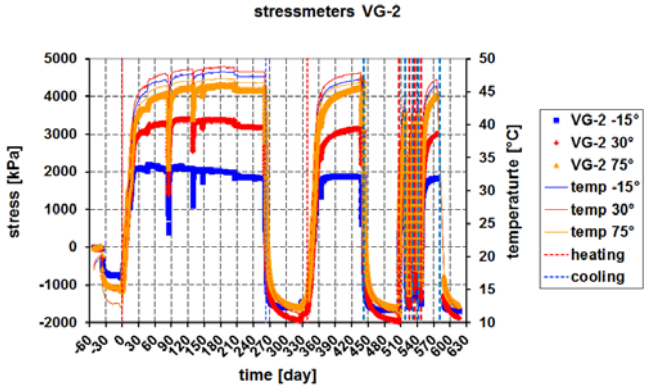

Figure 3. Stress and temperature changes in VG-2 borehole (0.24m from heater)

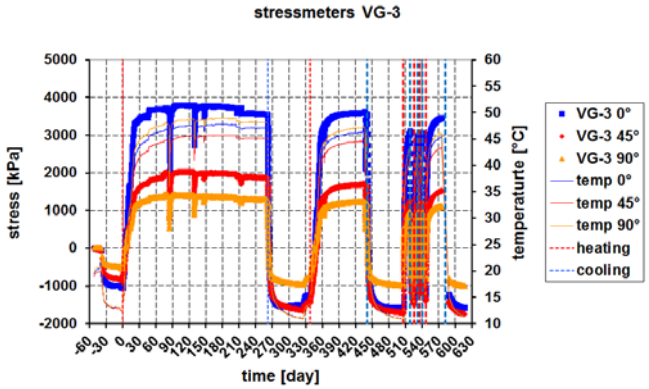

Figure 4. Stress and temperature changes in VG-3 borehole (0.32m from heater)

The stress progress in borehole VG-4 differs both in the shape of the curves and in the matching between the temperature and the stress (Figure 5). VG-4, as a representative of the remote place, is at first affected by the stress changes in the area closer to the heater until the thermal wave reaches the position of sensors. After that moment, the stress field responses to the temperature. The behavior of the stress field, observed for VG-4 (Figure 6), holds also for the parts of massif closer to the heater, but in the smaller scale. In the very starting phase of the cooling (or heating), the mechanical changes in the area quite near the

heater (where the heat transfer is instantaneous) affect the stress field at just a little more distant places immediately, before the thermal changes reach the particular place. For the heating/cooling switching, the common response for all sensors was the immediate short time stress increase in the direction perpendicular to the heater and decrease in the direction longitudinal to the heater. This time period differs according to the distance of the sensor from the heater and it is tons of minutes for the VG-2 (Figure 7) and VG-3, hours for VG-1 and weeks for VG-4. For the cooling /heating switching, inverse reaction occurs.

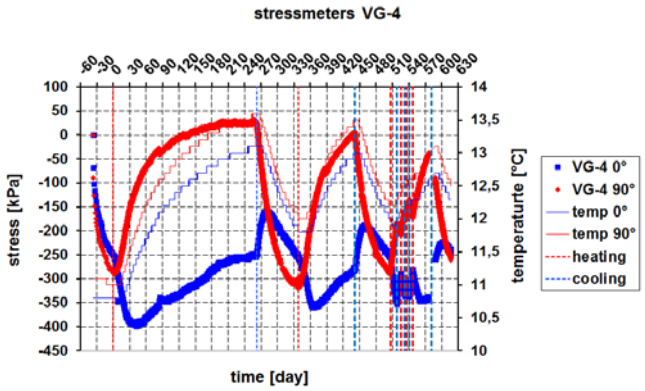

Figure 5. Stress and temperature changes in VG-4 borehole (3.80m from heater)

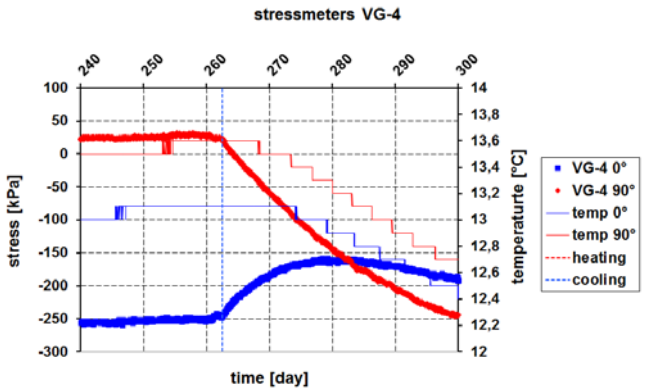

Figure 6. Detailed view of starting of the first cooling phase in VG-4 borehole

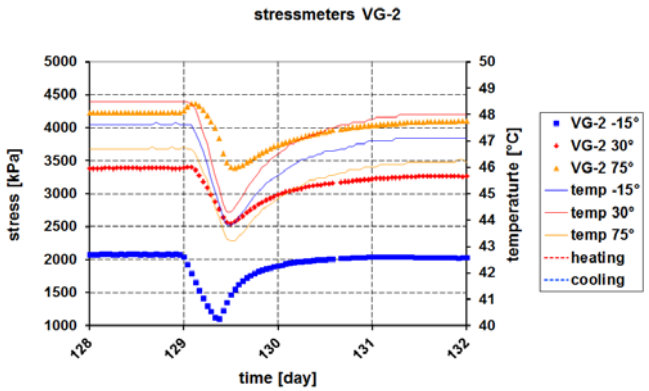

Figure 7. Detailed view of starting of the first cooling phase in VG-2 borehole

Groundwater pressure is monitored by piezometers (Figure 8). Groundwater pressures in the two longer boreholes increase with heating and then slowly dissipate. Groundwater pressure in the shortest borehole is only affected by packer tests. The sudden drops of displacement and temperatures near the 84., 129., 146., and 437. day of the experiment are again caused by the failure of power supply to the heater.

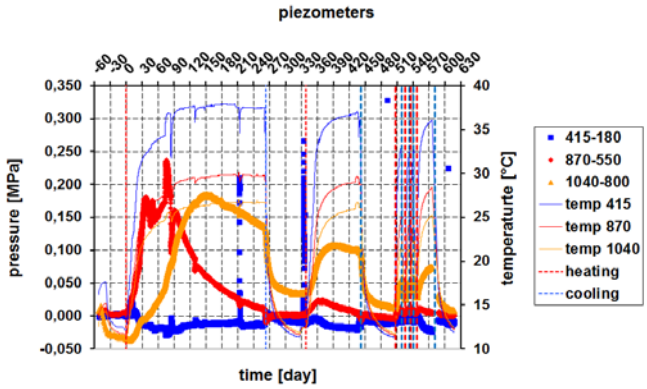

Figure 8. Groundwater pressure and temperature changes

4 CONCLUSIONS

Present results indicate very rapid reaction of the rock massif to fluctuations in rock heating intensity and large extent of these artificially induced stress changes. The changes appear without any observable hysteresis, i.e. they behave as reversible in respect to irregular experimental heat supply modifications. Stress changes dependence on temperature and stress changes reversibility could indicate low frequency of opened fissures of the granitic massif. The main mechanism of the rock massif movement is caused by reversible linear thermal expansion of the granite matrix. However some fissures enabled the dissipation of groundwater pressure.

5 ACKNOWLEDGEMENTS

The project has been supported by the Ministry of Industry and Trade of the Czech Republic (Project Number: FR-TI3/325). We would like to thank to the whole project realization team (Czech geological survey, ISATech ltd., Arcadis CZ corp., Institute of rock structure and mechanics of Czech academy of sciences and Technical University of Liberec).

6 REFERENCES

Andersson, J. & Martin, C. 2009. The Äspö pillar stability experiment: Part I—Experiment design. *International Journal of Rock Mechanics and Mining Sciences* 46(5): 865-878.

Berchenko, I. Detournay, E. Chandler, N. & Martino, J. 2004. An in-situ thermo-hydraulic experiment in a saturated granite I: design and results. *International Journal of Rock Mechanics and Mining Sciences* 41(8): 1377-1394.

Chan, T. Hood, M. & Witherspoon, P. 1981. Predicted and measured temperatures, displacements and stresses from the Stripa heater experiments. *Subsurface Space* 2: 829-837.

Dincer, I. & Rosen, M. 2010. *Thermal energy storage: Systems and Applications (2nd edition)*. New Jersey: Wiley.

Ercan Ataer, O. 2006. Storage of Thermal Energy; *Energy Storage Systems; Encyklopedia of Life Support Systems,* Developed under the Auspices of the UNESCO. (Y. A. Gogus, Ed.) Oxford, UK: Eolss Publishers. [http://www.eolss.net]

Heuze, F. 1984. Suggested method for estimating the in-situ modulus of deformation of rock using the NX-Borehole Jack. *Geotechnical Testing Journal GTJODJ* 7(4): 205-210.

Heuze, F. & Amadei, B. 1985. The NX-Borehole Jack: a lesson in trials and errors. *Int. J. Rock Mech. Min. Sci. & Geomech. Abstr.* 22(2): 105-122.

Janoušek, V. Braithwaite, C.J.R. Bowes, D.R. & Gerdes, A. 2004. Magma-mixing in the genesis of Hercynian calc-alkaline granitoids: an integrated petrographic and geochemical study of the Sázava intrusion, Central Bohemian Pluton, Czech Republic. *Lithos* 78: 67–99.

Kwon, S. Lee, C. Yoon, C.-H. & Cho, W.-J. 2013. In situ borehole heater test at the KAERI Underground Research Tunnel in granite. *Annals of Nuclear Energy* 62: 526-535.

Schneefuβ, J. Gommlich, G. & Noell, U. 1989. The heater test at the Grimsel Rock Laboratory: The thermo-mechanical response of the rock mass to a heat flux. *Nuclear Engineering and Design* 116(1): 25-31.

Spathis, A. T. 1990. The vibrating wire stressmeter – Calibration factors for a novel implementation, *Int. J. Rock Mech. Min. Sci. & Geomech. Abstr.* 27(4): 309-314.

Žák, J. Schulmann, K. Hrouda, F. 2005. Multiple magmatic fabrics in the Sázava pluton (Bohemian Massif, Czech Republic): A result of superposition of wrench-dominated regional transpression on final emplacement. *J. Struct. Geol.* 27(5): 805-822.

Geotechnical and Geophysical Site Characterisation 5 – Lehane, Acosta-Martínez & Kelly (Eds)

Site investigation, monitoring and stability analysis of a built-up slope involved by gas pipeline explosion

G. Totani
University of L'Aquila, DICEAA, L'Aquila, Italy

F. Totani
Consultant, L'Aquila, Italy

P. Monaco
University of L'Aquila, DICEAA, L'Aquila, Italy

L. Simeoni
University of Trento, DICAM, Trento, Italy

ABSTRACT: The paper describes the results of site investigations, monitoring and stability analyses of a build-up slope located near Pineto (Italy). In March 2015 the explosion of a gas pipeline in the upper portion of the slope caused extensive damage to existing buildings and lifelines. Soon after the event, a site investigation and monitoring program was planned. The site investigation included 3 boreholes (25-30 m depth) and 3 flat dilatometer tests DMT (15 to 30 m depth) carried out inside the boreholes by use of the "torpedo" system. The boreholes were instrumented for inclinometer and piezometer measurements. A detailed topographic survey was carried out to reconstruct the ground profile. Hydrological data were analysed for possible critical rainfall events. The slope is formed by OC clay, covered with an upper, 10-14 m thick clayey-sandy silt colluvial layer. The stability of the slope was analysed both in pre- and in post-explosion conditions. The pre-explosion conditions were back-analysed assuming different levels of the groundwater table (at the time of the explosion presumably close to the ground surface). The analyses, in agreement with field observations, indicated that the slope is unstable and possibly slope movements may have been one concurrent cause of failure of the pipeline. The profiles of the DMT horizontal stress index K_D helped identify multiple slip surfaces.

1 INTRODUCTION

When a buried pipeline is installed within an unstable slope in which large-scale ground movements might occur, these movements may induce substantial axial/bending strains and stresses in the pipeline, with possible risk of rupture. The methods to predict landslide-induced pipeline strains and stresses are not well described in design standards or codes of practice. Finite element analysis of soil-pipe interaction is potentially an effective tool to model the pipeline response to slope movements. All the above significant engineering issues have received particular attention in recent studies (for instance Hodder & Cassidy 2010, Lin et al. 2011, Zhang & Duan 2012, Zhou 2012, Contreras et al. 2013, Fredj & Dinovitzer 2014, Ho et al. 2014, Petro et al. 2014, Sahdi et al. 2014, Auflič et al. 2015, Fredj et al. 2015).

On March 6, 2015 the explosion of a gas pipeline in the upper portion of the slope of Colle Cretone (Pineto, Italy) caused extensive damage to existing buildings and lifelines. The explosion triggered a fire of gigantic proportions. The heat of the fire damaged the existing buildings, as well as trees and overhead power lines, in a radius of more than 200 m from the breaking point. A landslide occurred over an interval of about 1-2 hours with a speed of about 20-40 cm/hour, leaving numerous cracks on the ground surface and generating displacements/rotations on the retaining walls nearby.

This paper describes the results of the site investigation, the monitoring program and the stability analyses of the slope carried out in the months following the gas pipeline explosion. The analyses, in agreement with field observations, indicated that the slope movements have been one concurrent cause of failure of the pipeline. Geotechnical analyses revealed that the movements along the slope had a direction almost collinear with the longitudinal axis of the damaged pipeline. The information presented in this paper is the basis for further analysis of the mechanical behaviour of the pipeline interacting with the slope movement and evaluation of the pipeline strain demand.

2 GEOLOGICAL AND GEOMORPHOLOGICAL SETTING OF COLLE CRETONE SLOPE

The hillside area of Colle Cretone (Pineto, Italy) is composed of a Middle-Upper Pliocene grey-blue clay formation, whose top surface gently dips toward the Adriatic sea. Above these formation colluvial silty-clayey-sandy deposits, which reflect an intense recent evolutionary phase, are encountered. Due to

their widespread areal diffusion and significant thickness, which may exceed 10 m, the colluvial deposits can be regarded as a real geological formation.

The hills are shaped by the presence of ditches and small streams which flow into the major rivers in the Abruzzo region. The sides of the valleys excavated by these streams show a markedly asymmetrical profile. The side of the valley that slopes more gently is modelled in the colluvial deposits. Its morphology indicates the presence of slow movements in progress (about 15-20 mm/year). The only surficial evidence of such slow movements has the form of ground surface undulations. Ditches are in rapid erosion and make the slopes of the valley continuously steeper, which is the origin of the slow slope movements. Generally movements are reactivated in correspondence of continuous rainfall, while they cease completely in the dry periods.

Slow slope movements are not among the landslides that more directly recall the image of "catastrophe", intended as a phenomenon (more or less unexpected, or unforeseen) that produces substantial damage in a short time, even though it may be characterised by different stages (Leroueil 2001). Nevertheless slow movements are particularly insidious, due to their widespread diffusion and low surficial evidence. They typically affect gently sloping areas, usually selected for siting of settlements and infrastructures that are destined, sooner or later depending on the precautions that have been taken, to suffer (at times irreparable) damage during the evolution of the movement.

As noted above, in this area slow slope movements have a seasonal character, directly related with variations of the ground water level induced by rainfall. Based on the results of monitoring continued for over 10 years on similar slopes, the position of the slip surface generally lies within, and/or at the base, of an upper debris layer, at the contact between this layer and the weathered/softened portion of the base clay formation, or sometimes deeper, within the base clay formation.

As featured in various maps, including regional ones, the area of Colle Cretone has long been affected by slow movements. Figure 1 shows the area of reactivation/expansion of the movement which occurred on March 6, 2015, involving the gas pipeline. Figure 1 also shows an excerpt from a planimetric map retrieved from official cartography of the Abruzzo regional authority, dating back nearly 20 years ago.

Figure 2 shows a schematic section of the water flow system that affects the slope from Colle Cretone (Cretone Hill) towards the Cerrano stream at its toe. In this context, the continuous influx of stormwater promotes saturation/imbibition of the colluvial cover, causing a reduction of shear strength and thus giving rise to the reactivation of the movement.

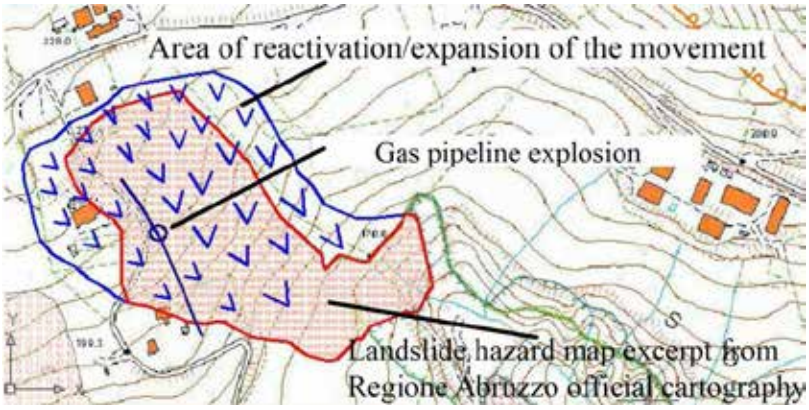

Figure 1. Area of reactivation/expansion of the movement occurred on March 6, 2015, involving the gas pipeline.

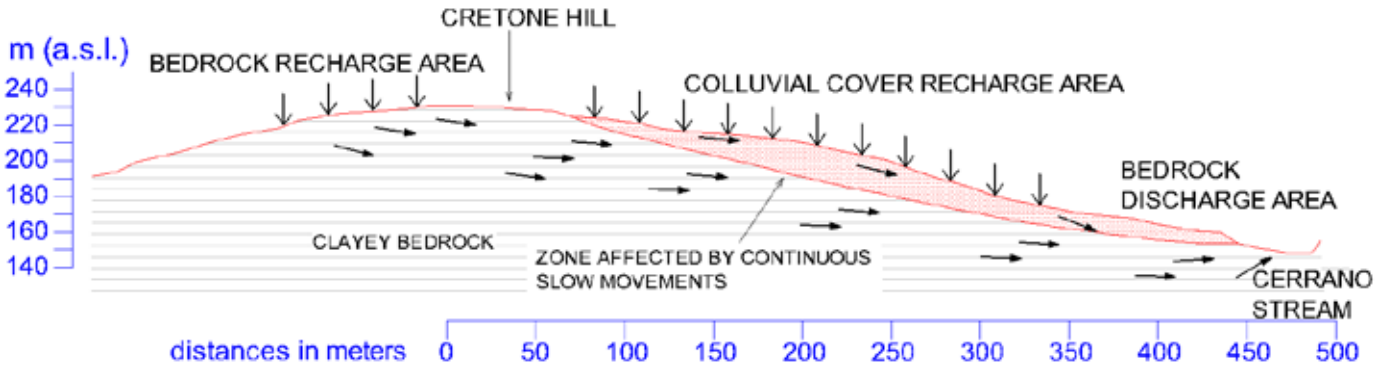

Figure 2. Schematic section of the water flow system across the slope.

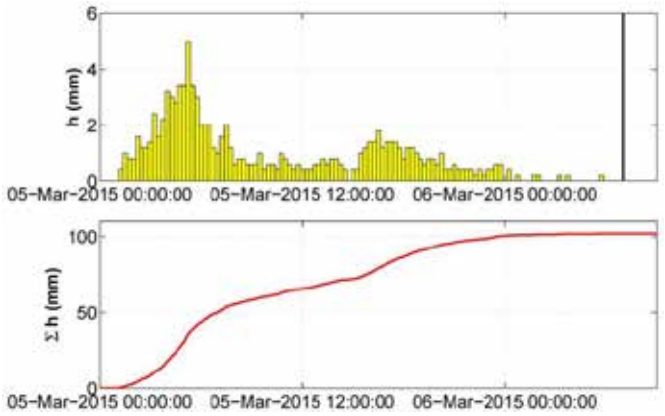

Figure 3. Height of rain recorded by pluviograph (March 5-6, 2015 event).

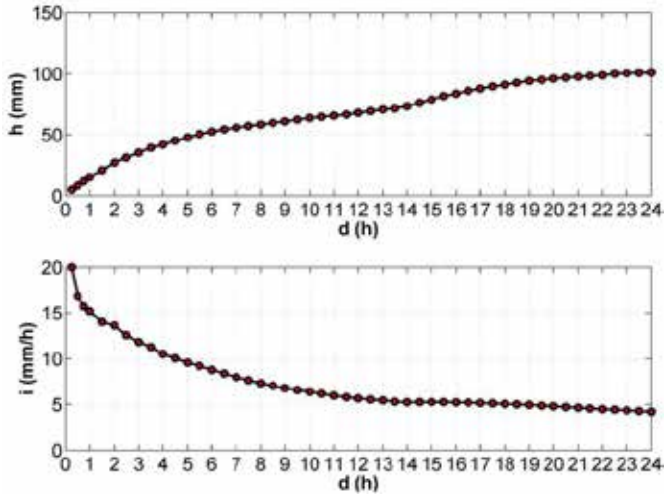

Figure 4. Height of rain cumulated during the March 5-6, 2015 event.

3 RAINFALL EVENTS OF FEBRUARY-MARCH 2015

During February-March 2015 the slope was subjected to particularly intense "rainfall paths". Following are the results of the analysis of the rain event happened on March 5 and 6, 2015. This analysis has permitted to evaluate the characteristics of the event in terms of duration and intensity, as well as the associated return period.

Figure 3 shows the values of the height of rain recorded by pluviograph. Figure 4 reports the height of rain cumulated during the event. The analysis of the data indicates that the event began on the night of March 5 (01:30 UTC) and lasted continuously until late in the evening (23:45 UTC), with a total height of rain of 102 mm. Peak intensity occurred at 5:15 UTC, in the first stage of the event, reaching the value of 20 mm/hour.

The analysis of rainfall data before the event of March 5 has shown the prior occurrence of two events lasting more than 20 hours, respectively on February 6-7 and on February 25-26. The total height of rain for this last event (occurred seven days before the event in question) was 97 mm.

4 SITE INVESTIGATION AND MONITORING

A site investigation and monitoring program was planned soon after the pipeline explosion (Figure 5).

Three boreholes were drilled along the slope to 25-30 m depth, in order to obtain detailed stratigraphic information. Flat dilatometer tests (DMT) were carried out inside the boreholes by use of the "torpedo" system to 15-30 m depth.

The DMT tests were aimed at identifying the slip surfaces involved by the expansion/retrogression of the landslide occurred on March 6, 2015, based on the method proposed by Totani et al. (1997). This method permits to detect quickly active/past slip surfaces in overconsolidated (OC) clay slopes, based on the inspection of the profiles of the DMT horizontal stress index K_D (Marchetti 1980). The method is based on the following two assumptions:

(a) The sequence of sliding-remoulding creates a remoulded zone of nearly normally consolidated (NC) clay, with loss of structure, aging, cementation.

(b) Since in NC clays $K_D \approx 2$, if an OC clay slope contains layers where $K_D \approx 2$, these layers are likely to be part of a slip surface (active or quiescent).

In essence, the method consists in identifying zones of NC clay in a slope which, otherwise, exhibits an OC profile, using $K_D \approx 2$ as the identifier of the NC zones (see also Marchetti et al. 2001).

The three borehole logs (Figure 6) show that the upper colluvial silty-clayey-sandy deposit has a thickness varying between 11 m (at the topmost borehole location) and 14 m (at lower elevation).

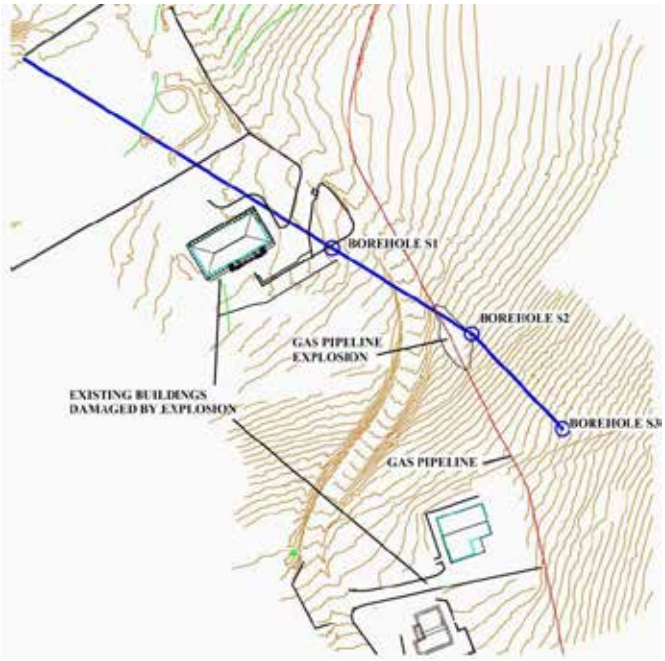

Figure 5. Plan layout of boreholes and DMT tests.

The base blue clays are found about 14 m below the ground surface, with a top surface dipping down toward the valley.

Significant evidence regarding the thickness of soil above the pipeline involved by the landslide is provided by the K_D profile from DMT 1. The section in Figure 6 shows that, above the pipeline, the soil is quite altered/remoulded to a depth of approximately 7.6 m, with a minimum peak of $K_D \approx 2$ just at that depth. Based on this information and taking into account the location of cracks and fissures on the surface, it was possible to reconstruct the geometry of the landslide mobilised by the rainfall event of March 5-6, 2015.

The inspection of the K_D profiles from DMT 2 and DMT 3 (Figure 6 and Figure 7, top) does not reveal any zones with $K_D \approx 2$ or recently remoulded soil layers. Hence it can be concluded that a "neo-formation" roto-translational landslide was triggered on March 6, 2015, involving the portion of slope above the pipeline. The investigation then confirms the geomorphological interpretation, which indicates an extension due to retrogression of a pre-existing slow slope movement.

Figure 7 shows the profiles of the constrained modulus M and of the undrained shear strength c_u obtained from DMT 1. It can be noticed that the landslide, by remoulding the soil, has produced a substantial deterioration of the mechanical properties in the upper 7-7.5 m.

Inclinometer casings and Casagrande piezometers were installed in the three boreholes, in order to monitor the landslide movements and the pore pressures. Inclinometer and piezometer measurements are in progress. A detailed topographic survey was also carried out to reconstruct the ground profile along the slope.

Direct shear tests, with measurement of the residual shear strength after several reversal cycles, were executed on samples retrieved from the colluvial, soft to stiff (when dry) clayey-silty-sandy layer. Figure 8 (left) shows typical shear strength vs. horizontal displacement curves. The interpreted shear strength values are shown in Figure 8 (right). The relatively high values of the residual friction angle of the soil may depend on the scarce activity of the clay minerals.

5 STABILITY ANALYSES

The stability of the slope in the zone of the landslide occurred on March 6, 2015 was back-analysed assuming two different ground water conditions (Figure 9): (1) ground water table at ground surface; (2) ground water table from about 3 to 6 m below ground surface.

If the peak shear strength is assumed in the colluvial cover, the safety factor (Fs) variations are scarcely influenced by changes in pore water pressures. If one refers to the residual shear strength, the values of Fs vary from 0.95 to 1.05. Such values may explain well the movement of the colluvial cover.

The fact that the equilibrium of the slope is governed by the residual strength implies the presence of a pre-existing slip surface, or at least of a soil band of narrow thickness, whose strength was reduced nearly to the residual value due to large or long lasting deformations.

This latter condition is in agreement with the morphological evolution of the slope, that suggests the permanence of the present conditions for a long time.

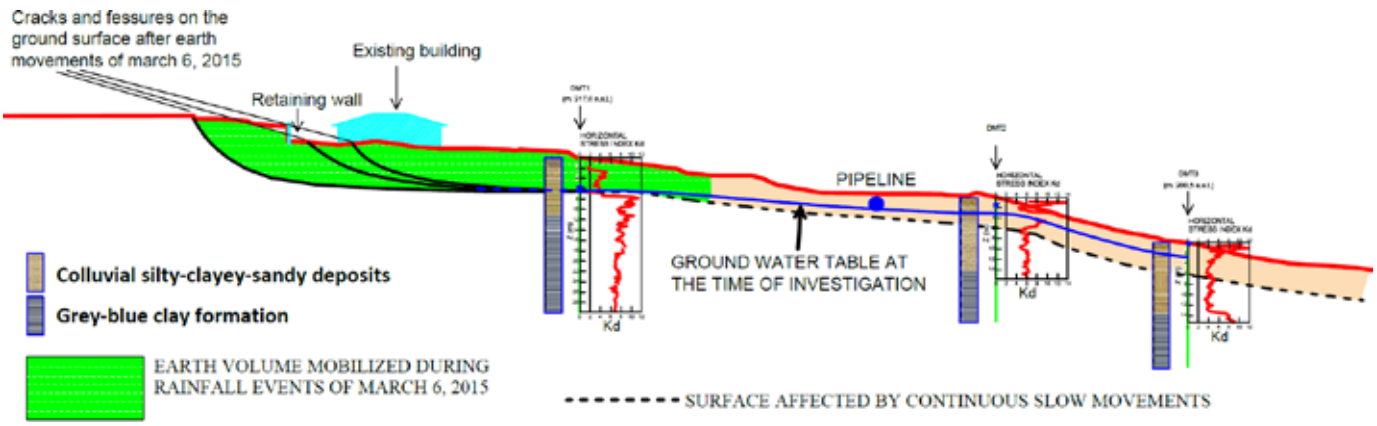

Figure 6. Longitudinal section of the slope and results of site investigation (boreholes and flat dilatometer tests).

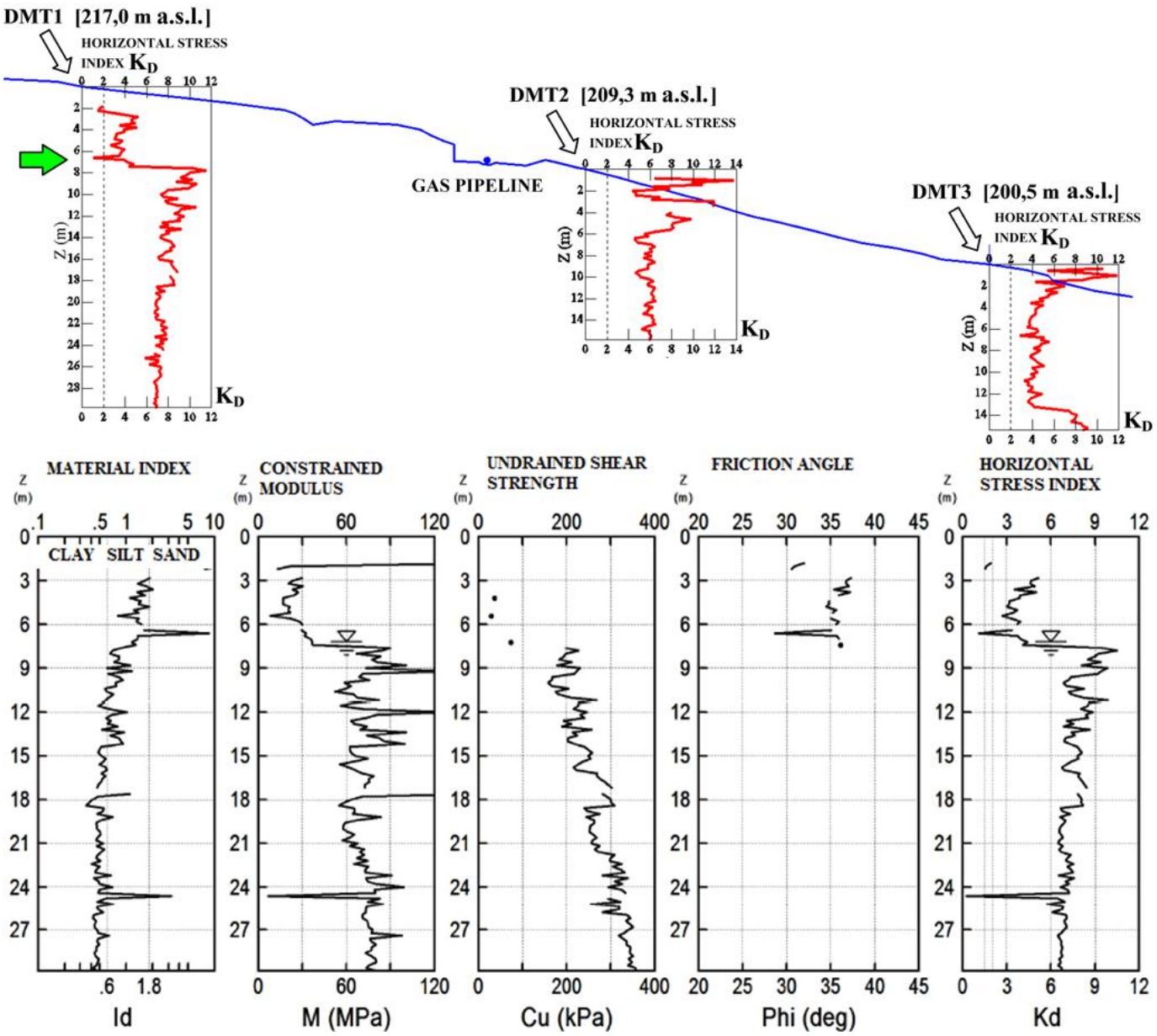

Figure 7. Profiles of K_D from all DMTs (top) and parameters interpreted from DMT 1 (bottom).

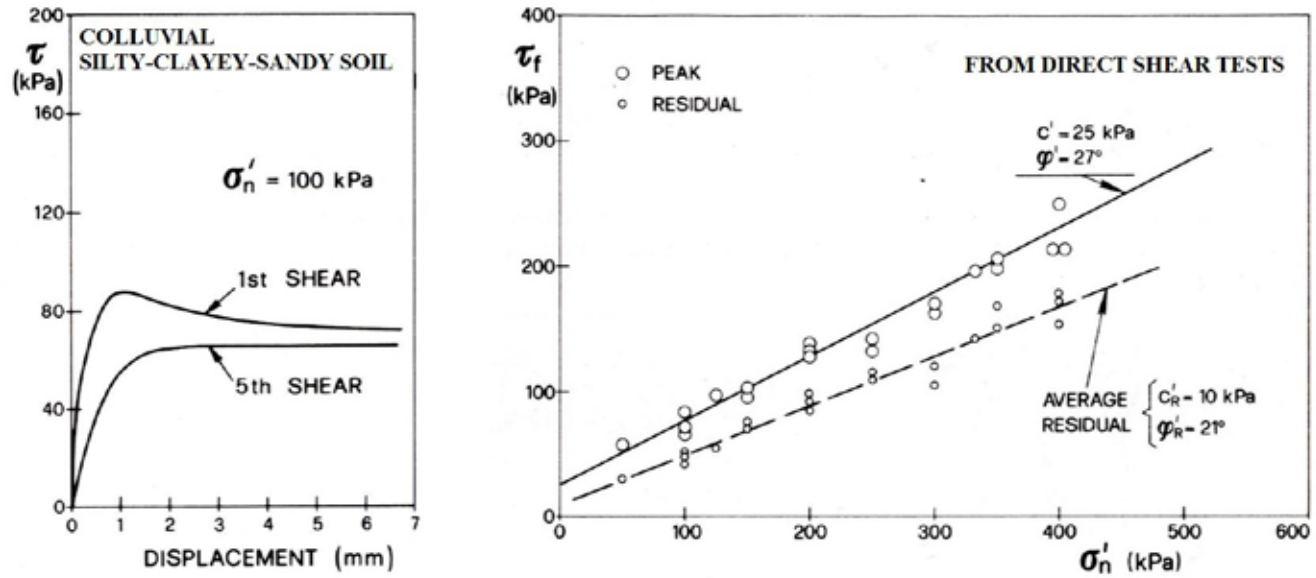

Figure 8. Results of direct shear test on a sample retrieved in borehole S1 (depth 6.00 m).

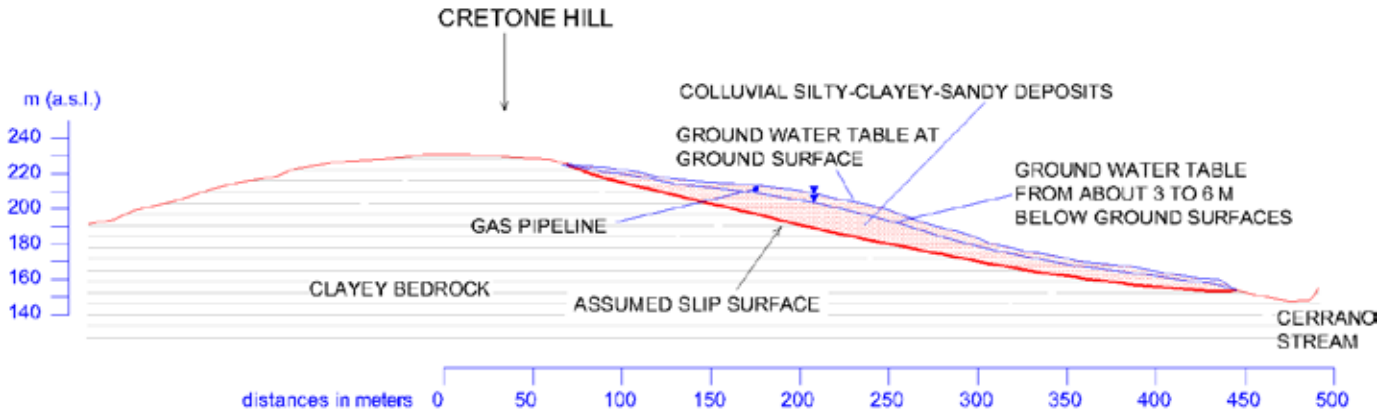

Figure 9. Slip surface and ground water conditions assumed in the back-analysis.

6 CONCLUDING REMARKS

The analysis illustrated in this paper indicates a possible relation between the rupture of the buried gas pipeline and slope movements.

The shallow colluvial cover, in which the pipeline is located, could be affected by continuous slow movements, governed by the pore water pressure regime.

The equilibrium conditions of the slope are controlled by shear strength near to the residual strength in a softened band within the colluvial cover and by pore water pressure variations in the same layer.

As a general conclusion, it can be said that exceptional climatic conditions may influence the equilibrium conditions of such colluvial covers.

7 ACKNOWLEDGEMENTS

Giuseppe Colagrande is acknowledged for assisting the authors in editing the paper.

8 REFERENCES

Auflič, M.J., Komac, M. & Šinigoj, J. 2015. Modern remote sensing techniques for monitoring pipeline displacements in relation to landslides and other slope mass movements. *Environmental Security of the European Cross-Border Energy Supply Infrastructure,* 31-48.

Contreras, M.F., Vergara, C., Pereira, M., Colonia, J.D. & García, H. 2013. Pipeline integrity assessment and mitigation techniques in unstable soil conditions based on comparison of in line inspection results. *Proc. 1st ASME International Pipeline Geotechnical Conference, Bogota, Colombia*.

Fredj, A. & Dinovitzer, A. 2014. Pipeline response to slope movement and evaluation of pipeline strain demand. *Proc. 10th International Pipeline Conference, Calgary, Alberta, Canada,* 4, doi: 10.1115/IPC2014-33611.

Fredj, A., Dinovitzer, A. & Sen, M. 2015. Application of the SPH Finite Element Method to evaluate pipeline response to slope instability and landslides. *Proc. 10th European LS-DYNA Conference, Würzburg, Germany*.

Ho, D., Wilbourn, N., Vega, A. & Tache, J. 2014. Safeguarding a buried pipeline in a landslide region. *Proc. Pipelines 2014: From Underground to the Forefront of Innovation and Sustainability, Portland, Oregon, USA,* 1162-1174, doi: 10.1061/9780784413692.105.

Hodder, M.S. & Cassidy, M.J. 2010. A plasticity model for predicting the vertical and lateral behaviour of pipelines in clay. *Géotechnique,* 60(4): 247-263.

Leroueil, S. 2001. Natural slopes and cuts: movement and failure mechanisms. *Géotechnique,* 51(3): 197-243.

Lin, D., Lei, Y., Xu, K., Huang, R., Luo, M. & Tao, H. 2011. An experiment on the effect of a transverse landslide on pipelines. *Acta Petrolei Sinica,* 32(4): 728-732.

Marchetti, S. 1980. In Situ Tests by Flat Dilatometer. *J. Geotech. Engrg. Div.,* 106(GT3): 299-321.

Marchetti, S., Monaco, P., Totani, G. & Calabrese, M. 2001. The Flat Dilatometer Test (DMT) in Soil Investigations – A Report by the ISSMGE Committee TC16. Official version approved by TC16 reprinted in *Flat Dilatometer Testing*, *Proc. 2nd Int. Conf. on the Flat Dilatometer, Washington D.C., USA,* 2006, Failmezger R.A. & Anderson J.B. (eds), 7-48.

Petro, L., Jánová, V., Žilka, A., Ondrejka, P., Liščák, P. & Balík, D. 2014. Catastrophic landslide in Nižná Myšla village (eastern Slovakia). *Landslide Science for a Safer Geoenvironment, Volume 3: Targeted Landslides,* 305-311.

Sahdi, F., Gaudin, C., White, D.J., Boylan, N. & Randolph, M.F. 2014. Centrifuge modelling of active slide-pipeline loading in soft clay. *Géotechnique,* 64(1): 16-27.

Totani, G., Calabrese, M., Marchetti, S. & Monaco, P. 1997. Use of in-situ flat dilatometer (DMT) for ground characterization in the stability analysis of slopes. *Proc. XIV ICSMFE, Hamburg, Germany,* 1: 607-610.

Zhang, P. & Duan, Y. 2012. Study on failure probability model of LanChengYu pipeline under landslide geological disaster. *Information, Special Issue on Reliability, Maintenance, and Safety Engineering: Recent Progress in China,* 15(12B): 5683-5692.

Zhou, W. 2012. Reliability of pressurised pipelines subjected to longitudinal ground movement. *Structure and Infrastructure Engineering: Maintenance, Management, Life-Cycle Design and Performance,* 8(12), doi: 10.1080/15732479.2010.505244.

Geotechnical and Geophysical Site Characterisation 5 – Lehane, Acosta-Martínez & Kelly (Eds)

A preliminary design of ground improvement by grouted stone columns for a shopping centre

A. M. Ünver

Department of Civil Engineering, Middle East Technical University, Ankara, Turkey

İ. S. Ünver

Department of Civil Engineering, İstanbul Technical University, İstanbul, Turkey

ABSTRACT: Stone column ground improvement method is not applicable in very soft soils since the stone columns with lack of lateral support bulge with time and this causes settlements. Therefore, it has been recommended to apply grouted stone columns instead of conventional stone columns at the preliminary design stage of the project considered. The details of a grouted stone column of ground improvement method recommended for a shopping centre project, for which the subsoils are very soft clays, is presented in this paper. Preliminary soil investigations have shown that the subsoils at the related site are composed of very soft organic clays for which high secondary consolidation settlements are expected. Standard Penetration Test (SPT) results are the main parameters utilized at the preliminary design stage. Out of 25 SPT blow counts in the clay layer, the blow count number was N=0 (zero) in 18 of them. This means that the clays at the site are extremely soft. The calculations and evaluations have shown that a conventional stone column of ground improvement technique is to be insufficient due to bearing capacity and settlement considerations in this one-storey shopping centre. Bearing capacity and secondary consolidation settlement calculation results are given. After all evaluations, the principles of a feasible preliminary design by grouted stone columns are given in the paper.

1 INTRODUCTION

It was planned to construct a shopping centre in Muğla-Milas region of Turkey. A preliminary design of foundation systems of the superstructure, for the purpose of quantity survey and cost estimate, was claimed. Six boreholes (BH-1, BH-2,.....) could be executed for the preliminary design of foundation systems. The borehole locations are given in Figure 1. There are several blocks to be constructed within the project. It was intended to locate the boreholes so that all the subsoils at construction area could be idealized. But due to an inundation problem, borehole machine could not work in A and B blocks area (Figure 1). Standard Penetration Test (SPT) was the main tool in this preliminary site investigation. This was also due to time limitation of the work claimed. There were generally one-storey buildings to be constructed within the scope of the project. According to borehole results it was understood that the subsoils are composed of very soft clays and they are called as "mud" in this preliminary investigation. Two alternatives were evaluated for a satisfactory foundation design. Stone column ground improvement method was the first alternative. A preliminary design of precast driven piles was done in the second alternative. The latter is out of the scope of this paper. Stone column method of ground improvement method has been examined in this paper. After bearing capacity and settlement calculations it has been understood that the application of conventional stone columns without a precaution like cement grouting or similar is not applicable due to extremely soft clay subsoils. Therefore, a preliminary design of grouted stone columns has been done. The principles and general calculation results are evaluated and the conclusions are presented in this paper.

2 SOIL PROFILES

Six boreholes were carried out at the related site as given in Figure 1. SPT was the main site test in this preliminary investigation. Soil profiles and site test (SPT) results are given in Figure 2. As understood in Figure 2, after a crust layer of 2.5m in thickness as an average there are very weak layers called "mud" during site investigation. This layer is quite unfavorable with regard to bearing capacity and settlement criteria. The thickness of the weak layer changes between 4 and 9m. The color of the "mud" is dark grey. Totally 25 SPT tests were executed in this layer. The recorded SPT blow counts revealed that the layer is extremely soft. Out of 25 SPT blow counts in weak clay layer, the blow count number was N=0 (zero) in 18 of them.

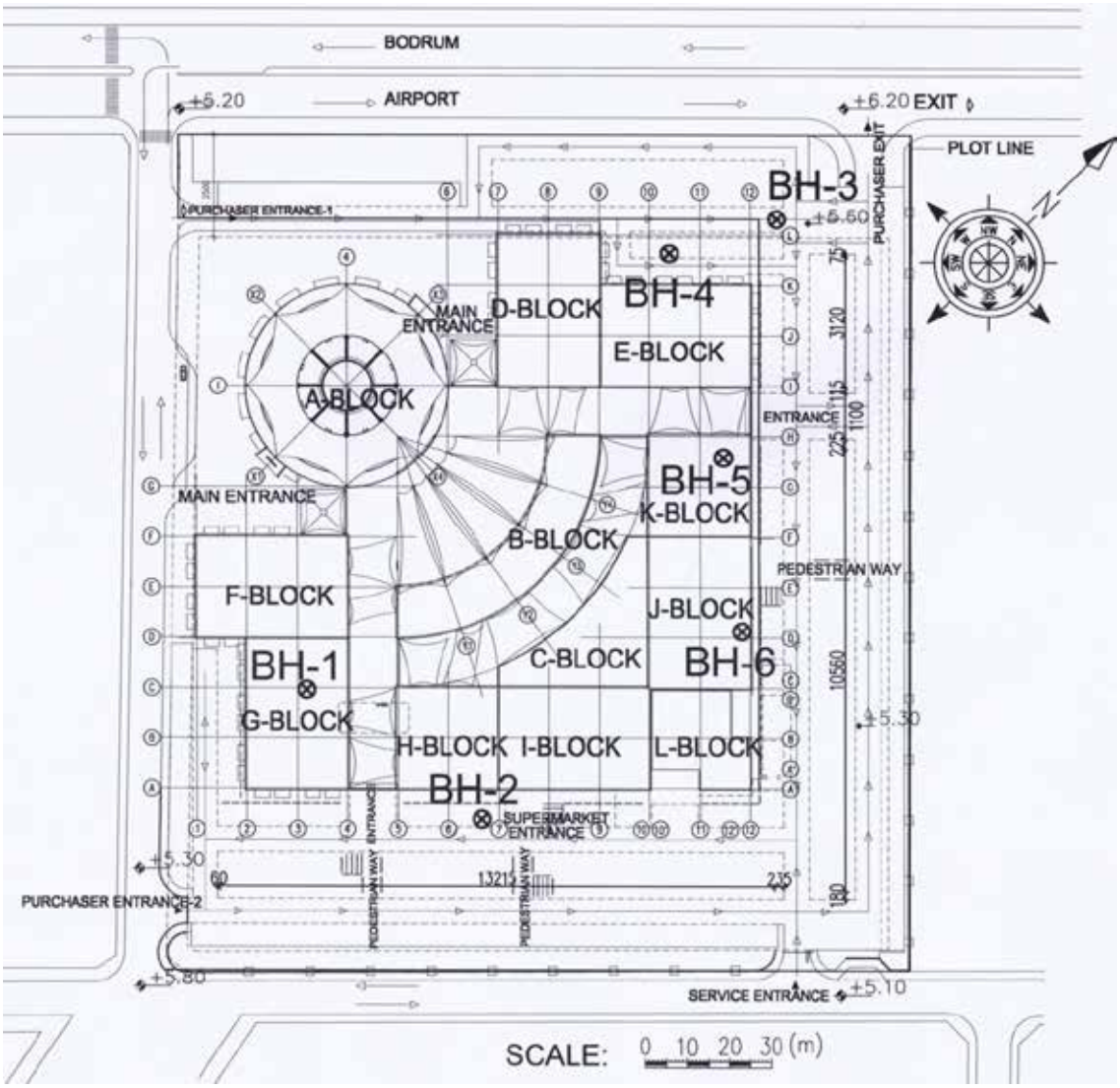

Figure 1. Borehole locations (BH-1, BH-2, BH-3, BH-4, BH-5, BH-6)

SPT numbers were N=2 in 6 of them and N=3 in one of them. This simple statistics shows that a very weak clay layer exists under the construction area. Since the clay layer is extremely soft, it was not possible to get enough soil samples for laboratory testing in this preliminary site investigation. It is known from past experience and information for the investigation area that the so called "mud" at this site is probably organic and the type of soil is peat. The undrained shear strength of the "mud" at the site is presumed as c_u=5-10 kPa at most. The stable gravel and/or weathered phyllite layers start under the weak mud layer at site as given in Figure 2.

3 SITE AND SUPERSTRUCTURE INFORMATION

Site area is almost flat topographically. The elevation of the Bodrum-Milas highway near site is about 1.5m higher than the elevations at the site area. One-story prefabricated and reinforced concrete buildings are to be constructed generally at the related site. Single footings and mat foundations have been designed at the preliminary design stage for these one-storey buildings. It is planned to excavate about 25cm vegetable soils and make controlled soil fills of thickness 50cm first and construct mat foundations later. The mat foundation areas of different buildings in the project can be given as 730 m^2, 930 m^2 and 2200 m^2. Maximum foundation pressures for these buildings are given about 40 to 65 kPa. It has been found suitable to make 50cm strip off excavations and settle foundations for the other single footings over which the prefabricated buildings are to be constructed. The dimensions of single footings are 4.8mx4.8m and 5.5mx5.5m generally. The spaces between these single footing areas will be filled with soil with an average depth of 2m. Maximum foundation pressure under single footings is given as 56 kPa. All the site will be filled with soil at the spaces between buildings and other car park areas with an average depth of 1.5 to 2m.

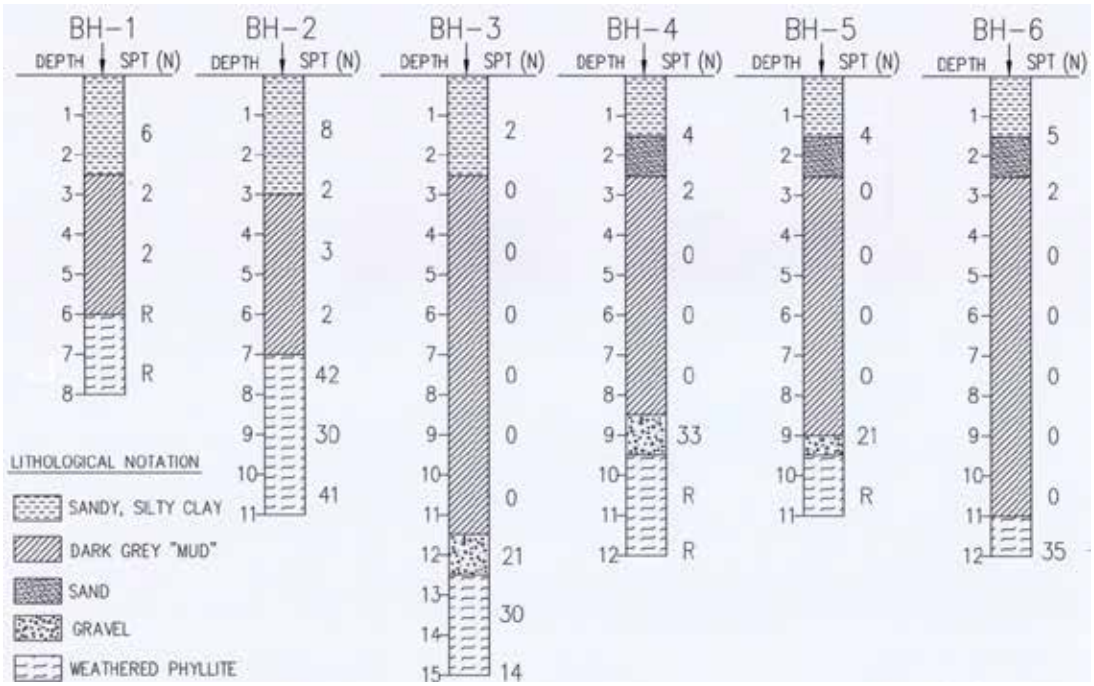

Figure 2. Soil profiles and site test (SPT) results

4 PRELIMINARY DESIGN OF FOUNDATION SYSTEMS

It is anticipated that stone column method of ground improvement is a feasible alternative when the site and cost conditions are taken into account. However, it is known from past experience that conventional stone columns are not applicable in clay soils having undrained shear strengths lower than about c_u=15 kPa (Barksdale and Bachus 1983, Moseley and Kirsch 2004). Because, in very soft soils the stone columns with lack of lateral support bulge with time and this causes settlements.

4.1 *Bearing capacity evaluations*

Average undrained shear strength of the "mud" layer at the site is c_u=5-10 kPa at most considering SPT blow counts. The bearing capacity of conventional stone columns can be computed by the Equation 1 below given in Bowles (1996).

$$q_u=\tan^2(45+Ø'/2)*6c_u \quad (1)$$

where q_u= ultimate bearing capacity of stone columns-kN/m^2; Ø'=internal friction angle of stone column material-40º~45º).

If a computation is carried out with c_u=10 kPa and considering 60cm diameter stone columns, the allowable bearing capacity of a conventional stone column is Q_u=57 kN (Safety factor=1.5). Although the undrained shear strength of the "mud" layer has been taken at the upper limits, the allowable bearing capacity of a conventional stone column is quite low as noticed. Therefore, designing with conventional stone columns seems not feasible.

4.2 *Settlement evaluations*

It is obvious that the very soft clay layers at the site have quite high compressibility. It is possible at this preliminary design stage that the coefficient of volume compressibility used in settlement computations can be estimated by considering the values for similar clays found in the past or by utilizing the typical values given in literature. It is inferred from this survey that coefficient of volume compressibility can be taken between, m_v=0.001-0.0015 m^2/kN. There are some values larger than the upper limit especially for organic and peat type of clays reported in literature (Carter and Bentley, 1991). Settlement calculations have been carried out for shallow foundations by using the lower limit of coefficient above, the acting loads due to buildings and fills, and the compressible layer thickness. It has been found that the estimated primary consolidation settlement for the building with mat foundation of 2200 m^2 is about s=35cm. The calculated settlements for prefabricated buildings with single footings are at the order of s=5-10cm excluding the fills between them. After filling the large areas with 2m of soils, approximately s=25cm settlements are expected. All the estimated settlements are unacceptable; and it is known that conventional stone columns can generally reduce these settlements by about 60% of untreated settlements at most.

Then, it is noticed that the settlements are still unacceptable for some buildings even conventional stone columns are designed.

Secondary settlements are known to be critical for organic clays. Therefore, these type of settlements have also been investigated for this project. Secondary settlements are generally estimated by the Equation 2 below given in Terzaghi et al. (1996).

$$s_{sec.}=C'_{\alpha}*H*\log(t/t_p) \quad (2)$$

Here, C'_{α} is the secondary compressibility index. It is given by a graph depending on natural water content in Mesri (1973). Although there is no data about water content, C'_{α} is generally between 0.007 and 0.025 as shown in Figure 3.

In Equation 2 above, H is the compressible layer thickness, t is the time for secondary settlements (It can be taken as economical life of the structure) and t_p is the time for primary consolidation settlement (It can vary from months to years depending on the soil and drainage conditions). It is seen that as t/t_p ratio increases secondary settlements also increase. This ratio rarely exceeds 100 at site conditions and it is frequently lower than 10 (Terzaghi et al., 1996). On the other hand, in the projects where the time for primary consolidation settlements are accelerated by vertical drains, this ratio may increase dramatically. It is well known that conventional stone columns act as vertical drains at the same time. Therefore when conventional stone columns are designed in our project, secondary settlement phenomenon will be more critical. When a quick computation is performed to estimate secondary settlements for untreated subsoils by taking C'_{α} between 0.007 and 0.025, and t/t_p between 40-50, about 10 to 30cm settlements are found. Thus, secondary settlements can even exceed primary consolidation settlements. It can be concluded that the settlement problem is still quite critical when conventional stone columns are designed.

4.3 *Preliminary design of grouted stone columns*

After above evaluations, it has been decided to make a preliminary design with a modified type of stone column method in this project. Modified methods are generally classified into three:

- Grouted stone columns
- Vibro mortar columns
- Vibro concrete columns

Grouted stone columns have been chosen, when a feasibility study is made considering Turkey's conditions. In this modified method, water-cement suspension is grouted additionally in conventional stone column application.

The bearing capacity calculations of grouted stone columns can be made by the same principles of end-bearing pile calculations. The stable gravel and weathered phyllite layers beneath the weak subsoils at site results in high bearing capacity of grouted stone columns. The diameter of grouted stone columns has been chosen as 60cm at the preliminary design stage. It has been anticipated to form 80cm enlarged bases at the tip of the columns. After calculations of bearing capacity of grouted stone columns by several approaches an average allowable bearing capacity of Q=400 kN has been found using a safety factor of 3. This is a reasonable load and a feasible preliminary design can be performed now.

Considering the superstructure loads, the layouts of the grouted stone columns have been prepared. 2.5mx2.5m and 3mx3m square patterns have been designed for the buildings with mat foundations. A symmetrical 4 no. grouted stone columns have been designed against probable rotational effects for footings. 3mx3m square patterns have been found to be suitable for the soil fill loads between single footings and under other car park fills (Fill heights are about 2m).

It has also been recommended to make good quality granular fills of 60cm thickness reinforced with 2 layers of geogrids under the prefabricated buildings with single footings and at the bottom of car park fills. The purpose was to get an arching effect by means of reinforced fills so that all the superstructure loads are to be transferred to grouted stone columns. Thus, the loading of weak subsoils will be prevented and the probability of forming negative skin frictions on grouted stone columns shall be minimized.

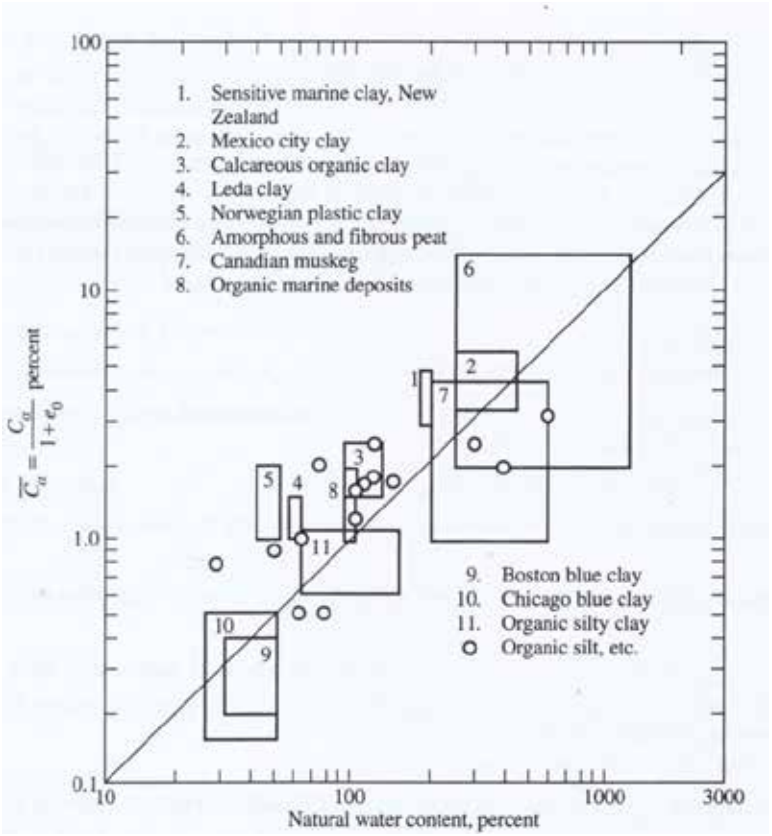

Figure 3. Relationship between secondary compression index and natural water content (Mesri, 1973)

5 CONCLUSION

At the preliminary design stage of foundation systems of a shopping centre project in Muğla-Milas region of Turkey, site investigations with boreholes have revealed that the subsoils are extremely soft. The weak layer is below the first crust layer at the site and its thickness is between 4m and 9m. The very soft clay is called as "mud". Standard Penetration Test (SPT) was the main tool in this preliminary soil investigation study. Out of 25 SPT blow counts in weak clay layer, the blow count number was N=0 (zero) in 18 of them. This simple statistics shows that the clay layer is extremely soft. This was the main reason of unavailability of enough soil samples during the site investigation.

Although Client requested an economical alternative ground improvement method like stone columns for the shopping centre, the calculations and evaluations resulted in that conventional stone column design was not possible for this project. Therefore, grouted stone columns were designed. Precast driven piles were recommended as the second alternative which is out of the scope of this paper. The principles of grouted stone column preliminary design are given in this paper. The geotechnical concepts like bulging of conventional stone columns, secondary consolidation settlement, controlled soil fills reinforced with geogrids and negative skin friction were taken into consideration during preliminary design.

Although it is highly probable that the very soft clays are organic based on site observations and past experience at the related region, it has been recommended to Client that more advanced site investigation techniques should be used for final design stage. By this way, it will be possible to get enough soil samples for definite descriptions of the soil layers and make strength and compressibility tests. It has been shown that determination of natural water content is even quite important to reasonably estimate the secondary settlements which may exceed the primary consolidation settlements in some cases.

6 REFERENCES

Barksdale, R. D., and Bachus, R. C. 1983. Design and construction of stone columns. *U.S. Department of Transportation, Federal Highway Administration, Report No. FHWA/RD-83/026*

Bowles, J. E. 1996. *Foundation analysis and design*. 5th edition, The McGraw-Hill Comp., Inc., 1175 pp.

Carter, M., and Bentley, S. P. 1991. *Correlations of soil properties.* Pentech Press.

Mesri, G. 1973. Coefficient of secondary compression. *Journal of the Soil Mech. and Found. Div., ASCE, Vol.99, No.SM1, 122-137.*

Moseley, M. P., and Kirsch, K. 2004. *Ground improvement.* 2nd edition, Spon Press, 431 pp.

Terzaghi, K., Peck, R. B., and Mesri, G. 1996. *Soil mechanics in engineering practice.* 3rd edition, John Wiley and Sons, Inc., 549 pp.

Geotechnical and Geophysical Site Characterisation 5 – Lehane, Acosta-Martínez & Kelly (Eds)

Comparison of pile design following two standards: EC7 and AS2159

S. Buttling
National Geotechnical Consulting, Brisbane, Australia

ABSTRACT: In normal design practice one method is chosen from the many available and applied to a site. In this paper two case histories are examined, where there is sufficient information to investigate and compare different design methods, including different methods of selecting design parameters. Because the projects are completed, there is information from boreholes and CPTs, from instrumented trial piles, working pile tests and dynamic load tests. Comparisons will include various design methods included in EC7, and also with AS 2159:2009.

1 INTRODUCTION

BS EN 1997-1 (BSI, 2010), or EC7 as it is commonly known, was published in 2004 after more than twenty years of drafting effort by a large group of people from many European countries, and was re-issued with corrigenda in 2009. It brought geotechnical engineering design in Europe into line with structural engineering design, by requiring the application of limit state design principles. In this paper we will look at the application of EC7 to the design of piles, where it was a welcome advance, since designing piled foundations using working stress design for a structure such as a cable stayed bridge being designed on limit state principles, had been extremely challenging.

In Australia, limit state design of piles has been incorporated into the standard, AS 2159 (Standards Australia, 2009), since 1995, and was revised in 2009. The opportunity will be taken to compare the two standards, in relation to two real projects.

2 PILE DESIGN TO EC7

Clause 7.4.2 gives a comprehensive list of matters to be taken into consideration in the design of piled foundations, including such things as installation effects, spacing and group behaviour, effect on adjacent properties, and chemical effects in the soil, amongst others. However, Clause 7.4.1 states:

"The design shall be based on one of the following approaches:

- the results of static load tests, which have been demonstrated, by means of calculations or otherwise, to be consistent with other relevant experience;
- empirical or analytical calculation methods whose validity has been demonstrated by static load tests in comparable situations;
- the results of dynamic load tests whose validity has been demonstrated by static load tests in comparable situations;
- the observed performance of a comparable pile foundation, provided that this approach is supported by the results of site investigation and ground testing."

2.1 *Pile design using the results of static load tests*

Taking design on the basis of static load tests first, the problem is, how is design on the basis of static load tests to be carried out? Bond and Harris (2008) refer to the fact that EC7 "places great emphasis on the use of static load tests, either as the primary design method or in providing validity to designs based on dynamic load tests or calculations". They then go on to recommend ISSMFE pile testing procedures, and to discuss how many tests should be carried out. However, they do not actually explain how static load testing could be used in practice to design a piled foundation. Bond and Simpson (2009) make many of the same points, but also include reference to the equations in EC7 which allow a characteristic value for ultimate pile resistance to be determined from test values. They include the equation for static load tests:

$$R_{c.k} = min\left\{\frac{(R_{c,m})_{mean}}{\xi_1}, \frac{(R_{c,m})_{min}}{\xi_2}\right\} \quad (1)$$

and discuss the values of ξ to be used, from EC7 and from the National Annex but, again, they do not actually explain how a pile may be designed using static load test results.

The best guidance has been found in Frank et al (2004) which was written by some of the key authors of the standard. Section 7.4 gives some very general explanation about design using static load test results, but the best information is in the worked example, Example 7.1. For this case a hypothetical foundation is to be designed for a major bridge, and the following information is available to the designer:

- Permanent Load 31 MN
- Accidental Load 16 MN
- The soil profile consists of 20 – 30 m of very soft clay, muddy sands, sands and clays, and, finally, sands and gravels at the level of the expected pile toe level
- Four static load tests were carried out on open ended driven piles, and of various lengths. The resulting ultimate resistances were rationalised to a length of 55.5 m and are included in Table 1.

Table 1: Measured (rationalised) ultimate pile resistances

Pile No	ULS Resistance (MN)
P8	14.0
P31	14.4
P79	12.1
P79b	13.9

In the hypothetical example the relevant correlation factors from Table A.9 of EC7 were applied to the mean and minimum resistances, in order to calculate a characteristic resistance, $R_{c,k}$=12.1 MN. The appropriate load factors were then applied to the permanent and accidental loads, and divided by the characteristic resistance to determine the number of piles required. This was checked for Load Combinations 1 and 2 of Design Approach 1, and also for Design Approach 2 and for accidental loads.

It is understood that this was only intended to be an illustrative example but, it is suggested, it is so far from reality as to actually be meaningless, because it does not give any real designer any assistance with designing a piled foundation using the results of static load tests. With over 40 years' experience of pile design and construction, the author is unable to conceive of a real project in which four static load tests are carried out, without even knowing how many piles are required on the project. As noted above, the pile lengths varied and were "rationalised to a length of 55.5 m", which begs the question as to how trial pile lengths were selected. In the event, the answer produced was that four piles were required, equal to the number of test piles! It also has to be noted that the example only works for purely vertical loads, which are extremely rare in practice. Most significant piled structures, be they moderate to high rise buildings, or infrastructure such as bridges, are subject to horizontal loads, which almost never are applied at the pile cap level. There are therefore moments to be combined with the vertical and horizontal forces, which means that the maximum pile load will be a function of its position, and that will in turn be a function of the number of piles. That will certainly be the case for a major bridge.

It is therefore believed that, for practical purposes, it is not possible to design piles purely on the basis of static load tests. When designing the foundations for high-rise buildings, it is necessary to iterate backwards and forwards with the structural engineers numerous times, in order to arrive at an optimised pile diameter and layout. This may involve several different load combinations, especially including wind loads on the high towers, and careful analysis of the stiffness of and bending moments in the mat foundation. Alternatively, in the design of foundations for balanced cantilever bridges, each extension of the balanced cantilever involves several new construction load cases, plus all the wind and flood load cases, together with the effects of age on the concrete (cracked modulus) and possible scour of the river bed. Many load cases need to be considered and, for the critical load cases, different layouts need to be tested using different numbers of piles of varying diameter, in order to arrive at an economic solution, which makes maximum reasonable use of available concrete stress.

2.2 *Other pile design methods according to EC7*

Since design using the results of static load tests has been ruled out as normally impractical, the other recommended design methods will be detailed in relation to two projects, one in Bangkok using large diameter bored piles, and one in Queensland using precast concrete driven piles. It is noted that, for design by calculation, as opposed to design by static load test, Clause 2.4.1 requires the use of a "model factor", which seems to be a way of ensuring that a lumped factor of safety is still about 2.5, as it was in working stress design. This has also been referred to by Orr (2012) and Vardenaga et al (2012a), but seems to be unfortunate, since all the finesse gained by the use of partial factors to assess different degrees of uncertainty is once again lost to a lumped factor which incorporates a whole range of disparate uncertainties. It is suggested that the ULS calculation is, in fact, a true representation of that limit state, but that, in many real situations, it is actually the serviceability

limit state which needs to control the design, and requires careful consideration. Design methods appropriate to the SLS are described in Vardenaga et al (2012b), but this is a step for which we appear to be ill prepared. Design has been strength controlled for so long that our site investigation industry is much more attuned to measuring strength than it is to measuring stiffness, and results of various pile performance prediction events would suggest that we still have some way to go in reliably predicting performance (Fellenius et al 2014).

The model factor is also referred to in Clause 7.6.2.3 (2), which precedes both 7.6.2.3 (5) which mentions "profiles of tests", and 7.6.2.3 (8) which refers to use of characteristic strength values. In Frank et al (2004) the pile designs based on profiles of tests are referred to as "model piles". The model factors are not set out in EC7, but have been left to each Country to provide in their National Annex. According to Bond and Simpson (2009) the value of the model factor recommended in the UK National Annex for a case of no static load testing, $\gamma_{Rd} = 1.4$.

3 CASE HISTORY FROM BANGKOK

3.1 *Structural design and action effects*

In practice pile design is a far more complex process than suggested by the Example from the Designer's Guide. The structure in Bangkok comprised three towers, each of 70 floors so about 200 m in height, linked together and built on a single mat foundation, as shown in Figure 1. Bangkok soils consist of alternating layers of sands and clays, laid down in marine, deltaic and fluvial environments, with bedrock reckoned to be at depths of about 500 to1000 m (Balasubramaniam et al, 2004). This meant that the mat could not be a raft foundation, since the superficial layer of about 15 m of soft clay is incapable of providing a useful bearing capacity in the long term, and subject to significant surface settlement, typically about 20 mm per year, as a result of ongoing consolidation caused by underdrainage. Loads in the framed structure were developed during the design, arising from permanent load from the structure as it was progressively sized, live loads on the floors, which are reduced according to local codes for high-rise buildings as it is too conservative to assume full floor loading for every one of 70 floors, together with wind loads and earthquake loads in appropriate combinations.

Typical structural design makes use of numerical analysis, in which foundations such as piles are generally represented by linear elastic springs on a rigid base. The first step was to try to persuade the structural engineers that this model, which showed maximum pile load under the lift core, with a mat foundation dished like a saucer, was not a true representation of load transfer. Use was made of a simple PIGLET model, utilising both rigid and flexible foundation options, in order to try to bracket the behaviour. However the effect of the three linked towers was to create a structural stiffness which, when combined with the flexibility of the real soil, meant that the model suggested maximum pile loads at the corners, the opposite of the structural model. Compatibility was achieved by an iterative process, in which spring stiffnesses in the structural model were adjusted individually, based on the results of the PIGLET analysis, both spatially and according to deflection. The optimum number of 1 m diameter piles under the mat was determined as 399 spaced out on an equilateral grid, and the average ULS action effect was about 6,500 kN. However, when factored in accordance with EC7 this increased to about 9,670 kN, while in accordance with AS 2159 (AS 1170) it was about 8,830 kN, and the maximum ULS action effect was found to be about 11,000 kN, assuming a rigid mat foundation and some yielding of extremely loaded piles.

Figure 1. High rise building for case history from Bangkok

3.2 *Pile design methods*

3.2.1 *Pile design using empirical calculation methods based on static load tests [7.6.2.3]*

The empirical method used here was developed based on a large number of static load tests, carried out in the early 1990s as part of the expansion of urban infrastructure in Bangkok. About 24 tests were carried out on one project, with another 20 undertaken at the Second Bangkok International Airport Project between 2001 and 2005. These tests, many of which were instrumented in order to allow determination of shaft friction values related to displacement, were correlated with the SPT N value since this is still the most widely used test in Bangkok soils. Stroud (1974, 1988) recommended a factor f_1 such that:

$$s_u = f_1 \times N_{60} \quad (2)$$

and suggested that, for low plasticity clays, f_1 = 5. Balasubramaniam et al (2004), quoting Sambhandharaksa and Pitupakorn (1994), stated that for Bangkok clays the equivalent relationship is:

$$s_u = f_2 \times N \quad (3)$$

with f_2 = 6.72, but note that N_{60} is not commonly used in Bangkok. For pile adhesion this is used with an adhesion factor = 0.4, giving a shaft friction value of 2.68 x N. By comparison the Stroud (1974, 1988) value is commonly used with an adhesion factor of 0.5 (Vardanega et al, 2012a), giving a shaft friction value of 2.5 x N. Balakrishnan et al (1999) suggested a value for K_s of 2.3 for the Kenny Hill Formation in Kuala Lumpur based on static load tests, where:

$$q_{sf} = K_s \times N \quad (4)$$

Chang and Broms (1991) recommended K_s = 2 as a design value, and hence with some degree of conservatism, based on static load tests in Singapore. All of these values are very similar and suggest that K_s = 2.5 is probably a reasonable non-conservative design value, although for Bangkok soils the value of K_s = 2.68 has been verified by many static load tests.

3.2.2 *Pile design using the model pile approach [7.6.2.3 (5)]*

Of the empirical methods included in EC7 the preferred approach is the use of "model piles". This involves taking each individual test location, such as a borehole, a CPT position or a series of pressuremeter tests, and designing a single pile, a "model pile" on the basis of the data provided. This is a method which the author used for many years in Bangkok, where it is particularly suitable. This is because it is widely known that Bangkok soils have very strong horizontal stratification, as a result of their deposition, over many cycles of marine regression, in a marine or fluvial environment leading to alternating layers of sands and clays over hundreds of metres of depth. Since the weak layers can occur at various depths, combining the data can lead to conservative estimates of characteristic strength related to the weaker strength values. On the other hand a pile, as a "rigid" vertical element, will tend to average the strength values out. It was found that "model piles" of the same length produced similar capacities from different boreholes as a result of this process.

On the subject site, eleven boreholes were available, as listed in Table 2.

Table 2: Borehole depths and calculated ultimate resistance

Borehole ID	Depth (m)	Ultimate geotechnical resistance (kN)
BH1	80	13269
BH2	80	14262
BH3	80	16620
BH4	80	13141
BH5	80	12464
BH6	80	15002
BH8	60	15366
BH9	60	16340
BH10	60	13183
BH11	60	14577
BH12	60	14264

These were used to create 11 model piles, in a spreadsheet incorporating conversion from SPT N value to shaft friction for both cohesive and granular soil layers. Assuming a 47 m long pile, the results were as shown in the table above, which have a mean of 14,408 kN and a minimum value of 12,464 kN. Table A.10 of EC7 gives ξ_3 = 1.25 and ξ_4 = 1.08 which leads to a characteristic ultimate geotechnical resistance = 11,526 kN.

3.2.3 *Pile design using the characteristic ground profile approach [7.6.2.3 (8)]*

In this method all of the data is considered, as plotted in Figure 2. It is apparent that there are roughly three depth zones below the upper 15 m which is the soft Bangkok marine clay, defined as 15 to 30 m, 30 to 60 m, and 60 to 80 m. These three layers were therefore treated separately. It was decided to use the method proposed by Bond (2011), in which the characteristic value of a parameter which varies with depth is defined by the 95% confidence level of the mean (the 50% fractile), and that proposed by Schneider (1997) in which the characteristic value is defined as half a standard deviation below the mean. For the former the relevant equations are:

$$X_{k,inf} = m_X - k_n s_X \quad (5)$$

Where m_x is the mean value, s_x is the standard deviation, and k_n is a statistical coefficient which depends on Student's t, as follows:

$$k_n = t_{n-1}^{95\%} \times \sqrt{1/n} \quad (6)$$

where $t_{n-1}^{95\%}$ is Student's t-value for *(n-1)* degrees of freedom at a 95% confidence level.

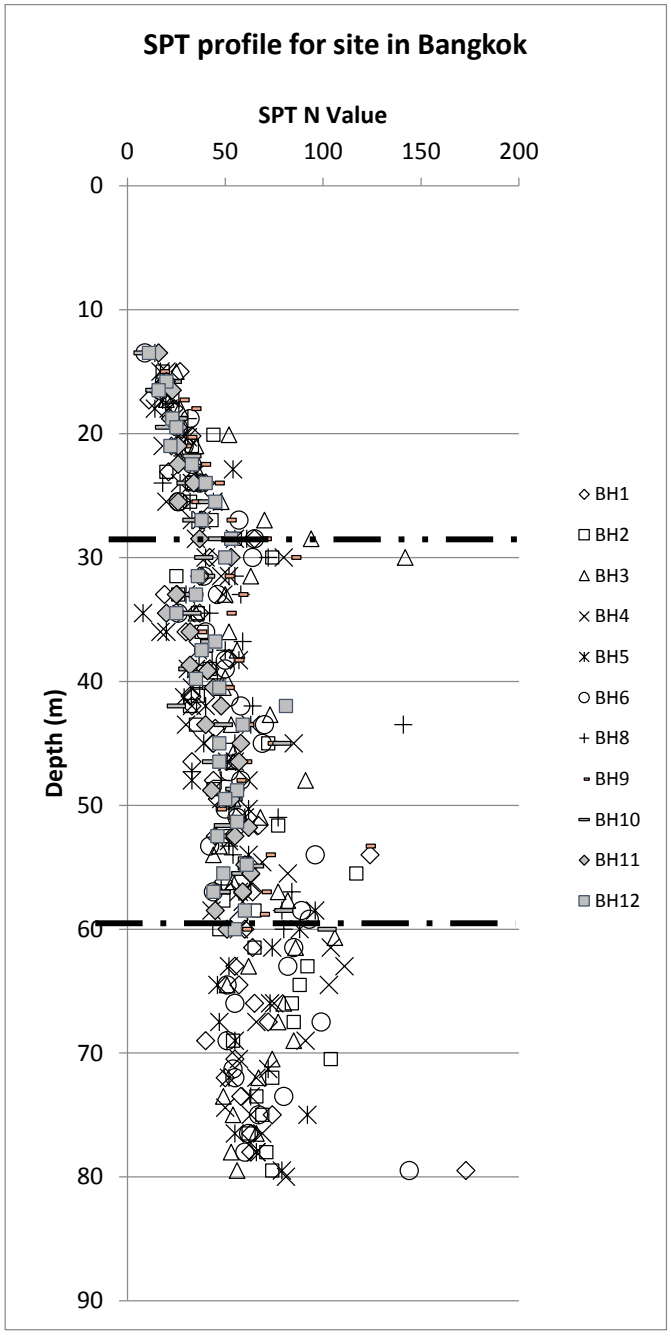

Figure 2. SPT data for first site

Figure 3 shows these two relationships plotted against depth, as well as the mean. It can just be made out that, because of the consistency of the data, the 50% fractile is less conservative than half a standard deviation below the mean for all three layers.

Entering these into the same design spreadsheet as used before, to convert SPT N values to shaft friction and end bearing, and making the calculations for a 47 m long pile, gave a characteristic ultimate geotechnical resistance of $R_{c,k}$ = 13,254 kN using the 50% fractile, and $R_{c,k}$ = 11,787 kN using the characteristic as half a standard deviation below the mean.

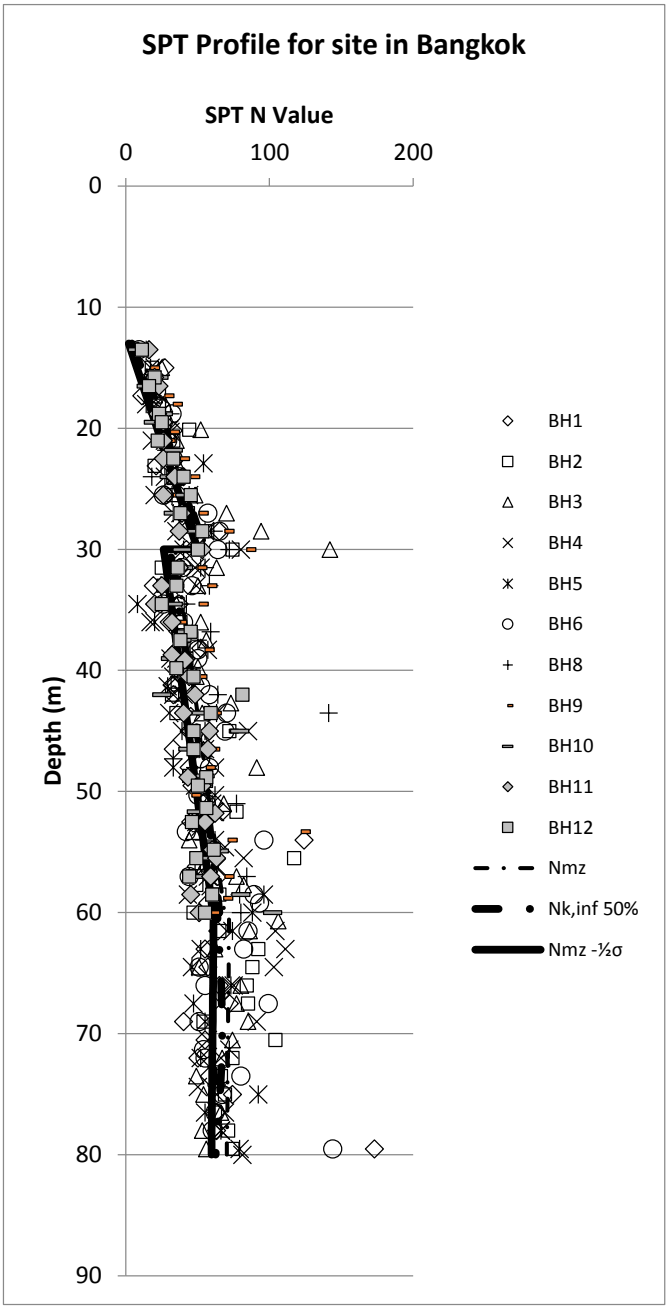

Figure 3. SPT data for first site with design lines

3.2.4 *Pile design using dynamic load test results [7.6.2.4]*

On this site, four dynamic pile tests were also carried out on working piles, and the stress wave records were subjected to signal matching using the CAPWAP software. The results were as shown in Table 3.

These give a mean value of 15,557 kN, and a minimum of 15,277 kN. Table A.11 of EC7 gives ξ_5 = 1.6 and ξ_6 = 1.5, to be applied to the mean and minimum values respectively to determine a characteristic ultimate geotechnical resistance. However, a footnote to the table allows these to be multiplied by 0.85 if signal matching is used. This leads to modified values of

$\xi_5 = 1.36$ and $\xi_6 = 1.275$, which in turn produce a characteristic ultimate geotechnical resistance, $R_{c,k}$ = 11,439 kN.

Table 3: Dynamic pile test results after CAPWAP analysis

Pile No	Ultimate geotechnical resistance (kN)
#P101	15277
#214	15810
#224	15716
#349	15424

3.2.5 *Pile design using static load test results [7.6.2.2]*

In fact, in this case study, a static load test was carried out as a part of the design process for confirmation purposes, allowing a comparison to be made with this method also. The pile behaved better than had been anticipated by the design, such that at the maximum planned test load of 16,795 kN, restricted by the capacity of test frames, jacks and anchor piles, the settlement was only 29.2 mm. The Cemset program (Fleming 1992) was used to extrapolate the load-settlement curve to estimate the load corresponding to a pile head settlement equal to 10% of the pile diameter, a definition of ultimate geotechnical resistance in accordance with EC7. This figure was 20,630 kN. Based on Table A.9 of EC7 the factors ξ_1 and ξ_2 are both equal to 1.4 for a single value, with the result that $R_{c,k}$ = 14,736 kN.

3.3 *Comparison of methods*

It is therefore possible to compare directly the characteristic ultimate geotechnical resistances determined from the different methods for this single site. The results are shown in Table 4.

Table 4: Characteristic ultimate geotechnical resistances by different methods

Pile design method	EC7 Clause	$R_{c,k}$ (kN)
Required ultimate resistance		11,000
Model pile method	7.6.2.3 (5)	11,526
Ground profile method (1)	7.6.2.3 (8)	13,254
Ground profile method (2)	7.6.2.3 (8)	11,787
Dynamic pile tests method	7.6.2.4	11,439
Static load tests method	7.6.2.2	14,736

Ground profile method (1) uses the 50% fractile

Ground profile method (2) uses a characteristic strength half a standard error below the mean

The agreement between three of the methods is startling, with the maximum and minimum within 2% of the mean. The 50% fractile characteristic value was seen to be less conservative than the value based on Schneider, and that is reflected in a characteristic geotechnical resistance 14% above the mean value from the results above. The static load test gave the highest result, demonstrating that the design method of converting SPT N value to shaft friction and end bearing is still conservative, as one would hope, although it has been based on many previous tests.

However, there are a number of factors included in EC7 which have not yet been taken into account. It is noted that they are not applied consistently. For example, the model factor is to be applied to characteristic values determined using ground test results, including model piles, but not to designs based on static load tests or dynamic load tests. It is also noted that the correlation factors for use with static load tests, and those for use with ground profiles, can be multiplied by 1.1 if the structure has enough stiffness to redistribute loads, but the same is not applied to designs based on dynamic load tests or ground test results other than model piles. The result is that Table 4 is modified as shown in Table 5.

Table 5: Characteristic ultimate geotechnical resistances when various additional factors have been applied

Pile design method	EC7 Clause	$R_{c,k}$ (kN)
Required ultimate resistance		11,000
Model pile method	7.6.2.3 (5)	12,464
Ground profile method (1)	7.6.2.3 (8)	9,467
Ground profile method (2)	7.6.2.3 (8)	8,419
Dynamic pile tests method	7.6.2.4	11,439
Static load tests method	7.6.2.2	16,209

It is immediately apparent that there is far less agreement between the different methods, and it is much harder to explain the differences. Since both the model pile method and the ground profile method are based on the same correlation between SPT N value and shaft friction, based on the same set of pile load test data, the significantly more conservative designs based on the ground profile method are very hard to justify.

4 CASE HISTORY FROM QUEENSLAND

4.1 *Structural design and action effects*

In this case the structure was a fluid storage tank associated with a water treatment plant. The pile load was determined from permanent load of the structure, plus permanent live load from the water in the tank, which was to be normally full. Various other load cases were considered, together with negative shaft friction as a result of consolidation of the near surface soft clays under new fill, and the result was a required ultimate geotechnical strength of 1,995 kN. As in the previous case study, the relationship between structural design, involving all the various imposed loads in different combinations with appropriate factors, and geotechnical design which accounts for soil structure interaction, and deformation within the soil particularly for large pile groups, is complex and required close cooperation and iterations between the designers. 270 mm square precast concrete piles were

to be used, and about 300 were required to support the structure.

4.2 *Pile design methods*

4.2.1 *Pile design using empirical calculation methods based on static load tests [7.6.2.3]*

The geotechnical investigations had involved a number of phases, over a number of years, as set out in Table 6.

Although a total of 13 CPT tests and 23 boreholes were carried out, only the last three boreholes in the later years were deep enough to be used for pile design. A weak alluvial layer in the top 10 m would not provide shaft friction support, but would in fact create negative shaft friction loads on the piles.

Because of a lack of static load testing results available for Queensland soils, the same relationship between SPT N value and shaft friction was used as was derived in Bangkok. This is clearly very poor in relation to site specific correlations, or even to correlations based on the same geology but, in some circumstances such as this may become necessary and will have to be taken into account in the selection of appropriate factors.

4.2.2 *Pile design using the model pile approach [7.6.2.3 (5)]*

In Figure 4 all of the SPT N values from the three boreholes are plotted. The individual boreholes were used to create three "model piles". The ultimate geotechnical resistances were calculated as shown in Table 7.

Table7: Ultimate geotechnical resistances from model pile approach

BH ID	Ultimate Geotechnical Resistance (kN)
BH101	2728.6
BH102	2904.5
BH103	2830.3

These in turn led to a mean value of 2821 and a minimum value of 2729 kN. For three model piles the correlation factors from Table A.10 of EC7 are ξ_3 = 1.33 and ξ_4 = 1.23. The resulting characteristic ultimate geotechnical resistance was $R_{c,k}$ = 2,121 kN.

4.2.3 *Pile design using the characteristic ground profile approach [7.6.2.3 (8)]*

Figure 5 shows the mean line after removal of data for the upper soft soils, with the inferior characteristic and the line half a standard deviation below the mean. The formulae from these two lines have then been entered into the same design spreadsheet as previously with the following results. The characteristic ultimate geotechnical resistance using the 50% fractile was $R_{c,k}$ = 2,947 kN, and using the values half a standard deviation below the mean was $R_{c,k}$ = 2,379 kN.

Table 6: Available ground investigation information

2006		2009		2010		2010	
BH ID	Depth (m)	BH ID	Depth (m)	BH ID	Depth (m)	BH ID	Depth (m)
BH01	5	BH01	3	BH01	23.95	BH101	38.5
BH02	5	BH02	3	BH02	23.75	BH102	40.06
BH03	5	BH03	3	CPT1	15.4	BH103	40.4
BH04	5	BH04	3	CPT2	15.73		
BH05	15.45	BH05	3	CPT3	15.08		
BH06	15.45	BH06	3	CPT4	14.85		
BH07	20.95	BH07	3	CPT5	15.08		
BH08	18.45	BH08	19.5	CPT6	15.23		
		BH09	18	CPT7	15.58		
		BH10	18	CPT8	15.25		
		CPT1	17	CPT9	15.38		
		CPT2	14.53	CPT10	21.35		
		CPT3	15.63				

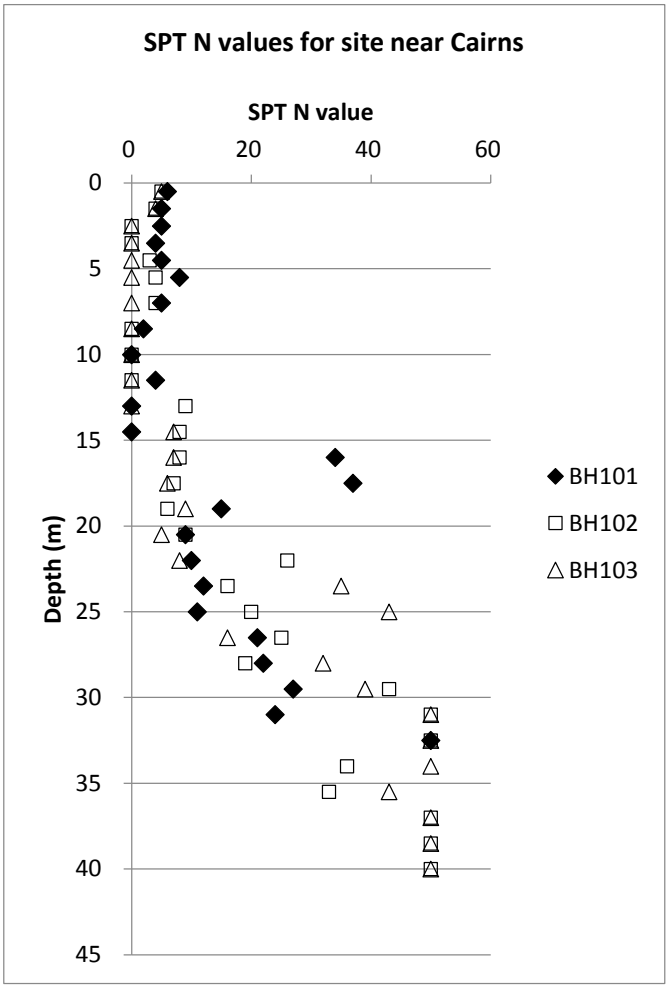

Figure 4. SPT data for second site

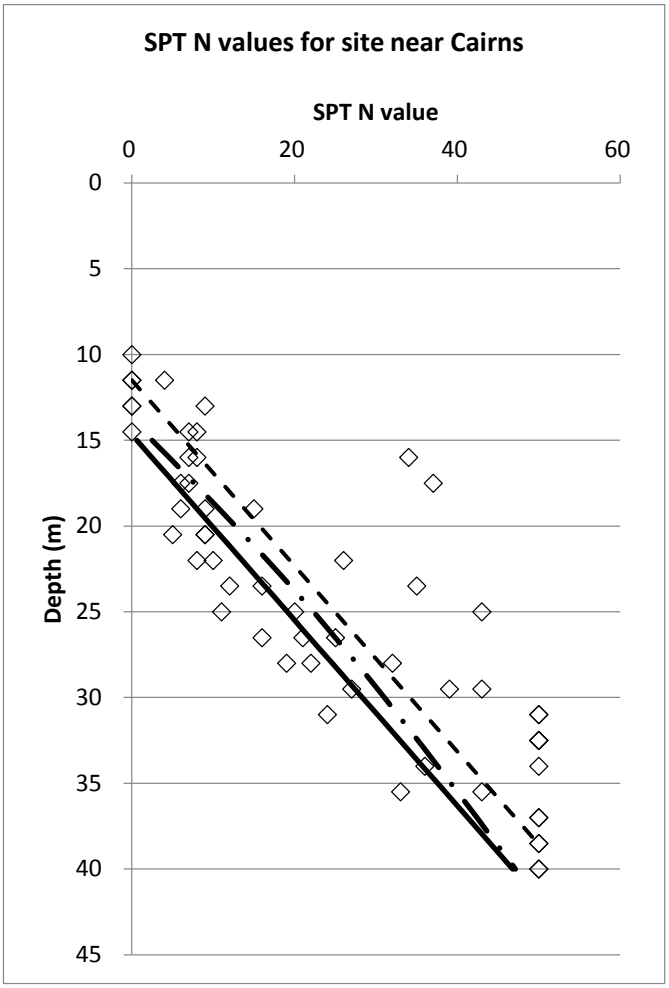

Figure 5. Selected SPT data for second site with design lines

4.2.4 *Pile design using dynamic load test results [7.6.2.4]*

On this site 15 dynamic pile tests were carried out, and the ultimate geotechnical resistances determined from the wave equation analysis (Case Method) were as given in Table 8.

Table 8: Ultimate geotechnical resistances from dynamic pile tests

Pile ID	DPT results	Pile ID	DPT results
CP21	2568	P36	2599
CP27	2581	P59	2712
CP32	2728	P95	2610
CP73	2554	P99	2665
CP79	2839	P113	2821
CP84	2541	P114	2867
IW4	2534	UP4	2650
P12	2453		

For 15 dynamic pile tests the correlation factors from Table A.11 of EC7 are $\xi_5 = 1.42$ and $\xi_6 = 1.25$, which lead to a characteristic ultimate geotechnical resistance $R_{c,k} = 1{,}869$ kN.

This value is clearly low, and reflects the large factors that need to be applied to wave equation analysis evaluations because of uncertainties over critical issues such as selection of damping factors which have a major impact on the outcome. As previously, Table A.11 of EC7 also allows a reduction of these correlation factors by 0.85 if signal matching is used, such as CAPWAP. On this site 5 of the DPT results were subject to CAPWAP analysis. The correlation factors increase because of the smaller number of tests, but this is more than offset by the reduction to 85%. The appropriate correlation factors are $\xi_5 = 1.275$ and $\xi_6 = 1.1475$ and these lead to a characteristic ultimate geotechnical resistance = 2,017 kN.

The results are summarised in Table 9.

Table 9: Summary of ultimate geotechnical resistance values by different methods

Pile design method	EC7 Clause	$R_{c,k}$ (kN)
Required ultimate resistance		1,995
Model pile method	7.6.2.3 (5)	2,121
Ground profile method (1)	7.6.2.3 (8)	2,947
Ground profile method (2)	7.6.2.3 (8)	2,379
Dynamic pile tests method (1)	7.6.2.4	1,869
Dynamic pile tests method (2)	7.6.2.4	2,017

Unfortunately no static load tests were carried out on this site to give that added correlation. Nevertheless it can be seen that the design satisfied the ULS inequality in every case except for the use of dynamic pile testing without signal matching.

As with the first case study, we have not yet applied the additional factors, such as model factors and superstructure stiffness factors, recommended by EC7. Again these are applied inconsistently, with characteristic ultimate geotechnical strengths increased due to load sharing only for the model pile method, since there are no static load tests, and reduced because of the application of the model factor, for the model pile method and both ground profile methods, but not for the dynamic pile test methods. The results are as set out in Table 10.

Table 10: Summary of ultimate geotechnical resistances after additional factors

Pile design method	EC7 Clause	$R_{c,k}$ (kN)
Required ultimate resistance		1,995
Model pile method	7.6.2.3 (5)	1,667
Ground profile method (1)	7.6.2.3 (8)	2,105
Ground profile method (2)	7.6.2.3 (8)	1,699
Dynamic pile tests method (1)	7.6.2.4	1,869
Dynamic pile tests method (2)	7.6.2.4	2,017

The obvious result is that now three of the methods fail to meet the required ultimate geotechnical strength, and this is considered to be unduly conservative.

5 PILE DESIGN METHODS ACCORDING TO AS 2159-2009

Australia has had a limit state design code for piling since 1985. This has used the resistance factor method applied to the overall resistance, rather than the strength factor method applied to individual components of strength, and has applied a geotechnical strength reduction factor, φ_g, selected by the designer. In the 1995 version there was a table, Table 4.1, which allocated a range of values to φ_g according to design method. These ranged from $0.7 < \varphi_g < 0.9$, for piles subject to static load testing, through $0.5 < \varphi_g < 0.85$ for dynamic load tests, to $0.4 < \varphi_g < 0.55$ for static analyses or pile driving formulae.

One of the problems with this method was that, even though guidance was given in Table 4.2 as to from where in the given range the reduction factor should be selected, based on quality and quantity of data and methods available, it was inevitably found that designers employed by clients in conventional roles would be more conservative than those employed by contractors in Design & Construct roles.

An attempt was made to reduce this discrepancy in the 2009 revision of the standard, and also to encourage static load testing, which has become extremely rare in Australia. The new derivation of the geotechnical resistance factor is now a risk based approach, in which nine influencing attributes are each evaluated on a scale of 1 to 5, 1 representing the lowest risk, and appropriate weightings are applied to each attribute.

The average risk rating, ARR, is then defined as the sum if the individual ratings each multiplied by its weighting, divided by the sum of the weightings. The ARR is then used to determine a basic geotechnical strength reduction factor, φ_{gb}, from which the final value of φ_g is determined based on the amount of static or dynamic load testing to be carried out. The appropriate geotechnical strength reduction factor is then applied to the design ultimate geotechnical strength, $R_{d,ug}$, to give the design geotechnical strength, $R_{d,g}$. The design ultimate geotechnical strength is to be determined from:

a. Analysis using data from a site investigation
b. Analysis based on dynamic data obtained during installation of test or working piles (pile driving formula, wave equation analysis, closed form solutions or signal matching)
c. Analysis of data collected during pile installation
d. Analysis using data from a static, rapid or bi-directional load test

Standard formulae for shaft and base resistance are recommended, using average shaft friction in compression, $f_{m,s}$ and base resistance, f_b, with the comment:

"In assessing $f_{m,s}$ and f_b, consideration shall be given to the pile type, the method of installation, the soil type and other factors which may influence $f_{m,s}$, and f_b, such as the installed condition of the shaft and base."

This gives no clear guidance as to what strength values should be used, and Vardenaga et al (2012a) commented "It does seem curious that partial factors can be assigned without knowledge of how conservatively engineers treat their soil data." It is noted that AS 2159 assigns a geotechnical strength reduction factor to the second decimal place, while Vardenaga et al selected a 25th percentile as the appropriate strength when others might well have chosen half a standard deviation below the mean, or even the mean, expecting the strength reduction factor to deal with uncertainty.

It is interesting that AS 2159 does not refer anywhere to "characteristic" strength for soil or rock, and reserves the term only for concrete. It does introduce a term, R_{ug}, within the definitions which is described as the "Ultimate geotechnical strength of a pile. This is estimated either by calculation ($R_{d,ug}$) or by test ($R_{t,ug}$)" and also as "The resistance developed by an axially or laterally loaded pile or pile group at which static equilibrium is lost or at which the supporting ground fails."

Since this value can only be *estimated* by design or by test, it would appear to be a notional ultimate strength. It is only subsequently used in relation to jacked piles and pile testing. Although guidance is given on the determination of $R_{d,ug}$, which is taken to be a good estimate of R_{ug}, there is much less help with $R_{t,ug}$. This will be discussed again later.

There is also a catch within AS 2159-2009, which is in the chapter on testing, Section 8, rather than in the design chapter where all the other material related to φ_g can be found. Clause 8.2.4 (c) states:

"Where the basic geotechnical strength reduction factor is greater than 0.4, the following testing shall be undertaken:

(i) In the absence of tests to verify design ultimate geotechnical strength, testing shall be performed to verify pile serviceability for all foundations with average risk rating of 2.5 or greater. The relevant acceptance criteria nominated in Clauses 8.4.3 and 8.5.2 shall apply. The minimum rate of testing will depend on the average risk rating, as tabulated in Table 8.2.4(A).

(ii) Testing shall be performed to verify the integrity of pile shafts. Assessment of pile shaft integrity may be by high-strain dynamic pie testing (see Clause 8.5), or other methods of integrity testing (see Clause 8.8).

(iii) (This clause sets out the percentage of piles for integrity testing, according to ARR)."

Thus, for any pile with a geotechnical strength reduction factor greater than 0.4, at least integrity testing is required, and, if ARR > 2.5 (i.e. the risk rating is higher than very low or low), proof load testing is also required. The corollary is that, if no testing is carried out, φ_g cannot be greater than 0.4.

6 CASE HISTORY FROM BANGKOK

6.1 *Structural design and action effects*

Using the load factors of AS 1170 (Australian Standards 2002), the design action effect was determined to be about 8830 kN. For no pile testing, with $\varphi_g = 0.4$ this is equivalent to $R_{d,ug} \geq 22{,}075$ kN. Based on the calculations considered earlier with regard to EC7, this would clearly be an uneconomic design.

With a significant amount of site investigation, including boreholes to 80 m, extensive experience in the Bangkok soils over many years an many load tests, the calculated ARR = 1.76, leading to $\varphi_g = 0.70$ for high redundancy systems, such as 399 piles under a single mat. If four dynamic load tests are carried out on bored piles, this increases to 0.71, and if a single static load test is carried out, it increases to 0.72. Thus the required $R_{d,ug} \geq 12{,}265$ kN.

6.2 *Geotechnical design*

The geotechnical design could be carried out by the model pile procedure of EC7, as was the author's standard practice, which would have led to a mean design ultimate geotechnical strength = 14,408 kN or a minimum = 12,464 kN. This satisfies the inequality. The four dynamic pile test results then all confirm the design, with a mean ultimate geotechnical strength = 15,557 kN and a minimum = 15,277 kN. The static load test, with a predicted ultimate geotechnical strength = 20,630 kN, also confirms the design.

7 CASE HISTORY FROM QUEENSLAND

7.1 *Structural design and action effects*

AS 2159-2009 does not require negative shaft friction to be taken into account at the geotechnical ultimate limit state, although it must be considered in relation to the structural ultimate limit state and at the serviceability limit state. The argument is that, if the ultimate geotechnical limit state were to occur, then any soil-pile movement which had mobilised negative shaft friction would be reversed. As a result the action effect, E_d = 1,500 kN. The piles were installed under a D&C contract allowing the piling contractor to select the geotechnical strength reduction factor. As stated previously, without any testing at all this would have been restricted to 0.4 by Clause 8.2.4 (c), and this would have required $R_{d,ug} \geq 3{,}750$ kN which would be very unlikely to be economic, especially for driven piling where dynamic load testing is readily available at little extra cost. In the event the contractor/designer opted for 10% pile testing allowing them to select a $\varphi_g = 0.74$, requiring $R_{d,ug} \geq 2{,}027$ kN.

7.2 *Geotechnical design*

Using the same geotechnical design method as for the EC7 design, the three model piles gave ultimate geotechnical resistances of 2,729, 2,904 and 2,830 kN, which would have been more than adequate. Fifteen dynamic pile test results with a mean of 2,654 kN and a minimum of 2,453 kN would also have confirmed the design, as would the five CAPWAP results with a mean of 2,572 kN and a minimum of 2,539 kN.

In the event, when the design was submitted to the structural engineer for comment, a number of queries were raised, mainly on structural issues. The contractor/designer then took the unusual step of withdrawing the calculations on the basis that the dynamic pile testing had proven the design, because the minimum test value was higher than the required ultimate geotechnical strength. However, this then created the dilemma that a design based on a "characteristic" strength was not available, and it was necessary to

consider, based on the dynamic load test results available, what results might have been obtained if all piles had been tested. No guidance is available for this situation in AS 2159-2009, as mentioned above.

It is a matter of statistics, and one approach would be to use the factors in EC7 applied to minimum and mean strengths. This gives a characteristic strength, as before, of 1,869 kN based on the dynamic load tests, and 2,017 based on the CAPWAP results, neither of which is enough. The problem is that, with the use of the geotechnical strength reduction factor and the correlation factors together, there is almost certainly too much conservatism built into the design. It also highlights the problems that can occur when mixing elements from more than one code.

8 COMPARISON OF CODES

It may be useful to compare the numerical results obtained by use of the two different codes. This is attempted in Table 11 below, and it appears that, for the same pile size and length. The EC7 values are more conservative than the AS 2159 values. However caution is advised, as it is not a matter of simply looking at the numbers. The ultimate geotechnical resistance values from EC7 are characteristic values, whereas there is no equivalent in AS2159. It must also be noted that these values are used in the basic inequality, of the form:

$$F_{c;d} \leq R_{c;d} \tag{7}$$

and that the magnitude of the design action effect may vary.

It also needs to be noted that these comparisons have been made at the ultimate limit state, which is often the first state to be examined, probably because of history in working stress design. AS2159 specifically requires examination of the serviceability limit state, whereas EC7 states in a note under 7.6.4.1 (2) that "for piles bearing in medium-to-dense soils …. The safety requirements for the ultimate limit state are normally sufficient to pre vent a serviceability limit state in the supported structure."

9 CONCLUSIONS

- The design of piled foundations in real situations is more complex than is implied by some of the published data, including examples of how to use design standards such as EC7.
- Although design of piled foundations using the results of static load tests directly is the preferred option according to EC7, the method is not likely to be practical for the design of real foundations.
- The design of piled foundations by empirical methods based on the results of static load tests is a practical solution, which can provide credible results.
- These methods can include the use of "model piles", where an empirical design is based on each individual investigation position, such as a borehole or an in situ test (e.g. CPT) profile.
- They can also involve methods in which characteristic strength profiles are determined from a number of boreholes, and these have been shown to give compatible results.
- With regard to site characterisation, the use of the model pile approach or the use of characteristic strength profiles gave very similar results when rational methods were used to produce the strength profiles.
- The design of piled foundations using the results of dynamic load tests has been shown to produce results which are compatible with the above methods, but this would still require the installation of a number of piles ahead of the main works in order to establish the design.
- The application of some of the additional factors according to EC7, such as the "model factor" and the foundation stiffness factor, appear to be somewhat inconsistent and, in some cases, unnecessary.
- Both foundations considered, one for bored piles and one for driven piles, appeared to be able to meet the requirements of both EC7 and AS2159-2009.

Table 11: Comparison of the results from the two codes

Site	With or without testing	Code	
		EC7 – $R_{c,k}$ (kN)	AS2159 – $R_{d,ug}$ (kN)
Bangkok	No testing	11,526	12,464
	With static load testing	11,434	15,277
	With dynamic testing	14,736	20,630
Queensland	No testing	2,121	2,379
	With dynamic testing	2,017	2,017

10 ENDNOTE

It should be noted that, while the author has a keen interest in EC7 and has followed its development over several decades, he does not use it on a regular basis nor is he subject to any National Annex, which is a crucial part of the application. Therefore the factors referred to, and comments made upon them, are from the base document and many of these will have been modified by a National Annex. The exception is the Model Factor, for which no value is given in the base document, so the value of 1.4 has been taken from the UK National Annex.

11 REFERENCES

Balakrishnan, E.G., Balasubramaniam, A.S., & Phien-wej, N. 1999. Load deformation analysis of bored piles in residual weathered formation. *ASCE, Journal of Geotechnical and Geoenvironmental Engineering,* 125, 2, 122-131.

Balasubramaniam, A.S., Phienwej, N., Gan, C.H. & Oh, Y.N. 2004. Piled foundations and basement excavations for tall buildings in Bangkok subsoils. *Proceedings of the Malaysian Geotechnical Conference, Kuala Lumpur.*

Bond, A.J. 2011. A procedure for determining the characteristic value of a geotechnical parameter. *Proceedings 3rd International Symposium on Geotechnical Safety and Risk, Munich, Germany,* 419-426.

Bond, A.J. & Simpson, B. 2009. Pile design to Eurocode 7 and the UK National Annex. Part 1: Eurocode 7. *Ground Engineering, London*, 42, 12, 27-31.

Bond, A.J. & Simpson, B. 2010. Pile design to Eurocode 7 and the UL National Annex. Part 2: UK National Annex. *Ground Engineering, London*, 43, 1, 28-31

Bond, A.J. & Harris, A. 2008. *Decoding Eurocode 7.* London, Taylor & Francis, 598 pp.

BSI. 2010. BS EN 1997-1. *Eurocode 7: Geotechnical Design, Part 1: General Rules.* British Standards Institution, London.

Chang, M.F. & Broms, B. 1991. Design of bored piles in residual soils based on field-performance data. *Canadian Geotechnical Journal,* 28, 200-209.

Fellenius, B.H. & Terceros, M.H. 2014. Response to Load for Four Different Bored Piles. *Proceedings of the DFI-EFFC International Conference on Piling and Deep Foundations, Stockholm*, May 21-23, pp. 99 120.

Fleming, W.G.K. 1992. A new method for single pile settlement prediction and analysis. *Geotechnique*, 42, 3, 411-425.

Frank, R., Bauduin, C., Driscoll, R., Kavvadas, M., Krebs Ovesen, N., Orr, T. and Schuppener, B. 2004. *Designers' Guide to EN 1997-1 Eurocode 7: Geotechnical design – General rules,* Thomas Telford, London, 216 pp.

Orr, T.L.L. 2012. How Eurocode 7 has affected geotechnical design: a review. *Proceedings of the Institution of Civil Engineers, Geotechnical Engineering*, 165, GE6, 337-350.

Sambhandharaksa, S. & Pitupakorn, W. 1985. Predictions of prestressed concrete pile capacity in Bangkok stiff clay and clayey sand. *Proceedings of the 8th Southeast Asian Geotechnical Conference, Kuala Lumpur*, F207- F212.

Schneider, H.R. 1997. Definition and determination of characteristic soil properties. *Proceedings of the 12th International Conference on Soil Mechanics and Foundation Engineering, Hamburg, Germany,* Balkema, 2271-2274.

Standards Australia. 2002. AS/NZS 1170.0:2002. *Structural design actions, Part 0: General principles.*

Standards Australia. 2009. AS 2159-2009. *Piling – Design and installation.*

Stroud, M. 1974. The standard penetration test in sensitive clays and weak rocks. *Proceedings of the European Symposium on Penetration Testing, Stockholm, Sweden*, 2:2, 366-375.

Stroud, M. 1988. The Standard Penetration Test – Its application and interpretation Part 2. *Proceedings of Penetration testing in the UK,* Thomas Telford, London, 29-47.

Vardenaga, P.J., Kolody, E., Pennington, S.H., Morrison, P.R.J. & Simpson, B. 2012a. Bored pile design in stiff clay I: codes of practice. *Proceedings of the Institution of Civil Engineers, Geotechnical Engineering*, 165, GE4, 213-232.

Vardenaga, P.J., Williamson, M.G. & Bolton, M.D. 2012b. Bored pile design in stiff clay II: mechanisms and uncertainty. *Proceedings of the Institution of Civil Engineers, Geotechnical Engineering,* 165, GE4, 233-246.

Geotechnical and Geophysical Site Characterisation 5 – Lehane, Acosta-Martínez & Kelly (Eds)

Different response of apparently identical structures: a far-field lesson from the Mirandola (Italy) 2012 earthquake

S. Castellaro
Dep. Physics and Astronomy, University of Bologna (Italy)

ABSTRACT: Twin structures, that is structures very similar in terms of geometry, materials, mass distribution etc., founded on the same soil and set at very close distance, are rationally expected to have an identical response to earthquakes. When this does not occur, a role is usually played by factors like the interaction with the surrounding structures or by other anomalies hidden behind the apparent similarity. The case of two apparently identical twin towers that showed a very different response to the 2012 Mirandola (Italy) earthquake ground shaking is presented: one remained perfectly intact while the other had a wide set of fractures on secondary walls. This resulted to be the effect of several contributing factors: the stiffness of the two structures, experimentally measured, provided unexpected differences. This reflected into different modal frequencies for the two towers, with the first and second modes of the damaged tower coincident or very close to the soil resonance. The final result was a coupled soil-structure resonance, implying a much higher displacement of one tower compared to the other, under the same input motion. In Italy, insurance against earthquake damage will probably become compulsory in the near future. This case suggests that the specific soil-structure and structure-structure interaction will have to be carefully evaluated since they can critically affect even apparently identical structures.

1 INTRODUCTION

North East off the Old City of Bologna (Northern Italy) there exist two modern structures (tower A and tower B) - identical to the sight - characterized by the same geometry and construction style, set at about 120 m distance one from the other (Figure 1). The height of both towers is 56 m and their basement area is approximately 20 by 40 m. The horizontal section of the towers is a portion of annulus with a common centre. The two structures are located at different distances from the centre, which results in a slightly different curvature, hardly perceptible to the sight.

However, the different curvature is mostly an architectonical element since the façade, built with lightweight steel elements, is separated from the main bearing structure. Two reinforced concrete (RC) shear walls and two RC stair cores, together with an irregular layout of steel columns, form the main bearing structure. The geometry and position of the shear walls and stair cores is very similar in the two structures, while the steel columns are located in slightly different positions. The structures were designed at the end of the '90s and built in the early 2000, according to building codes that did not take into account horizontal loads induced by seismic motion but only horizontal loads induced by wind.

Figure 1. Sketch of the two towers.

The two structures responded in a very different way to the Mirandola (Modena, 44.89°N, 11.23°E), May 20th 2012 M_L = 5.9 earthquake, the epicenter of which was located at a distance of about 45 km North. Specifically, tower A did not suffer from any damage while tower B presented extensive damage in the internal walls (though only aesthetic damages).
We attempt to provide an explanation for such a different behavior through a dynamic analysis of the structures and of the foundation soil.

2 DYNAMIC ANALYSIS OF THE STRUCTURES AND SOIL

2.1 *Experimental structure analysis*

As already stated, the main structural elements are two RC shear walls and two RC stair cores. An irregular layout of double-T steel columns complete the bearing structure. Both structures are set on a strip foundation (approx. 1 m thick) at 12 m depth under tower A and 10 m depth under tower B. In practice, tower A has one underground level more than tower B, even though the absolute depth of the foundations differ by 2 m only.

The dynamic characterization of the structures was conducted in passive mode, using seismic microtremors as an excitation function. On each tower we recorded the motion at all the even levels on a vertical alignment close to the barycentre (as close as possible, compatibly with the tower accessibility) and on a vertical alignment close to a corner. Since in passive surveys the source is spatially distributed and may change with time (e.g. due to wind, traffic etc.) a reference instrument was set at the foundation level of each structure while moving the other instruments at different levels along the same vertical axis. Eventually, all the measurements were referred to the reference instruments, which therefore acted as a 'normalization'. In order to ensure the stationarity of the excitation, the survey was conducted in a short time span (approximately 3 hours), by sampling microtremors for 15 minutes at each location and continuously at the reference sites. Longer measurements (6 hours) were conducted at the topmost levels of the two towers to characterize their damping.

The experiment was conducted simultaneously on the two structures using four Tromino® digital tromographs (MpHo srl). Each instrument is a stand-alone unit which can be linked to the others through the built-in radio and which measure both velocity and accelerations. The instruments were simply laid down on the surveyed floors with no particular anchorage other than the instrumental weight (~1 kg) The survey was conducted twice, the first time in July 2012 and the second time in May 2013. The analysis allowed us to obtain: 1) the modal frequencies, 2) the modal shapes and 3) the damping:

The modal frequencies appear as peaks in the horizontal spectra of the recorded motion at each floor. However, in order to normalize for the possible amplitude drifts of the natural input during the measurement, spectra recorded at each floor where divided by the corresponding (in time) spectrum measured by the reference instrument at the foundation floor. This results in plots with adimensional y-axis, since they represent ratios between amplitude velocity spectra. Due to the absence of wind during the surveys, we assumed that the main difference in the excitation function came from the subsoil and this is the reason for putting the reference instruments at the foundation level. Results are shown in Figure 2 and indicate that the first flexural mode of tower A is at 1.1 Hz in the transverse direction and at 1.2 Hz in the longitudinal direction. The modal shapes for the transversal and longitudinal direction are shown in Figure 3 and 4. This tower was analyzed also 3 years before (Castellaro e Mulargia, 2010) and the modal frequencies and shapes obtained from the present survey coincide with those obtained from the previous survey, thus indicating that neither earthquake nor ageing have caused any structural damage to the tower. Measurements on the B tower had unexpected features: the first flexural mode in the transversal direction appeared at 0.9 Hz (i.e 20% lower than the twin tower A) and at 1.1 Hz along the longitudinal axis (i.e. 8% lower than the twin tower B).

From the above comparison we observe that the dynamics of the two towers is rather similar along the longitudinal axis (in terms of both frequency and amplitude) while - as anticipated - the transversal behavior is very different for two supposedly almost identical structures. Since the mass distribution of the two towers is very similar, a lower stiffness of tower B compared to tower A must be responsible for this difference. The slightly different curvature of the two towers is mostly an architectural element, therefore it is not expected to play a role higher than a very small percentage in this difference. The different depth of the foundation embedment could instead play a bigger role but, as we will see later from the results of a numerical model, can only account for about 6% of the difference. Other factors must therefore determine this difference: variations in structural layouts, structural details and material properties are the best candidates. In fact, the dissimilar layout of steel columns might also explain why the variation between natural frequencies is larger among the transversal rather than among the longitudinal modes.

For what refers to higher modes, the modal analysis revealed that the second mode (1.6 Hz for tower A and 1.4 Hz for tower B) is a torsion mode. This emerges from the correlation of the intra-floor (corner to centre) measurements which emphasizes the torsion modes. The second flexion modes appear at frequencies of approximately 4-4.5 Hz and shapes the structures as illustrated in Figure 3.

Concerning modal shape amplitudes, we observe that under the excitation of ambient noise, tower B has an excursion which is 40% larger than tower A in the transversal direction while in the longitudinal direction the dynamics is identical both in frequency and amplitude. The displacement of tower B is 40% larger than tower A also for the first torsion mode.

The main hypotheses that could explain the differences in amplitudes are the same proposed to explain the difference in the natural frequencies, i.e., a) differences in the foundation embedment and b) differences in the structural stiffness, due to several possible factors.

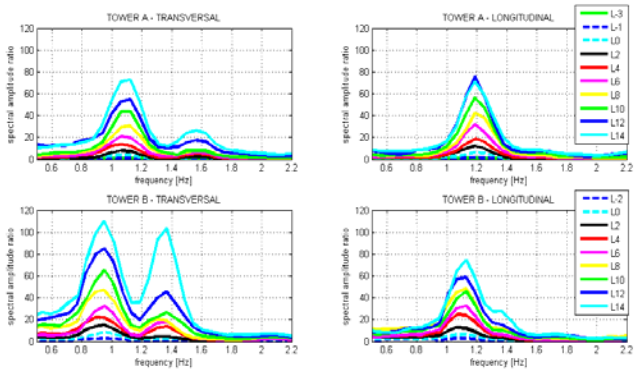

Figure 2. Modal frequencies of towers A and B obtained from the ratio of the spectra recorded at the different levels and those at the reference level (foundation floor). We observe that the behavior along the longitudinal axis is rather similar, while a substantial difference (both in terms of frequency and amplitude) appears on the transversal axis.

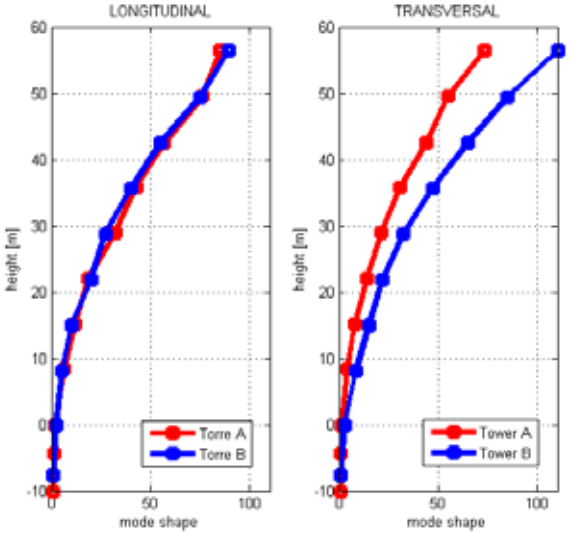

Figure 3. First flexion mode shapes (normalized to the foundation level) of tower A and B in the longitudinal and transversal direction.

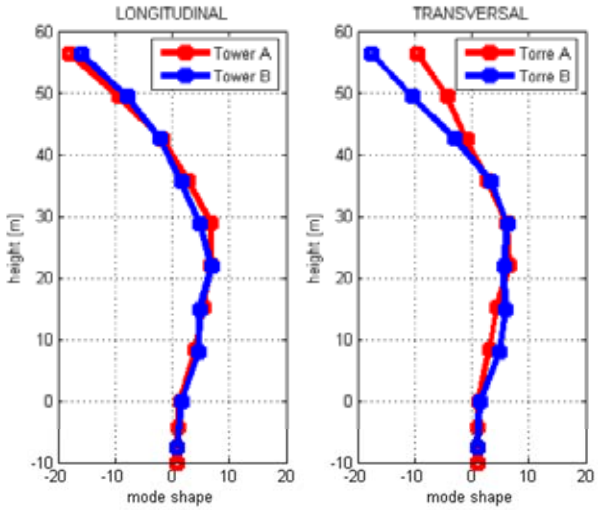

Figure 4. Second flexure mode shapes (normalized to the foundation level) of tower A and B in the longitudinal and transversal direction.

2.2 *Soil analysis*

The foundation soil of the tower has been surveyed several times in the past and presents shear wave velocity values (Vs) of about 200 m/s and a main resonance frequency, well known in this part of the river Po Plain, of 0.8 Hz. The results of the multichannel passive/active surface wave based surveys, of the H/V curves and their joint fit and interpretation are shown in Figure 5. The first observation is that tower B is in resonance with the soil: the first flexion mode is coincident and the first torsion mode is very close to the soil resonance frequency. This does not occur for tower A (red and blue shades in Figure 5)

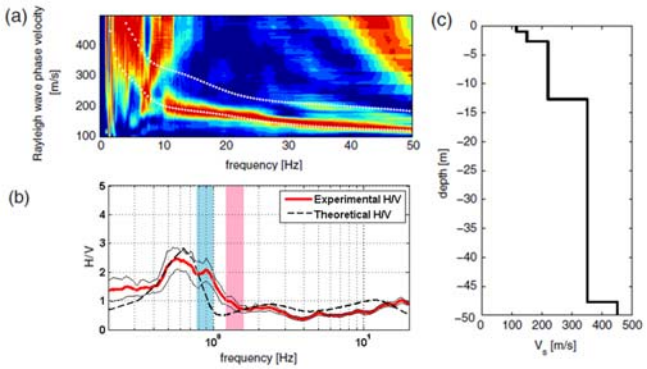

Figure 5. A) Rayleigh phase velocity spectra recorded on the free-field surrounding the towers, B) average H/V curve (red) ± standard deviation (thin black line) of the site. The shaded areas represent the frequency of the first flexion mode of tower A (red) and B (light blue).
The joint fit of A) and B) suggests the Vs model illustrated in C). The theoretical dispersion curve (first 2 modes) is given by the white circles in panel A) and by the black dashed line in panel B). The investigation depth reached by the survey A) is limited to 15 m. The remaining part of the model was obtained by the joint fit of A) and B) beyond this depth.

2.3 Soil-structure interaction

In a former study (Castellaro and Mulargia, 2010) we evaluated the soil-structure interaction in the case of large structures and we concluded that the radiation of the structure motion to the soil, which decays as the inverse of the distance, is more evident when the soil and structure resonances coincide.

In the case of the towers under analysis we expect that the motion of the undamaged tower A, which has resonances far from the soil resonance, is much less visible on the surrounding soil compared to the motion of the damaged tower B, which is in double-resonance with the soil. This is in fact what we observe: at 7 m distance from the foundation perimeter the effect of the radiation of the tower A to the soil is negligible.

In the case of tower B, where the first and second modes occur at frequencies very close to the soil one, the tower motion is radiated to the soil up to at least 40 m from the center of the tower (Figure 5).

We remind that the radiation of a structure motion to the soil appears as a sharp peak in the spectra recorded on the soil at the resonance frequency(ies) of the structure. This peak is more evident on the horizontal components but can also be evident on the vertical component, as a function of the rocking. As a further evidence, the peak fades while moving away from the structure. This cannot be confused with the soil resonances because in microtremor recordings the latter are identified by a local minimum in the vertical spectral component while the horizontal ones usually do not show any peak or, when they do it (as an effect of SH or Love waves), a) its amplitude does not decay with the distance from the structure, b) it has a much broader 'gaussian' shape than the sharp peaks typical of the structures.

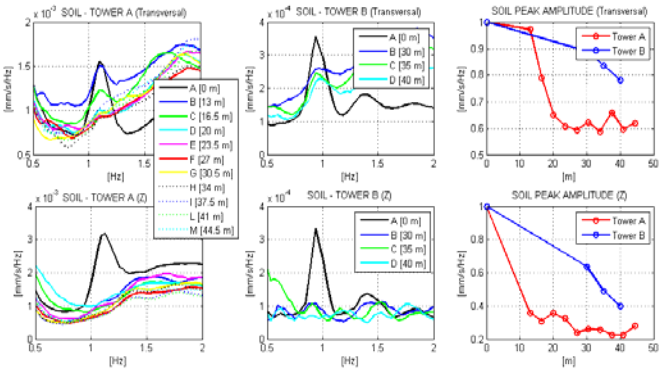

Figure 5. *Left column:* horizontal (top) and vertical (bottom) spectra recorded on the ground at different distances from tower A. *Center column:* same for tower B. The distance is calculated from the center of each tower (point A, 0 m) and increase outwards. The first measurement point outside the foundation of tower A is point C, at 16.5 m distance from the center of the tower. The first measurement point outside the foundation for tower B is point B, at 30 m distance from the center of the tower. *Right column:* spectral amplitude decay of the peak induced by the tower motion on the ground at the frequency of the tower first flexural mode frequency. The decay is much more evident for tower A than for tower B, due to the resonance of the latter with the soil.

3 DISCUSSION AND CONCLUSIONS

As a consequence of the Mirandola 20th May 2012 M_L = 5.9 earthquake, we observed a very different damage level on two esthetically identical residential structures located at 45 km from the epicenter. Through a passive modal analysis of the structures and of the foundation soil and specific numerical modeling, we have tried to identify the reasons for such a different behavior.

The detailed analysis showed that the two structures (tower A: undamaged, tower B: damaged) have approximately the same mass distribution and therefore the same rotation inertia. They have a slightly different ray of curvature, which is mostly an architectural feature, and which would potentially result in a slightly larger rotation stiffness for the more curved structure (tower A). They have also a slightly different foundation depth (2 m). Experimental evidence shows that the fundamental frequencies of the two towers differ of 20% in the transversal direction while numerical analyses suggest that the geometric difference can only explain a difference of the order of 6%. It follows that the two structures must have a different intrinsic stiffness, most probably explained by their complexity and irregularity and the fact that they were designed by independent engineers.

As a consequence of the lower stiffness, tower B is in full double resonance with the soil, while tower A is not. Double resonance is a well-known factor that induces much larger amplitudes in the structure than expected when the structure and soil eigenfrequencies are not far one from the other.

An evidence supporting the importance of the soil-structure interaction in this case is that the undamaged tower A does not radiate its motion to the surrounding soil in an appreciable way while the tower motion radiation is well measurable on the soil around the damaged tower B. This phenomenon is common under coincidence of resonances between soils and structures.

In conclusion, we have observed a very different dynamic behaviour in two esthetically and apparently identical structures, that led one of the two to suffer from damages during a recent seismic event, while the other was completely unaffected. A detailed analysis revealed that the damaged tower has lower natural frequencies, in such a way that the first transversal flexural mode coincides with the subsoil resonance. As a consequence of the double-resonance, the damaged tower has a mode displacement amplitude 40% larger than the undamaged tower even under ambient vibration excitation.

This case shows that two structures that would be defined identical to the sight (and for any insurance inspector) can react in a very different way for at least two “hidden” factors: a) structural stiffness and b) soil-structure coincidence of resonances. For this reason detailed experimental dynamic analyses taking into account also soil-structure interaction should be performed to anticipate possible differences and associated seismic risks.

The above issues cannot be considered as ‘details’ in design since in practice they led a modern building to be damaged by a M < 6 earthquake at 45 km distance.

4 REFERENCES

Castellaro S., Mulargia F., 2010. How far from a building does the ground motion free field start? The cases of three famous towers and of a modern building, *Bull. Seism. Soc. Am*., 100, 2080-2094.

Geotechnical and Geophysical Site Characterisation 5 – Lehane, Acosta-Martínez & Kelly (Eds)

In-situ performance assessment of ballasted railway track stabilised using geosynthetics and shock mats

S. Nimbalkar
School of Civil & Environmental Engineering, University of Technology Sydney, Australia

B. Indraratna
University of Wollongong, Wollongong City, NSW 2522, Australia

ABSTRACT: In Australia, ballasted railway tracks are one of major modes of transportation. The main objectives of Australian railways are to cater for the demands of the supply chain in the mining and agriculture sectors, as well as to provide quicker and cost effective commuter transport in urban areas. However several geotechnical problems in the populated coastal areas pose significant issues. Ballasted tracks are conventionally constructed on compacted granular embankments overlying the natural subsoil. The granular embankments comprises of ballast and capping layers which undergo substantial deformations and degradation under the heavy cyclic loading of passenger and freight trains. This in turn, may lead to a loss of track geometry, and require costly frequent maintenance. In order to rectify these issues, appropriate stabilization techniques for ballast and capping are necessary, the extent of which depends also on the type of subgrade. When appropriately designed and installed, synthetic inclusions such as geosynthetics and/or shock mats can provide a cost effective alternatives to traditional techniques of ground improvement. Comprehensive field trials were carried out on two railway networks in Bulli and Singleton in New South Wales, Australia. In these studies, several track sections were instrumented with precise sensors for real-time monitoring of stress-deformation response of granular embankments. Different types of geosynthetics were placed beneath the ballast embankment. Recoverable and irrecoverable components of vertical deformations of the track substructure were routinely monitored. The amount of ballast breakage was evaluated by collecting samples from the field and by performing sieve analysis in the laboratory. It was evident that geosynthetics in the form of geogrids can decrease the vertical strains of the ballast layer, resulting in reduced maintenance costs. This paper describes the comprehensive field instrumentation, site geology, construction procedures, and field performance evaluation of these full-scale geosynthetic- and shock mat- stabilized ballast embankments in Australia.

1 INTRODUCTION

In recent years, demand for rail travel has increased significantly due to ever growing demand from urban population and industry sector. Design maximum axle loads have increased over time, from 13.6 tons in 1880 to 22.5 tons in 1906 to 35.7 tons in 1998 (AREMA 1998) to 39 tons today. In addition to increasing axle loads, train traffic is increasing at the rate of about 20 million train miles per year (Sweedler 1999, Bilow and Randich 2007).

Two types of rail tracks, viz. ballasted and slab, are most common; former being used in majority of networks while later being adopted along high-speed rail corridors. The slab track construction costs are 30% to 50% higher than for standard ballasted track (Bilow and Randich 2007). The ballasted tracks are constructed on compacted granular embankments overlying the natural subsoil. Rail-sleeper assembly (i.e. track superstructure) is the most obvious part of a rail track, but the track sub-structure is equally as important in ensuring a safe and comfortable ride for the train and its passengers or freight (Selig and Waters 1994, Esveld 2001).

The quality of granular embankments, comprising of ballast and subballast layers, is important in ensuring a safe and comfortable ride for the train and its passengers or freight. However these embankments deform and degrade substantially under the heavy train traffic, which may lead to a loss of track geometry (Indraratna et al. 2013, 2014e, 2016, Sun et al. 2016). The need for substructure maintenance stems from the development of excessive track geometry deviations resulting from irrecoverable deformations in the ballast, subballast, and subgrade. The continuous degradation of ballast causes sharp angular particles to degrade into relatively less angular or semi-rounded grains, thereby reducing inter-particle friction. This reduced inter-particle frictional resistance decreases the track bearing capacity (Marshal 1973, Indraratna et al. 2010). Track stiffness play significant role on track settlements and track

geometry faults (Burrow et al., 2007; Banimahd et al., 2013, Nimbalkar & Indraratna 2016).

During normal train operations, regular harmonic stress patterns are exerted on track substructure including ballast. However, abnormalities in the wheels and/or rails impart high impact stresses onto the tracks and accelerate damage to track elements. These irregularities are distinct in nature and can cause train wheels to impose impact forces onto the rail (Bian et al., 2013; Indraratna et al., 2014a,b). At bridge approaches, road crossings, and track transitions such as where concrete slab tracks merge into ballasted track, or vice versa, these abrupt changes in stiffness lead to high impact forces that accelerate track degradation (Li & Davis, 2005). The use of resilient mats (shock mats) at such locations can attenuate impact forces substantially (Jenkins et al., 1974; Nimbalkar et al., 2012a,b, Schneider et al. 2011).

The applications of geosynthetics in two-dimensional (Selig & Waters 1994, Koerner 1998, Raymond 2002, Indraratna and Salim 2003, Brown et al. 2007, Liu et al. 2009, Indraratna and Nimbalkar 2013, 2015, Indraratna et al., 2014d, Woodward et al. 2014) and three-dimensional forms (Leshchinsky and Ling 2013, Hegde and Sitharam 2014, Tafreshi et al. 2014, Indraratna et al., 2015) is well known. However, only a few studies have assessed the relative benefits of geosynthetics and shock mats under in-situ track conditions. Therefore, extensive field trials on sections of instrumented railway track at Bulli and Singleton, New South Wales (NSW), Australia have been conducted. This paper discusses details of the instrumentation and monitoring processes, as well as the findings from these unique field studies.

2 FIELD STUDY AT BULLI

Geosynthetics have been widely and successfully used in new rail tracks and in track rehabilitation schemes for almost three decades (Selig and Waters 1994, Koerner 1998). When appropriately designed and installed, geosynthetics are a cost effective alternative to more traditional techniques. A field trial was conducted on a section of instrumented railway track in the town of Bulli, north of Wollongong City, New South Wales (NSW), Australia to study the effectiveness of a geocomposite installed at the ballast-sub-ballast interface. The relative performance of moderately graded recycled ballast in comparison with traditional highly uniform ballast was also evaluated.

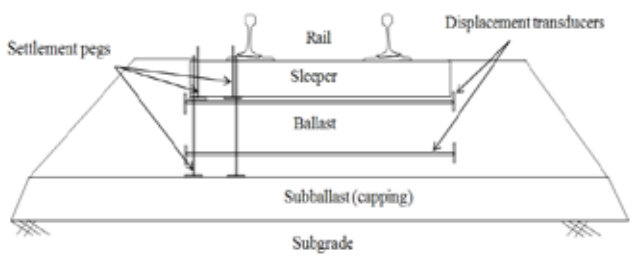

Figure 1. Installing settlement pegs and displacement transducers (data sourced from Indraratna et al. 2010, with permission from ASCE).

2.1 *Track Construction*

The proposed site for track construction was located between two turnouts at Bulli, along the south coast of NSW. The instrumented section of track was divided into four sections (Table 1). The ballast and subballast were 300 mm and 150 mm in thickness, respectively. A single layer of geocomposite was used below the fresh and recycled ballast. Concrete sleepers were used.

Table 1 Layout of experimental track sections using fresh ballast, recycled ballast and geocompolistes, and shock mats.

Section	Length (m)	Type of Ballast	Type of Geosynthetics
1	15	Fresh ballast	-
2	15	Fresh ballast	-
3	15	Recycled ballast	Geocomposite
4	15	Recycled ballast	Geocomposite

2.2 *Material Specifications*

The parent rock type of ballast was latite basalt (volcanic origin). Recycled ballast was collected from spoil stockpiles of a recycled plant near Sydney. The subballast material was a mixture of sand and gravel. A biaxial geogrid was placed over the nonwoven polypropylene geotextile to serve as the geocomposite layer installed at the ballast-subballast interface. The technical specifications of the geosynthetic material used at this site have been discussed elsewhere by Indraratna et al. (2010).

2.3 *Track Instrumentation*

The performance of each section of track under the repeated loads of moving trains was monitored using sophisticated instrumentation. The vertical and horizontal stresses that would develop in the track bed under repeated wheel loads were measured by rapid response hydraulic earth pressure cells with thick, grooved active faces based on semi-conductor type transducers. Settlement pegs were installed between the sleeper and ballast and between the ballast and sub-ballast to measure vertical deformations of the ballast. The settlement pegs consisted of 100 mm × 100 mm × 6 mm stainless steel base plates attached to 10 mm diameter steel rods.

Lateral deformations were measured by electronic displacement transducers connected to a computer controlled data acquisition system. These transducers were placed inside two, 2.5 m long stainless steel tubes that can slide over each other, with 100 mm × 100 mm end caps as anchors. The installation positions of settlement pegs and displacement transducers are shown in Figure 1.

2.4 *Peak stresses*

The peak vertical stresses (σ'_v) recorded in Section 1 are shown in Table 2. These stresses were measured during the passage of passenger train with 20.5 ton axle load and coal freight train with 25 ton axle load each travelling at a speed of 60 km/h. As expected, a greater axle load imposed a higher σ'_v. This resulted in increased deformation of the ballast as discussed in the following section.

Table 2 Maximum vertical stresses measured below the sleeper (data sourced from Indraratna et al., 2010, © ASCE)

Axle load	20.5 tons	25 tons
Sleeper-ballast	238	293
Ballast-capping	63	86

While most of the values of σ'_v were reached up to 238 kPa, one peak value of σ'_v reached 415 kPa which was later found to be associated with a wheel flat. This proved beyond doubt that large dynamic impact stresses are applied by wheel imperfections, a fact that should be carefully assessed and accounted for in the design and maintenance of ballasted track.

2.5 *Vertical and lateral deformations*

In order to investigate the overall performance of the ballast layer, the average vertical and lateral deformations were determined from the field measurements at sleeper-ballast and ballast-subballast interfaces. The average vertical and lateral deformations of the ballast layer are plotted against the number of load cycles (N) as shown in Fig. 2(a) and 2(b), respectively. The recycled ballast showed less vertical and lateral deformations because of its moderately-graded particle size distribution compared to the very uniform fresh ballast. Recycled ballast often has less breakage because they are less angular (more rounded), thereby reducing corner breakage caused by high stress concentrations.

It was evident that geocomposite reduced the vertical deformation of fresh ballast by 33% and that of recycled ballast by 9%. It also reduced lateral deformation of fresh ballast by about 49% and that of recycled ballast by 11%. The capacity of the ballast layer to distribute load was improved by the placement of a flexible and resilient geocomposite layer, and it also substantially reduced settlement under high cyclic loading.

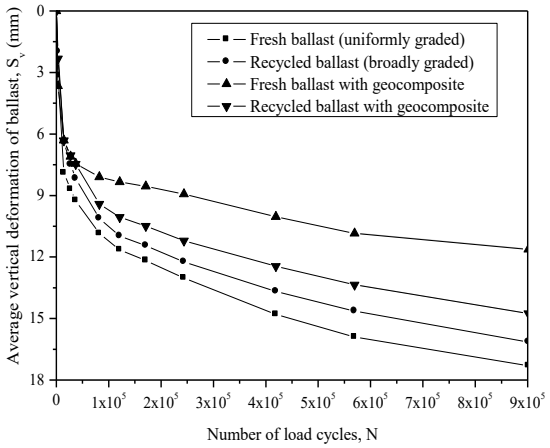

(a)

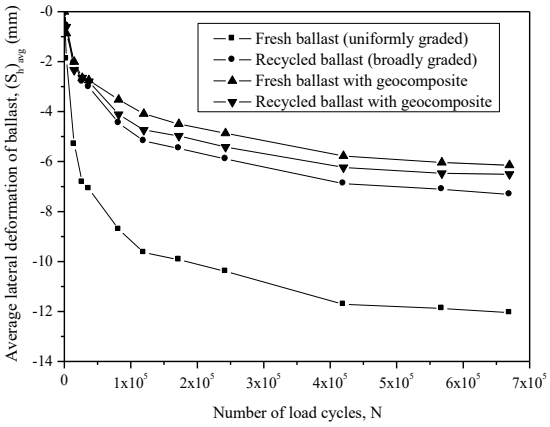

(b)

Figure 2. Average deformations of the ballast layer: (a) vertical; (b) lateral (data sourced from Indraratna et al. 2010, with permission from ASCE).

3 FIELD STUDY: SINGLETON TOWN

To investigate the 'in-situ' performance of different types of geosynthetics, an extensive study was undertaken on an instrumented track near Singleton, NSW [21].

3.1 *Track Construction*

The experimental sections were part of the track that extends from Bedford (chainage 224.20 km) to Singleton (235.06 km), New South Wales. The instrumented track was divided into eight 200 m long sections. These sections were built on three different types of sub-grades, including the soft alluvial silty clay deposit, the hard rock, and the concrete bridge deck. A layer of geosynthetics was placed below the fresh ballast. The details of track construction and material specifications can be found in Indraratna et al. [21].

Nine experimental sections were included in the Third Track while it was under construction (Table 3). Three types of subgrades were encountered, including (i) the relatively soft general fill and alluvial silty clay deposit (Sections 1-4 and Section A), (ii) the intermediate cut siltstone (Sections 5 and C), and (iii) the stiff reinforced concrete bridge deck supported by a piled abutment (Section B). The details of track construction and material specifications can be found in Indraratna et al. [17].

Table 3 Reinforcement at experimental sections using geogrids, geocompolistes, and shock mats.

Section	Location (Chainage)	Type of Geosynthetics
1	234.66	Geogrid 1
2	234.40	Geogrid 2
3	234.22	Geogrid 3
4	234.12	Geocomposite
5	228.44	Geogrid 3
A	234.86	-
B	232.01	Shock mat
C	228.24	-

3.2 *Track Instrumentation*

Different types of sensors were used as listed below. Strain gauges were used to study mobilised strains along the layers of geogrid. Traffic induced vertical stresses were monitored by pressure cells (Fig. 3a). Transient deformations of the ballast were measured by five potentiometers mounted on a custom built aluminum frame. Settlement pegs were installed to measure vertical deformations of the ballast in the similar fashion as shown in Fig. 3(b). Electrical analogue signals from the strain gauges, pressure cells, and potentiometers were obtained using a mobile data acquisition system.

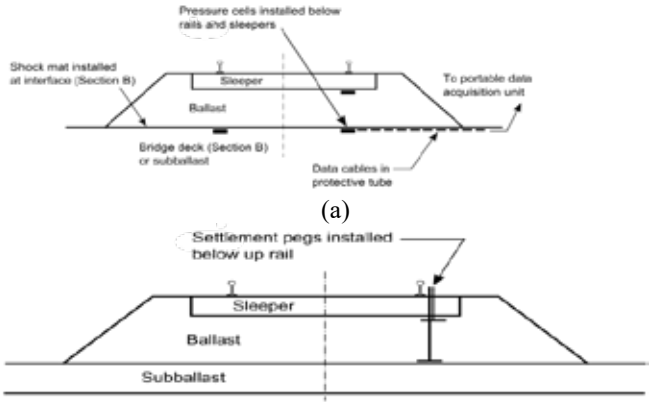

Figure 3. Details of instrumentation of experimental sections of track at Singleton using, (a) pressure cells and (b) settlement pegs.

3.3 *Traffic Induced Vertical Stresses*

The vertical stress (σ'_v) measured in the ballast layer are shown in Table 4. As expected (σ'_v) measured at the sleeper-ballast interfaces were significantly larger (about four-fold) than those at ballast-capping interfaces. This elucidates the role of the ballast layer for effective dissipation of stresses with depth. The vertical stresses (σ'_v) due to passage of coal freight train (axle load of 25 tons) travelling at 60 km/h were quite larger than those measured during the Bulli field trial. While a direct comparison between these two studies is not possible owing to variations in track substructure conditions, the data recording at higher frequency certainly offered more reliable estimation of maximum stresses from the wheel load. It was also found that higher train speeds increased the stresses at the sleeper-ballast and ballast-capping interfaces. Similar finding were reported in the past (Kempfert and Hu, 1999).

Table 4 Vertical cyclic stresses measured under the rail (σ′v) (data sourced from Indraratna et al. 2014c)

Axle load (tons)	At = 25		At = 30	
Speed, V (km/h)	40	60	40	60
Sleeper-ballast	290	301	315	338
Ballast-capping	85	89	94	102

3.4 *Vertical Deformations*

The ballast deformations (S_v) are plotted against the number of load cycles (N), as shown in Figs. 4 & 5. These results indicated that the non-linear variation of ballast deformations. The rate at which the deformations increased actually decreased as the number of load cycles increased.

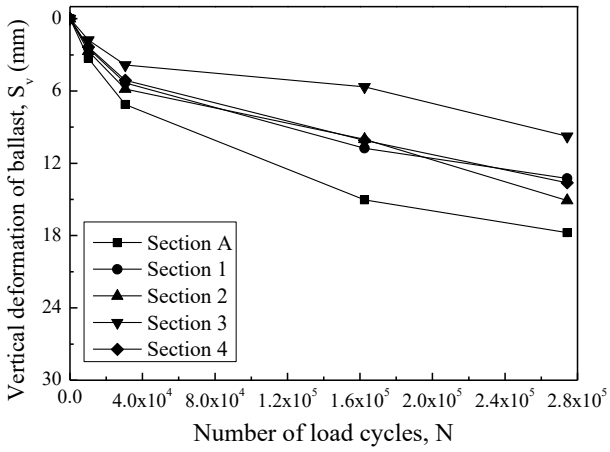

Figure 4. Vertical deformations of ballast layer for soft alluvial deposit (data sourced from Nimbalkar & Indraratna 2016).

The vertical deformations of the ballast reinforced with geogrids were 10-32% smaller than those without reinforcement. This pattern was similar to that observed in the laboratory (Indraratna & Nimbalkar 2013, 2015), and was mainly attributed to the interlocking between the ballast particles and

grids. It was also apparent that the ability of geogrid reinforcement to reduce ballast deformation was generally higher for softer subgrades. The larger deformations also caused significant particle breakage, as discussed below.

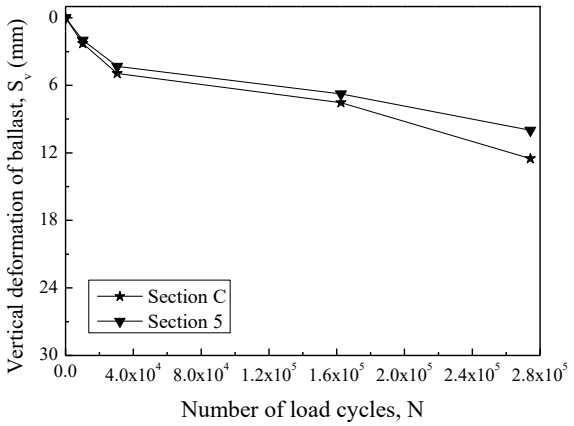

Figure 5. Vertical deformations of ballast layer for hard rock (data sourced from Nimbalkar & Indraratna 2016).

3.5 *Ballast breakage*

Indraratna et al. (2005) and Lackenby et al. (2007) introduced a new Ballast Breakage Index (BBI) specifically for railway ballast to quantify the extent of degradation, and it is based on the particle size distribution (PSD) curves. Breakage of corners of sharp angular ballast particles and attrition of asperities occur progressively under heavy traffic loading. Values of BBI for various subgrade and shock mat combinations are presented in Table 5.

Table 5. Measured breakage of ballast aggregates (data sourced from Indraratna et al. 2014d).

Subbase type	Top	Middle	Bottom
Alluvial deposit	0.17	0.078	0.064
Concrete bridge deck	0.064	0.031	0.022
Hard rock	0.21	0.11	0.087

The larger stresses also caused much more breakage of individual particles of ballast, as was anticipated. At alluvial deposit and hard rock, a larger vertical settlement was observed thus attributing to larger particle breakage in these sections. At concrete bridge deck, least breakage was observed, thus confirming the ability of shock mat to mitigate ballast degradation.

4 CONCLUSIONS

The performance of railroad tracks with geosynthetic reinforcement and shock mats was examined and discussed through full-scale instrumented field studies which used precise instrumentation schemes and monitoring methods for the field data collection.

The field tests carried out on the instrumented track at the town of Bulli highlight that recycled ballast performs satisfactorily under repeated train loads compared to the fresh ballast. This is due to moderately-graded composition of recycled ballast that interlock better within the granular assembly, in contrast to highly uniform fresh ballast recommended in Australian Standards. Test results further demonstrate the potential benefits of using a geocomposite in track, where it was able to reduce the lateral deformation of fresh ballast by about 50% and that of recycled ballast by 10%.

The results of the Singleton study showed that geogrids could decrease the vertical strains of the ballast, with the obvious benefits of reducing the rate of deterioration of track geometry and decreasing the cost of maintenance. The effectiveness of the geosynthetics increased as the subgrade decreased in stiffness. The geogrids with an optimum aperture size significantly reduced ballast deformations through improved interlock with the particles. The findings of these full-scale field studies in Australia allows for a better assessment of the ability of geosynthetic reinforcement to mitigate degradation caused by cyclic and impact wheel loads, as well as more economical and effective design and maintenance of ballasted rail tracks.

5 ACKNOWLEDGEMENTS

The authors are grateful to the CRC for Rail Innovation (established and supported under the Australian Government's Cooperative Research Centres program R3.106 & R3.117) for the funding of this research. The authors express their sincere thanks to the Australian Research Council, Sydney Trains (previously RailCorp), Australian Rail Track Corporation (ARTC) and Aurizon (previously Queensland Rail National) for their continuous support. The Authors would like to thank Dr Pongpipat Anantanasakul (Lecturer, Mahidol University, Thailand) for his help during the tenure of his postdoctoral fellowship at the University of Wollongong.

The assistance of Mr David Christie (formerly Senior Geotechnical Consultant, RailCorp), Mr Tim Neville (ARTC), Mr Michael Martin (Aurizon), Mr Damien Foun (Aurizon), and Mr Sandy Pfeiffer (formerly Senior Geologist, RailCorp) is gratefully acknowledged. The authors would like to thank Mr Alan Grant (laboratory manager), Mr Cameron Neilson and Mr Ian Bridge (technical staff) at the University of Wollongong for their assistance throughout the period of this study. The on-site assistance provided by Mr David Williams of ARTC, Carol Bolam, Tony Miller, and Darren Mosman of Hunt8r Alliance (Newcastle) is much appreciated.

Much of the research outcomes reported here are elaborated in Journal of Geotechnical & Geoenvironmental Engineering, Géotechnique, Transportation Geotechnics, Ground Improvement and SEAG's journal of Geotechnical Engineering. Selected contents are reproduced with kind permission.

6 REFERENCES

American Railway Engineering and Maintenance of Way Association (AREMA). Manual for Railway Engineering. Washington, D.C., 1998.

Banimahd, M., Woodward, P., Kennedy, J. & Medero G. 2013. Three-dimensional modelling of high speed ballasted railway tracks. *Proc of the Inst of Civil Engineers - Transport* 166(2):113-123.

Bian, J., Gu, Y. & Murray, M.H. 2013. A dynamic wheel–rail impact analysis of railway track under wheel flat by finite element analysis. *Vehicle System Dynamics* 51(6):784-97.

Bilow, D.N. & Randich, G.M. 2007. Slab track for the next 100 years. *In 2000 Annual Conf. Proc. of American Railway Engineering and Maintenance of Way Association* pp. 1-20.

Brown, S.F., Kwan, J. & Thom, N.H. 2007. Identifying the key parameters that influence geogrid reinforcement of railway ballast. *Geotextiles and Geomembranes* 25(6): 326-335.

Burrow, M.P.N., Bowness, D. & Ghataora, G.S. 2007. A comparison of railway track foundation design methods. *Proc. of the Institution of Mech. Engineers* 221(F1): 1-12.

Esveld, C. 2001. *Modern Railway Track*, MRT-Productions, Netherlands.

Hegde, A.M. & Sitharam, T.G. 2014. Effect of infill materials on the performance of geocell reinforced soft clay beds. *Geomechanics and Geoengineering* 10(3): 163-173.

Indraratna, B., Biabani, M. & Nimbalkar, S. 2015. Behavior of Geocell-Reinforced Subballast Subjected to Cyclic Loading in Plane-Strain Condition. *J. Geotech. Geoenviron. Eng., ASCE* 141(1): 1-16.

Indraratna, B. & Nimbalkar, S. 2015. An Australian perspective on modernization of rail tracks using geosynthetics and shockmats. *Ground Improvement Case Histories: Compaction, Grouting and Geosynthetics* p. 583-608.

Indraratna, B., Navaratnarajah, S.K., Nimbalkar, S. & Rujikiatkamjorn, C. 2014a. Use of shock mats for enhanced stability of railroad track foundation. *Australian Geomechanics Journal* 49(4): 101-111.

Indraratna, B., Nimbalkar, S., Navaratnarajah, S.K., Rujikiatkamjorn, C. & Neville, T. 2014b. Use of shock mats for mitigating degradation of railroad ballast. *Sri Lankan geotechnical journal - Special issue on ground improvement* 6(1):32-41.

Indraratna, B., Nimbalkar, S. & Rujikiatkamjorn, C. 2014c. Enhancement of rail track performance through utilisation of geosynthetic inclusions. *Geotechnical Engineering* 45(1): 17-27.

Indraratna, B., Nimbalkar, S. & Rujikiatkamjorn, C. 2014d. From theory to practice in track geomechanics – Australian perspective for synthetic inclusions. *Transportation Geotechnics* 1(4): 171-187.

Indraratna, B., Sun, Q.D. & Nimbalkar, S. 2014e. Observed and predicted behaviour of rail ballast under monotonic loading capturing particle breakage. *Canadian Geotechnical Journal* 52(1): 73-86.

Indraratna, B., Sun, Y. & Nimbalkar S. 2016. Laboratory assessment of the role of particle size distribution on the deformation and degradation of ballast under cyclic loading. *J. Geotech. Geoenviron. Eng., ASCE* 142(7): 2016:04016016. doi: 10.1061/(asce)gt.1943-5606.0001463.

Indraratna, B., Tennakoon, N., Nimbalkar, S. & Rujikiatkamjorn, C. 2013d. Behaviour of clay-fouled ballast under drained triaxial testing. *Géotechnique* 63(5): 410-419.

Indraratna, B. & Nimbalkar, S. 2013. Stress-strain-degradation response of railway ballast stabilised with geosynthetics, *J. Geotech. Geoenviron. Eng., ASCE* 139(5), 684-700.

Indraratna, B. & Salim, W. 2003. Deformation and degradation mechanics of recycled ballast stabilised with geosynthetics. *Soils & Foundations* 43(4): 35-46.

Indraratna, B., Lackenby, J. & Christie, D. 2005. Effect of confining pressure on the degradation of ballast under cyclic loading, *Géotechnique* 55(4) 325-328.

Indraratna, B., Nimbalkar, S., Christie, D., Rujikiatkamjorn, C., & Vinod, J.S. 2010. Field assessment of the performance of a ballasted rail track with and without geosynthetics. *J. Geotech. Geoenviron. Eng., ASCE* 136(7): 907-917.

Jenkins, H.M., Stephenson, J.E., Clayton, G.A., Morland, J.W., & Lyon, D. 1974. The effect of track and vehicle parameters on wheel/rail vertical dynamic forces. *Railway Engineering Journal* 3: 2-16.

Kempfert, H.G. & Hu, Y. 1999. Measured dynamic loading of railway underground. *Proc. of the 11th Pan-American Conference on Soil Mechanics and Geotechnical Engineering*, International Society for Soil Mechanics, Brazil, 843-847.

Koerner, RM. 1998. *Designing with geosynthetics*. 4th ed., Prentice Hall, Englewood Cliffs, New Jersey, USA.

Lackenby, J., Indraratna, B., McDowell, G. & Christie, D. 2007. Effect of confining pressure on ballast degradation and deformation under cyclic triaxial loading. *Géotechnique* 57(6), 527-536.

Leshchinsky, B. & Ling, H. 2013. Effects of geocell confinement on strength and deformation behavior of gravel. *J. Geotech. Geoenviron. Eng., ASCE* 139(2), 340-352.

Li, D. & Davis, D. 2005. Transition of railroad bridge approaches. *J. Geotech. Geoenviron. Eng., ASCE* 131(11): 1392-1398.

Marsal, R.J. 1973. Mechanical properties of rock fill. *In: Hirschfield R. C. and Pools, S. J. (eds) Embankment Dam Engineering*: Casagrande Vol, Wiley, New York, 109-200.

Nimbalkar, S., Indraratna, B. & Rujikiatkamjorn, C. 2012b. Performance improvement of railway ballast using shock mats and synthetic grids. *GeoCongress 2012, State of the Art and Practice in Geotechnical Engineering*, Gotechnical Special Publication, ASCE. 1622-1631.

Nimbalkar, S., Indraratna, B., Dash, S.K. & Christie, D. 2012a. Improved performance of railway ballast under impact loads using shock mats. *J. Geotech. Geoenviron. Eng., ASCE* 138(3): 281-294.

Nimbalkar, S. & Indraratna, B. 2016. Improved performance of ballasted rail track using geosynthetics and rubber shockmat. *J. Geotech. Geoenviron. Eng., ASCE* 142(8): doi: 10.1061/(ASCE)GT.943-5606.0001491.

Raymond, G.P. 2002. Reinforced ballast behaviour subjected to repeated load. *Geotextiles & Geomembranes* 20(1): 39-61.

RCA Australia 2008. Geotechnical investigation report for Minimbah Bank Third Track. RCA Australia, Newcastle, Australia.

Schneider, P., Bolmsvik, R. & Nielsen, J.C.O. 2011. In situ performance of a ballasted railway track with under sleeper pads. *Proc. of the Institution of Mechanical Engineers, Part F: Journal of Rail and Rapid Transit* 225(3): 299-309.

Selig, E.T. & Waters, J.M. 1994. *Track Geotechnology and Substructure Management* Thomas Telford, London. Reprint 2007.

Sun, Q.D., Indraratna, B. & Nimbalkar, S. 2016. Deformation and degradation mechanisms of railway ballast under high frequency cyclic loading. *J. Geotech. Geoenviron. Eng., ASCE* 142(1): 04015056.

Sweedler, B.M. 1999. Toward a Safer Future: National Transportation Safety Board Priorities. *TR News* 201, 3-6.

Tafreshi, S.N.M., Khalaj, O. & Dawson, A.R. 2014. Repeated loading of soil containing granulated rubber and multiple geocell layers. *Geotextiles & Geomembranes* 42(1), 25-38.

Woodward, P.K., Kennedy, J., Laghrouche, O., Connolly, D.P. & Medero, G. 2014. Study of railway track stiffness modification by polyurethane reinforcement of the ballast. *Transportation Geotechnics* 1(4): 214-224.

Geotechnical and Geophysical Site Characterisation 5 – Lehane, Acosta-Martínez & Kelly (Eds)

Measuring and comparing soil parameters for a large bridge on East coast of United States

R. Failmezger
In-situ Soil Testing, L.C., Morattico, Virginia, USA

G. Sedran
In-Depth Geotechnical, Hamilton, Ontario, Canada

D. Marchetti
Studio Prof. Marchetti, Roma, Italy

ABSTRACT: At a bridge site on the East coast of the United States, the subsurface soils varied from very soft clays to very dense sands. Seismic (p and s) dilatometer tests (SDMT), cone penetrometer tests with pore pressure measurements (CPTU), pressuremeter tests (PMT), vane shear tests (VST), and standard penetration tests (SPT) measured the geotechnical properties of these soils. A large crane lowered the direct push "seafloor" system to the mudline, which pushed the DMT and CPTU soundings. Underwater hammers generated either the compression wave or shear wave needed for the seismic tests. At the main span, the exploration holes were clustered together and those results are compared.

1 INTRODUCTION

In 1939 a U.S. Department of Transportation performed subsurface explorations by dynamically driving a 1 inch (25 mm) diameter sampling pipe with a 150 pound (68 kgf) hammer into those soils. This testing method predates the standard penetration test and as a result, we had little understanding of the existing soil properties.

In contrast, the new explorations included numerous high quality in-situ tests, such as pressuremeter, vane shear, cone penetrometer, dilatometer, and downhole seismic tests. While we carefully planned our methods to conduct these tests, the geology and shear strengths of these soils differed from what we anticipated. The upper clays were much softer than we anticipated and the lower clays were significantly stronger than anticipated. We modified our test procedures to efficiently perform the explorations.

At the main channel, where the new bridge will have its largest foundations, all of the above tests were performed. The soils' shear strengths and deformation properties are compared for the different tests.

2 PERFORMING THE EXPLORATIONS

A direct push seafloor system, weighing 13,600 kgf (15 tons), pushed the dilatometer and cone penetrometer test probes until penetration refusal occurred.

Figure 1 shows a large crane lowering the seafloor system into the river.

A Central Mine Equipment (CME) Model 75 truck drill rig completed pushing the dilatometer and cone penetrometer tests to the contract depth requirements. Its leveling jacks were welded to the barge keeping it in the same exact location as well as giving it maximum pushing power. This drill rig also performed the standard penetration tests, undisturbed sampling, and prepared the holes for the vane shear tests and pressuremeter tests.

Figure 1. Lowering the seafloor direct push system into the river with a large crane

2.1 *Standard penetration testing*

The drill crews made their drilling fluid by adding bentonite and polymer to the river water that they pumped into a mud tub. They added soda ash to lower its ph. The client had concerns about drilling fluid getting into the river, so the drill crew used 5-inch (125 mm) inner diameter casing telescoping inside 8-inch (200 mm) ID casing to make the hole. The larger casing contained any drilling fluid that may have escaped from the smaller casing from entering the river. After the drill crew completed each hole, they pumped the remaining drilling fluid into large steel drums that were later removed from the site.

The 8-inch (200 mm) casing weighed 110 pounds (50 kgf) for each 5 foot (1.5 m) long section and the 5-inch (125 mm) casing weighed 70 pounds (32 kgf) for each 5 foot (1.5 m) long section. The drill crew found this heavy casing cumbersome to handle and thread on/off. They wisely used the large crane that could lift items 120 feet (37 m) above the barge's deck to lower the casing into the soil when starting the hole and remove it as one long piece when they completed the hole.

Often, when drilling deep holes, the driller can spend a significant amount of time threading and unthreading drill rods. For this project, the drill crews used NWJ rods, which had high strength and enabled the drilling fluid to easily flow through them. The crane operator also picked-up long lengths of rods each time, avoiding numerous threading of rods. The driller would lower the front leveling jacks of the drill rig each time so that the crane's hoist would not strike the drill rig tower. This process significantly reduced the testing time.

The heavy casing penetrated the upper very soft clays as much as 40 feet (12 m). Unfortunately, the required two sets of large casing eliminated testing and sampling of these upper soils. The driller performed standard penetration tests according to ASTM D-1586). In the softer clays, the driller used a fixed piston sampler that he pushed into the clay, while in the harder clays he used a Denison piston sampler that he drilled into those clays.

2.2 *Pressuremeter Testing*

Our engineers carefully monitored the driller's preparation of the borehole for the pressuremeter tests. The drill rig turned the rods at a rate of about 1 turn per second and pumped the drilling mud at a flow rate of 10 gallons/minute (40 liters/minute). For the cohesive soil, a 2.93 inch (74.4 mm) diameter three-winged bit with down discharge made the test zone, while for the cohesionless soil, a 3.06 inch (77.8 mm) diameter tri-cone bit also with down discharge made the test zone. Above the test zone, the driller used a 4.88 inch (124 mm) tri-cone bit to create a large hole so that the mud flow for the test zone would not be impeded.

A Texam pressuremeter using a 74 mm diameter monocell probe performed strain-controlled pressuremeter tests. We calibrated each probe for membrane resistance in air and for system compressibility inside a heavy walled steel pipe. The raw test values were corrected for membrane resistance, system compressibility and hydrostatic pressure head. The membrane expanded into the soil and its resisting pressure was measured at each 40 cubic centimeter interval. After the pressuremeter failed the soil past its elastic behavior, the pressuremeter performed an unload-reload cycle. Often, after this unload-reload cycle the pressuremeter held its pressure for 10 minutes by slowly inflating and measured the soil's creep properties. Additionally, the pressuremeter performed up to two more unload-reload cycles at higher radial strains. Figure 2 shows us performing the pressuremeter test.

2.3 *Vane shear tests*

A computer controlled the rotation rate of the drive motor that turned the vane and measured the torque resistance of the vane with a calibrated electronic torque cell. The drive motor, positioned about 30 cm above the vane, eliminated the parasitic rod friction common to many other types of vane shear equipment. For each test, the computer turned the vane at 0.1 degrees per second for the first 90 degrees to obtain the peak shear strength, 6 degrees per second for ten revolutions and 0.1 degrees per second for the last 90 degrees to obtain the remolded shear strength.

The upper clays from the mudline to approximately 15 meters below it had low shear strengths and a 75 mm diameter and 150 mm long vanes performed the tests. The lower clays had much higher shear strengths and either 40 or initially 50 mm diameter and 80 and initially 100 mm long vanes attempted to measure their strengths. Unfortunately these clays had strengths that exceeded the maximum vane equipment's torque and as a result did not fail. Twice, when we pressed the vane into these strong clays, their shafts bent.

2.4 *Cone penetrometer tests*

The direct push seafloor system has the following significant advantages over pushing probes from the barge deck into the river deposits:

a) Testing starts at the mudline rather than the depth below the mudline where the casing stops settling. The engineer can measure the strength and deformation properties of these very soft deposits with the seafloor system.
b) Casing attached to the top of the seafloor system and extended to the barge deck serves to measure the tests depths. This depth reference does

not move with either waves or the tide and provides accurate measurements.

c) When pushing using a drill rig, the rods can move laterally between the push point and the mudline and rely on the casing for lateral support. The casing can also buckle requiring several different sizes of casing telescoped inside each other. The seafloor system avoids this zone of parasitic rod buckling.

Figure 4: Pushing the DMT with the seafloor system

The crane operator carefully set our direct push sea-

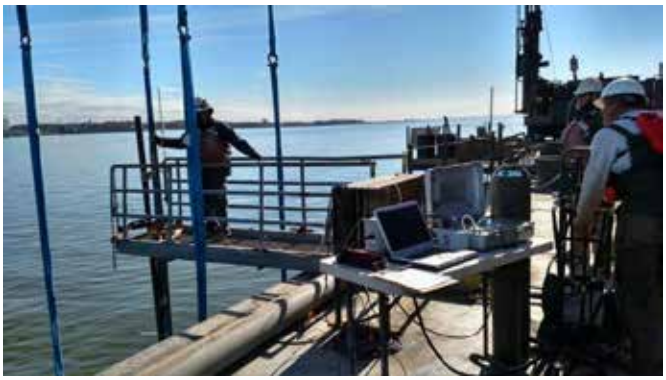

floor system on the river's mudline. Because of its large base area (192 square feet or 17.8 square meters) the seafloor system generally settled less than 20 cm. We estimated the amount of settlement by observing the thickness of mud on the base plates after the completing the sounding and lifting the seafloor out of the river. The upper clays had very low shear strengths and we initially lowered instead of pushed the CPT probe at a controlled penetration rate of 2 cm/second in the clays. Often we did not start pushing the probe into the clays until we had penetrated them about 12 meters. Their low strengths also caused unfortunately low lateral support for the push rods. For each sounding we pushed the CPT probe until we exceeded the lateral capacity of these soft clays and rod buckling began to occur. Many of the soundings could be pushed more than 30 meters below the mudline and the deepest penetration went about 41 meters.

The scheduled depths for the CPT soundings were about 180 feet (55 m) below mudline and the seafloor system had penetration refusal above those depths. Initially we continued these soundings by drilling a 3 inch (75 mm) diameter hole using casing and lowering the CPT and its rods into that hole. The drill rig pushed the CPT until penetration refusal occurred, withdrew the probe and unthreaded its push rods, drilled through the penetration zone and continued the push process. This procedure simply took too much time to do. We discovered that the lower clays had high shear strengths and high lateral earth pressures. They would adhere to the sides of the push rods and cause penetration refusal even though we used a friction reducer to try to eliminate this parasitic rod resistance.

Because we could only push about 5 meters or less each try, we decided to use the torpedo method with the crane to lower and remove the CPT probe and push rods. The CPT cable was threaded through the bottom 5 to 6 meters of AWJ rods (1.75 inch or 44 mm OD) and then exited to the outside of the NWJ rods. The driller taped the CPT cable to the outside of the NWJ rods at approximately 6 meter intervals to try to prevent it from being damaged. To prevent the cable from getting tangled, we rolled or unrolled it onto or off a 30 cm diameter reel.

A data acquisition computer recorded the tip resistance, sleeve friction, and pore water pressure at 5 cm depth intervals as the probe advanced into the soil. At many of the soundings, pore pressure dissipation tests were performed.

Figure 5: Typical shear wave set-up for SDMT

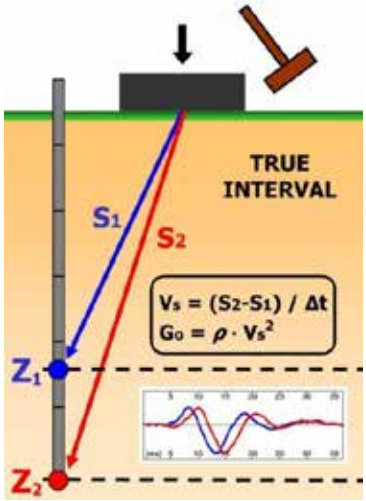

2.5 *Dilatometer tests*

At two locations at the two ends of the main span, we performed dilatometer test soundings. Like with the CPT soundings, the seafloor system pushed the DMT blade into the soils. Figure 4 shows the seafloor direct push system pushing the DMT blade into the soft clays.

Unfortunately at the two locations, a dense sand and gravel layer that caused penetration refusal existed below the very soft clays, which had thicknesses of 18 meters. While the seafloor system measured the soil properties of these very soft clays, we continued these soundings using the torpedo method after drilling through the sand and gravel formation.

For each DMT test, we measured the "A", "B", "C" and penetration thrust values. In the very soft clays the difference between the "A" and "B" reading were just slightly more than their calibration values. In these clays we slowly and carefully inflated and deflated the membrane to obtain accurate measurements.

2.6 *Seismic downhole tests*

This project required both shear and compression seismic wave velocities at two test locations to depths of 58 meters. We knew that we could not push the seismic probe to those depths using the seafloor direct push system and decided to drill to 58 meters with the drill rig and lower the seismic DMT probe to that depth. Fine well-graded washed gravel was placed into the annulus between the seismic DMT probe and the borehole sidewalls to achieve good coupling.

We also knew that we would need a lot of energy to successfully make measurements to those depths. A large shear plate and heavy shear and compression hammers mounted to the seafloor system and positioned about 3 meters away from the sounding created the energy waves. After lowering the probe to its bottom depth and orienting its shear sensors parallel to the direction of the seismic strike, the shear and compression tests started. After performing about 5 compression and shear strikes and recording those waves with the computer acquisition system, we raised the seismic probe 1 meter to perform the next set of seismic tests. We successfully continued this process until we raised the probe and performed tests 3 to 4 meter below the mudline, where the driller could no longer place the gravel and successfully couple the probe and the borehole sidewalls.

The SDMT combines the flat plate dilatometer with a seismic module for the measurement of the shear wave velocity. The seismic module instruments a rod placed above the DMT blade, equipped with two shear receivers located at 0.5 m distance apart and two compression receivers located 0.6 m apart. The shear wave, generated at the mudline, travels downward and arrives first to the upper receiver, then, after a delay Δt, to the lower receiver (Fig. 5). At each test depth, the seismic module amplifies and digitizes the seismograms acquired by the two receivers, and then transmits that data, using the single wire from the standard DMT cable, to a computer that determines the delay of the wave arrival. Vs equals the ratio between the difference in the distances of the shear wave travel paths from the source to each receiver (S2 - S1) and the time delay, Δt, in the wave arrival. The compression wave, also generated at the mudline by striking the plate vertically, travels to the compression receivers and its speed computes similarly to the shear wave. Performing compression waves below the water table offers little significance to the designer as the virtually incompressible water transmits the wave.

3 COMPARISON OF THE TEST RESULTS

Figures 4 and 6 show the undrained shear strengths versus depth for the DMT, VST, CPT, and PMT for the north and south ends of the proposed main span

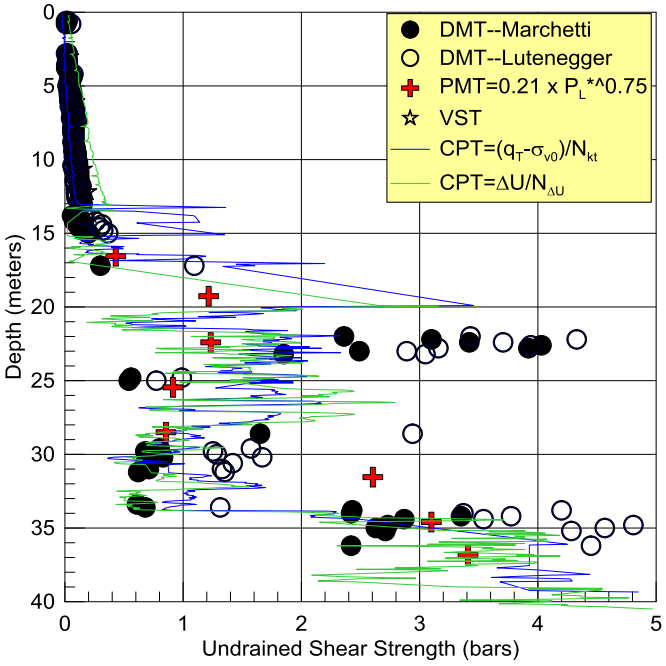

of the bridge, respectively. Because the upper clays had strengths much less than the lower clays, Figures 5 and 7 show the strength for the upper clays (0 to 15 meters) with an enlarged scale for the north and south ends, respectively.

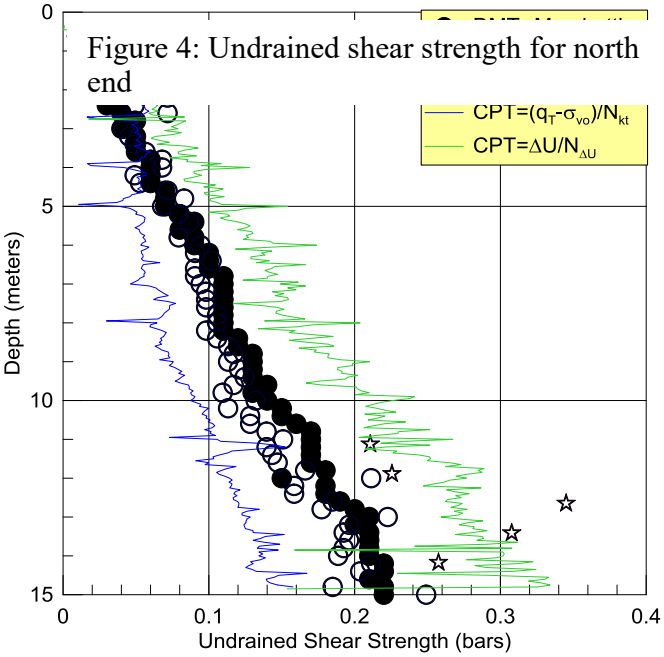

Figure 4: Undrained shear strength for north end

Figure 5: Undrained shear strength for north end for soft clays (0 to 15 m)

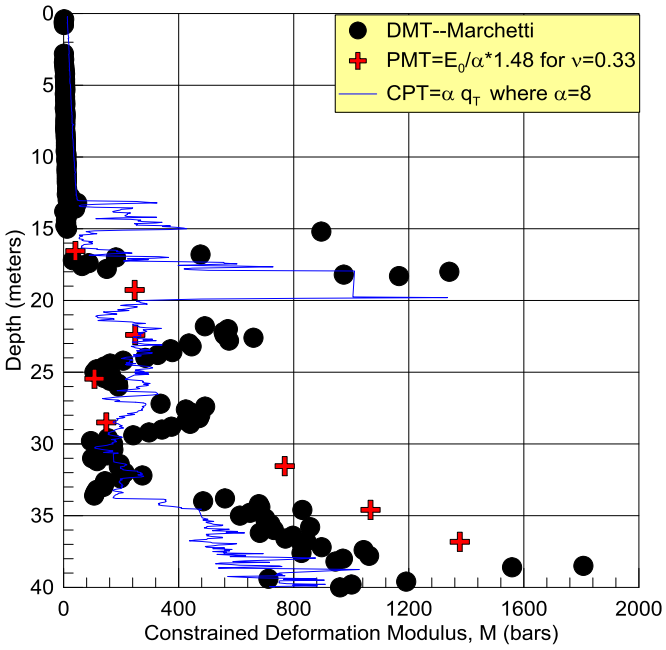

Figure 6. Undrained shear strength for south end

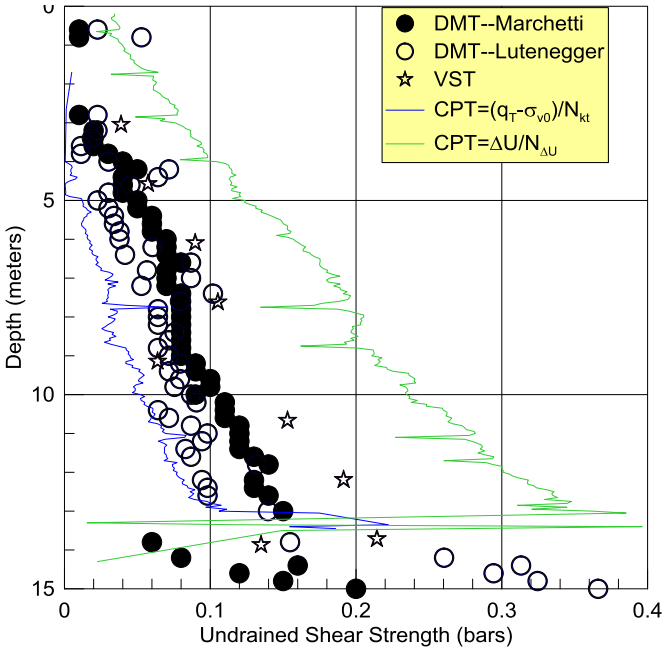

3.1 *Shear tests*

The DMT data computed the undrained shear strength of the clays using Marchetti (1980) and Lutenegger (2006) methods. Marchetti used an empirical relationship based on excellent comparisons of shear strength at eight well documented research sites. Many other researchers have since then shown that Marchetti's method accurately predicts the undrained strength at numerous sites, world-wide.

$Su = 0.22\sigma_{v0}'(0.5K_D)^{1.25}$ --Marchetti

Lutenegger used cylindrical cavity expansion theory to develop his method and showed how this method predicts shear strength in soft clays at several sites. For the hard clays at this site Lutenegger's method shows higher values than the other methods, but with similar trending patterns as the other methods.

$Su = (P_0-P_2)/2.65$ --Lutenegger

The CPTU data computed the undrained shear strength based on the corrected tip resistance and on the excess pore water pressure as follows:

$Su = (q_T-\sigma_{v0})/N_{kT}$, and

$Su = \Delta U/N_{\Delta U}$.

We selected N_{kT} = 15 and $N_{\Delta U}$ = 6 for the shear strength computations at this site. While these values predict the undrained shear strength for the stronger clays fairly well, different correlation factors would better predict the strengths in the very soft clays from 0 to 15 meters, demonstrating why engineers should choose these correlation factors based on site or geologic specific correlations.

The pressuremeter data predicted the undrained shear strength equal to $0.21\ (P_L^*)^{0.75}$, where P_L^* = the net limit pressure. The vane data computed the shear strength equal to $6T/(7\pi D^3)$, where T equals the torque and D equals the vane's diameter.

3.2 *Deformation tests*

Figures 8 shows the predicted constrained deformation moduli from correlations with DMT, CPT and PMT data for the North end. The DMT data computed the modulus using Marchetti (1980) equation. For the PMT data, Young's modulus equals E_0/α, where E_0 is the initial pressuremeter modulus and α is the rheological factor obtained from the Pressiorama chart (Baud, 2013). Based on a Poisson's ratio, ν, of 0.33, the constrained deformation modulus = 1.482 * the Young's modulus. The CPT data computed the constrained modulus equal to $\alpha * q_T$, where α was assumed as 8.

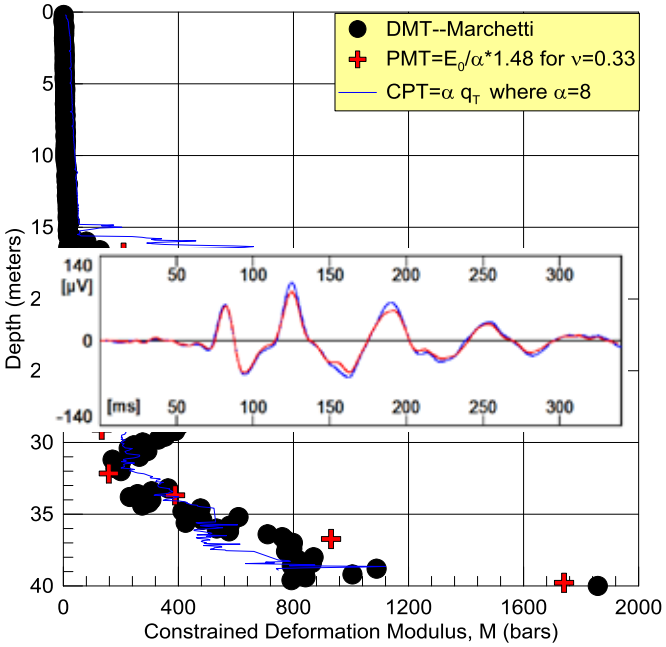

Figure 8. Constrained deformation modulus for the North end

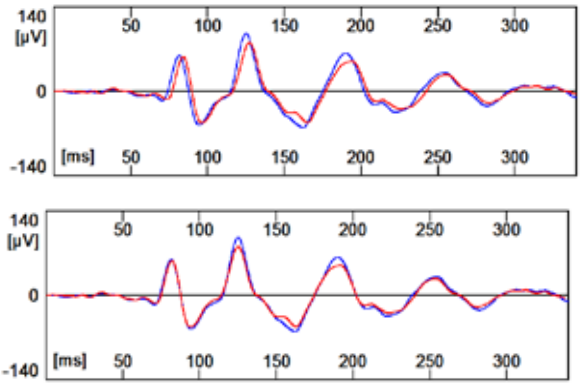

Figure 9a,b Seismic shear wave recorded at 30m

3.3 *Seismic shear wave tests*

The large scale shear wave source provided high quality signals to large depths. As an example, Fig 9a shows the seismograms recorded 30 m below the river bed. The delay of the shear wave arriving to the two receivers, vertically spaced 0.50 m, is clear and consistent. Fig 9b shows the same seismograms after the red trace, corresponding to the lower receiver, has mathematically shifted to the left by a delta time, Δt, until it superimposes on the blue trace, the upper receiver. The shear wave velocity simply computes as the difference in wave travel distance divided by Δt.

4 CONCLUSIONS

Direct pushing of the DMT and CPT probes from the mudline eliminates obstacles that occur when pushing those probes from the barge deck. Those obstacles include missing the tests from the mudline to the depth that casing stops settling, buckling of rods between the barge deck and mudline, and having inaccuracies in depth measurements from waves and tides changes.

The true interval seismic DMT accurately measured the shear and primary waves generated by heavy hammers striking a plate embedded at the seafloor.

The undrained shear strengths from the VST, CPT, DMT and PMT compared favorably with each other. The CPT correlation factors depend on the geological formation and its stress history and one should use different factors for different formations.

The constrained deformation moduli from the DMT, CPT and PMT compared favorably with each other.

5 REFERENCES

Baud, J.P., Gambin, M. (2013) "*Détermination du coefficient rhéologique α de Ménard dans le diagramme Pressiorama*" Proceedings of the 18th International Conference on Soil Mechanics and Geotechnical Engineering, Paris 2013.

Baud, J.P., Gambin, M. (2014) "*Soil and rock classification from high pressure borehole expansion tests*", Geotechnical and Geological Engineering. Springer. Volume 32, Issue 6, December 2014

Lutenegger, A. (2006) "Cavity expansion model to estimate undrained shear strength in soft clay from dilatometer", Proceedings from Second International Conference on the Flat Dilatometer, Washington, D.C., pp. 319-326.

Marchetti, S. (1980). "In Situ Tests by Flat Dilatometer." *ASCE Journal of Geotechnical Engineering Division,* Vol. 106, No. GT3, Paper 15290, pp. 299-321.

Marchetti, S., Monaco, P., Totani, G. & Marchetti, D. (2008), *In Situ Tests by Seismic Dilatometer (SDMT)*, Proc. from Research to Practice in Geotechnical Engineering, ASCE Geotech. Spec. Publ. No. 180 (honoring J.H. Schmertmann), 292-311.

Monaco, P., Marchetti, S., Totani, G. & Calabrese, M. (2005), *Sand liquefiability assessment by Flat Dilatometer Test (DMT),* Proc. XVI ICSMGE, Osaka, 4, 2693-2697.

Monaco, P. & Marchetti, S. (2007), *Evaluating liquefaction potential by seismic dilatometer (SDMT) accounting for aging/stress history*, Proc. 4th Int. Conf. on Earthquake Geotechnical Engineering ICEGE, Thessaloniki, 12pp.

Monaco, P., Marchetti, S., Totani, G. & Marchetti, D. (2009), *Interrelationship between Small Strain Modulus G0 and Operative Modulus*, International Symposium IS-Tokyo 2009 on Performance-Based Design in Earthquake Geotechnical Engineering, 8 pp.

Geotechnical and Geophysical Site Characterisation 5 – Lehane, Acosta-Martínez & Kelly (Eds)

Behavior of a model shallow foundation on reinforced sandy sloped fill under cyclic loading

M.J.I. Alam, C. T. Gnanendran & S.R. Lo
School of Engineering and Information Technology (SEIT), The University of New South Wales (UNSW), Canberra, ACT-2600, Australia

ABSTRACT: Investigations of shallow foundations with geogrid reinforcement under cyclic loading conditions are rather limited. In this study, an attempt has been made to experimentally investigate the behavior of a model shallow foundation on dense sandy sloped fill under cyclic loading. Special placement and compaction techniques were used to ensure a consistent and uniform soil density representative of the field condition. A high tenacity polyester geogrid reinforcement was embedded into the foundation soil mass using the wrap-around technique. Laboratory testing program covered a wide range of cyclic loading amplitudes. A large number of loading cycles, considering hold periods, were applied to the strip footing. The vertical soil stress at different depth was also measured using five individual earth pressure cells. The test results suggested that the cyclic loading amplitude had a significant effect on both the vertical and horizontal permanent deformation behavior of the soil. For a particular loading amplitude and frequency, permanent deformations showed negligible effect of hold periods when the load was held at the minimum value of the cyclic loading amplitude. However, significant increases of permanent deformations were observed after the hold periods when the load was totally released during the hold periods. Similar observations, as of permanent deformations, were also found for residual soil stresses.

1 INTRODUCTION

Loading is one of the most important design factors for a foundation. The static load due to the self-weight of the structure is the dominant contributor of the loads acting on a foundation. However, in addition to the static loads, the foundation is often subjected to live loads of different types such as cyclic loading. The strength and deformation characteristics of a foundation soil mass are significantly affected by cyclic loading due to stress repetitions (Seed et al. 1967). The number of loading cycles, amplitude and frequency are the most important factors that affect the behavior of foundation soil mass under cyclic loading (Diyaljee & Raymond 1982).

The materials used to support foundations may vary but, generally, well-graded granular materials such as sand and gravel are used due to their high bearing capacity, good drainage quality and frictional characteristics. In many practical cases shallow foundations may need to be constructed on or near the crest of a sloped soil mass. The behavior of a shallow foundation near slope of a granular soil mass becomes very complicated when it is subjected to cyclic loading in addition to the static loading due to its non-linear elasto-plastic behavior. Bridge abutment constructed on embankment slope under traffic loading is one of the common examples of such type of foundations which are subjected to a large number of loading cycles. To avoid potential complexity, deep foundations are normally preferred by the design engineers (Bauer et al. 1981). However, the use of shallow foundations may be necessary due to the type of structure and cost effectiveness in many practical conditions.

In practice, the design of a shallow foundation is often based on approximations of the bearing capacity under static loading conditions, despite the foundation experiencing cyclic loading. These approximations lead to the use of a large factor of safety and excessive cost. The main reason behind this practice is the lack of experimental and theoretical studies and understanding of the actual behavior of shallow foundation under cyclic loading conditions.

At present geogrids are widely used as soil reinforcement to improve the stability of the foundation soil mass. Related experimental studies considering single or multiple layers of geogrid reinforcement embedded in a sloped soil mass available in the literature are mainly focused on the investigations of the bearing capacity under static loading conditions (Bathurst et al. 2003; Choudhary et al. 2010; Gnanendran &

Selvadurai 2001; Lee & Manjunath 2000; Sawwaf 2007). Experimental studies on the behavior of foundation on geogrid reinforced sandy flat ground under cyclic loading can also be found in the literature (Boushehrian et al. 2011; Puri et al. 1993; Sawwaf & Nazir 2010; Yeo et al. 1993). However, experimental investigations on the behavior of shallow foundation on geogrid reinforced sloped granular fill under cyclic loading conditions are rather limited in the literature except some recent studies reported by Sawwaf & Nazir (2012) and Islam & Gnanendran (2013). Furthermore, shallow foundations (such as bridge abutment) also experience interruptions of cyclic loading due to the absence of vehicles on the road for an extended period of time. These interruptions may affect the deformation and residual stress behavior of the foundation soil mass. Nevertheless, at the time of conducting this research, the authors are not aware of any study which discusses the effect of any load interruptions during the cyclic loading period which experience a shallow foundation in practical conditions.

The objective of this research work is to experimentally investigate the behavior of a model shallow foundation on geogrid reinforced sandy sloped fill under cyclic loading conditions. The permanent deformation behavior and residual soil stress at different depth of the foundation soil mass subjected to cyclic loading were investigated. The effect of any load interruption on deformation and stress behavior was also investigated by providing hold periods during cyclic loading.

2 TESTED MATERIALS

2.1 *Tested soil*

A well-graded sand with about 5% of non-plastic fines was used for this study. The particle size distribution curve of the tested soil is shown in Figure 1. The maximum dry density (MDD) and optimum moisture content (OMC) of the soil were determined from Standard Proctor compaction test and found to be 1819.5 kg/m^3 and 4.75% respectively. A series of monotonic triaxial tests were also conducted at different confining pressures ranging from 50 to 200 kPa to determine the soil strength and deformation parameters. The measured friction angle (ϕ), dilation angle (ψ) and cohesion (c) was found to be 44^0, 13^0 and 8.2 kPa respectively. It should be noted that all the triaxial specimens were prepared maintaining the MDD and OMC which were consistent with the large scale laboratory model foundation tests as described later.

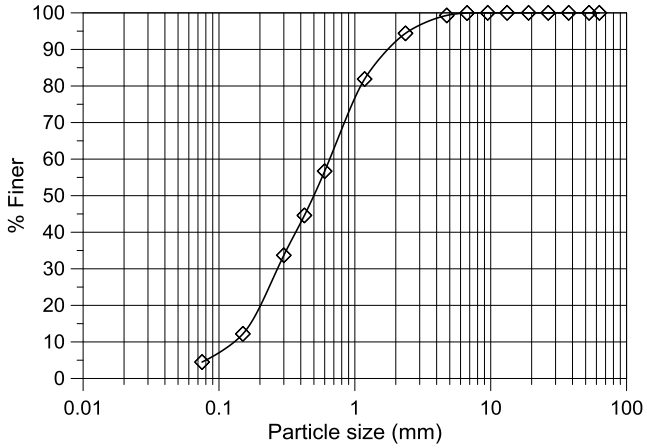

Figure 1. Particle size distribution curve of the tested soil

2.2 *Reinforcement*

A polyester geogrid was used in this experimental study as the reinforcing element. The geogrid, named as Miragrid 8XT, was manufactured by Tencate Geosynthetics. The geogrid was composed of high molecular weight with high tenacity multifilament yarns with a PVC coating to resist the geogrid from biological degradation. The width of the longitudinal and transverse members of the geogrid was 8 mm and 4 mm respectively with a thickness of 1 mm. The longitudinal members were placed at a spacing of 20 mm whereas the transverse members were placed at 30 mm spacing. A pictorial view of the geogrid reinforcement used in this study is shown in Figure 2. According to the manufacturer the tensile strength of the geogrid was 108 kN/m.

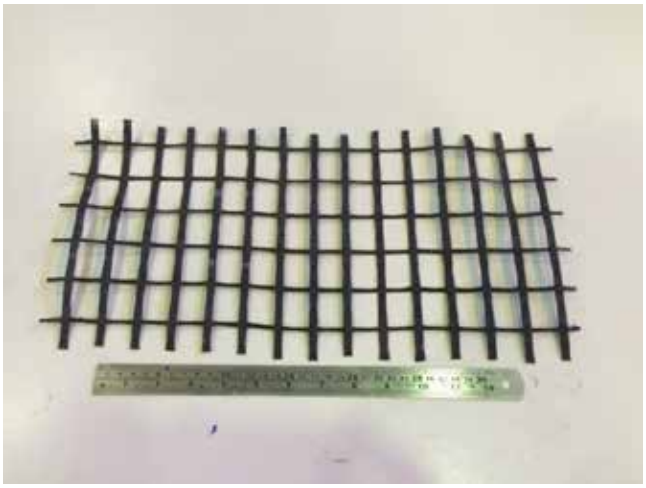

Figure 2. Pictorial view of the geogrid reinforcement

3 TEST CONFIGURATION

The testing arrangement used for this laboratory experiment comprised of a rectangular box, a strip footing, a polyester geogrid reinforcement, hydraulic actuator, load cell, displacement transducers, pressure cells and data acquisition system. The rectangular box was made of steel with dimensions of 2 m long, 1 m wide and 1 m height. Steel made strip footing of 1 m long and 0.2 m wide was used to apply cyclic loading on the soil mass. To replicate practical conditions, the base of the footing was roughened by cementing a thin layer of sand to it using epoxy glue. A schematic diagram of the laboratory testing arrangement is shown in Figure 3.

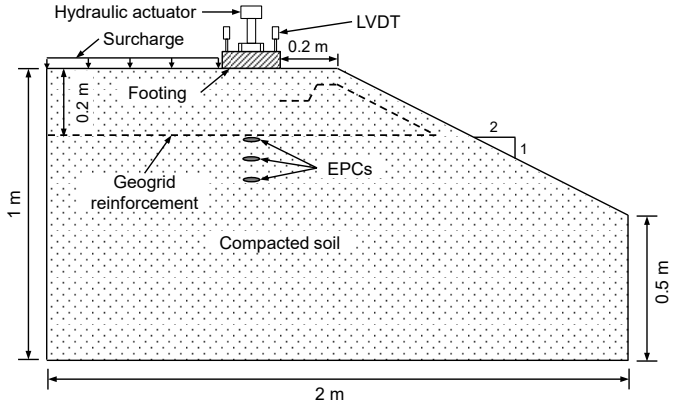

Figure 3. Schematic diagram of the model shallow foundation testing system

The tested soil was collected and stored in big air tight containers. To achieve desired moisture content, required amount of water was added to the soil during specimen preparation. Pre-weighted soil sample was placed in the box and compacted maintaining the MDD and OMC which were consistent with the triaxial tests as explained earlier. The whole compaction process was performed using a percussion compactor with 10 compaction layers maintaining the desired thickness to achieve target dry density. After filling the bottom eight layers, the geogrid reinforcement was placed. As the reinforcement was placed using wrap-around technique (as shown in Figure 3) on the sloping side, the top two layers were compacted very carefully using an additional drop hammer ensuring the uniform compaction around the reinforcement. It is to be noted that five individual earth pressure cells (EPCs) were placed in the soil mass at different depths of 200, 300 and 400 mm from the top surface to measure the vertical soil stresses under the footing as shown in Figure 3. After compacting all the layers, a slope of 1V:2H was made on one side of the foundation. The strip footing was then placed on the soil mass with a setback distance of 0.2 m from the crest of the slope (see Figure 3). A surcharge pressure of 8 kPa was also applied on non-slope side of the soil mass to replicate the static structural load. An external load cell was placed on top of the footing to measure the applied loading amplitude whereas eight individual linear variable differential transformers (LVDTs) were mounted directly on top of the footing to measure both the vertical and horizontal displacements. This ensured that the measured displacements were not be affected by compliance in the loading train.

Cyclic loading amplitude with a desired frequency was applied on the footing in load controlled mode using a hydraulic actuator which was connected to a strong reaction frame. The cyclic load was applied in such a way that a ramp-up load at a very slow rate up to the minimum value of the cyclic loading amplitude was applied first. Then the load was varied between the minimum and maximum values using a sinusoidal wave with the desired frequency of equal to 0.5 Hz for a total of 20000 cycles. To investigate the effect of any loading interruption, the applied cyclic loading was held for two hours at the minimum value of the loading amplitude after each 5000 cycles. The A data acquisition system was used to collect and store data from the measuring devices.

4 RESULTS AND DISCUSSIONS

A total of five large scale model foundation tests were conducted under cyclic loading conditions. A model foundation test is identified by a standardized naming system of F-XX-YY&ZZ. Letters ‘F’ represents large scale model foundation tests. The following letters ‘XX’ represent the frequency of the applied cyclic loading. The letters ‘YY’ and ‘ZZ’ indicate the minimum and maximum values of the cyclic loading amplitudes respectively. For example, F-0.5-27&45 indicates large scale cyclic load model foundation test performed at a frequency of 0.5 Hz with minimum and maximum values of the loading amplitude of 27 and 45 kN respectively. It is to be noted that, as the effect of cyclic loading amplitude is more prominent than the loading frequency, for this study, tests were performed at a constant frequency of 0.5 Hz.

4.1 *Permanent deformation behavior*

The vertical and horizontal permanent deformations occurred in each loading cycle were calculated for each test. The cumulative values of the vertical and horizontal permanent deformations were also calculated and plotted against the number of load cycle (N) to investigate their variation. It is to be noted that, for the

plot of cumulative permanent deformations the deformation value started from the first loading cycle and the deformation occurred during virgin loading (ramp-up and a cycle) was not considered. As the tests were performed in four different stages (5000 cycles in each stage) considering hold periods, test results were presented for each stage. Figure 4a and b represent the variation of the cumulative vertical and horizontal deformations with N obtained from the test of F-0.5-27&45. The four different plots in Figure 4a and b represent the variation of cumulative permanent deformations in those corresponding stages. According to the Figure 4, both the cumulative vertical and horizontal permanent deformations increased with the increase of N. In a particular loading stage, the increment rate was high within the first few thousand loading cycles and after about 2000 cycles, the curve remained almost constant up to the end of the cycle as considered. It is also evident that, for both the cumulative vertical and horizontal permanent deformations the values were significant for the first 5000 loading cycles (i.e., stage-1). However, after the first 5000 loading cycles, the permanent deformations decreased significantly (stage-2 to 4).

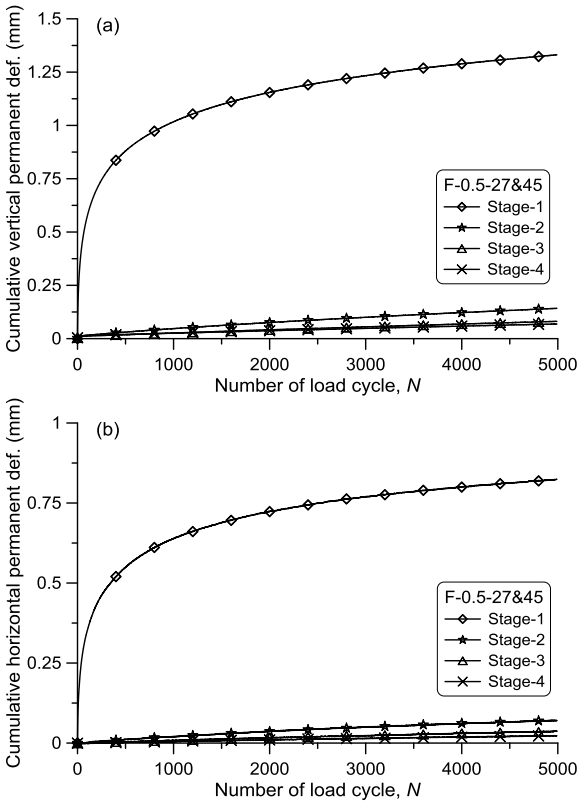

Figure 4. Variation of cumulative permanent deformations with N for F-0.5-27&45; (a) vertical permanent deformation and (b) horizontal permanent deformation

The effect of hold periods during the tests, where the load was held at the minimum value of the cyclic loading amplitude, were also investigated by summarizing the permanent deformations calculated in each stage. Figure 5 shows the cumulative vertical and horizontal deformations occurred in the entire test (20000 cycles) for all the tests as performed. Evidently, for both the vertical and horizontal permanent deformations, the curves did not show any deflection during the hold periods for all the tests which was indicative of a negligible effect of hold periods on the permanent deformations when the load was held at the minimum value of the cyclic loading amplitudes.

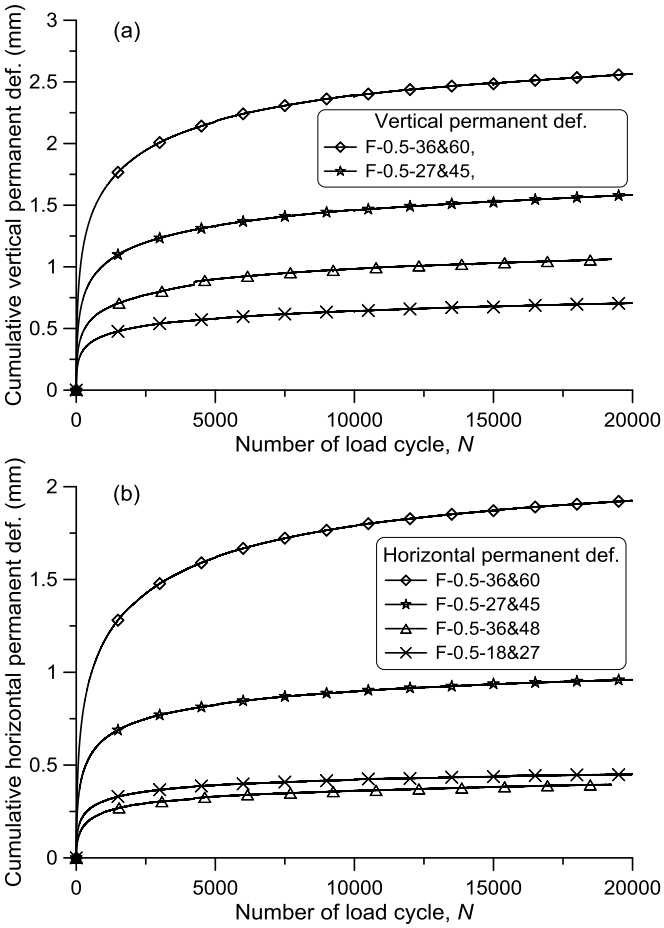

Figure 5. Variation of cumulative permanent deformations with N; (a) vertical permanent deformation and (b) horizontal permanent deformation

To further investigate the effect of hold period on permanent deformation, test F-0.5-27&45 was repeated (named as F-0.5-27&45*) with a different loading path where the load was totally released during the hold periods. A total of 30000 loading cycles were applied for this test maintaining hold periods after each 10000 cycles. It is to be noted that, after each hold period, the cyclic load was applied considering ramp-up followed by load cycles. The test results for the variation of cumulative vertical and horizontal permanent deformations for F-0.5-27&45* are shown in Figure 6.

It is pertinent to note that, for these plots the permanent deformation values started from the first loading cycle for stage-1 as consistent with F-0.5-27&45, and the deformations occurred in the ramp-up periods for stage-2 and 3 were not considered. Evidently, for this particular test, the hold period had a significant effect on the permanent deformations where sudden increases of both the vertical and horizontal permanent deformations were observed after each hold periods. This behavior of permanent deformations was expected to be due to the release of all loads on the soil mass during hold periods and the reloading acted as virgin loading for the next stage.

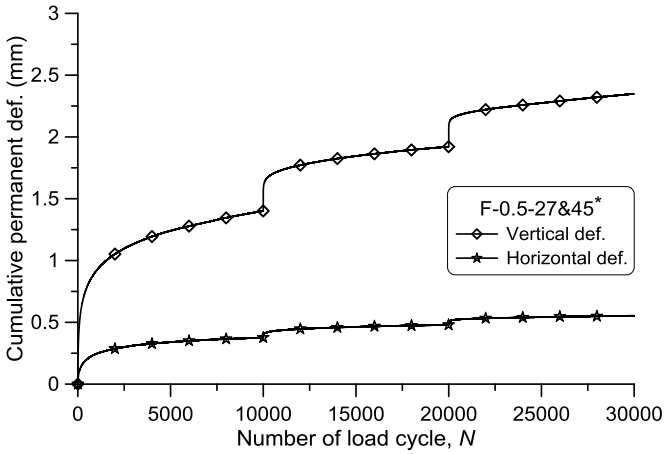

Figure 6. Variation of cumulative permanent deformations with N for F-0.5-27&45*

4.2 *Residual soil stress behavior*

The residual soil stresses at different depths (200, 300 and 400 mm) of the foundation soil mass were also observed and plotted against N to investigate their variation. A representative plot of the residual soil stress vs. N obtained at different depths for F-0.5-27&45 is shown in Figure 7a. Evidently, the residual soil stress increased with the increase of N. However, the increment rate was high at the first stage (i.e., first 5000 cycles) of the test and after that the soil stress remained almost consistent up to the end of the test. The residual soil stress was found to be maximum at a depth of 200 mm (i.e., at the geogrid reinforcement level) and reduced with the increment of depth. It is also evident that, the hold periods had almost negligible effect on the residual soil stress when the load was held at the minimum value of the cyclic loading amplitude.

The residual soil stresses at different depths of the foundation soil mass were also investigated for the test of F-0.5-27&45* where the load was entirely released during the hold periods. The variation of the residual soil stresses with N for the test of F-0.5-27&45* is shown in Figure 7b. A similar observation as of test F-0.5-27&45 was found where the residual stress increased with the increase of N and the maximum stress was found at 200 mm depth (i.e., at the geogrid reinforcement level). However, the reloading after each hold period showed significant increase of residual soil stress at every EPC level. This variation of residual soil stress is believed to be due to the release of load during the hold periods which releases all the stresses in the foundation soil mass. The reloading after hold periods acted as virgin loading in the soil mass which caused the sudden increase of residual soil stresses at the beginning of each stage.

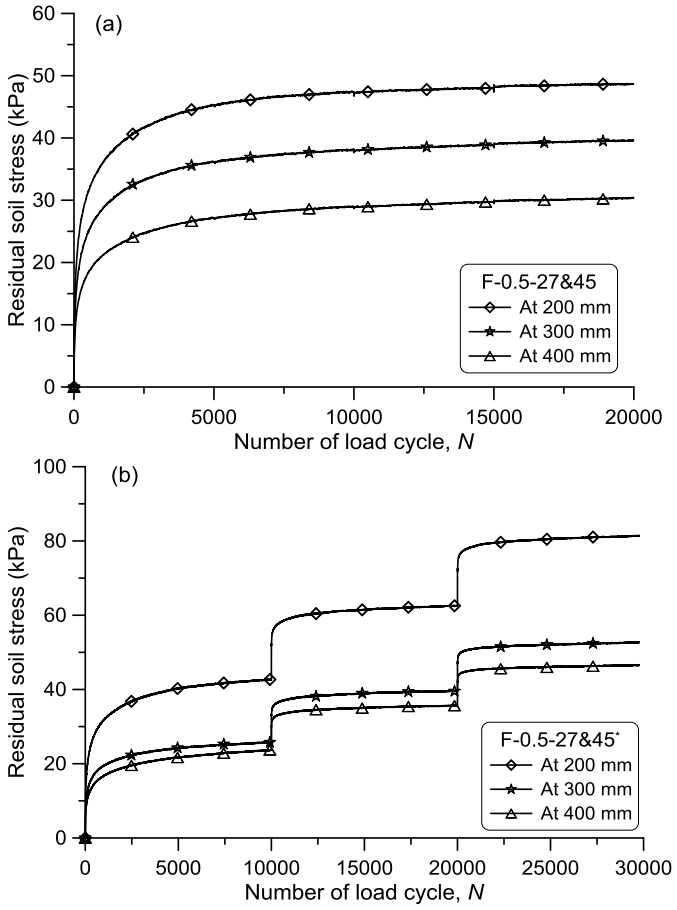

Figure 7. Variation of residual soil stresses with N; (a) for F-0.5-27&45 and (b) for F-0.5-27&45*

5 CONCLUSIONS

A comprehensive series of large scale experiments were performed in this study to investigate the behavior of a model shallow foundation on reinforced sandy sloped fill under cyclic loading conditions. A widely used geogrid reinforcement was embedded in to the foundation soil mass to improve stability. The main conclusions from this experimental study can be summarized as follows.

1. The cumulative vertical and horizontal deformations increased with the increase of N and the majority of the permanent deformations occurred within first few thousand loading cycles.

2. The hold periods showed negligible effect on permanent deformations when the load was held at the minimum value of the cyclic loading amplitude.

3. Significant increases of vertical and horizontal permanent deformations were observed in each stage when the load was entirely released during hold periods.

4. The residual soil stresses at different depth of the soil mass increased with the increase of N for first few thousand loading cycles and after that the stress remained almost constant up to the end of the test.

5. A negligible effect of hold periods on residual soil stresses was observed when the load was held at the minimum value of the cyclic loading amplitude. However, significant increase of residual soil stresses was evident for the test where the load was entirely released during hold periods.

6 REFERENCES

Bathurst, R.J., Blatz, J.A. & Burger, M.H. 2003. Performance of instrumented large-scale unreinforced and reinforced embankments loaded by a strip footing to failure. *Canadian Geotechnical Journal* 40 (6): 1067-1083.

Bauer, G.E., Shields, D.H., Scott, J.D. & Gruspier, J.E. 1981. Bearing capacity of footings in granular slopes. *Proceedings of the 10th International Conference on Soil Mechanics and Foundation Engineering, Stockholm, Sweden*, 33-36.

Boushehrian, A.H., Hataf, N. & Ghahramani, A. 2011. Modeling of the cyclic behavior of shallow foundations resting on geomesh and grid-anchor reinforced sand. *Geotextiles and Geomembranes* 29 (3): 242-248.

Choudhary, A.K., Jha, J.N. & Gill, K.S. 2010. Laboratory investigation of bearing capacity behaviour of strip footing on reinforced flyash slope. *Geotextiles and Geomembranes* 28 (4): 393-402.

Diyaljee, V.A. & Raymond, G.P. 1982. Repetitive load deformation of cohesionless soil. *Journal of Geotechnical Engineering Division, ASCE* 108 (10): 1215-1229.

Gnanendran, C.T. & Selvadurai, A.P.S. 2001. Strain measurement and interpretation of stabilising force in geogrid reinforcement. *Geotextiles and Geomembranes* 19 (3): 177-194.

Islam, M.A. & Gnanendran, C.T. 2013. Slope stability under cyclic foundation loading-Effect of loading frequency. *Stability and Performance of Slopes and Embankments III (Geo-Congress 2013), San Diego, California, USA*, 750-761.

Lee, K.M. & Manjunath, V.R. 2000. Experimental and numerical studies of geosynthetic-reinforced sand slopes loaded with a footing. *Canadian Geotechnical Journal* 37 (4): 828-842.

Puri, V.K., Yen, S.C., Das, B.M. & Yeo, B. 1993. Cyclic Load-Induced Settlement of a Square Foundation on Geogrid-Reinforced Sand. *Geotextiles and Geomembranes 12* 12: 587-597.

Sawwaf, M.A.E. 2007. Behavior of strip footing on geogrid-reinforced sand over a soft clay slope. *Geotextiles and Geomembranes* 25 (1): 50-60.

Sawwaf, M.E. & Nazir, A.K. 2010. Behavior of repeatedly loaded rectangular footings resting on reinforced sand. *Alexandria Engineering Journal* 49: 349-356.

Sawwaf, M.A.E. & Nazir, A.K. 2012. Cyclic settlement behavior of strip footings resting on reinforced layered sand slope. *Journal of Advanced Research* 3: 315-324.

Seed, H.B., Mitry, F.G., Monismith, C.L. & Chan, C.K. 1967. Prediction of flexible pavement deflections from laboratory repeated-load tests. National Cooperative Highway Research Program Report No. 35, Highway Research Board, Washington DC.

Yeo, B., Yen, S.C., Puri, V.K., Das, B.M. & Wright, M.A. 1993. A laboratory investigation into the settlement of a foundation on geogrid-reinforced sand due to cyclic load. *Geotechnical & Geological Engineering* 11 (1): 1-14.

Theme 14. Application of Statistical Techniques

Geotechnical and Geophysical Site Characterisation 5 – Lehane, Acosta-Martínez & Kelly (Eds)

Frequency Spectrum "Bell-Curve" Fitting as a Component of SCPT Interval Velocity Accuracy Assessment

E. Baziw & G. Verbeek
Baziw Consulting Engineers Ltd., Vancouver, Canada

ABSTRACT: Seismic Cone Penetration Testing (SCPT) is an important geotechnical testing technique for site characterization that provides low strain ($<10^{-5}$) *in-situ* interval compression (V_p) and shear (V_s) wave velocity estimates. A challenging problem is to obtain an accuracy assessment of the quality of these calculated interval velocities. The accuracy assessment should take into account various independent characteristics from the acquired data for each depth increment, which are then fused together into a classification or "rank" that quantifies the accuracy of the estimated interval velocities. In 2015, the authors introduced an initial reliable and unique interval velocity classification (IVC) technique which utilizes linearity estimates from Polarization Analysis (PA) in conjunction with Cross Correlation Coefficient (CCC) calculations of the full waveforms. At that time it was suggested that the quality assessment of the estimated interval velocities should be based on the equal weight of the PA linearity and the CCC between the full waveforms calculated at sequential depths. In this paper, the mathematical and implementation details of a new parameter introduced into the IVC are outlined. This new parameter quantifies the deviation of the source wave frequency spectrum from a desirable bell-shaped curve. SCPT seismic traces with high signal to noise ratios were found to have characteristically bell-shaped curves similar to the probability density of a normal distribution.

1 INTRODUCTION

1.1 *Background*

Seismic Cone Penetration Testing (SCPT) (ASTM D7400, 2013) is a common geotechnical technique for measuring *in-situ* compression and shear wave velocities (V_P and V_S respectively). The main goal in SCPT is to obtain arrival times as the source wave travels through the soil profile of interest, and from these arrival times interval velocities are then calculated. Once the velocities have been calculated it is highly desired to assign a confidence level to the estimate. Typically, investigators have utilized the Cross Correlation Coefficient (CCC) between seismic traces recorded at successive depths. The CCC gives an indication of the similarity between the traces (Baziw, 1993) and ranges in value from zero (no similarity) to unity (perfect similarity).

However, the CCC has proven to be an unreliable indicator of the accuracy of the calculated interval velocity, because measurement noise (both random and systematic) can also be correlated and generate erroneously high CCC values. In addition, the CCC values are affected by the digital frequency filters that are applied to increase the Signal to Noise Ratios (SNRs) of the acquired seismic data files.

In order to overcome the limitations of the CCC the authors developed (Baziw and Verbeek, 2016) a new and significantly more comprehensive approach to SCPT interval velocity classification (*IVC*) and assessment, similar to the methodology Ge (Ge and Mottahed, 1993 and 1994, Ge, 2003) developed for microseismic source location estimation. In this approach various seismic data characteristics obtained from the acquired microseismic data for each event are fused together based upon analytic, derived and evolving empirical relationships. The outcome is a microseismic source location estimate "rank", varying from A (very good), B (good), C (acceptable), and D (not acceptable).

In the initial approach the authors combined linearity estimates from Polarization Analysis (PA) (Baziw, 2004, Baziw and Verbeek, 2016, Kanasewich, 1981) with the CCC values to assess the quality of the calculated interval velocities. This approach assumes that full waveforms and ray path refraction are utilized within the interval velocity calculation (Aki and Richards, 2002, Baziw, 2002 and 2004, Baziw and Verbeek, 2012).

The PA linearity approaches unity when the rectilinearity of the responses on the X and Y axes is high, which will be the case for seismic traces recorded in a transverse isotropic (TI) medium (Shearer, 1999, Aki and Richards, 2002) with minimal measurement noise, clean source waves, and no signal distortions (e.g., reflections). The more any of these aspects are present the lower the linearity value will be and low linearity values will also be obtained when shear-wave splitting or shear wave birefringence occur (Gibowicz and Kijko, 1994).

The authors suggested that the quality assessment should be based on the equal weight of the linearity and the CCC between the full waveforms calculated at sequential depths:

$$IVC = (LinearityDepth_1 + LinearityDepth_2 + CCC_{between\ Depth1\ and\ Depth2})/3). \quad (1)$$

This initial weighting was based on a re-evaluation of many data sets previously processed (from over 40 different sites around the world, covering over 4000 seismic traces).

The *IVC* value was then converted into a grade ranging from *A* to *F* as shown below, where A is highly desirable and *F* is unusable:

Classification	
[0-1]	***[A-F]***
0.9 to 1.0	***A***
0.8 to 0.9	***B***
0.7 to 0.8	***C***
0.6 to 0.7	***D***
< 0.6	***F***

It should be noted that the authors indicated that this classification would be refined in the future as it is applied on a routine basis for new data sets.

After proposing the initial approach the authors have reviewed numerous SCPT data sets and attempted to identify other independent characteristics which define the quality of the acquired SCPT seismic data, especially for horizontal shear (SH) wave analysis where dominant responses reside on the X and Y axis. As part of this process they considered among others the amplitude responses on the Z component of a triaxial sensor package (minimal Z component responses would be expected for SH wave analysis), the correlation between right and left polarized wave interval velocity estimates, and how well true Vertical Seismic Profile (VSP) arrival times match–up with arrival times derived from relative arrival times obtained from cross-correlating full waveforms at successive depths. Unfortunately, the first proved to be ad hoc, while the last two were not conducive to automated data processing.

A more promising feature for incorporation into the *IVC* was the shape of the seismic trace frequency spectrum, or better the deviation of the source wave frequency spectrum from a desirable bell-shaped curve, as SCPT seismic traces with high signal to noise ratios were found to have characteristically bell-shaped curves similar to the probability density of a normal distribution. This approach is presented in this paper.

2 FREQUENCY SPECTRUM "BELL CURVE" FITTING

The probability density of a normal (or Gaussian) distribution is given as

$$f(x|\mu,\sigma^2) = \frac{1}{\sigma\sqrt{2\pi}} e^{-\frac{(x-\mu)^2}{2\sigma^2}} \quad (2)$$

where μ denotes the mean or expectation of the distribution and σ denotes the standard deviation with variance σ^2. The area under the normal pdf curve is unity. Figure 1 illustrates example of normal pdfs for varying μ and σ^2 values. All the curves in Fig. 1 have the classical bell-shape.

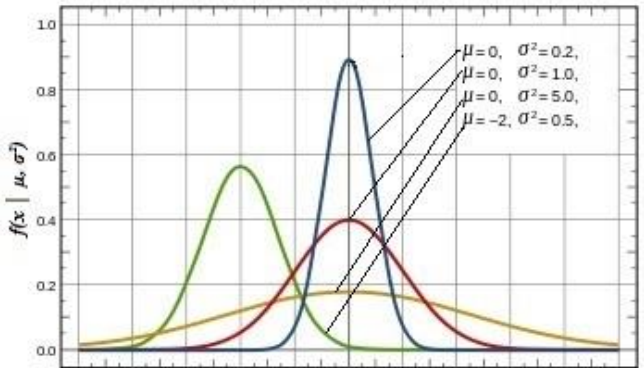

Figure 1. illustrates example of normal pdfs for varying μ and σ2 values. (after, http://www.dplot.com/probability-scale.htm)

Figure 2 illustrates a Berlage source wave (Baziw and

Ulrych (2006), Baziw and Verbeek (2014)), which is commonly used within seismic signal processing for simulation purposes. The Berlage source wave is analytically defined as

$$w(t) = AH(t)t^n e^{-ht}\cos(2\pi ft + \emptyset) \quad (3)$$

where $H(t)$ is the Heaviside unit step function [$H(t) = 0$ for $t \leq 0$ and $H(t) = 1$ for $t > 0$]. The amplitude modulation component is controlled by two factors: the exponential decay term h and the time exponent n. These parameters are considered to be nonnegative real constants. Figure 3 illustrates the frequency spectrum (solid black line) of the Berlage source wave shown in Fig. 2 with the normal pdf approximation shown as a dotted grey line, with $\mu = 69$ Hz and $\sigma = 32.5$. As is evident from Fig. 3, the frequency spectrum of the simulated Berlage source wave closely matches that of a bell-shaped curve.

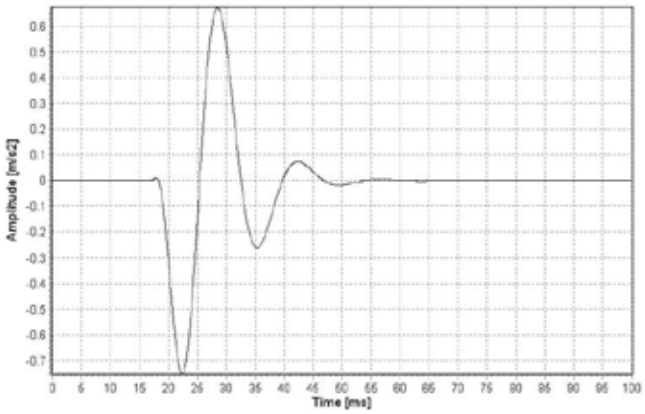

Figure 2. Berlage source wave with of $f = 70$ Hz, $n = 2$, $h = 270$ and $\phi = 40^o$ specified.

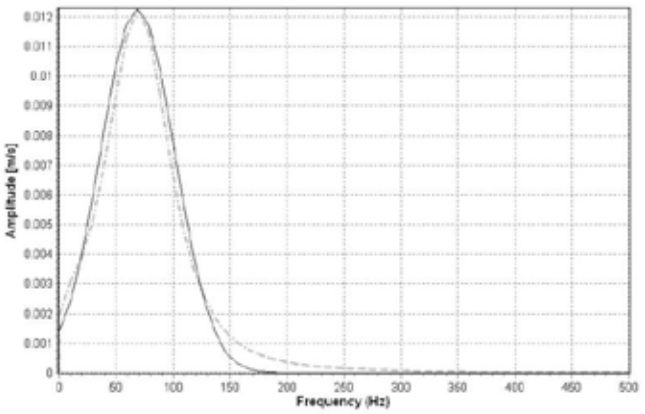

Figure 3. Frequency spectrum (solid black line) of Berlage source wave illustrated in Fig. 2 with the normal pdf approximation shown as a dotted grey line.

2.1 *Bell-Curve fitting algorithm, SNR estimation and incorporation into IVC*

To incorporate the deviation of the source wave frequency spectrum from a desirable bell-shaped curve into the *IVC* the following process is proposed:

1. Apply a digital zero-phase shift frequency filter (e.g., 200 Hz low pass frequency filter) to triaxial sensor data set so that high frequency measurement noise is removed.
2. For SH source wave analysis, calculate frequency spectra for $X(t)$ and $Y(t)$ recordings, $S_X(f)$ and $S_Y(f)$, and determine which axis has the dominant frequency response axis (denote as $S(f)$).
3. Force the area under $S(f)$ to approach unity by uniformly modifying the amplitudes within $S(f)$. This step is outlined below by eqs. 4(a) and 4(b).

$$Area_{S(f)} = \Delta f \sum_{i+1}^{n} S(f)_i \quad (4a)$$

$$\sum_{i+1}^{n} S(f)_i = S(f)_i / Area_{s(f)} \quad (4b)$$

In eq. 4(a), Δf denotes the frequency increment resolution.

4. Determine μ (dominant frequency), $p(\mu)$ (maximum spectral amplitude), and $\sigma = 1/(\, p(\mu)\, \sqrt{(2\pi)})$ utilizing an iterative forward modelling (IFM) technique such as the Simplex method (Baziw, 2002, 2011). In this IFM case the cost function to minimize is the RMS difference between the normalized area under $S(f)$ and the derived area (using eq. (2)) from a normal pdf which utilizes the currently estimated μ and σ values.
5. Calculate $p(f)$ via equation (1) utilizing the IFM estimates μ and σ from Step 4.
6. Calculate $\epsilon_1 = \sum_{i+1}^{n} abs\big(S(f)_i - pdf(f)_i\big)\,)$
7. Calculate $\epsilon_2 = \sum_{i+1}^{n} abs(S(f)_i)$
8. Calculate parameter R which is defined as $R = \varepsilon_1/\varepsilon_2$
9. Spectrum Rank (*SR*) component of the *IVC* is then calculated $SR = 1\text{-}R$.
10. The *IVC* is then calculated as the average of the linearity value determined by applying PA and the SR value.

$$IVC = ((Linearity_{Depth1} + SR_1)/2 + (Linearity_{Depth2} + SR_2)/2 + CCC_{between\ Depth1\ and\ Depth2})/3 \quad (5)$$

3 REAL DATA EXAMPLES

3.1 *High SNR SCPT data set*

Figure 4 illustrates a real data example of a high SNR SH source wave SCPT trace acquired in Alberta, Canada. The triaxial data was acquired at a depth of 5m by fast response accelerometers (5μs response time) with a bandwidth of 10 Hz to 10 KHz manufactured by PCB Piezotronics. The triaxial seismic data displayed in Fig. 4 had an option referred as *normalize locally* implemented. Normalize locally refers to normalizing the displayed amplitudes of the X(t), Y(t), and Z(t) axes with respect to the absolute maximum value. This provides for a clear visual of the dominant X(t), Y(t) and Z(t) dominant responses.

The frequency spectra are calculated from the filtered traces of Fig. 4 (200 Hz low pass filter applied) as outlined in Step 2. The dominant frequency components were determined to reside within the X axis recordings. Figure 5 illustrates the X axis frequency spectrum (solid black line) of triaxial source wave illustrated in Fig. 4 where the frequency spectrum amplitudes were uniformly modified so that the area under the curve was unity (Step 3).

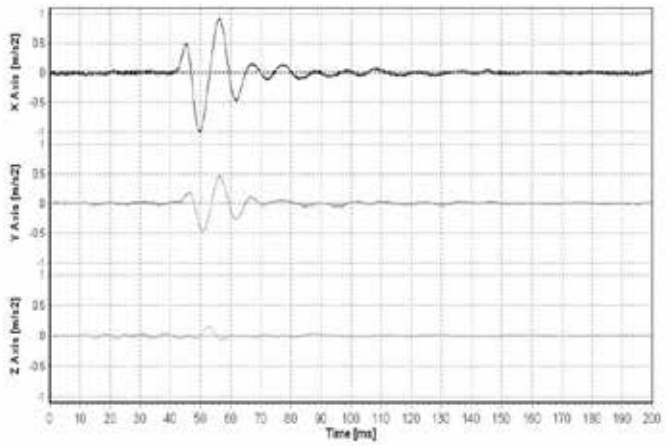

Figure 4. Unfiltered high SNR SCPT triaxial accelereometer data set.

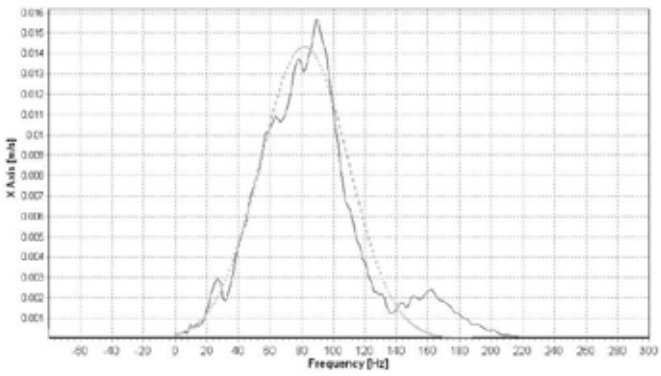

Figure 5. X axis frequency spectrum (solid black line) of triaxial source wave illustrated in Fig. 4 with the normal pdf approximation shown as a dotted grey line.

The spectrum in Fig. 5 is then fed into the IFM portion of the bell-curve fitting algorithm where optimal values of μ = 82 Hz and σ = 27.8 were obtained. Figure 5 illustrates the estimated normalized pdf superimposed upon the unity area frequency spectrum. Values of ε_1 = 0.163, ε_2 = 0.816, R = 0.20 and SR = 0.8 were obtained. This high SR value indicates a high quality seismic trace, which is confirmed by the linearity value for this trace of 0.976 (using a standard time window, see 3.2).

3.2 *Low SNR SCPT data set*

Figure 6 illustrates another real data example where we have a low SNR SH source wave SCPT trace acquired in New Zealand. The triaxial data was acquired at a depth of 8m by fast response accelerometers (5μs response time) with a bandwidth of 10 Hz to 10 KHz manufactured by PCB Piezotronics. The triaxial seismic data displayed in Fig. 6 had option *normalize locally* applied. The frequency spectrums are calculated from the filtered traces of Fig. 6 (200 Hz low pass filter applied) as outlined in Step 2. The dominant frequency components were determined to reside within the Y axis recordings. Figure 7 illustrates the 7 axis frequency spectrum (solid black line) of triaxial source wave illustrated in Fig. 6 where the frequency spectrum amplitudes were uniformly modified so that the area under the curve was unity (Step 3).

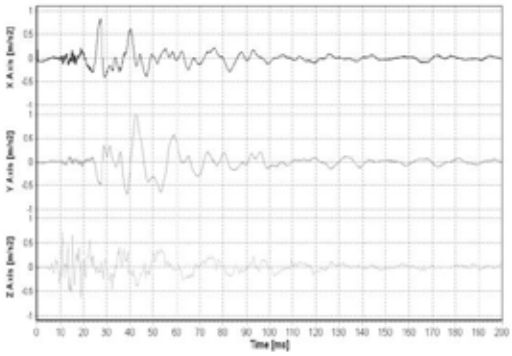

Figure 6. Unfiltered low SNR SCPT triaxial accelerometer data set

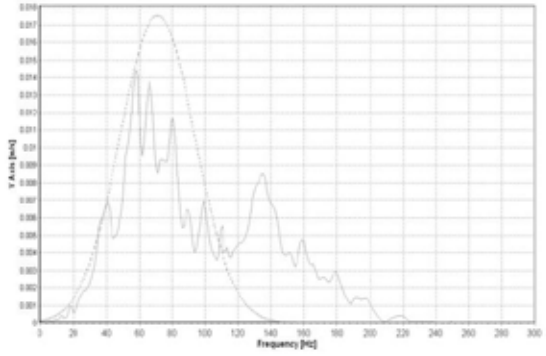

Figure 7. Y axis frequency spectrum (solid black line) of triaxial source wave illustrated in Fig. 6 with the normal pdf approximation shown as a dotted grey line.

The spectrum in Fig. 7 is then fed into the IFM portion of the bell-curve fitting algorithm where optimal values of μ = 71 Hz and σ = 22.7 were obtained. Figure 7 illustrates the estimated normalized pdf superimposed upon the unity area frequency spectrum. Values of ε_1 = 0.6, ε_2 = 0.907, R = 0.66 and SR = 0.34 were obtained. The value of SR = 0.34 identifies a low quality seismic trace. As could be expected the linearity value obtained for this trace is also lower (0.691).

It should be noted, however, that the linearity value can be significantly dependent upon the time window that is applied. The value listed above is based on a standard window covering 28 ms on either side of the first peak (the larger time window allows for greater source wave and trace characterization). If we were to reduce that to 14 ms the value increases to 0.779, and with an even narrower time the value can be as high as 0.82.

Whenever there is a low SR value and a low linearity value batch or automated processing should be avoided and arrival times should be obtained visually from VSPs and identifying first breaks or dominant peaks or trough.

4 CONCLUSIONS

SCPT is an important geotechnical testing technique for site characterization. SCPT provides low strain ($<10^{-5}$) in-situ interval compression (V_p) and shear (V_s) wave velocity estimates. A challenging problem in SCPT is to obtain an accuracy assessment of the quality of the calculated interval velocities. The accuracy assessment should take into account various independent seismic time series characteristics of the acquired data, which are then fused together into an interval velocity classification (*IVC*) or "rank" which quantifies the accuracy of the estimated interval velocities. This paper builds upon previous *IVC* development work where the authors have fused linearity estimates from polarization analysis in conjunction with cross correlation coefficient calculations of the full waveforms. In this paper, the mathematical and implementation details of a new parameter introduced into the *IVC* algorithm were outlined. This new parameter, denoted as *SR*, quantifies the deviation of the source wave frequency spectrum from a desirable bell-shaped curve. As outlined in this paper, SCPT seismic traces with high Signal to Noise Ratios (SNRs) were found to have characteristically bell-shaped curves similar to the probability density of a normal distribution. It was shown when processing real SCPT data sets that the bell-curve *SR* value is highly indicative of the SNR of the acquired trace. For seismic traces with low SNR batch or automated processing should be avoided and arrival times should be obtained visually from vertical seismic profiles identifying first breaks or dominant peaks or trough.

5 REFERENCES

Aki, K., and Richards, P.G. 2002. Quantitative Seismology (2nd Edition). Sausalito, CA: University Science Books.

ASTM. D7400-08. 2013. Standard Test Methods for Downhole Seismic Testing. ASTM Vol. 4.09 Soil and Rock (II): D5877-latest.

Baziw, E. 1993. Digital filtering techniques for interpreting seismic cone data, Journal of Geotechnical Engineering. ASCE, Vol. 119, No. 6, 98-1018.

Baziw, E. 2002. Derivation of Seismic Cone Interval Velocities Utilizing Forward Model. Can. Geotech. J., vol. 39,1-12.

Baziw, E. 2004. Two and three dimensional imaging utilizing the seismic cone penetrometer. In Proceedings of the 2nd International Conference on Geotechnical Site Characterization (ISC-2), Porto, Portugal, 19-22 Sept. Millpress Science Publishers, 1611-1618.

Baziw, E. and Ulrych, T.J. 2006. Principle Phase Decomposition - A New Concept in Blind Seismic Deconvolution, IEEE Transactions on Geosci. Remote Sensing (TGRS), vol. 44, no. 8, 2271-2281.

Baziw, E. 2011. Incorporation of Iterative Forward Modeling into the Principle Phase Decomposition Algorithm for Accurate Source Wave and Reflection Series Estimation. IEEE Transactions on Geosci. Remote Sensing (TGRS), vol. 49, no. 2, 650-660.

Baziw, E., and Verbeek, G. 2012. Deriving Interval Velocities from Downhole Seismic Data. Geotechnical and Geophysical Site Characterization 4 – Mayne (eds), CRC Press, 1019–1024.

Baziw, E. and Verbeek, G. 2014. Signal Processing Challenges when Processing DST and CST Seismic Data containing TIRs. ASTM International - Geotechnical Testing Journal (GTJ), vol. 37, no. 3, 1-21.

Baziw, E. and Verbeek, G. 2016. Classification Technique for Assessing Estimated Interval Velocity Estimates in DST, submitted to the ASTM International - Geotechnical Testing Journal.

GE, M. 2003. Analysis of source location algorithms, Parts 1 and II. J. of Acoustic Emission, vol. 21, 14-18 and 29-51.

Ge M., and Mottahed P. 1993. An automatic data analysis and source location system. Proceedings 3rd International Symposium on Rockbursts and Seismicity in Mines A A Balkema Rotterdam, 343-348.

Gelb, A. 1974. Applied Optimal Estimation, 4th ed., MIT Press: Cambridge, Mass, USA.

Gibowicz, S.J., and Kijko, A.1994. An Introduction to Mining Seismology, Academic Press, San Diego, CA, USA.

Kanasewich, E.R., 1981, Time sequence analysis in geophysics. 3rd ed., The University of Alberta Press, Edmonton, AB. Chapter 19.

Shearer, P.M. 1999. Introduction to Seismology. 1st edition, Cambridge: Cambridge University Press.

Geotechnical and Geophysical Site Characterisation 5 – Lehane, Acosta-Martínez & Kelly (Eds)

Enhanced data interpretation: combining in-situ test data by Bayesian updating

J. Huang
ARC Centre of Excellence for Geotechnical Science & Engineering, University of Newcastle, Australia

R. Kelly
SMEC, Brisbane, Queensland, Australia

S.W. Sloan
ARC Centre of Excellence for Geotechnical Science & Engineering, University of Newcastle, Australia

ABSTRACT: Combining data sets obtained during site characterization studies has the potential to enhance data interpretation. An example is provided where seismic data is combined with preconsolidation pressures obtained from laboratory tests. Semi-empirical relationships between preconsolidation pressure and shear wave velocity can be used to estimate the preconsolidation pressure. Conventionally, the uncertainties in the relationships are ignored. The Bayesian updating approach is used to take these uncertainties into account. Both trend analysis and kriging interpolation are used for the laboratory tests on the preconsolidation pressure to derive the prior distributions. The posterior preconsolidation pressures are then obtained by incorporating shear wave velocity measurements from a seismic dilatometer test. The analyses demonstrate that the seismic dilatometer data can be enhanced by the laboratory data set. This approach can be extended to enhance two-dimensional geophysical surveys by conditioning on a small number of accurate laboratory or in-situ test measurements.

1 INTRODUCTION

A typical site investigation program for a linear infrastructure project could include multiple types of site characterization techniques including geophysics, in-situ testing, borehole drilling and laboratory testing. Currently these data are often used in isolation from each other. For example, geophysical surveys could be used to assess site stratigraphy but not used to assess material parameters. When data are combined, they can have different resolutions. A profile of boreholes and in-situ tests can be overlain on geophysics data to help interpret stratigraphic boundaries from 'blurry' geophysics data. In-situ tests can be performed at different locations to boreholes and compared with the laboratory test data obtained from soil samples to develop material parameters. The soil between the in-situ tests and the borehole locations is assumed to have uniform properties.

Probabilistic numerical methods can be used to combine many of these different data sets to extract additional information from data that are routinely collected. The numerical methods have the potential to increase resolution of stratigraphic assessments using geophysics combined with other data, convert geophysics data to material properties, improve the resolution of in-situ tests combined with high quality laboratory measurements and to interpolate stratigraphy/material properties between test locations (e.g., Foti 2013).

Bayesian updating is a probabilistic numerical method that can be used to combine data. The advantage of Bayesian updating is that small data sets can be used. In this paper we demonstrate how Bayesian updating works by combining data from in-situ shear wave velocity measurements and laboratory tests with depth at a single location (one dimension). The theory can be extended to two and three dimensions. The example we present combines preconsolidation pressures obtained from constant rate of strain (CRS) consolidation tests with shear wave velocity data obtained from a seismic dilatometer test.

2 BAYESIAN UPDATING

Bayesian updating is a stochastic method that is well suited to geotechnical processes, particularly when limited information is available (e.g., Kelly and Huang 2015). Bayes' formula can be written as follows:

$$P(\boldsymbol{\theta}\,|\,\mathbf{y}) \propto P(\mathbf{y}\,|\,\boldsymbol{\theta})P(\boldsymbol{\theta}) \tag{1}$$

where $P(\boldsymbol{\theta})$ is the prior probability distribution of the material parameters, $P(\mathbf{y}\,|\,\boldsymbol{\theta})$ is the probability of measurements $(\mathbf{y})$ conditional on the material parameters $(\boldsymbol{\theta})$ and $P(\boldsymbol{\theta}\,|\,\mathbf{y})$ is the posterior

distribution of the material parameters updated by measurements.

The measurements ($\mathbf{y}$) represent the geophysics data and can be written as:

$$y_i = f(\boldsymbol{\theta}) + \mu_\varepsilon \tag{2}$$

where μ_ε is the mean "error" or difference between measurement and model function (or calculation) $f(\boldsymbol{\theta})$.

If the measured error is assumed to be normally distributed, the likelihood function of measurement y_i can be written as:

$$P(y_i \mid \boldsymbol{\theta}) = \phi\left(\frac{y_i - f(\boldsymbol{\theta}) - \mu_\varepsilon}{\sigma_\varepsilon}\right) \tag{3}$$

where σ_ε is the standard deviation of the measurement errors, and ϕ is the probability density function of the standard normal distribution.

The Markov Chain Monte Carlo sampling method (MCMC) has been used to sample the posterior distribution. This method involves stepping through a Markov Chain where, at each step, a test realization for $\boldsymbol{\theta}$ is proposed according the proposed distribution, and is then either accepted or rejected using a random decision rule based on the realization's predicted data misfit and the misfit of the previously accepted model. After a certain "burn-in" period, required for the procedure to stabilize and become independent of the initial starting realization, accepted samples drawn at regular intervals along the Markov Chain will represent independent realizations of the posterior distribution and will occur at a frequency corresponding to their posterior probability of occurrence. The basic idea goes back to Metropolis et al. (1953)).

3 EMPIRICAL RELATIONSHIP BETWEEN PRECONSOLIDATION PRESSURES AND SHEAR WAVE VELOCITY

Atkinson (2007)) proposed Eq. (4) relating small strain shear stiffness to yield stress ratio. In this Equation, G_0 is the small strain stiffness, p_a is a normalising pressure taken to be 1kPa, A, n and m are constants, p' is the effective mean pressure and R_0 is the yield stress ratio.

$$\frac{G_0}{p_a} = A\left(\frac{p'}{p_a}\right)^n R_0^m \tag{4}$$

The shear wave velocity should therefore be related to the yield stress ratio because G_0 and shear wave velocity are related parameters. Eq. (5) is written in terms of effective vertical stress and OCR as an analogy to Equation 5.

$$\frac{G_0}{p_a} = A\left(\frac{\sigma'_v}{p_a}\right)^n OCR^m \tag{5}$$

A relationship between preconsolidation pressure and shear wave velocity was obtained by adopting the values n = 0.9, m = 0.35 and A = 170 estimated from Atkinson (2007)) and rewriting OCR in terms of preconsolidation pressure.

Eq. (5) is the model function and we consider that its accuracy is uncertain. The model function is used to convert the geophysical data into a form that can be compared with more accurate laboratory test data.

Preconsolidation pressures assessed from constant rate of compression tests and the ones interpreted from a seismic dilatometer test are compared in Fig. 1. The laboratory test data are considered the prior set of material parameters and the seismic dilatometer data are the measurements.

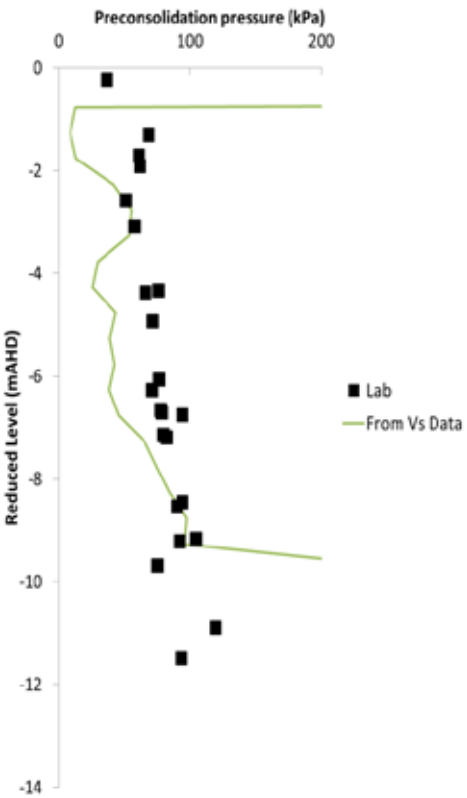

Figure. 1 Comparison between preconsolidation pressures assessed from constant rate of compression tests and interpreted from a seismic dilatometer test.

4 PRIOR INTERPRETATION OF PRECONSOLIDATION PRESSURES

The prior distribution is obtained from laboratory test data. A log-normal distribution has been assumed for the prior values.

A prior distribution of the measurements can be obtained by obtaining a linear trend through the data with depth and then assessing the standard deviation of the data from the trend. This is equivalent to assuming the preconsolidation pressure increases linearly with depth as

$$\sigma'_y = az + b \tag{6}$$

where z is reduced level, a and b are constants. The laboratory test data is fitted to Eq. (6) by the least square method, and $a = -6.38\text{kPa}$ and $b = 39.90\text{kPa}$. The standard deviation from the trendline is 6.39kPa and is assumed to be constant with depth.

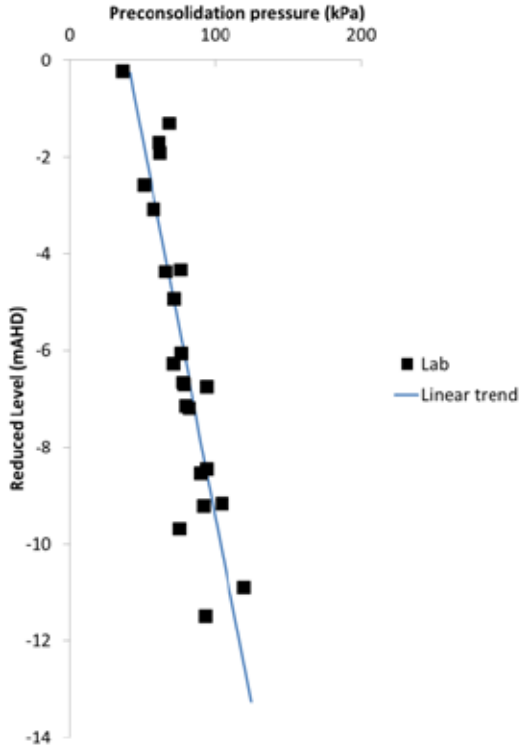

Figure. 2 Trend analysis of preconsolidation pressures assessed from constant rate of compression tests.

A prior distribution can also be obtained by kriging through the data set. Kriging provides a best estimate of a random field between known data. The basic idea is to estimate $X(z)$ at any point using a weighted linear combination of the values of X at each observation point. In kriging, high weights are given to the points that are closer to the unknown points. Interested readers are referred to Fenton and Griffiths (2008)). The kriged preconsolidation pressures assessed from constant rate of compression tests are shown in Fig. 3. In the example presented in this paper the scale of fluctuation is only used in the vertical direction but it can, in principle, be used to model 2D and 3D spatial variations.

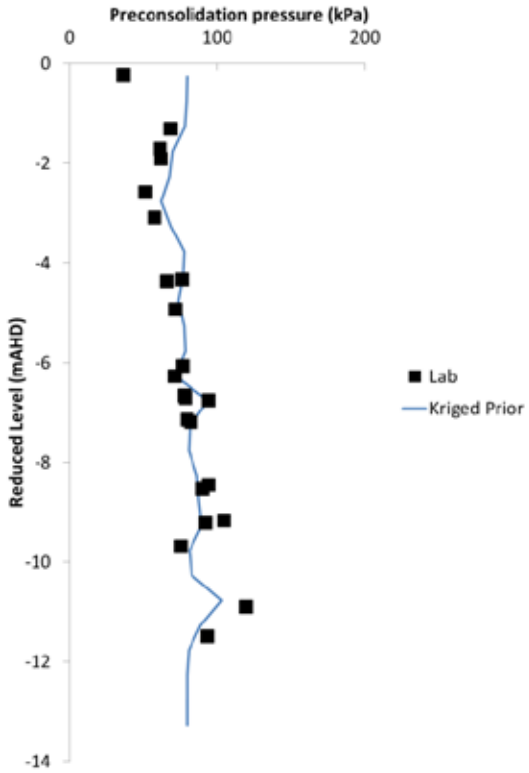

Figure. 3 Kriging interpolation of preconsolidation pressures assessed from constant rate of compression tests.

5 PRECONSOLIDATION PRESSURE UPDATED BY SHEAR WAVE VELOCITY

The mean and standard deviation of the error between the seismic dilatometer data and the model function are not known in advance. Shear wave velocities measured from seismic dilatometer tests are likely to be quite accurate, as is their conversion to small strain shear stiffnesses. However, the accuracy of the model function, Eq. (5), is quite uncertain. If we assume that there is no bias in the model function then the mean of the error can be set to zero. If we assume that the model function is highly uncertain then we can assign a large standard deviation to the error. In this case, the prior information will dominate the posterior solution, and in the extreme they will be equal. This is the same as assuming that the preconsolidation pressures measured in the laboratory apply everywhere in the domain. If we assume that the error has a small standard deviation then the solution will be more heavily influenced by the seismic dilatometer data and model function.

For the purpose of this example we have assumed that the standard deviation of the error is relatively small to highlight how the posterior is influenced by the prior and likelihood functions.

The posterior mean preconsolidation pressure is compared with the linear prior and model function from the seismic dilatometer in Fig. 4. The posterior prediction has updated the seismic dilatometer data

such that its trend and magnitude more closely approximates the laboratory values.

A similar comparison with the kriged prior is shown in Fig. 5. Kriging incorporating a scale of fluctuation provides a set of prior values that are conditioned on the laboratory data but vary between data points according to the scale of fluctuation. The posterior prediction is a better fit to the laboratory test data, possibly due to the standard deviation of the prior kriged data being smaller than that of the prior linear data. Use of a scale of fluctuation with the kriged prior also provides greater accuracy when interpolating between data points with depth compared with the linear prior.

6 DISCUSSION

The previous section demonstrated some of the principles adopted when combining data. This method of analysis can be extended into two dimensions where a geophysical data set could be conditioned on laboratory and in-situ test data obtained at different spatial locations, both horizontally and with depth. The combined data set creates a 2D geotechnical model, where material parameters can be assigned to geophysical grid points. This model would be an enhancement of conventional models, where material parameters are assigned uniformly to a particular stratigraphic layer.

In principle, this model could then be transformed into a finite element mesh. Further, mean and standard deviation of the parameter values are also associated with the grid points, which allows creation of 2D probabilistic models. Creation of such models is a fundamental precursor for the routine use of probabilistic analysis in design practice.

However, a number of technical challenges remain to be overcome. One significant challenge is to quantify model error. At the moment it is difficult to quantify the magnitude of model error. Therefore the analyst can choose how much error to adopt in an analysis to effectively tune the model towards uniform material properties based on laboratory test data at one extreme or geophysics data at the other extreme. Selection of model error is therefore based on engineering judgment and the skill of the analyst.

A second challenge is to incorporate Bayesian updating of stratigraphic boundaries into the process (e.g., Houlsby and Houlsby 2013) before updating the material properties. In the examples presented in

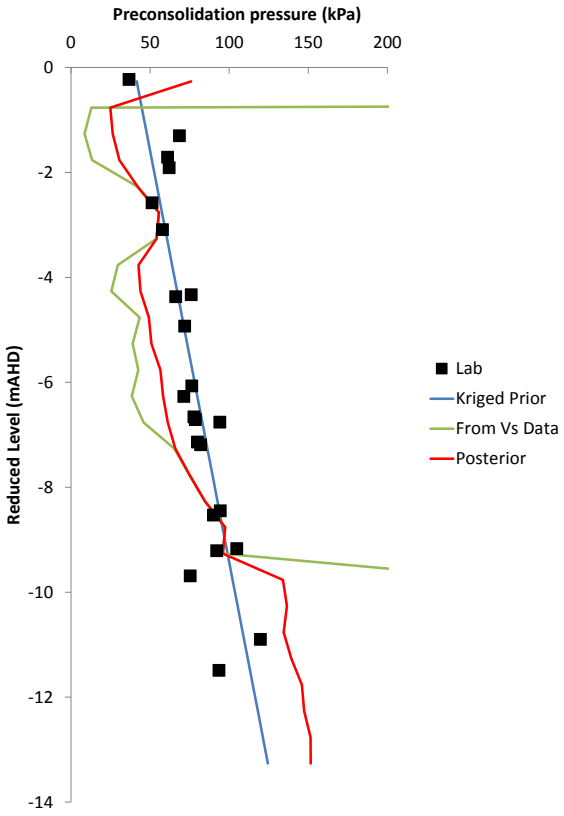

Figure. 4 Posterior mean preconsolidation pressures using trend analysis of constant rate of compression tests as prior distribution.

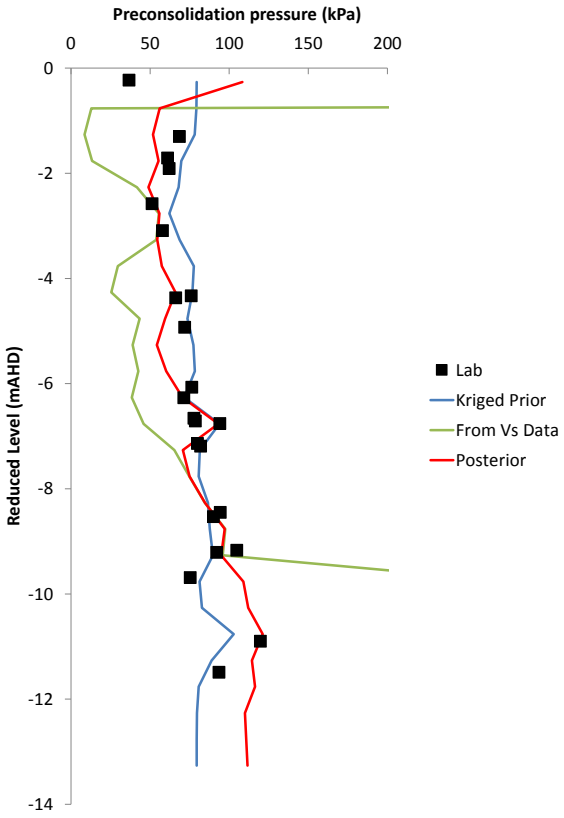

Figure. 5 Posterior mean preconsolidation pressures using kriging interpolation of constant rate of compression tests as prior distribution.

Section 5, the laboratory and dilatometer data sets were obtained from different physical locations and there is a difference in the depth to the base of the soft clay. The level at the base of the soft clay is approximately RL-9.5m at the location of the dilatometer and about RL-12m at the location of the laboratory test data. The Bayesian process, as presented here, updates both data sets irrespective of their stratigraphy.

7 CONCLUSIONS

This paper combines two different sets of geotechnical test data, namely results from laboratory constant rate compression tests and field seismic dilatometer tests. Empirical relationships between the preconsolidation pressure and shear wave velocity are firstly derived from the two sets of data. Unlike the traditional direct transformation, where the uncertainty associated with the transformation is ignored, the Bayesian updating approach is used to form a rigorous framework for combining the two sets of data. It is shown that the uncertainties of preconsolidation pressure can be significantly reduced by incorporating shear wave velocity measurements.

Further work is required to extend the process into two dimensions, incorporate stratigraphic updating and to investigate the magnitude of model error.

8 ACKNOWLEDGEMENTS

The authors wish to acknowledge the support of the Australian Research Council Centre of Excellence for Geotechnical Science and Engineering.

9 REFERENCES

Atkinson J *The Mechanics of Soils and Foundation*s, Second Edition, Taylor & Francis 2007.

Fenton GA and Griffiths DV Risk *Assessment in Geotechnical Engineering*, Wiley 2008.

Foti S (2013) Combined use of geophysical methods in site characterization. *Geotechnical and Geophysical Site Characterization* 4, Vols I and Ii: 43-61.

Houlsby NMT and Houlsby GT (2013) Statistical fitting of undrained strength data. *Geotechnique* 63(14): 1253 –1263.

Kelly R and Huang J (2015) Bayesian updating for one-dimensional consolidation measurements. *Canadian Geotechnical Journal* 52(9): 1318-1330.

Metropolis N, Rosenbluth AW, Rosenbluth MN, Teller AH and Teller E (1953) Equation of state calculations by fast computing machines. *The Journal of Chemical Physics* 21(6): 1087-1092.

Geotechnical and Geophysical Site Characterisation 5 – Lehane, Acosta-Martínez & Kelly (Eds)

Calibration of Vs Prediction Model based on SPT-N using Conditional Probability Theory

T. Kishida
Pacific Earthquake Engineering Research Center, University of California, Berkeley, USA
C-C. Tsai
National Chung Hsing University, Taiwan

ABSTRACT: Prediction models of shear wave velocity (V_s) based on the standard penetration test (SPT) blow counts (N) are widely used in design practice. However, application of these models is limited because these models are typically ranged between regions. Moreover, it is difficult to calibrate the regression parameters for a site specific condition if multicollinearity exists in the model. This paper proposes a calibration procedure for developing a site specific V_s prediction model. The framework is based on conditional probability theory by developing correlations of model parameters from a global database. An application example is presented to develop the site specific V_s prediction model based on the available local N measurements. The framework of the conditional probability theory provides the rational approach to calibrate the site specific V_s prediction model.

1 INTRODUCTION

Standard penetration test (*SPT*) blow count (N) is available at many sites throughout the world. On the other hand, shear wave velocities (V_s) are less available compared to N. Since V_s profiles are required for dynamic analysis and site characterization, the correlation of V_s and N is widely used for many design practice. Brandenberg et al. (2010) and Wair et al. (2012) summarized the previous studies and showed that most prediction models use the functional form of $V_s = AN^B$. Brandenberg et al. (2010) also presented multiple linear regression models for V_s by using N and effective overburden stress (σ'_{vo}) as predictor variables, showing that it improves the prediction capabilities. However, it is recognized that V_s prediction models range widely between sites that is an importance issue to improve the prediction capability (Brandenberg et al. 2010 and Wair et al. 2012). Based on this reason, this paper proposed an approach to calibrate V_s prediction model for the site specific condition based on the conditional probability framework.

2 V_S PREDICTION MODELS CONDITIONED ON N MEASUREMENTS

2.1 *Model Development*

It is assumed that N is modeled with σ'_{vo} by a simple regression equation,

$$\ln N = b_0 + b_1 \ln \sigma'_{vo} + \varepsilon_N \tag{1}$$

where ε_N represents the residuals that follows normal distribution with standard deviation of σ_N. Similarly, it is assumed that V_s is modeled with σ'_{vo} by a simple regression equation,

$$\ln V_s = c_o + c_1 \ln \sigma'_{vo} + \varepsilon_{Vs} \tag{2}$$

where ε_{Vs} are residuals following normal distribution with standard deviation of σ_{Vs}. Correlation between ε_N and ε_{Vs} is also defined as ρ_{NVs} from Equations (1) and (2). Based on the conditional prediction of V_s given N measurement, the following formula is obtained.

$$E[\ln Vs \mid \ln N] = \beta_0 + \beta_1 \ln N + \beta_2 \ln \sigma'_{vo} \tag{3}$$

where

$$\beta_0 = c_0 - b_0 \frac{\sigma_{Vs}}{\sigma_N} \rho_{NVs} \tag{4}$$

$$\beta_1 = \frac{\sigma_{Vs}}{\sigma_N}\rho_{NVs} \tag{5}$$

$$\beta_2 = c_1 - b_1\frac{\sigma_{Vs}}{\sigma_N}\rho_{NVs} \tag{6}$$

Standard deviation is calculated as;

$$\sigma^2_{Vs|N} = \sigma^2_{Vs}\left(1-\rho^2_{NVs}\right) \tag{7}$$

Equations (3) to (7) become the basis of conditional probability approach.

2.2 *Variation of Simple Regression Parameters*

Database of V_s and N was developed from three data resources of Taiwan Strong Motion Instrument Program (TSMIP), Kyoshin Network (K-NET) by National Research Institute for Earth Science and Disaster Prevention and Oakland International Airport (OAK). Data from TSMIP and K-NET are available for public. The data for OAK was obtained from the previous study (Arulnathan et al. 2009). The database includes approximately 1,400 soil profiles. Effective stresses were computed for each boring from the available unit weight and depth of water table. If the depth of water table is not available, it was determined when the P-wave velocity becomes 1,500 m/s. The N is corrected to N_{60} with the associated correction factors from past studies.

By running the simple regression analyses with Equations (1) and (2) for the developed database, Figure 1 was obtained. Mean, standard deviations, and correlations of these parameters are also presented in Equations (8) to (10).

2.3 *Variation of β_0, β_1, β_2 and σ_{VsN} for prediction model of Vs with N*

Figure 2 shows the scatter plots of β_0, β_1, and β_2 for clay, silt and sand obtained from the aforementioned data sources. The figure shows that there is no clear difference in the distribution of the parameters among clay, silt and sand. This observation implies that regional factors such as geologic conditions contribute more to the variation of β_0, β_1, and β_2 more than soil type.

$$\left[\hat{b}_0 \quad \hat{b}_1 \quad \hat{c}_0 \quad \hat{c}_1 \quad \hat{\sigma}_N \quad \hat{\sigma}_{Vs} \quad \hat{\rho}_{VsN}\right] = \left[0.484 \quad 0.489 \quad 4.21 \quad 0.251 \quad 0.840 \quad 0.322 \quad 0.400\right] \tag{8}$$

$$\left[\sigma_{b0} \quad \sigma_{b1} \quad \sigma_{c0} \quad \sigma_{c1} \quad \sigma_{\sigma N} \quad \sigma_{\sigma Vs} \quad \sigma_{\rho VsN}\right] = \left[1.97 \quad 0.436 \quad 0.763 \quad 0.163 \quad 0.212 \quad 0.115 \quad 0.276\right] \tag{9}$$

$$\begin{bmatrix} 1 & \rho_{b0b1} & \rho_{b0c0} & \rho_{b0c1} & \rho_{b0\sigma N} & \rho_{b0\sigma Vs} & \rho_{b0\rho VsN} \\ \rho_{b0b1} & 1 & \rho_{b1c0} & \rho_{b1c1} & \rho_{b1\sigma N} & \rho_{b1\sigma Vs} & \rho_{b1\rho VsN} \\ \rho_{b0c0} & \rho_{b1c0} & 1 & \rho_{c0c1} & \rho_{c0\sigma N} & \rho_{c0\sigma Vs} & \rho_{c0\rho VsN} \\ \rho_{b0c1} & \rho_{b1c1} & \rho_{c0c1} & 1 & \rho_{c1\sigma N} & \rho_{c1\sigma Vs} & \rho_{c1\rho VsN} \\ \rho_{b0\sigma N} & \rho_{b1\sigma N} & \rho_{c0\sigma N} & \rho_{c1\sigma N} & 1 & \rho_{\sigma N\sigma Vs} & \rho_{\sigma Vs\rho VsN} \\ \rho_{b0\sigma Vs} & \rho_{b1\sigma Vs} & \rho_{c0\sigma Vs} & \rho_{c1\sigma Vs} & \rho_{\sigma N\sigma Vs} & 1 & \rho_{\sigma N\rho VsN} \\ \rho_{b0\rho VsN} & \rho_{b1\rho VsN} & \rho_{c0\rho VsN} & \rho_{c1\rho VsN} & \rho_{\sigma Vs\rho VsN} & \rho_{\sigma N\rho VsN} & 1 \end{bmatrix} = \begin{bmatrix} 1 & -0.955 & 0.414 & -0.394 & 0 & 0 & 0 \\ -0.955 & 1 & -0.402 & 0.455 & 0 & 0 & 0 \\ 0.414 & -0.402 & 1 & -0.938 & 0 & 0 & 0 \\ -0.394 & 0.455 & -0.938 & 1 & 0 & 0 & 0 \\ 0 & 0 & 0 & 0 & 1 & 0.373 & 0 \\ 0 & 0 & 0 & 0 & 0.373 & 1 & 0 \\ 0 & 0 & 0 & 0 & 0 & 0 & 1 \end{bmatrix} \tag{10}$$

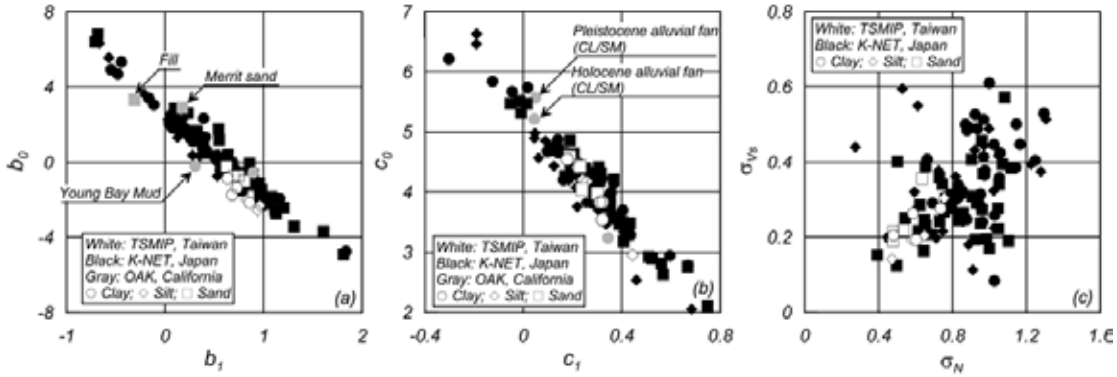

Figure 1. Variation of b_0, b_1, c_0, c_1, σ_{vs}, and σ_N for clay, silt, and sand

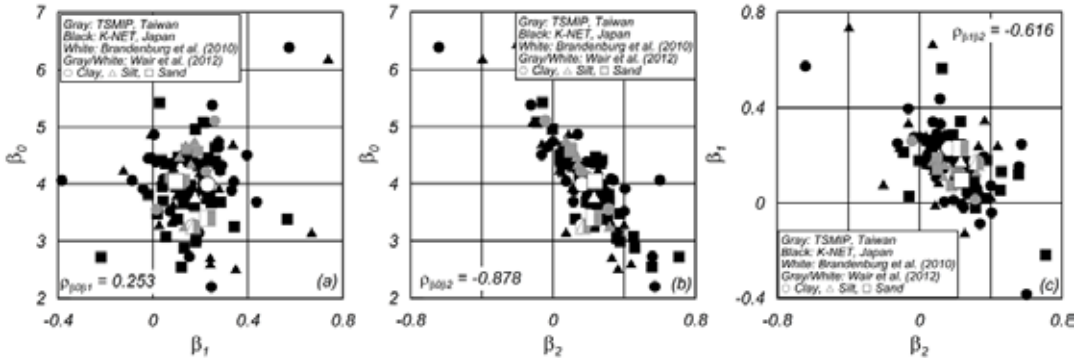

Figure 2. Variations of (a) β_0 and β_1, (b) β_0 and β_2, and (c) β_1 and β_2 for clay, silt and sand. Figures also show the parameters from the previous studies by Brandenberg et al. (2010) and Wair et al. (2012).

Figure 2 also shows the regression parameters by Brandenberg et al. (2010) and Wair et al. (2012) for comparison. The results by Brandenberg et al. (2010) locate nearly the center of distributions obtained from the database, where the results by Wair et al. (2012) are slightly shifted from the center of distributions, but still within the range of the parameter distributions.

3 CALIBRATION OF SITE SPECIFIC VS PREDICTION MODEL WITH AVAILABLE N

This section describes the development of a site specific V_s prediction model where only N measurements are available from several borings, but no V_s measurements. The c_0 and c_1 in Equation (2) are estimated conditioned on the b_0 and b_1 measurements as follows:

$$\begin{bmatrix} c_0 \\ c_1 \end{bmatrix} = \begin{bmatrix} \hat{c}_0 \\ \hat{c}_1 \end{bmatrix} + \Sigma_{12}\Sigma_{22}^{-1} \begin{bmatrix} b_0 - \hat{b}_0 \\ b_1 - \hat{b}_1 \end{bmatrix} \tag{11}$$

By substituting Equations (8), (9) and (10) into (11), the following expressions are obtained:

$$c_0 = 4.21 + 0.132 b_0 - 0.132 b_1 \tag{12}$$

$$c_1 = 0.0689 + 0.0381 b_0 + 0.335 b_1 \tag{13}$$

Similarly, the σ_{Vs} is obtained conditioned on σ_N as follows:

$$\sigma_{Vs} = 0.152 + 0.202 \sigma_N \tag{14}$$

Therefore, substituting Equations (12), (13) and (14) into (4), (5) and (6), β_0, β_1 and β_2 in Equation (3) are obtained conditioned on the b_0, b_1 and σ_N as follows:

$$\beta_0 = 4.21 + \left(0.0512 - \frac{0.0608}{\sigma_N} \right) b_0 - 0.132 b_1 \tag{15}$$

$$\beta_1 = 0.080 + \frac{0.0608}{\sigma_N} \tag{16}$$

$$\beta_2 = 0.0689 + 0.0381 b_0 + \left(0.254 - \frac{0.0608}{\sigma_N} \right) b_1 \tag{17}$$

Urayasu, Japan where the lateral spread was observed after 2011 Tohoku earthquake (Ashford et al. 2011) is selected as an example site. Figure 3 shows the variation of N_{60} against σ'_{vo} for sand deposit beneath the fill. The figure shows that b_0 and b_1 in Equation (1) are 1.77 and 0.182, respectively. The standard deviation of σ_N is obtained as 0.663. Based on these variables, β_0, β_1 and β_2 are obtained from Equations (15) to (17); hence the V_s prediction model conditioned on these measurements is obtained as follows:

$$\ln V_s = 4.11 + 0.172 \ln N + 0.166 \ln \sigma'_{vo} \quad (18)$$

Standard deviation is calculated based on Equations (14) as follows:

$$\sigma_{Vs|N} = 0.262 \quad (19)$$

By following this approach, the site specific V_s prediction models can be calibrated by using the global database and the available N measurements at application sites.

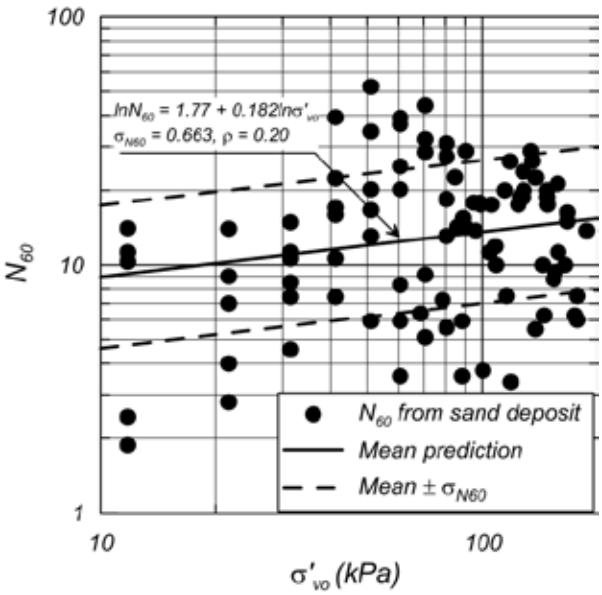

Figure 3. Variation of N_{60} for sand deposit beneath artificial fill against σ'_{vo}.

4 CONCLUSIONS

The V_s prediction model conditioned on SPT N is discussed in this paper. This study focuses on the calibration of V_s prediction model with the site specific database, where previous studies mainly focuses on the improvement of the model based on soil type such as clay, silt and sand.

Simple regression parameters of $\ln V_s$ and $\ln N$ against $\ln \sigma'_{vo}$ were computed from global database. Based on these analyses, means, standard errors and correlations of these regression parameters are obtained as a basis to develop the site specific V_s prediction models.

Methodology to obtain the site specific V_s prediction model is described when only N are available from several borings, but no V_s measurement. The proposed approach can reflect the trend observed in $\ln N$ vs. $\ln \sigma'_{vo}$ at application sites whereas previous studies have to assume the same site condition between where V_s prediction model was developed and the application site. This is a significant improvement to adjust the V_s prediction models to the local site conditions. The proposed approach can be applicable to any sites since no specific assumption exists behind the development of conditional V_s prediction model with N.

5 REFERENCES

Grove, A.T. 1980. Geomorphic evolution of the Sahara and the Nile. In M.A.J. Williams & H. Faure (eds), *The Sahara and the Nile*: 21-35. Rotterdam: Balkema.

Jappelli, R. & Marconi, N. 1997. Recommendations and prejudices in the realm of foundation engineering in Italy: A historical review. In Carlo Viggiani (ed.), *Geotechnical engineering for the preservation of monuments and historical sites*; *Proc. intern. symp., Napoli, 3-4 October 1996*. Rotterdam: Balkema.

Johnson, H.L. 1965. Artistic development in autistic children. *Child Development* 65(1): 13-16.

Polhill, R.M. 1982. *Crotalaria in Africa and Madagascar*. Rotterdam: Balkema.

Wair, B. R., DeJong, J. T., and Shantz, T. 2012, Guidelines for Estimation of Shear Wave Velocity Profiles, PEER Report 2012/08, Pacific Earthquake Engineering Research Center, Headquarters at the University of California.

Brandenberg, S. J. and Bellana, N. and Shantz T. 2010, Shear wave velocity as function of standard penetration test resistance and vertical effective stress at California bridge sites, Soil Dynamics and Earthquake Engineering, 30, 1026-1035.

Arulnathan, R., et al. 2009. Vulnerability assessment of perimeter dike system at Oakland International Airport, TCLEE 2009 Conf.: 7th Int. Conf. on Lifeline Earthquake Eng., ASCE, Reston, VA.

Ashford, S. A., Boulanger, R. W., Donahue, J. L. and Stewart, J. P. 2011, Geotechnical Quick Report on the Kanto Plain Region during the March 11, 2011, Off Pacific Coast of Tohoku Earthquake, Japan, GEER Association Report No. GEER-025a (April 5, 2011)

Taiwan Strong Motion Instrument Program 2014, Engineering Geological Database for TSMIP, http://egdt.ncree.org.tw/ (last accessed, 03/21/2015).

National Research Institute for Earth Science and Disaster Prevention. 2014. Strong-motion Seismograph Networks (K-NET, KiK-net). <http://www.kyoshin.bosai.go.jp> (last accessed, April. 1, 2015).

Geotechnical and Geophysical Site Characterisation 5 – Lehane, Acosta-Martínez & Kelly (Eds)

Identification of Geologic Depositional Variations using CPT-based Conditional Probability Mapping

C.P. Krage, J.T. DeJong & R.W. Boulanger
University of California, Davis, Davis, CA, USA

ABSTRACT: The purpose of site characterization is to perform a geological, quantitative assessment of the project site to develop an idealized representation of the subsurface conditions and engineering properties that will be used for geotechnical analysis and design. An integrated approach to site characterization provides a methodical framework to hypothesize, evaluate, and understand the project site conditions. Proper characterization requires an understanding of the performance mechanism(s) that govern the geotechnical system performance given the site geologic setting, with the sufficiency of a site investigation program determined by how well the spatial variability and engineering properties are defined for the length scales of interest. Failure to adequately determine the nature of spatial variability, the connectivity of particular layers, or the presence of weak/loose zones can result in inadequate design and geosystem performance. In this paper the use of transition probability geostatistics, conditioned to CPT soundings and combined with geologic information, is explored to improve the characterization and understanding of subsurface stratigraphy at a project site. Following a description of the methods employed, a project example with a detailed geologic study and 34 CPT soundings is used to assess subsurface stratigraphy and site variability with the purpose of identifying continuous depositional layers that are expected to liquefy for a given seismic loading. Transition probability geostatistics are used to model the spatial correlation of zones expected to liquefy within each geologic layer. The interpreted subsurface is obtained using kriging based simulation techniques, dependent on both the correlation model and conditioned CPT soundings. The results from the geostatistical simulations indicate the presence of a thin, continuous liquefiable layer across the site.

1 INTRODUCTION

The purpose of site characterization is to perform a geological, quantitative assessment of the project site to develop an idealized representation of the subsurface conditions and engineering properties that will be used for geotechnical analysis and design. The challenge in this task is the insufficiency of available data for describing site conditions (typically limited by cost and schedule) and the often complex nature of a site's geology. As a result, when selecting representative properties for design and analysis of geosystems it is important to understand the nature of spatial variability and how that spatial variability may influence or alter the performance mechanisms. Selection of representative properties relies on engineering judgement and assumptions for estimation of the subsurface properties and their variability (Duncan 2000).

An integrated site characterization methodology, such as the one presented in Figure 1, is useful to understand and assess the role of spatial variability in design and analysis of geosystems to better inform engineering judgement. This paper highlights some of the geostatistical techniques that are currently available to quantify spatial variability, including a transition probability approach originally developed in the field of hydrology. An example case is presented where geostatistical techniques are implemented to identify depositional variations, capture the lateral extent and continuity of potentially liquefiable deposits, and highlight the usefulness of this approach.

2 GEOSTATISTICS FOR INFORMING SITE CHARACTERIZATION

Geostatistics can be used to supplement traditional site characterization techniques, providing quantitative assessment of site variability to compliment typical judgement-based estimation of the subsurface variability. The role of geostatistics is to extend what is known from the geologic setting and from soil borings and in-situ tests to provide insights regarding both site conditions and the expected system performance at unsampled locations.

The application of geostatistical techniques to geotechnical applications are well documented where researchers have applied geostatistical methods to

develop random field models of subsurface variability (e.g. Fenton and Vanmarcke 1990), analyze the role of spatial variability on performance of geosystems (e.g. Fenton and Vanmarcke 1990, Griffiths et al. 2002, Elkateb et al. 2003, Al-Bittar and Soubra 2014, Li et al. 2015a) and analyze real data sets to develop representative models for spatially variable deposits (e.g. Fenton 1999, Lloret-Cabot et al. 2012, Lloret-Cabot et al. 2014, Li et al. 2015b).

These techniques can be used to quantify the variability of design parameters used in analysis, reducing reliance on qualitative judgements and assumptions in practice. Li et al. (2015a) investigated the failure mechanisms and bearing capacity of footings buried at various depths within simulated spatially variable soil and found that failure planes seek out and develop in weaker zones, resulting in the development of multiple failure planes not predicted in a typical analysis with uniform properties. This resulted in a range of bearing capacity factors of 60% to 120% of the uniform bearing capacity factor. Boulanger and Montgomery (2015) suggested that 30th to 50th percentile normalized SPT blow count values may be representative of spatially variable deposits for evaluating liquefaction induced deformations in an alluvial deposit beneath a large embankment dam. Munter et al. (2016) used a geostatistical approach to model the role of spatially variable mixtures of sand and clay on infinite slope lateral spreading analyses. They found that failure paths tended to concentrate within connected liquefiable sand pockets. Deformations were minimal when these sand pockets were sufficiently discontinuous and the clay sufficiently strong.

These studies demonstrate the benefit of an improved quantitative understanding of the geologic setting via geostatistical techniques. This understanding is particularly useful in fluvial environments where fluctuations in the depositional process produce heterogeneous deposits where both the soil type and soil properties often vary over lateral distances of even a few meters. The distance over which the soil type is similar can be described using different length scale terms, such as a correlation length.

Estimating the vertical correlation length tends to be more straightforward than estimating the horizontal correlation length in fluvial depositional environments. This is because in-situ tests, which obtain measurements versus depth at a high sampling frequency (e.g., CPT data every 50 mm, DMT every 0.3 m, SPT every 1.5 m, sonic coring is continuous), enable detailed characterization of the vertical variability of soil type and engineering properties. Methods for estimating the horizontal correlation length are less robust because the distance between data points (i.e. the distance between soundings or borings) is typically large to obtain coverage of the project site. In practice, it is rare that the spacing of soundings or borings for a project are selected with determination of the lateral variability being a priority. Nonetheless, DeGroot and Baecher (1992) did show that alteration of boring layout schemes can improve estimation of the horizontal correlation length.

Geostatistical analysis of subsurface conditions can aid in the site idealization process if performed thoroughly, thereby improving geotechnical engineering analysis and design. The challenge in this task is twofold: (1) to identify or estimate the soil type at unknown locations and (2) to estimate the engineering properties at these unknown spatial locations. These challenges are addressed in an integrated site characterization approach.

3 INTEGRATED SITE CHARACTERIZATION

3.1 *General Framework*

The framework for an integrated approach to site characterization by DeJong et al. (2016) spans from the desk study to observations during the long-term performance of the system. This is accomplished through a series of stages as shown in Figure 1: inductive reasoning, scenario assessment, site investigation, site idealization, analysis and design, and the observational method. The approach broadly encompasses the geotechnical engineering process, and as such extends beyond the single task of site investigation wherein in situ and laboratory techniques are used to obtain measurements of the soil conditions, and beyond the approaches described by others (Clayton et al. 1995, USACE 2001, Mayne et al. 2002, Clayton and Smith 2013). Ultimately, the purpose of the integrated site characterization approach is to develop a geological and performance mechanism-based quantitative assessment of site conditions for geotechnical engineering analysis and design.

3.2 *Development of Idealized Site Conditions*

The development of an idealized representation of site conditions requires that the site investigation program be guided by a hypothesis of subsurface stratigraphy that is based upon geology and the length-scale of the potential failure mechanisms. The site investigation program should be designed to validate these hypothesized conditions and therefore becomes a step of verification and refinement, rather than a step of pure discovery (although discovery may be a consequence of the investigation).

This approach requires development of a hypothesis of geologic conditions and identification of possible failure mechanisms prior to performing the site investigation. The anticipated geologic conditions are identified using regional geologic history, surficial geologic mapping, historical records, soil borings or soundings, and geophysical studies. Identification of possible failure mechanisms, including the

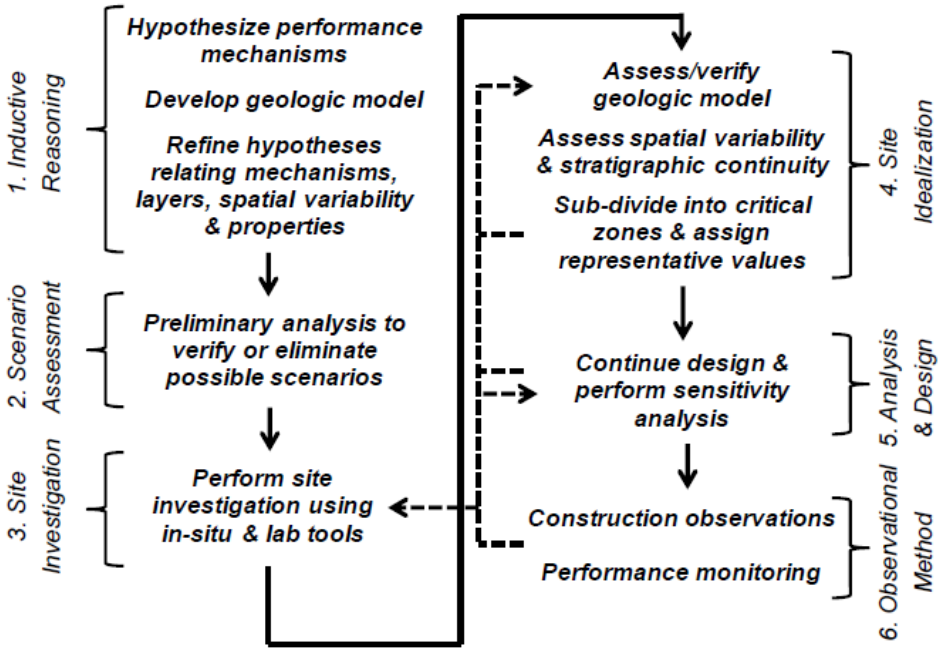

Figure 1. Schematic of the integrated site characterization framework.

length scale over which they act, can be guided by past performance at the project (or analogous) site and the results of preliminary quantitative analyses based on historical data (if available) and the geologic model hypothesis. These analyses can be used to determine the required lateral extent and depth of investigation, identify the length scale of spatial variability that is particularly relevant, reveal zones that may be of particular concern, and guide balancing the characterization of engineering properties and mapping of site spatial variability. In turn this guides the work distribution between geological, geophysical, in situ, laboratory, and hydro-geological studies.

An idealization of the site condition with its subsurface structure, variability, and representative engineering properties, can be developed after or preferably in parallel with the site investigation work. As described by DeJong et al. (2016), soil properties for particular layers can be effectively evaluated in a quantitative manner using analysis of cumulative distributions of normalized engineering properties. The representative percentile properties can be more effectively selected once the length scale of the failure mechanism relative to the length scale of spatial variability has been evaluated (Christian and Baecher 2006).

Identification of soil layers within which representative values can be defined requires mapping of of the subsurface variability (connectivity of lenses, layers, or zones). This is often a subjective process based on engineering judgement and conservative assumptions. Geostatistical techniques can provide an alternate approach to inform the engineer before employing engineering judgment in assessing spatial variability.

3.3 *Geostatistical Analysis*

The purpose of a geostatistical analysis is to use the information obtained from the site investigations to model and estimate conditions at unsampled locations. These geostatistical simulations can be used in iterative analysis and design procedures.

The use of geostatistical techniques generally requires that unique geologic units be identified and analyzed separately (e.g. not mixing data from an alluvial and colluvium unit together), and therefore be implemented after proper development and interpretation of geological site conditions. Quantitative geostatistics can complement geologic interpretation but is not a replacement as it cannot autonomously detect and delineate geologic depositional units.

Decisions must be made about what properties to treat geostatistically and if the distribution of those properties was fully captured in the site investigation program. In many cases, the description of property distributions requires supplementing the site investigation data with typical values for similar depositional environments. These fundamental assumptions to the geostatistical approach warrant scrutiny as they can dramatically affect the outcome of the analysis. Details of preparing a geostatistical analysis are highlighted in the following section.

4 GENERATING CONDITIONAL REALIZATIONS BASED ON CPT SOUNDINGS

4.1 *Spatial Correlation Model*

Several approaches to geostatistical simulation are used in geotechnical practice, with correlation and covariance functions tending to be the most common. While the approaches have different mathematical formulations, all methods serve the same

function to model site variability. Subsurface simulations generated via these approaches typically consist of a dataset, a model that describes the variation of that property in space, and some form of interpolation (e.g. kriging) technique. A geostatistical model must be fit to the dataset and serve to describe the change in spatial correlation with increased separation distance. A transition probability approach originally developed in the field of hydrology (Carle and Fogg 1996) is advantageous in that it can capture the order of depositional variations (i.e. facies models). This ordering is not typically captured in correlation or variogram models and as such the transition probability approach is used in this research (Carle and Fogg 1996).

Transition probability describes the likelihood of transitioning from one category (where categories are user defined; can be soil type or engineering property based) to another over some separation distance. The main advantage of this approach is the ability to model ordered systems (e.g. geologic facies environments), where the transition probability from category A to category B may not be the same as from B to A (i.e. upward fining sequence).

Scales of fluctuation, correlation length, and mean length terminology are specific to the type of model used and they describe the similarity or dissimilarity of two locations separated in space (Carle and Fogg 1996, Elkateb et al. 2003). The mean length is used in transition probability geostatistics to describe the expected length of a specific category across a horizon (horizontal or vertical). Properties that are similar across large distances have a large scale of fluctuation, correlation length and mean length while properties that are similar across smaller distances (more dissimilar at larger distances) have a small scale of fluctuation, correlation length and mean length.

The transition probability model is described by two parameters, the mean length and the sill for each category. The mean length describes the initial decay of transition probability and represents the average length of a category in a given horizon (X, Y, or Z) while the sill describes the global proportion of an individual category to the total number of categories and occurs at large separation distances.

A transition probability model is fit to a given dataset and used to simulate the subsurface stratigraphy using, for example, the software package TPROGS (Transition Probability Geostatistical Software; Carle 1999). This approach consists of an objective function (transition probability model), an algorithm to minimize the error of the objective function (sequential indicator simulation, SIS), and a quenching based algorithm to further reduce error in the objective function where the SIS and simulated quenching algorithms are used in tandem. The SIS kriging procedure defines the grid with categories that generally reflect the desired objective function. Kriging is an interpolation technique that honors the given data (conditioning points). SIS uses the information at known locations to estimate the category of an unknown location. Once this unknown location is estimated, it is used as a known location for the next (sequential) simulation.

Simulated annealing (quenching) can be applied iteratively to improve the simulation by eliminating "impurities" that throw off the objective function. This procedure cycles through each grid node and inquires whether a change in the node category will reduce the global error. This process continues until the global error is minimized or the maximum number of iterations are reached.

The successful implementation of SIS and simulated annealing results in a statistically robust simulation that honors conditioning data (if available) and the geostatistical model. As with any geostatistical approach, tuning of the model parameters will help improve the accuracy of the geostatistical simulation.

5 EXAMPLE CASE: LIQUEFACTION IN A WIDE ALLUVIAL BASIN

Site idealization incorporating geostatistical techniques is highlighted in the following example. Construction of a new embankment dam in a seismically active region requires site idealization for liquefaction assessment. The proposed dam (approximately 11 m tall and 550 m wide) is to be constructed in a wide alluvial basin where liquefaction of the sandy sediments is of concern. Due to the small height of the embankment, the zone of liquefiable material necessary to propagate large deformations up through the embankment is on the order of 15 to 24 m. CPTs were spaced approximately 15 m apart along the dam alignment to identify subsurface stratigraphy and identify the potential connectivity of loose, liquefiable zones.

5.1 *Geologic Setting*

The project site is located in a drainage basin bounded by alluvial fan deposits on the east and west. The deposits within the basin consist of Pliocene to Holocene alluvial fan and active channel deposits overlying sedimentary bedrock. These deposits consist of sand, silty sand, silt, and minor lenses of clay, silt, gravel, and cobbles and are divided into an upper and lower alluvial layer based on geologic interpretation and an extensive site investigation program. A geostatistical approach is used to identify loose, liquefiable zones in the upper alluvial layer (Zone 1) for this example, since liquefaction of the lower alluvium (Zone 2) contributes less to the potential for large deformations in the embankment dam.

5.2 *Category Binning Approach*

Screening for selecting transition probability category bins is first performed based on soil behavior type index (I_c), which indicates primarily sandy soil with 98% of I_c values between 1.3 to 2.6. Because preliminary analysis indicates prevalent sandy soil deposits prone to cyclic liquefaction, category bins are defined based on normalized cone penetration tip resistances (q_{c1N}) rather than I_c, since q_{c1N} is the parameter used in the liquefaction triggering correlations. The anticipated seismic hazard and measured q_{c1N} are used to estimate the demand and capacity of the deposits for liquefaction potential. A design earthquake with a moment magnitude of 7.75 and an 84th percentile peak ground acceleration (PGA) of 0.85g results in cyclic stress ratios of 0.4 to 0.6 in the Zone 1 alluvium. Ranges of q_{c1N} are selected for each category by overlaying the seismic demand on the Boulanger and Idriss (2015) liquefaction triggering relationship as shown in Figure 2. Category bins based on q_{c1N} of 0 to 110, 110 to 180, and greater than 180 are used to identify zones of expected liquefaction (L), possible liquefaction (PL) and no liquefaction (NL), respectively.

5.3 *Implementation of Geostatistical Approach*

Transition probabilities were calculated from available CPT q_{c1N} in the vertical and horizontal directions, then a Markov chain transition probability model was fit to these measured transition probabilities to use in the conditioning simulation. The transition probabilities matrix for the vertical direction are shown in Figure 3 with the sill calculated from the total proportion of each category and model parameters were chosen to ensure the best overall fit to the measured transition probabilities.

The geostatistical simulation in Figure 4 shows q_{c1N} values based on the transition probability model for the Zone 1 alluvium, conditioned on the CPT measured q_{c1N} values. The conditioned simulation was performed using a grid size of 100 mm and 620 mm in the vertical and horizontal directions respectively. The simulations indicate liquefaction in this unit is expected to be most prevalent at shallow depths, ranging from 1-2 m deep on the west side (left side of Figure 4) to 4-6 m deep on the east side (right side of Figure 4). In addition, liquefaction is also expected at a larger depth (elevation 1134 m) along a continuous thin, low tip resistance layer.

Geostatistical analysis is particularly useful when categorical bins are defined based on the engineering problem being analyzed; in this case liquefaction triggering. Modeling of categorical penetration tip resistances based on liquefaction potential allows for direct interpretation of the potential liquefaction hazard at the site. This example highlights the benefit of geostatistical interpretation of the subsurface

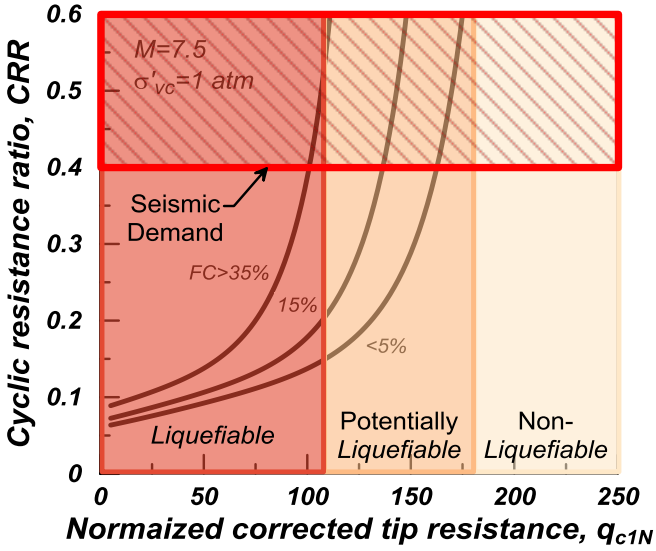

Figure 2. Selection of categories for the conditioned simulation based on the anticipated seismic demand and the Boulanger and Idriss (2015) triggering correlations.

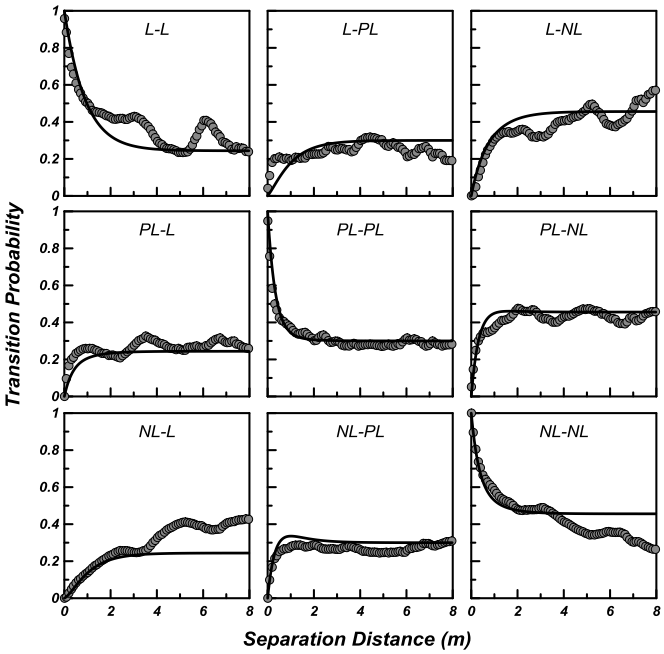

Figure 3. Calculated transition probabilities for the given CPT data (symbols) and the Markov chain transition probability model (line) for the vertical direction. Titles (e.g. L-PL) indicate the transition probability from one category (L) to the next (PL).

stratigraphy within the integrated site characterization framework.

6 CONCLUSIONS

This paper presented an approach to geostatistical simulation using an integrated site characterization framework. An example was presented, highlighting the usefulness of geostatistical techniques in the site idealization process.

The use of a geostatistical model conditioned to available CPT data aided in the identification and interpretation of geologic depositional variability, helping track the continuity of zones expected to liquefy at different seismic loadings. This was per-

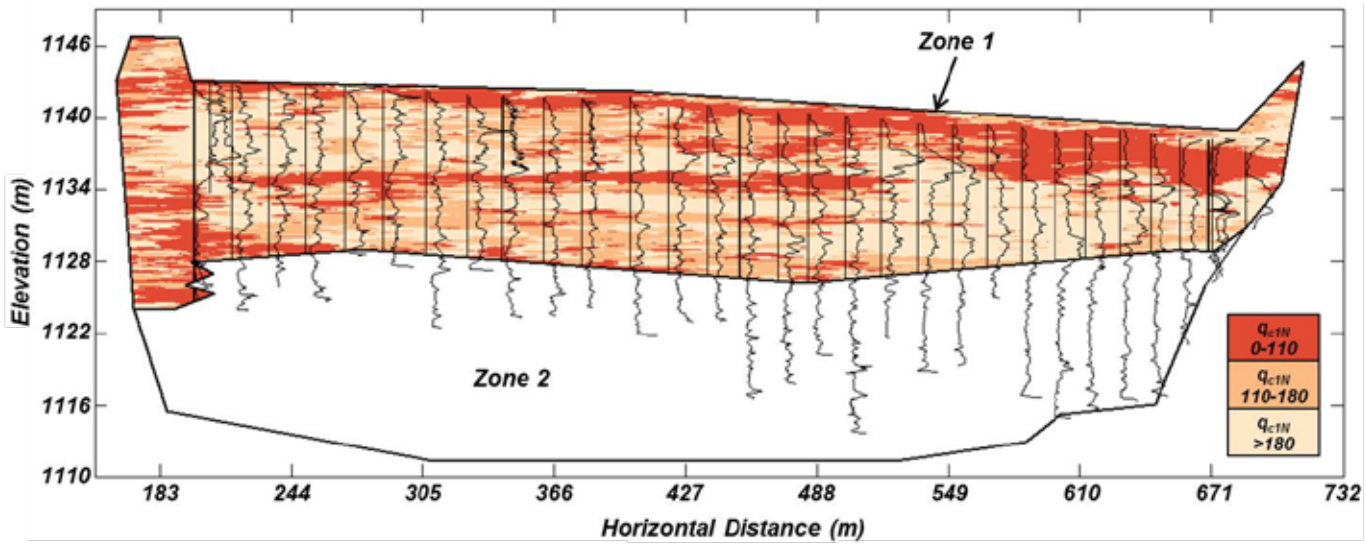

Figure 4. Boundary of the basin fill deposits, indicating Zone 1 and Zone 2 alluvium. The q_{1cN} profiles indicate the conditioning locations used in the geostatistical simulation. The presence of a thin continuous liquefiable to potentially liquefiable layer is detected at approximately 1134 m elevation.

formed after geologic interpretation binned the basin into primary geologic units.

Geostatistical analysis can be particularly useful when categorical bins are defined based on the engineering problem being analyzed. Modeling of categorical penetration tip resistances based on liquefaction potential allows for direct interpretation of the potential liquefaction hazard at the site. An example was presented that highlights the benefit of geostatistical interpretation of the subsurface stratigraphy within the integrated site characterization framework.

7 ACKNOWLEDGEMENTS

Funding from the National Science Foundation (CMMI-1436617) is appreciated. Any opinions, findings and conclusions or recommendations expressed in this material are those of the authors and do not necessarily reflect the views of the National Science Foundation. Provision of the data from the Los Angeles Department of Water and Power is gratefully acknowledged.

8 REFERENCES

Al-Bittar, T. and Soubra, A.H. 2014. Probabilistic analysis of strip footings resting on spatially varying soils and subjected to vertical or inclined loads. *J. of Geotech. and Geoenviron. Eng.* 140(4).

Boulanger, R. W., and Idriss, I. M. (2015). "CPT-based liquefaction triggering procedure." *J. of Geotech. and Geoenviron. Eng.* 142(2).

Boulanger, R.W. and Montgomery, J. 2015. Nonlinear deformation analyses of an embankment dam on a spatially variable liquefiable deposit. *Proceedings of 6ICEGE, New Zealand.*

Carle, S.F. 1999. *TPROGS: Transition Probability Geostatistical Software: Users Guide.* University of California, Davis

Carle, S.F. and Fogg, G.E. 1996. Transition probability-based indicator geostatistics. *Mathematical Geology* 28(4): 453-476.

Christian, J.T. and Baecher, G.B. 2006. The influence of spatial correlation on the performance of earth structures and foundations. *Proceedings of Geocongress 2006*.

Clayton C., Matthews M., Simons N. 1995. *Site Investigation* (2nd ed.). Oxford: Blackwell Science.

Clayton CRI, Smith DM. 2013. *Effective Site Investigation* (2nd ed.). Site Investigation Steering Group, Institution of Civil Engineers, London: ICE Publishing.

DeGroot, D.J., and Baecher, G.B. 1993.Estimating the autocovariance of in-situ soil properties. *J. Geotech. and Geoenviron. Eng.* 119(1): 147-166.

DeJong, J.T., Sturm, A.P. and Ghafgazhi, M. 2016. Characterization of gravelly alluvium. *Proceedings of 6ICEGE, New Zealand.*

Duncan, J.M. 2000. Factors of safety and reliability in geotechnical engineering. *J. Geotech, and Geoenviron. Eng.* 126(4): 307-316.

Elkateb, T. Chalaturnyk, R. and Robertson, P.K. 2003. An overview of soil heterogeneity: quantification and implications on geotechnical field problems. *Can. Geotech. J.* 40(1): 1-15.

Fenton, G.A. 1999. Random field modeling of CPT data. *J. Geotech. and Geoenviron. Eng.* 125(6): 486-498.

Fenton, G.A. and Vanmarcke, E.H. 1990. Simulation of random fields via local average subdivision. *J. Geotech. and Geoenviron. Eng.* 116(8): 1733-1749.

Griffiths, D.V., Fenton, G.A., and Manoharan, N. 2002. Bearing capacity of rough rigid strip footing on cohesive soil: probabilistic study. *J. Geotech and Geoenviron. Eng.* 128(9): 743-755.

Li, J., Tian, Y., and Cassidy, M.J. 2015a. Failure mechanism and bearing capacity of footings buried at various depths in spatially random soil. *J. Geotech. and Geoenviron. Eng.* 141(2).

Li, X.Y., Zhang, L.M., and Li, J.H. 2015b. Using conditioned random field to characterize the variability of geologic profiles. *J. Geotech. and Geoenviron. Eng.* 142(4).

Lloret-Cabot, M., Hicks, M.A., and van den Eijnden, A.P. 2012. Investigation of the reduction in uncertainty due to soil variability when conditioning a random field using kriging. *Geotechnique Letters* 2(3): 123-127.

Lloret-Cabot, M., Fenton, G.A., and Hicks, M.A. 2014. On the estimation of scale of fluctuation in geostatistics. *Georisk: Assessment and management of risk for engineering systems and geohazards* 8(2): 129-140.

Mayne PW, Christopher BR, and DeJong, JT. 2002. *Subsurface Investigations*. National Highway Institute. U.S. Department of Transportation. Federal Highway Administration.

Munter, S.K., Krage, C.P, Boulanger, R.W., DeJong, J.T., and Montgomery, J. 2016. Potential for liquefaction-induced lateral spreading in interbedded deposits considering spatial variability. *Proceedings from GEOSEI 2016, Pheonix, AZ.*

Vanmarcke, E.H. 1977. Probabilistic modeling of soil profiles. *J. Geotech. Eng. Div.* 103(11): 1227-1246.

U.S. Army Corps of Engineers. 2001. EM 1110-1-1804 Geotechnical Investigations. Washington, DC.

Geotechnical and Geophysical Site Characterisation 5 – Lehane, Acosta-Martínez & Kelly (Eds)

Probabilistic assessment of laterally loaded pile performance in sand

B.M. Lehane, F. Glisic & J.P. Doherty
School of Civil, Environmental & Mining Engineering, University of Western Australia, Australia

ABSTRACT: A probabilistic assessment of the lateral response of a pile in a uniformly graded dune sand is presented using CPT and load test data from a site in Perth, Western Australia. The assessment, which employs a new CPT-based design method, provides designers with an appreciation of the level of uncertainty associated with serviceability limit state design for laterally loaded piles in sand. It is shown that the lateral load range likely to induce a pile head rotation gradient of 1% (=0.57°) is significantly lower than the range anticipated from the CPT variability. Predictions of lateral response using the CPT method are not very sensitive to randomly generated q_c profiles with assigned mean and standard deviation values at each depth.

1 INTRODUCTION

The performance of laterally loaded piles is currently the subject of considerable attention due to the rapid growth in the numbers of wind turbines being constructed around the world. These turbines are usually founded on a single pile (or monopile) and experience large wind loads (as well as wave loads for offshore turbines). The lateral displacements of these piles generally govern their design as rotations of the mast in excess of about 1% can render the turbine un-serviceable. This paper presents a probabilistic assessment of lateral pile response using a new CPT based design method with the aim of providing designers with an appreciation of the level of uncertainty associated with serviceability limit state design for laterally loaded piles in sand.

The paper examines the effects of spatial variability of the ground parameters using an intensive series of CPTs performed at the site of lateral pile tests conducted in Perth, Western Australia. The primary calculation method for the sand's *p-y* curves is the direct CPT approach for sands proposed by Suryasentana & Lehane (2014, 2016) and this is shown to provide a reasonable prediction for the lateral response measured by the test piles using the average measured q_c profile and the *LAP* laterally loaded pile program (Doherty 2014). A Monte Carlo simulation is performed involving generation of random q_c profiles consistent with the assessed site variability and their combination with the *LAP* program to generate probability density functions for the load that would cause 1% rotation gradient (=0.57°) at the pile head. These functions are then used to examine the relationship between the uncertainty in the load required to cause a 1% rotation and the variability of the ground parameters. The paper also examines this relationship when employing the widely used American Petroleum Institute (API 2011) recommendations for lateral pile design in sand.

2 LATERALLY LOADED PILE ANALYSIS

The lateral load-displacement (*p-y*) curves recommended by the American Petroleum Institute (API 2011) are commonly used for the design of laterally loaded piles in sand. These recommendations are based on physical tests on relatively small diameter piles and simply require assessment of an operational friction angle for the sand. However, calculated lateral pile responses show a wide variability in practice, primarily because of the range of methods used by designers to determine ϕ' and the sensitivity of the *p-y* curves to the value of ϕ'. Such variability prompted the method developed by Suryasentana & Lehane (2014, 2016) which makes direct use of the CPT q_c value rather than inferred friction angles. This method, referred to here as the S&L method, was derived via a regression analysis on a large series of 3D Finite Element computations that predicted the lateral pile response in a variety of different

sands and a cavity expansion approximation using Finite Elements to predict corresponding CPT q_c profiles in each sand deposit. The updated S&L formulation for a circular pile is provided in Equation (1) (Suryasentana & Lehane 2016), where D is the pile diameter and z, σ_v, σ'_v, q_c and G_{max} are the depth, vertical total stress, vertical effective stresses, CPT end resistance and small strain shear modulus at the level of the p-y spring. u_g is the water pressure at the ground surface (which is non-zero for offshore applications).

$$p = 4.5\, G_{max}\, y\,; \quad y/D \leq 0.0001 \qquad (1a)$$

$$p = p_u\, f(y); \quad y/D \geq 0.01 \qquad (1b)$$

where

$$f(y) = 1 - exp\left(-8.9\left(\frac{y}{D}\right)\left(\frac{\sigma_v - u_g}{\sigma'_v}\right)^{0.5}\left(\frac{z}{D}\right)^{-1.25}\right) \qquad (1c)$$

$$p_u = 2.4\,\sigma'_v D\left(\frac{q_c}{\sigma'_v}\right)^{0.67}\left(\frac{z}{D}\right)^{0.75} \leq q_c D \qquad (1d)$$

For simplicity, the very small strain component of the p-y curves (Equation 1a) is ignored in the following and Equation 1b is assumed to be applicable at all y/D values.

The *LAP*, laterally loaded pile program (Doherty 2014), was used to calculate lateral pile response as it incorporates Equation (1) in one of its available p-y options. The program uses beam elements to represent pile sections and requires specification of the diameter and flexural rigidity of these sections and their corresponding yield moments. The soil unit weight and position of the water table are specified in addition to the CPT q_c profile (which can be copied directly from the CPT Contractor's data files). The program generates about ten p-y springs per metre depth.

3 SHENTON PARK LATERAL LOAD TEST

This paper uses Equation (1) to examine the sensitivity of variations in CPT q_c to the performance of a laterally loaded test pile conducted at Shenton Park, Perth, Western Australia. The stratigraphy at the Shenton Park site comprises a 5m to 7m thick deposit of siliceous dune sand overlying weakly cemented limestone. The sand is sub-angular to sub-rounded with D_{50}, D_{60} and D_{10} values of 0.42mm, 0.47mm and 0.21mm respectively. The water table is typically just above the top of the limestone and the sand has a low level of saturation (< 15%), which varies seasonally by up to about 5%. A full description of the properties of the Shenton Park sand is provided in Lehane et al. (2004).

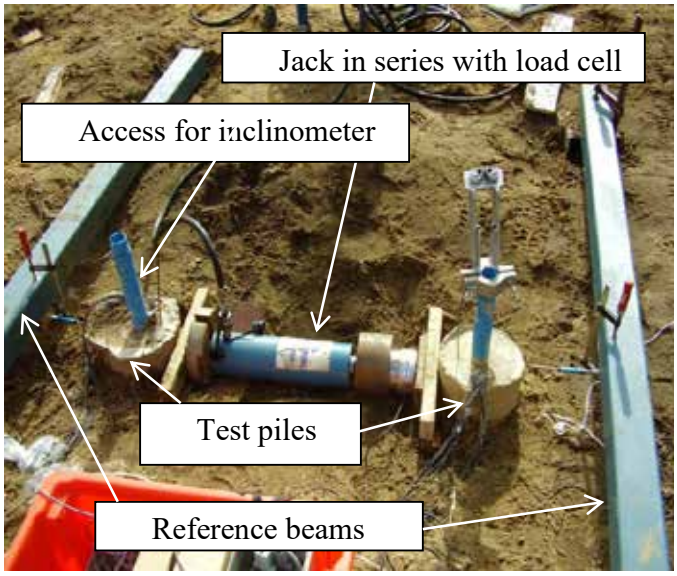

Figure 1. Lateral load test set up at Shenton Park

Two, 225mm diameter, 3.5m long grout piles were constructed using the continuous flight auger (CFA) technique. Lateral tests were performed as shown on Figure 1 by pushing the piles apart using a jack aligned approximately 0.15m above ground level. The q_c values recorded in 12 No. CPTs performed within 10m of the test piles are plotted on Figure 2. The coefficient of variations (CoVs) of the q_c values in the lateral direction are also shown on this figure and indicate a higher level of variability near the surface (which is typical of many sites).

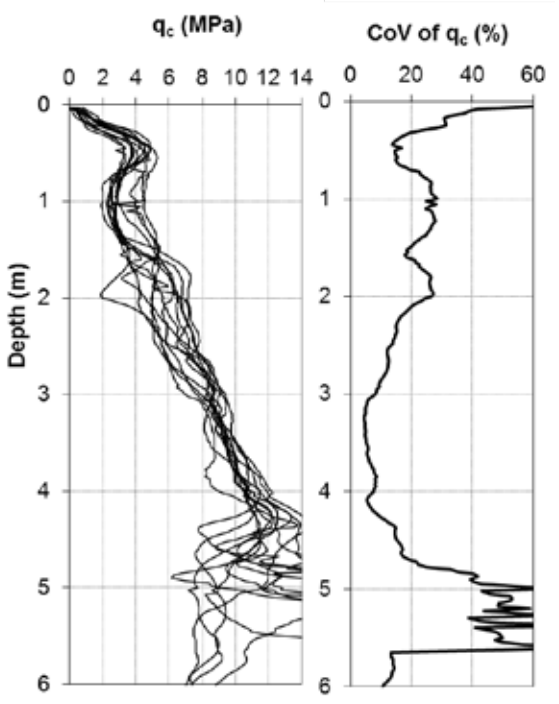

Figure 2. CPT end resistances and their variation at Shenton Park

The lateral load – displacement variation calculated with *LAP* using an initial uncracked EI value of 2420 kNm^2 and yield moment (M_y) of 9 kNm is compared with the average measured response (of the two test piles) on Figure 3. It is noteworthy that the lateral displacements of each of the two test piles at any given load differed by less than 5 to 10%.

The LAP calculation on Figure 3 adopted the mean q_c profile derived using the CPTs plotted on Figure 2. The EI and M_y values employed were measured directly in a separate on-site calibration exercise, which involved lateral loading at the heads of identical piles after excavation of a large 1m deep pit in the vicinity of the piles (Luff 2007).

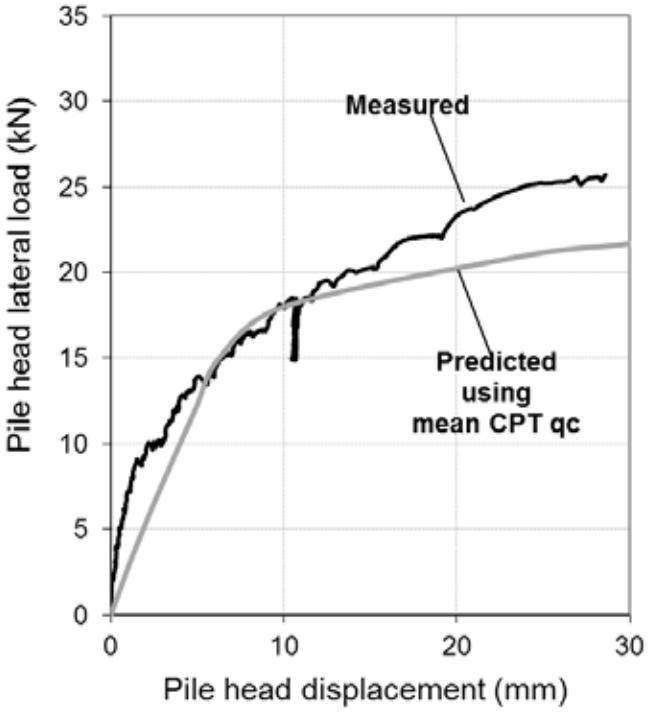

Figure 3. Measured and calculated pile head lateral load-displacement variations

Figure 3 shows that the S&L method provides a reasonable prediction of the lateral pile response, although the initial lateral stiffness is underestimated. The lateral load required to cause a rotation of 1/100 at the location of the applied load is referred to here as $H_{0.01}$, and was approximately 18 kN for the case on Figure 3 (at which stage the pile head displacement was about 11.5 mm).

4 PROBALISTIC ANALYSIS

4.1 Predictions for Shenton Park using Equation 1

Fifty random CPT profiles for the Shenton Park site were generated using Microsoft Excel © for a Monte Carlo analysis. The random generator employed to generate these profiles assumed a normal distribution and hence required specification of a mean CPT q_c value and corresponding standard deviation. As described by Phoon & Kulhawy (1999) and illustrated in Figure 4, the spatial variation of q_c at any depth z can be decomposed into a smoothly varying trend function (q_{ct}) and a fluctuating component q_{cf}, i.e.

$$q_c\,(z) = q_{ct}\,(z) + q_{cf}\,(z) \qquad (2)$$

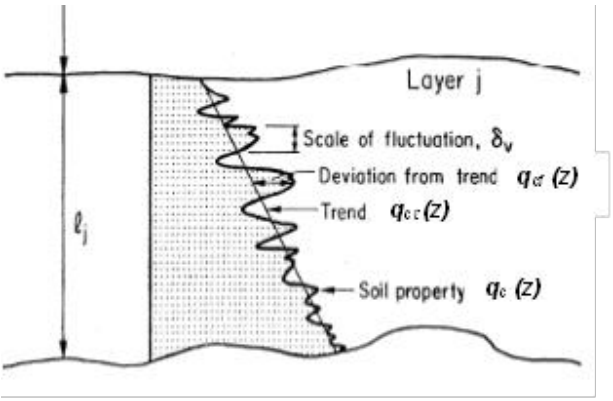

Figure 4. Statistical representation of q_c profile (Phoon & Kulhawy 1999)

The fluctuating component, q_{cf} *(z)*, represents the inherent variability of q_c and its mean and variance should not be depth dependant. The vertical scale of fluctuation (δ_v) at the Shenton Park site was assessed to be 0.5m (but 0.25m in the upper 0.5m) assuming a general trend for q_c increasing from zero at the surface to about 3.8 MPa at 0.5m, reducing to about 2.5 MPa at 1m depth and then increasing linearly with depth to 7.3 MPa at 3m depth. The coefficient of variation assumed for lateral variability of q_c is shown on Figure 2.

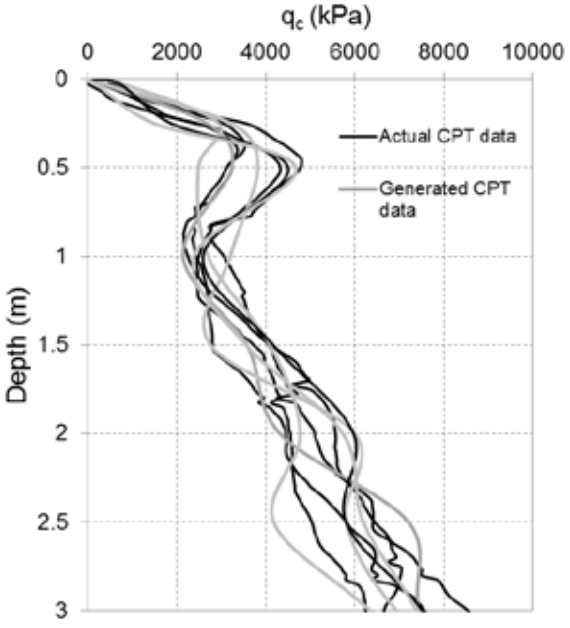

Figure 5. Comparison of actual and typical generated q_c profiles

Examples of randomly generated q_c traces are compared in Figure 5 with CPT data recorded at the site. The randomly generated data reflect the measurements well, although some minor localised peaks are not captured. Trials using a smaller δ_v value led to far greater 'peakiness' in the generated profiles which did not reflect the measurements.

The *LAP* program was then used to derive $H_{0.01}$ values with a node spacing of 0.025m for each of these fifty CPT profiles, assuming the *p-y* response of the sand is given by the S&L method. Calculations were performed assuming (i) the pile yield moment of 9 kNm and (ii) the pile remained elastic during lateral loading. Mean values of $H_{0.01}$ of 18.7 kN and 26 kN were calculated for analysis set (i) and (ii) respectively. The larger $H_{0.01}$ values determined for the elastic pile may be anticipated from extrapolation of the initial stages of the *LAP* calculated load-displacement curve on Figure 3.

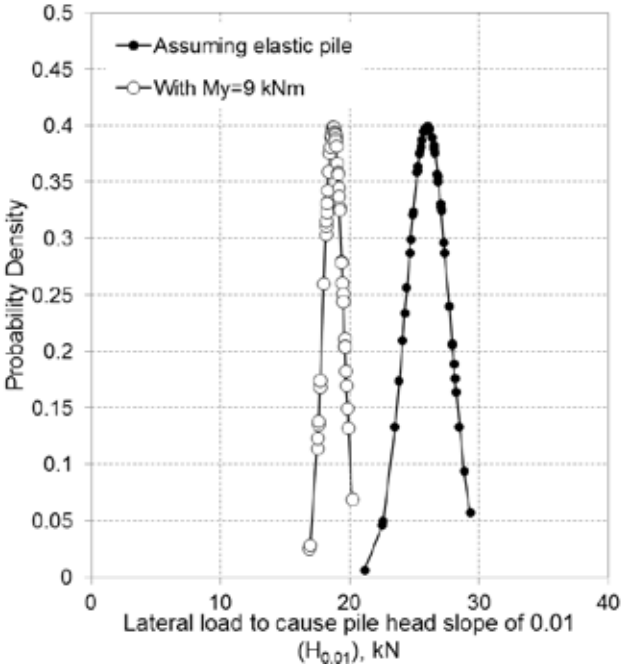

Figure 6. Probability densities for $H_{0.01}$ at Shenton Park, with and without pile yield

The probability density functions determined using the 50 computations of $H_{0.01}$ for each analysis set are plotted on Figure 6. It is clear that there is a very narrow spread in calculated $H_{0.01}$ values, despite the relatively wide range of q_c resistances; this trend is consistent with the close similarity of the measured responses of the two test piles.

The calculated coefficients of variation (CoV) of $H_{0.01}$ allowing for pile yield and assuming elastic piles are 0.042 and 0.064 respectively. These coefficients are more than five times smaller than the mean CoV for the q_c data at Shenton Park. It is therefore clear that high, normally distributed, variability in q_c values at a site does not lead to a correspondingly high variability in $H_{0.01}$ values.

The significantly lower CoV for $H_{0.01}$ compared to that of the CPT q_c arises because of the assumption of randomly distributed q_c values. Separate analyses to confirm this observation were performed using the following two q_c profiles:

$$q_c \text{ (lower)} = q_{c,mean}\,(1 - \text{CoV}) \quad (3a)$$

$$q_c \text{ (upper)} = q_{c,mean}\,(1 + \text{CoV}) \quad (3b)$$

Output from the analyses indicated that, in line with Equation (1d), the ratios of the ultimate pressures developed on the piles in the q_c (lower) profile to those developed in the q_c (upper) profile were equal to $[(1\text{-CoV})/(1+\text{CoV})]^{0.67}$, which amounts to 0.76 at CoV=0.2 and 0.23 at CoV=0.8. The corresponding ratios of $H_{0.01}$ were a little higher than these values because of the dependence on y/D (Equation 1c) and varied from 0.84 for a CoV=0.2 to 0.37 for CoV=0.8.

4.2 Additional calculations using Equation 1 and the stratigraphy at Shenton Park

Further analyses were performed adopting the same pile configuration as the test piles at Shenton Park, assuming the mean q_c profile, with the pile *EI*=2420 kNm^2 and yield moment, M_y= 9 kNm. However, for these cases, the random generation of 50 CPT profiles adopted a constant CoV for q_c over the depth of the piles. The probability density functions determined in these analyses using *LAP* (with *p-y* curves given by Equation 1) for q_c CoVs of 0.2, 0.4, 0.6 and 0.8 are presented on Figure 7. These again confirm the low sensitivity of the computed $H_{0.01}$ values to the variability in q_c values. The mean $H_{0.01}$ value was about 18 kN for all cases. More significantly, the calculated CoV for $H_{0.01}$ was only 10% of the CoVs of the q_c profiles for CoV=0.2 increasing to 20% of the of the CoVs of the q_c profiles at CoV=0.8.

An appreciation of the relative insensitivity of $H_{0.01}$ values at Shenton Park to variability of the q_c values may be better understood in terms of probabilities. If, for example, the CoV for q_c at the sand site is 0.4 (this CoV is considered relatively high) and the expected $H_{0.01}$ value is the mean given by equation 1 i.e. 18.6 kN, the foregoing analyses suggest that there is a probability of less than 0.001 that $H_{0.01}$ exceeds 22 kN.

Separate analyses were also performed assuming that CPT q_c values at Shenton Park. These showed that:

- closely comparable trends are observed if the q_c values are assumed to be log normally distributed (for CoV<0.5);
- as for the variable CoV analyses, the CoVs of $H_{0.01}$ assuming an elastic pile were about 50% higher than those adopting M_y=9kNm

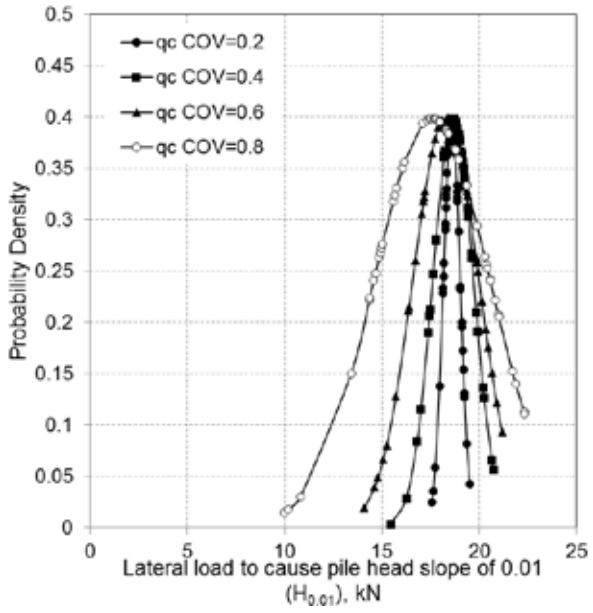

Figure 7 Probability densities for various (constant) COVs for q_c at Shenton Park (M_y=9 kNm)

4.3 Predictions for Shenton Park using the API (2011) method

One of the most popular means of determining the lateral response of piles in sand is the method recommended in API (2011). The *p-y* curves derived using this method are a function of the relative depth (*z*/D) and the sand's friction angle (ϕ').

For the purposes of this study, use is made of the site specific correlation given in Lehane et al. (2004) between the relative density (D_r) of the Shenton Park sand and the CPT q_c value. The sand's friction angle was then determined using the correlations with D_r presented by Bolton (1986). The mean of Bolton's expressions for triaxial compression and plane strain ϕ' values was used in calculations. The CoVs for q_c from which D_r values were derived were the same as the site specific values shown on Figure 2; the associated randomly generated profiles of ϕ' at Shenton Park are shown on Figure 8. The mean value of ϕ' determined was 39.6°, which is about 3 degrees less than the operational angle backfigured by Li & Lehane (2010) for a cantilever retaining wall at Shenton Park. Interestingly, the average generated CoV for ϕ' over the whole profile (to 3.5m depth) is only 0.068, which is considerably less than the CoV for q_c.

The calculations made using LAP and the API (2011) sand model with the randomly generated friction angle profiles plotted on Figure 8 show an even smaller spread of $H_{0.01}$ compared to that calculated using the direct CPT method (i.e. Equation 1). The CoV calculated for $H_{0.01}$ for an elastic pile using API is only 0.047 compared with 0.064 obtained using Equation 1. This trend arises because of the low CoV for ϕ', which effectively leads to very similar average ϕ' values and hence *p-y* curves within the lateral zone of influence of the pile.

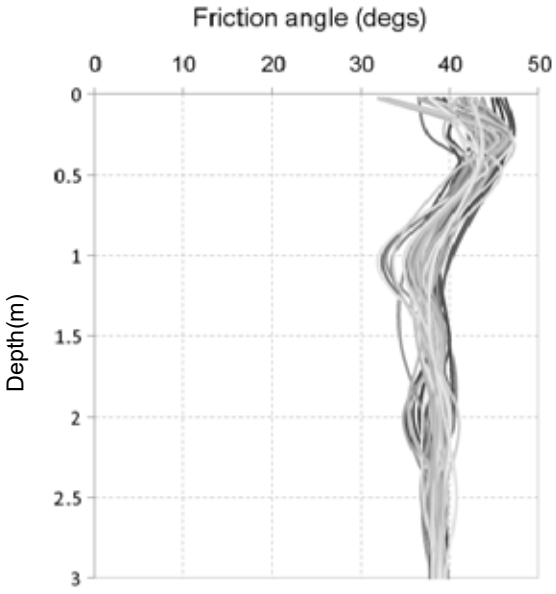

Figure 8. Randomly generated ϕ' values at Shenton Park

The mean $H_{0.01}$ value of 27.6 kN determined using API and the ϕ' values on Figure 7 was very close to that calculated an elastic pile using Equation 1 (=26 kN; see Figure 3). Given the very low variability in calculated $H_{0.01}$ values, it follows that, when using API, it is more important to obtain confidence in the method employed to determine ϕ'. Unfortunately there are a wide range of methods in common use to assess ϕ', with the consequence that most assessments are highly subjective. Back-analysis of the Shenton Park tests using the API method suggests that the mean operational friction angle was about 40° whereas, as part of a settlement prediction exercise at Shenton Park (Lehane et al. 2009), practitioners estimated ϕ' values at Shenton Park of between 30° and 36°. In this respect, direct methods, such as Equation (1), provide a clear advantage over indirect methods such as API (2011).

5 EXTRAPOLATION TO LARGE DIAMETER PILES AND LARGER ROTATIONS

4.1 *Extrapolation to larger diameter*

A number of analyses were performed involving application of a lateral load at pile head level to 2m diameter, 20m long, 50mm wall thickness (t), steel tubular piles in saturated sand; the sand surface was 1.3m below the point of lateral load application. The same statistical approach as outlined above for the (relatively small scale) Shenton Park tests was employed. The analyses adopted Equation (1) to derive *p-y* springs and assumed that the sand had a constant relative density (D_r). The following relationship proposed by Jamiolkowski *et al.* (1985) for a normally

consolidated sand of medium compressibility was used to relate q_c with D_r:

$$q_c \text{ (kPa)} = 97 (\sigma'_v)^{0.5} 10^{1.52 D_r} \quad (3)$$

where σ'_v is given in kPa and D_r is expressed as a fraction. The pile was assumed elastic and the CoV for q_c at any given depth was taken as 0.4 i.e. q_c had a relatively high variability.

These analyses showed that the value of $H_{0.01}$ had approximately the same level of sensitivity to q_c variability as that shown by the smaller pile at Shenton Park i.e. for a q_c CoV of 40%, the CoV for $H_{0.01}$ was only 5.5%.

4.2 *Extrapolation to larger pile head rotation*

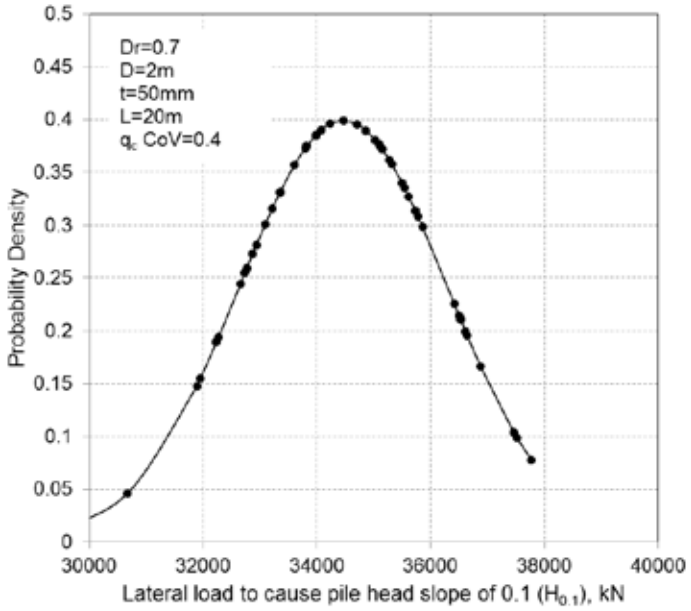

Figure 9 $H_{0.1}$ values for steel pipe pile in saturated sand with D_r=0.7

To further examine the sensitivity to random variations of q_c profiles with a given CoV, calculations were carried out using Equation (1) to determine the likely range of loads causing a pile head rotation of 10%; the same pile geometry and sand conditions as employed above were employed i.e. a 2m diameter pipe pile in a uniform saturated sand with D_r=0.7. The CoV for q_c at any given depth was also taken as 0.4 and the pile was assumed elastic.

The results from the computations are presented on Figure 8. The results equate to a CoV of about 5.5% for loads causing a rotation of 10% of the pile head, $H_{0.1}$ i.e. the CoV for both $H_{0.1}$ and $H_{0.01}$ was about 14% of the CoV for CPT q_c variability. As for the Shenton Park case, a much wider range of $H_{0.1}$ values are obtained if the lower-bound and upper-bound q_c values are employed in the calculations (rather than randomly generating q_c profiles with a given mean and CoV).

6 CONCLUSIONS

The calculations summarised in this paper have shown that the lateral load range likely to induce a given level of pile head rotation for a pile in sand is significantly lower than the range anticipated from the CPT q_c variability.

The CPT-based method for laterally loaded piles proposed by Suryasentana & Lehane (2014,2016) is seen to provide good predictions for the lateral response of a test pile at a medium dense sand site. Predictions using this method and using the API sand method have a low sensitivity to randomly generated q_c or ϕ' profiles that are normally distributed at any given depth.

7 REFERENCES

API (American Petroleum Institute) 2011. *Geotechnical and foundation design considerations*, ANSI/API RP 2GEO, 1st edn. Washington DC, USA: API Publishing Services.

Bolton M. 1986. The strength and dilatancy of sands. *Geotechnique*, 36(1), 65-78.

Doherty, J. P. 2014. User manual for LAP, Laterally loaded pile analysis. School of Civil, Environmental & Mining Engineering, University of Western Australia, Perth WA 6009.

Jamiolkowski M., Ladd C.C., Germaine J.T. and Lancellotta R. 1985. New developments in field and laboratory testing of soils. *Proc. 11th Int. Conf. On Soil Mech. and Fdn. Engrg.*, San Francisco, 1, 57-153, Balkema (Rotterdam).

Phoon K.K. and Kulhawy F.H. 1999. Characterization of geotechnical reliability. *Canadian Geotechnical J.*, 36, 612-624.

Lehane B.M., Doherty J.P. and Schneider J.A. 2009. Settlement prediction for footings on sand. Keynote Lecture, *Proc. 4th International Symposium on deformation characteristics of Geomaterials*, Atlanta, 1, 133-152, IOS press, The Netherlands.

Lehane B.M., Ismail M. and Fahey M. 2004. Seasonal dependence of in-situ test parameters in sand above the water table. *Geotechnique*, 54 (3), 215-218.

Li, A. and Lehane B.M. 2010. Embedded cantilever retaining walls in sand. *Geotechnique*, 60 (11), 813-823.

Luff B. 2007. Backanalysis of pile behaviour in Perth dune sand. Final Year thesis project, School of Civil, Environmental & Mining Engineering, The University of Western Australia, Crawley 6009.

Suryasentana S. K. and Lehane B. M. 2014. Numerical derivation of CPT-based p–y curves for piles in sand. *Géotechnique* 64(3), 186–194.

Suryasentana S.K. and Lehane B.M. 2016. Updated CPT-based p-y formulation for laterally loaded piles in cohesionless soil under static loading. *Geotechnique*, *dx.doi.org/10.1680/jgeot.14.P.156*

Geotechnical and Geophysical Site Characterisation 5 – Lehane, Acosta-Martínez & Kelly (Eds)

Stochastic Waveform Inversion for Probabilistic Geotechnical Site Characterization

S.S. Parida & K. Sett
Department of Civil Structural and Environmental Engineering, University at Buffalo, New York, United States of America

P. Singla
Department of Mechanical and Aerospace Engineering, University at Buffalo, New York, United States of America

ABSTRACT: This study develops a stochastic inverse analysis methodology to probabilistically estimate site-specific soil modulus from geophysical test measurements by accounting for the uncertain spatial variability of the soil deposit, any measurement uncertainty and uncertainty due to limited data. Hypothesizing the soil modulus to be a three-dimensional, heterogeneous, anisotropic random field, the methodology first formulates and solves a forward model that mimic a geophysical experiment using a stochastic collocation approach to characterize the effect of spatially variable, uncertain soil modulus on the model response variables, for example, accelerations at the sensor locations. The stochastic collocation approach utilizes recently developed non-product quadrature method, conjugate unscented transformation, to accurately estimate statistical moments corresponding to the model response variables in a computationally efficient manner. The methodology then employs a minimum variance framework to merge the information obtained from the model prediction and the sparse geophysical test measurements to update the statistical information pertaining to the soil modulus. The methodology is illustrated using synthetic data from a fictitious geophysical experiment.

1 INTRODUCTION

Quantification of site-specific uncertainties in soil properties through standard geotechnical site characterization approach of drilling and measuring soil properties at a few locations in a soil deposit poses a challenge due to the very limited amount of (borehole) measurements typically available at any geotechnical site. This leads to data uncertainty in the estimation process and it gets carried over unaccounted for in subsequent probabilistic design/simulation of the behavior of geostructures.

Geophysical tests, which are increasingly being used in characterizing geotechnical sites, offer an advantage that they typically yield larger volume of data for more accurate statistical analysis. Traditionally, geophysical test measurements are analyzed deterministically with simplifying assumptions so that the inversion process remains tractable. Spectral analysis of surface waves (SASW) is one such widely used approach that assumes ground waves to consist only of Rayleigh waves and neglects the effects of P- and S-waves (Nazarian 1984). Moreover, it relies on one-dimensional conjecture and hence only produces horizontally layered soil profile (Fathi 2015). In recent years, with advancement of mathematical machineries and availability of faster computers, partial differential equation (PDE) constrained full waveform inversions, which inherently account for all types of waves in a solid medium, have also been successfully attempted to image heterogeneous soil deposits (see, for example, Kallivokas *et al*. 2013). However, such inversion processes, due to their deterministic nature, fail to account for uncertain spatial variability of soil parameters and any measurement uncertainty associated with the geophysical experiments

This paper develops a methodology for PDE-constrained stochastic waveform inversion to not only estimate constitutive parameters of any soil deposit but also to quantify uncertainties associated with them by accounting for uncertain spatial variability and measurement uncertainty as well as uncertainty due to limited data The authors anticipate that such a tool, when properly verified and validated, will tremendously benefit geotechnical engineers in accurately visualizing (in terms of confidence intervals) the heterogeneity of subsurface at any site. This will not only result in more accurate simulation of the behavior of any civil infrastructure objects but also allow for estimation of site-specific resistance factors for the load and resistance factor design (LRFD) of geotechnical components of any civil infrastructure objects. Note that due to very limited amount of soil data typically available at any geotechnical site for a meaningful statistical analysis, the current American Association of State Highway and Transportation Officials (AASHTO) recommended LRFD resistance factors for substructures were derived by just calibrating the LRFD equation

to the factors of safety used in the past with the working stress design (WSD) approach. The factors are indifferent to any site-specific information e.g., variability of soil properties at a particular site, the extent of soil exploration (little versus extensive), etc. The anticipated ability to compute fully site-specific resistance factors will lead to safer and more economical designs of civil infrastructure objects.

2 PROBLEM STATEMENT

We will analyze synthetic data from a fictitious geophysical experiment shown schematically in Figure 1. Assuming a three-dimensional, heterogeneous profile of soil modulus, we will numerically simulate a geophysical experiment to obtain sensor measurements (acceleration/velocity/displacement time histories) due to a known excitation at the source location. We will assume them to represent actual sensor measurements after polluting them a bit by adding Gaussian white noise to mimic real measurements. Finally, using these few measurements and hypothesizing the soil modulus to be a three-dimensional random field, we will inversely estimate its parameters.

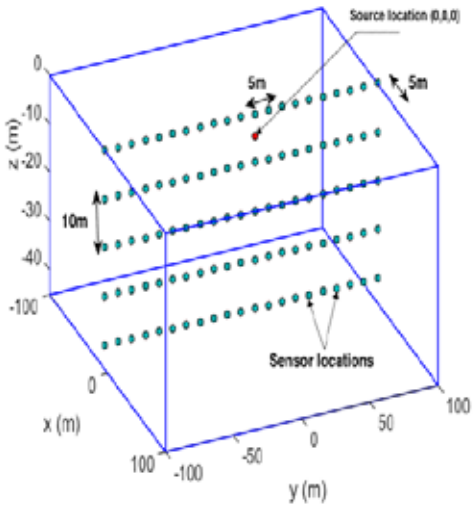

Figure 1. Schematic of the fictitious site to be probed showing sensor and source locations.

3 THE FORWARD PROBLEM

Solution of any PDE-constrained probabilistic inverse problem is, in essence, an iterative process. Each iteration starts with the propagation of the target parameter, with some prior belief about its uncertainties, through the governing PDE ("the model") and then updating the target parameter with the help of a suitable estimator that aims to maximize the likelihood of the observed response by minimizing the error between "the model" predictions and true responses. Thus setting up "the model", propagating prior uncertainties through it and obtaining "the model" response are tantamount to any other stage of the inversion process and constitute the forward problem. In a deterministic setting, forward problems that
are governed by PDEs are typically solved numerically, for example, using the finite element method

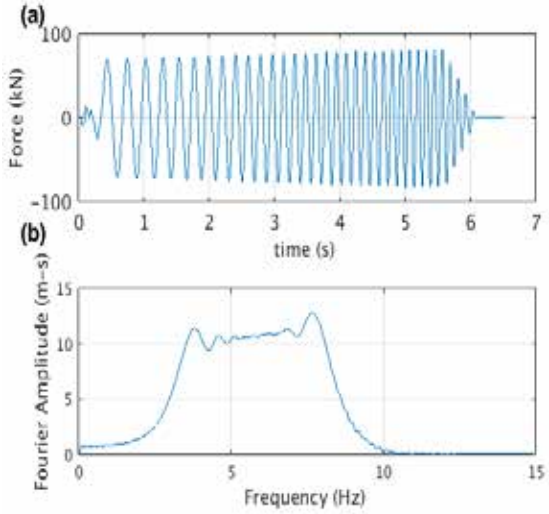

Figure 2. (a) Forcing function at (0,0,0) and (b) its Fourier spectrum

or the finite difference method. In a probabilistic setting where the model parameters are uncertain, the governing PDE becomes a stochastic PDE. Monte Carlo (MC) approach (Doucet *et al* 2001) is the most widely used approach for solving stochastic PDEs. MC approach, in general, is very straightforward and can be used to probabilistically simulate any problem whose deterministic solution – either analytical or numerical – is known. However, its accuracy depends upon the number of realizations (N) used in the simulation process; the MC estimates approach their true values as the number of deterministic runs, N, approaches infinity. Because of the above, accurate probabilistic simulation using MC approach becomes extremely computational intensive, especially for problems which do not have analytical solutions; for large scale problems, like nonlinear dynamic problems in a finite element setting, it will probably be intractable. Among the alternate approaches, the stochastic Galerkin and the stochastic collocation approaches are more common. Stochastic Galerkin approaches (see, for example, Ghanem & Spanos 1991) usually represent all the uncertain parameters of a model using some type of finite series expansions and then employ a Galerkin technique to minimize the errors of finite representation which result in a system of coupled (deterministic) equations. Stochastic collocation approaches (see, for example, Babuska et al. 2007), on the other hand, can be viewed as a Monte Carlo type sampling technique, with the exception that, instead of at random, the sampling points are selected following some kind of numerical quadrature schemes that are

used to estimate the statistical moments of the response variable. Stochastic collocation approaches are, in general, non-intrusive approaches in the sense they do not require modifications of underlying deterministic (finite element or finite difference) code.

This study employs the finite element method in conjunction with the stochastic collocation approach to probabilistically solve the forward problem corresponding to the geophysical experiment shown schematically in Figure 1. The soil deposit is modelled using 8-noded standard brick elements of dimension 5m × 5m × 5m. The horizontal and vertical extents of the soil domain – that theoretically extend to infinity – are restricted by using artificial absorbing boundaries. Widely used Lysmer-Kuhlemeyer (Lysmer and Kuhlemeyer 1969) local boundaries are used for this purpose. A chirp signal (Figure 2) with dominant frequencies between 3Hz and 10Hz was used to excite the ground at the source location for a duration of 6 sec. The soil material is assumed to be linear elastic as the chirp signal is not expected to plastify the soil. While the Poisson's ratio of soil is assumed to be deterministic with a constant value of 0.3 throughout the domain, the Young's modulus of soil is assumed to be a three-dimensional heterogeneous, cross-anisotropic random field.

The random field parameters up to the second order marginal mean values, marginal coefficients of variation (COVs), and vertical and horizontal correlation structures that are the unknowns for the inverse problem – will initially be guessed for the forward simulation. In concurrence with the general soil behavior, marginal mean and COV are assumed to increase with depth. In the horizontal directions, however, they are assumed to be constant. Typically, due to the nature of soil formation process, soil parameters are less correlated in vertical direction than in the horizontal directions (Lacasse & Nadim 1996). Accordingly, the correlation length of Young's modulusin the vertical direction is assumed to be smaller than that in the horizontal directions. It is assumed that there is no correlation between the moduli in x-y plane and vertical direction. Mathematically, we capture the above-assumed spatial variation of uncertain Young's modulus in terms of Gaussian shape functions and weights as:

$$Y(x,y,z) = w_0 + w_1 z + \sum_1^n W_i N_i(\mu_{c_i}, P) \quad (1)$$

$$P = \begin{bmatrix} \sigma & \sigma_{xy} & 0 \\ \sigma_{xy} & \sigma & 0 \\ 0 & 0 & \sigma \end{bmatrix} \quad (2)$$

$$W_i = w_2 r + w_3 \theta \quad (3)$$

where Y is the Young's modulus, μ_{c_i} is the center of each Gaussian shape function and n is the number of Gaussian shape functions. The parameters w_1, w_2, w_3, σ and σ_{xy} are assumed to be random variables that give rise to the uncertainty in Y. z, r and θ are polar coordinates of a spatial point with origin at (0,0,0). The correlation in Y is indirectly captured here by the summation in Equation (1) since we hypothesize that the magnitude of Y at a point in space is a result of all the Gaussians shape functions. With this we can write $\Theta = [w_1, w_2, w_3, \sigma, \sigma_{xy}]$ to be the uncertain parameter vector of the system. Notice that the assumed structure of Eq. (1) on the Young's modulus field allows us to represent a random field with the help of only 6 parameters Assuming uniform distribution for the random vector Θ, we can write it as:

$$\theta_i(\xi) \cong \theta_{i_0} + \theta_{i_1}\xi_i \qquad \forall\ \theta_i \in \Theta \quad (4)$$

where $\boldsymbol{\xi} = [\xi_1, \xi_2, \dots]^{\mathrm{T}}$ is a known vector of uniform random variables. Further, since the acceleration at a spatial location is a function of Y, and given that Y itself is a function of Θ, acceleration at any geospatial location in the domain becomes a function of the random parameter vector Θ. Therefore, the expected value of any scalar function of acceleration, a, can be computed as:

$$\mathcal{E}\left[f\left(a(\Theta)\right)\right] = \int_\Theta f(a(\Theta))p(\Theta)d\Theta \cong \sum_q w_q f\left(a\left(\Theta(\xi_q)\right)\right) \quad (5)$$

where $\Theta(\xi_q)$ is evaluated at quadrature points ξ_q and and w_q are the respective weights. Only values of the response variable corresponding to these quadrature points are necessary to calculate the expectation and hence the model is simulated for values of Y corresponding to those $\Theta(\xi_q)$s. Many quadrature rules ex-ist in the literature of stochastic collocation for choosing the sample points like Gaussian closure (Iyengar & Dash 1978), unscented transform and Smyolak sparse grid quadrature (Nagavenkat 2012). The major problem with these quadrature rules is that they get computationally very expensive as the dimensionality
of the problem increases. Recently, a non-product quadrature rule known as the conjugate unscented transformation (CUT) has been developed (Nagavenkat 2012, Nagavenkat et al 2013, Mandankan 2014, Mandankan et al 2014). The CUT approach can be considered as an extension of the conventional unscented transform method that satisfies additional higher order moment constraints. It uses just a small number of points, relative to the Gauss quadrature scheme, to compute an integral with the same accuracy. Thus, we start by generating 5-dimensional CUT points (and respective weights) corresponding to the 5 random variables w_1, w_2, w_3, σ and σ_{xy} and evaluate their values at these quadrature according to Equation (4). For example, the random variable w_1 can be evaluated as:

$$w_1(\xi_{1q}) = a_0 + a_1\xi_{1q} \quad (6)$$

where ξ_{1q} corresponds to the q[th] quadrature point.

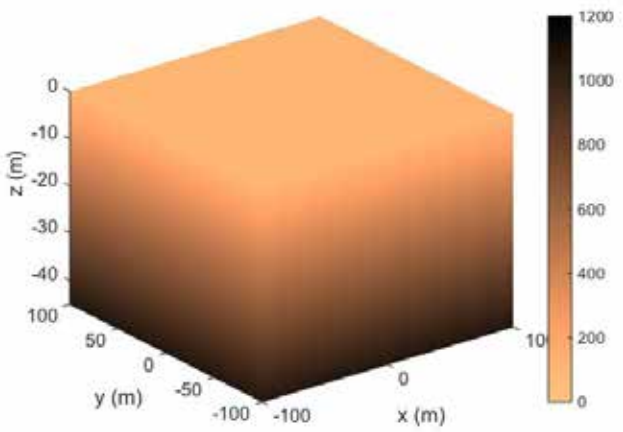

Figure 3. Distribution of true value of Young's modulus (MPa).

Table 1. Coefficients of random variables.

Random Variable	1st coefficient MPa	2nd coefficient MPa
$\boldsymbol{w_1}$	22.4	2
$\boldsymbol{w_2}$	0.035	0.0071
$\boldsymbol{w_3}$	0.79	0.15
$\boldsymbol{\sigma}$	3.70	0.74
$\boldsymbol{\sigma_{xy}}$	3.70	0.74

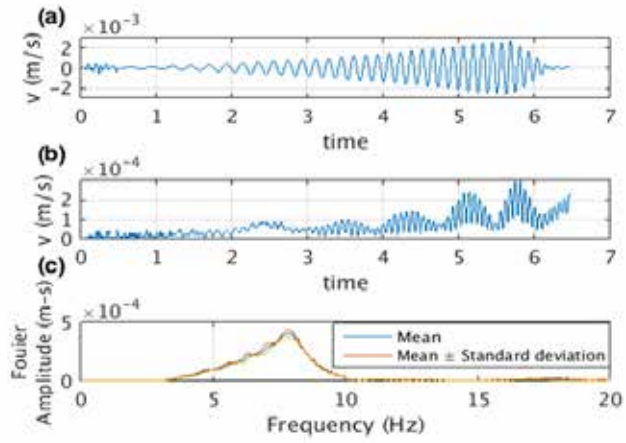

Figure 4. (a) Mean, (b) standard deviation of the simulated velocity time history at (-5,0,0) and (c) corresponding Fourier spectra.

Note that $\boldsymbol{\xi}$ are uniform random variables with zero mean and unit variance. Prior values of coefficients a_0 and a_1 are assumed to be 22.4 MPa and 2 MPa respectively. Similar prior assumptions of other random variables lead to the coefficient values listed in Table 1. We state that the CUT approach needs just 425 quadrature points for our 5-D problem to accurately compute the expectations and hence our model requires as many forward runs, each run corresponding to a realization of Y. For shape functions, we assumed 10 Gaussian functions in each direction initially. Due to much smaller extent of the target domain in the vertical direction this assumption ensures smaller correlation length along it than in horizontal directions. The 3D soil domain corresponding to the true value of Young's modulus is shown in Figure 3. Once the computational model is set up it is run for all the quadrature realizations of Y. Mean and standard deviation of the simulated velocity time history and corresponding Fourier spectra at a node located at (-5,0,0) are shown in Figure 4.

4 THE INVERSION PROCESS

For the inversion process the acceleration time histories recorded at sensor locations are used to compute our posterior moments. To this end, we employ the minimum variance framework (Madankan 2014).

4.1 *Minimum Variance*

Consider a sensor model given by Equation (6), where $h(\Theta)$ corresponds to the true value of the response of the corresponding dynamic system, ν represents the sensor noise with a zero mean and covariance matrix R, and y is the measured response. For such a system, according to the minimum variance framework, the first two posterior moments of the parameter vector Θ, are given by Equations (7) and (8), respectively.

$$y = h(\Theta) + \nu \tag{7}$$

$$\mu_{\Theta}^{+} = \mu_{\Theta}^{-} + K[y - \mathcal{E}^{-}[h(\Theta)]] \tag{8}$$

$$\Sigma_{\Theta}^{+} = \Sigma_{\Theta}^{-} - K\Sigma_{\theta y}^{T} \tag{9}$$

where superscripts – and + denote prior and posterior value of the corresponding random variable. The matrix K is called the Kalman gain matrix and is a measure of the information gained due to the observation y. It is given by:

$$K = \Sigma_{\theta y}(\Sigma_{\mathrm{hh}}^{-} + R)^{-1} \tag{10}$$

where $\Sigma_{\theta y}$ is the covariance matrix between Θ and y and Σ_{hh}^{-} is the prior covariance matrix of the model response for different quadrature realizations of Y. These expectations can be evaluated by the CUT approach. For example Σ_{hh}^{-} is approximately given by:

$$\Sigma_{\mathrm{hh}}^{-} \cong \sum_{q=1}^{N} w_q(h_q - \mu_{\mathrm{h}}^{-})(h_q - \mu_{\mathrm{h}}^{-})^T \tag{11}$$

where N is the number of quadrature points (425 in our case) and μ_{h}^{-} is the mean of the model response. We point out that $h_q$is the computed model response for the realization of Y corresponding to the quadrature point ξ_q.

4.2 *Posterior Moments*

Using the aforementioned framework, the posterior moments for the parameter vector is calculated. Due to the absence of true field measurements we use one of the realizations of Y as its true value and after polluting the corresponding acceleration time history with a Gaussian noise we get the measured response y in Equation (6). 50 randomly sampled time steps from the acceleration time history obtained from every sensor shown in Figure 1 is used, for each of the 425 runs, to compute the posterior moments according to Equations (8)-(11).

Table 2. Comparison between true value, prior and posterior means and standard deviations (SD).

RVs	True Value (MPa)	Prior Mean (MPa)	Post Mean (MPa)	Prior SD (MPa)	Post SD (MPa)
w_1	24.09	22.4	24.13	1.15	0.07
w_2	0.03	0.035	0.035	0.004	0.004
w_3	0.93	0.79	0.79	0.092	0.09
σ	4.32	3.70	3.65	0.43	0.32
σ_{xy}	4.32	3.70	3.70	0.43	0.42

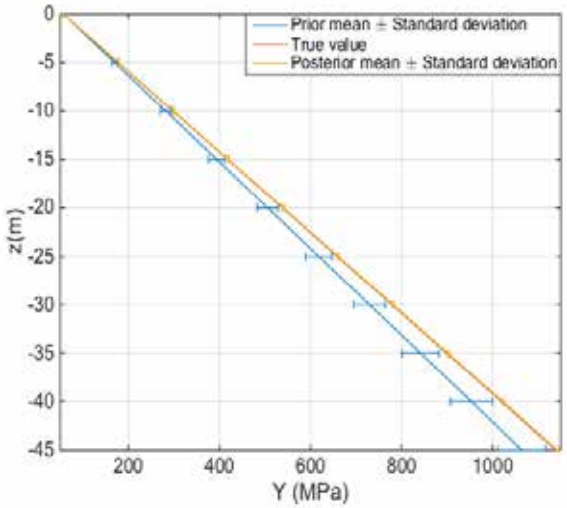

Figure 5. True value, prior mean and posterior mean and standard deviation of Young's modulus at (-5, -5, z).

5 RESULTS

The true values along with the prior and posterior moments of the random parameter vector, obtained after the inverse analysis, are listed in Table 2. We have also shown a comparison between the variation of prior mean, true value and posterior mean (with one standard deviation bound) of Y along depth at (x,y) = (-5,-5) in Figure 5. We can observe that the posterior mean of the Young's modulus is very close to the true value of Y with small error. In Figures 6 (a) and (b) we have shown the errors between the true value of Young's modulus distribution and the prior and posterior means respectively. In Figure 6 (c) the error between the posterior and the prior means of Young's modulus is plotted. Along with this an analysis to understand the information gain about the unknown parameters with respect to number of sensors and time steps was also conducted. In Figure 7 (a) the L_2-norm of error is plotted with respect to the number of time steps and sensors where error (e) is given by difference between the true value and posterior mean. For this we started by taking acceleration time history from sensors, along a line with offset 5 meter from source and depth 40m, in our analysis, and further added sensors while moving up the vertical direction. It was observed that the error decreases with increasing number of sensors and time-steps. An interesting thing to note is that the sensors bottom most layer did not contribute much to reducing error while the maximum error was reduced after inclusion of sensors from the surface. With this premise we went on to analyze the variation of $\Sigma_{\theta y}$across the soil domain, which represents the correlation of measurement data with random parameter vector $\boldsymbol{\theta}$. Since, from Equation (10), the Kalman gain matrix (K) is directly proportional to it, $\Sigma_{\theta y}$ gives us an idea about the amount of information gain at various locations in space. In Figure 7(b) we plot the trace of each column of $\Sigma_{\theta y}$ with respect to its spatial location for two different time instants. It can again be observed that amount of information gain decreases with increasing depth. An implication of this could be that only a few sensors located on and close to the surface give us almost all information about the domain. However further analysis on optimal location of sensor needs to be conducted to confirm this conjecture.

6 CONCLUSIONS

A methodology is developed to perform PDE-constrained stochastic waveform inversion using geophysical test measurements. It is illustrated by probabilistically characterizing a geotechnical site -- hypothesizing the Young's modulus of soil at the site to be a three-dimensional, heterogeneous, anisotropic random field and inversely estimating its parameters by using synthetic data from a fictitious geophysical experiment performed numerically at that site. Towards optimizing the number and locations of sensors in a geophysical experiment, a preliminary analysis is carried out using the developed methodology to. It is observed that the amount of information gain decreases with depth implying that the measurements at the bottom sensors do not contribute much to the inverse estimation process. The developed methodology is mathematically rigorous and computationally efficient. Moreover, it is general enough to be extended widely including inverse estimation of additional elastic as well as elastic-plastic soil parameters

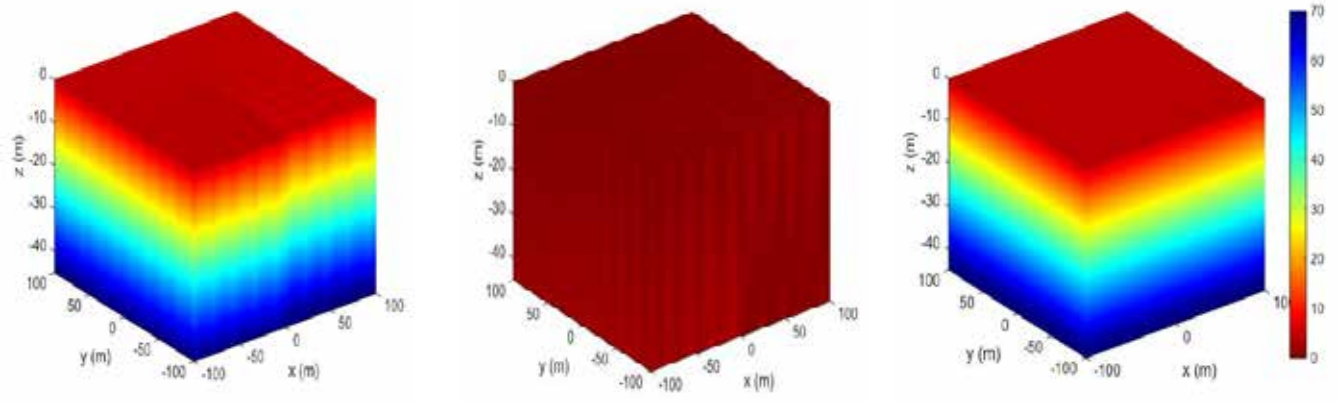

(a) (b) (c)

Figure 6. Spatial distribution of error between (a) prior mean of Young's modulus (MPa) and its true value, (b) posterior mean of Young's modulus (MPa) and its true value and (c) posterior and prior means of Young's modulus (MPa).

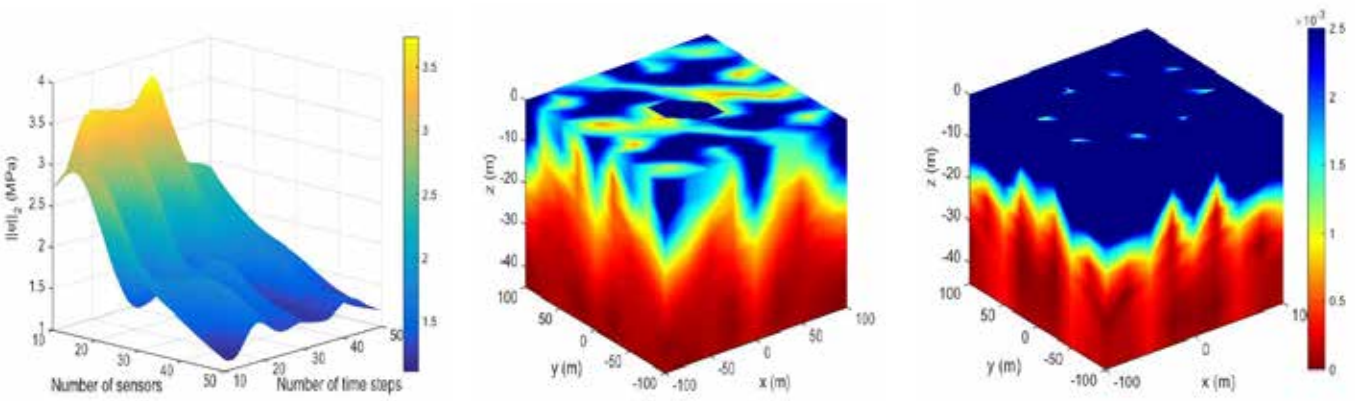

(a) (b) time = 4.5s. time = 5.5s.

Figure 7. (a) L_2-norm of error with respect to number of sensors and time steps, and (b) spatial distribution of $\Sigma_{\theta y}$ at 4.5s and 5.5s.

7 REFERENCES

Babuska, I.M., Nobile, F. & Tempone, R. 2007. A stochastic collocation method for elliptic partial differential equation with random input data. *SIAM Journal on Numerical Analysis* 43(3):1005-1134

Doucet, A., Freitas de, N. & Gordon, N. 2001. *Sequential Monte-Carlo Methods in Practice*. Springer-Verlag

Fathi,A. 2015. *Full-waveform inversion in three-dimensional PML-truncated elastic media: theory, computations and field experiments,* PhD Dissertation, The University of Texas at Austin

Ghanem,R.G. & Spanos,P.D.1991. *Stochastic finite elements:A spectral approach*, Springer

Kallivokas, L.F., Fathi, A., Kucukcoban, S., Stokoe K.H., Bielak, J. & Ghattas,O. 2013. Site Characterization using full waveform inversion. *Soil Dynamics and Earthquake Engineering* 47:62-82

Lacasse S. & Nadim F.1996. Uncertainties in characterizing soil properties. In Shackelford C.D.& Nelson,P.P.,(eds), *Uncertainty in Geologic Environment: From Theory to Practice, Proceedings of Uncertainty'96, July 31-August 3,1996,Madison, Wisconsin, Geotechnical Special Publication No. 58(1)*: 49–75 : ASCE, New York

Lysmer, J. & Kuhlemeyer, A.M. 1969. Finite dynamic model for infinite media, *Journal of the Engineering Mechanics Division*, ASCE 95: 859-877.

Iyengar,R.N. & Dash P.K. 1978. Study of the random vibration of nonlinear systems by the Gaussian closure technique. *Journal of Applied Mechanics* 45: 393–399

Madankan, R. 2014. *Model-data fusion and adaptive sensing for large scale systems:Application to atmospheric release*, PhD Dissertation, State University of New York at Buffalo.

Madankan, R., Pouget, S., Singla, P.,Bursik, M., Dehn, J., Jones, M., Patra, A.,Pavolonis, M., Pitman, E.B., Singh, T. & Webley, P. 2014. Computation of probabilistic hazard maps and source parameter estimation for volcanic ash transport and diffusion, *Journal of Computational Physics* 271:39-59

Nagavenkat, A.,2013. *The conjugate unscented transform - a method to evaluate multidimensional expectation integrals*, Master's thesis, State University of New York at Buffalo.

Nagavenkat, A., Singla P. & Singh T. 2012. The conjugate unscented transform-an approach to evaluate multi-dimensional expectation integrals, *Proceedings of the American Control Conference*

Nazarian,S. 1984. *In situ determination of elastic moduli of soil deposits and pavement system by Spectral-Analysis-of-Surface-Waves-method*, PhD Dissertation, The University of Texas at Austin

Geotechnical and Geophysical Site Characterisation 5 – Lehane, Acosta-Martínez & Kelly (Eds)

Automatic methodology to predict grain size class from dynamic penetration test using neural networks

C. Sastre, M. Benz & R. Gourvès
Sol Solution Géotechnique Réseaux, Riom, France

P.Breul & C.Bacconnet
Université Blaise Pascal, Laboratoire de Génie Civil Polytech, Clermont-Ferrand, France

ABSTRACT: The Panda 2®, developed by Roland Gourvès in 1991, is a lightweight dynamic cone penetrometer. It provides the dynamic cone resistance (q_d) and depth in real time with a high sampling frequency. Nevertheless it cannot take soil samples so the penetration test is called 'blind'. The aim of this paper is to propose an automatic methodology to predict the soil grading from the cone resistance using artificial neural networks. We have built a database based on the Panda® laboratory tests on soil samples and on in situ tests conducted next to boreholes during various geotechnical studies performed in France. Then the neural network was used to classify the cone resistance logs according to grain size distributions of the tested soils by means of feature extraction using different signal analysis. The results show that we are able to separate 4 soil classes with 98% accuracy.

1 THE PANDA 2®, VARIABLE ENERGY DYNAMIC CONE PENETROMETER (DCP)

The dynamic penetrometer Panda 2® has been designed to geotechnical investigation at shallow depth up to about 5 meters (Benz 2009). It is a light-weight dynamic, highly portable cone penetrometer, which uses variable energy manually delivered by the blow of a normalized hammer. After each blow, the dynamic cone resistance q_d is calculated at the current depth using the Dutch formula. One of the major interest is the high acquisition resolution. Therefore the plot of the cone resistance values against the depth, the Panda penetrogram, is a rich amount of information on the stratigraphy of site and soil properties (Shahour & Gourvès 2005) with a large number of data.

Despite all the benefits provided by the Panda 2® soil samples cannot be taken during the test thus there is no information about the nature of soil. However we notice empirically that the form of the cone resistance curve might differ between different types of soil. An example shows (Fig.1), with 3 Panda® tests conducted on laboratory calibration chamber of 80 cm height. The tested soils have a different nature and granulometry but a similar density and moisture content. We can easily note the morphological differences between the 3 resistance logs. The underlying idea for the methodology described in this paper relies on this observation: the expert knowledge and perspective of an experienced engineer can detect indices in the signal form to estimate the nature of the tested soil. In this study, we have developed a model based on artificial neural network to accomplish this empiricism.

Table 1. Soil parameters for the samples (Fig.1)

Nature		DGA Silt	Laschamps Clay	Sayat Sand
GTR		A1	A2	B2
γ_h	kN/m^3	17.8	17.6	17.3
γ_d	kN/m^3	16.2	15.6	16.0
W	kN/m^3	10.0	12.9	7.9
W_{OPN}	%	18.4	18.1	11.0
Moisture state		Dry	Dry	Dry

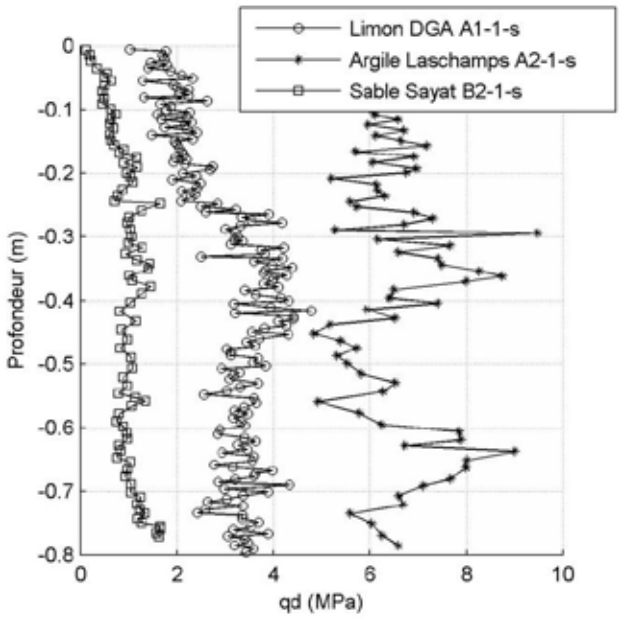

Figure 1. An example of a resistance log for different types of soils with similar state parameters.

2 ARTIFICIAL NEURAL NETWORKS

2.1 *Introduction*

ANN are mathematical models inspired in the human nervous system and has been effectively applied in many engineering applications. ANN are artificial intelligence (AI) tools to analyse the raw data and extract useful knowledge (Fayad et al. 1996) and to support selection problems. Furthermore ANN is known to be an alternative method for modelling complex problems in different fields of engineering (Shahin et al. 2001, Waszcsyszyn 2011).

2.2 *Proposed ANNs models*

Among several types of ANNs models used for data-analytic applications, multilayer perceptron MLP (Rumehart et al. 1986) and probabilistic neural network PNN (Spetch 1990) have been chosen. These models are feedforwards networks consist of multiple layers of interconnected neurons. We can distinguish 3 types of layers, input layer, hidden layer and output layer (Fig. 2). The neurons of the input layers are just used to stock the inputs values. The neurons of hidden and output layer are calculation cells. They compute a weighted sum of their inputs and then the activation function is applied to the sum in order to generate their output value. They are called feedforward networks because the input signal always moves one direction only, from input to output, and it never goes backwards.

The current training algorithm for this networks is the back-propagation method (Rumerhart et al. 1986). This algorithm involves 2 phases. Firstly the propagation phase where the training pattern's input are propagated from the input to the output layer. The second phase is the backward phase where the output error at a defined layer backwards through the connections with the previous layer in order to update the weights to find the minimum of the error function. That is known as the learning process of the ANN. The goal of the learning process is to find the optimal set of weights which would produce the right output for any input ideal case.

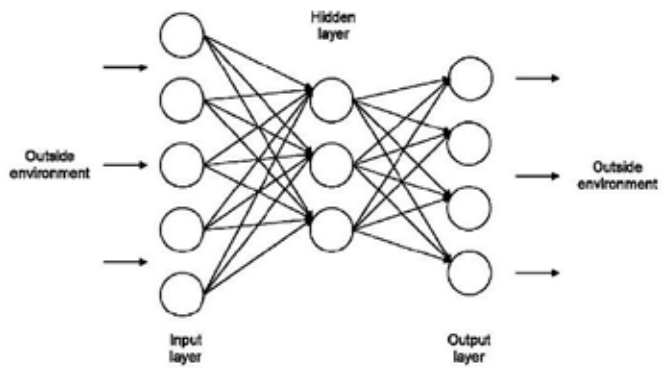

Figure 2. An example of a simple feedforward neural network.

Consequently the algorithm requires the target value for each input value to calculate the loss function gradient. It is for this reason that it is considered to be a supervised learning algorithm fundamentally. The term supervised refer to the labeled training data. In our context it may be possible to apply a supervised learning if we develop a cone resistance log data base and each sample has an appropriated soil class as output. In this way we could think about a model with an associative memory which would be able to predict the soil class from the cone resistance log based on a knowledge obtained from a labeled database.

MLP modelling has been used most often in geotechnical literature (Shahin et al. 2008). Furthermore MLP are universal approximators in the sense that they can compute an approximation that is good as we want even with only one hidden layer. On the other hand, PNN are frequently used in classification problems. They have a similar structure to MLP. The main difference is the change of the sigmoid or hyperbolic activation function often used in MLP topology by a statistically derived one, a radial base function, normally the Gaussian function. Unlike MLP, PNN approaches optimal Bayes classification and the outputs could also be used to estimate a posteriori probability that an output belongs to a defined category. On the other hand, one of the main difficulty of MLP paradigm is the fact to estimate the number of hidden layers and the number of neurons of each layer. However the PNN has always 2 hidden layers the pattern layer and the summation layer respectively. The first layer always contains one neuron for each case in the training data set and the second layer contains a number of neurons equal to number of defined targets. I

2.3 *ANNs in geotechnical problems*

In the geotechnical context, ANNs are considered as powerful modelling tools to deal with the uncertainty and extreme variability of most of the problems. In addition, ANNs have also demonstrated a major performance when compared with traditional statistical models. Therefore, since the early 1990s, ANNs have been applied successfully to several problems in geotechnical engineering (Shahin et al. 2009). Interested reader can refer to (Shahin et al. 2001, 2008, 2009) where the application of ANNs in geotechnical problems are examined.

(Sulewska 2011) pointed out the following six selected problems: 1) prediction of the Overconsolidation Ratio, 2) estimation of potential soil liquefaction, 3) prediction of foundation settlement, 4) evaluation of piles bearing capacity, 5) prediction of cohesive parameter for cohesive soils, 6) compaction built of cohesionless soils. The ANNs applied are all MLP with only one hidden layer. The number of

hidden neurons varies from 1 to 8. The excellent results confirm the interest of the application of ANNs in the geotechnical field, where the choice of ANNs models to regression problems is constantly increasing.

Despite all the benefits presented by ANNs, one of the major criticisms is that they are black boxes models, since no satisfactory explanation of their behavior could be achieved so far. The knowledge extraction is one of principal research topics in this field. In addition, ANN models often need a large database to perform an effective learning of the patterns. The number of samples dependent upon the problem to solve and cannot be estimated a priori. This fact could be a constraint on the application for certain geotechnical problems.

3 PROPOSED METHODOLOGY

The aim of this study is to propose an automatic methodology able to classify a sol according to its granulometry from a cone resistance signal provided by Panda2® test. This project is divided into 4 phases: Panda test database creation; input variable selection; output model; performance model validation.

3.1 *Panda test database*

The first step in a machine learning problem is the database acquisition. The database creation is necessary to allow the ANNs models observe the environment and learn to make reasonable decisions about the categories of the patterns.

A database of penetrograms provided by the Panda2® test has been created. It contains 218 penetrograms obtained from sufficiently homogeneous soils with no grain size over 50mm. Their nature and geotechnical properties have been characterized by means of laboratory test. Samples have been provided by laboratory and in situ test. The soil classification available for the tested soils based on GTR guide (SETRA & LCP 1992).

The laboratory Panda test were realized in a 37 cm diameter and 80 cm height calibration chamber, by using static loading under oedometric conditions (Chaigneau 2000). These tests were performed in more than 20 different soil types. Panda tests were carried out for each sample constituted. The part of the penetration curve where the cone resistance exhibit constant values was extracted and submitted to the posterior signal analysis. A total of 149 laboratory test have been recollected with a dry and medium water moisture.

On the other hand, there are 69 Panda2® in situ tests performed during several site characterization studies by the French company Sol Solution. In situ test are located in France, specifically in Auvergne department.

3.2 *Feature extraction and variable selection*

The second step involves the definition of entries of ANN model. The choice of input variables is fundamental to assure the model performance. This stage is called feature extraction and mainly consists of a short-term processing technique that is applied on the observed data in order to generate a feature sequence, the pattern.

We have carried out a feature extraction based on four analysis signal applied to cone resistance curve Inspired by analysis processing for speech recognition or bioelectrical signal analysis (Shannon 1948a, b, Kannatey-Asibu 1982, Hayes 1996, Betancourt 2004, Romo et al. 2007). We have applied 4 signal analysis: statistical, nonlinear, and morphological and spectral and a pattern vector of 26 parameters for each penetrogram have been obtained.

Variable selection is intended to select the best subset of predictors, removing redundant predictors and defying the curse of dimensionality to improve classification performance. In this work we have performed a local sensitivity analysis using one -at-a-time approach (OAT). One benefit of OAT is one of the simplest approach and it can be applied to all numerical models so we have chosen this method for practical reasons. Rabitz H. (1989) and Saltelli (2006) offer an interesting review about the use of sensitivity analysis strategies for model-based inference in different articles.

OAT techniques analyze the effect of one parameter on the cost function at a time, keeping the other parameters fixed. Note that they explore only a small fraction of the design space but is enough to allow a quick detection of model inputs what don't have any significant influence in the output value. In this instance 3 perturbation values have been considerate, calculated as a percentage of the standard deviation for each input variable (Fig.3). Another perturbation equal to input variable variance have been also used. After each modification the variation of error is calculated in order to measure the individual impact of each entry parameter.

Table 2. Parametrization of cone resistance log.

Number of parameter		
1. q_d mean	7. q_d interquartile range	13. q_d slope changes
2. q_d median	8. q_d skew	14. q_d waveform
3. q_d standar deviation	9. q_d kurtosis	15. Linear coefficient of linear trend
4. q_d coefficient of variation	10. q_d Shannon entropy	16. Independent coefficient of linear trend
5. q_d variance	11. q_d logarithm entropy range	
6. q_d range	12. q_d skew	17. Maximum spectral power

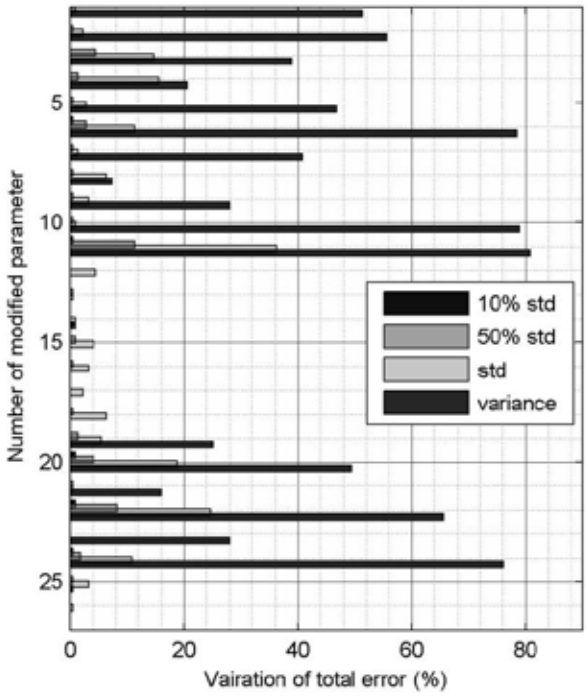

Figure 3. Results of the sensitivity analysis for the 26 original characteristics.

Analyzing the results of OAT approach used, we have realized that there are 9 inputs variables relative to cone penetration analysis which modification have no influence on the ANN accuracy classification. They are rejected and the number of input variables have been reduced to 17. In other terms, for every cone resistance log of the database, a final feature vector of 17 parameters (Tab.2) is thus constructed to be the entry for the ANN model.

3.3 *Target classes*

The next stage is to decide what outputs are the neural network expected to learn. The aim is to classify the nature soils in terms of granulometry. As we have explained in the previous section 3.1, the database soils collected are classified in GTR classification. In the following, the 4 output classes proposed (Tab.3) are based on this soil classification. We have used a binary coding, namely "dummy". Each dummy variable is given the value zero except for the one corresponding to the correct category, which is given the value one.

Table 3. Target classes based on tested soils.

Target	GTR	Nature	Codification
Class 1	A1 A2 A3 A4	Fine soils	1 0 0 0
Class 2	B5 B6	Fine sands	0 1 0 0
Class 3	D1 B1 B2	Sands, gravel	0 0 1 0
Class 4	D2 B3 B4	Gravel	0 0 0 1

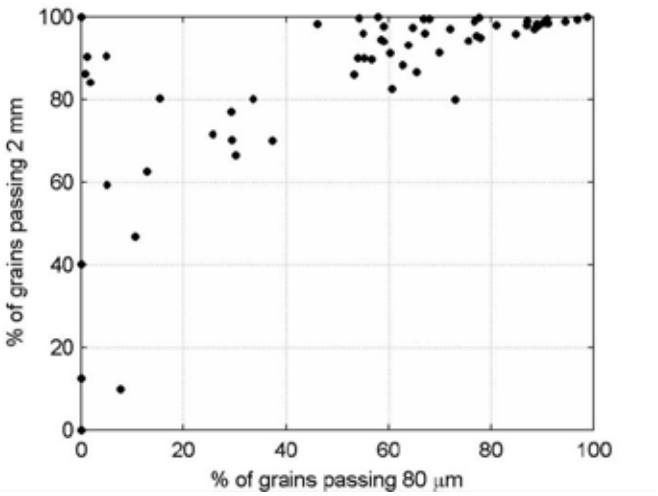

Figure 4. Percentage passing through the sieve opening 2 mm and 80 μm for the database soils.

The 2 opening size of sieves used to classify the soils in GTR are 2 mm and 80 μm. The percentage of grains passing through these openings is plotted (Fig.4) for the database soils.

3.4 *Design phase for MLP classifier*

The precise network topology required for an MLP to solve a particular problem usually cannot be determined (Leverington 2009), although research efforts continue in this regard. In contrast, PNN networks don't have this issue because their architecture is fixed by the size of the problem as we have explained in section 2.2.

In this regard we have trained several networks in order to choice the best MLP parameters architecture using the root mean squared error RMSE as error function (Hetch-Nielsen 1990). It is the most popular measure of error and has the advantage that large errors receive much greater attention than small errors.

We note that the input and output data must be preprocessed for ANNs problems. Data preprocessing will allow the model produce accurate forecasts. Normalization and standardizing are the two most used preprocessing methods so we have tested it. Specifically we have applied a normalization scaling the data to the interval [-1, 1] and a standardization scaling inputs to have mean 0 and variance 1. The better results have been obtained with a normalization preprocessing and the hyperbolic function as activation function for the hidden and the output layer.

Finally to estimate the optimal number of hidden units we have varied the number of hidden neurons of the trained networks from 2 to 25, and we also have run several test to take account of the random initialization weights effect. We have also tested MLP with one and two hidden layers and we have obtained a better generalization with just one. The final MLP model proposed has one hidden layer with 12 neurons and the Levenberg-Marquardt (Levenberg 1944, Marquardt 1963) as training function.

Finally we add that early stopping method was used in all the run test to avoid overfitting.

3.5 *Performance of proposed ANN models*

To avoid overfitting, the ANN model should use a set different set unknown for the ANN. For that purpose, we carried out a Hold-Out validation (Bishop 1995). This method needs to divide the large dataset to three subset. Then the classifier is tested by new databases called validation and test sets. In this study the data have been randomly divided into these three subsets. The fraction of the data that is placed in the training set is 70% and 15% for the validation and test sets. However, the way the data are divide can have an important impact on model performance (Shahin et al. 2004) and the statistical properties of the various data subsets should be taken into account as a part of any data division procedure.

The matrix confusion summarize the classification of each dataset for MLP final model (Tab.3). This table is often used to describe the performance of a classification model. In this matrix, each column number represents the instance in target or actual class while each number row number represents the instance of predicted class.

Table 4. Confusion matrix for MLP proposed

		Training				Validation			
Output	Class 1	75	2	0	0	17	1	0	0
	Class 2	1	18	0	0	0	2	0	0
	Class 3	0	0	25	0	0	0	7	0
	Class 4	0	0	0	31	0	0	0	6
		Test				Total			
Output	Class 1	18	0	0	0	110	3	0	0
	Class 2	0	3	0	0	1	23	0	0
	Class 3	0	0	5	0	0	0	37	0
	Class 4	1	0	1	5	1	0	1	42
		Target class				Target class			

We note that MLP proposed has assigned the right class to 212 samples from a total of 218 that means an accuracy of 97% from the total database. The 97% and 94% accuracy have achieved for the validation and test sets respectively.

4 DISCUSSIONS AND CONCLUSIONS

In this paper we have proposed an automatic methodology to predict grain size class from dynamic penetration test and the classification task is carried out by 2 different ANN, an MLP and a PNN. The both network have achieved excellent results. Nevertheless further studies and samples may be needed to assess its application in situ.

Regarding performance of each model of ANN used in this study, we think that the 2 topologies have proved their efficiency. Nevertheless, PNN may be more interesting than MLP to detect novel cases since it is a model based on probability density estimation.

It can be noted that the application of ANNs have been possible due to characteristics of cone resistance log provided by Panda test. In addition, incorporation of other soil measurements as soil images by means of geo-endoscopy technique (Breul 1999, Haddani 2004) or Panda3 measures (Benz 2009, Escobar 2014) could be helpful. Work in this area is ongoing.

5 REFERENCES

Benz-Navarrete M.A. 2009. Mesures dynamiques lors du battage du pénétromètre PANDA 2. *Chemical and Process Engineering. Université Blaise Pascal-Clermont-Ferrand II.*

Betancourt G., Giraldo E., Franco J. 2004. Reconocimiento de patrones de movimiento a partir de señales electromiográficas. *Scientia et Técnica* vol.26: 53-58.

Breul P. 1999. Caractérisation endoscopique des milieux granulaires couplée à l'essai de pénétration. *Thèse de doctorat Physique Clermont-Ferrand 2.*

Chaigneau L., Bacconnet C., Gourvès R. 2000. Penetration test coupled with geotechnical classification for compacting control. *Proceedings of International Conference on Geotechnical & Geological Engineering, GeoEng2000 (Melbourne, Australia.*

Escobar E.J. (2015). Mise au point et exploitation d'une nouvelle technique pour la reconnaissance des sols : le Panda 3. *Thèse de doctorat Génie Civil Clemont-Ferrand.*

Fayyad U., Piattetsky-Shapiro G., Smyth P. 1996. The KDD process for extracting useful knowledge from volumes of data. *Commun ACM* 39 vol.11: 27-34.

Hadanni Y. 2004. Caractérisation et classification des milieux granulaire par géondoscopie. *Thèse de doctorat Génie Physique Clermont-Ferrand 2.*

Hayes M.H. 1996. *Statistical Digital Signal Processing and Modeling.* Ed Wiley.

Hecht-Nielsen, R. 1990. *Neurocomputing.* Addison-Wesely Publishing Company, Reading, MA.

Hornik K. and Stinchcombe M. and Halbert W. 1989. Multilayer feedforward networks are universal approximators. *Neural Networks* vol.2 (5): 359-366.

Kannatey-Asibu E., Dornfeld D.A. 1982. *Wear* vol.76: 247-261.

Levenberg K. 1944. A Method for the Solution of Certain Problems in Least Squares. *Quart. Appl.Math.* vol.1: 431-441.

Leverington D. 2009. A Basic Introduction to Feedforward BackPropagation Neural Network. *Geosciences Department Texas Tech University*.

Marquardt D. 1963. An Algorithm for Least-Squares Estimation of Nonlinear Parameters. *SIAM J. Appl. Math.* vol.2: 164-168.

Rabitz H. 1989. Systems analysis at the molecular scale. *Science* vol.246 (4927): 221-6.

Romo H.A., Realpe J.C., Jojoa P.E. 2007. Análisis de Señales EMG Superficiales y su Aplicación en Control de Prótesis de Mano. *Revista Avances en Sistemas e Informática* vol.4 (1): 128-136.

Rumelhart D.E., Hinton G.E., Williams R.J. 1986. Learning internal representations by error propagation. Parallel distributed processing: *Explorations in the microstructure cognition* vol.1: 318-362.

Saltelli A., Ratto M., Tarantola S., Campolongo F, European Commision, Joint Research Centre of Ispra(I) 2006. Sensitivity analysis practices: strategies for model-based inference. *Reliability Engineering & System Safety* vol.91 (10-11): 1109-1125.

Sarle W.S. 2002. The Neural Networks FAQ. *ftp://ftp.sas.com/pub/neural/FAQ.html*

SETRA & LCP 1992. *Technical Guidelines on Embankement and Capping Layers Construction.* Guide technique.

Shahin M.A., Jaksa M.B., Maier H.R. 2001. Artificial Neural Network applications in geotechnical engineering. *Australian Geomechanics-March.*

Shahin M.A., Jaksa M.B., Maier H.R. 2004. Data Division for Developing Neural Networks Applied to Geotechnical Engineering. *Journal of Computing in Civil Engineering* vol.18 (2), 105-114.

Shahin M.A., Jaksa M.B., Maier H.R. 2008. State of the art of artificial neural networks in geotechnical engineering. *Electronic Journal of Geotechnical Engineering.*

Shahin M.A., Jaksa M.B., Maier H.R. 2009. Recent Advances and Future Challenges for Artificial Neural Systems in Geotechnical Engineering Applications. *Advances in Artificial Neural Systems* vol. 2009: 9.

Shahrour I., Gourvès R. 2005. *Reconnaissance des terrains in-situ.* Hermès-Lavoisier.

Shannon C.E. 1948a. A mathematical theory of communication Part I. *Bell System Technical Journal* vol.27: 379-423.

Shannon C.E. 1948b. A mathematical theory of communication Part II. *Bell System Technical Journal* vol.27: 623-656.

Spetch D.F. 1990. Probabilistic neural network. *Neural Networks* vol.3: 109-118.

Sulewska M.J. 2011. Applying Artificial Neural Networks for analysis of geotechnical problems. *Computer Assisted Mechanics and Engineering Sciences* vol.18 (4): 231-241.

Waszczyszyn Z. 2011. Artificial Neural Networks in civiel engineering: another five years of research in Poland. *Computer Assisted Mechanics and Engineering Sciences* vol.18: 131-146.

Geotechnical and Geophysical Site Characterisation 5 – Lehane, Acosta-Martínez & Kelly (Eds)

Quantifying and reducing uncertainty in down-hole shear wave velocities using signal stacking

M.A. Styler & I. Weemees
ConeTec Investigations, Ltd., Richmond, Canada

ABSTRACT: In down-hole seismic testing, shear wave velocities are interpreted from measured shear wave signals and the geometric positioning of the seismic source and receivers. The quality of the shear wave signals can be improved through signal stacking, however signal stacking decreases the production rate of down-hole seismic testing and has diminishing returns with each subsequent trace. In this paper we quantify the improvement in the interpreted shear wave propagation time that can be realized through signal stacking up to six traces. Results are presented for a seismic cone penetration test performed to a depth of over 30 m at a site in San Leandro, CA, America. We used an automatic seismic source to generate reproducible seismic waves. Each seismic test comprised of at least five left-side and right-side (reverse polarity) generated shear waves. In this paper we show how to quantify noise for each seismic test, how to calculate the signal to noise ratio for the shear wave, and how to calculate a probability distribution for the shear wave propagation time. We show that SNR increases with signal stacking; which results in a decrease in the shear wave interval time error. We quantified the interval time error by propagating the measurement uncertainty through the cross-correlation function and characterizing a probability distribution for the location of the peak cross-correlation. Quantifying down-hole seismic uncertainty does not require any special equipment or field procedures beyond recording at least two seismic traces. This work has implications in the engineering applications of shear wave velocity profiles. Sensitivity analyses can be performed considering the reported uncertainty in the shear wave velocity profile.

1 INTRODUCTION

Down-hole shear wave velocity profiles are interpreted by comparing adjacent recorded seismic traces. The quality of the traces can be improved through signal stacking, where the seismic test is repeated at a single depth and the recorded traces are added together. Signal stacking amplifies the systematic features in the trace – such as the shear wave, compression wave, and any reflected waves. The improvement from signal stacking is diminished with each additional trace. Signal stacking also adversely affects the production rate of down-hole seismic testing.

In this paper we evaluate the benefit of signal stacking on down-hole seismic tests performed during a seismic cone penetration test (SCPTu). We quantify the noise and the signal to noise ratio (SNR) for each recorded trace. We calculate the SNR for the stacked signals. We then compared the error in the interval shear wave time to the calculated SNR.

This work was demonstrated using down-hole seismic tests performed during a SCPTu in San Leandro, California, United States. An automatic hammer was used to generate reproducible seismic waves at the ground surface. Seismic tests were repeated at least ten times, with half being inverse polarity, at each depth. The noise was quantified by subtracting signals to remove systematic features. The SNR was calculated by comparing the square of the amplitude of the seismic wave to the square of the amplitude of the noise. We assumed that the noise could be represented by a zero-mean Gaussian distribution. The noise-distribution was propagated through the cross-correlation function to estimate the error in the interval shear wave velocity time.

This paper contains three contributions to improve down-hole seismic profiles. First, we show how to calculate the noise in a set of down-hole seismic traces. Second, we show how to quantify the SNR for a trace and for stacked signals. Third, we show how to evaluate the error in the propagation time when comparing two seismic traces. Unsurprising-

ly, we observed that an increase in SNR reduces the error in the shear wave propagation time.

2 DOWN-HOLE SEISMIC TESTING

2.1 *Cone Penetration Testing (CPTu)*

Cone penetration testing (CPTu) is performed by advancing an instrumented probe into the soil at a rate of 2 cm/sec. The standard CPTu probe includes measures of the tip resistance (q_c), sleeve friction (f_s), dynamic fluid pressure (u_2), inclination, and temperature every 2.5 or 5 cm of depth. The cone tip resistance requires a systematic correction from q_c to a corrected value of q_t using $q_t = q_c + u_2(1 - a)$. The net tip resistance (q_t-σ_{v0}) depends primarily on the soil type, in-situ effective stress, and in-situ density. The fluid pressure depends on the ambient fluid pressure and induced fluid pressure due to cone insertion and soil shearing. The CPTu is a reproducible and efficient site investigation technique for profiling soil deposits and estimating soil properties.

2.2 *Seismic Cone Penetration Testing (SCPTu)*

Rice (1984) described the combination of cone penetration testing with down-hole seismic testing to create the SCPTu. The seismic cone penetrometer includes a seismic sensor behind the friction sleeve. This push-in tool provides excellent coupling between the sensor and the in-situ soil; which can be a significant challenge in bore-hole seismic testing. In the work by Rice (1984), seismic shear waves were generated at the ground surface by striking the ends of a normally loaded wooden plank with a sledge hammer. Opposite ends of the plank were struck to invert the polarity of the shear wave. Seismic testing with a sledge hammer source was performed every metre of cone penetration, coinciding with the cone deployment rod lengths. Adjacent signals were compared to determine the interval propagation time. Rice (1984) found that the first cross-over point provided the most consistent characteristic point in the seismic trace. The first cross-over point is the point where the shear-wave and reverse-polarity shear wave traces cross. The first cross-over point for each seismic test depth was compared to determine the interval shear wave propagation time. The geometry of the seismic source and in-situ receiver are used to determine the interval propagation length. The shear wave velocity is the ratio of the interval propagation length to the interval propagation time.

Rice (1984) also compared a true-interval module to a pseudo-interval module. A true-interval cone uses two receivers at a fixed spacing along the cone probe. Signals from both receivers are recorded simultaneously when a seismic wave is generated at the ground surface. A pseudo-interval seismic cone uses a seismic receiver at a single location. The receiver is advanced through the soil to subsequent depths to collect a set of seismic traces. Rice (1984) observed a discrepancy between the true-interval and pseudo-interval results. He rebuilt the true-interval module using geophones that were paired based on similar resonant frequencies and oscillation characteristics. This revised true-interval probe provided results that were closer to the pseudo-interval technique. Styler et al. (2013) also observed a discrepancy using true-interval probes. True-interval modules may have a difficult to characterize systematic error due to slight variations in the sensors and mounting within the seismic tool. Furthermore, true-interval testing is still suspect to trigger-time errors when signal stacking is performed. Conversely, the errors in the pseudo-interval test are known and can be controlled and mitigated. For example, seismic testing at the end of the rod-stroke results in a very consistent and reproducible rod-stick up length and essentially eliminates the error due to probe insertion depth. Multiple tests and rejecting signals can resolve any significant trigger-time errors.

Robertson et al. (1986) presented the preliminary work on the development of the SCPTu technique. They demonstrated the viability of obtaining a down-hole seismic profile with the SCPTu. They stated that a typical survey included 40 hammer blows, but generally only 1 blow was required on each side of the beam.

Gillespie (1990) demonstrated the importance of generating reproducible seismic signals. He also interpreted the arrival of the shear wave using the first cross-over point. He showed that the generation of slightly different waveforms from the sledge hammer strike could shift the cross-over point. He showed that a metal beam provided a better seismic source than a wooden plank. To generate reproducible seismic waves, he created a pendulum with a fixed drop height to strike the metal beam.

Campanella and Stewart (1992) recommended cross-correlation over the first cross-over point. They said that the cross-over location can suffer from interference as it uses the time information at a single point. They show an example set of signals where the cross-over time had been delayed due to interference from a "step" distortion in the signal. Alternatively, the cross-correlation function compares the entire shear wave signal. For the same set of example signals, the cross-correlation interpretation was not as affected as the cross-over point.

Cross-correlation compares the entire seismic trace to determine the time shift which best aligns the two signals. The cross-correlation function can be solved with Equation 1. In this equation N is the number of discrete measurements in the signal, it is the length of the digital recorded data. The two signals are represented by x(i) and y(i). The first value of the cross-correlation function is at $CC_{xy}(n=0)$, and

is simply the sum of the element-by-element multiplication of the two signals. When the two signals are aligned, the positive peaks and negative peaks are matched. The sum of the products for aligned signals is maximized as two negatives multiplied together results in a positive. Cross-correlation values are calculated for each time shift of n, as the top signal is shifted in time. The maximum cross-correlation value corresponds to the time shift when the signals are most aligned. This time shift is taken as the propagation time.

$$CC_{xy}(n) = \sum_{m=1}^{m=N-n} x(m)y(m-n) \quad (1)$$

Howie and Amini (2005) further examined the interpretation methods for down-hole seismic testing. They performed numerical simulations of the down-hole seismic test and evaluated field data from a site in Richmond, British Columbia, Canada. They found generally good agreement between the first cross-over point and cross-correlation. They showed that soil-damping caused signal widening a dispersion with depth; but that this effect was somewhat countered by an increase in stiffness with depth.

Improved automatic seismic sources have been developed (Styler et al. 2014, Mayne and McGillivray 2008, Casey and Mayne 2002) since the SCPTu was introduced. Casey and Mayne (2002) presents an automatic hammer source using internal solenoids. Mayne and McGillivray (2008) present five iterations of a compact automatic spring loaded rotating hammer source. Styler et al. (2014) used a continuous vibrating source instead of a hammer-strike generated shear wave. The work presented in this paper used an automatic hammer-strike seismic wave source.

2.3 *Signal stacking*

Signal stacking is performed by repeating a test and summing up the results. In down-hole seismic testing, all of the left side hits would be summed up to form a left-side stack. For a series of identical tests with random error, the signal to noise ratio increases by a factor equal to $\sqrt{n}$. For example, stacking 4 hits should double the signal to noise ratio.

Signal stacking is commonly used to improve bender element seismic signals measured in a laboratory. Bender elements are used to obtain the shear wave velocity across laboratory soil specimens. Lee and Santamarina (2006) emphasized the use of signal stacking over amplifiers and filters that can alter the signal spectrum. Brandenberg et al. (2008) developed a fast stacking procedure for bender element testing. This technique avoided the need to wait for residual seismic signals to dissipate before sending the next pulse. The time between pulses was randomized so that only the primary arrival of the shear wave was systematic and amplified during signal stacking. They note that this approach magnifies the SNR, but not as much as $\sqrt{n}$.

Signal stacking is also used to improve in-situ seismic measurements. Hunter et al. (2002) recommended the use of signal stacking during down-hole seismic testing if interference from tube waves occurs due to poorly grouted borehole casing. They also suggested signal stacking during non-invasive shear wave refraction investigations as traffic and wind noise may coincide with the frequency range of interest. If the noise is at the same frequencies as the shear wave it cannot be easily filtered.

Meunier et al. (2001) used signal stacking to develop a permanent seismic monitoring technique using low energy stationary seismic sources. The objective was to monitor gas storage in a deep reservoir. Permanent seismic sensors were installed in-situ on the casing of three wells. To monitor small changes in the reservoir they needed permanent stationary seismic sources. This constraint prevented the use of a mobile 30000 lb vibrator. Their solution was a low energy piezoelectric seismic source. After stacking 1280 signals the results were comparable to the large vibrator results.

Signal stacking is a powerful technique to increase the signal to noise ratio. It is used for seismic testing in the laboratory and in-situ.

3 SITE INVESTIGATION AND INTERPRETATION METHODS

Our objective for this paper was to evaluate how much signal stacking improves the interpretation of the down-hole V_S profile from a SCPTu. We achieved this by quantifying the SNR from the recorded traces and the stacked traces. We compared the calculated SNR to the 95% coverage window for the uncertainty in the shear wave propagation time. Calculating the propagation time error compares two signals, so we compared the error to the smaller SNR of the two signals.

This evaluation was performed on a SCPTu in San Leandro, California, United States. This site geological surface map indicates that this area comprises Young Quaternary Alluvium overlying Older Quaternary Alluvium with possible channels of Quaternary Intertidal Deposits. Figure 1 shows the SCPTu profile for this site. There are three fine grained layers from 0.5 m to 9.0 m, 12.0 m to 17.5 m, and 22.0 to 28.5 m. These layers are separated by free-draining sands. The interpretation of the velocities in the fourth column of SCPTu profile are described within this paper.

The seismic waves were generated using an automatic hammer source and received down-hole using a pseudo-interval seismic cone. The seismic

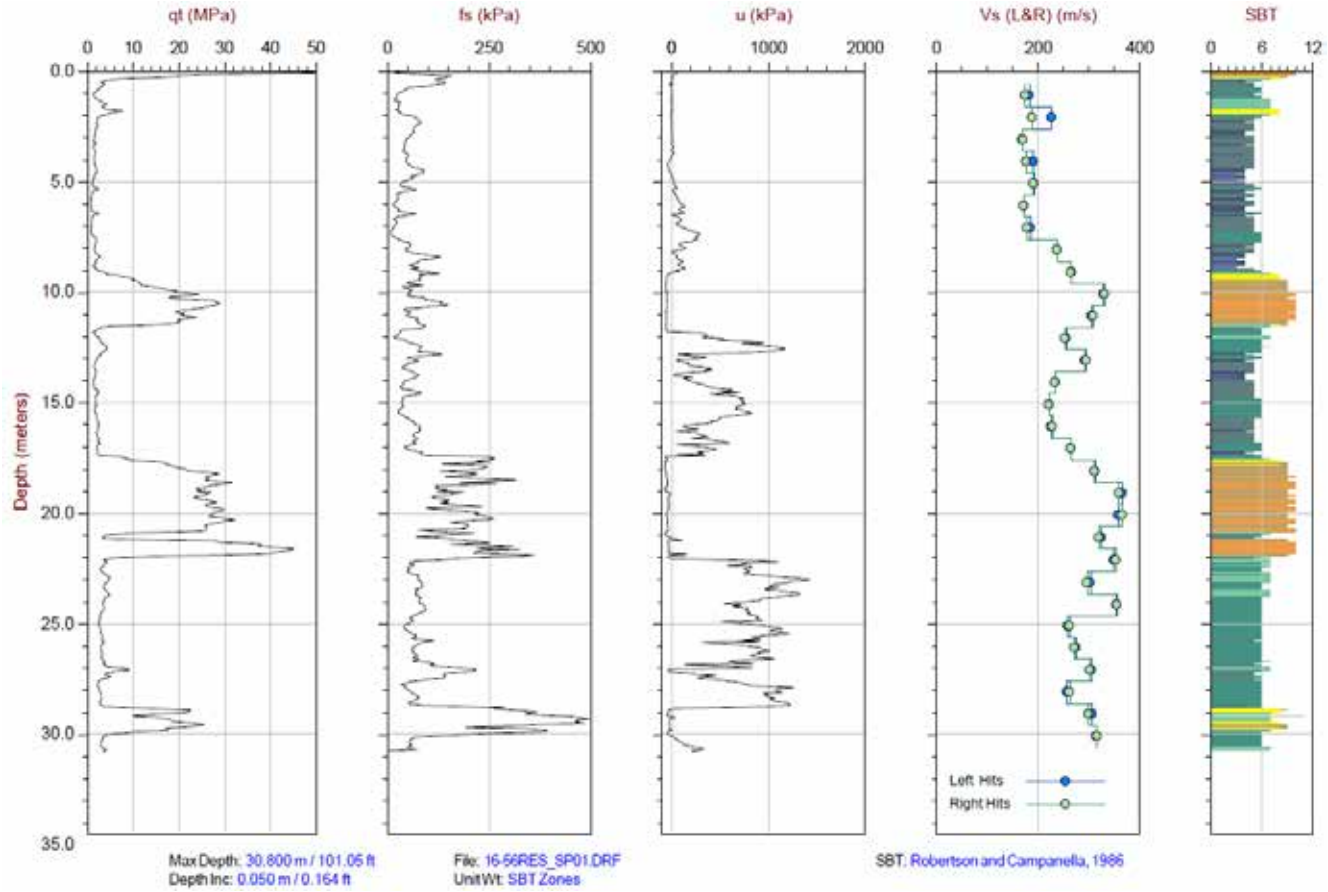

Figure 1. SCPTu profile including corrected tip resistance, sleeve friction, pore pressure, interpreted shear wave velocity profile, and inferred soil behaviour type showing desiccated crust over three thick layers of fines each separated by thick sand layers

source was located 57 cm from the test-hole. The data acquisition system included amplification, analog-to-digital conversion, and data recording. The amplification was manually adjusted by the CPT operator during the SCPTu. The analog signal from the geophone is amplified prior to digital conversion. The operator had the option of accepting or rejecting each recorded seismic trace. Reasons for rejection included over or under amplification, oversaturated geophone signals, or a subjective evaluation of the quality of the seismic trace. Data was recorded at a sampling rate of 20 kHz. The seismic tests were performed at 1 m intervals corresponding to the end-of-stroke rod breaks. Seismic testing consisted of automatic striking of left and right side hits. Each test was repeated at least five times per side.

3.1 *Reproducible seismic signals*

Figure 2 presents a cascade plot of the seismic traces to the end of hole. In this figure the raw data from each seismic trace was stacked, divided by 10 to avoid overlapping for figure clarity, and then plotted at the seismic sensor depth. In a cascade plot, the shear wave velocity is approximately the slope of the characteristic points in the signals. This figure indicates that the shear wave velocity increases at 8 m and 18 m depth. The exact shear wave velocity is different than this approximation as the shear wave propagation length is longer than the seismic sensor depth. A cascade plot provides a quick visual review of the collected seismic dataset.

Figure 3 shows two sets of recorded seismic tests in detail. This figure shows ten traces at 18.6 m and eleven traces at 19.6 m that have been scaled to plot in clarity on the depth-axis scale. Sets of adjacent seismic traces are compared to interpret shear wave interval propagation time. Small errors in the interpretation for the propagation time can result in larger errors in the shear wave velocity.

Figure 4 shows a close-up view of the raw recorded seismic signals at a geophone depth of 19.6 m. These signals have not been filtered. They have not been scaled to a common amplitude. This figure includes six right side (red) and five left side (blue) seismic traces. It is difficult to discern the individual traces at this scale due to the reproducibly of the seismic hits and received signals.

3.2 *Quantifying noise*

A digital signal is a finite time-series of measurements. Each measurement is the sum of the underlying value and noise: Trace = Signal + Noise. We have assumed that the noise can be represented as a

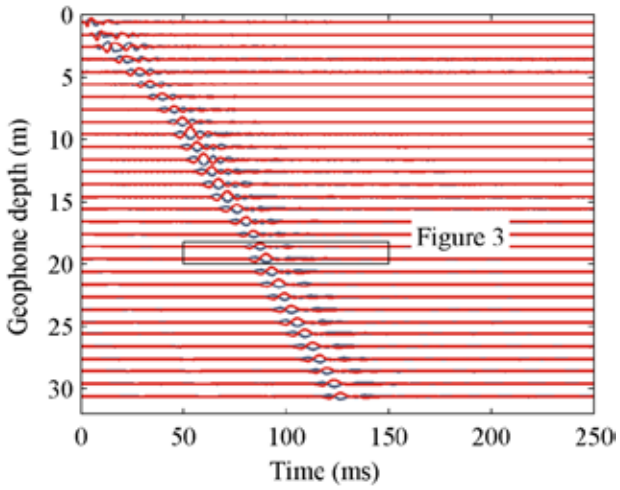

Figure 2. Cascade plot of stacked down-hole seismic traces with reverse polarity waves by striking opposite ends of the seismic beam

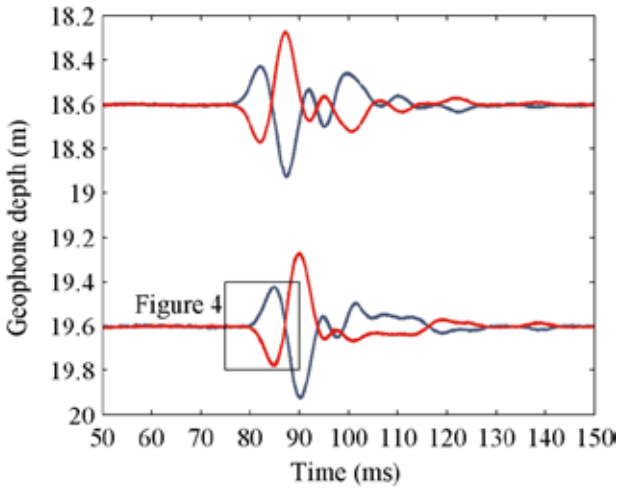

Figure 3. Scaled seismic traces from subsequent tests performed with the geophone at a depth of 18.6 and 19.6 m

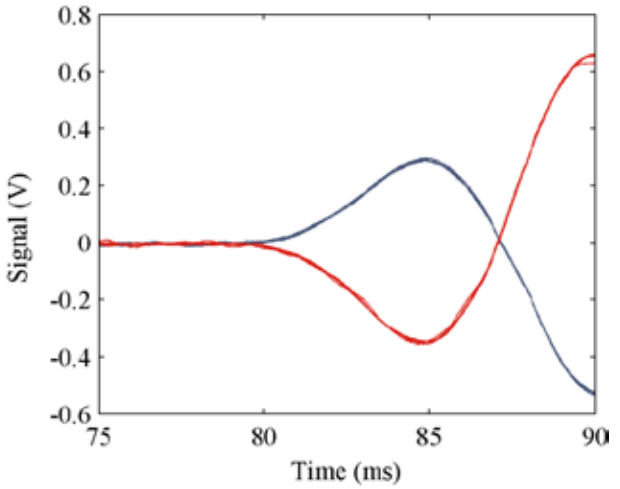

Figure 4. Close up view of raw recorded five left traces (blue) and six right traces (red) showing reproducibility

normal distribution with zero mean. This assumed distribution is required for a subsequent analysis of the uncertainty of the location for the cross-correlation peak. It represents the measurement uncertainty in our digital signals.

In a down-hole seismic test a long trace is recorded to capture a seismic wave that may only occur over a time window less than 100 ms. Based on this, we incorrectly assumed that the noise could be characterized over the first 50 ms or last 50 ms of each recorded trace. These windows can be seen in Figure 2. We unexpectedly observed systematic features over these time-windows. The first 50 ms of the signals collected at a geophone depth of 19.6 m are shown in Figure 5. This figure shows eleven raw traces. What is immediately apparent is that every trace is aligned. They are in-phase – this shows that the variation is not random. Figure 6 shows the last 50 ms. Again, repeated tests show systematic features in the signal; but the left and right are not in-phase. This may be due to continued resonance of the geophones or from reflected waves. It is clear from these reproducible seismic tests that the noise cannot be characterized over small time-windows before or after the main shear wave signal.

We separate the signal from the noise, the systematic from the random, by comparing repeated seismic traces. We calculated the mean trace (T_m) and the average deviation from the mean trace. The mean trace is simply the stacked trace divided by N, the number of stacked signals. The standard deviation for the noise is the average deviation from this mean trace. It is calculated over all N signals with Equation 2. In this equation n is the total number of sample points. For 5 recorded traces with 5,000 points each, n is 25,000.

$$\sigma_n = \sqrt{\frac{\sum_1^N (T_i - T_m)^2}{n-1}} \qquad (2)$$

Figure 7 shows a scatter plot of the dispersion of the data for the right-side hits at a depth of 19.6 m. The noise was calculated with Equation 2 to a value of 0.0029 V. This figure includes two lines representing ±1.

3.3 *Calculating the signal to noise ratio (SNR)*

The SNR quantifies the quality of the recorded seismic trace. It represents how strongly the underlying seismic signal (T_i) is separated from the background noise (σ_n). We calculated the SNR with Equation 3 as the ratio of the maximum absolute value of the signal divided by three times the standard deviation of the noise. We used extreme values for the signal and noise in order to avoid penalizing traces that were recorded over longer durations. The extreme value for the signal typical occurs as a peak

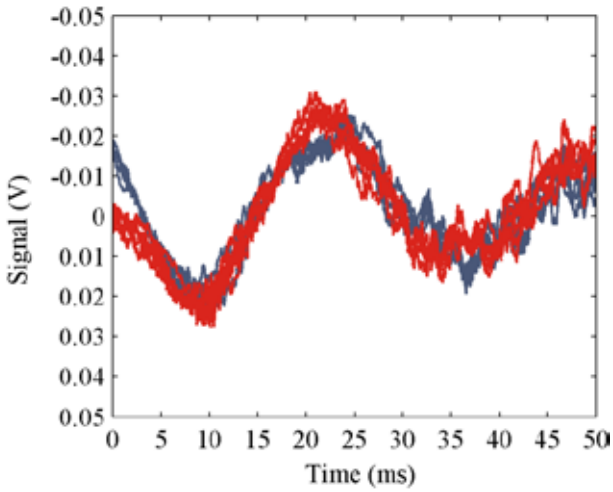

Figure 5. Fist 50 ms of seismic traces collected at a geophone depth of 19.6 m showing systematic variations in the recorded traces

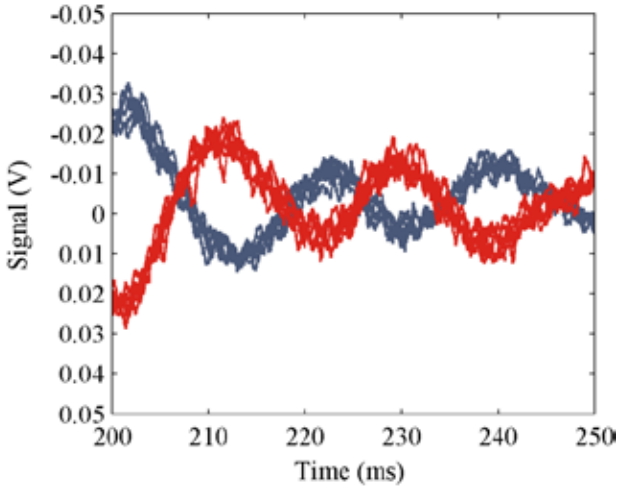

Figure 6. Last 50 ms of seismic traces collected at a geophone depth of 19.6 m showing systematic variations in the recorded traces

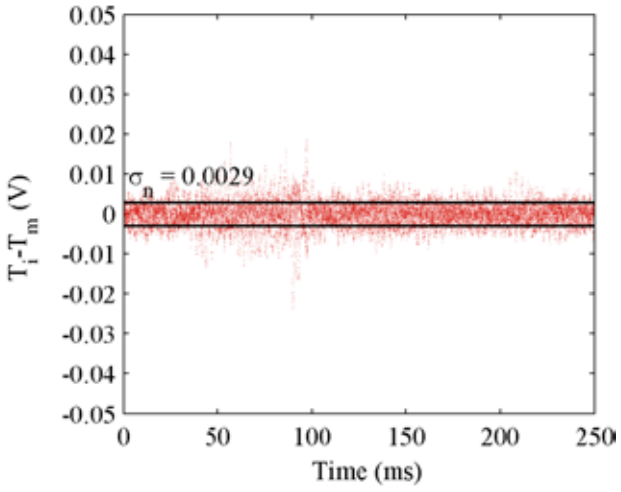

Figure 7. Calculating the random noise by subtracting the mean trace from each recorded trace

in the first shear wave cycle. We used three times the standard deviation of the noise (Equation 2) as the maximum value for the noise.

$$SNR = \frac{Max\left(abs(T_i)\right)}{3\sigma_n} \tag{3}$$

Signal-stacking traces increases the amplitude of the trace and the variance noise. The amplitude of the trace is increased by approximately a factor equal to the number of stacked signals (N). The increase in noise is calculated as the square root of the sum of the variances of the individual trace. The effect of signal stacking on SNR is shown in Equation 4. If both the trace and the variance (σ_n^2) increase by N, then the SNR increases by $N^{0.5}$. Stacking 4 traces should increase the SNR by a factor of 2.

$$SNR = \frac{Max\left(abs(\sum_1^N T_i)\right)}{3\sqrt{N\sigma_n^2}} \tag{4}$$

At a depth of 19.6 m there were six right-side seismic traces recorded. Each of these six traces is shown on the left side of Figure 8. These are the raw data plots and have not been normalized or scaled. Each plot includes an annotation for the signal to noise ratio. The right side of Figure 8 shows the effect of stacking each subsequent seismic trace. The signal to noise ratio increases with each hit. It increases by the expected rate – a factor equal to the square root of the number of stacked traces.

3.4 *Quantifying V_S uncertainty*

We developed a technique to quantify the uncertainty in the estimated propagation time using the cross-correlation function. This was accomplished by characterizing the measurement uncertainty in our recorded seismic signals and propagating it through the cross-correlation function. We then created a probability distribution for the location of the cross-correlation peak; which corresponds to the propagation time.

The characterized measurement uncertainty is propagated through the cross-correlation function, Equation 1. Each point in the cross-correlation function is the result of a large summation. Following the central limit theorem, a large sum of independent random variables will be approximately normally distributed. To calculate this distribution, we only need to determine the mean and variance of the inner product. We do not need a complete characterization of the product of two normal random variables. The first step is to normalize both signals using the characterized standard deviation of the noise. In these normalized signals, every single point has a standard deviation of 1. The variance of

the product of two independent normal distributions, each with a standard deviation of 1, is given in Equation 4 – as shown by Donahue (1964).

$$\sigma^2 = \mu_x^2 + \mu_y^2 + 1 \tag{4}$$

The variance of a sum is simply the sum of the variances. We have shown (Eq. 4) that the variance of a product of independent normal random variables, each with a standard deviation of 1, is also a sum. Therefore, simply using the associative property of addition, we can calculate the variance of the cross-correlation function using Equation 5. The variance is simply the sum of the square of each noise-normalized signal plus the length of the recorded signals.

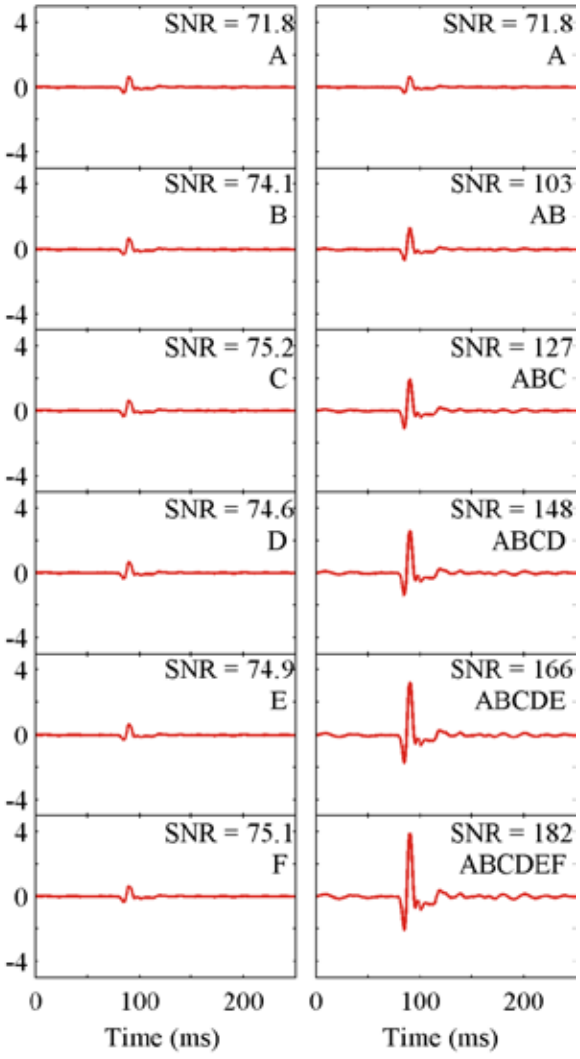

Figure 8. Effect of signal stacking individual traces from right-side seismic testing performed at a geophone depth of 19.6 m with the left side figures representing each trace and the right side figures representing the stacked trace; each plot is annotated with the calculated SNR showing the increase with signal stacking

$$\sigma^2 = \sum_{m=1}^{m=N} \left(\left(\frac{x(m)}{\sigma_x} \right)^2 + \left(\frac{y(m)}{\sigma_y} \right)^2 + 1 \right) \tag{5}$$

The mean of the cross-correlation function is solved using Equation 1 with the noise-normalized signals.

Evaluating the uncertainty in the cross-correlation function does not yet provide a probability distribution for the shear wave propagation time. Figure 9 shows the cross-correlation function of the first right-side hits of the signals shown in Figure 3. Figure 9 includes the range of the standard deviation calculated with Equation 5. The axis limits in Figure 9 were selected to show the detail in the cross-correlation peak. When uncertainty in the cross-correlation value is considered, it can be seen that the exact location of the peak of the cross-correlation function becomes uncertain.

We have been unable to determine a closed-form solution for the probability that each point in the cross-correlation function is larger than every other point. The two options are to perform numerical integration or a Monte-Carlo simulation. We selected a Monte Carlo simulation for the simplicity in execution. We generated 100,000 realizations of the cross-correlation function and calculated a histogram for the location of the maximum value. This histogram is converted into a probability density function, as shown in Figure 10, by dividing the histogram by the number of realizations.

A cumulative distribution function is an alternative representations of the results shown in Figure 11. It is an integration of the probability distribution function. It is a cumulative sum, or running sum, of the probability distribution function. The y-axis is the probability that the propagation time is less than the value on the x-axis. At 50% the propagation time may equally be higher or lower. This 50% value is an average, but not necessarily the arithmetic

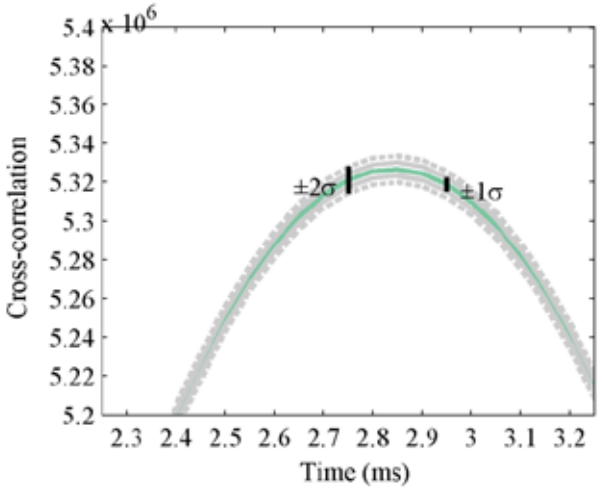

Figure 9. Maximum peak from cross-correlation (Eq. 1) of the first right side hit at 18.6 m and 19.6 m with a calculated (Eq. 5) cross correlation standard deviation of 3144

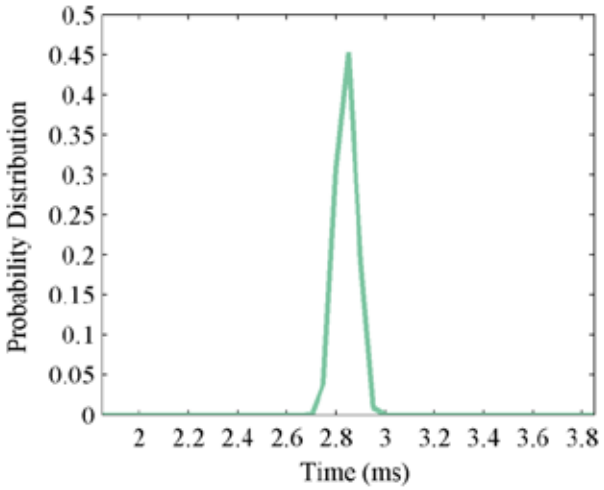

Figure 10. Probability distribution function for the location of the peak from 100,000 Monte Carlo simulations of the cross-correlation shown in Figure 9

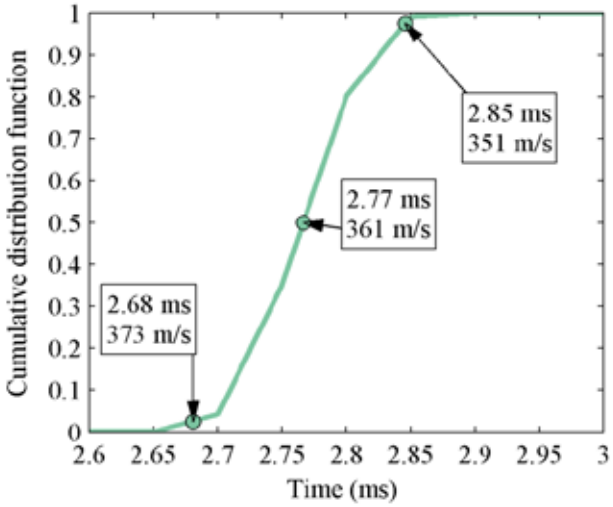

Figure 11. Cumulative distribution function for the cross-correlation results from the first right side-hits at 18.6 and 19.6 m depth showing an average V_S of 361 m/s with a 95% coverage range of 22 m/s

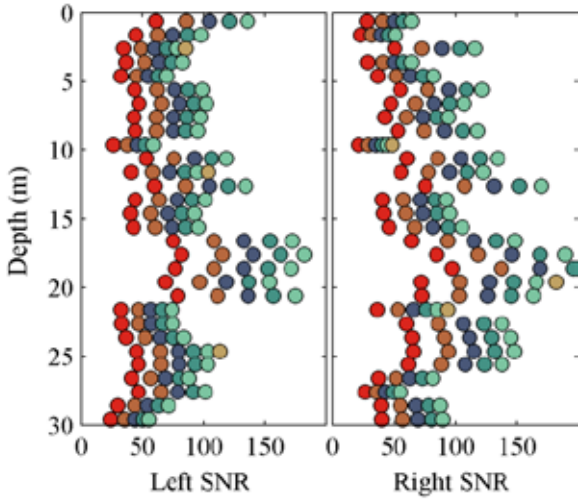

Figure 12. SNR calculated for the left side hits (circles) and stacked left side hits (squares) along with profile of 95% V_S bounds from stacked traces

at 2.5%, 50%, and 97.5%. These three numbers provide an average propagation time and the width of a 95% coverage window. The results in Figure 11 have an average velocity of 361 m/s with a 95% coverage window of 22 m/s.

This approach quantifies the uncertainty. It permits engineering applications to use the reported data appropriately and to perform sensitivity analyses. In this paper we evaluated how signal stacking can be used to reduce the uncertainty in the shear wave propagation time.

4 RESULTS

Figure 12 shows depth profiles for the SNR for both the left and right side results. Signal stacking always increased the SNR. The left-most point represents the SNR from just the first trace. As each subsequent trace was stacked the SNR increases. In this SCPTu, the SNR generally increased to 20 m depth, then decreases below 20 m. In this SCPTu, the changes in SNR did not appear to coincide with any particular features in the profile. We did not see a loss of signal strength immediately below interfaces with high tip resistance that could reflect a portion of the seismic signal.

Figure 13 includes three depth profiles. The first one shows both the left-side and right-side interpreted shear wave velocities using the completely stacked signals. Each depth interval is represented by a block that indicates the range of the 95% coverage window. The error in this profile was so low that these windows are difficult to discern on this scale. This profile also showed remarkable consistency between the left-side and right-side interpreted shear wave velocities. Unlike cross-over points, the use of cross-correlation allows both the left-side and right-side set of data to be interpreted independently. The reproducibility of the left-side and right-side confirms the interpreted results. The middle profile shows the interval propagation time. This is the 50% value from the CDF calculated for

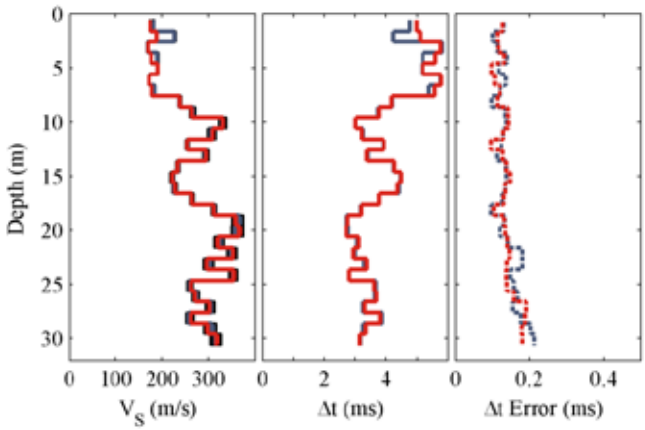

Figure 13. Shear wave velocity profiles for left and right side hits with propagation time and a profile of 95% Δt error

Figure 14 compares the width of the 95% coverage window to the calculated SNR. These results were calculated for each additional signal from signal stacking. Calculating the uncertainty of the shear wave interval propagation time requires comparing two signals, each with their own SNR. The results presented in Figure 14 show the minimum SNR. It was assumed that the smaller SNR would govern the error in the propagation time. This figure shows that increase the SNR decreases the error in the propagation time.

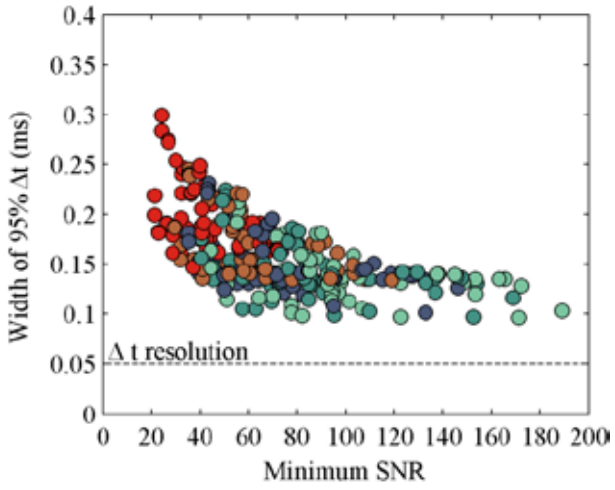

Figure 14. Comparing the width of the 95% coverage window for the shear wave propagation time versus the minimum SNR of the two compared signals showing improved VS characterization with higher SNR

5 DISCUSSION

Signal stacking raw seismic traces amplifies the systematic features in the signal. This is shown clearly in Figure 8. A stronger signal, with a higher signal to noise ratio, corresponds with a lower error in the estimated propagation time. This is shown in Figure 14. Therefore, signal stacking can be used to improve the estimate of the shear wave propagation time and shear wave velocity.

At depth the signal strength decreases. This is due to geometric attenuation and soil damping. A decrease in SNR with depth below 20 m was observed and is shown in Figure 12. This decrease can be countered by signal stacking. Figure 8 and Figure 12 both show that stacking signals increases the SNR.

The required number of signals to stack to achieve an acceptable error in V_S may exceed what can reasonably be accomplished while maintaining acceptable SCPTu production rates. Signal stacking has a positive impact on SNR, but it may not be enough to achieve V_S uncertainty objectives. An alternative to signal stacking is to increase the propagation interval. Increasing the propagation interval reduces the significance of the error in the propagation time.

In this paper we presented the effect of signal stacking at one SCPTu using a reproducible automatic seismic source. We have not examined or isolated equipment-specific or site-specific effects on these results. We expect that the observed SNR is equipment and site dependent. Consequently, the results shown in Figure 14 cannot yet be used to specify SNR targets for other field programs. Further work is needed to examine the effect of different sites and different equipment on the SNR and propagation time error.

6 CONCLUSIONS

From this work analyzing a single profile we have supported the following conclusions:

- SNR increases with signal stacking,
- The error in the propagation time decreases with higher SNR, and
- The decrease in SNR with depth can be countered by signal stacking.

These general conclusions are completely expected, however the specific observed trends may be site-dependent and equipment dependent. The equipment used at this site produced remarkably consistent shear wave signals which provided a small quantified noise and high SNR.

The main contributions contained within this paper are the techniques we used to demonstrate the effect of SNR and signal stacking on the uncertainty in the shear wave velocity. We presented interpretation methods that can be used to:

- Quantify signal noise through signal-subtraction,
- Quantify SNR in down-hole seismic signals, and
- Calculate the error in the shear wave propagation time using the cross-correlation function.

These techniques are applicable beyond the SCPTu presented within this paper. They can be applied to any SCPTu that recorded more than one trace per seismic test.

7 REFERENCES

Brandenberg, S.J., Kutter, B.L. & Wilson, D.W. 2008. Fast Stacking and Phase Corrections of Shear Wave Signals in a Noisy Environment. *Journal of Geotechnical and Geoenvironmental Engineering,* 134(8):1154–1165.

Campanella, R.G. & Stewart, W.P. 1992. Seismic cone analysis using digital signal processing for dynamic site characterization. *Canadian Geotechnical Journal*. 29:477-486.

Casey, T.J. & Mayne, P.W. 2002. Development of an electrically-driven automatic downhole seismic source. *Soil Dynamics and Earthquake Engineering*, 22:951-957.

Donahue, J.D. 1964. Products and quotients of random variables and their applications. *Aerospace research laboratories office of aerospace research*, ARL 64-115.

Gillespie, D.G. 1990. Evaluating shear wave velocity and pore pressure data from the seismic cone penetration test. Ph.D. Thessis, The University of British Columbia, Department of Civil Engineering, Vancouver, Canada.

Howie, J.A. & Amini, A. 2005. Numerical simulations of seismic cone signals. *Canadian Geotechnical Journal*, 42(2):574-586.

Hunter, J.A., Benjumea, B., Harris, J.B., Miller, R.D., Pullan, S.E., Burns, R.A., & Good, R.L. 2002. Surface and Downhole Shear Wave Seismic Methods for Thick Soil Site Investigations. *Soil Dynamics and Earthquake Engineering,* 22(9-12):931–941.

Lee, J.-S. & Santamarina,J.C. 2006. Discussion: Measuring Shear Wave Velocity Using Bender Elements. *ASTM Geotechnical Testing Journal*, 29(5):3–5.

Mayne, P.W. & McGillivray, A.V. 2008. Improved shear wave measurements using autoseis sources. In Deformational Characteristics of Geomaterials Volume 2, Ed. Burns, Mayne, & Santamarina.

Meunier, J., Huget, F., & Meynier, P. 2001. Reservoir Monitoring Using Permanent Sources and Vertical Receiver Antennae : The Céré-la-Ronde Case Study. *The Leading Edge*, 20(6):622-629.

Rice, A.H. 1984. The seismic cone penetrometer. MaSc Thesis, The University of British Columbia, Department of Civil Engineering, Vancouver, Canada.

Robertson, P.K., Campanella, R.G., Gillespie, D. & Rice, A. 1986. Seismic CPT to measure in situ shear wave velocity. *Journal of Geotechnical Engineering*, 112(8):791-803.

Styler, M.A., Woeller, D., & Howie, J.A. 2013. Measuring down-hole shear waves from a vibrating perpetual source during Cone Penetration Testing. *In Canadian Geotechnical Conference: GeoMontreal,* Montreal.

Styler, M.A., Howie, J.A., & Sharp, J.T. 2014. Perpetual source SCPTu: signal stacking shear waves during continuous penetration. *In CPT'14*, Las Vegas.

Geotechnical and Geophysical Site Characterisation 5 – Lehane, Acosta-Martínez & Kelly (Eds)
© 2016 Australian Geomechanics Society, Sydney, Australia, ISBN 978-0-9946261-2-7

3D mapping of organic layers by means of CPTU and statistical data analysis

J. Wierzbicki & A. Smaga
Institute of Geology, Adam Mickiewicz University, Poznań, Poland

K. Stefaniak
Institute of Construction and Geoengineering, Poznań University of Life Sciences, Poland

W. Wołyński
Faculty of Mathematics and Computer Science, Adam Mickiewicz University, Poznań, Poland

ABSTRACT: The article presents the possibilities of using selected methods of statistical data analysis to determine the spatial extent of soft soils layers. The test site is characterized by the occurrence of a complex geological structure which is a result of alternating deposition of organic sediments and alluvial sand. As data for the analysis, the CPTU results (calculated to parameters: q_t, Q_t, F_r, I_c) were used. In the analysis, various techniques of data grouping and interpolation were used, including 2D nad 3D IDW methods. Advantages and limitations of each statistical techniques are discussed, both with respect to the geological model of the substrate, and in terms of determining the representative values of geotechnical parameters.

1 INTRODUCTION

Designing the foundation of large-area engineering constructions in complex geological conditions makes it necessary to consider the subsoil structure as a three-dimensional task. The fact, that in geotechnical site characterization we have mostly only point, local and discontinuous data is well known. Simultaneously the construction design assumes a continuous model of the subsoil, in which strength and deformation characteristics are well defined in each point of the space.

The potential solution of this problem is to use the interpolation techniques which can help us to fill in sometimes over of 95% of unknown space, according to some mathematical rules. There are many of interpolation methods, from basic triangulation technique, through a purely analytical technique of square interpolation between testing points – ABOS, a technique based on statistical analysis of the effect of individual observations (Inverse Distance Weighting) to Kriging, in which values of a parameters are determined on the basis of the adopted statistical model of variation of the data. Most of them are developed in two-dimentional space. In this case data distribution is analysed in one plane only, horizontal (a map) or vertical (a cross-section).

A disadvantage of such models is the fact that only data lying on a specific plane is interpolated, and data from the close vicinity, but lying on other levels (for example of depth) are omitted. In the case of complex geology of the site it can lead to inadequate site characterization, for example resulting in miscalculations of settlements of different parts of the construction.

Another important problem is the locality of carried out investigations and the use of different techniques for this purpose. For example borings and CPTU's are carried out simultaneously, but very often in different locations, creating a grid of complementary researches.

The geotechnical models, e.g. a stiffness model, can be assessed using CPTU data, subjected to statistical analysis, quite well (Młynarek et al. 2013). In the case of simple and predictable geology it can be sufficient to use relatively rarely spaced testing points (e.g. testing every 50m). In the case of more complex geology, sometimes it could be necessary, to complete the data set, using some observations from additional and not so advanced investigations. In this case, the problem may occur with the use of analog data from e.g. a drilling log for the assessment of geotechnical models, using digital data, eg. from CPTU.

In this paper authors deal with above problems, and try to show an example of procedure of data interpretation for simultaneous use of a boring log and the CPTU data for a mapping the organic layer in the case of structure sensitive to unequal settlements. The proposed methodology, helps to avoid an important mistakes in the geotechnical site characterization, without any additional time and financial costs.

2 TESTING SITE

2.1 *Geographical and geological characterization*

Research has been carried out in an area in Września, 50 km from Poznań. Września is located on the Wrzesinska Plain in central-western Poland (Fig. 1). Wrzesińska Plain is built of glacial clay, and in the north-western part of the area is an out-wash plain built of layered sand and gravel. In the study area Holocene deposits in the form of silts, glaci-fluvial sands and organic soils also occures.

Deposition of organic soils was an uneven process. Organic deposits on the out-wash plain sedimentation were temporarily backfilled by sandy sediments. As a result of the interim backfill organic soil by sandy deposits, they can be assumed as a sligtly consolidated soil. In addition, analyzed organic soils occurs at different depths and they are characterized by high volatility and lack of regularity in the level, which shows lack of a one main sedimentary basin.

Figure 2 shows examples of drilling profiles. Organic deposits in the form of gyttia and peat are presented at different depths under the fine and medium sand or silty soils. Under the layer of organic soil most frequently a glacial clay is observed.

2.2 *Geotechnical testings*

The test site covered area of a large-area warehouse, designed on a large number of individual footings. Due to the Eurocodes Serviceability Limit State requirements the crucial in this case was to minimize differences between settlements of individual footings. This requires as much as possible precise localization of organic soils layers and as many data as possible for the design.

As part of the research tests the cone pentration tests CPTU and drilling research were carried out. CPTU tests were performed in accordance with the International Reference Test Procedure for Cone Penetration Testing TC-16 Committee ISSMGE (1999). Test points were determined in evenly in the grid after 15 points CPTU and 15 points drilling (Fig.3).

In addition, 3 drilling and 3 CPTU were made at the same points, which were adopted as reference points. Results of drilling were used to identify the occurrence of organic soil in the research profile. In turn, the CPTU were used to determine the mechanical parameters of the organic soils (Fig. 4)

Figure 1. Location of testing site on the country map.

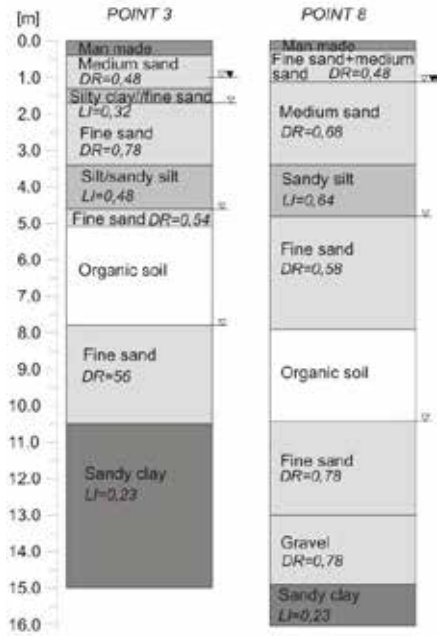

Figure 2. Example of geological profile from the test site (DR – relative density, LI – liquidity index).

.

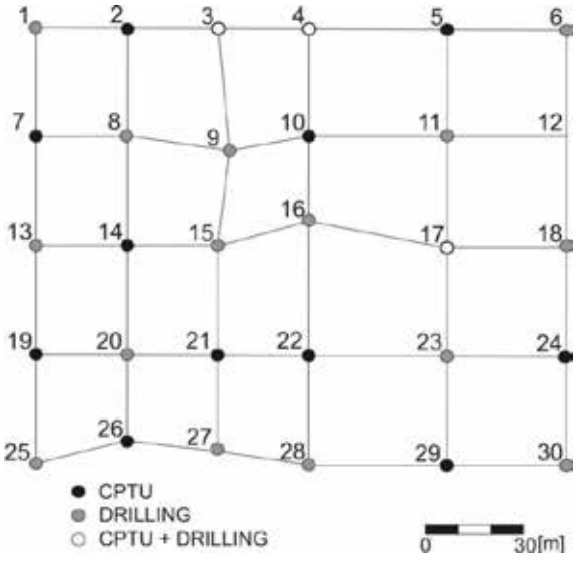

Figure 3. The grid research points.

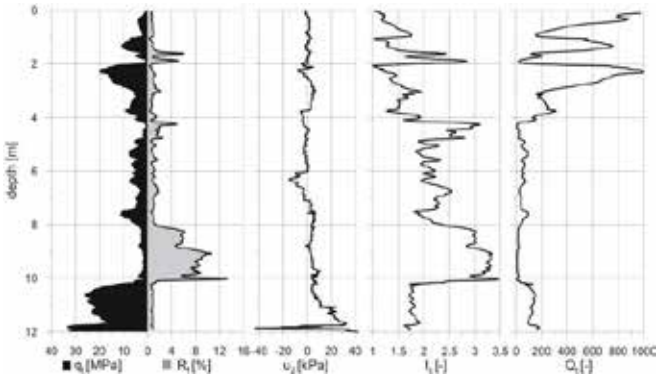

Figure 4. Typical CPTU results (Wrzesnia test site).

A description of organic soils in terms of strength is complicated, and in order to adopt an interpretation procedure for CPTU characteristics, the first step is to verify their position in the Soil Behaviour Type Chart (SBT) (Fig. 5) (Robertson 2009).

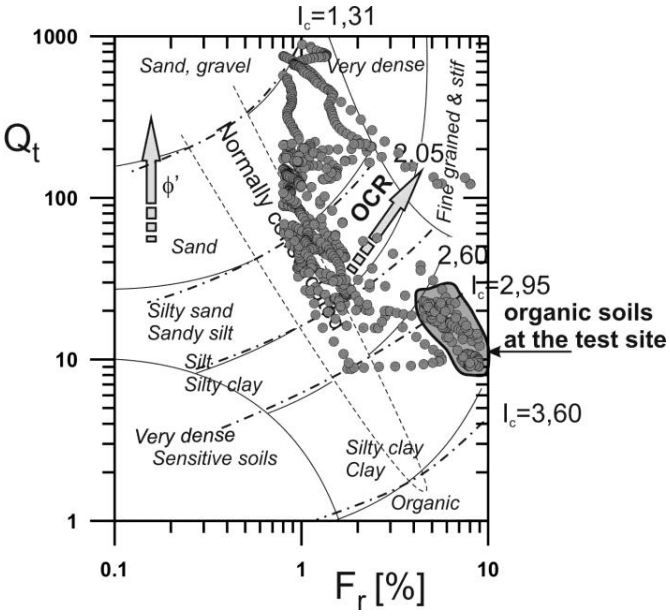

Figure 5. Location of the investigated soils on SBT classification chart.

3 METHODS

3.1 *General assumptions of subsoil model*

As it was stated above, the CPTU and drillings, consisted the almost rectangular grid of 30 testing points, but only half of them provided the complete information about the strength and deformation parameters along the profile. This mean, that in the assessment of e.g. stiffness geostatistical model, the only 50% of gathered information about the configuration of the organic layer, can be used. To omit this disadvantage, the following procedure was proposed. Firstly the CPTU data were calculated to the form of: net cone resistance (q_n), normalized cone resistance (Q_t), normalized friction ratio (F_r), pore pressure parameter (B_q) and soil classification index (I_c). For this purpose the data collected from boring logs were used as well. Secondly, all the CPTU data were mixed all together, and clustered using one of cluster analysis methods. Then the clustered CPTU profiles were compared to the reference profiles, and the average values of CPTU parameters in particular clusters were assigned to individual layers from the boring logs. This let to "digitalize" the lithological profiles and to include the analog information, into the digital set used for the assessment of a geotechnical model. The last step of proposed procedure was to carry out the interpolation of all gathered data. The advantage of this procedure is the possibility of carrying out the geotechnical analysis for the whole investigated space, using so called representative (averaged and statistically grouped) values of the CPTU parameters.

3.2 *Clustering methodology*

Values of the CPTU parameters were subjected to clustering analysis using k-means method which is widely describe and recommended by Młynarek et al. (2005). K-means method is non-hierarchical clustering, consisting in creating defined number of clusters, which differ from each other the greatest extent possible. Every cluster creates a distinct data set. Initial amount of clusters is selected randomly. Objects have been moved between clusters until the minimal intra-cluster variability and maximal inter-cluster variability be achieved (Everitt, 1974). Assigning an object to particular cluster is consisting in comparing the distance of the object from the center of gravity of the cluster.

However, k-means method leads to many possible solutions therefore the problem is the choice of the most appropriate. To dissolve the problem analysis of Calinski-Harabasz index (CH) is conducted. This analysis allows to obtain optimal from a statistical point of view number of clusters (Caliński & Harabasz, 1974). Additionally, optimal number of clusters can be obtained by diagram of weighted average of the coefficient of variation for particular number of clusters (ACV) (Wierzbicki, 2007). The analysis of diagram of weighted average of the coefficient of variation is more engineering tool, because minimalizing the intra-cluster variability simultaneously marginalizing minor clusters. The both methods, analysis of Calinski-Harabasz index and analysis of diagram of weighted average of the coefficient of variation, were used to interpretation of cone penetration tests.

3.3 *2-D and 3-D data interpolation*

The method chosen for interpolation procedure, was the modified Inverse Distance Weighting – IDW. The detailed background of its assumptions was given by Młynarek et al. (2007). In this method

the interpolated value of characteristic v_0 in a given point with coordinates (x_0,y_0,z_0) (z_0 is the determined depth) is established on the basis of values of neighbouring v_i, coming from observations in points (x_i,y_i,z_0). Each of these values affects the interpolated value of v_0 with the weight, which is inversely proportional to the distance between these points. The formula used in IDW takes the form:

$$v_0 = \frac{\sum_{i=1}^{|N(v_0)|} w_i v_i}{\sum_{i=1}^{|N(v_0)|} w_i}, \tag{1}$$

where $|N(v_0)|$ denotes the number of included observations from the neighbourhood of v_0, and weight w_i take the form:

$$w_i = \frac{1}{(d_i + s)^p}. \tag{2}$$

The value of d_i found in formula (2) denotes the distance between points (x_0,y_0,z_0) and (x_i,y_i,z_i) in the form:

$$d_i = \sqrt{(x_0 - x_i)^2 + (y_0 - y_i)^2}, \tag{3}$$

in the 2-dimensional case, and:

$$d_i = \sqrt{(x_0 - x_i)^2 + (y_0 - y_i)^2 + \varsigma(z_0 - z_i)^2}, \tag{4}$$

in the case of 3-dimensional interpolation,where $s>0$ and p serve the role of smoothing parameters. By neighborhood $N(v_0)$ we mean here a set of these observations (testing points) at depth z_0, which distance d_i from point (x_0,y_0,z_0) does not exceed a certain fixed threshold value which parameter ζ ($\zeta>0$) was introduced, determining the effect of observations in the direction of axis z, i.e. depth.

4 RESULTS

The cluster analysis carried out on the set of all CPTU data, provided a large number of potential solutions, form 2 to 20 clusters. The choice of the most appropriate one was made using the graphs of the relation of CH and AVC indexes to the number of obtained clusters. As can be seen in the Fig. 6, the CH index shows the statistically best solutions within the frame between 4 and 9 clusters. Simultaneously the value of weighted average of the coefficient of variation (AVC), has the local minimum at 8 clusters. In this case the division of the investigated subsoil into 8 groups was assumed as the most appropriate one.

The next step of analysis was to calculate the representative values of the CPTU parameters for each cluster, and correlate them to the given parts of boring profiles. For this aim the three reference points were used. As the representative values of CPTU parameters the average value was used (Fig. 7). It resulted in the "digitalization" of boring profiles, in which every distinguished layer had been correlated and replaced by representative values of the adequate cluster (Fig. 8).

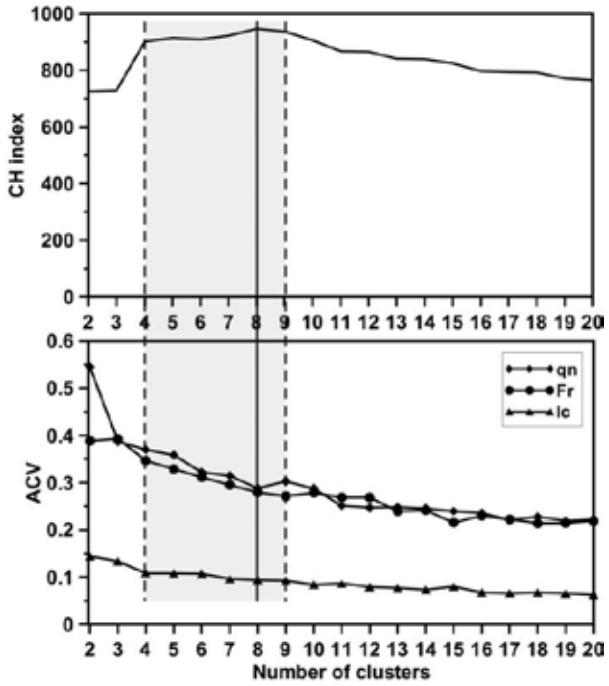

Figure 6. The Caliński-Harabasz CH index and AVC index values, calculated for different numbers of clusters.

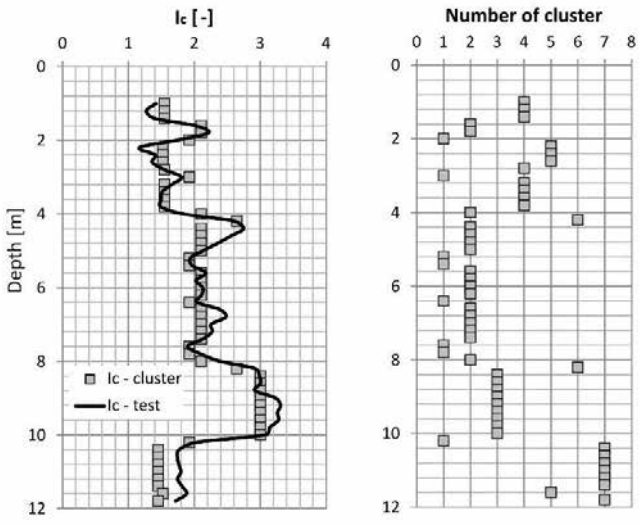

Figure 7. An example of the I_c profile from CPTU (test) and obtained after cluster analysis on the background of the profile division into the clusters.

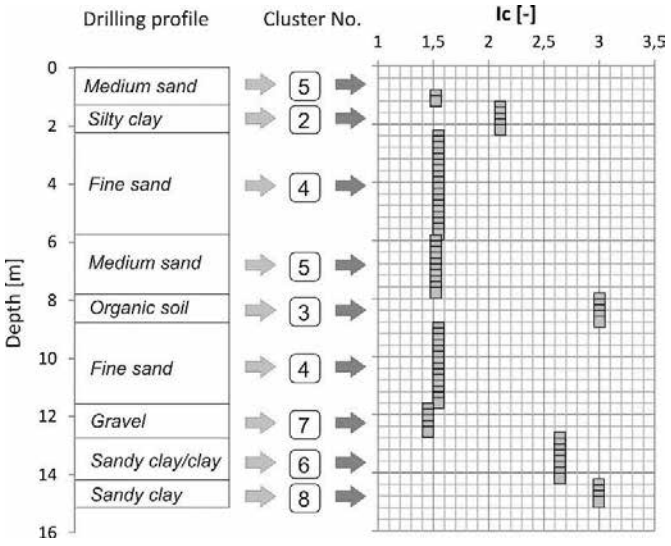

Figure 8. An example of the conversion of drilling profile into I_c profile on the basis of correlated clusters.

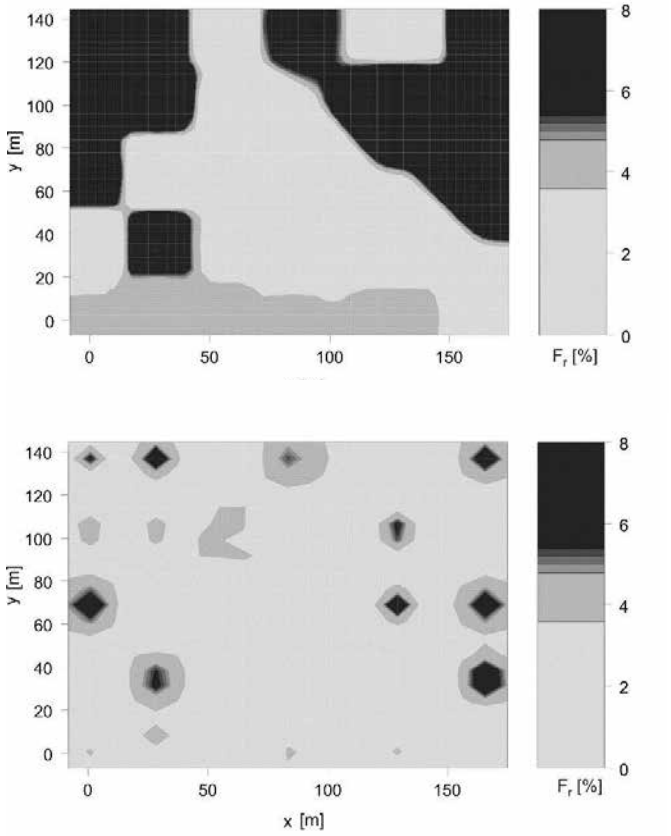

Figure 9. The 2-D interpolation model (above) and 3-D interpolation model (below) of Fr, showed at the depth of 8,4 m.

So prepared set of the data was subjected to the interpolation analysis. For the purpose of this part of analysis two CPTU parameters were chosen: F_r and I_c. This selection of the first of them resulted from the fact that, as it was observed during the cluster analysis, the value of F_r above 5,3 indicates an organic soil very well. At the same time the I_c values not allows to distinguish clearly boundary between organic soils and sandy clays, but can be very helpful for the analysis of the strength properties of subsoil.

Both the 3-D and 2-D analysis were carried out, resulting in the models of distribution of analyzed parameters in the investigated space and providing almost continuous data at the whole investigated area. As an example of obtained results the maps created at the depth of 8,4 m are presented and discussed.

Despite to the results obtained by Młynarek et al. (2007), present investigations show almost complete inadequacy of the 3-D model in comparison to 2-D model (Fig. 9). The organic layer, indicated by F_r values above 5,3 %, is almost not identified in the case of 3-D model, despite to 2-D model. The 2-D model clearly allows to determine the extent of organic soil at a given depth, using F_r parameter. Additionally, a level of risk of adopting the incorrect geotechnical model in the analyzed case, can be observed if we calculate the 2-D model, at the same depth, but using only CPTU data (Fig. 10). It is clearly seen that additional data from drillings provide an important knowledge about the extent of the organic layer. This fact results in the possibility of distinguish the potentially week zones within the subsoil, by means of analysis of I_c parameter (Fig. 11). In the analyzed case a value of I_c above 2,8 indicated not consolidated clays or organic soils, which may result in increased settlements of footings.

5 CONCLUSIONS

Proper site characterization is one of the most important stages of any investments. In the described example the crucial for the footings design of warehouse was to localize the organic layer, and to digitalize the information on the geotechnical properties for the purpose of structural model. For this purpose both CPTU measurements and drilling logs were used, providing data for statistical model of subsoil.

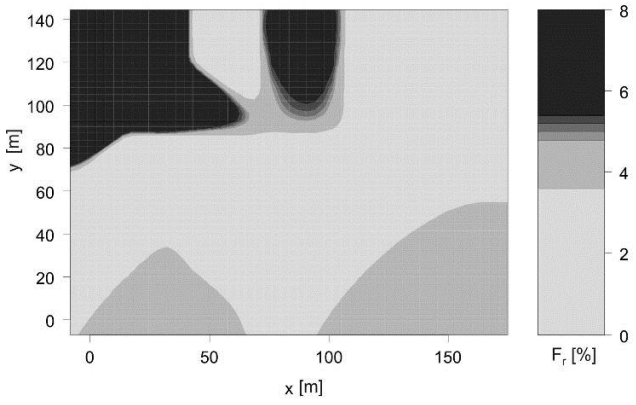

Figure 10. The 2-D interpolation model of F_r at the depth of 8,4 m, calculated for the CPTU data only.

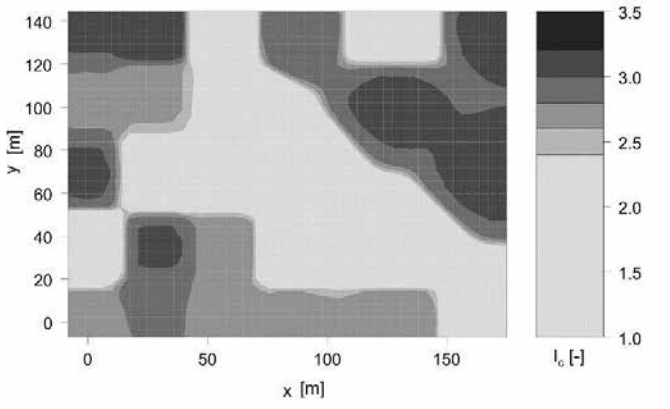

Figure 11. The 2-D interpolation model of I_c at the depth of 8,4 m.

It was clearly seen that only simultaneous use of all available data allowed the detailed identification of organic soil layer. This in turn was possible by subjecting the CPTU data to cluster analysis and then to use all data for computation of interpolation IDW model.

Despite to the arrangement done by Młynarek et al. (2007), the full 3-D IDW model has not yielded a satisfactory results. This is probably due to highly horizontal extent of the mapped organic layer and also a high contrast in values of analyzed parameters between organic soil and the rest of subsoil.

Finally, on the basis of computed IDW model of CPTU parameters it is possible to calculate geotechnical parameters, as constrained modulus or shear strength parameters, in any point of investigated space.

6 REFERENCES

Caliński, T. & Harabasz, J. 1974. A dendrite method for cluster analysis. *Communication in Statistics*, 3: 1-27.

Everitt, B. 1974. Cluster Analysis. Halsted-Wiley. N.Y.

Młynarek, Z., Wierzbicki, J. & Wołyński, W. 2005. Use of cluster method for in situ tests. *Stud. Geotech. Mech*, 27, 3/4: 16-27.

Młynarek, Z., Wierzbicki, J. & Wołyński, W. 2007. An approach to 3D subsoil model based on CPTU results. V. Cuellar et. al (eds.) *Geotechnical Engineering in Urban Enviornment,*. Vol. 3, 1721-1726. Millpress, Rotterdam.

Młynarek, Z., Wierzbicki, J. & Stefaniak, K. 2013. Deformation characteristics of overconsolidated subsoil from CPTU and SDMT tests. R. Q. Coutinho& P.W. Mayne (eds.) *Geotechnical and Geophysical Site Characterization 4,. Proc. of 4th International Conference on Geotechnical and Geophisical Site Investigations:* 1189-1193.Taylor & Francis Group, London.

Robertson, P. K. 2009. Interpretation of Cone Penetration Testing – a unified approach, Canadian Geotechnical Journal, 46 (11), 1337–1355.

TC-16 (1999) ISSMGE International Reference Test Procedure for Cone Penetration Test (CPT) and Cone Penetration Test with Pore Pressure (CPTU).

Wierzbicki, J. 2007. Determination of homogenous geotechnical layers in strongly laminated soil by means of CPTU and cluster analysis. V. Cuellar et. al (ed.) *Geotechnical Engineering in Urban Enviornment,*. Vol. 5, 575-579. Millpress, Rotterdam.

Geotechnical and Geophysical Site Characterisation 5 – Lehane, Acosta-Martínez & Kelly (Eds)

Assessment of ground improvement on silt based on spatial variability analysis of CPTU data

H.F. Zou, G. J. Cai, S.Y. Liu & J. Lin
Jiangsu Key Laboratory of Urban Underground Engineering and Environmental Safety, Southeast University, Nanjing, Jiangsu, China

T.V. Bheemasetti & A.J. Puppala
The University of Texas at Arlington, Arlington, Texas, USA

ABSTRACT: A novel resonance deep compaction technique was used to improve the strength and density of loose saturated silts in northern Jiangsu Province, China. In this research, the random field theory is applied in modeling the characteristics of the cone tip resistance (q_t) obtained from the piezocone penetration tests to evaluate the performance of the compaction improvement. The three random field model parameters including the mean value, vertical scale of fluctuation and coefficient of variation of the q_t data before and after the compaction are analyzed. It is shown that the mean values and scales of fluctuation of q_t decrease immediately after the compaction but then they increase as the density of the silt recovers. The coefficient of variation consistently decreases with respect to the recovery age. These observations demonstrate the successful application of the resonance compaction in improving the stiffness and homogeneity of the silt.

1 INTRODUCTION

Ground improvement techniques have been widely used to increase the density, strength and stiffness of saturated loose sands and silts (Massarsch & Fellenius 2002, 2005). Assessing the performance of ground improvement is a major task and can be achieved using either in situ or laboratory tests. In routine projects, assessment of improvement effect based on laboratory tests suffers the disadvantages of high cost, long testing period and difficulty in obtaining the representative undisturbed cohesionless soil samples. Therefore, in situ tests have been widely applied.

The modern advanced piezocone penetration test (CPTU) has been accepted as one of the most useful tools for assessing the quality of ground improvement (Lunne et al. 1997; Ku & Juang 2011). The CPTU provides three separate readings, total cone tip resistance (q_t) simultaneously with sleeve frictional resistance (f_s) and pore water pressure (u), and offers near continuous and economical information about the in situ subsurface stratification (Cai et al. 2011, 2012). The q_t and f_s indices represent the failure strength and density of cohesionless soils, while the u measurements describe the flow characteristics. However, most traditional application of CPTU for the quality control either only took the mean soil properties into consideration or compared the soil property records in a qualitative sense (e.g. Lunne et al. 1997; Ku & Juang 2011). The impact of ground improvement on the spatial variability of soil is not considered in above studies.

This paper performs spatial variability analysis on the CPTU data obtained from a silt site located in the floodplain of abandoned Yellow River in Jiangsu province, China. The silts were enhanced using a new deep resonance compaction technique to increase the liquefaction resistance of the silt. In this study, the random field theory (RFT) is applied to model the spatial variability of the CPTU cone tip resistance of the silts and to assess the performance of compaction. To achieve this study, the theory of random field is briefly summarized first. Then the site information, resonance vibratory compaction technique, and also the piezocone penetration tests are introduced. The variations of the RFT model parameters of the q_t data are analyzed to illustrate the performance of the compaction.

2 RANDOM FIELD MODEL

The spatial variability of a soil property can be modeled as a zero-mean weakly stationary random field (Uzielli et al. 2005). Despite of measurement error associated with the CPTU data, the measured q_t profile is expressed as the linear combination of a trend and fluctuation component about the trend:

$$g(z) = t(z) + x(z) \tag{1}$$

in which $g(z)$ = measured q_t at location z; $t(z)$ = trend function at z; $x(z)$ = fluctuation component or residual at z; and z = depth coordinate in this research.

The trend is generally determined using the ordinary regression analysis. Extensive researches on the selection of trend function revealed that the trend functions should be simple but still doing justice to the data (e.g. Baecher & Christian 2003; Uzielli et al. 2005; Stuedlein et al. 2012). In this research it is found that a linear trend function is sufficient to describe the deterministic component within the q_t data and hence is adopted.

The fluctuation component, $x(z)$, represents the spatial variability of a soil property. Two parameters including the scale of fluctuation (δ) and coefficient of variation (COV) are used to describe the fluctuation component. The δ provides an indication of the distance within which the property values show relatively strong correlation, whereas the COV provides the magnitude of variation (Phoon & Ching 2012). The COV is defined as:

$$COV = \frac{\sigma}{t_M} = \frac{\sqrt{\frac{1}{n-1}\sum_{i=1}^{n}[x(z_i)]^2}}{t_M} \tag{2}$$

where σ = standard deviation; t_m = mean of q_t; n = number of data points; z_i = depth coordinate of ith sampling point.

Several methods have been developed to estimate δ (e.g., DeGroot & Baecher 1993; Jaksa et al. 2000; Phoon et al. 2003; Vanmarcke 2010). The method of moments is simple and accurate to achieve this estimation. In this method, the sample autocorrelation function (ACF) representing the strength of the autocorrelation with respect to the lag distance between two observations are calculated. Then a theoretical autocorrelation model (ACM) is fitted to the ACF to provide a continuous description of the spatial autocorrelation. The δ is estimated from the model parameter of ACM. The ACF is estimated using the following approximation (Phoon et al. 2003):

$$R(\tau = j\Delta z) \approx \frac{1}{s^2(n-j-1)}\sum_{i=1}^{n-j}[x(z_i)x(z_{i+j})] \tag{3}$$

where Δz = sampling interval and Δz = 0.05 m in this research; n = number of data points; s^2 = sample variance [evaluated from Equation (3) using j = 0 with $R(0)$ = 1].

Equation (3) is only accurate up to 1/4 length of the record. To further improve the accuracy of the curve fitting, it has been suggested that only the data points with autocorrelation coefficients larger than the Bartlett's limit (r_B) should be used (Uzielli et al. 2005). The Bartlett's limit is given by $r_B = 1.96/\sqrt{n}$.

Several ACMs have been presented in geotechnical literatures (Uzielli et al. 2005; Stuedlein et al. 2012). Four theoretical autocorrelation models (ACM) along with the estimates of scale of fluctuation have been widely used in geotechnical literatures, as shown in Table 1. These autocorrelation models include the single exponential (SNX), cosine exponential (CSX), second-order Markov (SMK), and squared exponential (SQX). These four ACMs are sufficient for the curve fitting in the estimation of δ. The ACM providing best fit to the ACF should be used to represent the actual autocorrelation structure of soil property. The best fit can be determined as providing the largest coefficient of determination (R^2) in the curve fitting.

Table 1. Common ACMs and corresponding scale of fluctuation (Phoon et al. 2003)

ACM	Mathematic expression	Scale of fluctuation (δ)
SNX	$R(\tau) = \exp(-\lambda\|\tau\|)$	$\delta = 2/\lambda$
CSX	$R(h) = \exp(-b\|h\|)\cos(bh)$	$\delta = 1/b$
SMK	$R(h) = (1+d\|h\|)\exp(-d\|h\|)$	$\delta = 4/d$
SQX	$R(h) = \exp[-(ah)^2]$	$\delta = \sqrt{\pi}/a$

An important assumption of the random field theory is that the fluctuation component is weakly stationary. The weak stationarity assumes that the mean and variance are constant along space, and that the autocorrelation structure only depends on the lag distance between the observations. The weak stationarity can be checked using the modified Bartlett's statistics test proposed by Phoon et al. (2003). However, this test is generally too strict for soil data in practice (e.g. Stuedlein et al. 2012). The geotechnical evidence of the weak stationarity of soil data is the homogeneity of a soil unit. If the fluctuation component of q_t data is collected from a homogeneous soil unit, then it can be considered as a weak stationary random field in a qualified sense. Therefore, in this study the weak stationarity is not tested rigorously because only the q_t data corresponding to the middle silt will be studied, whereas the non-stationarity induced by the scattered soil seam will be neglected. Before applying the random field theory, the site conditions and testing program will be presented in the subsequently section.

3 SITE CONDITIONS AND TESTINGS

In this section, the main physical properties of the subsoil determined from laboratory tests are introduced first. To increase the density and liquefaction resistance of the subsoil, a novel vibratory compacting technique is applied. Four sets of piezocone penetration tests are performed in the testing site both

before and after the improvement. Using these tests, the performance of the ground improvement technique on the site is then analyzed and discussed.

3.1 *Geological conditions*

The testing site is located at the Suqian-Xinyi highway in Suqian, northern Jiangsu Province, China. The sediments at this site mainly consist of silt and silty sand. A test section with 95 m in length and 20 m in width at the highway site was chosen to investigate the performance of a new resonance compaction technique. Locations of the highway and test section are shown in Figure 1.

(a) China map with Jiangsu province

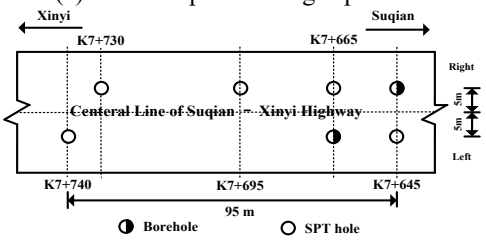

(b) Testing section

Figure 1. Location and layout of testing site

Quaternary sediments form the soil stratigraphy in the upper 20 m depth beneath the embankment surface. The uppermost soil unit is a sandy silt unit with scattered silty clay seams. The followed soil layer is a loose silt (upper silt) unit with silty sand and silty clay seams. A loose silt unit (middle silt) with thin silty sand seams is located just beneath the upper silt unit. The lower soil unit is a median to dense silt with scattered silty sands interlayer. Main physical characteristics of the subsoil including the specific gravity (G_s), clay content (CC), moisture (w), liquid limit (LL), and plasticity index (PI) are presented in Table 2, according to results of laboratory tests on collected disturbed soil samples. The ground water table location is about 3.8 to 5.5 m below the ground surface. The middle silt is the major concern of the improvement and is considered in this study.

Table 2. Main physico characteristics of soils

Stratum	Depth (m)	G_s	CC (%)	w (%)	LL	PI
Sandy silt	0 – 2.0	2.74	8.62	11.4	26.2	8.8
Upper silt	2.0 – 6.5	2.70	6.34	25.8	28.9	7.0
Middle silt	6.5 – 16.0	2.69	7.59	29.5	28.4	5.8
Lower silt	16.0 – 26.4	2.68	8.57	27.6	27.5	4.5

3.2 *Resonance compaction*

A new resonance compaction technique is developed for increasing the density and strength of the cohesionless soils by Southeast University, China. Figures 2(a) and 2(b) show a schematic of the resonance compaction equipment along with the details of the compaction probe. The resonance compaction points are set in a triangular manner as shown in Figure 2(c). The spacing interval for two adjacent compaction points is 1.5 to 2.0 m.

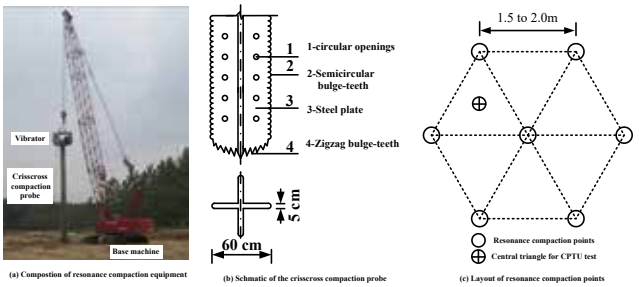

(a) Compostion of resonance compaction equipment (b) Schmatic of the crisscross compaction probe (c) Layout of resonance compaction points

Figure 2. Schematic and specification of the resonance compaction

The compaction equipment consists of a vibrator with a powerpack, a compaction probe and a base machine. The compaction probe is inserted into the ground under the control of vibrator. The compaction probe transmits the energy provided by the vibrator to the sounding soils. The most effective energy transfer occurs when the compaction probe is allowed to operate at the resonance frequency, which is determined according to pre-compacting tests. The resonance compaction probe in this research is a crisscross section vibratory probe of 15 m in length and 0.6 m in width. To reduce probe impedance and increase the drainage of excess pore water pressure induced by the compaction, circular openings of 0.1 m in diameter are spaced at 0.8 m along the probe. To evaluate the performance of the compaction, several CPTU tests have been performed in this testing section and will be introduced subsequently.

3.3 *Piezocone penetration test*

The CPTU system consists of a hydraulic pushing and leveling system, 1-m length segmental rods, cone penetrometers and a data acquisition system. The 10 cm^2 piezocone has a sleeve area of 150 cm^2 with a pore pressure transducer located 5 mm behind the base (u_2 configuration). All CPTU tests were conducted at a penetration rate of 2 cm/sec, and measurements were collected every 5 cm.

Piezocone penetration tests were performed at the testing section for four times, one set before the compaction and the other three sets after the compaction. The first set of CPTU tests was performed on the soil before compaction and consisted of 17 soundings to provide the referential background of site information. Later the resonance compaction

was conducted at the testing section. The second set of CPTU tests was performed on the soils after 14 days of recovery and consisted of 9 soundings. The third set of CPTU tests was performed after 54 days of recovery and consisted of 7 soundings at the center of the triangle of three adjacent compaction points (as shown in Fig. 2(c)). The fourth set of CPTU tests were performed after 60 days of recovery and consisted of 10 soundings. The layouts of these CPTU soundings are shown in Figure 3. All the CPTU soundings were performed either along or adjacent to the central line of the highway. Representative CPTU profiles are illustrated in Figure 4.

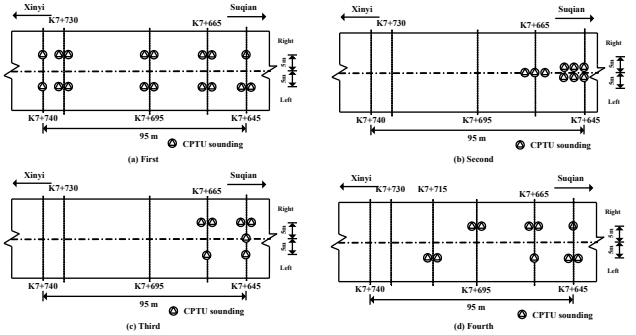

Figure 3. Layout of four sets of CPTU soundings of: (a) First; (b) Second; (c) Third; (d) Fourth dataset

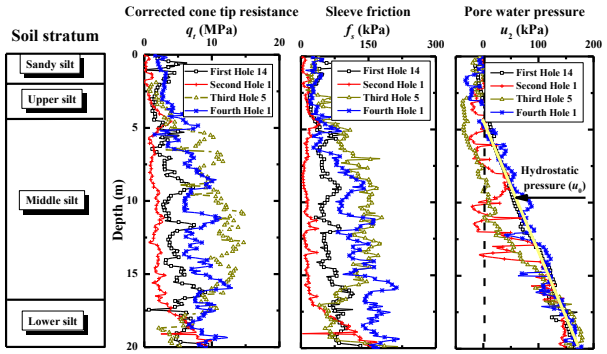

Figure 4. Typical CPTU profiles at the Suqian site for the four CPTU data sets

4 VERTICAL RANDOM FIELD MODEL PARAMETERS

Literature revealed that the spatial variability of a soil property is generally anisotropic, mainly reflected in the much higher spatial autocorrelation in the horizontal direction compared to that in the vertical direction. Due to the limitation of the sample volume in the horizontal direction, this research mainly focuses on the vertical spatial variability. The random field model parameters including mean value, COV and the vertical scale of fluctuation (δ_v) of the q_t data before and after the compaction will be analyzed. Based on the results, the performance of the resonance compaction technique in improving the density of the silt is discussed.

4.1 *Interpretation of vertical scale of fluctuation*

The estimate of vertical scale of fluctuation is impacted by the trend removal procedure which is applied to generate the stationary random field. In this section, two types of analyses are conducted to describe the variation of the spatial autocorrelation of q_t with respect to the ground improvement. In the first type of analysis (denoted as generic analysis hereafter), a generic two-dimensional trend is removed from all the q_t data of each dataset using the ordinary linear regression analysis. In the second type of analysis (denoted as specific analysis), a specific one-dimensional linear trend is removed from each q_t profile of each dataset. Then the fluctuation component of each q_t profile is determined by measured profile subtract the corresponding trend.

Figure 5 presents the estimated sample ACFs of all fluctuation components of q_t records for each dataset in the generic analysis. To obtain a generic estimate of the vertical scale of fluctuation, the ACFs of each corresponding dataset at each lag distance are averaged. The averaged ACFs are then used for estimating the generic δ_v. Using the inserting Bartlett's limit method (BLM) proposed by Jaksa et al. (2000), the horizontal Bartlett's line of $r_B = 1.96/\sqrt{n}$ is superimposed on the ACF plots. Then the lag distance corresponding to the intersection between the Bartlett's line and the sample ACFs approaches the estimate of the vertical scale of fluctuation. The ACFs, averaged ACFs, fitted ACM and statistics including the measurement interval, Bartlett's limit, number of ACF data points, estimates of generic δ_v and the coefficient of determination (R^2) are all presented in Figure 5.

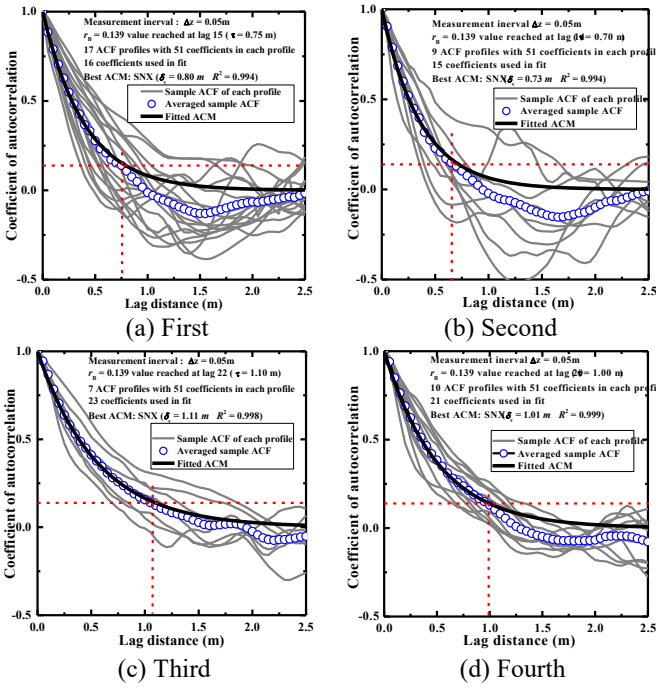

Figure 5. Estimates of vertical scale of fluctuation using generic analysis for: (a) First; (b) Second; (c) Third; (d) Fourth dataset

It can be seen from Figure 5 that before compaction, the generic δ_v of q_t data of the middle silt is 0.80 m. After 14, 54, and 60 days of recovery, the generic δ_v values of q_t data are 0.73, 1.11, and 1.01 m, respectively. A slight decrease of the generic δ_v is observed immediately after the compaction, whereas it increases later. This observation indicates that the resonance compaction should make influence on the autocorrelation structure of the soil data. Hence, the variation of the spatial variability of the q_t data could reflect the impact of the compaction. This conclusion will be further demonstrated using the specific analysis.

Figure 6 presents four representative examples of curve fitting of ACMs to ACFs. To evaluate the performance of fitted ACMs to the ACFs, the coefficients of determination (R^2) are also calculated and presented in Figure 6. Basic statistics including the insertion of Bartlett's limit, numbers of the autocorrelation coefficients in both ACFs and curve fitting for ACMs are also shown in Figure 6.

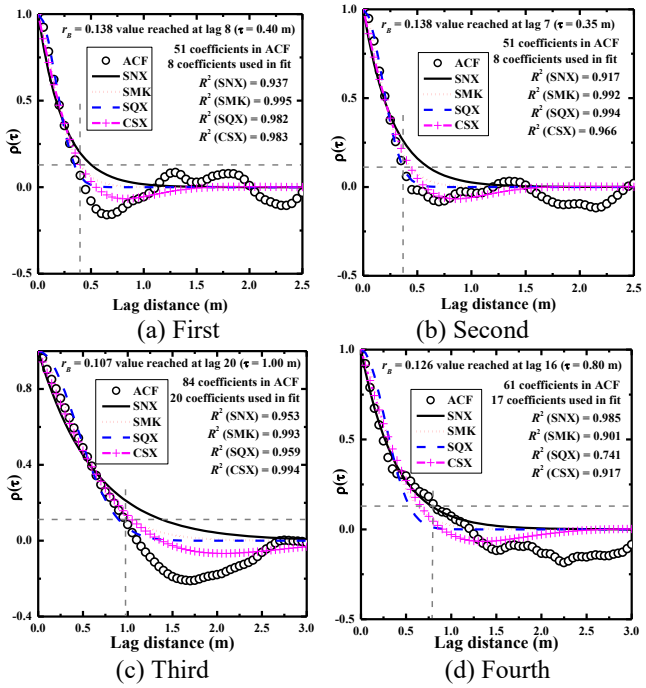

Figure 6. Representative example of best-fit case in: (a) First; (b) Second; (c) Third; (d) Fourth dataset

Figure 7 presents the estimated vertical scales of fluctuation (δ_v) and mean values of q_t records of the middle silt in the four datasets in the specific analysis. Variations of the mean q_t values are quite significant. Before compaction (first dataset), the mean q_t of the middle silt varies from 2 to 7.6 MPa. After 14 days of recovery (second dataset), the mean q_t decreases to the range of 1.5 to 4.8 MPa. However, after 54 and 60 days of recovery, it increases to the range of 7.7 to 12.4 MPa. This observation illustrates that a preliminary reduction of the density of the middle silt occurred immediately after the compaction, whereas the density will increase remarkably during the recovery. Besides, it can be also observed that the mean q_t of the third dataset is slightly higher than that of the fourth dataset, although the recovery age of the former is shorter. This feature shows that the performance of the compaction is more effective at the center of the triangle of three adjacent compaction points, compared to that at the compaction points

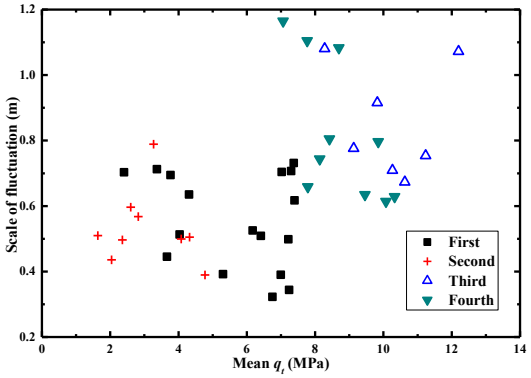

Figure 7. Vertical scales of fluctuation against mean values of q_t record using specific analysis.

The behavior of specific δ_v is similar to that of mean q_t. On the whole, all the specific δ_v values vary from 0.3 to 1.2 m and are consistently in the same magnitude for all the four datasets. Hover, variations of the specific δ_v values of different datasets can be also observed. The specific δ_v values of q_t data before compaction vary widely from 0.3 to 0.8 m with the mean value of 0.55 m. After 14 days of recovery, the specific δ_v values seem to remain the same as those of silt before compaction. However, as the density further grows, the specific δ_v values tend to increase slightly to the range of 0.6 to 1.2 m after 54 and 60 days of recovery. A preliminary decrease and the subsequent increase are observed on the specific δ_v of the q_t data.

The variation of either generic or specific δ_v values could be potentially explained by the mechanism of the penetration test and resonance compaction. The q_t measurements are viewed as the mechanical response of CPTU probe to the surrounding soils. The size of influence zone induced by the penetration of the cone probe increases with the stiffness and strength of the surrounding soils, whereas the vertical scale of fluctuation representing the autocorrelation strength of the soil data should be correlated to the size of the influence zone. During the resonance compaction, the insertion and vibration of the compaction probe destroyed the geotechnical formation of the undisturbed silt. Hence, a preliminary reduction of the strength and stiffness of the subsoil and furthermore the size of the CPTU influence zone can be expected. However, with the recovery of the soil strength, the size of the CPTU influence zone will increase gradually. Therefore, both the mean value and δ_v of the q_t data should decrease immediately after compaction, but these two parameters will gradually increase with the recovery age.

4.2 *Interpretation of coefficients of variation*

The COV quantifies the magnitude of variability of a soil property. Using Equation (2), the COV of q_t can be determined for each record. Figure 8 presents the COVs of q_t for the four datasets using specific analysis. It can be seen clearly that the COVs of q_t decrease with the mean values. Before compaction the COVs of q_t vary from 25 to 45%. This range of COV still remains after 14 days of recovery. However, after 54 and 60 days of recovery, the COV values reduced to 15 to 30%. It is concluded that the resonance compaction technique effectively reduces the uncertainties of q_t of the middle silt.

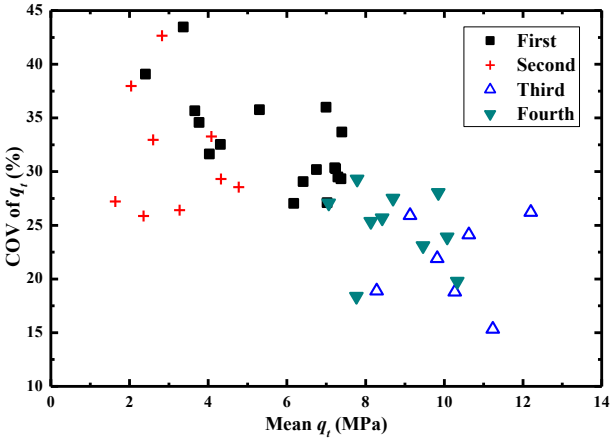

Figure 8. Vertical coefficient of variation against mean values of q_t record using specific analysis.

5 CONCLUSIONS

A novel resonance compaction technique was applied for improving the liquefaction resistance of silts located at the Suqian, China. To evaluate the performance of the compaction, piezocone penetration tests (CPTU) were performed both before and after the improvement. The random field theory was utilized to describe the variation of the spatial variability of q_t data due to the compaction. Three random field model parameters, including mean value, vertical scale of fluctuation (δ_v) and coefficient of variation (COV) of q_t, were analyzed and compared. Results showed that both the mean value and the δ_v decreased immediately after the compaction, but these two parameters gradually increased with the strength and density recovery, whereas the COV consistently decreased after the compaction. This observation could be potentially related to the mechanism of the cone penetration and the resonance compaction. The spatial variability analysis on q_t of the silt demonstrated the effectiveness of the resonance compaction technique in improving the mean strength and density of the silt and simultaneously reducing its uncertainties.

6 ACKNOWLEDGMENTS

Majority of the work presented in this paper was funded by the Foundation for the New Century Excellent Talents of China (NCET-13-0118), the Foundation of Jiangsu Province Outstanding Youth (Grant No. BK20140027), the Foundation for the Author of National Excellent Doctoral Dissertation of PR China (Grant No. 201353), and the High Level Talent Project of Peak of Six Talents in Jiangsu Province (Grant No. 2015-ZBZZ-001). These financial supports are gratefully acknowledged.

7 REFERENCES

Baecher, G. B. & Christian, J. T. 2003. *Reliability and statistics in geotechnical engineering*. John Wiley and Sons, New York.

Cai, G.Y., Liu, S.Y., Puppala, A.J. & Tong, L.Y. 2011. Assessment of the coefficient of lateral earth pressure at rest (Ko) from in situ seismic tests. *Geotechnical Testing Journal*, Vol. 34, No. 4, pp. 310-320.

Cai, G.J., Liu, S.Y. & Puppala, A.J. 2012. Liquefaction assessments using seismic piezocone penetration (SCPTU) test investigations in Tangshan region in China. *Soil Dynamics and Earthquake Engineering*, Vol. 41, pp. 141-150.

DeGroot, D.J. & Baecher, G.B. 1993. Estimating autocovariance of in-situ soil properties. *Journal of Geotechnical Engineering*, ASCE, Vol. 119, No. 1, pp. 147-166.

Jaksa, M.B., Kaggwa, W.S. & Brooker, P.I. 2000. Experimental evaluation of the scale of fluctuation of a stiff clay. *Proceedings of the 8th International Conference on Applications of Statistics and Probability in Soil and Structural Engineering*, Balkema, Rotterdam, pp. 415-422.

Ku, C.S. & Juang, C.H. 2011. Variation of CPTU parameters and liquefaction potential at a reclaimed land induced by dynamic compaction. *Journal of GeoEngineering*, Vol. 6, No. 2, pp. 89-98.

Lunne, T., Robertson, P.K. & Powell, J.J.M. 1997. *Cone penetration testing in geotechnical practice*. Blackie Academic and Professional, London.

Massarsch, K.R. & Fellenius, B.H. 2002. Vibratory compaction of coarse-grained soils. *Canadian Geotechnical Journal*, Vol. 39. No. 3, pp. 695-709.

Massarsch, K.R. & Fellenius, B.H. 2005. Deep vibratory compaction of granular soils. *Chapter 19 in Ground Improvement-Case Histories*, Elsevier publishers, B. Indranatna and C. Jian, Editors, pp. 633 - 658.

Phoon, K.K. & Ching, J. 2012. Beyond coefficient of variation for statistical characterization of geotechnical parameters. *Keynote lecture of Geotechnical and Geophysical Site Characterization 4*, ISC 4, 113-130.

Phoon, K.K., Quek, S.T. & An, P. 2003. Identification of statistically homogeneous soil layers using modified Bartlett statistics. *Journal of Geotechnical and Geoenvironmental Engineering*, Vol. 129, No. 7, pp. 649–659.

Stuedlein, A.W., Kramer, S.L., Arduino, P. & Holtz, R.D. 2012. Geotechnical characterization and random field modeling of desiccated clay. *Journal of Geotechnical and Geoenvironmental Engineering*, Vol. 138, No. 11, pp. 1301-1313.

Uzielli, M., Vannucchi, G. & Phoon, K.K. 2005. Random field characterization of stress-normalized cone penetration testing parameters. *Géotechnique*, Vol. 55, No. 1, pp. 3–20.

Vanmarcke, E.H. 2010. *Random fields: Analysis and synthesis.* World Scientific, Singapore.

Theme 15. Environmental Testing

Geotechnical and Geophysical Site Characterisation 5 – Lehane, Acosta-Martínez & Kelly (Eds)

Observed influence of ambient temperature variations on the analysis of ground thermal response tests

S. Colls
Golder Associates Pty Ltd, Melbourne, Australia

ABSTRACT: The thermal response test (TRT) is used for in-situ assessment of the thermal characteristics of the ground (principally thermal conductivity and temperature). These characteristics are required for the design of the ground heat exchanger (GHE) of a closed-loop ground-source heat pump system. Previous studies of the influence of ambient temperature on TRT results typically focus on how temperature variations affect experimental accuracy (e.g. due to poorly insulated surface pipes connecting the GHE to test equipment). The focus of this paper is on how ambient temperature fluctuations affect the net energy applied to the ground during the TRT, which can affect the interpretation of the test, particularly for relatively shallow depth energy piles. The results of a seventeen day long TRT performed on an energy pile installed in Melbourne, Victoria, together with the results of ground temperature measurements over a two-year period at the same site, are presented and discussed. Analysis of the test results suggests that ambient temperature variations could result in the calculation of thermal conductivity at different periods during the test varying by up to 20%. The implications of the observed behaviour for the performance of ground-source heat pump systems are also discussed.

1 INTRODUCTION

The ground heat exchanger (GHE) is an integral component of ground-source heat pump (GSHP) systems that use sustainable geothermal energy to efficiently heat and cool buildings. GHEs usually comprise a closed loop of absorber pipes embedded in grouted boreholes (typically up to about 100 m deep), backfilled trenches (typically about 2 m deep), or 'energy piles' (foundation piles fitted with absorber pipes, typically 10 m to 30 m deep) (Brandl, 2006). A heat transfer fluid circulates in the absorber pipes; if the fluid is cooler than the ground it absorbs heat, and if it is warmer than the ground it emits heat. A heat pump connects the GHEs and any distribution pipes (collectively, the ground circuit) to a building circuit. To heat the building, heat is extracted from the circulating fluid and to cool the building, heat is rejected to the circulating fluid.

To optimise GHE design, an accurate assessment of the in situ thermal properties of the ground is required: thermal conductivity (λ, in W/(mK)), thermal diffusivity (α, in mm^2/s) and vertical temperature profile or T_0, the average far-field temperature over some depth (in °C or K). Assessment of thermal conductivity is particularly important as the total design length of GHEs in a GSHP system is inversely proportional to the ground's thermal conductivity. Accurate assessment of T_0 is required so that the range in absorber fluid temperature during GSHP system operation, which should remain within a desired range for efficient heat pump performance, can be estimated. Although the thermal properties of samples recovered from the ground can be assessed in the laboratory (e.g. Barry-Macaulay et al, 2013; Clarke et al, 2008), there can be issues associated with sample disturbance, scale and the degree to which discrete samples are representative of the ground as a whole, and in situ assessment of the ground's thermal properties is recommended practice for the design of energy piles (GSHP Association, 2012).

In situ assessment of the ground's thermal properties can be undertaken with a thermal response test (TRT), details of which are presented in Section 2. TRTs are usually performed in vertical borehole GHEs, but can also be undertaken in energy piles (e.g. Loveridge et al., 2014). It is recognised that ambient temperature variation can have an impact on test accuracy (e.g. Bandos et al., 2011 and Abdelaziz et al., 2015). However, previous studies of the influence of ambient temperature on TRT results typically focus on experimental considerations such as heat loss in surface pipes connecting TRT equipment to the GHE (which can cause the power applied to the GHE during testing to fluctuate) or the accuracy of temperature sensors.

The focus of this paper is on how ambient temperature fluctuations affect the net energy applied to the ground during the TRT, which can affect the interpretation of the test, particularly for relatively shallow depth energy piles. The effects are illustrated using the results of a seventeen day long TRT performed on a 30 m deep energy pile GHE and ground temperature measurements over a two year period at the same site. The ground temperature measurements also indicate that T_0 will vary depending on the time of year of the TRT and depth over which the average temperature is measured. The implications of these observations for energy pile design and performance are discussed.

2 THERMAL RESPONSE TESTS

A detailed summary of the development and application of this test, for which there is now an international standard (ISO, 2015) is presented in Spitler & Gehlin (2015). In summary, the test setup is typically similar to that shown in Figure 1. A constant heat flux or power (Q, in W, often expressed as a power $q = Q / L_{GHE}$ per metre GHE length) is applied to the circulating heat transfer fluid. The variation in inlet and outlet fluid temperature (T_{in} and T_{out}, in °C or K) over time is measured and (as will be discussed) the rate of change in mean fluid temperature [$T_{mean} = (T_{in} + T_{out}) / 2$] provides information on the ground's thermal properties.

TRT results are typically analysed using a line-source equation approach, whereby the mean fluid temperature after some elapsed time (t, in seconds), can be estimated using Equation 1.

$$T_{mean} = T_0 + \left(\frac{2.303q}{4\pi\lambda}\right)\log\left(\frac{4\alpha t}{\gamma' r_b^2}\right) + qR_b \quad (1)$$

where, in addition to terms defined previously, r_b is the GHE radius (in m), R_b is the GHE thermal resistance term (in mK/W) and $\gamma' = 1.78$ is a constant [ln(1.78) = Euler's number].

For TRT analysis, Equation 1 is re-written in the form of the equation for a straight line ($y = mx + c$), relating ΔT_{mean} (equal to $T_{mean} - T_0$) to log(t). In this form:

$$\Delta T_{mean} = \left(\frac{2.303q}{4\pi\lambda}\right)\log(t) + \left(\frac{2.303q}{4\pi\lambda}\right)\log\left(\frac{4\alpha}{\gamma' r_b^2}\right) + qR_b \quad (2)$$

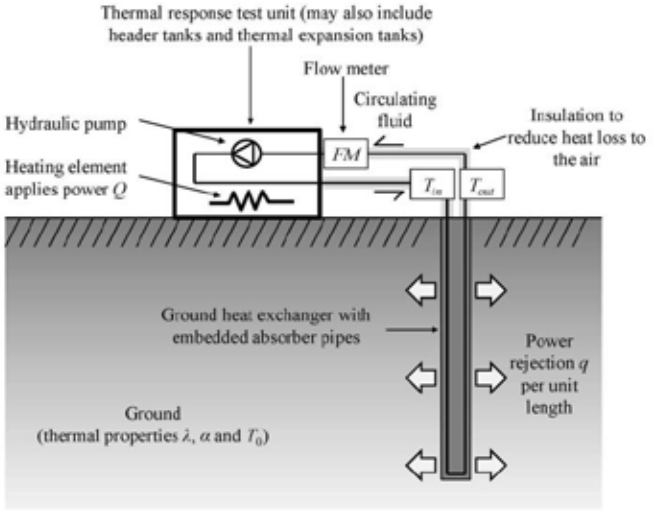

Figure 1. Typical thermal response test setup

Once T_0 has been established (methods for doing this are compared in Gehlin and Nordell, 2003), plotting ΔT_{mean} for a measured and constant q against log(t) eventually yields a linear relationship. Because of limitations on the accuracy of the line-source equation over short time periods, data from $t < 5r_b^2 / \alpha$ is usually ignored in TRT analysis and the trend-line is drawn tangential to later data. The slope (m) and vertical axis intercept (c) of the trend-line can then provide an estimate of (in turn) the ground's thermal conductivity and GHE thermal resistance (these estimates are averages over the length of the GHE):

$$\lambda = \frac{2.303q}{4\pi m} \quad (3)$$

$$R_b = \left(\frac{c}{q}\right) - \left(\frac{2.303}{4\pi\lambda}\right)\log\left(\frac{4\alpha}{\gamma' r_b^2}\right) \quad (4)$$

Note that in Equation 4, it is necessary to estimate the ground's volumetric specific heat capacity (S_{vc}, in J/m^{3}K) to calculate thermal diffusivity $\alpha = \lambda / S_{vc}$, with λ calculated from Equation 3. Specific heat capacity is an important thermal characteristic – it is a measure of the temperature change that occurs in some material volume due to the application or extraction of energy. For soil and rock, S_{vc} is typically about 2000 kJ/m^{3}K.

It is important for the power applied to the GHE during the test to be accurately measured – this measurement should be made using Equation 5 by measuring the change in inlet to outlet temperature as the fluid (usually water, for which $S_{vc} \approx 4180$ kJ/m^{3}K) flows through the GHE, and the flow rate of the fluid (F, in m^3/s).

$$Q = F(T_{in} - T_{out})S_{vc} \quad (5)$$

Because of the potential for heat loss in pipes connecting the TRT equipment to the GHE, measurement of the electrical power applied by the heating element should not be relied on as an accurate estimate of the power applied to the GHE (this power should nonetheless be measured). Measurement of inlet and outlet temperature should be made at the top of the GHE (i.e. immediately before and after fluid flows in or out of it) rather than at the inlet and outlet of the TRT equipment which may be separated from the GHE by connecting pipes.

3 EXPERIMENTAL RESULTS

3.1 *Experimental setup*

The TRT discussed in this paper was undertaken in a 31.2 m deep, 600 mm diameter energy pile (known by site convention as GHE-A) at the Beaurepaire Geothermal Experiment (BGE), a full-scale experimental facility constructed at the University of Melbourne's Parkville campus. The setup of the BGE facility is described in Colls (2013) and Colls et al. (2012). The upper 1 m of GHE-A was thermally insulated.

Subsurface conditions at the BGE site comprise a 0.3 m thick layer of sand fill (imported topsoil) over silty clay (residual soil) and variably weathered Melbourne Mudstone (Silurian age sedimentary rock). Extremely weathered siltstone with minor interbedded sandstone was encountered below 1.0 m, grading to moderately weathered below about 20 m depth. The frequency and thickness of sandstone beds increased below 20 m. The depth to groundwater was about 13 m. Laboratory testing (refer Colls, 2013) indicates the thermal conductivity of the ground generally increases with increasing depth.

The variation in the vertical ground temperature profile was measured using thermistors grouted at various depths into a 30 m deep, 100 mm diameter borehole known by site convention as BH1. BH1 was located about 2.7 m from GHE-A (centre to centre spacing). Measurement of the ambient air temperature was also recorded.

3.2 *Ground temperature profile*

The ground temperature variation in BH1 was measured over a 2-year period at depths of 0.1 m, 0.5 m, 1 m, 2 m, 5 m, 10 m, 20 m and 30 m. Figure 2 shows data from selected depths in BH1 (selected for clarity of presentation). Over the period shown in Figure 2, the ambient air temperature fluctuated between about 2°C and 41°C. Sources of experimental error and accuracy are described in Colls (2013).

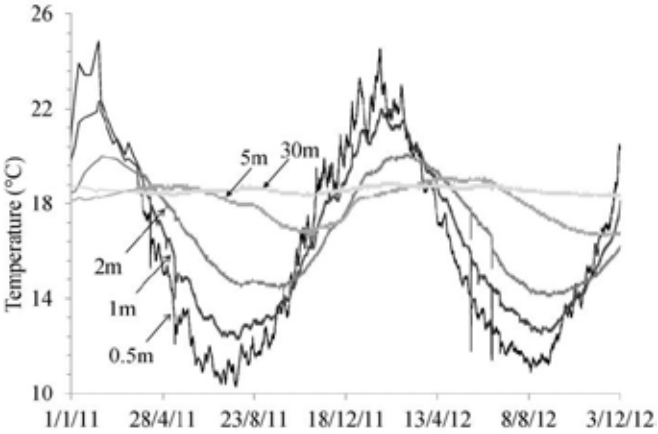

Figure 2. Selected results of ground temperature measurement in BH1

Figure 2 illustrates that the ground temperature varies seasonally; the ground absorbs heat energy from the warmer ambient air in summer, and rejects heat energy to the cooler air in winter. Any energy applied during a TRT (noting that energy is the product of power and time) will be in addition to this 'background' heat flux.

For interpretation of TRTs and GHE design, it is also important to recognise that the average ground temperature, T_0, will vary depending on the time of the year it is measured and the depth range it is measured over. Table 1 presents the range in measured average ground temperature in BH1 over different depth ranges.

Table 1. Average ground temperature measured over different depth ranges, BH1.

Depth range	Range of average temperature	Mean average temperature
	°C	°C
0 to 5 m	14.5 to 20.5	17.5
0 to 10 m	16.3 to 19.6	17.8
0 to 20 m	17.4 to 19.4	18.4
0 to 30 m	17.8 to 19.4	18.6

For ground at a constant temperature year on year the 'average' heat flux from the air to the ground will be zero. A simplified estimate of the heat flux that occurs as the ground warms from winter to summer and cools from summer to winter can be made by assuming the yearly temperature range in Table 1 occurs over a six month period and that the ground has a specific heat capacity of 2000 kJ/m^{3}K (the volume of ground affected to 5 m depth, for example, would be 5 m^3 per m^2 surface area). By this approach, the average 'background' heat flux is estimated to be about 3.8 W/m^2 to 6.0 W/m^2.

Note that the surface temperature boundary conditions above the GHE could change from the time of the TRT to operation of the GSHP system. For example, energy piles are generally located beneath buildings, which may not be present during testing.

Any change in the surface temperature boundary could therefore change both the shallow vertical temperature profile and the average ground temperature over the GHE depth. It is therefore important that the vertical ground temperature profile, and not just the initial mean ground temperature over the GHE depth, is measured during TRTs so that the effect of any change in the surface temperature over time can be assessed during GHE design.

3.3 *TRT results*

Figure 3 shows the measured change in T_{mean} during a seventeen day long TRT (known by site convention as TRT18) performed in GHE-A, together with the variation in the average daily ambient temperature (based on hourly measurements in a location shaded from direct sunlight). During the test, which commenced on 5 December 2011, a nominal 3kW power was applied to the GHE by an electrical heating element (the average power applied to the GHE as measured using Equation 5 was 2.86 kW). Note that for this paper, data from the first four days of the test has been ignored because of the minimum time criteria typically applied to TRT interpretation (see Section 2). The average ground temperature over the length of the GHE at the start of the test (T_0) was 18.1°C.

During TRT18, four time periods (4 to 6 days, 7 to 10 days, 11 to 13 days and 14 to 17 days) have been identified during which the average daily ambient temperature (based on hourly measurements) is 2.8°C to 3.5°C above or below the average ambient temperature (21.3°C) over the 'overall' test period.

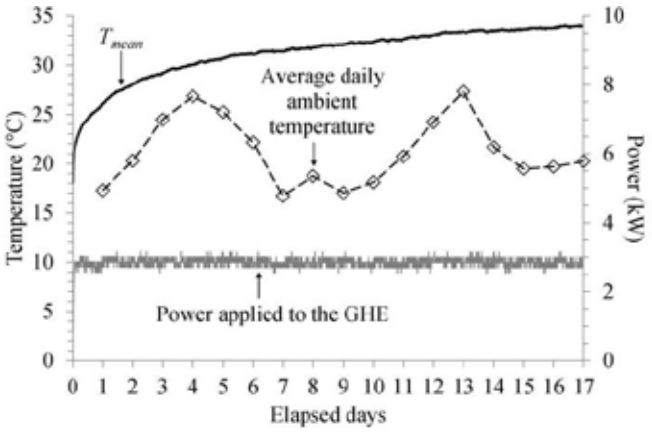

Figure 3. Data from TRT18 in GHE-A

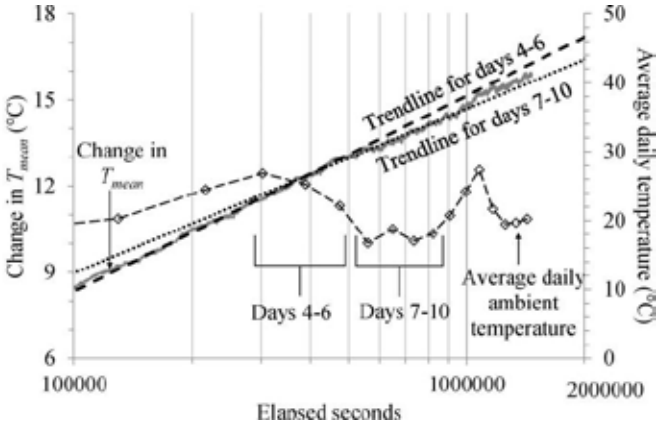

Figure 4. Influence of ambient temperature variations on the change in mean water temperature during TRT18, GHE-A.

The impact of ambient temperature on the results of TRT18 is not readily apparent on the scale of Figure 3. However, as Figure 4 shows, there is a distinct change in the slope of the TRT analysis plot (the change in T_{mean} from T_0 versus log time) during the relatively warm and cool periods. This change occurs despite the power applied to the GHE (measured using Equation 5, refer Table 3 and discussion below) remaining relatively constant during the warmer and cooler periods. If the slope of the TRT plot changes while the applied power remains relatively constant, from Equation 3 the estimate of thermal conductivity will also change; a steeper slope indicates relatively low thermal conductivity (heat dissipates more slowly into the ground around the GHE) and a shallower slope indicates relatively high conductivity (heat dissipates more rapidly).

Estimates of thermal conductivity and GHE thermal resistance, based on the applied power measured (over the 30.2 m long GHE-A below the 1 m long thermally insulated section) and the slope of the TRT analysis plot during different time periods, are presented in Table 3. The trend-lines used to estimate the thermal conductivity and GHE thermal resistance for days 4 to 6 and days 7 to 10 are shown on Figure 4. Trend-lines were also drawn for the other time periods but for clarity are not shown on Figure 4.

Table 2. Influence of ambient temperature on the interpretation of TRT18.

Time period	Ave. ambient temperature	q	λ	R_b
	°C	W/m	W/mK	mK/W
4 to17 days	21.3	94.5	2.73	0.055
4 to 6 days	24.8	95.4	2.57	0.051
7 to 10 days	17.7	94.0	3.02	0.060
11 to 13 days	24.1	94.7	2.47	0.047
14 to 17 days	17.8	94.0	2.89	0.060

Important points to note from Table 3 are as follows:

The variation in ambient temperature results in small fluctuations in the applied power (less than 1% of the average power applied over for the total test duration). This result suggests that for the test setup, pipes connecting the TRT equipment to the GHE are relatively well insulated, noting that the inlet and outlet temperature measurements used to calculate this power were from thermistors in direct contact with the circulating water. Slightly more power is applied during warmer periods and slightly less power is applied during cooler periods.

The estimated thermal conductivity based on the different time periods varies between about -9.5% and +10.5% of the estimated value for the total test duration. The estimate of thermal conductivity is lower during relatively warm periods than in relatively cool periods. The estimated GHE thermal resistance varies by a similar proportion. This suggests that, for the range in the ambient temperatures during the test, estimates of these parameters could range by about 20% if protracted warm or cool periods are observed during testing. Larger variations could potentially be observed between tests undertaken in winter and summer.

Possible reasons for the observed variation in the estimate of thermal conductivity are discussed below. At this time it is unclear what the relative contribution of these mechanisms to the observed change is, or if there are other contributing factors that have not been considered.

Firstly, it is reasonable to assume that the average thermal conductivity of the ground adjacent to the GHE will not change over the course of the test. Although some thermal properties are temperature dependent, given the relatively small change in ground and average ambient temperature, it is not considered to be a significant contributing factor.

With reference to Equation 3 and the discussion of background heat flux in Section 3.2, it is likely that the *measured* power applied to the GHE during the relatively warm periods underestimates the *net* power applied by the TRT equipment plus the background heat flux. If, for example, the net power applied fluctuates by about ±10% during the relatively warm and cool periods, it would explain the different thermal conductivity estimates. The background heat flux would then need to be in the order of 300 W compared to the nominal 3 kW heating power. This value seems high given the estimate of average background heat flux of up to about 6.0 W/m^2; i.e. the test result would need to be affected by about 50 m^2 of ground (the ground to a radial distance of about 4 m from the centre of the GHE), which for the initial part of the test in particular seems large given the slow speed at which heat propagates through the ground. However, the 'background' heat flux is based on average temperature changes over a six month period, and there are many days in summer when the air is cooler than the ground (and vice versa in winter) hence there will be periods when the background heat flux is much higher – Banks (2012) indicates that solar insolation can be up to a few hundred watts per square metre.

In some situations there may be 'external' sources of heat, such as sewers, subway tunnels or basements near GHEs that add or extract heat from the ground during the TRT, and will not be accounted for in the measured power. However, the BGE site is not known to be close to external heat sources.

Another explanation could be that variation in the near surface temperatures affects the power rejected at different depths along the GHE axis. Although a constant rate of power rejection per metre GHE length is assumed in TRT analysis, in reality the heat rejection rate is unlikely to be constant with depth because the temperature gradient between the circulating fluid and surrounding ground will vary, and is typically highest near the surface where the warm fluid first enters the ground. Changes to the vertical temperature profile due to ambient temperature variations may therefore alter the relative contribution different ground layers make to the average thermal conductivity measured over the total GHE length. However, at the BGE site the thermal conductivity of the ground typically increases with depth and an increase in the average thermal conductivity (not observed) would be expected if warmer ambient temperatures mean a higher proportion of the heat is rejected at depth than when the near surface but lower conductivity ground is relatively cool.

Note that the influence of ambient temperatures on TRT interpretation and GSHP system performance is in general expected to be more significant for relatively shallow energy pile GHEs than for typical borehole GHEs, which can extend to depth of 100 m or more hence have a greater proportion of their length below the depth of the seasonal temperature influence. The relatively long duration of TRTs in energy piles compared to TRTs in narrower diameter borehole GHEs (typically about 50 hours' duration) could also contribute to the impact of ambient temperatures on TRT analysis, as the area/volume of ground around the GHE affected by a TRT increases over time, hence the ratio of 'background' heat flux to applied power could increase over time.

It is also important to recognise that changes in ambient temperatures will affect the operation of GSHP systems as well as TRT results. For example, in summer the ground around the GHE should be expected to heat more rapidly than if only the power rejected by the GSHP system (to cool a building) was applied.

4 CONCLUSIONS

In this paper, observations from full-scale field experiments are presented to illustrate the potential impact of ambient air temperatures on the measurement of the average ground temperature, T_0, and estimates of thermal conductivity and GHE thermal resistance interpreted from energy pile TRT results. These are important parameters for the design of GHEs. The key points raised are summarised as follows:

T_0 will be affected by the time of year and depth over which it is measured. It may change from the time of testing to when the GSHP system is operating if ground surface conditions are altered, for example due to construction of a building floor slab.

TRT interpretation should take into account the time of year of testing and whether, in addition to the measured power applied to the GHE by the TRT equipment, the ground surrounding the GHE is gaining or losing power from the ambient air or external energy sources. From the results presented in this paper, the variation in the estimates of thermal conductivity and GHE thermal resistance could be up to about 20%. However, larger variation could potentially be observed where the ambient temperature variation is greater than occurred during this test.

These points should be taken into account in the interpretation of TRTs and the design of GSHP systems based on TRT results.

5 ACKNOWLEDGEMENTS

The Beaurepaire Geothermal Experiment could not have been built without seed funding from the Melbourne Energy Institute, and the generous assistance of Geotechnical Engineering Pty Ltd and Melbourne University Sport. The significant contribution of Professor Ian Johnston, Dr Guillermo Narsilio, the Department of Infrastructure Engineering at Melbourne University and Golder Associates Pty Ltd is also acknowledged.

6 REFERENCES

Abdelaziz, S., Olgun, C. & Martin, J. 2015. Counterbalancing ambient interference on thermal conductivity tests for energy piles. *Geothermics* 56: 45-59.

Banks, D. 2012. *An introduction to thermogeology: ground source heating and cooling (2nd edition)*, West Sussex: John Wiley & Sons, Ltd.

Bandos, T., Montero, A., Fernandez de Cordoba, P . & Urchueguia, J. 2011. Improving parameter estimates obtained from thermal response tests: Effect of ambient air temperature variations. *Geothermic*s 40: 136-143.

Barry Macaulay, D., Bouazza, M., Singh, R., Wang, B. & Ranjith, P. 2013. Thermal conductivity of soils and rocks from the Melbourne (Australia) region. *Engineering Geology* 164: 131-138.

Brandl, H. 2006. Energy foundations and other thermo-active ground structures. *Géotechnique* 56(2): 81-122.

Clarke, B., Agab, A. & Nicholson, D. 2008. Model specification to determine thermal conductivity of soils. In *Proc. Institution of Civil Engineers Geotechnical Engineering* 161(GE3): 161-168.

Colls, S., Johnston, I. & Narsilio, G. 2012. Experimental study of ground energy systems in Melbourne, Australia. *Australian Geomechanics* 47(4): 15-20.

Colls, S. 2013. Ground heat exchanger design for direct geothermal energy systems. *PhD thesis, Department of Infrastructure Engineering, The University of Melbourne,* Australia.

Gehlin, S. & Nordell, B. 2003. Determining the undisturbed ground temperature for thermal response test. *ASHRAE Transactions* 109: 151-156.

GSHP Association 2012. Thermal pile design, installation & materials standards. *Ground Source Heat Pump Association, National Energy Centre, Milton Keynes*.

International Standards Organisation 2015. Geotechnical investigation and testing – geothermal testing – determination of thermal conductivity of soil and rock using a borehole heat exchanger, *ISO17628:205(E)*.

Loveridge, F., Brettman, T., Olgun, C. & Powrie, W. 2014. Assessing the applicability of thermal response testing to energy piles. In *Proc. Global Perspectives on the Sustainable Execution of Foundation Works*, Stockholm, Sweden.

Spitler, J. & Gehlin, S. 2015. Thermal response testing for ground source heat pump systems – an historical review. *Renewable and Sustainable Energy Reviews* 50: 1125-1137.

Geotechnical and Geophysical Site Characterisation 5 – Lehane, Acosta-Martínez & Kelly (Eds)

Monitoring the plume of potassium chloride from wells used as ground improvement in highly sensitive clays

T.E. Helle
Norwegian University of Science and Technology (NTNU), & the Directorate of Public Roads, Trondheim, Norway

P. Aagaard
University in Oslo, Norway

A. Emdal & S. Nordal
Norwegian University of Science and Technology (NTNU), Trondheim, Norway

ABSTRACT: Potassium chloride (KCl) may be used as ground improvement in low-saline, highly sensitive clays termed quick clays. KCl improves the mechanical behaviour of quick clays to such an extent that they no longer appears as quick. Six salt wells filled with potassium chloride were installed in January 2013 at the Dragvoll research site, Trondheim, Norway. The migration of KCl from of the salt wells into the quick clay deposit, is monitored by Schlumberger Divers, BAT ground water monitoring system and a CPTU with resistivity module (RCPTU). The resistivity, normalised tip resistance and pore-pressure parameter clearly indicate the changed behaviour of the clay. In particular, the salt treated clay shows a significant increase in remoulded shear strength and do no longer liquefy when remoulded. The arrival of the plume to the divers and BAT filters reflects a non-symmetrical flow and diffusion pattern around the wells.

1 INTRODUCTION

The Holocene clays in Scandinavia were deposited in a marine environment at the end of the last ice age. Leaching and diffusion has in many clay deposits decreased the originally high salt content in the pore water (~30-35 g/l), and changed the ion composition (Rosenqvist 1946). Clays with a remaining salt content of less than 1 g/l may liquefy completely when remoulded (Bjerrum et al. 1969; Moum et al. 1971, Torrance 1975). In Norway, quick clays are defined by a remoulded shear strength of less than 0.5 kPa. The liquid limit in quick clays is lower than the natural water content, and the clay particles float in their own pore water when remoulded.

This paper presents results from research on improving the properties of the highly sensitive Dragvoll quick clay by installing salt wells. Potassium chloride (KCl) has a beneficial effect on increasing the undrained and remoulded shear strength, as well as the Atterberg limits of quick clays (Moum et al. 1968; Eggestad & Sem 1976; Helle et al. 2015).

It should be noted that low salt content does not necessarily imply that the clay is quick, as the specific ion composition at low salt content highly affects the geotechnical properties (Moum et al. 1971). The clays' negatively charged mineral surfaces attract cations to maintain neutral charge. At the normally occurring pH in Norwegian clays (~8) (Løken 1970; Mitchell and Soga 2005), calcium (Ca^{2+}) is favoured over magnesium (Mg^{2+}), and potassium (K^{+}) over sodium (Na^{+}) due to valence, hydrated radius and available concentration (Løken 1970; Appelo and Postma 2005; Mitchell and Soga 2005).

Na^{+} is the abundant ion in the pore water in quick clays, whereas Ca^{2+} and Mg^{2+} dominate the adsorbed positions. Ca^{2+} and Mg^{2+} are introduced by the leaching water and weathering of the soil minerals (Moum et al. 1971). Under ordinary pore water compositions in clays, Ca^{2+} and Mg^{2+} are favoured over K^{+} by the mineral surface. However, introducing a high concentration of K^{+}, Ca^{2+} and Mg^{2+} are replaced by K^{+} on the mineral surface regardless of its lower exchange power (Mitchell and Soga 2005). K^{+} has a greater impact than Na^{+}, Mg^{2+} and Ca^{2+} on improving the undrained and remoulded shear strength as well as the Atterberg limits (Moum et al. 1968; Løken 1968). According to Moum et al. (1968), as little as 0.5 g K^{+}/l is sufficient to increase the remoulded shear strength to more than 0.5 kPa.

Salt wells filled with KCl were successfully used as ground improvement in a quick clay deposit at Ul-vensplitten, Oslo, Norway in the 1970s (Eggestad and Sem 1976). Two years after installation, the remoulded shear strength was increased from less than 0.5 kPa to the order of 10-45 kPa, reducing the sensitivity from 12-80 to 1-3. The liquid limit increased beyond the natural water content (Eggestad and Sem 1976). Ground investigations carried out thirty to forty years after installation confirm that the non-quick properties remain in an engineering time scale (Helle et al. 2016).

To further investigate the correlation between geochemistry and geotechnical properties, six salt wells filled with KCl were installed at the Dragvoll research site in Trondheim, Norway (Fig. 1). Monitoring over time is carried out to quantify the extent of the salt plume and the effectiveness of the ground improvement over time.

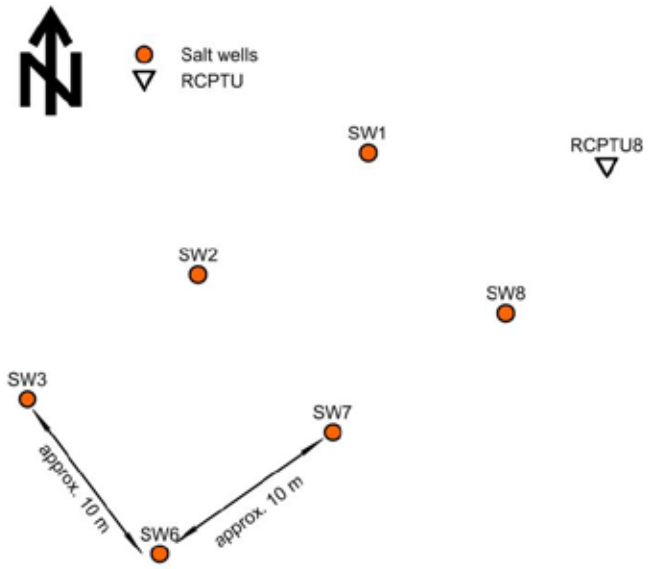

Figure 1. The salt wells are positioned with ~10 m spacing. RCTU8 is located in the outskirt of the test site.

2 SITE DESCRIPTION AND GROUND INVESTIGATION METHODS

2.1 *Dragvoll research site*

The Dragvoll research site is located in an area with clay deposit thickness of up to 40 m (Hafsten and Mack 1990). The marine limit in the Trondheim area is 175-180 m above current sea level (Kjemperud 1981; Hafsten 1983), whereas the research site is located at 156 m above current sea level.

Six salt wells were installed in January 2013 in the quick clay deposit at the Dragvoll research site. The wells are constructed of PE pipes with an outer diameter of 63 mm. The pipes are perforated with slits from 4 m to 8 m depth, allowing the salt to migrate into the quick clay deposit (Fig. 2). To prevent clay entering the salt well, a geotextile is lashed around the perforated pipes. The wells are refilled with granular KCl regularly to maintain a high concentration of KCl in the wells (~4 mol/kgw).

Salt well no. 6 is monitored by BAT groundwater monitoring system (www.bat-gms.com), and Schlumberger divers. The divers log the water head, conductivity and temperature once a day. Ground water samples are extracted from the BAT standard filter tips every 2-3 months. The four instruments are installed at 6 m depth, in a distance of 0.5 m and 1.0 m on opposite sides of the well (Fig. 3).

2.2 *Ground investigations*

A GeoTech CPTU connected to a resistivity module (RCPTU) was used to survey the migration of the salt plume from Salt-well no. 8. The electrodes on the resistivity module are placed in a Wenner-α configuration with electrode spacing of 5 cm. The signals are sent as impulses of direct current of equal intensity, 200 times per second. Seven RCPTU soundings to 12 m depth were carried out around SW8 in September/October 2015; 2 yrs and 9 months after installation. Undisturbed samples were extracted from 4.0 m to 8.8 m depth in a distance of 0.5 m from the salt well (borehole P8A). In the following, most emphasis is made on the results from RCPTU9 correlated to the samples extracted from borehole P8A.

2.3 *Laboratory tests*

The soil samples were tested in the NTNU geotechnical laboratory within 24 hours after extraction from the ground. Index testing was carried out on all samples.

The pore water composition was analysed at the laboratory at the Department for Geosciences at the University in Oslo. The cations were analysed using a Dionex ICS-1000 Ion Chromatography System (ICS-1000). The anions were analysed using a Dionex ICS-2000 Ion Chromatography System (ICS-2000).

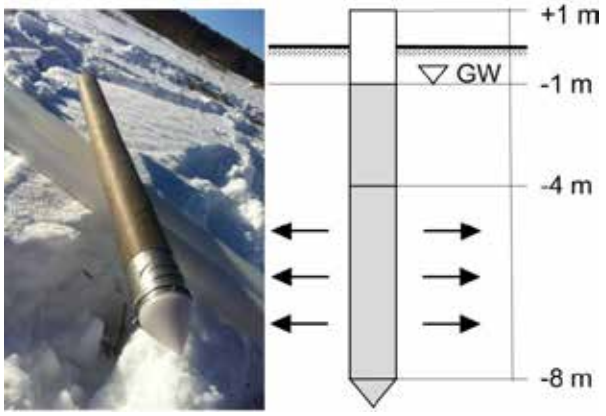

Figure 2. The salt wells are constructed using PE- pipes with an outer diameter of 63 mm. The pipes have slits covered with a geotextile in the depth interval 4-8 m.

3 RESULTS

3.1 *Plume arrival around Salt-well no. 6*

Divers and BAT filters placed around SW6, monitor the progression of the salt plume over time (Fig. 3). The conductivity started to increase in the diver well 0.5 m from SW6 approx. 80 days after installation. Around 450 days, the conductivity increase stopped.

At the same time, the salt concentration in the salt well may have been low due to long refill intervals. The diver conductivity started to increase immediately after refilling the well with salt. This indicate a direct contact between the diver well and the salt well, either due to a communicating silt layer, or a rift caused by installation. A slight increase in the conductivity was observed 1.0 m from the well ~600 days after installation.

The chloride concentration arrived 0.5 m approx. 300 days after installation (Fig. 4a). The K-front is retarded due to ion exchange reactions, and arrived around 600 days after installation. Similar findings were made for the Cl-front 1.0 m from the well (Fig. 4b). The salt plume propagates faster in an eastward direction due to a small hydraulic gradient in that direction (Helle et al. In prep).

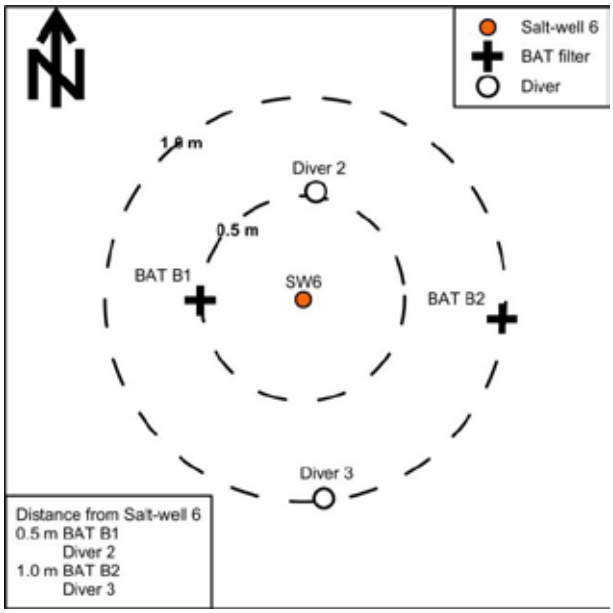

Figure 3. Positioning of BAT filter tips and divers used for monitoring the salt plume arrival over time.

3.2 *Extent of the salt plume around SW8 – 2 years and 9 months after installation*

The salt plume did not spread uniformly around salt-well no. 8 (Fig. 5). The resistivity correlates to the salt content in the pore water (Fig. 6a). Initially, the resistivity in the quick clay at Dragvoll was around 50 Ωm. RCPTU9 correlates well with the increased salt content along the whole depth range of the perforated screen (Fig. 6a). However, on the opposite side of the well (RCPTU 11 north of SW8, Fig. 6b), the resistivity decrease is not as significant as in RCPTU9. Consequently, the salt migration from the salt wells is most likely not only driven by molecular diffusion, but may also be influenced by advective flow. The salt plume surrounding SW8 seem to migrate in a south-western direction. The plume had not yet arrived the locations of RCPTU5 and -7 at the time of investigation; 1 m and 1.5 m from the well respectively.

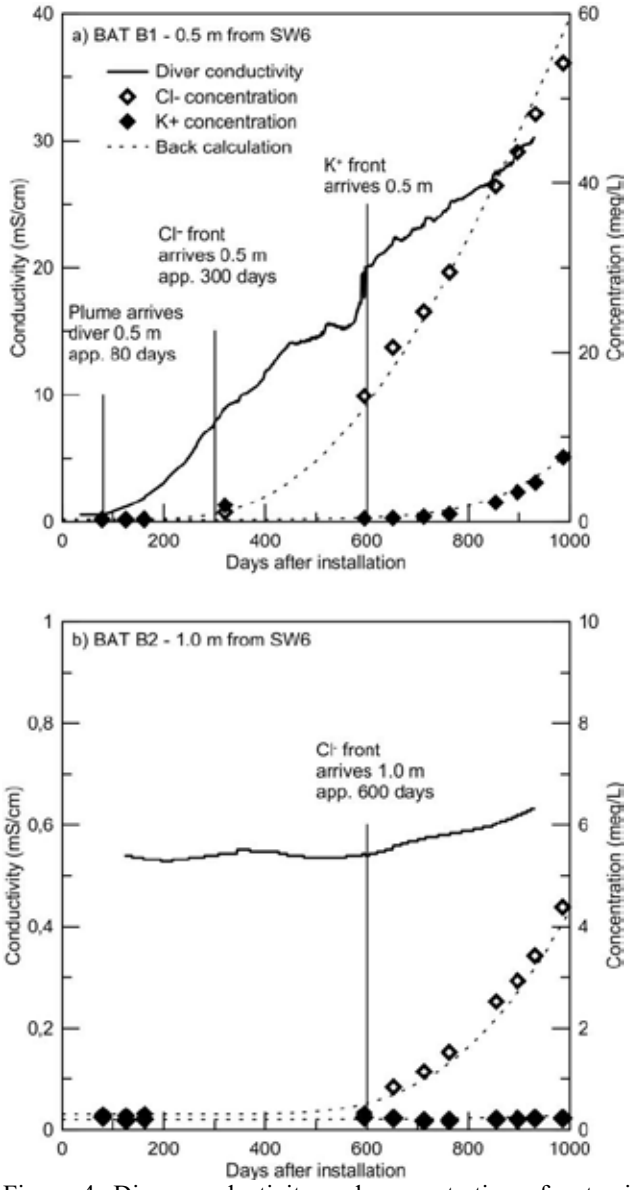

Figure 4. Diver conductivity and concentration of potassium (K^+) and chloride (Cl^-) in the extracted pore water in the BAT filters positioned a) 0.5 m and b) 1.0 m from salt-well no. 6.

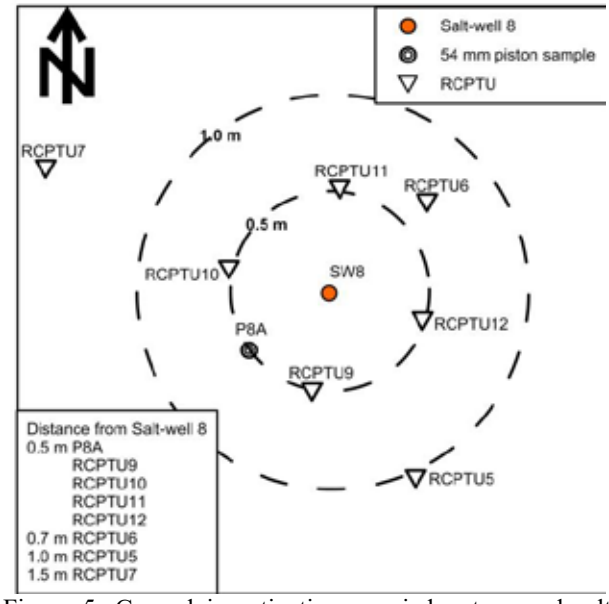

Figure 5. Ground investigations carried out around salt-well no. 8 2 years and 9 months after installation.

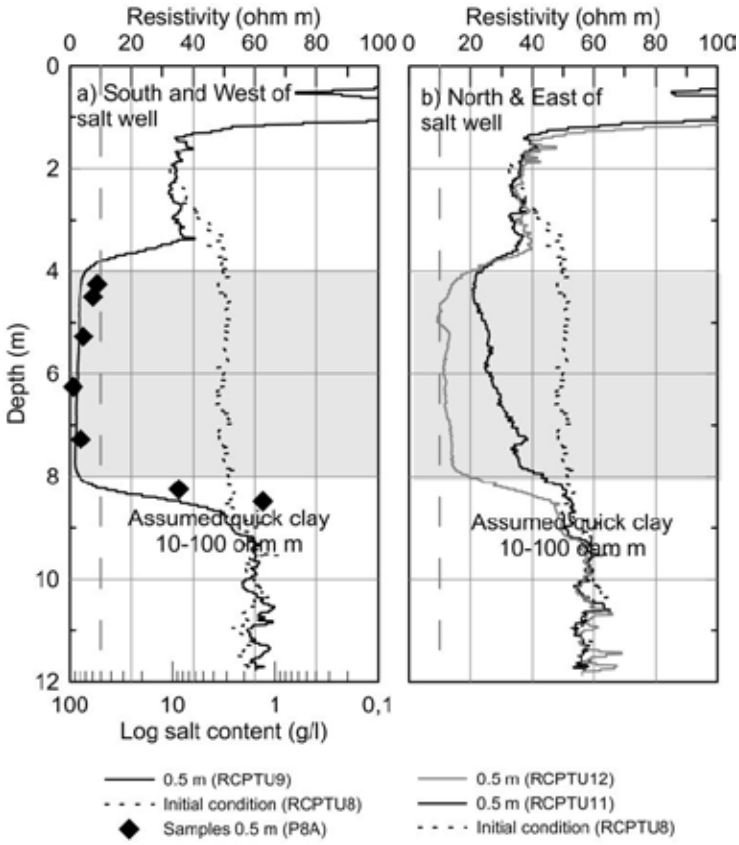

Figure 6. Resistivity profiles 0.5 m from salt-well no. 8. The initial condition is shown by dotted line. a) RCPTU9 and salt content 0.5 m west of salt-well no. 8. Note that the axis for the salt content is in log scale and reverse order. b) RCPTU11 and 12 north and east of the well.

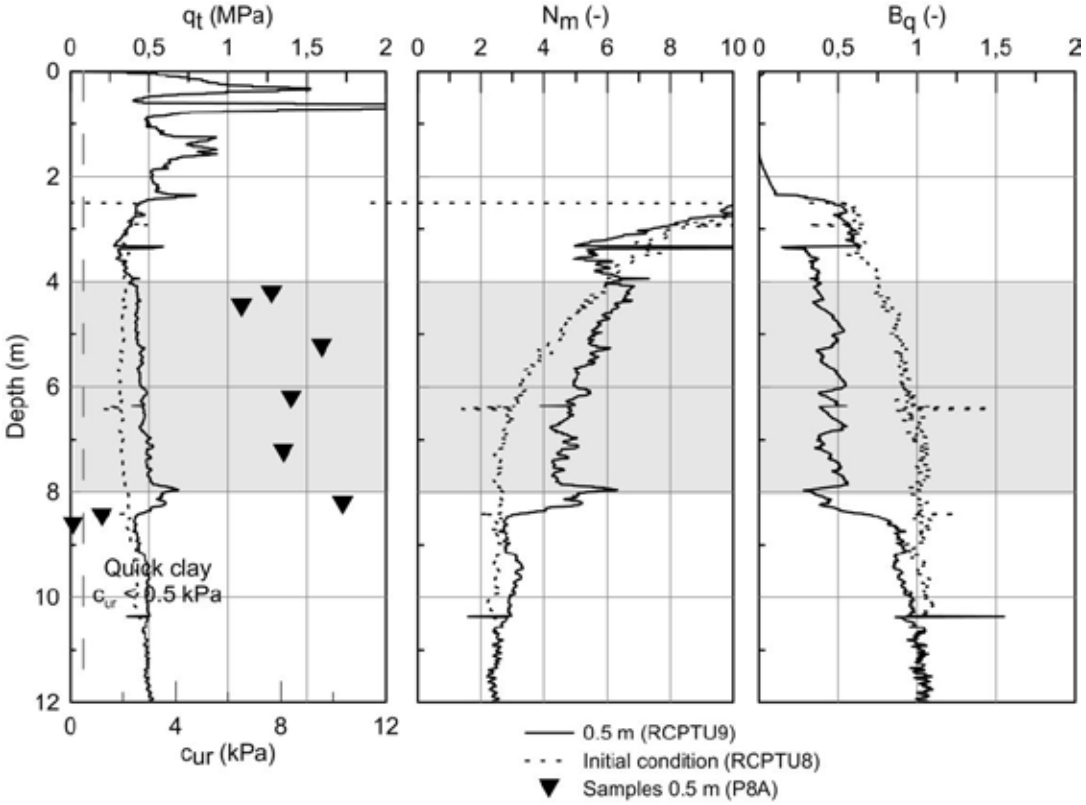

Figure 7. Corrected tip resistance (q_t), normalised tip resistance (N_m) and pore pressure parameter (B_q) in RCTPU, 2 years and 9 months after installation of salt well no. 8 The remoulded shear strength (c_{ur}) found in the samples extracted 0.5 m from the well is shown with black triangles. The initial condition is shown by dotted line.

The remoulded shear strength (c_{ur}) is greatly affected by the salt content in the pore water. The salt content in the salt treated clay is increased to as much as 98 g/l. The improved remoulded shear strength (c_{ur}) in the clay samples extracted 0.5 m from SW8, is in the range 6.5 to 10.4 kPa (Fig. 7).

A slight increase is seen in the corrected tip resistance (q_t) in the salt treated clay 0.5 m from SW8 (RCPTU9). Both the normalised tip resistance (N_m) and pore-pressure parameter (B_q) may indicate the occurrence of quick clay. The normalised tip resistance (N_m) is calculated by dividing the net tip resistance on the effective overburden pressure and an average attraction of 5 kPa. According to Sandven et al. (2015), N_m of less than 4 may indicate quick clay, as was also detected in the Dragvoll quick clay. However, at around 4 m depth, N_m is around 6, even though the clay is quick. N_m exceeds 4 in the salt treated clay. B_q decreases from approximately 1 in the quick clay, to around 0.5 in the salt treated clay.

4 DISCUSSION AND CONCLUSIONS

The non-symmetrical flow pattern around the wells at Dragvoll makes it difficult to monitor the salt plume. The instruments should be placed in the fastest and slowest flow-path directions. These directions were not known prior to installing the wells and instruments at Dragvoll. The salt plume seem to expand slightly different in various directions at the test site. Around SW8, it seems to expand more in a west-ward and slightly southward direction. Around SW6, however, it seems to expand more in an east-ward direction.

RCPTU is a powerful tool to track the salt plume extent, as well as providing valuable information on the soil properties. The remoulded shear strength exceeds 0.5 kPa in the salt treated clay. Considering both resistivity, N_m and B_q, the salt-treated, improved clay can be distinguished from quick clay. According to Long et al. (2012), the resistivity seems to be unaffected by salt contents exceeding 8 g/l. The resistivity data from the RCPTUs correlated to the salt content from nearby boreholes confirm this (Fig. 8a).

Even though, resistivity measured by RCPTU clearly identifies the increased salt content, resistivity measured by electrical resistivity tomography (ERT) with an electrode spacing of 0.5 m, was not able to detect the increased salt content due to poor resolution at depth (Bazin et al. 2016).

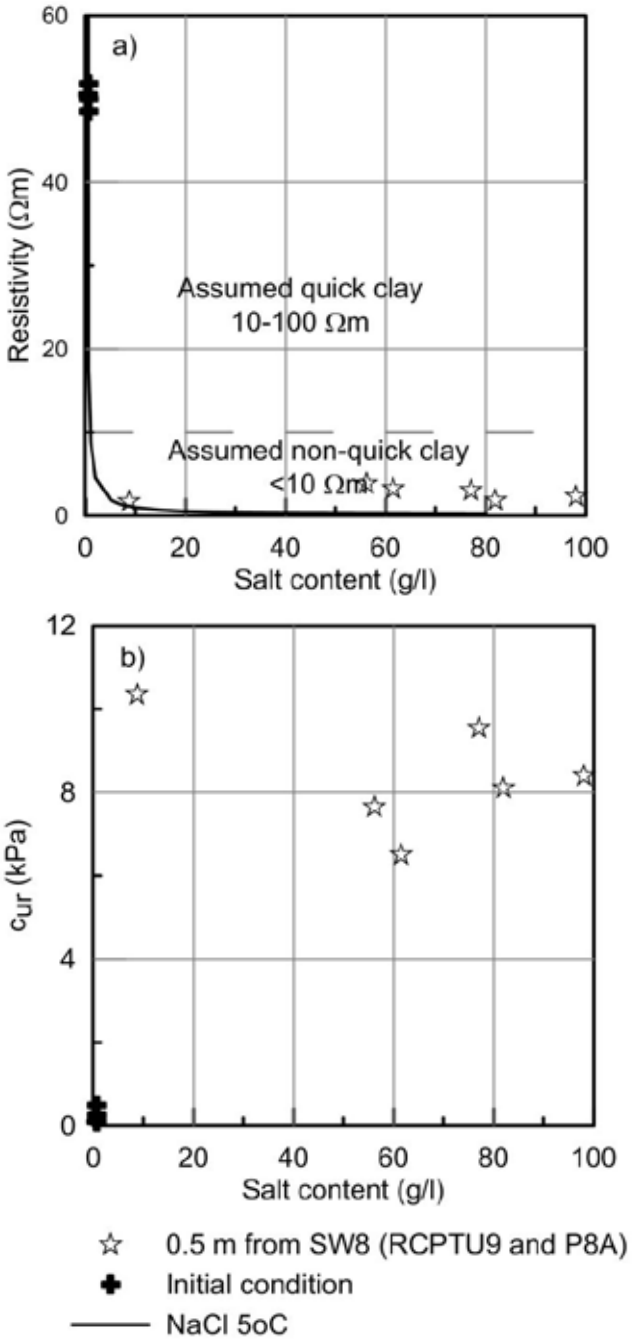

Figure 8. a) RCPTU resistivity correlated to salt content found in nearby samples. The dashed line shows the limit where the resistivity may indicate quick clay (10-100 Ωm) and non-quick clay (<10 Ωm) (Solberg et al. 2012). The black line shows PHREEQC calculated resistivity versus TDS equivalent to NaCl solutions at 5ºC. b) Remoulded shear strength correlated to salt content found in nearby samples.

5 ACKNOWLEDGMENTS

The authors express their sincere gratitude to Jan Jønland, Einar Husby and Gunnar Winter at NTNU Geotechnical Research Group for their thorough work carrying out the ground investigations. Anders Samstad Gylland, formerly at NTNU, and Elisabeth Gundersen in the Directorate of Public Roads are acknowledged for their contributions to discussing well design and installation methods. The tidy work

by Mufak Naoroz at the laboratory at the University in Oslo analysing the pore water chemistry on small sample volumes, is highly appreciated. The work is funded by the Norwegian re-search program "Naturfare - infrastruktur, flom og skred (NIFS)".

6 REFERENCES

Appelo, C. & Postma, D. 2005. Geochemistry. groundwater and pollution. 2nd edn. Balkema, Leiden, Netherlands.

Bazin, S., Anschütz, H., Sauvin G., Helle T.E., Gribben S., Donohue, S. & Long, M. 2016. Geophysical characterisation of marine and quick clay sites: field and laboratory tests. 5th International Conference on Geotechnical and Geophysical Site Characterization.

Bjerrum, L., Løken, T., Heiberg, S. & Foster, R. 1969. A field study of factors responsible for quick clay slides. Proceedings of 7th ICSMFE, 2, Mexico 1969, 531-540.

Eggestad. A. & Sem. H. 1976. Stability of excavations improved by salt diffusion from deep wells. Proceedings of the European conference on soil mechanics and foundation engineering, 6, Vienna, March 1976: 211-216.

Hafsten, U. (1983). Shore-level changes in South Norway during the last 13,000 years, traced by biostratigraphical methods and radiometric datings. Norsk geografi tidsskrift 37: 63-79.

Hafsten, U. & Mack, G. 1990. Den postglaciale landskapsutviklingen på Dragvoll universitetsområde, Trondheim. Norsk Geografisk Tidsskrift 44(3): 131-148.

Helle, T.E., Bryntesen, R.N., Amundsen, H.A., Emdal, A., Nordal, S. & Aagaard, P. 2015. Laboratory setup to evaluate the improvement of geotechnical properties from potassium chloride saturation of a quick clay from Dragvoll, Norway. Proceedings of GeoQuebec2015, Canada, September 2015.

Helle, T.E., Nordal, S., Aagaard, P. & Lied, O.K. 2016. Long-term-effect of potassium chloride treatment on improving the soil behaviour of highly sensitive clay – Ulvensplitten, Norway. Canadian Geotechnical Journal 53(3): 410-422.

Helle, T.E., Aagaard, P. & Nordal, S (In prep). In-situ improvement of highly sensitive clays by potassium chloride migration.

Kjemperud, A. 1981. A shoreline displacement investigation from Frosta in Trondheimsfjorden, Nord-Trøndelag, Norway. Norsk geologisk tidsskrift 61: 1-15.

Long, M., Donohue, S., L'Heureux, J.S., Solberg, I.-L., Rønning, J.S., Limacher, R., O'Connor, P., Sauvin, G., Rømoen, M. & Lecomte, I. 2012. Relationship between electrical resistivity and basic geotechnical parameters for marine clays. Canadian Geotechnical Journal 49(10): 1158-1168.

Løken, T. 1970. Recent research at the Norwegian Geotechnical Institute concerning the influence of chemical additions on quick clay. Proceedings of the Geologiska Föreningen i Stockholm, Förhandlingar 92(2): 133-147.

Mitchell. J.K. & Soga K. 2005. Fundamentals of soil behaviour. 3rd edn. John Wiley & Sons Inc. New Jersey, USA.

Moum, J., Sopp. O.I. & Løken T. 1968. Stabilization of undisturbed quick clay by salt wells. Available from Norwegian Geotechnical Institute, Oslo, Norway. NGI Publication no. 81.

Moum, J., Løken, T. & Torrance, J.K. 1971. A geochemical investigation of the sensitivity of a normally consolidated clay from Drammen, Norway. Géotechnique, 21(4): 329-340.

Rosenqvist, I.T. 1946. Om leirers kvikkaktighet. Available from the Norwegian Public Road Administrations, Meddelelsen fra Vegdirektøren, No. 3: 29-36.

Sandven, R., Montafia, A., Gylland, AS, Pfaffhuber, AA, Kåsin, K., Long, M. 2015. Detektering av kvikkleire-Sluttrapport. NIFS-report no. 126-2015.

Solberg, I.-L., Hansen, L., Rønning, J.S., Haugen, E.D., Dalsegg, E. & Tønnesen, J.F. 2012. Combined geophysical and geotechnical approach to ground investigations and hazard zonation of a quick clay area, mid Norway. Bulletin of Engineering Geology and the Environment 71(1): 119-133.

Torrance, J.K. 1975. On the role of chemistry in the development and behaviour of the sensitive marine clays of Canada and Scandinavia. Canadian Geotechnical Journal 12: 326-335.

Geotechnical and Geophysical Site Characterisation 5 – Lehane, Acosta-Martínez & Kelly (Eds)

The effects of preload surcharge on arsenic and aluminium mobilization in pyritic sediment

O. Karikari-Yeboah[a,b]*, W. Skinner[a] and J. Addai-Mensah[a]

[a]*Future Industries Institute, University of South Australia, Mawson Lakes, Adelaide, SA 5095. Australia;* [b]*Maiden Geotechnics, Queensland, Australia.*

ABSTRACT: The preload technique is employed in geotechnical engineering to improve the shear strength and load-carrying capacity of saturated fine-grained sediments. The technique is based on transient flow of pore water in response to excess pore pressure build-up in the sediment pores under surface surcharge. In pyritic sediment, the preload has an additional advantage of suppressing pyrite oxidation and associated acidity through obstruction of atmospheric oxygen influx. The resulting DO depletion creates severely reduced conditions within the sediment, which may be favourable for the mobilization of toxic metals. This study investigated the mobilization of As and Al in a pyritic sediment under preload surcharge. The objectives were to establish the effects of redox changes under preload surcharge on the mobilization of arsenic and aluminium. It was demonstrated that the severely reduced conditions beneath the surcharge was conducive for As mobilization. However, the abundant supply of iron minerals in pyrite-rich sediment provided natural attenuation of As through sorption onto the iron minerals. For Al, the dissolution was found to be pH dependent with minimum concentration of Al in the pore water occurring around pH 4.5. Imposition of surcharge was accompanied by pH increase with potential increase in Al mobilization into the pore waters. The study outcome shows that the preload technique over pyrite-rich sediment is not a mere physical phenomenon. It has geochemical consequences to be taken into consideration.

1 INTRODUCTION

Pyritic sediments occur commonly in marine deposits and in waterlogged conditions within sedimentary deposits (Hurtgen et al., 1999, Wildman et al., 2004, Bolton et al., 2006). These sediments are associated with acidic leachate from pyrite oxidation, which occurs when the sediment is exposed to aqueous oxygen. The dissolution of phyllosilicate clay minerals is markedly boosted in the resulting acidic environment, leading to the release and proliferation of hydrolysable, heavy or light and alkali earth metal ions such as Al(III), Fe(II/III), Mg(II), Ca(II), Pb(II), K^+ and Na^+. In high concentrations, these metal ions may invariably pose serious toxicity problem to the environment. Infrastructural developments in pyritic sediment environment have been on the increase in recent times, due principally to shortage of other suitable lands in prime locations in cities around the world (Karikari-Yeboah and Gyasi-Agyei, 2000).

This has necessitated frequent use of the preload technique for ground improvement. The technique is based on induced consolidation through transient flow of pore water out of the sediment, due to the creation of hydraulic gradient in response to the application of surface surcharge. Pyritic sediments are characterized by oxic zone, overlying an anoxic region with distinct redox interface. The application of surface surcharge interrupts oxygen supply to the sediment, leading to oxygen depletion, transformation of the previously oxic zone into reduced environment and the creation of severely reduced conditions within the sediment, as the dissolved oxygen is used up by microorganisms for metabolic activities. Consequently, pyrite oxidation and associated acidic leachate are suppressed (Karikari-Yeboah and Addai-Mensah, 2014, Karikari-Yeboah et al., 2014). However, the reduced conditions so created beneath the surcharge may be conducive for mobilization of toxic metals, including arsenic and aluminium. This study involved field testing and laboratory analyses of pyrite-rich sediment hydrogeology,

Pore water geochemistry and solid-phase speciation. Improvement in the groundwater quality through carbonate dissolution and decrease in acidity through the suppression of pyrite oxidation (Johnston et al., 2009) and natural attenuation of arsenic (Carrero et al., 2015) have been demonstrated. However, increase in aluminium concentration was also observed in the severely reduced environment.

2 MATERIALS AND METHODS

2.1 *The study Site*

The study site is situated at Murwillumbah, in the northern New South Wales (NSW), Australia (Figure 1). The original site topography comprised isolated hills rising to reduced level RL 38.60 (Australian Height Datum, AHD), with low-lying areas of pyrite-rich sediment at RL 0.9 m to RL 1.2 m (AHD) at the bottom of the hills. During an infrastructure development, a section of the low-lying area was placed under preload and permanent surcharge. The surcharge thicknesses varied between 9.0 and 16.2 m. The low-lying area with the imposed surcharge is, herein, referred to as the surcharged area (SA).

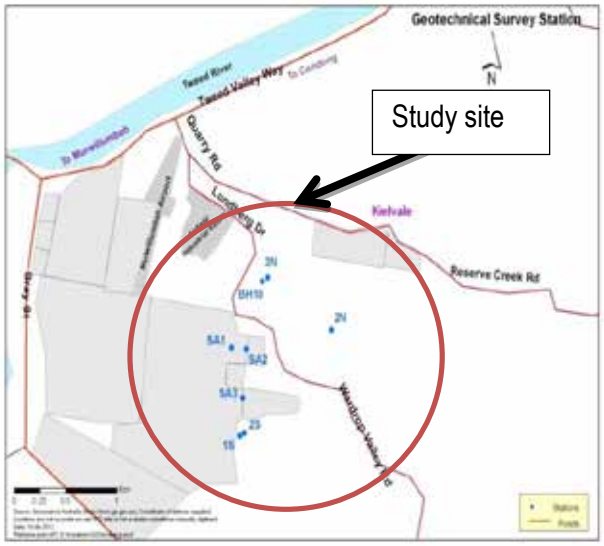

Figure 1: Locality Plan

2.2 *Methodology*

2.2.1 *Fieldwork*

Soil samples were obtained from boreholes across the study site. Several boreholes were established within the original sediment (OS) and at the surcharged area. Samples were collected at close depth intervals with 50 mm diameter (U50) and 0.5m long, thin-wall steel tubes. The sample tubes were sealed at both ends immediately upon withdrawal from the ground, and kept in iced compartment, en route to the laboratory, where they were immediately refrigerated pending laboratory analyses. Standpipes were installed in the boreholes for in-situ water quality monitoring. Dissolved oxygen (DO), electrical conductivity (EC), salinity, oxidation reduction potential (ORP), pH, and temperature were monitored with in-situ calibrated standard instrument. Measurements were taken using a TPS 90FL-MV field/lab analyzer with a 20-metre length cable. The field measurements extended over a period of two years. Target parameters were determined simultaneously at the various depths.

2.2.2 *Elemental Analyses*

The elemental analyses targeted the determinations of metal concentrations in pore water and soil samples. Pore water samples were extracted by the pressure exertion and centrifugal extraction procedures. The sediments were loaded into tightly sealed centrifugation tubes, which were filled and capped under inert atmospheric conditions. Pore water metal concentrations were measured using a Perkin Elmer Optima 7300 DV ICP-OES. Calibration and certified standards were made in 1% nitric acid solution. The acid extractable metal content of soil samples was measured in the digest liquor of soil samples. 200 mg of dry soil was digested with 3 ml of 70% nitric acid and 9 ml of 32% HCl. The mixture was then filtered through Whatman paper followed by 0.45 µm PTFE membranes. The filtrate was subsequently analysed by ICP-OES as described above. The acid generating potential of the soil samples was assessed using the NAG test method[1]. Briefly, 2.5 g of dried and pulverised (<75 µm) soil sample was treated overnight at room temperature with 250 ml of 15% hydrogen peroxide, followed by boiling for 2 hrs. The sample was cooled and filtered and the filtrate titrated with the appropriate concentration of sodium hydroxide solution to pH 4.5 and pH 7 (where the NAG pH was < 7). As and Mn were read in axial-view. Raw spectra were processed using the multicomponent spectral fitting (MSF) algorithm with WinLab 32 (Ver. 4.0) software. Arsenic was speciated as As (III), As(V), monomethylarsonic acid (MMA) and dimethylarsinic acid (DMA). Separation of arsenic species was achieved using an Agilent 1100 liquid chromatography module equipped with a Hamilton PRP-X100 anion exchange column. Detection was achieved using an Agilent 7500c ICP-MS. Arsenic was quantified using the m/z 75 ion with Agilent ChemStation software.

3 RESULTS AND DISCUSSION

The water table was intercepted at the original sediment (OS) at depths within 0.5 m below the ground surface at normal times, and above the ground sur-

face during periods of peak and prolonged rainfalls. At the surcharged area (SA), it rose into the surcharge material in response to the total stress increase. Dissolved oxygen (DO), pH, temperature, Eh, EC and salinity profiles in the Murwillumbah sediment have been reported elsewhere (Karikari-Yeboah et al., 2014). Redox partitioning of the sediment environment has been confirmed, with the redox interface at or around RL -1.2 m. The reduced level at the ground surface was RL 0.9. Table 1 is a summary of the monitored parameters.

Table 1: Summary of physico-chemical properties

Parameter	Oxic Zone (OS)	Anoxic Zone (OS)	SA
DO (%Sat)	0 to 26	0	0
pH	4	7	8 to 9
Temp (°C)	19 to 22	20	21
Eh (Mv)	200 to 600	100	200
EC (µS/cm)	1200	6000	1200
Salinity (ppm)	800	3800	600

In the original sediment, DO was completely depleted at and below the redox interface. The pH was around 4 in the oxic zone and 7 in the anoxic zone. Temperature was highest at 22 °C within the top 1.0 m of the original sediment, but fell with depth to a minimum value of 19 °C at the redox interface. In the anoxic zone, the temperature was kept uniform at 20 °C. Eh was highest within the oxic zone of the original sediment but dropped significantly at or immediately beneath the redox interface. The electrical conductivity and salinity were low in the oxic zone, but experienced significantly increase immediately below the redox interface. At the surcharge area, the pH ranged between 8 and 9 beneath the surcharge. The temperature was kept uniform around 21 °C. Eh, EC and salinity were all significantly lower beneath the surcharge. These changes have impacted on the speciation of toxic metals, including As and Al, in the sediment. The measured arsenic concentrations in the sediment and in the pore water are summarized in Table 2 (a & b). Total As concentrations in the sediment were generally higher in the reducing environments of the anoxic zone of the original sediment and beneath the surcharge, compared to the levels in the oxic zone of the original sediment. There was no significant difference in the measured concentrations in the pore waters. Published literature indicates that arsenic is generally present in reduced environment as As (V), with adequate supply of organic matter and strongly reduced environment as the major contributory factors for its mobilization (Acharyya and Shah, 2006, Aggarwall et al., 1991). A reductive dissolution mechanism involving hydrated iron oxide was proposed by Acharyya and Shah for the release of arsenic into ground water. Consequently, the strongly reduced environments in the anoxic zone of the original sediment, and beneath the surcharge, would be expected to complete the necessary conditions for the mobilization of arsenic in the sediment environment. However, in pyrite-rich sediment, arsenic mobilization has been noted to be controlled by As (V) sorption onto schwertmannite (Burton et al., 2009). Consequently, the low As concentration levels observed, with values below detection limits, confirm the roles of iron as effective removal of As in acidic sediment (Burton et al., 2009, Carrero et al., 2015).

Table 2a: Arsenic concentrations in pore water

Parameter	Oxic Zone (OS)	Anoxic Zone (OS)	SA
Total As	0.006-0.021	0.007-0.015	< 0.02
As (III)	0.001	0.01-0.002	< 0.005
As (V)	0.005-0.021	0.009-0.015	< 0.005

Table 2b: Arsenic concentrations in sediment

	Depth (RL)	Total As (mg/kg)
Oxic Zone - OS	0.2	8.4
	-0.8	5.3
Anoxic Zone - OS	-1.8	7.5
	-2.8	8.5
SA	0.02	4.2
	-1.56	9.2
	-3.06	7.8

Aluminium occurs in sediments as water soluble, and particulate matter in the form of exchangeable and secondary mineral phases (Yvanes-Giuliani Yliane et al., 2014). Its partitioning and dissolution in the sediment and into the pore waters were controlled by the sediment chemical characteristics, including the pH, salinity, total organic matter, represented by total organic carbon, and presence of other metals such as Fe (Yvanes-Giuliani Yliane et al., 2014, Upadhyay, 2008, Carrero et al., 2015). The typical range of Al in soils is 1% to 30 % (10,000 to 300, 000 mg/kg) (US-EPA, 2003). The levels encountered in the Murwillumbah sediment were in the range of 20 to 25 mg/kg in the pore water, and 100 to 120 mg/kg as particulate matter in the soil (Figure 2). In the soil, Al concentration levels were quite similar in the original sediment and beneath the surcharge.

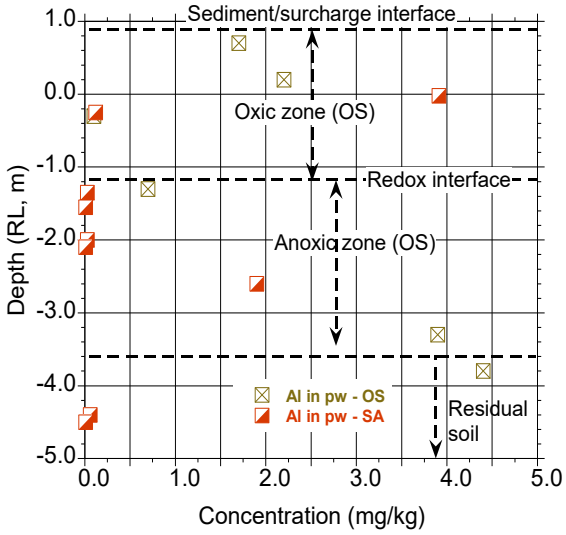

Figure 2a: Al concentration–depth profiles - pw

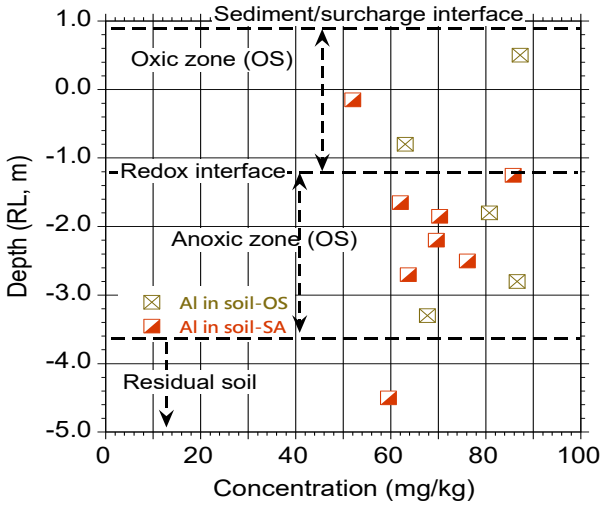

Figure 2b: Al concentration–depth profile - soil

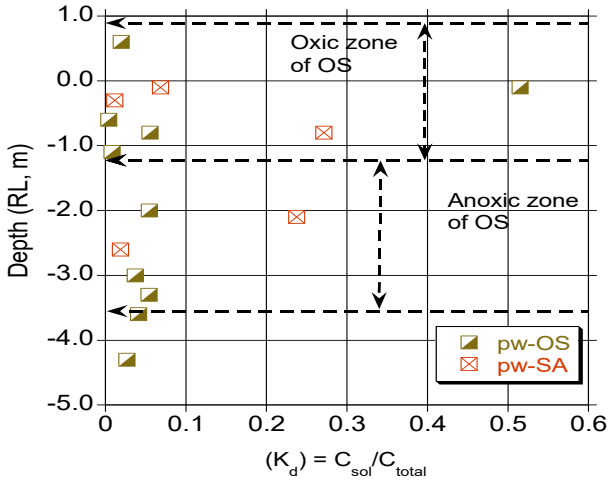

Figure 3: K_p with depth: OS and SA

In the pore waters, however, the concentration levels were far greater at and immediately beneath the redox interface in the original sediment, and beneath the surcharge.

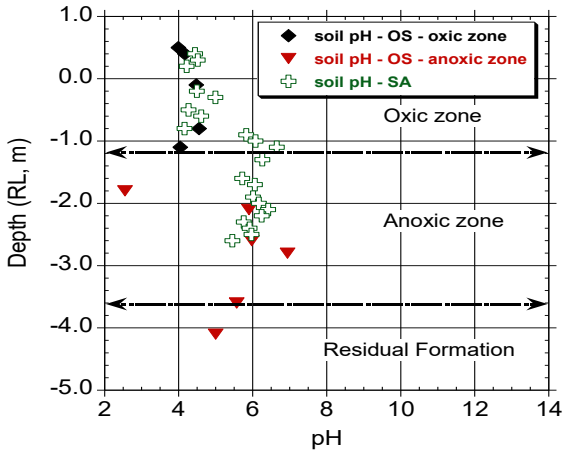

Figure 4: Sediment pH profile – OS & SA

The concentration levels in the pore water were less than the levels in the soil. The difference reflected the proportionate soluble and particulate aluminium that were present in the sediment. A solid–solution partitioning coefficient (K_p) (Fig. 3) (Upadhyay, 2008) can be established to described the dissolution in the various redox zones. K_p is defined here as $Kp = C_{sol}/C_{total}$, where C_{sol} was the Al concentration in the pore water (mg/kg) and C_{total} was the sum of the concentrations in the pore water and in the particulate phase. In the original sediment, dissolution was more active at and below the redox interface, with up to 0.1 of the total aluminium going into solution. Up to 0.3 of the total aluminium went into solution beneath the surcharge. Al dissolution into the pore water was noted to be pH dependent. It decreased with pH increase in the oxic zone of the original sediment, up to pH of about 4.5, at depth of RL -1.0. Thus, maximum concentration of Al in the sediment and minimum concentration in the pore water occurred around the redox interface RL -1.2 (Fig. 2) at pH of about 4.5 (Fig. 4). Similar pH conditions have been reported by others (Carrero et al., 2015, Yvanes-Giuliani Yliane et al., 2014). At pH of 4 and 7 that existed in the oxic and anoxic zones of the original sediment, Al concentration in the pore water would had been at about the minimum levels in the oxic zone, and would had been on the increase in the anoxic zone.

The application of surcharge, accompanied by pH increase, would have triggered further increase in Al mobilization into the pore water. As the re-course of Figure 3 shows, the dissolution factor beneath the surcharge was more than double that in the original sediment. Figures 5, 6 and 7 show the effects of organic carbon, Fe and Cl on the dissolution of Al in pore water.

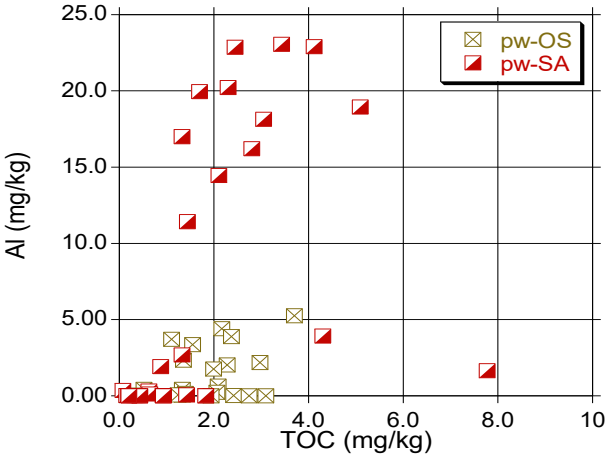

Figure 5: Al concentration versus Total organic carbon (TOC) concentration in pore water–OS & SA

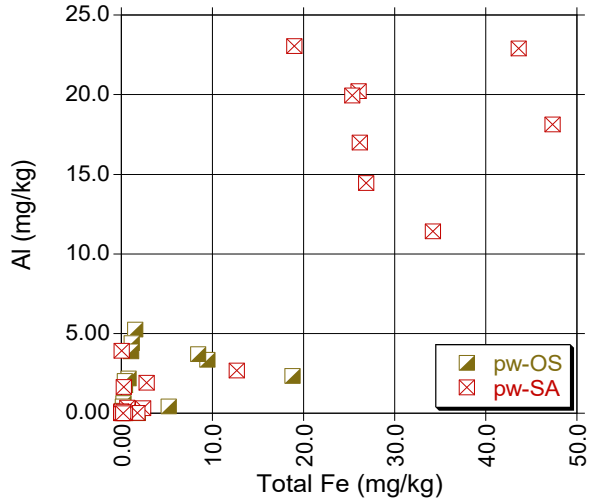

Figure 6: Al concentration versus total iron (Fe) concentration in pore water – OS & SA

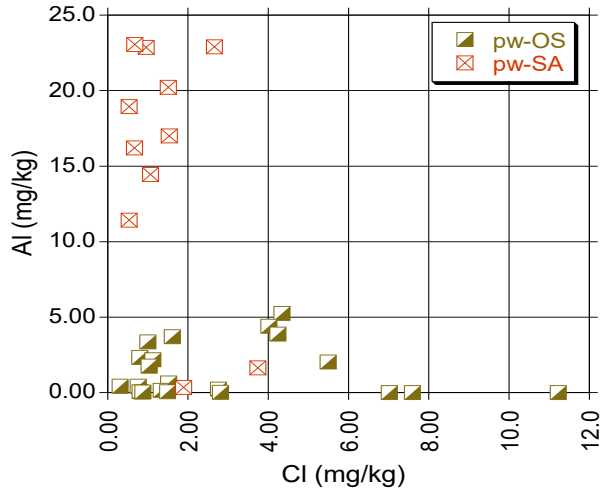

Figure 7: Al concentration versus chloride (Cl) concentration in pore water – OS & SA

Al concentration in the pore water generally remained high until a concentration level of TOC, Fe and Cl reached a certain level, and then decreased thereafter. The same trend was also observed beneath the surcharge. The phenomenon can be ascribed to the formation and precipitation of complexes. The same trend was also observed beneath the surcharge.

4 CONCLUSIONS

The effects of surcharge on the dissolution of As and Al into the pore waters of pyritic sediment have been investigated. The results demonstrate reduced As concentration in the original sediment and beneath the surcharge. This may be associated with high concentration of iron minerals and their consequent precipitation, and favoured As (V) removal from pore waters through sorption onto the iron minerals surfaces, leading to natural attenuation of As contamination in the sediment environment.

The increase in pH associated with imposition of surcharge appeared to favour the dissolution of Al into the pore water. Al in pore water is associated with the weathering of phyllosilicate clay minerals of the host formation and dissolution of the reactive, water-soluble portions. The dissolution process is mediated by pH, presence of adequate organic matter and other metallic ions. Al concentration in the pore water increased with decrease in pH in the oxic zone of the original sediment, with minimum concentration occurring around pH of 4.5. Thereafter, the concentration in the pore water increased with increase in pH. In the oxic zone, the pH was typically around 4 to 4.5. Consequently, Al concentration in the pore water would have been around its lowest levels. The imposition of surcharge and the associated pH increase would have triggered further mobilization of Al into the pore water.

Al concentration in the pore water also appeared to be affected by the concentrations of organic matter, total Fe and chloride in the sediment.

5 REFERENCES

Acharyya, S. K. & Shah, B. A. 2006. Arsenic-contaminated groundwater from parts of Damodar fan-delta and west of Bhagirathi River, West Bengal, India: influence of fluvial geomorphology and quaternary morphostratigraphy. *Environmental Geology,* 52**,** 489-501.

Aggarwall, P. K., Means, J. L. & Hinchee, R. E. Formulation of nutrients solutions for in situ bioremediation. *In:* HINCHERE, R. E. O., R. F., ed. In situ Bioremediation, 1991 Butterworth, Boston, MA.

Bolton, E. W., Berner, R. A. & Petsch, S. T. 2006. The weathering of sedimentary organic matters as a control on atmospheric O_2: II. Theoretical Modeling. *American journal of science,* 306.

Burton, E. D., Bush, R. T., Johnston, S. G., Watling, K. M., Hocking, R. K., Sullivan, L. A. & Parker, G. K. 2009. Sorption of arsenic by iron-oxides and oxyhydroxides in soils. *Environmental Science Technology,* 43**,** 9202-9207.

Carrero, S., Perez-Lopez, R. & Fernandez-Martinez, A. 2015. The potential role of aluminium hydroxysulphates in the removal of contamiants in acid mine drainage. *Chemical Geology,* 417**,** 414-423.

Hurtgen, M. T., Lyons, T. W., Ingakll, E. D. & Cruse, A. M. 1999. Anomalous enrichments of iron monosulfide in euxinic marine sediments and the role of H_2S in iron sulfie transformations: examples from Effingham Inlet, Orca

Basin and The Black Sea. *American journal of science,* 299**,** 556-588.

Johnston, S. G., Bush, R. T., Sullivan, L. A., Burton, E. D., Smith, D., Martens, M. A., Mcelnea, A., Ahern, C. R., Powell, B., Stephens, L. P., Wilbraham, S. T. & Heel, S. V. 2009. Changes in water quality following tidal inundation of coastal lowland acid sulfate soil landscapes. *Estuarine, Coastal and Shelf Science,* 81**,** 257-266.

Karikari-Yeboah, O. & Addai-Mensah, J. 2014. Pyrite-rich sediment pore water quality transformations under preload surcharge. *3rd Biennial UMat International Mining and Mineral Conference.* Tarkwa, Ghana.

Karikari-Yeboah, O. & Gyasi-Agyei, Y. 2000. Stability of Slopes Characterised by Colluvium: investigation, analysis and stability. *GeoEng2000.* Melbourne, Australia.

Karikari-Yeboah, O., Manzies, N. W. & Addai-Mensah, J. Transformations in pyritic sediment redox dynamics during burial beneath preload surcharge. 7th International Congress on Environmental Geotechnics, Novemberr, 2014 2014 Melbourne, Australia.

Upadhyay, S. 2008. Sorption model for dissolved and particulate aluminium in the Conway estuary, U.K. *Estuarine, Coastal and Shelf Science,* 76**,** 914-919.

US-EPA 2003. Ecological Soil Screening level for Aluminium - Interim Final OSWER Directive 9285.7-60. *In:* RESPONSE, O. O. S. W. E. (ed.). Washington, D. C.

Wildman, R., Berner, R. A., Petsch, S. T., Bolton, E. W., Eckert, J. O., Mok, U. & Evans, J. B. 2004. The weathering of sedimentary organic matters as a control on atmospheric O_2: I. Analysis of a Black Shale. *American journal of science,* 304**,** 234-249.

Yvanes-Giuliani Yliane, A. M., Waite, D. T. & Collins, R. N. 2014. Exchangeable and secondary mineral reactive pools of aluminium in coastal lowland acid sulfate soils. *Science of the Total Environment,* 485-486**,** 232-240.

Geotechnical and Geophysical Site Characterisation 5 – Lehane, Acosta-Martínez & Kelly (Eds)

Electrical Conductivity Breakthrough Curve of Soil Column with Residual Diesel Fuel

Myounghak Oh
Korea Institute of Ocean Science & Technology, Ansan, Republic of Korea

Yong Sung Kim
Global Green Growth Institute, Seoul, Republic of Korea

ABSTRACT: In order to demonstrate the applicability of bulk electrical conductivity breakthrough curves for estimating solute transport in soil with residual diesel fuel, electrical conductivity breakthrough curves on column test was investigated. In addition, the electrical conductivity breakthrough curves were compared with Mobile-Immobile Model to verify the amount of solute in the immobile fraction of the pore volume. Changes in the electrical conductivity represented as a relative parameter with time gives information about solute transport in both clean saturated soils and saturated soils with residual diesel fuel. This illustrates the advantage of electrical conductivity BTC to monitor solute concentration continuously with time based on instantaneous electrical measurements. Electrical conductivity BTCs can provide an effective means of qualitative monitoring on solute transport with longitudinal direction of transport.

1 INTRODUCTION

In order to conduct an accurate predition of flow and transport processes, accurate measurement methods and approapriate modelling approaches is necessary. Soil column tests provides a reliable means of evaluating the solute transport characteristics in soil. To provide an effective means of analyzing solute transport in soil medium, a column test device installed with 4-electrode electrical conductivity sensors have been developed(Kim 2009). Detection and monitoring by means of measuring the electrical properties of soils is advantageous in that it can be performed quickly with little data processing needed to obtain accurate and repeatable results (Rinaldi & Cuestas 2002; Oh et al. 2007; Oh et al. 2008). In many cases, contaminants are introduced into the subsurface at concentrations sufficient to alter the electrical properties of soil. The electrical conductivity of saturated soils is a measure of how well a soil-fluid mixture accommodates the transport of electric charge, and is a physical property which changes significantly according to the type and concentration of contaminant present.

The objective of this study is to demonstrate the applicability of bulk electrical conductivity breakthrough curves(BTCs) for estimating solute transport in mixed contaminated soils. The influence of residual diesel fuel, which is NAPL(Non Aqueous Phase Liquid) and non-conductive contaminant, on electrical conductivity breakthrough curves on column test was investigated. The electrical conductivity BTCs were analyzed based on Mobile-Immobile Model (MIM) to verify the amount of solute in the immobile fraction of the pore volume.

2 MOBILE-IMMOBIEL MODEL

Advection-dispersion equation has been adapted for transport of conservative solute in a homogeneous porous medium. However, soils often poses heterogenieties in the pore space, simply from the spatial difference in the soil particle size, composition and the degree of compaction, or even from biological activities which can create large pores with time. Conceptualizing the transport of chemicals in such soils becomes a challenging process. Generally, BTCs from solute transport experiments in heterogeneous media or soils with macropores can be characterized by early breakthrough and tailing, which results in highly asymmetrical shapes. Such phenomenon can be understood in terms of the presence of fast transport through the macropores and diffusion of solute into and out from the less mobile pores.

Dubè et al.(2003) found that soils contaminated by non-aqueous phase liquids(NAPLs) experience such heterogeneities, since NAPLs change the transport by the aqueous phase by changing the network of pores assessable to aqueous flow, namely by creating circuits of pores that by-pass porous zones occupied by residual NAPL. Many other studies (Rao et al., 1980; Nkedi-Kizza et al., 1983; Lee et al., 2000)

have shown that MIM model can describe some forms of preferential solute movement.

Transport in soils with macropores can be conceptualized by assuming advective transport in the macropore region and diffusion into or out of the less mobile regions by using a first-order kinetic diffusion process (Coats & Smith, 1964; Van Genuchten & Wierenga, 1976). The model is refered to as physical non-equillibrium, mobile-immobile(MIM) model. In the MIM model, the liquid phase is assumed to be divided into mobile and immobile regions. Advective-dispersice solute transport only occurs in the mobile region, and the movement of solute between the mobile and immobile regions are described as first-order diffusive mass transfer. The two governing equations of the MIM model for conservative solute are as follows.

$$\theta_m \frac{\partial c_m}{\partial t} = \theta_m D_m \frac{\partial^2 c_m}{\partial x^2} - J\frac{\partial c_m}{\partial x} - \lambda(c_m - c_{im}) \quad (1)$$

$$\theta_{im} \frac{\partial c_{im}}{\partial t} = \lambda(c_m - c_{im}) \quad (2)$$

where; θ is the volumetric water content, J is the solute flux, λ is the mobile-immobile first-order diffusive mass transfer coefficient, D_m is the dispersion coefficient for the mobile region, c_m and c_{im} are the resident solute concentrations in the mobile and immobile regions, respectively. Note that θ is equal to $\theta_m+\theta_{im}$, the sum of the volumetric water content corresponding to mobile and immobile regions, respectively. Parameter β is used to describe the fraction of mobile region, equal to the ratio between mobile and total porosity($\beta=\theta_m/\theta$). Solution to Equations (1) and (2) can be obtained by substituting appropriate inlet and outlet boundary conditions.

3 TEST METHOD

3.1 *Column test device*

Sensor for measuring electrical conductivity was designed to be composed of 4 electrodes with the geometry (or curvature) following the inner wall of the column test. Since the current drawn through the measurement electrodes is very small on the four-electrode array, there is no appreciable buildup of ions at the electrodes and it can operate at very low frequencies without being polarized. In addition, electrode geometry following the inner wall of the column allowed avoiding sample disturbance. The design follows the basics of the four-electrode measurements but the array is directed parallel to the direction of solute transport. Each fan-shaped electrode has a thickness of 2mm; such design ensured sufficient area of contact between the soil and electrodes. The electrodes are placed 3mm apart, which gives a total of sensor thickness of 17 mm. Figure 1 shows a schematic diagram of fan-shaped 4-electrode measuring sensor and column test device. Three conductivity sensors are located at 58.5mm, 200mm, and 341.5mm away from the influent/effluent boundary. The 400mm long, 50mm diameter column is made of acryl to avoid flow of electrical current between the fan-shaped electrodes. In addition, porous stone of 10mm thickness was placed as a diffuser at the influent and effluent boundaries to induce 1-D flow and minimize disturbance in flow through the boundary.

The three electrical sensors are connected to the 4263B LCR meter (Agilent Technologies, Japan) for conductance measurements via channel selector, specially designed and produced for the developed column test device. The channel selector allows measurements at the three different sensors to be made using a single LCR meter by functioning as an electrical bridge. Since electrical measurements can be conducted instantaneously, measurements on sensors E1~E3 can be made at desired time intervals.

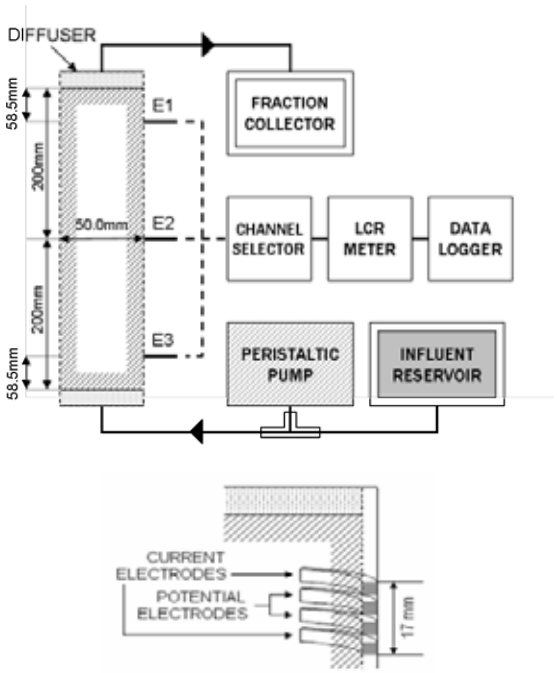

Figure 1. Schematic diagram of the fan-shaped 4-electrode conductivity sensor and column test devices (modified after Kim (2009))

3.2 *Test materials and method*

Silica sand that is commercially available in Korea was used as the material for experimental study. Referred to as Jumunjin sand, it is classified as poorly graded sand(SP) under the Unified Soil Classification System(USCS). The test soils were prepared by washing using deionized water several times prior to oven drying at 100˚C for 24 hours. The soil was thoroughly washed in order to minimize the presence of soluble excess salts which can affect the pore water conductivity. The prepared soil was evenly compacted into four 10cm thick layers into

the column. In order to completely saturate the soil columns, CO_2 purging was performed for 2 hours prior to injecting the saturating solution. The high solubility of CO_2 gas into water enables interconnected pores to be easily saturated. Complete saturation was assumed in all tests conducted. For solute injection tests on soils, DI water was injected as the solution of saturation using the peristaltic pump. In order to induce steady-state flow condition, injection was maintained for more than 48 hours. Such procedure also contributed to minimizing the excess salt remaining in the soil samples.

In order to minimize the uncertainties in data analysis, a simple uniform 1-D steady state solute flow was simulated by injecting non-reactive solute into soil columns. To obtain the solute BTC at the exit boundary, solute samples were collected by using a fraction collector in minute intervals dependent on the volumetric discharge rate. Verification was conducted by comparing the electrical conductivity BTC to the conventional BTC obtained from chemical analysis of effluent samples.

In tracer injection tests on soils contaminated by residual diesel, diesel fuel was trapped in the soil column similar to several methods reported in the literature (Pennell et al., 1993; Dawson & Roberts 1997; Fortin et al., 1998; Dubè et al., 2002). Diesel fuel dyed using Sudan IV was introduced into a soil column at a rate of 0.3 mL/min. Diesel fuel injection was followed by DI water injection at 0.6 mL/min to displace the diesel. Such process continued until no free diesel was collected at the effluent. Note that the diesel was injected and displaced at a high flow rate relative to that of tracer injection test. High rate of diesel injection was aimed at minimizing fingering of the displacement front from the difference in viscosity between DI water and diesel. A possibility of irregular displacement front which may produce undisplaced lenses of diesel was visually verified. In addition, a high rate of flow selected for displacing free diesel was designed to avoid displacement of free diesel during tracer-injection tests which were conducted at a flow rate of 0.3 mL/min.

4 RESULTS AND ANAYSIS

In order to investigate the influence of residual diesel on water flow, Figures 2 and 3 show the BTCs obtained from column tests. BTCs shown as solid lines were fitted BTCs by least-squares analysis and transport parameters were estimated by using the CXTFIT code. The saturation degree of diesel fuel in soil column was about 23.1%. Note that the BTCs are results obtained from identical volumetric discharge. Relative concentrations are plotted against the effective PV time units for a simple comparison. Note that the 1 pore volume for clean sand was 1,059 minutes while that of diesel-contaminated sand was 816 minutes based on effluent BTCs(c(x,t)=0.5). Such values indicate 22.95% acceleration for breakthrough due to residual diesel, are in good accord with the residual diesel saturation of 23.08%. The amount of accelerated breakthrough computed based on bulk soil conductivity BTCs were 17.22%, 31.39%, and 25.94% for sensors E3, E2 and E1, respectively. The amount of accelerated breakthrough is similar for effluent BTC and E1 BTC. However, values from sensors E2 and E3 indicate possibilities of heterogeneity in with depth. Again, such results demonstrate the applicability of multiple BTCs for 2-D analysis. Tendency of earlier breakthrough, tailing and asymmetrical shape is clear in the results of pulse injection tests. These characteristics are usually recognized as indications of heterogeneous flow characterized by a rapid preferential flow through a small fraction of the pore volume (Reedy et al. 1996). Preferential flow is usually related to structural heterogeneities in soil such as interaggregate regions and discrete macropores (Bouma et al. 1977).

The hypothesis of heterogeneous flow is also supported by the inadequacy of the advection-dispersion equation to fit the experimental data. As shown in Figure 4, mobile-immobile representation was found to be more adequate in fitting the experimental data shown in Figure 3(b), especially for effluent BTC. Effluent BTC indicated a significant amount of immobile water fraction at a high mobile-immobile diffusive mass transfer coefficient. Results suggest that the mobile phase was rapidly conducted through the flow domain producing earlier breakthrough and solute remaining in the immobile phase produced tailing of the breakthrough curve.

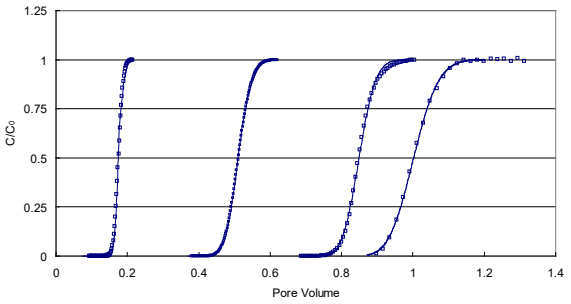

(a) clean soil

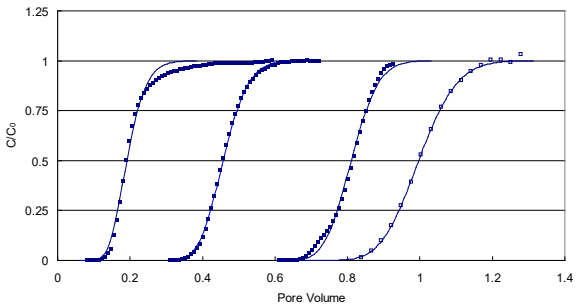

(b) soil with residual diesel fuel

Figure 2. Breakthrough curves obtained from continuous tracer injection test

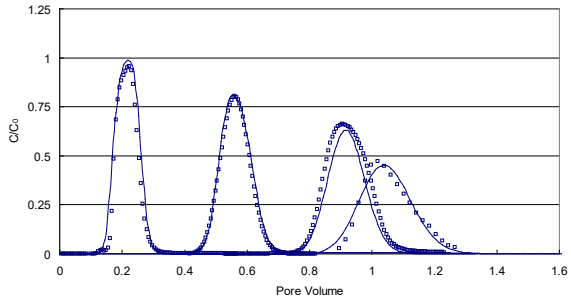

(a) clean soil

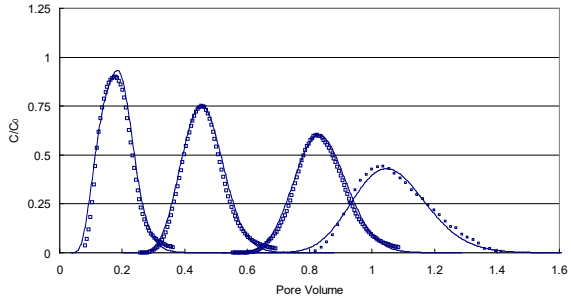

(b) soil with residual diesel fuel

Figure 3. Breakthrough curves obtained from pulse tracer injection test

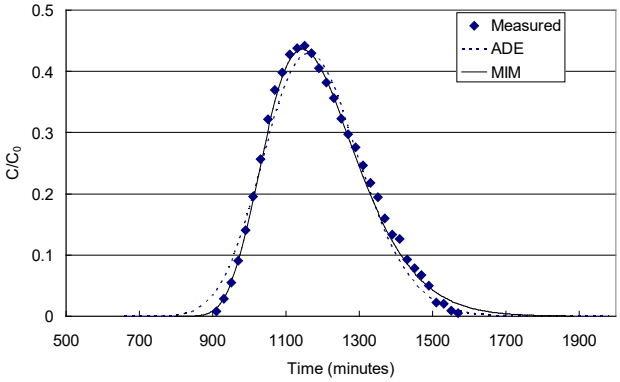

Figure 4. Regression of experimental data on diesel-contaminated soil into MIM model

5 CONCLUSIONS

The electrical conductivity BTC provides an economical and time-effective means of analyzing solute transport through soil since it can be obtained without efforts required in sampling and analysis.

Changes in the electrical conductivity represented as a relative parameter with time gives information about solute transport in both clean saturated soils and saturated soils with residual diesel fuel. This illustrates the advantage of electrical conductivity BTC to monitor solute concentration continuously with time. Electrical conductivity BTCs can provide an effective means of qualitative monitoring on solute transport with longitudinal direction of transport. The hypothesis of heterogeneous flow is also supported by the inadequacy of the advection-dispersion equation to fit the experimental data. The mobile-immobile representation was found to be more adequate in fitting the experimental data.

6 ACKNOWLEDGEMENT

This study was supported by Korea Institute of Ocean Science & Technology (PE99422).

7 REFERENCES

Bouma, J., Jongerious, A., Boersma, O., Jager, A., and Schoonderbeek, D. 1997. The function of different types of macropores during saturated flow through four swelling soil horizons. *Soil Science Society of America Journal* 41: 945-950.

Coats, N.H. & Smith B.D. 1964. Dead end pore volume and dispersion in porous media, *Society of Petroleum Engineers Journal* 4: 73-84.

Dawson, H.E. & Roberts, P.V. 1997. Influence of viscous, gravitational, and capillary forces on DNAPL saturation. *Groundwater* 35: 261-269.

Dubè J.S., Winiarski, T. & Galvez-Cloutier, R. 2003. Effect of the initial soil water saturation on the behavior of a mixed LNAPL and heavy metal contaminated glaciofluvial deposit. *European Journal of Soil Science* 54: 517-530.

Dubè, J.S., Galvez-Cloutier, R. & Winiarski, T. 2002. Heavy metal transfer in soil contaminated by residual LNAPLs. *Canadian Geotechnical Journal* 39: 279-292.

Fortin, J., Jury, W.A. & Anderson, M.A. 1998. Dissolution of trapped nonaqueous phase liquids in sand columns. *Journal of Environmental Quality* 27: 38-45.

Kim, Y.S. 2009. *Contaminant detection and analysis of solute transport in the subsurface using the electrical properties of soil*. Dissertation, Seoul National University.

Lee, J., Jaynes, D.B. & Horton, R. 2000. Evaluation of a simple method for estimating solute transport parameters: Laboratory studies. *Soil Science Society of America Journal* 64: 492-498.

Nkedi-Kizza, P., Biggar, J.W., van Genuchten, Werenga, P.J., Seilm, H.M., Davidson, J.M. & Nielsen, D.R. 1983. Modeling tritium and chloride 36 transport through an aggregated Oxisol. *Water Resources Research* 19: 691-700.

Oh, M., Kim, Y. & Park, J. 2007. Factors affecting the complex permittivity spectrum of soil at a low frequency range of 1 kHz-10 MHz. *Environmental Geology* 51: 821-833.

Oh, M., Seo, M.W., Lee, S. & Park, J. 2008. Applicability of grid-net detection system for landfill leachate and diesel fuel release in the subsurface. *Journal of Contaminant Hydrology* 96: 69-82.

Pennell, K.D., Abriola L.M. & Weber W.J. 1993. Surfactant-enhanced solubilization of residual dodecane in soil columns: 1. Experimental investigation. *Environmental Science and Technology* 27(12): 2332–2340.

Rao, P.S.C., Rolston, D.E., Jessup, R.E. & Davidson, J.M. 1980. Solute transport in aggregated porous media: Theoretical and experimental evaluation. *Soil Science Society of America Journal* 44: 1139-1146.

Reedy, O.C., Jardine, P.M., Wilson, G.V. & Selim, H.M. 1996. Quantifying the diffusive mass transfer of nonreactive solutes in columns of fractured saprolite using flow interruption. *Soil Science Society of America Journal* 60: 1376-1384.

Rinaldi, V.A. & Cuestas, G.A. 2002. Ohmic conductivity of compacted silty clay. *Journal of Geotechnical and Geoenvironmental Engineering* 128: 111-121.

van Genuchten, M.Th. & Wierenga, P.J. 1976. Mass transfer studies in sorbing porous media: I. Analytical solution. *Soil Science Society of America Journal* 40: 473-480.

Geotechnical and Geophysical Site Characterisation 5 – Lehane, Acosta-Martínez & Kelly (Eds)

Experimental study on water content and density effects on dielectric permittivity of selected Victorian soils

A. Orangi, D. S. Langley, N. M. Withers & G.A. Narsilio
Department of Infrastructure Engineering
The University of Melbourne, Parkville, Victoria, Australia

WSP | Parsons Brinckerhoff Engineering Services
Southbank, Victoria, Australia

ABSTRACT: The use of electromagnetic (EM) techniques in site investigations is becoming increasingly common all over the world. Thus, it is imperative to thoroughly understand the effects of soil geotechnical parameters on soil electromagnetic properties. While focused on compaction, this study investigates the effect of dry density, water content and soil type on the dielectric properties of 3 soils from Melbourne (Victoria) at 1 GHz, using Frequency Domain Reflectometry (FDR). Understanding the relationships between soil dielectric properties with geotechnical parameters is a key step in developing correlations. Whilst the real dielectric constant is strongly linked to the volumetric water content, an inversely proportional trend has been found between dry density and the real dielectric constant, presumably affected by the soil specific surface area. Furthermore, based on the experimental data presented herein, the Dobson Soil Mixing Dielectric Model (SMDM) for estimating the real dielectric constant has been modified and improved.

1 INTRODUCTION

1.1 *Dielectric properties of soil*

Electromagnetic wave based measurement techniques rely on changes on dielectric constant or relative permittivity. Dielectric constant κ is a complex number that describes the behaviour of a material when it is subjected to an electrical field and can be represented as described in (Rinaldi & Francisca, 2006):

$$\kappa = \kappa' - j\kappa'' \quad (1)$$

where κ′ and κ″ are the real and imaginary component of the dielectric permittivity and $j = \sqrt{-1}$. The real component κ′ represents the polarisability of the material and it is proportional to the number of dipoles that exist within the material. The out of phase (imaginary) component of permittivity κ'', is in phase with the conductivity σ. Therefore, losses due to polarisation and conduction are measured together by the imaginary dielectric constant. Thus, considering these losses, an effective imaginary dielectric constant can be expressed as (Santamarina, Klein, & Fam, 2001):

$$\kappa''_{eff} = \kappa'' + \sigma/(\omega\varepsilon_o) \quad (2)$$

where $\varepsilon_o \approx 8.85 \times 10\text{-}12$ F/m; ω is the angular frequency; and σ is the electrical conductivity of the sample at very low frequency. At high frequencies:

$$\sigma''_{eff} = \kappa''\omega\varepsilon_0 \quad (3)$$

where σ''_{eff} is the effective electrical conductivity..

1.2 *Dielectric mixing models*

Each phase of unsaturated soils has distinct real dielectric constants: $\kappa' = 1$ for air, $\kappa' = (2-7)$ for soil solid particles, and $\kappa' \cong 80$ for water. Therefore, the average dielectric constant of soils is related to the dielectric constant of the individual phases, their volume fractions, their spatial distributions and their orientations relative to the direction of the incident electrical field. These can be captured by means of mixture models with the simplest model known as the Lichtenecker and Rother Model (LRM):

$$\kappa_{eff}{}^{\alpha} = \sum_i \frac{V_i}{V}\kappa_i{}^{\alpha} \quad (4)$$

where κ_i is the permittivity of phase *i*; V_i is the volume of phase *i*, V is the total volume of the soil; and α is a constant varying from -1 to 1 depending on the geometrical arrangement of the components (Lichtenecker & Rother, 1931). Based on the LR model, Dobson et al. (1985) proposed a semi-empirical model on the basis of measurements covering 5 soil types ranging from a sandy loam to silty clay. This model, known as SMDM, can be used for predicting the real dielectric constant of soils, for frequencies between 1.4 GHz to 18 GHz:

$$\kappa'_{soil} = \left[1 + \frac{\rho_b}{G_s}(\kappa'_s - 1) + \theta^{\beta'}\kappa'_{fw}{}^{\alpha} - \theta\right]^{\frac{1}{\alpha}} \quad (5)$$

which was further adjusted for Low Frequencies (300 MHz to 1.4 GHz) by Peplinski et al. (1995):

$$\kappa'_{soil_{(LF)}} = 1.15 \times \kappa'_{soil} - 0.68 \quad (6)$$

where ρ_b is the dry bulk density g/cm^3; G_s is specific gravity g/cm^3; κ_s' is the real dielectric constant of solid particles; θ is the volumetric water content; κ_{fw}' is the frequency dependent real dielectric constant of free water; $\alpha = 0.65$; and β' = a soil type dependent coefficient defined as:

$$\beta' = 1.2748 - 0.00519\, Sand\% - 0.00152\, Clay\% \quad (7)$$

It can be seen that the dielectric behaviour of the soil matrix is strongly linked to the volumetric water content θ, as confirmed by various experimental studies that suggested empirical correlations between soil dielectric constant and volumetric water content (e.g., Roth, Malicki, & Plagge, 1992; Topp, Davis, & Annan, 1980; Wensink, 1993). These correlations, however, appear to respond more accurately to the conditions that they were originally based upon (e.g., soil type and frequency).

The most widely used empirical correlation is known as the Topp correlation. Topp et al. (1980) has suggested that the apparent dielectric constant κ_a for low loss and nearly homogeneous materials is proportional to the real dielectric constant as:

$$\kappa_a = -76.7\,\theta^3 + 146\,\theta^2 + 9.3\,\theta + 3.03 \quad (8)$$

Very few studies have investigated the impact of density on the dielectric properties of soils. Some studies have reported a proportional trend between the real dielectric constant and dry density for dry samples (Dirksen & Dasberg, 1993; Lauer, Albrecht, Salat, & Felix-Henningsen, 2010; Salat & Junge, 2010).

This paper investigates the effect of compaction on the dielectric properties of different soil types (at 1 GHz) and aims to enhance and develop a better understanding of the effects of dry density (or compaction) on electromagnetic properties of soil.

2 METHODOLOGY

2.1 *Laboratory Testing*

2.1.1 *Soil sample characterisation*

Soil samples were collected from the greater Melbourne region, Australia, encompassing different Melbourne geological formations, which are categorised as Silurian and Tertiary (Newer Volcanic and Brighton Group) formations.

Geotechnical properties of soil samples were determined during the experimental program. Grain size distributions including sieve analysis (Standards Australia, 2009) and hydrometer tests (Standards Australia, 2003a) were conducted to classify the soil in accordance with Unified Soil Classification System (USCS). In addition, standard compaction tests (Standards Australia, 2003b) were performed to obtain the optimum moisture content and the corresponding dry density for each sample. Specific Surface Area for soil samples was estimated based on the correlation suggested in (Ersahin, Gunal, Kutlu, Yetgin, & Coban, 2006):

$$SSA = 0.042 + 4.23\, Clay\% + 1.12\, Silt\% - 1.16\, Sand\% \quad (9)$$

2.1.2 *Soil sample preparation*

To obtain homogeneous samples at specific water contents, an adequate amount of distilled water was added to a batch of oven dried soil based on the amount of dry soil present and then mixed thoroughly. The batch was allowed to equilibrate for at least 24 hours in a sealed container. Distilled water was used to minimise the introduction of any foreign ions to the mixture. Next, different densities were achieved as follows: instead of applying 25 blows per layer (standard compaction test), each specimen was prepared with a different number of blows at a given gravimetric water content. After each specimen was prepared, dielectric measurements were performed (explained in next section) and a small portion was taken out for gravimetric water content measurement by oven drying and subsequently, converted to volumetric water content, which is called water content hereafter in this manuscript. This method was repeated for the subsequent gravimetric water contents up to the saturation point.

2.1.3 *Soil dielectric measurements*

Soil dielectric properties were measured using an Agilent dielectric Slim Form Probe connected to a FieldFox Vector Network Analyser. Before each dielectric measurement, a three step calibration was performed. Then, each specimen was placed on a lab jack and moved towards the probe to minimise any error from cable or probe movements until a penetration of at least 10 mm was maintained. Measurements were conducted and the coefficient of reflection S_{11} was measured and was converted to real dielectric constant at 1 GHz by means of proprietary software (the full discussion of this conversion is beyond the scope this study). Errors associated with the electromagnetic measurements were minimised by 3 repeated measurements in a triangular pattern for each specimen, such that the measurements were representative of the entire

specimen. Predrilling was adapted to all specimens to compensate for the ones which the probe insertion may have been hard otherwise.

3 EXPERIMENTAL RESULTS, ANALYSIS AND DISCUSSION

3.1 *Soil geotechnical properties*

Grain size distribution analysis has revealed that samples are categorised as (locally known) Brighton Group Sand (A), extremely weathered Silurian Mudstone (B) and Basaltic clay (C). Table 1 provides a summary of fine and coarse fractions as well as other parameters including, optimum gravimetric water content w_{opt}, the corresponding dry density $\rho_{dry\ (opt)}$ and the estimated Specific Surface Area A_s.

Table 1. Soil sample characteristics

Sample	**Clay**	**Silt**	**Sand**	**W_{opt}**	**$P_{dry\ (opt)}$**	**A_s**
	(%)	(%)	(%)	(%)	(g/cm^3)	(m^2/g)
A (SP)	0	3	97	9	2.0	—
B (ML)	20	51	29	13	1.8	108
C (CH)	63	29	8	27	1.4	290

3.2 *Soil dielectric properties*

Having prepared the specimens and conducted the dielectric measurements for each soil, dielectric data was grouped based on volumetric water content and dry density. The effect of water content and dry density among other parameters, on soil dielectric properties, could therefore be explicitly investigated. Results of real dielectric constant measurements at 1 GHz frequency were compared against volumetric water content and density. In addition, results of measurements were compared against the SMDM model, whilst the Topp correlation was also examined in predicting the real dielectric constant.

3.2.1 *Real dielectric constant versus water content*

By increasing the volumetric water content, the number of dipoles in a soil matrix increases and this results in more polarisation under an electromagnetic field, hence a larger real dielectric constant (Santamarina et al., 2001). This behaviour is well illustrated in Figure 1 for all 3 samples. However, the rate of these proportional trends is different for each type of soil. This can be explained as follows. As the clay content in the soils increases, the number of water molecules bounded to the soil particle increases for a given water content due to the increase in the soil Specific Surface Area and this will result in a lower real dielectric constant at a given water content. The bound water molecules are tightly held by clay particles and are unable to move freely compared to free water molecules when subjected to an electromagnetic field hence, they exhibit a lower real dielectric constant.

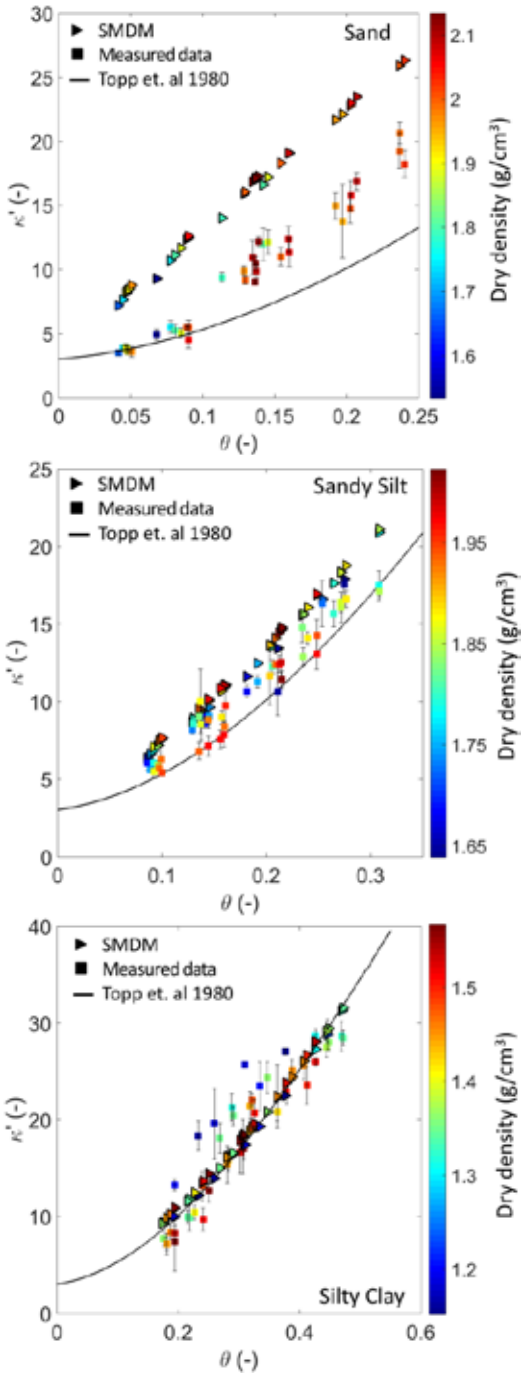

Figure 1. Real dielectric constant at 1 GHz compared against SMDM and Topp et. al 1980

One can see in Figure 1 that the SMDM significantly overestimates the real part over the range of water content tested for the sand sample. For the sandy silt sample, the errors of the overall predictions have greatly reduced, but below approximately 20% water content the differences between the measured and predicted real dielectric constant are larger compared to the errors corresponding to the higher water contents. With the silty clay sample, SMDM predictions for the real dielectric constant are in good agreement with the measured data. Moreover, considering samples with

dry density larger than 1.4 g/cm^3 and water content above approximately 25%, the performance of the model is relatively better compared to the remainder of the data.

For the sand sample, the Toop correlation performs with considerably smaller errors below 10% water content. However, the real part of the dielectric constant deviates from the measurements at higher water contents and is underestimated. With the sandy silt sample, the performance of the Topp correlation has improved significantly, however, the real dielectric constants are generally underestimated especially for samples with dry densities less than 1.9 g/cm^3. Conversely, for dry densities greater than 1.9 g/cm^3 and water contents below 15% the Topp correlation performs reasonably well. For the silty clay sample, Topp predicts the real dielectric constant with a reasonable agreement with relatively small errors for samples with dry densities greater than 1.4 g/cm^3. Nonetheless, for samples with lower dry densities, Topp underestimates the real dielectric constant. A similar performance of Topp correlation was reported in Dirksen and Dasberg (1993) for samples with dry densities greater than 1.3 g/cm^3 where it was found that Topp underestimated the real dielectric constant.

3.3 *Real dielectric constant versus dry density*

As explained earlier in the sample preparation section, through applying different compaction energies at constant gravimetric water contents, samples with different dry densities have been obtained. Furthermore, samples of similar volumetric contents have been regrouped to explicitly investigate the effect of compaction on the real dielectric constant of soil.

Figure 2 shows the change in the real dielectric constant at constant water contents (grouped at approximate 2% increments). In an attempt to explain these results, one must first recognize that water in soil can exhibit in terms of bound and free water. It is suggested by Dobson et al. (1985) that as the dry density increases, the volumetric bound water increases as:

$$\theta_b = \delta \cdot \rho_b \cdot A_s \tag{10}$$

where θ_b is the volumetric bound water content; δ is the thickness of the water molecule attached to the solid particles (~9Å); ρ_b is the dry bulk density (g/cm^3); and A_s is the Specific Surface Area (m^2/g).

The higher A_s, the higher the ability of the soil solid particles to attract water molecules. Hence, at a constant volumetric water content, soils with higher A_s contain more bound water molecules than free water. A proportional trend between dry density and real dielectric constant has been repeatedly reported in the literature, and it has been suggested that through increasing the dry density, more solid particles are being introduced into the matrix and it is assumed that overall real dielectric constant of the matrix will increase accordingly. However, Equation 10 suggests that the effect of surface area also needs to be taken into account. By increasing the dry density of the matrix, for soils with high A_s, the amount of bound water starts to increase accordingly. Since bound water has a significantly lower dielectric constant compared to free water, it is hypothesised that for soils with certain A_s, the effect of density on real dielectric constant is inversely proportional.

In view of the above, the sand sample is first to be examined. The range of densities achieved with the aforementioned method for this sample is from 1.53 g/cm^3 to 2.13 g/cm^3 and the volumetric water content varies between 4.1% and 24%. The tested sand comprises of 97% sand and 3% silt. The A_s associated with the sand is very small compared to the other two samples, hence, it is suggested that the volume of bound water relative to the total volumetric water content is considerably low within this soil matrix. Thus, different compaction energies are not expected to change the proportion of bound to free water significantly and variations are expected to be subtle at a given volumetric water content. It is not expected therefore to find any inversely proportional trend between density and the real dielectric constant for this sample. Thus, as the dry density increases at constant water content (in the absence of the bound water state) and more air voids are being taken up by solid particles, it is expected to see an increase in the total dielectric constant of the matrix. This is due to the larger real dielectric constant of solid particles compared to air (i.e., $\kappa'_{solid} = 4.7 > \kappa'_{air} = 1$).

As Figure 2 shows, for the sand sample, the real component changes proportionally with dry density, however, insignificantly for samples with water content below approximately 15% (zone A). Nevertheless, while approaching the optimum volumetric water content (approximately 20% for this soil), a more obvious increasing trend can be observed (zone B).

For the sandy silt sample, the sensitivity of dielectric constant to the dry density is expected to be larger due to its higher A_s. It can be seen in Figure 2 that the variation of real dielectric constant for a change in dry density from 1.64 g/cm^3 to 2.03 g/cm^3 is indeed more significant for this sample over the previous sand sample.

Moreover, the water content has changed from approximately 8% to 31%. At lower volumetric water contents (i.e., below 10%), the effect of dry density on the real component of dielectric constant is minimal (zone A).

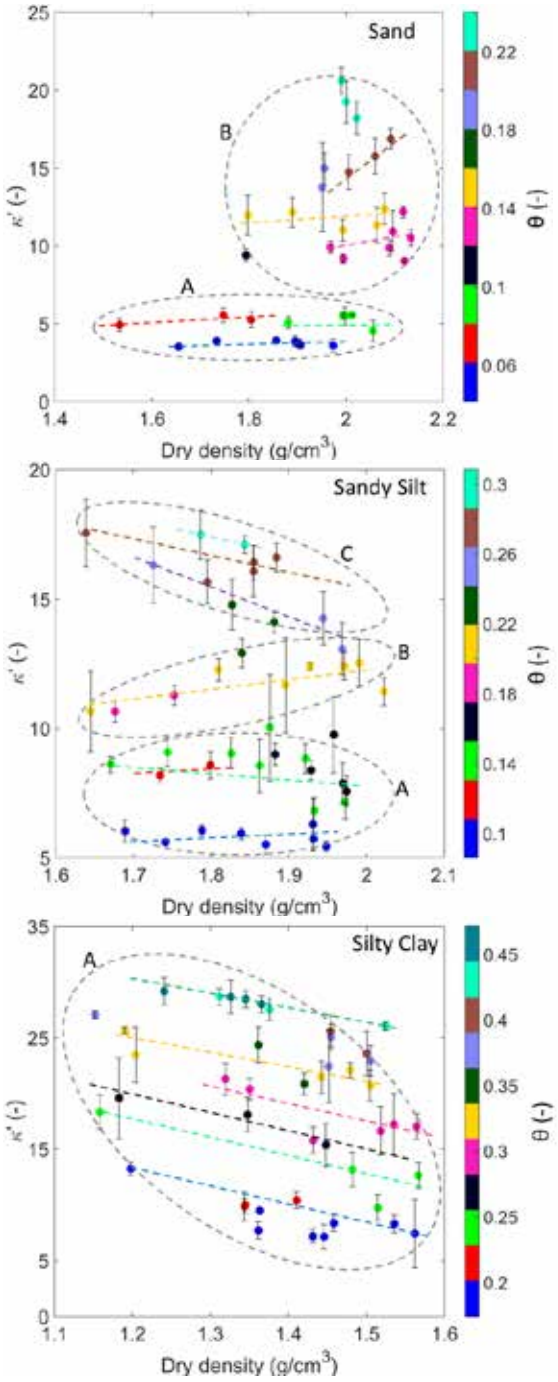

Figure 2. Effect of density on the real dielectric constant (1 GHz) at constant water content (dotted lines to guide the eye)

There is no significant variation for the real dielectric constant against dry density for low water content samples, however, as the volumetric water content increases to approximately 20%, a proportional trend is observed. Still, as the volumetric water content increases above 20% (Zone C), there can be seen an inversely proportional trend between the dry density and the real dielectric constant due to the increase in the number of bound water molecules with increasing dry density.

Lastly, for the silty clay sample, the ranges of variation of water content and dry density are 1.15 g/cm^3 to 1.57 g/cm^3 and 17% to 47% respectively. Different compaction energies have been applied to the clay samples starting from a moist condition, hence, the effect of dry density on the dielectric properties of clay particle below 20% volumetric water content could not be investigated. As Figure 2 shows, there is a clear negative trend between dry density and the real dielectric constant (zone A) for the tested water content range. This behaviour is attributed to the increase in the number of bound water molecules as the dry density increases at a given water content (Equation 10). This effect is dominant over the water content range and more obvious for this soil sample due to the significantly larger specific surface area (see Table 1.)

4 IMPROVEMENT TO THE SMDM MODEL

Based on the preceding experimental results and the discussions, an improvement is suggested to the SMDM model which focuses on the textural coefficient β'. The values for the soil texture coefficient β' were optimised and the following equation is suggested:

$$\beta' = 1.2695 - 0.00279\, Sand\% - 0.00288\, Clay\% \qquad (11)$$

Based on this improved equation, results of the predictions using the improved SMDM model are presented in Figure 3 (as MSMDM).

The predictions of real dielectric constant using the modified model improved significantly for the sand and slightly for the sandy silt sample. Conversely, for the silty clay sample, the performance of the model is improved only for samples with dry density below 1.4 (g/cm^3), however, the errors are larger for samples with higher densities. Further modifications could be implemented to the SMDM model to capture the effect of specific surface area and dry density.

5 CONCLUSION

This study investigated the effect of soil geotechnical parameters on the real dielectric constant of soil samples from 3 different geological formations from Melbourne (Australia). Proportional trends between volumetric water content and real dielectric constant have been observed and are soil type dependent. Although the overall trends observed from experimental data follow the trends predicted by the SMDM model and Topp correlation, discrepancies were observed. The discrepancies seem to be attributed to the limitations of the models in capturing the effects of texture and dry density. Additionally, the empirical correlations are generally based on the original conditions on which they were originally derived upon and might not properly capture other soils/conditions.

An improvement to the SMDM model has been suggested for soils with no to low plasticity.

More importantly, it was found (and hypothesised) that for soils with high Specific Surface Area, density can exhibit an inversely proportional relationship with the real dielectric constant. This effect has only been briefly mentioned in a very limited number of other studies.

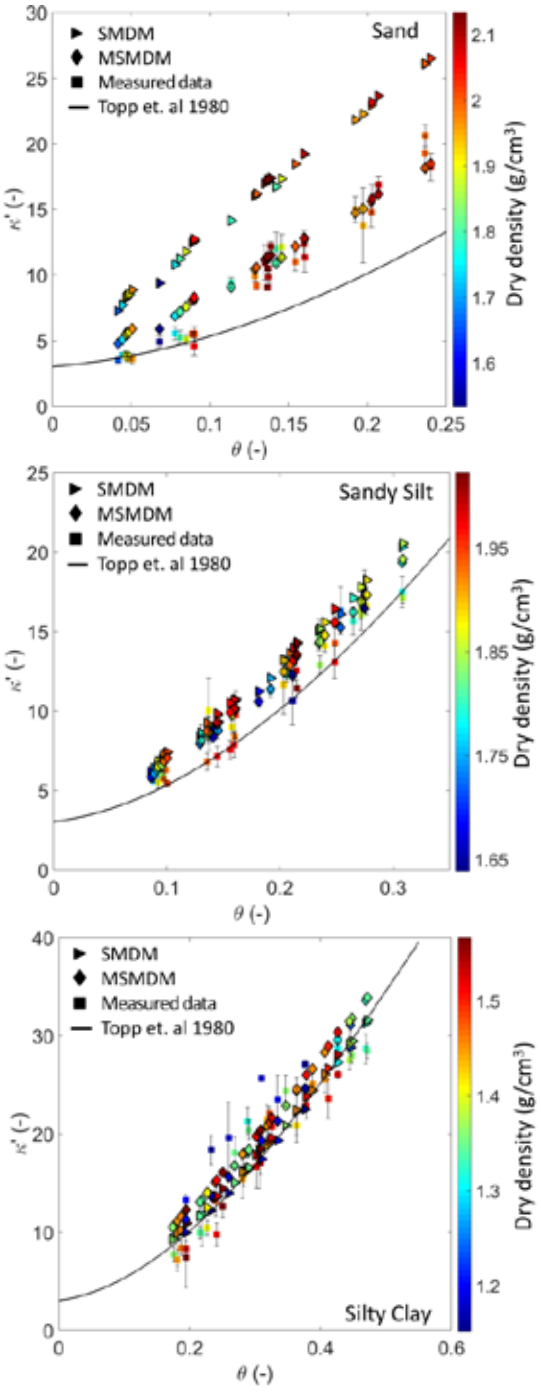

Figure 3. Predicted real dielectric constant at 1 GHz compared against, measured data, SMDM and Topp et. al 1980.

6 ACKNOWLEDGMENTS

The authors would like to thank Geotechnical Engineering (Mr Nick Morgan) and Withers Civil Contractors (Mr Wayne Withers) for providing soils.

7 REFERENCES

Dirksen, C., & Dasberg, S. (1993). Improved calibration of time domain reflectometry soil water content measurements. *Soil Sci. Soc of America Jl, 57*(3), 660-667.

Dobson, M. C., Ulaby, F. T., Hallikainen, M. T., & El-Rayes, M. A. (1985). Microwave dielectric behavior of wet soil-Part II: Dielectric mixing models. *Geoscience and Remote Sensing, IEEE Transactions on*(1), 35-46.

Ersahin, S., Gunal, H., Kutlu, T., Yetgin, B., & Coban, S. (2006). Estimating specific surface area and cation exchange capacity in soils using fractal dimension of particle-size distribution. *Geoderma, 136*(3), 588-597.

Lauer, K., Albrecht, C., Salat, C., & Felix-Henningsen, P. (2010). Complex effective relative permittivity of soil samples from the taunus region (Germany). *Journal of Earth Science, 21*(6), 961-967.

Lichtenecker, K., & Rother, K. (1931). Die Herleitung des logarithmischen Mischungsgesetzes aus allgemeinen Prinzipien der stationären Strömung. phys. *Z, 32*, 255-260.

Peplinski, N. R., Ulaby, F. T., & Dobson, M. C. (1995). Dielectric properties of soils in the 0.3-1.3-GHz range. *IEEE Geoscience and Remote Sensing, 33*(3), 803-807.

Rinaldi, V. A., & Francisca, F. M. (2006). Removal of immiscible contaminants from sandy soils monitored by means of dielectric measurements. *Journal of Environmental Engineering, 132*(8), 931-939.

Roth, C., Malicki, M., & Plagge, R. (1992). Empirical evaluation of the relationship between soil dielectric constant and volumetric water content as the basis for calibrating soil moisture measurements by TDR. *Journal of Soil Science, 43*(1), 1-13.

Salat, C., & Junge, A. (2010). Dielectric permittivity of fine-grained fractions of soil samples from eastern Spain at. *Geophysics, 75*(1), J1-J9.

Santamarina, J. C., Klein, K., & Fam, M. (2001). Soils and waves: particulate materials behavior, characterization and process monitoring, J. *England: John Wiley and Sons Ltd*.

Standards Australia. (2003a). Methods of testing soils for engineering purposes *Soil classification tests - Determination of the particle size distribution of a soil - Standard method of fine analysis using a hydrometer* (pp. 18). Australia.

Standards Australia. (2003b). Methods of testing soils for engineering purposes *Method 5.1.1: Soil compaction and density tests—Determination of the dry density/moisture content relation of a soil using standard compactive effort*. Sydney, NSW 2001, Australia: Standards Australia International Ltd.

Standards Australia. (2009). Methods of testing soils for engineering purposes *Soil classification tests - Determination of the particle size distribution of a soil - Standard method of analysis by sieving* (pp. 9). Australia.

Topp, G., Davis, J., & Annan, A. P. (1980). Electromagnetic determination of soil water content: Measurements in coaxial transmission lines. *Water Resources Research, 16*(3), 574-582.

Wensink, W. (1993). Dielectric properties of wet soils in the frequency range 1-3000 MHz. *Geophysical Prospecting, 41*(6), 671-696.

Geotechnical and Geophysical Site Characterisation 5 – Lehane, Acosta-Martínez & Kelly (Eds)

In-situ soil water content estimation using new capacitive based sensors

A. Orangi, N.M. Withers, D.S. Langley & G.A. Narsilio
Department of Infrastructure Engineering
The University of Melbourne, Parkville, Victoria, Australia

WSP | Parsons Brinckerhoff Engineering Services
Southbank, Victoria, Australia

ABSTRACT: Water content and density measurements are important to many industries. At present, the most common ways of obtaining these parameters are time and labour intensive destructive methods or indirect invasive techniques, such as the nuclear densometer. Additionally, large scale remote sensing measurements are currently being implemented to acquire information such as water content in environmental studies. However, the integration between remote sensing and in-situ methods for soil investigation has not been examined thoroughly. Through an experimental study, this paper investigates the sensitivity of three new cost effective capacitance-based sensors to estimate in-situ soil water content and density non-invasively. Measurements with the sensors have been compared against oven dried water content and real dielectric constant measured with an Agilent 85070E dielectric probe. The capacitance sensors have been proven to detect changes in volumetric water content, with some limitations of contact area and soil composition, but show very low sensitivity to density variations.

1 INTRODUCTION

Quality control of soil compaction is an integral activity in civil engineering, agriculture, hydrology and forestry; with water content and dry density defining the level of compaction. The evaluation of these parameters in subgrades of civil construction projects bears significant influence on the overall performance of the project, with the strength and deformation attributes of geomaterials significantly correlated to the water content and density of the specific soil (Bryson, Jean-Louis, & Gabriel, 2012).

Current methods for the quality control of compaction include the nuclear densometer, sand-cone density apparatus and indirectly from dynamic cone penetrometer alongside the oven-drying method, with the nuclear densometer being the most commonly used method in civil engineering projects (Campbell, Soane, & Ouwerkerk, 1994). However, concerns about the use of hazardous radioactive materials, the cost of the required equipment, and the reliance on soil invasion for the transmission gauge insertion highlight the limitations and potential undesirability of this method (Campbell et al., 1994; Topp, Davis, & Annan, 1980; Yu & Drnevich, 2004). Despite these concerns, the use of nuclear densometers remains the preferred method. Alternative techniques for determining the water content and density rely on milder (non-radioactive) electromagnetic methods which involve the measurements of electrical properties of soils.

The dielectric constant κ of a material can be described as the degree that an electrical charge distributed in the material can be polarised by the application of an electric field (Xu et al., 2014). The dielectric constant is a complex number consisting of a real component κ', representing the electric field storage capacity of the material, and an imaginary component κ'', known as the dielectric loss term representing attenuation and dispersion (Martinez & Byrnes, 2001). Typically, soils are a three phase heterogeneous mixtures comprised of air, solid particles and water which each has values of $\kappa' = 1$, $\kappa' = (2 – 7)$ and $\kappa' = 80$, respectively. Given the significantly higher real dielectric constant of water compared to the other components, soils' dielectric properties are extremely sensitive to water content (Francisca & Rinaldi, 2003).

Furthermore, the capacitance of a material can be described by the following equation:

$$C = \kappa . g . \varepsilon_0 \quad (1)$$

where C = capacitance (F); g = geometric constant; and ε_0 = permittivity of a vacuum (F/m). As can be seen from Equation 1, given a constant sensor geometry, the capacitance is directly proportional to the dielectric constant, thus, the potential exists to capture changes in soil water content using capacitive measurements as proxies for soil dielectric constant. Several methods and relationships therefore exist in relating soil dielectric properties to volumet-

ric water content (θ) with the Topp correlation being the most common relationship (Topp et al., 1980):

$$\kappa' = 3.03 + 9.3\theta + 146.0\,\theta^2 - 76.7\,\theta^3 \quad (2)$$

Relationships such as this tend to be derived from indirect methods such as Time Domain Reflectometry (TDR) and invasive capacitive techniques, which involve sending waves into the ground using probes and measuring the reflected signals to acquire the material's real dielectric constant. These methods are usually invasive, requiring probe insertion.

This paper explores the effectiveness of three new non-invasive capacitance-based sensors to detect changes in soil water content through surface measurements, thus requiring no soil insertion.

2 MATERIALS AND EXPERIMENTAL PROCEDURE

2.1 *Materials*

Disturbed soil samples were collected from three different sites within Victoria as detailed in Figure 1. The three soil samples used in this research are a Brighton Group sand from Caulfield (Sample 1, poorly graded sand), an extremely weathered Silurian mudstone from Doncaster (Sample 2, sandy silt), and a Basaltic clay from Mt. Ridley (Sample 3, silty clay). Thus, the samples come from different Melbourne geological formations.

Table 1 summarises each sample's grain size distributions, the optimum θ, and Unified Soil Classification System (USCS) classification.

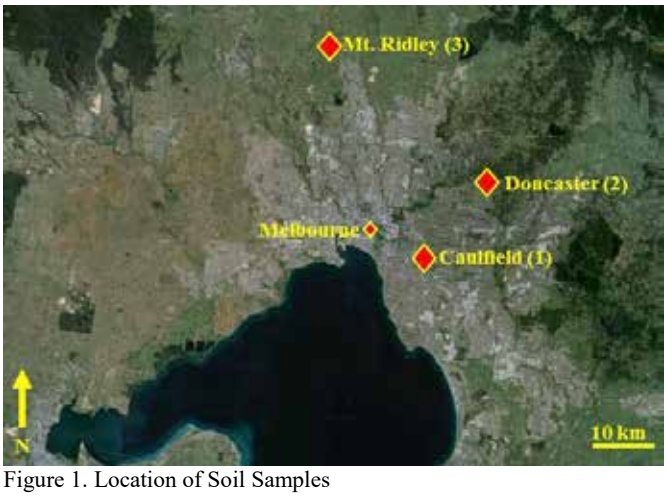

Figure 1. Location of Soil Samples

2.2 *Sensors*

The three new capacitance-based sensors utilised for this research are the AD7746 capacitive sensor board (denoted as "Circular Sensor" in this research), the MPR121 capacitive keypad sensor (denoted as "Rectangular Sensor" in this research) and a PCB capacitive sensor (denoted as "PCB Sensor" in this research). These sensors are Capacitance-to-Digital Converters (CDC) and are used to measure the capacitance of the sample, within the defined geometry of the particular sensor. The Circular Sensor and Rectangular Sensor are connected to an Arduino board, which utilises a C++ platform and transmit the measured capacitance through a USB cable. The capacitance readings have been stored and displayed on Arduino computer programs. Similarly, the PCB sensor transmits the capacitance reading through a USB cable to a CoolTerm computer program.

Table 1. Soil sample characteristics.

Sample	Optimum θ	Clay	Silt	Sand	USCS
	%	%	%	%	(-)
1	18	0	3	97	SP
2	21	20	51	29	ML
3	38	63	29	8	CH

Regarding sensor specifications, the Circular Sensor can measure up to 24 pF capacitance. Furthermore, its architecture features inherent high resolution, linearity (±0.01%) and accuracy (±4 fF factory calibrated), the positive supply voltage can vary between -0.3 V and +6.5 V, and it has an operational frequency of approximately 32 kHz (Analog Devices, 2005). The Rectangular Sensor has 12 capacitance sensing inputs that can measure in a range from 0.45 pF to over 2880 pF capacitance, and also has a positive supply voltage of 1.71 V to 3.6 V operated at 400 kHz (Freescale Semiconductor Inc, 2010). The PCB sensor is a capacitive sensor to measure changes in the capacitance of material. The sensors are shown in Figure 2.

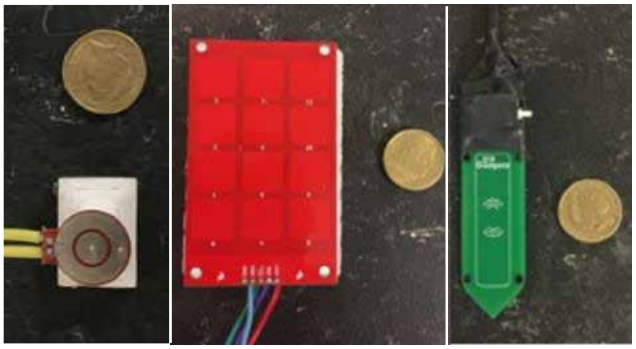
Figure 2. Three New Sensors: Circular Sensor (left), Rectangular Sensor (middle), PCB Sensor (right).

2.3 *Soil sample preparation*

A standard compaction curve was first defined for each soil (Standards Australia, 2003). Once defined, further samples were prepared in bulk at regular gravimetric water content intervals to achieve a range of samples on both the 'dry' and 'wet' side of the optimum water content.

For each of these samples, the soils were portioned into PVC compaction moulds of known di-

mensions, such that a variety of different compactive energies were inflicted on samples of specific gravimetric water contents. This was done using a standard compaction hammer and applying blows in the range of 2.5 to 40 blows per layer. This allowed specimens with different dry densities to be achieved whilst holding gravimetric water contents. The 'exact' gravimetric water content was measured using the oven dried method (Standards Australia, 2005), and dry densities were subsequently calculated. This allowed the gravimetric water contents to be converted to volumetric water content θ (water content hereafter) for the subsequent analyses.

2.4 *Experimental setup and tests*

The general setup of the experiments includes all three sensors connected to personal computers, a dielectric probe, a FieldFox Vector Network Analyser (VNA), a lab jack and a PVC compaction mould containing the soil specimen (to negate any effects the standard metal compaction mould would have on measurements). An example of a typical experimental setup is shown in Figure 3.

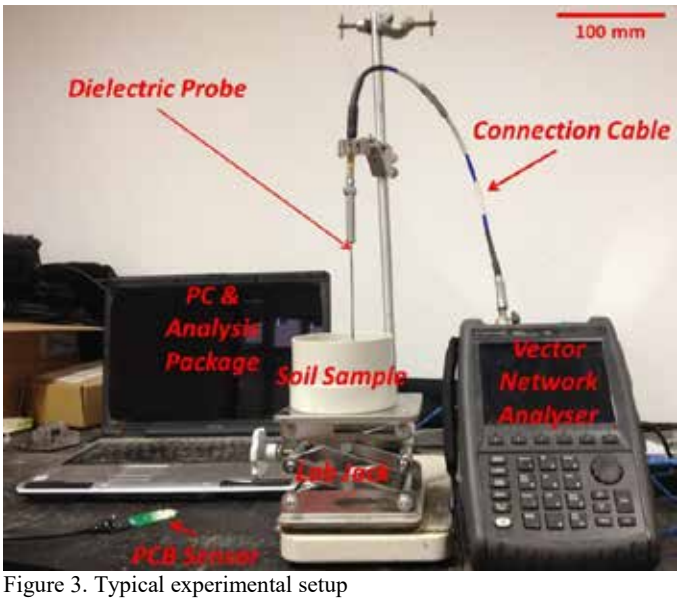

Figure 3. Typical experimental setup

2.4.1 *Circular Sensor test*

Upon trimming the surface of the soil specimen, electric measurements followed. The Circular Sensor test was typically performed first, where the sensor was held against the soil surface until a consistent reading with minimal noise is obtained. Following that, two extra surface measurements were taken with the sensor so that the measurements were representative of the entire surface. This also allowed means and standard deviations to be taken in the analyses to ensure the reliability of results.

2.4.2 *Rectangular Sensor test*

The Rectangular Sensor test was performed exactly the same way as the Circular Sensor, with the exception that a weight was placed on top of the sensor's handle to ensure even and constant pressure against the soil surface when acquiring a reading. The amount of pressure was tested and proved to have no impacts on the sensor readings. Moreover, it is noted that the Rectangular Sensor actually retrieves twelve readings due to having twelve sensing electrodes. For the purpose of this research, the overall mean of these readings has been taken as the Rectangular Sensor reading.

2.4.3 *PCB Sensor test*

Three surface measurements were also conducted with the PCB Sensor. This sensor also operates slightly different to the other two, where a mean reading of the air (which was nearly constant all the time) was taken for calibration. Subsequently, the average of the three surface measurements was subtracted from the air reading, to compute the sensor reading.

2.4.4 *Dielectric probe test*

The dielectric properties of each soil were also measured through a Frequency Domain Reflectometry (FDR) technique, under controlled environmental conditions in a frequency range of 200 MHz – 6 GHz with an Agilent 85070E Slim Form Dielectric Probe. The probe was inserted a minimum depth of 10 mm into each specimen for 3 measurements in a triangular manner to minimise any errors. The probe insertion was facilitated with pre-drilling to compensate for specimens which may have been too hard or dense for the dielectric probe to otherwise penetrate. This probe measurement was always performed last to avoid any disturbance to the soil structure before performing the sensor measurements. The κ' obtained with the probe at 1 GHz through converting the reflection coefficient S_{11} to the real dielectric constant, has been used to compare to the sensors' readings. It is important to note that the operational frequency of the probe is different form the operational frequencies of the sensors however, choosing 1 GHz, is solely for the purpose of investigating the trends between the measurements taken by the sensors and the dielectric probe.

3 RESULTS AND DISCUSSION

The results of experiments for each sensor for all three soil samples are detailed in the following sections. Each sensor reading is plotted using green triangles and a dotted line, whilst κ' obtained from the dielectric probe at a measurement frequency of 1 GHz is plotted with purple squares and an accompanying dashed trend line. All trend lines are fitted as 3rd order polynomials based on the Topp calibration. κ' has also been plotted based on the Topp calibration (Equation 2) with a solid red line.

3.1 *Circular Sensor*

Figure 4 shows the response of the Circular Sensor and the measured dielectric constants for each of the three soil types.

Firstly, for the sand sample, the sensor is able to detect changes in water content accurately for the entire range tested. Up to approximately the optimum water content of 18% the sensor reading pattern obtained follows the measured κ' closely. Above optimum volumetric water content however, the sensor reading pattern plateaus, likely due to it being close to the maximum capacitance that the sensor can measure. The relatively good readings correlation obtained from this soil sample are linked to the smooth surface and homogeneity of the material allowing good contact surface to be maintained. A similar response to the surface roughness has been also reported in Orangi and Narsilio (2015).

For the sandy silt sample, there is an initial decreasing trend from about 8% to 15% water contents for the Circular Sensor reading. The sensor reading values then stay relatively constant till approximately the optimum water content of 21%. Above this value, the sensor reading increases with water content, now reflecting the measured κ' trend line quite well. This may be explained by the variable surface mineralogy of this highly weather mudstone. It is likely that effect of the variable surface mineralogy on the 'dry' side (below optimum volumetric water content) is far more dominant causing the unexpected decreasing trend. However, as water starts to dominate, on the 'wet' side (above optimum volumetric water), the sensor is able to detect changes in water content as the variable surface mineralogy effect is less pronounced.

Lastly, for the silty clay, the Circular Sensor was able to achieve good contact between the soil surface and sensor, despite the 'rough' and uneven soil surface, due to the trimming of the soil specimen at the end of the compaction. Between water contents from 15% to 38% (optimum), the measured capacitance remains relatively unchanged. However, there is a transition point at roughly optimum water content, where the measured capacitance values significantly increase with moisture content, then to decrease, but still showing an increasing trend with moisture in the 'wet' side. Despite the Circular Sensor not being able to pick up changes in water content in the lower range of moisture in the 'dry' side, the sensor displays its ability to detect the optimum moisture content.

3.2 *Rectangular Sensor*

Figure 5 shows the responses of the Rectangular Sensor and real dielectric constant measured with the Agilent probe for each of the three soils as well as the predictions made with the Topp equation.

With the sand sample, it is apparent that there is little change in the measured capacitance from water contents between 4% and 18%. However, at approximately 18% (coinciding with the optimum water content of the soil) there is a noticeable transition point where the measured capacitance values increase continually up to the highest water content tested of approximately 24%. This highlights the ability of the Rectangular Sensor to capture the transition from the 'dry' to 'wet' side of the compaction curve in this particular soil where good contact surface area could be maintained and there were no observable variations in surface mineralogy which was observed with the Silurian mudstone sample (sandy silt). The sensor, however, is unable to accurately detect changes in water content on the 'dry' side.

With the sandy silt, the sensor reading decreases initially with increasing water content in the range of approximately 8% to 16%. Beyond this range, the sensor reading remains essentially constant with no

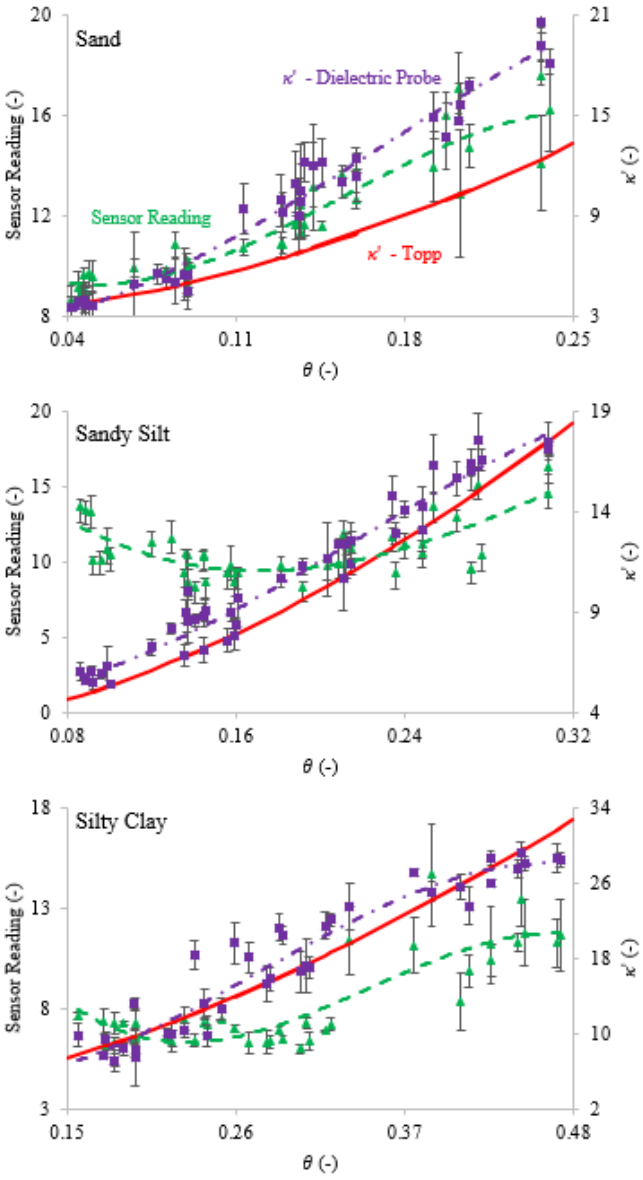

Figure 4. Circular Sensor readings compared against real dielectric constant at 1 GHz and Topp Equation.

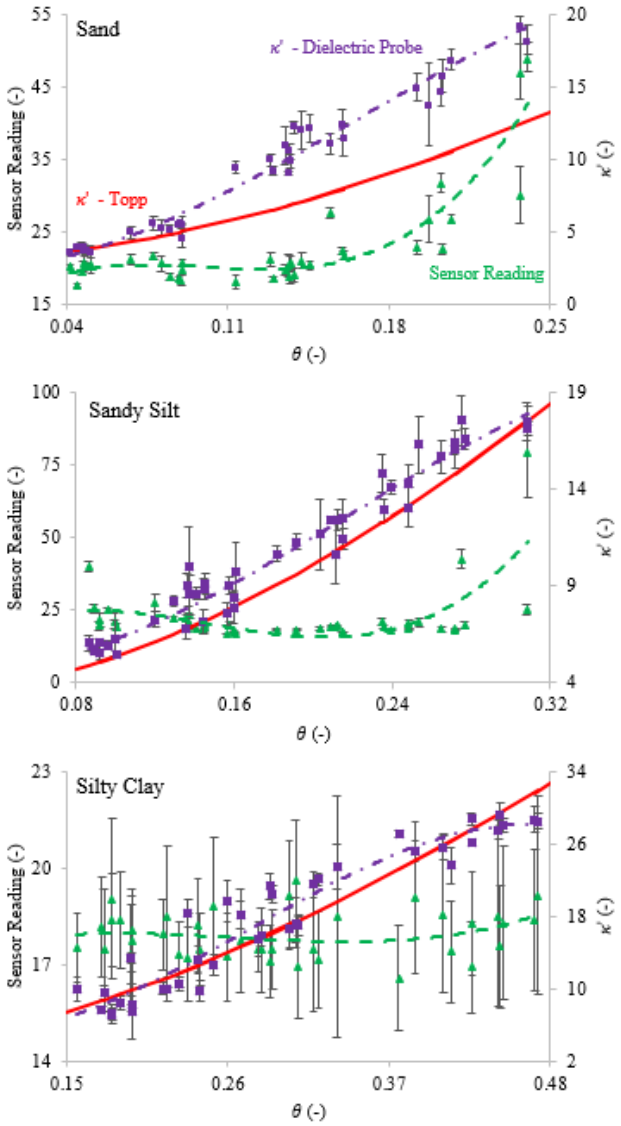

Figure 5. Rectangular Sensor readings compared against real dielectric constant at 1 GHz and Topp Equation.

increasing trend till the last three measurements beginning at approximately 27% which increases significantly. This may again be explained by the observation of the variable surface mineralogy of the Silurian mudstone which was also mentioned in the previous section. For water contents below optimum, this behavior may have more of an effect resulting in the more averaged response detected by the Rectangular Sensor, due to its larger footprint. As the effects of water start to truly dominate the soil behavior in the last three measurements, this variable mineralogy has less of an effect, resulting in a significant increase in sensor reading here. Overall the Rectangular Sensor is ineffective at detecting changes in soil water content and does not follow the same trend as the κ' values obtained with the dielectric probe for the sandy silt.

Turning to the silty clay sample, there is no apparent trend. It is suggested that this is due to the method of testing, where the specimen had to be trimmed after compaction resulting in a visibly 'rough' and uneven surface in the silty clay due to the higher fines content. This 'rough' and uneven surface in combination with the larger footprint of the rectangular sensor, meant it was difficult to maintain complete contact with the soil surface and thus, measurements were affected by more air voids being present between the soil specimen surface and the sensor, than in the actual specimen, hence, disturbing the measurements. This is reflected by the averaged response of the sensor readings, as well as the much higher standard error illustrated here relative to the range of sensor readings obtained.

3.3 *PCB Sensor*

Figure 6 details the response of the PCB Sensor, the measured real dielectric constant and the Topp correlation predictions for each soil sample tested.

With the sand sample, the PCB sensor performs exceptionally well for the range of water contents tested. The general trend of the sensor reading increasing with increasing water content is apparent for all water contents tested for this sample and the $R^2 = 0.97$ for the fitted cubic trend line.

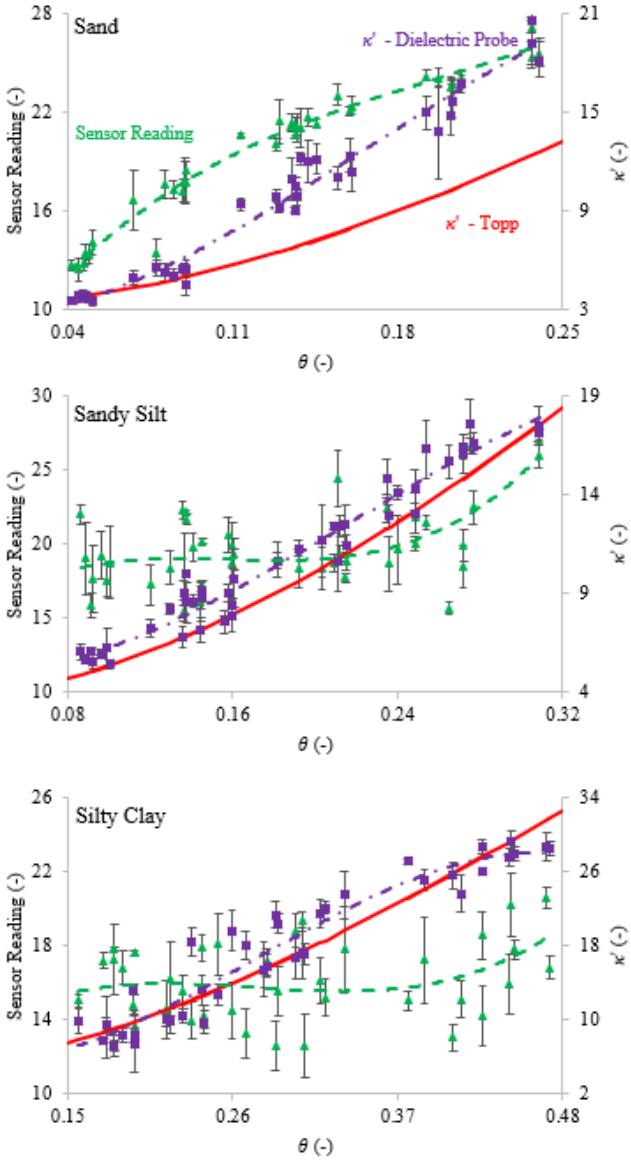

Figure 6. Rectangular Sensor readings compared against real dielectric constant at 1 GHz and Topp Equation.

The PCB sensor reflects the measured κ' here well, supporting the theory that they are directly proportional for a constant geometry. It is proposed that such a good fit is present here due to a good contact surface between the soil sample and the sensor.

For the sandy silt, there is no prominent increasing trend for the sensor readings on the 'dry' side for the range of water contents tested, where an averaged response similar to the Rectangular Sensor is present. However, beyond the optimum water content of 21%, there is a noticeable increase in the sensor reading as it starts to follow the shape of the κ' measurement obtained from the probe.

For the silty clay, there is no increasing trend apparent for the sensor. Similar to the previous scenarios, this can be attributed to the specimens' 'rough' and uneven surface after trimming where a good contact surface between the sensor and soil could not be achieved due to the sensors large footprint.

4 CONCLUSIONS

Based on the experimental work and analysis carried out in this research all three new sensors have shown the ability to detect changes in water content using a non-invasive surface measurement technique, with some limitations and to varying degrees of accuracy. This supports the initial theory that an increase in water content will increase the soil's dielectric constant and correspondingly increase capacitance. This preliminary assessment supports the potential for these fast and cost effective sensors to be developed as an alternative to current methods of estimating in-situ water content.

Comparing the results of the three sensors, the Circular Sensor performs the best across all three soils. It renders the highest R^2 for all trend lines, shows an overall increasing trend throughout (excluding the 'dry' side of the Silurian mudstone) and is most effective sensor due to its smaller geometry allowing good contact surface to be easily achieved. It is recommended that further testing of this sensor is performed for a larger range of water contents and soils.

The Rectangular Sensor appears to be able to detect changes in soil water content, especially on the 'wet' side but is largely limited by its larger footprint. In its current form, it is the least effective of the three sensors. It is recommended that this sensor is further tested with a method where a 'smooth' and even soil surface can be maintained or the sensor is cut into its smaller twelve electrodes to improve contact with the tested soil.

The PCB Sensor shows the best results for the Brighton Group Sand where a good contact surface area could be maintained, however, with an average response for the Silurian mudstone despite a smooth surface being achieved. Moreover, for the tested fine grained soil, the Basaltic Clay, a good contact surface area was unable to be maintained so results were not representative of its effectiveness in fine grained soils. Therefore, it is recommended that the PCB Sensor is further tested in clays where a method is adapted for a smoother contact surface.

Overall, the sensors show the potential to be a fast and cost effective replacement of current in-situ water content estimation techniques but need further research before they are ready to be utilised in field applications.

5 ACKNOWLEDGMENTS

Authors are grateful to Mr Gonzalez-Armayor for coding and calibrating two of the sensors. Geotechnical Engineering (Mr N Morgan) and Withers Civil Contractors (Mr W Withers) provided soil samples.

6 REFERENCES

Analog Devices. (2005). 24-Bit Capacitance-to-Digital Converter with Temperature Sensor (AD7745/AD7746). In Analog Devices (Ed.). USA.

Bryson, L., Jean-Louis, M., & Gabriel, C. (2012). Determination of in situ moisture content in soils from a measure of dielectric constant. *International Journal of Geotechnical Engineering, 6*(2), 251-259.

Campbell, D., Soane, B., & Ouwerkerk, C. v. (1994). Determination and use of soil bulk density in relation to soil compaction. *Soil compaction in crop production.*, 113-139.

Francisca, F. M., & Rinaldi, V. ı. c. A. (2003). Complex dielectric permittivity of soil-organic mixtures (20 MHz-1.3 GHz). *J. of Environmental Engineering, 129*(4), 347-357.

Freescale Semiconductor Inc. (2010). MPR 121 Proximity Capacitive Touch Sensor Controller.

Martinez, A., & Byrnes, A. P. (2001). *Modeling dielectric-constant values of geologic materials: An aid to ground-penetrating radar data collection and interpretation*: Kansas Geological Survey, University of Kansas.

Orangi, A., & Narsilio, G. A. (2015). *New capacitive sensor for in-situ soil moisture estimation*. in Manzanal and Sfriso (Eds), XV Pan-American Conf. on Soil Mechanics and Geotechnical Eng., Buenos Aires, Argentina. pp. 422-429.

Standards Australia. (2003). Methods of testing soils for engineering purposes *Method 5.1.1*. Sydney, NSW 2001.

Standards Australia. (2005). AS 1289.2.1.1: Methods of testing soils for engineering purposes - Soil moisture content tests -- Oven drying method (standard method) (pp. 3).

Topp, G., Davis, J., & Annan, A. P. (1980). Electromagnetic determination of soil water content: Measurements in coaxial transmission lines. *Water Res. Res., 16*(3), 574-582.

Xu, J., Logsdon, S. D., Ma, X., Horton, R., Han, W., & Zhao, Y. (2014). Measurement of Soil Water Content with Dielectric Dispersion Frequency. *Soil Science Society of America Journal, 78*(5), 1500-1506.

Yu, X., & Drnevich, V. P. (2004). Soil water content and dry density by time domain reflectometry. *J. of Geotechnical and Geoenvironmental Engineering, 130*(9), 922-934.

Geotechnical and Geophysical Site Characterisation 5 – Lehane, Acosta-Martínez & Kelly (Eds)

Site characterization for a new refinery in a disposal area for bituminous residue

B. Pasqualini, E. Nicotera, A. Liberati, R. Marcellini

Technip, Rome, Italy

P. Ascari & R. Galbiati

Studio Geotecnico Italiano, Milan, Italy

ABSTRACT: This paper presents and discusses results of the first 25 weeks of monitoring on trial embankments aimed to obtain parameters for foundation design for an industrial development. The area (60 ha) is covered by a thick (2÷6 m) layer of a material denominated "pitch", constituted by a mix of natural soil and residual bituminous material from past industrial processes. The design involves the construction of an embankment, 3÷4 meters thick, acting as a capping, and avoiding excavations and dewatering in the contaminated soil. For the estimate of parameters for foundation design, it has been deemed unrealistic to use the traditional correlations with the most common in-situ tests. Reliability of laboratory tests to estimate site behavior is also questionable. Hence, a monitoring system of three trail embankments has been built on an area (about 30 m width) that is reasonably representative of the stress increase in the operating conditions.

Development of industrial site utilizing neighboring areas generally represents a cost-effective and practical solution. However, it happens sometimes that areas nearby existing industrial facilities present severe environmental problems, especially in light of the existing Laws and Standards, which have become more stringent meantime. However, if the removal of such materials is not required by current Laws and Rules and it is impracticable or very expensive, the left-in-place solution, providing that environmental, health and safety countermeasures are taken, in compliance with local Laws, becomes attractive and viable. This is the case of the site in question, which has been used, through the decades, as disposal site for bituminous materials, mixed with the natural soil on site in various and uncontrolled percentages and methodologies.

The actual thickness of this layer of "pitch" material is ranging from 2 to 6 m, as an average. Its consistency range from relatively firm material (where the pitch has been mixed with high percentages of existing natural soils, constituted by silty sands and sandy silts), to almost "fluid" state, where very little, if no mixing at all, has been carried out. The pitch material overlies weathered limestone, becoming relatively intact at depth.

The basic project includes a capping of a clean, coarse grained material, 3÷4 m thick. In addition to the function of capping, this solution reduce issues related to future excavation/dewatering for foundation and underground services installation. The basic design problem related to this solution is the assessment of the potential settlement due to the compressibility of "pitch" material. This also defines the need and governs the design of soil improvement methods, and, in some case, requires the use of piles as foundation solutions.

Considering the peculiarity of the behavior of such materials, it has been concluded that the usual correlation between deformability parameters of natural soils and results of in situ tests (such as SPT, CPT or other) would results unreliable for the relevant case. Even more questionable would be the adoption of laboratory testing for the scope, involving some tricky problems related to the "undisturbed" sampling of this material and to the representativeness of the sample behavior with respect to the site conditions. In addition, the required duration of tests, that would unavoidably consider the expected "viscous" behavior of this "pitch", constitutes severe limita-

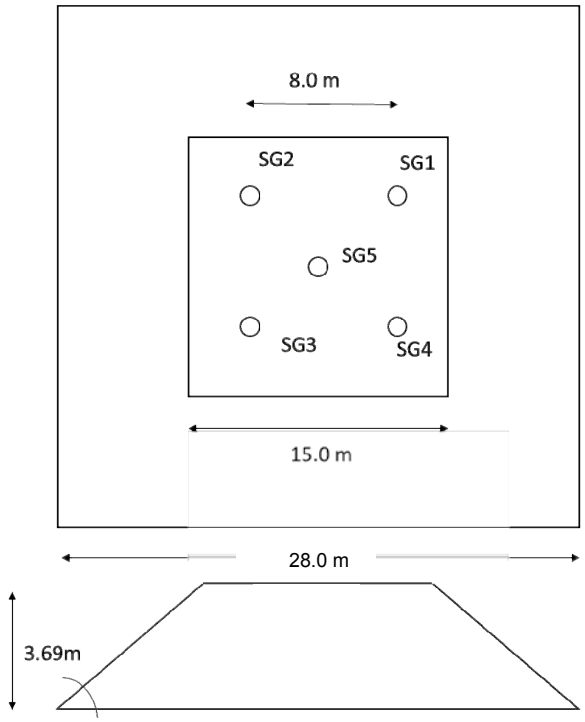

Figure 1. Plan arrangement of the settlement plates and typical cross section.

tions of this approach.
Owing the above, it has been decided to investigate the settlement behavior of this material erecting three trail embankments, having an height of in the range 3.5 to 3.7 m, and a square base of about 27 m. Adopting a slope of about 30°, the top of the embankment resulted in approximately 15*15 m in plan.
Under this conditions, it is reasonable to consider that the stress increase, in the centre of the embankment, is constant through the depth of the pitch material, even considering its maximum thickness of 6 m, such that the settlement of the centre of the embankment are representative of the effect of the construction of design final fill.

At the base of the embankment, 5 settlement plates have been installed, as shown in Figure 1, where a cross section of a typical embankment has been reported.

During embankment construction, the density was checked, indicating an average unit weight of about 17.5 kN/m3. The applied stress is therefore of about 65 kPa, that is considered as representative of the stress increase due to the design fill construction.

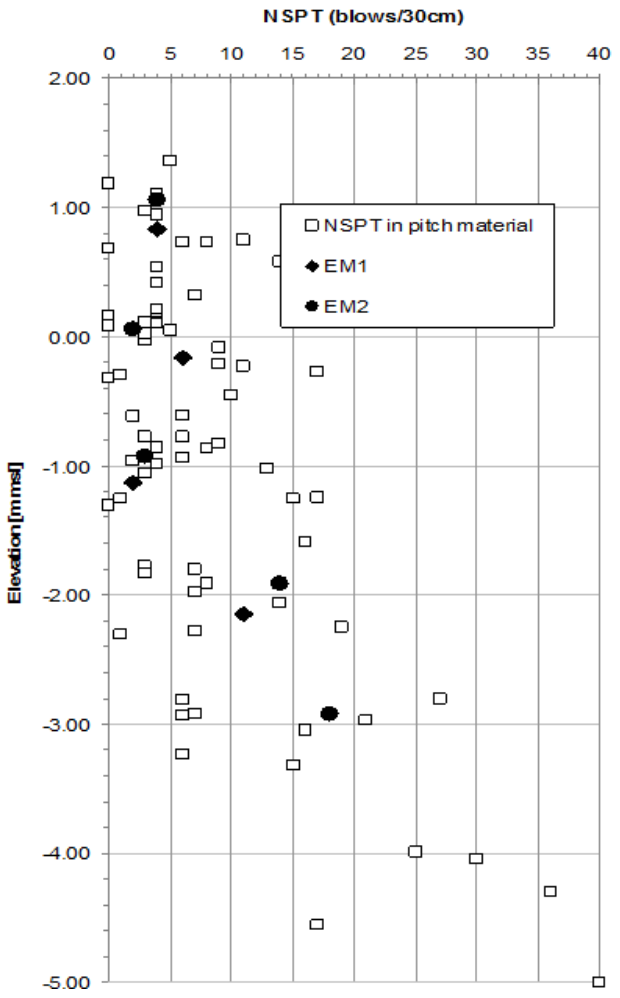

Figure 2. Results of SPT tests in the Pitch area and under EM1 and EM2.

1 RESULTS OF "TRADITIONAL" SITE INVESTIGATIONS

1.1 *SPT tests*

Figure 2 shows the results of the SPT tests carried out in the whole Pitch area, relative to about 27 boreholes, carried out in the pitch material only. Ground level in the area is ranging from 1.5 to 2.5 m msl.

Also reported in the figure are the results of the SPT carried out in the boreholes beneath embankment 1 and 2 (EM1 and EM2). Embankment 3 has been constructed on the area with very small thickness of pitch, and no SPT tests are available.
Maximum thickness of very soft pitch, having SPT of less than 5blows/30 cm, are in the order of 2-4 m. As can be seen, the general pattern of NSPT indicate a fairly tendency of increasing with depth, therefore suggesting a "soil-like" type of behavior.
As can be seen, the conditions found beneath the EM1 and EM2 can be considered as representative as a reasonably "lower bound" condition of the site, with thicknesses of soft pitch material in the order of 2.5 to 3.5 meters.

The estimate of constrained modulus in soft soils on the basis of SPT can be carried out according to Stroud (1974), even it has been recognized during recent decades that these relationships lead to remarkable approximations (see for example Kulhawy and Mayne, 1990). In addition, these relationships do not allow for a definition of the development of settlements vs. time.

Using Stroud, and a multiplier coefficient of SPT equal to 5, one could obtain constrained modulus in the order of 1-2 MPa, for the lowest values of SPT (less than 5blows/30cm). This still leave great uncertainty in the estimate of settlement, in addition to give no information regarding the development of settlement during the lifetime of the structure.

1.2 *Flat dilatometer tests*

At three location beside the embankments 1 and 2 (EM1 and EM2), denominated A, B and C, flat dilatometer (DMT) have been carried out through the thickness of the pitch material. Results are reported in Figure 3, in terms of dilatometer modulus Ed as a function of elevation (ground level shall be taken at an elevation of +2 m msl, as an average).

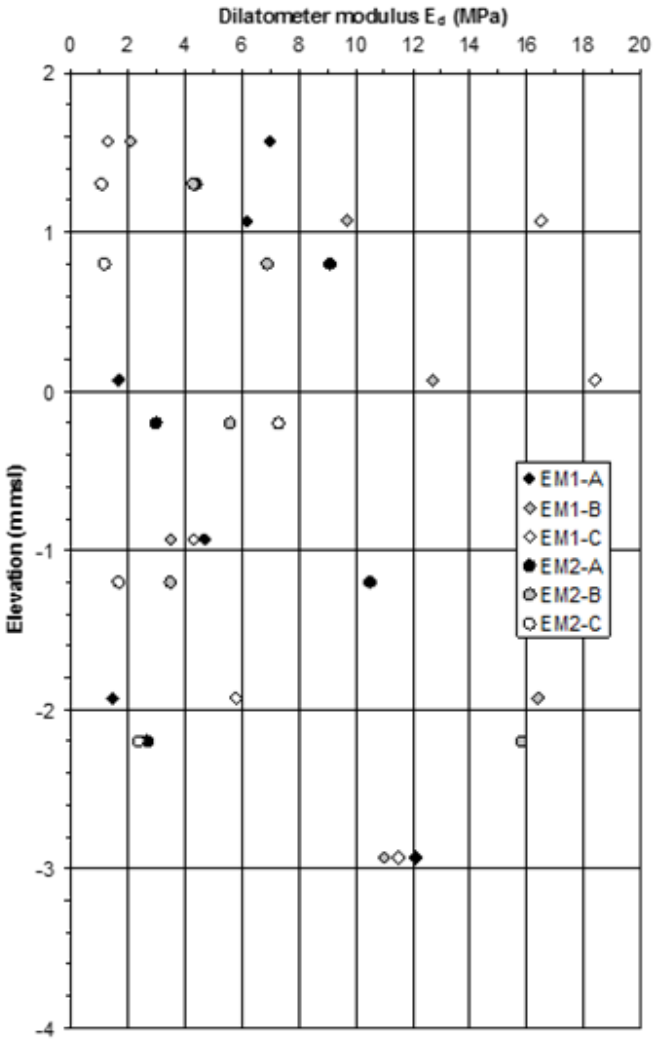

Figure 3. Results of DMT tests under EM1 and EM2.

For the reasons already discussed in the introduction, it is considered that the adoption of the usual correlation between the results of the DMT tests and the deformability parameters to be adopted for design (such as those proposed by Marchetti et al. (2001)) is questionable for the relevant location. It shall however be noted that results indicate that an interpretation using the correlation recommended for clayey soils gives values of constrained modulus M of few MPa, that shall be considered as reasonably representative of the expected values of this peculiar material. However, it shall be kept in mind that the long terms deformability could be of major importance for the settlement estimate at this location, and that DMT interpretation does not consider this contribution.

1.3 *Plate Loading Test*

Under the embankment EM1, a Plate Loading Tests (D=600mm), has been carried out, showing the result presented in Figure 4. Inferred operative Young modulus between 100 and 225 kPa is in the order of 5÷6 MPa. As it will be discussed later, however, this value of the modulus do not incorporate the "long term settlement" (due to evident practical restriction in time for the conduction of in situ tests), and therefore the above values of modulus cannot be taken as a safe estimate of the operative parameters for foundation design.

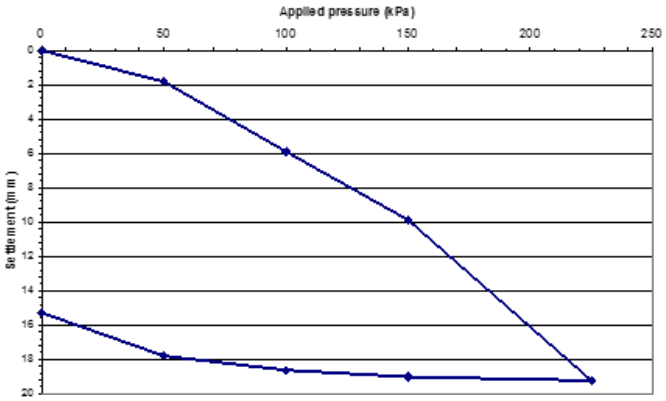

Figure 4. Results of PLT D=600mm under EM1.

As can be seen, the settlement recovery upon unloading is very small, indicating that a remarkable yielding of the pitch material took place.
Similar results have been found at other locations, showing different values of Young modulus, but all showed a very small recovery upon unloading.

2 EMBANKMENT SETTLEMENTS

Figure 5. Picture of trial embankment

Figure 5 shows a picture of one of the embankments at the end construction.
Figures 6 and 7 show the settlements of the various plates installed beneath EM-1 and EM-2. Settlement monitoring started immediately after the end of the construction of the embankment. Therefore, the "immediate" settlement has not been measured.
In relation to the observed pattern of the settlement vs time, the following is noted:

– Embankments 1 and 2 are located in similar soil conditions, i.e. with pitch material with low consistency (i.e. NSPT≤ 5 blows/feet) in the order of 2.5÷3.5 m thickness. Reasonably, they also show similar results, being the maximum settlement in the order of 65 to 70 mm.

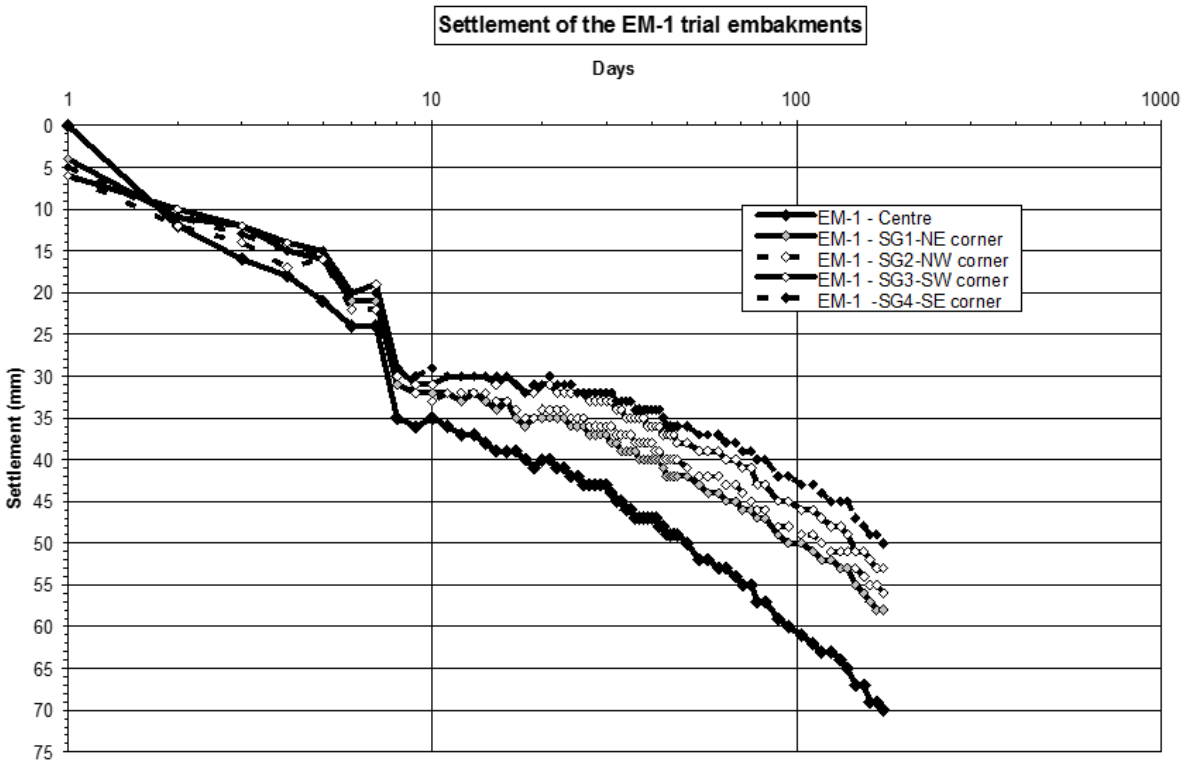

Figure 6. Settlement records of EM-1.

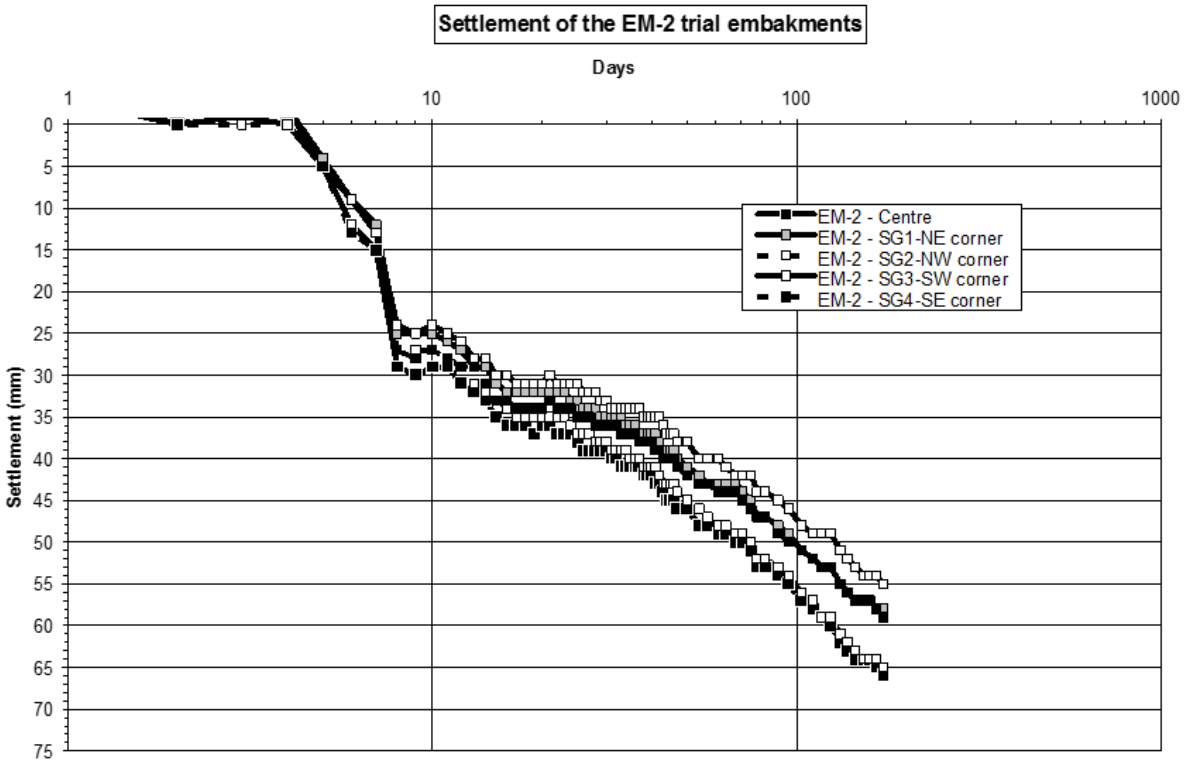

Figure 7. Settlement records of EM-2.

- Settlement vs time curves for EM1 and 2 show two different slopes: in the first part, immediately after the end of construction (about 10 days), settlement rate is relatively fast and irregular. In both cases, the settlement of the centre is equal to about the half of what measured up to now. It can be assumed that these settlements shall be interpreted as being mainly dominated by the "consolidation" component, it the sense of a rearrangement of the structure of the material due to the induced change in effective stress.
- About 10 days after, the settlement curves show a more regular pattern. It is supposed that this second part is mainly governed by the viscous compressibility of the pitch material.
- The records show a tendency of an acceleration of the settlement rate with log of time, for all points. This is consistent with found by Soleimanbeigi et al. (2014), A.,Soleimanbeigi and Tuncer (2015), and by Viyanant et al (2007), during the execution of oedometer tests on bituminous material mixed with sand or fly ashes, and on recycled asphalt shingle.
- Also, data suggest that the slope of the curve is lower for corner points, where the stress increase is also small. This is also consistent with the aforementioned laboratory findings, that indicate that the value of $C\alpha\varepsilon$ (where $C\alpha\varepsilon = \Delta\varepsilon/\Delta\log t$) is dependent on effective stress level.
- As expected, the settlement at the center is greater than the ones at the corners. This is certainly true for EM1, while for EM2 the NW corner settled almost identically to the center. This is possibly due to a particularly unfavorable soil condition at that location.

Based on the above, it can be assumed that the "viscous" component of the settlement is the remarkable part of the settlement. Actually, not being recorded the "immediate" settlement upon construction, it is not possible to establish the actual percentage with respect to "consolidation" process. However, the absolute value of these settlements, after 200 days from the end of construction, is equal to 35 mm at the centre for both embankments, showing possible increasing in settlement rate in the *s-log t* plot.

Even if these findings are consistent with literature data, it shall be considered the peculiarity and variability of the soil condition at the relevant site, and the differences with the typically carefully controlled conditions of the laboratory. Therefore, this tendency shall be confirmed by additional monitoring data relative to longer period of observation.

For what design considerations are concerned, it shall be considered that, in the engineering practice, a limit of 25 mm is usually taken as an allowable limit for the "post-construction" settlement (i.e. the settlement that the structure experiences during its lifetime).

It can be observed that the settlement occurred in the first 200 days after the end of the construction of the embankments already exceed this limit. If this tendency will be confirmed by additional data, this involves considerable design consequences, and in particular:

- the most loaded structures will require the support of foundation piles;
- some smaller and ancillary structures, or other structures that typically accept higher settlements (e.g. steel tanks), could be founded on improved ground (for example, installing stone columns);
- the estimate of the long-term settlement of the platform can determine the need or not for soil improvement under areas of remarkable extension, such as those occupied by roads, paved areas and storage areas. For these areas, it will be then decided whether to accept the estimated settlement, possibly providing occasional interventions aimed at the preservation of the functionality of the area, or if a soil improvement is required, with a dramatic increase in foundation costs.

It is finally observed that under no circumstances this observed behavior would have been reasonably predicted by the usual method methods of investigations.

3 CONCLUSION

The monitoring of the settlements of two embankments, 3.7 m, built on top of a layer of material constituted by a mix of soils (sands and silts), and bituminous wastes, 5 to 6 meters thickness, overlying stiff limestone, indicate a remarkable component of a "viscous" settlements.

After 200 days from the end of construction, the total measured settlements is in the order of 65-70 mm, half of which is reasonably attributed, on the basis of the pattern of the log t vs settlement plot, to a "viscous" component. Settlement rate in the s vs. log t plot shows some sign of increasing with time, supporting literature findings coming from laboratory tests.

Practical implication of such amount of settlement, and the pattern of settlement in time, are dramatic in the definition of the foundation works, and soil improvement, in the light of the use of this area for industrial facilities development.

The area of the embankments has also been investigated with SPT tests, PLT's and DMT tests. Values of deformability parameters obtainable from these tests, using the available correlation in the literature, where not able to predict the actual behaviour of the embankment, with particular reference to the amount of settlements in the long-term conditions.

Therefore, in the relevant case, only the monitoring of these settlements, for a remarkable period of time, can give reliable and useful indications regarding foundation design.

4 REFERENCES

Kulhawy, F.H. and Mayne, P.W. 1990. *Manual on estimating soil properties for foundation design*. New York: Cornell University, Geotechnical Engineering Group, Ithaca, EL-6800, Research Project 1493-6

Marchetti, S., Monaco P., Totani, G. and Calabrese, M. 2001. The Flat Dilatometer Test (DMT) in soil investigations. A Report by the ISSMGE Committee TC16. *Proceedings 2nd International Flat Dilatometer Conference.*

Soleimanbeigi, A., Tuncer, B.E. and Craig H.B. 2014. Creep response of recycled asphalt shingles. *Can. Geotech. Jou.* Vol.51, 103-114.

Soleimanbeigi, A. and Tuncer, B.E. 2015. Compressibility of recycled materials for use as highway embankment fill. *J. Geotch. Geoenviron.Eng,* 2015, Vol.141, no.5.

Stroud M.A. 1974. The standard penetration test in insensitive clays and soft rocks. *ESOPT. Proceedingsof European Symposium on Penetration Testing.* Stokholm: National Swedish Buildng Research

Viyanant, C., Rathje, E.M., and Rauch, F.A. 2007. Creep of compacted reclyced asphalt pavement. *Can. Geotech. Jou.* Vol.44, 687-697.

Geotechnical and Geophysical Site Characterisation 5 – Lehane, Acosta-Martínez & Kelly (Eds)

Influence of periodic hydrocarbon contaminated bentonite on strength and settlement characteristics of stone column

M.V. Shah & H.C. Chokhawala
Applied Mechanics, L.D. College of Engineering, Ahmedabad-380015, India

ABSTRACT: Many coastal areas (marine soils) is largely facing oil/gas spillage which leads to hydrocarbon contamination of this soils. With period of time this hydrocarbon creates major changes in soil engineering properties. Present research is attempt to study the geotechnical properties of hydrocarbon contaminated bentonite (Less expansive) using singular and group of stone columns. Experimental work is contingent on IS 15284 (part-1) to evaluate the settlement response of stone column in 3% and 6% artificially hydrocarbon contaminated calcium bentonite clay as single (Unit cell) and in a group of column (triangular pattern). Compressibility characteristics of stone column and improved shear strength of soil mass is major concern of this research work. Overall results depicted that there is major influence of periodic hydrocarbon contamination on compressibility characteristics of soft clays and can be sufficiently reduced by infusing stone column.

1 INTRODUCTION

Hydrocarbon soil contamination is very common in marine clays. Petrochemicals, hydrocarbons (oil spills), are extensively liberated onto the surrounding soil and get penetrated into the deep ground soil further affecting its physico-chemical properties. This necessitated the use of land, which has weak strata, wherein the geotechnical engineers are challenged by presence of different problematic soils with varied engineering characteristics. Many of these areas are covered with thick soft marine clay deposit, with very low shear strength and high compressibility.

Several researchers have worked on stone column by varying the spacing between column, length of column, diameter of column, different materials of column and also varying of surrounding soils condition like soft soil to fine sand and layered soils. Some has also reinforced stone column by different geosynthetic materials. Very few work has been done to improve hydrocarbon contaminated soft clays by stone column.

In experimental approach, Hughes and Withers (1974) carried out series of model tests in normally consolidated clay. The test results indicated that ultimate capacity of stone column was governed primarily by the maximum radial reaction of the soil against the bulging and the extend of vertical movement in the stone column was limited to about 4 times the diameter. Shankar and Shroff (1997) conducted experimental studies to study the effect of pattern of installation of stone columns and showed that triangular pattern seems to be optimum and rational. Madhav (2000) presented an overview of recent contributions for the analysis and design of stone columns. Different equations available in the literature for finding bearing capacity and settlement of stone column improved ground have also being given. Aimbly & Gandhi (2007) carried out several test by varying spacing between column, shear strength of soft clay and loading pattern. Result observed that by increasing spacing and decreasing shear strength of column axial load carrying capacity is decreasing. Tandel & Solanki (2012) tested performance of stone column with and without geosynthetics and result showed that with reinforcement stone column axial load carrying capacity is increased by two folds and in that role of different geosynthetic had also played a vital role in the performance of stone column.

2 EXPERIMENTAL INVESTIGATIONS

Following objectives are conducted in present work.

1.) To evaluate Index and Engineering properties

of non-contaminated and periodic hydrocarbon contaminated calcium bentonite clay.

2.) To evaluate the axial load carrying capacity of stone column in Non-contaminated clay, 3% and 6% hydrocarbon contaminated clay.

3.) To evaluate the improved shear strength of ground after infusion of stone column by means of van shear test.

Accordingly two type of test were carried out in the large size oedometer of different size (d=250mm & d=600mm). For single column and group of three column in triangular pattern.

2.1 Experimental set-up

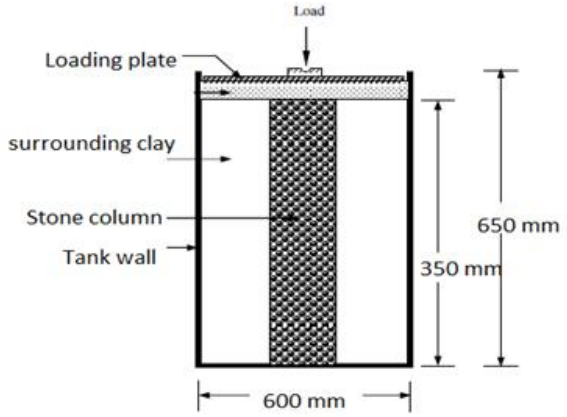

Figure 1 Schematic diagram of stone column arrangement

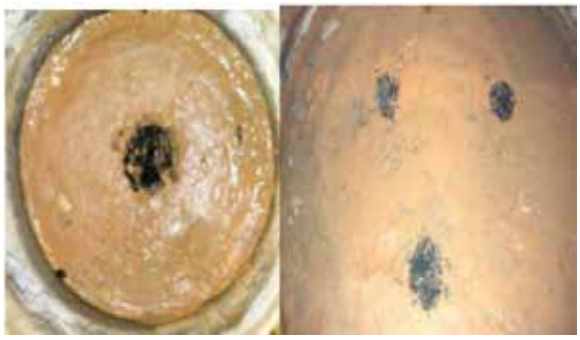

Figure 2 Installation pattern of stone column

All experiments were carried out on a 50 mm diameter stone column surrounded by soft clay in cylindrical tanks of 650 mm high and a diameter varying from 250 to 600 mm to represent the required unit cell area of soft clay around each column assuming triangular pattern of installation of columns. For single column tests the diameter of the tank was taken 250 mm and for group tests on 3 columns, 600 mm diameter was used. Tests with entire area loaded were used to study the stiffness of improved ground.

2.2 Test set-up

The stone column was extended to the full depth of the clay placed in the tank for a height of 350 mm so that *l* /*d* ratio (length of the column/diameter of the column) is a minimum of7, which is required to develop the full limiting axial stress onthe column (Mitra and Chattopadhyay 1999). Vertical stress wasapplied either over the entire tank area. The loading pattern and displacement observation pattern was thoroughly follow IS: 15284 Part-1 (2003).

Tests were also carried out on a group of three columns arranged in a triangular pattern where the clay area corresponding to an equivalent area of three unit cells is represented by the tank area as shown in Fig. 2 to compare the behaviour with a single column and to check the stress distribution between stone column and clay. The load was applied through a 16 mm thick wooden plate to ensure negligible structural deformation.

2.3 Properties of material

Three basic materials are used in the testing program. Non-contaminated calcium bentonite, Hydrocarbon contaminated (3%, 6%) calcium bentonite clay, Hydrocarbon sample and stone aggregates.

2.3.1 Properties of clay

Table 1 Properties of NC clay and 3%, 6% C clay

Properties	NC	3%C	6%C
Specific gravity	2.1	2.18	2.25
Liquid Limit (%)	249	205	186
Plastic limit (%)	57	85	110
Plasticity index (%)	192	95	76
Maximum dry density (kN/m ^{3})	18.36	18.69	19.1
Optimum water content (%)	20	18	16.5

Table 2 periodic contamination effect on Liquid Limit, plastic limit & shrinkage limit

Properties	Period in days			
	0	15	30	45
LL_3%	242	239	205	197
LL_6%	235	170	186	150
PL_3%	118	115	85	102
PL_6%	125	122	110	114
SL_3%	45	38	22	21.5
SL_6%	43	29	23	27

2.3.2 Properties of stones

Crushed stones (aggregates) of size below 8mm have been used to form stone column. The finer fraction

passing through 2mm was removed by wet sieving and used after drying. Typical properties of aggregate for stone column are:

Table 3 Properties of stone aggregates

Internal friction angle	35^0
Particle Size	2mm-8mm
Coefficient of curvature	1.125
Uniformity coefficient	2

2.3.3 Preparation of clay bed

Initially clay was mixed with water equal to 2 times the liquid limit of the soil by kneading in a large tank to form a slurry that was free from lumps and remove past stress if any. This pressure is allow to consolidate under its own weight for 1 day and then after consolidate under 20 kPa to make a clay bed. Drainage is permitted at the top and the bottom layer by placing porous plates. This process continued for 8-10 days until the required clay bed shear strength is been achieved. This procedure yielded clay beds of uniform moisture content and consistency.

2.3.4 Construction of Stone Column

All stone columns were constructed by a replacement method. A thin open-ended seamless PVC pipe of 50 mm outer diameter and wall thickness 2 mm was pushed into the clay at the centre of the tank up to the bottom. Stones were charged into the hole in layers with a measured quantity of 0.65 kg to achieve a compacted height of 50 mm. The pipe was then raised in stages ensuring a minimum of 5 mm penetration below the top level of the placed gravel. To achieve a uniform density, compaction was given with a 2.5 kg circular steel tamper with 10 blows of 100 mm drop to each layer. The corresponding density was found to be 16.62 kN/m^3. The procedure was repeated until the column is completed to the full height

3 RESULT AND DISCUSSION

Following are the results and discussion on settlement characteristics of stone column in hydrocarbon contaminated clays.

1. Axial load carrying capacity of stone column
2. The load resistance offered by stone column is computed at different settlement interval in N/mm.

Load resistance = *change in load/change in settlement*

3. Improved shear strength of soil mass
4. Moisture content profile
5. Bentonite-hydrocarbon interaction, Bentonite-hydrocarbon-Stone column interaction

3.1 Axial capacity of stone column and load resistance

This analysis aims at evaluating the improvement of the stiffness of the treated ground. The loading of both the stone column and the surrounding equivalent area with confinement of the tank wall represents an actual field condition for the interior columns of a large group of stone columns. Fig. 3 & 4 shows typical axial stress versus settlement behaviour for non-contaminated as well as 3%, 6% contaminated clay.

1. The ultimate load obtain from the graph for NC clay is 1080, 3%C clay it is 1020N and 6%C clay it is 960N for single column.
2. The ultimate load obtain from the graph for NC clay is7200N, for 3%C clay it is 6840N, and 6%C clay it is 6660N.
3. It is observed that load carrying capacity of stone column is decreasing 12.5% in 3% hydrocarbon contaminated clay and 20% in 6% hydrocarbon contaminated clay with compare to non-contaminated clay.
4. Resistance offered is quite high initially; moderate in between 8-12mm and beyond 12mm resistance offering rate is decreased respeactively for single stone column in non-contaminated, 3% and 6% contaminated clays.
5. Axial load carrying capacity decrease with increase in percentage of hydrocarbon in the clay mass.The hydrocarbon presence in the clay mass react with it and try to change clay engineering properties so compatibility between clay mass and stone column get disturbed and ultimately result in decrement in load carrying capacity of a stone column. Here attempt is made to see the performance of stone column as one of the soil improvement method particularly for hydrocarbon contaminated soft clays with increasing percentage of hydrocarbon and with increase in period of contamination there is a considerable change in index properties (Atterberg's limit) of Hd contaminated calcium bentonite. Decrease in plasticity characteristics of calcium bentonite may prove to be use-full in terms of either swell pressure / swell index but it has not benefited increasingly axial load carrying capacity of stone column.

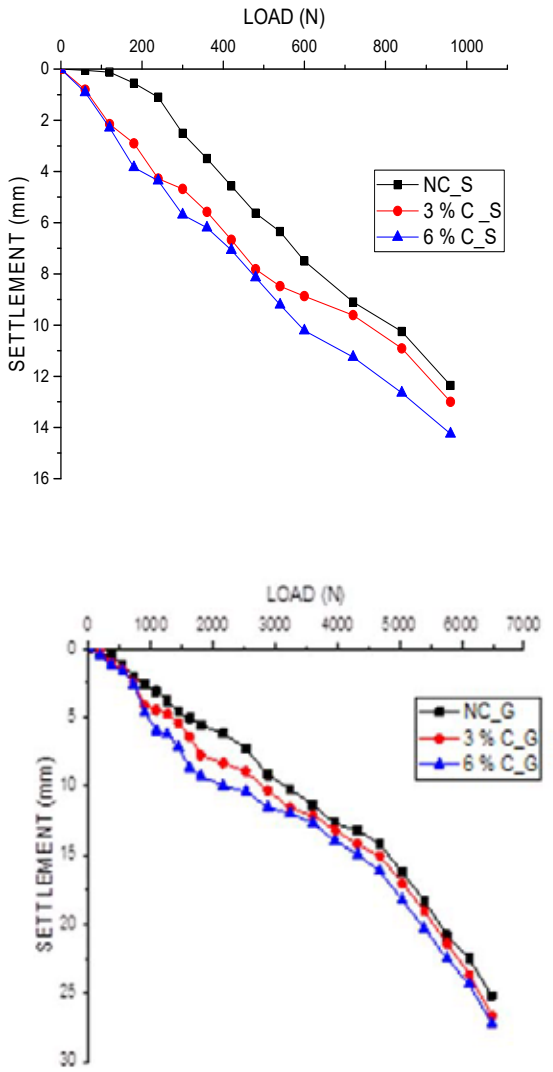

Figure 3(a) & 3(b) P-Δ curve for single column & group columns

3.2 Water content profile

From figure 5 it is observed that water content before test and after test has great fluctuation due to the working of the stone column as vertical drains in clay mass. But in hydrocarbon contaminated clays water dissipation is low due to layer formation of hydrocarbon above the clay particles. Vertical permeability decrease with increase in hydrocarbon contamination. The decrease in permeability attributed to the shrinkage of double layer surrounding the particle of clay. Absorption of H_d in clay causes displacement if H^+ ions result decrease in permeability.Calcium bentonite has Ca+2 valance cations on the surface of particles that attracts more water molecules towards it and water particles get attracted towards the basal surface of the clay minerals and therefore it will not release the water easily from the clay mass. If we observed both vertical and horizontal moisture profile of clay mass (along the height of sample and radius of sample) increasing moisture content with increase in depth shows that drainage path is not uniform along the length of stone column though the sample is homogenous and in case of calcium bentonite the zone of influence (taken as per IS 15284) is inefficient in attracting radial water in plain strain conditions.

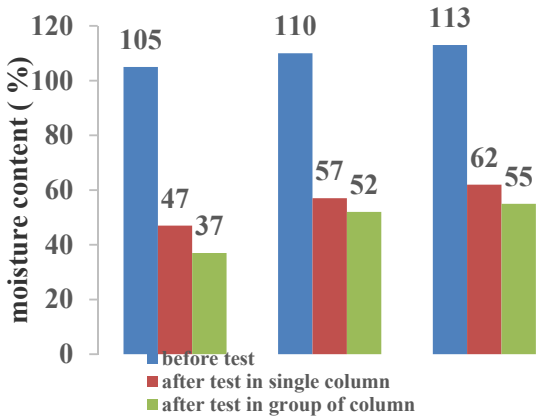

Figure 3. Moisture content profile

Table 4. Shear strength profile

	shear strength profile		
	NC	3%C	6%C
before test	15	15	15
After test single column	22.4	21.5	20.3
After test group of column	25.3	24.2	22.5

3.3 Shear strength

Table 4 shows the shear strength variation in the clay mass before and after test. By infusing the stone column in soil mass it sufficiently removes water from it and increase the shear strength. But in H_d contaminated clays due to the hydrocarbon internal slippage increases between the clay particles. During consolidation, the undrained strength and stiffness of the soil increase progressively. But as the percentage of contamination increases for the same contamination period, more and more surface of the clay is covered with hydrocarbon owing to lower mobility of water through the system and this lead to low shear strength value of clay mass containing hydrocarbon as compare to virgin clay mass.

1. In single column test shear strength is improved by 33%, 30%, 26% respectively in NC, 3%C and 6%C clays.
2. In group of column test shear strength is improved by 40%, 38%, 33% respectively in NC, 3% C and 6%C clays.

3.4 Bentonite-hydrocarbon interaction, bentonite-hydrocarbon-stone column interaction

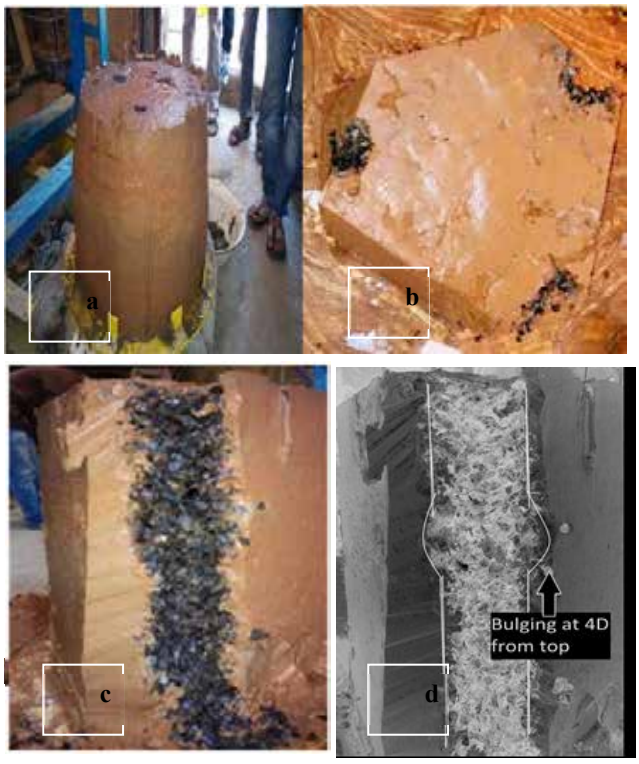

Figure 4. Post test analysis (a) soil after test (b) isometric view of soil mass (c) sectional view of stone column and clay (d) bulging of column in soil mass

i. Due to compressibility of soft mass and dissipation of pore water under constant magnitude of stress the overall height of column is found reduced by 30mm with respect to original height.
ii. If the length of column is equal to or greater than 4D (diameter of column) then it fail by bulging (IS 15284 part-1 2003). Column fails by bulging equal to 2D (10 cm) at the centre of the column.
iii. Calcium bentonite used as clay bed, has high cohesion and adhesion inherently. Such high plastic clay having very low shear strength and stiffness when it comes in contact with water. Such type of soil are susceptible to the marine deposit having problem of high pore water pressure generation.
iv. During the compression test on entire clay bed, soft clay would not give sufficient resistance to carry load, and column angular material will penetrate under the soft clay bed. This will lead to column bulging t certain depth of column.

4 CONCLUSIONS

- Single column tests with an entire unit cell area loaded compare well with the group test results. Hence the single column behaviour with unit cell concept can simulate the field behaviour for an interior column when large number of columns is simultaneously loaded.
- It is remarkably observed that stiffness of soil and stiffness of stone column has vast difference so due to such difference, compatibility between stone column and soil is not form and stone column does not work sufficiently.
- The hydrocarbon contamination leads to decrement in liquid limit as compared to liquid limit of non-contaminated bentonite clay. The mineralogical composition of hydrocarbon (Dodecane) comprises of long chains of carbon-hydrogen atoms, which when comes in contact with water leads to decrease in inter-molecular bond and leads to development of viscous layer over the clay mass, and also hydrocarbon has low density in comparison to water, it tends to float and thus leads to reduction in liquid limit.
- Water is covered by the hydrocarbon particles and it reduces effectively by means of radial consolidation provide by infusion of stone column in it.
- This decrement in load carrying capacity is due to the internal slippage of particle due to the oil contamination and presence of high moisture in the mass, both together reducing the strength of the whole system.
- Axial capacity of column is decreasing in Non-contaminated clay, 3% H_d Contaminated and 6% H_d contaminated clay by 20 % in singular column and 12.5% in group of three column.
- Shear strength is sufficiently improved by inducing the stone column. But as increases the % contamination in clay, shear strength decreases due to the internal slippage of the clay particles.
- The load settlement behaviour of a unit cell with an entire area loaded is almost linear and it is possible to find the stiffness of improved ground.
- Decrease in bulge depth and increase in diameter of bulge have been observed in Non-contaminated clay to 3%, 6% H_d contaminated clays.
- Load resistance offered by stone column with increasing percentage of contamination depends on two aspects. First integrity of stone column (uniform density of stone column throughout its length) and uniform settlement of clay mass compatible with structural rearrangement of gravel under increment of various stress levels. Second is load resistance offered by the stone column is very high in the initial portion of the curve up to 3-5 mm settlement, moderate between 5-10 mm and very low beyond 10 mm in non-contaminated and hydrocarbon contaminated bentonite clay. The effect of lower load resistance with increase in settlement is due to low dissipation rate of pore water even under higher loads because of smear wall created by calcium bentonite and swelling properties of clay.

- Rate of decrease in water expulsion under higher loads with increase in % contamination depicts that rate of inward radial flow of water was decreasing though load was increasing which is even noted in settlement measurements also.

There is a definite impact of both percentage hydrocarbon contamination and periodic contamination on the index and engineering properties of calcium bentonite, though it is stabilize by inducing singular stone column and group of stone columns. This leads us advance assessment of influence of both percentage contamination and periodic contamination on strength characteristics of such marine clays. It is necessary to provide a remedy which will not increase only it load carrying capacity/bearing power but which also reduces differential settlement. This study was an attempt to project stone column as one of the remedy technique for hydrocarbon contaminated clay and to estimate load carrying capacity for various percentages of contamination. It is further observed that behaviour of stone column embedded in calcium bentonite shows very progressive results and can be very well adopted for greater depths of clay deposits. For such hydrocarbon marine deposits especially of calcium bentonite, stone column proves to be most efficient and ecological technique if adopted with proper understanding of bentonite-hydrocarbon-water interaction chemistry.

ACKNOWLEDGEMENTS

The authors are highly thankful to Prof. (Dr) G.P. Vadodariya, Dean, L.D.College of Engineering and Prof. A.R. Gandhi, Head, Applied Mechanics Department, LDCE, Ahmedabad, India for extending research facilities for this project.

REFERENCES

Ambily and Gandhi (2004) "Experimental and Theoretical Evaluation of Stone Column in Soft Clay" Page 201-206, Year of Publish 2004, ICGGE.

Ambily and Shailesh R. Gandhi (2007) "Behavior of Stone Columns Based on Experimental and FEM Analysis" Journal of Geotechnical and Geo environmental Engineering Volume 133 number 4, April 2007, American Society of Civil Engineers.

Bora Mukul C and Dash Sujit Kumar "Load Deformation Behaviour of Floating Stone Columns in Soft Clay" December 16-18, 2010, page 250-255, Indian Geotechnical Conference

Bowles (1988). Foundation Analysis and Design, 4th edition, McGraw – Hill International Editions,New Delhi.

Datye, K.R. and Nagaraju,S.S. (1981). Design Approach and Field Control for Stone Columns, Proc. Tenth Int. Conf. On SMFE., Stockholm, Vol. 3, 637 – 640.

Greenwood, D.A. (1970). Mechanical Improvement of Soils Below Ground Surfaces, Proc. Ground Engineering Conf., Institution of Civil Engineers, London, 11-22.

Hughes, J.M.O. and Withers, N.J. (1974). Reinforcing of Soft Cohesive Soils with Stone Columns, Ground Engineering, Vol.7, No.3, 42-49.

Hughes, J.M.O., Withers, N.J. and Greenwood, D.A. (1975). A Field Trial of Reinforcing Effect of Stone Column in Soil ,Geotechnique, Vol.25, No.1, 32-44.

Ling Zhang and Minghua Zhao "Deformation Analysis of Geotextile-Encased Stone Columns" International journal of geo mechanics (2014), page 04014053(1) - 04014053(10), American Society of Civil Engineers.

Madhav, M.R. (2000).Granular Piles- Recent Contributions. A short term course on Ground Improvement and Deep foundations held at IIT Madras, Dec 2000, MRM1 - MRM38.

Geotechnical and Geophysical Site Characterisation 5 – Lehane, Acosta-Martínez & Kelly (Eds)

A preliminary study on evaluating the performance of aged landfill covers using DC and CC resistivity methods

Y.X. Wu & Y.H. Wang
The Hong Kong University of Science and Technology, HKSAR, China
Z. Zhang
China Institute of Water Resources and Hydropower Research, Beijing 100084, China

ABSTRACT: A preliminary study, using the electrical resistivity tomography, was conducted to evaluate the performance of landfill cover in response to different weather conditions at an aged landfill site in Hong Kong. Both the direct current (DC) resistivity method and the capacitively coupled (CC) resistivity method (with line antenna) were adopted. The measured results suggest that both the DC and CC resistivity methods can be used to effectively monitor the ground resistivity change of a landfill cover in response to different weather conditions. Besides, the DC resistivity method can be used to identify the location of geomembrane layer and then examine the associated deformation since a clear boundary, below which there exists a high resistivity regime due to the presence of nonconductive geomembrane to hider to DC transmission, was found. As to the CC resistivity method, it can be used to investigate the electrical resistivity distribution and associated changes for the regimes above and below the geomembrane layer since the alternative current (AC) can be capacitively coupled into the ground below the geomembrane.

1 INTRODUCTION

Many landfills have been built for the disposal of municipal solid waste. When landfills are closed, landfill covers are commonly put to minimize the quantity of surface water infiltrating into the waste deposits and then protect waste containment system from rainfall percolation (e.g, Benson et al. 2001). However, since the local conditions, such as seasonal weather conditions and the growth of vegetation roots, etc., will change the pores and peds in the cover soils (Buol et al. 2011; Henken-Mellies & Schweizer 2011), the hydraulic properties of the cover soils, e.g., the saturated hydraulic conductivity (Ks), may change with time (Meiers et al. 2006). Benson et al. (2007) carried out a long-term monitoring on the hydraulic properties of water balance covers using a flexible-wall permeameter, and the results indicated that Ks could increase as much as 10,000 times four years after the construction of those covers. Such an increase in Ks was also reported in Henken-Mellies & Schweizer (2011). They found that the hydraulic conductivity in a simple soil barrier and in compacted clay liners may increase considerably with time if there was no long-lasting protection method. Such an increasing trend of Ks may weaken the performance of the landfill covers.

In addition to the increase in Ks of the cover soils, the properties of the geomembrane liner in the landfill cover may also deteriorate with time as a result of exposure to the field conditions. This in turn may also affect the long-term performance of a landfill cover. Therefore, there are concerns on the performance of the aged landfill covers, especially those more than 20 years old.

In Hong Kong, there are 13 closed landfills aged from 20 to 41 years. Considering the large amount of stored waste in those landfills, which is about 66 megatons, to assess the performance of those aged landfill covers in order to better control rainfall percolation into the underlying waste is crucial to Hong Kong.

Compared with the traditional sampling method to determine soil properties, geophysical methods, e.g., electrical resistivity tomography (ERT), have non-destructive, low-cost and fast speed features. The direct current (DC) ERT method (termed as DC resistivity method in the following discussion) has been successfully applied to detect defects and heterogeneity in loamy-clay cover (Genelle et al. 2012), to trace subsurface migration of contaminants from landfill (Bahaa-eldin et al. 2011), and to investigate top cover effectiveness and internal structure of sealed landfill (Hermozilha et al. 2010). Hence, it seemly feasible to apply DC resistivity method in assessing the performance of aged landfill covers. In addition to the DC resistivity method, capacitively coupled (CC) ERT method (termed as CC resistivity method in the following discussion) can also be used in the assessment. A CC resistivity system, usually

working at kilohertz frequency, can inject an electrical current into the ground and measure the potential of the ground surface capacitively without galvanic coupling. That is, there is no need to install electrodes while using the CC resistivity method. Indeed, the CC resistivity method has a higher ratio of measurement speed to data density compared with DC resistivity method (Niu et al. 2014). In this context, the CC resistivity method seems to be economically preferred to evaluate the performance of aged landfills because this method, compared with the DC method, is less time consuming and relatively easy to be operated (to be further discussed later).

In summary, this study aims to evaluate the performance of aged landfill covers using both the DC and CC resistivity methods. A series of resistivity surveys was carried out at Tseung Kwan O (TKO) Stage II/III Landfill, which is an aged landfill site in Hong Kong, to evaluate the landfill cover performance in response to different weather conditions. In addition, for the same survey line, comparisons between the measurements obtained from the two methods are made to highlight the different features between them.

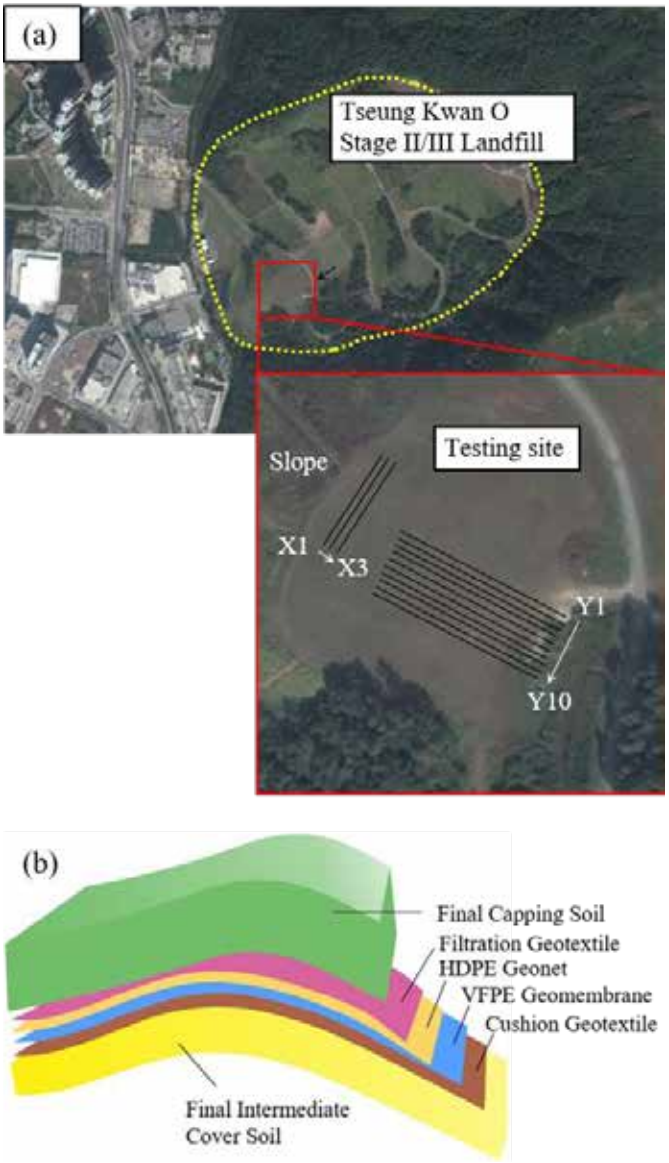

Figure 1. Landfill site: (a) location of test site and measurement lines and (b) profile of landfill cover.

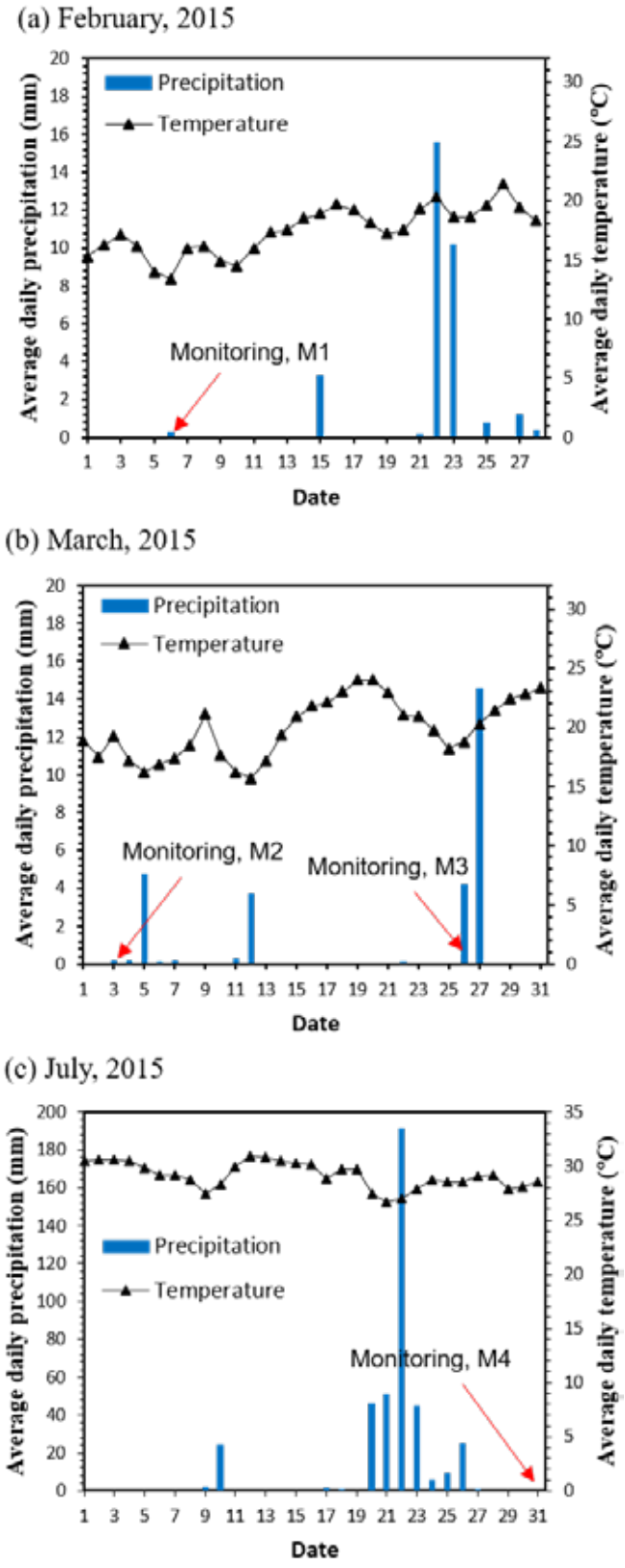

Figure 2. Weather conditions, in terms of the daily averaged precipitation and temperature, for each measurement. Note that the scale set for precipitation is different in order to show the details.

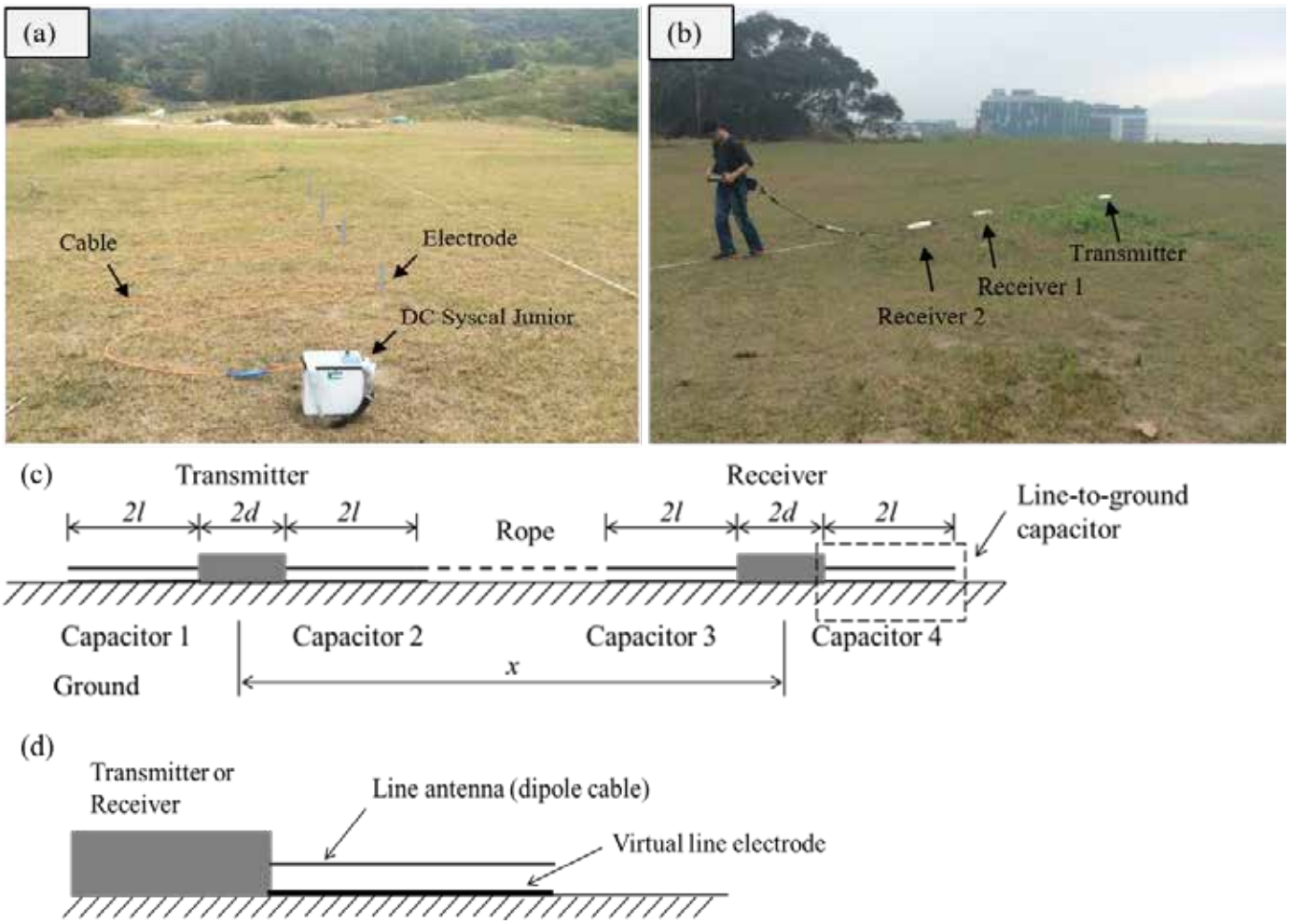

Figure 3. Instruments used in the resistivity surveys: (a) for the DC method; (b) for the CC method; (c) a schematic diagram with one transmitter and one receiver; and (d) the line-to-ground capacitor (b, and c are adopted from Niu and Wang 2013).

2 SITE DESCRIPTION

Figure 1a gives a satellite image of TKO Stage II/III Landfill. The landfill is located at TKO development area 105, New Territories, Hong Kong. The landfill site is subjected to a monsoon-influenced humid subtropical climate. The average annual precipitation ranges from 1400 to 3000 millimetres, and the daily mean temperature ranges from 16.3 to 28.8 °C. The landfilling operation of TKO Stage II/III Landfill commenced in 1989 and ceased in 1994. The flat area of the landfill is approximately 42 hectares, and the amount of stored waste is about 12.6 megatons, which accounts for 19% of the total amount of stored waste in the closed landfills in Hong Kong. As shown by Figure 1a, a platform, which is approximately 0.7 hectares large, is selected as the testing site, because this area is flat enough to carry tests.

Figure 1b presents the cover profile of TKO Stage II/III landfill. The designed thickness of the final capping soil is about 0.8 m

3 EXPERIMENTAL DETAILS

Four different surveys have been carried out using SYSCAL Junior Switch 48 resistivity meter and OhmMapper at different weather conditions. 10 lines (from Y1 to Y10) in y direction and 3 lines (from X1 to X3) in x direction were monitored as shown in Figure 1a. RES2DINV inversion software (Loke and Barker 1996) was used to interpret the measured resistivity data by two dimensional (2D) resistivity tomography. The absolute error of each inversion result is less than 5%. Details are described in the following.

a. The DC resistivity method

As shown in Figure 3a, in the DC resistivity survey, the dipole-dipole array with equal electrode spacing of 2 m for the survey lines Y1 to Y10 and 1m for the survey lines X1, X2 and X3 was adopted. The SYSCAL Junior resistivity meter was used and each measurement array consists of 24 electrodes.

b. The CC resistivity method

In the CC resistivity survey, as shown in as shown in Figure 3b, the OhmMapper (Geometrics, CA, USA) was used. The OhmMapper is a CC resistivity system (meter), which consists of one transmitter and

several receivers as also shown in Figure 3b. The receivers and transmitter are linked by a nonconductive rope and therefore the whole equipment can be towed by an operator at a walking speed. As shown

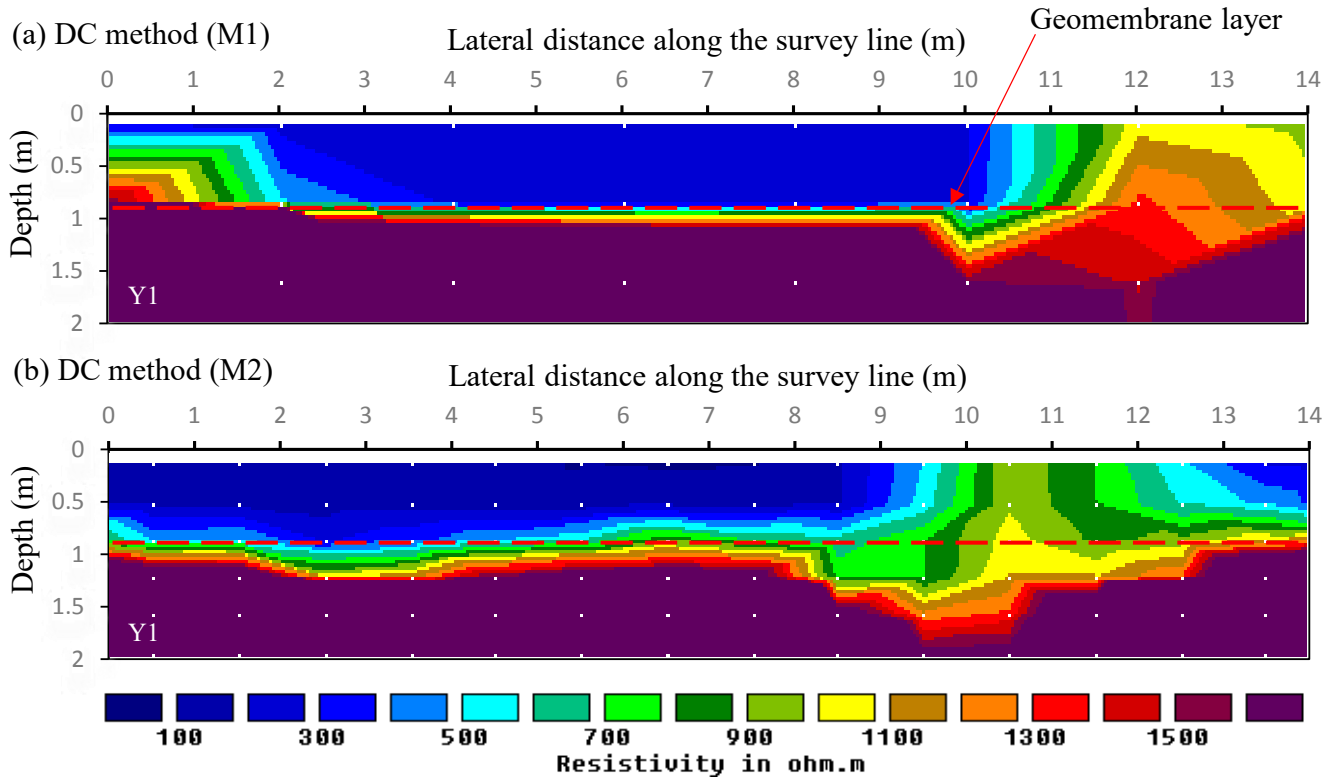

Figure 4. Results of ground resistivity measured by the DC resistivity method along the survey lines Y1 for (a) measurement M1 and (b) measurement M2.

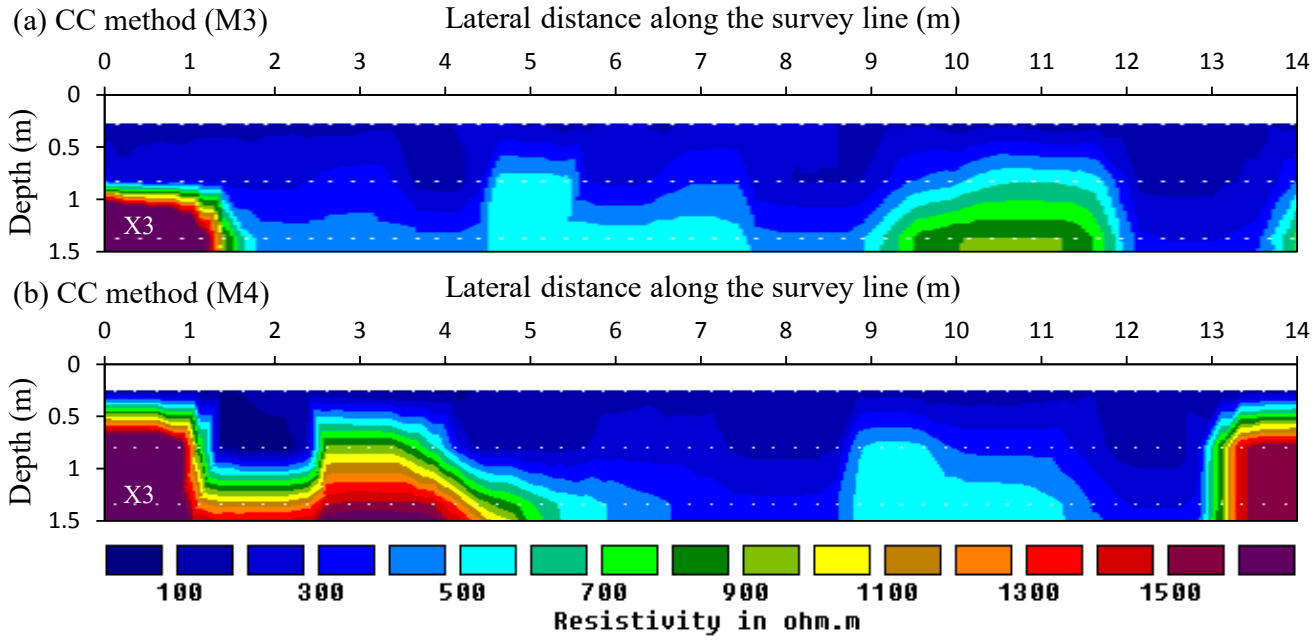

Figure 5. Results of ground resistivity measured by the CC resistivity method along the survey lines X3 for (a) measurement M3 and (b) measurement M4.

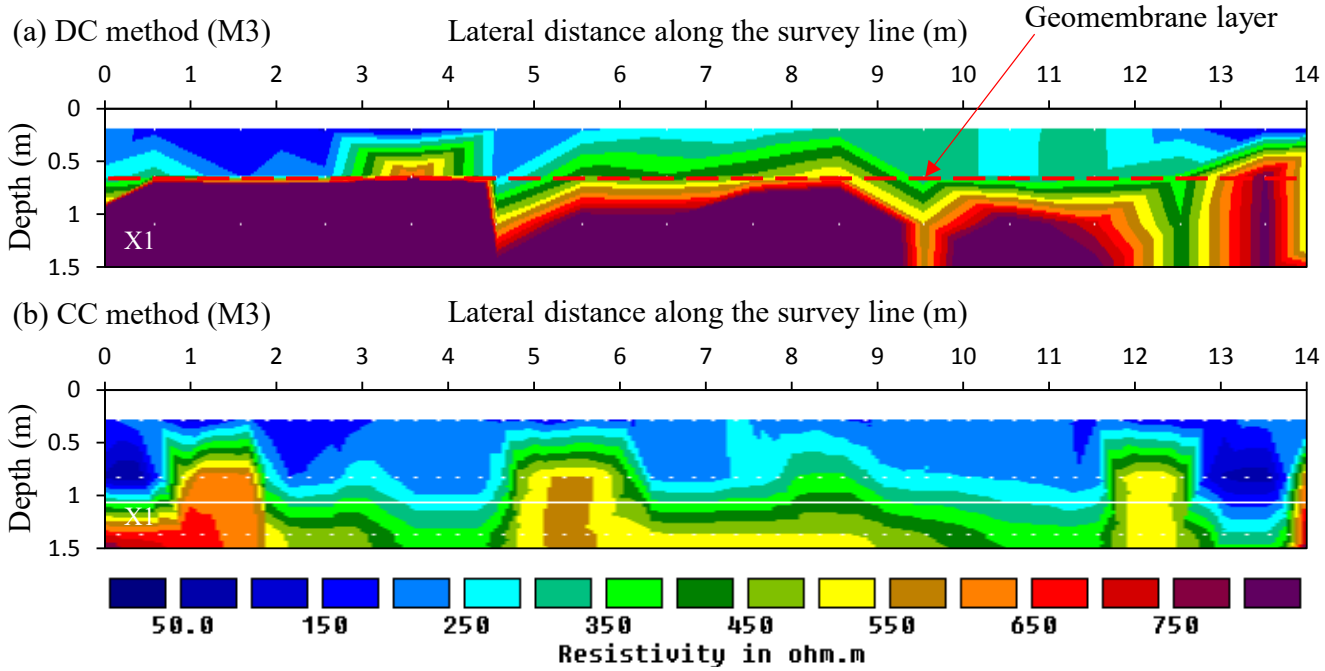

Figure 6. Results of ground resistivity along the survey line X1 for measurement M3 using (a) the DC resistivity method and (b) the CC resistivity method.

in Figure 3c, each transmitter or receiver has two line antennas (i.e., the dipole cables) and each line antenna together with the ground surface forms a line-to-ground (or cable-to-ground) capacitor as illustrated in Figures 3c, d. That is, the upper plate of the capacitor is formed by the line antenna (dipole cable), and the lower capacitor plate is established by the ground surface and is envisaged as a virtual line electrode herein to facilitate the discussion. During the measurement, the alternating current (AC) generated from the transmitter can be capacitively coupled into the ground through this virtual line electrode, which has galvanic coupling with the ground. In the same principal, the potential on the ground surface (see Figs. 2c, d) can also be measured by the receiver. Note that the current frequency is fixed at 16.5 kHz for OhmMapper. In this study, the dipole length is selected as 2.5 m and the rope length between the receiver and transmitter was 1 m for all measurements. The equivalent dipole length used in the inversion should be corrected by a factor 0.74 as suggested in Niu and Wang (2014).

c. Measurements

The weather conditions, in terms of the daily averaged precipitation and temperature for each measurement are indicated in Fig. 2. As shown in Figure 3a, the first measurement (M1) was carried out after a long arid weather condition. The second measurement (M2) was carried out two days after several rainfall events with ~30 mm precipitation in total (Fig. 2b), the third measurement (M3) was carried out right after a rainfall event with 4.2 mm precipitation (Fig. 2b), and the fourth measurement (M4) was carried out four days after several rainfall events taking place within 10 days with 379 mm precipitation in total (Fig. 2c).

4 RESULTS AND DISCUSSION

The center parts of some tomography results are compared together. Figure 4 compares the tomography images measured by the DC resistivity method along the survey line Y1 for the first and the second measurements (i.e., M1 and M2). It can be found that both images show a sudden resistivity increase area about 0.9 m beneath the ground surface, and this phenomenon should be caused by the presence of the geomembrane layer. The region above the geomembrane layer has the electrical resistivity about 300 Ω.m, and the electrical resistivity suddenly reaches a quite high value in the regime below the geomembrane layer. This is due to that the direct current is difficult to flow through the non-conductive geomembrane during testing, thus the area below the geomembrane is considered as media with a high resistivity value based on the measurement. Besides, an area with relatively high resistivity on the right side above geomembrane can be observed. This phenomenon is supposed to be caused by the existence of a concrete exhaust shaft. When comparing the two measurement results, it can be found that the resistivity value of the region above the geomembrane is higher in the measurement M2 (see Fig. 4a) than in the measurement M2 (see Fig. 4b). This is consistency with the precipitation conditions that the weather is drier during measurement M1 than during measurement M2.

Figure 5 presents the results along the survey line X3 from the measurements M3 and M4 using the

CC resistivity method. As shown in the figure, the geomembrane layer cannot be clearly identified and the ground resistivity below the geomembrane can still be measured. This is because an alternative current was used by OhmMapper and the current can also be capacitively coupled into the ground below the membrane. When comparing the two measurement results, the ground electrical resistivity is decreased after a heavy rainfall (see Fig. 5b), even for the region beneath the geomembrane.

Figure 6 compares the results along the survey line X1 measured by both the DC and CC resistivity methods. Once again, the DC resistivity measurements, as shown in Figure 6a, can clearly identify the location of geomembrane below which the resistivity suddenly jumps to a high value. It can also be found that the boundary that separates the low and high resistivity regime due to the presence of geomembrane wavy along the survey line. This might be caused by the ground settlement and movement since line X1 is near the slope along the test site. For the CC resistivity measurement, as shown in figure 6b, the ground electrical resistivity can be detected for the regimes above and below the membrane. The comparison between the results shown in Figures 6a and 6b suggests that the DC resistivity method is good to identify the location of geomembrane and then check the deformation and condition of the geomembrane layer, and the CC resistivity method is good to survey the ground resistivity changes below the geomembrane layer.

5 CONCLUSIONS

A preliminary study, using the electrical resistivity tomography, was carried out on an aged landfill site to evaluate the performance of landfill cover. Four different resistivity surveys were carried out at different weather conditions. Both the direct current (DC) resistivity method and the capacitively coupled (line antenna) resistivity method were adopted in the monitoring. The testing landfill site is located at Tseung Kwan O development area 105, New Territories, Hong Kong; the landfilling operation commenced in 1989 and ceased in 1994.

The measured results suggest that both the DC and CC resistivity methods can be used to monitor the ground resistivity change of landfill covers in response to different weather conditions. Besides, the DC resistivity method can be used to detect the location of geomembrane layer and then examine the associated deformation since a clear boundary, below which the resistivity value suddenly jumps to a high value due to the DC cannot penetrate through the nonconductive geomembrane, can be identified in the survey results. As to the CC resistivity method, it can be used to investigate the electrical resistivity distribution and associated changes in response to different weather conditions for the regimes above and below the geomembrane layer. The alternative current (AC) used by OhmMapper can also be capacitively coupled into the ground below the geomembrane.

6 ACKNOWLEDGEMENTS

This research was supported by the Hong Kong Research Grants Council (HKUST6/CRF/12R).

7 REFERENCES

Bahaa-eldin ER, Yusoff I, Rahim SA, Zuhairi WW, Ghani MA. 2011. Tracing subsurface migration of contaminants from an abandoned municipal landfill. *Environmental Earth Sciences* 63(5):1043-55.

Benson C, Abichou T, Albright W, Gee G, Roesler A. 2001. Field evaluation of alternative earthen final covers. *Int J Phytoremediation* 3(1):105-27.

Benson CH, Sawangsuriya A, Trzebiatowski B, Albright W. 2007. Postconstruction changes in the hydraulic properties of water balance cover soils. *J Geotech Geoenviron Eng* 133(4):349-59.

Buol SW, Southard RJ, Graham RC, McDaniel PA. 2011. Soil genesis and classification. John Wiley & Sons.

Genelle F, Sirieix C, Riss J, Naudet V. 2012. Monitoring landfill cover by electrical resistivity tomography on an experimental site. *Eng Geol* 145:18-29.

Henken-Mellies WU and Schweizer A. 2011. Long-term performance of landfill covers - results of lysimeter test fields in bavaria (germany). *Waste Manag Res* 29(1):59-68.

Hermozilha H, Grangeia C, Matias MS. 2010. An integrated 3D constant offset GPR and resistivity survey on a sealed landfill—Ilhavo, NW portugal. *J Appl Geophys* 70(1):58-71.

Loke MH and Barker R. 1996. Rapid least-squares inversion of apparent resistivity pseudosections by a quasi-newton method. *Geophys Prospect* 44(1):131-52.

Meiers Greg P., Barbour SL and Qualizza Clara V. 2006. The use of in situ measurements of hydraulic conductivity to provide an understanding of cover system performance over time. Proc., 7th int. conf. on acid rock drainageInternational Network for Acid Prevention Tehachapi, Calif.

Niu Q and Wang YH 2013. Theoretical and experimental examinations of the capacitively-coupled resistivity (line antenna) method, *Geophysics*. 78(4): E189-E199.

Niu Q and Wang Y. 2014. Inversion of capacitively coupled resistivity (line-antenna) measurements. *Geophysics* 79(3):E125-35.

Niu Q, Wang Y, Zhao K. 2014. Evaluation of the capacitively coupled resistivity (line antenna) method for the characterization of vadose zone dynamics. *J Appl Geophys* 106:119-27.

Geotechnical and Geophysical Site Characterisation 5 – Lehane, Acosta-Martínez & Kelly (Eds)

Assessment of the Infiltration capacity of a Retention pond by the TDR measurements

I. A. Ichola
LGCIE 34 avenue des Arts INSA-LYON Villeurbanne F-69621 France
C. Anzoras
BG Consulting Engineers, Villeurbanne, France

ABSTRACT: Four years after the construction of a storm-water retention pond of a highway, TDR measurements were performed on the bottom surface of the pond. The distribution of water content in the surface layer is very variable but once of the electrical conductivity proves that the surface is characterised by three different values. These three values of electrical conductivity correspond to three zones of different texture so three zones of different permeability. The correspondence between the coefficient of permeability and the electrical conductivity of the soil shows that the values of the coefficient under estimate the infiltration rate of water in the basin. The infiltration capacity of the retention pond is under estimates by the value of the saturated soil coefficient of permeability. During the filing of the basin, the distribution of the water content becomes lesser variable as shown the water migration in the upper layer of the sealing layer. Thus it is noticed that TDR measurements can locate wetlands in surface layer and track its migration into the deeper layers.

1 INTRODUCTION

During many years, studies have been conducted on the permeability of manufactured products like GCL or geomembrane, for the realization of sealing layers of waste containers and retention basins. These sealing systems are difficult to maintain and difficult to repair. So it is projected to built the sealing system of a highway retention pond with the natural soil material as loam or run pit. Usually, these soils, after compaction, have not a very low coefficient of permeability.

Two local materials are proposed as sealing product. The first is produced during the pond excavation and the second is from a quarry near the site. To get information on these soils, several geotechnical tests are carried out in the laboratory. These results are used for the earthwork during the pond construction. Many standard permeability tests are carried out to evaluate the compacted soil permeability. The results of these tests prove that the coefficients of the permeability are low enough for using as sealing products for the pond.

To detect the water movement in the sealing layer of the pond, thirty TDR probes are embedded on three levels, ten probes by level. The TDR measures are acquired automatically every thirty minutes and stored on computer. Four years after pond installation, surface TDR measurements are performed to correlate water content on the bottom of the pond and in the sealing layer. Water content repartition on the surface is compare to that observed in the sealing layer. One day after surface TDR measurements in the basin, a rainfall event has caused the filling of the basin. Process water migration in the sealing layer is described by the water content increase according to the water height in the basin. The decrease of the water height in the basin is used to determine the infiltration rate and the change in the coefficient of permeability during the upper layer saturation in the basin. The limit value of the permeability coefficient is compared with the value assessed by the electrical conductivity of the soil on the basin surface.

2 DESCRIPTION OF THE TESTED HIGHWAY ROAD RETENTION POND

The surface of the water retention pond is about 2000 m^2 (76m length, 26m width). The barrier thickness is 400mm. To reduce the number of probes, long rod probes made in laboratory are used. The rods have 2m length with a diameter of 5mm and there is 13mm between the rod axes as shown on Figure 1b.TDR probes are installed in five trenches. Two probes are put on three levels in every trench. The sealing material used in the basin is from a quarry near the basin. The geotechnical analyses allow identifying it as

clayey gravel. The compaction tests on the used material allow reaching a dry density of 2g/cm^3 in the wetting natural water content. Standard permeability tests prove that the average value of the saturation coefficient of permeability is 10^{-7}m/s. This value can be decreased to 10^{-9}m/s when the soil material contains more fine grains than the average value of fine grain content in the samples used for the standard permeability tests.

Once the sealing layer achieved, the excavated soil is brought into coverage and seeded with grass. Geotechnical tests on the excavated material used allow identifying it as clayey sand. Compacted at its natural water content to a layer of 20cm, the average value of dry density reaches 1.85g/cm^3. Standard permeability tests performed on the samples of excavated soil show an average value of coefficient of permeability of 10^{-9}m/s when it is wetted at the natural water content.

The photo on Figure 1a represents the basin after TDR probe installation. Layer of 300mm of the excavated soil is compacted as the barrier system. So the pond can retain 1.50m height of water. The level gauge installed in the oil separator chamber allows the monitoring of the water level in the basin.

Figure 1. Photos of the basin after TDR probes installation and type of long length probes used

3 TDR MEASUREMENT TECHNIQUES

TDR probes allow the measurements of the volumetric water content and the electrical resistance of the soil. These measures are obtained with the relationships between soil dielectric constant and water content and between the reflection coefficient of an EM wave and soil electrical resistance. When the probes are composed of short rods of length less than 50cm, the most commonly used relationship is that of Topp et al. (1980). In this condition the dielectric constant is determined by the transit time of the EM wave in the probe. So the apparent dielectric constant which is the relative real part of the permittivity can be computed by:

$$\varepsilon_r = \left(\frac{c}{v}\right)^2 = \left(\frac{ct}{2L}\right)^2 \quad (1a)$$

where t is the transit time, L the length of the probe and c light speed in free space.

The load of the transmission line Z_L embedded in the investigated soil can be calculated with the voltage reflection coefficient ρ defined by:

$$\rho = \frac{Z_L - Z_0}{Z_L + Z_0} \quad (1b)$$

Z_0 is the characteristic impedance of the cable

The ρ values can be read directly on the signal curve for large propagation time. So the load Z_L can be calculated and converted to σ_a by using probe's geometric constant. The geometric constant K_c, is experimentally obtained by immersing the probe in a solution of known salinity σ_a, measuring the impedance Z_L by TDR, using an equation identical to one of Rhoades and Schilfgaarde (1976):

$$K_c = \sigma_{ref}(25°) Z_L / f \quad (1c)$$

f is temperature correction; $\sigma_{ref}(25°C)$ is the permeant electrical conductivity; $\sigma_{ref}(25°C)$ is the permeant electrical conductivity.

For probes made of rods of large length, the TDR signal inversion method is used to obtain the distribution of the soil impedance along the probe (Pereira Dos Santos 1997). When the medium tested has low dissipation, soil impedance change along the probe is given by:

$$Z(t) = Z_c \exp(2\rho(t)) \quad (2a)$$

where the voltage reflection coefficient between probe entrance time ti and exit time tf; Zc is the cable impedance.

The measurement position at the time t is defined by:

$$z(t) = L \times \frac{\int_{ti}^{t} Zdt}{\int_{ti}^{tf} Zdt} \quad (2b)$$

The two equations (2a) and (2b) give the value of the soil impedance at the position z(t). The dielectric constant is obtained by the ratio:

$$\varepsilon(t) = \frac{Z(t)}{Z_a} \quad (2c)$$

Z_a is the impedance of the probe in the air.

The relationship between the soil dielectric constant and the volumetric water constant used, is one proposed by Topp et al. gives by the following equation:

$$\theta = -0.053 + 0.29\varepsilon - 5.5\ 10^{-4}\varepsilon^2 + 4.3\ 10^{-6}\varepsilon^3 \quad (3)$$

4 TDR MEASUREMENT TECHNIQUES

TDR measurements allow obtaining the distribution of the volumetric water content and the electrical conductivity of the soil. The distribution of electrical conductivity indicates the permeability of different zones of the basin. The distribution of coefficient of permeability is used to explain the water movement in depth.

4.1 *Distribution of volumetric water content in the basin bottom*

The distribution of the water content on the basin bottom surface is obtained by TDR measurements carried out on 40 points. The measurement points are made up of mesh of 5m side lengthwise and 3m in the direction of the width of the basin. Measurements were performed after one week without rain. During a rainfall event, the filling of the basin by the runoff water occurs, entering by the eastern zone and exiting by the western zone. The water content distribution shown in Figure 2 proves that the zone of the entrance of the runoff water remains wetter than the exit zone after the basin becomes empty. In the entrance zone, it is found water content value near the saturation value. Low values of the water content are located in the exiting zone. Water content distribution is characterised by the moisture value variation in the surface layer of the basin. These different values of the volumetric content must be correlated to the coefficient of the permeability. Alimi et al. (2012), shows that the value of the soil coefficient of permeability can be described by the electrical conductivity value of the soil.

4.2 *Distribution of electrical conductivity in the basin bottom*

The distribution of electrical conductivity in the surface layer of the basin in Figure 3 shows that three main zones of different electrical property can be distinguished. The values of the electrical conductivity decrease from 5mS/cm in the water inlet zone to 3.8mS/cm in the water outlet zone of the pond. While the distribution of the water content in the surface layer of the basin is characterised by six different values that of the electrical conductivity is represented by three values. This shows that the electrical conductivity is rather influenced by the texture of the soil than by the arrangement of the soil grains. Simultaneous measurements of the electrical conductivity and the permeability coefficient on compacted soil samples show that the two physical quantities may be related as shown in Table1.

It is noticed that the coefficient of permeability decreases when the electrical conductivity increases. So the distribution of the electrical conductivity proves that the central zone on the surface layer in the basin is more permeable than the inlet and outlet zones of the retention basin. This distribution of estimated coefficient of permeability in the surface layer can be verified by examining the distribution of the water content in the upper layer of the sealing layer during infiltration.

Table 1. Correlation between electrical conductivity and coefficient or permeability

Electrical Conductivity (mS/cm)	3.8	4	4.5	5
Coefficient of Permeability (m/s)	$6.58\text{x}10^{-8}$	$6.40\text{x}10^{-8}$	$5.95\text{x}10^{-8}$	$5.50\text{x}10^{-8}$

5 DISTRIBUTION OF WATER CONTENT IN THE UPPER LAYERS OF THE SEALING LAYER

In effect after the TDR measurements on the surface of the basin, 04/28/2004 from 11:30 to 16:23, the basin received rain that begins 04/28/2004 at 23:00 and ends the 04/29/2004 at 10:00. It notes a water level of 35cm in the basin 9 hours after stopping the rain.

The distribution of the water content in the upper layer of the sealing layer presented in Figure 4 proves that the central zone is more wetted than inlet and outlet of the retention pond. That means this zone receives more infiltrated water from the surface layer. The water migration through the surface layer is in agreement with the distribution of the values of coefficient of permeability estimated by the distribution of the soil electrical conductivity. It is shown that TDR measurements on the basin surface allow estimation of permeability coefficients and to locate the zones of higher permeability during retention pond maintenance.

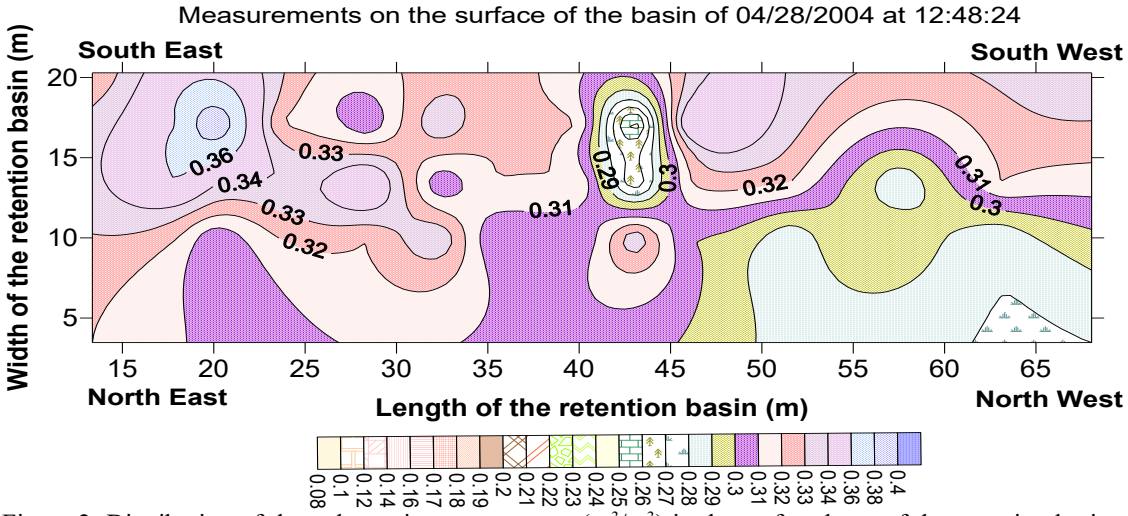

Figure 2. Distribution of the volumetric water content (m^3/m^3) in the surface layer of the retention basin after a week without the rainfall event

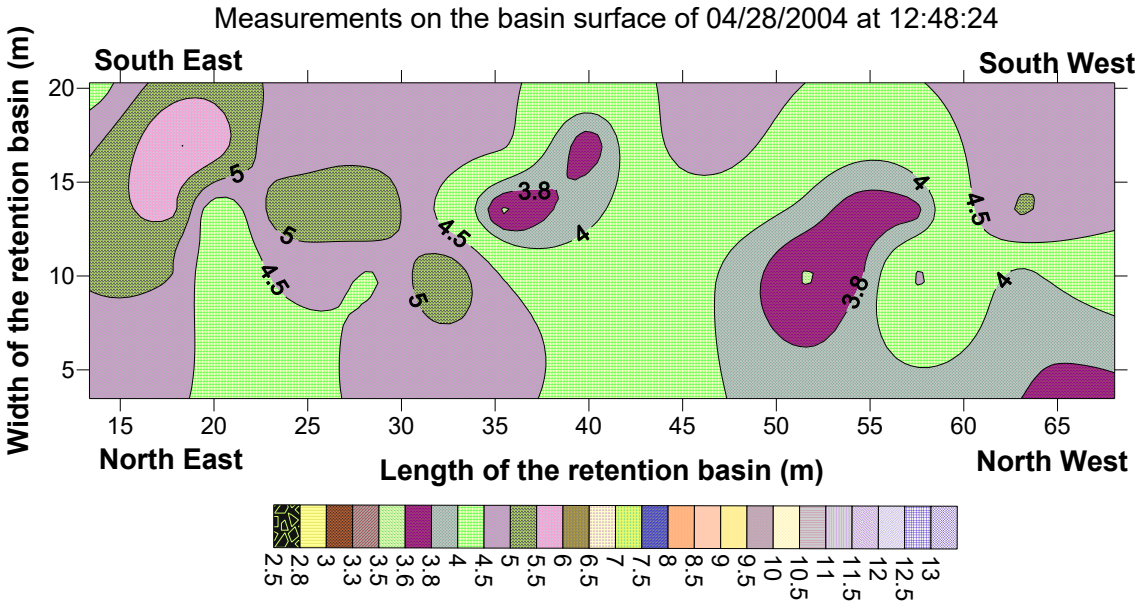

Figure 3. Distribution of the electrical conductivity in the surface layer of the retention basin after a week without the rainfall event

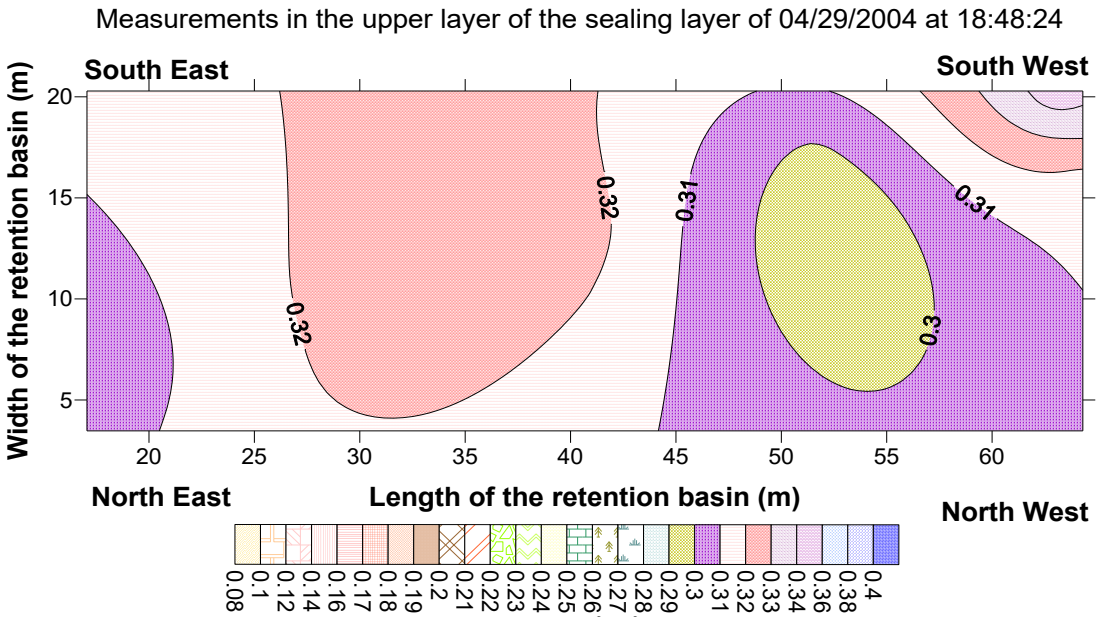

Figure 4. Distribution of the volumetric water content (m^3/m^3) on the retention basin after 9hours the rain stop

Figure 5. Photos of the retention pond during surface TDR measurements and 9 hours after the rainfall began

Figure 5a shows the pictures of the basin during TDR measurements on the surface of the pond bottom and 9hours after the end of the rain the next day. It is noticed that the grass on the surface of the pond bottom does not reveal the zones of different textures except when there are pebbles. The filling provides uniform coverage of the pond surface with runoff water (Fig 5b). The average value of water level reached at the end of the rain is 0.37m and real infiltration is observed 9hours after. In this time the average level water decreases to 0.346m. This means that the average infiltration rate can be assessed to 7.10^{-7}m/s. Average value of the coefficient of permeability of the surface layer of the basin, estimated to 6.10^{-8}m/s, proves that the gravity water movement inside the layer remains slow compared to infiltration. It is always observed that the coefficient of permeability computed with the infiltration rate is early higher than the coefficient of permeability of saturated soil. It decreases during long time of infiltration to reach the value of saturated coefficient of permeability of the soil. The high infiltration rate in early time proves that the coefficient of permeability of the saturated soil underestimates the soil layer infiltration capacity.

When the water content distribution in the upper layer of the sealing layer is examined, the change in water content values appeared 4hours after the rain begins. The average water level value in this time reaches 0.16m. The change is not in the all zones at the same time. The water infiltration is delayed according to the soil permeability in the probe position in the upper layer of the sealing layer. But, considering water content distribution in sub layer, the moisture migration continues in depth before the saturation of the upper layer of the sealing layer. This kind of water migration increases the layer capacity of infiltration.

6 CONCLUSION

The purpose of this study is to identify the surface moisture state of the bottom of a retention basin to predict the movement of water in the soil during the filling. The rain that fell overnight after the surface TDR measurements gave the opportunity to examine the movement of water in the soil once the initial state of the soil moisture compiled. Despite the sod on the retention pond bottom, the distribution of moisture in the surface layer is more varied. This means that the surface layer is formed of different zones of different structures. But the water migration in depth revealed by the TDR probes in the upper layer shows that during the filling of the pond the moisture distribution becomes less variable. It is characterised by three values of water content in the upper layer of the sealing layer.

The TDR measurements also enabled the estimation of values of permeability coefficients of the bottom surface soil layer of the retention basin. It is discovered that the surface layer of the basin has zones of different texture. The estimated average value of saturation permeability coefficient is low compared to the average infiltration rate. Then it can be said that the infiltration capacity of the retention basin is higher than might indicate the value of permeability coefficient.

7 REFERENCES

Alimi-Ichola, I., Bouchemella, S. and Mahler, F.C. (2012) "Use of geophysical techniques for the localisation of the restricting zones of permeability in the bottom of basin: forecast the zones of clogging." Proceeding of ICS'4, Sep. 18-21, 2012, Porto de Galinas, Permambuco, Brazil, vol. 2, 1367-1374.

Dos Santos, P. (1997) "Développement d'une nouvelle méthode de détermination des profils de teneur en eau dans les sols par inversion d'un signal TDR." Thèse de doctorat (Université Joseph Fourier – Grenoble I).

Roades, J.D. and van Schilfgaarde (1976) “An electrical conductivity probe for determining soil salinity.” Soil Sci. Am. J.40:647-651.
Topp G.C., Davis J.L., Annan A.P. (1980) “Electromagnetic determination of soil water content: Measurement in coaxial transmission lines.” Water Resour. Res. 16, 574-582.

Geotechnical and Geophysical Site Characterisation 5 – Lehane, Acosta-Martínez & Kelly (Eds)
© 2016 Australian Geomechanics Society, Sydney, Australia, ISBN 978-0-9946261-2-7

Author index

VOLUME 2

This volume includes papers presented at the **Fifth International Conference on Geotechnical and Geophysical Site Characterisation** (ISC'5) on the following topics:

- Geophysics
- General site characterisation
- Characterisation in rock and residual soil
- Characterisation of non-standard soils
- Design using in-situ tests
- Case histories
- Application of statistical techniques
- Environmental testing

Geotechnical and Geophysical Site Characterisation 5 is particularly aimed at academics and professionals interested in in-situ site characterisation. The conference was organised under the auspices of the Australian Geomechanics Society and the International Society for Soil Mechanics and Geotechnical Engineering (ISSMGE) Technical Committee TC102 (Ground Property Characterization from In-Situ Tests). ISC'5 is the latest in a series which began in Atlanta in 1985 (ISC'1), and was followed by conferences in Porto (ISC'2, 2004), Taipei (ISC'3, 2008) and Porto de Galinhas, Brazil (ISC'4, 2012).

AUSTRALIAN GEOMECHANICS SOCIETY
PO Box 955, St Ives, NSW 2075, Australia
www.australiangeomechanics.org

ISBN 978-0-9946261-2-7

GEOTECHNICAL AND GEOPHYSICAL SITE CHARACTERISATION 5

ISC'5

Lehane
Acosta-Martínez
Kelly
Editors

VOLUME 2